A&A, 705, A204 (2026)
https://doi.org/10.1051/0004-6361/202556637
© The Authors 2026

Astronomy & Astrophysics

The ALMA survey to Resolve exoKuiper belt Substructures (ARKS)

X. Interpreting the peculiar dust rings around HD 131835

M. R. Jankovic[1,⋆], N. Pawellek[2,3], J. Zander[4], T. Löhne[4], A. V. Krivov[4], J. Olofsson[5], A. Brennan[6], J. Milli[7], M. Bonduelle[7], M. C. Wyatt[8], A. A. Sefilian[9], T. D. Pearce[10], S. Mac Manamon[6], Y. Han[11], S. Marino[12], L. Matrà[6], A. Moór[3], M. Booth[13], E. Chiang[14], E. Mansell[15], P. Weber[16,17,18], A. M. Hughes[15], D. J. Wilner[19], P. Luppe[6], B. Zawadzki[15], C. del Burgo[20,21], Á. Kóspál[3,22,23], S. Pérez[16,17,18], J. M. Carpenter[24], and T. Henning[23]

(Affiliations can be found after the references)

Received 28 July 2025 / Accepted 3 September 2025

ABSTRACT

Context. Dusty discs detected around main-sequence stars are thought to be signs of planetesimal belts in which the dust distribution is shaped by collisional and dynamical processes, including interactions with gas if present. The debris disc around the young A-type star HD 131835 is composed of two dust rings at ∼65 au and ∼100 au, a third unconstrained innermost component, and a gaseous component centred at ∼65 au. New ALMA observations show that the inner of the two dust rings is brighter than the outer one, in contrast with previous observations in scattered light.

Aims. We explore two scenarios that could explain these observations: the two dust rings might represent distinct planetesimal belts with different collisional properties, or only the inner ring might contain planetesimals while the outer ring consists entirely of dust that has migrated outwards due to gas drag.

Methods. To explore the first scenario, we employed a state-of-the-art collisional evolution code. To test the second scenario, we used a simple dynamical model of dust grain evolution in an optically thin gaseous disc. In each case we identified the parameters of the planetesimal and the gaseous disc that best reproduce the observational constraints.

Results. Collisional models of two planetesimal belts cannot fully reproduce the observations by only varying their dynamical excitation, and matching the data through a different material strength requires an extreme difference in dust composition. The gas-driven scenario can reproduce the location of the outer ring and the brightness ratio of the two rings from scattered light observations, but the resulting outer ring is too faint overall in both scattered light and sub-millimetre emission.

Conclusions. The dust rings in HD 131835 could be produced from two planetesimal belts, although how these belts would attain the required extremely different properties needs to be explained. The dust–gas interaction is a plausible alternative explanation and deserves further study using a more comprehensive model.

Key words. minor planets, asteroids: general – circumstellar matter – stars: individual: HD 131835

1. Introduction

Main-sequence stars are often surrounded by dusty belts, known as debris discs (e.g. Thureau et al. 2014; Sibthorpe et al. 2018; Lestrade et al. 2025). This dust is believed to be continually destroyed in mutual collisions (with the smallest dust grains also blown out by radiation pressure), and thus must be continually produced in collisions of kilometre-sized or larger bodies (planetesimals). The observed dusty belts are thus commonly interpreted as signposts of planetesimal belts, analogous to the asteroid and Kuiper belts in the solar system (Wyatt 2008; Krivov 2010; Matthews et al. 2014; Hughes et al. 2018; Wyatt 2020; Marino 2022; Pearce 2024).

Unlike in the solar system, some of these belts also have a gaseous component. There is a growing number of debris discs in which cold gaseous CO and neutral carbon have been observed (e.g. Kóspál et al. 2013; Dent et al. 2014; Lieman-Sifry et al. 2016; Moór et al. 2017; Higuchi et al. 2017; Cataldi et al. 2018; Kral et al. 2020). The origin of this gas is uncertain; it could be a secondary product of collisions (Zuckerman & Song 2012; Dent et al. 2014) or of planetesimal thermophysical evolution (Bonsor et al. 2023), or it could be tracing larger amounts of molecular hydrogen left over from the star and planet formation process (Kóspál et al. 2013; Moór et al. 2017). Protoplanetary molecular hydrogen can persist around A-type stars for up to ∼100 Myr (i.e. up to the age of most of the gaseous debris discs), but this requires the small micron-sized dust grains to be depleted so that photo-evaporation of the gas disc is slowed down (Nakatani et al. 2021; Ooyama et al. 2025). The secondary scenario can readily explain discs with low CO mass but the CO-rich systems need to be shielded from photo-dissociation for the CO to persist long term. This requires either self-shielding or shielding by neutral carbon (a product resulting from photo-dissociation; Kral et al. 2016, 2019; Marino et al. 2020), and this in turn requires weak vertical mixing of the gas species (Cataldi et al. 2020; Marino et al. 2022). The strength of vertical mixing is currently unconstrained but observed low CI/CO ratios indicate

⋆ Corresponding author: marija.jankovic@ipb.ac.rs

Open Access article, published by EDP Sciences, under the terms of the Creative Commons Attribution License (https://creativecommons.org/licenses/by/4.0), which permits unrestricted use, distribution, and reproduction in any medium, provided the original work is properly cited.
This article is published in open access under the Subscribe to Open model. Subscribe to A&A to support open access publication.

that carbon shielding is unlikely to be efficient enough to explain the amount of CO observed in some discs (Cataldi et al. 2023; Brennan et al. 2024).

Meanwhile, the unknown origin of the gas presents a challenge to our interpretation of observed dust structures because gas can change the orbits of dust grains relative to orbits of unseen planetesimals. Gas drag damps particle orbital eccentricities and inclinations, and the combination of gas drag and radiation pressure in an optically thin dust disc pushes small dust grains outwards from their nascent planetesimal belt (Takeuchi & Artymowicz 2001). These effects could change the morphology of debris disc haloes observed in scattered light (Thébault & Augereau 2005; Krivov et al. 2009), as well as the vertical structure of debris discs (Olofsson et al. 2022). The outward migration of the small dust can even result in the formation of an additional, separate dust belt (Takeuchi & Artymowicz 2001). These effects of the gas on the dust depend on the gas mass and composition, which are very different in the two gas origin scenarios.

One of the gas-rich debris discs is that surrounding HD 131835 (HIP 73145), an A-type star located at a distance of 130 pc (Gaia Collaboration 2023) in the 15–16-Myr-old (Mamajek et al. 2002; Pecaut et al. 2012) Upper Centaurus Lupus moving group (de Zeeuw et al. 1999). The dusty disc is very bright, with a fractional luminosity of 3×10^{-3} dominated by its cold component (Moór et al. 2015), and it has been extensively observed through thermal emission at multiple wavelengths (Hung et al. 2015b; Moór et al. 2015; Lieman-Sifry et al. 2016; Moór et al. 2017; Kral et al. 2019) and in scattered light (Hung et al. 2015a; Feldt et al. 2017; Milli et al. 2026). A gaseous disc of CO and neutral carbon has been detected and coincides spatially with the dusty disc (Moór et al. 2015; Lieman-Sifry et al. 2016; Kral et al. 2019; Hales et al. 2019; Mac Manamon et al. 2026). The most detailed imaging of the disc was achieved using the SPHERE instrument (Spectro-Polarimetric High-contrast Exoplanet REsearch; Beuzit et al. 2019) in scattered light, at 1.6 μm, which revealed that the disc contains at least two dusty rings (at ∼65 au and ∼100 au, with the outer ring being much brighter than the inner ring, and a third less definite structure closer to the star; Feldt et al. 2017). The morphology of the disc led researchers to propose that dust-gas interactions may play a critical role in shaping its two rings (Feldt et al. 2017; Kral et al. 2019). However, the disc had not yet been resolved adequately at longer wavelengths to allow a detailed comparison between theoretical models and observational data.

The debris disc around HD 131835 was one of the targets in the Atacama Large Millimeter/submillimeter Array (ALMA) survey to Resolve exoKuiper belt Substructures (ARKS; Marino et al. 2026a). ARKS is an ALMA large program designed to resolve the radial and vertical structure of 24 debris discs at millimetre wavelengths, and to investigate the gas distribution and kinematics in the gas-bearing subset of the sample. One of the key findings from the ARKS program is that a number of discs show an unexpected radial offset between the peak of their thermal emission at millimetre wavelengths and the peak of their scattered light brightness profile, with the scattered light peaking further away from the star than the millimetre thermal emission (Milli et al. 2026). In the disc around HD 131835, this offset between brightness maxima is extreme. The new ARKS observations show that thermal emission peaks in the inner dust ring at millimetre wavelengths, and the outer ring is much less bright, contrary to what is seen in scattered light observations (Feldt et al. 2017).

The dust surface densities inferred from the two observations (Milli et al. 2026) suggest that the size distribution of dust in the two rings is very different, such that the ratio of the micron-sized dust grains (traced by the scattered light observations) to the number of mm-sized dust grains (traced by ALMA) is larger in the outer ring. There are two likely explanations for this. First, two planetesimal belts can produce different ratios of small and large dust if, for example, their dynamical excitation is sufficiently different (Thébault & Wu 2008). Second, the gas present in the system could induce migration of the small dust to the outer gas disc edge, producing a secondary dust belt (without a second planetesimal belt; Takeuchi & Artymowicz 2001).

In this paper, we use numerical models of collisional evolution and dynamical models of dust-gas interaction to explore the two explanations for the peculiar dust rings in HD 131835. In Section 2, we discuss the observations that motivate this study. In Section 3, we first show that explaining these observations requires the inner ring of HD 131835 to be under-abundant in small, micron-sized dust, and the outer ring to be over-abundant in it, compared to the standard model of a collisional cascade at steady-state. We then explore a scenario in which the different dust size distributions in the two rings can be explained by the disc containing two planetesimal belts with different properties. In Section 4, we consider a scenario in which only the first ring has a belt and the outer ring is made up purely of small dust that migrated there due to gas drag. In Section 5, we discuss which of the two scenarios is more likely to be at play in HD 131835, and in Section 6, we summarize our conclusions.

2. Observations

Our theoretical work is motivated by two high-resolution observations: the disc image in total-intensity scattered light from SPHERE (Feldt et al. 2017) and the recent ARKS image in thermal emission from ALMA (Marino et al. 2026a). In this section we discuss these observations.

2.1. SPHERE

HD 131835 has been previously observed in the near-infrared (at ∼1.6 μm), in total-intensity scattered light, with SPHERE (Feldt et al. 2017). Using angular differential imaging (ADI), Feldt et al. (2017) constructed a high-resolution image of the disc, which we show in Fig. 1. We also re-derive the surface brightness radial profile based on their data with a similar procedure, by de-projecting the image and azimuthally averaging the flux, and we show it in Fig. 2 in blue.

Three features can be identified from the image and from the radial profile: a bright ring located at the radial distance of ∼100 au (ring 'B1' in Feldt et al. 2017), a less bright ring at ∼65 au (their ring 'B2') and a further, unresolved feature at <50 au. The morphology and the brightness of the innermost feature are highly uncertain. Observations at radial distances smaller than ∼0.2" (∼ 26 au at the distance of HD 131835; d = 130 pc, Gaia Collaboration 2023) are affected by the presence of the coronagraph (the grey region in Fig. 2). Additionally, the negative flux around 50 au, caused by self-subtraction induced by the observing strategy (ADI; Milli et al. 2012), indicates that systematic effects are strong up to at least this radius. For these reasons, in this work we only focus on the two rings at 65 and 100 au. We denote these as the inner and the outer ring, and we consider these two rings as collisionally and dynamically independent from the innermost asymmetric component.

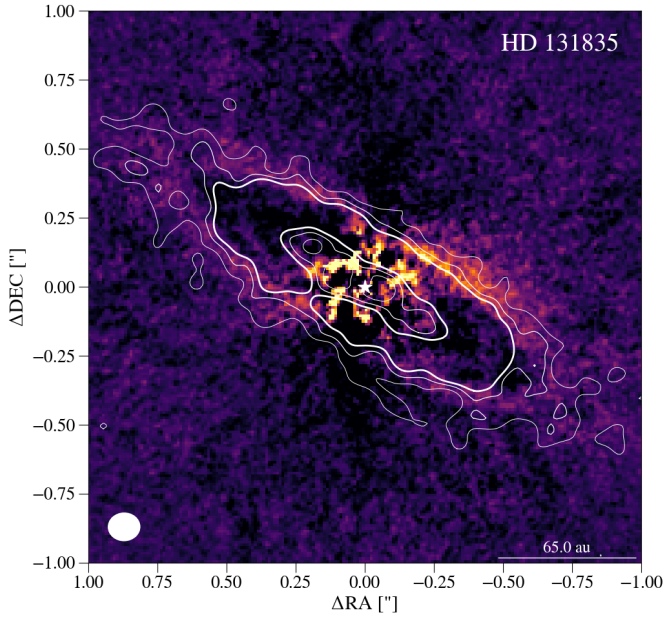

Fig. 1. HD 131835 observed in scattered light, using the VLT/SPHERE instrument. The white star at the centre denotes the position of the star. The white bar at the bottom right corner represents a distance of 0.5", with the corresponding value in au. In addition to the scattered light image, the contours of the corresponding ALMA dust continuum observations (thermal emission of bigger dust grains) are plotted. There are three contour levels, corresponding to [3, 5, 7] sigma. The white ellipse at the bottom left represents the beam size for the ALMA observation, using a robust value of 0.3. North is up and east is left.

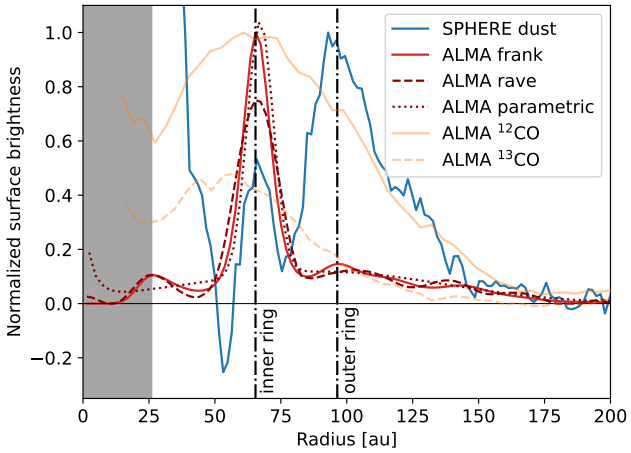

Fig. 2. Normalized surface brightness of thermal emission from HD 131835 inferred from ALMA continuum (solid, dashed, and dotted red lines for the best-fit `frank`, `rave`, and parametric radial profiles, respectively) and of scattered light from VLT/SPHERE (blue line), and radial profile of intensity of molecular line emission of ^{12}CO and ^{13}CO observed with ALMA (solid and dashed orange lines; ^{13}CO intensity is normalized in such a way that the ^{13}CO/^{12}CO intensity ratio is preserved). The vertical dash-dot lines indicate the locations of the inner and the outer ring based on local maxima at 65.4 au and 96.5 au in the `frank` radial profile. The third, innermost component is partially within a region of high uncertainty for the scattered light observation (grey region) and appears to be asymmetric, and we do not include it in our theoretical models. For further details, see Section 2.

Due to artefacts of ADI, the relative brightness of the two rings extracted from the image is unreliable. Forward modelling can account for the self-subtraction that may be affecting the inner ring brightness, yet the inner ring is too faint in the image for its full morphology to be meaningfully constrained. Milli et al. (2026) only include the outer ring in their model and find a good overall fit to the data. This model has a peak surface brightness of 0.679 ± 0.041 mJy/arcsec^2 at around 100 au, measured along the disc semi-major axis. Overall, the model shows an extended halo of small particles with an outer slope consistent with the slope previously constrained by Feldt et al. (2017), and also consistent with a 'classical' halo of small particles under effect of radiation pressure in a collisional cascade (Thebault et al. 2023).

To put some constraints on the inner ring, Milli et al. (2026) further add a narrow inner ring of fixed morphology into their model and only vary a subset of the usual parameters. Based on visual inspection of the residuals, they derive an upper limit on the brightness ratio between the inner and the outer ring of ~ 1, also measured along the major axis of the disc in the non-deprojected image. In other words, at the wavelength of 1.6 µm, at the scattering angle of 90 degrees, the inner ring is less bright than the outer ring. Taking into account that the scattered light brightness falls off with distance to the star at fixed dust density, this result shows that the outer ring is overabundant in µm-sized dust grains relative to the inner ring. This is in contrast to the ALMA results at 890 µm, which we discuss next.

2.2. ALMA

The debris disc around HD 131835 has been recently observed at millimetre wavelengths as part of the ALMA large program ARKS (2022.1.00338.L, PI: S. Marino). The disc was observed in band 7, centred at the wavelength of 0.89 mm, with a resolution (beam size) of 17 au (0.13"). All details of the observations, data reduction and imaging are presented in Marino et al. (2026a).

The resulting image of the dust continuum emission is shown as white contours in Fig. 1, which shows clearly a large difference in the spatial distribution of the ALMA dust emission and the scattered light observed with SPHERE. The ALMA dust emission peaks at around 65 au from the star, and becomes much fainter at 100 au, where the scattered light is brightest.

Han et al. (2026b) fitted models of the de-projected radial brightness profiles to all of the ARKS targets. They used three approaches: a non-parametric model fit to the raw interferometric data (`frank`; Jennings et al. 2020; Terrill et al. 2023), a non-parametric model fit to the image (`rave`; Han et al. 2022, 2025), and a parametric radial profile model. All three of the ALMA radial profiles show a clear maximum in surface brightness at around 65 au from the star, corresponding to the bright dusty ring evident in the disc image (see Fig. 2). All three profiles also show that there is extended dust continuum emission both inside and outside of this ring. However, the three profiles disagree in terms of the structure of the extended emission. The `frank` profile (solid red line) features at least two local maxima in addition to the main ring, at 25 au and at 100 au, and also a 'shoulder' at around 150 au. The `rave` profile (red dashed line) features two local maxima in the outer disc, but at different radii to the `frank` profile. Finally, the best-fit parametric profile (red dotted line), a sum of two Gaussians, shows instead only the main ring and an extended halo-like emission, with no distinct ring in the outer disc.

Since the three approaches have these disagreements and since all three come with their own caveats (see Han et al. 2026b, for details), it remains uncertain how many dusty rings

there are in the ALMA continuum emission. In the outer region, on which we focus in this work, the `frank` profile shows a faint ring at ∼ 100 au, coinciding with the outer ring previously seen with SPHERE. Therefore, for the purpose of comparing the outer ring properties from the two observations, we use the `frank` profile throughout this paper, and its two local maxima in the surface brightness of 8.9 ± 0.6 mJy/arcsec^2 at 65.4 au, and 1.3 ± 0.2 mJy/arcsec^2 at 96.5 au. However, the possibility remains that the outer disc is merely a gradual extension of the inner (main) ring at 65 au, and not a separate component.

In any case, the outer region being much fainter relative to the main ring at 65 au is in contrast to the scattered light observations, where the ring at ∼ 100 au is at least as bright as the ring at 65 au. Further taking into account that at fixed dust density the scattered light brightness falls off faster with radius than thermal emission, it can be inferred that the density of small/large grains is greater in the outer/inner belt (Milli et al. 2026). This suggests a very different local dust size distribution at the two radii.

The ARKS observation of HD 131835 also covered ^{12}CO and ^{13}CO J = 3–2 emission lines. From the spatially resolved images of the molecular emission, azimuthally averaged, spectrally integrated intensity radial profiles have been extracted (Mac Manamon et al. 2026). The radial profiles show a broad distribution peaking slightly interior to the inner dust ring at ∼65 au (see the orange lines in Fig. 2). The gas emission is likely optically thick as demonstrated for HD 121617 (Brennan et al. 2026), which in addition to the gas radial profiles not being deconvolved, means that the shown radial profiles are potentially much broader than the true profile of the gas distribution.

3. Two planetesimal belts

In this section we test if the ALMA and the SPHERE observations can be explained by the dust in the system being produced in two distinct planetesimal belts with different properties. We first use an empirical model to illustrate that a 'standard' collisional model is completely inconsistent with the observed data. Then, we use a detailed numerical approach to produce a suite of model planetesimal belts. Within that suite of models we identify pairs of model belts whose colours match the colours of the rings in HD 131835.

3.1. First modelling attempt and the challenge

3.1.1. Approach

To demonstrate why explaining the ALMA and SPHERE observations simultaneously is challenging, we started with a simple, intuitive model. Following Pawellek et al. (2024), we assumed that the surface brightness profile inferred from the ALMA data reflects the spatial distribution of dust-producing planetesimals in the system. This is expected because the ALMA continuum emission is dominated by mm-sized dust grains, which are unaffected by radiation pressure, and therefore simply inherit orbits of their parent bodies (Krivov 2010). We calculated a normalized surface density radial profile of planetesimals from the `frank` surface brightness radial profile assuming a black-body temperature profile, and we assumed that the planetesimals are on circular orbits. We then assumed that a simplified collisional cascade (Dohnanyi 1969) operates in the system, grinding the planetesimals to dust. We did not model the collisional evolution in this simple model, and instead assumed that at each radius planetesimals produce dust with a fixed size distribution as in Pawellek et al. (2024). The basis of this size distribution is a power law,

$$n(s)\,\mathrm{d}s \propto s^{-q}\,\mathrm{d}s, \tag{1}$$

where n is the number density, s the grain radius, and q = 3.5 the size distribution index. We further included radiation pressure from stellar light (Burns et al. 1979) by putting dust grains on eccentric orbits determined by their size and optical properties (e.g. Strubbe & Chiang 2006; Krivov et al. 2006, see also Eq. (9)). The smallest dust grains are unbound due to the radiation pressure, which we accounted for by putting them on hyperbolic orbits and by reducing their number density according to their escape velocity.

Finally, having generated the dust distribution, we computed the dust temperature assuming thermal equilibrium, simulated thermal emission (890 µm) and scattered light (1.6 µm) images and calculated the radial surface brightness profiles. Here and throughout this paper we assume dust grains are perfect spheres with a simple astrosilicate composition (Draine 2003) and we calculate the optical properties of the dust using Mie theory. For the scattered light we fix the scattering angle to 90 degrees, corresponding to the ansae of a well resolved thin inclined disc, so that our model scattered light radial profile is directly comparable to the surface brightness constraint discussed in Section 2.1. We adopt a stellar mass of $M_* = 1.7\,M_\odot$ and a stellar luminosity of $L_* = 9\,L_\odot$ (Marino et al. 2026a).

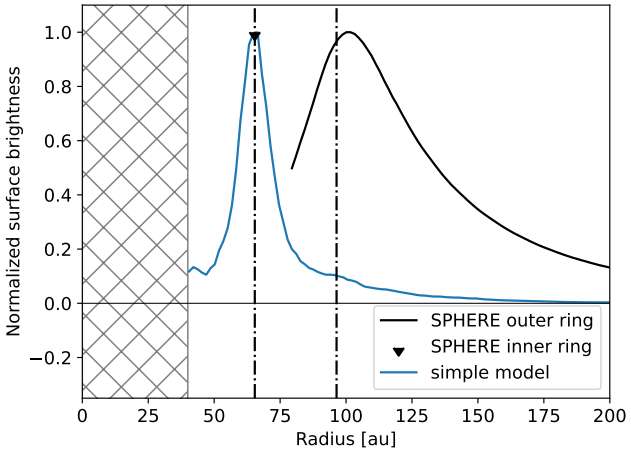

Fig. 3. Surface brightness profile of scattered light from the first modelling attempt (blue line). This is based on an assumption that the thermal emission observed with ALMA indicates the spatial distribution of planetesimals feeding an ideal collisional cascade, and the constraints on the SPHERE radial profile based on forward modelling (black line for the outer ring and upper limit for the inner ring). Vertical dash-dot lines indicate the locations of the inner and the outer ring based on local maxima at 65.4 au and 96.5 au in the `frank` radial profile. The inner 40 au are not included in the model as we focus on the outer regions. See Section 3.1 for details.

3.1.2. Results

The obtained surface brightness profile for scattered light is shown in Fig. 3. It fails to reproduce the one inferred from SPHERE observations completely. Although the scattered-light profile is radially extended, there are no signs of the pronounced outer ring at ∼100 au seen with SPHERE. This result shows that the first-guess model, which only includes a simplified collisional cascade combined with radiation pressure, falls short of describing the system.

The weakest point of this simple approach is the assumption of an ideal collisional cascade in which the size distribution index q is fixed in the entire disc, that is, where the only radial variations in the size distribution are due to small dust being more spread out by the radiation pressure. It is unlikely that changing our other assumptions (e.g. assumed dust optical properties) could change the shape of the radial profile to account for such a large difference between our result and the SPHERE observation. Therefore, in order to explain the observations, the outer ring of HD 131835 must be rich in micron-sized dust relative to millimetre-sized dust and/or the inner ring must be poor in small dust. In the following sections we investigate possible scenarios explaining the different size distributions in the two rings.

3.2. Numerical models of collisional evolution

3.2.1. Approach

We used the state-of-the art numerical code ACE (Analysis of Collisional Evolution; Krivov et al. 2005, 2006; Löhne et al. 2008; Löhne et al. 2017) to find combinations of two planetesimal belts, collisionally evolved independently, that could explain both the SPHERE and ALMA datasets. ACE models a disc as a distribution of objects over a phase space, discretized into bins. Three dimensions are treated explicitly: object mass (or size), orbital pericentre distance (or semi-major axis) and eccentricity. The code evolves numbers of objects in bins defined by different combinations of these three parameters. Other orbital parameters such as inclinations and apsidal angles are averaged over (e.g. when calculating collision rates). The kinetic Boltzmann–Smoluchowski equation that is solved considers catastrophically disruptive, cratering, and bouncing collisions, all treated as fully inelastic. Orbits of collision fragments are computed from momentum conservation and size-dependent stellar radiation pressure efficiency (see Krivov et al. 2005, 2006; Löhne et al. 2012, 2017).

For comparison with the observations we used the ratios of surface brightnesses at ALMA and SPHERE wavelengths, that is, colours. Since our belts are assumed to be mutually independent, and their individual radial profiles can be scaled with the free parameters of total belt masses, our model belts are best characterized by colours calculated from the maxima of surface brightnesses at each wavelength. To compare our models against the observations, we calculated the colours of the two rings of HD 131835 using the peak surface brightnesses from the `frank` profile, and using the constraints on the scattered light profile discussed in Section 2.1. For the inner ring only a lower limit on the colour is available. In Figs. 4 and 6, these are shown with grey symbols. To calculate thermal emission and the scattered light model observations, we assumed the same dust optical properties, disc orientation and stellar properties as in Section 3.1.

3.2.2. Results

The first possibility we explored is that different size distributions could arise from different levels of excitation in the two belts. Results of ACE simulations for this scenario are shown in Fig. 4. The eccentricities are initially uniformly distributed between zero and $e_{\max}$. Each symbol represents a single belt with a relative width of 10% in semi-major axis space at either 65 or 100 au, and with the same properties except for the maximum initial (free) eccentricity $e_{\max}$. The radii in the figure correspond to peaks of thermal emission, which vary slightly with the belt excitation and with collisional evolution. The semi-opening angle of the disc (ϵ, corresponding to the maximum orbital inclination) is set to $\sin(\epsilon) = e_{\max}/2$.

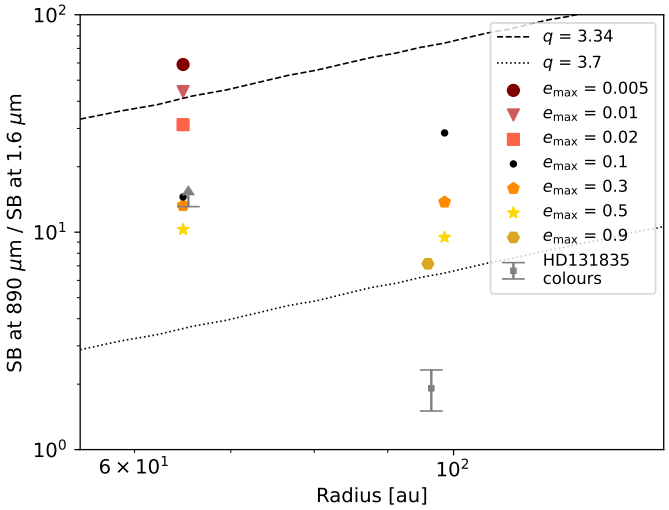

Fig. 4. Ratios of peak surface brightnesses at 890 μm and 1.6 μm (colours) shown as function of radii of peak thermal emission, for belt models with various initial excitations. Black dots represent reference cases with a maximum eccentricity $e_{\max} = 0.1$, other symbols are as in the plot legend, with different sets of values explored in the two rings. The grey error bars show HD 131835 colours based on the ALMA and the SPHERE observations. Dashed and dotted lines give the expected surface brightness ratios for fiducial, unevolved discs with a fixed power-law size distribution and a minimum grain size of 1 μm. For details, see Section 3.2.

In general, it can be seen that low eccentricities in the inner belt and high eccentricities in the outer belt provide the closest match to the observed colours of the two belts. As shown by Thébault & Wu (2008), a low excitation of the parent belt reduces the relative abundance of small grains. This is because the production rate of small grains from fragmentation of larger grains is reduced at lower excitation, while their destruction rate remains high due to their high eccentricities set primarily by radiation pressure. Both the production and the destruction of the large grains are affected similarly by the excitation, so that their steady-state density changes very little. The lower the excitation, the larger the dominant grain size and the less scattered light is expected relative to thermal emission at longer wavelengths.

To further illustrate the need for a difference in size distribution between the two belts, in Fig. 4 we show colours of unevolved belts with fixed power-law size distributions, placed at different radii. The dashed and the dotted line correspond to size distributions poorer and richer in small grains, respectively. Note, however, that the size distribution in our collisionally evolved belts is not a simple power law.

We find that our inner belt models with maximum eccentricity of $e_{\max} \lesssim 0.3$ are within the lower limit on the colour of the inner ring in HD 131835. The colour of the outer ring cannot be matched by varying $e_{\max}$ only. Even for our model with $e_{\max} = 0.9$, the ratio of the surface brightnesses at 890 μm and at 1.6 μm is about 3.5 times higher than that measured for the outer ring in HD 131835. In principle, a different assumption about grain composition and optical properties could change the colours of our model belts, to bring them closer to agreement with the observations.

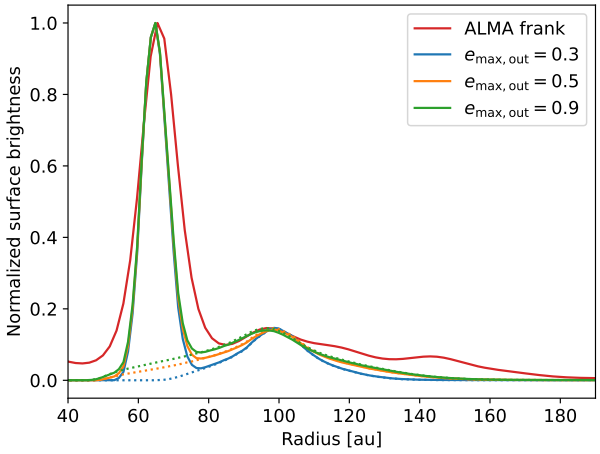

Fig. 5. Sum of surface brightness profiles for some combinations of our inner and outer belt models, at 890 µm (solid lines). In each combination the inner belt is the same (e_{max} = 0.1) and the outer belt has a different maximum eccentricity, as shown in the plot legend. Dotted lines only show the surface brightness of the outer belt models. The belts are modelled independently, and their peak surface brightness values are re-scaled to ring peak values from `frank`. The `frank` profile of HD 131835 is shown in red. For details, see Section 3.2.

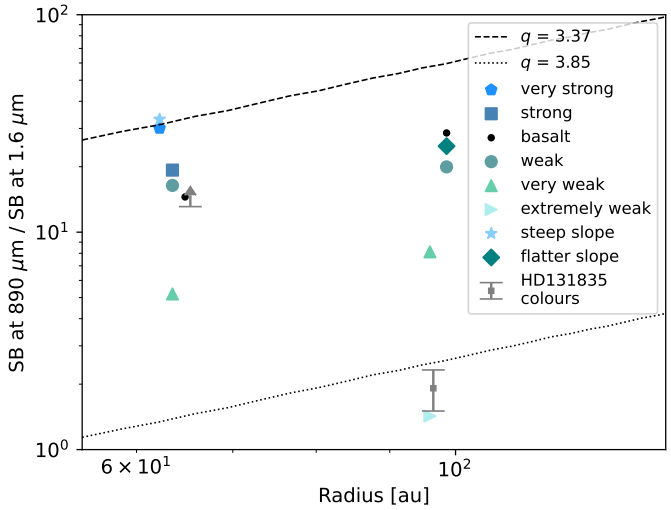

Fig. 6. Same as Fig. 4 for belt models with various disruption energy (Q^*_D) prescriptions (see plot legend and Table 1). Here, all models have a maximum eccentricity e_{max} = 0.1. Dashed and dotted lines are as in Fig. 4, only for slightly different power laws. For details, see Section 3.2.

Table 1. Different $Q^*_{D,s}$ and b_s values for the modelled belts.

Identifier	$Q^*_{D,s}$ [erg/g]	b_s
Basalt	$5 \cdot 10^6$	–0.37
Very strong	$5 \cdot 10^8$	–0.37
Strong	$5 \cdot 10^7$	–0.37
Weak	$5 \cdot 10^5$	–0.37
Very weak	$5 \cdot 10^4$	–0.37
Extremely weak	$5 \cdot 10^3$	–0.37
Steep slope	$5 \cdot 10^6$	–1
Flatter slope	$5 \cdot 10^6$	–0.05

The very strong excitation of the model outer belt is compatible with the observed radial profile in the sub-millimetre. While the wide range of orbital eccentricities could lead to a belt that is too broad to show up as a discrete ring, Fig. 5 shows that this is not the case because the excited belts have cores of sufficiently low excitation. The resulting (outer) edges are actually more pronounced than in the observed profile, which Han et al. (2026b) find well-fitted by a broad halo-like distribution. A caveat of our current model is that any interaction between the two belts is ignored.

In a second scenario, the rings could develop different size distributions through different material strengths. Collisional outcomes in ACE are determined by the specific energy for disruption, parametrized as a double power law in object radius s:

$$Q^*_{\rm D}(s) = \left[Q^*_{\rm D,s} \left(\frac{s}{1\,{\rm m}} \right)^{b_{\rm s}} + Q^*_{\rm D,g} \left(\frac{s}{1\,{\rm km}} \right)^{b_{\rm g}} \right] \left(\frac{v_{\rm imp}}{3\,{\rm km/s}} \right)^{0.5}, \quad (2)$$

where $v_{\rm imp}$ is the impact velocity for any given collision, $Q^*_{\rm D,s}$ and $b_{\rm s}$ are the critical specific energy at a reference size and the size-dependence slope, respectively, in the strength regime (at small object sizes), and analogously $Q^*_{\rm D,g}$ and $b_{\rm g}$ describe the critical specific energy in the gravity regime. Fig. 6 shows the results of ACE simulations where we keep eccentricities the same in both belts (e_{max} = 0.1), but the belts have different specific energies for disruption in the strength regime. Values for the coefficients in Eq. (2) are listed in Table 1. The reference case (black dots) is based on standard basalt from Leinhardt & Stewart (2012). For the gravity regime all models assume $Q^*_{\rm D,g} = 5 \cdot 10^6$ erg/g and $b_{\rm g}$ = 1.38 (cf. Benz & Asphaug 1999).

Again, a general trend is apparent that goes in the direction of explaining the observations where the colour of the inner belt can be explained by dust having the standard basalt material strength or by particles being slightly weaker, strong or very strong, while the outer belt needs to have extremely weak particles. Weaker material is more easily destroyed in collisions causing a large overabundance of small grains just above the blowout limit at around 2 µm. This means a higher surface brightness in scattered light and thus a smaller surface brightness ratio, similar to higher eccentricity values. If the material has such extreme values as explored here, in the strong case grains below a certain size cannot be destroyed anymore. This results in an overabundance of ~50 µm-sized grains. The collisional production of even smaller particles is reduced, leading to a low surface brightness in scattered light and a higher surface brightness ratio. However, only an extreme pair of belts could explain the observed colour ratio with the inner ring producing dust made of standard basalt-like or weak material and the outer ring of extremely weak material. The total difference between the materials would need to amount to about two to three orders of magnitude in $Q^*_{\rm D}$ at a given dust size. For comparison, even if the belts harboured completely different material, such as basalt in the inner one and water ice in the outer one, the difference in material strengths should not exceed one or two orders of magnitude (e.g. Benz & Asphaug 1999).

4. Single planetesimal belt and dust-gas interaction

We now consider a different scenario that might explain the peculiar dust rings around HD 131835, one that relies on dust–gas interactions. Gas in the system exerts a drag force on the dust grains (Takeuchi & Artymowicz 2001). The drag force makes

large grains drift radially in the direction of the gas pressure gradient (towards a pressure maximum), while small grains that are strongly affected by radiation pressure move radially outwards (towards the outer edge of the gas disc). In this section, we explore the possibility that the small (micron-sized) grains released in the main ALMA ring at 65 au might be brought outward by gas, to ∼100 au, making this region bright in scattered light.

First, we present our model of the gas disc (Section 4.1) and the dust grain dynamics (Section 4.2) and we discuss conditions under which gas can lead to the formation of the outer ring (Section 4.3). Then, we produce a grid of dynamical models, varying key gas and dust parameters, to identify parameters for which the two model rings resemble the morphology of HD 131835 (Section 4.4). Lastly, we consider if such rings can still form when we account for destructive collisions (Section 4.5).

4.1. Model of gas disc

We assume that the gas surface density in the disc follows a Gaussian profile,

$$\Sigma_{\rm g}(r) = \Sigma_{\rm g,0} \exp\left(-\frac{(r-r_{\rm g})^2}{2\sigma_{\rm g}^2}\right), \tag{3}$$

where $\Sigma_{\rm g,0}$ is the surface density at the reference radius $r_{\rm g}$, and $\sigma_{\rm g}$ is the width of the radial profile. This choice is motivated by the new ARKS observations of CO molecular emission in HD 131835 (Mac Manamon et al. 2026). The deprojected radial emission profile of CO is similar to a Gaussian (see Fig. 2). The true CO density profile is likely to deviate from the emission profile due to radial variations in gas temperature, excitation levels and optical depth. Nevertheless, our assumed density profile captures the features that are certain: the gas surface density peaks at some radius and decreases smoothly, but rapidly, both inwards and outwards.

The assumed profile is also loosely consistent with theoretical expectations if the gas is secondary. Secondary CO gas, continually produced in planetesimal collisions, viscously spreads from its point of release, while also being subject to photo-dissociation (Kral et al. 2016, 2017; Hales et al. 2019; Marino et al. 2020). At early times following the onset of collisional cascade these processes need not be in equilibrium, and the CO radial profile resembles a Gaussian (Marino et al. 2020). In a similar scenario in which the entire gas mass was released at once at radius $r_{\rm g}$ and viscously spread to its present structure, assuming radially constant viscosity, there exists a well-known analytic solution to the disc evolution equation for the gas radial profile (Lynden-Bell & Pringle 1974). Early on in the evolution of such a disc, this analytic solution agrees very well with a Gaussian profile, especially outwards from the release radius.

In the secondary gas scenario, the system should also contain carbon and oxygen, products of CO photo-dissociation. These species are expected to have different, more radially extended profiles. Carbon has been detected in HD 131835; however, its mass appears to be lower than that of CO (possibly an order of magnitude) and its radial profile is not as well-constrained (Kral et al. 2019). Therefore, we neglect the contribution from these species and for the secondary scenario we assume a mean molecular weight of $\mu = 28$ (in units of hydrogen atom mass $m_{\rm H}$).

In addition to the secondary gas scenario, we also consider the primordial scenario, in which the observed CO is merely a tracer species of much more abundant molecular hydrogen. In this scenario, we also assume a Gaussian radial profile, but with a different mean molecular weight ($\mu = 2.3$).

For all models we assume the gas to have a black-body temperature profile,

$$T_{\rm g}(r) = 278\ {\rm K}\left(\frac{L_*}{L_\odot}\right)^{1/4}\left(\frac{r}{\rm au}\right)^{-1/2}, \tag{4}$$

with temperature vertically constant at any given radius, and we assume that the gas is in vertical hydrostatic equilibrium. The midplane gas density is then given by

$$\begin{aligned}\rho_{\rm g}(r) &= \rho_{\rm g,0}\frac{H_{\rm g}(r_{\rm g})}{H_{\rm g}(r)}\exp\left(-\frac{(r-r_{\rm g})^2}{2\sigma_{\rm g}^2}\right)\\ &= \rho_{\rm g,0}\left(\frac{r}{r_{\rm g}}\right)^{-5/4}\exp\left(-\frac{(r-r_{\rm g})^2}{2\sigma_{\rm g}^2}\right),\end{aligned} \tag{5}$$

where $H_{\rm g} = c_{\rm s}/\Omega_{\rm K}$ is the gas vertical scale height, $c_{\rm s}(r) = \sqrt{k_{\rm B}T(r)/(\mu m_{\rm H})}$ is the isothermal sound speed, and $\rho_{\rm g,0} = \Sigma_{\rm g,0}/(\sqrt{2\pi}H_{\rm g}(r_{\rm g}))$. Due to thermal pressure, the gas azimuthal velocity deviates from a Keplerian velocity (e.g. Takeuchi & Artymowicz 2001),

$$v_{\rm g} = v_{\rm K}\sqrt{1-\eta}, \tag{6}$$

where $v_{\rm K}$ is the Keplerian velocity at a given radius, and η is the ratio between the pressure gradient force and the stellar gravitational force acting on the gas (Takeuchi & Artymowicz 2001),

$$\eta(r) = -\frac{r^2}{GM_*\rho_{\rm g}(r)}\frac{\rm d}{{\rm d}r}\left(\rho_{\rm g}(r)c_{\rm s}^2(r)\right). \tag{7}$$

For our assumed gas structure, the parameter η is given by

$$\eta(r) = \frac{c_{\rm s}^2(r)r}{GM_*}\left(\frac{7}{4} + \frac{r^2 - rr_{\rm g}}{\sigma_{\rm g}^2}\right). \tag{8}$$

At large radii, η can become non-physically high in this model[1]. However, this only occurs at such large radii where the gas density is so small that the dust is completely unaffected by the gas, and this is always at distances larger than the radius of the outer dusty ring. For numerical reasons, we limit η to 1 if Eq. (8) evaluates to a higher value[2].

We assume that the gas surface density peaks at the location of the inner belt, at $r_{\rm g} = 65$ au[3]. The gas midplane density at radius $r_{\rm g}$, $\rho_{\rm g,0}$ (this is not the same as the maximum midplane density), the Gaussian width $\sigma_{\rm g}$ and the mean molecular weight μ are considered as free parameters in our model. While there are some constraints on these parameters from gas observations, we first explore which values of these parameters result in rings resembling those in HD 131835, and then in Section 5 we discuss how these values compare to those from gas observations.

[1] This is because a strictly Gaussian radial profile for the surface density is not entirely physical. While a Gaussian shape can be justified as an approximation for some physical scenarios, as discussed above, such an approximation evidently fails at large radii. In reality the gas radial profile deviates from a Gaussian tail at large radii.

[2] We verified that this is unimportant by re-running one of our simulations, setting $\rho_{\rm g} = 0$ in the region where we set $\eta = 1$. We obtained the exact same results as in the original run.

[3] The observed CO emission profile peaks at a slightly smaller radius (Fig. 2). Given the uncertain relationship between the emission profile and the gas surface density, we pick this value of $r_{\rm g}$ for simplicity.

4.2. Model of dust grain dynamics

To produce a model of the dust in this gaseous disc, we followeded the approach of Krivov et al. (2009). We assumed that dust particles are produced at the location of the inner belt from parent bodies with semi-major axes distributed uniformly in the range of 60–70 au and eccentricities in the range of 0–0.1. Small dust grains affected by radiation pressure instantly end up on more eccentric orbits, according to their β parameter (ratio between the radiation pressure force and the stellar gravity force acting on the particle). The particle β parameter is given by

$$\beta = \frac{3L_* Q_{\rm pr}}{16\pi G M_* c s \rho_s}, \tag{9}$$

where $Q_{\rm pr}$ is the radiation pressure efficiency coefficient of particles of size s, ρ_s is the particle material density, G is the gravitational constant, and c is the speed of light.

We integrated equations of motion of individual dust grains of various sizes (500 particles log-spaced from 2 µm to 1 cm, corresponding to a range of $\beta = 0.5$ to $\beta = 0.0001$), following particle motion in the disc midplane due to gas drag and radiative forces for 10 Myr. This is shorter than the estimated system age of 16 Myr, but in all relevant cases small particles reach their equilibrium orbits within 10 Myr. We assumed grain material density of $\rho_s = 3.3\,{\rm g\,cm^{-3}}$ and we calculated particle β parameters assuming $Q_{\rm pr} = 1$. Note that the assumed grain density corresponds to astrosilicate composition, for which we check that indeed $Q_{\rm pr} \approx 1$ for $\beta < 0.5$.

From the resulting trajectories, we took particle locations at points equidistant in time. This set of particle locations is taken to represent a sample of individual model particles. We binned these model particles according to their stellocentric radii r, obtaining the vertically integrated number of particles in every given size and radius interval. Then, we calculated the column number density of dust grains per log-unit of size by dividing the number of particles in different radial bins with the corresponding annulus area, and we scaled the number of model particles according to our assumed power-law size distribution with exponent q (see Eq. (1)).

The resulting dust density represents a disc in which dust is produced at a constant rate, with a power-law size distribution, and in which all particles survive for the entire simulated time of 10 Myr. Therefore, the assumed global power-law size distribution is preserved. This purely dynamical model does not account for particle lifetimes which could be both shorter and size-dependent due to destructive collisions, in turn affecting how far particles can migrate. We discuss the effect of collisions a posteriori in Section 4.5. For our model discs, we also calculated surface brightness radial profiles in both scattered light and thermal emission, in the same manner as described in Section 3.1.

4.3. Formation of an outer dust ring

Takeuchi & Artymowicz (2001) showed that in a gaseous disc of primordial (hydrogen-dominated) composition, featuring a sharp, sigmoid outer edge, µm-sized grains accumulate at that edge and form an additional dust ring that could be observed at short wavelengths. Here, we consider a different, Gaussian-like decrease of gas surface density in the disc outer regions, and the gas may be of secondary origin with a high mean molecular weight.

In general, for there to be a distinct outer ring, the small dust that migrates outwards ought to accumulate within a narrow range of radii. Two illustrative models are shown in Fig. 7, in which the gas has different mean molecular weight, μ. To isolate the effects of changing μ, we assume the same midplane density profile in both models, even though in reality we expect vastly different gas masses in different gas origin and gas composition scenarios. For $\mu = 2.3$ (in units of $m_{\rm H}$), corresponding to a gas composed primarily of molecular hydrogen, the surface brightness at 1.6 µm peaks at the location of the assumed planetesimal belt and features a very modest secondary peak around 120 au (see the bottom left panel in Fig. 7). Looking at the spatial distribution of dust particles of various sizes (after 10 Myr, see the yellow-red colour-plot in the top left panel), we see that the density of small particles indeed peaks at larger radii, showing that those particles drifted outwards due to gas drag and radiation pressure. However, they are distributed smoothly in the disc, and do not accumulate significantly at any particular location.

For $\mu = 28$, on the other hand, as would be found in a secondary gaseous disc dominated by CO, we find that the surface brightness profile has two prominent peaks, indicative of two dust rings (shown in the bottom right panel of Fig. 7). In this case, dust grains of 10–30 µm in size all end up in a narrow range of radii at ~120 au by the end of our simulation, producing the outer ring. Note that in both cases, formally, there are small dust grains also in the main belt where they are produced. However, this does not show up in the figures as their number density there is negligible under these model assumptions.

To explain these results, we can consider a simplified description of grain dynamics, under the assumption that particle orbits are circularized quickly. In that case, particles quickly reach a steady-state drift velocity (Takeuchi & Artymowicz 2001),

$$v_{\rm drift} = \frac{\beta - \eta - 2\beta\,{\rm St}\,{\rm v_K/c}}{{\rm St} + {\rm St}^{-1}} v_{\rm K}, \tag{10}$$

where St is the Stokes number, the dimensionless ratio between the gas drag stopping time for particles of size s and the dynamical timescale, and c is the speed of light. In a sufficiently dense gaseous disc, where St is not too large, the third term in the numerator, related to Poynting–Robertson (PR) drag, can be neglected. Then, small particles with $\beta(s) > \eta(r)$ drift outwards to their "stationary" radius where $\beta(s) = \eta(r)$ and $v_{\rm drift} = 0$. If, on the other hand, gas density is low, inwards drift due to PR drag cannot be neglected, and particle drift may be stopped ($v_{\rm drift} = 0$) before particles reach radii where $\beta(s) = \eta(r)$. A similar effect is described by Pearce et al. (2020), who found that dust drifting inwards due to PR drag can become trapped close to the star, by the gas produced at the dust sublimation radius.

In the models of Takeuchi & Artymowicz (2001), the assumption of a sharp edge ensures that both the drop in the gas density and a sharp increase in $\eta(r)$ occur at nearly the same location, where particles reach their $\beta(s) = \eta(r)$ stability loci and accumulate. In our simulations with $\mu = 2.3$, particles also reach $\beta(s) = \eta(r)$ loci: the density of particles of different sizes peaks at these loci, indicated by the dashed grey curve, in the top left panel of Fig. 7. For $\mu = 28$, these loci are effectively outside of the gas disc. This is because a higher mean molecular weight results in lower sound speed, and consequently a lower $\eta(r)$ at any given radius. In dust size-radius plane, $\beta(s) = \eta(r)$ loci move upwards. Then, the gas density drops and particle drift velocity drops to $v_{\rm drift} = 0$ at radii shorter than the $\beta(s) = \eta(r)$ radii. These 'true' stationary radii depend on particle size in such a way that

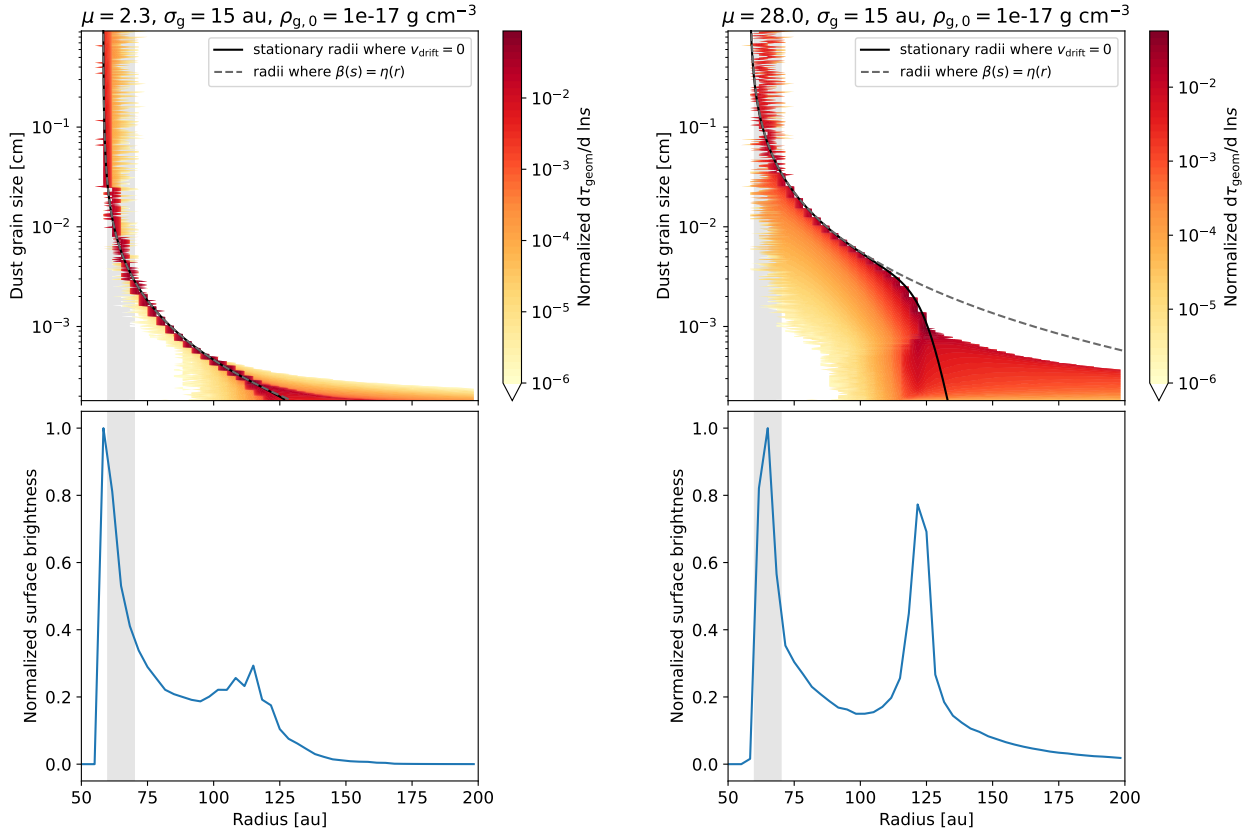

Fig. 7. Dynamical models of dust evolution in discs with mean molecular weight $\mu = 2.3$ (left column) and $\mu = 28$ (right column), with the same density profile (with the gas midplane density at 65 au equal to $\rho_{g,0} = 10^{-17}$ g cm^{-3}, and the Gaussian profile width $\sigma_g = 15$ au), at 10 Myr after particle release in the assumed belt indicated by grey bands. Top panels show the normalized geometric optical depth per log unit of size as a function of radius and particle size from the results of our dynamical models (yellow-red colour plots), the stationary radii where the drift velocity due to gas and radiative effects is zero (solid black lines; see Eq. (10)), and the radii where $\beta(s) = \eta(r)$. Bottom panels show normalized surface brightness as a function of radius in the disc for scattered light at 1.6 µm assuming a face-on disc. For details, see Section 4.3.

particles in a wider range of sizes end up in a narrower range of radii, producing the second ring.

It is also notable that it is not the smallest bound particles that make this ring bright. The smallest bound particles drift outwards, but remain distributed over a wider radial range. This is because these particles are produced on highly eccentric orbits due to radiation pressure and their orbits are slow to circularize; additionally, their eccentricity is 'pumped' at the outer gas edge (see Takeuchi & Artymowicz 2001). In the top right panel of Fig. 7 there are two dark bands of high particle density for these smallest particles, indicative of their pericentres (vertical band at around 120 au) and apocentres (along the upper edge of the red region). It is ∼10 µm-sized particles that contribute most to the outer ring optical depth.

It is not only the mean molecular weight that affects whether an outer ring forms, but rather a combination of the model parameters. We also expect the gas in real debris discs to have vastly different densities in the secondary (high mean molecular weight) and the primordial (low mean molecular weight) scenarios. The left panel of Fig. 8 shows the stationary radius (the solutions to $v_{drift} = 0$; Eq. (10)) as a function of grain size for different combinations of μ and $\rho_{g,0}$. Unlike the $\beta(s) = \eta(r)$ loci, these stationary radii depend on the gas density. For very low gas densities and large dust grain sizes there is no stationary solution at all, PR drag is the dominant effect and $v_{drift} < 0$ at all radii. Furthermore, in a more massive gas disc, the effective outer gas edge is further radially outwards. For $\mu = 2.3$, the $\beta(s) = \eta(r)$ loci can also fall outside of the gas disc, albeit only at lower densities than for $\mu = 28$. A narrower radial distribution of gas also works in favour of forming the outer ring, at fixed $\rho_{g,0}$ and for either value of μ, because it increases $\eta(r)$ and decreases the gas density at any given radius, so that a wider dust size range accumulates in a narrower radius range.

Another key parameter is the gas temperature. Like the mean molecular weight, it affects stationary orbits by changing the sound speed and the $\eta(r)$ profile (Eq. (8)). So far, we assumed the black-body temperature profile, which need not hold for the gas. Overall, a lower temperature (see Brennan et al. 2026) would decrease $\eta(r)$ and produce a similar effect to an increase in the mean molecular weight.

It must also be noted that in real discs, particles may not reach these stationary radii if the gas density is too low and the drift timescale too long. To illustrate this, we used the steady-state drift assumption and integrated Eq. (10) to estimate the radii at which particles end up after time t,

$$r = r_{belt} + \int_0^t v_{drift}(r(t))\mathrm{d}t. \tag{11}$$

The results are shown in the right panel of Fig. 8 for one particular fixed gas midplane density profile, but different mean molecular weights. For the given gas density and for $\mu = 2.3$, particles reach their stationary radii already in 0.1 Myr. For $\mu = 28$, the stationary radii are further away and the drift timescales

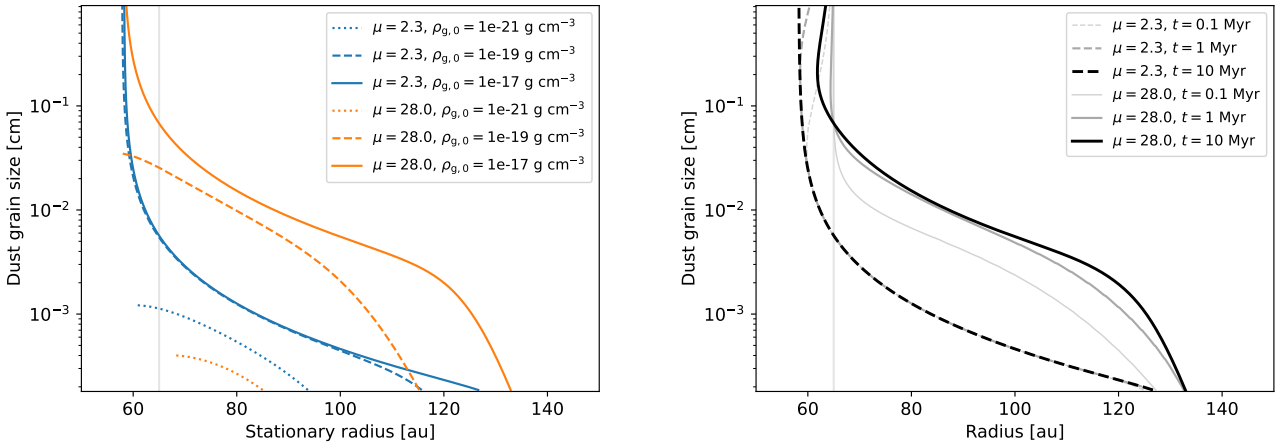

Fig. 8. Left: stationary radii ($v_{\rm drift} = 0$) as a function of particle size, computed for different values of mean molecular weight and gas midplane density at the location of the belt (see plot legend). Right: dependence of the radial location of particles on time, assuming $\rho_{\rm g,0} = 10^{-17}$ g cm^{-3}, calculated using the steady-state drift approximation. In both panels, the horizontal grey line shows the dust release radius of 65 au. The Gaussian profile width is assumed to be the same in all calculations here ($\sigma_{\rm g} = 15$ au). For details, see Section 4.3.

longer; the radius as a function of size also becomes more shallow for small sizes with time. This suggests an outer ring may form before dust reaches the stationary radii, and it only becomes more pronounced the longer particles survive.

4.4. Application to HD 131835

In this section, we explore a grid of dynamical models to identify which model parameters produce a dust structure resembling the morphology of HD 131835. Unlike in the collisional scenario in Section 3.2, our gas-driven model needs to explain not only the colours, but also the location where the outer dust ring hypothetically formed and the relative brightness of the two rings at both wavelengths. In our search for 'optimal' model parameters we freely varied the gas structure width and the gas mass for both primordial-like and secondary gas composition. This allows us to show how the dust structure varies with different model parameters. In Section 5.1.2, we discuss how these optimal parameters compare to observational constraints on the gas structure (e.g. if the required gas densities are realistic).

First, we aim to match the location of the outer ring. Fig. 9 shows a grid of models in which we vary the gas midplane density at the location of the belt ($\rho_{\rm g,0}$), Gaussian radial profile width ($\sigma_{\rm g}$), and mean molecular weight (μ). These dynamical models are produced as described in Section 4.2, integrating equations of motion of dust particles for 10 Myr. We find that a minimum density is required for the outer ring to appear ($\rho_{\rm g,0} > 10^{-21}$ g cm^{-3} for most models), above which higher density leads to a ring that is further away from the star. As expected, a wider Gaussian profile (higher $\sigma_{\rm g}$) also results in the ring forming further away. For each combination of μ and $\sigma_{\rm g}$ one can find the value of $\rho_{\rm g,0}$ for which the small dust is distributed at ~ 100 au (i.e., the observed location of the outer ring in HD 131835). Therefore, the location of the outer ring constrains the combination of the gaseous disc's width, density, and mean molecular weight, but not the individual parameters themselves.

Next, we aim to match the surface brightness ratio of the two rings in scattered light. From the grid of models shown in Fig. 9, for each combination of μ and $\sigma_{\rm g}$ we select the value of $\rho_{\rm g,0}$ for which the small dust is distributed at ~ 100 au. In all of these models, the outer ring is fainter than the inner ring, in contrast with what is observed in HD 131835 in scattered light (Fig. 2). The ratio of the two rings, however, can be reconciled by increasing the size distribution exponent q, as shown in Fig. 10. In doing so, we mimic a likely effect whereby particles that drift out of the planetesimal belt should have longer lifetimes and become more numerous relative to an ideal collisional cascade. Steeper distributions (larger q, favouring small grains) result in a fainter inner region and a brighter outer region in all models, because in all models the inner region consists of larger particles and the outer region of smaller ones. For sufficiently large q, the outer ring becomes brighter than the inner one in scattered light, in line with the observations.

Finally, we compare these models to the observed surface brightness of the two rings in both scattered light at 1.6 μm and in 890 μm emission. We re-scaled the dust mass of each model so that the peak sub-millimetre surface brightness is equal to the peak in the `frank` radial profile (shown with black dashed line in Fig. 10). The constraints on the peak surface brightness of the two rings in scattered light are shown using a solid black line for the outer ring and a black symbol for the upper limit on the inner ring.

In all models, the outer ring is fainter than the observed 890 μm emission, and both rings are fainter than what is observed in scattered light. Considering only the peak brightness of both rings and at both wavelengths, the two most favourable models are: (i) $\mu = 28$, $\sigma_{\rm g} = 10$ au and $\rho_{\rm g,0} = 10^{-17}$ g cm^{-3} (total gas mass of 0.26 $M_\oplus$), and (ii) $\mu = 28$, $\sigma_{\rm g} = 15$ au and $\rho_{\rm g,0} = 10^{-19}$ g cm^{-3} (total gas mass of 0.004 $M_\oplus$), both with $q \gtrsim 3.75$. Some of the models with $\mu = 2.3$ have a similar (dis)agreement with the observed scattered light peak brightness, but the outer ring is always much fainter than observed at 890 μm. This is because, for $\mu = 28$, the outer ring brightness is dominated by 10 μm-sized grains at their equilibrium orbits, whereas for $\mu = 2.3$, the outer ring consists of smaller particles of few microns in size, whose orbits have not circularized within the simulated time and whose pericentres are concentrated around 100 au. Nevertheless, all of the models struggle to reproduce the broad component observed at both wavelengths, which extends to radii >200 au.

4.5. Effect of collisions

The models presented thus far in this section are purely dynamical; they only account for the spatial motion of the dust grains for

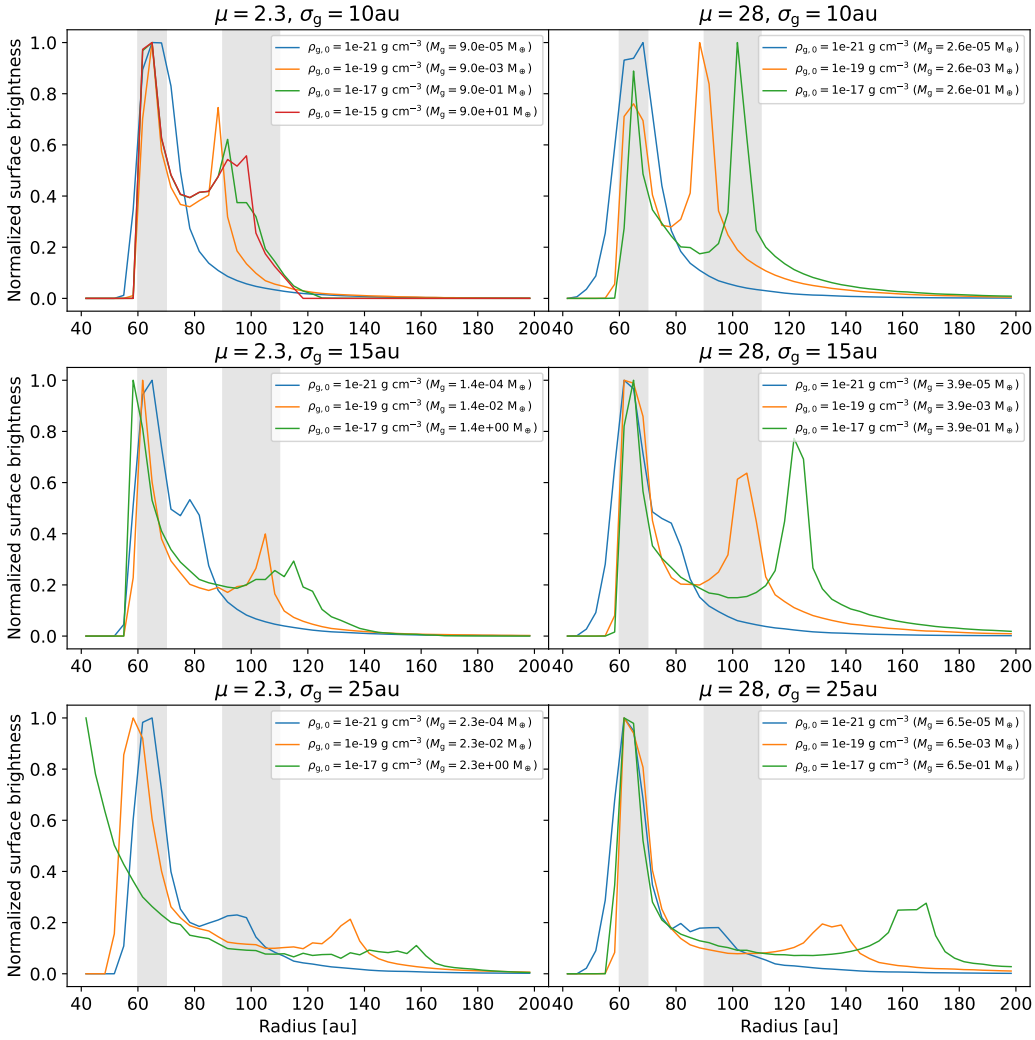

Fig. 9. Normalized surface brightness of scattered light at 1.6 μm as a function of radius 10 Myr after particle release for a grid of dynamical dust models with varying gas disc parameters. The panels on the left-hand side are for the mean molecular weight of $\mu = 2.3$ and those on the right-hand side are for $\mu = 28$. From top to bottom, the radial width of the Gaussian radial profile of the gas disc is varied from 10 au to 25 au. The different colours show different gas densities at the radius of 65 au, as indicated in the plot legends. Collisions are not accounted for in these models and the size distribution exponent is fixed to $q = 3.5$. The grey bands show the approximate locations of the observed rings we aim to match. For details, see Section 4.4.

10 Myr, comparable to the estimated system age of 16 Myr. Lifetimes of particles may be significantly shorter than 10 Myr due to destructive collisions. Here we test if collisions can prevent the formation of the outer ring by destroying particles faster than they can drift outwards (see also Olofsson et al., in prep.). We do so by comparing the dust collisional lifetime within the belt with the time it takes particles to drift out of the belt. Once they are outside of the belt, particles are much safer from destructive collisions because the dust density is lower and collision velocities are damped by the gas.

The collisional lifetime of particles while they are still in the belt, $t_{\rm coll}$, can be estimated using a simple particle-in-a-box model. Here we follow Wyatt et al. (2007) and Rigley & Wyatt (2020) with some changes. The details of this simple model are presented in Appendix A. To calculate the collisional lifetime we need to choose values of three key parameters: specific critical disruption energy $Q^*_{\rm D}$, typical particle inclination i and the total mass $M_{\rm dust}$ of dust grains smaller than 1 cm. For the dust mass, we adopt $M_{\rm dust} = 0.45\,{\rm M}_\oplus$, which is estimated based on the ARKS continuum emission (Marino et al. 2026a). We assumed the typical orbital inclination is equal to the disc aspect ratio, which is measured as the half-width half-maximum of the disc vertical profile of the ARKS observation at mm wavelengths (Weber et al. 2026). Values of the aspect ratio obtained are $0.022^{+0.007}_{-0.006}$, $0.039^{+0.006}_{-0.006}$ and $0.058^{+0.038}_{-0.037}$ from a parametric approach, code `frank` and code `rave`, respectively. To do our calculations here, we considered a range of aspect ratios encompassing all three confidence intervals (0.016–0.096). For $Q^*_{\rm D}$ we considered a range an order of magnitude below and above 10^8 erg g^{-1}, which is roughly the value studies have found for 10 μm-sized rocky dust grains (Benz & Asphaug 1999; Stewart & Leinhardt 2009), at the impact velocities expected in HD 131835 based on the derived aspect ratios. We calculated the collisional lifetime of 10 μm-sized particles within these parameter intervals and show it as a colour map in Fig. 11. The white region indicates the values of the aspect ratio and $Q^*_{\rm D}$ for which collisions at the average impact velocity cannot destroy these particles.

We calculated the time it takes for a particle to drift out of the belt as follows. Assuming the belt has a width $\Delta r = 10$ au,

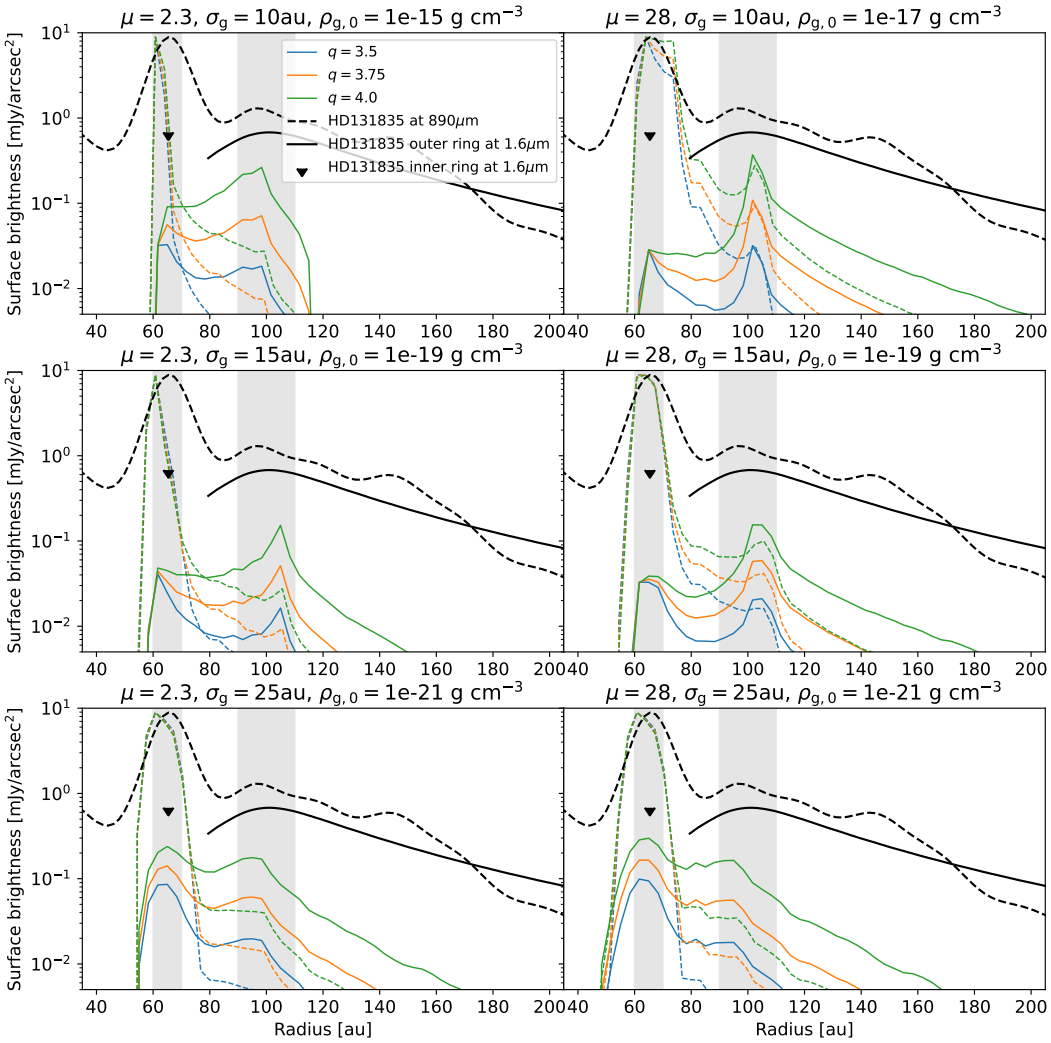

Fig. 10. Surface brightness of scattered light at 1.6 μm (solid lines) and thermal emission at 890 μm (dashed lines) as functions of radius for a grid of models that match the location of the outer ring of HD 131835. The gas disc parameters are selected from Fig. 9 and are shown in each panel title. Different line colours (blue, orange, green) represent a different size distribution exponent q, which changes the brightness ratio of the inner and the outer ring. Black lines and black symbols show the observational constraints on the brightness of the rings in HD 131835. For details, see Section 4.4.

and that the orbits are circularized quickly[4], a particle exits the belt after a time

$$t_{\rm drift} \approx \frac{\Delta r}{v_{\rm drift}}, \tag{12}$$

where $v_{\rm drift}$ is the drift velocity at the belt centre, calculated using Eq. (10). To calculate the drift velocity, we need to choose the value for the gas midplane density. Using our dynamical models (Section 4.4), we find that the outer dust ring forms if the Gaussian radial profile of gas has a width $\sigma_{\rm g}$ of 10–15 au. For $\sigma_{\rm g}$ = 15 au, the outer ring forms at the desired location (at 100 au) for a gas midplane density of $\rho_{\rm g,0} = 10^{-19}\,{\rm g\,cm^{-3}}$ at the centre of the belt. Assuming this midplane density, we show the drift timescale in Fig. 11 as a black contour – this is the line at which the collisional lifetime and the drift timescale are equal. Below and to the right from this contour, particle lifetime exceeds the drift timescale, and particles can escape the belt before they are destroyed in collisions. A large part of the parameter space we explore is within this region. For the median value of the aspect ratio fitted with `rave` and for the most likely critical specific energy ($10^8\,{\rm erg\,g^{-1}}$), that is not the case. The other two constraints (with the code `frank` and the parametric approach), even though indicating only a slightly smaller aspect ratio, point to dust being able to escape from the belt. We therefore conclude that the current constraints on the disc aspect ratio and thus on the impact velocities in the disc are consistent with either outcome, if $\rho_{\rm g,0} = 10^{-19}\,{\rm g\,cm^{-3}}$ at the centre of the planetesimal belt.

For $\sigma_{\rm g}$ = 10 au, the midplane gas density that places the outer ring at the correct location was found to be $\rho_{\rm g,0} = 10^{-17}\,{\rm g\,cm^{-3}}$. In this case, the drift timescale is shorter than the collisional lifetime within the entire explored parameter space (not shown in a figure). Collisions could be a danger even at these higher densities if dust grains are much weaker (e.g. recently Sommer et al. 2025, found an empirical value of $Q_{\rm D}^{*} = 3 \times 10^6\,{\rm erg\,g^{-1}}$ for icy grains). For gas densities of

[4] The orbits of the smallest bound, micron-sized grains are not, in fact, circularized quickly for the relevant gas densities. Their drift timescale should thus be longer than that given by Eq. (12), because they spend the majority of their time at longer circumstellar radii, where the gas density is lower. However, we are primarily interested in ∼10 μm-sized grains, which make the outer ring bright in our dynamical models, and for which this approximation is sufficiently accurate.

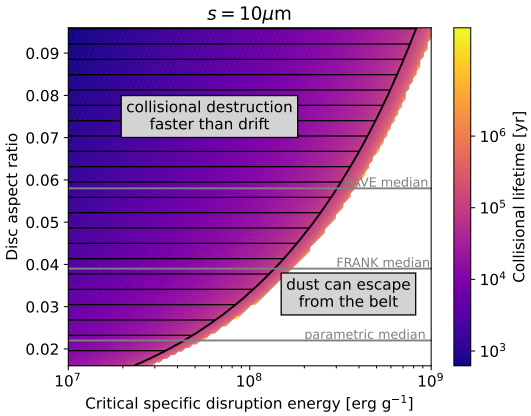

Fig. 11. Collisional lifetime (shown as a colour map) of 10 µm-sized particles in the inner ring of HD 131835, as a function of the disc aspect ratio and the critical specific energy for dispersal (Q^*_D). The overlaid hashed region indicates the parameter space where collisional destruction is faster than drift from the belt caused by gas drag (assuming a midplane gas density of $\rho_{g,0} = 10^{-19}$ g cm^{-3} and disc width σ_g = 15 au at the radius of 65 au). The shown range of disc aspect ratios corresponds to a significance interval from fits to ALMA data with median values from three different fitting methods shown with grey lines (Weber et al. 2026). The white region is where particles cannot be collisionally destroyed at all, at the average impact velocity. For details, see Section 4.5.

$\rho_{g,0} = 10^{-21}$ g cm^{-3}, we find that disruptive collisions would prevent any migration of the small dust outwards from the inner belt, except in the part of parameter space where fragmentation cannot destroy particles at all in our simple model. However, for such parameters, based on the results above, we expect that cratering or erosion of grains in collisions would render the gas unimportant at such low gas densities.

Collisions, had they been included in our dynamical model, would also affect the brightness of the outer ring, which would depend on the lifetime of the particles that arrive there. It is not possible to estimate what this lifetime would be with the simplified collisional model described herein. Collisional velocities between 10 µm particles are expected to diminish completely because their radial movement is halted in the outer ring, and their orbital eccentricities and inclinations are damped by the time they arrive to the outer ring. This would imply that these particles can survive indefinitely. However, they are impacted by smaller grains whose orbital eccentricities are still large at the outer gas disc edge (see Section 4.3 and Takeuchi & Artymowicz 2001). It is not possible to account for these time- and size-dependent eccentricities within the simple framework employed here. Future work should consider a more self-consistent, dynamical *and* collisional model of gaseous debris discs.

5. Discussion

In this section, we first discuss which mechanisms are likely to produce the two peculiar rings in the debris disc of HD 131835 (Section 5.1). We then discuss the implications of our results for other debris discs where offsets between thermal emission and scattered light have also been observed (Section 5.2).

5.1. The peculiar dust rings of HD 131835

There are two main possibilities for the rings of HD 131835. One is that the two rings are representative of two planetesimal belts with different properties. The other is that it is only the inner ring that contains planetesimals and where the dust is mainly produced, and that the outer ring is made up of only the small dust that is dragged there by interaction with the gas present in the system. In Sections 3 and 4, we showed results of numerical simulations of these two scenarios and for each scenario we identified the properties of the debris required to produce rings similar to those in HD 131835. Here, we critically examine both scenarios and assess whether their respective theoretical requirements could realistically be fulfilled in this system. We also discuss some other possible explanations.

5.1.1. Two very different planetesimal belts

To explain the observations, the dust grains in the two rings need to have a very different size distribution. In this scenario, we assumed both rings host planetesimals feeding a collisional cascade, and the different dust grain size distributions arise from a difference in either dynamical excitation or material strength.

Different excitation. Our collisional belt models with different dynamical excitation cannot explain the difference in the observed colours of the two rings in HD 131835. We hypothesize that the models could be brought into agreement with the observations if different dust grain optical properties were assumed, such that the colour of our model outer belts would be reduced by a factor of at least 3.5. Assuming still that the two belts are made of the same material, the colour of our model inner belts would also change, albeit not by the same factor due to the belts having very different dust size distributions. We can therefore draw a limited conclusion that in this scenario the inner ring needs to have a moderate to low excitation, as in our models with a uniform distribution of eccentricities and a maximum eccentricity of $e_{max} \leq 0.3$ (corresponding to an average eccentricity of $\leq$0.15), and the outer ring needs to be more strongly excited, with a maximum/average eccentricity likely at least several times higher. Here we discuss if an extreme difference in dynamical excitation of two neighbouring belts is likely.

One way to explain dynamical excitation of debris discs in general is self-stirring, a mechanism in which large bodies comprising the disc stir surrounding material to higher eccentricities and inclinations through gravitational scattering (e.g. Quillen 2007; Matrà et al. 2019a; Kenyon & Bromley 2002a, 2004a; Kenyon & Bromley 2008, 2010; Krivov & Booth 2018). From the semi-analytic model of Ida & Makino (1993), in a gravitationally stirred planetesimal belt the eccentricities increase over time t as $e_{rms} = \sqrt{\langle e^2 \rangle} \propto (M\Sigma M_*^{-3/2} r^{1/2} t)^{1/4}$, where M is the mass of a stirrer, Σ is their (effective) surface density, and r is the stellocentric radius of the belt. Assuming the two hypothetical belts in HD 131835 have both been stirred from their formation to the present system age, the product $M\Sigma$ characterizing their large stirrers would have to higher by a factor of $\sim 0.8(e_{rms,out}/e_{rms,in})^4$ in the outer belt. An extreme difference in the excitation of the two belts would thus open a question of why much larger and/or more numerous bodies formed in a belt further out, where the dynamical timescale is longer, unless the bodies in the inner belt have been collisionally destroyed on a faster timescale. The semi-analytic theory invoked here may also be inapplicable to the hypothetical high excitation of the outer ring in HD 131835, as it is derived from short-term simulations of planet-planetesimal interactions. On longer timescales, as the excitation increases, so do inhomogeneities around the planet (Ida & Makino 1993).

Alternatively, if self-stirring processes are inefficient, there are multiple ways in which yet-unseen planets can excite the outer belt more strongly than the inner one. For instance, this

could occur via secular perturbations due to an eccentric planet (Mustill & Wyatt 2009). This planet would likely need to be located exterior to both rings, because a planet in-between the two belts would stir the belts at a comparable rate, and to a comparable excitation (Wyatt 2005; Murray & Dermott 1999). A planet exterior to both belts would stir the inner belt to a smaller excitation. In this case, the collective gravity of planetesimals (if massive enough) might further increase the excitation contrast between the two rings. This is because the disc's gravity may suppress the planet-induced secular perturbations, with the suppression being stronger at larger separations from the planet, in this case in the inner belt (Sefilian et al. 2021; Sefilian 2024). A similar effect could arise if there is a low-eccentricity planet inwards of the inner belt and a high-eccentricity planet exterior to the outer belt (Farhat et al. 2023). One caveat is that if the outer ring needs to be excited up to eccentricities of 0.45–0.9, the planet would also need to be on a highly eccentric orbit and it would impart a massive asymmetry on the disc (Faramaz et al. 2014; Pearce & Wyatt 2014), which is not observed in HD 131835 (Lovell et al. 2026). Alternatively, a planet on either an eccentric or a circular orbit could excite the outer ring via mean motion resonances (MMRs; e.g. Faramaz et al. 2017; Pearce et al. 2024). Excitation via MMRs is even more effective if a planet has migrated through the outer belt in the past, either inwards or outwards (Friebe et al. 2022; Booth et al. 2023). However, to achieve such high eccentricities would require material to be trapped in MMRs, which would also result in their distribution being clumpy, yet there is no strong evidence of disc asymmetry in the ARKS observation of this disc (Lovell et al. 2026). Another possibility is that a planet migrated outwards through the disc and excited the outer belt via scattering (e.g. Malhotra 1993). This may have created the broad mm dust distribution observed with ALMA.

In a companion ARKS paper (Weber et al. 2026), the new ALMA observation of HD 131835 is fitted with a radially constant aspect ratio, with three different modelling approaches. As in Section 4.5, we can consider the lowest and the highest value from the three confidence intervals obtained therein, resulting in a range of $h \sim 0.016$–0.096. Assuming that the root-mean-square inclination is approximately equal to the measured aspect ratio ($i_{\rm rms} \sim h$) and that the eccentricities are in energy equipartition with the inclinations ($e_{\rm rms} \sim 2i_{\rm rms}$), this corresponds to $e_{\rm rms} \sim$ 0.03–0.19. This is consistent with our match for the inner ring, and lower than what is likely required for the outer ring. Note that, while it is generally expected that in a gravitationally stirred disc the orbital inclinations are stirred to around the same level as the eccentricities, this is not the case if a planet excites very large eccentricities (Ida & Makino 1993). Likewise, a hypothetical eccentric planet could excite high eccentricities without simultaneously exciting large inclinations if it is coplanar with the rings (Pearce & Wyatt 2014). Weber et al. (2026) also found that the best parametric shape for the disc vertical profile is a double Gaussian, which could signify planet-disc interactions (Malhotra 1995; Matrà et al. 2019b; Sefilian et al. 2025). Future modelling of the disc vertical structure should include a radial dependence to probe a possible change in the disc excitation between the inner and the outer ring.

Different material strength. We also explored whether the two rings can be explained by two belts made of materials of different strengths. We found that the observations can be explained if the two belts have the same excitation, but the critical specific disruption energy ($Q^*_{\rm D}$) of the dust is different by at least 2 to 3 orders of magnitude. In contrast, studies of material strength report less than 2 orders of magnitude difference between rocky and (weak) ice materials (see figure 11 in Leinhardt & Stewart 2009).

The rings could be of different composition if they formed on different sides of an ice line of a major planetesimal building component. The present-day black-body temperature in the two rings is 60 K and 48 K at 65 and 100 au, respectively, assuming $L_* = 9\,L_\odot$. In the nascent protoplanetary disc the temperature would have been lower. Although the protostar is expected to have been more luminous in the past, the dust in the protoplanetary disc obscures stellar light and heating is reduced in the disc midplane (Chiang & Goldreich 1997; Chiang et al. 2001). Therefore, the water ice line has always been much closer to the star than both belts, at the temperature of ~ 150 K. It is not clear if comet-like fraction of CO or CO_2 would make any change in particle strength.

We did not explore combinations of both different excitation and different material strength for the two rings. The difference in the predicted colour of the outer ring is quite large between the 'very weak' and 'extremely weak' models in Fig. 6. We therefore expect that for combinations including stronger materials, the outer belt would still have to be significantly more dynamically excited than the inner one to be consistent with observations of HD 131835, which would be qualitatively the same as the case discussed above. However, the effects are not additive in any simple manner. For example, particles are stronger at higher impact velocities (and thus they are stronger at higher dynamical excitation), see Eq. (2). Therefore, it is not possible to make predictions with certainty using the models presented here and we leave this for future work when further observational constraints from scattered light and/or James Webb Space Telescope (JWST) may be available. Future work should also consider the collisional interaction between the two belts if there is an overlap between particle orbits, and the influence of the gas present in the system (gas drag likely influences one or both belts even if it is not creating the outer ring).

Finally, note that the absence of a separate ring of CO emission at 100 au (Fig. 2) does not necessarily indicate the absence of a separate planetesimal belt. From the ALMA radial profile, the outer ring is much fainter at millimetre wavelengths compared to the inner ring, and therefore a hypothetical outer planetesimal belt could be much less massive than the inner one. Even if the outer belt is of the same composition and also releases CO gas, it may do so at a much lower rate compared to the inner ring. The amount of CO gas released from the belt at 100 au could be small compared to the amount produced in the inner ring that viscously spread to the outer belt. On the other hand, the gas production rate depends not only on the belt mass, but also on other properties of the belt such as its excitation. This is another aspect of the two-belt scenario that deserves further study.

5.1.2. Migration of small dust due to gas

We found that in our gas discs with a Gaussian surface density radial profile, an outer dusty ring typically forms at the radius at which the gas density drops sufficiently so that the effects of gas drag, radiation pressure and PR drag cancel out. Radially wider profiles (higher $\sigma_{\rm g}$) require lower gas densities (lower $\rho_{\rm g,0}$) to form the outer ring at a particular location. We identified combinations of these parameters that place the outer ring at the location it is observed at in HD 131835. However, we can exclude some of these combinations based on other arguments.

There are three measurements of CO gas mass that we can compare our models against: $M_{CO} = (1.7 \pm 0.3) \times 10^{-2}\,M_\oplus$ (Cataldi et al. 2023), $M_{CO} = (4.1 \pm 0.4) \times 10^{-4}\,M_\oplus$ and $M_{CO} = (3.2 \pm 0.3) \times 10^{-2}\,M_\oplus$ (Mac Manamon et al. 2026). The large difference in these masses is due to different assumptions about the observed line optical thickness and the gas microphysics, which are well known uncertainties in obtaining the gas mass from the observed flux. Furthermore, it is known that there is atomic carbon gas in the system, with a mass similar to or smaller than the mass of CO (Cataldi et al. 2023). The total gas mass is not known because of the possible presence of other gas species that are difficult to detect, such as water vapour that could be released in similar manner to secondary CO (and its photodissociation products, OH, H and O), or ample H_2 that could be remnant from the protoplanetary disc phase. We can estimate an upper limit on the total gas mass by assuming the observed CO is a tracer of a protoplanetary disc-like gas in which the CO/H_2 number density ratio is about 10^{-4}. This yields a possible H_2-rich gas mass of $0.36\,M_\oplus$ or $26\,M_\oplus$ (corresponding to the lowest and the highest among the three measurements of M_{CO}).

We can compare our models in Fig. 9 to these constraints (model gas masses are shown in plot legends). First, for the secondary gas composition (CO-rich, $\mu = 28$), our lowest-mass models ($\rho_{g,0} = 10^{-21}\,g\,cm^{-3}$) have mass close to the lower limit on M_{CO} obtained by Mac Manamon et al. (2026), while their higher mass measurement and the mass measured by Cataldi et al. (2023) fall between our two higher-mass models ($\rho_{g,0} = 10^{-19}\,g\,cm^{-3}$ and $\rho_{g,0} = 10^{-17}\,g\,cm^{-3}$). However, we can exclude our lowest-mass model on the basis that collisions would prevent the small grains from migrating outwards from the planetesimal belt (see Section 4.5).

This implies that the width of the radial profile of the gas needs to be between 10 au and 15 au, in order for the outer ring to be formed at the correct location (around 100 au). These radial gas profiles are narrower than the observed CO line radial profiles (see Fig. 2, or Figure 4 in Mac Manamon et al. 2026). To check whether the observed radial profiles could be wider as a result of optical depth effects, we produced a synthetic observation of our gas disc model with $\sigma_g = 15$ au and $\rho_{g,0} = 10^{-19}\,g\,cm^{-3}$. We assumed local thermal equilibrium, and we used RADMC3D (Dullemond et al. 2012) to perform radiative transfer calculations and to produce a data cube of ^{12}CO line emission. The data cube is then convolved by the spectral and spatial resolution of the data. We assumed the same disc inclination and position angle, and we used the same method for extracting the radial profile as Mac Manamon et al. (2026). We find that the radial profile of our synthetic observation is indeed narrower than the observed radial profile (see Fig. 12). However, in this simple exercise we assumed a black-body temperature for the gas. In a companion ARKS study, Brennan et al. (2026) found that another gas-rich debris disc (HD 121617) features gas that is colder than the black-body temperature at the same radius. Had we assumed a lower temperature in this calculation, our model gas radial profile would better match the observations in terms of both the intensity and the width, if the line is assumed to be optically thick. Therefore, this exercise provides important insights, but it does not rule out the gas scenario.

Some of our models with a primordial gas composition ($\mu = 2.3$) also feature an outer dust ring. However, only our highest-mass models are consistent with the likely total gas mass in this case. Then, our models imply a radial width of the gas disc of only ~10 au. While Fig. 12 shows the observed CO line intensity is distributed more widely than the required width of 10 au, we cannot rule out primordial origin for the gas, because the true radial distribution of the gas could be narrower if the observed CO line is very optically thick (as seen in HD 121617, Brennan et al. 2026).

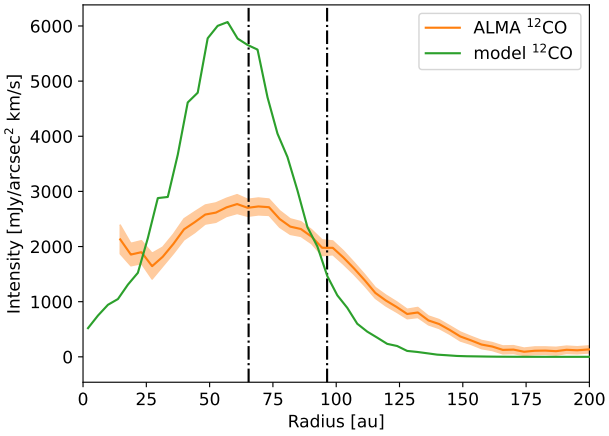

Fig. 12. Radial profile of molecular line emission of ^{12}CO observed with ALMA (orange line; Mac Manamon et al. 2026) and from a synthetic observation of our favoured gas structure model with $\sigma_g = 15$ au and $\rho_{g,0} = 10^{-19}\,g\,cm^{-3}$ (green line). The vertical dash-dot lines indicate the locations of the inner and the outer dust rings at 65.4 au and 96.5 au. For details, see Section 5.1.2.

Overall, for either gas composition, there are discrepancies between our 'optimal' gas structures and the existing observational constraints. Additionally, all of our models under-predict the brightness of the outer dust ring, especially at 890 µm. Nevertheless, there are several important effects that have not been accounted for in our simple dynamical model, as discussed next.

(1) Collisions: Collisions may work both in favour of and against the gas-driven scenario. Disruptive collisions may destroy particles in the inner ring before their collision velocities are damped and before they escape the belt, in which case the outer ring would not form. We tested if this happens in Section 4.5 by comparing a simple estimate for the collisional lifetime of the small dust with the timescale of their migration out of the belt. The results were inconclusive due to the large uncertainty in particle material strength, and the sensitivity of results to the belt excitation (as probed by the different aspect ratio measurements). Note also that, even if the average particle is destroyed quickly, it is possible that only a fraction of small particles escape the belt and survive long enough to accumulate into a bright outer ring.

Furthermore, collisions could help to produce a global size distribution that makes the outer ring bright. Particles that manage to leave the belt end up in a lower density environment than those in the belt, and we expect their orbital inclinations and eccentricities to decrease due to gas drag, as well as the velocities at which they collide. This means these their collisional lifetimes would be longer than if they remained in the belt, and they would increase in number. In our models all particles survive for 10 Myr, but we mimicked this effect by considering global power-law size distributions with different exponents q, demonstrating that steeper size distributions result in a brighter outer belt.

Finally, collisions do not always need to be disruptive. Hypothetically, if small dust grains reach 100 au, their collisional velocities may be sufficiently damped so that collisions result in growth instead of fragmentation. This would increase the

brightness of the outer ring at mm wavelengths. A comprehensive numerical model that would account for both dynamical and collisional evolution of the dust is needed to check these hypotheses.

(2) Gas distribution evolves with time: We assumed that the gas disc structure is fixed for a period of 10 Myr, comparable to the age of this system. The assumed Gaussian radial profile of the gas itself is expected if the gas is *not* at steady-state, but instead is radially spreading (assuming the gas is of secondary origin; Kral et al. 2019; Marino et al. 2020). The gas may also not have been produced early on if the planetesimal belt was formed dynamically cold. It may have taken some time for the belt to become dynamically excited sufficiently for the collisions among the bodies to be disruptive (e.g. Kenyon & Bromley 2002b, 2004b) and to start producing dust and gas. The outer dust ring could still have formed in such a case, but the dust would have had less time to migrate outwards (see Section 4.3 and Fig. 8). Our models imply that the current gas density would have to be higher than what we find in this work to still produce the outer ring at a desired distance from the star. On the other hand, it is not known when (or even if) the primordial gas disc dissipated and what structure may be left over from the transition phase, and the gas may also be produced through mechanisms other than collisions (Bonsor et al. 2023; Huet et al. 2025).

(3) Gas distribution may be affected by dynamical feedback: The gas disc structure may be affected by the dust itself. If the dust mass density is not negligible, and if the dust density approaches the gas density at some location (counting the dust grains that at least marginally couple to the gas), conservation of angular momentum dictates that the outward migration of the dust would exert a force on the gas (Nakagawa et al. 1986). This is bound to happen towards the outer edge of the gas disc and this dynamical feedback on the gas might prevent accumulation of large amounts of dust. If the gas mass is as small as the CO mass lower limit by Mac Manamon et al. (2026), the dynamical feedback cannot be neglected anywhere in the disc.

(4) Shape of the outer gas edge is uncertain: We only considered a Gaussian radial profile for the gas. The gas disc could have a sharper outer edge than what we assumed here (e.g. like the one in the models of Takeuchi & Artymowicz 2001) and if that edge was located at ∼100 au, it could be easier to construct a model in which gas leads to a bright outer ring. The gas density would only need to be high enough for the migration timescale to be sufficiently short to escape collisions, while the outer ring location would be independent of it. There is no evidence that the CO radial profile has a sharp outer edge, or that there is an external companion or a passing star that would carve out a sharp edge. Local perturbations in the gas density could have a similar effect (e.g. due to dynamical feedback discussed above, or due to local temperature variations discussed below). Notably, the gas outer edge could also be less sharp than the Gaussian profile ($\exp(-x^2)$) assumed here: in a well-known self-similar model of a viscously spreading gas disc at steady-state, gas surface density at the outer edge drops off exponentially ($\exp(-x)$; Lynden-Bell & Pringle 1974), and a similar drop off is seen in simulations of secondary gas in debris discs (Marino et al. 2020).

(5) Gas temperature is uncertain: We assumed a fixed blackbody temperature profile for the gas. For a given gas surface density profile, gas temperature affects the gas scale-height, gas midplane density, gas pressure and radial gas pressure gradient. Both the dust drift velocity and the dust stationary orbits would thus be affected. We do not expect that our results would be fundamentally different if temperature is uniformly increased everywhere. If the dust increases gas temperature locally by photoelectric heating, this would lead to local changes in the gas pressure profile and potentially non-trivial consequences for the evolution of the dust (Klahr & Lin 2005; Besla & Wu 2007; Mac Manamon et al. 2026). Such thermal feedback of dust on the gas would be in addition to the dynamical feedback discussed above.

(6) Unbound grains contribute to scattered light brightness: In our simulations, we did not include sub-micron dust grains that are expected to be gravitationally unbound due to radiation pressure. Unbound grains may strongly contribute to scattered light brightness in bright debris discs such as HD 131835 (Thebault & Kral 2019). It has been suggested that gas drag could trap some of the unbound grains or at least slow them down on their way out of the system (Bhowmik et al. 2019; Moór et al. 2019; Marino et al. 2020; Pearce et al. 2020; Milli et al. 2024; Pawellek et al. 2024), further enhancing their abundance. However, for majority of the gas densities explored here the friction timescale of sub-micron grains is of the order of the orbital period or longer and thus we do not expect that in this system their quick escape is much affected by gas drag (see also Takeuchi & Artymowicz 2001).

(7) Grains may be porous: We assumed the dust grains have a simple compact astrosilicate structure. A lower grain material density from a higher porosity would increase the particle β parameter at a fixed dust grain size. This would put larger dust in the outer ring by increasing the radii where $\beta(s) = \eta(r)$, similar to the effect of a higher mean molecular density. In turn, this could increase the brightness of the outer ring in both thermal emission and scattered light. However, this hypothesis needs to be tested by also considering the effect of grain porosity on the optical properties of the dust.

Ultimately, dust growth in the outer ring could increase the ring brightness at mm wavelengths, and local perturbations in the gas density could allow for ring formation near 100 au with the gas extending further outwards. It is not clear under what conditions a gas-driven scenario could also produce an extended halo seen both in scattered light and sub-millimetre.

5.1.3. Other possibilities

There is a possibility that the gas is moving the small dust from the inner to the outer region and that there are also planetesimals producing dust around 100 au (with either the same or different properties as the planetesimals around 65 au). At first sight, it would be a great coincidence for the gas to deliver the small dust from the inner belt exactly to the location of the outer belt. However, there could be a single cause for the outer dust and gas edge, such as a planet sculpting the outer edge. Additionally, it is possible the outer peak in the `frank` radial profile does not correspond to a true separate ring in reality. Radial profiles of ALMA data obtained with two other methods do not recover the same outer ring (see Section 2.2). Instead, the true distribution of mm dust and the planetesimals could be a smooth extension of the inner belt, and the region around 100 au may not represent a special place in the sub-millimetre from the disc. This would make it more likely that there is both gas-driven dust in this region, and an extended planetesimal belt.

Another possibility is that there are indeed two planetesimal belts, and that some process is preferentially removing the smallest dust grains from the inner belt, relative to the outer belt. Candidate processes include gas drag (with or without placing the small dust at the peak of the outer belt), PR drag (removes dust faster closer to the star) and removal of water ice from small dust grains by photo-desorption (also called photo-sputtering or UV sputtering; acting faster closer to the star because of the

higher incident stellar flux Grigorieva et al. 2007). However, our collisional modelling in Section 3.2 shows that the observed colour of the inner belt can be explained with fairly straightforward assumptions, without invoking any of these processes, and it is in the outer belt that the size distribution is more difficult to explain.

Yet another possibility is that the inner belt hosts a collisional cascade, while the outer belt, or at least its peculiar colour, was formed more recently by a giant impact. The fragment size distribution from a single impact can be steeper than the size distribution of a collisional cascade (e.g. Leinhardt & Stewart 2012). This is perhaps the least likely possibility because the time since such an impact would have to be short enough for the size distribution to have remained steep and not collisionally processed, while it would also have to be long enough for the impact-related strong asymmetries in scattered light (see Jackson et al. 2014; Jones et al. 2023) to be sheared out.

Finally, returning to the gas-dust interaction as the possible culprit, it could be that the true nature of the two rings is inverted from what we assumed in this work. Namely, it is possible that it is the outer ring/halo that produces dust, and that the inner ring is a result of mm-sized dust grains migrating inwards due to gas drag (as they are unaffected by radiation pressure). In this scenario mm dust becomes trapped around the gas pressure maximum (slightly inwards of the gas surface density maximum), starting a collisional cascade which produces the micron-sized dust seen with SPHERE. For this to be a plausible explanation, the gas needs to be of primordial origin, dense enough at 100 au to marginally couple the mm-sized grains, to cause their inward radial drift.

5.2. Other discs with offset between thermal emission and scattered light

Milli et al. (2026) identified a total of six debris discs among the ARKS targets for which there is significant outwards radial offset between the peak of their thermal emission and the peak of their scattered light radial profiles (HD 131835, HD 121617, HD 131488, HD 32297, HD 9672 and HD 145560). Only one of these six discs does not have a gas detection (HD 145560), but also the existing upper limit on the CO is not stringent compared to e.g. HD 131835. Furthermore, only one disc in the sample has gas detected and does not have an offset, and this is the relatively gas-poor disc of β Pic. Overall, thus, it appears that this offset is related to the presence of gas.

Among these discs, HD 131835 is the disc with the largest offset. For HD 131835 there is also the least overlap between the outer ring seen in scattered light and the inner ring seen in thermal emission, while the other discs do not show a separate outer dust ring in the same sense. One explanation for this could be that in all discs gas effects are causing the offset, but only in HD 131835 the small dust has managed to escape the planetesimal belt and accumulate at the outer gas disc edge. The other explanation is that HD 131835 hosts two planetesimal belts and the offset should be measured between the outer ring seen in the `frank` profile and the peak of scattered light profile, which would make it much less of an outlier.

The simple dynamical models of gas-driven dust evolution that we used in this work are not directly applicable to these other discs with offset. That is because in other discs the small grains overlap significantly with the mm dust, meaning the small grains definitively remain a part of the collisional cascade inside the planetesimal belt. Therefore, for these discs radial drift due to gas drag should be accounted for together with collisional destruction to model how far the small grains can move. Additionally, HD 121617 has an azimuthal symmetry which also requires a different numerical approach. The arc-like feature seen with ALMA (Lovell et al. 2026; Marino et al. 2026b) motivated a dedicated study by Weber et al. (2026), where the dynamical evolution of both gas and dust was modelled using full hydrodynamical simulations. That work shows that the azimuthal asymmetry can arise from aerodynamic trapping of grains in a pressure maximum of a vortex developing in a gas-rich ring. The simulations also successfully reproduce the observed offset between the ALMA continuum and scattered light emission, thanks to the size-dependent combined effects of radiation pressure and gas drag. Interestingly, this model requires HD 121617 to have a substantial amount of primordial gas, whereas for HD 131835 our modelling does not rule out either origin for the gas.

Outside of the ARKS sample, the disc around HD 141569A is well known to have a significantly different structure at long and short wavelengths and to have ample CO gas (Clampin et al. 2003; Perrot et al. 2016; White & Boley 2018; Miley et al. 2018; Di Folco et al. 2020). While the exact nature of this disc is uncertain (e.g., if it is a debris disc, a protoplanetary disc or a transitional disc), the disc is gas-rich and optically thin and so its dust should be subject to much of the same physics as considered here. However, its much more complex structure (e.g. a larger number of rings and asymmetries) almost certainly requires a more complex theoretical explanation accounting for gas thermal evolution and the photoelectric instability (Lyra & Kuchner 2013), dynamical effects from potential planets (Wyatt 2005), or slow modes of self-gravitating discs (Jalali & Tremaine 2012).

6. Conclusions

Observations of thermal emission and scattered light from around HD 131835 paint a complex picture of the debris disc in this system. There are two certain substructures in it: an inner dusty ring at $\sim$65 au and an outer ring at $\sim$100 au. In thermal emission, the inner ring is brighter than the outer one, while the opposite is seen in scattered light. We explored two different interpretations of these observations using numerical simulations and found that:

1. The observed brightness ratios of the two rings are completely incompatible with a simple paradigm of millimetre-wavelengths tracing the distribution of the planetesimals and dust being in an idealized collisional cascade with a standard power-law size distribution with a slope of 3.5;
2. The two dust rings could be signs of two planetesimal belts with different properties. However, extreme assumptions are required to explain the colour of the outer belt. The colour of the inner belt is consistent with a maximum initial orbital eccentricity of $\leq$0.3 and with dust grains that have a basalt-like material strength. The particles in the outer belt need to be of much weaker material (a difference of two to three orders of magnitude in the specific critical disruption energy). Alternatively, a higher dynamical excitation in the outer belt also moves our models closer to observational constraints, yet even an extreme maximum eccentricity of 0.9 is insufficient to explain the observations if the belts are of the same material and if their optical properties are similar to those of astrosilicates. Further study is needed to determine if combinations of different excitations and different materials, and/or different optical properties would help to match the observational constraints;
3. Our simple model of an inner ring that contains planetesimals that produce the dust, with the outer ring formed entirely of 1–10 µm-sized dust grains that migrated away

from the belt due to gas present in this system provides valuable insights. For example, the location of the outer ring and the relative brightness of the rings in scattered light could be matched with reasonable assumptions in this scenario. However, such an outer ring would be much fainter in both thermal emission and in scattered light than what is observed. We hypothesize that a model accounting for dust growth in the outer ring and evolution of the gas could better match the observations, although collisions and dust feedback on the gas structure could also prevent the formation of such an outer ring. Another possibility is that dust-gas interaction indeed creates the bright ring seen at short wavelengths, but only on top of an extended planetesimal disc (a smooth extension of the inner planetesimal belt);

4. Improved observations of the disc in scattered light that would better constrain the inner ring at short wavelengths would help to further test both scenarios. JWST observations would help to understand the distribution of the mid-sized dust grains, how they may or may not be affected by the gas drag, and possible radial variations in the grain composition.

Data availability

The ARKS data used in this paper can be found in the ARKS dataverse. For more information, visit arkslp.org.

Acknowledgements. We thank the referee for their thoughtful comments. MRJ acknowledges support from the European Union's Horizon Europe Programme under the Marie Sklodowska-Curie grant agreement no. 101064124 and funding provided by the Institute of Physics Belgrade, through the grant by the Ministry of Science, Technological Development, and Innovations of the Republic of Serbia. AB acknowledges research support by the Irish Research Council under grant GOIPG/2022/1895. JM acknowledges funding from the Agence Nationale de la Recherche through the DDISK project (grant No. ANR-21-CE31-0015) and from the PNP (French National Planetology Program) through the EPOPEE project. MB acknowledges funding from the Agence Nationale de la Recherche through the DDISK project (grant No. ANR-21-CE31-0015). A.A.S. is supported by the Heising-Simons Foundation through a 51 Pegasi b Fellowship. TDP is supported by a UKRI Stephen Hawking Fellowship and a Warwick Prize Fellowship, the latter made possible by a generous philanthropic donation. SMM acknowledges funding by the European Union through the E-BEANS ERC project (grant number 100117693), and by the Irish research Council (IRC) under grant number IRCLA-2022-3788. Views and opinions expressed are however those of the author(s) only and do not necessarily reflect those of the European Union or the European Research Council Executive Agency. Neither the European Union nor the granting authority can be held responsible for them. SM acknowledges funding by the Royal Society through a Royal Society University Research Fellowship (URF-R1-221669) and the European Union through the FEED ERC project (grant number 101162711). LM acknowledges funding by the European Union through the E-BEANS ERC project (grant number 100117693), and by the Irish research Council (IRC) under grant number IRCLA-2022-3788. Views and opinions expressed are however those of the author(s) only and do not necessarily reflect those of the European Union or the European Research Council Executive Agency. Neither the European Union nor the granting authority can be held responsible for them. EC acknowledges support from NASA STScI grant HST-AR-16608.001-A and the Simons Foundation. EM acknowledges support from the NASA CT Space Grant. PW acknowledges support from FONDECYT grant 3220399 and ANID – Millennium Science Initiative Program – Center Code NCN2024_001. AMH acknowledges support from the National Science Foundation under Grant No. AST-2307920. Support for BZ was provided by The Brinson Foundation. CdB acknowledges support from the Spanish Ministerio de Ciencia, Innovación y Universidades (MICIU) and the European Regional Development Fund (ERDF) under reference PID2023-153342NB-I00/10.13039/501100011033, from the Beatriz Galindo Senior Fellowship BG22/00166 funded by the MICIU, and the support from the Universidad de La Laguna (ULL) and the Consejería de Economía, Conocimiento y Empleo of the Gobierno de Canarias. This work was also supported by the NKFIH NKKP grant ADVANCED 149943 and the NKFIH excellence grant TKP2021-NKTA-64. Project no.149943 has been implemented with the support provided by the Ministry of Culture and Innovation of Hungary from the National Research, Development and Innovation Fund, financed under the NKKP ADVANCED funding scheme. SP acknowledges support from FONDECYT Regular 1231663 and ANID – Millennium Science Initiative Program – Center Code NCN2024_001. This paper makes use of the following ALMA data: ADS/JAO.ALMA# 2022.1.00338.L, 2012.1.00142.S, 2012.1.00198.S, 2015.1.01260.S, 2016.1.00104.S, 2016.1.00195.S, 2016.1.00907.S, 2017.1.00167.S, 2017.1.00825.S, 2018.1.01222.S and 2019.1.00189.S. ALMA is a partnership of ESO (representing its member states), NSF (USA) and NINS (Japan), together with NRC (Canada), MOST and ASIAA (Taiwan), and KASI (Republic of Korea), in cooperation with the Republic of Chile. The Joint ALMA Observatory is operated by ESO, AUI/NRAO and NAOJ. The National Radio Astronomy Observatory is a facility of the National Science Foundation operated under cooperative agreement by Associated Universities, Inc. The project leading to this publication has received support from ORP, that is funded by the European Union's Horizon 2020 research and innovation programme under grant agreement No. 101004719 [ORP]. We are grateful for the help of the UK node of the European ARC in answering our questions and producing calibrated measurement sets. This research used the Canadian Advanced Network For Astronomy Research (CANFAR) operated in partnership by the Canadian Astronomy Data Centre and The Digital Research Alliance of Canada with support from the National Research Council of Canada the Canadian Space Agency, CANARIE and the Canadian Foundation for Innovation.

References

Benz, W., & Asphaug, E. 1999, Icarus, 142, 5
Besla, G., & Wu, Y. 2007, ApJ, 655, 528
Beuzit, J. L., Vigan, A., Mouillet, D., et al. 2019, A&A, 631, A155
Bhowmik, T., Boccaletti, A., Thébault, P., et al. 2019, A&A, 630, A85
Bonsor, A., Wyatt, M. C., Marino, S., et al. 2023, MNRAS, 526, 3115
Booth, M., Pearce, T. D., Krivov, A. V., et al. 2023, MNRAS, 521, 6180
Brennan, A., Matrà, L., Mac Manamon, S., et al. 2026, A&A, 705, A201
Brennan, A., Matrà, L., Marino, S., et al. 2024, MNRAS, 531, 4482
Burns, J. A., Lamy, P. L., & Soter, S. 1979, Icarus, 40, 1
Cataldi, G., Brandeker, A., Wu, Y., et al. 2018, ApJ, 861, 72
Cataldi, G., Wu, Y., Brandeker, A., et al. 2020, ApJ, 892, 99
Cataldi, G., Aikawa, Y., Iwasaki, K., et al. 2023, ApJ, 951, 111
Chiang, E. I., & Goldreich, P. 1997, ApJ, 490, 368
Chiang, E. I., Joung, M. K., Creech-Eakman, M. J., et al. 2001, ApJ, 547, 1077
Clampin, M., Krist, J. E., Ardila, D. R., et al. 2003, AJ, 126, 385
de Zeeuw, P. T., Hoogerwerf, R., de Bruijne, J. H. J., Brown, A. G. A., & Blaauw, A. 1999, AJ, 117, 354
Dent, W. R. F., Wyatt, M. C., Roberge, A., et al. 2014, Science, 343, 1490
Di Folco, E., Péricaud, J., Dutrey, A., et al. 2020, A&A, 635, A94
Dohnanyi, J. S. 1969, JGR, 74, 2531
Draine, B. T. 2003, ARA&A, 41, 241
Dullemond, C. P., Juhasz, A., Pohl, A., et al. 2012, RADMC-3D: A multi-purpose radiative transfer tool, Astrophysics Source Code Library [record ascl:1202.015]
Faramaz, V., Beust, H., Thébault, P., et al. 2014, A&A, 563, A72
Faramaz, V., Ertel, S., Booth, M., Cuadra, J., & Simmonds, C. 2017, MNRAS, 465, 2352
Farhat, M. A., Sefilian, A. A., & Touma, J. R. 2023, MNRAS, 521, 2067
Feldt, M., Olofsson, J., Boccaletti, A., et al. 2017, A&A, 601, A7
Friebe, M. F., Pearce, T. D., & Löhne, T. 2022, MNRAS, 512, 4441
Gaia Collaboration (Vallenari, A., et al.) 2023, A&A, 674, A1
Grigorieva, A., Thébault, P., Artymowicz, P., & Brandeker, A. 2007, A&A, 475, 755
Hales, A. S., Gorti, U., Carpenter, J. M., Hughes, M., & Flaherty, K. 2019, ApJ, 878, 113
Han, Y., Wyatt, M. C., & Matrà, L. 2022, MNRAS, 511, 4921
Han, Y., Wyatt, M. C., & Marino, S. 2025, MNRAS, 537, 3839
Han, Y., Mansell, E., Jennings, J., et al. 2026, A&A, 705, A196
Higuchi, A. E., Sato, A., Tsukagoshi, T., et al. 2017, ApJ, 839, L14
Huet, P., Kral, Q., & Guillot, T. 2025, A&A, 699, A278
Hughes, A. M., Duchêne, G., & Matthews, B. C. 2018, ARA&A, 56, 541
Hung, L.-W., Duchêne, G., Arriaga, P., et al. 2015a, ApJ, 815, L14
Hung, L.-W., Fitzgerald, M. P., Chen, C. H., et al. 2015b, ApJ, 802, 138
Ida, S., & Makino, J. 1993, Icarus, 106, 210
Jackson, A. P., Wyatt, M. C., Bonsor, A., & Veras, D. 2014, MNRAS, 440, 3757
Jalali, M. A., & Tremaine, S. 2012, MNRAS, 421, 2368
Jennings, J., Booth, R. A., Tazzari, M., Rosotti, G. P., & Clarke, C. J. 2020, MNRAS, 495, 3209
Jones, J. W., Chiang, E., Duchêne, G., Kalas, P., & Esposito, T. M. 2023, ApJ, 948, 102
Kenyon, S. J., & Bromley, B. C. 2002a, AJ, 123, 1757
Kenyon, S. J., & Bromley, B. C. 2002b, ApJ, 577, L35
Kenyon, S. J., & Bromley, B. C. 2004a, AJ, 127, 513

Kenyon, S. J., & Bromley, B. C. 2004b, ApJ, 602, L133
Kenyon, S. J., & Bromley, B. C. 2008, ApJS, 179, 451
Kenyon, S. J., & Bromley, B. C. 2010, ApJS, 188, 242
Klahr, H., & Lin, D. N. C. 2005, ApJ, 632, 1113
Kóspál, Á., Moór, A., Juhász, A., et al. 2013, ApJ, 776, 77
Kral, Q., Wyatt, M., Carswell, R. F., et al. 2016, MNRAS, 461, 845
Kral, Q., Matrà, L., Wyatt, M. C., & Kennedy, G. M. 2017, MNRAS, 469, 521
Kral, Q., Marino, S., Wyatt, M. C., Kama, M., & Matrà, L. 2019, MNRAS, 489, 3670
Kral, Q., Matrà, L., Kennedy, G. M., Marino, S., & Wyatt, M. C. 2020, MNRAS, 497, 2811
Krivov, A. V. 2010, Res. Astron. Astrophys., 10, 383
Krivov, A. V., & Booth, M. 2018, MNRAS, 479, 3300
Krivov, A. V., Sremčević, M., & Spahn, F. 2005, Icarus, 174, 105
Krivov, A. V., Löhne, T., & Sremčević, M. 2006, A&A, 455, 509
Krivov, A. V., Herrmann, F., Brandeker, A., & Thébault, P. 2009, A&A, 507, 1503
Leinhardt, Z. M., & Stewart, S. T. 2009, Icarus, 199, 542
Leinhardt, Z. M., & Stewart, S. T. 2012, ApJ, 745, 79
Lestrade, J. F., Matthews, B. C., Kennedy, G. M., et al. 2025, A&A, 694, A123
Lieman-Sifry, J., Hughes, A. M., Carpenter, J. M., et al. 2016, ApJ, 828, 25
Löhne, T., Eiroa, C., Augereau, J.-C., et al. 2012, Astron. Nat., 333, 441
Löhne, T., Krivov, A. V., Kirchschlager, F., Sende, J. A., & Wolf, S. 2017, A&A, 605, A7
Löhne, T., Krivov, A. V., & Rodmann, J. 2008, ApJ, 673, 1123
Lovell, J. B., Hales, A. S., Kennedy, G. M., et al. 2026, A&A, 705, A200
Lynden-Bell, D., & Pringle, J. E. 1974, MNRAS, 168, 603
Lyra, W., & Kuchner, M. 2013, Nature, 499, 184
Mac Manamon, S., Matrà, L., Marino, S., et al. 2026, A&A, 705, A198
Malhotra, R. 1993, Nature, 365, 819
Malhotra, R. 1995, AJ, 110, 420
Mamajek, E. E., Meyer, M. R., & Liebert, J. 2002, AJ, 124, 1670
Marino, S. 2022, arXiv e-prints [arXiv:2202.03053]
Marino, S., Flock, M., Henning, T., et al. 2020, MNRAS, 492, 4409
Marino, S., Cataldi, G., Jankovic, M. R., Matrà, L., & Wyatt, M. C. 2022, MNRAS, 515, 507
Marino, S., Gupta, V., Weber, P., et al. 2026a, A&A, 705, A202
Marino, S., Matrà, L., Hughes, A. M., et al. 2026b, A&A, 705, A195
Matrà, L., Öberg, K. I., Wilner, D. J., Olofsson, J., & Bayo, A. 2019a, AJ, 157, 117
Matrà, L., Wyatt, M. C., Wilner, D. J., et al. 2019b, AJ, 157, 135
Matthews, B. C., Krivov, A. V., Wyatt, M. C., Bryden, G., & Eiroa, C. 2014, in Protostars and Planets VI, eds. H. Beuther, R. S. Klessen, C. P. Dullemond, & T. Henning, 521
Miley, J. M., Panić, O., Wyatt, M., & Kennedy, G. M. 2018, A&A, 615, L10
Milli, J., Olofsson, J., Bonduelle, M., et al. 2026, A&A, 705, A199
Milli, J., Mouillet, D., Lagrange, A. M., et al. 2012, A&A, 545, A111
Milli, J., Choquet, E., Tazaki, R., et al. 2024, A&A, 683, A22
Moór, A., Henning, T., Juhász, A., et al. 2015, ApJ, 814, 42
Moór, A., Curé, M., Kóspál, Á., et al. 2017, ApJ, 849, 123
Moór, A., Kral, Q., Ábrahám, P., et al. 2019, ApJ, 884, 108
Murray, C. D., & Dermott, S. F. 1999, Solar System Dynamics (Cambridge University Press)
Mustill, A. J., & Wyatt, M. C. 2009, MNRAS, 399, 1403
Nakagawa, Y., Sekiya, M., & Hayashi, C. 1986, Icarus, 67, 375
Nakatani, R., Kobayashi, H., Kuiper, R., Nomura, H., & Aikawa, Y. 2021, ApJ, 915, 90
Olofsson, J., Thébault, P., Kral, Q., et al. 2022, MNRAS, 513, 713
Ooyama, W., Nakatani, R., Hosokawa, T., Mitani, H., & Turner, N. J. 2025, ApJ, 983, 153
Pawellek, N., Moór, A., Kirchschlager, F., et al. 2024, MNRAS, 527, 3559
Pearce, T. D. 2024, arXiv e-prints [arXiv:2403.11804]
Pearce, T. D., & Wyatt, M. C. 2014, MNRAS, 443, 2541
Pearce, T. D., Krivov, A. V., & Booth, M. 2020, MNRAS, 498, 2798
Pearce, T. D., Krivov, A. V., Sefilian, A. A., et al. 2024, MNRAS, 527, 3876
Pecaut, M. J., Mamajek, E. E., & Bubar, E. J. 2012, ApJ, 746, 154
Perrot, C., Boccaletti, A., Pantin, E., et al. 2016, A&A, 590, L7
Quillen, A. C. 2007, MNRAS, 377, 1287
Rigley, J. K., & Wyatt, M. C. 2020, MNRAS, 497, 1143
Sefilian, A. A. 2024, ApJ, 966, 140
Sefilian, A. A., Rafikov, R. R., & Wyatt, M. C. 2021, ApJ, 910, 13
Sefilian, A. A., Kratter, K. M., Wyatt, M. C., et al. 2025, MNRAS, 543, 3123
Sibthorpe, B., Kennedy, G. M., Wyatt, M. C., et al. 2018, MNRAS, 475, 3046
Sommer, M., Wyatt, M., & Han, Y. 2025, MNRAS, 539, 439
Stewart, S. T., & Leinhardt, Z. M. 2009, ApJ, 691, L133
Strubbe, L. E., & Chiang, E. I. 2006, ApJ, 648, 652
Takeuchi, T., & Artymowicz, P. 2001, ApJ, 557, 990
Terrill, J., Marino, S., Booth, R. A., et al. 2023, MNRAS, 524, 1229
Thébault, P., & Wu, Y. 2008, A&A, 481, 713
Thébault, P., & Augereau, J. C. 2005, A&A, 437, 141
Thebault, P., & Kral, Q. 2019, A&A, 626, A24
Thebault, P., Olofsson, J., & Kral, Q. 2023, A&A, 674, A51
Thureau, N. D., Greaves, J. S., Matthews, B. C., et al. 2014, MNRAS, 445, 2558
Weber, P., Pérez, S., Baruteau, C., et al. 2026, A&A, 705, A203
White, J. A., & Boley, A. C. 2018, ApJ, 859, 103
Wyatt, M. C. 2005, A&A, 440, 937
Wyatt, M. C. 2008, ARA&A, 46, 339
Wyatt, M. 2020, in The Trans-Neptunian Solar System, eds. D. Prialnik, M. A. Barucci, & L. Young, 351
Wyatt, M. C., Smith, R., Greaves, J. S., et al. 2007, ApJ, 658, 569
Zuckerman, B., & Song, I. 2012, ApJ, 758, 77

[1] Institute of Physics Belgrade, University of Belgrade, Pregrevica 118, 11080 Belgrade, Serbia
[2] Institut für Astrophysik, Universität Wien, Türkenschanzstraße 17, 1180 Wien, Austria
[3] Konkoly Observatory, HUN-REN Research Centre for Astronomy and Earth Sciences, MTA Centre of Excellence, Konkoly-Thege Miklós út 15–17, 1121 Budapest, Hungary
[4] Astrophysikalisches Institut und Universitätssternwarte, Friedrich-Schiller-Universität Jena, Schillergäßchen 2–3, 07745 Jena, Germany
[5] European Southern Observatory, Karl-Schwarzschild-Strasse 2, 85748 Garching bei München, Germany
[6] School of Physics, Trinity College Dublin, the University of Dublin, College Green, Dublin 2, Ireland
[7] Univ. Grenoble Alpes, CNRS, IPAG, 38000 Grenoble, France
[8] Institute of Astronomy, University of Cambridge, Madingley Road, Cambridge CB3 0HA, UK
[9] Department of Astronomy and Steward Observatory, The University of Arizona, 933 North Cherry Ave, Tucson, AZ 85721, USA
[10] Department of Physics, University of Warwick, Gibbet Hill Road, Coventry CV4 7AL, UK
[11] Division of Geological and Planetary Sciences, California Institute of Technology, 1200 E. California Blvd., Pasadena, CA 91125, USA
[12] Department of Physics and Astronomy, University of Exeter, Stocker Road, Exeter EX4 4QL, UK
[13] UK Astronomy Technology Centre, Royal Observatory Edinburgh, Blackford Hill, Edinburgh EH9 3HJ, UK
[14] Department of Astronomy, University of California, Berkeley, Berkeley, CA 94720-3411, USA
[15] Department of Astronomy, Van Vleck Observatory, Wesleyan University, 96 Foss Hill Dr., Middletown, CT 06459, USA
[16] Departamento de Física, Universidad de Santiago de Chile, Av. Víctor Jara 3493, Santiago, Chile
[17] Millennium Nucleus on Young Exoplanets and their Moons (YEMS), Chile
[18] Center for Interdisciplinary Research in Astrophysics Space Exploration (CIRAS), Universidad de Santiago, Chile
[19] Center for Astrophysics | Harvard & Smithsonian, 60 Garden St, Cambridge, MA 02138, USA
[20] Instituto de Astrofísica de Canarias, Vía Láctea S/N, La Laguna, 38200 Tenerife, Spain
[21] Departamento de Astrofísica, Universidad de La Laguna, La Laguna, 38200 Tenerife, Spain
[22] Institute of Physics and Astronomy, ELTE Eötvös Loránd University, Pázmány Péter sétány 1/A, 1117 Budapest, Hungary
[23] Max-Planck-Insitut für Astronomie, Königstuhl 17, 69117 Heidelberg, Germany
[24] Joint ALMA Observatory, Avenida Alonso de Córdova 3107, Vitacura 7630355, Santiago, Chile

Appendix A: Particle-in-a-box collisional model

We employ a particle-in-a-box collisional model from Wyatt et al. (2007) and Rigley & Wyatt (2020) with some changes. We assume that particles are moving within a ring centred at stellocentric radius r, of width Δr and aspect ratio h, whose volume is given by

$$V = 4\pi r^2 \Delta r h. \tag{A.1}$$

These particles are colliding, on average, at a velocity proportional to their average orbital inclination i,

$$v_{\rm imp} = i v_{\rm K}. \tag{A.2}$$

We assume a fixed power-law size distribution with exponent $q = 3.5$ (Eq. (1)) and normalization factor K given by

$$K = \frac{3(4-q)}{4\pi\rho_{\rm s}} s_{\rm max,dust}^{q-4} M_{\rm dust}, \tag{A.3}$$

where $M_{\rm dust}$ is the total mass of grains smaller than $s_{\rm max,dust} = 1$ cm in radius. Furthermore, all particles in the disc collide with each other, but only some of the collisions result in catastrophic disruption. *If* there is a minimum, critical projectile size s_c that can break up targets of size $s_{\rm t}$, that is not too close to either the minimum or the maximum size of bodies in the disc, the collisional lifetime of targets of size $s_{\rm t}$ is given by

$$t_{\rm coll} \approx \frac{(q-1)V}{\pi K v_{\rm imp}} s_{\rm c}^{q-1} s_{\rm t}^{-2}. \tag{A.4}$$

In general, for a projectile of mass $m_{\rm p}$ to destroy a target of mass $m_{\rm t}$, the impact energy must exceed the minimum energy required to break up the target,

$$\frac{m_{\rm t} m_{\rm p}}{m_{\rm t} + m_{\rm p}} \frac{v_{\rm imp}^2}{2} > Q_{\rm D}^* m_{\rm t}, \tag{A.5}$$

where $Q_{\rm D}^*$ is the specific critical energy for dispersal (a quantity dependent on the target size, material and impact velocity, e.g., Benz & Asphaug 1999). The critical projectile size is the minimum projectile size to fulfill that condition. *If* the critical projectile size is much smaller than the target size,

$$\frac{m_{\rm c}}{m_{\rm t}} = \frac{2Q_{\rm D}^*}{v_{\rm imp}^2}. \tag{A.6}$$

However, we find that the critical projectile size calculated in this way can exceed the target size within the ranges of relevant parameters in HD 131835. Thus, we modify this model in the following way.

We assume that regardless of the projectile-target size ratio, the entire impact energy is always used up to destroy the target. That leads to a slightly more general expression for the critical projectile size,

$$\frac{m_{\rm c}}{m_{\rm t}} = \frac{\frac{2Q_{\rm D}^*}{v_{\rm imp}^2}}{1 - \frac{2Q_{\rm D}^*}{v_{\rm imp}^2}}. \tag{A.7}$$

As projectile size reaches the target size, some of the impact energy should also be spent on destroying or cratering the projectile. How the impact energy would be partitioned depends on the complex physics of collisions and material deformation. By neglecting any deformation to the 'projectile', we obtain a lower limit on the target lifetime.

Furthermore, if $2Q_{\rm D}^*/v_{\rm imp}^2 \geq 1$, or if $s_{\rm c}$ exceeds the maximum size of bodies in the disc, particles of size $s_{\rm t}$ cannot be destroyed, at least not at the average impact velocity $v_{\rm imp}$. Most particles like this should thus survive from the time they are produced to the system age, in this simple model.

A&A, 705, A203 (2026)
https://doi.org/10.1051/0004-6361/202556855
© The Authors 2026

Astronomy & Astrophysics

The ALMA survey to Resolve exoKuiper belt Substructures (ARKS)

IX. Gas-driven origin for the continuum arc in the debris disc of HD 121617

P. Weber[1,2,3,⋆], S. Pérez[1,2,3], C. Baruteau[4], S. Marino[5], F. Castillo[1,2,3], M. R. Jankovic[6], T. Pearce[7], M. C. Wyatt[8], A. A. Sefilian[9], J. Olofsson[10], G. Cataldi[11,12], J. B. Lovell[13], C. del Burgo[14,15], A. M. Hughes[16], S. Mac Manamon[17], A. Brennan[17], L. Matrà[17], J. Milli[18], B. Zawadzki[16], E. Chiang[19], M. A. MacGregor[20], D. J. Wilner[13], M. Bonduelle[18], J. M. Carpenter[21], Y. Han[22], Á. Kóspál[23,24,25], and P. Luppe[17]

(Affiliations can be found after the references)

Received 14 August 2025 / Accepted 25 September 2025

ABSTRACT

Context. Debris discs were long considered to be largely gas-free environments, where dynamical evolution is governed primarily by collisional fragmentation, gravitational stirring, and radiative forces. Recent detections of CO molecular line emission in debris discs demonstrate that gas is present, but its abundance and origin are still uncertain. The *ALMA survey to Resolve exoKuiper belt Substructures (ARKS)* observed both the gas and dust of several debris discs at high resolution and revealed a narrow ring of gas and dust in the disc HD 121617, with an asymmetric arc-like feature that is 40% brighter than the rest of the ring.

Aims. An important open question is how representative the estimated CO masses are for the total gas mass in debris discs. We aim to constrain the total gas mass in HD 121617 using numerical models under the assumption that the dust arc is produced by hydrodynamical processes involving the gas.

Methods. We used the hydrodynamical code Dusty FARGO-ADSG, in which dust is modelled as Lagrangian particles. We explored the effects of radiation pressure and dust feedback, as well as of varying the total gas mass on the dynamical evolution of the system. We compared these simulations with observations via radiative transfer calculations.

Results. We find that an unstable gas ring can create a size-dependent radial and azimuthal dust trap. The total gas mass dictates the efficiency of particle trapping as a function of grain size. We find that two of our models, $M_{\rm gas} = 50\,M_{\oplus}$ and $M_{\rm gas} = 5\,M_{\oplus}$, can simultaneously reproduce the observed arc in the ALMA band 7 continuum image and the radial outward offset of the VLT/SPHERE scattered light ring, driven by the combined effects of gas drag and radiation pressure. We further find a conservative lower limit of $M_{\rm gas} > 2.5\,M_{\oplus}$ and a conservative upper limit of $M_{\rm gas} < 250\,M_{\oplus}$.

Conclusions. If the ALMA band 7 asymmetry is caused by gas drag, reconciling the required gas mass with the observed ^{12}CO emission suggests the presence of significant amounts of H_2, consistent with the gas being primordial, that is, long-lived remnant material from the protoplanetary disc phase. In this scenario, HD 121617 would represent a hybrid disc, bridging the protoplanetary and debris disc stages. As an arc-shaped emission can alternatively be reproduced by a planet's gravitational forcing, future observations are crucial to distinguish between these two scenarios.

Key words. methods: numerical – methods: observational – surveys – planets and satellites: general – protoplanetary disks – Kuiper belt objects: individual: HD 121617

1. Introduction

Debris discs consist of a dust population that is predominantly generated by collisions between larger bodies (e.g., Hughes et al. 2018; Marino 2022; Pearce 2024). Therefore, they are generally regarded as second-generation discs in which dust is continually replenished. The advent of the Atacama Large Millimetre/Submillimetre Array (ALMA) has not only provided unprecedented angular resolution to investigate thermal emission from these structures, but has also revealed that some debris discs harbour substantial amounts of gaseous carbon monoxide (CO, e.g. Kóspál et al. 2013; Hughes et al. 2018; Cataldi et al. 2023) with mass estimates ranging from $10^{-6}\,M_{\oplus}$ to $10^{-1}\,M_{\oplus}$ (Cataldi et al. 2023; Mac Manamon et al. 2025). In the pre-ALMA era, the prevailing view (apart from the case of 49 Ceti, Zuckerman et al. 1995) was that debris discs should be gas-free environments, since the primordial gas in protoplanetary discs is expected to be dispersed near the end of the disc phase by a combination of processes, including photoevaporation, magnetically driven (magnetothermal) winds, and viscous draining (e.g. Clarke et al. 2001; Alexander et al. 2014; Ercolano & Pascucci 2017; Bai et al. 2016). Therefore, the detection of CO is of utmost interest, as it challenges this classical notion of gas-free debris discs.

In several systems, the estimated CO mass is too large to be consistent with the expected gas production rate from cometary mass loss (Kral et al. 2017), prompting questions about the origin of the CO. Two favoured scenarios have been proposed: either the gas from the protoplanetary phase persists for longer than previously thought (primordial gas, e.g. Kóspál et al. 2013; Nakatani et al. 2021), or it is released during the debris disc phase from the volatile-rich solid bodies, either by collisions (e.g. Czechowski & Mann 2007; Bonsor et al. 2023) or photodesorption (Grigorieva et al. 2007) and subsequently shielded

⋆ Corresponding author: philipppweber@gmail.com

Open Access article, published by EDP Sciences, under the terms of the Creative Commons Attribution License (https://creativecommons.org/licenses/by/4.0), which permits unrestricted use, distribution, and reproduction in any medium, provided the original work is properly cited.
This article is published in open access under the Subscribe to Open model. Subscribe to A&A to support open access publication.

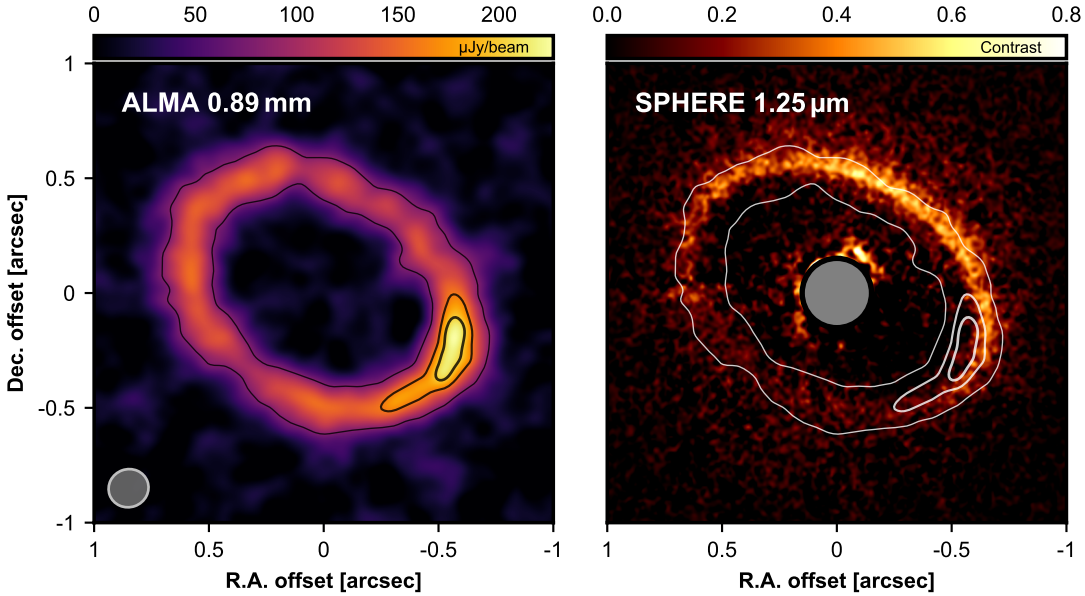

Fig. 1. Observations of HD 121617. The left panel shows the ALMA band 7 continuum observation (λ_{obs} = 0.89 mm) from Marino et al. (2026a). The contours at [80, 160, 200] μJy/beam highlight the ring's azimuthal asymmetry. The clean beam is displayed as a white ellipse in the bottom left. The right panel shows the SPHERE/IRDIS J-band scattered light image (λ_{obs} = 1.25 μm) from Milli et al. (2026), with the same ALMA continuum contours. The grey circle indicates the coronagraphic mask of the observation.

from ultraviolet (UV) radiation (secondary gas; Kral et al. 2019; Marino et al. 2020).

The chemical composition in the primordial and secondary scenarios differs considerably (e.g. Klusmeyer et al. 2021; Smirnov-Pinchukov et al. 2022). In the secondary gas scenario, CO, C and O are the principal constituents; in contrast, the primordial-gas scenario implies a total gas mass dominated by molecular hydrogen, H_2, leading to a total gas mass significantly larger than that inferred from CO observations. Although direct observation of gas tracers often struggles to distinguish between these scenarios, each has markedly different implications for dust dynamics. Gas and dust co-located in the disc exchange momentum through friction, whose strength depends on both the grain surface area per unit mass and the local gas density (e.g. Safronov 1972; Whipple 1972). Consequently, a sufficiently dense gas phase is needed to exert a notable drag force on dust grains. If composed of second-generation gas, the total gas mass would be relatively low and frictional coupling with millimetre-sized dust would remain negligible (Marino et al. 2020). In contrast, if the gas composition resembles that of typical protoplanetary discs (i.e. abundant, yet undetected in H_2), even the mm dust would likely experience significant dust–gas interactions.

While the interaction between dust and gas has been extensively investigated in protoplanetary discs (see Lesur et al. 2023, for a recent review), relatively few studies have focused on this process in the context of debris discs. One of the main differences between the two environments is that debris discs are optically thin to stellar radiation, and studies of optically thick protoplanetary discs cannot be directly applied. In optically thin discs, radiation pressure works in conjunction with gas drag to reshape the spatial distribution of small dust grains (Takeuchi & Artymowicz 2001). Resulting effects on the dust radial and vertical structure have often been studied assuming a fixed gas distribution and an azimuthally symmetric disc (Thébault & Augereau 2005; Krivov et al. 2009; Olofsson et al. 2022; Jankovic et al. 2026), although there are several studies that considered frictional coupling between the dust and the gas (e.g. Klahr & Lin 2005; Besla & Wu 2007; Lyra & Kuchner 2013; Castrejon et al. 2019). In studies focusing on gas production, destruction, and evolution of secondary gas (e.g. Kral et al. 2016, 2017, 2019; Hales et al. 2019; Marino et al. 2020), or the effect of a planet on secondary gas dynamics (Bergez-Casalou & Kral 2024), dust was treated only as a tracer species or omitted altogether. Overall, these works highlight that hydrodynamical processes, previously assumed to be negligible in debris discs, may indeed be essential to understanding observed structures.

Within the sample of objects observed by the ALMA survey to Resolve exoKuiper belt Substructures (ARKS, Marino et al. 2026a), the debris disc around HD 121617 stands out as a specifically interesting case. The left panel of Fig. 1 shows the ARKS ALMA band 6 observation of HD 121617 (Marino et al. 2026a) that exhibits an arc to the southwest in the dust continuum (Marino et al. 2026b; Lovell et al. 2026) reminiscent of protoplanetary disc structures formed through dust trapping in a gas vortex (e.g. Meheut et al. 2012; Baruteau et al. 2019). Comparable examples in protoplanetary discs include the systems MWC 758 (Baruteau et al. 2019), HD 143006 (Pérez et al. 2018) and PDS 70 (Doi et al. 2024, Daza et al. in prep.). The right panel of Fig. 1 shows the VLT/SPHERE J-band image of HD 121617 presented in Milli et al. (2026) with the original data presented in Perrot et al. (2023). The comparison shows that, in addition to its pronounced azimuthal asymmetry at mm wavelengths, the ring around HD 121617 shows a radial outward offset in the J-band scattered light image relative to the radial peak of mm emission. This is indicative of radial segregation between dust grains of different sizes, and a small eccentricity, but no significant asymmetry (Milli et al. 2026). The combination of azimuthally confined continuum emission (Lovell et al. 2026; Marino et al. 2026b), substantial CO gas content (Moór et al. 2017; Mac Manamon et al. 2025), lack of an arc in the distribution of small grains, and the observed radial offset in scattered light (Milli et al. 2026) makes HD 121617 a compelling target for

investigating whether, and under which conditions, gas drag can shape the dust distribution in a debris disc.

HD 121617 is an A1-type pre-main-sequence star located at a distance of 117.9±0.4 pc (Gaia Collaboration 2023), with an estimated age of 16 ± 2 Myr and a luminosity of $14.0^{+0.4}_{-0.3}$ $L_\odot$(Matrà et al. 2025), a mass of 1.901 ± 0.009 $M_\odot$, a radius of 1.553 ± 0.01 $R_\odot$, and an effective temperature of 9029 ± 34 K (Marino et al. 2026a). HD 121617's age places it as an object of interest possibly transitioning from the protoplanetary disc phase to a debris disc stage, marking it as a potential hybrid system with primordial gas. The dust mass is estimated to be 0.21 ± 0.02 $M_\oplus$ (Marino et al. 2026a, see also Perrot et al. 2023), while radiative transfer models of HD 121617 show that the molecular line emission from ^{13}CO and ^{12}CO are optically thick indicating (model dependent) masses as high as $M\left(^{13}\mathrm{CO}\right)=2^{+0.5}_{-0.7}\times10^{-3}$ $M_\oplus$ and $M\left(^{12}\mathrm{CO}\right)\sim0.15$ $M_\oplus$, respectively (Brennan et al. 2026). If the disc retains a significant fraction of primordial gas inherited from the protoplanetary disc stage, the total gas mass would likely exceed the measured CO mass by several orders of magnitude (see Williams & Best 2014, for a discussion). In particular, HD 121617 exhibits several signatures that we investigate in the context of dust–gas interactions in a debris disc. The key observables are: (i) an azimuthally confined dust overdensity producing a local brightness enhancement of about 40% at 0.89 mm, with an azimuthal extent characterised by a full width at half maximum (FWHM) of roughly 90° (Marino et al. 2026b); (ii) a near-infrared scattered-light ring located about 9.5% farther out than the submillimetre ring (Milli et al. 2026); and (iii) a mirror symmetry of the scattered-light ring with respect to the semi-minor axis (Milli et al. 2026).

In this paper, we present a model that qualitatively explains these features as the outcome of dust–gas interactions. Our results show that an unstable gas ring can simultaneously explain the azimuthal brightness variations seen in the ALMA band 7 continuum and the radial offset of the scattered light ring. At the outset, however, we note that our proposed explanation for the observations of HD 121617 is not unique; a gas-free scenario in which gravitational forcing by a migrating planet produces the observed structure will be explored in future work (Pearce et al., in preparation).

The rest of the paper is structured as follows: We present the simulation setup and numerical methods in Sect. 2. We present the main results in Sect. 3. An observational comparison based on radiative transfer and image synthesis is presented in Sect. 4. We discuss our findings and suggest tests for future observations in Sect. 5 and conclude in Sect. 6. Technical details of calculations are presented in Appendices A and B.

2. Hydrodynamical simulations

Hydrodynamical simulations are commonly used to explore protoplanetary disc dynamics, where it is generally assumed that the total disc mass is dominated by gas. On the other hand, hydrodynamics had long been considered irrelevant for the study of debris discs, until the discovery of significant CO emission in various exoKuiper belts raised the possibility that gas could affect dust structures and evolution. A key distinction between protoplanetary discs and debris discs is the difference in both dust and gas densities. The higher dust masses of protoplanetary discs generally make them optically thick to the stellar irradiation, and their gas densities are sufficiently high for micron-sized grains to remain tightly coupled to the gas flow. By contrast, debris discs are commonly believed to be optically thin at all wavelengths (inferred from their small fractional luminosities), making small dust grains susceptible to radiation pressure. Furthermore, the lower gas density in debris discs (especially for the secondary gas origin) implies that even micron-sized grains decouple from the gas dynamics. While an interstellar medium–like (ISM-like) dust-to-gas ratio of about 1% is typically assumed in protoplanetary discs (Williams & Cieza 2011), this ratio can be much larger in debris discs (e.g. Moór et al. 2017).

These differences in gas density imply that not all techniques developed for protoplanetary disc simulations can be directly applied to debris discs. For example, the low gas densities expected in debris discs imply long momentum stopping times for the dust. This opens up the possibility that multiple streams of dust moving in multiple directions can be present at a single location, making it inappropriate to treat dust as a pressureless fluid with a single velocity at a given location (as already highlighted in a simplistic approach by Lynch et al. 2024). Meanwhile, stellar irradiation exerts a significant radiation pressure on dust particles throughout the disc that can become relevant for small dust grains of a high surface-to-mass ratio, necessitating an explicit numerical treatment of this force, as done here. Finally, because of the potentially high dust-to-gas ratio in debris discs, we include both the frictional effect of the gas onto the dust and the back-reaction of the dust onto the gas dynamics.

We set up numerical simulations to determine whether gas friction influences dust structures around HD 121617, specifically the arc observed in the ALMA band 7 continuum (Marino et al. 2026a) and the offset seen in scattered light (Milli et al. 2026). We used the hydrodynamical code Dusty FARGO-ADSG[1] (Baruteau & Zhu 2016), which is based on the FARGO algorithm (a fast Eulerian transport algorithm for differentially rotating discs, Masset 2000), and allows gas and dust to evolve in two dimensions (radial and azimuthal). In this framework, the gas is defined as an Eulerian fluid on a fixed grid, while the dust is represented by Lagrangian particles, i.e. discrete fluid elements that are tracked as they move through the flow field. Here, each computational particle (superparticle) in the simulation can be thought of as a collection of physical dust grains. The following subsections describe how we initialise the key hydrodynamic fields and outline essential numerical details.

2.1. Disc setup

We initialised the gas density as an azimuthally smooth ring around the central star, represented by a Gaussian radial profile atop a Gaussian background function, motivated by the radial profiles presented in Han et al. (2026). Specifically, we set the initial gas surface density to

$$\Sigma_\mathrm{g} = \Sigma_0 \times \exp\left(-\frac{(r-r_0)^2}{2\sigma^2}\right) + \Sigma_\mathrm{bg} \times \exp\left(-\frac{(r-r_\mathrm{bg})^2}{2\sigma_\mathrm{bg}^2}\right), \quad (1)$$

where r_0 and r_bg are the characteristic radii of the ring centre and the background centre, respectively, and σ and σ_bg are the ring's and the background's half-widths. The ring's stability is particularly sensitive to its width σ and to the contrast between the ring's maximum density Σ_0 and the background density (e.g. Ono et al. 2018). In our simulations, the initial density distribution corresponded to a narrow ring (small σ) with a high contrast, defined as $C \equiv \Sigma_0/\Sigma_\mathrm{bg} \gg 1$. In Section 3.2, we chose these parameters such that the ring became susceptible to the

[1] https://github.com/charango/dustyfargoadsg

Rossby Wave Instability (RWI; Lovelace et al. 1999). The RWI can be triggered when the disc's vortensity (the ratio of flow vorticity to density) exhibits a local extremum (necessary but not sufficient criterion, Lovelace et al. 1999)[2].

Even in protoplanetary discs, where gas dynamics has long been seen as the most important driver of evolution, the magnitude and origin of viscosity remain poorly constrained (see Lesur et al. 2023; Rosotti 2023, for comprehensive reviews). This uncertainty is even greater in debris discs, where the relevance of gas dynamics has only been considered in recent years. For a comprehensive review of potential viscosity sources in these environments, we refer to Cui et al. (2024). Here, we employed the α-viscosity model (Shakura & Sunyaev 1973) for the kinematic viscosity, $\nu = \alpha\, c_s^2\, \Omega_K^{-1}$, where c_s is the sound speed and Ω_K the Keplerian angular frequency. We assumed a locally isothermal equation of state and adopted a gas temperature profile of $T \sim r^{-0.5}$, a standard choice for debris discs (e.g. Kral et al. 2017). From this, we obtained the pressure scale height $H = c_s \Omega_K^{-1} \sim r^{1.25}$ and the aspect ratio $h = H/r \sim r^{0.25}$. We emphasise that this flaring index of 0.25 remains open to debate, as it is often motivated by a black-body dust profile (Backman & Paresce 1993). Different heating and cooling mechanisms for dust and gas mean that they are not necessarily thermally coupled (e.g. Zagorovsky et al. 2010); in fact, in HD 121617, gas and dust temperatures were assumed to be partially different (Brennan et al. 2026).

To account for non-Keplerian rotation due to the radial pressure gradient, we modified the initial azimuthal gas velocity as

$$u_\phi = v_K \sqrt{1-\eta}\,; \qquad \eta \equiv -h^2 \frac{d\ln P}{d\ln r}, \tag{2}$$

where v_K is the Keplerian velocity, and $P = \Sigma_g c_s^2$ is the vertically integrated locally isothermal gas pressure. The quantity η, therefore, characterises how much the azimuthal velocity of the gas deviates from Keplerian rotation. Conceptually, if the pressure decreases with radius, η will be positive and the gas will, therefore, orbit sub-Keplerian (and vice versa for an increasing pressure profile). The change in gas density across the ring implies positive and negative radial pressure gradients at the inner and outer parts of the ring, respectively. At the pressure maximum, η becomes zero and the gas orbits with a Keplerian speed. We note that the prescription for u_ϕ in Eq. (2) only holds as long as the momentum feedback from dust grains is negligible (a more complex solution when including dust feedback is given in Benítez-Llambay et al. 2019).

2.2. Gas drag and radiation pressure

In protoplanetary disc studies, a standard way to characterise the dynamical behaviour of a particle is through the Stokes number, St. This dimensionless quantity compares the timescale over which friction forces the particle to move with the gas to the characteristic orbital timescale, Ω_K^{-1} (e.g. Birnstiel et al. 2010). In the linear regime, which is applicable to both protoplanetary and debris discs, St does not depend on the relative velocity between dust and gas. It is commonly expressed as

$$\mathrm{St} = \frac{\pi}{2}\frac{\rho_{\mathrm{mat}}\, a}{\Sigma_g}, \tag{3}$$

where ρ_{mat} is the grain's material density, a is its physical radius, and Σ_g is the gas surface density. The Stokes number thus quantifies the extent to which a dust particle is affected by gas drag, with the drag force often written as

$$\mathbf{f}_{\mathrm{drag}} = \frac{\Omega_K}{\mathrm{St}}\,(\mathbf{u}-\mathbf{v})\,, \tag{4}$$

with the velocity vectors, $\mathbf{u}$ and $\mathbf{v}$ for gas and dust, respectively. Eq. (3) shows that the coupling of a grain to the gas depends mainly on its size and the local abundance of gas. Consequently, at very low gas densities, like those expected in the secondary gas scenario in debris discs, even small dust grains ($\sim$1 µm) can potentially only be weakly (or not at all) coupled to the gas flow. To compute the momentum exchange between Lagrangian particles and gas that is modelled on a grid, two numerical steps are critical: first, the interpolation of the gas density and velocities from the Eulerian mesh to each particle's position, and second the projection of the particle's momentum feedback onto the gas, updating the gas velocities that are stored at the fixed interfaces between neighbouring grid cells. We used the implemented cloud-in-cell method for interpolation. In Appendix A, we compare the code's performance against analytical solutions for a radial drift test. We further activated dust diffusion due to stochastic kicks between the dust particles and the gas (Fuente et al. 2017; Charnoz et al. 2011), following Youdin & Lithwick (2007) who derived an expression for the radial diffusivity of passive solid particles, $D_d = \nu(1+4\mathrm{St}^2)(1+\mathrm{St}^2)^{-2}$.

In addition to frictional interactions with the gas and the central star's gravitational force, we implemented the effect of radiation pressure on the dust dynamics. We neglected the disc's self-gravity and the Poynting–Robertson drag (Burns et al. 1979), which operates on a much longer time scale than what is relevant in our simulations ($t_{\mathrm{P-R}} \sim 1$ Myr, cf. Eq. (50) in Burns et al. 1979). If the disc is optically thin to stellar irradiation, we can approximate the stellar flux at a certain location independently of the dust distribution. Under this assumption, the radiation pressure force is given by

$$\mathbf{f}_{\mathrm{rad}} = \frac{\beta G M_\star}{r^2}\,\frac{\mathbf{r}}{|\mathbf{r}|}\,, \tag{5}$$

where β is a dimensionless parameter that depends on the grain's material properties and the stellar parameters (Burns et al. 1979). Most importantly, β is a function of the particle's radius, with $\beta(a) = \beta_{1\,\mu\mathrm{m}} \times (1\ \mu\mathrm{m}/a)$, where $\beta_{1\,\mu\mathrm{m}} = \beta(a{=}1\ \mu\mathrm{m})$.

Notably, the radiation pressure force shares the same radial dependence as the star's gravitational force,

$$\mathbf{f}_{\mathrm{grav}} = -\frac{G M_\star}{r^2}\,\frac{\mathbf{r}}{|\mathbf{r}|}\,. \tag{6}$$

Because of this similarity, we can account for radiation pressure by replacing the original gravitational potential, ϕ_g, with an effective gravitational potential:

$$\phi_g^\star = (1-\beta)\,\phi_g. \tag{7}$$

In practice, we modified the code in a way that each dust particle experiences this effective gravitational potential, which depends on the particle size via $\beta(a) = \beta_{1\,\mu\mathrm{m}} \times (\ \mu\mathrm{m}/a)$. For simplicity, we initialised the dust grains with their local Keplerian velocity.

[2] A sufficient criterion has been found empirically in Chang et al. (2023).

2.3. Numerical setup

In the following section, we present results of one-dimensional (radial; Section 3.1) and two-dimensional (radial/azimuthal; Section 3.2) simulations. The grid on which the gas density was evaluated extended from $0.1\,r_0$ to $3\,r_0$ with $N_r = 512$ logarithmically spaced grid cells. In the two-dimensional case, the azimuthal angle, φ, spanned from $-\pi$ to π on $N_\varphi = 1024$ cells. We used wave killing zones (de Val-Borro et al. 2006) at the inner and outer boundaries to prevent spurious reflections.

For the dust particles, to ensure equal sampling across different grain sizes, we drew superparticles from a logarithmically spaced size distribution using a uniform kernel. Each superparticle was then assigned a representative mass (similar to Baruteau et al. 2019) assuming a dust number density profile of $n(a) \sim a^{-3.5}$ over the size range $a_{\rm min} = 0.8$ µm to $a_{\rm max} = 1$ cm. This distribution was motivated by that derived by Perrot et al. (2023) for HD 121617 based on the SED fit. For the material density of the particles, we used $\rho_{\rm mat} = 3.3\,{\rm g\,cm^{-3}}$, which represents silicate grains. For the initial setup, we positioned the particles inside the gas ring, between $0.9\,r_0$ and $1.1\,r_0$. Our numerical treatment did not consider collisions between the dust particles themselves. We ran the simulation for 200 orbits at r_0 and output density and velocity fields for every orbit.

3. Results

3.1. One-dimensional case

Dust trapping at gas-pressure maxima is well established in protoplanetary discs (e.g. Pinilla et al. 2012; Dullemond et al. 2018). In contrast, debris discs are optically thin, leaving grains directly exposed to stellar radiation. Radiation pressure must therefore be included. We began with 1D, axisymmetric simulations to examine how radiation pressure and gas drag set the radial structure of a coupled dust-gas ring before extending to more complex setups.

First, we note the differences to the scenario in which radiation pressure is not relevant, typical for protoplanetary discs. As shown in Eq. (2), the azimuthal gas velocity differs from the Keplerian velocity depending on the radial pressure gradient. In the absence of radiation pressure, dust grains orbit with a Keplerian velocity. This velocity mismatch between gas and dust generates friction, causing an exchange of angular momentum and leading to a radial drift of the dust grains towards regions of higher gas pressure (e.g. Whipple 1972). As a result, in a ring-shaped gas distribution, dust grains accumulate at the maximum pressure, where both dust and gas rotate at the same (Keplerian) speed.

On the other hand, in optically thin debris discs, radiation pressure reduces the effective gravitational potential (Eq. (7)), causing dust grains to orbit at $v_\varphi = \sqrt{1-\beta(a)}\,v_{\rm K}$. Since $\beta(a) \geq 0$, the dust moves sub-Keplerian. Additionally, if $\beta(a) > \eta$ the dust orbits slower than the gas, it experiences a headwind, and this frictional interaction transfers angular momentum from the gas to the dust. As a result, the dust drifts outward to regions of lower gas pressure. This drift continues until $\beta(a) = \eta$, at which point no further angular momentum exchange occurs (see Takeuchi & Artymowicz 2001, for a detailed discussion). To conserve angular momentum, the gas moves in the opposite direction (i.e. inward where dust drifts outward).

To test these expectations, we performed one-dimensional simulations of dust co-located with a gas ring using Dusty FARGO-ADSG with just one azimuthal cell. We represented the dust using 1000 particles, initialised around the peak of the gas density distribution, and ascribed a Keplerian velocity. The ring is centred at $r_0 = 75$ au, matching the location observed in HD 121617 (see Marino et al. 2026a; Mac Manamon et al. 2025). We set $\beta_{1\,\mu{\rm m}} = 0.4$, which corresponds to a blow-out size (particles for which $\beta = 0.5$) of 0.8 µm, approximately the observationally inferred minimum grain size (Perrot et al. 2023, see also Sect. 3.1). We then considered three scenarios: (i) a gas-free disc, where particles were influenced solely by gravity and radiation pressure, (ii) a gas-rich disc with a total gas mass of $10\,M_\oplus$, a molecular weight of $\mu = 2.3$, and a dust-to-gas ratio of 0.01, representative of the primordial scenario, where particles felt the gas drag but momentum feedback from dust to gas was small, and (iii) a gas-reduced disc with a total gas mass of $0.1\,M_\oplus$, a molecular weight of $\mu = 14$, and a dust-to-gas ratio of unity, representative of a secondary gas scenario. When included, the gas ring was characterised by a temperature of $T(r_0) = 38$ K (motivated by Brennan et al. 2026), a radial width of $\sigma = 0.14 \times r_0$, a contrast to the background of $C = 20$, and a viscosity level of $\alpha = 10^{-4}$. As both gaseous scenarios used the same temperature at different molecular weights, the aspect ratio was different in the two cases. Scenario (ii) was characterised by an aspect ratio of $h(r_0) = 0.07$, while scenario (iii) used $h(r_0) = 0.028$. This setup produced a maximum surface density of $\Sigma_{\rm max} = 0.17\,{\rm g\,cm^{-2}}$ for case (ii) and $\Sigma_{\rm max} = 3.1 \times 10^{-3}\,{\rm g\,cm^{-2}}$ for case (iii). Each simulation was evaluated after 150 orbits at r_0, corresponding to approximately 71 kyr.

Fig. 2 shows the particles' radial distance from the star, with the vertical axis indicating the particle size. The left panel shows the gas-free scenario. Because radiation pressure depends on particle size, only the smallest grains ($a \lesssim 10$ µm) deviate significantly from their initial radial region (shaded area). The horizontal line marks the blowout size $a_{\rm bound} = 0.8$ µm (at which $\beta(a) = 0.5$), above which particles remain on bound orbits. Particles smaller than $a_{\rm bound}$ escape the system, while those just above $a_{\rm bound}$ follow highly eccentric orbits. The resulting broad spread in the radial distance for particles of $a_{\rm bound} \leq a \lesssim 10$ µm arises from these high eccentricities, with the simulation snapshot capturing each particle at a different point in its eccentric orbit.

The central panel of Fig. 2 corresponds to case (ii), where we examined a gas ring that encases the dust grains, where the dust-to-gas mass ratio is $f_{\rm dtg} = 0.01$. The shaded region indicates the initial radial extent of the dust particles, while the solid blue curve shows the gas surface density after 150 orbits. For each radial cell, the particle size at which $\beta(a) = \eta(r)$ is indicated by the black dashed line. This simulation reveals three distinct regimes of particle behaviour. First, the largest particles ($\gtrsim$100 µm) remain mostly unaffected by radiation pressure. Beyond the pressure maximum, the gas orbits sub-Keplerian because the inward pressure gradient implies $\eta > 0$ (see Eq. (2)). The large particles, for which $\beta < \eta$, orbit faster than the gas, thus, they lose angular momentum due to friction. Consequently, they drift towards the pressure maximum at the ring's radial centre.

Particles of $\lesssim$50 µm, start to be affected by radiation pressure and thus orbit with a sub-Keplerian velocity. For those particles, there is a location where $\beta(a) > \eta$ and the particles orbit slower than the gas and thus experience a tailwind. This induces an outward drift until they reach a location where $\beta = \eta$ (marked by the dashed line). Notably, dust grains do not maintain significant eccentricities here because gas drag efficiently damps any non-circular motion.

For particles of $\lesssim$5 µm the relation $\beta > \eta$ holds everywhere in the domain; these grains experience a net outward drift with no

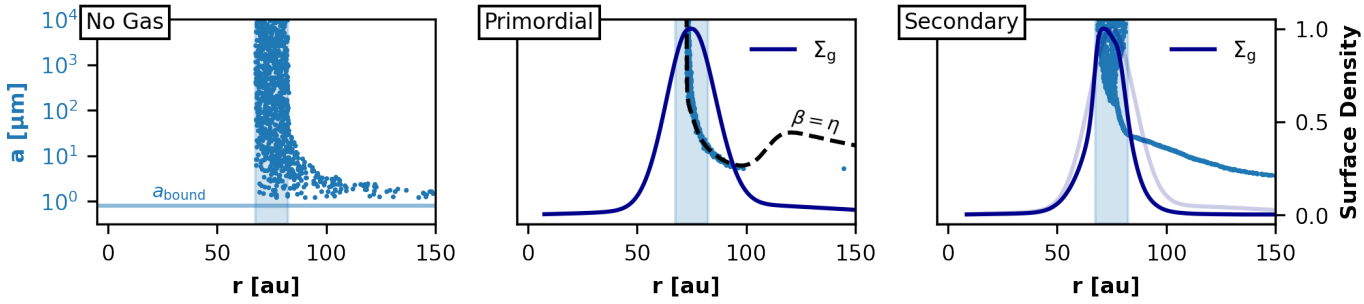

Fig. 2. One-dimensional simulations of a dust ring. All setups included radiation pressure with $\beta_{1\,\mu m} = 0.4$, and are shown after 150 orbits at r_0. *Left*: simulation without gas. The horizontal line indicates the minimum particle size for which the dust remains on bound orbits, and the shaded area marks the initial radial range of the dust particles. *Centre*: includes gas density specified by Eq. (1), with gas density (Σ_g, blue curve) normalised to its maximum value, which was set to represent a gas ring of 10 $M_\oplus$, representing a primordial scenario. The dust-to-gas ratio is 0.01. The dashed curve shows where $\beta = \eta$. *Right*: same as the centre panel, but with $M_{gas} = 0.1\ M_\oplus$, and a dust-to-gas ratio of unity, reflecting a scenario of secondary gas origin. Large particles are affected by neither radiation pressure nor gas drag, and they remain on their initial circular Keplerian orbits. For sizes $\lesssim$100 μm, both gas drag and radiation pressure become efficient, and the particles move outward. The momentum feedback from the dust changes the gas density profile from its initial distribution (transparent blue line).

equilibrium point and thus leave the domain through the outer boundary. In this primordial–gas scenario, the minimum size that remains bound in the ring is therefore substantially larger than in the gas–free case (where $a_{bound} \simeq 0.8$ μm), because gas drag transfers angular momentum to the grains and assists their outward motion. The grains that do remain trapped align with the local balance condition $\beta(a) = \eta$. As η is size-independent, changing the radiation pressure normalisation $\beta_{1\,\mu m}$ by a certain factor simply shifts the dashed line in the central panel vertically by the same factor. This yields three immediate implications: (i) the minimum retained size is set by the threshold $\beta(a_{min}) = \eta$; for compact grains with $\beta \sim a^{-1}$, this implies $a_{min} \sim \eta^{-1}$; (ii) a warmer ring (larger sound speed c_s and hence larger aspect ratio h) retains smaller grains, because $\eta \sim h^2$; (iii) a narrower ring (steeper radial pressure gradient) also retains smaller grains, since $\eta \sim h^2\,|\mathrm{d}\ln P/\mathrm{d}\ln r|$ increases with the pressure slope.

Finally, the right panel of Fig. 2 illustrates the outcome for scenario (iii), a secondary origin gas-poor disc, with a dust-to-gas ratio of unity. Here, particles $\gtrsim$1 cm are neither affected by radiation pressure nor gas drag, on the simulated time scales, and remain on their initial circular Keplerian orbits. For sizes $\lesssim$30 μm, both the gas drag and radiation pressure become efficient and the particles move outward. The momentum feedback from the dust changes the gas density profile from its initial distribution (transparent blue line). As the dust orbits even slower than the gas, it receives angular momentum from the gas via friction. Hence, as the gas loses angular momentum, it is forced to move inwards, steepening the outer slope of the density distribution. We highlight that once dust feedback becomes significant, the azimuthal gas velocity is modified by the friction and Eq. (2) does no longer apply. Hence, the equilibrium location is no longer represented by the $\beta = \eta$-line.

3.2. Two-dimensional fiducial model

In this section, we investigate how the system develops under an azimuthally asymmetric instability. To this end, we need a mechanism that triggers an azimuthally asymmetric profile in the gas structure. Here, we used as an initial condition an idealised Gaussian-like gas density profile (described in Eq. (1)) that is tailored to trigger such instability, when the azimuthal coordinate is included in the simulation. In particular, we set the parameters of the simulation such that the ring is susceptible to the Rossby Wave Instability (RWI, Lovelace et al. 1999; Ono et al. 2016; Chang et al. 2023). The occurrence of this instability can be controlled by the width, σ, of the density profile in Eq. (1). Ono et al. (2018) presented a dedicated study that analyses the conditions and evolution of the RWI in a gas ring and which azimuthal mode is most unstable. We emphasise that the results by Ono et al. (2018) are relevant but not directly applicable, as we include the momentum feedback from the dust onto the gas in our simulation. This was not included in their study; it changes the equations of motion and adds a dependency on the dust-to-gas ratio to the gas dynamics. We adopted a viscosity level of $\alpha = 10^{-4}$. The (magneto)hydrodynamical processes that transport angular momentum in protoplanetary discs (Lesur et al. 2023; Rosotti 2023) may partially apply to debris-disc gas as well (Cui et al. 2024). In the low-density regime, Cui et al. (2024) further argue that molecular viscosity can become non-negligible. For our fiducial model this is probably not relevant as we estimate a molecular viscosity level of $\alpha \sim 10^{-7}$, but this contribution increases linearly with decreasing gas mass. The magnetorotational instability (MRI, Balbus & Hawley 1991) is not expected to be active in the midplane at the densities of our fiducial model (Cui et al. 2024); but turbulence generated in upper layers could be transported there. Overall $\alpha = 10^{-4}$ should be regarded as a conservative upper limit for the scenarios considered here. We note, however, that at significantly lower gas densities than our fiducial case, α could be significantly larger because both the molecular viscosity and MRI-turbulence contribution increase.

In the linear regime, the RWI grows rapidly, typically within 10–20 dynamical periods, and is only weakly affected by viscosity (Lin 2014). Once the non-linear regime is reached, however, viscosity plays a central role in setting the vortex lifetime, with higher α accelerating vortex dissipation (Lin 2014).

As the dust mass can be estimated from the spectral energy distribution (0.21 $M_\oplus$; Marino et al. 2026a; Perrot et al. 2023), and the gas temperature from the CO molecular line emission (38 K at r_0; Brennan et al. 2026), we keep these values fixed. We model the dust population using 10^5 superparticles. When considering a molecular mass of $\mu = 2.3$ this temperature corresponds to an aspect ratio of $h_0 = 0.07$. We found that the ring becomes unstable when its radial width is $\sigma \lesssim 1.5 \times H_p$, with $H_p = h \times r$ being the gas pressure scale height. In the fiducial model we therefore set a moderately unstable width of

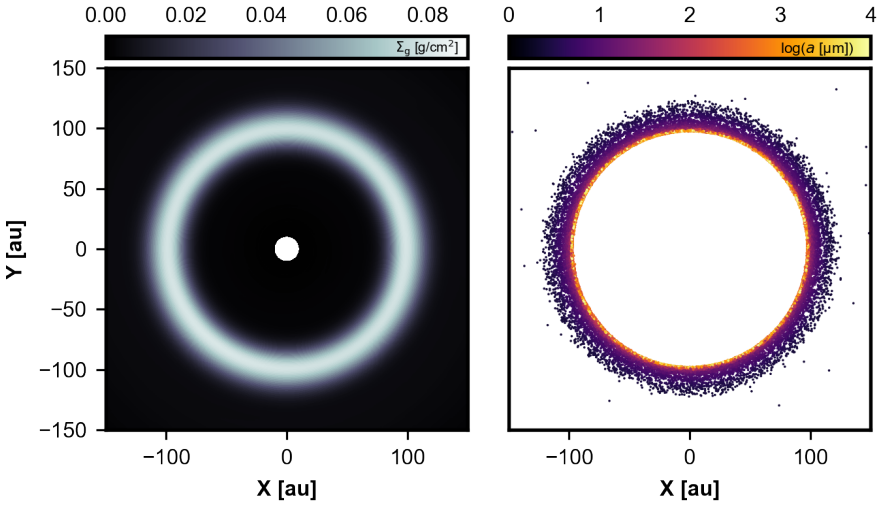

Fig. 3. Fiducial hydrodynamical model after 150 orbits at r_0 (corresponding to about 71 kyr). The total gas mass of the Gaussian ring is $M_g = 50\,M_\oplus$, with a dust-to-gas mass ratio of 4.2×10^{-3}. *Left*: gas surface density distribution. *Right*: particle distribution with colour indicating the grain size.

Table 1. Fiducial model parameters adopted in Sect. 3.2.

Quantity	Parameter	Value
Viscosity	α	10^{-4}
Ring Gas Density	Σ_0	$0.12\,\mathrm{g\,cm^{-2}}$
Background Density	Σ_{bg}	$6\times10^{-3}\,\mathrm{g\,cm^{-2}}$
Density Contrast	C	20
Ring location	r_0	75 au
Ring width	σ	7.4 au
Background peak location	r_{bg}	103 au
Background width	σ_{bg}	43 au
Total gas mass	M_{gas}	$50\,M_\oplus$
Temperature at r_0	T_0	38 K
Aspect Ratio	h	0.07
Dust material density	ρ_{mat}	$3.3\,\mathrm{g\,cm^{-3}}$
Radiation strength	$\beta_{1\,\mu m}$	0.4
Dust-to-gas ratio	f_{dtg}	4.2×10^{-3}
Mean-molecular weight	μ	2.3
CO mass ratio	χ_{CO}	3×10^{-3}

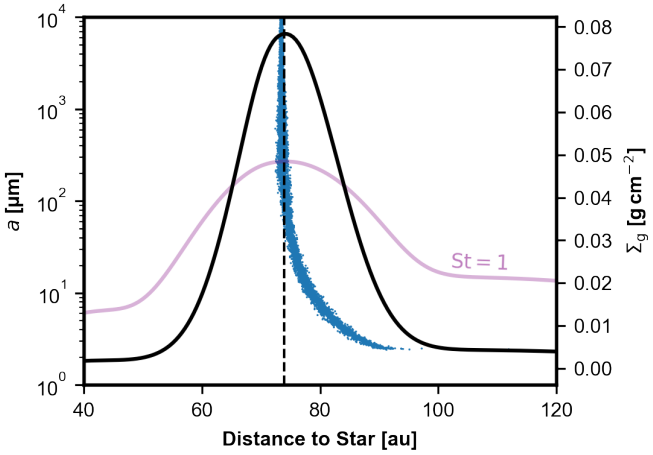

Fig. 4. Radial distribution of particles corresponding to Fig. 3. The figure incorporates every tenth particle. The black curve traces the azimuthally-averaged gas surface density profile. The vertical dashed line marks the pressure maximum. The purple curve indicates the particle size that corresponds to a Stokes number of unity.

$\sigma = 1.4\times H_p(r_0) = 1.4\times h_0 r_0 = 7.4$ au. This is very similar to the condition found in Brennan et al. (2026) that the FWHM of the radial gas density distribution must be narrower than ~17.3 au, corresponding to a width of $\sigma = 7.3$ au. We defined the ratio between the estimated CO mass ($m_{CO} = 0.15\,M_\oplus$, Brennan et al. 2026) and the total gas mass, $\chi_{CO} \equiv m_{CO}/m_{gas}$. The typical value adopted for protoplanetary discs, $\chi_{CO} \sim 10^{-3}$ (e.g. Williams & Best 2014), is inherited from the interstellar medium. However, the fractional abundance of CO is highly uncertain and depends on thermal and chemical processes during the disc's lifetime. Direct measurements of hydrogen have found that CO tends to be reduced in evolved discs (e.g. Bergin et al. 2013; McClure et al. 2016; Trapman et al. 2017), indicating depletion caused by freeze-out, photodissociation, and chemical reactions. Finally, the CO mass fraction also depends on whether the gas is of primordial or secondary origin – or a mixture. Table 1 lists the parameters that we use for the fiducial run. Note that some of these parameters are interdependent, such as the dust-to-gas ratio and the CO mass ratio, or the temperature and the aspect ratio.

In the fiducial simulation, a vortex emerges after around 10 orbits at r_0 ~4.7 kyr. The instability grows rapidly until 25 orbits (~11.8 kyr), but then starts to abate. The system reaches an azimuthally symmetric state after about 200 orbits (~94 kyr). We show a time series of the azimuthal asymmetry caused by the instability in Appendix B.

The left panel of Fig. 3 shows the gas surface density distribution after 150 orbits at r_0 (~71 kyr), while the right panel shows the particle positions with the colour indicating the grain size. The size-dependent distribution of the solids is better illustrated by the radial and azimuthal profiles in Figs. 4 and 5, respectively.

Figure 4 shows that dust grains of about 30 μm and larger are efficiently trapped at the pressure maximum of the gas ring, indicated by the vertical dashed line. The purple curve in Fig. 4 indicates where St = 1 (roughly 250 μm at the peak). For particles with $a \lesssim 30$ μm, radiation pressure becomes increasingly significant, shifting the distribution slightly outward relative to larger grains.

Fig. 5 highlights the distinct behaviours of the dust grains more clearly. Namely, the azimuthal distribution reveals three regimes: (i) small grains ($a \lesssim 10$ μm) that closely trace the azimuthal gas structure, (ii) partially decoupled grains ($10\,\mu m \lesssim a \lesssim 300\,\mu m$) that are still strongly affected by the gas flow, and (iii) very decoupled grains ($a \gtrsim 300$ μm) that are affected

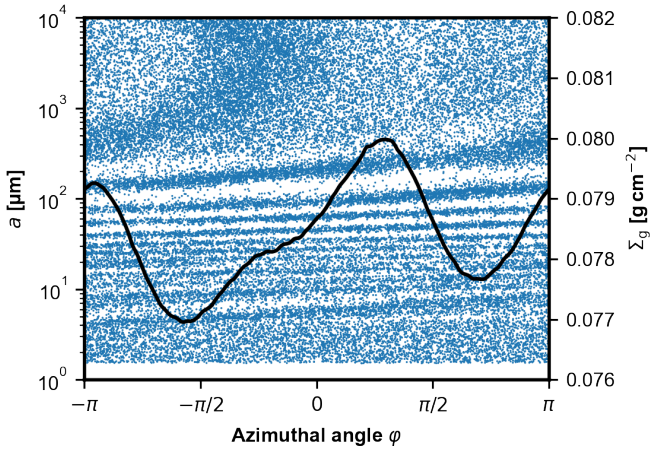

Fig. 5. Azimuthal distribution of particles of different sizes corresponding to Fig. 3. The figure incorporates every tenth particle. The black curve traces the radial peak value of the gas surface density and corresponds to the right y-axis.

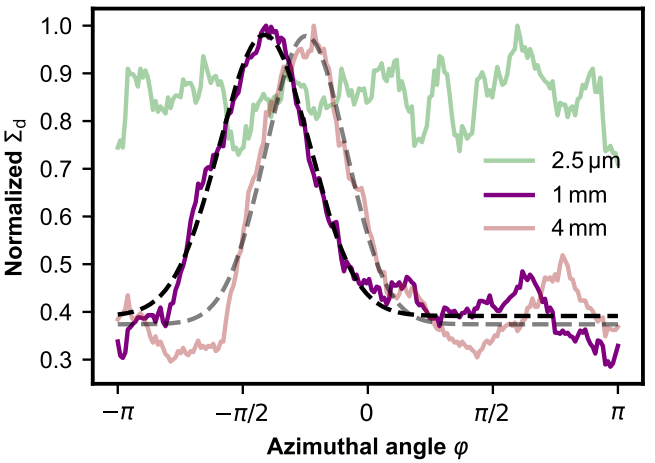

Fig. 6. Azimuthal dust distribution for representative sizes of 2.5 μm, 1 mm and 4 mm. The profiles were produced by selecting the particles within ±10% of the respective size over the full radial domain and normalising to the maximum value of the large grains. The dashed black curve represents a Gaussian fit to the data 1 mm profile.

by the gas flow only on extended timescales. Between 10 μm and 300 μm, the response to the azimuthal gas variations is noticeably size-dependent. That dust particles of different Stokes number are trapped at different azimuths in the case of a strong vortex has been investigated in detail in several studies (Baruteau & Zhu 2016; Fuente et al. 2017; Hammer et al. 2019). The shift away from the gas maximum in larger particles is attributable to their increased inertia relative to the gas flow, which corresponds to a longer frictional stopping time.

To study the azimuthal distribution more quantitatively, we present three representative normalised dust density profiles in Fig. 6. Here, we binned the particles around 2.5 μm (St ∼ 0.01), 1 mm (St ∼ 3.5) and 4 mm (St ∼ 14), respectively, summing those within ±10% of each central particle size. The figure shows that, apart from noise, the small particles are azimuthally spread. The two larger species are azimuthally confined but the 4 mm particles are shifted in the positive azimuthal direction with respect to the 1 mm grains. Gaussian fits to the 1 mm and 4 mm distributions are plotted as dashed black curves in Fig. 6. The fits yield widths of $\sigma_{1\mathrm{mm}} = 32.0° \pm 0.2°$ and $\sigma_{4\mathrm{mm}} = 28.9° \pm 0.2°$, and an azimuthal shift between the two species of $30.0° \pm 0.3°$. This is a much larger shift than that found in Baruteau & Zhu (2016) for the corresponding Stokes numbers and is due to the fact that at the time plotted the gas vortex has weaken due to dissipative effects (see Appendix B). Similar to the azimuthal asymmetry in the gas, the azimuthal accumulation of dust grains is also time-dependent and both the shift and the contrast of the asymmetry depend on the snapshot at which the simulation is evaluated.

Grain size transitions in gas coupling depend on the gas surface density, and thus on the total gas mass. Effects of varying the gas mass (while all else is kept the same, including the dust mass) is discussed next in Section 4.

4. Radiative transfer and image synthesis

We employed the radiative transfer code RADMC-3D (version 2.0; Dullemond et al. 2012), a grid-based method that requires density fields as input. Accordingly, we constructed a three-dimensional spherical grid with $N_r \times N_\theta \times N_\varphi = 512 \times 30 \times 1024$ cells. For the dust component, we separated the superparticles into fifty logarithmically spaced representative size bins and transformed the discrete superparticle distribution into a grid-based dust density via cloud-in-cell interpolation. Because our hydrodynamical simulations are two-dimensional, we first computed the dust surface density $\Sigma_\mathrm{d}(r, \varphi)$ and then extended the distribution in the vertical direction according to the following:

$$\rho_\mathrm{d}(r, \varphi, z) = \frac{\Sigma_\mathrm{d}(r, \varphi)}{\sqrt{2\pi}\, H_\mathrm{d}} \exp\left(-\frac{z^2}{2 H_\mathrm{d}^2}\right), \tag{8}$$

where the dust scale height, following Dubrulle et al. (1995), is given by

$$H_\mathrm{d} = \sqrt{\frac{\alpha_\mathrm{D}}{\alpha_\mathrm{D} + \mathrm{St}}}\, H_\mathrm{g}. \tag{9}$$

We assumed that the diffusion coefficient α_D is equal to the viscous α parameter used in the simulations, which in our case served as a numerical convenience rather than a physically constrained quantity. While this approach does not yield physically motivated dust scale heights, we found that the choice has little impact on the resulting synthetic images, as most of the emission arises near the disc midplane where the vertical dust distribution is densest. We computed the opacities for each representative dust size using the `optool`[3] package (Dominik et al. 2021), assuming compact grains with a material composition of pyroxene silicates. We then used RADMC-3D to compute the dust temperature with the `mctherm` task, employing $n_\mathrm{phot} = 10^8$ photon packages. Because the disc is optically thin, the dust temperature varies only weakly with height: grains at virtually all altitudes are directly exposed to stellar radiation. At the ring radius, grains larger than 10 μm are of ∼62 K, essentially the black-body equilibrium temperature reported by Mac Manamon et al. (2025). Smaller grains absorb stellar photons more efficiently than they re-emit at long wavelengths and therefore become slightly hotter; the smallest grains we consider (0.8 μm) reach roughly 65 K at the same location. Next, we performed ray-tracing simulations of the thermal emission at $\lambda_\mathrm{obs} = 0.89$ mm and of scattered stellar light at $\lambda_\mathrm{obs} = 1.25$ μm, using anisotropic scattering based on the scattering matrices calculated with `optool`. We assumed an inclination of 44.1° and a position angle of 58.7°, as reported in Marino et al. (2026a).

[3] https://github.com/cdominik/optool

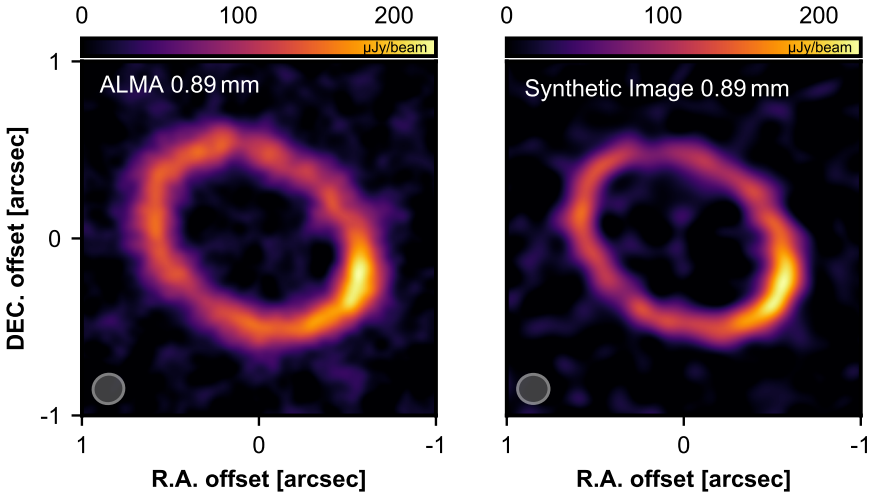

Fig. 7. Comparison between ALMA observation and simulation. *Left*: ALMA band 7 observation of HD 121617 (Marino et al. 2026a,b). *Right*: synthetic image of the fiducial hydrodynamical model at 0.89 mm using `CASA`-simobserve. In both images, the beam is shown as a grey ellipse in the bottom left corner.

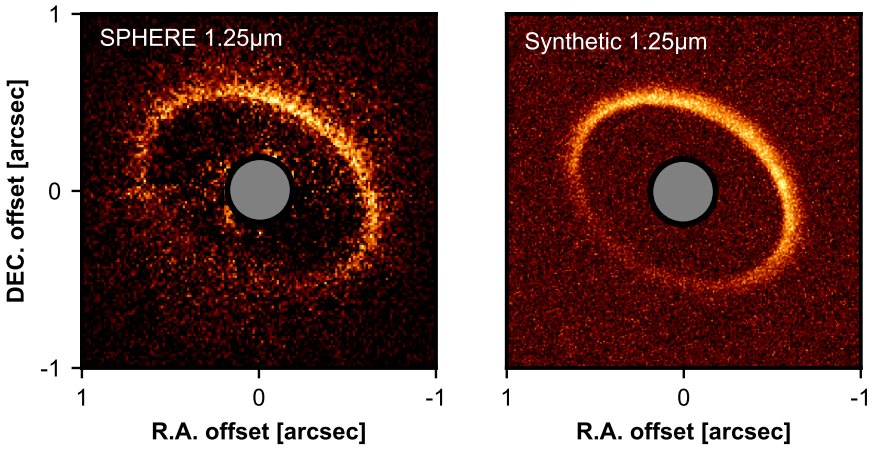

Fig. 8. Comparison between scattered light observation and simulation. *Left*: VLT/SPHERE J-band (λ_{obs} = 1.25 μm) observation of HD 121617 (see Milli et al. 2026). *Right*: synthetic image of polarised light at 1.25 μm for the fiducial hydrodynamical model. In both panels, the grey circle indicates the coronagraphic mask of the observation.

To generate more realistic comparisons with actual observations, we applied image synthesis techniques to replicate each telescope's finite resolution and sensitivity. In the case of ALMA band 7, we used the CASA `simobserve` task, including realistic noise contributions from atmospheric fluctuations and antenna responses. We found a good match with the observational beam when using a combination of configurations C-5 (with integration time τ_{int} = 345 min) and C-3 (τ_{int} = 84 min) and weights of `robust`=`0.5`.

For the polarised J-band image, we convolved the model output with the diffraction-limited resolution of an 8.2 m telescope at λ_{obs} = 1.25 μm, then added Poisson noise to approximately match the observed signal-to-noise ratio.

4.1. Fiducial model

Fig. 7 compares the ALMA band 7 observation of HD 121617 (Marino et al. 2026a) with the corresponding synthetic image of our hydrodynamical model. Qualitatively, the simulated image represents the observation to a high degree; in particular, the ring's radial extent and the arc's azimuthal distribution and contrast are well reproduced. In a more detailed inspection, the right panel reveals a brighter arc in the ring where dust grains are azimuthally concentrated, superimposed on an azimuthally symmetric emission component. This combination results in a slightly stronger contrast between the arc and the rest of the ring (see Sect. 5.2) in the synthetic image compared to the real observation.

Fig. 8 presents the VLT/SPHERE polarised J-band image of HD 121617 (Milli et al. 2026) alongside its simulated counterpart. Polarised J-band observations primarily capture starlight scattered off small dust grains in the circumstellar environment. Since small particles ($a \lesssim 10$ μm) follow the largely azimuthally symmetric gas distribution, the brightness pattern is dominated by angle-dependent scattering efficiency and phase function, rather than azimuthal density variations. Even in polarised light, forward scattering is typically enhanced, while backward scattering is suppressed (e.g. Min et al. 2012). As a result, the near (northwest) side of the ring, where forward scattering prevails, appears brighter, while the far side is scarcely visible. We note that the simulated scattered light image appears more radially extended than the actual observation, which may indicate an overestimate of dust diffusion in our model.

As previously stated, in addition to the azimuthal trapping of mm grains, the most important effect of the gas drag is the radial mismatch of the ring observed by ALMA (r = 73.6 au) and in scattered light (r = 80.6 au) (Milli et al. 2026). This shift corresponds to 9.5%. Fig. 9 shows the deprojected radial intensity profiles of the synthetic ALMA band 7 observation (cf. right panel of Fig. 7) and the synthetic scattered light image (cf. right panel of Fig. 8), both normalised to their respective maximum values. The dashed lines in Fig. 9 mark the measured ring locations from the observations (Milli et al. 2026). By fitting Gaussians to the radial profiles of the synthetic images, we find the scattered light ring to be shifted outward by 8.2% with respect to the ALMA ring. This is qualitatively in good agreement with the real observations.

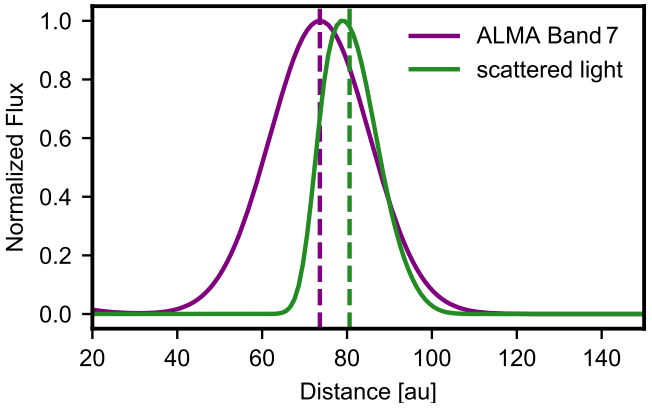

Fig. 9. Deprojected radial intensity profiles of ALMA band 7 synthetic observation (purple, corresponding to right panel of Fig. 7) and J-band scattered light (green, corresponding to right panel of Fig. 8). The vertical dashed lines mark the corresponding maxima measured from the real observations at 73.6 au and 80.6 au for sub-mm emission and scattered light, respectively (see Milli et al. 2026).

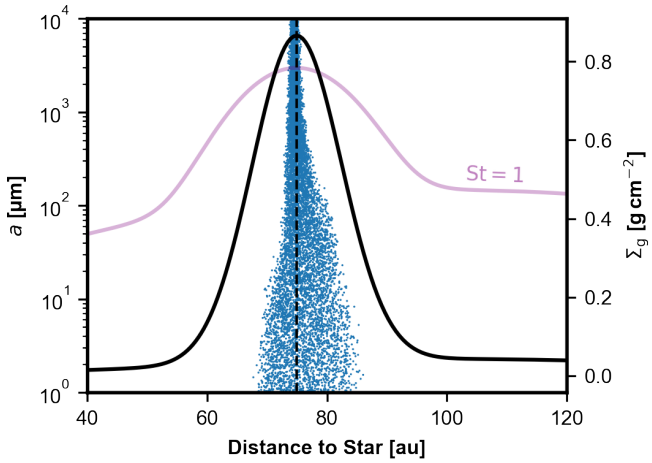

Fig. 10. Radial particle distribution for different sizes from a two-dimensional hydrodynamical simulation with $M_{\rm gas}$ = 250 $M_\oplus$. The vertical dashed line marks the ring location at 75 au. The purple profile marks the particle sizes that correspond to St = 1.

4.2. The gas mass upper limit

We attribute the offset between ALMA and SPHERE rings to radiation pressure, which predominantly affects small dust grains. This additional force changes their radial force balance, resulting in a sub-Keplerian equilibrium orbital velocity. However, for these small grains to be radially displaced from the gas, they must be at least partially decoupled from the gas dynamics; otherwise, any relative motion with respect to the gas dynamics will be immediately dampened. We demonstrate this with a simulation in which the gas mass is increased by a factor of five relative to our fiducial model (from 50 $M_\oplus$ to 250 $M_\oplus$): although the ALMA arc can still be reproduced at this higher gas mass, particles of $a \lesssim 10$ μm are tightly coupled to the gas dynamics.

Fig. 10 shows the radial distribution of the particles. Compared to the distribution of the fiducial model shown in Fig. 4, particles of $a \lesssim 10$ μm are much more radially spread in the case of increased gas mass. Additionally, those particles extend to inside the pressure maximum (marked by the vertical dashed line). The radiation pressure does not dislocate the particles as significantly as in the fiducial model. Gaussian fits to the rings

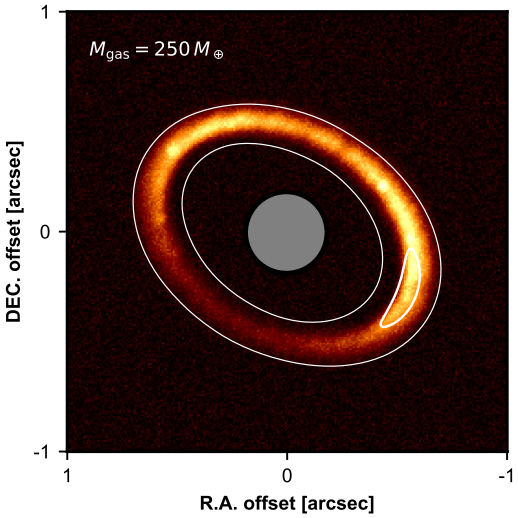

Fig. 11. Same as right panel of Fig. 8 but for the model that assumes a higher gas mass, with $M_{\rm gas} = 250\,M_\oplus$. The contours delineate the ALMA band 7 continuum emission. The model fails to reproduce the characteristic features of the J-band image (cf. right panel of Fig. 1), i.e. the radial dislocation with respect to the ALMA ring, and the ring's sharpness.

indicate that the peak of the scattered light ring lies only 0.8% farther out than that of the ALMA band 7 ring. This model of increased gas density would fail to reproduce both the outward shift and the sharpness of the ring seen in scattered light. We demonstrate this by producing the J-band polarised light image for the increased gas mass, shown in Fig 11. The image shows the corresponding ALMA band 7 continuum emission overlaid as white contours. This shows a rough agreement between the scattered light and sub-mm ring radii, inconsistent with the observations. Additionally, it shows that the scattered light ring is more radially spread.

Therefore, the upper limit for the gas mass is between the value used in the fiducial model (50 $M_\oplus$) and the 250 $M_\oplus$ analysed here. In particular, this demonstrates that the ring around HD 121617 is not consistent with the gas content of a typical Class II disc around a 1.9 $M_\odot$ star (~1 $M_{\rm J}$, e.g. Ansdell et al. 2016).

4.3. The gas mass lower limit

4.3.1. $M_{\rm gas} = M_{\rm CO}$

First, we probed the scenario where the reported CO mass of 0.15 $M_\oplus$ represents the total gas mass, $M_{\rm gas}$ = 0.15 $M_\oplus$. This change affects the ring dynamics in two ways. Every grain's Stokes number rises by more than two orders of magnitude compared to the fiducial model. Particles that were mildly influenced by drag in the fiducial model now move independently, while previously well-coupled grains become only weakly coupled. Second, with the total dust mass held constant, the dust-to-gas ratio in the ring increases to above unity, $f_{\rm dtg} = 1.4$. Crnkovic-Rubsamen et al. (2015) found that once dust accumulates in a vortex the dust feedback destroys the vortex if the trapped dust density reaches about 30% of the gas density (see also Fu et al. 2014; Raettig et al. 2015). Here, we find that if we initiate the simulation above that value, the vortex does not even develop. Even if we decrease the ring width considerably to $\sigma = H$, the instability remains suppressed by the dust.

However, an alternative is that the gas is secondary but dominated by species other than CO. In secondary gas scenarios

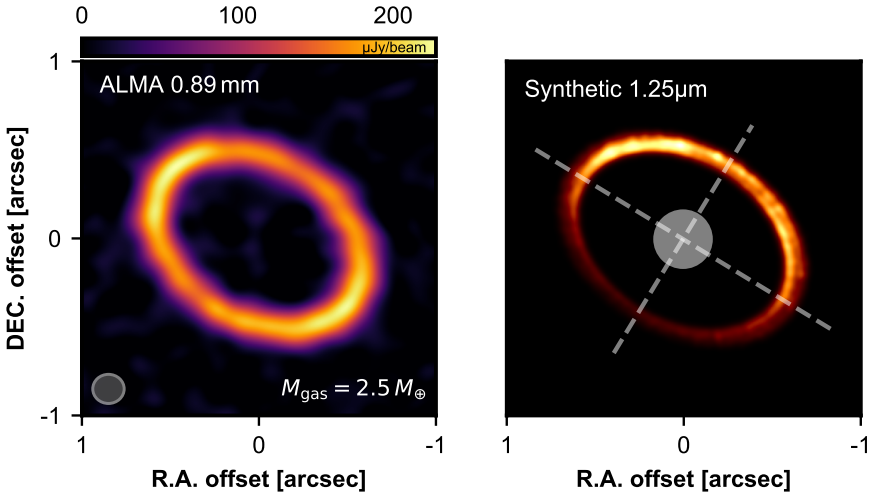

Fig. 12. Synthetic images for the $M_{gas} = 2.5\,M_\oplus$ model: ALMA band 7 continuum (left) and J-band polarised intensity (right). Dashed lines in the right panel mark the projected semi-major and semi-minor axes, according to the employed PA of 58.7° (Marino et al. 2026a).

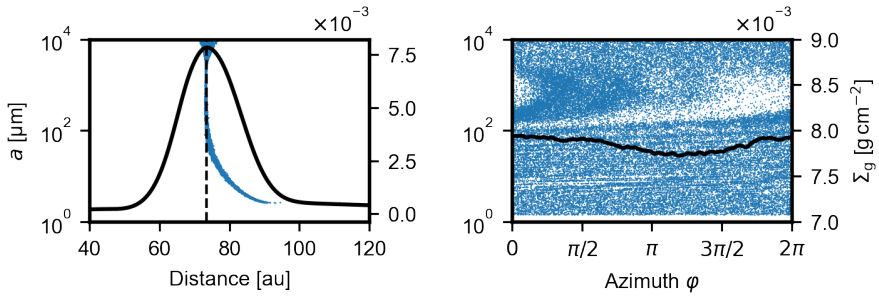

Fig. 13. Particle distributions for the $M_{gas} = 5\,M_\oplus$ model after 150 orbits at r_0. Left: radial profiles (cf. Fig. 4); Right: azimuthal profiles (cf. Fig. 5). In both panels the black curve shows the gas surface density (right-hand axis).

the instantaneous CO mass is set by the volatile mix of the parent bodies and how fast CO photodissociates into C and O. Unshielded CO around debris discs typically survives only ~100–200 yr (often quoted as ≈ 120 yr for the interstellar radiation field; e.g. Matrà et al. 2015; Marino et al. 2016; Kral et al. 2017), so most of the total gas mass may reside in atomic carbon and oxygen unless CO is shielded in which case CO tends to dominate the gas mass in secondary models (Kral et al. 2019; Marino et al. 2020; Marino 2022). This is because CO shielding by carbon can dramatically prolong the CO lifetime. Once CO becomes shielded, its photodissociation rate can drop by orders of magnitude. In such shielded discs, the carbon abundance is regulated: higher carbon abundance increases shielding and thus carbon and oxygen production from CO is diminished. Whether this applies to HD 121617 remains open.

For HD 121617, the currently reported C mass is $M_{CI} \approx 4 \times 10^{-3}\,M_\oplus$, corresponding to a column density of $N \sim 2{\times}10^{17}$ cm^{-2} (Cataldi et al. 2023). In other words, given the observational estimates at the time of writing, the carbon mass in HD 121617 is significantly lower than the CO mass and close to the value where shielding starts to become efficient ($\gtrsim 10^{-17}$ cm^{-2}, Kral et al. 2019; Marino et al. 2020; Marino 2022). Still, we carried out two additional simulations with total gas masses of 2.5 $M_\oplus$ and 5 $M_\oplus$, adopting dust-to-gas mass ratios of $f_{dtg} = 0.084$ and $f_{dtg} = 0.042$, respectively. These runs are meant to represent cases in which CO is abundant but does not dominate the overall gas mass budget.

In this simulation the instability does develop in the gas, but the largest dust grains ($a \gtrsim 3$ mm) have St $\gg 1$ and are therefore only weakly affected by gas drag. Owing to the combination of low gas surface density and the resulting high St, no clear azimuthal asymmetry appears in the mm-sized grains that dominate the band 7 continuum. By contrast, small grains of ~10 μm decouple from the gas and do develop an azimuthal asymmetry. Consequently, this model fails to reproduce the observed combination in HD 121617 of an asymmetric ALMA continuum arc and a symmetric SPHERE scattered-light image (Fig. 12).

The 5 $M_\oplus$ case behaves differently. After the gas asymmetry weakens, only a specific grain-size window, 100 μm $\lesssim a \lesssim$ 3 mm, retains a strong azimuthal contrast (Fig. 13). In the radial dimension, $a \lesssim 50$ μm grains are gradually pushed outward by the combined action of radiation pressure and gas drag; particles with 50 μm $\lesssim a \lesssim$ 2 mm are efficiently confined at the pressure maximum; and $a \gtrsim 3$ mm grains, with St $\gg 1$, remain largely on their initial orbits. Thus, the azimuthal asymmetry is carried primarily by those grains that are radially trapped (and hence concentrated) but not so large as to be entirely decoupled.

Fig. 14 presents the corresponding synthetic observations: ALMA band 7 (left panel), SPHERE J-band polarised intensity (central panel), and deprojected radial profiles of both (right panel). The model qualitatively reproduces the main features seen in HD 121617: an asymmetric mm continuum ring coupled with a more uniform scattered-light ring, with a fidelity comparable to the fiducial ($M_{gas} = 50\,M_\oplus$) model. The radial offset between the rings in the synthetic ALMA and SPHERE images is 10.9%, in good agreement with the observations, though slightly larger.

5. Discussion

5.1. Hybrid rather than debris disc

Protoplanetary discs have been detected around stars as old as 23 Myr (V4046 Sgr, Mamajek & Bell 2014). Considering HD 121617's estimated age of 16 Myr, evidence for a primordial origin of the detected gas would question its classification as a traditional debris disc. Instead, it might represent a rather old,

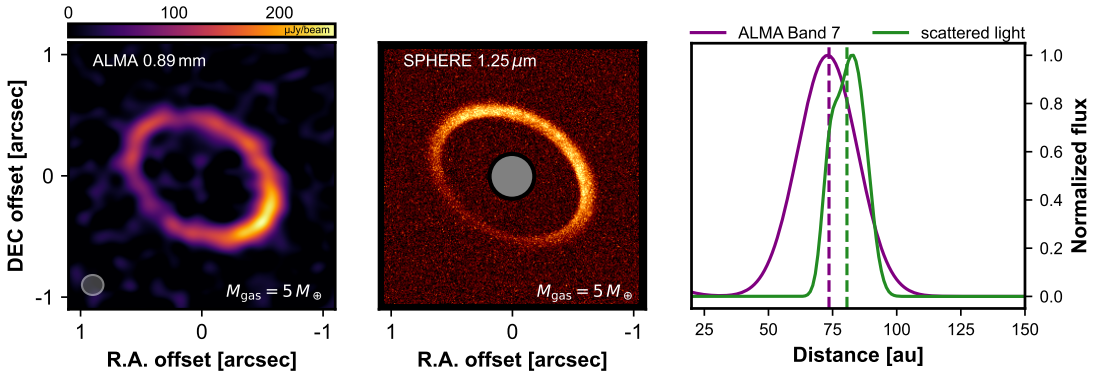

Fig. 14. Synthetic observables for the $M_{gas} = 5\,M_\oplus$ model. Left: ALMA band 7 continuum; Centre: SPHERE J-band polarised intensity; Right: deprojected radial profiles of the two rings.

dispersing protoplanetary disc in a transitional phase. Unfortunately, the term "transition disc" has historically been connoted with discs that host large inner cavities that were classified through dust continuum deficits at near- or mid-infrared wavelengths (e.g. Strom et al. 1989; Espaillat et al. 2014). However, it has since been found that most of these so-called transition discs are actually steady, persistent environments, contradicting the notion of an imminent transition. To differentiate from the classical connotation of transition discs, we will here use the term "hybrid disc", following Kóspál et al. (2013), for a system that mainly retains its gas from the protoplanetary disc while its solids are at debris-like levels (although not necessarily collisionally generated as in standard debris disc definitions).

Moór et al. (2017) surveyed several young A-type stars and detected CO in 11 out of 16 young (≤42 Myr) classified debris discs, suggesting that they might indeed be such hybrid discs, a sub-population of late-stage discs around intermediate-mass stars that still harbor significant gas. As argued in Sect. 4.3, the observations are incompatible with the gas drag scenario for total gas masses of $M_{gas} \lesssim 2.5\,M_\oplus$. Consequently, a confirmation of the gas drag shaping the continuum emission in HD 121617 would strongly point to the hybrid disc scenario. In this case, HD 121617 might be undergoing final dispersal through mechanisms such as photoevaporation (e.g. Nakatani et al. 2021, 2023).

Under photoevaporation, high-energy stellar photons heat the gas to sufficiently high temperatures to drive mass loss from the disc (e.g., Owen et al. 2012; Ercolano et al. 2018). As gas is removed from the inside out, the outer ring may become progressively "steepened" or radially compressed, while radiation pressure and stellar winds further erode any remaining material. Thus, the presence of ~0.15 $M_\oplus$ of CO in HD 121617 could reflect late stage gas dispersal rather than a purely secondary gas origin (i.e., collisionally generated, see also Kral et al. 2017 for secondary gas origins). If so, HD 121617 may well illustrate how a disc in the final stages of protoplanetary evolution can masquerade as a debris disc while retaining enough gas to affect dust dynamics and reveal ongoing gas dispersal. The co-location of dust and gas in this case could be simply explained via dust-gas interactions that drive the large dust grains towards the pressure maximum.

In this picture, gas retention beyond ~10 Myr implies that photoevaporation and disc winds operate inefficiently, as expected when the stellar high-energy drivers are intrinsically weak. This naturally explains the prevalence of gas detections around A-type stars (Moór et al. 2017), implying low X-ray and extreme-UV output (e.g. Nakatani et al. 2023). Moreover, if very small grains and Polycyclic Aromatic Hydrocarbons are depleted, the efficiency of far-UV (FUV) photoelectric heating drops sharply, further suppressing FUV-driven photoevaporation (e.g. Nakatani et al. 2021; Coleman & Haworth 2022; Nakatani et al. 2023; Ooyama et al. 2025). Thus, the classification of HD 121617 as an A-type star and the proposed lack of grains with $a \lesssim 1$ μm (Perrot et al. 2023) support the notion of slow protoplanetary disc dispersal and thereby the primordial gas scenario.

5.2. Observational tests for trapping by gas drag

5.2.1. 50 $M_\oplus$ versus 5 $M_\oplus$

The three key observables in HD 121617 are (i) a confined arc in the ALMA band 7 continuum, (ii) a J-band morphology dominated by the scattering phase function, and (iii) a radial offset between the sub-mm and NIR rings. They are reproduced by both our fiducial model with $M_{gas} = 50\,M_\oplus$ and the lower-mass model with $M_{gas} = 5\,M_\oplus$. The hydrodynamical simulations, however, reveal a crucial difference: the size-dependence of the azimuthal structure near the arc. In the low-mass case, the largest grains remain largely unaffected by gas drag and show little or no azimuthal trapping. Because different ALMA bands probe different characteristic grain sizes, multi-band continuum imaging offers a way to break this degeneracy in M_{gas}.

To test this, we perform additional continuum radiative transfer at 0.45, 1.25, and 2.2 mm, representative of ALMA bands 9, 6, and 4, respectively. From each image, we deproject the ring and extract an azimuthal profile by integrating the flux over a narrow radial window (±2 au) centred on the radial peak. We fit the deprojected profile by a Gaussian function atop a constant background (representing the azimuthally symmetric ring component), and normalise the profile by the background.

Figure 15 compares the azimuthal profiles for the two gas masses. We focus on two diagnostics: (i) the contrast of the intensity maximum relative to the smooth (axisymmetric) component, and (ii) the azimuth of the intensity maximum, obtained by fitting a Gaussian to each profile.

For $M_{gas} = 50\,M_\oplus$ (left panel), the peak-to-background contrast at 0.89 mm is 2.08 ± 0.02, the PA of the peak location is 28.0°±0.2° and the azimuthal FWHM of the arc is 67° ± 1°. In the multi-band analysis, we see that the contrast increases systematically with wavelength from band 9 to band 4, while the azimuth of the maximum remains constant within the margin of error. In the $M_{gas} = 5\,M_\oplus$ model (right panel), the peak-to-background contrast at 0.89 mm is 2.35 ± 0.03, the PA of the peak location is 27.9° ± 0.2° and the azimuthal FWHM of the arc is 87° ± 2°.

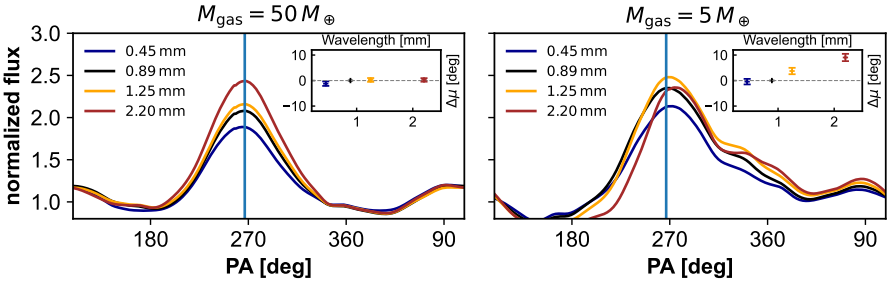

Fig. 15. Normalised azimuthal brightness profiles of the deprojected ring at four wavelengths, 0.45, 0.89, 1.25, and 2.20 mm (ALMA bands 9, 7, 6, and 4), as a function of position angle (PA). PA increases east of north, in the direction of the system's orbital motion. Left: model with $M_{gas} = 50\,M_\oplus$. Right: model with $M_{gas} = 5\,M_\oplus$. Profiles are normalised to the azimuthally smooth ring component (unity corresponds to the smooth-ring level). Insets show the offset of the peak PA at each wavelength relative to the band 7 peak measured in Marino et al. (2026b). In the high-mass model, the peak PA is nearly wavelength-independent and the contrast increases with wavelength; in the low-mass model, the contrast drops at 2.2 mm and the peak shifts systematically toward larger PA with increasing wavelength.

In the multi-wavelength analysis, both diagnostics behave differently: the contrast rises from band 9 to band 6 but then declines towards band 4, and the peak shifts in azimuth by $3.7° \pm 1.3°$ (band 6) and $9.1° \pm 1.4°$ (band 4) relative to the observed band 7 maximum (Marino et al. 2026b).

The declining contrast between bands 6 and 4 in the low-mass case arises because the largest grains, which contribute more to the longer-wavelength emission, are azimuthally more symmetric when the gas mass is lower. As the observing wavelength increases, the measurement becomes more sensitive to this nearly axisymmetric population, diluting the arc contrast. The systematic azimuthal shift is likewise a consequence of size-dependent dust–gas coupling: grains with longer stopping times respond differently to gas asymmetries and tend to lead smaller grains in azimuth (Baruteau et al. 2019).

In summary, a monotonic increase of arc contrast with wavelength and a stationary arc azimuth favour the higher gas mass, whereas a non-monotonic contrast (peaking near band 6) together with a wavelength-dependent azimuthal shift point to the lower-mass scenario.

5.2.2. Planet versus gas drag

While our hydrodynamical simulations demonstrate that the azimuthally asymmetric mm ring observed in HD 121617 can be reproduced through gas–dust interactions, this does not provide a conclusive explanation for such a phenomenon.

An alternative explanation is that the disc asymmetry arises from interactions with an unseen planet (Pearce et al., in prep.). In this scenario, a planet located interior to the debris disc is (artificially) forced to undergo outward migration, similar to Neptune's planetesimal-driven migration in the Solar System (Malhotra 1993; Hahn & Malhotra 1999). As the planet migrates, its mean-motion resonances sweep through the disc, capturing debris bodies in resonances and creating asymmetric clumps in their distribution. The structure, location, and number of these clumps depend on the specific resonances in which the debris becomes trapped, which is a probabilistic event depending on the planetary migration rate (Wyatt 2003). This simple migration model has previously been proposed to explain a clump of planetesimals around β Pic (Matrà et al. 2019), an asymmetric disc around q^1 Eri (Lovell et al. 2021), and tentative clumps in the debris disc around ϵ Eri (Booth et al. 2023). In this purely planetary explanation, it remains to be seen how the measured content of CO gas would impact the dust distribution. Additionally, collective gravity of debris particles may play an important dynamical role by hindering the planet's migration (Hahn & Malhotra 1999), detuning the resonances (Murray et al. 2022), and/or suppressing the debris eccentricities (Sefilian 2024). Consequently, further tests are needed to distinguish between these two possibilities.

One test to differentiate between the planetary and gas drag scenario involves observations in the time domain. As shown by Wyatt (2006), planetesimals in an outward-migrating planetary system become predominantly trapped in 2:1 or 3:2 mean-motion resonances. This implies a planetary orbit at $r_{2:1} = 57$ au or $r_{3:2} = 47$ au. If the arc is sculpted by mean-motion resonances, it should orbit with the planet's own period, rather than the local Keplerian period. At the ring's radius, the Keplerian orbital period is approximately 474 years, so if the dust arc is induced by gas drag it will complete one full rotation on that timescale. However, if the ring was in a 2:1 resonance with an interior planet, it would orbit in 237 years; in a 3:2 resonance, 316 years. Future measurements of the arc's azimuthal shift can be compared against these predictions to distinguish between the two scenarios. If we require a minimum shift of half the beam size (~7 au, Marino et al. 2026a) to confidently register an azimuthal displacement, then for the 2:1, 3:2, and gas-dominated scenarios the necessary intervals are $\Delta t_{2:1} = 4.6$ yr, $\Delta t_{3:2} = 6.1$ yr, and $\Delta t_{gas} = 9.2$ yr, respectively. Given that the initial dataset was obtained between October 2022 and May 2023, a second observational epoch in or after 2033 would detect a positional shift of the arc even under local Keplerian motion. An observation in 2030 could already confirm or rule out the scenario of resonant trapping.

5.3. Caveats and prospects

This study demonstrates a new avenue for simulating debris disc dynamics by adapting numerical techniques originally developed for protoplanetary discs. However, several important considerations remain unaddressed and invite further investigation. An obvious question is about the origin of the radially confined ring, which we imposed as an arbitrary initial condition, assuming that the ring is an inherited structure from the protoplanetary disc phase. Indeed, Orcajo et al. (2025) found that at the latest stage of a surveyed protoplanetary disc sample, the dust typically converges to a narrow isolated ring. One plausible explanation for the inner cavity and the concentration of material at its edge is the presence of a sufficiently massive planet. In fact, in protoplanetary discs, planet–disc interactions have previously been shown to induce vortices at the edge of the gap, similar to what has been observed for HD 121617 (e.g. de Val-Borro et al. 2007).

For HD 121617, only planets more massive than 7 $M_{\rm Jup}$ are ruled-out at the inner edge of the disc (Milli et al. 2026). Even in the absence of planets, similar structures can be induced by steep transitions of the viscosity profile, as expected between active and passive turbulent zones (Flock et al. 2015). Future work should therefore focus on examining debris disc hydrodynamics under the influence of planetary perturbations, aiming to capture both the formation and evolution of these rings in a more comprehensive manner.

Another important flaw is the omission of dust growth, fragmentation, and production by planetesmals (if present) in the numerical evolution of the ring. In debris discs, dust is continuously generated by collisions between larger bodies and may be destroyed in collisions between smaller particles. This ongoing process may introduce a constant redistribution of particle sizes and reduce the size-dependence of the overall density distribution. The collisional timescale can be shorter than the timescale on which gas drag imposes a spatial size seggregation in the disc, depending on the gas density and other parameters. This is discussed in the context of another gas-bearing debris disc, HD 131835, in a companion ARKS study (Jankovic et al. 2026). In a study dedicated primarily to size-dependent radial trapping in debris discs, Olofsson et al. (in prep.) carry out a parameter sweep and find that the SPHERE–ALMA offset is governed primarily by the competition between gas mass and optical depth (a proxy for the collisional timescale). They find that there is a "sweet spot" in dust-to-gas ratio where the offset is maximised. They find that at high gas mass and low optical depth, a secondary mm ring can appear and mimic a gap carved by a planet.

However, the high collision rates typically assumed in debris discs rely on large relative velocities driven by orbital eccentricities and inclinations. In the presence of substantial gas, these orbital elements are rapidly damped unless there is a continuous mechanism re-exciting them, thereby lowering the collisional velocities compared to a gas-free scenario. Hence, if the gas is primordial, its damping of relative velocities would suppress destructive collisions and increase the survival time of solids. This raises the possibility that the dust population is at least partly primordial rather than maintained solely by planetesimal collisions. For a detailed consideration of dust trapped inside a gas ring and the relevance of collisions in the context of a debris disc, we further refer to the discussion Section 4.1 of Pearce et al. (2020).

Gas drag might also play an important role in other systems that are classified as debris discs. A prominent example is the exoKuiper belt around HD 181327, where CO is co-located with a band 6 continuum ring (Marino et al. 2016). In this system, the observational evidence reveals notable differences: the millimetre continuum appears comparatively smooth, whereas optical scattered-light observations with the Hubble Space Telescope show an azimuthal asymmetry (Stark et al. 2014; Fox & Wiegert 2025). This trend is qualitatively consistent with a reduced gas content compared to HD 121617 (as illustrated, for example, in Fig. 12) and is in agreement with the low CO mass inferred for HD 181327 ($M_{\rm CO} \sim 2 \times 10^{-6}\,M_{\oplus}$; Marino et al. 2016). A definitive test of this interpretation would require dedicated, system-specific simulations, which are beyond the scope of this work.

6. Conclusions

We used hydrodynamical simulations with self-consistent dust-gas coupling to test whether gas drag can explain the submillimetre continuum arc observed in the debris disc of HD 121617. Our main findings can be summarised as follows:

1. Gas drag trapping can reproduce the ALMA arc: a marginally stable gas ring naturally produces azimuthal dust concentrations when the aerodynamic coupling is sufficiently high. In particular, models with total gas masses of $M_{\rm gas} = 50\,M_{\oplus}$ and $5\,M_{\oplus}$ both reproduce the observed ALMA band 7 continuum arc;
2. Size-dependent dynamics and radiation pressure explain NIR/mm differences: stellar radiation pressure from the A-type host causes small grains to orbit sub-Keplerian and drift outward, while millimetre-sized particles concentrate at the pressure maximum. As a result, μm grains traced in scattered light are displaced outward relative to the mm continuum ring, whereas mm grains form the azimuthal arc. The observed offset between the near-infrared and sub-mm rings thus arises naturally from the different responses of grain sizes to radiation pressure and gas drag;
3. Constraints on the gas mass: the outward shift of the scattered-light ring requires that μm grains are not perfectly entrained, implying a limit on the coupling and therefore on the total gas content. From our models we infer an upper limit of $\sim 250\,M_{\oplus}$ for the total gas mass; conversely, the presence of a pronounced sub-mm arc and the absence of scattered-light asymmetries with respect to the semi-minor axis require at least a few Earth masses of gas, with a conservative lower bound of $\sim 2.5\,M_{\oplus}$. Together, these limits suggest that HD 121617 may contain more gas than its estimated CO content and that predicted from secondary models, favouring a hybrid-disc (primordial gas) scenario;
4. Observational tests: the simulations predict a wavelength-dependent azimuthal contrast because only a restricted range of grain sizes is efficiently azimuthally confined. In the $5\,M_{\oplus}$ model, the largest grains remain closer to an azimuthally uniform distribution than in the $50\,M_{\oplus}$ model, reducing the contrast at longer wavelengths. Moreover, the azimuthal overdensity should orbit at the local Keplerian rate. Multi-wavelength ALMA imaging that probes different grain sizes and a second band 7 epoch to track the pattern's orbital motion would provide decisive tests of gas drag trapping versus alternatives such as resonant confinement by an outward-migrating interior planet.

We note that the quoted gas mass bounds are model-dependent. They are expected to vary with assumptions about the turbulent viscosity, gas temperature and scale height, ring width, and the dust size distribution and opacities that set the relative contributions of trapped versus background grains.

More broadly, our results show that hydrodynamical modelling of continuum substructures can place meaningful constraints on the hidden gas and its origin in debris discs. For HD 121617, a hybrid-disc interpretation can resolve apparent spatial differences between the emission profiles of CO gas and dust structures, yet it implies a more complex evolutionary pathway bridging the protoplanetary and debris disc phases. Future work that couples dust production and destruction with planet-disc interactions will be crucial to establish whether HD 121617 and analogous systems trace the final stages of protoplanetary disc dispersal or a predominantly secondary gas origin.

Data availability

The ARKS data used in this paper can be found in the ARKS Dataverse (https://dataverse.harvard.edu/dataverse/arkslp). For more information, visit https://arkslp.org.

Acknowledgements. PW and SP acknowledge support from FONDECYT grants 3220399 and 1231663 and ANID – Millennium Science Initiative Program – Center Code NCN2024_001. SM acknowledges funding by the Royal Society through a Royal Society University Research Fellowship (URF-R1-221669) and the European Union through the FEED ERC project (grant number 101162711). MRJ acknowledges support from the European Union's Horizon Europe Programme under the Marie Sklodowska-Curie grant agreement no. 101064124 and funding provided by the Institute of Physics Belgrade, through the grant by the Ministry of Science, Technological Development, and Innovations of the Republic of Serbia. TDP is supported by a UKRI Stephen Hawking Fellowship and a Warwick Prize Fellowship, the latter made possible by a generous philanthropic donation. A.A.S. is supported by the Heising-Simons Foundation through a 51 Pegasi b Fellowship. JBL acknowledges the Smithsonian Institute for funding via a Submillimeter Array (SMA) Fellowship, and the North American ALMA Science Center (NAASC) for funding via an ALMA Ambassadorship. CdB acknowledges support from the Spanish Ministerio de Ciencia, Innovación y Universidades (MICIU) and the European Regional Development Fund (ERDF) under reference PID2023-153342NB-I00/10.13039/501100011033, from the Beatriz Galindo Senior Fellowship BG22/00166 funded by the MICIU, and the support from the Universidad de La Laguna (ULL) and the Consejería de Economía, Conocimiento y Empleo of the Gobierno de Canarias. AMH acknowledges support from the National Science Foundation under Grant No. AST-2307920. SMM acknowledges funding by the European Union through the E-BEANS ERC project (grant number 100117693), and by the Irish research Council (IRC) under grant number IRCLA- 2022-3788. Views and opinions expressed are however those of the author(s) only and do not necessarily reflect those of the European Union or the European Research Council Executive Agency. Neither the European Union nor the granting authority can be held responsible for them. AB acknowledges research support by the Irish Research Council under grant GOIPG/2022/1895. LM acknowledges funding by the European Union through the E-BEANS ERC project (grant number 100117693), and by the Irish research Council (IRC) under grant number IRCLA-2022-3788. Views and opinions expressed are however those of the author(s) only and do not necessarily reflect those of the European Union or the European Research Council Executive Agency. Neither the European Union nor the granting authority can be held responsible for them. JM acknowledges funding from the Agence Nationale de la Recherche through the DDISK project (grant No. ANR-21-CE31-0015) and from the PNP (French National Planetology Program) through the EPOPEE project. Support for BZ was provided by The Brinson Foundation. EC acknowledges support from NASA STScI grant HST-AR-16608.001-A and the Simons Foundation. MB acknowledges funding from the Agence Nationale de la Recherche through the DDISK project (grant No. ANR-21-CE31-0015). This work was also supported by the NKFIH NKKP grant ADVANCED 149943 and the NKFIH excellence grant TKP2021-NKTA-64. Project no.149943 has been implemented with the support provided by the Ministry of Culture and Innovation of Hungary from the National Research, Development and Innovation Fund, financed under the NKKP ADVANCED funding scheme. This research was partially supported by the supercomputing infrastructure of the NLHPC (CCSS210001). This work made use of the Puelche cluster hosted at CIRAS/USACH. This paper makes use of the following ALMA data: ADS/JAO.ALMA# 2022.1.00338.L, 2012.1.00142.S, 2012.1.00198.S, 2015.1.01260.S, 2016.1.00104.S, 2016.1.00195.S, 2016.1.00907.S, 2017.1.00167.S, 2017.1.00825.S, 2018.1.01222.S and 2019.1.00189.S. ALMA is a partnership of ESO (representing its member states), NSF (USA) and NINS (Japan), together with NRC (Canada), MOST and ASIAA (Taiwan), and KASI (Republic of Korea), in cooperation with the Republic of Chile. The Joint ALMA Observatory is operated by ESO, AUI/NRAO and NAOJ. The National Radio Astronomy Observatory is a facility of the National Science Foundation operated under cooperative agreement by Associated Universities, Inc. The project leading to this publication has received support from ORP, that is funded by the European Union's Horizon 2020 research and innovation programme under grant agreement No 101004719 [ORP]. We are grateful for the help of the UK node of the European ARC in answering our questions and producing calibrated measurement sets. This research used the Canadian Advanced Network For Astronomy Research (CANFAR) operated in partnership by the Canadian Astronomy Data Centre and The Digital Research Alliance of Canada with support from the National Research Council of Canada the Canadian Space Agency, CANARIE and the Canadian Foundation for Innovation.

References

Alexander, R., Pascucci, I., Andrews, S., Armitage, P., & Cieza, L. 2014, in Protostars and Planets VI, eds. H. Beuther, R. S. Klessen, C. P. Dullemond, & T. Henning, 475
Ansdell, M., Williams, J. P., van der Marel, N., et al. 2016, ApJ, 828, 46
Backman, D. E., & Paresce, F. 1993, in Protostars and Planets III, eds. E. H. Levy, & J. I. Lunine, 1253
Bai, X.-N., Ye, J., Goodman, J., & Yuan, F. 2016, ApJ, 818, 152
Balbus, S. A., & Hawley, J. F. 1991, ApJ, 376, 214
Baruteau, C., & Zhu, Z. 2016, MNRAS, 458, 3927
Baruteau, C., Barraza, M., Pérez, S., et al. 2019, MNRAS, 486, 304
Benítez-Llambay, P., Krapp, L., & Pessah, M. E. 2019, ApJS, 241, 25
Bergez-Casalou, C., & Kral, Q. 2024, A&A, 692, A156
Bergin, E. A., Cleeves, L. I., Gorti, U., et al. 2013, Nature, 493, 644
Besla, G., & Wu, Y. 2007, ApJ, 655, 528
Birnstiel, T., Dullemond, C. P., & Brauer, F. 2010, A&A, 513, A79
Bonsor, A., Wyatt, M. C., Marino, S., et al. 2023, MNRAS, 526, 3115
Booth, M., Pearce, T. D., Krivov, A. V., et al. 2023, MNRAS, 521, 6180
Brennan, A., Matrà, L., Mac Manamon, S., et al. 2026, A&A, 705, A201
Burns, J. A., Lamy, P. L., & Soter, S. 1979, Icarus, 40, 1
Castrejon, A., Lyra, W., Richert, A. J. W., & Kuchner, M. 2019, ApJ, 887, 6
Cataldi, G., Aikawa, Y., Iwasaki, K., et al. 2023, ApJ, 951, 111
Chang, E., Youdin, A. N., & Krapp, L. 2023, ApJ, 946, L1
Charnoz, S., Fouchet, L., Aleon, J., & Moreira, M. 2011, ApJ, 737, 33
Clarke, C. J., Gendrin, A., & Sotomayor, M. 2001, MNRAS, 328, 485
Coleman, G. A. L., & Haworth, T. J. 2022, MNRAS, 514, 2315
Crnkovic-Rubsamen, I., Zhu, Z., & Stone, J. M. 2015, MNRAS, 450, 4285
Cui, C., Marino, S., Kral, Q., & Latter, H. 2024, MNRAS, 530, 1766
Czechowski, A., & Mann, I. 2007, ApJ, 660, 1541
de Val-Borro, M., Edgar, R. G., Artymowicz, P., et al. 2006, MNRAS, 370, 529
de Val-Borro, M., Artymowicz, P., D'Angelo, G., & Peplinski, A. 2007, A&A, 471, 1043
Doi, K., Kataoka, A., Liu, H. B., et al. 2024, ApJ, 974, L25
Dominik, C., Min, M., & Tazaki, R. 2021, OpTool: Command-line driven tool for creating complex dust opacities, Astrophysics Source Code Library [record ascl:2104.010]
Dubrulle, B., Morfill, G., & Sterzik, M. 1995, Icarus, 114, 237
Dullemond, C. P., Juhasz, A., Pohl, A., et al. 2012, RADMC-3D: A multi-purpose radiative transfer tool, Astrophysics Source Code Library [record ascl:1202.015]
Dullemond, C. P., Birnstiel, T., Huang, J., et al. 2018, ApJ, 869, L46
Ercolano, B., & Pascucci, I. 2017, Roy. Soc. Open Sci., 4, 170114
Ercolano, B., Weber, M. L., & Owen, J. E. 2018, MNRAS, 473, L64
Espaillat, C., Muzerolle, J., Najita, J., et al. 2014, in Protostars and Planets VI, eds. H. Beuther, R. S. Klessen, C. P. Dullemond, & T. Henning, 497
Flock, M., Ruge, J. P., Dzyurkevich, N., et al. 2015, A&A, 574, A68
Fox, C., & Wiegert, P. 2025, arXiv e-prints [arXiv:2501.01387]
Fu, W., Li, H., Lubow, S., Li, S., & Liang, E. 2014, ApJ, 795, L39
Fuente, A., Baruteau, C., Neri, R., et al. 2017, ApJ, 846, L3
Gaia Collaboration (Vallenari, A., et al.) 2023, A&A, 674, A1
Grigorieva, A., Thébault, P., Artymowicz, P., & Brandeker, A. 2007, A&A, 475, 755
Hahn, J. M., & Malhotra, R. 1999, AJ, 117, 3041
Hales, A. S., Gorti, U., Carpenter, J. M., Hughes, M., & Flaherty, K. 2019, ApJ, 878, 113
Hammer, M., Pinilla, P., Kratter, K. M., & Lin, M.-K. 2019, MNRAS, 482, 3609
Han, Y., Mansell, E., Jennings, J., et al. 2026, A&A, 705, A196
Hughes, A. M., Duchêne, G., & Matthews, B. C. 2018, ARA&A, 56, 541
Jankovic, M., Pawellek, N., Löhne, T., et al. 2026, A&A, 705, A204
Klahr, H., & Lin, D. N. C. 2005, ApJ, 632, 1113
Klusmeyer, J., Hughes, A. M., Matrà, L., et al. 2021, ApJ, 921, 56
Kóspál, Á., Moór, A., Juhász, A., et al. 2013, ApJ, 776, 77
Kral, Q., Wyatt, M., Carswell, R. F., et al. 2016, MNRAS, 461, 845
Kral, Q., Matrà, L., Wyatt, M. C., & Kennedy, G. M. 2017, MNRAS, 469, 521
Kral, Q., Marino, S., Wyatt, M. C., Kama, M., & Matrà, L. 2019, MNRAS, 489, 3670
Krivov, A. V., Herrmann, F., Brandeker, A., & Thébault, P. 2009, A&A, 507, 1503
Lesur, G., Flock, M., Ercolano, B., et al. 2023, in Astronomical Society of the Pacific Conference Series, 534, Protostars and Planets VII, eds. S. Inutsuka, Y. Aikawa, T. Muto, K. Tomida, & M. Tamura, 465
Lin, M.-K. 2014, MNRAS, 437, 575
Lovelace, R. V. E., Li, H., Colgate, S. A., & Nelson, A. F. 1999, ApJ, 513, 805
Lovell, J. B., Marino, S., Wyatt, M. C., et al. 2021, MNRAS, 506, 1978
Lovell, J. B., Hales, A. S., Kennedy, G. M., et al. 2026, A&A, 705, A200
Lyra, W., & Kuchner, M. 2013, Nature, 499, 184
Lynch, E. M., Lovell, J. B., & Sefilian, A. A. 2024, MNRAS, 529, L147
Mac Manamon, S., Matrà, L., Marino, S., et al. 2025, A&A, 705, A198
Malhotra, R. 1993, Nature, 365, 819
Mamajek, E. E., & Bell, C. P. M. 2014, MNRAS, 445, 2169
Marino, S. 2022, arXiv e-prints [arXiv:2202.03053]
Marino, S., Matrà, L., Stark, C., et al. 2016, MNRAS, 460, 2933
Marino, S., Flock, M., Henning, T., et al. 2020, MNRAS, 492, 4409
Marino, S., Gupta, V., Weber, P., et al. 2026a, A&A, 705, A202
Marino, S., Matrà, L., Hughes, A. M., et al. 2026b, A&A, 705, A195

Masset, F. 2000, A&AS, 141, 165
Matrà, L., Panić, O., Wyatt, M. C., & Dent, W. R. F. 2015, MNRAS, 447, 3936
Matrà, L., Wyatt, M. C., Wilner, D. J., et al. 2019, AJ, 157, 135
Matrà, L., Marino, S., Wilner, D. J., et al. 2025, A&A, 693, A151
McClure, M. K., Bergin, E. A., Cleeves, L. I., et al. 2016, ApJ, 831, 167
Meheut, H., Meliani, Z., Varniere, P., & Benz, W. 2012, A&A, 545, A134
Milli, J., Olofsson, J., Bonduelle, M., et al. 2026, A&A, 705, A199
Min, M., Canovas, H., Mulders, G. D., & Keller, C. U. 2012, A&A, 537, A75
Moór, A., Curé, M., Kóspál, Á., et al. 2017, ApJ, 849, 123
Murray, Z., Hadden, S., & Holman, M. J. 2022, ApJ, 931, 66
Nakatani, R., Kobayashi, H., Kuiper, R., Nomura, H., & Aikawa, Y. 2021, ApJ, 915, 90
Nakatani, R., Turner, N. J., Hasegawa, Y., et al. 2023, ApJ, 959, L28
Olofsson, J., Thébault, P., Kral, Q., et al. 2022, MNRAS, 513, 713
Ono, T., Muto, T., Takeuchi, T., & Nomura, H. 2016, ApJ, 823, 84
Ono, T., Muto, T., Tomida, K., & Zhu, Z. 2018, ApJ, 864, 70
Ooyama, W., Nakatani, R., Hosokawa, T., Mitani, H., & Turner, N. J. 2025, ApJ, 983, 153
Orcajo, S., Cieza, L. A., Guilera, O., et al. 2025, ApJ, 984, L57
Owen, J. E., Clarke, C. J., & Ercolano, B. 2012, MNRAS, 422, 1880
Pearce, T. D. 2024, arXiv e-prints [arXiv:2403.11804]
Pearce, T. D., Krivov, A. V., & Booth, M. 2020, MNRAS, 498, 2798
Pérez, L. M., Benisty, M., Andrews, S. M., et al. 2018, ApJ, 869, L50
Perrot, C., Olofsson, J., Kral, Q., et al. 2023, A&A, 673, A39
Pinilla, P., Benisty, M., & Birnstiel, T. 2012, A&A, 545, A81
Raettig, N., Klahr, H., & Lyra, W. 2015, ApJ, 804, 35
Rosotti, G. P. 2023, New A Rev., 96, 101674
Safronov, V. S. 1972, Evolution of the protoplanetary cloud and formation of the earth and planets
Sefilian, A. A. 2024, ApJ, 966, 140
Shakura, N. I., & Sunyaev, R. A. 1973, A&A, 24, 337
Smirnov-Pinchukov, G. V., Moór, A., Semenov, D. A., et al. 2022, MNRAS, 510, 1148
Stark, C. C., Schneider, G., Weinberger, A. J., et al. 2014, ApJ, 789, 58
Strom, K. M., Strom, S. E., Edwards, S., Cabrit, S., & Skrutskie, M. F. 1989, AJ, 97, 1451
Takeuchi, T., & Artymowicz, P. 2001, ApJ, 557, 990
Thébault, P., & Augereau, J. C. 2005, A&A, 437, 141
Trapman, L., Miotello, A., Kama, M., van Dishoeck, E. F., & Bruderer, S. 2017, A&A, 605, A69
Whipple, F. L. 1972, in From Plasma to Planet, ed. A. Elvius, 211
Williams, J. P., & Best, W. M. J. 2014, ApJ, 788, 59
Williams, J. P., & Cieza, L. A. 2011, ARA&A, 49, 67
Wyatt, M. C. 2003, ApJ, 598, 1321
Wyatt, M. C. 2006, ApJ, 639, 1153
Youdin, A. N., & Lithwick, Y. 2007, Icarus, 192, 588
Zagorovsky, K., Brandeker, A., & Wu, Y. 2010, ApJ, 720, 923
Zuckerman, B., Forveille, T., & Kastner, J. H. 1995, Nature, 373, 494

[1] Departamento de Física, Universidad de Santiago de Chile, Av. Víctor Jara 3493, Santiago, Chile
[2] Millennium Nucleus on Young Exoplanets and their Moons (YEMS), Chile
[3] Center for Interdisciplinary Research in Astrophysics Space Exploration (CIRAS), Universidad de Santiago, Chile
[4] IRAP, Université de Toulouse, CNRS, CNES, 31400 Toulouse, France
[5] Department of Physics and Astronomy, University of Exeter, Stocker Road, Exeter EX4 4QL, UK
[6] Institute of Physics Belgrade, University of Belgrade, Pregrevica 118, 11080 Belgrade, Serbia
[7] Department of Physics, University of Warwick, Gibbet Hill Road, Coventry CV4 7AL, UK
[8] Institute of Astronomy, University of Cambridge, Madingley Road, Cambridge CB3 0HA, UK
[9] Department of Astronomy and Steward Observatory, The University of Arizona, 933 North Cherry Ave, Tucson, AZ 85721, USA
[10] European Southern Observatory, Karl-Schwarzschild-Strasse 2, 85748 Garching bei München, Germany
[11] National Astronomical Observatory of Japan, Osawa 2-21-1, Mitaka, Tokyo 181-8588, Japan
[12] Department of Astronomy, Graduate School of Science, The University of Tokyo, Tokyo 113-0033, Japan
[13] Center for Astrophysics | Harvard & Smithsonian, 60 Garden St, Cambridge, MA 02138, USA
[14] Instituto de Astrofísica de Canarias, Vía Láctea S/N, La Laguna, 38200 Tenerife, Spain
[15] Departamento de Astrofísica, Universidad de La Laguna, La Laguna, 38200 Tenerife, Spain
[16] Department of Astronomy, Van Vleck Observatory, Wesleyan University, 96 Foss Hill Dr., Middletown, CT 06459, USA
[17] School of Physics, Trinity College Dublin, the University of Dublin, College Green, Dublin 2, Ireland
[18] Univ. Grenoble Alpes, CNRS, IPAG, 38000 Grenoble, France
[19] Department of Astronomy, University of California, Berkeley, Berkeley, CA 94720-3411, USA
[20] Department of Physics and Astronomy, Johns Hopkins University, 3400 N Charles Street, Baltimore, MD 21218, USA
[21] Joint ALMA Observatory, Avenida Alonso de Córdova 3107, Vitacura 7630355, Santiago, Chile
[22] Division of Geological and Planetary Sciences, California Institute of Technology, 1200 E. California Blvd., Pasadena, CA 91125, USA
[23] Konkoly Observatory, HUN-REN Research Centre for Astronomy and Earth Sciences, MTA Centre of Excellence, Konkoly-Thege Miklós út 15–17, 1121 Budapest, Hungary
[24] Institute of Physics and Astronomy, ELTE Eötvös Loránd University, Pázmány Péter sétány 1/A, 1117 Budapest, Hungary
[25] Max-Planck-Insitut für Astronomie, Königstuhl 17, 69117 Heidelberg, Germany

Appendix A: Validation of momentum feedback from a size-distribution

Accurate modelling of dust-to-gas momentum feedback is crucial when the dust-to-gas mass ratio is large. In such cases, the simulation outcome strongly depends on a sufficiently precise implementation of the drag forces exerted by the dust on the gas. Since this aspect has not yet been tested in Dusty FARGO-ADSG, we performed a simple drift test on a one-dimensional grid.

We initialised the gas surface density with a radial power-law:

$$\Sigma_g(r) = \Sigma_{g,0} \left(\frac{r}{r_0}\right)^{-0.5} . \quad \text{(A.1)}$$

We also set the dust density, sampled by the particles, to follow the same power-law profile, ensuring an initial constant dust-to-gas ratio across all radii. We considered an inviscid scenario and discard stochastic kicks between particles. No exact analytical solution exists for dust and gas velocities under a continuous size distribution, only for multiple discrete species (Benítez-Llambay et al. 2019). We therefore compared our numerical results to the analytical expressions for radial and azimuthal velocities derived for discrete sizes (Benítez-Llambay et al. 2019, their Eqs. 70–73). Instead of randomly sampling sizes from a continuous distribution, we split the dust into a small number of discrete bins. In all the tests, we used the cloud-in-cell interpolation scheme. For improved display of the results, we binned every ten simulated particles to a representative data point.

A.1. Single-sized grains

In an initial test, we set $\Sigma_{g,0} = 0.15\,\mathrm{g\,cm^{-2}}$ and distributed 10^3 particles of the same size, $a = 0.1$ mm, over 512 cells. This configuration corresponded to a dust-to-gas ratio of 0.1 and the particles Stokes number corresponded to $\mathrm{St} \sim 0.1 - 1$, depending on the location in the disc. Both dust and gas started with zero radial velocity. The gas azimuthal velocity was set to its pressure-supported sub-Keplerian profile (Eq. 2), the dust particles' azimuthal velocity was set to Keplerian. We find that the particles' velocities rapidly converge to the analytical predictions. Figure A.1 shows the radial velocities and azimuthal deviation from Keplerian velocities after five orbits at $r_0 = 75$ au.

A.2. Multi-sized grains

Next, we considered two discrete dust sizes in the same setup, $a = 0.1$ mm and $a = 1$ mm, using 10^4 total particles. We examined two scenarios, first with $\Sigma_{g,0} = 0.15\,\mathrm{g\,cm^{-2}}$ and $f_{dtg} = 0.1$, then $\Sigma_{g,0} = 0.015\,\mathrm{g\,cm^{-2}}$ and $f_{dtg} = 1$.

Figure A.2 displays the resulting radial velocities and azimuthal deviations from Keplerian rotation for both dust species and the gas, in both the $f_{dtg} = 0.1$ and $f_{dtg} = 1$ cases. We further tested five discrete sizes, each contributing the same dust mass, to achieve an overall dust-to-gas ratio of unity (see Figure A.3). In all those tests, the analytical velocity profiles are well matched by the numerical solution.

A.3. Continuous size distribution

In the simulations presented in this study, we drew particle sizes from a continuous dust size distribution. For a given dust size distribution, dust-to-gas ratio, and gas density profile, we can derive semi-analytic solutions for the corresponding gas radial and azimuthal velocities. Specifically, we discretised the continuous distribution into a large number of bins ($N_{dust} = 1000$) and numerically solve Eqs. 70–71 of Benítez-Llambay et al. (2019). We then compare these solutions with the hydrodynamical results from Dusty FARGO-ADSG at ten orbits. Because each dust size exhibits a different drift behaviour, the local dust-to-gas ratio and size distribution begin to deviate from their initial profiles after only a few orbits, so limiting the evolution to ten orbits ensured closer adherence to the initial conditions, while giving enough time for the numerical solution (markers) to approach the semi-analytical solution (lines).

Figure A.4 illustrates this comparison for $f_{dtg} = 0.2$. Overall, there is good agreement between the two approaches. Any differences are not necessarily due to numerical inaccuracies, but may instead arise from gradual departures in the actual dust-to-gas ratio and size distribution from their assumed initial state in the semi-analytic model.

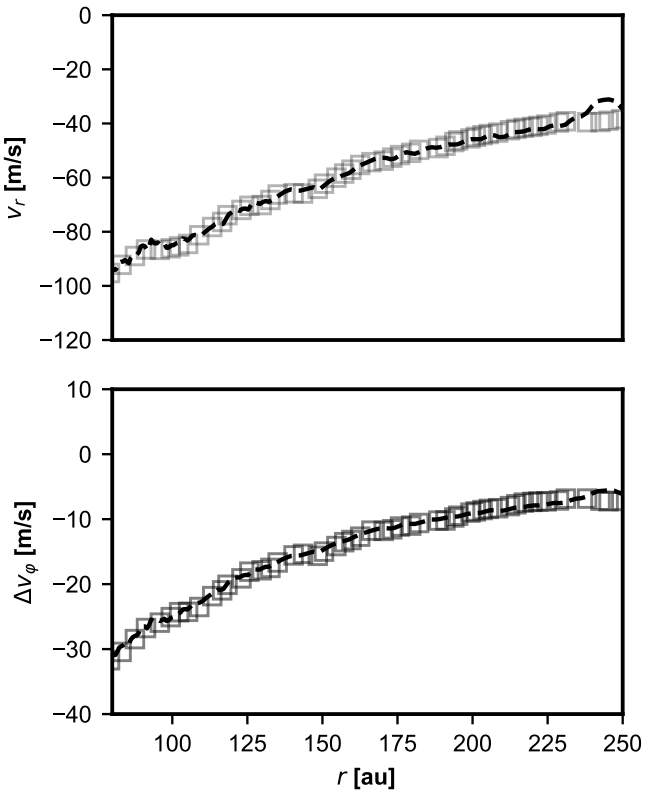

Fig. A.1: Validation of the dust feedback implementation for single-sized grains ($a = 0.1$ mm, $\Sigma_{g,0} = 0.15\,\mathrm{g\,cm^{-2}}$, $f_{dtg} = 0.1$). Top: Radial velocity; Bottom: Difference between azimuthal velocity and local Keplerian velocity. The dashed lines are the analytical solutions (Benítez-Llambay et al. 2019, Eqs. 72–73), and the squares represent the dust particle velocities. For clarity, we binned the velocity of ten neighbouring particles to one representative data point.

Appendix B: Evolution of the asymmetry in the gas ring

The initial condition of our setup is unstable to the Rossby-Wave Instability. This instability generates the asymmetric gas structure that is then imparted onto the solids via friction. However, the instability leads to a radial spreading of the dust ring and, without external forcing, the asymmetry dissipates with time.

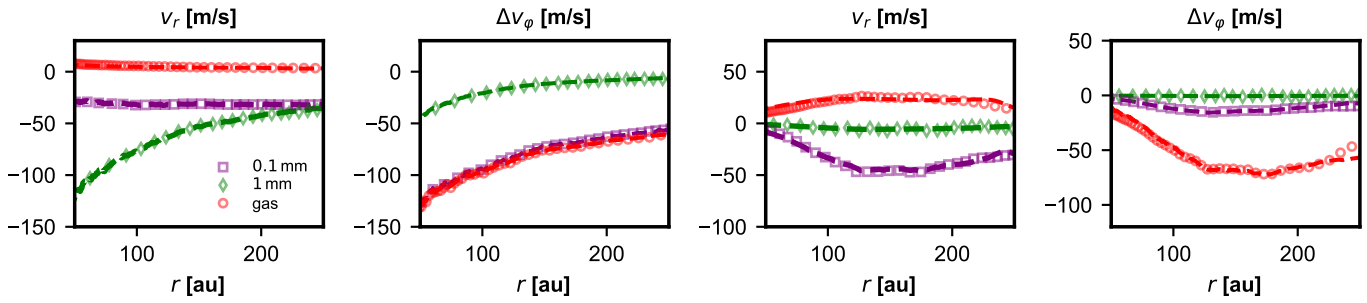

Fig. A.2: Drift test with two discrete dust sizes. Left panels: Radial velocity and azimuthal deviation for $f_{\rm dtg} = 0.1$. Right panels: Same, but with the gas density lowered by a factor of 10, resulting in $f_{\rm dtg} = 1$. The dashed lines show the analytical solutions.

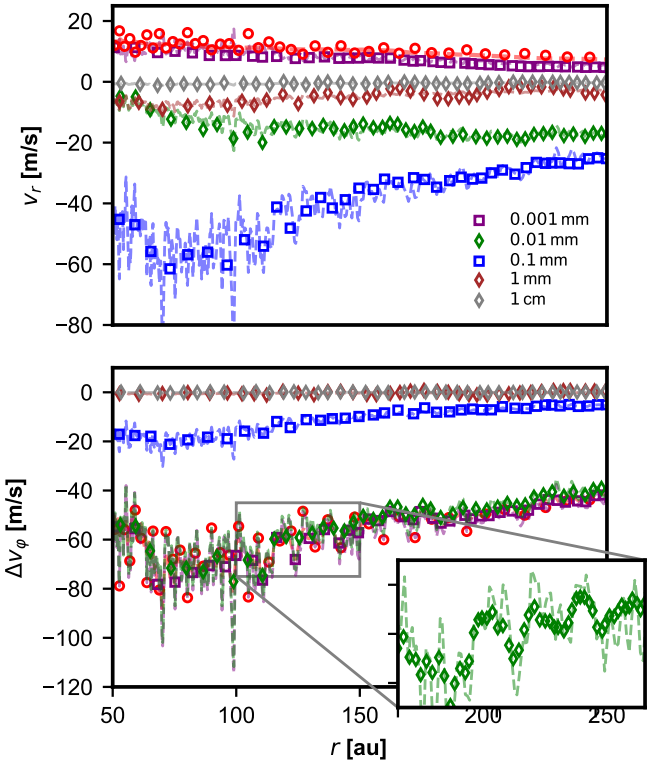

Fig. A.3: Same as Fig. A.2, but with 5 discrete sizes. The total dust-to-gas ratio was unity, and each dust-size bin carried an equal fraction of the total dust mass.

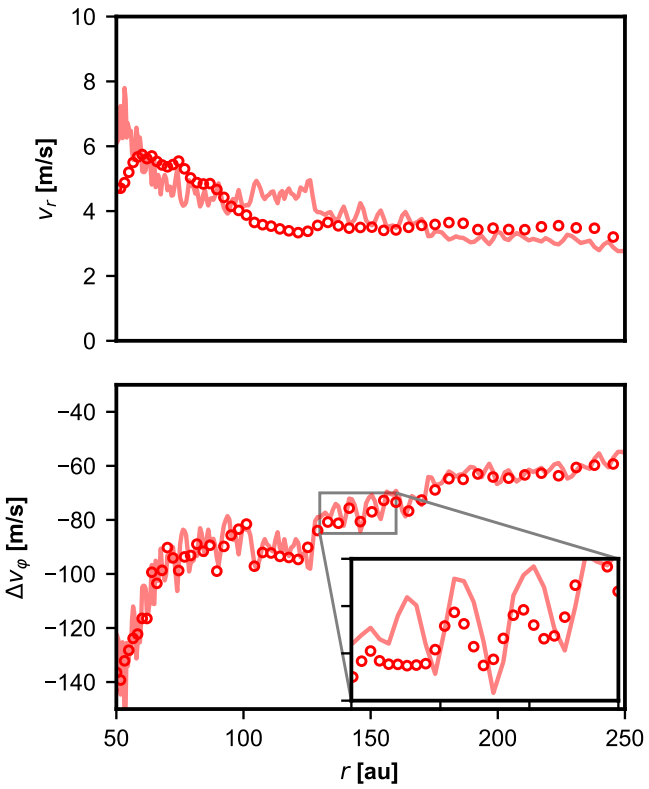

Fig. A.4: Gas velocities for a continuous dust size distribution with a power-law index of −3.5, ranging from 0.1 µm to 1 cm at a dust-to-gas ratio of $f_{\rm dtg} = 0.1$. The solid lines show the semi-analytic solutions from Eqs. 70 (top panel) and 71 (bottom panel) in Benítez-Llambay et al. (2019), based on the gas density profile after ten orbits. Circles indicate the corresponding gas velocities computed by Dusty FARGO-ADSG at the same output time.

Fig. B.1 presents the evolution of the azimuthal asymmetry. 1For each snapshot we divided the gas surface density by its azimuthally averaged profile. In the figure, blue marks regions denser than the local mean, and red marks depleted sectors of the ring. We display this deviation only for regions where the local mean is larger than 0.01 g cm^{-2} (corresponding to ∼7% of Σ_0) to not be confused by contributions from low-density regions. The instability generates its strongest contrast after about 25 orbits. By the time the fiducial model is analysed, after 150 orbits, the asymmetry in the gas has already weakened significantly.

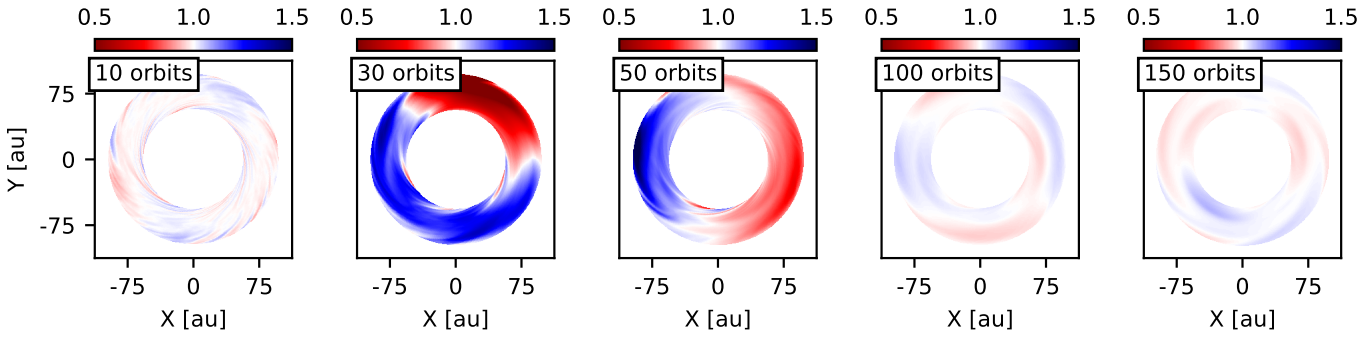

Fig. B.1: Evolution of the asymmetry generated by the unstable gas ring. The colour shows the gas surface density divided by the azimuthally averaged gas surface density. The displayed outputs correspond to 4.7 kyr, 14.1 kyr, 23.6 kyr, 47 kyr and 71 kyr, respectively.

A&A, 705, A202 (2026)
https://doi.org/10.1051/0004-6361/202556493
© The Authors 2026

Astronomy & Astrophysics

The ALMA survey to Resolve exoKuiper belt Substructures (ARKS)

VIII. A dust arc and non-Keplerian gas kinematics in HD 121617

S. Marino[1,⋆], V. Gupta[1], P. Weber[2,3,4], T. D. Pearce[5], A. Brennan[6], S. Pérez[2,3,4], S. Mac Manamon[6], L. Matrà[6], J. Milli[7], M. Booth[8], C. del Burgo[9,10], G. Cataldi[11,12], E. Chiang[13], Y. Han[14], Th. Henning[15], A. M. Hughes[16], M. R. Jankovic[17], Á. Kóspál[18,19,15], J. B. Lovell[20], P. Luppe[6], E. Mansell[16], M. A. MacGregor[21], A. Moór[18], J. Olofsson[22], A. A. Sefilian[23], D. J. Wilner[20], M. C. Wyatt[24], and B. Zawadzki[16]

(Affiliations can be found after the references)

Received 18 July 2025 / Accepted 24 November 2025

ABSTRACT

Context. ExoKuiper belts around young A-type stars often host CO gas, whose origin is still unclear. The ALMA survey to Resolve exoKuiper belt Substructures (ARKS) includes six of these gas-bearing belts, to characterise their dust and gas distributions and investigate the gas origin.

Aims. As part of ARKS, we observed the gas-rich system HD 121617 with a 0.″12 (14 au) resolution and discovered an arc of enhanced dust density. In this paper, we analyse in detail the dust and gas distributions and the gas kinematics of this system.

Methods. We extracted radial and azimuthal profiles of the dust (in the millimetre and near-infrared) and gas emission (^{12}CO and ^{13}CO) from reconstructed images. To constrain the morphology of the arc, we fitted an asymmetric model to the dust emission. To characterise the gas kinematics, we fitted a Keplerian model to the velocity map and extracted the gas azimuthal velocity profile by deprojecting the data.

Results. We find that the dust arc is narrow (1–5 au wide at a radius of 75 au), azimuthally extended with a full width at half maximum of ∼90°, and asymmetric; the emission is more azimuthally compact in the direction of the system's rotation, and represents 13% of the total dust mass (0.2 $M_\oplus$). From analysis of the scattered light and CO images, we conclude that the arc is much less pronounced or absent for small grains and gas. Finally, we find strong non-Keplerian azimuthal velocities at the inner and outer wings of the ring, as was expected due to strong pressure gradients.

Conclusions. The dust arc resembles the asymmetries found in protoplanetary discs, often interpreted as the result of dust trapping in vortices. If the gas disc mass is high enough (≳20 $M_\oplus$, requiring a primordial gas origin), both the radial confinement of the ring and the azimuthal arc may result from dust grains responding to gas drag. Alternatively, it could result from planet-disc interactions via mean motion resonances. Further studies should test these hypotheses and may provide a dynamical gas mass estimate in this CO-rich exoKuiper belt.

Key words. hydrodynamics – methods: data analysis – methods: observational – techniques: interferometric – circumstellar matter – planetary systems

1. Introduction

ALMA observations of debris discs, in particular those analogous to the Kuiper belt (exoKuiper belts), have the potential to constrain the formation and architecture of planetary material at tens of astronomical units (Miller et al. 2021; Najita et al. 2022; Pearce et al. 2022). The recent REASONS survey (Matrà et al. 2025) revealed a great diversity in the morphology of exoKuiper belts using ALMA observations. However, the low resolution of these observations hampered a systematic study of substructures in these discs. The ALMA survey to Resolve exoKuiper belt Substructures (ARKS, Marino et al. 2026) is the first ALMA Large Program dedicated to studying substructures in the dust and gas of 24 exoKuiper belts. One of the key findings of ARKS is the presence of significant asymmetries in 10/24 belts (Lovell et al. 2026).

Among the belts in ARKS, six belong to the particular class of gas-bearing debris discs that are frequently found around young A-type stars (Kóspál et al. 2013; Lieman-Sifry et al. 2016; Moór et al. 2017; Cataldi et al. 2023). The origin of gas (CO, atomic carbon, and other atomic species) is uncertain in these discs. On the one hand, it could be residual protoplanetary disc gas that has not yet dispersed and is dominated by molecular hydrogen (Nakatani et al. 2021, 2023; Ooyama et al. 2025). On the other hand, the CO gas could be released from the solids via thermal desorption, photodesorption, or collisions, and be dominated by volatiles such as CO, carbon, and oxygen (Zuckerman & Song 2012; Dent et al. 2014; Marino et al. 2016; Kral et al. 2019; Marino et al. 2020, 2022; Bonsor et al. 2023).

Of the ten asymmetric belts in ARKS, HD 121617 stands out. This system is composed of a 16 Myr old A1V type star at 118 pc (Pecaut & Mamajek 2016; Houk 1978; Gaia Collaboration 2023) that hosts the brightest gas disc in the sample (Mac Manamon et al. 2026), and displays an asymmetry in the form of a dust

⋆ Corresponding author: s.marino-estay@exeter.ac.uk

Open Access article, published by EDP Sciences, under the terms of the Creative Commons Attribution License (https://creativecommons.org/licenses/by/4.0), which permits unrestricted use, distribution, and reproduction in any medium, provided the original work is properly cited.
This article is published in open access under the Subscribe to Open model. Subscribe to A&A to support open access publication.

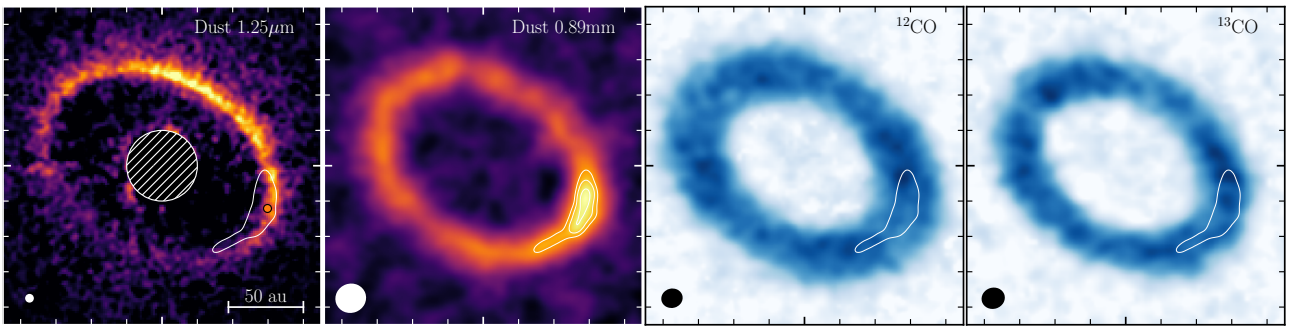

Fig. 1. Dust and gas images of HD 121617. Left panel: scattered light VLT/SPHERE Q_ϕ image at 1.25 μm (J band) observed in polarised light with IRDIS (Milli et al. 2026), smoothed with a Gaussian with a standard deviation of 1 pixel (12 mas). The central hatched region masks an area dominated by strong artefacts. The small orange circle in the SW ansa marks the pericentre location as constrained by Milli et al. (2026). Middle left panel: ALMA dust continuum image at 0.89 mm (Marino et al. 2026). Middle right panel: ^{12}CO J=3-2 moment 0 image (Mac Manamon et al. 2026). Right panel: ^{13}CO J=3-2 moment 0 image (Mac Manamon et al. 2026). The white contours in the middle left image represent 75, 85, and 95% of the peak intensity. The 75% contour is also shown in the other images for reference. The ALMA continuum and CO images were obtained with CLEAN using robust parameters of 1.0 and 0.5, respectively. The beam and PSF sizes are shown as ellipses in the bottom left of each panel. The minor ticks in all panels are spaced by 0.″2.

overdensity or arc (Lovell et al. 2026). Its debris disc was first identified as an infrared excess detected from the mid-infrared with IRAS, AKARI, and WISE to the far-infrared with Herschel (Mannings & Barlow 1998; Fujiwara et al. 2013; Perrot et al. 2023). It was later resolved with ALMA at low resolution (Moór et al. 2017) and more recently in scattered light as a narrow dusty debris disc (Perrot et al. 2023). The disc has a fractional luminosity of 5×10^{-3} (Marino et al. 2026), which is among the highest in the sample of known gas-rich debris discs (Moór et al. 2017, 2025).

The scattered light data, and their re-analysis as part of ARKS, revealed a narrow belt of small dust grains and a potential small eccentricity of 0.03, with a pericentre towards the southwest (SW) ansa where the dust arc peaks (Perrot et al. 2023; Milli et al. 2026). The new ALMA observations revealed an azimuthally extended overdensity in millimetre dust (Lovell et al. 2026) that resembles the overdensities seen in protoplanetary discs, typically attributed to dust trapped in vortices (e.g. Casassus et al. 2013; van der Marel et al. 2013; Marino et al. 2015; Baruteau & Zhu 2016; Regály et al. 2017). The CO gas emission, on the other hand, does not show any strong asymmetry (Mac Manamon et al. 2026). HD 121617's low inclination and high CO flux make it the ideal ARKS target to study dust and gas asymmetries, as well as gas kinematics in exoKuiper belts.

Motivated by the dust overdensity, this paper closely examines the dust asymmetry and gas kinematics to assess the nature of this feature. In Sect. 2, we examine the dust and gas distributions and fit a parametric model to the millimetre dust distribution to constrain the morphology of the arc. In Sect. 3, we analyse the ^{12}CO J=3-2 (hereafter ^{12}CO, unless otherwise stated) gas kinematics and find strong deviations from Keplerian rotation using the ARKS new high spectral (velocity) resolution. Sect. 4 discusses the origin of the arc, the presence of non-Keplerian kinematics in exoKuiper belts, and the gas origin in this system. Finally, Sect. 5 summarises our findings and conclusions.

2. Dust and gas distribution

To constrain the distribution of large millimetre-sized grains and CO gas, in this section we use the new ALMA images obtained as part of ARKS (2022.1.00338.L, PI: S. Marino, co-PIs: A. M. Hughes & L. Matrà). HD 121617 was observed in band 7 (0.89 mm) between October 2022 and May 2023 using two antenna configurations to sample small and large scale structures, which yielded a resolution of 0.″12 or 14 au and a maximum recoverable scale of ∼5″ or 600 au. The observations included four spectral windows targeting the dust continuum emission that is dominated by millimetre-sized grains and the ^{12}CO and ^{13}CO gas J=3-2 emission. The ^{12}CO and ^{13}CO observations had a spectral resolution of 26 and 850 m/s, respectively. This means that only the ^{12}CO data is suitable for a detailed analysis of its kinematics. Imaging of the continuum and CO data was performed using the Clean algorithm (for more details see Marino et al. 2026; Mac Manamon et al. 2026).

To constrain the distribution of small grains, we used VLT/SPHERE polarised data that traces the scattered light by small micron-sized grains. We used a re-reduced Q_ϕ image at 1.25 μm (J band), obtained using IRDIS on 18 April 2018 and achieving a resolution of 0.″04 or 5 au. The data were originally presented in Perrot et al. (2023) and re-reduced by Milli et al. (2026) as part of ARKS.

The SPHERE and ALMA images are shown in Figure 1. The peak signal-to-noise (S/N) of the SPHERE image, ALMA dust, ^{12}CO, and ^{13}CO images is 10, 24, 21, and 19, respectively. The asymmetry is only strong in the dust emission at 0.89 mm, which is highlighted with white contours in all images. Note that the increased emission towards the NW in the scattered light image at 1.25 μm is due to the polarised scattering phase function, which favours forward scattering, i.e. scattering from the near-side of the belt (Min et al. 2012).

2.1. Radial and azimuthal profiles

Here, we focus on characterising the distribution of the micron-sized grains, millimetre-sized grains, and CO gas uniformly. For this, we extracted radial and azimuthal intensity profiles from the SPHERE scattered light image, ARKS dust continuum image, and ARKS ^{12}CO and ^{13}CO J=3-2 moment 0 images.

The top left panel of Figure 2 shows the radial profiles extracted directly from the CLEAN images using the same approach as presented in Han et al. (2026)[1] and assuming the

[1] For the ALMA dust continuum and CO images we use two opposing 120° wide wedges aligned with the disc major axis, whereas for the SPHERE image we use narrower wedges of 60° since the emission is affected by the phase function.

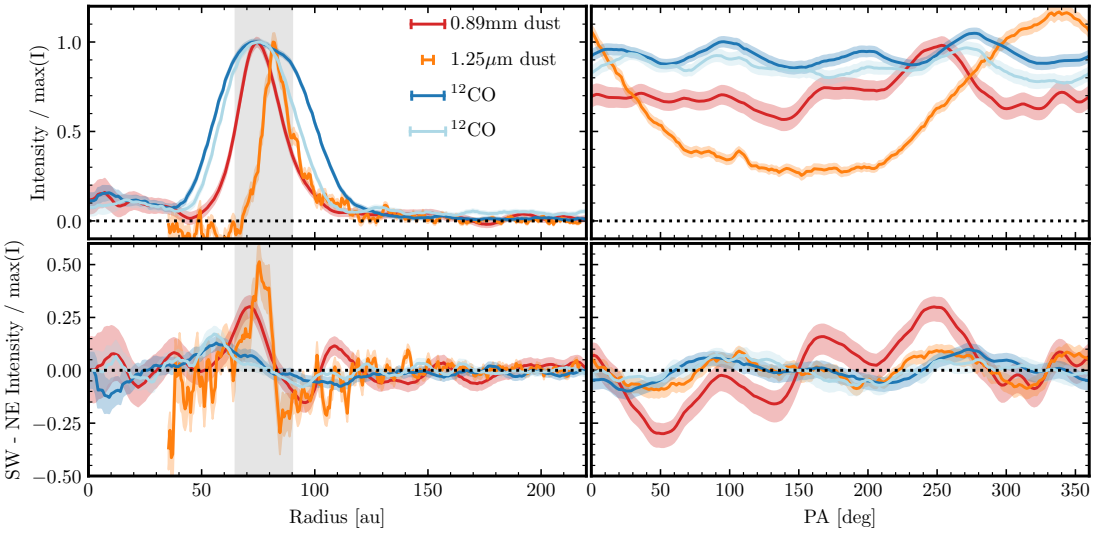

Fig. 2. Radial and azimuthal profiles extracted from the SPHERE and ALMA dust and gas images (produced with a robust parameter of 0.5). Top left panel: de-projected and azimuthally averaged intensity radial profiles extracted from wedges towards the NE and SW ansae with a width of 120° for ALMA and 60° for SPHERE. The bars on the top right indicate the resolution of each profile. Bottom left: residual radial profiles after subtracting the average intensity of the NE from the SW ansa. Top right: intensity azimuthal profiles obtained by averaging the emission between 65 and 90 au and over 40° rolling windows. Bottom right: residual azimuthal profiles after subtracting the mirrored profile relative to the NW minor axis of the disc (PA of 330°). The shaded coloured region in all panels represents the 1σ uncertainty taking into account the image noise and number of independent points being averaged (i.e. points spaced by a beam). The vertical shaded grey region in the left panels shows the radial region that was averaged when extracting the azimuthal profiles. The dust and gas intensities are normalised by their radial profile peaks.

images to be well centred on the stars[2]. As is discussed in Milli et al. (2026), the small dust distribution traced at 1.25 μm peaks ∼7 au further out than the millimetre emission, which could be due to the combined effect of radiation pressure and gas-drag (as explored in Jankovic et al. 2026). The ^{12}CO emission profile, on the other hand, peaks at a radius of 73 au that is similar to the peak radius of large dust grains (74 au). However, the CO emission is more radially extended with a full width at half maximum (FWHM) of 48 au (Mac Manamon et al. 2026) compared to the 12 au for the small and 22 au for the large dust components (as measured from the radial profiles in Fig. 2). The ^{13}CO emission is less extended with a FWHM of 37 au compared to the ^{12}CO, although still more extended than both the millimetre- and micron-sized dust profiles. The wider radial span of ^{12}CO compared to ^{13}CO and the dust can be simply explained by its high optical depth as demonstrated in Brennan et al. (2026), with the surface density profile having a width that is consistent with that of the dust.

In addition, we investigate whether the emission profiles along the NE and SW ansae display any shift due to the belt being eccentric, as found in the scattered light emission (Perrot et al. 2023; Milli et al. 2026). The bottom left panel of Figure 2 shows the difference between radial profiles extracted from wedges towards the SW and NE ansae, hereafter called residuals. The residuals from the scattered light (orange) display an 'S' profile, indicating that the SW emission is slightly closer to the star relative to the NE emission. The fact that the positive and negative have roughly the same amplitude implies that there is no strong excess of emission on the SW side of the scattered light, in contrast to the millimetre emission, but an offset in position. Because the SW is slightly closer to the star than the NE due to the 0.03 eccentricity, the SW side would be expected to be ∼10% brighter in scattered light, which may explain why the positive residual has a larger amplitude than its negative counterpart in the scattered light profile.

The ^{12}CO and ^{13}CO residuals also display a significant signal with an 'S' profile as the scattered light profile, indicating a potential eccentricity in the CO emission. The ^{12}CO emission peaks at 80 au on the NE side versus 75 au on the SW side. This difference is consistent with that expected from an eccentricity of ∼0.03. The residual is still significant if we assume a different stellar location; for example, the centre derived from the millimetre emission (Sect. 2.2) or the ^{12}CO kinematics (Sect. 3). However, we note that the stellar location uncertainty of $\lesssim$10 mas (Marino et al. 2026) is of the same order as the expected belt offset from a 0.03 eccentricity (20 mas) towards the NE direction. Additionally, an apparent offset in the minor axis direction would be expected if the ^{12}CO and ^{13}CO emission is optically thick and tracing a vertically elevated $\tau \sim 2/3$ layer (Brennan et al. 2026), as is seen for protoplanetary discs. In that case, the offset would differ between ^{12}CO and ^{13}CO due to the different heights of this layer, but this difference is too small to be disentangled with the current uncertainties. Therefore, we cannot confirm this eccentricity in the CO emission.

The millimetre dust residual displays a peak that corresponds to the arc location. Beyond the positive residual at 75 au, we find a 3σ negative residual at 95 au. This suggests that the millimetre dust distribution could also be eccentric, with the NE side being more extended. However, the significance of this feature drops to 2.5σ if we assume a stellar location at the centre derived from the millimetre emission fit (Sect. 2.2). The SW profile peaks at 74.2 au and NE at 75.2, which is a difference much smaller than expected for the 0.03 eccentricity seen in scattered light. However, the fact that the millimetre emission is highly asymmetric makes it challenging to assess whether the disc is

[2] The stellar location is well known in the SPHERE observations and corresponds to the image centre (Milli et al. 2026). For ALMA, the star is not detected. However, from Gaia DR3's astrometric solution and ALMA astrometric precision, we know the star should be at the centre with an uncertainty of $\lesssim$10 mas (Marino et al. 2026).

eccentric. Therefore, we can neither confirm nor rule out that the millimetre emission is eccentric.

The top right panel of Figure 2 shows the azimuthal intensity profiles with a PA of 0° aligned with north increasing anti-clockwise on the plane of the sky. The profiles are extracted by averaging the emission between 65 and 90 au (roughly the FWHM of the millimetre emission) using a rolling azimuthal window of 40° projected in the sky plane, which boosts the S/N and smooths the recovered profile. The asymmetry in the millimetre dust emission (solid red line) peaks at a position angle (PA) of ∼250°, but it spans a wide range of PA. The peak excess is about ∼40% of the average intensity beyond the arc. However, we note that both the beam and azimuthal averaging could make this excess appear lower than its true value. For example, our modelling in Sect. 2.2 shows that the overdensity could have a peak density that is twice the background density or even larger. Finally, the excess seems to have a sharper edge towards larger PAs (anti-clockwise from the peak) than to the opposite side.

The scattered light emission (solid orange line) has a strong azimuthal dependence due to the polarised scattering phase function that favours forward-scattering. To account for this effect, we self-subtracted the emission mirroring the azimuthal profile with respect to the semi-minor axis at the near side of the ring (at a PA of 330° as derived from scattered light, Milli et al. 2026, and consistent with the ALMA continuum and CO gas kinematics modelling in Sects. 2.2 and 3). The self-subtracted profile (orange line in the bottom right panel of Figure 2) shows a 2σ excess centred at ∼250°, and that is ∼20% of the emission at the corresponding PA. However, this feature only appears when averaging the emission between 65 and 90 au. If we extend this range to 110 au, this asymmetry disappears. This is because the scattered light emission is slightly eccentric as described above, with the SW side being closer in than the NE side (Milli et al. 2026). Overall, these findings suggest that the arc, if any, is less prominent in the distribution of small grains.

The ^{12}CO and ^{13}CO emission displays an azimuthal modulation with four maxima 45° away from the major and minor axes. This is common in moment 0 maps for optically thick line emission, as the Keplerian shear along the line of sight and within a beam makes the line wider and the integrated line flux higher in those locations (Brennan et al. 2026). Apart from this modulation, we do not find any significant feature (e.g. the residual azimuthal profile is consistent with zero). We also analyse the azimuthal profile of the moment 8 maps (i.e. peak intensity image) and find no significant excess at any PA. Therefore, we conclude that there is no significant asymmetry in the ^{12}CO and ^{13}CO emission (apart from a small eccentricity). However, since both the ^{12}CO and ^{13}CO emissions are optically thick, we cannot rule out the presence of an asymmetry in the gas density distribution similar to that seen in the millimetre-sized dust.

2.2. Arc parametric fit to continuum emission

To constrain the morphology of the arc in the distribution of millimetre-sized grains, we fitted a parametric model to the continuum visibilities following the same approach as in Marino et al. (2026) using `disc2radmc` (a python wrapper to use RADMC3D[3], Marino et al. 2022) and an MCMC to sample the parameter space. Simply put, we used a parametric model to define the disc density distribution, produced a synthetic image using radiative transfer calculations, Fourier transformed the image and calculated the model likelihood using Galario (Tazzari et al. 2018), and sampled the posterior distribution using the Python package EMCEE (Foreman-Mackey et al. 2013) to fit the free parameters using the Affine Invariant MCMC Ensemble sampler (Goodman & Weare 2010).

We modelled the dust surface density as the sum of two components: an axisymmetric component, $\Sigma_a(r)$, described as a double power law as a function of the radial cylindrical coordinate, r, which was found to provide a good fit to the azimuthally averaged radial profile (Han et al. 2026); and an asymmetric component $\Sigma_c(r,\phi)$ described as a 2D Gaussian as a function of r and the azimuthal angle, ϕ, measured anti-clockwise in the plane of the disc from the SW ansa. This parametrisation offers adequate flexibility to constrain the radial and azimuthal widths of the arc. The surface density is thus defined as

$$\Sigma(r,\phi) = \Sigma_a(r) + \Sigma_c(r,\phi), \tag{1}$$

$$\Sigma_a(r) = 2^{1/\gamma}\Sigma_0 \left[\left(\frac{r}{r_0}\right)^{-\alpha_{\rm in}\gamma} + \left(\frac{r}{r_0}\right)^{-\alpha_{\rm out}\gamma}\right]^{-1/\gamma}, \tag{2}$$

$$\Sigma_c(r,\phi) = A_c\Sigma_0 \exp\left[-\frac{(r-r_c)^2}{2\sigma_r^2} - \frac{(\phi-\phi_c)^2}{2\sigma_\phi^2}\right], \tag{3}$$

$$\sigma_\phi = \begin{cases}\sigma_{\phi 1}, & \text{if } \phi > \phi_c \\ \sigma_{\phi 2}, & \text{if } \phi < \phi_c\end{cases} \tag{4}$$

where $\alpha_{\rm in}$ and $\alpha_{\rm out}$ control how steep the inner and outer edges of the belt are, γ controls how smooth or sharp the surface density radial peak is, and r_0 determines the peak radius of the axisymmetric component. For the asymmetric component, A_c controls the peak density of the arc relative to the axisymmetric component, r_c and σ_r control the radial location and width of the arc, whereas ϕ_c and σ_ϕ control its azimuthal location and width.

Furthermore, we split σ_ϕ into two parameters to allow the arc to be azimuthally asymmetric as the azimuthal profile suggests. We thus use $\sigma_{\phi 1}$ for $\phi > \phi_c$ and $\sigma_{\phi 2}$ for $\phi < \phi_c$. From the scattered light image, we can infer that the NW side is the near side, and from the CO line-of-sight velocities, the SW has a projected velocity towards us. Therefore, the disc is rotating counterclockwise. This means that $\sigma_{\phi 1}$ determines the azimuthal width in the leading side of the arc, while $\sigma_{\phi 2}$ does for the trailing side. Finally, we also leave as free parameters the disc inclination and position angle (longitude of ascending node), and RA and Dec offsets.

As in Marino et al. (2026), we modelled the dust as a size distribution from 1 µm to 1 cm, with a power law exponent of −3.5. We assumed a dust composition made of 70% astrosilicates, 15% crystalline water ice, and 15% amorphous carbon by mass (mixed using the Bruggeman's formula, Draine 2003; Li & Greenberg 1998). We assumed grains to be compact and spherical and used Mie theory to calculate their opacities. This results in an opacity of 1.9 cm^2 g^{-1} at 0.89 mm (the only wavelength being fitted here). The minimum grain size may be smaller, as inferred from the SED, or larger if equal to the blow-out size (∼3 µm, Perrot et al. 2023). Nevertheless, it does not affect the derived dust masses, which are dominated by the maximum grain size given the assumed size distribution exponent. The maximum size of solids in the belt is likely much larger than 1 cm (especially if planetesimals are present), meaning that the derived dust mass only accounts for grains smaller than 1 cm, which dominate the millimetre emission (Terrill et al. 2023).

The best-fit parameters for the arc and their posterior distribution are presented in Figure 3 (the posterior distribution of

[3] https://www.ita.uni-heidelberg.de/~dullemond/software/radmc-3d/

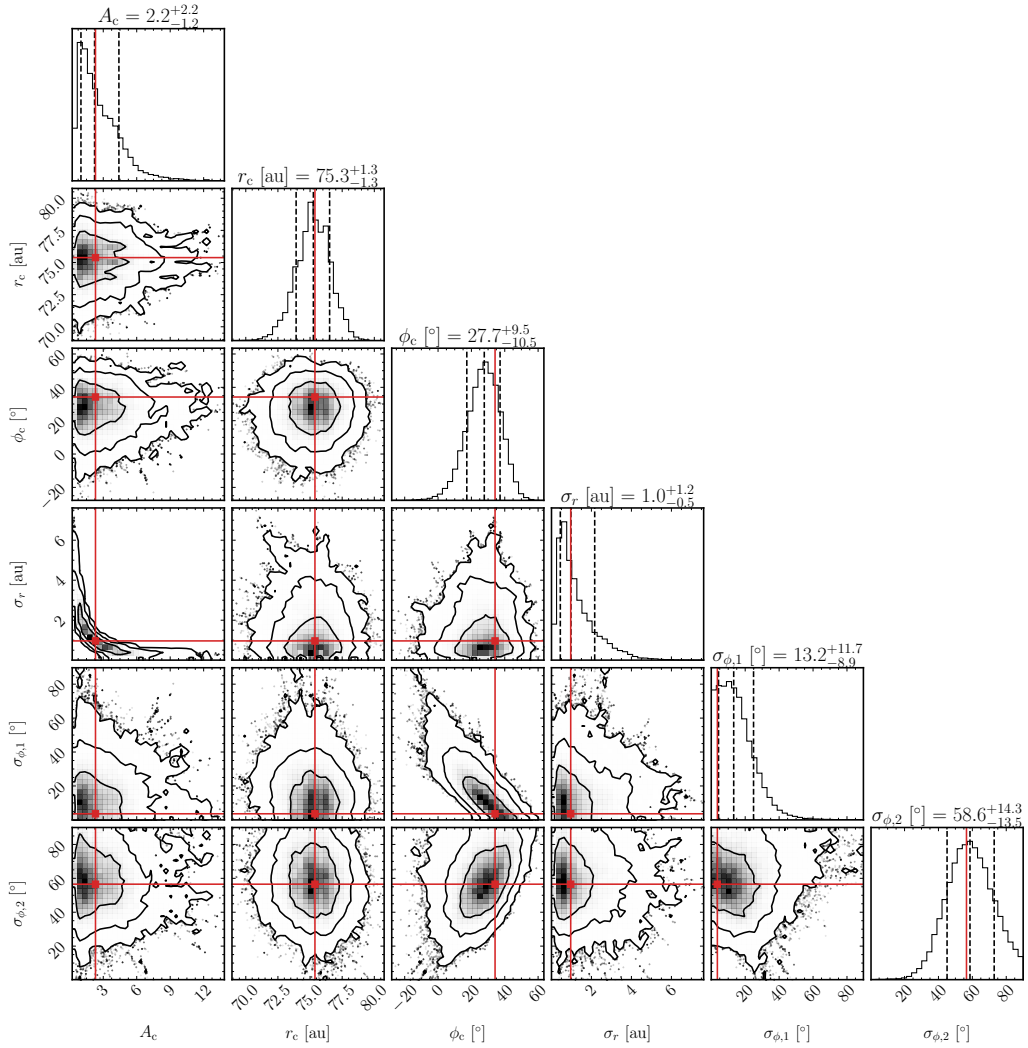

Fig. 3. MCMC posterior distribution of the arc parameters used to fit the dust continuum observations: the peak amplitude of the arc A_c; the central radius of the arc r_c; the azimuthal location of the arc peak ϕ_c; the arc radial standard deviation σ_r; and the azimuthal standard deviations for the leading and trailing side of the arc $\sigma_{\phi,1}$ and $\sigma_{\phi,2}$, respectively. The contour levels in the 2D marginalised distributions correspond to the 68, 95 and 99.7% confidence levels. The dashed vertical lines in the marginalised distributions display the 16th, 50th and 84th percentiles. The red lines represent the best-fit value (lowest χ^2). The posterior distribution of the other parameters is presented in Figure B.1.

the remaining parameters is presented in Figure B.1). For the axisymmetric component, we find it is centred at $r_0 = 70 \pm 1$ au, with an inner slope $\alpha_1 > 10$ (3σ) and outer slope $\alpha_2 = -6.5 \pm 0.3$, consistent with the values derived in Han et al. (2026). The peak of the surface density is likely sharp, but it is only marginally constrained by γ. Combined, these parameters set the surface density peak of the axisymmetric component at 70 ± 1 au.

The total dust mass is constrained to be $0.233 \pm 0.004\ M_\oplus$, but we note that the small uncertainties do not include the uncertainties in the assumed dust opacity. The derived value agrees well with the dust mass of $0.21 \pm 0.02\ M_\oplus$ derived by Perrot et al. (2023) fitting the spectral energy distribution. However, these dust masses are not directly comparable since there are subtle differences between the size distribution parameters (e.g. slope and maximum grain size) and composition between both modelling efforts. Depending on the assumed dust opacity, the derived dust mass could vary by a factor of a few (e.g. Kim et al. 2019). Despite these large systematic uncertainties, our results and conclusions do not depend on the exact value of the dust mass.

For the asymmetric component, we find that the arc peak, r_c, is centred at 75 ± 1 au (i.e. slightly further out than the axisymmetric component) at an azimuth, ϕ_c, of 28^{+10}_{-11}°, which translates to a PA of ~270°, given the disc inclination and longitude of ascending node. The radial width of the arc, σ_r, is marginally resolved with a standard deviation of $1.0^{+1.2}_{-0.5}$ au (a FWHM of $2.4^{+2.8}_{-1.2}$ au) and a 3σ upper limit of 5.4 au. Azimuthally, we find strong evidence that the arc's trailing side is wider, with a standard deviation of 59 ± 14° ($\sigma_{\phi,2}$) on the trailing side versus 13^{+12}_{-9}° on the leading side ($\sigma_{\phi,1}$). Using the posterior distribution, we estimate the azimuthal FWHM $(2.355(\sigma_{\phi,1} + \sigma_{\phi,2})/2)$ to be 85^{+18}_{-21}°, confirming the wide azimuthal extension of this dust overdensity. Finally, the arc peak amplitude, A_c, is not well constrained as its value is degenerate with the radial width, which is not well constrained. However, from the posterior distribution, we calculated and found that the overall millimetre dust mass contribution of the arc is $13 \pm 1\%$ of the total dust mass of $0.23\ M_\oplus$.

Figure 4 shows the ALMA continuum image, the model image, the beam-convolved model image, and the residuals.

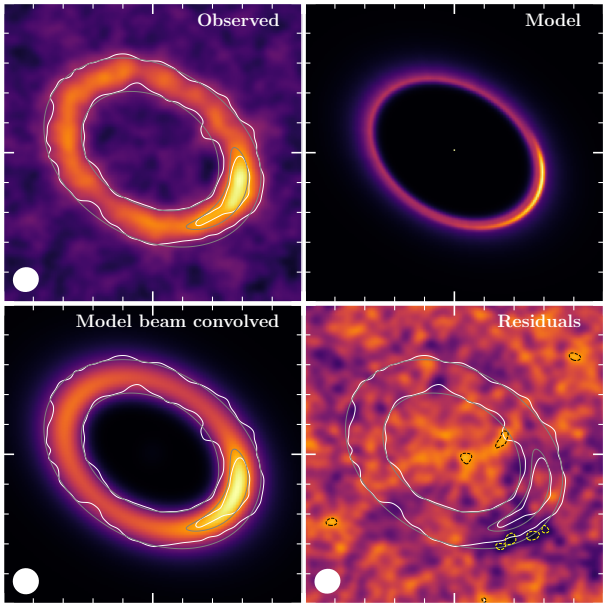

Fig. 4. Comparison between observations and best-fit model. Top left: ALMA dust continuum image. Top right: synthetic image of the best-fit model. Bottom left: best-fit model image that has been beam-convolved. Bottom right: dirty image of the residuals after subtracting the best-fit model from the observed visibilities. The dashed black and yellow contours represent positive and negative 3σ values, respectively. The white (grey) contours represent an intensity that is 30 and 75% the intensity peak of the observed (convolved model) image. The beam sizes are displayed in the bottom left corners. All images correspond to a CLEAN robust parameter of 1.0. The small white ticks are spaced by 0.2″.

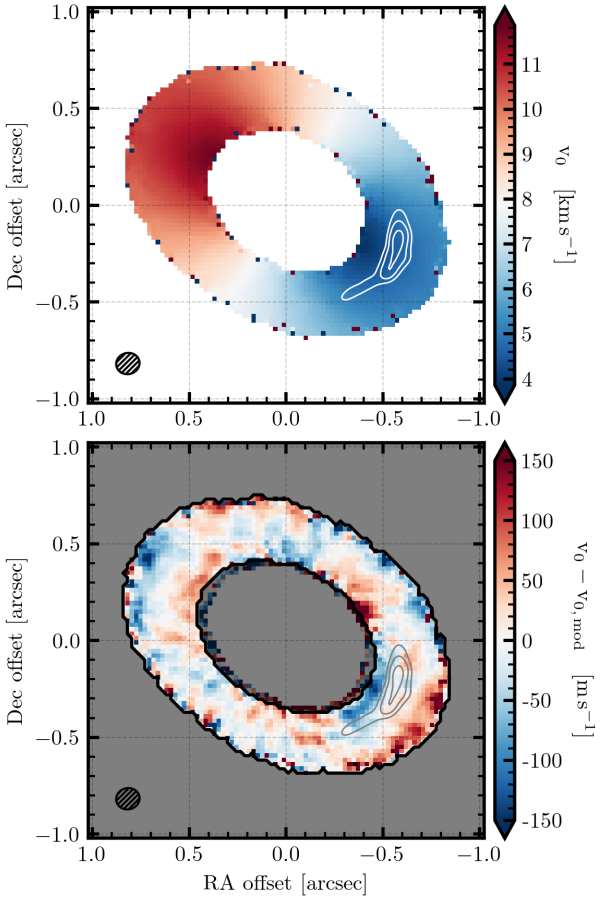

Fig. 5. Top panel: line of sight ^{12}CO velocity map. Bottom panel: residual velocity map after subtracting a Keplerian model. The white-shaded region in the top panel represents pixels that did not have an S/N high enough to extract the line-of-sight velocity. The grey-shaded region in the bottom panel represents the area that was not included in the fit to avoid low-S/N areas. The white and grey contours display the location of the dust arc. The beam size is displayed in the bottom left corner.

Overall, we find a good match between the observed morphology and the model. The only significant discrepancy is found at the SW side just exterior to the trailing side of the arc, where the residual map shows a few 3σ negatives (dashed yellow contours). The circular model is more extended than the data in this area of the disc. This may be related to the eccentricity found in scattered light with a pericentre towards the SW and the slight negatives in the residuals near 100 au found in the SW-NE subtracted radial profiles. These findings suggest that the millimetre dust distribution may be eccentric, too. Alternatively, the arc radial distribution may be more complex than our model; for example, with the trailing side being closer to the star.

3. CO gas kinematics

In addition to constraining the CO gas distribution in Sect. 2.1, here we investigate the kinematics of the CO gas traced by the ^{12}CO ARKS observations with a resolution of 26 m/s (13 m/s channels). We use the clean data cube corresponding to a robust value of 0.5 (Mac Manamon et al. 2026).

3.1. 2D velocity map

We extracted a 2D line-of-sight velocity map from the clean cube using the package BETTERMOMENTS and the Gaussian method that fits a Gaussian line profile to each pixel (using a sigma clipping of 5, Teague & Foreman-Mackey 2018; Teague 2019b). The resulting velocity map is presented in the top panel of Figure 5, displaying a typical rotational pattern.

We fitted a Keplerian model to this velocity map using the EDDY package (Teague 2019a) to determine the orientation of the system, systemic velocity, and stellar mass. The best-fit values are −3 mas for the RA offset, 20 mas for the Dec offset, 59.6° for the position angle, 43.8° for the inclination, 1.89 $M_\odot$ for the stellar mass, and 7.86 km/s for the system line of sight velocity in the Barycentric reference frame. The uncertainties on these values extracted by EDDY are below 1%, but they are likely underestimated as they do not take into account the spatial correlation between pixels. The derived values for the inclination and position angle are consistent with those derived for the dust emission (44.8 ± 0.6° and 58.5 ± 0.8°, respectively). The kinematically derived stellar mass is consistent with the value of 1.901 ± 0.009 $M_\odot$ presented in Marino et al. (2026), which was derived based on the available photometry, estimated age (16 ± 2 Myr, Pecaut & Mamajek 2016), and the PARSEC v1.2S stellar evolution models (Bressan et al. 2012; Chen et al. 2014, 2015; Tang et al. 2014). We note that the derived values based on the kinematics could be slightly biased by the potential gas eccentricity of ~0.03 with a pericentre towards the SW, as found in Sect. 2.1.

Figure 5 presents the line-of-sight velocity map and residuals after subtracting the best-fit Keplerian model. The dust arc is shown with white and grey contours. We do not find a significant velocity residual feature at the arc location. However, we do find on both ansae (where the projected azimuthal velocity is highest)

that the velocities are slower near the outer edge and faster near the inner edge than Keplerian. This effect cannot be explained by an incorrect inclination or stellar mass in the model, since that would not produce residuals with a velocity flip from the inner to the outer regions, which is reversed in the two ansae. Other strong residuals near the inner edge and minor axis (e.g. the strong ~200 m/s residual in the NE side) are likely due to the lower S/N near the inner edge and systematic errors due to the finite resolution of the data. They are stronger in lower-resolution cubes (with a robust parameter of 2) and also appear in simulated data (see Appendix C).

We also explored models with an elevated emission surface as commonly found in protoplanetary discs (e.g. Teague et al. 2018), but we found height values consistent with zero. We note, however, that the emission height for a narrow ring is strongly degenerate with RA and Dec offsets that we fit. Moreover, even if the ^{12}CO emission is optically thick and elevated, it might not be elevated enough to clearly see in the moment 1 and channel maps, especially if the vertical distribution of the total gas density is narrower than in protoplanetary discs due to a higher mean molecular weight or photodissociation (e.g. Hughes et al. 2017; Marino et al. 2022; Brennan et al. 2026). Therefore, for the following analysis, we assume that the emission arises from the midplane.

3.2. De-projected azimuthal velocity

To constrain and deproject the gas velocities as a function of radius, we used the EDDY package (Teague 2019a), again using the cube as input. We divided the disc into a set of concentric annuli spaced by 20% of the beam size (same as the pixel size) and oriented at the same position angle and inclination as the disc (as derived when fitting the line-of-sight velocities). Within each annulus, EDDY finds the best azimuthal, radial, and systemic velocity (used to extract the vertical velocity) that reproduces how the centroid velocity changes as a function of azimuth. We used the Gaussian method to derive the line centroid and the 'simple harmonic oscillator (SHO)' method to derive the 3D velocities at each radius. The SHO method models the line-of-sight velocity, $v_{\rm los}$, as a function of azimuth within each annuli, as the combined projection of an azimuthal (v_ϕ), radial (v_r), vertical (v_z) and systemic velocity ($v_{\rm sys}$),

$$\begin{aligned} v_{\rm los}(r,\phi) = & \, v_\phi(r)\cos(\phi)\sin(i) \\ & - v_r(r)\sin(r,\phi)\cos(i) \\ & - v_z(r)\cos(i) + v_{\rm sys}. \end{aligned} \tag{5}$$

Note that there is a degeneracy between the vertical and systemic velocities. This means that the absolute values of vertical velocities are unconstrained (Teague et al. 2019). Nevertheless, we can fix and approximate the systemic velocity to be the systemic velocity extracted from the Keplerian fit.

In addition, we also restricted the fit to position angles within 20° from the major axis of the disc since emission and velocities closer to the minor axis are more affected by the finite beam size due to the disc inclination (44°). To account for the uncertainty on the disc orientation, we ran EDDY ten times, randomising the disc orientation according to the posterior distribution of the Keplerian fit. For each orientation, EDDY performs ten retrievals using a different random sample of pixels within each annulus, which also helps to derive more realistic uncertainties.

We examined the azimuthal, radial, and vertical velocities, but found that the radial and vertical components are consistent with zero at all radii with upper limits below 1% of the Keplerian speed. This upper limit applies to global radial or vertical velocities. Locally, radial or vertical velocities could be higher and remain undetected due to the noise. Therefore, hereafter, we focus on the azimuthal component of the velocity.

The left top panel in Figure 6 shows the measured azimuthal velocities (blue) as a function of radius compared to the expected Keplerian velocities (i.e. $v_\phi \propto r^{-1/2}$ in grey) and those measured from a simulated observation of a Keplerian model taking into account the effect of the beam and noise (Appendix C). The expected Keplerian profile assumes a mass of 1.91 $M_\odot$. If the large millimetre-sized grains are radially trapped by the gas due to gas-drag, the dust ring should peak where the gas azimuthal velocity is equal to the Keplerian velocity ($v_{\rm K}$), which occurs for $M_\star = 1.91\ M_\odot$. The simulated Keplerian model assumes a mass of 1.89 $M_\odot$ to roughly match the extracted velocity at 75 au. These values are well in agreement with the $1.90 \pm 0.01\ M_\odot$ inferred using stellar evolution models (as presented in Marino et al. 2026). The bottom left panel shows the residuals after subtracting the expected Keplerian velocities from the observed and simulated data. Overall, we find deviations of the order of 1% with the azimuthal velocity decreasing with radius faster than Keplerian. This finding is also present if we fit all azimuths, although less strongly, and if we fit the moment 1 instead of the cube. Note that the stellar mass is independently constrained only from stellar models ($1.90 \pm 0.01\ M_\odot$, Marino et al. 2026). Hence, it is uncertain where the extracted azimuthal velocity intersects the Keplerian rotation curve.

The profile extracted from the simulated Keplerian model decreases with radius more slowly than the Keplerian profile. This is due to beam smearing, which contaminates the velocity at the inner and outer edges with the velocities from the peak of emission (Pezzotta et al. 2025). This means that the deviations that we measure from the data are likely even stronger and closer to 2% the Keplerian speed towards 65 and 85 au.

The right panels in Figure 6 show the line-of-sight velocity residuals after subtracting the best Keplerian (top) and the more flexible model that fits the 3D velocities as a function of radius (bottom). We find that the latter makes the residuals significantly smaller along the major axis of the disc. The other strong residuals near the disc inner edge and minor axis are still present in the data and are most likely a systematic error due to the limited spatial resolution of the data. For example, the residuals of the simulated Keplerian observations show the same residual pattern near the minor axis (see Figure C.1).

These kinematic deviations are qualitatively what would be expected near a gas ring with a strong pressure maximum at its centre. The azimuthal velocity for a stable and low mass disc ($M_{\rm gas} \ll M_\star$) is expected to be

$$\frac{v_\phi(r,z)^2}{r} = \frac{GM_\star r}{(r^2+z^2)^{3/2}} + \frac{1}{\rho}\frac{\partial P(r,z)}{\partial r}, \tag{6}$$

where P is the gas pressure, which can be defined as

$$P = \rho c_s^2, \tag{7}$$

$$c_s^2 = \frac{k_{\rm B}T}{\mu m_p}, \tag{8}$$

where ρ is the gas density, c_s is the sound speed, T is the gas temperature, μ is the mean molecular weight of the gas, $k_{\rm B}$ is the Boltzmann constant, and m_p is the mass of hydrogen. From Equation (6), we can see that a positive pressure gradient (e.g. interior to the pressure maximum) results in a super-Keplerian

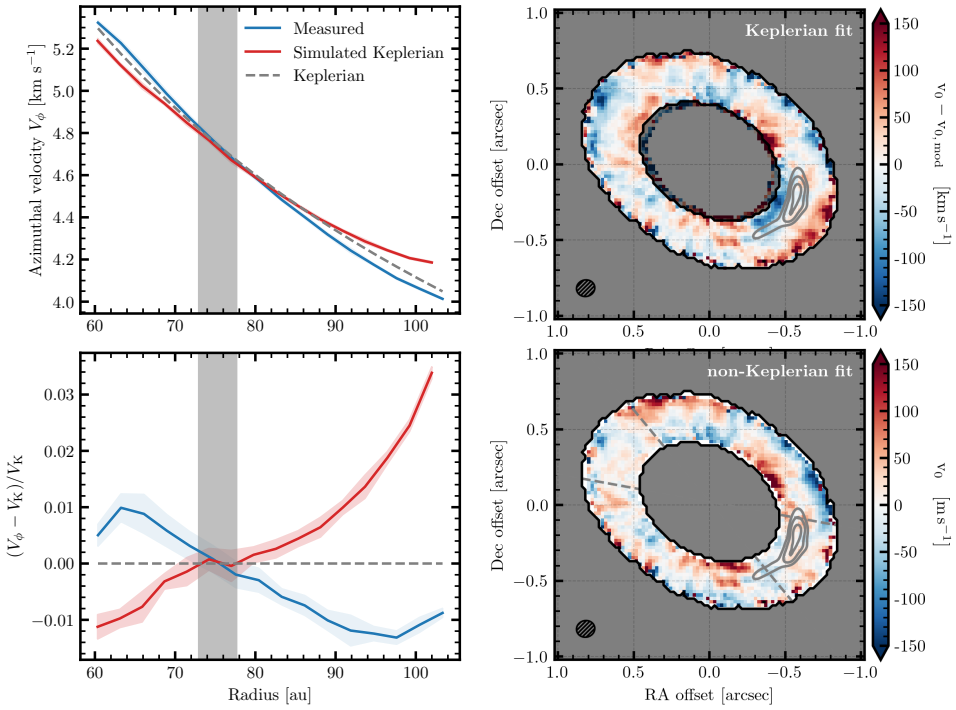

Fig. 6. Azimuthal velocity profile fit. Top left: azimuthal velocity profile extracted from the observed image cube (blue line), from a simulated image cube of a Keplerian model (red line), and the expected Keplerian profile ($v_\phi \propto r^{-1/2}$, dashed grey line). Bottom left: azimuthal velocity profile residual after subtracting the expected Keplerian profile. The blue- and red-shaded regions represent the 1σ uncertainty. The shaded grey region in the left panels represents the dust arc peak and extent. Top right: velocity map residuals after subtracting the best-fit Keplerian model. Bottom left: velocity map residuals after subtracting a model using the measured non-Keplerian azimuthal velocity profile. The dashed grey lines represent wedges used to fit the data near the disc's major axis.

velocity, whereas a negative pressure gradient (e.g. exterior to the pressure maximum) results in a sub-Keplerian velocity.

The azimuthal velocity profile residuals (bottom left panel in Figure 6) also display an apparent dip at 60 and 100 au. These could be due to a change in the slope of the density or temperature profile. However, the low S/N at these radii mean that these features may be due to noise.

Finally, to test our interpretation of the residual pattern, Appendix C presents simulated observations with and without deviations from Keplerian rotation. Our simulations confirm that the observed pattern is consistent with velocity deviations due to the pressure gradient of a gas ring, and inconsistent with a purely Keplerian rotation pattern.

3.3. Retrieving the radial density profile

In this section, we aim to retrieve the gas density profile using the Keplerian deviations as a proxy for the pressure gradient. We start by defining

$$T = T_0 \left(\frac{r}{r_0}\right)^\beta, \tag{9}$$

where T_0 is a reference temperature at radius r_0, and β a power law exponent for the temperature. We rearrange Equation (6) with $z = 0$ and find

$$\frac{1}{\rho}\frac{\partial \rho}{\partial r} = \frac{\mu m_p}{k_B (\frac{r}{r_0})^\beta}\left(\frac{v_\phi^2}{rT_0} - \frac{GM_\star}{r^2 T_0}\right) - \frac{\beta}{r}, \tag{10}$$

where the quantities on the right-hand side can be estimated from the data (v_ϕ, T_0, $M_\star$) or assumed to take standard values. We assume that $\beta = -0.14$, $T_0 = 38$ K, and r_0=73 au as found in Brennan et al. (2026) by fitting the ^{13}CO data cube. Moreover, we assume that $M_\star = 1.91\ M_\odot$, which makes the Keplerian speed at the arc location (75 au) the same as the extracted azimuthal velocity. This would be expected if the dust arc corresponds to dust trapped at the pressure maximum. Since we do not know the gas composition, we assume two values for μ: 14 for a disc dominated by C and O (secondary gas), and 2.3 for an H_2-dominated disc (primordial gas). Integrating the right-hand side over r, we obtain $\ln[\rho(r)]$ plus a constant that becomes a normalisation factor.

Figure 7 shows the gas density profiles derived from the deviations from Keplerian motion assuming $\mu = 14$ (orange) or 2.3 (blue). The dashed black line shows the frequency-integrated CO surface brightness profile for comparison (derived in Sect. 2.1). The dashed line shows the best fit midplane density profile of ^{13}CO derived in Brennan et al. (2026). We find a remarkable similarity between the kinematically derived profile assuming $\mu = 14$ (orange) and that retrieved from the ^{13}CO emission (dotted black), with only a slight radial shift that disappears if we assume a stellar mass of 1.92 $M_\odot$. This μ is also remarkably consistent with the value obtained when fitting the ^{13}CO cube ($12.6^{+1.3}_{-1.1}$), though see Brennan et al. (2026) for model assumptions and caveats likely affecting this measurement. The ^{12}CO emission profile (dotted line) appears much wider than the retrieved density profiles, as expected given its high optical depth.

The kinematically derived profile assuming $\mu = 2.3$ (blue) appears ~3 times wider than the ^{13}CO density distribution. This does not, however, rule out the gas having a low mean molecular weight and being primordial. This is because the profile derived from the kinematics traces the total gas distribution, which could

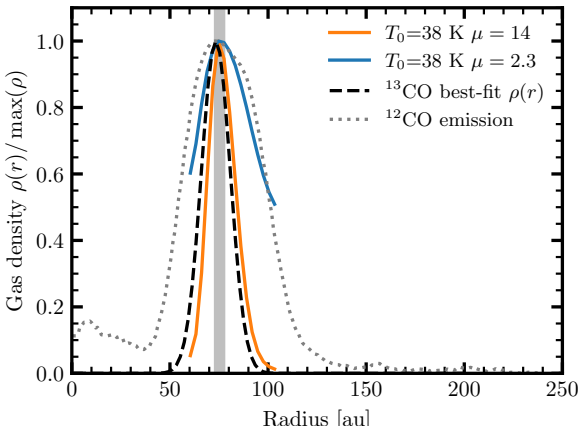

Fig. 7. Retrieved gas density profile (solid coloured lines) using different gas temperatures and mean molecular weights. The dashed black line displays the midplane density profile of ^{13}CO as derived in Brennan et al. (2026). The dotted grey line displays the ^{12}CO gas emission profile (normalised). The vertical shaded grey region shows the location of the arc and dust surface density peak.

differ from that of ^{12}CO and ^{13}CO due to CO photodissociation in a primordial or secondary origin scenario (Trapman et al. 2019; Marino et al. 2020).

Assuming a lower μ results in a broader density profile because of the sound speed. Decreasing μ increases the sound speed if we keep the temperature fixed. With a higher sound speed, the density profile can be shallower and still reproduce the same strong pressure gradients and velocity perturbations. Increasing the gas temperature has a similar effect. Decreasing $M_\star$ from 1.91 to 1.89 $M_\odot$ shifts the pressure maximum from 75 to 83 au as v_ϕ and v_K intersect at a larger radius. Increasing β shifts the density peak to smaller radii if the density profile is shallow.

Considering how the beam, optical depth and CO photodissociation affect the CO intensity distribution and azimuthal velocity profiles in different ways, we do not attempt to find a perfect fit between the kinematically derived density and the emission profile. Moreover, an important caveat to note is that the true azimuthal velocity profile is likely steeper than the extracted one because the latter is affected by beam smearing (as is discussed in Sect. 3.2). This means that the deviations from Keplerian rotation could be underestimated. Nevertheless, our simulated observations presented in Appendix C show that our kinematic method can reliably recover the density profile that we input to the model.

In conclusion, we find that the gas kinematics show significant deviations from Keplerian rotation, which can be explained by the pressure gradient of the observed ring of CO gas. Given the degeneracies involved in fitting the density profile, we cannot distinguish between a secondary gas scenario (dominated by C, O or CO) and a primordial one (H_2-dominated) using the azimuthal velocity alone. However, if we assume that ^{13}CO traces well the total gas density distribution, giving consistent results to the μ measurement in Brennan et al. (2026), the CO-dominated scenario would be preferred.

4. Discussion

4.1. A vortex as the origin of the arc

We found that the dust overdensity in the millimetre is radially narrow and azimuthally elongated and asymmetric, with the leading side being more azimuthally compact. The dust overdensity is absent or less prominent in the distribution of small grains. All these properties are found in models of vortices in protoplanetary discs (e.g. Baruteau et al. 2019). Gas drag via a vortex can trap dust, creating strong overdensities. This effect is grain size-dependent, which may be the reason why the distribution of small grains does not display a strong overdensity. Grains with frictional timescales comparable to the orbital timescales (i.e. with a Stokes number close to 1) are more efficiently trapped, whereas grains with much shorter frictional timescales tend to follow the gas distribution (e.g. Baruteau et al. 2019). For gas drag to significantly affect the millimetre-sized grains that dominate the observed continuum emission, the gas surface density must be high and comparable to that in protoplanetary discs. If we require millimetre-sized grains to have a fractional timescale of 10 times the orbital period or shorter, i.e. a Stokes number $\lesssim$10, this translates to a minimum gas surface density of 5×10^{-2} g cm^{-2} (2×10^{-3} $M_\oplus$ au^{-2}) or a minimum total gas mass of 20 $M_\oplus$ (supported by simulations in Weber et al. 2026).

This high minimum gas mass of 20 $M_\oplus$ may be at odds with the gas surface density if the gas is CO-dominated (estimated to be ~0.2 $M_\oplus$ depending on the ^{12}CO/^{13}CO abundance ratio, Brennan et al. 2026). Nevertheless, it is still possible that H_2 dominates the gas mass, with an ISM-like H_2/CO abundance ratio of 10^4, resulting in a much larger total mass above the minimum required to affect the millimetre-sized dust, and making the gas a protoplanetary disc leftover (i.e. of primordial origin). A vortex in HD 121617 may be a natural consequence of the gas distribution, as vortices can be produced by the Rossby wave instability, which is triggered by strong pressure gradients (Lovelace et al. 1999; Li et al. 2001; Lyra et al. 2009; Meheut et al. 2012; Flock et al. 2015). Weber et al. (2026) explores this scenario using hydrodynamical simulations to constrain what range of gas masses is necessary and to assess whether models can reproduce the amplitude as well as radial and azimuthal extents of the dust arc.

A vortex is also expected to leave a trace in the gas distribution and kinematics. The CO emission distribution does not display any hint of an overdensity. However, there could still be a hidden overdensity in the gas as both ^{12}CO and ^{13}CO emissions are optically thick (Brennan et al. 2026). In addition, as a vortex is a significant local deviation from Keplerian rotation, we may expect to see a feature on the SW side of the disc. The expected local velocity deviations by a vortex may be up to a few % of the average azimuthal velocity (e.g. Pérez et al. 2018), which is at the limit of our sensitivity (the noise in our velocity map residuals is of the order of ~3% the maximum line of sight velocities). We do not find any significant feature near the dust arc in the residuals after subtracting our non-Keplerian model in Sect. 3.2.

Therefore, the observed dust and gas distributions and kinematics are roughly consistent with the presence of a vortex, assuming that there is enough gas to affect the millimetre-sized dust dynamics ($\gtrsim$20 $M_\oplus$). This would require the gas to be of primordial origin.

4.2. Narrow gas rings

The radial distribution of CO gas in debris discs has been challenging to study due to the lack of high spatial resolution observations (e.g. Lieman-Sifry et al. 2016; Moór et al. 2017), low S/N (e.g. Marino et al. 2016), and the edge-on orientation of many of these discs, making it harder to extract radial information (e.g. β Pic, Matrà et al. 2017a). ARKS has allowed us to constrain the CO spatial distribution for three non-edge-on gas

discs with ages ranging from 16 to 45 Myr (HD 9672, HD 121617 and HD 131835), and HD 121617 appears to host the narrowest gas disc among these three (Mac Manamon et al. 2026). Several of the known gas-rich debris discs may be as narrow, but their edge-on orientation demands a more complex modelling to extract the gas radial distribution (e.g. HD 32297, Mac Manamon et al. 2026), or the current observations do not have the resolution to determine this (e.g. HD 9985, Moór et al. 2025). Higher-resolution observations and radiative transfer modelling of those edge-on discs with sufficient observations are needed to constrain how common narrow gas discs are among debris discs.

Rings of gas (or discs with large cavities) are relatively common among the much brighter protoplanetary discs with ages ranging from 4 to 20 Myr, and in particular transition discs around early type stars where millimetre-sized grains become radially trapped (e.g. van der Marel et al. 2021; Martinez-Brunner et al. 2022; Weber et al. 2022). Moreover, several of those discs display strong asymmetries that resemble the arc in HD 121617 and are interpreted as dust trapping by vortices. If gas in debris discs is primordial, the asymmetry in HD 121617 may be caused by the same processes as in the more massive protoplanetary discs.

What processes make HD 121617's gas disc narrow is uncertain and may depend on its origin. If gas is primordial, the ring-like distribution of CO gas may be a consequence of photoevaporation carving an increasingly large cavity (Nakatani et al. 2021, 2023; Ooyama et al. 2025), in which case, the different cavity sizes between gas-rich debris discs may be due to different evolutionary stages. Alternatively, the cavity could be produced by multiple planets interior to the disc, which prevents the gas disc from expanding (e.g. Bae et al. 2019; Toci et al. 2020). If gas is secondary, the ring-like distribution may be a consequence of a very long viscous timescale or the presence of planets (e.g. Moór et al. 2019; Marino et al. 2020; Kral et al. 2020).

4.3. Vortices in other debris discs

A vortex has also been proposed to explain an overdensity of CO gas and small dust grains in β Pic (Skaf et al. 2023). In that disc, the large dust grains' distribution is more symmetric than the gas (Dent et al. 2014; Matrà et al. 2017b, 2019) and small grains (Telesco et al. 2005; Li et al. 2012; Han et al. 2023), which is the opposite of what we found in HD 121617. If the overdensity in both discs is due to vortices, this would suggest that the gas densities in β Pic are much lower than in HD 121617 (as expected, given their CO fluxes). A lower gas density would decouple the large millimetre grains from the gas while efficiently trapping the μm grains in a vortex. Similarly, the HD 181327 debris disc shows an overdensity in the distribution of small grains (Stark et al. 2014), contains sufficient CO gas to affect the dynamics of micron-sized grains (although it is not detected at a sufficient S/N to see any asymmetry), and its millimetre grains are more symmetric (Marino et al. 2016). If this interpretation is correct, then vortices may be common in debris discs with gas and explain dust asymmetries that are grain-size dependent. Determining the gas surface density or kinematics will be crucial to proving or ruling out their presence.

4.4. A giant collision as the origin of the arc

A second possible scenario often invoked to explain overdensities in debris discs is giant collisions (e.g. Wyatt & Dent 2002; Michel et al. 2001; Kenyon & Bromley 2005; Grigorieva et al. 2007; Kral et al. 2013; Thebault & Kral 2018; Jackson et al. 2014; Dent et al. 2014; Wyatt & Jackson 2016). Models of (gas-free) giant collisions predict overdensities in the dust distributions that can last for thousands of orbits. Initially, the collision generates a dense cloud of dust that expands and orbits at a roughly Keplerian speed; however, it quickly shears out due to the differing orbital elements of the debris (partly due to radiation pressure acting on small grains), forming a spiral feature. Subsequently, the produced debris returns to the collision point, where new collisions occur, resulting in more debris being generated. The initial clumpy phase is very short, only lasting a few orbits and thus is unlikely to explain the overdensity in HD 121617.

After a few orbits, the collisional fragments form a smooth but asymmetric disc with a strong overdensity at the collision point that can last for thousands of orbits, or ∼0.5 Myr for orbits near 75 au (Wyatt & Jackson 2016). Due to radiation pressure, grains slightly larger than the blow-out size (∼3–30 μm) that are produced in the collision point form a disc that is much wider on the opposite side (e.g. Jones et al. 2023). The even smaller grains below the blow-out size that are produced in the collision point are ejected by radiation pressure, forming a leading outward-propagating spiral structure from the collision point (Jackson et al. 2014). The net effect is that scattered light observations tracing small grains should display an asymmetric collision point and a disc that is wider on the opposite side. The distribution of longer-lived millimetre-sized dust traced by ALMA is predicted to be symmetric about the collision point (Jackson et al. 2014).

The key features to assess this scenario are therefore the radial width of the arc, its azimuthal extent and asymmetry, and its apparent absence in the distribution of micron-sized dust and CO gas. The fact that the arc is extremely narrow and potentially unresolved is consistent with the pinch point that occurs at the collision point. The large azimuthal extent could also be consistent with a giant collision scenario. However, the fact that it is asymmetric, with the trailing side being more extended or denser, is inconsistent with the collisional scenario. Moreover, there is no significant overdensity in the distribution of micron-sized dust. Even if the gas affects the dynamics and distribution of the micron-sized dust, larger solids should continuously create small dust at the collision point, generating an asymmetry. Finally, the CO gas does not display any asymmetries, which could be consistent with its continuous release at the collision point. Since the CO gas could be long-lived, its distribution should become axisymmetric as gas pressure would smooth any strong overdensity at the collision point. Additionally, given that the CO gas is very optically thick, an overdensity would be easily hidden.

The interpretation above relies on gas not affecting the dust dynamics. In Sect. 4.1 we estimated that 20 $M_\oplus$ of gas would be required to significantly affect the dynamics of millimetre-sized grains. A similar calculation leads to a gas mass of 0.02 $M_\oplus$ in gas to affect the dynamics of micron-sized grains. Since the CO gas mass estimated from observations is 0.2 $M_\oplus$ (although there could be more gas Brennan et al. 2026), the small grains are likely affected by the gas, and thus we cannot use the distribution of small grains alone to rule out this scenario. The CO gas mass could be underestimated, or there could be a large reservoir of H_2 gas, in which case even the millimetre-sized grains could be affected by the gas.

The estimated CO gas mass is too large to be consistent with the potential gas released from a giant collision between dwarf or terrestrial planets (e.g. Schneiderman et al. 2021). A collision between gas giant planets may be able to release the required

gas, although those collisions are very unlikely as close encounters between gas giants at tens of au are more likely to result in ejections than collisions (Wyatt et al. 2017). Gas could, however, have a different origin from the arc and be dense enough to affect the dust dynamics. Unfortunately, there are no models that predict the evolution of solids after a giant collision in the presence of gas.

In summary, a giant collision scenario by itself is unlikely to explain the multiple observables. However, we cannot rule out the possibility of gas levels being high enough to affect the dynamics of both small and large grains and make the existing giant collision models inapplicable. If that is the case, gas-dust interactions alone may be enough to explain the arc without the need for a giant collision (as discussed in Sect. 4.1).

4.5. Planet-disc interactions as the origin of the arc

An alternative third scenario to explain the dust asymmetry is the influence of an unseen planet, interacting with the disc through mean-motion resonances (MMRs). Planetesimals and smaller solids trapped in MMRs would form asymmetric structures at specific locations, which could explain the clump in HD 121617. This would require a large number of planetesimals trapped in resonance, which can occur if the planet migrates; this migration causes MMRs to sweep through the disc, trapping large numbers of planetesimals in resonance (Wyatt 2003, 2006; Reche et al. 2008; Krivov et al. 2007; Booth et al. 2023). This would be the case for a planet located interior to the disc that migrated outwards. This migration could have been driven by planetesimal scattering, akin to Neptune's historical migration into the Kuiper Belt (Malhotra 1993), or by gas interactions in the protoplanetary disc phase. The number of clumps and their shapes depend on the specific MMRs, as well as the planet mass, eccentricity, migration speed and migration distance. This scenario was previously invoked to explain tentative clumps in ϵ Eri's debris disc (Booth et al. 2023), as well as features in the β Pic and q^1 Eri discs (Matrà et al. 2019; Lovell et al. 2021b). The model will be explored in detail for HD 121617 in Pearce et al., (in prep.).

Dust trapped in planetary MMRs would have a size-dependent structure. Larger dust would be more strongly constrained in clumps, whilst smaller dust would have a more axisymmetric distribution due to radiation pressure driving grains out of resonance (Wyatt 2006). A similar outcome would arise in the alternative explanation, where the clump is driven by a gas vortex; in the gas scenario, small grains would have a smoother distribution as they are coupled more strongly to the gas (Birnstiel et al. 2013). However, the two scenarios could be observationally distinguished by considering clump rotation. If the clump were resonant, then it would rotate at the orbital speed of the interior planet, which is faster than the Keplerian speed of the disc. Conversely, a vortex clump would rotate at roughly the disc's Keplerian speed (Weber et al. 2026). Furthermore, a clump generated by a giant impact (Sect. 4.4) would not rotate at all, because the clump would be caused by the intersection of orbits at the collision point (Jackson et al. 2014). So future observations could distinguish between these scenarios by determining the clump-rotation speed.

4.6. Non-Keplerian kinematics in debris discs

This paper presents the first well-resolved non-Keplerian gas kinematics in a debris disc. While these have been frequently found in protoplanetary discs (e.g. Pinte et al. 2023), previous observations of debris discs lacked the sensitivity and resolution to systematically search for non-Keplerian kinematics (e.g. Moór et al. 2017). The only previously known case is the debris disc-bearing class III star, NO Lup, which presents strong evidence of a radial outflow or wind, but remains only marginally resolved by ALMA (Lovell et al. 2021b). HD 121617's low inclination and high CO flux make it the ideal ARKS target to study gas kinematics in debris discs, opening the door to future kinematic studies of gas in debris discs over a larger sample of discs with low to moderate inclinations.

In addition to the azimuthal velocity perturbations, gas in debris discs could also present kinematic deviations from Keplerian rotation due to outflows or winds (Lovell et al. 2021a), kinks due to planets (Perez et al. 2015; Bergez-Casalou & Kral 2024), vertical flows due to winds (Nakatani et al. 2021), and vortices (Perez et al. 2015). A future ALMA survey tailored to studying the gas at high spatial and spectral resolutions is needed to assess if these are common features in the gas kinematics of debris discs. Finding any of these features could help us understand the origin and evolution of the gas and the potential presence of planets in these systems.

4.7. On the origin of HD 121617's gas

What is the origin of gas in debris discs remains one of the most pressing questions for this field. Depending on its origin, which determines its composition and overall abundance, this gas may affect planets in these systems (Kral et al. 2020; Marino et al. 2020). Typically, secondary models predict gas levels $\lesssim$10 $M_\oplus$ that are dominated by CO, carbon, and oxygen, with this upper limit depending on the belt mass, volatile abundances, and gas viscosity (Marino et al. 2020). In a primordial scenario, the main constraint is that the CO must be shielded enough by H_2 to have a lifetime comparable to the age of the system. This can be achieved by a column density greater than 10^{22} cm^{-2} (Visser et al. 2009), which can be translated to a minimum mass of 10 $M_\oplus$ if it has a similar radial distribution as CO. This minimum gas mass to shield CO is consistent with the gas mass necessary to trap millimetre-sized grains (Weber et al. 2026).

In this and the two companion papers by Brennan et al. (2026) and Weber et al. (2026), we have studied this CO gas-rich system in detail, revealing multiple properties that can help us to assess its origin. Below we summarise the most important:

- The ^{12}CO line is optically thick and thus the total CO mass is unconstrained. Although the ^{13}CO line is optically thick too, its mass can be constrained to 2×10^{-3} $M_\oplus$ (in the assumption of LTE and a radially Gaussian, vertically isothermal model), which we can convert to a total CO mass of 0.2 $M_\oplus$ by assuming an ISM-like ^{12}CO/^{13}CO abundance ratio of 77 (Brennan et al. 2026). This CO gas mass could be consistent with both secondary and primordial scenarios, depending on the abundance of shielding species such as CI and H_2, respectively. Cataldi et al. (2018) constrained the CI mass and column density in this disc, and found it to be insufficient to shield CO, which disfavours a secondary origin. The H_2 abundance is unconstrained, but if we assume an ISM-like CO/H_2 abundance ratio of 10^{-4}, the total H_2 gas mass would be 200 $M_\oplus$, which is sufficient to shield CO for the age of the system.
- If the millimetre dust asymmetry is explained by dust trapping, there must be $\gtrsim$20 $M_\oplus$ of gas to effectively drag the millimetre-sized dust (Weber et al. 2026). This would favour the gas primordial origin as secondary models struggle to reach those high levels (Marino et al. 2020).

– The non-Keplerian kinematics and the density profile fit to the ^{13}CO emission point towards a high mean molecular weight of ∼13, favouring a secondary origin. This assumes, however, that the ^{13}CO traces well the total gas density distribution, which may not be the case due to CO photodissociation.
– The peak of the small micron-sized dust distribution is significantly further out than the peak of the millimetre-sized grains, which suggests that gas drag is shaping the distribution of small grains (Milli et al. 2026; Jankovic et al. 2026). Both secondary and primordial gas levels could be consistent with this effect (Weber et al. 2026).

These features alone and modelled independently cannot be used to reach a definitive conclusion about the origin of the gas for this and other gas-rich debris discs. Additional high spatial and spectral resolution observations of CO and its isotopologues, combined with detailed radiative transfer modelling, are required to reconcile the CO line profiles, moment 0's, line ratios and kinematic deviations. This would give a definitive answer to the optical depths, abundance of CO, kinetic and excitation temperatures, and potentially the mean molecular weight (or sound speed) of the disc. Secondary models of the gas could then be used to reproduce the CO abundance, its radial distribution, and the gas mean molecular weight. Their success or failure could serve as a definitive answer as to the origin of the CO gas.

5. Conclusions

In this paper, we have analysed high spatial and spectral resolution ALMA observations of HD 121617 from the large programme ARKS, characterising an asymmetry in the distribution of large millimetre-sized grains and the gas kinematics of this gas-rich exoKuiper belt. In particular, we investigated how strong this asymmetry is in the sub-millimetre continuum emission, whether it is present in the distribution of small grains (traced by scattered light) and gas (traced by CO line emission), and whether the gas displays any non-Keplerian kinematics. Our main results and conclusions are:

– At the observed resolution, the arc has a peak intensity at 0.89 mm that is 40% brighter than the baseline emission around the belt. We do not find any evidence of an arc in the scattered light and CO gas emission. However, we recovered a previous result that the small dust distribution is slightly eccentric (Perrot et al. 2023). We also find evidence that the CO gas and millimetre dust distribution could be eccentric, but this cannot be confirmed with the current astrometric precision.
– We fitted a parametric radiative transfer model to the millimetre dust distribution to constrain the arc morphology. The model is composed of an axisymmetric component and an asymmetric arc component. We inferred that the arc component is radially narrow and only marginally resolved with a FWHM between ∼1 and 5 au. The azimuthal extent of the arc has a FWHM of ∼90°, with the leading side being more compact than the trailing side. Overall, the arc component is inferred to be 13% of the total dust mass of 0.2 $M_\oplus$.
– When examining the gas kinematics of the ring, we found that the azimuthal velocity decreases with radius more steeply than Keplerian. This effect can be explained by the density and pressure profile of a narrow ring of gas. Interior to the density and pressure maximum, there is a strong positive pressure that results in super-Keplerian velocities. Exterior to the density and pressure, there is a strong negative pressure gradient that results in sub-Keplerian velocities. We used the extracted azimuthal velocity profile to retrieve the gas density profile, assuming gas molecular weights corresponding to a primordial or secondary origin. Overall, we find that a high molecular weight of 14 (valid for a secondary origin scenario) reproduces best the retrieved ^{13}CO gas density profile. Assuming a mean molecular weight of 2.3 (expected if the gas is dominated by H_2) produces a density profile that is much wider than that of ^{13}CO. However, our kinematically derived profile traces the bulk of the gas whose distribution could be different to that of CO due to CO photodissociation, skewing its distribution towards the densest parts of the disc.
– We discussed how the arc asymmetry could originate from a vortex in the gas or via planet-disc interactions. In the former case, the arc would have a similar origin to those found in protoplanetary discs that are suspected of being due to dust trapping in a vortex and would require the disc gas mass to be $\gtrsim$20 $M_\oplus$, which would imply a primordial origin for the gas and be enough to shield CO by H_2 (Weber et al. 2026). In the second scenario, we hypothesise that a migrating planet could have trapped solids in mean motion resonances, producing an overdensity in the form of an arc (Pearce et al., in prep.).

Finally, we note that the HD 121617 arc asymmetry was only found with ARKS' high-resolution and high-S/N observations. Additional arc asymmetries have been found in other ARKS targets (Lovell et al. 2026) and could be present in many other exoKuiper belts not included in ARKS.

Data availability

The ARKS data used in this paper and others can be found in the ARKS dataverse. The continuum image used in this work can be found within the ARKS I's dataset (doi.org/10.7910/DVN/VNGHPQ). The CO gas images used in this work can be found within the ARKS IV's dataset (doi.org/10.7910/DVN/PXGNNZ). The SPHERE scattered light image used in this work can be found within the ARKS V's dataset (doi.org/10.7910/DVN/RGRKTJ). For more information, visit arkslp.org.

References

Bae, J., Zhu, Z., Baruteau, C., et al. 2019, ApJ, 884, L41
Baruteau, C., & Zhu, Z. 2016, MNRAS, 458, 3927
Baruteau, C., Barraza, M., Pérez, S., et al. 2019, MNRAS, 486, 304
Bergez-Casalou, C., & Kral, Q. 2024, A&A, 692, A156
Birnstiel, T., Dullemond, C. P., & Pinilla, P. 2013, A&A, 550, L8
Bonsor, A., Wyatt, M. C., Marino, S., et al. 2023, MNRAS, 526, 3115
Booth, M., Pearce, T. D., Krivov, A. V., et al. 2023, MNRAS, 521, 6180
Brennan, A., Matrà, L., Mac Manamon, S., et al. 2026, A&A, 705, A201
Bressan, A., Marigo, P., Girardi, L., et al. 2012, MNRAS, 427, 127
CASA Team, (Bean, B., et al.) 2022, PASP, 134, 114501
Casassus, S., van der Plas, G. M., Perez, S., et al. 2013, Nature, 493, 191
Cataldi, G., Brandeker, A., Wu, Y., et al. 2018, ApJ, 861, 72
Cataldi, G., Aikawa, Y., Iwasaki, K., et al. 2023, ApJ, 951, 111
Chen, Y., Girardi, L., Bressan, A., et al. 2014, MNRAS, 444, 2525
Chen, Y., Bressan, A., Girardi, L., et al. 2015, MNRAS, 452, 1068
Dent, W. R. F., Wyatt, M. C., Roberge, A., et al. 2014, Science, 343, 1490
Draine, B. T. 2003, ApJ, 598, 1017
Flock, M., Ruge, J. P., Dzyurkevich, N., et al. 2015, A&A, 574, A68
Foreman-Mackey, D., Hogg, D. W., Lang, D., & Goodman, J. 2013, PASP, 125, 306
Fujiwara, H., Ishihara, D., Onaka, T., et al. 2013, A&A, 550, A45
Gaia Collaboration (Vallenari, A., et al.) 2023, A&A, 674, A1
Goodman, J., & Weare, J. 2010, Commun. Appl. Math. Comput. Sci., 5, 65
Grigorieva, A., Artymowicz, P., & Thébault, P. 2007, A&A, 461, 537
Han, Y., Wyatt, M. C., & Dent, W. R. F. 2023, MNRAS, 519, 3257

Han, Y., Mansell, E., Jennings, J., et al. 2026, A&A, 705, A196
Houk, N. 1978, Michigan Catalogue of Two-dimensional Spectral Types for the HD stars (USA: University of Michigan)
Hughes, A. M., Lieman-Sifry, J., Flaherty, K. M., et al. 2017, ApJ, 839, 86
Jackson, A. P., Wyatt, M. C., Bonsor, A., & Veras, D. 2014, MNRAS, 440, 3757
Jankovic, M. R., Pawellek, N., Zander, J., et al. 2026, A&A, 705, A204
Jones, J. W., Chiang, E., Duchêne, G., Kalas, P., & Esposito, T. M. 2023, ApJ, 948, 102
Kenyon, S. J., & Bromley, B. C. 2005, AJ, 130, 269
Kim, M., Wolf, S., Potapov, A., Mutschke, H., & Jäger, C. 2019, A&A, 629, A141
Kóspál, Á., Moór, A., Juhász, A., et al. 2013, ApJ, 776, 77
Kral, Q., Thébault, P., & Charnoz, S. 2013, A&A, 558, A121
Kral, Q., Marino, S., Wyatt, M. C., Kama, M., & Matrà, L. 2019, MNRAS, 489, 3670
Kral, Q., Davoult, J., & Charnay, B. 2020, Nat. Astron., 4, 769
Krivov, A. V., Queck, M., Löhne, T., & Sremčević, M. 2007, A&A, 462, 199
Li, A., & Greenberg, J. M. 1998, A&A, 331, 291
Li, H., Colgate, S. A., Wendroff, B., & Liska, R. 2001, ApJ, 551, 874
Li, D., Telesco, C. M., & Wright, C. M. 2012, ApJ, 759, 81
Lieman-Sifry, J., Hughes, A. M., Carpenter, J. M., et al. 2016, ApJ, 828, 25
Lovelace, R. V. E., Li, H., Colgate, S. A., & Nelson, A. F. 1999, ApJ, 513, 805
Lovell, J. B., Kennedy, G. M., Marino, S., et al. 2021a, MNRAS, 502, L66
Lovell, J. B., Marino, S., Wyatt, M. C., et al. 2021b, MNRAS, 506, 1978
Lovell, J. B., Hales, A. S., Kennedy, G. M., et al. 2026, A&A, 705, A200
Lyra, W., Johansen, A., Zsom, A., Klahr, H., & Piskunov, N. 2009, A&A, 497, 869
Mac Manamon, S., Matrà, L., Marino, S., et al. 2026, A&A, 705, A198
Malhotra, R. 1993, Nature, 365, 819
Mannings, V., & Barlow, M. J. 1998, ApJ, 497, 330
Marino, S., Casassus, S., Perez, S., et al. 2015, ApJ, 813, 76
Marino, S., Matrà, L., Stark, C., et al. 2016, MNRAS, 460, 2933
Marino, S., Flock, M., Henning, T., et al. 2020, MNRAS, 492, 4409
Marino, S., Cataldi, G., Jankovic, M. R., Matrà, L., & Wyatt, M. C. 2022, MNRAS, 515, 507
Marino, S., Matrà, L., Hughes, A. M., et al. 2026, A&A, 705, A195
Martinez-Brunner, R., Casassus, S., Pérez, S., et al. 2022, MNRAS, 510, 1248
Matrà, L., Dent, W. R. F., Wyatt, M. C., et al. 2017a, MNRAS, 464, 1415
Matrà, L., MacGregor, M. A., Kalas, P., et al. 2017b, ApJ, 842, 9
Matrà, L., Wyatt, M. C., Wilner, D. J., et al. 2019, AJ, 157, 135
Matrà, L., Marino, S., Wilner, D. J., et al. 2025, A&A, 693, A151
Meheut, H., Meliani, Z., Varniere, P., & Benz, W. 2012, A&A, 545, A134
Michel, P., Benz, W., Tanga, P., & Richardson, D. C. 2001, Science, 294, 1696
Miller, E., Marino, S., Stammler, S. M., et al. 2021, MNRAS, 508, 5638
Milli, J., Olofsson, J., Bonduelle, M., et al. 2026, A&A, 705, A199
Min, M., Canovas, H., Mulders, G. D., & Keller, C. U. 2012, A&A, 537, A75
Moór, A., Curé, M., Kóspál, Á., et al. 2017, ApJ, 849, 123
Moór, A., Kral, Q., Ábrahám, P., et al. 2019, ApJ, 884, 108
Moór, A., Ábrahám, P., Kóspál, Á., et al. 2025, A&A, 703, A15
Najita, J. R., Kenyon, S. J., & Bromley, B. C. 2022, ApJ, 925, 45
Nakatani, R., Kobayashi, H., Kuiper, R., Nomura, H., & Aikawa, Y. 2021, ApJ, 915, 90
Nakatani, R., Turner, N. J., Hasegawa, Y., et al. 2023, ApJ, 959, L28
Ooyama, W., Nakatani, R., Hosokawa, T., Mitani, H., & Turner, N. J. 2025, ApJ, 983, 153
Pearce, T. D., Launhardt, R., Ostermann, R., et al. 2022, A&A, 659, A135
Pecaut, M. J., & Mamajek, E. E. 2016, MNRAS, 461, 794
Perez, S., Dunhill, A., Casassus, S., et al. 2015, ApJ, 811, L5
Pérez, S., Casassus, S., & Benítez-Llambay, P. 2018, MNRAS, 480, L12
Perrot, C., Olofsson, J., Kral, Q., et al. 2023, A&A, 673, A39
Pezzotta, V., Facchini, S., Longarini, C., Lodato, G., & Martire, P. 2025, A&A, 694, A108
Pinte, C., Teague, R., Flaherty, K., et al. 2023, ASP Conf. Ser., 534, 645
Reche, R., Beust, H., Augereau, J.-C., & Absil, O. 2008, A&A, 480, 551
Regály, Z., Juhász, A., & Nehéz, D. 2017, ApJ, 851, 89
Schneiderman, T., Matrà, L., Jackson, A. P., et al. 2021, Nature, 598, 425
Skaf, N., Boccaletti, A., Pantin, E., et al. 2023, A&A, 675, A35
Stark, C. C., Schneider, G., Weinberger, A. J., et al. 2014, ApJ, 789, 58
Tang, J., Bressan, A., Rosenfield, P., et al. 2014, MNRAS, 445, 4287
Tazzari, M., Beaujean, F., & Testi, L. 2018, MNRAS, 476, 4527
Teague, R. 2019a, J. Open Source Softw., 4, 1220
Teague, R. 2019b, Res. Notes Am. Astron. Soc., 3, 74
Teague, R., & Foreman-Mackey, D. 2018, Res. Notes Am. Astron. Soc., 2, 173
Teague, R., Bae, J., & Bergin, E. A. 2019, Nature, 574, 378
Teague, R., Bae, J., Bergin, E. A., Birnstiel, T., & Foreman-Mackey, D. 2018, ApJ, 860, L12
Telesco, C. M., Fisher, R. S., Wyatt, M. C., et al. 2005, Nature, 433, 133
Terrill, J., Marino, S., Booth, R. A., et al. 2023, MNRAS, 524, 1229
Thebault, P., & Kral, Q. 2018, A&A, 609, A98
Toci, C., Lodato, G., Christiaens, V., et al. 2020, MNRAS, 499, 2015
Trapman, L., Facchini, S., Hogerheijde, M. R., van Dishoeck, E. F., & Bruderer, S. 2019, A&A, 629, A79
van der Marel, N., van Dishoeck, E. F., Bruderer, S., et al. 2013, Science, 340, 1199
van der Marel, N., Birnstiel, T., Garufi, A., et al. 2021, AJ, 161, 33
Visser, R., van Dishoeck, E. F., & Black, J. H. 2009, A&A, 503, 323
Weber, P., Casassus, S., & Pérez, S. 2022, MNRAS, 510, 1612
Weber, P., Pérez, S., Baruteau, C., et al. 2026, A&A, 705, A203
Wyatt, M. C. 2003, ApJ, 598, 1321
Wyatt, M. C. 2006, ApJ, 639, 1153
Wyatt, M. C., & Dent, W. R. F. 2002, MNRAS, 334, 589
Wyatt, M. C., & Jackson, A. P. 2016, Space Sci. Rev., 205, 231
Wyatt, M. C., Bonsor, A., Jackson, A. P., Marino, S., & Shannon, A. 2017, MNRAS, 464, 3385
Zuckerman, B., & Song, I. 2012, ApJ, 758, 77

[1] Department of Physics and Astronomy, University of Exeter, Stocker Road, Exeter EX4 4QL, UK
[2] Departamento de Física, Universidad de Santiago de Chile, Av. Víctor Jara 3493, Santiago, Chile
[3] Millennium Nucleus on Young Exoplanets and their Moons (YEMS), Chile
[4] Center for Interdisciplinary Research in Astrophysics Space Exploration (CIRAS), Universidad de Santiago, Chile
[5] Department of Physics, University of Warwick, Gibbet Hill Road, Coventry CV4 7AL, UK
[6] School of Physics, Trinity College Dublin, the University of Dublin, College Green, Dublin 2, Ireland
[7] Univ. Grenoble Alpes, CNRS, IPAG, 38000 Grenoble, France
[8] UK Astronomy Technology Centre, Royal Observatory Edinburgh, Blackford Hill, Edinburgh EH9 3HJ, UK
[9] Instituto de Astrofísica de Canarias, Vía Láctea S/N, La Laguna, 38200 Tenerife, Spain
[10] Departamento de Astrofísica, Universidad de La Laguna, La Laguna, 38200 Tenerife, Spain
[11] National Astronomical Observatory of Japan, Osawa 2-21-1, Mitaka, Tokyo 181-8588, Japan
[12] Department of Astronomy, Graduate School of Science, The University of Tokyo, Tokyo 113-0033, Japan
[13] Department of Astronomy, University of California, Berkeley, Berkeley, CA 94720-3411, USA
[14] Division of Geological and Planetary Sciences, California Institute of Technology, 1200 E. California Blvd., Pasadena, CA 91125, USA
[15] Max-Planck-Insitut für Astronomie, Königstuhl 17, 69117 Heidelberg, Germany
[16] Department of Astronomy, Van Vleck Observatory, Wesleyan University, 96 Foss Hill Dr., Middletown, CT, 06459, USA
[17] Institute of Physics Belgrade, University of Belgrade, Pregrevica 118, 11080 Belgrade, Serbia
[18] Konkoly Observatory, HUN-REN Research Centre for Astronomy and Earth Sciences, MTA Centre of Excellence, Konkoly-Thege Miklós út 15-17, 1121 Budapest, Hungary
[19] Institute of Physics and Astronomy, ELTE Eötvös Loránd University, Pázmány Péter sétány 1/A, 1117 Budapest, Hungary
[20] Center for Astrophysics | Harvard & Smithsonian, 60 Garden St, Cambridge, MA 02138, USA
[21] Department of Physics and Astronomy, Johns Hopkins University, 3400 N Charles Street, Baltimore, MD 21218, USA
[22] European Southern Observatory, Karl-Schwarzschild-Strasse 2, 85748 Garching bei München, Germany
[23] Department of Astronomy and Steward Observatory, The University of Arizona, 933 North Cherry Ave, Tucson, AZ, 85721, USA
[24] Institute of Astronomy, University of Cambridge, Madingley Road, Cambridge CB3 0HA, UK

Appendix A: Acknowledgments

Acknowledgements. We thank the anonymous referee for their comments and suggestions that have improved the quality and clarity of this paper. We thank Richard Teague for helpful discussions and for providing help using the packages BETTERMOMENTS, EDDY and GOFISH. S.M. acknowledges funding by the Royal Society through a Royal Society University Research Fellowship (URF-R1-221669) and the European Union through the FEED ERC project (grant number 101162711). P.W. acknowledges support from FONDECYT grant 3220399 and ANID – Millennium Science Initiative Program – Center Code NCN2024_001. T.D.P. is supported by a UKRI Stephen Hawking Fellowship and a Warwick Prize Fellowship, the latter made possible by a generous philanthropic donation. A.B. acknowledges research support by the Irish Research Council under grant GOIPG/2022/1895. S.P. acknowledges support from FONDECYT Regular 1231663 and ANID – Millennium Science Initiative Program – Center Code NCN2024_001. S.M.M. acknowledges funding by the European Union through the E-BEANS ERC project (grant number 100117693), and by the Irish research Council (IRC) under grant number IRCLA- 2022-3788. Views and opinions expressed are however those of the author(s) only and do not necessarily reflect those of the European Union or the European Research Council Executive Agency. Neither the European Union nor the granting authority can be held responsible for them. L.M. acknowledges funding by the European Union through the E-BEANS ERC project (grant number 100117693), and by the Irish research Council (IRC) under grant number IRCLA- 2022-3788. Views and opinions expressed are however those of the author(s) only and do not necessarily reflect those of the European Union or the European Research Council Executive Agency. Neither the European Union nor the granting authority can be held responsible for them. J.M. acknowledges funding from the Agence Nationale de la Recherche through the DDISK project (grant No. ANR-21-CE31-0015) and from the PNP (French National Planetology Program) through the EPOPEE project. C.d.B. acknowledges support from the Spanish Ministerio de Ciencia, Innovación y Universidades (MICIU) and the European Regional Development Fund (ERDF) under reference PID2023-153342NB-I00/10.13039/501100011033, from the Beatriz Galindo Senior Fellowship BG22/00166 funded by the MICIU, and the support from the Universidad de La Laguna (ULL) and the Consejería de Economía, Conocimiento y Empleo of the Gobierno de Canarias. E.C. acknowledges support from NASA STScI grant HST-AR-16608.001-A and the Simons Foundation. A.M.H. acknowledges support from the National Science Foundation under Grant No. AST-2307920. M.R.J. acknowledges support from the European Union's Horizon Europe Programme under the Marie Sklodowska-Curie grant agreement no. 101064124 and funding provided by the Institute of Physics Belgrade, through the grant by the Ministry of Science, Technological Development, and Innovations of the Republic of Serbia. This work was also supported by the NKFIH NKKP grant ADVANCED 149943 and the NKFIH excellence grant TKP2021-NKTA-64. Project no.149943 has been implemented with the support provided by the Ministry of Culture and Innovation of Hungary from the National Research, Development and Innovation Fund, financed under the NKKP ADVANCED funding scheme. J.B.L. acknowledges the Smithsonian Institute for funding via a Submillimeter Array (SMA) Fellowship, and the North American ALMA Science Center (NAASC) for funding via an ALMA Ambassadorship. E.M. acknowledges support from the NASA CT Space Grant. A.A.S. is supported by the Heising-Simons Foundation through a 51 Pegasi b Fellowship. Support for B.Z. was provided by The Brinson Foundation. This paper makes use of the following ALMA data: ADS/JAO.ALMA# 2022.1.00338.L. ALMA is a partnership of ESO (representing its member states), NSF (USA) and NINS (Japan), together with NRC (Canada), MOST and ASIAA (Taiwan), and KASI (Republic of Korea), in cooperation with the Republic of Chile. The Joint ALMA Observatory is operated by ESO, AUI/NRAO and NAOJ. The National Radio Astronomy Observatory is a facility of the National Science Foundation operated under cooperative agreement by Associated Universities, Inc. The project leading to this publication has received support from ORP, which is funded by the European Union's Horizon 2020 research and innovation programme under grant agreement No 101004719 [ORP]. We are grateful for the help of the UK node of the European ARC in answering our questions and producing calibrated measurement sets. This research used the Canadian Advanced Network For Astronomy Research (CANFAR) operated in partnership by the Canadian Astronomy Data Centre and The Digital Research Alliance of Canada with support from the National Research Council of Canada the Canadian Space Agency, CANARIE and the Canadian Foundation for Innovation.

Appendix B: Posterior distribution of the dust arc model

Figure B.1 shows the posterior distribution retrieved from the MCMC fit to the dust ALMA data, except those that define the arc, which are shown in Figure 3.

Appendix C: ^{12}CO radiative transfer models

To understand the systematics in the velocity profiles derived in Sect. 3, we simulate ^{12}CO J=3-2 ALMA observations using Keplerian and non-Keplerian models to test the sensitivity of our methods. We start by simulating synthetic image cubes using DISC2RADMC (Marino et al. 2022). Our model consists of a disc of gas around a 1.91 $M_\star$ central star. The gas is distributed with a Gaussian radial surface density distribution, centred at 74 au, with a FWHM of 17 au (Brennan et al. 2026), and a vertical aspect ratio $h = 0.05$.

The gas is assumed to be in local thermodynamic equilibrium, and we set the kinetic and excitation temperature at the belt centre to be 38 K and decaying with radius with an exponent β of -0.14 (as derived in Brennan et al. 2026). The mean molecular weight (μ) is assumed to be either 14 (representative of a secondary origin scenario) or 2.3 (primordial scenario). A lower μ results in a higher sound speed and larger deviations from Keplerian rotation. The model azimuthal velocities are set to be Keplerian or non-Keplerian rotation due to pressure support (following Eq. 6). The radial and vertical velocities are set to zero.

We simulate image cubes with a spectral resolution of 26 m/s and spatial resolution of 10 mas. We use these synthetic cubes to simulate ALMA observations using the task SIMOBSERVE in CASA (CASA Team et al. 2022), using the same antenna configuration as the observations and inputting the same noise level per channel. The simulated ALMA observations are then imaged using TCLEAN using a Briggs weighting, a robust parameter of 0.5, a Keplerian mask and the same pixel size as in Mac Manamon et al. (2026). The resulting image cubes have approximately the same beam size and root-mean-square level. Finally, we follow the same procedure as with the real data, and extract the line-of-sight velocities, residuals after a Keplerian model subtraction, and azimuthal velocities from the simulated observations.

The line-of-sight velocity residuals for three different models and the observations are presented in Figure C.1. The left panel presents a Keplerian model, which does not display any clear residual pattern along the disc major axis as in our observations. The central panels present two non-Keplerian models. The middle left and right panels present non-Keplerian models of a disc with a high μ of 14 and one with a low value of 2.3, respectively. Both simulated models display a similar pattern to the observations, with the inner NE (SW) region being more red-shifted (blue-shifted) than the Keplerian model, indicating a super-Keplerian velocity. Similarly, the outer regions display sub-Keplerian velocities. The residual velocities of the observations are similar to those in the high μ model, but much lower than those in the low μ model.

To better compare the simulated models and data, the top panel of Figure C.2 shows the azimuthal velocities extracted using the same method as for the data. The velocities extracted from the simulated observation of a Keplerian model (red line) decrease with radius more slowly than both the observations (dark blue line) and a Keplerian profile (dashed grey line). The

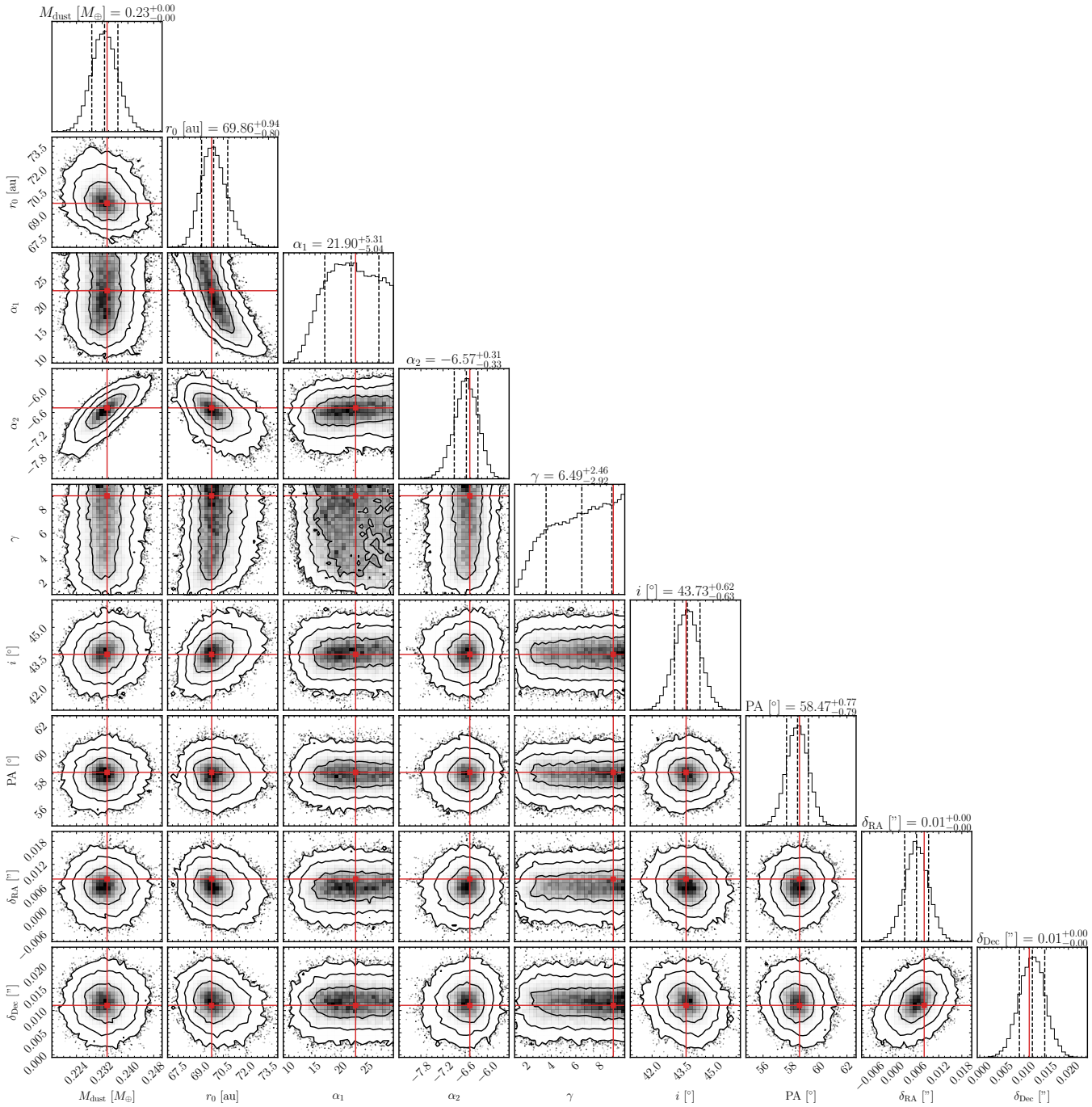

Fig. B.1: MCMC posterior distribution of the parameters used to fit the dust continuum observations, except those that define the arc. The contour levels in the 2D marginalised distributions correspond to the 68, 95, and 99.7% confidence levels. The dashed vertical lines in the marginalised distributions display the 16th, 50th, and 84th percentiles. The red lines represent the best-fit value (lowest χ^2).

latter is likely due to beam smearing (Pezzotta et al. 2025). The two profiles extracted from non-Keplerian simulated models (purple and light blue) have slopes that are steeper than Keplerian, as in the observations. The best-fit $M_\star$ for the Keplerian, and non-Keplerian $\mu = 14$, and $\mu = 2.3$ models was 1.93, 1.93 and 1.80 $M_\odot$, significantly different from the 1.91 $M_\odot$ used as input. This demonstrates that the stellar mass derived from Keplerian fits can be easily wrong by a few per cent.

The middle panel of Figure C.2 displays the azimuthal velocity residuals of the simulated and real observations after subtracting a Keplerian profile that intersects the corresponding azimuthal velocities at 75 au. The two non-Keplerian simulated observations (purple and light blue lines) produce residuals with the same pattern as the observations (dark blue), demonstrating how the effect of pressure support can lead to the non-Keplerian signal that we found. The deviations from the model with a low μ, and thus a high sound speed, are much stronger than observed. We note, however, that there are strong degeneracies between the density distribution of the gas and its sound speed (determined by its temperature and μ); therefore, we do not attempt to find a best fit here.

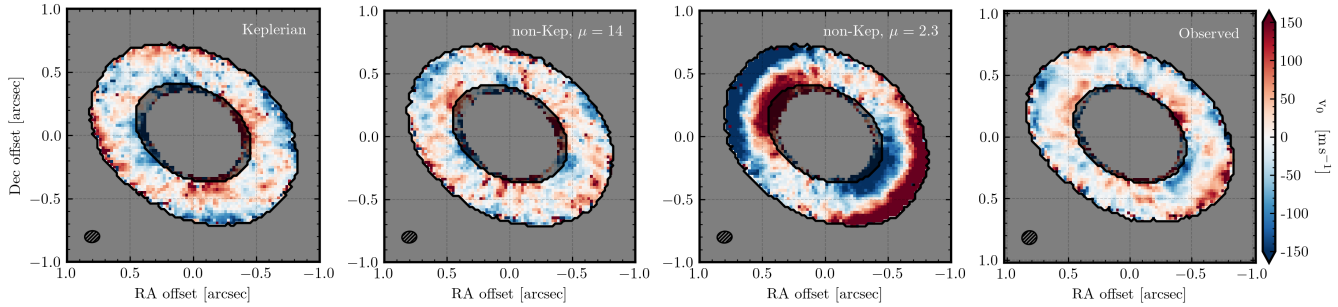

Fig. C.1: Velocity map residuals after subtracting the best fit line-of-sight Keplerian model from simulated (left, middle left and middle right panels) and the real observations (right panel). The grey-shaded region represents the area that was not included in the fit to avoid low S/N areas. The beam size is displayed in the bottom left corner.

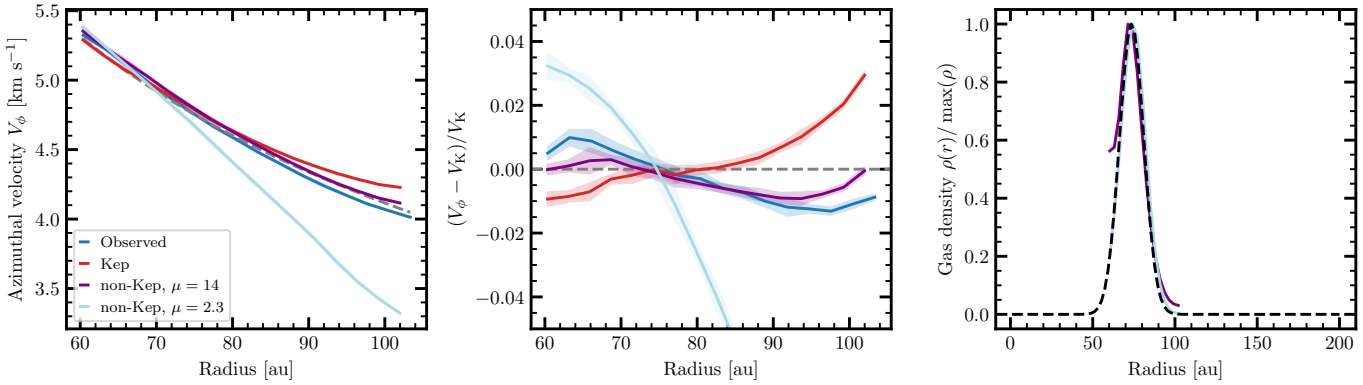

Fig. C.2: Left panel: Azimuthal velocity profile extracted from the simulated and real image cubes vs the best-fit Keplerian model of the real data (dashed grey line). Middle panel: Azimuthal velocity profile residual after subtracting a Keplerian profile. The shaded regions represent the 1σ uncertainty. Right panel: Gas density extracted from the two models with non-Keplerian velocities (solid coloured lines) compared to the input gas density (dashed black line). The dark blue line represents the profiles extracted from the real data. The light blue, purple, and red lines represent different models as indicated in the legend in the top panel.

The Keplerian simulated observations produce a deviation opposite to what is observed, with sub-Keplerian at the inner edge and super-Keplerian at the outer edge due to beam smearing. This demonstrates that a Keplerian model is strongly disfavoured by our observations.

The bottom panels show the inferred gas density radial profiles extracted from the two models with non-Keplerian velocities. We use as input the known model gas temperature, mean molecular weight, and a stellar mass such that the retrieved velocities match the Keplerian velocity at 75 au. For both non-Keplerian models, the derived profiles reproduce well the true input profile despite the effects of beam smearing and optical depth effects.

However, if we use as input the stellar mass of the radiative transfer model of 1.91 $M_\odot$, the retrieved profiles do not recover as well the input density. For $\mu = 2.3$, the peak density shifts to 70 au. For $\mu = 14$, the retrieved profile monotonically rises with radius, creating a positive pressure gradient that is necessary to match the observed azimuthal velocity that is higher than Keplerian at all radii. The difference in behaviour between these two models is likely due to the velocity deviations being stronger and easier to extract for the $\mu = 2.3$ model.

The examples shown in this section demonstrate that the non-Keplerian kinematics of HD 121617 can be reasonably reproduced by radiative transfer models that incorporate the effect of pressure support on the azimuthal velocity of the gas. While we do not attempt to fit the data with these models due to strong degeneracies between model parameters, this could be done, in principle, in the future by incorporating other observables such as the line profile (constraining the gas temperature) and intensity distribution (constraining the spatial distribution).

A&A, 705, A200 (2026)
https://doi.org/10.1051/0004-6361/202556568
© The Authors 2026

Astronomy & Astrophysics

The ALMA survey to Resolve exoKuiper belt Substructures (ARKS)

VI. Asymmetries and offsets

J. B. Lovell[1,⋆], A. S. Hales[2,3,4], G. M. Kennedy[5,6], S. Marino[7], J. Olofsson[8], A. M. Hughes[9], E. Mansell[9], B. C. Matthews[10,11], T. D. Pearce[6], A. A. Sefilian[12], D. J. Wilner[1], B. Zawadzki[9], M. Booth[13], M. Bonduelle[14], A. Brennan[15], C. del Burgo[16,17], J. M. Carpenter[3], G. Cataldi[18,19], E. Chiang[20], A. Fehr[1], Y. Han[21], Th. Henning[22], A. V. Krivov[23], P. Luppe[15], J. P. Marshall[24], S. Mac Manamon[15], J. Milli[14], A. Moór[25], M. C. Wyatt[26], S. Ertel[12,27], M. R. Jankovic[28], Á. Kóspál[25,29,22], M. A. MacGregor[30], L. Matrà[15], S. Pérez[31,4,32], and P. Weber[31,4,32]

(Affiliations can be found after the references)

Received 23 July 2025 / Accepted 13 November 2025

ABSTRACT

Context. Asymmetries in debris discs provide unique clues to understand the evolution and architecture of planetary systems. Previous studies of debris discs at (sub)millimetre wavelengths have suggested the presence of asymmetries in a wide variety of systems, yet the lack of sufficiently sensitive high-resolution observations means that the typical properties of debris disc asymmetries have not been studied at the population level. The aim of the ALMA survey to Resolve exoKuiper belt Substructures (ARKS) is to expand our understanding of radial and vertical dust structures, as well as gas distributions and kinematics, in debris discs. The ARKS sample of 24 highly resolved targets in ALMA's Bands 6 and 7 (1.1–1.4 mm and 0.8–1.1 mm, respectively) provided a unique opportunity to study their asymmetries.

Aims. Here, in ARKS VI, we present a systematic analysis of the asymmetries and stellocentric offsets present in the ALMA continuum data for the ARKS survey. Our aims are to (i) identify asymmetries in debris disc dust distributions, (ii) quantify debris disc asymmetry properties, and (iii) discuss the potential origins of debris disc asymmetries. This work is the first systematic analysis of asymmetries in a large sample of well-resolved discs at (sub)millimetre wavelengths.

Methods. We utilised empirical methods to identify emission asymmetries (relative to disc major and minor axes, and azimuthal disc locations) and the presence of offset emission between disc centres and the locations of the host stars, via an analysis of their calibration procedures and disc properties. We associated observational asymmetry types (offset, major and/or minor axis, azimuthal) and plausible physical classes (arcs, eccentricities, and possible clumps and warps) associated with each source.

Results. We show that there are ten systems, almost half of the ARKS sample, that host either a continuum emission asymmetry or offset emission. Three systems host offsets (HD 15115, HD 32297, and HD 109573 (HR 4796)), four host azimuthal asymmetries (HD 9672 (49 Ceti), HD 92945, HD 107146, and HD 121617), two host an asymmetry in their major axis (HD 10647 (q^1 Eri), and HD 39060 (β Pic)), and one hosts an asymmetry in their minor axis (HD 61005). We attribute the offset asymmetries to non-zero eccentricities, and three of the azimuthal asymmetries to arcs. The presence of an asymmetry or offset in the ARKS sample appears to be correlated with the fractional luminosity of cold dust. We tentatively suggest that continuum asymmetries are more prevalent in CO-rich debris discs, suggesting that gas interactions may drive debris dust asymmetries. We identify seven other tentative asymmetries, including four in distinct ARKS systems and three in systems with otherwise significant asymmetries.

Conclusions. This study demonstrates that debris disc asymmetries in the ARKS sample are common, and plausibly so in the wider population of debris discs at (sub)-millimetre wavelengths. This means that (sub)-millimetre asymmetries plausibly await discovery in debris discs as we probe these with higher sensitivity and resolution. Throughout, we highlight future studies to further investigate the origins of debris disc asymmetries, and build on the work presented here.

Key words. circumstellar matter – planetary systems

1. Introduction

Debris discs are dusty rings around stars that are sustained by continual planetesimal belt collisions over megayear to gigayear timescales (Wyatt 2008; Matthews et al. 2014; Hughes et al. 2018; Marino 2022). As mature circumstellar discs, debris discs provide critical insights into the evolution of planetary systems following the dispersal of their protoplanetary discs, through the stellar main sequence, and beyond to post-main sequence planetary systems (see e.g. Bonsor & Wyatt 2010; Wyatt et al. 2015; Farihi 2016). Improvements in sensitivity and angular resolution over recent years at (sub)millimetre wavelengths – in particular, with the James Clerk Maxwell Telescope (JCMT), Submillimeter Array (SMA), and Atacama Large Millimeter/submillimeter Array (ALMA) – have shown the diversity of debris disc structures and substructures. This diversity can now provide a greater understanding as to how planetary systems evolve, via studies of their continuum dust and carbon monoxide

⋆ Corresponding author: joshualovellastro@gmail.com

Open Access article, published by EDP Sciences, under the terms of the Creative Commons Attribution License (https://creativecommons.org/licenses/by/4.0), which permits unrestricted use, distribution, and reproduction in any medium, provided the original work is properly cited.
This article is published in open access under the Subscribe to Open model. Subscribe to A&A to support open access publication.

(CO) gas morphologies (see e.g. the surveys of Holland et al. 2017; Moór et al. 2017; Lovell et al. 2021b; Matrà et al. 2025, and references therein).

Asymmetries and offsets have been strongly associated with some of the best-studied debris discs, particularly in scattered light images. The warp in the β Pictoris disc (Mouillet et al. 1997; Heap et al. 2000), later identified as due to a second disc component (Kalas et al. 2005; Golimowski et al. 2006), is one of the earliest and most well-known examples. The offset of the Fomalhaut disc centre from the stellar position is obvious at all wavelengths at which the star is detectable (e.g. Acke et al. 2012; Su et al. 2013; MacGregor et al. 2017; Gáspár et al. 2023; Chittidi et al. 2025; Lovell et al. 2025). Asymmetries that vary over time have even been detected in the AU Mic disc (Boccaletti et al. 2015), with various potential explanations (Sezestre et al. 2017; Chiang & Fung 2017; Grady et al. 2020; Thebault & Kral 2018). Though these asymmetries are among the most well-known and pronounced, many discs exhibit asymmetries of some kind. Crotts et al. (2024) conducted an empirical analysis of 26 debris discs, many of them less well-studied, imaged with the Gemini Planet Imager (GPI) and found that the majority of imaged discs (>70%) have one or more discernibly asymmetric features, such as brightness, radial extent, or *JHK* colours, as well as warps and azimuthal features. However, studies have not yet found comparably high occurrence rates of debris disc asymmetries at longer wavelengths.

Asymmetries in debris discs at millimetre wavelengths have been reported in data prior to ALMA, for example from the Submillimeter Array (SMA; see e.g. MacGregor et al. 2015, in the case of HD 15115) and the *James Clerk Maxwell* Telescope (JCMT; see e.g. Holland et al. 2003; Panić et al. 2013; Holland et al. 2017, in the case of Fomalhaut, and other targets in the SONS – SCUBA-2 Observations of Nearby Stars – sample). Moreover, several millimetre asymmetric structures in debris discs were known before ARKS, including the CO gas clump in the south of the β Pic (HD 39060) disc (e.g. Dent et al. 2014), the continuum (dust) emission clump in the main ring of q^1 Eri (HD 10647; Lovell et al. 2021a), and the eccentric discs of Fomalhaut (HD 216956), HD 53143, and HD 202628 (e.g. MacGregor et al. 2017; Faramaz et al. 2019a; Kennedy 2020; MacGregor et al. 2021). In other cases, pre-ARKS ALMA data have suggested hints of asymmetric emission that have not been definitively proven, for example in the case of the ARKS target HD 92945 (Marino et al. 2019) and ε Eri (HD 22049; see Booth et al. 2023). In some cases, asymmetric clumps have been found in systems that were then found to originate from galactic or extra-galactic confusion (e.g. in the case of background sources being co-located in the discs of HD 95086, Fomalhaut and HD 22049; see Booth et al. 2019; Kennedy et al. 2023; Booth et al. 2023) highlighting the need for long-term monitoring of asymmetries to verify their origins. Moreover, asymmetries have been detected in a range of systems in scattered light images without counterpart asymmetries in (sub)millimetre thermal emission images (see e.g. Olofsson et al. 2019, 2022), which may result from either observational differences (i.e. differences in their signal-to-noise ratio (S/N) or resolution) or physical differences (with different wavelength observations being more or less sensitive to distinct physical features that trace underlying asymmetric structures), highlighting the need for multi-wavelength monitoring to quantify their origins and behaviour.

Asymmetries in circumstellar discs more generally contain vital clues to the processes driving their evolution. These are present at early evolutionary stages in protoplanetary discs (see e.g. Andrews 2020) and at later evolutionary stages in debris discs (see also Hughes et al. 2018; Marino 2022). Arcs and crescents are the rarest type of substructure in protoplanetary discs (less common than rings or spirals) based on their occurrence rates (Bae et al. 2023), and are detected in up to 30% of massive discs, falling to around 5% in less massive discs.

Asymmetries in debris discs have been uniquely linked to a range of dynamically induced substructures. A commonly invoked scenario is one in which these asymmetries can be driven directly by planet–disc interactions (see e.g. Dong et al. 2020). Examples include scenarios in which eccentric planets drive eccentricities (e.g. Quillen & Faber 2006; Pearce & Wyatt 2014; Kennedy 2020; Lynch & Lovell 2022; Lovell & Lynch 2023) or spirals into discs (Hahn 2003; Wyatt 2005; Pearce & Wyatt 2015; Rodet et al. 2017; Sefilian et al. 2021, 2023). Circular but migrating planets, on the other hand, can trap planetesimals in mean-motion resonances, which can produce clumps in discs (e.g. Wyatt 2003, 2006; Reche et al. 2008; Booth et al. 2023; Friebe et al. 2022). Planets can also carve gaps in discs beyond their own orbital radii via secular resonances (e.g. Pearce & Wyatt 2015; Yelverton & Kennedy 2018; Sefilian et al. 2021, 2023). Orbital inclination misalignments between planets and discs can also cause vertical warps in the discs (see e.g. Mouillet et al. 1997; Augereau et al. 2001; Sefilian et al. 2025). However, planets are not uniquely responsible for inducing asymmetries in discs. Other scenarios may also drive these features, for instance stellar flybys (Reche et al. 2008; Rodet et al. 2017; Pfalzner et al. 2024), stellar binary interactions (Farhat et al. 2023), gas–dust interactions (Lyra & Kuchner 2013), inheritance from earlier stages of evolution (Nealon et al. 2018; Kennedy 2020), slow modes of self-gravitating discs (Jalali & Tremaine 2012), or via giant impacts between large planetesimals in the disc (Jackson et al. 2014; Dent et al. 2014; Jones et al. 2023). Quantifying asymmetric emission features therefore allows one to understand their origins, and details the histories of planetary systems.

Debris discs show wavelength-dependent architectures. Whilst larger millimetre- to centimetre-sized grains typically trace the orbits of their parent planetesimals, smaller (sub)micron-sized grains are more strongly affected by radiation forces, which can drag material inwards, for example via the Poynting–Robertson effect, or blow small grains out of discs via radiation pressure (Matthews et al. 2014; Hughes et al. 2018). The physics that dictate how grains are transported in debris discs can alter their observed asymmetric morphologies as a function of wavelength, for example with scattered light observations being able to observe dust out to much larger radii (i.e. where ISM interactions may plausibly shape their morphologies) and with millimetre observations being more sensitive to asymmetries inherent in planetesimal belts (see e.g. Wyatt 2006; Lee & Chiang 2016; Lynch & Lovell 2022; Jones et al. 2023, where planetary system dynamics are more likely to dominate their morphologies). These distinctions mean it is important to study asymmetries from a multi-wavelength perspective to understand the origins of asymmetric debris disc structures.

The ALMA survey to Resolve exoKuiper belt Substructures (ARKS) is the first ALMA large programme dedicated to studying the structures and dynamics of a sample of the nearest and brightest debris discs, providing unprecedented sensitivity and resolution, sufficient to resolve their radial and vertical morphologies. Most pertinent to the analysis and discussion in this paper are papers ARKS I (Marino et al. 2026b), which discusses the overview, reduction, and calibration of the sample; ARKS II (Han et al. 2026), which models and presents (axisymmetric) disc radial profiles; ARKS III (Zawadzki et al. 2026),

Table 1. ARKS debris discs determined to be asymmetric.

Name	Asym. Type	Class
HD 9672 (49 Ceti)	Az.	Warp?
HD 10647 (q^1 Eri)	Maj.	Clump?
HD 15115	Off.	Eccentric
HD 32297	Off.	Eccentric
HD 39060 (β Pic)	Maj.	?
HD 61005	Min.	?
HD 92945	Az.	Arc
HD 107146	Az.	Arc
HD 109573 (HR 4796)	Off.	Eccentric
HD 121617	Az.	Arc

Notes. Asymmetries with unknown or ambiguous classes are denoted with a '?'. All ten systems are presented as a gallery in Fig. 1.

which models and presents (axisymmetric) disc vertical profiles; and ARKS V (Milli et al. 2026), which presents SPHERE scattered light images and profiles of discs. In this paper we present a systematic analysis of the sample's continuum asymmetries and offsets. We performed most of our analysis empirically and solely on dust continuum emission products, as provided by the work presented in ARKS I, and further detailed in Appendix A. Assessment of the CO gas asymmetries will be presented in a future ARKS paper.

The rest of this paper is structured as follows. In Sect. 2, we present our methods for identifying dust continuum asymmetries or offsets. In Sect. 3, we discuss our findings for each source, and then in Sect. 4 in terms of the population. We summarise our findings and conclude in Sect. 5. Technical details are presented in Appendices A–C.

2. Stellocentric offsets and emission asymmetries

There are principally four types of observational asymmetry that we investigated for with these ARKS data. We searched for observational asymmetries based on these presenting asymmetric emission about their (i) major axes (Maj), (ii) minor axes (Min), (iii) at some localised azimuthal location (Az), or (iv) if these systems are host to a stellocentric offset (Off), i.e. a global offset between the disc emission centre and its central star. These asymmetry types are noted beside each relevant system in Table 1, each of which we conclude on per system in Sect. 3. Whilst asymmetric emission and/or offsets may be present in any given system, disc geometries can challenge our ability to definitively interpret their physical origin, thus in some cases we cannot ascribe to these a physical classification. In this section, we discuss the methodologies by which we assess ARKS data to be host to either a stellocentric offset or asymmetric emission. The data we analysed is described in Appendix A.

2.1. Offset assessments

We assessed all 24 ARKS targets for the presence of stellocentric offsets by analysing which discs have Gaia DR3 stellar locations significantly offset from their best-fit disc centre positions. These checks were made based on each target's fitted ΔRA and ΔDec values that were measured consistently for the full ARKS sample using symmetric Gaussian radial distribution models, as presented in ARKS I (see their Table B.1 Marino et al. 2026b).

In ARKS I (Marino et al. 2026b), HD 15115, HD 32297, HD 39060, HD 95086, and HD 109573 all have best-fit ΔRA and/or ΔDec offsets that are significantly offset from 0 (by more than 3σ). Since HD 95086's data suffers from the undersubtraction of a background source (as noted in Marino et al. 2026b), we deem this disc centre offset too biased to conclude that it is real. In the case of HD 39060, we attributed the disc centre offset to the data having a systematically poorer astrometric solution, evident in the large phase centre offset (see Table D.1 in Marino et al. 2026b) resulting from these data being collected prior to the release of accurate Gaia astrometric stellar solutions.

The observations of HD 15115, HD 32297, and HD 109573 have phase centre offsets from their Gaia stellar positions in both RA and Dec smaller than 20 mas, showing that the star was positioned at (or very close to) the phase centre throughout their observations. We present in Table B.1 the best-fit check source positions derived in both the visibility and image domain, i.e. with `uvmodelfit` and `imfit` respectively, as well as the best-fit disc centre offsets for HD 15115, HD 32297, and HD 109573. The offset uncertainties associated with these three targets are very small, in most cases just a few milliarcseconds, whereas their disc centres are offset by many tens of milliarcseconds. These three systems are amongst the nine ARKS targets with 'check source' observations. Check source observations enable the quantification of the typical astrometric uncertainties during ALMA observations, which we estimated for our science targets as described in Appendix B. The check source positions have tightly constrained locations consistent with no offset, and uncertainties that are smaller than the best-fit disc centre uncertainties. This comparison suggests that HD 15115, HD 32297, and HD 109573 have disc centres significantly offset from their stellar locations that cannot be explained by instrumental/calibration errors. We therefore concluded that these offsets are due to a physical offset from the centre of these three discs and their stars, and discuss this further in Sect. 3.

2.2. Assessment of asymmetric (sub)millimetre emission

Appendix A presents the images analysed in this paper for emission asymmetries. We note here that for 23/24 sources, we use the standard ARKS continuum data, except for HD 107146, for which we use the Band 6 data alone[1]. We primarily utilised two empirical methods to investigate whether systems host emission asymmetries. With these methods, we define significant asymmetries as those where we find evidence of residual asymmetric emission exceeding 5σ, and tentative asymmetries where there is evidence of residual asymmetric emission in the range 3–5σ.

2.2.1. Method one: Two-dimensional asymmetry analysis

We conducted image self-subtraction analysis in the three disc symmetry-axes on the cleaned images of all 24 systems. These disc symmetry axes are the major axis (which we use interchangeably here with position angle; PA), the minor axis (90°

[1] The ARKS image for HD 107146 includes both Band 7 and Band 6 data imaged in `tclean` with multi-frequency synthesis (mfs) and achieves exceptional S/N.

However, due to an issue with the short baselines in the Band 7 data which led to significant fringes in the final cleaned image (that could not be corrected for during the cleaning process; see Imaz Blanco et al. 2023) we removed the higher-frequency data and re-imaged the Band 6 data only. Whilst the Band 6 data have slightly worse resolution, the overall S/N is better than the Band 7 data and thus we find it more reliable for studying asymmetric emission.

anti-clockwise to the PA), and the rotation axis (i.e. symmetry about a rotation of 180°). Measuring for these non-axisymmetries requires knowledge of the image coordinate centre, which we fix to be the Gaia DR3 location of each system's star[2], unless these systems are host to a significant stellocentric offset (HD 15115, HD 32297 and HD 109573), in which case we shift the centre by this offset to hunt for asymmetries in their brightness distributions not caused by their offset alone, or the best-fit disc centres derived in Marino et al. (2026b) provided significantly smoother residual maps in comparison to those produced assuming the image centre was the Gaia DR3 stellar location (HD 131488, and HD 131835), given the best-fit disc centre can be subtly shifted due to the presence of disc substructures; see Zawadzki et al. (2026). The major and minor axis self-subtractions also require knowledge of the system position angles, and we use those provided by symmetric Gaussian model fits to each system's visibilities as presented in Table B.1 of Marino et al. (2026b). To produce these residual maps, we simply mirrored or rotated each image about the coordinate centre and subtracted the mirrored or rotated map from un-mirrored or un-rotated map[3]. Whilst this method is effective at finding strong asymmetries, it has the downside of inflating the noise properties of the residual images by $\sqrt{2}$. In addition, since these images are not spatially averaged, these properties can make subtler asymmetric features less pronounced. Using this method, we only find strong evidence of asymmetric emission towards HD 121617 (the most asymmetric disc in ARKS, as discussed in Marino et al. 2026a; Brennan et al. 2026; Weber et al. 2026), as well as tentative evidence in the cases of HD 9672, HD 10647, HD 39060, HD 92945, HD 107146, HD 131488, HD 131835, and HD 218396, each of which we discuss in Sect. 3. In each case, we verified that the observed asymmetric features are robust to whether we use the coordinate centres derived in Marino et al. (2026b) as outlined above, or those derived in the ARKS axisymmetric parametric modelling papers, i.e. Han et al. (2026) and Zawadzki et al. (2026).

2.2.2. Method two: One-dimensional asymmetry analysis

To search for subtler asymmetries, we computed azimuthal, major axis, and minor axis profiles by averaging emission over particular regions of ARKS target images. This process effectively integrates 2D emission into 1D profiles, which allowed us to detect fainter asymmetric emission features. To produce these profiles, we de-projected the image data into system-specific bases, which requires knowledge of a target's bulk disc position angle, inclination, and reference coordinate centre. We adopted the values presented in Table B.1 from ARKS I (Marino et al. 2026b) for these parameters, and present these here for completeness in Table A.2. We discuss each of these asymmetries per source in Sect. 3. In all cases, we considered residual emission found at levels above 5σ in intensity, or integrated (accounting for the number of independent resolution elements within the integrated region) to be conclusive evidence of the presence of an asymmetry. We considered residual emission, either in intensity or integrated, at the level 3–5σ to be tentative evidence of asymmetric emission. We verified the robustness of these asymmetries to the reference coordinate centre by checking if these persist when we adopt the ΔRA and ΔDec values in the ARKS axisymmetric modelling papers, i.e. Han et al. (2026) and Zawadzki et al. (2026).

Due to the diversity of disc geometries, although we computed these profiles for all systems, some are much poorer at providing diagnostics of disc emission asymmetries, and so we do not utilise these in our analysis. For example, we do not interpret the azimuthal profiles of highly inclined or edge-on discs since their de-projections are too uncertain. Details of the profiles used in the analysis of each system are provided in Sect. 3.

A point that we highlight here is that the subtraction of sub-millimetre galaxies (SMGs) from the ARKS data pre-imaging (as noted in ARKS I Marino et al. 2026b) might remove some non-axisymmetric emission from each data set. Five systems were shown to host SMGs that are spatially co-located within their discs: HD 76582, HD 95086, HD 107146, TYC 9340-437-1, and HD 218396 (HR 8799). In the case of HD 107146, the subtracted emission originates from the inner cavity of the disc, inside the region where we assessed that there is asymmetric emission and thus, these subtractions do not affect our conclusions. In the case of HD 218396, one such clump is coincident with one of the clump features that we identified as a tentative asymmetry, and hence we do not ascribe significance to this being a disc-related asymmetry.

2.3. Assessment of asymmetric scattered light emission

We checked for any signs of asymmetries in near-IR scattered light observations. We refer to ARKS V (Milli et al. 2026) for a summary of the data availability and reduction process. Here we focus on targets for which the discs have been detected with the VLT/SPHERE instrument (Beuzit et al. 2019), either in total intensity or in linear polarimetry. For polarimetric observations, we used the Q_ϕ image (Milli et al. 2026). For observations in total intensity, we first computed an estimate of the telescope's point spread function from the cube of images, using a principal component analysis (automatically selecting the number of principal components so that 95% of the variance is taken into account); see also Soummer et al. (2012). We then subtracted this estimated point spread function to each frame of the cube, de-rotated them according to their parallactic angle at the time of the observations, and median-stacked the cube. Afterwards, with the final image of the disc, we mirrored it along its minor axis (Marino et al. 2026b, with the position angle taken from Table A.2, see also ARKS I), and subtracted it from the original image. If a target has both total intensity and linear polarimetric observations, both are used. The residual maps are shown in the top gallery of Fig. C.6, where each map is convolved by a 2D Gaussian with a standard deviation of 1.5 pixels to reduce the shot noise.

To further investigate the presence of asymmetries in these residual maps, we computed radial profiles, shown in the lower gallery of Fig. C.6. The profiles are computed in wedges along the major axis of the discs (indicated on top of the residual images), and we computed the mean in radial bins, on both sides of the disc's minor axis. To estimate the uncertainties, we computed the standard deviation in the same radial bins on the uncertainties maps: we used the U_ϕ image for polarimetric observations, while for total intensity datasets, we used the same principal component analysis as mentioned before but de-rotate the cube in the opposite direction (to cancel out any disc signal).

[2] All ARKS systems (per observational execution block) had their data shifted to this same reference location, which was conducted in `CASA` using the `fixvis` and `fixplanets` tasks; see Marino et al. (2026b) Table D.1 for further details.

[3] For this analysis, we utilised the non-primary beam-corrected images for each source, but scale the contour levels by the primary beam correction, such that the contours reflect the underlying significance of residual features.

3. Results

3.1. Asymmetries and offsets in ARKS: System-by-system analyses

Using the methods outlined in Sect. 2, we identified asymmetries and offsets in ten ARKS targets (at levels above 5σ), which we detail individually below. These are shown in Fig. 1.

3.1.1. HD 9672 (49 Ceti): An azimuthally asymmetric disc

HD 9672 hosts a unique azimuthal asymmetry. With reference to Fig. 1, we note that the peaks in the disc ansae appear shifted (i.e. rotated or twisted) relative to the disc major axis, i.e. these are on opposing sides of the disc as can be seen by comparing the peak locations relative to the black dotted line which marks the disc position angle. To confirm this twisted feature asymmetry, we analysed both the ARKS image, and the best-fit model-subtracted residual map presented in ARKS III (Zawadzki et al. 2026), the latter of which we present in the top panel of Fig. 2. We constructed and compared averaged intensity profiles parallel to the minor axis of the disc, through both disc ansae (averaged over a major axis extent of 0.75″). After reversing the direction of the profile through the western ansa and averaging this with the profile through the eastern ansa, we show in the residual intensity profile (lower panel of Fig. 2) that about the major axis there is a significant enhancement and decrement feature, showing the twisted feature to be significant. Indeed, by integrating the modulus of the residual intensity profile between ±0.5″, we found that the twisted feature has a significance of 5.2σ. The twisted feature is somewhat evident in the self-subtraction maps for HD 9672 (see Fig. C.1, in particular the minor axis map); however, the residual intensity profile is necessary to determine its presence as significant.

This analysis demonstrates that there is a significant azimuthal asymmetry in HD 9672's continuum disc, the only source in the ARKS sample to present this type of twisted asymmetric morphology. To highlight how this asymmetric feature manifests at other submillimetre data, we overplot on the top panel of Fig. 2 the ^{12}CO (3–2) moment-zero residual map presented in Hughes et al. (2017), where a similar twisted feature is present[4]. Although these archival data have a resolution that is two times lower than the ARKS continuum data and also have lower sensitivity, the CO residuals appear stronger, and more significantly twisted from the disc position angle than the continuum dust. Whilst there are multiple physical interpretations of this azimuthal structure, including the possibility that there is a warp, a physical twist, or a spiral, the origin of this feature is nevertheless difficult to determine given the available data, and without recourse to detailed modelling efforts, which are beyond the scope of this paper. Spiral patterns and twists are yet to have been reported in the literature in a debris disc at (sub)millimetre wavelengths (though these have been seen in scattered light data, for the young discs around HD 141569A and TWA 7; see e.g. Clampin et al. 2003; Ren et al. 2021, respectively); however, there are now a number of reported warps, i.e. asymmetric vertical or inclination distributions, that have appeared in both scattered light and (sub)millimetre observations, for example towards HD 39060 (β Pic; see e.g. Mouillet et al. 1997; Augereau et al. 2001; Golimowski et al. 2006; Dent et al. 2014) and HD 110058 (see e.g. Kasper et al. 2015; Hales et al. 2022; Stasevic et al. 2023). In these two systems, their warps have been interpreted as resulting from secular interactions with misaligned planets (see also Crotts & Matthews 2024), including scenarios where the disc's gravity plays a significant role in shaping the warp structure (e.g. via secular-inclination resonances; Sefilian et al. 2025). In such models, the discs exhibit a (leading) two-armed spiral pattern, which is most prominent beyond the warp (Nesvold & Kuchner 2015; Farhat et al. 2023; Sefilian et al. 2025). That other systems have been found to be warped which share morphological similarity to HD 9672 may suggest a preference to interpret HD 9672's structure as being warped, and likewise driven by similar phenomena. Nevertheless, any conclusion that this disc is warped, or due to some other type of structure, requires further work.

[4] To overplot these data, we shifted the image centre of the CO data by the phase centre offset noted in Hughes et al. (2017).

3.1.2. HD 10647 (q^1 Eri): A major axis asymmetry

The HD 10647 disc shows a significant major axis asymmetry, arising from an emission enhancement in its south-west ansa. Although this asymmetry is visible in HD 10647's emission map, which hosts contours that show enhanced emission in the south-west ansa in comparison to the north-east (see Fig. 1), this feature is best characterised by its major axis profile that we present in Fig. 3. In this figure we show the major axis intensity profiles (upper panel, averaged over the full minor axis of the disc) as a function of distance along the disc major axis from the central star for the ALMA data, separately for the archival data, ARKS-only data, or combined datasets and their self-subtracted intensity difference profiles (lower panel), and indicate the radial location of the reported clump (from Lovell et al. 2021a) in blue. Multiple independent peaks exceed 3σ along the south-east ansa region of the disc's combined data difference profile, and by integrating from 0 to either ±7.5″, we found that the integrated difference profile is significant at the 5.5σ level. An interesting feature towards this source is that the significance of this asymmetry is strongly dependent on whether archival HD 10647 baselines are included within the imaged data. For example, considering the archival-only (ARKS re-processed) data, the asymmetry significance increases to $\approx 9.1\sigma$, with a net flux enhancement in the south-west of ≈1.5 mJy, consistent with that reported in Lovell et al. (2021a). However, this significance falls to $<2\sigma$ if only the newest (higher-resolution) ARKS-only data are considered. Since the asymmetry is present in the fully combined data set, we report this here as significant. The lack of a significant asymmetry in the ARKS-only data cannot be explained by the difference in observational resolution or sensitivity between the archival and ARKS-only data. We note these data achieved approximately the same sensitivity, (13.6 μJy beam^{-1} for the archival data, and 13.1 μJy beam^{-1} for the ARKS-only data), and by smoothing the ARKS-only data with a Gaussian kernel matching the restored (clean) beam properties of the archival data, we found no significant flux enhancement in the south-west.

Although we conclude that the major axis of HD 10647's disc is asymmetric, it appears less conclusive that this major axis asymmetry originates in an extended dust clump, as suggested by Lovell et al. (2021a). The clump asymmetry interpretation of Lovell et al. (2021a) showed broad agreement between the ALMA data and the HST images (which shows the scattered light is extended asymmetrically further out in the north-west of the disc, presented also in Milli et al. 2026). The clump hypothesis suggested that the clump was produced as a Neptune-analogue planet migrated outwards and trapped planetesimals in its 2:1 mean motion resonance, similar to that expected in the

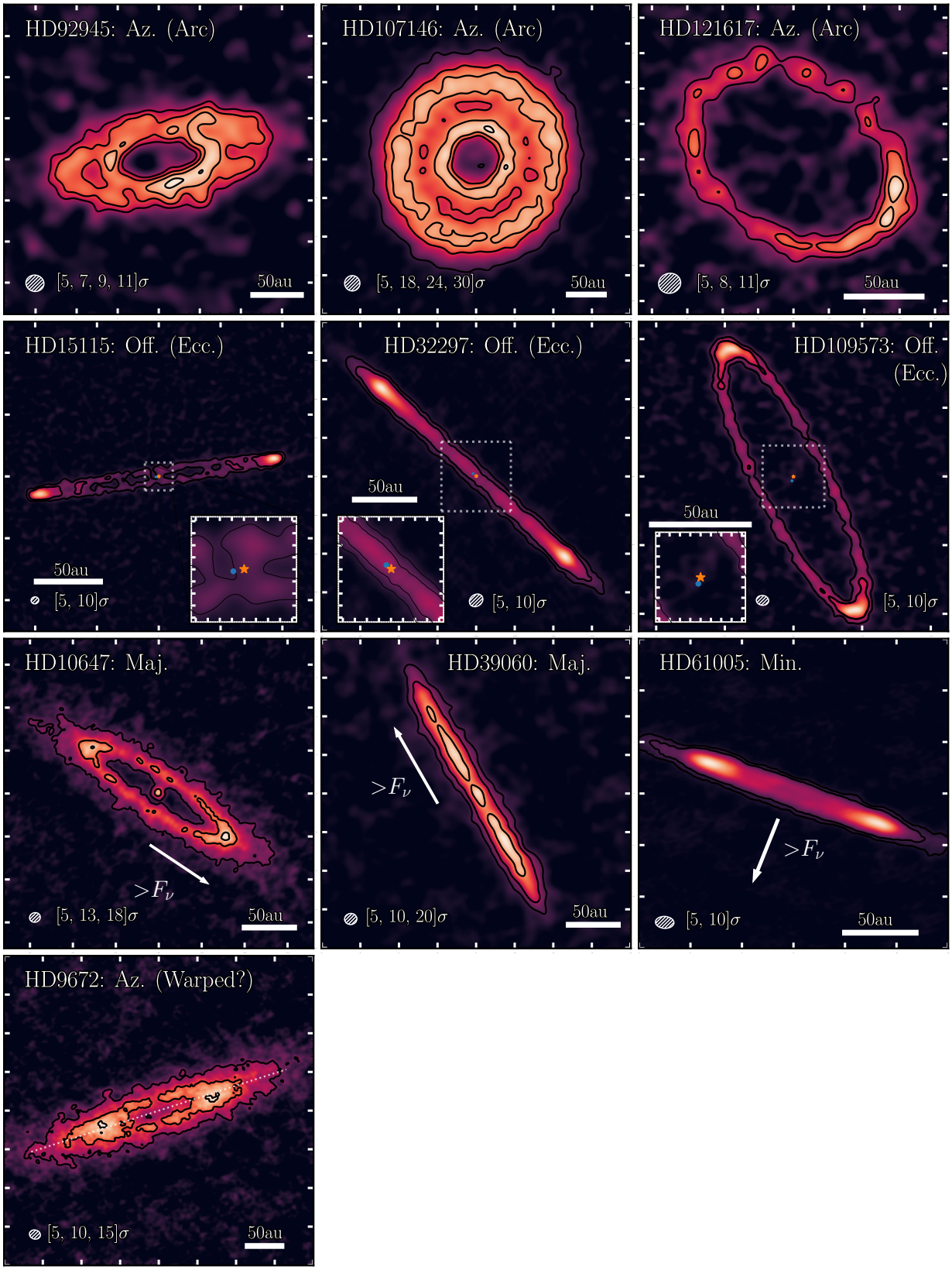

Fig. 1. Gallery of the ten ARKS systems with evidence of asymmetric or offset emission, and their respective observational asymmetry type. The arrows indicate systems that host a major or minor axis with the directionality pointing towards the brighter side. All systems are shown with different contour levels to accentuate their asymmetric features. We present the synthesised beams in the lower left of each panel, as well as 50 au scale bars in the lower right. For systems with significant offsets, we show insets zoomed into their central regions, denoting their phase (stellar) centres as orange stars and best-fit disc centres as blue dots. In all panels north is up and east is left. From left to right, then top to bottom, the images are cropped to fields of view that in both axes are ±7.5″, ±8″, ±0.875″, ±2.5″, ±1″, ±1.125″, ±9″, ±8″, ±3″, and ±4″, respectively.

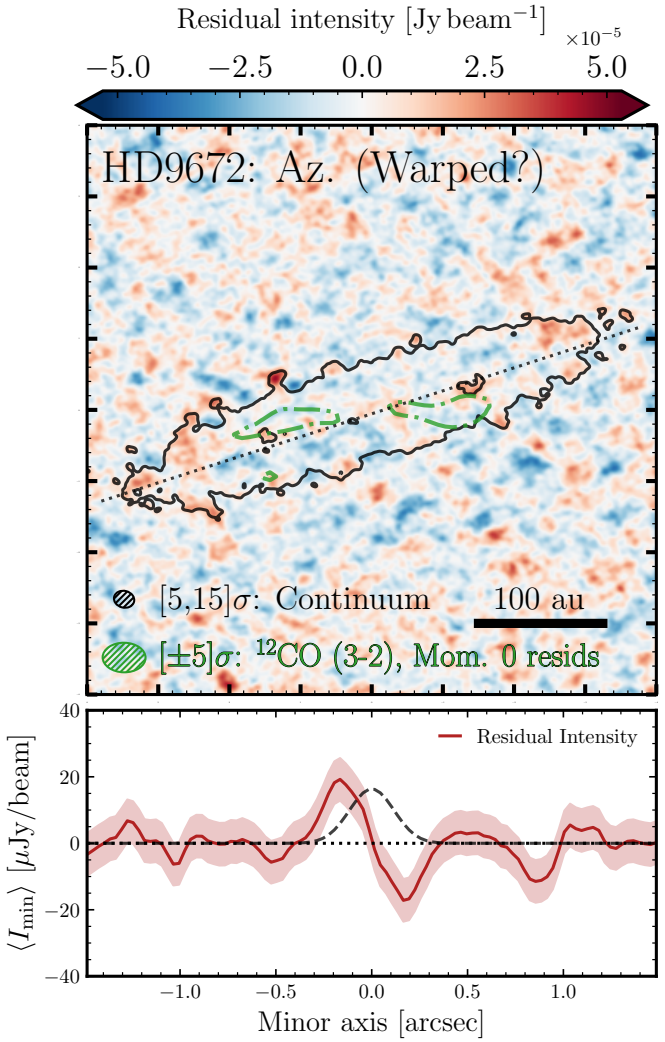

Fig. 2. Top: HD 9672 residual map as presented in ARKS III, Zawadzki et al. (2026), with the ARKS continuum image shown in solid black contours, and the ^{12}CO (3–2) moment-zero residuals overplotted as thick dash-dot green contours, as presented in Hughes et al. (2017), cropped to a ±4″ region of the sky. The continuum disc position angle is shown as the black dotted line across the disc. Clean beams, contour scales, and a scale bar are shown on the map. North is up; east is left. Bottom: Minor axis residual intensity profile across a major axis averaged region about the ansae regions, shown in solid red (after reversing the direction of the western ansae). Errors are shown at the ±1σ level, scaled to account for the mean and difference profiles.

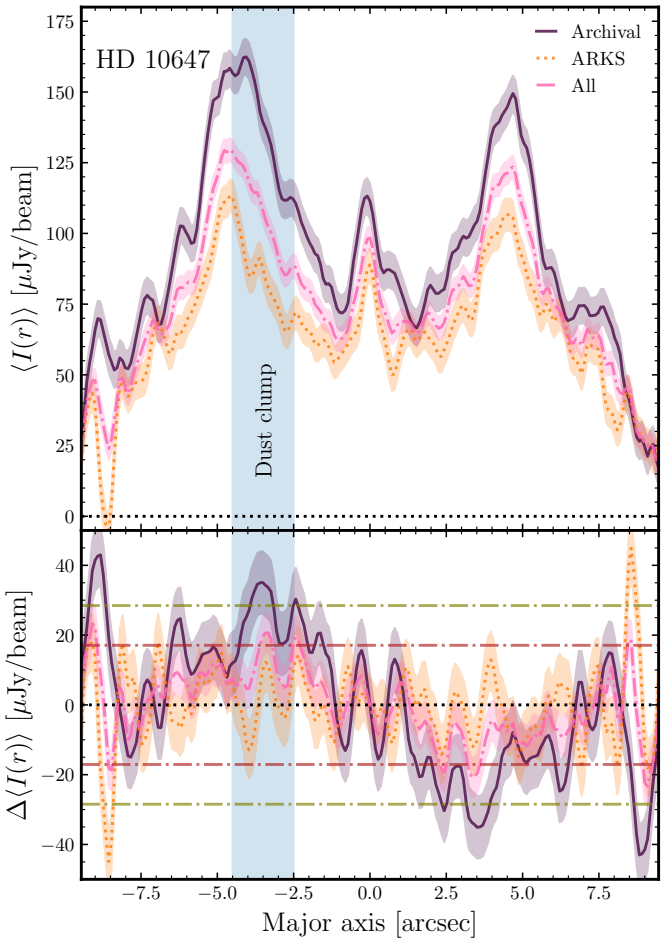

Fig. 3. HD 10647 major axis profiles (top) for each of the archival-only, ARKS-only, or combined ('All') baselines, and their associated difference profiles (bottom) obtained by self-subtracting the profiles about 0.0″. The major axis direction is negative towards the south-east of the disc. The red and green dash-dot lines represent the ±3σ and ±5σ profile differences for the combined data; the shading gives the error associated with each of the difference profiles, scaled by $\sqrt{2}$ to account for the self-subtraction. We also show the ≈40−80 au radial location (in blue) associated with q^1 Eri's dust clump from Lovell et al. (2021a).

Solar System (see e.g. Fernandez & Ip 1984). Although this scenario remains consistent with the combined ARKS data, that the asymmetry significance has fallen suggests alternative hypotheses should be considered, in particular those that may explain the transience of this feature, for example, if this may be more plausibly due to planetesimal collisions (see e.g. Jones et al. 2023), or alternatively, something external to the disc, for example a variable background source (such as a variable star or a variable submillimetre galaxy). Consequently, longer term monitoring of this feature is warranted to investigate its temporal behaviour.

3.1.3. HD 15115: An eccentric disc

HD 15115 is host to a stellocentric offset, as initially discussed in Sect. 2.1. From the self-subtraction map in Fig. C.1 there is no evidence of emission enhancements in any of the three asymmetry axes considered. Given the highly inclined geometry of this source, we produced a major axis profile that showed tentative signs of an emission asymmetry; however, this was not robust to the choice of coordinate centre (within the range implied by this source's RA and Dec offsets; see Table A.2). We likewise found no evidence of an emission asymmetry about the minor axis. This means that, although the system hosts a significant offset, it presents as a symmetric disc in emission relative to the disc centre.

From the derived stellocentric offsets in Table B.1, we found that the inferred pericentre direction is towards the western ansa. However, due to the disc's highly inclined geometry, there is a large range of pericentre directions (i.e. argument of pericentre) and by extension, eccentricities, compatible with the data. Nevertheless, by assuming that the pericentre direction is aligned with the plane of the sky and oriented along the disc major axis, via the disc geometry the derived offsets imply a lower bound on the forced eccentricity of HD 15115 of $e_f > 0.02$. Although it is possible to place an upper bound on this value, this is subject

Table 2. ARKS debris discs determined to be tentatively asymmetric.

Name	Asym. Type
HD 32297	Min
HD 39060 (β Pic)	Min
HD 61005	Maj
HD 84870	Az and Min
HD 131488	Maj
HD 131835	Maj and Min
HD 218396 (HR8799)	Az

Notes. Overlap with systems in Table 1 demonstrate that some systems show tentative hints of asymmetries in multiple features.

to more uncertainty and will be constrained by future modelling work (Lovell et al., in prep.).

The significant offset between the disc centre and stellar location for this system means that, by definition, it is eccentric and adds to the small but increasing number of (sub)millimetre-resolved eccentric discs. There is nevertheless a possible inconsistency between the ALMA-derived eccentricity and the scattered light emission. For example, although the ALMA offset analysis suggests that the pericentre direction is pointed westwards, the scattered light emission is dominated by asymmetric emission strongly extended westwards (see e.g. Kalas et al. 2007; Schneider et al. 2014) which may instead suggest the pericentre direction is directed eastwards, for example based on the models of Lee & Chiang (2016). One plausible hypothesis may be that a recent collision in the disc occurred closer to orbital apocentre (rather than at orbital pericentre, where collision rates are typically more frequent), resulting in small grains being scattered preferentially westwards. Indeed, in Jones et al. (2023) impact sites on both sides of the star were modelled to re-produce the scattered light morphology of the disc, which may result in the observed multi-wavelength morphology of HD 15115. Our analysis of the SPHERE total intensity observations (see Fig. C.6) further confirm that the disc is asymmetric at near-IR wavelengths, with the west side brighter than the east side. Given the low signal-to-noise ratio of the SPHERE data, (Milli et al. 2026) assumed a centro-symmetric model to reproduce the observations, which cannot be used to further investigate the location of the pericentre. Further work is needed to address this potential difference between the submillimetre and scattered light analysis.

3.1.4. HD 32297: An eccentric disc

The debris disc of HD 32297 is host to a stellocentric offset, and we thus interpret this as being eccentric. This finding is supported by observations of HD 32297 in ALMA Band 8 (Luppe et al., in prep.) in which the fitted RA and Dec offsets match those in ALMA Band 7. This system, similarly to HD 15115, also hosts no significant asymmetries in its emission along its major or minor axis. The symmetry in these profiles is corroborated by HD 32297's self-subtraction maps in Fig. C.1 which are measured about the disc centre. We note that if the stellar centre is instead adopted, strong self-subtraction residual emission artefacts are present given the significant stellocentric offset. Nevertheless, there is a tentative minor axis asymmetry at the level of 3–4σ, that presents as an emission enhancement on the southern side of the disc, as noted in Table 2 suggesting future observations may reveal there are subtle emission asymmetries in this disc.

From the derived stellocentric offsets in Table B.1, we found that the inferred pericentre direction is towards the south-west ansa. However, due to the disc's edge-on geometry, there is a large range of pericentre directions, and by extension, eccentricities, compatible with the data. Nevertheless, by assuming that the pericentre direction is aligned with the plane of the sky and oriented along the disc major axis, via this geometry the offsets imply a lower bound on the forced eccentricity of HD 32297 of $e_f > 0.03$.

Our finding that HD 32297 is eccentric at submillimetre wavelengths is in good agreement with previous interpretations of scattered light observations. One example is from the HST images of HD 32297 which shows large extension vertically northwards from the disc (Schneider et al. 2014). The HST data presents a strong match to the 'double-wing' morphology as produced both by the models of Lee & Chiang (2016), resulting from perturbations from a highly eccentric internal planet, or by the models of Jones et al. (2023) via a giant impact scenario. In addition, the SPHERE polarimetric data in scattered light presents a strong radial extension northwards, implying further that the pericentre direction is preferentially towards the south-west of the disc, i.e. in the same direction that we derived here based on the analysis of the stellocentric offset. This result is best observed in the polarimetric residual map of Fig. C.6 (top, third panel from the left); the disc is brighter in the south-west direction, close to the star, but the asymmetry is reversed farther out ($r \geq 0.8''$). On the north-east side, the disc is dimmer at short separation but becomes brighter beyond $r \geq 0.8''$. A similar pattern can be seen in the total intensity residual map, though there is strong residual speckle noise in the inner regions. Although Milli et al. (2026) modelled the disc assuming a circular birth ring, these SPHERE residuals are suggestive that HD 32297 hosts an eccentric disc, with a pericentre direction towards the south-west side. Crotts et al. (2024) and Duchêne et al. (2020) come to a similar conclusion based on GPI data, measuring modest eccentricities of 0.04 and 0.05, respectively, in an otherwise axisymmetric disc, which appear to be in very good agreement with our analysis of these ALMA data.

3.1.5. HD 39060 (β Pic): A major axis asymmetry

The HD 39060 (β Pic) disc is host to a significant asymmetry along its major axis. This presents as a positive emission peak in the minor axis self-subtraction map in Fig. C.2, where this appears in the northern ansa of the disc. By averaging emission over the disc minor axis $\pm 2''$ from the mid-plane, and extracting the disc major axis intensity profile, as plotted in Fig. 4, we found that emission is enhanced towards the north of the disc versus the south. We obtained a major axis difference profile for HD 39060 in the same manner described in Sect. 3.1.2. By integrating the difference profile between of 0 and $10''$ (accounting for the beam size) or equivalently, the modulus of the integral from –10 to $0''$, we found this total flux enhancement at the level of 5.5σ. This northern enhancement is on the opposite side of the disc to the known CO, CI and dust clumps, and the 'cat's tail' (see e.g. Dent et al. 2014; Cataldi et al. 2018; Han et al. 2022; Rebollido et al. 2024) which we discuss further below, which for the CO clump, we indicate in blue on Fig. 4. Separately, HD 39060 shows tentative evidence of a minor axis asymmetry, at the level of 3–4σ, with the western side presenting brighter on the (northern) side of the disc from which the cat's tail protrudes (also see Rebollido et al. 2024).

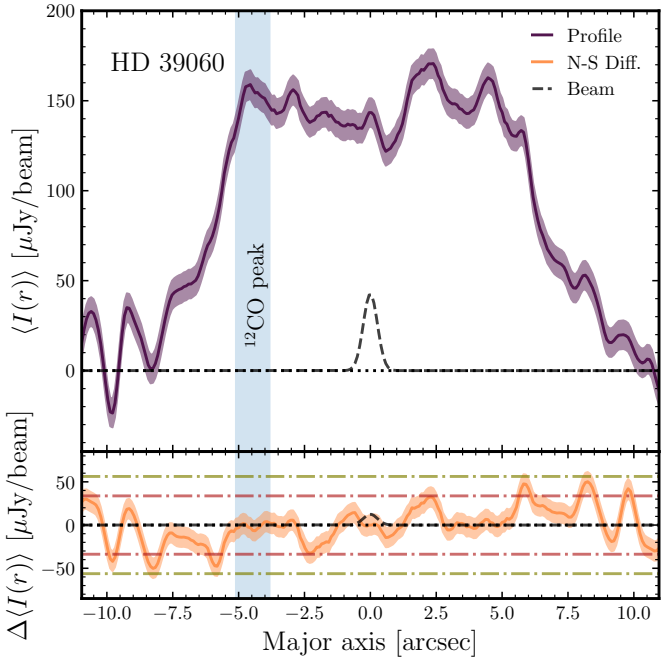

Fig. 4. HD 39060 (β Pic) major axis profile (top) from the south (minus major axis direction) to the north (positive radial direction), and its associated major axis difference profile about the image centre (bottom). We show in red and green dash-dot lines $\pm3\sigma$ and $\pm5\sigma$ profile differences, and in amber the error associated with the difference profile, scaled by $\sqrt{2}$ to account for the uncertainty in the self-subtraction of the profile. We also show the ≈85 au radial location (in blue) associated with β Pic's known CO clump from Dent et al. (2014).

The SPHERE residual map in Fig. C.6 shows a unique asymmetric pattern for HD 39060, as we see positive and negative patterns on each side of the disc's minor axis. Since there is a known warped component in the disc and we used the position angle inferred from the submillimetre ARKS data, this suggests that the SPHERE polarimetric data are not probing the same component as the ALMA observations. However, the scattered light and mid-infrared observations that are sensitive to HD 39060's extended emission may corroborate the asymmetry that we detect in these data. For example, when imaged with HST, JWST and the University of Hawai'i Telescope (UHT), HD 39060 is always seen to be more extended towards northwards (see Kalas & Jewitt 1995; Golimowski et al. 2006; Rebollido et al. 2024). Indeed, in a giant impact scenario, the clumps in the south may trace a collisional impact location, and the northern extended emission may trace the radii out to which this material is preferentially ejected. Therefore, whilst the SPHERE data may be tracing a different asymmetry to ALMA, the northern extension traced by HST, JWST and UHT may be tracing the same physical feature. Although we found no evidence for a significant stellocentric offset with the available ALMA data, this northward extension may imply that the HD 39060 debris disc is eccentric, which future observations should aim to constrain. We note that in the theoretical work of Smallwood (2023), which modelled the HD 39060 system including both known planets, it was shown that the disc may also be eccentric, resulting from interactions with these two planets, which may also drive the more famous warp asymmetry. Further work to study this disc's multiple asymmetries is thus warranted.

3.1.6. HD 61005: A minor axis asymmetry

The HD 61005 disc is host to a minor axis asymmetry – the only ARKS source to host such a feature at a significant level – in which the southern half of the disc is enhanced in emission in comparison to the north. We present the minor axis profile, produced over a major axis averaged extent of ±3.8″, and the associated minor axis difference profile for HD 61005 in Fig. 5, in the upper and lower panels respectively. An enhancement exceeding 3σ in intensity is evident on the south side of the disc over a relatively broad span of ≈2−3 beams, which integrated, is 5.6σ significant. By averaging over ±1″ regions (parallel to the minor axis) along the disc major axis, in addition to the minor axis asymmetry, we found tentative evidence at the ≈4σ level that the east side of the disc is brighter than the west.

HD 61005 is known as 'The Moth' (Hines et al. 2007) as it is host to an iconic vertically extended (halo) emission distribution towards the south of the disc, as imaged in scattered light (Schneider et al. 2014; Olofsson et al. 2016), which appear like 'swept-back wings'. The asymmetry about this axis is clearly detected both in total intensity and linear polarimetry in the SPHERE observations, as seen in Fig. C.6. In both datasets, the east side is brighter than the west side, and this holds true close to the minor axis, the major axis, and the swept-back wings. This suggests that the disc might be eccentric, with the pericentre located in the north-east side, possibly close to the semi-minor axis on the front side of the disc (e.g. Olofsson et al. 2016, and consistent with the eccentric disc models of Lee & Chiang 2016), though we note that no significant stellocentric offset was observed for this source with the ALMA data. That we observe an asymmetry on this same side of the disc in thermal emission with ALMA suggests that the ARKS data may be sensitive to the extended halo emission as yet only seen at shorter wavelengths. Comparatively, for both HD 32297 and HD 61005, MacGregor et al. (2018) reported the detection of an extended halo emission towards the edges of the major axis, previously only traced by scattered light. As with MacGregor et al. (2018), we remain agnostic as to whether the larger grains traced by the submillimetre ALMA data favour or disfavour the vertical asymmetry as being forced from ISM-gas ram pressure interactions with HD 61005's debris disc, without conducting further modelling of the disc, but we note that such modelling is now required to investigate this scenario.

3.1.7. HD 92945: An arced disc

The HD 92945 disc is host to an arc asymmetry, that is strongest on its innermost ring, in the south-west of the disc. We note that HD 92945 has been identified as host to two rings separated by a gap in between (Marino et al. 2019), as corroborated by the ARKS data re-reduction (see Marino et al. 2026b; Han et al. 2026). HD 92945's arc asymmetry is amongst the strongest asymmetries we find in the sample, with this one clearly visible in its gallery image in Fig. 1, and plausibly too in its self-subtraction maps, i.e. Fig. C.2. To quantify this brightness enhancement, we constructed azimuthal profiles around the disc over three radial spans, one for each of the two rings separately, and one spanning both rings and the gap. These regions are shown in the radial profile of Fig. 6 (top panel), alongside their corresponding azimuthal profiles (lower panel). A strong enhancement is evident in the south-west of the disc in the inner ring (purple profile), which has a peak-enhancement at the level of ≈30% which spans a broad azimuthal extent of ≈140°, which is resolved as an extended arc. In comparison, the outer ring

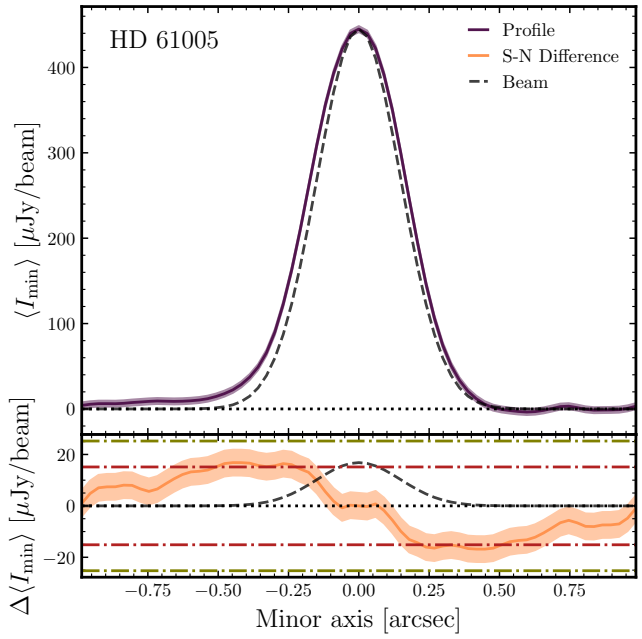

Fig. 5. HD 61005 minor axis profile (top) from the south (minus minor axis direction) to the north (positive minor axis direction), and its associated difference profile about the image centre (bottom). We show as red and green dash-dot lines the $\pm3\sigma$ and $\pm5\sigma$ profile differences, and in amber the error associated with the difference profile, scaled by $\sqrt{2}$ to account for the uncertainty in the self-subtraction of the profile.

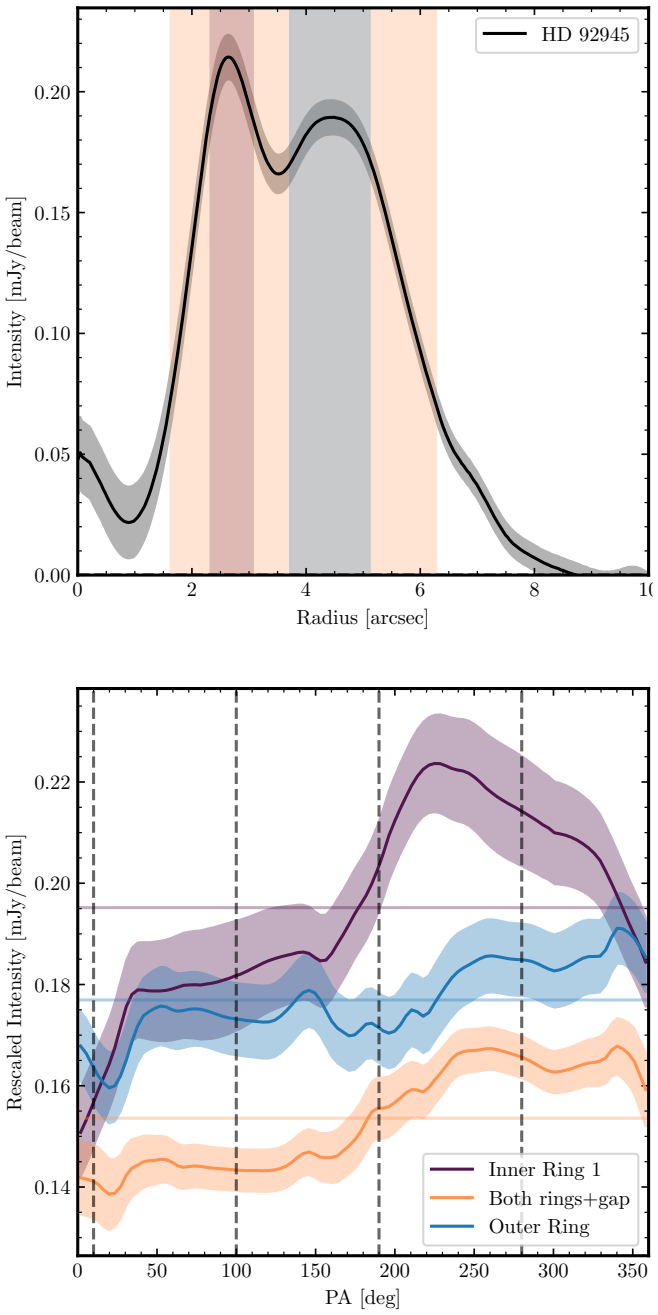

Fig. 6. HD 92945 radial profile (top) and azimuthal profiles (bottom, as per indicated regions in top panel). The (top) shaded regions indicate the radial span over which profiles are extracted. The shaded regions about each profile in the bottom panel show $\pm1\sigma$ error ranges. The vertical dashed lines indicate the PA, PA+90°, PA+180°, and PA+270° where the PA of HD 92945 is 100.0° (see Table A.2), the horizontal purple, blue, and amber lines represent the mean profile for the inner ring, outer ring, and both ring profiles, respectively.

shows no evidence of a comparable enhancement, suggesting that the asymmetries in this disc are localised to, or dominated by, the arc in the inner ring. We note that this asymmetry was first identified in Marino et al. (2019); however, since this could have been due to a background galaxy, this was not considered to be physically confirmed. However, recent scattered light observations with JWST NIRCam confirms that this asymmetry is also present in the distribution of small grains (Lazzoni et al. 2025), and hence here we report this asymmetry to be physically located in the disc.

There are multiple explanations to interpret the azimuthal asymmetry present in HD 92945's inner ring. Given the large azimuthal extent of the arc, one possibility is that this is due to limb-brightening from the underlying disc being eccentric (see e.g. Lynch & Lovell 2022; Lovell & Lynch 2023, though we note the intensity enhancement might be too large for this to be feasible). An alternative, is that this is due to planet–disc interactions in the inner ring. Marino et al. (2019) present models that include secular resonances that induce both the main gap and the asymmetry, and thus provide a plausible interpretation for this system. Although not specific to the HD 92945 system, we note that the system TWA 7 has recently been identified to host similar sinusoid-like variations in its scattered light azimuthal profile (see Olofsson et al. 2018; Ren et al. 2021; Crotts et al. 2025) due to direct planet-clearing, and thus an alternative explanation may be that this feature arises from a planet embedded in the disc. In any case, deeper observations and further modelling of this target are warranted to investigate the nature of this arc, and its potential relationship with putative planets.

3.1.8. HD 107146: An arced disc

The HD 107146 disc, like that of HD 92945, is host to an azimuthally extended arc asymmetry. In the HD 107146 disc, this is present in its northern side. Another similarity with HD 92945, is that HD 107146 has also been identified as being host to rings and gaps (Marino et al. 2018; Imaz Blanco et al. 2023), likewise corroborated by the ARKS data re-reduction (Marino et al. 2026b; Han et al. 2026, see ARKS I and II), although HD 107146 hosts three rings and two gaps (compared to HD 92945's two rings and single gap). We recall that for this system, we have only used the available archival Band 6 ALMA data; see Sect. 2.2.

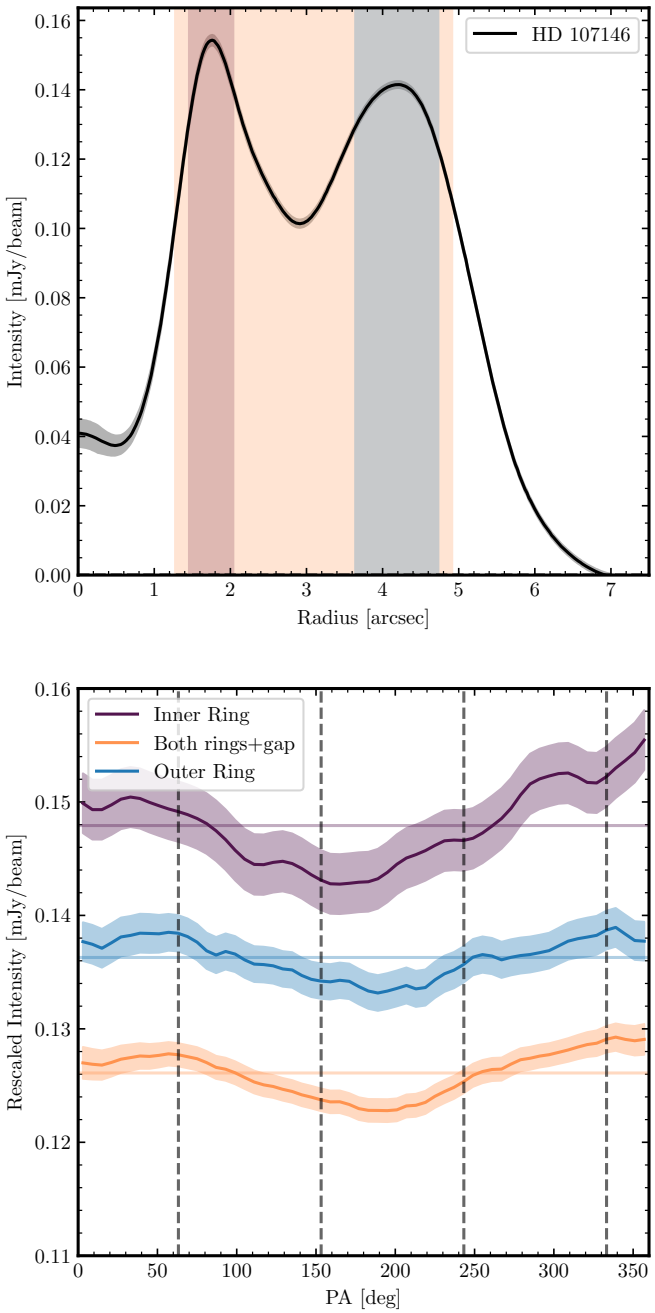

Fig. 7. HD 107146 radial profile (top) and azimuthal profiles (bottom, as per indicated regions in top panel). The shaded regions in the top panel indicate the radial span over which profiles are extracted. The shaded regions about each profile in the bottom panel show $\pm 1\sigma$ error ranges. The vertical dashed lines indicate the PA, PA+90°, PA+180°, and PA+270°, where the PA of HD 107146 is 153.2° (see Table A.2), the horizontal purple, blue, and amber lines represent the mean profile for the inner ring, outer ring, and both ring profiles, respectively.

In Fig. 7 we show the radial profile for HD 107146 and three associated azimuthal profiles that span the innermost and outermost bright rings separately, and a third one that spans the full disc extent (i.e. also covering the gap between the rings, where this main gap is the combination of the two narrower gaps visible in higher-resolution data along with the third or centre ring). These profiles demonstrate similar broad features as HD 92945, though in this case, there is evidence that the outer radial span contributes to the observed asymmetry, given the enhancement in the significance of the asymmetry in the profile which spans the largest radial extent across the disc (see the amber 'Both rings+gap' profile). We measured a peak-trough enhancement of ~3% for the full disc span, and a higher level of ~7% in the inner disc when considered separately (though the latter of these has larger uncertainty by ≈2×. It is difficult to assess the extent of this arc, given that this feature appears to span almost fully around the disc (in an almost sinusoid-like pattern), and in this regard appears distinct to HD 92945, where the arc appeared more localised. Neither SPHERE nor GPI scattered light data are available for HD 107146 to compare with this ALMA analysis, and we note that the HST study of HD 107146 (Ertel et al. 2011) presented no evidence of an arc asymmetry. The HST STIS scattered light image of HD 107146 is presented in Milli et al. (2026).

The arc asymmetry in HD 107146's disc presents a number of interesting hypotheses as to its origin. HD 107146 hosts a strong proper motion anomaly from a ~3 $M_{\rm Jup}$ body orbiting within 20 au (1.37″) from its star (see ARKS I Marino et al. 2026b), which lends weight to the possibility that the millimetre disc asymmetry may be tracing interactions with such a planet. This means that one possibility is that this millimetre brightness modulation is due to the disc hosting an underlying eccentricity, driven by this inner planet (since near face-on eccentric discs can produce sinusoidal-like emission variations in systems shaped by internal eccentric planets; see e.g. Lynch & Lovell 2022). Although we found no evidence of a stellocentric offset in HD 107146's data, the ALMA configurations adopted to observe this system did not include long baseline configuration data (which were necessary to determine the stellocentric offsets in HD 15115, HD 32297 and HD 109573) and thus these data are intrinsically less sensitive to the presence of an offset. An alternative possibility could be that a planet initially between the two brighter rings migrated inwards, creating the deeper gap between the rings, and trapped planetesimals in mean-motion resonances in the inner-ring (as discussed by Friebe et al. 2022), the latter of which may contribute to the observed azimuthal emission structure. Finally, we highlight again the similarity to HD 92945, and thus the possibility here too of a planet embedded in the disc producing this azimuthal modulation (via a similar comparison to Crotts et al. 2025). Further work, such as new modelling and follow-up observations, is now important to uncover which of these scenarios, or indeed another scenario, may best interpret the arc in HD 107146.

3.1.9. HD 109573 (HR 4796): An eccentric disc

The HD 109573 disc is the third system in ARKS that we determined to host a significant stellocentric offset, and thus, we interpret this as eccentric at submillimetre wavelengths. HD 109573 is geometrically distinct from HD 15115 and HD 32297; being less inclined, its minor axis is clearly resolved, meaning that its azimuthal structure can be more readily probed. By considering the azimuthal emission around the full radial extent of the ring, and separately on the disc's inner edge and outer edge, we found no evidence that the emission is significantly asymmetric about the disc centre, corroborated by Fig. C.3 which shows HD 109573's self-subtraction residual maps to be solely from noise. We note that if instead of the coordinates of the disc centre, the coordinates of the star are adopted, HD 109573's azimuthal profiles, and its self-subtraction maps, presented very strong asymmetries, supporting the conclusion that the disc is eccentric.

Whilst in the cases of HD 32297 and HD 15115 their geometries meant that deriving a pericentre direction and eccentricity was not possible (only lower bounds on e_f could be derived), the resolved nature of HD 109573's disc means that a direct estimate of the pericentre direction and eccentricity can be made. Based on simple geometrical arguments, i.e. the direction vector from the disc centre to the stellar position (see the offset values in Table B.1), we find that the pericentre direction is oriented approximately 17° clockwise from north (conspicuously located at an azimuthal emission minima in the disc). Assuming this pericentre location, based on the relative distance between the stellar position and the ring at pericentre and apocentre, we approximate a value of the disc eccentricity of $e_f \approx 0.10$. Whilst determining uncertainties on these values is beyond the scope of this study, a future ARKS paper (Lovell et al., in prep.) will model these data in detail, to extract stronger constraints on this disc's eccentric morphology.

The conclusion that HD 109573 is eccentric, and with a value of $e_f \approx 0.10$, is largely corroborated by scattered light observations, which have measured eccentricities in the literature ranging from 0.01 to 0.08 (see e.g. Perrin et al. 2015; Milli et al. 2017; Olofsson et al. 2019; Milli et al. 2019; Chen et al. 2020; Crotts et al. 2024), although we note the value we derive here is on the upper end of this implied distribution. In all such scattered light images, both the total intensity and linear polarimetry observations showed that HD 109573's disc surface brightness is asymmetric. The scattered light asymmetries are most evident in SPHERE polarimetric data that we present in the lower left panel of Fig. C.6. In the radial profiles for HD 109573, these are first positive, then negative along the north side, with the opposite pattern along the south side, a typical sign of an eccentric disc (as stated above, these same patterns appear in the submillimetre self-subtraction residuals, if the star's coordinates instead of the disc centre coordinates are adopted). We also found that the pericentre direction implied by the disc centre offset towards the north (in the ALMA data) is consistent with modelling of HD 109573's scattered light emission (see e.g. Olofsson et al. 2019).

From the disc's geometry, it is evident that the pericentre direction is not pointing towards one of the disc ansae; it is perhaps less surprising that the disc ansae do not have strong brightness asymmetries (as one might expect if the disc position angle was aligned with either the pericentre or apocentre direction of eccentric planetesimal orbits; see e.g. Pan et al. 2016; Lynch & Lovell 2022), and as pointed out in previous studies of HD 109573, for example Wyatt et al. (1999) and Kennedy et al. (2018). Nevertheless, minimal or absent emission enhancement in HD 109573's disc ansae may imply that HD 109573's eccentric disc has a different underlying density distribution of planetesimals to other eccentric rings which are host to strong ansae emission enhancements (e.g. Fomalhaut, HD 53143, and HD 202628; see MacGregor et al. 2017; Faramaz et al. 2019a; Kennedy 2020; MacGregor et al. 2022), as likewise postulated for this system by Kennedy et al. (2018) with lower-resolution ALMA data of HD 109573. Further modelling of this system is warranted to interpret these findings, and differences with respect to the wider eccentric debris disc population.

3.1.10. HD 121617: An arced disc

The HD 121617 disc hosts the most significant continuum asymmetry in the ARKS sample, evident in both its image; see Fig. 1, and self-subtraction maps; see Fig. C.3. The self-subtraction maps show multiple $>3\sigma$ peak enhancements coincident with the arc in the south-west of the disc. We do not present the azimuthal profile of HD 121617 here, since this is presented in ARKS VIII (Marino et al. 2026a) Fig.2, in which the arc enhancement spans an angular extent of ∼90°, and is brighter than the mean disc intensity by ∼40%. The arc itself also hosts an asymmetry, being brighter in its northern side, i.e. there is an azimuthal gradient in the intensity of the arc, as evident in the major-axis self-subtraction map (Fig. C.3). The SPHERE polarimetric observations of the disc show a pattern comparable to the one of HD 109573, with an inversion of the radial profiles (from positive to negative on the east side, and the opposite on the west side), indicative that this system has an eccentric ring in scattered light (as reported at the level of $e = 0.03$ by Perrot et al. 2023), though we did not find evidence that this system was host to a stellocentric offset in the ALMA data, and so do not interpret this system as necessarily eccentric at submillimetre wavelengths. We note that the brightness enhancements in the arc (detected by ALMA) do not present consistently in the near-IR scattered light observations. We limit discussion to this source here since other ARKS papers are dedicated to further discussion of HD 121617 (see e.g. Brennan et al. 2026; Marino et al. 2026a; Weber et al. 2026, which collectively model and analyse the structure of the continuum and gas kinematics in detail).

3.2. Tentative asymmetries

In three discs so far, we described the presence of additional tentative asymmetries, i.e. two in the minor axes of HD 32297, HD 39060, and one in the major axis of HD 61005. In the wider ARKS sample we found evidence of tentative asymmetries in the discs of HD 84870, HD 131488, HD 131835, and HD 218396 that we briefly discuss here to motivate future observations. We present the self-subtraction maps of these four systems in Fig. C.5 (alongside HD 95086 in Fig. C.4 which we cannot confidently ascertain if this source is symmetric or asymmetric due to the imperfect-subtraction of a background source; see ARKS I Marino et al. 2026b). Discussing these in turn, HD 84870 is host to a 3–4σ clump in the south of the disc that appears in both the rotation subtraction and minor axis subtraction maps. HD 131488 is host to residual emission features about its minor axis (see Fig. C.5), which may indicate the presence of a clump, or an emission enhancement in the western ansa. HD 131835 is host to a $\approx 3\sigma$ negative residual feature in its major axis and minor axis self-subtraction plots in Fig. C.5 towards the south-east, near to its minor axis. Given the negative feature is co-located in both the major and minor axis self-subtraction maps, this may indicate the disc has a dearth of emission (an azimuthal gap) located in the inner disc (in Han et al. 2026; Zawadzki et al. 2026; Milli et al. 2026; Jankovic et al. 2026, this system is shown to have a two-component disc, with the first (inner) component brighter in thermal emission and fainter in scattered light, and the second (outer) component fainter in thermal emission, but brighter in scattered light). HD 218396 (HR 8799) is host to two clumps in the north and north-west of the disc, that present most significantly in the major axis subtraction map. Whilst the north-west clump is most likely due to the imperfect subtraction of a known background source (see ARKS I, our discussion in Sect. 2.2, as well as Faramaz et al. 2021, where this bright point source is noted), the northern clump (present, just below 3σ) is not co-located with any known background sources. Given the presence of multiple giant planets in the inner tens of au of HD 218396 (see e.g. Marois et al. 2008; Apai et al. 2016; Wertz et al. 2017; Boccaletti et al. 2024), and the possibility that this clump may

arise from planet-disc interactions with one of those, this clump in particular may warrant further investigation.

Overall, whilst we do not wish to overstate the significance of these tentative features (none of these exceed 5σ), we report these given the possibility that future observations may confirm their presence. For example, since some number of these present as unresolved clumps, these should be determined as to whether they are co-moving, to rule out the possibility that these are all due to background confusion (see e.g. the method of Kennedy et al. 2023).

4. Discussion

4.1. Discussion of asymmetries and offsets in ARKS

4.1.1. Continuum asymmetries in debris discs are common

Overall, we showed that 10/24 (42%) ARKS targets are host to asymmetric emission or stellocentric offsets in their dust distributions, and that four further systems host tentative asymmetries. We summarise these asymmetries and offsets in Table 1 and Table 2 noting in both their asymmetry classes, and in the first table, and where these are unambiguous, their physical class. For each source, we have identified and briefly discussed plausible physical origins of the asymmetries, including planet-disc interactions, stellar-disc interactions (e.g. flybys), and collisions as plausible origins of those identified.

That nearly half of all ARKS systems host a significant continuum asymmetry suggests that asymmetries are common in the population of bright debris discs that the ARKS programme has analysed. In ARKS I (Marino et al. 2026b), the sample's (cold dust) fractional luminosities ($L_{\rm cold}/L_{\star}$) are presented. Excluding HD 95086 (for which we cannot determine the presence of a real asymmetry), we find that whilst 8/10 of the brightest discs, i.e. those with $L_{\rm cold}/L_{\star} > 5 \times 10^{-4}$ host significant asymmetries, just 2/13 of the fainter discs with $L_{\rm cold}/L_{\star} < 5 \times 10^{-4}$ host significant asymmetries. We note that the two discs in the brighter population that do not host significant asymmetries are HD 131488 and HD 131835, which we showed tentative evidence that these may host asymmetries. This bias implies that either the most luminous discs in the ARKS sample are intrinsically more asymmetric, or that with higher S/N data on the fainter discs, these discs may also host similarly asymmetric emission. The latter of these possibilities is corroborated by scattered light observations, given the near-80% fraction of debris discs measured as asymmetric in the GPI survey (Crotts et al. 2024), i.e. it is plausible that debris discs are more likely to present as asymmetric than symmetric. The former of these possibilities could imply, however, that a number of asymmetries are driven by giant impacts, as collisional events not only produce asymmetric clumps and arcs, but overall raise the dust content of discs in general, and would thus be accompanied with a rise in $L_{\rm cold}/L_{\star}$ (see e.g. Jones et al. 2023).

Whilst debris disc asymmetries may be common, (sub)-millimetre wavelength debris disc asymmetries in general appear to be mostly very subtle (this appears in contrast to scattered light asymmetries, which often appear far stronger; Schneider et al. 2014; Jones et al. 2023; Crotts et al. 2024). This may plausibly relate to the underlying physics and origins of asymmetries in debris discs, given the strong wavelength-dependence of their structures, the scales on which distinct asymmetries are observed, and the typical S/N required to observe asymmetric emission (see further discussion in Sect. 1, and e.g. Matthews et al. 2014; Hughes et al. 2018). We note that in just one ARKS disc, HD 121617, was the self-subtraction map analysis sufficiently conclusive on the presence of significant asymmetry, whereas for all nine other asymmetries, we had to resort to additional analyses (though we note in the case of the offset systems, these host strong residual patterns if their stellar centres are used instead of their disc centres). This overall suggests that in general (sub)-millimetre debris discs can be understood as being dominated by axisymmetric morphologies, with a subset hosting fainter, non-axisymmetric features. This means that modelling debris discs in the paradigm of axisymmetric emission generally remain a well-justified approach for interpreting their bulk properties (Kennedy 2025; Han et al. 2026; Zawadzki et al. 2026).

The subtlety of debris disc asymmetries appears in contrast to those observed in large, structured protoplanetary discs, as evident in the uniform analyses of ALMA data in, for example, the DSHARP survey (Andrews et al. 2021) and the exoALMA survey (Curone et al. 2025). In these works, it is evident that in a number of cases (e.g. MWC 758, HD 135344B), the emission structures of some protoplanetary discs are near-dominated by asymmetric features (e.g. some of these sources have non-axisymmetry index values above 0.4), as would not be the case in any single ARKS debris disc, as evident in Figs. C.1, C.2, and C.3[5]. These differences between protoplanetary disc asymmetries and debris disc asymmetries may therefore highlight the importance of dust–gas interactions in driving the majority of strong asymmetries in circumstellar discs. This appears to be corroborated by our finding that the system with the strongest continuum asymmetry (HD 121617) is also the most CO-rich disc in the sample (Mac Manamon et al. 2026), as well as our discussion of the possible bias towards CO-detections in asymmetric discs; see Sect. 4.1.3.

4.1.2. A diverse suite of asymmetries in debris discs

We identified four broad asymmetry types present in the data; four discs are azimuthally asymmetric, three discs have stellocentric offsets, two discs have major axis asymmetries, and one disc has a minor axis asymmetry. Whilst this is the largest sample of debris discs host to (sub)-millimetre asymmetries to date, these fractional subpopulations of asymmetries are too small to conclude that the presence of any one type of asymmetry is more common than any other. This conclusion remains true even if the tentative asymmetry classes are included.

Importantly, the physical origins of some asymmetry types can be confused by their observing geometries. For example, an arc or a clump in a highly inclined debris disc may present a major axis asymmetry observationally. This places a limitation on our ability to identify the physical origin of some asymmetries, and in particular, systems identified with either major or minor axis flux asymmetries. Moreover, some physical asymmetries can manifest in degenerate observational signatures. For example, as discussed earlier in the case of HD 9672, we demonstrated the presence of a significant azimuthal asymmetry, though we are unable to conclude on this being a warp, twist or spiral based on the available data. This further challenges our ability to infer the frequency of any specific physical classes of debris disc asymmetries.

[5] In the cases of HD 15115, HD 32297, and HD 109573, if these were instead considered about their stellar locations, then they would be considered hosts to strong non-axisymmetric residuals. The comparison we make is therefore only valid for disc-centred residuals, and thus should be accounted for in any comparison of the relative non-axisymmetries of eccentric discs.

Nevertheless, in six cases we are more confident about the origins of their asymmetries. For example, in the case of HD 92945, HD 107146 and HD 121617 these are spatially resolved as arc asymmetries, where each of these systems is host to a significant dust column enhancement over an azimuthally extended region of the disc. Further, in the case of HD 15115, HD 32297 and HD 109573, the systems with offsets, such offsets can only be induced if these systems are eccentric. The discovery of three eccentric systems at submillimetre wavelengths with ARKS observations doubles the number of previously resolved eccentric debris rings at these wavelengths. We thus add HD 15115, HD 32297 and HD 109573 to the ranks of Fomalhaut (HD 216956; see e.g. MacGregor et al. 2017; Matrà et al. 2017; Kennedy 2020; Chittidi et al. 2025; Lovell et al. 2025), HD 202628 (e.g. Faramaz et al. 2019a; Kennedy 2020), and HD 53143 (e.g. MacGregor et al. 2022; Lovell & Lynch 2023). A key distinction between these three eccentric discs in ARKS and the three previously known is the lack of any observed stellar emission towards HD 15115, HD 32297, and HD 109573, whereas stellar (sub)-millimetre emission is strongly detected towards Fomalhaut, HD 53143 and HD 202628. This study therefore demonstrates the potential for identifying new eccentric discs with high-resolution ALMA data, even in the absence of detectable (sub)-millimetre stellar emission.

A lack of spiral patterns in debris discs? It is likely that even with the sensitivity and resolution of ARKS data, spiral patterns would have gone undetected. Although the asymmetry in HD 9672 disc's could be due to a spiral pattern, we see no strong evidence of this type of asymmetry in the ARKS sample of debris discs, nor in the (less sensitive) REASONS survey of debris discs (Matrà et al. 2025). This type of asymmetry therefore appears to be especially rare in debris discs. This is in contrast to protoplanetary discs where multiple spiral morphologies have been detected at submillimetre wavelengths (see e.g. Andrews et al. 2018; Huang et al. 2018; Andrews 2020). Spiral patterns in protoplanetary discs are understood to be produced by hydrodynamical processes, i.e. gas-driven, which are then reflected in the dust (see e.g. Goldreich & Tremaine 1979; Bae & Zhu 2018). In debris discs, which are in general much more gas-poor than protoplanetary discs, the mechanisms driving spiral substructures are likely to be fundamentally different, for example resulting from planet-induced secular differential precession of planetesimal orbits (see e.g. Wyatt 2005; Sende & Löhne 2019; Farhat et al. 2023), in which case these would be transient in nature, or resulting from density waves launched at secular resonances (if any) in discs with non-zero mass, in which case spirals may be long-lived (Ward & Hahn 1998; Hahn 2003; Sefilian 2022). Such features, however, may be damped due to viscosity effects and/or collisional activity (see e.g. Hahn 2003; Nesvold & Kuchner 2015), making them less discernible in observations.

4.1.3. Are CO-rich debris discs more commonly asymmetric?

In the ARKS sample there are 6 CO-rich debris discs (namely, HD 9672, HD 32297, HD 39060, HD 121617, HD 131488 and HD 131835; Mac Manamon et al. 2026), and 18 CO-poor debris discs (where no CO detections have yet been reported). We found that the presence of CO gas in a debris disc may be a good indicator of whether its dust continuum will be asymmetric. For example, whilst 4/6 of these CO-rich debris discs host significant continuum asymmetries, only 6/18 of the debris discs without a CO detection are asymmetric. If the tentative asymmetries that we report are determined to be real, then these figures both rise to 6/6 and 8/18 respectively. Whilst these numbers remain too small for us to conclude that this trend is significant, it remains indicative that where CO gas has been detected, continuum asymmetries are more likely to be found. Plausibly, this may mean that hydrodynamic interactions between the gas and dust are driving at least some of these asymmetric features. This possibility is further discussed in Weber et al. (2026) where the arc in HD 121617 is modelled as the result of dust trapped in a vortex.

4.2. Comparison with ARKS visibility modelling

In this work, we have uniformly analysed ARKS images to assess the presence of asymmetries, almost solely analysing the ARKS continuum images. In ARKS II and ARKS III (Han et al. 2026; Zawadzki et al. 2026) all ARKS targets were fitted with parametric axisymmetric disc models in the visibility domain (ARKS III only modelled the $i > 66^\circ$ systems), producing best-fit models and residual maps. Given the systematic difference in these two methods to analyse the ARKS sample, here we compare the conclusions drawn between our respective methods.

For the three eccentric discs, HD 15115, HD 32297, and HD 109573, which we found to be axisymmetric but significantly offset, the parametric modelling of ARKS III found consistent offsets were needed to fit these data, and thus our studies agree on this conclusion. We note that for HD 109573, the parametric modelling presented in ARKS III finds residual emission excesses in the disc ansae that we did not find strong evidence of in this study. We estimate that HD 109573 is highly eccentric ($e_f \approx 0.10$), and thus will be host to a non-axisymmetric surface density distribution. Therefore, by fitting and subtracting an axisymmetric ring model, i.e. with a different surface density distribution to that of an eccentric ring, these residual artefacts are likely to appear. HD 109573 will be studied in a future ARKS paper to understand if these excesses can be accounted for with such an eccentric disc model (Lovell et al., in prep.).

For the three systems with arc asymmetries, we can only directly compare with the parametric modelling efforts in two cases i.e. HD 121617 and HD 92945, since we only used archival Band 6 data to analyse HD 107146, whereas ARKS II analysed the Band 6 and Band 7 data combined. In Han et al. (2026), both HD 92945 and HD 121617 are host to significant residual emission co-located with the arc features that we identified in this work, and we thus find very good agreement between our analysis here and the parametric modelling.

For the four systems analysed via profiles for asymmetries, HD 9672, HD 10647, HD 39060, and HD 61005, we likewise find good agreement between our conclusions and those of ARKS III (Zawadzki et al. 2026). For HD 9672, since we analysed the image domain of the best-fit parametric model residuals, our results agree with ARKS III by definition. For HD 10647, ARKS III present residuals that have a number of 3σ peaks along the south-west inner edge, in the same locations that we integrated over to produce the significant asymmetry that we present here. For HD 39060, the parametric models presented in ARKS III find a number of residual peaks in the north of the disc, which also agree with the major axis asymmetry that we present here. Although few 3σ peaks appear in the ARKS III residuals for HD 61005, we note that an analysis of the residual map reveals, on the northern side of the disc, that there is a relative model oversubtraction (leading to an integrated negative flux) in comparison to the south where there is a relative undersubtraction (leading to an integrated positive flux). We thus also find general agreement between the ARKS III residuals and our

conclusion that HD 61005 has an asymmetry along the minor axis.

Overall therefore, the findings of the asymmetries in this work are in very good general agreement with the results presented by the ARKS parametric modelling in ARKS II and III.

5. Conclusions

We present the sixth paper of The ALMA survey to Resolve exoKuiper belt Substructures (ARKS). ARKS is studying a sample of 24 debris discs at unprecedented resolution to understand their radial and vertical structures, including asymmetries. In this work we presented our study of the dust continuum asymmetries and offsets in ARKS data. From our analyses we conclude the following:

1. In the ARKS sample, 10 out of 24 systems are hosts to either a continuum asymmetry or an offset, with tentative signs of asymmetries in four further systems. Of the ten significant asymmetries, three host stellocentric offsets (non-zero eccentricities), three host arc asymmetries, two host major axis asymmetries, one hosts a minor axis asymmetry, and one hosts an azimuthal asymmetry with a twisted pattern. Overall, these results demonstrate that there is a broad diversity of asymmetries in the ARKS sample;
2. Our investigation suggests that continuum asymmetries are a common feature in debris discs, when observed with sufficiently high resolution and sensitivity, which prior to ARKS was inconclusive. Nevertheless, these (sub)millimetre asymmetries mostly present as subtle features. We find that the presence of an asymmetry is correlated with the cold dust fractional luminosity in the sample. We also find a tentative enhancement in the fraction of systems hosting a continuum asymmetry and in those that are CO-rich;
3. We discussed plausible interpretations for the origins of these asymmetries, including planet–disc interactions, stellar–disc interactions, and collisions. We compared the ARKS asymmetries to those present in protoplanetary discs, which in general appear to be both qualitatively and quantitatively distinct. We highlighted upcoming planned work that will investigate systems in detail, and proposed future studies to follow up targets with new observations, modelling, and simulations to better constrain these asymmetric features and the processes driving them.

Acknowledgements. We thank the anonymous referee for their careful review of our study, and many helpful suggestions which helped improved this manuscript. JBL acknowledges the Smithsonian Institute for funding via a Submillimeter Array (SMA) Fellowship, and the North American ALMA Science Center (NAASC) for funding via an ALMA Ambassadorship. SM acknowledges funding by the Royal Society through a Royal Society University Research Fellowship (URF-R1-221669) and the European Union through the FEED ERC project (grant number 101162711). AMH acknowledges support from the National Science Foundation under Grant No. AST-2307920. EM acknowledges support from the NASA CT Space Grant. TDP is supported by a UKRI Stephen Hawking Fellowship and a Warwick Prize Fellowship, the latter made possible by a generous philanthropic donation. A.A.S. is supported by the Heising-Simons Foundation through a 51 Pegasi b Fellowship. Support for BZ was provided by The Brinson Foundation. MB acknowledges funding from the Agence Nationale de la Recherche through the DDISK project (grant No. ANR-21-CE31-0015). A.B. acknowledges research support by the Irish Research Council under grant GOIPG/2022/1895. C.d.B. acknowledges support from the Spanish Ministerio de Ciencia, Innovación y Universidades (MICIU) and the European Regional Development Fund (ERDF) under reference PID2023-153342NB-I00/10.13039/501100011033, from the Beatriz Galindo Senior Fellowship BG22/00166 funded by the MICIU, and the support from the Universidad de La Laguna (ULL) and the Consejería de Economía, Conocimiento y Empleo of the Gobierno de Canarias. EC acknowledges support from NASA STScI grant HST-AR-16608.001-A and the Simons Foundation. This material is based upon work supported by the National Science Foundation Graduate Research Fellowship under Grant No. DGE 2140743. JPM acknowledges research support by the National Science and Technology Council of Taiwan under grant NSTC 112-2112-M-001-032-MY3. S.M.M. acknowledges funding by the European Union through the E-BEANS ERC project (grant number 100117693), and by the Irish research Council (IRC) under grant number IRCLA-2022-3788. Views and opinions expressed are however those of the author(s) only and do not necessarily reflect those of the European Union or the European Research Council Executive Agency. Neither the European Union nor the granting authority can be held responsible for them. J.M. acknowledges funding from the Agence Nationale de la Recherche through the DDISK project (grant No. ANR-21-CE31-0015) and from the PNP (French National Planetology Program) through the EPOPEE project. S.E. is supported by the National Aeronautics and Space Administration through the Exoplanet Research Program (Grant No. 80NSSC23K0288, PI: Faramaz). M.R.J. acknowledges support from the European Union's Horizon Europe Programme under the Marie Sklodowska-Curie grant agreement no. 101064124 and funding provided by the Institute of Physics Belgrade, through the grant by the Ministry of Science, Technological Development, and Innovations of the Republic of Serbia. This work was also supported by the NKFIH NKKP grant ADVANCED 149943 and the NKFIH excellence grant TKP2021-NKTA-64. Project no.149943 has been implemented with the support provided by the Ministry of Culture and Innovation of Hungary from the National Research, Development and Innovation Fund, financed under the NKKP ADVANCED funding scheme. L.M. acknowledges funding by the European Union through the E-BEANS ERC project (grant number 100117693), and by the Irish research Council (IRC) under grant number IRCLA-2022-3788. Views and opinions expressed are however those of the author(s) only and do not necessarily reflect those of the European Union or the European Research Council Executive Agency. Neither the European Union nor the granting authority can be held responsible for them. SP acknowledges support from FONDECYT Regular 1231663 and ANID – Millennium Science Initiative Program – Center Code NCN2024_001. PW acknowledges support from FONDECYT grant 3220399 and ANID – Millennium Science Initiative Program – Center Code NCN2024_001. This paper makes use of the following ALMA data: ADS/JAO.ALMA# 2022.1.00338.L, 2012.1.00142.S, 2012.1.00198.S, 2015.1.01260.S, 2016.1.00104.S, 2016.1.00195.S, 2016.1.00907.S, 2017.1.00167.S, 2017.1.00825.S, 2018.1.01222.S and 2019.1.00189.S. ALMA is a partnership of ESO (representing its member states), NSF (USA) and NINS (Japan), together with NRC (Canada), MOST and ASIAA (Taiwan), and KASI (Republic of Korea), in cooperation with the Republic of Chile. The Joint ALMA Observatory is operated by ESO, AUI/NRAO and NAOJ. The National Radio Astronomy Observatory is a facility of the National Science Foundation operated under cooperative agreement by Associated Universities, Inc. This research used the Canadian Advanced Network For Astronomy Research (CANFAR) operated in partnership by the Canadian Astronomy Data Centre and The Digital Research Alliance of Canada with support from the National Research Council of Canada the Canadian Space Agency, CANARIE and the Canadian Foundation for Innovation. SPHERE is an instrument designed and built by a consortium consisting of IPAG (Grenoble, France), MPIA (Heidelberg, Germany), LAM (Marseille, France), LESIA (Paris, France), Laboratoire Lagrange (Nice, France), INAF–Osservatorio di Padova (Italy), Observatoire de Genève (Switzerland), ETH Zurich (Switzerland), NOVA (Netherlands), ONERA (France) and ASTRON (Netherlands) in collaboration with ESO. SPHERE was funded by ESO, with additional contributions from CNRS (France), MPIA (Germany), INAF (Italy), FINES (Switzerland) and NOVA (Netherlands). SPHERE also received funding from the European Commission Sixth and Seventh Framework Programmes as part of the Optical Infrared Coordination Network for Astronomy (OPTICON) under grant number RII3-Ct-2004-001566 for FP6 (2004–2008), grant number 226604 for FP7 (2009–2012) and grant number 312430 for FP7 (2013–2016). The SPHERE data presented here is based on observations collected at the European Southern Observatory under ESO programme(s) 095.C-0298(A), 0101.C-0420(A), 598.C-0359(F), 098.C-0686(B), 096.C-0388(A), 0102.C-0916(B), 095.C-0273(A), 0101.C-0753(B), 0104.C-0436(B), and 098.C-0686(A, B). We also acknowledge financial support from the Programme National de Planétologie (PNP) and the Programme National de Physique Stellaire (PNPS) of CNRS-INSU in France. This work has also been supported by a grant from the French Labex OSUG@2020 (Investissements d'avenir – ANR10 LABX56).

Data availability

The ARKS data used in this paper can be found in the ARKS dataverse. For more information, visit arkslp.org. Additional non-standard ARKS products used within this work are stored in Lovell (2025), where we have also made available

the code used to produce the self-subtraction plots presented in Figs. C.1–C.5. This code is also stored on `github`.

References

Acke, B., Min, M., Dominik, C., et al. 2012, A&A, 540, A125
ALMA Partnership (Brogan, C. L., et al.) 2015, ApJ, 808, L3
Andrews, S. M. 2020, ARA&A, 58, 483
Andrews, S. M., Huang, J., Pérez, L. M., et al. 2018, ApJ, 869, L41
Andrews, S. M., Elder, W., Zhang, S., et al. 2021, ApJ, 916, 51
Apai, D., Kasper, M., Skemer, A., et al. 2016, ApJ, 820, 40
Augereau, J. C., Nelson, R. P., Lagrange, A. M., Papaloizou, J. C. B., & Mouillet, D. 2001, A&A, 370, 447
Bae, J., & Zhu, Z. 2018, ApJ, 859, 118
Bae, J., Isella, A., Zhu, Z., et al. 2023, in ASPCS, 534, Protostars and Planets VII, eds. S. Inutsuka, Y. Aikawa, T. Muto, K. Tomida, & M. Tamura, 423
Beuzit, J. L., Vigan, A., Mouillet, D., et al. 2019, A&A, 631, A155
Boccaletti, A., Thalmann, C., Lagrange, A.-M., et al. 2015, Nature, 526, 230
Boccaletti, A., Mâlin, M., Baudoz, P., et al. 2024, A&A, 686, A33
Bonsor, A., & Wyatt, M. 2010, MNRAS, 409, 1631
Booth, M., Matrà, L., Su, K. Y. L., et al. 2019, MNRAS, 482, 3443
Booth, M., Pearce, T. D., Krivov, A. V., et al. 2023, MNRAS, 521, 6180
Brennan, A., Matrà, L., Mac Manamon, S., et al. 2026, A&A, 705 A201
Cataldi, G., Brandeker, A., Wu, Y., et al. 2018, ApJ, 861, 72
Chen, C., Mazoyer, J., Poteet, C. A., et al. 2020, ApJ, 898, 55
Chiang, E., & Fung, J. 2017, ApJ, 848, 4
Chittidi, J. S., MacGregor, M. A., Lovell, J. B., et al. 2025, ApJ, 990, L40
Clampin, M., Krist, J. E., Ardila, D. R., et al. 2003, AJ, 126, 385
Crotts, K. A., & Matthews, B. C. 2024, ApJ, 975, 136
Crotts, K. A., Matthews, B. C., Duchêne, G., et al. 2024, ApJ, 961, 245
Crotts, K. A., Carter, A. L., Lawson, K., et al. 2025, ApJ, 987, L41
Curone, P., Facchini, S., Andrews, S. M., et al. 2025, ApJ, 984, L9
Dent, W. R. F., Wyatt, M. C., Roberge, A., et al. 2014, Science, 343, 1490
Dong, J., Dawson, R. I., Shannon, A., & Morrison, S. 2020, ApJ, 889, 47
Duchêne, G., Rice, M., Hom, J., et al. 2020, AJ, 159, 251
Ertel, S., Wolf, S., Metchev, S., et al. 2011, A&A, 533, A132
Faramaz, V., Krist, J., Stapelfeldt, K. R., et al. 2019a, AJ, 158, 162
Faramaz, V., Marino, S., Booth, M., et al. 2021, AJ, 161, 271
Farhat, M. A., Sefilian, A. A., & Touma, J. R. 2023, MNRAS, 521, 2067
Farihi, J. 2016, New Astron. Rev., 71, 9
Fernandez, J. A., & Ip, W.-H. 1984, Icarus, 58, 109
Friebe, M. F., Pearce, T. D., & Löhne, T. 2022, MNRAS, 512, 4441
Gáspár, A., Wolff, S. G., Rieke, G. H., et al. 2023, NatAst, 7, 790
Goldreich, P., & Tremaine, S. 1979, ApJ, 233, 857
Golimowski, D. A., Ardila, D. R., Krist, J. E., et al. 2006, AJ, 131, 3109
Grady, C. A., Wisniewski, J. P., Schneider, G., et al. 2020, ApJ, 889, L21
Hahn, J. M. 2003, ApJ, 595, 531
Hales, A. S., Marino, S., Sheehan, P. D., et al. 2022, ApJ, 940, 161
Han, Y., Wyatt, M. C., & Dent, W. R. F. 2022, MNRAS, 519, 3257
Heap, S. R., Lindler, D. J., Lanz, T. M., et al. 2000, ApJ, 539, 435
Han, Y., Mansell, E., Jennings, J., et al. 2026, A&A, 705, A196
Hines, D. C., Schneider, G., Hollenbach, D., et al. 2007, ApJ, 671, L165
Holland, W. S., Greaves, J. S., Dent, W. R. F., et al. 2003, ApJ, 582, 1141
Holland, W. S., Matthews, B. C., Kennedy, G. M., et al. 2017, MNRAS, 470, 3606
Huang, J., Andrews, S. M., Pérez, L. M., et al. 2018, ApJ, 869, L43
Hughes, A. M., Lieman-Sifry, J., Flaherty, K. M., et al. 2017, ApJ, 839, 86
Hughes, A. M., Duchêne, G., & Matthews, B. C. 2018, ARA&A, 56, 541
Imaz Blanco, A., Marino, S., Matrà, L., et al. 2023, MNRAS, 522, 6150
Jackson, A. P., Wyatt, M. C., Bonsor, A., & Veras, D. 2014, MNRAS, 440, 3757
Jalali, M. A., & Tremaine, S. 2012, MNRAS, 421, 2368
Jankovic, M. R., Pawellek, N., Zander, J., et al. 2026, A&A, 705, A204
Jones, J. W., Chiang, E., Duchêne, G., Kalas, P., & Esposito, T. M. 2023, ApJ, 948, 102
Kalas, P., & Jewitt, D. 1995, AJ, 110, 794
Kalas, P., Graham, J. R., & Clampin, M. 2005, Nature, 435, 1067
Kalas, P., Fitzgerald, M. P., & Graham, J. R. 2007, ApJ, 661, L85
Kasper, M., Apai, D., Wagner, K., & Robberto, M. 2015, ApJ, 812, L33
Kennedy, G. M. 2020, Roy. Soc. Open Sci., 7, 200063
Kennedy, G. M. 2025, RAS Tech. Instrum., 4, rzaf004
Kennedy, G. M., Marino, S., Matrà, L., et al. 2018, MNRAS, 475, 4924
Kennedy, G. M., Lovell, J. B., Kalas, P., & Fitzgerald, M. P. 2023, MNRAS, 524, 2698
Lazzoni, C., Bendahan-West, R., Marino, S., et al. 2025, A&A, 704, A176
Lee, E. J., & Chiang, E. 2016, ApJ, 827, 125
Lestrade, J. F. 2008, in IAU Symposium, Vol. 248, A Giant Step: from Milli- to Micro-arcsecond Astrometry, eds. W. J. Jin, I. Platais, & M. A. C. Perryman, 170
Lovell, J. 2025, Dataset for: The ALMA survey to Resolve exoKuiper belt Substructures (ARKS) VI: Asymmetries and Offsets
Lovell, J. B., & Lynch, E. M. 2023, MNRAS, 525, L36
Lovell, J. B., Marino, S., Wyatt, M. C., et al. 2021a, MNRAS, 506, 1978
Lovell, J. B., Wyatt, M. C., Ansdell, M., et al. 2021b, MNRAS, 500, 4878
Lovell, J. B., Lynch, E. M., Chittidi, J., et al. 2025, ApJ, 990, 145
Lynch, E. M., & Lovell, J. B. 2022, MNRAS, 510, 2538
Lyra, W., & Kuchner, M. 2013, Nature, 499, 184
Mac Manamon, S., Matr'a, L., Marino, S., et al. 2026, A&A, 705, A198
MacGregor, M. A., Wilner, D. J., Andrews, S. M., & Hughes, A. M. 2015, ApJ, 801, 59
MacGregor, M. A., Matrà, L., Kalas, P., et al. 2017, ApJ, 842, 8
MacGregor, M. A., Weinberger, A. J., Hughes, A. M., et al. 2018, ApJ, 869, 75
MacGregor, M. A., Weinberger, A. J., Loyd, R. O. P., et al. 2021, ApJ, 911, L25
MacGregor, M. A., Hurt, S. A., Stark, C. C., et al. 2022, ApJ, 933, L1
Marino, S. 2022, arXiv e-prints [arXiv:2202.03053]
Marino, S., Carpenter, J., Wyatt, M. C., et al. 2018, MNRAS, 479, 5423
Marino, S., Yelverton, B., Booth, M., et al. 2019, MNRAS, 484, 1257
Marino, S., Gupta, V., Weber, P., et al. 2026a, A&A, 705, A202
Marino, S., Matrà, L., Hughes, A. M., et al. 2026b, A&A, 705, A195
Marois, C., Macintosh, B., Barman, T., et al. 2008, Science, 322, 1348
Matrà, L., MacGregor, M. A., Kalas, P., et al. 2017, ApJ, 842, 9
Matrà, L., Marino, S., Wilner, D. J., et al. 2025, A&A, 693, A151
Matthews, B. C., Krivov, A. V., Wyatt, M. C., Bryden, G., & Eiroa, C. 2014, in Protostars and Planets VI, eds. H. Beuther, R. S. Klessen, C. P. Dullemond, & T. Henning, 521
Maud, L. T., Asaki, Y., Fomalont, E. B., et al. 2020, ApJS, 250, 18
Maud, L. T., Asaki, Y., Dent, W. R. F., et al. 2022, ApJS, 259, 10
Milli, J., Vigan, A., Mouillet, D., et al. 2017, A&A, 599, A108
Milli, J., Engler, N., Schmid, H. M., et al. 2019, A&A, 626, A54
Milli, J., Olofsson, J., Bonduelle, M., et al. 2026, A&A, 705, A199
Moór, A., Curé, M., Kóspál, Á., et al. 2017, ApJ, 849, 123
Mouillet, D., Larwood, J. D., Papaloizou, J. C. B., & Lagrange, A. M. 1997, MNRAS, 292, 896
Nealon, R., Dipierro, G., Alexander, R., Martin, R. G., & Nixon, C. 2018, MNRAS, 481, 20
Nesvold, E. R., & Kuchner, M. J. 2015, ApJ, 815, 61
Olofsson, J., Samland, M., Avenhaus, H., et al. 2016, A&A, 591, A108
Olofsson, J., van Holstein, R. G., Boccaletti, A., et al. 2018, A&A, 617, A109
Olofsson, J., Milli, J., Thébault, P., et al. 2019, A&A, 630, A142
Olofsson, J., Thébault, P., Kral, Q., et al. 2022, MNRAS, 513, 713
Pan, M., Nesvold, E. R., & Kuchner, M. J. 2016, ApJ, 832, 81
Panić, O., Holland, W. S., Wyatt, M. C., et al. 2013, MNRAS, 435, 1037
Pearce, T. D., & Wyatt, M. C. 2014, MNRAS, 443, 2541
Pearce, T. D., & Wyatt, M. C. 2015, MNRAS, 453, 3329
Perrin, M. D., Duchene, G., Millar-Blanchaer, M., et al. 2015, ApJ, 799, 182
Perrot, C., Olofsson, J., Kral, Q., et al. 2023, A&A, 673, A39
Pfalzner, S., Govind, A., & Portegies Zwart, S. 2024, NatAst, 8, 1380
Quillen, A. C., & Faber, P. 2006, MNRAS, 373, 1245
Rebollido, I., Stark, C. C., Kammerer, J., et al. 2024, AJ, 167, 69
Reche, R., Beust, H., Augereau, J. C., & Absil, O. 2008, A&A, 480, 551
Ren, B., Choquet, É., Perrin, M. D., et al. 2021, ApJ, 914, 95
Rodet, L., Beust, H., Bonnefoy, M., et al. 2017, A&A, 602, A12
Schneider, G., Grady, C. A., Hines, D. C., et al. 2014, AJ, 148, 59
Sefilian, A. A. 2022, PhD thesis, University of Cambridge, UK
Sefilian, A. A., Rafikov, R. R., & Wyatt, M. C. 2021, ApJ, 910, 13
Sefilian, A. A., Rafikov, R. R., & Wyatt, M. C. 2023, ApJ, 954, 100
Sefilian, A. A., Kratter, K. M., Wyatt, M. C., et al. 2025, MNRAS, 543, 3123
Sende, J. A., & Löhne, T. 2019, A&A, 631, A141
Sezestre, É., Augereau, J. C., Boccaletti, A., & Thébault, P. 2017, A&A, 607, A65
Smallwood, J. L. 2023, MNRAS, 523, 3526
Soummer, R., Pueyo, L., & Larkin, J. 2012, ApJ, 755, L28
Stasevic, S., Milli, J., Mazoyer, J., et al. 2023, A&A, 678, A8
Su, K. Y. L., Rieke, G. H., Malhotra, R., et al. 2013, ApJ, 763, 118
Thebault, P., & Kral, Q. 2018, A&A, 609, A98
Ward, W. R., & Hahn, J. M. 1998, AJ, 116, 489
Weber, P., Pérez, S., Baruteau, C., et al. 2026, A&A, 705, A203
Wertz, O., Absil, O., Gómez González, C. A., et al. 2017, A&A, 598, A83
Wyatt, M. C. 2003, ApJ, 598, 1321
Wyatt, M. C. 2005, A&A, 440, 937
Wyatt, M. C. 2006, ApJ, 639, 1153
Wyatt, M. C. 2008, ARA&A, 46, 339
Wyatt, M. C., Dermott, S. F., Telesco, C. M., et al. 1999, ApJ, 527, 918

Wyatt, M. C., Panić, O., Kennedy, G. M., & Matrà, L. 2015, Ap&SS, 357, 103
Yelverton, B., & Kennedy, G. M. 2018, MNRAS, 479, 2673
Zawadzki, B., Fehr, A., Hughes, A. M., et al. 2026, A&A, 705, A197

[1] Center for Astrophysics | Harvard & Smithsonian, 60 Garden St, Cambridge, MA 02138, USA
[2] National Radio Astronomy Observatory, 520 Edgemont Road, Charlottesville, VA 22903-2475, USA
[3] Joint ALMA Observatory, Avenida Alonso de Córdova 3107, Vitacura 7630355, Santiago, Chile
[4] Millennium Nucleus on Young Exoplanets and their Moons (YEMS), Chile
[5] Malaghan Institute of Medical Research, Gate 7, Victoria University, Kelburn Parade, Wellington, New Zealand
[6] Department of Physics, University of Warwick, Gibbet Hill Road, Coventry CV4 7AL, UK
[7] Department of Physics and Astronomy, University of Exeter, Stocker Road, Exeter EX4 4QL, UK
[8] European Southern Observatory, Karl-Schwarzschild-Strasse 2, 85748 Garching bei München, Germany
[9] Department of Astronomy, Van Vleck Observatory, Wesleyan University, 96 Foss Hill Dr., Middletown, CT, 06459, USA
[10] Herzberg Astronomy & Astrophysics, National Research Council of Canada, 5071 West Saanich Road, Victoria, BC V9E 2E9, Canada
[11] Department of Physics & Astronomy, University of Victoria, 3800 Finnerty Rd, Victoria, BC V8P 5C2, Canada
[12] Department of Astronomy and Steward Observatory, The University of Arizona, 933 North Cherry Ave, Tucson, AZ 85721, USA
[13] UK Astronomy Technology Centre, Royal Observatory Edinburgh, Blackford Hill, Edinburgh EH9 3HJ, UK
[14] Univ. Grenoble Alpes, CNRS, IPAG, 38000 Grenoble, France
[15] School of Physics, Trinity College Dublin, the University of Dublin, College Green, Dublin 2, Ireland
[16] Instituto de Astrofísica de Canarias, Vía Láctea S/N, La Laguna, 38200 Tenerife, Spain
[17] Departamento de Astrofísica, Universidad de La Laguna, La Laguna, 38200 Tenerife, Spain
[18] National Astronomical Observatory of Japan, Osawa 2-21-1, Mitaka, Tokyo 181-8588, Japan
[19] Department of Astronomy, Graduate School of Science, The University of Tokyo, Tokyo 113-0033, Japan
[20] Department of Astronomy, University of California, Berkeley, Berkeley, CA 94720-3411, USA
[21] Division of Geological and Planetary Sciences, California Institute of Technology, 1200 E. California Blvd., Pasadena, CA 91125, USA
[22] Max-Planck-Insitut für Astronomie, Königstuhl 17, 69117 Heidelberg, Germany
[23] Astrophysikalisches Institut und Universitätssternwarte, Friedrich-Schiller-Universität Jena, Schillergäßchen 2-3, 07745 Jena, Germany
[24] Academia Sinica Institute of Astronomy and Astrophysics, 11F of AS/NTU Astronomy-Mathematics Building, No.1, Sect. 4, Roosevelt Rd, Taipei 106319, Taiwan.
[25] Konkoly Observatory, HUN-REN Research Centre for Astronomy and Earth Sciences, MTA Centre of Excellence, Konkoly-Thege Miklós út 15–17, 1121 Budapest, Hungary
[26] Institute of Astronomy, University of Cambridge, Madingley Road, Cambridge CB3 0HA, UK
[27] Large Binocular Telescope Observatory, The University of Arizona, 933 North Cherry Ave, Tucson, AZ 85721, USA
[28] Institute of Physics Belgrade, University of Belgrade, Pregrevica 118, 11080 Belgrade, Serbia
[29] Institute of Physics and Astronomy, ELTE Eötvös Loránd University, Pázmány Péter sétány 1/A, 1117 Budapest, Hungary
[30] Department of Physics and Astronomy, Johns Hopkins University, 3400 N Charles Street, Baltimore, MD 21218, USA
[31] Departamento de Física, Universidad de Santiago de Chile, Av. Víctor Jara 3493, Santiago, Chile
[32] Center for Interdisciplinary Research in Astrophysics Space Exploration (CIRAS), Universidad de Santiago, Santiago, Chile

Appendix A: Source data

The ARKS data have been consistently imaged with a range of robust parameters (0.5, 2.0) and with uv-tapers for some low surface brightness, extended sources. Asymmetric features can be more or less pronounced in different images, and thus we catalogue which images were used to produce various maps and/or profiles in this study in Table A.1, and for each source their respective inclination, position angle (PA), and right ascension (RA) and declination (Decl.) offset values in Table A.2.

Appendix B: Offset systems

ALMA's astrometric accuracy depends on a number of factors, including the atmospheric phase conditions, the separation between the science target and the phase calibrator(s), errors in antenna positions, and the delay model used during data correlation (see ALMA Technical Handbook, Chapter 10.5.2, Astrometric Observations). The astrometric accuracy for a given observation can be estimated empirically by measuring the offset position of a well-known calibrator across multiple observations. In the case of these 'check sources', these have locations that are known with extremely high precision, and are typically ICRF quasars with positions determined by Very Long Baseline Interferometry (VLBI) observations. The a-priori positions of these ICRF quasars are accurate to <0.0001″, thus based on the baseline configurations during ARKS ALMA observations, the check source phases should have offsets consistent with zero. In other words, if the stellocentric offsets observed towards any ARKS targets, though most pertinent to this appendix, HD 15115, HD 32297 and HD 109573, were solely due to phase calibration uncertainties, the same offsets would be present in the data for the check sources.

Check source selection from the ALMA Calibrator Source Catalogue is based on criteria that ensures check sources are at comparable distances from the phase calibrator as the science target, and that the check source must be sufficiently bright to achieve a S/N greater than 15 across all scans and spectral windows. The check source should also maintain adequate strength to support reliable imaging during both the QA0+ analysis and the ALMA Pipeline data processing stages. Research on long baseline observations from 2017 indicates that the peak-to-total flux density ratio serves as a dependable metric for evaluating observation quality. This metric is influenced by the root-mean-square (rms) phase difference between phase calibrator scans and the angular separation from the phase calibrator (refer to ALMA Technical Handbook, Sect. 10.4.10).

We used the check sources present in the observations of HD 109573, HD 15115, and HD 32297 to assess the positional accuracy of the calibrated data. In all cases, the same check source was observed for all execution blocks (EBs) per-science target, allowing for a consistent comparison of astrometric accuracy between different observations. Comparison between the offset position in different days and observing conditions provides an estimate of the absolute astrometric precision of ALMA. We measured the check source location for all execution blocks, and in both the image and visibility planes. Specifically, we imaged the check source after averaging all scans using the same `CASA tclean` parameters as were used to image the science target, and fitted a 2D Gaussian to the images with `CASA's imfit` tool. We compared the centroid coordinates of this Gaussian fit to the phase centre of the check source observation, corresponding to the ICRS/J2000 VLBI position from the ALMA Calibrator Source Catalogue. Likewise, we modelled the check source visibilities as point sources in `CASA's uvmodelfit` tool, and made the same comparison between the fitted centroid location and that of the check source. Check sources are expected to have an absolute positional errors <0.002″ and appear as point sources at ALMA's resolution (though decoherence may cause artificial source extension). To estimate the astrometric accuracy, we then calculated the repeatability of the measured positions, defined as the dispersion in the measured check source positions across all execution blocks for the three check sources. The resulting mean offset and dispersion for all execution blocks (per target or check source) are presented in Table B.1. For both RA and Decl., the first value represents the mean, while the quoted error corresponds to the dispersion of all measurements.

For HD 109573, two observations were conducted using J1254-4424 as the check source. The science target and the check source are located 4.99° and 4.90° from the phase calibrator, respectively. Given their similar distances from the phase calibrator, the astrometric accuracy measured for the check source serves as a reliable proxy for the accuracy toward HD 109573. For HD 32297, four observations were conducted using J0519+0848 as the check source. The science target and the check source are located 2.47° and 3.49° from the phase calibrator, respectively. Since the target is closer to the phase calibrator than the check source, the astrometric accuracy measured for the check source can be considered an upper limit for the target. Finally, for HD 15115, 12 observations were conducted using J0239+0416 as the check source. In this case, the science target and the check source are located 0.82° and 4.69° from the phase calibrator, respectively. Since the phase RMS is proportional to $\sqrt{d}$, with d being the geometric distance between the lines of sight of the target and the phase calibrator (see Maud et al. 2020, 2022, and references therein), the estimated astrometric accuracy toward HD 15115 is $\approx 1/\sqrt{\text{diff}}$ of the accuracy estimated for the check source, i.e. given the angular difference of $4.69° - 0.82° = 3.87°$, a factor of $1/\sqrt{3.87} \approx 1/2$. We note that one observation was excluded from the analysis of HD 15115's data to a phase RMS close to 60°, approximately four times higher than the average phase RMS of the other observations. Thus, 11 observations were included in total.

Both the mean offset and scatter (standard deviation) are of the order of a few milliarcseconds, a factor of 5–10 below ALMA's predicted astrometric accuracy (Lestrade 2008), but consistent with phase referencing experiments (carried out during long baselines campaigns; these experiments indicate that ALMA's measured absolute calibrator positions have a scatter of a few milliarcseconds; see ALMA Partnership 2015).

Appendix C: Self-subtraction maps

Here we present galleries of the self-subtraction maps of sources host to asymmetric emission or tentative asymmetries in Figs. C.1, C.2, C.3, C.4, and C.5. For the systems HD 9672, HD 10647, HD 39060, HD 61005, HD 92945, HD 107146, HD 121617, HD 95086, HD 84870, and HD 218396 we used image centres based on the Gaia DR3 stellar location, whereas for the systems HD 15115, HD 32297, HD 109573, HD 131488 and HD 131835 we used image centres based on the best-fit disc centres derived in Marino et al. (2026b); see also Table A.2. In Fig. C.6 we also present a gallery of SPHERE self-subtracted (minor axis) maps and their associated radial profiles, showing the extent to which these sources are asymmetric in scattered light.

Table A.1: Images and image properties used to analyse the ARKS sample in this paper.

Science Target	Gallery			Self-sub.			Profile		
	R	UVT [″]	$\sigma_{\rm RMS}$ [μJy beam^{-1}]	R	UVT [″]	$\sigma_{\rm RMS}$ [μJy beam^{-1}]	R	UVT [″]	$\sigma_{\rm RMS}$ [μJy beam^{-1}]
HD 9672	2.0	–	11	2.0	–	11	2.0	–	11
HD 10647 (All)	2.0	–	9.4	2.0	–	9.4	2.0	–	9.4
HD 10647 (Archival)	2.0	–	13.6	–	–	–	–	–	–
HD 10647 (ARKS)	2.0	–	13.1	–	–	–	–	–	–
HD 15115	0.5	–	6.5	0.5	–	6.5	–	–	–
HD 32297	2.0	–	15	2.0	–	15	–	–	–
HD 39060	2.0	0.5	20	2.0	0.5	20	2.0	0.5	20
HD 61005	2.0	–	19	2.0	–	19	2.0	–	19
HD 92945	2.0	0.7	21	2.0	0.7	21	2.0	0.7	21
HD 107146	2.0	–	5.6	2.0	–	5.6	2.0	–	5.6
HD 109573	0.5	–	20	0.5	–	20	–	–	–
HD 121617	0.5	–	11	0.5	–	11	–	–	–
HD 84870	–	–	–	2.0	–	12	–	–	–
HD 95086	–	–	–	2.0	1.0	28	–	–	–
HD 131488	–	–	–	2.0	0.1	11	–	–	–
HD 131835	–	–	–	0.5	–	11	–	–	–
HD 218396	–	–	–	2.0	0.8	11	–	–	–

Notes. ‘R’ here refers to the robust parameter of the image, and ‘UVT’ to the angular size of the uv-taper. 14/15 images are standard ARKS products, all except HD 107146, which we detail in Sect. 3. No profile analyses were used to quantify asymmetries towards HD 15115, HD 32297, HD 109573, and HD 121617. The lower half of the table presents target information for the systems with tentative asymmetries, including HD 95086, whose asymmetry is strong, but may not be physical. $\sigma_{\rm RMS}$ defines the RMS associated with each image (all values are presented to two significant figures).

Table A.2: Geometric and offset parameters used to analyse the ARKS data in this study.

Science Target	Inc. [°]	PA [°]	ΔRA [mas]	ΔDecl. [mas]
HD 9672	78.7 ± 0.2	107.9 ± 0.2	68 ± 76	−33 ± 30
HD 10647	77.8 ± 0.1	57.3 ± 0.1	90 ± 56	28 ± 51
HD 15115	86.7 ± 0.0	98.5 ± 0.0	44 ± 12	−8 ± 5
HD 32297	88.3 ± 0.0	47.5 ± 0.0	19 ± 4	18 ± 4
HD 39060	86.4 ± 0.2	29.9 ± 0.1	−54 ± 14	−2 ± 20
HD 61005	85.9 ± 0.1	70.4 ± 0.1	8 ± 22	−4 ± 8
HD 92945	65.4 ± 0.6	100.0 ± 0.6	−84 ± 55	12 ± 35
HD 107146	19.3 ± 0.6	153.2 ± 1.7	36 ± 35	−48 ± 35
HD 109573	76.6 ± 0.1	26.5 ± 0.0	11 ± 2	−32 ± 2
HD 121617	44.1 ± 0.6	58.7 ± 0.7	8 ± 8	14 ± 7
HD 84870	47.1 ± 2.6	−25.7 ± 4.1	81 ± 57	−103 ± 63
HD 95086	31.6 ± 3.5	100.0 ± 5.7	−91 ± 45	127 ± 34
HD 131488	85.0 ± 0.1	97.2 ± 0.0	0 ± 2	1 ± 1
HD 131835	74.2 ± 0.2	59.2 ± 0.2	6 ± 6	3 ± 6
HD 218396	28.8 ± 3.3	49.7 ± 5.7	−41 ± 65	−57 ± 69

Notes. The parameters defined here all match those of ARKS I, Table B.1; see Marino et al. (2026b).

Table B.1: Offset analysis table.

Science Target	Check Source	Number of EBs	`imfit` offset ΔRA, ΔDecl. [mas]	`uvmodelfit` offset ΔRA, ΔDecl, [mas]	Disc centre offset ΔRA, ΔDecl. [mas]
HD 15115	J0239+0416	11	1.6±6.7, 3.3±6.4	0.7±5.8, −3.3±5.8	44±12, −8±5
HD 32297	J0519+0848	4	0.5±3.9, −0.5±4.8	−0.7±1.7, 1.7±2.6	19±4, 18±4
HD 109573	J1254-4424	2	−2.4±0.8, 5.9±2.4	1.3±0.7, −5.4±2.6	11±2, −32±2

Notes. This table compiles the image and uv-plane analysis metrics for check source offsets, their number of execution blocks (EBs) for the three science targets, and the best-fit disc centres (from ARKS I; Marino et al. 2026b) for the sources determined to have significant offsets between those positions and their stellar locations.

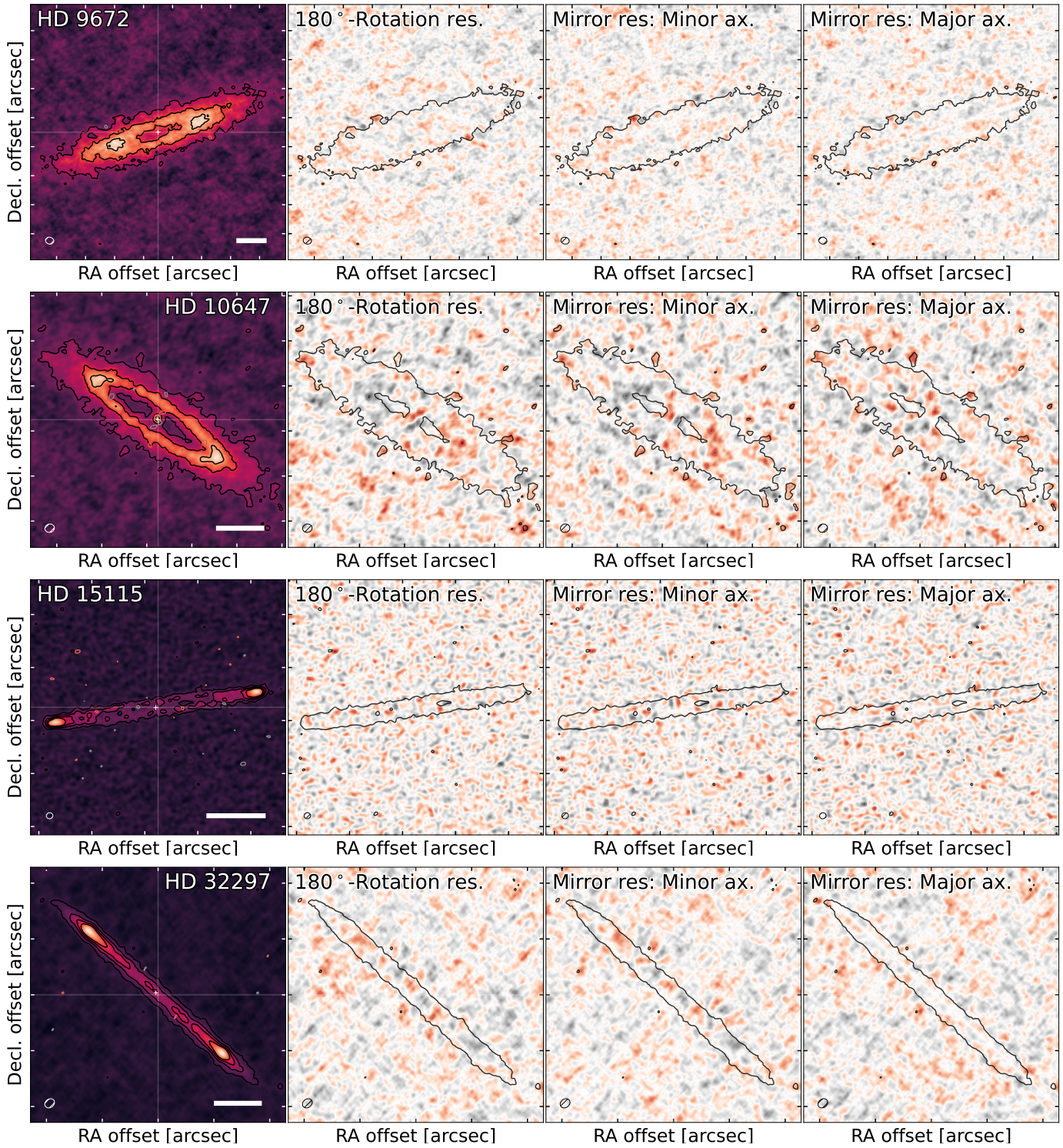

Fig. C.1: Self-subtraction residual maps for HD 9672, HD 10647, HD 15115, and HD 32297. The plots show their images (left), rotation-subtraction residuals (centre left), and mirror-subtractions along the minor and major axes (centre right and right, respectively). Residual maps show the 3σ image emission contour (black), and $\pm 3\sqrt{2} \times \sigma$ and $5\sqrt{2} \times \sigma$ residual emission contours (grey and red respectively for negative and positive). The colour scale ranges from $\pm 5\sigma$ of the rms in the residual maps. Beams are shown in the lower left of each panel, and 50 au scale bars are shown on the lower right of the left panel. We present the primary beam-corrected contours of the rotation self-subtraction residuals on the left panel to highlight where these arise from in the image plane for HD 9672, HD 15115, and HD 32297, and from the minor axis self-subtraction residuals for HD 10647.

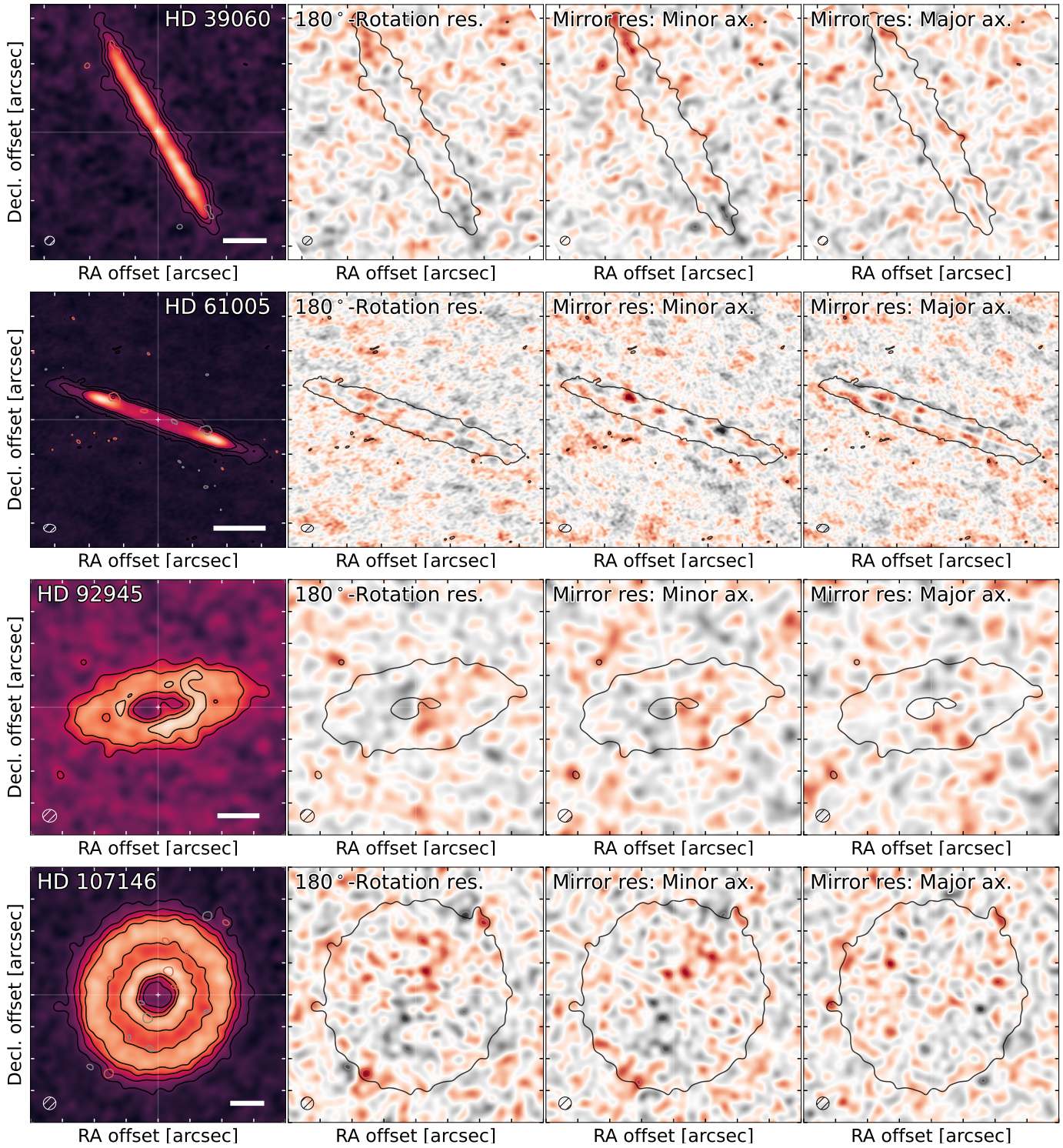

Fig. C.2: Self-subtraction residual maps for HD 39060, HD 61005, HD 92945, and HD 107146. This figure presents data in the same manner as Fig. C.1. We present the contours of the rotation self-subtraction residuals in the left panels to highlight where these arise from in the image plane for HD 92945 and HD 107146, and the minor axis self-subtraction residuals for HD 39060 and HD 61005.

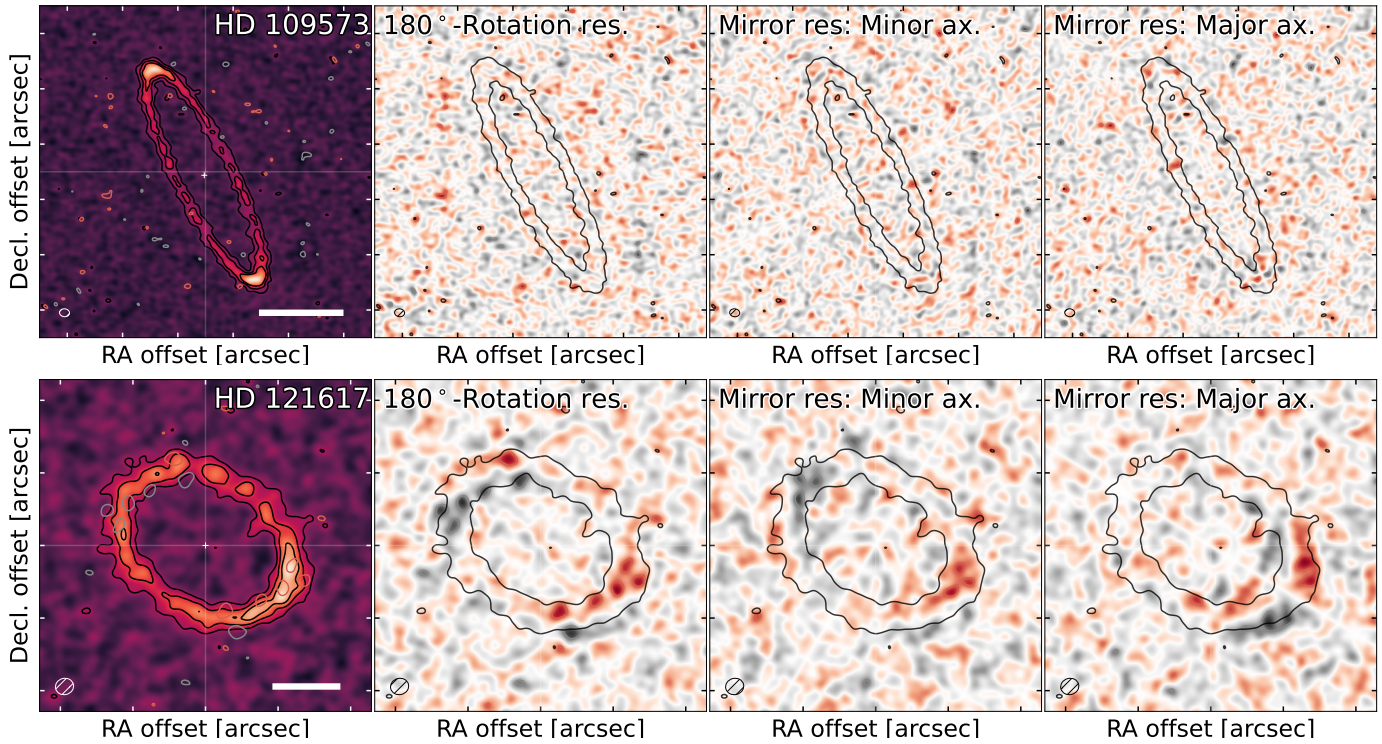

Fig. C.3: Self-subtraction residual maps for HD 109573 and HD 121617. This figure presents data in the same manner as Fig. C.1. We present the contours of the rotation self-subtraction residuals in the left panels to highlight where these arise in the image plane for both sources.

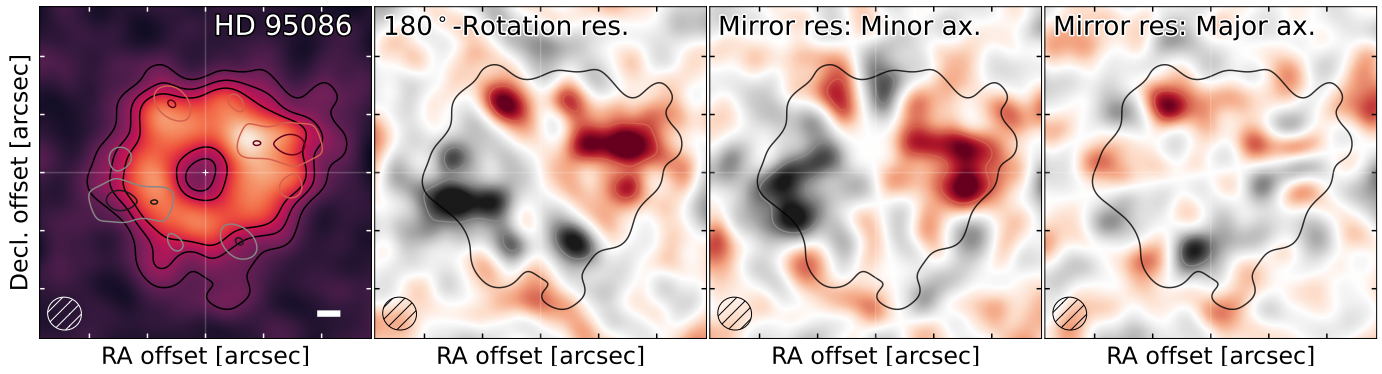

Fig. C.4: Self-subtraction residual maps for HD 95086, which due to undersubtraction of a background galaxy is host to a strong asymmetry that is unlikely to be physically located in the disc. This figure presents data in the same manner as Fig. C.1.

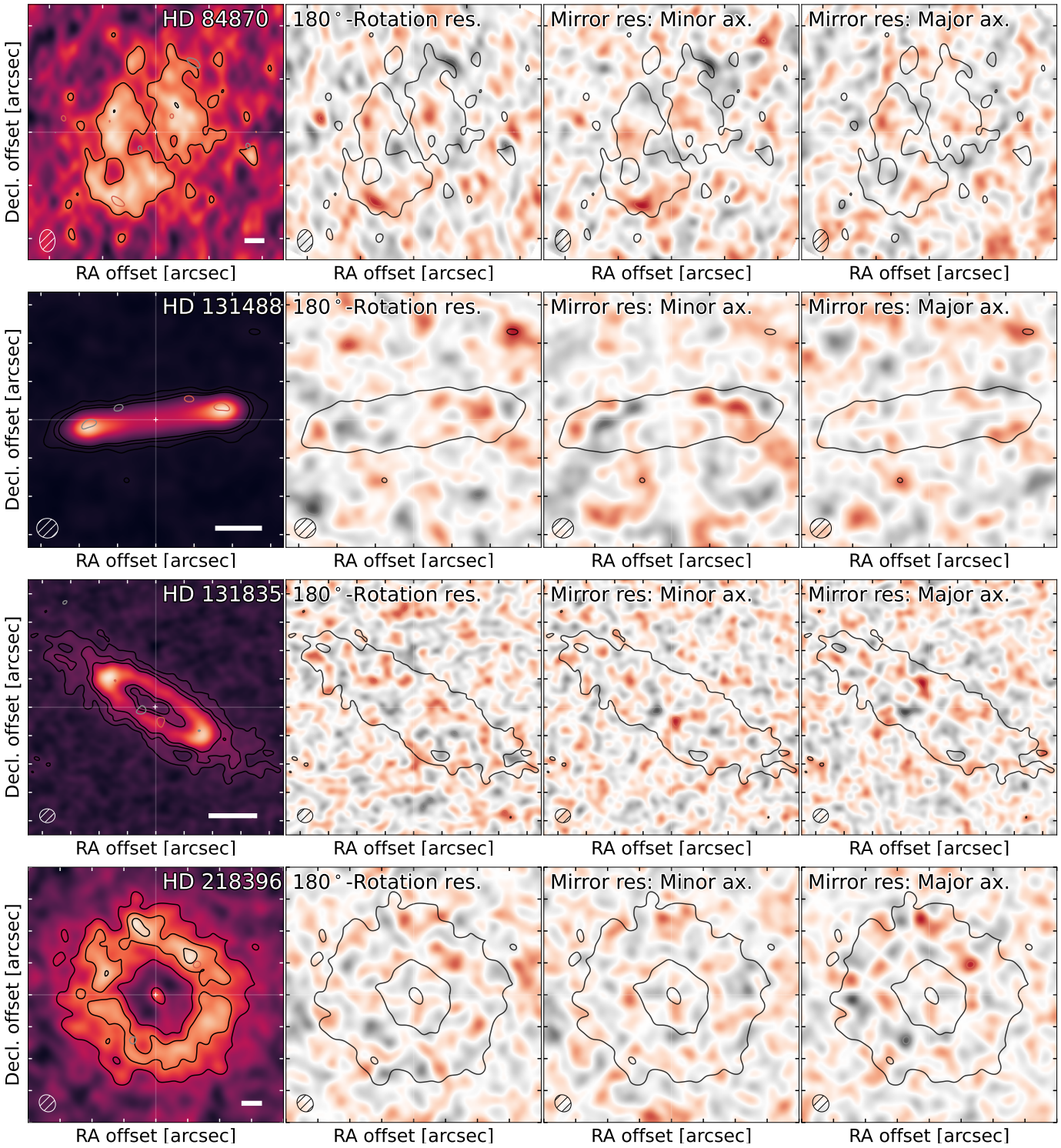

Fig. C.5: Self-subtraction residual maps for systems with tentative signs of asymmetries (HD 84870, HD 131488, HD 131835, and HD 218396). This figure presents data in the same manner as Fig. C.1. We present the contours of the rotation self-subtraction residuals in the left panel to highlight where these arise from in the image plane for HD 84870, of the minor axis self-subtraction residuals for HD 131488 and HD 131835, and of the major axis self-subtraction residuals for HD 218396.

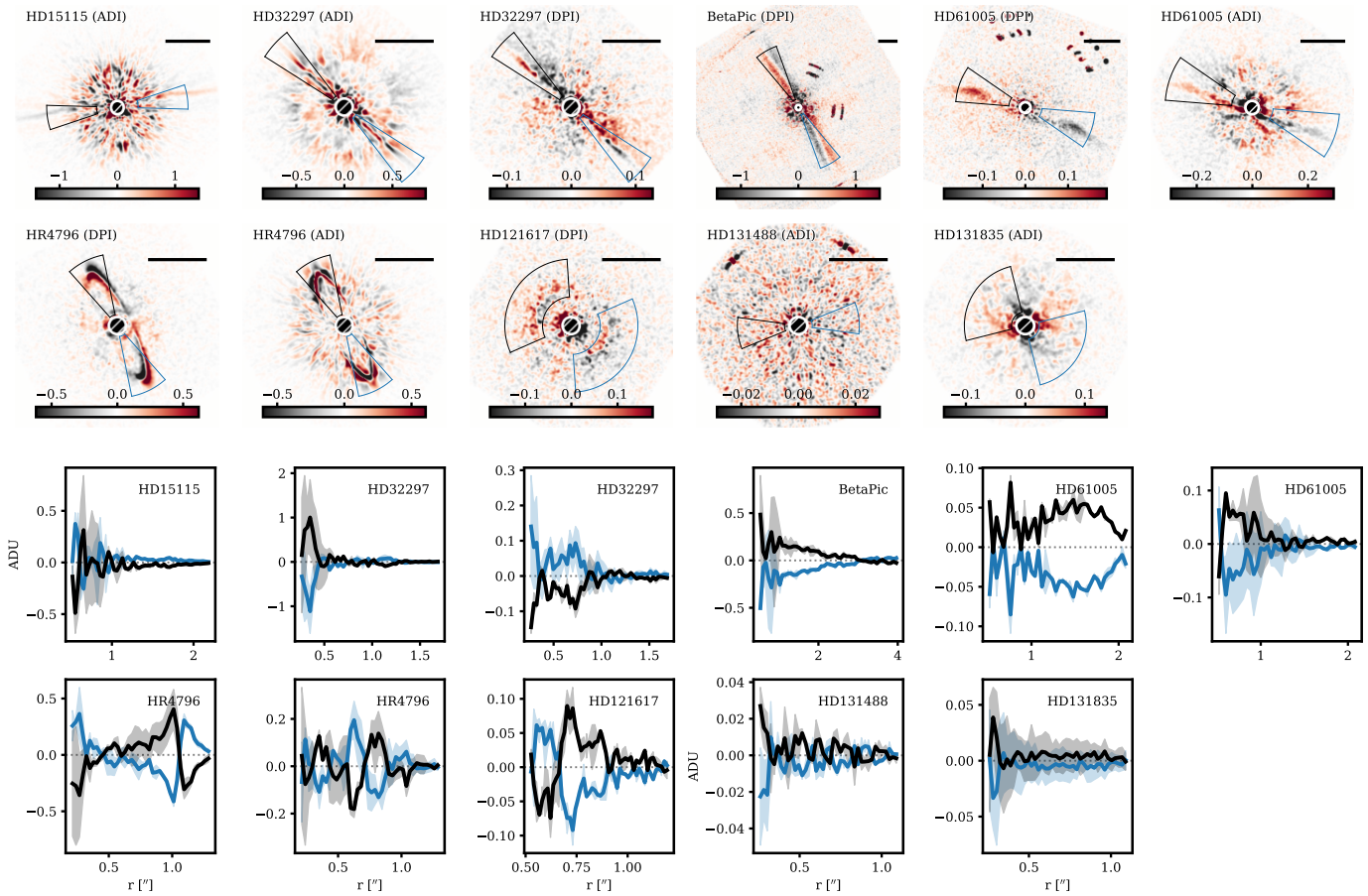

Fig. C.6: Top: Minor-axis self-subtraction residual maps for systems with SPHERE-detected emission. The black bar in the top right corner of each panel indicates 1″, denoted as either angular differential imaging (ADI) or dual polarisation imaging (DPI), depending on whether the total intensity maps or the Stokes Q_ϕ component from Milli et al. (2026) are used. Bottom: Radial profiles through the self-subtracted residual maps, estimated inside the wedges shown in the top panel for each corresponding image. The colour-coding of the wedges matches the colour-coding of the radial profiles (black and blue). The profiles present estimated $\pm 1\sigma$ uncertainties.

A&A, 705, A199 (2026)
https://doi.org/10.1051/0004-6361/202556523
© The Authors 2026

Astronomy & Astrophysics

The ALMA survey to Resolve exoKuiper belt Substructures (ARKS)

V. Comparison between scattered light and thermal emission

J. Milli[1,⋆], J. Olofsson[2], M. Bonduelle[1], R. Bendahan-West[3], J. P. Marshall[4], E. Choquet[5], A. A. Sefilian[6], Y. Han[7], B. Zawadzki[8], S. Mac Manamon[9], E. Mansell[8], C. del Burgo[10,11], J. M. Carpenter[12], A. M. Hughes[8], M. Booth[13], E. Chiang[14], S. Ertel[6,15], Th. M. Esposito[16,17], Th. Henning[18], J. Hom[6], M. R. Jankovic[19], A. V. Krivov[20], J. B. Lovell[21], P. Luppe[9], M. A. MacGregor[22], S. Marino[3], B. C. Matthews[23,24], L. Matrà[9], A. Moór[25], N. Pawellek[25,26], T. D. Pearce[27], S. Pérez[28,29,30], V. Squicciarini[3], P. Weber[28,29,30], D. J. Wilner[21], and M. C. Wyatt[31]

(Affiliations can be found after the references)

Received 21 July 2025 / Accepted 3 December 2025

ABSTRACT

Context. Debris discs are analogues to our own Kuiper belt around main-sequence stars and are therefore referred to as exoKuiper belts. They have been resolved at high angular resolution at wavelengths spanning the optical/near-infrared to the submillimetre-millimetre regime. Short wavelengths can probe the light scattered by such discs, which is dominated by micron-sized dust particles, while millimetre wavelengths can probe the thermal emission of millimetre-sized particles. Determining differences in the dust distribution between millimetre- and micron-sized dust is fundamental to revealing the dynamical processes affecting the dust in debris discs.

Aims. We aim to compare the scattered light from the discs of the 'ALMA survey to Resolve exoKuiper belt Substructures' (ARKS) with the thermal emission probed by ALMA. We focus on the radial distribution of the dust, and we also put constraints on the presence of giant planets in those systems.

Methods. We used high-contrast scattered light observations obtained with VLT/SPHERE, GPI, and the *HST* to uniformly study the dust distribution in those systems and compare it to the dust distribution extracted from the ALMA observations carried out in the course of the ARKS project. We also set constraints on the presence of planets by using these high-contrast images combined with exoplanet evolutionary models.

Results. Fifteen of the 24 discs comprising the ARKS sample are detected in scattered light, with TYC 9340-437-1 being imaged for the first time at near-infrared wavelengths. For six of those 15 discs, the dust surface density seen in scattered light peaks farther out compared to that observed with ALMA. These six discs except one are known to also host cold CO gas. Conversely, the systems without significant offsets are not known to host gas, except one. Moreover, with our scattered light near-infrared images, we achieve typical sensitivities to planets from 1 to 10 $M_{\rm Jup}$ beyond 10 to 20 au, depending on the system age and distance.

Conclusions. This observational study suggests that the presence of gas in debris discs may affect the small and large grains differently, pushing the small dust to greater distances where the gas is less abundant.

Key words. instrumentation: high angular resolution – Kuiper belt: general – protoplanetary disks – circumstellar matter

1. Introduction

Debris discs, analogues to our own Kuiper belt, have been detected around more than a thousand main-sequence stars (Cao et al. 2023), mainly through the infrared excess emitted by cold circumstellar dust (typically $T \leq 100$ K). This dust is thought to originate from kilometre-sized or larger planetesimals orbiting in a birth ring and colliding to produce smaller and smaller debris (Wyatt 2008). This continuous collisional cascade explains the presence of short-lived dust particles after millions or billions of years around a star.

The first debris disc was detected by the *InfraRed Astronomical Satellite* (IRAS, Aumann et al. 1984). Before the 2000s, the limited angular resolution and contrast capabilities of ground- and space-based instruments led to the resolved optical or near-infrared imaging of only two such systems: β Pictoris and HR 4796 (Smith & Terrile 1984; Schneider et al. 1999). Recent advances in high-contrast imaging have enabled observations of many debris discs in scattered light, either in total intensity or polarimetry (e.g. Schneider et al. 2014; Esposito et al. 2020; Ren et al. 2023) using the *Hubble Space Telescope* (*HST*), Spectro-Polarimetric High-contrast Exoplanet REsearch (SPHERE; Beuzit et al. 2019) on the *Very Large Telescope* (*VLT*), and the Gemini Planet Imager (GPI; Macintosh et al. 2014). Such optical or near-infrared observations are sensitive to the starlight scattered by particles with sizes similar to or smaller than the wavelength, which dominate the scattering cross-section (Thebault & Kral 2019) and still have a sufficient scattering efficiency.

In parallel, over the past decade, millimetre and submillimetre interferometry has yielded images of such systems, including the recent REsolved ALMA and SMA Observations of Nearby Stars (REASONS; Matrà et al. 2025) survey, opening the path for a population study based on high spatial resolution images of 74 of such systems. The subsequent 'ALMA survey to Resolve exoKuiper belt Substructures' (ARKS; Marino et al. 2026b)

⋆ Corresponding author: julien.milli@univ-grenoble-alpes.fr

Open Access article, published by EDP Sciences, under the terms of the Creative Commons Attribution License (https://creativecommons.org/licenses/by/4.0), which permits unrestricted use, distribution, and reproduction in any medium, provided the original work is properly cited.
This article is published in open access under the Subscribe to Open model. Subscribe to A&A to support open access publication.

acquired the highest angular resolution on a subsample of 24 discs, reaching, for some systems, a similar resolution as optical or near-infrared imaging (~40 mas). As observations of dust thermal emission are most sensitive to particles with sizes similar to the observational wavelength (Hughes et al. 2018), the high resolution offered by the ARKS program presents the possibility to study, in detail, where the millimetre-sized dust grains are located. Comparing ALMA observations (millimetre-sized grains) to scattered light images (micron-sized particles or below, at the bottom of the collisional cascade) therefore allows mapping of the spatial distribution of grains with different sizes in the disc.

In optically thin discs, the orbits of the dust particles depend on various mechanisms on top of the stellar gravitational field. These include radiation and wind forces from the central star (Burns et al. 1979), collisions, gravitational perturbation due to planets, stellar companions (Mustill & Wyatt 2009; Nesvold et al. 2016; Farhat et al. 2023) or even the debris disc itself (Sefilian 2024), in addition to gas drag (Takeuchi & Artymowicz 2001). Small grains are typically affected more strongly by these non-gravitational forces than their larger counterparts (Pawellek et al. 2019).

The outward force induced by the star's radiation pressure is usually defined by its ratio, called β, to the opposing gravitational pull from the star. The value of β determines the nature of the orbits. In particular, the smallest dust grains created by collisions have a higher β value than larger grains, resulting in more elliptical orbits (with an eccentricity $e \sim \beta/(1-\beta)$, Strubbe & Chiang 2006). This effect naturally creates a dust size segregation that extends beyond the birth ring, with smaller dust particles seen at larger distances (Krivov 2010). This can result in an extended halo of small dust particles, which are detectable in scattered light with sensitive wide-band optical imagers (e.g. Schneider et al. 2018, for HR 4796) or with polarimetry (e.g. Olofsson et al. 2024, for HD 129590).

Conversely, Poynting-Robertson drag, which causes dust grains to lose angular momentum due to stellar radiation, can induce inward migration (Kennedy & Piette 2015; Pawellek et al. 2019; Su et al. 2024; Sommer et al. 2025). In late-type stars, strong stellar winds may also induce an inward migration, possibly even exceeding the Poynting-Robertson drag effect (Plavchan et al. 2005; Pawellek et al. 2019).

In the birth ring, where the dust density is the highest, the high collision rate will also impact the dust population through the grinding of bigger grains into smaller particles. Other dynamical effects in the debris disc may be due to the gravitational perturbation of planetary companions or gas drag for discs hosting a sufficient amount of gas. We now know of more than 20 debris discs that contain gas, both hot (Rebollido et al. 2018) and cold (Iglesias et al. 2018; Cataldi et al. 2023).

Theoretical studies have shown that small and large grains may undergo different migration in the presence of cold gas at a few tens of au (Takeuchi & Artymowicz 2001; Krivov et al. 2009). To test those theories against observational evidence, we propose using the ARKS sample to compare in detail the surface density of the millimetre-sized dust detected with ALMA in thermal emission with that of the micron-sized dust seen in scattered light with optical or near-infrared imagers.

The remainder of the paper proceeds as follows. After presenting the scattered light observations of the ARKS sample and the methodology in Sect. 2, we present the detections in Sect. 3. We compare the dust surface density as estimated from the scattered light images and thermal emission in Sect. 4. We place constraints on the presence of planets in Sect. 5 and discuss the results in Sect. 6 before concluding in Sect. 7.

2. The ARKS scattered light sample and methods

2.1. Description of the ARKS sample and scattered light observations

The 24 discs comprising the ARKS sample are listed in Table A.1 of Appendix A.1 along with important stellar properties. We refer the reader to Marino et al. (2026b) for a comprehensive description of the sample and its selection. All targets were observed with various high-contrast imagers. In particular, all of them were scrutinised by the SPHERE instrument and its near-infrared imager IRDIS (Beuzit et al. 2019). The shaded rows in Table A.1 show the 15 discs detected in scattered light and analysed in this paper. All but one of the scattered light detections are archival observations that have already been presented in the literature. The last column of Table A.1 lists those references. The only exception is TYC 9340-437-1, for which we present the first scattered-light detection obtained with the *HST* in Appendix B. For each target in this study, we used the instrument and observation that achieve the highest angular resolution while maintaining a sufficient signal-to-noise ratio (S/N) to allow for a meaningful analysis. In most cases, we used observations taken with SPHERE – IRDIS, either in linear polarisation or in total intensity. In one case, we used *GPI* in its polarimetric mode. For the faintest discs, or those with a low inclination, they could only be detected with the *HST*, with one of the following three instruments: the *Advanced Camera for Surveys* (ACS), the *Near Infrared Camera and Multi-Object Spectrometer* (NICMOS) or the *Space Telescope Imaging Spectrograph* (STIS).

2.2. Surface density extraction

The surface brightness of a disc scales differently with the distance to the star r in scattered light and thermal emission. Assuming a constant scattering efficiency across the disc, the scattered light scales as $1/r^2$ while the thermal emission scales as $1/\sqrt{r}$ in the Rayleigh-Jeans blackbody approximation of a dust temperature profile $T = 278.3 L_\star^{1/4} r^{-1/2}$ (Wyatt 2008), where T is in Kelvin, $L_\star$ is the stellar luminosity in solar units and r is in au. To be able to consistently compare the radial profiles from scattered light and thermal emission, we decided to compare the surface density profiles rather than the surface brightness profiles.

2.2.1. ALMA

For ALMA, we used the surface density as estimated with the non-parametric technique called *frank*[1] (Jennings et al. 2020; Terrill et al. 2023). Compared to the alternative non-parametric technique *rave* (Han et al. 2022, 2025), which uses images obtained with the *clean* image reconstruction technique when fitting to ALMA data, which can be imperfect, *frank* works directly in visibility space and can be more sensitive to very sharp features. As a double-check, we also compared the surface density with that extracted from a double power-law parametric modelling, because we employed the same functional form for the scattered light modelling. This form is often employed

[1] For one target, β Pictoris, *frank* is not reliable because it does not handle multiple pointings, so we used the alternative non-parametric technique *rave* operating in the image space.

to measure the steepness of the inner and outer profiles and infer the dynamical excitation of the disc. For single belts, the double power-law parametric modelling is consistent with the non-parametric approach, but this form does not fit well all the data, especially structured belts or multiple-ring which are better fit by more complex parametric forms (triple power law, double gaussian, possibly including gaps). In all cases (parametric or non-parametric approaches), the 1D radial brightness profiles of discs are converted to surface density profiles assuming a blackbody equilibrium temperature profile, stellar luminosities and the mass opacity as described in Marino et al. (2026b), i.e. $1.9\,\mathrm{cm^2\,g^{-1}}$ for ALMA Band 7, $1.3\,\mathrm{cm^2\,g^{-1}}$ for ALMA Band 6. A full description of the surface density extraction from the ALMA data is provided in Han et al. (2026) and Zawadzki et al. (2026).

2.2.2. Scattered light

For the scattered light observations, we fitted a scattered light model to the disc images where the dust surface density is parameterised with a double power-law, following the model introduced in Augereau et al. (2001) and detailed in Appendix C. This is a simple ray-tracing model without any dust physics. It assumes a constant scattering efficiency across the disc, and a non-isotropic scattering phase function (either a parametric form or an empirical scattering phase function). Because retrieving the total intensity image of a disc is different from retrieving the polarised intensity, the fitting procedure is also specific to each case.

In polarised intensity (written *pI* in Table A.1, which applies to HD 121617, AU Mic, β Pictoris, HR 4796, HD 145560 and HD 32297), we used the image corresponding to the azimuthal Stokes parameter Q_ϕ to directly fit a disc model convolved with the instrumental Point-Spread Function (PSF), following the methodology described in Olofsson et al. (2020).

For observations carried out in total intensity (written *I* in Table A.1), the processing is different whether the image comes from the *VLT – SPHERE*, from *HST – ACS* or from *HST – NICMOS*. For SPHERE images (HD 131835, HD 131488, AU Mic, HD 15115, 49 Ceti, HD 61005, HD 32297, HR 4796), the post-processing technique that allows the disc detection is angular differential imaging (ADI). In this case, finding the best model requires forward modelling, a technique where the disc model is subtracted from the data, which are then re-processed to analyse the residual image. These steps are repeated by adapting the disc model until the residuals are minimised. For the *HST – ACS* image of HD 10647 (q^1 Eri), we directly fitted a disc model to the image presented in Lovell et al. (2021). We did not perform any forward modelling, as the PSF subtraction technique applied is roll subtraction with a roll amplitude of ~25°. This amplitude is sufficiently large with respect to where the disc is detected to not be biased by self-subtraction artefacts (see Lovell et al. 2021, for details on the data reduction). For the *HST – NICMOS* image of TYC 9340-437-1, the post-processing technique to reveal the disc is reference differential imaging (see Appendix B), and the same forward modelling procedure as for the *VLT – SPHERE* images is applied.

There are three discs for which the dust surface densities were already extracted and presented in previous publications, namely HD 92945, HD 107146, and 49 Ceti (Golimowski et al. 2011; Ertel et al. 2011; Choquet et al. 2016). Therefore, we did not carry out dedicated forward modelling for these systems. For 49 Ceti, the exact same double-power law modelling was already presented in Choquet et al. (2016) based on VLT – SPHERE and *HST* – NICMOS data. We therefore re-used the published results, and show in this paper the best model detailed in their Table 1 for the VLT – SPHERE dataset, as both images had a similar S/N but VLT – SPHERE provides the highest angular resolution. For HD 92945, we used the published non-parametric surface density extracted in Golimowski et al. (2011), as this disc contains radial substructures that are not well represented by a double-power law profile. For HD 107146, the surface density was extracted in Ertel et al. (2011) with a parametric modelling akin to a double-power law profile.

We determined the best models with a Nested Sampling Monte Carlo framework (implemented in the Python package *PyMultiNest*, Buchner et al. 2014) using uniform priors. In particular, we did not use any prior information based on the ALMA best-fit models (Marino et al. 2026b). This was done on purpose not to bias the results. The only exception is TYC 9340-437-1, for which the S/N is poor, and therefore we had to fix the inclination and position angle to the best value found with ALMA. The best-fitting parameters are shown in Appendix D along with their associated uncertainty. For most discs, the inclination and position angle extracted from the ALMA and scattered light images are compatible at a 3σ level. However, there are six exceptions, highlighted in grey in Table D.1, corresponding to discs inclined by >74°: β Pictoris, HD 32297, HD 15115, AU Mic, HD 131835 and q^1 Eri. A discussion of these differences is given in Appendix D.

3. The ARKS discs detected in scattered light

3.1. Detection versus non-detection

Among the 24 discs of the ARKS sample, we detected 15 of them in scattered light and have nine non-detections (shaded vs non-shaded rows in Table A.1, respectively). Fig. 1 shows a mosaic of the scattered light images, overlaid with contours from the ALMA continuum. From the detections vs non-detections, some trends already emerge. Among the ten highly inclined discs (last ten rows in Table A.1), all except one (HD 14055, which has the lowest fractional luminosity $L_{\rm disc}/L_* < 10^{-4}$) are detected in scattered light. However, only six out of the 14 moderately inclined discs are recovered in scattered light, and these six discs are among the seven brightest in terms of fractional luminosity. More quantitatively, the faintest highly inclined disc detected in scattered light is q^1 Eri (HD 10647) with a fractional luminosity of 2.6×10^{-4} and the faintest moderately inclined disc detected in scattered light is HD 92945 with a fractional luminosity of 6.6×10^{-4} (Matrà et al. 2025). Previous scattered light surveys have indeed already shown that detections are strongly correlated with high infrared excess and highly inclined discs (Esposito et al. 2020; Engler et al. 2025). This is a combination of two effects: more dust intercepts the line of sight for inclined systems, and the scattering phase function generally favours forward scattering (Hapke 2012).

3.2. Systems with CO gas detections

Six of the 15 discs detected in scattered light also contain CO gas detected with ALMA and they are highlighted in bold face in Table A.1. We therefore also compared the dust surface density with the CO intensity extracted from the ALMA data, as detailed in the companion ARKS paper by Mac Manamon et al. (2026). The scattered light images are overlaid with the contours

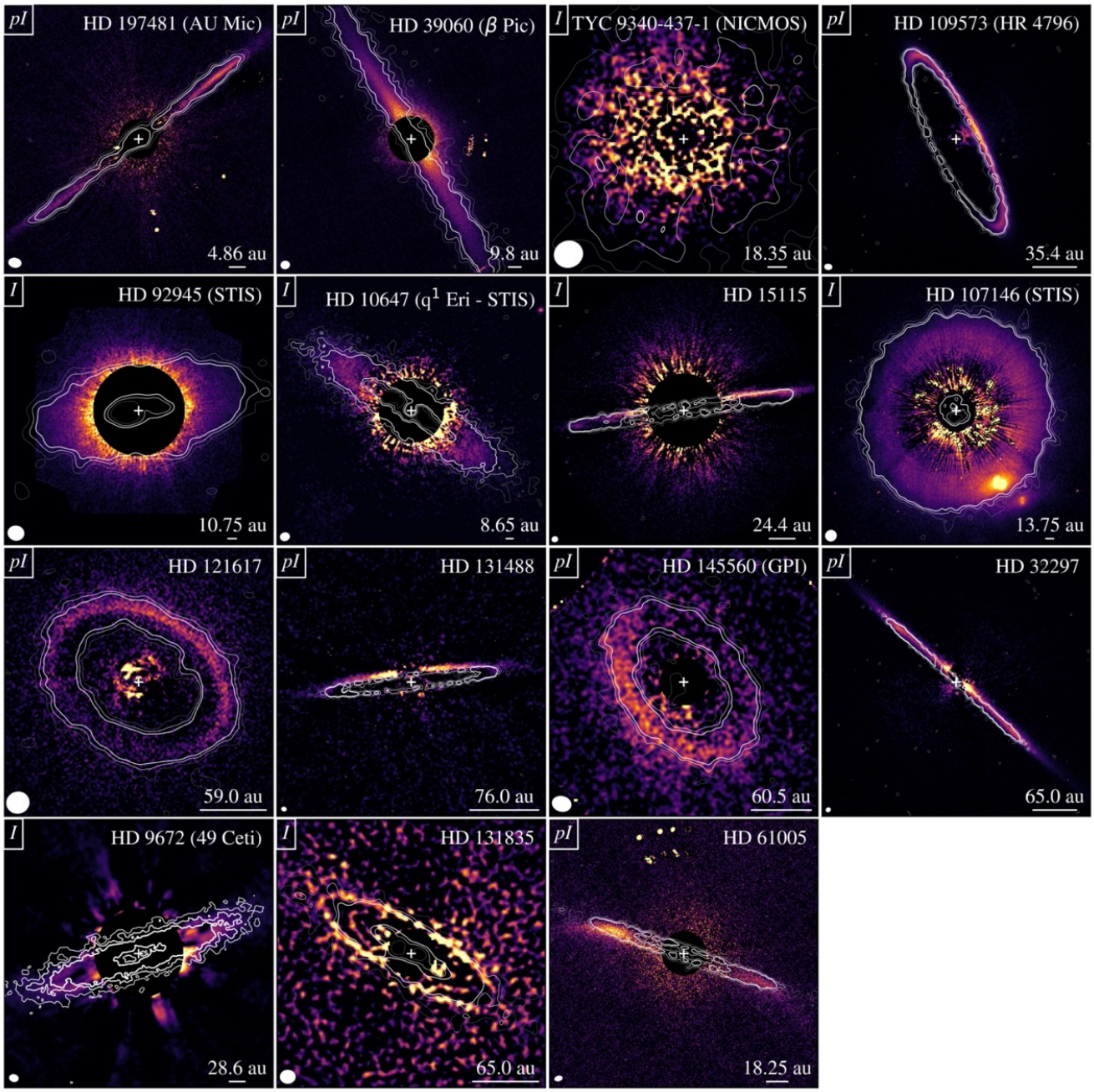

Fig. 1. ARKS discs detected in scattered light. The observations were made using the VLT – SPHERE instrument, unless otherwise specified. The discs denoted by '*I*' were observed in total intensity, whereas the ones with '*pI*' were observed in polarised light. The white line at the bottom right corner represents an angular scale of 0.5″, with the corresponding projected distance in au labelled in each panel. The white contours show the ALMA continuum observations, with three contour levels at a S/N of 3, 5 and 7 σ (see the corresponding ALMA image in Paper I Fig. 3 Marino et al. 2026b, for each disc). The white ellipse at the bottom left represents the ALMA image resolution and the white cross is the stellar position from GAIA DR3. For HD 131835, we show the image post-processed with the PACO algorithm (Flasseur et al. 2018), best highlighting the two rings. In all panels, North is up, East to the left.

of the ALMA ^{12}CO and ^{13}CO (J = 3–2) moment 0 maps (velocity integrated intensity) in Fig. 2 (for β Pictoris this is the J = 2–1 transition). Five of them are considered gas-rich, whereas HD 39060 (β Pictoris) is considered gas-poor ($M_{\rm CO} \lesssim 10^{-4}\ M_\oplus$).

4. Comparison of the radial profiles

The radial profiles of the dust surface density are shown in Fig. 3 and 4. The uncertainty on the scattered light profile is the 1-σ error estimated from the Monte Carlo fitting process[2]. The uncertainty on the ALMA surface density is the 1-σ error estimated from the *frank* algorithm[3] (Han et al. 2026).

[2] We sampled 100 profiles from the Monte Carlo posterior distribution parametrising the surface density, and defined the lower and upper uncertainty shown in Figs. 3 and 4 as the 16$^{\rm th}$ and 84$^{\rm th}$ percentile of the surface density for each distance in au.

[3] For β Pic where *rave* was used instead of *frank* to extract the ALMA dust surface density, the uncertainty is the 1-σ error estimated from *rave*.

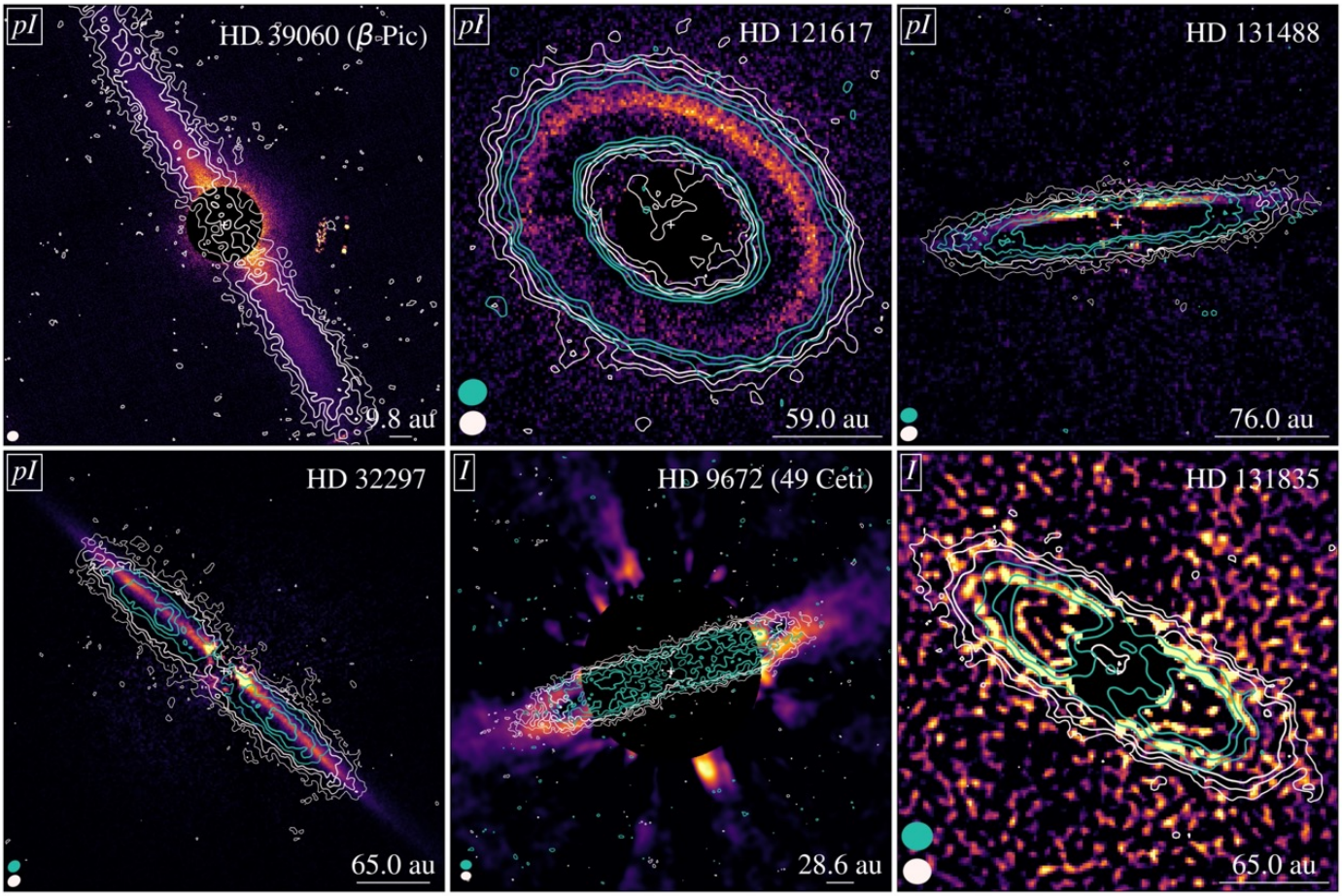

Fig. 2. Discs from the ARKS sample that have gas detections. The scattered light observations are the same as in Fig. 1. Overlaid on the scattered light images are the moment 0 maps for the gas observed with ALMA, using the robust values shown in Mac Manamon et al. (2026), i.e. 0.5 for β Pictoris, HD 121617, 49 Ceti, HD 131835 and 2.0 for HD 131488 and HD 32297. The ^{12}CO (J = 3–2 line) is plotted in white and the ^{13}CO (J = 3–2 line) in green, with the exception of β Pictoris where only the ^{12}CO (J = 2–1 line) is plotted, as this disc is not detected in ^{13}CO. For every disc, there are 3 contour levels, corresponding to 3, 5, and 7 σ. The ellipses at the bottom left (white for ^{12}CO and green for ^{13}CO) represent the beam size for the ALMA observations. In all panels, North is up, East to the left.

Table 1 displays the peak locations of the dust surface density. For the surface density extracted from the scattered light image, the peak location can be computed analytically based on the dust density parametrisation (see Appendix C.1 and Eq. (C.4)). The same can be done with the surface density extracted from the ALMA image (see Appendix C.2 and Eq. (C.6)). For the ALMA surface density extracted with the non-parametric approaches *frank* (or *rave* for β Pictoris), we defined the uncertainty on the peak location as the range of separations where the 1σ upper bound profile of the surface density is above the lower bound of the maximum surface density. Based on these values and uncertainties for the maximum surface density, we computed the relative offset between scattered light and ALMA. We describe the comparison to the ALMA parametric profiles only when there is disagreement with the ALMA non-parametric profiles.

We can distinguish three categories of discs, depending on this offset. When a zero offset is compatible with the 1σ uncertainty, we classify the offset as not significant (group described in Sect. 4.1). In the other cases, the offset can be either positive (meaning micron-sized dust is seen further out than millimetre-sized dust, described in Sect. 4.2) or negative (described in Sect. 4.3, for a single disc HD 61005).

4.1. Discs with no detectable offset

For eight out of the 15 considered discs, we found no detectable offset within our error bars. We outline these discs below.

HD 197481 (AU Mic). The main belt is resolved with ALMA into two separate peaks, the second one having a slightly higher surface density based on the *frank* extraction as reported in Table 1. The parametric modelling employed in scattered light does not allow this level of detail to be captured, and the surface density extracted in scattered light (total and polarised intensity) peaks at ~ 33 au, which is exactly in the middle of the two peaks seen with ALMA. When the ALMA observation is parametrised with the double power-law surface density profile as in scattered light, we find a relative offset of 2.6 ± 3.2%, and therefore we cannot offer a conclusion on the significance of an offset for AU Mic.

HD 39060 (β Pictoris). The ALMA dataset of β Pictoris used multiple pointings, and the *frank* algorithm does not appropriately deal with this observational setting. Therefore, we used instead the surface density extracted with the *rave* algorithm (see Fig. 3). In scattered light, we used the high S/N image of the disc obtained from deep polarimetric imaging in the H

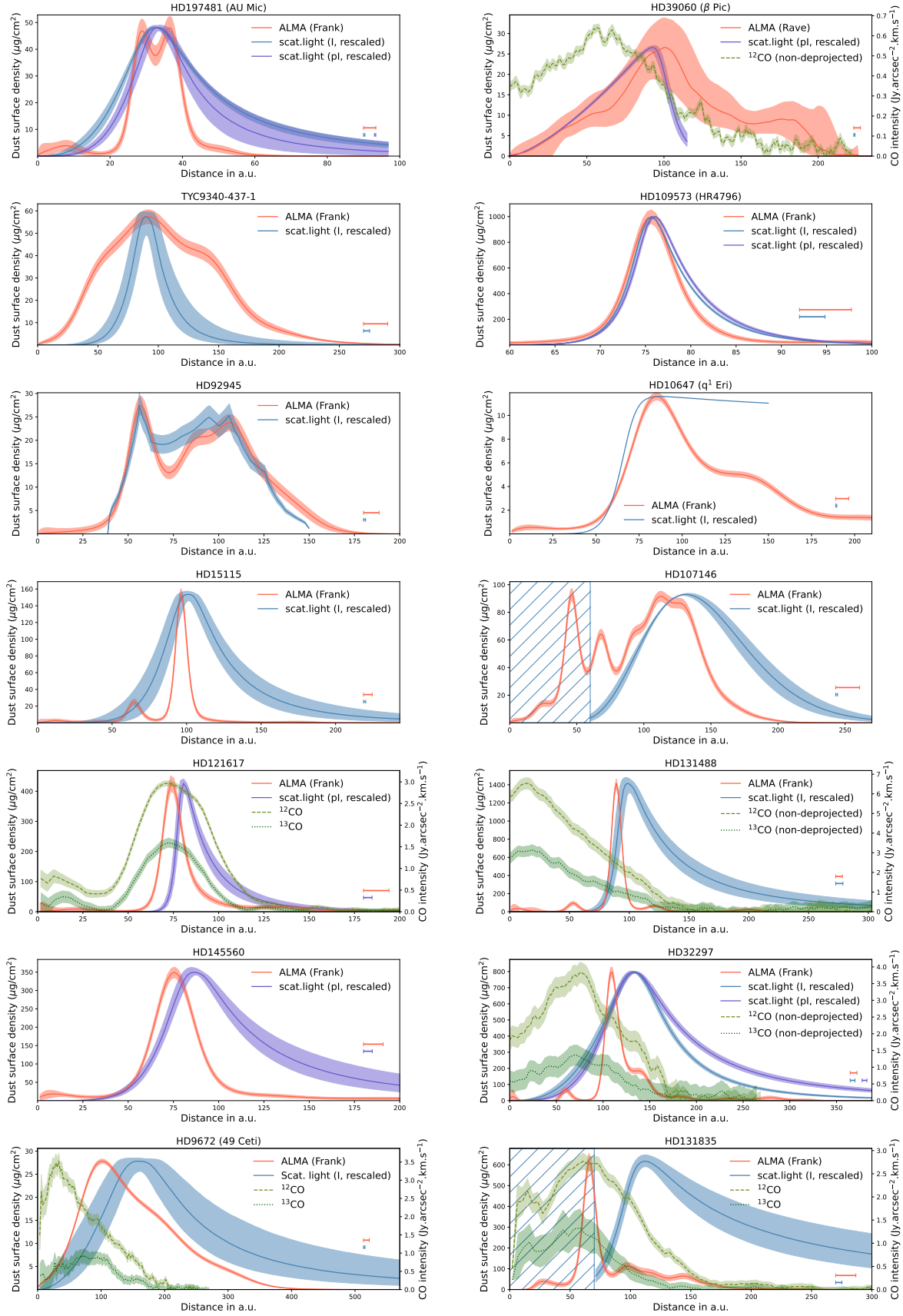

Fig. 3. Comparison of the dust surface densities extracted from the ALMA continuum image and from the scattered light image in total intensity (I) or polarised intensity (pI). The scattered light profiles are rescaled to the ALMA profiles for display. For systems with CO detected, the ^{12}CO or ^{13}CO intensity profile is overplotted. Blue hatched regions correspond to inner regions where no scattered light modelling could be performed. The scale in the bottom right-hand corner in each panel indicates the ALMA and scattered light image resolution.

Table 1. Radii of the maximum dust surface density measured in scattered light (second column) and in the ALMA continuum (third and fifth columns) together with the corresponding relative offset (fourth and sixth columns).

Name	Scatt. light au	ALMA (*frank*[a]) au	Rel. offset %	ALMA (double power law) au	Rel. offset %
Disc with no detectable offset in scattered light					
HD 197481	32.6 ± 0.6	$36.4^{+2.0}_{-2.5}$ [b]	$-10.5^{+6.4}_{-5.1}$	$31.8^{+1.1}_{-0.6}$	2.6 ± 3.2
HD 39060	$91.8^{+1.7}_{-1.9}$	$100.9^{+34.7}_{-63.7}$	-9^{+34}_{-31}	114.6 ± 5.0	-20.0 ± 4.0
TYC 9340-437-1	90.0 ± 4.9	$91.9^{+15.6}_{-15.9}$	-2 ± 17	$97.8^{+6.0}_{-7.0}$	-7.9 ± 7.8
HD 109573	75.6 ± 0.1	75.7 ± 1.1	0.0 ± 1.4	$76.7^{+0.3}_{-0.4}$	-1.4 ± 0.5
HD 92945	$56.1^{+4.4}_{-1.9}$	$56.5^{+4.6}_{-3.5}$	$-0.7^{+10.0}_{-8.8}$	$53.3^{+1.3}_{-1.2}$	$6.8^{+8.7}_{-4.2}$
HD 10647	87.3 ± 0.1	$86.0^{+4.6}_{-1.6}$	$1.5^{+1.9}_{-5.5}$	$75.6^{+1}_{-0.5}$	16.9 ± 1.2
HD 15115	$100.9^{+3.8}_{-4.0}$	96.3 ± 1.6	$4.7^{+4.3}_{-4.6}$	99.5 ± 0.4	$1.3^{+3.8}_{-4.1}$
HD 107146	$131.3^{+2.7}_{-1.8}$	$112.1^{+19.9}_{-5.6}$	$17.1^{+6.4}_{-20.8}$	NA	NA
Discs with an outward offset $> 1\sigma$ in scattered light					
HD 121617	$80.6^{+1.4}_{-1.1}$	$73.6^{+3.6}_{-2.0}$	$9.6^{+3.5}_{-5.6}$	$69.6^{+0.7}_{-0.5}$	15.8 ± 2.1
HD 131488	98.7 ± 3.6	$89.1^{+1.6}_{-1.4}$	$10.8^{+4.6}_{-4.3}$	$89.7^{+0.4}_{-0.3}$	10 ± 4
HD 145560	86.6 ± 2.5	$75.6^{+4.2}_{-4.4}$	$14.5^{+7.5}_{-7.2}$	73.8 ± 1.2	16.2 ± 3.9
HD 32297	133.3 ± 2.1	$108.4^{+1.9}_{-2.2}$	$23.0^{+3.2}_{-2.9}$	$106.6^{+0.7}_{-0.5}$	25.0 ± 2.1
HD 9672	159.4 ± 19	102.3 ± 11	$55.8^{+25.8}_{-24.4}$	106.1 ± 4	49.3 ± 19
HD 131835	$112.2^{+3.6}_{-3.2}$	$65.4^{+4.0}_{-2.1}$	$71.5^{+7.8}_{-11.6}$	61.9 ± 1	81 ± 7
Disc with an inward offset $> 1\sigma$ in scattered light					
HD 61005	$59.7^{+2.7}_{-2.4}$	$69.5^{+2.5}_{-2.8}$	$-14.1^{+5.2}_{-4.6}$	66.2 ± 0.6	-10.3 ± 3.4

Notes. Relative offsets are with respect to ALMA, and a positive offset indicates the scattered light surface density peaks at a larger distance. The discs are grouped in three categories, within which they are sorted with increasing relative offsets. The six discs with a CO detection are indicated with grey shading. [a]For β Pic, the *rave* profile was used instead of *frank* (see text for details). [b]For HD 197481, ALMA (*frank*) reveals two peaks. The maximum surface density is in the second peak, which is the value provided here, and it explains the negative offset. [c]For HD 107146, ALMA (*frank*) also displays three peaks, the offset is computed relative to the third peak, which corresponds to the ring seen in scattered light.

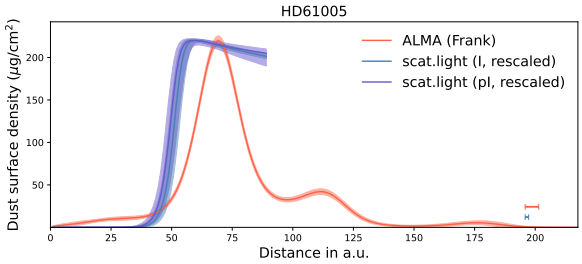

Fig. 4. Continued from Fig. 3.

band originally intended to measure the polarisation fraction of the planet β Pictoris b (van Holstein et al. 2021). Additionally, polarised images are not subject to self-subtraction (Milli et al. 2012, 2014), which gives more confidence in the extracted surface density. However, due to the large uncertainties on the ALMA dust surface density extracted from *rave*, the measured offset of $-8.6^{+22.1}_{-26.2}$% is not significant. While Fig. 3 may seem to show that the dust surface density seen in scattered light drops to zero beyond ~115 au, one should bear in mind that the SPHERE – IRDIS field of view does not go beyond that separation, but dust is detected up to several thousands of au in the β Pictoris system (Janson et al. 2021). The $1/r^2$ dependence of the scattered light intensity also makes it very challenging to probe the outermost regions.

TYC 9340-437-1. The S/N is poor, both in the *HST* – NICMOS scattered light image and in the ALMA continuum image (see Fig. 1). Therefore, the relative offset of -2 ± 17% has large uncertainty and is not significant. We also note that the surface density profiles in Fig. 3 may seem narrower in scattered light compared to the ALMA continuum. However, the poor S/N does not allow us to confidently determine whether there is a significant difference in width. Thus, a higher sensitivity scattered light observation is required to confidently compare both profiles.

HD 109573 (HR 4796). The ring around HR 4796 is very narrow and slightly eccentric (Milli et al. 2017) and the location of the peak surface density is identical between the scattered light measurements (both total and polarised intensity) and the ALMA continuum extracted with *frank*. The steep inner edge is similar between ALMA and SPHERE: $\alpha_{\rm in} = 34^{+5}_{-3}$ for the ALMA surface density and $\alpha_{\rm in} = 35.7 \pm 0.3$ for the SPHERE surface density. The smoother outer profile in scattered light ($\alpha_{\rm out} = -17.6 \pm 0.5$) compared to ALMA ($\alpha_{\rm out} = -21.7 \pm 1.8$) is real and likely due to the smallest dust particles being very sensitive to the stellar radiation pressure forming an extended halo already known from *HST* – STIS optical observations (Schneider et al. 2018).

HD 92945. The dust surface density profile shown in Fig. 3 is the best non-parametric model proposed by Golimowski et al. (2011) to reproduce the disc surface brightness of the *HST* – ACS image, assuming a 10% uncertainty on this profile. The

shape of this profile very closely matches the dust surface density extracted from the ALMA continuum, although with a slightly shallower gap. The peak positions reported in Table 1 correspond to the innermost ring, but both peak locations are compatible within error bars, showing no offset between the micron-sized and millimetre-sized dust.

HD 10647 (q^1 Eri). The best scattered light model shows a very smooth outer profile with a power-law exponent $\alpha_{\rm out} = -1.1$ up to ∼150 au, where the disc signal becomes too faint. Conversely, the ALMA continuum falls off steeply beyond 90 au but shows an extended halo centered at ∼160 au with a FWHM of ∼100 au (Han et al. 2026). Unlike most other systems, the disc is only detected in scattered light in the optical with *HST* – ACS in the F606W filter (central wavelength 589 nm), likely more sensitive to small eccentric submicron dust particles, which may tentatively explain the smooth surface density. Despite those differences, the offset in the peak surface density between scattered light and ALMA, as extracted from *frank*, is not significant. There is a significant offset with the ALMA peak profile when parametrised with a double power-law (16.9 ± 1.2%, see Table 1). However, this parametrisation is not the best functional form fitting the ALMA data (Han et al. 2026) compared to the double Gaussian, which peaks at 88 ± 4 au and for which no significant offset is detectable.

HD 15115 (the needle)[4]. HD 15115 is a double-ringed disc (MacGregor et al. 2019) seen close to edge-on. The polarised intensity of this disc is faint (Engler et al. 2019); therefore we used the SPHERE – IRDIS J-band total intensity image presented in Engler et al. (2019) for the surface density modelling. In the ALMA (*frank*) profile, the second peak at 96 ± 2 au is six times higher than the first peak at 65 ± 4 au, so we computed the relative offset between SPHERE and ALMA with respect to this second (and highest) peak. While the tentative offset of $4.7^{+4.3}_{-4.6}$% is just at 1σ, the offset computed with the ALMA double power law modelling of $1.3^{+3.8}_{-4.1}$% is not significant. Though this parametric modelling did not provide a good fit to the data, because of the second ring seen with ALMA, the double power law parametrisation with a gap is the preferred fit (Han et al. 2026), and it does not show an offset either ($3.9^{+4.3}_{-4.5}$%). We therefore cannot confirm the presence of an offset in this system. However, upon the assumption that the dust is being produced in the first and fainter ALMA ring, then the offset would be 56 ± 10%, and it would be statistically significant.

HD 107146. HD 107146 is a wide belt extending from 40 to 140 au with a gap at 56 au and a second one at 78 au. The ALMA *frank* profile suggests that an intermediate ring may be present within the gap (see companion paper Han et al. 2026). The disc is only detected in scattered light with the *HST* instruments (ACS, NICMOS and STIS, Ertel et al. 2011; Schneider et al. 2014). Using the ACS filter F606W (deemed more reliable than the F814W due to instrumental artefacts at short separations), Ertel et al. (2011) modelled the surface density of the disc with a parametric form (a product of a power-law and an exponential function analogous to Planck's law). The fitted profile is shown in Fig. 3. Due to the large coronagraph and the starlight residuals, the region within 60 au (orange-shaded region in Fig. 3) is not reliable in the ACS image used to extract the surface density profile (Ertel et al. 2011). More recent STIS images shown in Schneider et al. (2014) and reproduced in Fig. 1[5] show some level of emission in the inner 2″, suggesting that the region within 60 au may not be devoid of material as shown with ALMA, but we cannot confidently confirm this statement. We focus instead on the outer ring. An offset of $17.1^{+6.4}_{-20.8}$% is detected in the peak location between the scattered light and ALMA continuum. This offset is not statistically significant, and therefore we cannot rule out the fact that millimetre- and micron-sized dust grains are spatially collocated based on these observations. We note that the scattered light profile extends to larger separations, similar to q^1 Eri, and this again may be due to the fact that ACS images at optical wavelengths are sensitive to the halo of small grains extending farther from the star.

4.2. Discs with an outward offset in scattered light

For six out of the 15 considered discs, we find significant offsets, as outlined below.

HD 121617. HD 121617 is a narrow ring which shows a clear offset of $9.6^{+3.5}_{-5.6}$% between the polarised scattered light of the disc and the ALMA continuum surface density extracted with *frank*. This shift is also confirmed with the double power law parametrisation, and even more significant (15.8 ± 2.1%). This mismatch is visible with the naked eye in the image itself due to the low inclination of the disc (Fig. 1). CO gas is detected in this system and both ^{12}CO and ^{13}CO peak at a radius smaller than the location of the maximum scattered light peak (74.4 au vs $80.6^{+1.4}_{-1.1}$ au, see Mac Manamon et al. 2026; Brennan et al. 2026). This indicates that the millimetre-sized grains surface density peaks at a location consistent with the ^{13}CO, which is also the gas pressure maximum (Marino et al. 2026a). On the other hand, the micron-sized grains traced by scattered light are shifted outward, nearly 1sigma outward from the pressure maximum (based on the ^{13}CO best-fit radially Gaussian model).This is a location where the gradient is such that micron-sized dust could get stalled there if gas drag combined with radiation pressure play a dominant role in the grain dynamics, assuming sufficiently high total gas densities are present (Weber et al. 2026).

The scattered light image shows no azimuthal asymmetry (beyond the forward/backward side asymmetry, which is an effect of the anisotropy of scattering and not an azimuthal asymmetry in the surface density). This in contrast to the ALMA image, which is discussed in the companion ARKS papers Lovell et al. (2026); Marino et al. (2026a); Weber et al. (2026).

HD 131488. HD 131488 is another narrow ring (Pawellek et al. 2024) with a significant offset of $10.8^{+4.6}_{-4.3}$% detected between the total intensity scattered light and the ALMA continuum. The offset is consistent whether the ALMA surface density is extracted with *frank* or with the double power law parametrisation. Because of the close to edge-on geometry, the CO intensity profile cannot be reliably deprojected (Mac Manamon et al. 2026), but the non-deprojected profile still allows us to conclude that most of the CO resides inside the dust ring, with the micron-sized dust peaking close to the outer edge of the CO disc.

HD 145560. Despite the faintness of the disc in scattered light (Hom et al. 2020), with a detection only in polarised intensity and not in total intensity, an offset of $14.5^{+7.5}_{-7.2}$% at a 2σ confidence level is measured for HD 145560. This result should be taken with caution because of the poor S/N of the disc. This

[4] The term needle was coined by Kalas et al. (2007) because the disc is edge-on and very thin.

[5] The clump seen in the South of the image is a background galaxy.

is the only disc with an offset that is not known to contain CO gas. Gas may still be present but undetected in the system: the 3σ upper limit on the integrated line flux of ^{12}CO (3–2) is 67 mJy km/s, for a comparison, HD 131835, at a similar distance and age but with an earlier spectral type A2IV compared to F5V has a ^{12}CO (3–2) integrated line flux of 1.9 ± 0.2 Jy km/s (Mac Manamon et al. 2026).

HD 32297. HD 32297 is an edge-on disc (Bhowmik et al. 2019; Olofsson et al. 2022) with a significant offset of $23.0^{+3.2}_{-2.9}$% detected. This offset is consistent with both the total and polarised intensity images, and with the ALMA *frank* and the double power law parametrisation. We note that the location of the maximum surface density for micron-sized dust corresponds also to a small plateau in the millimetre-sized dust density seen with ALMA. HD 32297 is a CO-rich system, with the CO peak located interior to the dust ring. Due to the edge-on geometry of the disc, the CO line intensity cannot be deprojected, but the non-deprojected CO profile visible in Fig. 1 shows that the peak of the micron-sized dust particles occurs at a radius where the CO has dropped by more than 50%, similar to the case of HD 131488 discussed above.

HD 9672 (49 Ceti). A significant offset of $55.8^{+25.8}_{-24.4}$% is detected for 49 Ceti. Despite a large error bar due to the faintness of the disc in scattered light, the offset of 49.3 ± 19% using the double power-law rather than *frank* confirms this large offset. Both the SPHERE – IRDIS model presented here and the *HST* – NICMOS model presented in Choquet et al. (2016) confirm this offset. 49 Ceti is another gas-rich disc, with CO detected within the dust ring (see Fig. 3). The deprojected ^{12}CO intensity shows that the peak micron-sized dust surface density occurs where the ^{12}CO line intensity has already dropped by more than a factor of seven compared to its peak value.

HD 131835. This disc shows the largest offset among the ARKS targets, with a value of $71.5^{7.8}_{-11.6}$%. It is the subject of a dedicated companion paper (Jankovic et al. 2026) because of its complex structure. It hosts at least two rings detected in scattered light at 66 and 96 au (Feldt et al. 2017), the outer one being the brightest in scattered light (see Fig. 1 and Appendix E for more details taking into account possible post-processing biases), while ALMA only sees one prominent ring at ∼65 au. In this paper, we focus on and model the outer ring only, because the S/N is not sufficient to perform a full exploration of the inner and outer ring parameters. The micron-sized dust surface density shown in Fig. 3 only represents this outer ring, while regions within 70 au have been hatched. The peak in surface density from the scattered light modelling is located at $112.2^{+3.6}_{-3.2}$ au[6].

The ARKS paper Jankovic et al. (2026) explores two scenarios to explain this large offset: two planetesimal belts that appear very different in ALMA and SPHERE due to very different collisional properties, and a single planetesimal belt at 65 au with micron-sized dust pushed to >100 au by gas drag, creating the outer ring.

Intriguingly, the ALMA *frank* surface density profile shows a secondary peak with a lower amplitude slightly inward from the peak surface density of the outer ring, at 98 au. If there is indeed an outer parent belt distinct from the inner one at 98 au, the offset seen in scattered light would become $14.5^{+5.9}_{-5.7}$%, a value similar to the typical offset also found for the three other CO-rich discs HD 121617, HD 131488, and HD 32297. Comparing the peak surface density location with the deprojected CO intensity, we find, as for the other gas-rich discs, that the CO is mostly located within the dust rings, and that the scattered light peak radius occurs when the CO intensity has significantly dropped by more than half its maximum value. However, we note that *frank* modeling is not very robust for low S/N emission and oscillations can appear mimicking rings.

4.3. Disc with an inward offset in scattered light

HD 61005 (the moth). HD 61005 is a disc with an inner edge at ∼45 au, a main ring up to ∼80 au and a more diffuse 'swept-back' component, best seen with *HST* – STIS up to ∼240 au (Schneider et al. 2014). No gas has been detected in this system (Mac Manamon et al. 2026). With SPHERE, we detect the main ring and the halo up to ∼90 au (Fig. 4). It is the only ARKS disc with a significant negative relative offset between scattered light and thermal emission (see Table 1). Both the SPHERE total and polarised intensity images agree with a peak surface density occurring at a radius −14.1% ± 4.9% smaller than the ALMA continuum peak surface density. However, one must note that HD 61005 has a relatively broad belt seen in scattered light and the double-power law profile parametrised in Eq. (C.1) is not well adapted for broad belts without a clear peak. Secondly, the diffuse dust halo is not reproduced by the simple parametrisation of the dust surface density used in this work, because this halo is not aligned with the main ring. There are several possible explanations for that feature being seen misaligned with the main ring. The most likely is that the dust is pushed back from the disc plane as the system travels through the interstellar medium (Debes et al. 2009; Maness et al. 2009). The interstellar medium (ISM) can indeed blow the small grains from a system and influence the morphology of debris discs (Heras et al. 2025). An alternative scenario invokes a giant collision (Jones et al. 2023) although ISM sculpting is preferred for HD 61005.

5. Sensitivity to planets

Planetesimal belts can be influenced by the presence of giant planets in a system: they can sculpt the inner edge of a belt (as for the Kuiper belt, e.g. Malhotra 2019), carve a gap within a belt or trap planetesimals in resonance (as in TWA 7, see Lagrange et al. 2025), or interact with the dust creating asymmetries or warps (as in β Pictoris, e.g. Mouillet et al. 1997). We used the scattered light images obtained with SPHERE to derive uniform upper limits on the presence of planets among the ARKS sample, complemented by Gaia astrometric data. We present these results in Section 5.2, following a brief summary of the known planets in our sample in Section 5.1.

5.1. Known planets in the ARKS sample

Planets have been confirmed in six ARKS systems, all interior to the cold debris belts. Half of those debris belts are detected in scattered light: β Pictoris, AU Mic and HD 10647 (q^1 Eri), none of them which have a significant offset between the peak surface brightness seen with ALMA and in scattered light. There are 2 transiting planets orbiting AU Mic, both Neptune-sized bodies with periods of 8.5 and 18.9 days (Plavchan et al. 2020;

[6] This location of the peak surface density is larger than the value obtained with the best model presented in Feldt et al. (2017) and Eq. (C.4), which is 105 ± 4 au after taking into account the updated distance to the star of 129.7 pc compared to 123 pc in Feldt et al. (2017). Both values are still compatible within 1σ.

Gilbert et al. 2022). A radial-velocity planet was detected at 2 au around HD 10647, with a minimum mass of $\sim 1 M_{\rm Jup}$ (Butler et al. 2006; Marmier et al. 2013). The other planets were detected with direct techniques (direct imaging or interferometry, sometimes confirmed with radial-velocity or astrometry). Two giant planets orbit β Pictoris at ~10 and ~3 au, with masses of 10–11$M_{\rm Jup}$ and $7.8 \pm 0.4 M_{\rm Jup}$, respectively (Lagrange et al. 2009, 2020).

The other three systems known to host planets do not have their disc detected in scattered light. HD 95086 host a 4–5 $M_{\rm Jup}$ giant planet orbiting in ~51–73 au range (Rameau et al. 2013; Desgrange et al. 2022). HD 206893 contains a giant planet of $\sim 13 M_{\rm Jup}$ at ~3.5 au and a brown dwarf of $\sim 28 M_{\rm Jup}$ at ~10 au (Hinkley et al. 2023). Four giant planets of 6 to $12 M_{\rm Jup}$ orbit the HR 8799 system between 15 and 65 au (Marois et al. 2008; Thompson et al. 2023).

5.2. Constraints on the presence of additional planets

To assess the sensitivity to planets in our sample of stars, we generate detection probability maps (DPMs) based on the achieved contrast limits from archival SPHERE observations. All 24 targets in our sample have archival SPHERE data, and for each system, we select the observation that provides the deepest contrast using the dual-band H23 or broad-band H filters. We refer the reader to Appendix A.2 for the list of observations and filters. To ensure consistency across the sample, all contrast curves have been uniformly reduced using a Principal Component Analysis algorithm (Soummer et al. 2012; Amara & Quanz 2012), as implemented in the SPHERE High-Contrast Data Center (HC-DC, Delorme et al. 2017).

The DPMs were computed on a 2D grid of planet mass and semi-major axis using the *MADYS* (Squicciarini & Bonavita 2022) and *ExoDMC* (Bonavita 2020) tools. Because contrast curves are expressed as a function of projected separation, and DPMs operate in deprojected orbital space, we account for each system's inclination (taken from Marino et al. 2026b, and also reported in Table A.1) and sample a range of orbital configurations at every grid point. We also sample planet eccentricity by using a half-Gaussian distribution[7] centred at 0 with a standard deviation of 0.1 for all the systems. For each orbit, the planet's projected separation is calculated, and its mass is converted into magnitude using the system's age and the *bex-atmo2023-ceq* planet evolutionary model in *MADYS*, which combines the ATMO (Phillips et al. 2020) and BEX (Linder et al. 2019) models as in Carter et al. (2021). A planet is considered detectable if its brightness exceeds the SPHERE contrast limit at the corresponding projected separation. This process is repeated across different ages, accounting for the system's age uncertainty. The detection probability at each grid point is then defined as the fraction of simulated planets that would be detectable.

The DPMs can be seen in Fig. 5 for the moderately inclined systems and Fig. 6 for the very inclined systems. The blue shaded region in these plots indicates the probability of making a 5σ detection of a planet, if such a planet existed, with the contours representing the 99.7%, 95% and 50% levels. For three systems: HD 92945, HD 107146, and HD 206893, we also show the 99.7% contour from JWST MIRI coronagraphy at 11.4 μm for comparison (Bendahan-West et al., in prep.).

Additional planet constraints are overlaid on the SPHERE DPMs. Vertical dashed lines indicate the inner and outer edges of the disc, as well as the boundaries of any observed gaps, where the disc information comes from the ALMA modelling detailed in Han et al. (2026). Dynamically unstable regions, defined as the zones within three Hill radii ($\rm R_{Hill}$) of the disc or gap edges, are highlighted in orange hatching, with $1\rm R_{Hill}$ defined as

$$\rm R_{Hill} \equiv a_p \left(\frac{m_p}{3 m_*} \right)^{1/3}, \quad (1)$$

where a_p is the planet semi-major axis, and m_p and m_* are the planet and star masses, respectively. A planet on a circular orbit within $3\rm R_{Hill}$ of a disc edge, i.e. within the orange hatched region, would likely disrupt the observed disc morphology (e.g. Gladman 1993; Pearce & Wyatt 2014; Pearce et al. 2022, 2024). We use Gaia astrometry and the renormalised unit weight error (RUWE) to construct the grey dotted region and exclude more planet parameters, only when RUWE < 1.4. We follow the approach of Limbach et al. (2024) for constraining companions with orbital periods shorter than the Gaia DR3's 1038-day baseline, and that of Kiefer et al. (2025) for longer-period systems. In systems with significant proper motion anomaly (PMa), i.e. S/N > 3 in the Kervella et al. (2022) catalogue, we include a blue curve showing the planet parameters capable of reproducing the observed PMa. This curve is calculated following the approach described in Kervella et al. (2019) and assuming a single planet in a circular orbit as done in Marino et al. (2020). Finally, known planets in the systems are shown as orange dots. Full details on the construction of these DPMs are presented in Bendahan-West et al. (under review).

Interpreting the DPMs enables us to place observational upper limits on undetected planets across our sample. These limits on planet mass and semi-major axis, reported in Table 2, are given at the 99.7% and 50% confidence level for three specific scenarios. First, we consider a single planet sculpting the inner edge of the disc via scattering, with upper limits identified by the intersection of the DPM contours and the $3\rm R_{Hill}$ dynamically unstable orange region. The corresponding minimum mass for such planet would be defined by the diffusion timescale (e.g. Pearce et al. 2022, 2024), which in all cases is below the mass upper limits that we report. This means that we cannot rule out the presence of a planet that carved the disc inner edge via scattering. Second, we report observational upper limits on planet mass at the location(s) of the observed gap(s). While the presence of a planet within a gap is a plausible explanation for its origin, many other mechanisms can also produce similar features (e.g. Pearce et al. 2015; Zheng et al. 2017; Yelverton & Kennedy 2018; Sefilian et al. 2021, 2023); exploring the full range of gap-carving scenarios lies beyond the scope of this work. Third and finally, the full DPMs allow us to place tighter constraints on companions responsible for the significant PMa observed in some systems. For systems with known PMa companions, the corresponding parameters are listed in Table 2.

Except for the two Gigayear-old systems HD 15257 and HD 76582 for which our sensitivity is poor because of their age, direct imaging achieves typical sensitivity between 1 and 10 $M_{\rm Jup}$ beyond 10 to 20 au. This region can be further restrained by considering the dynamically unstable regions within 3 Hill radii of the disc edges. All the discovered planets with direct imaging are well within this region. We note that for inclined systems (see Fig. 6), the 50% probability contour and the 95% are well apart, indicating that single-epoch imaging does not entirely rule out the presence of giant planets even at relatively large separations depending on their projected separation. We obtained the deepest dataset on the young nearby low-mass star AU Mic, achieving a 50% sensitivity of $0.8 M_{\rm Jup}$ at ~30 au.

[7] Negative values are discarded.

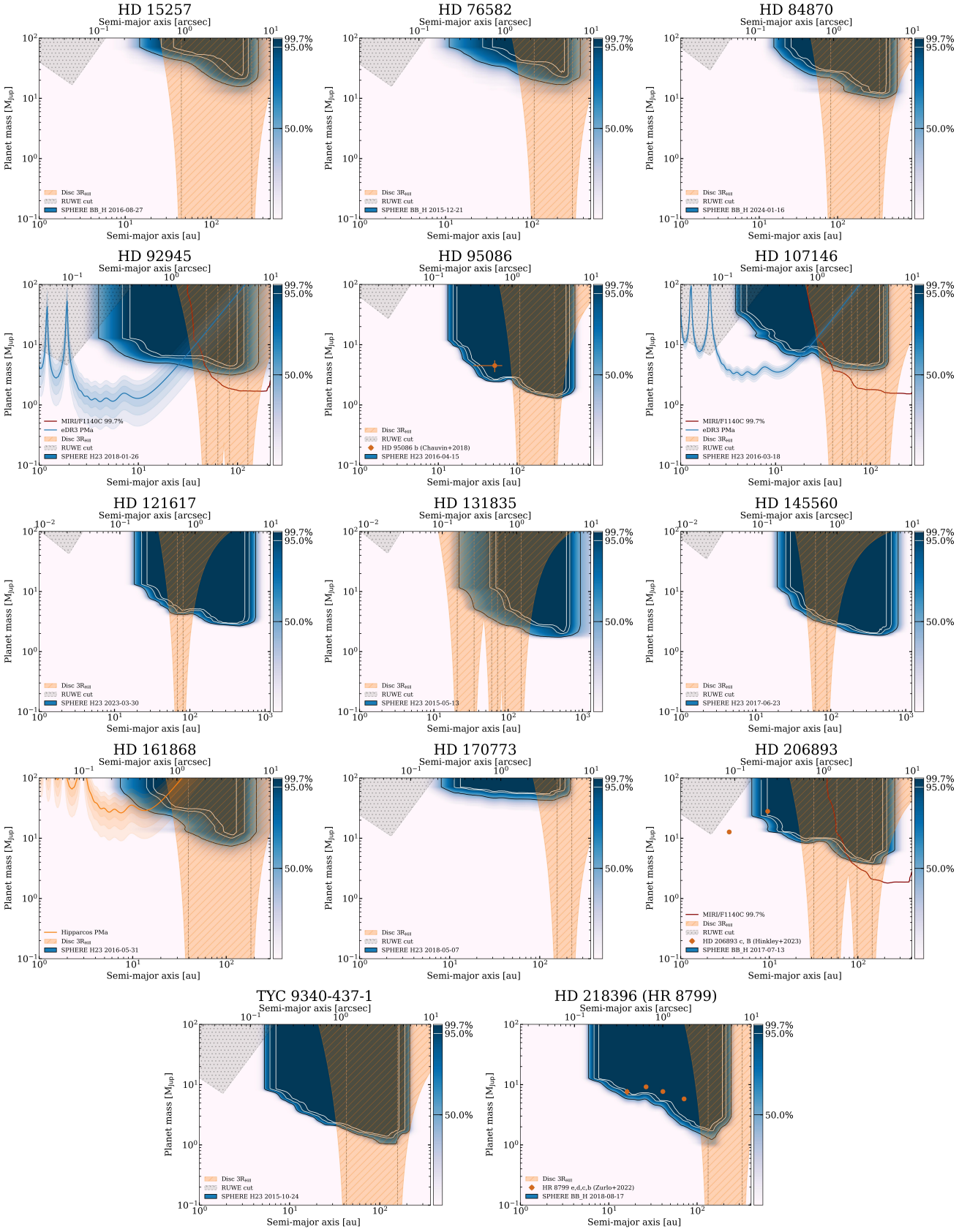

Fig. 5. SPHERE DPMs for the moderately inclined systems. The blue regions with contours at 99.7%, 95%, and 50% indicate the probability of detecting a planet at a 5σ level with SPHERE. For three systems, HD 92945, HD 107146, and HD 206893, the 99.7% JWST/MIRI F1140C contour is shown in red for comparison. The orange hatched areas denote the 3R$_{Hill}$ regions from the disc edges, where 1R$_{Hill}$ is defined as Eq. (1). Constraints from Gaia RUWE are indicated by grey dotted regions. The light blue curve marks the mass and location of a planet required to explain the significant proper motion anomaly. In systems with known planets, their positions are shown as orange dots.

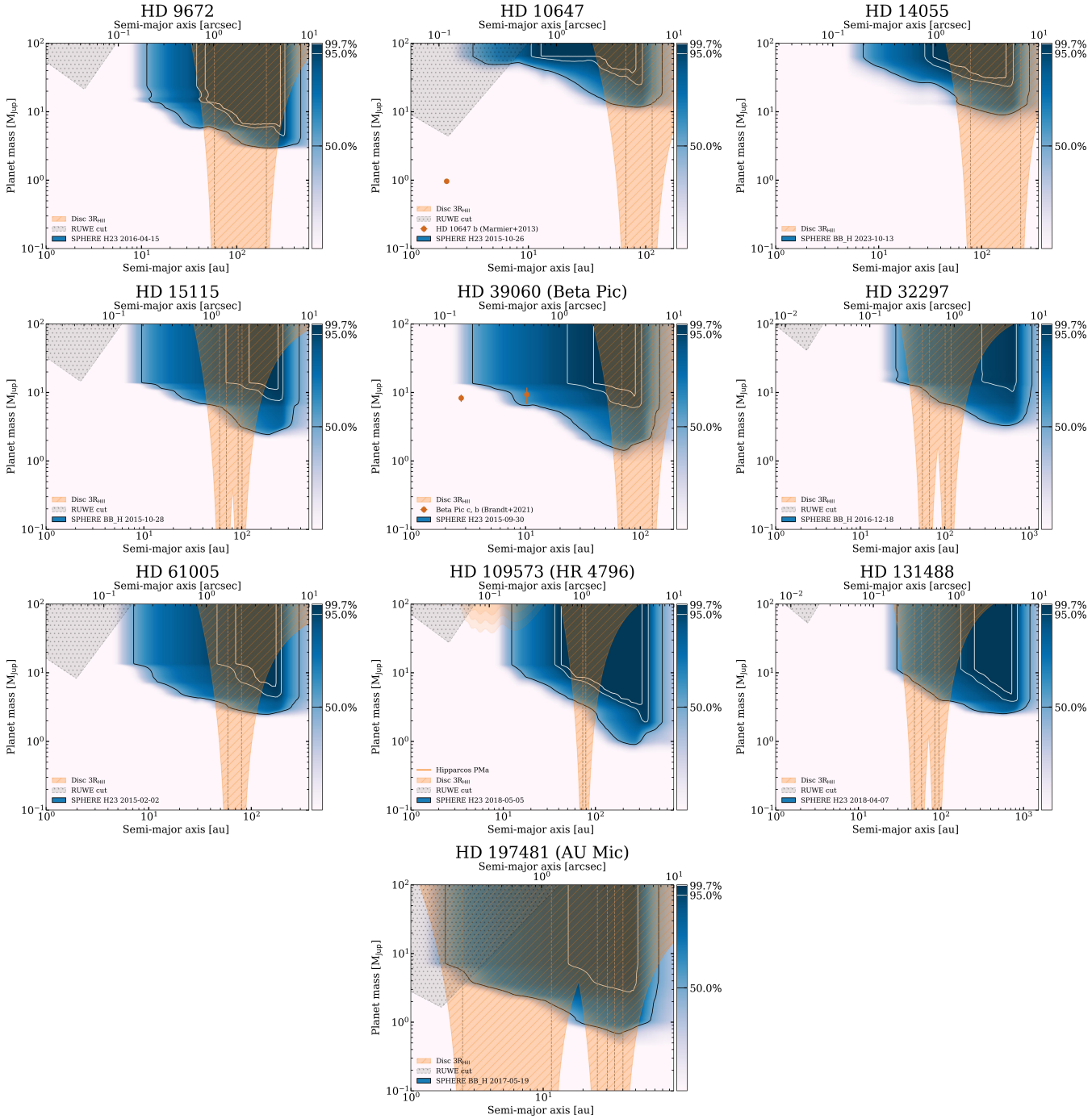

Fig. 6. Same as for Fig. 5 but for the highly inclined systems.

6. Discussion

For the first time, we can compare near-infrared and sub-millimetre images with comparable angular resolution for a sample of debris discs. This opens a new discovery space, allowing to determine offsets in the peak surface density as probed by scattered light and the ALMA continuum. Determining these offsets is fundamental to reveal the dynamical processes affecting the dust and the possible signatures of unseen planets (Thebault et al. 2014). It requires a careful methodology to take into account the different resolution and sensitivity of both regimes. Depending on the system considered, we are typically sensitive to offsets between 1 and 10 au. Our comparison between the disc surface density as probed by ALMA and scattered light images, summarised in Table 1, shows that there are no significant offsets ($>1\sigma$) between millimetre-sized and micron-sized grains for about half of the ARKS discs detected in scattered light. Interestingly, for five of the six discs with CO gas detection, an offset $>1\sigma$ is measured. There are two exceptions, β Pictoris and HD 145560. β Pictoris is a CO-bearing disc with no significant offset. However, there is a large uncertainty on the offset. This is because the edge-on geometry of this disc makes the scattered light surface density extraction less reliable than less inclined systems, and the presence of an asymmetric CO clump

Table 2. Planet mass upper limits and corresponding semi-major axes from the DPMs.

Star	Planet carving inner edge		Planet in gap(s)		PMa companion	
	a_p (au)	m_p (M_{Jup})	a_p (au)	m_p (M_{Jup})	a_p (au)	m_p (M_{Jup})
HD 9672	– (45)	– (6)	x	x	x	x
HD 10647 (q^1 Eri)	38 (46)	60 (13)	x	x	x	x
HD 14055	50 (55)	50 (17)	x	x	x	x
HD 15115	– (44)	– (7)	79	– (4.5)	x	x
HD 15257	– (28)	– (49)	x	x	x	x
HD 32297	– (39)	– (13)	80	– (8)	x	x
HD 39060 (β Pictoris)	49 (58)	13 (1.5)	x	x	2.74 ± 0.03 (2)	8.3 ± 1.0 (2)
HD 61005	– (44)	– (4)	x	x	x	x
HD 76582	65 (71)	50 (24)	x	x	x	x
HD 84870	52 (55)	34 (23)	x	x	x	x
HD 92945	34 (36)	6.5 (4)	72	4.5 (3) [a]	2–30	0.4–5
HD 95086	87 (85)	2.9 (2.4)	x	x	x	x
HD 107146	28 (29)	9 (6)	57, 79	5 (4), 4.5 (3.8) [b]	2.5–20	2.5–8
HD 109573 (HR 4796)	54 (58)	10 (4)	x	x	4–38	30–400
HD 121617	52 (54)	7 (4.5)	x	x	x	x
HD 131488	– (35)	– (10)	69	– (5.5)	x	x
HD 131835	– (–)	– (–)	42, 85	– (4.5), 9 (3)	x	x
HD 145560	47 (49)	5.5 (4)	x	x	x	x
HD 161868	26 (27)	37 (22)	x	x	3–25	9–100
HD 170773	92 (95)	53.5 (42)	x	x	x	x
HD 197481 (AU Mic)	– (–)	– (–)	17, 32	– (1.1), – (0.7)	x	x
HD 206893	22.5 (23)	10 (8.5)	73	6.5 (4.5) [c]	3.53 ± 0.07 (1)	12.7 ± 1.1 (1)
TYC 9340-437-1	33 (33)	2.3 (2)	x	x	x	x
HD 218396 (HR 8799)	109 (110)	2 (1.5)	x	x	16.10 ± 0.03 (3)	7.6 ± 0.9 (3)

Notes. All values are quoted at the 99.7% confidence level, with those in brackets indicating the 50% level. Dashes indicate regions where the observation lack sensitivity. A cross (x) marks systems with no detected gaps and no significant proper motion anomaly (PMa). Upper limits are provided for three scenarios: a planet carving the disc's inner edge, a planet located at the gap(s), and a planet responsible for the PMa. [(a)]Deeper mass upper limit observed in gap location with JWST – MIRI F1140C: 2 M_{Jup} (3σ); Bendahan-West et al. (under review). [(b)]Deeper mass upper limit observed in gap location with JWST – MIRI F1140C: 3 M_{Jup}, 1.8 M_{Jup} (3σ); Bendahan-West et al. (under review). [(c)]Deeper mass upper limit observed in gap location with JWST – MIRI F1140C: 5 M_{Jup} (3σ); Bendahan-West et al. (under review). Planet references: [(1)]Hinkley et al. (2023), [(2)]Brandt et al. (2021), [(3)] Zurlo et al. (2022).

(Matrà et al. 2017) makes the interpretation of this system more difficult. It is also worth noting that while β Pictoris has gas detections, it is relatively gas poor compared to the other ARKS gas-bearing discs, with a line luminosity a factor 4 to 22 times fainter. We should note that this factor does not account for optical depth which is likely significantly above 1 for the gas-rich ARKS discs (Brennan et al. 2026; Mac Manamon et al. 2026), and would push the gas-to-dust mass ratios higher. In that sense, all gas-rich discs in the sample have scattered light profiles that peak further out than ALMA. Conversely, all discs with a further out scattered light peak than ALMA but HD 145560 are gas-rich. HD 145560 is not known to host CO gas and has a significant offset detected. If CO gas is present in this system, the derived upper limit excludes a CO integrated line flux higher than 5% than that of HD 131835 (Mac Manamon et al. 2026), a disc of similar age and distance with a somewhat earlier spectral type.

Figure 7 provides a summary of the offsets measured between the peak surface densities of millimetre and micron-sized dust. The vertical axis shows the amount of CO detected in those systems (blue circles) or the CO upper limits for systems without detected CO (black triangles). Despite a large scatter, the offsets seem to be higher for systems with more gas. Part of the scatter can be minimised if the outer ring of HD 131835 seen in scattered light corresponds to the marginally detected outer ring seen with ALMA, resulting in a smaller offset of $14.5^{+5.9}_{-5.7}$%.

Considering the individual CO-bearing systems, the peak of the micron-sized dust surface density probed in scattered light usually occurs when the gas intensity has significantly dropped (see Fig. 3). We should keep in mind that this statement would only be stronger if we consider that the ^{12}CO and ^{13}CO are optically thick, because the CO surface density will likely have dropped more steeply than the (saturated) intensity profile suggests. This observation is in a good accordance with the theoretical prediction of Takeuchi & Artymowicz (2001). If the gas pressure decreases with radius, as seen in those systems at radii where dust is detected, the gas orbital motion is sub-Keplerian. It orbits at a velocity $v_K\sqrt{1-\eta}$ where v_K is the Keplerian velocity and $\eta > 0$ is the ratio between the pressure gradient and the gravitational force. Without any drag force, the dust orbits at a velocity $v_K\sqrt{1-\beta}$, meaning that large grains with small $\beta < \eta$ rotate faster than the gas and small grains with larger $\beta > \eta$ rotate slower than the gas. In this case, the back-wind felt by the small grains causes an outward migration and the head-wind felt by the large grains causes an inward migration. The migration halts when the grains feel no net torque. For small grains close to the blow-out size ($\beta = 0.5$), simulations show that they tend to concentrate in the regions where the gas density is rapidly declining with radius (Takeuchi & Artymowicz 2001). The case of HD 121617 seems to defy this quantitative explanation looking at the integrated CO line flux in Fig. 3, but because

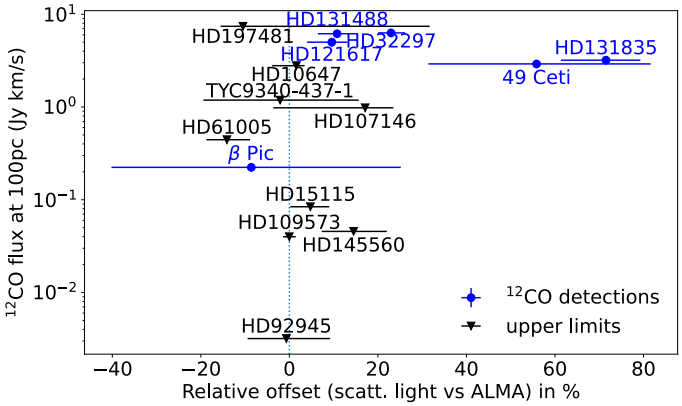

Fig. 7. Integrated intensity of ^{12}CO (J = 3–2) scaled at 100 pc (from Mac Manamon et al. 2026) as a function of the relative offset of the millimetre- and micrometre-sized dust surface densities (positive offset means the micrometre-sized dust peaks further than the millimetre-sized dust). The six discs with a CO detection are shown in blue, while CO non-detections appear in black. The upper limit for AU Mic refers to the ^{12}CO (J = 2–1) as no (J = 3–2) is available (Mac Manamon et al. 2026).

of optical depth effect, the intensity profile is much broader than the actual CO surface density profile, and the ^{12}CO will indeed have dropped significantly at the location of the scattered light peak.

7. Conclusions

Out of the 24 discs included in the ARKS sample, 15 are detected in scattered light, comprising the targets that are most highly inclined or have the greatest fractional luminosities. The reported detections were made with at least one of these three facilities: *VLT* (SPHERE), *Gemini* (GPI), or *HST* (NICMOS, STIS or ACS). Moreover, the entire ARKS sample has been observed by the VLT – SPHERE instrument. TYC 9340-437-1 is detected for the first time in scattered light with *HST* – NICMOS, but follow-up observations with a higher sensitivity are necessary to compare the micron-sized dust surface density with that from millimetre-sized dust seen with ALMA in this system. With a parametric modelling approach, we show that six of the 15 discs show a significant offset in the peak surface density of the dust detected in scattered light with respect to that in thermal emission. The six discs are HD 32297, HD 131488, HD 131835, 49 Ceti, HD 121617, and HD 145560. Such dust segregation by size may happen for dust particles exposed to the gas drag on top of the radiation pressure of the central star, and CO gas has been confirmed in five of the six discs (Mac Manamon et al. 2026). This effect was predicted in theoretical works (Takeuchi & Artymowicz 2001; Krivov 2010). Detailed hydrodynamical modelling is now required to confirm this observation (Olofsson et al., in prep.).

For many systems, interpretation is limited by the low S/N of the scattered light disc image, with bright stellar residuals that are difficult to disentangle from the disc brightness. Higher sensitivity images would allow us to perform a non-parametric surface density extraction, for instance, with the *rave* algorithm, which was recently adapted to also handle polarised scattered light in addition to thermal emission images (Han et al. 2022, 2025). The comparison to mid-infrared images also represents a promising and complementary future prospect to confirm the offsets measured in this work and probe thermal emission of warmer dust closer to the star compared to ALMA, as shown for Fomalhaut, Vega, or ϵ Eri with JWST (Gáspár et al. 2023; Su et al. 2024; Wolff et al. 2025).

Acknowledgements. This paper makes use of the following ALMA data: ADS/JAO.ALMA# 2022.1.00338.L, 2012.1.00142.S, 2012.1.00198.S, 2015.1.01260.S, 2016.1.00104.S, 2016.1.00195.S, 2016.1.00907.S, 2017.1.00167.S, 2017.1.00825.S, 2018.1.01222.S and 2019.1.00189.S. ALMA is a partnership of ESO (representing its member states), NSF (USA) and NINS (Japan), together with NRC (Canada), MOST and ASIAA (Taiwan), and KASI (Republic of Korea), in cooperation with the Republic of Chile. The Joint ALMA Observatory is operated by ESO, AUI/NRAO and NAOJ. The National Radio Astronomy Observatory is a facility of the National Science Foundation operated under cooperative agreement by Associated Universities, Inc. The project leading to this publication has received support from ORP, that is funded by the European Union's Horizon 2020 research and innovation programme under grant agreement No 101004719 [ORP]. We are grateful for the help of the UK node of the European ARC in answering our questions and producing calibrated measurement sets. This research used the Canadian Advanced Network For Astronomy Research (CANFAR) operated in partnership by the Canadian Astronomy Data Centre and The Digital Research Alliance of Canada with support from the National Research Council of Canada the Canadian Space Agency, CANARIE and the Canadian Foundation for Innovation. We respectfully acknowledge the University of Arizona is on the land and territories of Indigenous peoples. Today, Arizona is home to 22 federally recognised tribes, with Tucson being home to the O'odham and the Yaqui. Committed to diversity and inclusion, the University strives to build sustainable relationships with sovereign Native Nations and Indigenous communities through education offerings, partnerships, and community service. JM thanks the members of the EPOPEE project (Etude des POussières Planétaires Et Exoplanétaires) for the useful discussions. EPOPEE is a research group funded by the 'Programme National de Planétologie' (PNP) of CNRS-INSU in France, from which JM and MB acknowledge financial support. JM thanks Steve Ertel, Stanimir Metchev and Andras Gaspàr for providing the HD 107146 *HST* – STIS data, which was published by the sorely missed Glenn Schneider (Schneider et al. 2014). SPHERE is an instrument designed and built by a consortium consisting of IPAG (Grenoble, France), MPIA (Heidelberg, Germany), LAM (Marseille, France), LESIA (Paris, France), Laboratoire Lagrange (Nice, France), INAF Osservatorio di Padova (Italy), Observatoire de Genève (Switzerland), ETH Zurich (Switzerland), NOVA (Netherlands), ONERA (France) and ASTRON (Netherlands) in collaboration with ESO. SPHERE was funded by ESO, with additional contributions from CNRS (France), MPIA (Germany), INAF (Italy), FINES (Switzerland) and NOVA (Netherlands). SPHERE also received funding from the European Commission Sixth and Seventh Framework Programmes as part of the Optical Infrared Coordination Network for Astronomy (OPTICON) under grant number RII3-Ct-2004-001566 for FP6 (2004–2008), grant number 226604 for FP7 (2009–2012) and grant number 312430 for FP7 (2013–2016). This work has made use of the High Contrast Data Centre, jointly operated by OSUG/IPAG (Grenoble), PYTHEAS/LAM/CeSAM (Marseille), OCA/Lagrange (Nice), Observatoire de Paris/LESIA (Paris), and Observatoire de Lyon/CRAL, and supported by a grant from Labex OSUG@2020 (Investissements d'avenir – ANR10 LABX56). MB acknowledges funding from the Agence Nationale de la Recherche through the DDISK project (grant No. ANR-21-CE31-0015). RBW was supported by a Royal Society Grant (RF-ERE-221025). JPM acknowledges research support by the National Science and Technology Council of Taiwan under grant NSTC 112-2112-M-001-032-MY3. E.C. acknowledges funding from the European Union (ERC, ESCAPE, project No 101044152). SMM acknowledges funding by the European Union through the E-BEANS ERC project (grant number 100117693), and by the Irish research Council (IRC) under grant number IRCLA-2022-3788. Views and opinions expressed are however those of the author(s) only and do not necessarily reflect those of the European Union or the European Research Council Executive Agency. Neither the European Union nor the granting authority can be held responsible for them. Support for BZ was provided by The Brinson Foundation. A.A.S. is supported by the Heising-Simons Foundation through a 51 Pegasi b Fellowship. TDP is supported by a UKRI Stephen Hawking Fellowship and a Warwick Prize Fellowship, the latter made possible by a generous philanthropic donation. SM acknowledges funding by the Royal Society through a Royal Society University Research Fellowship (URF-R1-221669) and the European Union through the FEED ERC project (grant number 101162711). S.E. is supported by the National Aeronautics and Space Administration through the Exoplanet Research Program (Grant No. 80NSSC23K0288, PI: Faramaz). MRJ acknowledges support from the European Union's Horizon Europe Programme under the Marie Sklodowska-Curie grant agreement no. 101064124 and funding provided by the Institute of Physics Belgrade, through the grant by the Ministry of Science, Technological Development, and Innovations of the Republic of Serbia. PW acknowledges support from FONDECYT grant 3220399 and ANID –

Millennium Science Initiative Program – Center Code NCN2024_001. LM acknowledges funding by the European Union through the E-BEANS ERC project (grant number 100117693), and by the Irish research Council (IRC) under grant number IRCLA-2022-3788. AB acknowledges research support by the Irish Research Council under grant GOIPG/2022/1895. CdB acknowledges support from the Spanish Ministerio de Ciencia, Innovación y Universidades (MICIU) and the European Regional Development Fund (ERDF) under reference PID2023-153342NB-I00/10.13039/501100011033, from the Beatriz Galindo Senior Fellowship BG22/00166 funded by the MICIU, and the support from the Universidad de La Laguna (ULL) and the Consejería de Economía, Conocimiento y Empleo of the Gobierno de Canarias. AMH acknowledges support from the National Science Foundation under Grant No. AST-2307920. JBL acknowledges the Smithsonian Institute for funding via a Submillimeter Array (SMA) Fellowship, and the North American ALMA Science Center (NAASC) for funding via an ALMA Ambassadorship. SP acknowledges support from FONDECYT Regular 1231663 and ANID – Millennium Science Initiative Program – Center Code NCN2024_001.

References

Amara, A., & Quanz, S. P. 2012, MNRAS, 427, 948
Apai, D., Schneider, G., Grady, C. A., et al. 2015, ApJ, 800, 136
Ardila, D. R., Golimowski, D. A., Krist, J. E., et al. 2004, ApJ, 617, L147
Artymowicz, P., Burrows, C., & Paresce, F. 1989, ApJ, 337, 494
Augereau, J. C., Lagrange, A. M., Mouillet, D., Papaloizou, J. C. B., & Grorod, P. A. 1999, A&A, 348, 557
Augereau, J. C., Nelson, R. P., Lagrange, A. M., Papaloizou, J. C. B., & Mouillet, D. 2001, A&A, 370, 447
Aumann, H. H., Gillett, F. C., Beichman, C. A., et al. 1984, ApJ, 278, L23
Beuzit, J. L., Vigan, A., Mouillet, D., et al. 2019, A&A, 631, A155
Bhowmik, T., Boccaletti, A., Thébault, P., et al. 2019, A&A, 630, A85
Boccaletti, A., Thalmann, C., Lagrange, A.-M., et al. 2015, Nature, 526, 230
Boccaletti, A., Sezestre, E., Lagrange, A. M., et al. 2018, A&A, 614, A52
Bonavita, M. 2020, Exo-DMC: Exoplanet Detection Map Calculator, Astrophysics Source Code Library [record ascl:2010.008]
Brandt, G. M., Brandt, T. D., Dupuy, T. J., Li, Y., & Michalik, D. 2021, AJ, 161, 179
Brennan, A., Matrà, L., Mac Manamon, S., et al. 2026, A&A, 705, A201
Buchner, J., Georgakakis, A., Nandra, K., et al. 2014, A&A, 564, A125
Burns, J. A., Lamy, P. L., & Soter, S. 1979, Icarus, 40, 1
Butler, R. P., Wright, J. T., Marcy, G. W., et al. 2006, ApJ, 646, 505
Cao, P.-C., Liu, Q., Liao, N.-H., Yang, Q.-C., & Huang, D. 2023, Res. Astron. Astrophys., 23, 085002
Carter, A. L., Hinkley, S., Bonavita, M., et al. 2021, MNRAS, 501, 1999
Cataldi, G., Aikawa, Y., Iwasaki, K., et al. 2023, ApJ, 951, 111
Chauvin, G., Gratton, R., Bonnefoy, M., et al. 2018, A&A, 617, A76
Choquet, É., Pueyo, L., Hagan, J. B., et al. 2014, SPIE Conf. Ser., 9143, 914357
Choquet, É., Perrin, M. D., Chen, C. H., et al. 2016, ApJ, 817, L2
Choquet, É., Milli, J., Wahhaj, Z., et al. 2017, ApJ, 834, L12
Choquet, É., Bryden, G., Perrin, M. D., et al. 2018, ApJ, 854, 53
Debes, J. H., Weinberger, A. J., & Kuchner, M. J. 2009, ApJ, 702, 318
Delorme, P., Meunier, N., Albert, D., et al. 2017, in SF2A-2017: Proceedings of the Annual meeting of the French Society of Astronomy and Astrophysics
Desgrange, C., Chauvin, G., Christiaens, V., et al. 2022, A&A, 664, A139
Duchêne, G., Rice, M., Hom, J., et al. 2020, AJ, 159, 251
Engler, N., Boccaletti, A., Schmid, H. M., et al. 2019, A&A, 622, A192
Engler, N., Milli, J., Pawellek, N., et al. 2025, A&A, 704, A21
Ertel, S., Wolf, S., Metchev, S., et al. 2011, A&A, 533, A132
Esposito, T. M., Kalas, P., Fitzgerald, M. P., et al. 2020, AJ, 160, 24
Farhat, M. A., Sefilian, A. A., & Touma, J. R. 2023, MNRAS, 521, 2067
Feldt, M., Olofsson, J., Boccaletti, A., et al. 2017, A&A, 601, A7
Flasseur, O., Denis, L., Thiébaut, É., & Langlois, M. 2018, A&A, 618, A138
Gáspár, A., Wolff, S. G., Rieke, G. H., et al. 2023, Nat. Astron., 7, 790
Gilbert, E. A., Barclay, T., Quintana, E. V., et al. 2022, AJ, 163, 147
Gladman, B. 1993, Icarus, 106, 247
Golimowski, D. A., Krist, J. E., Stapelfeldt, K. R., et al. 2011, AJ, 142, 30
Hagan, J. B., Choquet, É., Soummer, R., & Vigan, A. 2018, AJ, 155, 179
Han, Y., Wyatt, M. C., & Matrà, L. 2022, MNRAS, 511, 4921
Han, Y., Wyatt, M. C., & Marino, S. 2025, MNRAS, 537, 3839
Han, Y., Mansell, E., Jennings, J., et al. 2026, A&A, 705, A196
Hapke, B. 2012, Icarus, 221, 1079
Henyey, L. G., & Greenstein, J. L. 1941, ApJ, 93, 70
Heras, A. M., Eiroa, C., del Burgo, C., Marshall, J. P., & Montesinos, B. 2025, A&A, 694, A325
Hinkley, S., Lacour, S., Marleau, G. D., et al. 2023, A&A, 671, L5
Hom, J., Patience, J., Esposito, T. M., et al. 2020, AJ, 159, 31
Hughes, A. M., Duchêne, G., & Matthews, B. C. 2018, Annu. Rev. Astron. Astrophys., 56, 541
Iglesias, D., Bayo, A., Olofsson, J., et al. 2018, MNRAS, 480, 488
Jankovic, M. R., Pawellek, N., Zander, J., et al. 2026, A&A, 705, A204
Janson, M., Brandeker, A., Olofsson, G., & Liseau, R. 2021, A&A, 646, A132
Jennings, J., Booth, R. A., Tazzari, M., Rosotti, G. P., & Clarke, C. J. 2020, MNRAS, 495, 3209
Jones, J. W., Chiang, E., Duchêne, G., Kalas, P., & Esposito, T. M. 2023, ApJ, 948, 102
Kalas, P., Fitzgerald, M. P., & Graham, J. R. 2007, ApJ, 661, L85
Kennedy, G. M., & Piette, A. 2015, MNRAS, 449, 2304
Kervella, P., Arenou, F., Mignard, F., & Thévenin, F. 2019, A&A, 623, A72
Kervella, P., Arenou, F., & Thévenin, F. 2022, A&A, 657, A7
Kiefer, F., Lagrange, A.-M., Rubini, P., & Philipot, F. 2025, A&A, 702, A76
Krivov, A. V. 2010, Res. Astron. Astrophys., 10, 383
Krivov, A. V., Herrmann, F., Brandeker, A., & Thébault, P. 2009, A&A, 507, 1503
Lagrange, A.-M., Gratadour, D., Chauvin, G., et al. 2009, A&A, 493, L21
Lagrange, A. M., Rubini, P., Nowak, M., et al. 2020, A&A, 642, A18
Lagrange, A. M., Wilkinson, C., Mâlin, M., et al. 2025, Nature, 642, 905
Limbach, M. A., Vanderburg, A., Venner, A., et al. 2024, ApJ, 973, L11
Linder, E. F., Mordasini, C., Mollière, P., et al. 2019, A&A, 623, A85
Lovell, J. B., Marino, S., Wyatt, M. C., et al. 2021, MNRAS, 506, 1978
Lovell, J. B., Wyatt, M. C., Kalas, P., et al. 2022, MNRAS, 517, 2546
Lovell, J. B., Hales, A. S., Kennedy, G. M., et al. 2026, A&A, 705, A200
Mac Manamon, S., Matrà, L., Marino, S., et al. 2026, A&A, 705, A198
MacGregor, M. A., Weinberger, A. J., Nesvold, E. R., et al. 2019, ApJ, 877, L32
Macintosh, B., Graham, J. R., Ingraham, P., et al. 2014, PNAS, 111, 12661
Maire, A.-L., Langlois, M., Dohlen, K., et al. 2016, SPIE Conf. Ser., 9908
Malhotra, R. 2019, Geosci. Lett., 6, 12
Maness, H. L., Kalas, P., Peek, K. M. G., et al. 2009, ApJ, 707, 1098
Marino, S., Zurlo, A., Faramaz, V., et al. 2020, MNRAS, 498, 1319
Marino, S., Gupta, V., Weber, P., et al. 2026a, A&A, 705, A202
Marino, S., Matrà, L., Hughes, A. M., et al. 2026b, A&A, 705, A195
Marmier, M., Ségransan, D., Udry, S., et al. 2013, A&A, 551, A90
Marois, C., Lafrenière, D., Macintosh, B., & Doyon, R. 2008, ApJ, 673, 647
Marshall, J. P., Milli, J., Choquet, É., et al. 2018, ApJ, 869, 10
Marshall, J. P., Milli, J., Choquet, E., et al. 2023, MNRAS, 521, 5940
Matrà, L., Wyatt, M. C., Kraal, Q., et al. 2017, MNRAS, 464, 1415
Matrà, L., Marino, S., Wilner, D. J., et al. 2025, A&A, 693, A151
Milli, J., Mouillet, D., Lagrange, A.-M., et al. 2012, A&A, 545, A111
Milli, J., Lagrange, A.-M., Mawet, D., et al. 2014, A&A, 566, A91
Milli, J., Vigan, A., Mouillet, D., et al. 2017, A&A, 599, A108
Mouillet, D., Lagrange, A.-M., Beuzit, J.-L., & Renaud, N. 1997, A&A, 324, 1083
Mustill, A. J., & Wyatt, M. C. 2009, MNRAS, 399, 1403
Nesvold, E. R., Naoz, S., Vican, L., & Farr, W. M. 2016, ApJ, 826, 19
Olofsson, J., Samland, M., Avenhaus, H., et al. 2016, A&A, 591, A108
Olofsson, J., Milli, J., Bayo, A., Henning, T., & Engler, N. 2020, A&A, 640, A12
Olofsson, J., Thébault, P., Kennedy, G. M., & Bayo, A. 2022, A&A, 664, A122
Olofsson, J., Thébault, P., Bayo, A., Henning, T., & Milli, J. 2024, A&A, 688, A42
Pawellek, N., Moór, A., Pascucci, I., & Krivov, A. V. 2019, MNRAS, 487, 5874
Pawellek, N., Moór, A., Kirchschlager, F., et al. 2024, MNRAS, 527, 3559
Pearce, T. D., & Wyatt, M. C. 2014, MNRAS, 443, 2541
Pearce, T. D., Wyatt, M. C., & Kennedy, G. M. 2015, MNRAS, 448, 3679
Pearce, T. D., Launhardt, R., Ostermann, R., et al. 2022, A&A, 659, A135
Pearce, T. D., Krivov, A. V., Sefilian, A. A., et al. 2024, MNRAS, 527, 3876
Perrot, C., Olofsson, J., Kral, Q., et al. 2023, A&A, 673, A39
Phillips, M. W., Tremblin, P., Baraffe, I., et al. 2020, A&A, 637, A38
Plavchan, P., Jura, M., & Lipscy, S. J. 2005, ApJ, 631, 1161
Plavchan, P., Barclay, T., Gagné, J., et al. 2020, Nature, 582, 497
Rameau, J., Chauvin, G., Lagrange, A.-M., et al. 2013, ApJ, 772, L15
Rebollido, I., Eiroa, C., Montesinos, B., et al. 2018, A&A, 614, A3
Ren, B., Pueyo, L., Perrin, M. D., Debes, J. H., & Choquet, É. 2017, SPIE Conf. Ser., 10400, 1040021
Ren, B. B., Rebollido, I., Choquet, É., et al. 2023, A&A, 672, A114
Schneider, G., Smith, B. A., Becklin, E. E., et al. 1999, ApJ, 513, L127
Schneider, G., Grady, C. A., Hines, D. C., et al. 2014, AJ, 148, 59
Schneider, G., Debes, J. H., Grady, C. A., et al. 2018, AJ, 155, 77
Sefilian, A. A. 2024, ApJ, 966, 140
Sefilian, A. A., Rafikov, R. R., & Wyatt, M. C. 2021, ApJ, 910, 13
Sefilian, A. A., Rafikov, R. R., & Wyatt, M. C. 2023, ApJ, 954, 100
Smith, B. A., & Terrile, R. J. 1984, Science, 226, 1421
Sommer, M., Wyatt, M., & Han, Y. 2025, MNRAS, 539, 439
Soummer, R., Pueyo, L., & Larkin, J. 2012, ApJ, 755, L28
Soummer, R., Perrin, M. D., Pueyo, L., et al. 2014, ApJ, 786, L23
Squicciarini, V., & Bonavita, M. 2022, A&A, 666, A15

Strubbe, L. E., & Chiang, E. I. 2006, ApJ, 648, 652
Su, K. Y. L., Gáspár, A., Rieke, G. H., et al. 2024, ApJ, 977, 277
Takeuchi, T., & Artymowicz, P. 2001, ApJ, 557, 990
Tanner, A., Plavchan, P., Bryden, G., et al. 2020, PASP, 132, 084401
Terrill, J., Marino, S., Booth, R. A., et al. 2023, MNRAS, 524, 1229
Thebault, P., & Kral, Q. 2019, A&A, 626, A24
Thebault, P., Kral, Q., & Augereau, J. C. 2014, A&A, 561, A16
Thompson, W., Marois, C., Do Ó, C. R., et al. 2023, AJ, 165, 29
van Holstein, R. G., Stolker, T., Jensen-Clem, R., et al. 2021, A&A, 647, A21
Weber, P., Pérez, S., Baruteau, C., et al. 2026, A&A, 705, A203
Wolff, S. G., Gáspár, A., Rieke, G., et al. 2025, AJ, 170, 244
Wyatt, M. C. 2008, ARA&A, 46, 339
Yelverton, B., & Kennedy, G. M. 2018, MNRAS, 479, 2673
Zawadzki, B., Fehr, A., Hughes, A. M., et al. 2026, A&A, 705, A197
Zheng, X., Lin, D. N. C., Kouwenhoven, M. B. N., Mao, S., & Zhang, X. 2017, ApJ, 849, 98
Zurlo, A., Goździewski, K., Lazzoni, C., et al. 2022, A&A, 666, A133

[1] Univ. Grenoble Alpes, CNRS, IPAG, 38000 Grenoble, France
[2] European Southern Observatory, Karl-Schwarzschild-Strasse 2, 85748 Garching bei München, Germany
[3] Department of Physics and Astronomy, University of Exeter, Stocker Road, Exeter EX4 4QL, UK
[4] Academia Sinica Institute of Astronomy and Astrophysics, 11F of AS/NTU Astronomy-Mathematics Building, No.1, Sect. 4, Roosevelt Rd, Taipei 106319, Taiwan
[5] Aix Marseille Université, CNRS, CNES, LAM, Marseille, France
[6] Department of Astronomy and Steward Observatory, The University of Arizona, 933 North Cherry Ave, Tucson, AZ 85721, USA
[7] Division of Geological and Planetary Sciences, California Institute of Technology, 1200 E. California Blvd., Pasadena, CA 91125, USA
[8] Department of Astronomy, Van Vleck Observatory, Wesleyan University, 96 Foss Hill Dr., Middletown, CT 06459, USA
[9] School of Physics, Trinity College Dublin, the University of Dublin, College Green, Dublin 2, Ireland
[10] Instituto de Astrofísica de Canarias, Vía Láctea S/N, La Laguna, 38200 Tenerife, Spain
[11] Departamento de Astrofísica, Universidad de La Laguna, La Laguna, 38200 Tenerife, Spain
[12] Joint ALMA Observatory, Avenida Alonso de Córdova 3107, Vitacura 7630355, Santiago, Chile
[13] UK Astronomy Technology Centre, Royal Observatory Edinburgh, Blackford Hill, Edinburgh EH9 3HJ, UK
[14] Department of Astronomy, University of California, Berkeley, Berkeley, CA 94720-3411, USA
[15] Large Binocular Telescope Observatory, The University of Arizona, 933 North Cherry Ave, Tucson, AZ 85721, USA
[16] Astronomy Department, University of California, Berkeley, CA 94720, USA
[17] SETI Institute, Carl Sagan Center, 339 Bernardo Ave., Suite 200, Mountain View, CA 94043, USA
[18] Max-Planck Institute für Astronomie, Königstuhl 17, 69117 Heidelberg, Germany
[19] Institute of Physics Belgrade, University of Belgrade, Pregrevica 118, 11080 Belgrade, Serbia
[20] Astrophysikalisches Institut und Universitätssternwarte, Friedrich-Schiller-Universität Jena, Schillergässchen 2–3, 07745 Jena, Germany
[21] Center for Astrophysics | Harvard & Smithsonian, 60 Garden St, Cambridge, MA 02138, USA
[22] Department of Physics and Astronomy, Johns Hopkins University, 3400 N Charles Street, Baltimore, MD 21218, USA
[23] Herzberg Astronomy & Astrophysics, National Research Council of Canada, 5071 West Saanich Road, Victoria, BC V9E 2E9, Canada
[24] Department of Physics & Astronomy, University of Victoria, 3800 Finnerty Rd, Victoria, BC V8P 5C2, Canada
[25] Konkoly Observatory, HUN-REN Research Centre for Astronomy and Earth Sciences, MTA Centre of Excellence, Konkoly-Thege Miklós út 15–17, 1121 Budapest, Hungary
[26] Institut für Astrophysik (IfA), University of Vienna, Türkenschanzstraße 17, 1180 Vienna, Austria
[27] Department of Physics, University of Warwick, Gibbet Hill Road, Coventry CV4 7AL, UK
[28] Departamento de Física, Universidad de Santiago de Chile, Av. Víctor Jara 3493, Santiago, Chile
[29] Millennium Nucleus on Young Exoplanets and their Moons (YEMS), Chile
[30] Center for Interdisciplinary Research in Astrophysics Space Exploration (CIRAS), Universidad de Santiago, Chile
[31] Institute of Astronomy, University of Cambridge, Madingley Road, Cambridge CB3 0HA, UK

Appendix A: The ARKS sample and the scattered light dataset

A.1. Overall ARKS sample

Table A.1 lists the 24 discs comprising the ARKS sample, along with important stellar properties.

A.2. SPHERE data sets

Table A.2 details the VLT - SPHERE datasets used for the modelling of the ARKS discs detected in scattered light and for the derivation of the planet sensitivity limits.

Appendix B: TYC 9340-437-1

TYC 9340-437-1 is an M dwarf debris disc member of the β Pictoris moving group at a distance of 36.7 pc. It was spatially resolved for the first time by *Herschel*-PACS at a wavelength of 100 µm (Tanner et al. 2020) suggesting a face-on inclination. ALMA revealed a higher resolution view of the disc at a wavelength of 1.33 mm, suggesting the disc architecture is a broad ring at 130 au (100 au width) and moderate inclination ($i = 40^{\circ}{}_{-20^{\circ}}^{+10^{\circ}}$).

HST - NICMOS observations were carried out on UT date 2004-09-15, with the F160W filter ($\lambda = 1.601$ µm, $\Delta\lambda = 0.390$ µm). Although Tanner et al. (2020) reported a non-detection from *HST* - NICMOS observations, we revisited the NICMOS data that were obtained as part of the coronagraphic program # 10176 (PI: I. Song). The total on-source integration time was 1855 seconds. Eight frames were taken at two different spacecraft orientations 30° apart. Instead of using this angular diversity to subtract the stellar Point-Spread Function (PSF), we used the multi-reference star differential imaging PSF-subtraction method developed for the ALICE program (Choquet et al. 2014; Hagan et al. 2018). We assembled and registered large and homogeneous libraries of 33 coronagraphic images from the NICMOS archive, gathering images from multiple reference stars observed as part of several *HST* programs. These libraries were used to subtract the star Point-Spread Function (PSF) from each exposure of the science target with the Principal Component Analysis (PCA) KLIP algorithm (Soummer et al. 2012). This technique has proven successful in detecting many faint discs in scattered light (Soummer et al. 2014; Choquet et al. 2016, 2017, 2018; Marshall et al. 2018, 2023).

We present the signal-to-noise (S/N) map of the *HST* - NICMOS observation of TYC 9340-437-1 in Figure B.1. The noise maps used to build the S/N were calculated with the same method as in Choquet et al. (2018). 136 reference star images from the PSF libraries were processed with the same method and reduction parameters as the science images. The PSF-subtracted libraries were then partitioned into 17 sets with the same number of frames as the science targets, rotated with the target image orientations, and combined. The noise maps were computed from the pixel-wise standard deviation across these sets of processed reference star images. The disc is detected at low significance with a peak S/N $\simeq$ 3 (per pixel). The scattered light from the disc appears asymmetric in the image with the eastern side being substantially brighter. Assuming the same orientation (position angle, inclination) in both images, the disc extent and architecture are consistent between the scattered light and millimetre wavelengths (see Table 1).

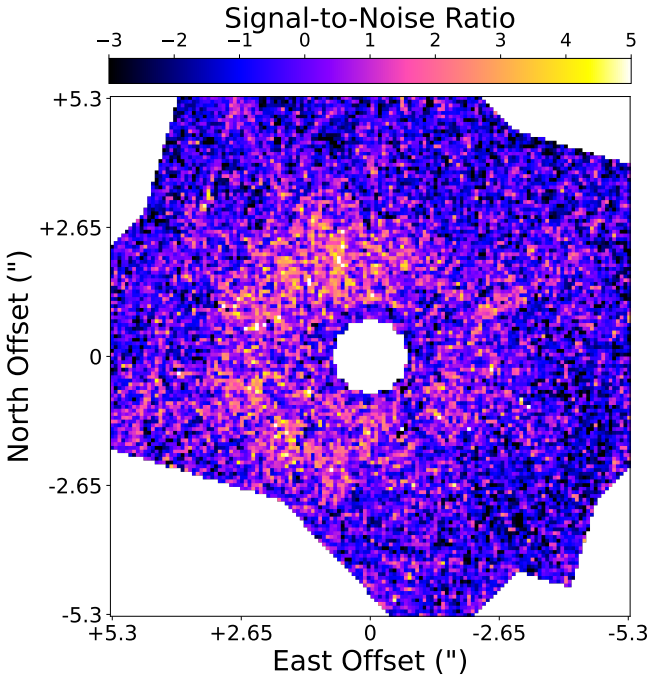

Fig. B.1. Signal-to-noise map of the *HST* - NICMOS detection of the debris disc of TYC 9340-437-1. Orientation: north is up, east is left.

Appendix C: Parametrisation

C.1. Scattered light parametric modelling

The dust parametrisation follows the model introduced in Augereau et al. (1999) (and originally presented in Artymowicz et al. 1989). In a cylindrical coordinate system (r, θ, z), the dust volume density $\rho(r, \theta, z)$ is expressed as

$$\rho(r,\theta,z) = \rho_0 \left(\left(\frac{r}{r_0}\right)^{-2\alpha_{\rm in}} + \left(\frac{r}{r_0}\right)^{-2\alpha_{\rm out}} \right)^{-1/2} \times e^{-z^2/2(r\tan\psi)^2}, \quad \text{(C.1)}$$

where $\alpha_{\rm in}$ and $\alpha_{\rm out}$ are the inner/outer slopes of the volume density distribution and $h = r\tan\psi$ is the vertical scale height of the disc (linearly increasing with r), parametrised by the opening angle ψ.

In case of an elliptical disc (case of HR 4796), the reference radius r_0 depends on the azimuthal angle θ. Therefore, the parameter r_0 is superseded by the semi-major axis of the disc a_0, the eccentricity e and the argument of pericenter ω, such that

$$r_0(\theta) = \frac{a_0(1-e^2)}{1 + e\cos(\omega+\theta)}. \quad \text{(C.2)}$$

The surface density $\Sigma(r)$ can be written as

$$\Sigma(r) = \int_{-\infty}^{+\infty} \rho(r,z)\,dz = \Sigma_0 \left(\left(\frac{r}{r_0}\right)^{-2\alpha_{\rm in}} + \left(\frac{r}{r_0}\right)^{-2\alpha_{\rm out}} \right)^{-1/2} \times \frac{r}{r_0}, \quad \text{(C.3)}$$

where Σ_0 is a constant.

For such a parametrisation, the radius of the maximum of the surface density $\Sigma(r)$ is not r_0 but also depends on $\alpha_{\rm in}$, $\alpha_{\rm out}$. Augereau et al. (1999) showed that it is

$$r_{\max,\Sigma} = r_0 \left(-\frac{\alpha_{\rm in}+1}{\alpha_{\rm out}+1} \right)^{1/2(\alpha_{\rm in}-\alpha_{\rm out})}. \quad \text{(C.4)}$$

Table A.1. List of the 24 ARKS targets, with the main system parameters from Marino et al. (2026b, see there for uncertainties) and their detection or non-detection in scattered light.

Name	Distance [pc]	Spectral type	$L_\star$ [$L_\odot$]	Age [Myr]	$L_{\rm cold}/L_\star$ [$\times 10^{-4}$]	Incl.[(a)] [°]	Detected in scattered light ? if yes: Instrument / Filter / Mode[(b)] / Ref[(c)]
Moderately inclined belts ($i < 75°$)							
HD 15257	49.0	F1V	14	1000^{+800}_{-800}	0.61	59.4 ± 4.9	No
HD 161868	29.7	A1V	24	300^{+200}_{-200}	0.65	66.1 ± 1.5	No
HD 76582	48.9	A7V	9.9	1200^{+900}_{-900}	2.0	72.6 ± 0.7	No
HD 206893	40.8	F5V	2.8	160^{+20}_{-20}	2.7	45.2 ± 2.5	No
HD 218396 (HR 8799)	40.9	A9V	5.5	33^{+7}_{-10}	2.5	28.8 ± 3.3	No[(d)]
HD 84870	88.8	A9V	7.9	300^{+200}_{-200}	4.3	47.1 ± 2.6	No
HD 170773	36.9	F4V	3.6	200^{+100}_{-100}	4.9	32.9 ± 1.9	No
HD 92945	21.5	K0V	0.37	200^{+100}_{-100}	6.6	65.4 ± 0.6	ACS / F606W and F814W / I / Golimowski et al. (2011); Ren et al. (2017)
HD 107146	27.5	G0V	1.0	150^{+100}_{-50}	9.8	19.3 ± 0.6	ACS / F606W and F814W / I / Ardila et al. (2004); Ertel et al. (2011)
TYC 9340-437-1	36.7	K7V	0.19	23^{+3}_{-3}	10	18.0 ± 8.0	NICMOS / F160W / I / this work
HD 95086	86.5	A9V	6.4	$13^{+1}_{-0.6}$	16	31.6 ± 3.5	No[(e)]
HD 145560	121	F5V	3.3	16^{+2}_{-2}	20	47.6 ± 0.6	GPI / H / pI / Hom et al. (2020)
HD 131835	130	A8V	8.9	16^{+2}_{-2}	23	74.2 ± 0.2	SPHERE / H / I / Feldt et al. (2017); Jankovic et al. (2026)
HD 121617	118	A1V	14	16^{+2}_{-2}	51	44.1 ± 0.6	SPHERE / J / pI / Perrot et al. (2023)
Highly inclined belts ($i > 75°$)							
HD 14055 (γ Tri)	35.7	A1V	29	300^{+200}_{-200}	0.89	80.7 ± 0.2	No[(f)]
HD 10647 (q^1 Eri)	17.3	F8V	1.6	1700^{+600}_{-600}	2.6	77.8 ± 0.1	ACS / F606W / I / Lovell et al. (2021)
HD 197481 (AU Mic)	9.71	M1V	0.098	23^{+3}_{-3}	3.9	88.3 ± 0.1	SPHERE / H / I and pI / Boccaletti et al. (2015, 2018)
HD 15115	48.8	F3V	3.7	45^{+5}_{-5}	4.7	86.7 ± 0.0	SPHERE / J / I (Engler et al. 2019)
HD 9672 (49 Ceti)	57.2	A2V	15	45^{+5}_{-5}	7.2	78.7 ± 0.2	SPHERE / H / I / Choquet et al. (2017)
							NICMOS / F110W / I / (Choquet et al. 2017)
HD 39060 (β Pic)	19.6	A4V	8.7	23^{+3}_{-3}	25	86.4 ± 0.2	SPHERE / H / pI / van Holstein et al. (2021)
HD 61005	36.5	G6V	0.62	45^{+5}_{-5}	25	85.9 ± 0.1	SPHERE / H / I and pI / Olofsson et al. (2016)
HD 131488	152	A3V	12	16^{+2}_{-2}	26	85.0 ± 0.1	SPHERE, H, I Pawellek et al. (2024)
HD 109573 (HR 4796)	70.8	B9.5V	25	10^{+3}_{-3}	42	76.6 ± 0.1	SPHERE / H / I / Milli et al. (2017)
							SPHERE / J / pI / Bonduelle et al. (in prep)
HD 32297	130	A8V	7.0	30^{+10}_{-10}	61	88.3 ± 0.0	SPHERE / H / I and pI / Bhowmik et al. (2019)

Notes. The list is grouped into moderately and highly inclined discs, and within each group, the discs are listed in increasing fractional luminosity $L_{\rm cold}/L_\star$. The discs detected in scattered light and analysed in this paper are highlighted in grey. The discs in bold face have been detected in CO with ALMA.
[(a)]Inclination of the disc, as estimated from the ARKS ALMA image (Marino et al. 2026b). [(b)] I stands for total intensity while pI stands for polarised intensity. [(c)]Reference corresponding to the scattered light dataset used in this work. Additional scattered light dataset may exist. [(d)]Engler et al. (2025) detected the inner warm disc with SPHERE in polarisation, but the outer cold disc remains elusive. [(e)]A marginal detection in polarised light with SPHERE in the J band is claimed in Chauvin et al. (2018, see their Fig. 15). However, our reanalysis of the data does not recover the signal. [(f)]HD 14055 was observed with IRDIS in the H band in polarised light on 2023-10-14 (PI: Moor) but not detected (private com.).

Table A.2. List of the 24 targets comprising the ARKS sample. Included are the ESO program ID of the SPHERE observations (if the disc was detected with SPHERE) and the corresponding IRDIS filter.

Name	Planet search dataset		Disc dataset	
	ESO program ID	Filter[a]	ESO program ID	Filter
Moderately inclined belts ($i < 75°$)				
HD 15257	096.C-0388(A)	BB_H	-	-
HD 161868	097.C-0865(B)	DB_H23	-	-
HD 76582	096.C-0388(A)	BB_H	-	-
HD 206893	099.C-0708(A)	BB_H	-	-
HD 218396 (HR 8799)	0101.C-0315(A)	BB_H	-	-
HD 84870	112.25YJ.001	DP_0_BB_H	-	-
HD 170773	1100.C-0481(G)	DB_H23	-	-
HD 92945	1100.C-0481(D)	DB_H23	-	-
HD 107146	095.C-0374(A)	DB_H23	-	-
TYC 9340-437-1	096.C-0241(A)	DB_H23	-	-
HD 95086	097.C-0865(A)	DB_H23	-	-
HD 145560	099.C-0177(A)	DB_H23	-	-
HD 131835	095.C-0298(A)	DB_H23	095.C-0298(A)	DB_H23
HD 121617	1101.C-0092(J)	DB_H23	0101.C-0420(A)	DP_0_BB_J
Highly inclined belts ($i > 75°$)				
HD 14055 (γ Tri)	112.25YJ.001	DP_0_BB_H	-	-
HD 10647 (q^1 Eri)	097.C-0750(A)	DB_H23	-	-
HD 197481 (AU Mic)	598.C-0359(B)	BB_H	598.C-0359(F)	DP_0_BB_H
HD 15115	096.C-0640(A)	BB_H	098.C-0686(B)	DP_0_BB_J
HD 9672 (49 Ceti)	097.C-0865(A)	DB_H23	096.C-0388(A)	BB_H
HD 39060 (β Pic)	097.C-0865(A)	DB_H23	0102.C-0916(B)	DP_0_BB_H
HD 61005	095.C-0298(H)	DB_H23	095.C-0273(A)	DP_0_BB_H
HD 131488	0101.C-0753(B)	DB_H23	0.101.C-0753(B)	DB_H23
HD 109573 (HR 4796)	1100.C-0481(G)	DB_H23	0104.C-0436(B)	DP_0_BB_J
HD 32297	098.C-0686(A)	BB_H	098.C-0686(A) 098.C-0686(B)	BB_H DP_0_BB_J

Notes. The discs detected in scattered light and analysed in this paper are highlighted in grey.
[a]BB, DB and DP_0 stand respectively for broadband, dual-band and dual-polarimetric. These acronyms correspond to the '*ESO INS COMB IFLT*' keyword in the SPHERE fits headers.

C.2. ALMA continuum parametric modelling

As explained in Sect. 2.2.1 and in more details in Han et al. (2026), discs brightness profiles are converted to surface density profiles assuming a blackbody equilibrium temperature profile, then a parametric modelling using a double power-law was fitted to the ALMA continuum surface density profile:

$$\Sigma_{\rm ALMA}(r,\theta,z) = \Sigma_0 \left(\left(\frac{r}{r_0}\right)^{-2\alpha_{\rm in}} + \left(\frac{r}{r_0}\right)^{-2\alpha_{\rm out}} \right)^{-1/2} . \quad \text{(C.5)}$$

We note here that this functional form parameterises the *volume density* in scattered light (Eq. C.1) but the *surface density* for the ALMA continuum data (Eq. C.5), resulting in a different expression for the location of the maximum radius of the ALMA surface density:

$$r_{\rm max,\Sigma_{ALMA}} = r_0 \left(-\frac{\alpha_{\rm in}}{\alpha_{\rm out}} \right)^{1/2(\alpha_{\rm in}-\alpha_{\rm out})} . \quad \text{(C.6)}$$

For the same reason, the parameters $\alpha_{\rm in}$, $\alpha_{\rm out}$ and r_0 cannot be directly compared between the parametric modelling done in scattered light and with ALMA. However, given that we have used a vertical scale height linearly increasing with the radius r, the two parameterisations are rigorously equivalent.

Appendix D: Modelling results

The best parameters from the disc forward modelling are presented in Table D.1. The two discs HD 107146 and HD 92945 do not appear in this table because the surface density was extracted in previous papers with a different parametrisation (Ertel et al. 2011; Golimowski et al. 2011).

We have made the scattered light data and best models publicly available on our dedicated website `arkslp.org` and `ARKS dataverse`.

The comparison of the ALMA and scattered light surface density profile is presented in Sect. 4. The comparison of the vertical profiles of the discs is done in the companion paper Zawadzki et al. (2026). A comparison to the position angle and inclination extracted from the ARKS ALMA images is done in the last two columns of Table D.1 and a discussion is provided below in Sect. D.1. The best scattering phase functions derived for the discs' models are shown below in Sect. D.2.

D.1. Comparison of the position angle and inclination between scattered light and ALMA

An accurate estimation of the inclination for edge-on or highly inclined systems is difficult in scattered light, as this parameter can be slightly degenerate with the vertical scale height and because the semi-minor axis which is critical to constrain the inclination is often hidden behind the coronagraphic mask or

located in a noisy area of the image. The inclination differs by more than 3σ for five systems.

For AU Mic and HD 32297, the inclination derived from total intensity is incompatible with ALMA, but that derived from polarised intensity is compatible. Polarimetry gives more weight to the 90° scattering angles (e.g. larger projected distances to the star), while total intensity gives more weight to the small scattering angles (e.g. small projected separations). Therefore given the distortions in the AU Mic disc (Boccaletti et al. 2015, 2018), such a difference likely reflects the complex structure of the disc.

For HD 32297, the value derived from polarised intensity is compatible with that derived from GPI in the same mode (Duchêne et al. 2020), which tends to show that there is no real discrepency between ALMA and scattered light. For β Pictoris, in polarised intensity, both the inclination and position angle are incompatible with ALMA. This difference also likely reflects the complex structure of the disc at short separations, with an inner warp inclined by several degrees from the main disc (Apai et al. 2015).

For HD 131835, there is a 2° difference in inclination between the scattered light and ALMA models, corresponding to a 3.2σ difference. As the semi-minor axis of the ring is poorly seen in scattered light, this may explain this difference.

For HD 10647, the disc inclination in scattered light is 7° less than with ALMA. As the vertical opening angle $\psi = 0.1 \pm 0.07$ rad appears poorly constrained, we also tried to fix this value to a small ($\psi = 0.04$ rad) or a large ($\psi = 0.14$ rad) value, but that did not change the best disc inclination. Because the *HST* / ACS inner working angle is large, we could only use disc signals beyond 3.5″ (61 au) which may explain the difference in inclination found with ALMA. However we cannot rule out a true misalignment between micrometre- and millimetre-size grains, as suggested for instance on the disc around η Crv (Lovell et al. 2022).

The position angles are typically very consistent between scattered light and ALMA, except for the two edge-on systems β Pictoris already discussed above and HD 15115. For the latter, the position angle is 0.7° higher in scattered light, corresponding to a 3.5σ difference with ALMA. This position angle differs by 0.5° with that derived in Engler et al. (2019) from the same dataset but with a different technique (ellipse fitting). The structural features seen inside the belt and described in (Engler et al. 2019) may therefore have an impact on the determination of the position angle.

D.2. Scattering phase functions

As a by-product of the modelling, we also show in Fig. D.1, the scattering phase functions (SPF) and polarised SPF (pSPF). In total intensity, the SPF is parametrised with a two-component Henyey-Greenstein phase function (Henyey & Greenstein 1941, see the top panel in Fig. D.1). In polarised intensity, the pSPF is non-parametric and estimated empirically following the method described in Olofsson et al. (2020) (bottom panel in Fig. D.1).

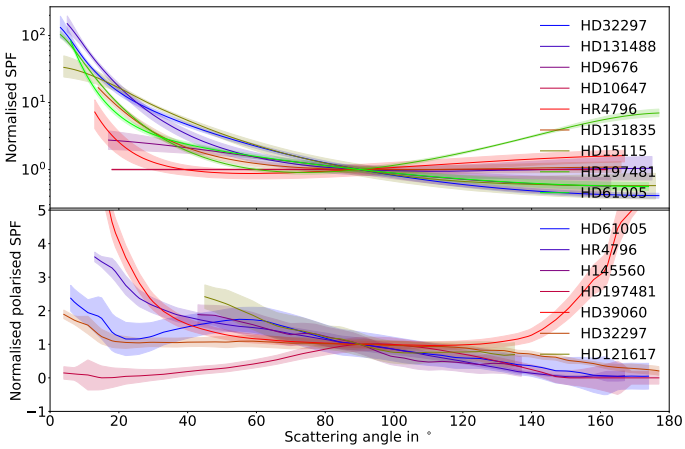

Fig. D.1. Scattering phase functions (top) and polarised scattering phase functions (bottom) of the ARKS discs modelled in this work.

Appendix E: Modelling of the inner and outer rings in the HD 131835 disc

Even though the outer ring of HD 131835 is brighter than the inner ring in the scattered light image post-processed with ADI, self-subtraction inherent to this post-processing technique may bias this conclusion. Self-subtraction is typically stronger at short separations (Milli et al. 2012). We therefore tried to constrain the intrinsic brightness ratio between the inner and the outer ring seen in scattered light. To limit the number of degrees of freedom, we assumed a similar inclination and position angle for the inner ring as for the outer ring, and varied the semi-major axis, brightness ratio and the scattering anisotropy parameter. This exercise showed that we can confidently rule out models with a surface brightness of the inner ring as bright as that of the outer ring in scattered light (as measured along the semi-major axis of the disc). This constraint is used in the dedicated companion paper (Jankovic et al. 2026).

Table D.1. Best disc parameters.

Target	Mode[(a)]	r_0[(b)] [mas]	$\alpha_{\rm in}$	$\alpha_{\rm out}$	ψ [rad×10^{-2}][(c)]	i [°]	PA [°]	e ×10^{-2}	ω [°]	i (ALMA) [°]	PA (ALMA) [°]
HD9672	I	2186 ± 169	$2.6^{2.1}_{-1.3}$	−2.1 ± 0.5	3.5	73 ± 3	109 ± 2	-	-	78.7 ± 0.2	107.9 ± 0.2
HD 10647	I	3895 ± 10	9.9 ± 0.2	−1.1 ± 0.1	10 ± 7	71.8 ± 0.1	56.9 ± 0.1	-	-	78.8 ± 0.1	57.3 ± 0.1
HD 15115	I	2042 ± 100	4.9 ± 2.5	−5.4 ± 1.3	2.8 ± 0.6	86.4 ± 0.4	−80.8 ± 0.2	-	-	86.7 ± 0.0	−81.5 ± 0.0
HD 32297	I	1057 ± 23	1.7 ± 0.3	−5.0 ± 0.2	0.8 ± 0.3	87.1 ± 0.1	−132.7 ± 0.1	-	-	88.3 ± 0.0	−132.5 ± 0.0
	pI	1000 ± 36	2.6 ± 0.5	−3.6 ± 0.2	1.3 ± 0.3	88.2 ± 0.2	−132.3 ± 0.1	-	-		
HD 39060	pI	5007 ± 88	0.4 ± 0.1	−17.0 ± 2.4	10.0 ± 0.5	84.6 ± 0.03	−148.6 ± 0.2	-	-	86.4 ± 0.2	−150.0 ± 0.1
HD 61005	I	1445 ± 59	15.8 ± 3.0	−1.3 ± 0.1	3.9 ± 0.4	86.1 ± 0.3	70.5 ± 0.2	-	-	85.9 ± 0.1	70.4 ± 0.1
	pI	1399 ± 69	14.7 ± 3.2	−1.2 ± 0.1	4.9 ± 1.2	83.9 ± 0.8	71.9 ± 0.8	-	-		
HD 109573	I	1062 ± 1	34.7 ± 0.3	−18.6 ± 0.5	0.2 ± 0.1	76.6 ± 0.1	−153.5 ± 0.1	3 ± 1	−137 ± 2	76.6 ± 0.1	−153.5 ± 0.0
	pI	1066 ± 2	34.3 ± 0.7	−17.9 ± 0.5	1.7 ± 0.2	77.1 ± 0.2	−153.3 ± 0.1	7 ± 1	−109 ± 3		
HD 121617	pI	668 ± 11	28.7 ± 5.0	−6.9 ± 1.1	4.1 ± 2.9	44.8 ± 1.4	−119.5 ± 2.1	3 ± 1	−10 ± 36	44.1 ± 0.6	−121.3 ± 0.7
HD 131488	I	619 ± 24	15.1 ± 3.7	−3.8 ± 0.6	1.8 ± 0.8	84.9 ± 0.3	−82.9 ± 0.2	-	-	85.0 ± 0.1	−82.8 ± 0.0
HD 131835	I	785 ± 24	6.0 ± 1.5	−2.4 ± 0.5	3.5 ± 1.4	76.2 ± 0.6	−120.6 ± 0.3	-	-	74.2 ± 0.2	−120.8 ± 0.2
HD 145560	pI	686 ± 30	4.3 ± 0.9	−3.8 ± 0.7	5.8 ± 3.3	46.8 ± 2.0	36.8 ± 2.0	-	-	47.6 ± 0.6	39.4 ± 0.9
HD 197481	I	3336 ± 234	1.8 ± 0.5	−3.5 ± 0.3	2.7 ± 0.1	89.0 ± 0.1	128.1 ± 0.1	-	-	88.3 ± 0.1	128.6 ± 0.1
	pI	3406 ± 234	2.7 ± 0.6	−4.5 ± 1.5	1.0 ± 0.7	86.5 ± 0.8	128.2 ± 0.5	-	-		
TYC 9340-437-1	I	2460 ± 119	5.4 ± 1.7	−7.9 ± 2.1	18.0 ± 4.2	18[(d)]	149.2[(d)]	-	-	18.0 ± 8.0	149.2 ± 20.2

Notes. The uncertainty is given at a 1σ confidence level and comes from the MCMC alone, except for the position angle, where a systematic uncertainty of 0.04° from the true north calibration of VLT - SPHERE (Maire et al. 2016) was added quadratically (when SPHERE was used). The last two columns show, as a comparison, the best-fit inclination and position angle as extracted from the ALMA images in Marino et al. (2026b) and the corresponding scattered light values are highlighted in grey if they are incompatible at a > 3σ confidence level. Values without uncertainty are fixed parameters in the fit.
[(a)]The observing mode is either I for total intensity or pI for polarised intensity. [(b)]If the disc is eccentric, the reference radius r_0 is replaced with the reference semi-major axis a_0 described in Eq. C.2, and the eccentricity e and the argument of pericentre ω are specified. [(c)]When expressed in radians, the opening angle, ψ, can also be understood as the ratio between the vertical scale height, h, and the reference radius, r_0. Therefore, the numerical value expressed in this column in rad×10^{-2} can be understood as a percentage. [(d)]The inclination and position angle for TYC 9340-437-1 were fixed parameters set to the best values derived from the modelling of the ALMA images (Marino et al. 2026b) because the S/N was too low in scattered light to leave them as free parameters.

A&A, 705, A198 (2026)
https://doi.org/10.1051/0004-6361/202556605
© The Authors 2026

Astronomy & Astrophysics

The ALMA survey to Resolve exoKuiper belt Substructures (ARKS)

IV. CO gas imaging and overview

S. Mac Manamon[1,⋆], L. Matrà[1], S. Marino[2], A. Brennan[1], Y. Han[3], M. R. Jankovic[4], P. Weber[5,6,7], M. Bonduelle[8], J. M. Carpenter[9], G. Cataldi[10,11], A. M. Hughes[12], A. Kóspál[13,14,15], J. P. Marshall[16], B. C. Matthews[17,18], J. Milli[8], A. Moór[13], K. Öberg[19], S. Pérez[5,6,7], A. A. Sefilian[20], D. J. Wilner[19], M. C. Wyatt[21], E. Chiang[22], A. S. Hales[23,9,6], J. B. Lovell[19], P. Luppe[1], M. A. MacGregor[24], T. Pearce[25], M. Booth[26], C. del Burgo[27,28], A. Fehr[19], E. Mansell[12], and B. Zawadzki[12]

(Affiliations can be found after the references)

Received 25 July 2025 / Accepted 24 September 2025

ABSTRACT

Context. CO gas is detected in a significant number (~20) of debris discs (exoKuiper belts), but understanding its origin and evolution remains elusive. Crucial pieces of evidence are its mass and spectro-spatial distribution, which are coupled through optical depth and have only been analysed at low to moderate resolution so far. The ALMA survey to Resolve exoKuiper belt Substructures (ARKS) is the first ALMA large program to target debris discs at high spectro-spatial resolution.

Aims. We used ^{12}CO and ^{13}CO J=3–2 line data of 18 debris belts observed by ARKS, 5 of which were already known to be gas-bearing, in order to analyse the spectro-spatial distribution of CO and constrain the gas mass in discs that were known to host gas previously, and to search for gas in the remaining 13 discs without previous CO detections.

Methods. We developed a line-imaging pipeline for ARKS CO data with a high spectro-spatial resolution. Using this tool, we produced line cubes for each of the ARKS targets, with a spatial resolution down to about 70 mas and a spectral resolution of 26 m s^{-1}. We used spectro-spatial shifting and stacking techniques to produce a gallery of maps with the highest possible signal-to-noise ratio (S/N) and with radial and spectral profiles that reveal the distribution and kinematics of gas in five gas-bearing discs at unprecedented detail.

Results. For each of the five gas-bearing discs (HD 9672/49 Ceti, HD 32297, HD 121617, HD 131488, and HD 131835), we constrained the inner radius of the ^{12}CO ($r_{\rm min}$ ~ 3–68 au), and we found that the radial brightness profile of CO peaked interior to the dust ring, but that CO was also more radially extended than the dust. In a second-generation scenario, this would require significant shielding of CO that would allow it to viscously spread to the observed widths. We present the first radially resolved ^{12}CO/^{13}CO isotopologue flux ratios in five gas-bearing debris discs and found them to be constant with radius for the majority (four out of five) of systems. This indicates that ^{12}CO and ^{13}CO are both optically thick or optically thin throughout the discs. We report CO line fluxes or upper limits for all systems and optical depth dependant masses for the five systems with detected CO. Finally, we analysed the ^{12}CO J=3–2 line luminosities for a range of ARKS debris discs and for debris discs from the literature. We confirm that gas is mostly detected in young systems. However, the high scatter seen in young/high fractional luminosity systems indicates no trend within the systems with detected gas. This could be caused by different system properties and/or evolution pathways.

Key words. techniques: interferometric – submillimeter: planetary systems

1. Introduction

Planetesimal belts (debris discs) are belts of icy dust, comets, asteroids, and planetesimals. They are analogous to the Kuiper and asteroid belts in the Solar System (for reviews, see Wyatt 2008; Matthews et al. 2014; Hughes et al. 2018, and references therein). These belts can be observed because the surface area that is covered by small dust grains is so large. The dust, comets, asteroids, and planetesimals collide constantly with one another, grind each other down, and create more dust. Debris discs were originally thought to be gas-free environments that solely consist of solids, but molecular gas emission has recently been observed in multiple discs (e.g. Kóspál et al. 2013; Moór et al. 2013, 2017; Dent et al. 2014; Lieman-Sifry et al. 2016; Matrà et al. 2015, 2017a). We now know of over 20 debris discs (most commonly found around intermediate-mass stars) that contain gas (Marino et al. 2020), and we know this not only through molecular emission observed at millimetre (mm) wavelengths, but also atomic C and O emission in the far-infrared (IR) (e.g. Cataldi et al. 2014; Brandeker et al. 2016; Roberge et al. 2013), CO absorption in the near-IR (Troutman et al. 2011), and CO and atomic absorption in the ultraviolet (UV) (e.g. Roberge et al. 2000, 2014; Wilson et al. 2019; Wu et al. 2025; Brennan et al. 2024). CO is the most commonly observed species (and the only molecule) to be observed in debris discs, however, which is largely due to the significant increase in sensitivity provided by the Atacama Large Millimetter/submillimeter Array (ALMA) (e.g. Matrà et al. 2019a; Klusmeyer et al. 2021; Smirnov-Pinchukov et al. 2022).

Two possible origins have been proposed for the debris disc gas. The first proposition was that the gas is of primordial origin and is left over from the protoplanetary disc phase. This would be surprising because gas is expected to have dissipated by the

⋆ Corresponding author: macmanas@tcd.ie

Open Access article, published by EDP Sciences, under the terms of the Creative Commons Attribution License (https://creativecommons.org/licenses/by/4.0), which permits unrestricted use, distribution, and reproduction in any medium, provided the original work is properly cited.
This article is published in open access under the Subscribe to Open model. Subscribe to A&A to support open access publication.

time the debris disc formed. Gas dissipation is thought to be a pre-condition for the escalation of collisional evolution of the planetesimals that characterise a debris disc (Wyatt 2008). The second proposition was that the gas is of secondary origin and was released from the planetesimals via collisional evolution of a shared origin with the dust.

In the primordial scenario, the gas could potentially remain in discs around A-type stars due to inefficient photoevaporation of protoplanetary discs, around intermediate-mass stars if their discs were depleted in small grains ($\lesssim$0.01 μm) so that far ultraviolet (FUV) photoelectric heating is ineffective, thus prolonging the disc lifetime through a delayed photoevoporation of the disc (Nakatani et al. 2021, 2023), and in general, if the gas densities are high enough that the photodissociation lifetime of CO gas can be extended through shielding (Kóspál et al. 2013). Without any shielding, the lifetime of a CO molecule against photodissociation by the interstellar radiation field would be 130 years (Heays et al. 2017) because there is not enough dust to shield the CO from the stellar and the interstellar UV radiation field (Kóspál et al. 2013).

The CO masses in CO-rich debris discs (e.g. HD 21997, HD 121617, HD 131488, HD 131835; Kóspál et al. 2013; Moór et al. 2017; Hales et al. 2019) were inferred to be sufficiently high that if H_2, the dominant shielding agent for CO in a primordial scenario, were present in primordial amounts (with a primordial CO/H_2 ratio), it could allow the CO to survive for the entire disc lifetime. The origin of CO in these systems could therefore plausibly be primordial. Kóspál et al. (2013) found that for these young debris discs (10–20 Myr) with masses of CO that are too high to be explained by just the destruction of exocomets, gas that persisted from the protoplanetary disc phase is a likely explanation. In particular, the masses of CO in these discs are of the order of $M_{\rm CO} \gtrsim 10^{-3}\ M_\oplus$ (Cataldi et al. 2023).

As mentioned above, the same processes that create dust in debris discs are also capable of releasing gas and are a viable alternative explanation for the origin of gas in debris discs. Gas can be released by sublimation of icy planetesimals (exocomets), photodesorption from dust grains (Grigorieva et al. 2007), vaporisation of colliding dust particles (Czechowski & Mann 2007), or collision of exocomets/icy planetesimals (Zuckerman & Song 2012; Kóspál et al. 2013; Bonsor et al. 2023). In this second-generation gas scenario, which is based on the composition of comets in the Solar System, the gas is dominated by CO, CO_2, and H_2O, with much smaller amounts of H_2 compared to a primordial scenario (e.g. Kóspál et al. 2013). CO self-shielding and shielding by C I, a photodissociation product of CO, are likely to play a significant role in extending the lifetime of the gas in the more CO-rich discs if they are secondary in origin (e.g. Matrà et al. 2017a; Kral et al. 2019; Marino et al. 2020).

Gas-removal processes operate continuously in debris discs. CO can be depleted via photodissociation and freeze-out onto dust grains, though the latter is inefficient at the temperatures and small collective surface area of dust grains in debris discs (Matrà et al. 2015). For gas to be observable in debris discs, it must therefore be continuously replenished and/or shielded from photodissociation over lifetimes comparable to the system age (Kóspál et al. 2013).

For low-mass CO (or CO-poor) discs (e.g. β Pic, Fomalhaut, HD 181327, TWA 7, and η Corvi), the survival timescale of CO is much shorter than the ages of their systems, even if the CO is being shielded by unseen H_2 (Dent et al. 2014; Matrà et al. 2018, 2017b; Marino et al. 2016a,b). Gas production by exocomets can explain discs with low CO masses ($M_{\rm CO} \lesssim 10^{-4}\ M_\oplus$) because the required production rate of CO agrees reasonably well with the destruction rates of exocomets in these debris discs (Cataldi et al. 2023).

If the gas is being replenished from solids (icy dust or larger exocomets), as in the secondary origin scenario, the naive expectation would be that the gas should be radially co-located with the dust component, as was found by Dent et al. (2014) and Matrà et al. (2017a) for β Pic. However, we expect the gas to radially viscously spread over time, and to create an accretion disc inwards and a decretion disc outwards, where the viscous spreading rate would depend on the viscosity of the gas (Kral et al. 2016). This was not observed for β Pic, however, where the radial distribution of long-lived CI gas, a daughter product of CO and CO_2 destruction, was inconsistent with the expectation of an accretion disc (Cataldi et al. 2018). If CI production started only ~5000 yr ago, however, not enough time has passed yet for the gas to viscously spread in to the star to form the accretion disc. Kral et al. (2019) similarly studied the radial distributions of CI and CO in the lower-resolution observations of HD 131835 and reported that they were consistent with one another, but inconsistent with an accretion disc. A potential explanation for why an accretion disc might not be visible is that the gas is accreted onto a planet orbiting interior to the disc.

We investigate the distribution of ^{12}CO and ^{13}CO in debris discs at an unprecedented spectro-spatial resolution by exploiting the ALMA survey to Resolve exoKuiper belt Substructure (ARKS, project number 2022.1.00338.L, PI: S. Marino), which is the first ALMA large program to target debris discs. ARKS targets 18 nearby debris discs (and 6 archival sources). The ARKS goals include understanding the diversity and ubiquity of radial and vertical substructures in dust continuum emission and imaging CO in gas-bearing discs at a level that allows us to carry out the first radial, vertical, and gas kinematic study. High-resolution CO observations will allow us to carry out detailed comparisons between the dust and the gas and to constrain the origin and evolution of CO gas in these discs (for sample characteristics and stellar parameters we used, see Marino et al. 2026b).

We used ALMA to observe the ^{12}CO J=3–2 line (henceforth ^{12}CO, unless specified otherwise) and ^{13}CO J=3–2 line (henceforth ^{13}CO, unless specified otherwise) in order to characterise the spectro-spatial structure of the five previously known gas-bearing targets and conduct a search for ^{12}CO in the other 13 discs that are as yet devoid of CO gas detections (henceforth gas-free discs). We did not reanalyse the six archival targets, including the CO detection around β Pic (Matrà et al. 2019b), that are included in the ARKS sample because the spectro-spatial resolution is very different and the CO line that was targeted by these archival observations was different as well. In Sect. 2 we describe the observations and the imaging pipeline we developed for ARKS. In Sect. 3 we present our results and and discuss their implications in Sect. 4. We conclude with a summary in Sect. 5.

2. Observations

To image CO gas in the ARKS data, we developed a line-imaging pipeline in Python using the Common Astronomy Software Applications (CASA) package, version 6.4.1.12 (CASA-Team 2022). The detailed calibration and preparation of the interferometric visibilities for imaging are described in Marino et al. (2026b), but we provide a brief summary here. The calibration of the interferometric visibilities for all observations in time, baseline, and frequency was carried out using the ALMA pipeline. The frequencies were transformed into the barycentric reference frame, and the data were time-averaged to reduce the data size

without compromising imaging quality. A phase centre offset (derived from basic fitting of a disc to the continuum visibilities tracing dust emission) was then introduced to ensure no relative astrometric offsets were present across different observing dates for the same system, and to ensure the visibility weights were correct in an absolute sense for each observing date, configuration, and system. Finally, for each of the ARKS sources and each array configuration, two CASA Measurement Sets containing the calibrated visibilities ready for imaging were produced for the spectral windows containing the ^{12}CO line (rest frequency of 345.796 GHz) and the ^{13}CO line (rest frequency of 330.599 GHz).

The ^{12}CO and ^{13}CO lines were observed for every system, though the spectral resolution varied depending on whether the system was previously known to be gas-bearing or not. For the 5 gas-bearing discs, the spectral resolution was set to 26 m s^{-1} (the finest spectral resolution possible with ALMA) for the ^{12}CO spectral window and to 886 m s^{-1} for the ^{13}CO spectral window, which corresponds to two times the native channel width. The gas-bearing discs' ^{12}CO spectral resolution was set such that the maximum possible kinematic information could be extracted. The ^{13}CO spectral window uses the maximum bandwidth to not compromise continuum sensitivity. For the discs without previous gas detections, the spectral resolution was set to 846 m s^{-1} for ^{12}CO and 886 m s^{-1} for ^{13}CO to maximise bandwidth and therefore sensitivity to dust continuum emission.

For each source and each line, we simultaneously imaged the calibrated and preprocessed visibilities from all baseline configurations using the CLEAN algorithm (Högbom 1974), as implemented through CASA's `tclean` task. We developed an imaging pipeline where `tclean` is called three times. For all three `tclean` iterations implemented as part of our pipeline, the `start`, `width`, and `nchan` parameters represent the barycentric velocity of the first channel, the width of each channel, and the number of channels in the cube outputted by the pipeline. These were set depending on the system and in particular on whether they were known to contain gas; the spectral information used to derive these values was obtained directly from each observations' Measurement Set header file. The parameter `width` was set to be the same as the observations native channel width, to maximise spectral resolution. In the ^{12}CO observations, this resulted in channel widths of 13 m s^{-1}, which corresponds to a resolution of 26 m s^{-1}; in the ^{13}CO observations, the native channel spacing was 443 m s^{-1}, which corresponds to a resolution of 886 m s^{-1}. The parameters `start` and `nchan` were calculated based on the expected range of Keplerian orbital velocities of the gas in each system. The range of velocities included in the cube for gas-bearing systems was estimated using the maximum expected Keplerian line-of-sight velocity,

$$v_{\rm los,max} = C v_{\rm los,\,kep}(r_{\rm min}), \tag{1}$$

where

$$v_{\rm los,\,kep}(r_{\rm min}) = 30 \text{ km s}^{-1} \sqrt{\frac{M_\star}{r_{\rm min}}} \sin i \tag{2}$$

is the Keplerian projected line of sight velocity at the inner edge $r_{\rm min}$ (in au) of the disc (given by Eq. (A.3)), $M_\star$ is the mass of the star in Solar masses, $M_\odot$, estimated as described in Appendix A of Marino et al. (2026b), and i is the inclination of the disc, measured from the best fit parameters derived by MCMC sampling carried out by Marino et al. (2026b, see Table C.1). Eq. (1) corresponds to the maximum line-of-sight velocity at which we expect to detect the gas, given prior ARKS continuum observations of $r_{\rm min}$. In Eq. (1), C is a constant factor adjusted for each system following the first iteration of the pipeline to correct for the inaccurate prior on $r_{\rm min}$ and for any departure of gas speed from purely Keplerian velocities (pressure gradients providing radial support), if any, and ensure all emission was included in the cube. Typically, we find values of C between 1.6 and 8.3, depending on the gas-bearing system, reflecting CO disc inner radii that were generally lower than initially estimated based on the dust distribution. For gas-free systems, $v_{\rm los,max}$ was set to 50 km s^{-1}. $v_{\rm los,max}$ was then divided by the width of the channels to calculate `nchan` for the `tclean` calls. `start` was calculated through $v_{\rm start} = V_* \pm \frac{v_{\rm los,max}}{2}$, where V_* is the stellar velocity in the barycentric frame as obtained from the literature (Table C.1). The ± sign depends on whether the visibility file had channels in order of ascending or descending velocity.

The parameter `restfreq` in each of the `tclean` calls is set to ^{12}CO and ^{13}CO rest frequencies. For the gas-bearing discs viewed at an inclination away from edge-on ($i = 90°$), we employed Briggs weighting, with a robust parameter of 0.5. This gives a good compromise between resolution and sensitivity for these gas-bearing discs. For the close to edge-on gas-bearing discs around HD 32297 and HD 131488, where the emission was spread over a much larger number of channels (leading to lower S/N per beam, per channel), and for the gas-free/non-detected discs, we employed Briggs weighting with a robust parameter of 2, which is close to Natural weighting (Briggs 1995), to achieve maximum sensitivity.

The first iteration of `tclean` was run without any deconvolution, with a very small pixel size to create a dirty image and obtain the size of the synthesized beam. We used this beam size to optimise the pixel size in later `tclean` runs, which we chose to be $\frac{1}{5}$ of the beam size (averaged between the major and minor axis). We then chose the image size to be equal to the full width at half maximum (FWHM) of the primary beam of the ALMA 12 m antenna. We carried out no deconvolution in the first two rounds of `tclean`. The second iteration of `tclean` is run to create another dirty image, now with an appropriate pixel and image size, which is needed to create a CLEAN mask around the emission in each channel in the cube.

Given the large number of 13 m s^{-1} channels covering the velocity extent of the ^{12}CO line ($\gtrsim$1000), manual masking is unfeasible and masks covering the gas emission in every channel have to be defined automatically. We use a Keplerian mask to leverage the expected near-Keplerian rotation pattern to produce channel-based masks (Teague 2020; Czekala et al. 2021). To create these, we use prior knowledge of each disc's geometry, assuming gas is co-located with the dust. Creation of these Keplerian masks is described in full in Appendix A.

In the third and final `tclean` iteration, the deconvolver parameter was set to `multiscale` (Cornwell 2008). We set the scales for the tclean deconvolution to be [0, 5, 10], corresponding to a point source, a scale of the same size as the synthesised beam, and twice the synthesised beam. The iterative CLEAN process is repeated until the peak emission within all masks in the residual images obtained after subtracting the latest iteration's CLEAN model was below a threshold of 4 times the RMS noise level. We adopted this threshold of 4 times the RMS noise level, in line with the CLEANing methodology of Czekala et al. (2021), as it ensured no significant disc emission remained within the mask in each channel while ensuring no artefacts of the dirty beam was present in the final, CLEANed image, which we confirmed by visual inspection. As is standard in the CLEAN process, the final CLEAN model cube was convolved with the

CLEAN beam and added to the final residual cube to obtain final image cubes of ^{12}CO and ^{13}CO emission for every disc. Along with these, we produced FITS files of the final cubes of the primary beam, the mask used, and the residuals[1].

For the five discs with previously detected gas (HD 9672, HD 32297, HD 121617, HD 131488, HD 131835), the imaging pipeline led to beam sizes ranging from 70 to 150 mas (corresponding to physical scales projected on the sky of 8 to 16 au) for ^{12}CO and 70 to 160 mas (corresponding to physical scales projected on the sky of 9 to 18 au) for ^{13}CO. The RMS levels in the ^{12}CO cubes ranged between 3 to 5 mJy/beam and from 0.6 to 1.0 mJy/beam in the ^{13}CO cubes (Table B.1).

For the 13 discs not previously known to host CO gas, we only ran the first two tclean rounds without masking or deconvolution. This led to beam sizes between 130 and 950 mas (corresponding to physical scales projected on the sky of 9–62 au) for ^{12}CO and 140–1000 mas (corresponding to physical scales projected on the sky of 10–65 au) for ^{13}CO. The noise levels were in the range of 0.4–1.6 mJy/beam in the ^{12}CO cubes and 0.5–1.6 mJy/beam in the ^{13}CO cubes (Table B.1).

While we do not include β Pic in the analysis in this paper as the archival data covers a different CO line and has a different spectro-spatial resolution to the ARKS targets, the archival data included in the ARKS sample of this disc was imaged in the same manner described here (with Briggs robust parameter set to 0.5) in order to be included in other ARKS papers (see Marino et al. 2026b; Milli et al. 2026).

3. Results

3.1. Image galleries

To best display the spectro-spatial structure of the ARKS gas-bearing sources, we created three different moment maps of each system; the line of sight peak velocity map (henceforth peak velocity map), the spectrally integrated-intensity map (henceforth integrated-intensity map) and the peak intensity/brightness temperature map. The peak velocity map displays the velocity field of the disc, in other words, the projected line-of-sight velocity (in the barycentric frame) of the gas in any given pixel. To calculate this, we fit a quadratic function to the peak and its two neighbouring channels in each of the pixels' spectra, and take this velocity of peak emission to describe the bulk velocity of the gas in each pixel. In the absence of a double-surface morphology typical of a protoplanetary disc – such as that produced by CO freeze-out in the disc midplane – the velocity structure along each line of sight can typically be approximated by a single-peaked emission profile. In this case, a simple quadratic fit to the line profile at each pixel yields a reliable estimate of the bulk gas velocity. Using this quadratic fitting method has been shown to be better than using the intensity weighted average velocity method implemented by CASA for inferring line centroids (Teague & Foreman-Mackey 2018).

The peak velocity maps for ^{12}CO and ^{13}CO are shown in the second and fifth column in Fig. 1, respectively. To ensure a good balance of reducing the noise from disc-free pixels while retaining velocity field information where the disc is faint, we clipped velocity values in pixels where the peak of the emission was detected at a significance below 3.5 σ. We take the maximum of this quadratic to be the peak emission (in mJy beam^{-1}) in the spectrum of each given pixel. We converted the peak intensity maps to peak-brightness temperature, $T_{\rm B}$, units using Planck's law. This leads to the brightness temperature maps in Fig. 1 (third and sixth columns), where a smoothing of 10 channels has been applied to the ^{12}CO maps as a compromise between S/N and retaining as accurate a measure of peak T_B as possible, though formally this leads to a slight underestimate of the brightness temperature.

Finally, we applied spectro-spatial shifting to the cube; this consists of shifting each pixel's spectrum so that its emission peak, originally located at the velocity shown in the peak velocity maps, was relocated to the stellar velocity. In particular, we spectrally integrated over all channels in the shifted cube where the disc was detected above 4 σ, which significantly reduced the number of channels containing disc signal to integrate over to create the integrated-intensity map of the discs. This consequently significantly increased the S/N of the final integrated-intensity maps.

All three moment maps for each gas-bearing system are shown in Fig. 1 for ^{12}CO and ^{13}CO, ordered by right ascension (RA) from top to bottom. We detect at high S/N and resolve ^{12}CO and ^{13}CO in each system over tens of resolution elements, with a variety of radial and vertical structure features seen in the integrated-intensity and the brightness temperature (peak intensity) maps, and the expected Keplerian velocity fields seen in the peak velocity maps.

3.2. Spectral and radial profiles

We created 1D spectra of ^{12}CO and ^{13}CO emission by spatially integrating the cube intensity between an inner and outer radius for each of the gas-bearing discs, using Gofish (Teague 2019). We iteratively varied the radii until all detectable emission was included. The resulting spectra, which are shown on the left column of Fig. 2, reveal the typical double peaked profile expected for a disc in Keplerian rotation around the central star. These spectra were shifted to the stellar velocity of each system – the stellar velocity was measured from the spectro-spatially shifted spectra, which will be discussed in Sect. 3.3.

We also extracted azimuthally averaged intensity profiles of the ^{12}CO and ^{13}CO emission in each disc, seen on the right hand side of Fig. 2. To create these profiles, we split the disc emission into concentric elliptical annuli, $\frac{1}{4}$ of the beam's major axis wide, each corresponding to a radial annulus in the orbital plane, accounting for the discs' inclination and position angle (Table C.1). For each radial annulus, we spectro-spatially stacked the emission by first shifting spectra in each of the annulus' pixels by the negative of their expected Keplerian line of sight velocity, and then averaging all the spectra from the annulus' pixels. We then integrated over the spectra to extract the intensity of the line at each radius, in mJy beam^{-1} km s^{-1}, which we converted to mJy arcsec^{-2} km s^{-1} to allow direct comparison between discs. This was implemented through Gofish's radial_profile function.

We find two of the gas-bearing discs, HD 32297 and HD 131488, to be too close to edge-on for the above technique to successfully produce radial profiles in the orbital plane; this is because for edge-on discs it is not possible to uniquely map an image pixel to an orbital radius (for a given inclination and PA). Therefore, we here present non-deprojected (on-sky) radial profiles (Fig. 2). These were created by averaging spectrally integrated emission perpendicular to each disc's midplane, within a region ±0.″3, 0.″2 perpendicular to the midplane of each disc,

[1] We make these available to the community at https://doi.org/10.7910/DVN/PXGNNZ and the imaging pipelines can be found on https://arkslp.org/

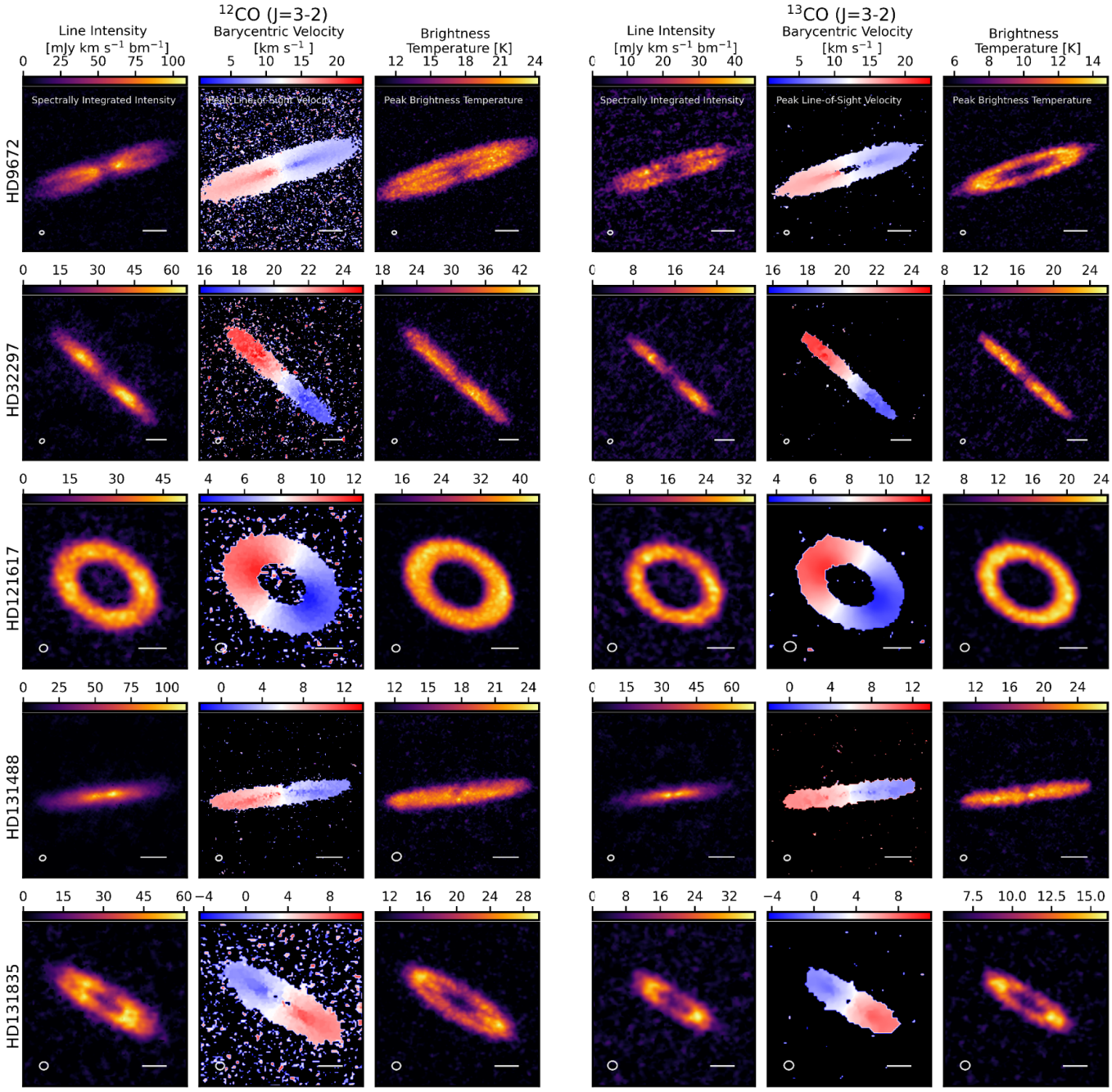

Fig. 1. ^{12}CO (left) and ^{13}CO (right) emission of the five gas-bearing disks in ARKS, HD 9672, HD 32297, HD 121617, HD 131488, and HD 131835 (from top to bottom). The first and fourth column in each row shows the spectrally integrated-intensity map of each disc for ^{12}CO and ^{13}CO, respectively. The minimum line intensity of these integrated-intensity maps was set at 0 mJy km s^{-1} beam^{-1}. The second and fifth columns shows the peak velocity map of each disc for ^{12}CO and ^{13}CO, respectively. Each is centred on the stellar velocity of the systems, and any pixel outside of the velocity range shown in the colour bar is set to black. The peak-intensity (brightness temperature) map of each disc is shown in the third and sixth column for ^{12}CO and ^{13}CO, respectively. The minimum brightness temperature shown in the colour bar is the mean of the emission far from the discs. The ellipse in the lower left corners of the maps is the synthesized beam of the observations. The white scale bar in the bottom right corners indicates 50 au.

respectively, and taking the mean for each vertical stack of pixels. As there are significant differences in the emission between the two sides of HD 32297, which could indicate a potential asymmetry requiring confirmation, we plot the radial profiles from both sides of this edge-on disc for ^{12}CO and ^{13}CO in Fig. 2. As there is no significant differences between both sides of HD 131488's disc, we plot the average radial profiles ^{12}CO and ^{13}CO in Fig. 2. To measure the uncertainty on these radial profiles, the vertical averaging method was applied to many equally sized, ±0.″3, 0.″2 slices of the image, in noise-only regions of the image to measure the noise in the background. This region-drawing and averaging (bootstrapping) was repeated many times in different parts of the image and the standard deviation of each of the average measurements was measured. Once the standard

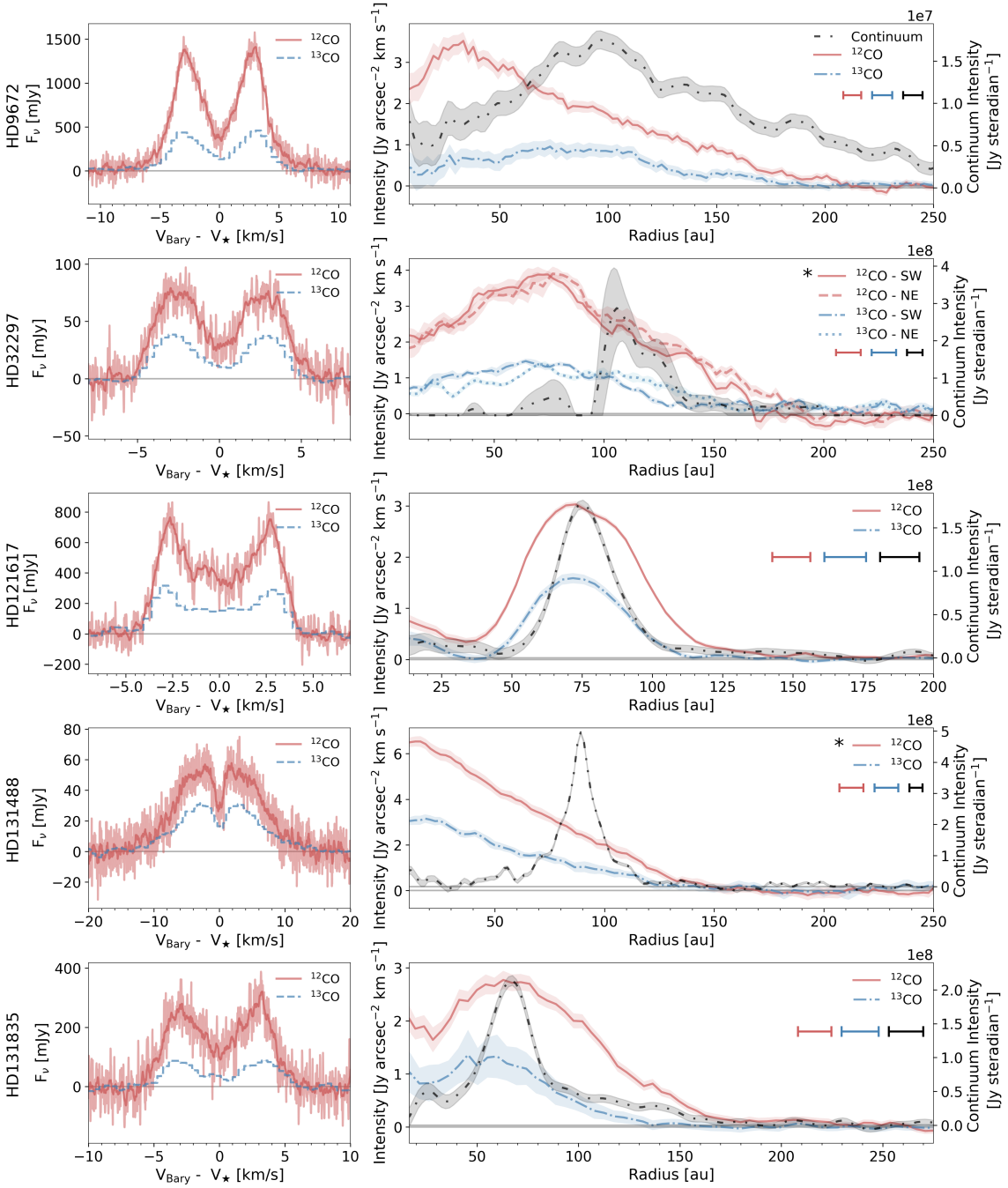

Fig. 2. Left column: spatially integrated spectrum of the ^{12}CO(3–2) (red) and ^{13}CO(3–2) (blue) emission from HD 9672, HD 32297, HD 121617, HD 131488, and HD 131835 in the barycentric velocity frame. The ^{12}CO spectra are additionally shown smoothed with a running mean (window size = 20), chosen to remove noise variation while preserving spectral features. Right column: radial profiles for the same discs. Radial profiles for HD 9672, HD 121617 and HD 131488 were created by azimuthally integrating the emission in each disc. The radial profiles for HD 32297 and HD 131488 (marked by *) are surface brightness profiles as a function of projected separation from the star along the major axis (rather than as a function of radius). For HD 32297, the radial distribution varies for each side of the discs so both sides are shown, in both ^{12}CO and ^{13}CO. For HD 131488, there is no significant differences between both sides of the disc, so an average radial profile is shown. The black radial profiles show the CLEAN dust profiles (Han et al. 2026). In each panel, the minimum value of R corresponds to the first resolution element of the observations. The red, blue and black horizontal bars indicate the resolution of the observations.

deviation of each of the average vertical measurements converged to a constant value for each vertical stack of pixels, it was taken as the error on each radial position in the radial profile.

The resulting radial profiles of each disc are shown in the right column of Fig. 2, and are compared to the continuum radial profiles from the same ARKS ALMA data (Han et al. 2026). Radial profiles comparing the gas distribution with the millimetre-sized dust grains observed with ALMA and with smaller, micron-sized dust grains observed in scattered light/NIR with SPHERE are presented in Milli et al. (2026).

As can be seen in Fig. 2, in each system the ^{12}CO gas appears to extend in all the way to the star. Thus, we can present an upper limit on the inner radius, r_{min}, in each system, being half the resolution element (beam size) of our observations. These upper

Table 1. Upper limits on the inner radii of ^{12}CO, integrated line flux, and corresponding gas masses of ^{12}CO(J=3–2).

	$r_{\min^{12}\mathrm{CO}}$ [au]	^{12}CO (J=3–2) Integrated Line Flux [Jy km s^{-1}]	^{13}CO (J=3–2) Integrated Line Flux [Jy km s^{-1}]	^{12}CO (J=3–2) $\tau_{^{12}\mathrm{CO}} << 1$ Mass [$10^{-4} M_\oplus$]	^{12}CO (J=3–2) $\tau_{^{12}\mathrm{CO}} = 77$ Mass [$10^{-2} M_\oplus$]
HD 9672	3	8.9 ± 0.9	3.0 ± 0.3	2.8 ± 0.3	2.2 ± 0.2
HD 32297	68	3.7 ± 0.4	1.3 ± 0.1	5.8 ± 0.6	4.5 ± 0.5
HD 121617	28	3.6 ± 0.4	1.5 ± 0.2	4.6 ± 0.5	3.5 ± 0.3
HD 131488	6	2.7 ± 0.3	1.3 ± 0.1	5.9 ± 0.7	4.5 ± 0.5
HD 131835	21	1.9 ± 0.2	0.61 ± 0.06	2.9 ± 0.3	2.2 ± 0.2

Notes. Upper limits on $r_{\min}$ correspond to the highest velocity and on-sky along-midplane distance from the star at which a 3 σ detection is achieved anywhere in each system. Integrated line fluxes were measured by spectro-spatially stacking the spectra of the ARKS gas-bearing targets. ^{12}CO gas masses derived assuming ^{12}CO are optically thin ($\tau_{^{12}\mathrm{CO}} << 1$) and assuming that the ^{12}CO and ^{13}CO is optically thick, and the ^{12}CO/^{13}CO ratio is 77 (ISM-like). The optically thin gas mass was calculated using Eq. (2) in Matrà et al. (2015) and by taking the peak-brightness temperatures from the peak-brightness temperature maps. Optically thin masses were scaled by the ISM ^{12}CO/^{13}CO ratio to calculate the optically thick mass.

limits are in the few au range, from 4.2 au around HD 9672 to 8.3 au around HD 131488. We note that for the edge-on systems HD 32297 and HD 131488, this is based on the sky-projected profile and should not strictly be interpreted as an orbital radius.

To more accurately estimate an inner radius for all systems, we therefore present an alternative approach where we calculate the orbital radius corresponding to the highest velocity and on-sky along-midplane distance from the star at which a 3 σ detection is achieved anywhere in each system, accounting for the stellar mass and system inclination (see Appendix C in Matrà et al. 2017a). This is applicable to systems with any inclination and leads to a likely better estimate for the inner ^{12}CO radii of each system (though still formally an upper limit as fainter emission may extend further in) and is reported in Table 1.

Figure 3 shows how the ^{12}CO/^{13}CO (spectrally integrated intensity) ratios change with radius for the gas-bearing sources. We only calculated this ratio in regions where both ^{12}CO and ^{13}CO are at least marginally detected; in other words, out to the radius at which point the ^{13}CO radial profile is detected above the 2 σ level. This threshold was chosen as it gave the best compromise of showing the ^{12}CO/^{13}CO ratio without displaying radii with high uncertainties due to the ^{13}CO becoming undetected. Note that for the edge-on systems, the ratio radial profile is on-sky (non-deprojected) and was calculated for both sides of each disc. As we found no significant differences in the ratio radial profile between the two, in Fig. 3 we present an average of the two sides.

We find that the ^{12}CO/^{13}CO intensity ratios at the radial ^{12}CO intensity peaks of each system are ∼2.0–5.5, and are well constrained with typical uncertainties of ±6–33% at the peak of the ^{12}CO radial profiles. Additionally, we do not find a strong dependence of the ratio with radius, within the fractional error, with ratios changing only by a factor ∼2–3 across broad radial ranges of ∼120–160 au. The implications of these findings are discussed in Sect. 4.2.

3.3. Spectro-spatial shifting and stacking

Of the 18 discs in the ARKS sample, thirteen were not previously known to host any gas. To investigate whether these discs have any detectable CO gas, we ran the first two `tclean` rounds on each disc to create the dirty image cubes (with the robust parameter set to two to ensure the highest possible S/N) without any CLEAN deconvolution, as no signal was obviously present from visual inspection of the cubes.

To further boost the S/N and extract signals that would be too faint to see in each channel and in single resolution elements, we carried out spectro-spatial stacking (Yen et al. 2016; Teague et al. 2016; Matrà et al. 2017b) using the `GoFish` package (Teague 2019). To spectro-spatially stack the emission, we assigned a sky-projected line-of-sight velocity to every pixel under the assumption of Keplerian rotation and that the CO emission is co-located with the dust emission. Given the known disc inclination, position angle (PA), both derived from MCMC sampling carried out by Marino et al. (2026b), and stellar mass, estimated as described in Appendix A in Marino et al. (2026b), the spectrum in each pixel was then shifted by the negative of its assigned sky-projected (line of sight) Keplerian velocity to the spectral (stellar) velocity (using literature values as listed in Table B.1). The minimum and maximum orbital radii of pixels to be shifted and stacked were selected by $r_{min/max}$ as in Eq. (A.3). For the edge-on systems, as mentioned in Sect. 2, it is not possible to assign a Keplerian velocity uniquely to each pixel. Therefore, we conservatively set $r_{min} = 0$ to ensure that the radial selection includes all on-sky pixels that are likely to contain emission. For the gas-free systems, the spectro-spatial shift was repeated twice, once assuming an orbital inclination i (from the known geometry of dust emission) and once with inclination $i + 180°$, to account for the two possible rotation directions of the disc.

Once all the spectra in the different pixels are aligned in velocity, they can be summed to significantly boost the S/N, as demonstrated for the gas-bearing disc HD 121617 in Fig. 4. This shows the spectrum integrated spatially over pixels that correspond to orbital (as opposed to on-sky) radii between r_{min} and r_{max}, as extracted directly from the image cube of HD 121617 in blue. We show the same spectrum following the spectro-spatial stacking (S.S. spectrum) process in red. Thus, if gas is present in the previously undetected systems, the stacked profile will present a single peak at the stellar velocity rather than a Keplerian profile, with the same noise level, leading to a significant peak S/N boost, as demonstrated in Fig. 4.

The spectro-spatially shifted and stacked spectra for each of the 13 systems where no CO was previously detected are shown in Fig. D.1 (two spectra plotted to represent each rotation direction). Despite application of the S/N-boosting spectro-spatial stacking technique, we do not detect ^{12}CO in any of the systems.

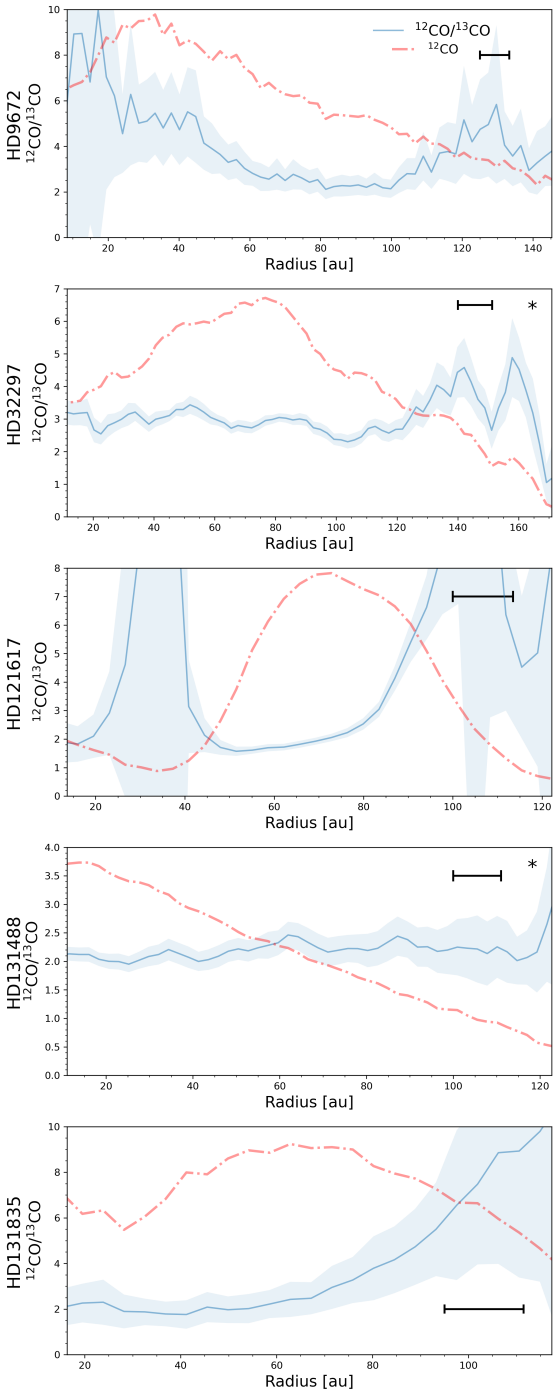

Fig. 3. Radial profiles of ^{12}CO/^{13}CO intensity ratios for HD 9672, HD 32297, HD 121617, HD 131488, and HD 131835 (blue). The ^{12}CO radial profile is overplotted in red to show the gas distribution in each system. The ^{12}CO/^{13}CO ratios for HD 32297 and HD 131488 (marked by an asterisk) were created from the average of the non-deprojected on-sky radial profiles. In each panel, the minimum value of R corresponds to the first resolution element of the observations. The black bar indicates the resolution of the observations.

For the gas-bearing disks, to measure the barycentric velocity of each system, we fitted a Gaussian to the spectro-spatially stacked spectra such as shown for HD 121617 in Fig. 4. Although Gaussians are not a perfect fit to the detailed shape of the single peaks, they are sufficient to determine the velocity centroid of the emission.

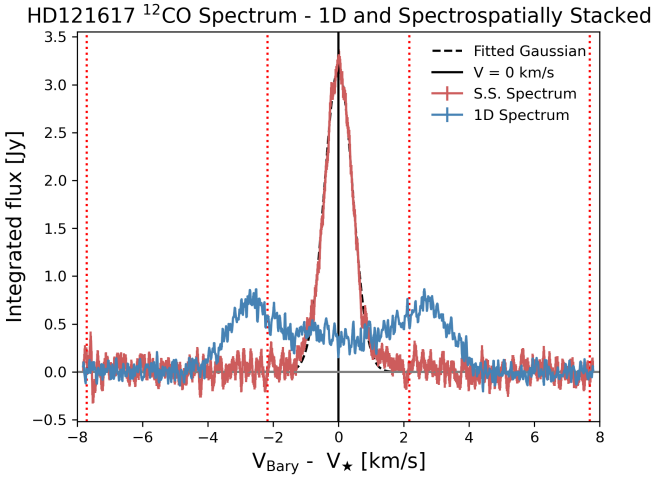

Fig. 4. ^{12}CO spatially integrated spectrum of HD 121617 (blue) and its spectro-spatially stacked (S.S.) spectrum (red). The dotted red lines indicate the velocities in which integration was carried out to calculate the error on the line flux measurement. V_* represents the stellar velocity of HD 121617, determined by fitting a Gaussian profile to the spectro-spatially shifted spectrum.

These velocities are presented in Table C.1 and are consistent with the stellar velocities used in the mask making process. Note that the uncertainties listed on these velocities are just statistically based from the Gaussian fit and do not include possible systematic errors causes by imperfect shifting or asymmetric disc velocity fields. As a check of the validity of the velocities measured with this method, we compared to the stellar velocity of HD 121617 to the stellar velocity measured by Brennan et al. (2026) for the same star ($V_* = 7858^{+2}_{-3}$ m s^{-1}) through fitting a Keplerian model to the peak velocity map. We found the two measured velocities to be consistent within 3 σ of each other. Additionally, we checked the stellar velocity of HD 131488 measured through high-resolution near-IR CRIRES+ spectroscopy ($V_* = 5.860^{+0.096}_{-0.012}$ km s^{-1}, Smith et al. 2025), and found it to be also consistent with our measurement.

3.4. Flux and mass lower limit measurements

To measure the line flux of the ^{12}CO and ^{13}CO lines in each of the three non-edge-on gas-bearing discs, we used the spectro-spatially shifted and integrated spectra described in Sect. 3.3. For example, the red spectrum in Fig. 4 was used to measure the integrated line flux of HD 121617. This way, we can take advantage of the narrower line width (for the same spectral RMS before and after spectro-spatial stacking) to obtain a lower uncertainty on the velocity integrated line flux.

We integrated over the red, spectro-spatially stacked spectrum created and shown in Fig. 4. To include all the emission while avoiding unnecessary noisy regions, we used the standard deviation sigma from the Gaussian fit described in Sect. 3.3 to guide the limits for the integration. We set the limits of integration to $V_* \pm 5\,\sigma$. We then visually confirmed that this covered the entirety of the line emission from each disc.

We use bootstrapping to calculate the error on these line flux measurements. To do so, we repeat the integration to calculate the error on this line flux measurement a large number (>100) of times over the exact same number of channels as the actual measurement, but in noise-only regions of the spectro-spatially stacked spectrum. We choose the standard deviation of these

bootstrap integrations as the statistical uncertainty on our line flux measurement. The number of iterations over which the integration was repeated was set by visually inspecting the standard deviations of the integration and was accepted as the error once it had converged to a constant value, making sure to use a sufficient number of noisy regions to allow this standard deviation value to converge. This statistical uncertainty was then added in quadrature to the systematic flux density calibration error associated with ALMA band 7 observations, which is 10% of the measured flux (Cortes et al. 2023); we find that the flux calibration systematic dominates the uncertainty for all discs.

For the edge-on gas-bearing systems, this method of measuring the line flux was ineffective, as due to their edge-on inclination, emission above and below the midplane was missed in the shifting and stacking process. Thus, to measure the integrated line flux for the two edge-on systems, we simply spatially integrated the intensity over the region where disc emission is present. For HD 32297 and HD 131488 respectively, the regions chosen were (78 × 500) au and (61 × 500) au boxes with the long sides along the midplane and short sides perpendicular to it, centered on their respective stellar positions. We obtained the integrated flux uncertainty by multiplying the RMS in the spectrally integrated intensity maps (in units of Jy km s^{-1} beam^{-1}) by the square root of the number of independent resolution elements (beams) in the respective boxes, and added this in quadrature to the systematic absolute flux calibration error, where the latter dominates the error budget. The integrated line fluxes of ^{12}CO and ^{13}CO for gas-bearing discs are presented in Table 1.

We used Eq. (2) in Matrà et al. (2015) to calculate the ^{12}CO optically thin ($\tau_{^{12}\mathrm{CO}} << 1$) gas mass in each disc using the integrated line fluxes. The calculation requires knowledge of the upper level (in our case, J=3) population of the CO molecule. For simplicity, we calculate this assuming local thermodynamic equilibrium (LTE) and a CO excitation temperature equal to the peak-brightness temperature measured from the ^{12}CO brightness temperature maps. If the gas is optically thin, this will lead to an underestimation of the excitation temperature (as $T_B < T_{exc}$), but that would mean that the masses presented in Table 1 remain lower limits as higher T_{exc} would lead to higher derived masses. These values (Table 1) are of order ∼1–6 × 10^{-4} M$_\oplus$. The relationship between this optically thin mass and the one that would be derived for any optical depth value is

$$M_{^{12}\mathrm{CO,thick}} = \frac{\tau_{^{12}\mathrm{CO}}}{1 - e^{-\tau_{^{12}\mathrm{CO}}}} M_{^{12}\mathrm{CO,thin}}, \quad (3)$$

with the caveat that this is in the simple assumption of a disc of spatially uniform CO density and temperature. This allows us to also report a mass in the assumption that the ^{12}CO is optically thick with an assumed optical depth of 77 (Table 1), motivated our findings in Sects. 4.2–4.3, showing that the ^{12}CO/^{13}CO ratio radial profiles are likely explained by both isotopologues being optically thick everywhere they are detected in the majority of systems. Then, if ^{13}CO is optically thick, its optical depth is at least 1. If the ISM ^{12}C/^{13}C abundance ratio of 77 applies, that implies that the ^{12}CO optical depth must be at least 77 (Wilson & Rood 1994). As such, our mass derived in the assumption of a ^{12}CO optical depth of 77 is to be considered a lower limit in a scenario where both ^{12}CO and ^{13}CO are optically thick, which we deem likely for most detected systems.

For the discs with non-detected gas, we calculated upper limits of the ^{12}CO integrated line flux by using the same bootstrapping method as described above, applied to the spectro-spatially shifted spectra in Fig. D.1. We spectrally integrated over 7 km s^{-1} wide noisy regions, located in random regions of each spectrum, and measured the standard deviation of the bootstrapped samples to derive the uncertainty σ on the spectrally integrated flux of any line, if present. We chose 7 km s^{-1} because the gas-bearing spectro-spatially stacked spectra were on average 7 km s^{-1} wide across a range of disc radial profiles and inclinations. We used this to set 3 σ upper limits on the line flux for all our undetected discs, presented in Table D.1. Given that ^{12}CO is not detected, we do not report upper limits for the rarer ^{13}CO isotopologue, as it would not be detected either.

4. Discussion

4.1. Radial CO distribution

With the high spatial resolution ARKS delivers, we were able to extract resolved radial profiles for the gas-bearing discs. Remarkably, we find that in all systems the CO emission is significantly broader and extends much closer to the star compared to the dust emission. Of the five gas-bearing discs in ARKS, only HD 121617 has a ring-like appearance, though even this disc has gas interior to the dust ring, with emission rising again inwards of a radial minimum at ∼34 au (Fig. 2). Interestingly, in each of the gas-bearing discs, the CO intensity distribution peaks interior to the millimetre-sized dust grains observed within ARKS. This could be an optical depth effect if the gas in each disc is optically thick, or an indication that the gas release is modulated by the temperature of solids which is higher closer to the star (Bonsor et al. 2023). In three discs, HD 9672, HD 32297, and HD 131488, we see large differences (>40 au) in the peak locations between the CO and the dust (Fig. 2). In HD 121617 and HD 131835, we see smaller, but still significant, offsets between the gas and the millimetre-sized dust grains.

This raises the question of whether CO can be continuously produced in a second-generation scenario, given it is not entirely co-located with the dust (Kóspál et al. 2013). However, gas released from exocometary ice is expected to viscously spread radially inwards and outwards of the belt (Kral et al. 2016). For ^{12}CO to have time to spread (as opposed to the long-lived atomic dissociation products), significant amounts of shielding would need to be in place. This is because for CO gas to persist past ∼130 years (the unshielded CO photodissociation timescale due to interstellar FUV photons) a shielding agent such as H_2, C, or CO itself is required (Heays et al. 2017; Matrà et al. 2015). The fact that we observe the CO to be broad/spreading throughout these systems means it must be shielded in the vertical direction from the Interstellar Radiation Field (ISRF) and in the radial direction from stellar UV photons, as in regions sufficiently close to the star, stellar photons dominate the UV field and photodissociation processes. In order for the gas to persist and inwardly propagate in this region, its shielding against the stellar UV photons must also be efficient enough (especially for HD 9672 and HD 131488, where the CO gas is present very close to the luminous star). This shielding could be done by CI and/or CO self-shielding (Marino et al. 2020). Therefore, in a secondary-generation scenario, the observed broad CO radial profiles of these CO-bearing discs can only be explained if the CO and/or CI column densities are sufficiently high to provide significant shielding or the viscosity of the gas is sufficiently high to allow the gas to spread within its photodissociation timescales. On the other hand, the CO could be primordial in origin, with large amounts of unseen H_2 shielding it. Whether the gas is primordial or secondary in HD 121617 is further discussed in Brennan et al. (2026), Marino et al. (2026a), and Weber et al. (2026).

4.2. Resolved isotopologue ratios and optical depth

The ^{12}CO/^{13}CO intensity ratio was radially resolved in each of the gas-bearing discs and are found to be between ∼2.0–5.5 at the peak ^{12}CO locations, which also corresponds to the peak location for ^{13}CO in all systems but HD 9672 (Figs. 2 and 3). These low peak or otherwise disc-averaged ^{12}CO/^{13}CO line ratios were previously interpreted to indicate optically thick ^{12}CO as they are much lower than the expected values from the ISM, ^{12}CO/^{13}CO = 77 (Wilson & Rood 1994). Interestingly, we find most ratio profiles in Fig. 3 to be consistent with being radially flat across the entire radial region where ^{13}CO is detected at the 2σ level (note that the shaded region shown in Fig. 3 is ±1σ). This radial change of the isotopologue ratio can be interpreted in terms of the optical depth of the five gas-bearing systems.

If we assume that optically thick ^{12}CO is co-located with optically thin ^{13}CO, that the CO is in local thermodynamic equilibrium (LTE), and that $T = T_{^{12}\mathrm{CO}} = T_{^{13}\mathrm{CO}}$, we could write the specific intensity of the line describing the spectrum at a specific radius as

$$I_{\nu_{^{12}\mathrm{CO}}} \simeq S_\nu(T), \tag{4}$$

$$I_{\nu_{^{13}\mathrm{CO}}} = S_\nu(T)(1 - e^{-\tau_{^{13}\mathrm{CO}}}), \tag{5}$$

where the source function is equal the Planck function, $S_\nu(T) = B_\nu(T)$, as the gas is in LTE and $\tau_{^{13}\mathrm{CO}}$ is the optical depth of the ^{13}CO. This assumption is based on previous studies where the ^{12}CO was calculated to be very optically thick in all discs but where ^{13}CO was assumed to be optically thin (e.g. HD 9672, HD 121617; Moór et al. 2017, 2019). This relation still holds if we do not assume LTE for the co-located ^{12}CO and ^{13}CO if they are subject to the same excitation conditions. Accordingly, we arrive at the following expression for the specific intensity ratio:

$$\frac{I_{\nu_{^{12}\mathrm{CO}}}}{I_{\nu_{^{13}\mathrm{CO}}}} = \frac{1}{1 - e^{-\tau_{^{13}\mathrm{CO}}}} \sim \frac{1}{\tau_{^{13}\mathrm{CO}}} \tag{6}$$

as $\tau_{^{13}\mathrm{CO}} << 1$ for optically thin ^{13}CO. We know that the optical depth is proportional to the column density of the gas, $\tau_{^{13}\mathrm{CO}} \propto N_{^{13}\mathrm{CO}}$, and therefore that the ^{13}CO specific intensity is also proportional to the column density, $I_{\nu_{^{13}\mathrm{CO}}} \propto N_{^{13}\mathrm{CO}}$. Thus, if we see a decrease radially in optically thin ^{13}CO specific intensity from a peak, this indicates a decrease in ^{13}CO optical depth and column density; in turn, from Eq. (6) above we should see an increase in the ^{12}CO/^{13}CO specific intensity ratio. Overall, for optically thick ^{12}CO and optically thin ^{13}CO, a decrease in ^{13}CO intensity should be accompanied by an increase in the ^{12}CO/^{13}CO specific intensity line ratio.

We highlight that in Fig. 2 we are showing the spectral integral of specific intensity (i.e. the intensity I) rather than the specific intensity I_ν discussed above, and that the line ratio profiles in Fig. 3 also show ratios of intensities rather than specific intensities. However, a similar behaviour as described above would be expected for intensity ratios as for specific intensity ratios, as the integral of an optically thick line changes much more slowly than an optically thin line. In conclusion, this indicates that the flat intensity ratios with radius shown in Fig. 3 rule out that the ^{12}CO is optically thick and co-located with optically thin ^{13}CO.

Radially flat ^{12}CO/^{13}CO ratios can thus be explained if both isotopologues are optically thick everywhere they are significantly detected, as inferred by Brennan et al. (2026) for HD 121617. In this case, both ^{12}CO and ^{13}CO specific intensities (and also integrated intensities) would trace the radial temperature distribution, which is likely to be monotonically decreasing with radius (e.g. ^{12}CO for HD 9672, and both isotopologues for HD 131488). It is important to note that if both isotopologues were optically thick, the underlying abundance ratios would be completely unconstrained. On the other hand, it remains formally possible that for discs other than HD 121617 both isotopologue lines could be optically thin everywhere they are detected. However, it is not clear what physical mechanism could be responsible for such a large change in the abundance ratio from the ISM abundance ratio, if both isotopologues are optically thin.

Thus, to explain our largely radially constant (within ±1σ) ^{12}CO/^{13}CO ratios, both isotopologues have to be either optically thick, or optically thin, at every location where they are detected. To break this degeneracy, radiative transfer modelling needs to be carried out, as in Brennan et al. (2026) for HD 121617.

Interestingly, Zhang et al. (2021) found the ^{12}CO/^{13}CO ratio to be ∼2–4 (see their Fig. 2, top two rows) in the gas-rich protoplanetary discs observed in the ALMA MAPS large program, which they interpreted to be due to the optical thickness of the CO gas. Combining this with the results of Brennan et al. (2026), it is likely that we are observing the same phenomenon with our comparably low ^{12}CO/^{13}CO ratios being caused by optically thick gas in each of the gas-bearing discs included in this study.

4.3. Temperature and CO mass estimates

If ^{12}CO and ^{13}CO are optically thick, the peak intensity and therefore brightness temperature is a direct probe of the excitation temperature, which if in LTE, also corresponds to the gas kinetic temperature. Interestingly, we measure peak-brightness temperatures of ∼25–50 K from the ^{12}CO peak-intensity/brightness temperature maps (Fig. 1). Each measured peak-brightness temperature is lower than the corresponding blackbody temperature at the discs' peak radial location (which range from 54 K < T_{BB} < 137 K), which is consistent with what was found with lower resolution observations of gas-bearing debris discs (e.g. Moór et al. 2019).

This difference in temperature could be caused by several mechanisms: the first possibility is that LTE does not apply and thus the kinetic temperature might be higher and closer to the black body temperature. This could be caused by low gas densities (e.g. in the absence of H_2) in which case, these temperatures could be lower limits to the gas kinetic temperature. The second possibility is that LTE does apply but differing heating/cooling processes (decoupling) of gas from dust is causing the difference.

With co-located optically thick ^{12}CO and ^{13}CO, we could naively expect the measured peak-brightness temperatures of both isotopologues would be equal (as we would expect $T_{^{12}\mathrm{CO}} = T_{^{13}\mathrm{CO}} = T_{\mathrm{exc}} = T_{\mathrm{B}}$). However, as can be seen when comparing between the peak-brightness temperatures for ^{12}CO and ^{13}CO for the majority of the discs (Fig. 1), there is a factor of ∼2 difference between the peak-brightness temperatures between ^{12}CO and ^{13}CO. This is likely due to the much lower spectral resolution in the ^{13}CO observations; the saturated line was convolved by the lower resolution element, and thus the resulting observed peak intensity/brightness temperature would be lower that the true peak intensity/brightness temperature. An example that potentially showcases this issue is HD 131488, in which the local line profiles are wider and therefore better resolved, likely because the gas extends closer to the star where broadening by Keplerian shear is more significant (Brennan et al. 2026, Appendix A); the ^{13}CO line was resolved and in this disc, we observe comparable peak temperatures for both ^{12}CO and ^{13}CO.

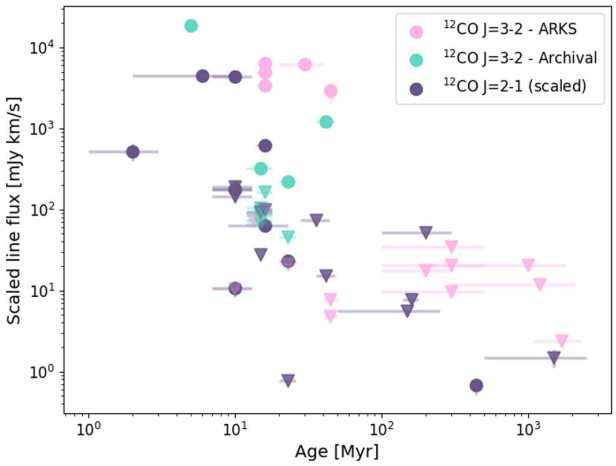

Fig. 5. Line flux of ^{12}CO (J=3–2) scaled to 100 pc as a function of the stellar age. The pink points show ^{12}CO (J=3–2) fluxes measured in this work, the green points show archival ^{12}CO (J=3–2) fluxes, and the purple points show archival ^{12}CO (J=2–1) fluxes that were scaled by the average ^{12}CO J=3–2/J=2–1 ratio of all discs for which both lines were observed (1.67). The archival sources and the corresponding references are listed in Table E.1. The circles represent resolved data points, and the triangles represent upper limits on ^{12}CO.

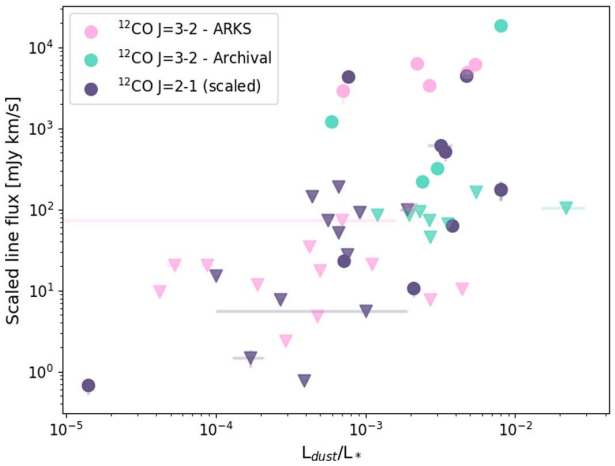

Fig. 6. Similar to Fig. 5, but for the line flux of ^{12}CO scaled to 100 pc as a function of the fractional luminosities (L_{dust}/L_*) of the systems.

As many of the ^{12}CO/^{13}CO intensity radial profiles can be explained by both isotopologues being both optically thick or both optically thin, in Sect. 3.4 (Table 1) we reported ^{12}CO masses for both scenarios. In the optically thick case however, it is not formally possible to directly determine CO gas masses from line fluxes, so we calculated an optically thick mass assuming $\tau_{^{12}CO}$ = 77. This assumption is based on the fact that if ^{12}CO is optically thick, then ^{13}CO must be as well ($\tau_{^{13}CO}$ >> 1), as demonstrated in Sect. 4.2. Assuming ISM abundance ratios (^{12}CO/^{13}CO = 77, Wilson & Rood 1994), $\tau_{^{12}CO} = 77\tau_{^{13}CO}$, and therefore $\tau_{^{12}CO}$ >> 77. Therefore, our reported $\tau_{^{12}CO}$ = 77 masses, while giving a more realistic idea of the ^{12}CO optical depth if both isotopologues are thick, should be interpreted as lower limits, as $\tau_{^{13}CO}$ is potentially much higher than 1.

4.4. ^{12}CO (J=3–2) population study

To compare the ARKS sample to the broader population, we combine ARKS line fluxes (including 13 upper limits) with any archival discs observed with ALMA with a reported line flux for the ^{12}CO J=3–2 line. We also include archival ^{12}CO J=2–1 ALMA observations by scaling the ^{12}CO J=2–1 line flux by the average of the ^{12}CO J=3–2/J=2–1 ratio (= 1.67) of all discs with both lines observed.

We scaled all line flux measurements to 100 pc to compare the intrinsic line luminosity of all discs. Figure 5 shows the scaled line fluxes as a function of system age. We see that gas detections are mostly found in systems younger than 50 Myr, though Fomalhaut (440 ± 40 Myr, Mamajek 2012) and η Corvi (HD 109085, 1500^{+1000}_{-500} Myr, Pearce et al. (2022) and references therein) are notable exceptions. Although the figure shows there is a clear trend of detection rate with age, no trend is present within detected systems, which could be due to a large scatter caused by different system properties and/or evolution pathways.

In Fig. 6, we show the relationship between the scaled line fluxes and the fractional luminosity of the discs. We observe a positive trend in which discs with higher fractional luminosities correspond to the gas-bearing debris discs implying that systems in which the most dust is being released/created corresponds to the systems with gas in the discs. This could indicate a secondary origin for the gas in these systems as the CO gas could originate in the same collisional cascade that creates the dust (Matrà et al. 2019a). However, this could simply be a consequence of the age trend, given that younger systems will typically also have larger fractional luminosities due to collisional evolution (e.g. Wyatt et al. 2007b). Nonetheless, the presence of upper limits for the highest fractional luminosities (and youngest ages) implies there is a large amount of scatter for dusty/young systems, which again could be caused by different system properties and/or evolutionary pathways (Marino et al. 2020).

4.5. Individual discs

For a discussion on each individual disc, their unique CO distributions and comparisons with previous, low resolution observations, please see Appendix F.

5. Conclusions

We presented the ALMA ^{12}CO and ^{13}CO observations of 18 debris discs in the ARKS sample. Our conclusions are listed below:

- The distributions of ^{12}CO and ^{13}CO are observed to be broader than the continuum in each of the five gas-bearing discs in our sample. In each disc, the CO peaks interior to the dust, although the offset between the dust and gas varies with each system. The radial distribution for CO is much broader, and we detected CO that extended in as far as the inner resolution element of the observations in all systems. We calculated velocity-based upper limits to the inner disc radii of 3–68 au;
- We presented radially resolved ^{12}CO/^{13}CO isotopologue flux ratios for the five gas-bearing discs in our sample. This allowed us to infer the optical depth of the CO. Based on the ^{12}CO/^{13}CO ratios that are consistent with being radially flat at the 3σ level presented for HD 32297, HD 121617, HD 131488, and HD 131835, we rule out that ^{12}CO is optically thick and co-located with optically thin ^{13}CO. We instead conclude that the isotopologues are either both optically thick or both optically thin in the discs. HD 9672 alone shows different radial profiles for ^{12}CO and ^{13}CO, which could imply optically thick ^{12}CO with optically thin ^{13}CO.

This is further supported by the shape of its global spectral line profile;
- We measured the integrated line flux of ^{12}CO and ^{13}CO in each gas-bearing system. Based on this, we calculated the optically thin and optically thick masses of ^{12}CO. The optically thick masses should be considered a strict lower limit because they were calculated by assuming ISM ratios of ^{12}CO/^{13}CO and that $\tau_{^{12}CO} = 77$, which is likely an underestimate of $\tau_{^{12}CO}$, and a higher $\tau_{^{12}CO}$ would increase the optically thick mass we calculated;
- We conducted a deep search for ^{12}CO in the 13 gas-free discs in the ARKS sample and did not detect CO in any of them. This allowed us to set strict upper limits on the integrated line flux in these 13 systems;
- We combined ARKS-derived CO J=3–2 line luminosities (or upper limits) with literature values to confirm that gas is preferentially detected in younger systems and/or in systems with a high fractional luminosity, but we highlight the large scatter in the line luminosities within the cohort of systems that are younger or have a higher fractional luminosity. This could potentially be caused by a range of host star properties and/or evolutionary pathways.

Acknowledgements. SMM and LM acknowledge funding by the European Union through the E-BEANS ERC project (grant number 100117693), and by the Irish research Council (IRC) under grant number IRCLA-2022-3788. Views and opinions expressed are however those of the author(s) only and do not necessarily reflect those of the European Union or the European Research Council Executive Agency. Neither the European Union nor the granting authority can be held responsible for them. SM acknowledges funding by the Royal Society through a Royal Society University Research Fellowship (URF-R1-221669) and the European Union through the FEED ERC project (grant number 101162711). AB acknowledges research support by the Irish Research Council under grant GOIPG/2022/1895. MRJ acknowledges support from the European Union's Horizon Europe Programme under the Marie Sklodowska-Curie grant agreement no. 101064124 and funding provided by the Institute of Physics Belgrade, through the grant by the Ministry of Science, Technological Development, and Innovations of the Republic of Serbia. PW acknowledges support from FONDECYT grant 3220399 and ANID – Millennium Science Initiative Program – Center Code NCN2024_001. MB acknowledges funding from the Agence Nationale de la Recherche through the DDISK project (grant No. ANR-21-CE31-0015). AMH acknowledges support from the National Science Foundation under Grant No. AST-2307920. This work was also supported by the NKFIH NKKP grant ADVANCED 149943 and the NKFIH excellence grant TKP2021-NKTA-64. Project no.149943 has been implemented with the support provided by the Ministry of Culture and Innovation of Hungary from the National Research, Development and Innovation Fund, financed under the NKKP ADVANCED funding scheme. JPM acknowledges research support by the National Science and Technology Council of Taiwan under grant NSTC 112-2112-M-001-032-MY3. JM acknowledges funding from the Agence Nationale de la Recherche through the DDISK project (grant No. ANR-21-CE31-0015) and from the PNP (French National Planetology Program) through the EPOPEE project. SP acknowledges support from FONDECYT Regular 1231663 and ANID – Millennium Science Initiative Program – Center Code NCN2024_001. A.A.S. is supported by the Heising-Simons Foundation through a 51 Pegasi b Fellowship. EC acknowledges support from NASA STScI grant HST-AR-16608.001-A and the Simons Foundation. JBL acknowledges the Smithsonian Institute for funding via a Submillimeter Array (SMA) Fellowship, and the North American ALMA Science Center (NAASC) for funding via an ALMA Ambassadorship. TDP is supported by a UKRI Stephen Hawking Fellowship and a Warwick Prize Fellowship, the latter made possible by a generous philanthropic donation. CdB acknowledges support from the Spanish Ministerio de Ciencia, Innovación y Universidades (MICIU) and the European Regional Development Fund (ERDF) under reference PID2023-153342NB-I00/10.13039/501100011033, from the Beatriz Galindo Senior Fellowship BG22/00166 funded by the MICIU, and the support from the Universidad de La Laguna (ULL) and the Consejería de Economía, Conocimiento y Empleo of the Gobierno de Canarias. This material is based upon work supported by the National Science Foundation Graduate Research Fellowship under Grant No. DGE 2140743. EM acknowledges support from the NASA CT Space Grant. Support for BZ was provided by The Brinson Foundation. This paper makes use of the following ALMA data: ADS/JAO.ALMA# 2022.1.00338.L, 2012.1.00142.S, 2012.1.00198.S, 2015.1.01260.S, 2016.1.00104.S, 2016.1.00195.S, 2016.1.00907.S, 2017.1.00167.S, 2017.1.00825.S, 2018.1.01222.S and 2019.1.00189.S. ALMA is a partnership of ESO (representing its member states), NSF (USA) and NINS (Japan), together with NRC (Canada), MOST and ASIAA (Taiwan), and KASI (Republic of Korea), in cooperation with the Republic of Chile. The Joint ALMA Observatory is operated by ESO, AUI/NRAO and NAOJ. The National Radio Astronomy Observatory is a facility of the National Science Foundation operated under cooperative agreement by Associated Universities, Inc. The project leading to this publication has received support from ORP, that is funded by the European Union's Horizon 2020 research and innovation programme under grant agreement No. 101004719 [ORP]. We are grateful for the help of the UK node of the European ARC in answering our questions and producing calibrated measurement sets. This research used the Canadian Advanced Network For Astronomy Research (CANFAR) operated in partnership by the Canadian Astronomy Data Centre and The Digital Research Alliance of Canada with support from the National Research Council of Canada the Canadian Space Agency, CANARIE and the Canadian Foundation for Innovation.

References

Ballering, N. P., Rieke, G. H., Su, K. Y., & Montiel, E. 2013, ApJ, 775, 55
Bergez-Casalou, C., & Kral, Q. 2024, A&A, 692, A156
Bonsor, A., Wyatt, M. C., Marino, S., et al. 2023, MNRAS, 526, 3115
Booth, M., Matrà, L., Su, K. Y., et al. 2019, MNRAS, 482, 3443
Booth, M., del Burgo, C., & Hambaryan, V. V. 2021a, MNRAS, 500, 5552
Booth, M., Schulz, M., Krivov, A. V., et al. 2021b, MNRAS, 500, 1604
Brandeker, A., Cataldi, G., Olofsson, G., et al. 2016, A&A, 591, A27
Brennan, A., Matrà, L., Marino, S., et al. 2024, MNRAS, 531, 4482
Brennan, A., Matrà, L., Mac Manamon, S., et al. 2026, A&A, 705, A201
Briggs, D. S. 1995, PhD Thesis, New Mexico Institute of Mining and Technology, USA
CASA-Team (Bean, B., et al.) 2022, PASP, 134, 114501
Cataldi, G., Brandeker, A., Olofsson, G., et al. 2014, A&A, 563, A66
Cataldi, G., Brandeker, A., Wu, Y., et al. 2018, ApJ, 861, 72
Cataldi, G., Wu, Y., Brandeker, A., et al. 2020, ApJ, 892, 99
Cataldi, G., Aikawa, Y., Iwasaki, K., et al. 2023, ApJ, 951, 111
Chen, C. H., Mittal, T., Kuchner, M., et al. 2014, ApJSS, 211, 25
Cornwell, T. J. 2008, IEEE J. Selected Top. Signal Process., 2, 793
Cortes, P. C., Vlahakis, C., Hales, A., et al. 2023, ALMA Technical Handbook, Tech. Rep. 10.3, ALMA
Currie, T., Guyon, O., Tamura, M., et al. 2017, ApJ, 836, L15
Czechowski, A., & Mann, I. 2007, ApJ, 660, 1541
Czekala, I., Loomis, R. A., Teague, R., et al. 2021, ApJSS, 257, 2
Daley, C., Hughes, A. M., Carter, E. S., et al. 2019, ApJ, 875, 87
Dent, W. R., Wyatt, M., Roberge, A., et al. 2014, Science, 343, 1490
Duffell, P. C., & MacFadyen, A. I. 2013, ApJ, 769, 41
Faramaz, V., Marino, S., Booth, M., et al. 2021, AJ, 161, 271
Flaherty, K. M., Hughes, A. M., Andrews, S. M., et al. 2016, ApJ, 818, 97
Gaia Collaboration (Vallenari, A., et al.) 2023, A&A, 674, A1
Gontcharov, G. 2006, Astron. Lett., 32, 759
Gratton, R., Bonavita, M., Mesa, D., et al. 2024, A&A, 685, A119
Grigorieva, A., Thébault, P., Artymowicz, P., & Brandeker, A. 2007, A&A, 475, 755
Hales, A., Gorti, U., Carpenter, J. M., Hughes, M., & Flaherty, K. 2019, ApJ, 878, 113
Han, Y., Mansell, E., Jennings, J., et al. 2026, A&A, 705, A196
Heays, A. N., Bosman, A. D., & Van Dishoeck, E. F. 2017, A&A, 602, A105
Högbom, J. 1974, A&AS, 15, 417
Horne, K., & Marsh, T. 1986, MNRAS, 218, 761
Hughes, A. M., Lieman-Sifry, J., Flaherty, K. M., et al. 2017, ApJ, 839, 86
Hughes, A. M., Duchêne, G., & Matthews, B. C. 2018, Annu. Rev. A&A, 56, 541
Jankovic, M. R., Pawellek, N., Zander, J., et al. 2026, A&A, 705, A204
Kennedy, G. M., Marino, S., Matra, L., et al. 2018, MNRAS, 475, 4924
Klusmeyer, J., Hughes, A. M., Matrà, L., et al. 2021, ApJ, 921, 56
Kóspál, Á., Moór, A., Juhász, A., et al. 2013, ApJ, 776, 77
Kral, Q., Wyatt, M., Carswell, R., et al. 2016, MNRAS, 461, 845
Kral, Q., Marino, S., Wyatt, M. C., Kama, M., & Matra, L. 2019, MNRAS, 489, 3670
Kral, Q., Matrà, L., Kennedy, G. M., Marino, S., & Wyatt, M. C. 2020, MNRAS, 497, 2811
Lieman-Sifry, J., Hughes, A. M., Carpenter, J. M., et al. 2016, ApJ, 828, 25
Lin, D. N. C., & Papaloizou, J. 1993, in Protostars and Planets III, eds. E. H. Levy, & J. I. Lunine (Tucson, AZ: University of Arizona Press), 749
Lovell, J., Kennedy, G. M., Marino, S., et al. 2021a, MNRAS, 502, L66
Lovell, J., Wyatt, M., Ansdell, M., et al. 2021b, MNRAS, 500, 4878
Lovell, J. B., Hales, A. S., Kennedy, G. M., et al. 2026, A&A, 705, A200
Mamajek, E. E. 2012, ApJ, 754, L20
Marino, S., Matrà, L., Stark, C., et al. 2016a, MNRAS, 460, 2933

Marino, S., Wyatt, M., Panić, O., et al. 2016b, MNRAS, stw2867
Marino, S., Carpenter, J., Wyatt, M., et al. 2018, MNRAS, 479, 5423
Marino, S., Yelverton, B., Booth, M., et al. 2019, MNRAS, 484, 1257
Marino, S., Flock, M., Henning, T., et al. 2020, MNRAS, 492, 4409
Marino, S., Cataldi, G., Jankovic, M. R., Matrà, L., & Wyatt, M. 2022, MNRAS, 515, 507
Marino, S., Gupta, V., Weber, P., et al. 2026a, A&A, 705, A202
Marino, S., Matrà, L., Hughes, A. M., et al. 2026b, A&A, 705, A195
Matrà, L., Panić, O., Wyatt, M., & Dent, W. 2015, MNRAS, 447, 3936
Matrà, L., Dent, W., Wyatt, M., et al. 2017a, MNRAS, 464, 1415
Matrà, L., MacGregor, M. A., Kalas, P., et al. 2017b, ApJ, 842, 9
Matrà, L., Wilner, D., Öberg, K., et al. 2018, ApJ, 853, 147
Matrà, L., Öberg, K. I., Wilner, D. J., Olofsson, J., & Bayo, A. 2019a, AJ, 157, 117
Matrà, L., Wyatt, M. C., Wilner, D. J., et al. 2019b, AJ, 157, 135
Matrà, L., Marino, S., Wilner, D. J., et al. 2025, A&A, 693, A151
Matthews, B. C., Krivov, A. V., Wyatt, M. C., Bryden, G., & Eiroa, C. 2014, arXiv preprint [arXiv:1401.0743]
McDonald, I., Zijlstra, A. A., & Boyer, M. L. 2012, MNRAS, 427, 343
Melis, C., Zuckerman, B., Rhee, J. H., & Song, I. 2010, ApJ, 717, L57
Melis, C., Zuckerman, B., Rhee, J. H., et al. 2013, ApJ, 778, 12
Mellon, S. N., Mamajek, E. E., Zwintz, K., et al. 2019, ApJ, 870, 36
Milli, J., Olofsson, J., Bonduelle, M., et al. 2026, A&A, 705, A199
Moór, A., Juhász, A., Kóspál, Á., et al. 2013, ApJ, 777, L25
Moór, A., Henning, T., Juhász, A., et al. 2015, ApJ, 814, 42
Moór, A., Kóspál, Á., Ábrahám, P., et al. 2016, ApJ, 826, 123
Moór, A., Curé, M., Kóspál, Á., et al. 2017, ApJ, 849, 123
Moór, A., Kral, Q., Ábrahám, P., et al. 2019, ApJ, 884, 108
Nakatani, R., Kobayashi, H., Kuiper, R., Nomura, H., & Aikawa, Y. 2021, ApJ, 915, 90
Nakatani, R., Turner, N. J., Hasegawa, Y., et al. 2023, ApJ, 959, L28
Nederlander, A., Hughes, A. M., Fehr, A. J., et al. 2021, ApJ, 917, 5
Pearce, T. D., Launhardt, R., Ostermann, R., et al. 2022, A&A, 659, A135
Pecaut, M. J., & Mamajek, E. E. 2016, MNRAS, 461, 794
Perrot, C., Olofsson, J., Kral, Q., et al. 2023, A&A, 673, A39
Rebollido, I., Ribas, Á., de Gregorio-Monsalvo, I., et al. 2022, MNRAS, 509, 693
Roberge, A., Feldman, P., Lagrange, A., et al. 2000, ApJ, 538, 904
Roberge, A., Kamp, I., Montesinos, B., et al. 2013, ApJ, 771, 69
Roberge, A., Welsh, B. Y., Kamp, I., Weinberger, A. J., & Grady, C. A. 2014, ApJ, 796, L11
Schneiderman, T., Matrà, L., Jackson, A. P., et al. 2021, Nature, 598, 425
Shakura, N. I., & Sunyaev, R. A. 1973, A&A, 24, 337
Smirnov-Pinchukov, G. V., Moór, A., Semenov, D. A., et al. 2022, MNRAS, 510, 1148
Smith, K. D., Matrà, L., Zhang, K., et al. 2025, arXiv e-prints [arXiv:2511.01708]
Sylvester, R., Skinner, C., Barlow, M., & Mannings, V. 1996, MNRAS, 279, 915
Teague, R. 2019, J. Open Source Softw., 4, 1632
Teague, R. 2020, https://doi.org/10.5281/zenodo.4321137
Teague, R., & Foreman-Mackey, D. 2018, RNAAS, 2, 173
Teague, R., Guilloteau, S., Semenov, D., et al. 2016, A&A, 592, A49
Torres, C. A., Quast, G. R., Melo, C. H., & Sterzik, M. F. 2008, arXiv preprint [arXiv:0808.3362]
Troutman, M. R., Hinkle, K. H., Najita, J. R., Rettig, T. W., & Brittain, S. D. 2011, ApJ, 738, 12
Weber, P., Pérez, S., Baruteau, C., et al. 2026, A&A, 705, A203
Wilson, T. L., & Rood, R. 1994, Annu. Rev. A&A, 32, 191
Wilson, P., Kerr, R., Des Etangs, A. L., et al. 2019, A&A, 621, A121
Wu, Y., Worthen, K., Brandeker, A., & Chen, C. 2025, ApJ, 982, 123
Wyatt, M. C. 2008, Annu. Rev. Astron. Astrophys., 46, 339
Wyatt, M. C., Smith, R., Greaves, J., et al. 2007a, ApJ, 658, 569
Wyatt, M. C., Smith, R., Su, K., et al. 2007b, ApJ, 663, 365
Yen, H.-W., Koch, P. M., Liu, H. B., et al. 2016, ApJ, 832, 204
Zawadzki, B., Fehr, A., Hughes, A. M., et al. 2026, A&A, 705, A197
Zhang, K., Booth, A. S., Law, C. J., et al. 2021, ApJSS, 257, 5
Zuckerman, B., & Song, I. 2012, ApJ, 758, 77
Zúñiga-Fernández, S., Bayo, A., Elliott, P., et al. 2021, A&A, 645, A30

[1] School of Physics, Trinity College Dublin, the University of Dublin, College Green, Dublin 2, Ireland
[2] Department of Physics and Astronomy, University of Exeter, Stocker Road, Exeter EX4 4QL, UK
[3] Division of Geological and Planetary Sciences, California Institute of Technology, 1200 E. California Blvd., Pasadena, CA 91125, USA
[4] Institute of Physics Belgrade, University of Belgrade, Pregrevica 118, 11080 Belgrade, Serbia
[5] Departamento de Física, Universidad de Santiago de Chile, Av. Víctor Jara 3493, Santiago, Chile
[6] Millennium Nucleus on Young Exoplanets and their Moons (YEMS), Chile
[7] Center for Interdisciplinary Research in Astrophysics Space Exploration (CIRAS), Universidad de Santiago, Santiago, Chile
[8] Univ. Grenoble Alpes, CNRS, IPAG, 38000 Grenoble, France
[9] Joint ALMA Observatory, Avenida Alonso de Córdova 3107, Vitacura 7630355, Santiago, Chile
[10] National Astronomical Observatory of Japan, Osawa 2-21-1, Mitaka, Tokyo 181-8588, Japan
[11] Department of Astronomy, Graduate School of Science, The University of Tokyo, Tokyo 113-0033, Japan
[12] Department of Astronomy, Van Vleck Observatory, Wesleyan University, 96 Foss Hill Dr., Middletown, CT 06459, USA
[13] Konkoly Observatory, HUN-REN Research Centre for Astronomy and Earth Sciences, MTA Centre of Excellence, Konkoly-Thege Miklós út 15-17, 1121 Budapest, Hungary
[14] Institute of Physics and Astronomy, ELTE Eötvös Loránd University, Pázmány Péter sétány 1/A, 1117 Budapest, Hungary
[15] Max-Planck-Insitut für Astronomie, Königstuhl 17, 69117 Heidelberg, Germany
[16] Academia Sinica Institute of Astronomy and Astrophysics, 11F of AS/NTU Astronomy-Mathematics Building, No.1, Sect. 4, Roosevelt Rd, Taipei 106319, Taiwan
[17] Herzberg Astronomy & Astrophysics, National Research Council of Canada, 5071 West Saanich Road, Victoria, BC V9E 2E9, Canada
[18] Department of Physics & Astronomy, University of Victoria, 3800 Finnerty Rd, Victoria, BC V8P 5C2, Canada
[19] Center for Astrophysics | Harvard & Smithsonian, 60 Garden St, Cambridge, MA 02138, USA
[20] Department of Astronomy and Steward Observatory, The University of Arizona, 933 North Cherry Ave, Tucson, AZ 85721, USA
[21] Institute of Astronomy, University of Cambridge, Madingley Road, Cambridge CB3 0HA, UK
[22] Department of Astronomy, University of California, Berkeley, Berkeley, CA 94720-3411, USA
[23] National Radio Astronomy Observatory, 520 Edgemont Road, Charlottesville, VA 22903-2475, USA
[24] Department of Physics and Astronomy, Johns Hopkins University, 3400 N Charles Street, Baltimore, MD 21218, USA
[25] Department of Physics, University of Warwick, Gibbet Hill Road, Coventry CV4 7AL, UK
[26] UK Astronomy Technology Centre, Royal Observatory Edinburgh, Blackford Hill, Edinburgh EH9 3HJ, UK
[27] Instituto de Astrofísica de Canarias, Vía Láctea S/N, La Laguna, 38200 Tenerife, Spain
[28] Departamento de Astrofísica, Universidad de La Laguna, La Laguna, 38200 Tenerife, Spain

Appendix A: Keplerian mask creation

We created the Keplerian masks used in the CLEANing process through the `keplerian_mask` package (Teague 2020), with disc and stellar parameters as in Table C.1. As the CO lines at any given disc location, or pixel on the sky, are not infinitely thin in the spectral direction, we need to account for their intrinsic line widths, dV, in the mask-making process. We assume the intrinsic line width is set by Doppler broadening, with

$$dV = 2\sigma_v \sqrt{2\ln 2} \text{ where } \sigma_v = \sqrt{\frac{k_B T}{m_{\rm CO}}}, \tag{A.1}$$

where $m_{\rm CO}$ is the mass of a CO molecule in kg. For simplicity we take the temperature T of the gas to be the same as blackbody-like dust, leading to

$$T = 278.3{\rm K}\sqrt{\frac{L_\star^{0.5}}{r}} \tag{A.2}$$

where $L_\star$ is the luminosity of the star in solar luminosities ($L_\odot$) and r is disc radius in au. The assumed inner and outer radii of the CO discs for the mask are

$$r_{\rm min/max}[''] = \frac{r_{\rm mid} \pm 2\sigma_r}{d} \text{ where } \sigma_r = \frac{\Delta r}{2\sqrt{2\ln 2}} \tag{A.3}$$

and d is the distance to the system in pc. $r_{\rm mid}$ is the radius to the centre of the disc and Δr is the FWHM of the disc, both in au. As an initial guess, we take $r_{\rm mid}$ and Δr for the dust grains' distribution in each system (Table 3, Marino et al. 2026b).

The mask was then convolved with a Gaussian kernel of FWHM equal to `nbeams` times the synthesised beam by using `make_mask`'s `nbeams` parameter. This ensures the mask covers more area than just the area covered by the Keplerian orbit. This parameter, effectively setting the area of the mask per channel, was adjusted after visually inspecting the cube to ensure all of the emission was included in the masks. Any inaccuracy in our assumptions to create the mask (e.g. gas radius, width, temperature, etc) are mitigated by the conservative choice of the `nbeams` parameter smoothing in the final convolution step, which varied between 1.5 – 10, depending on the system. The `nbeams` parameter was particularly large for edge-on discs, for which it is not possible to assign a unique sky-projected velocity to each pixel, as each pixel probes a large range of orbital radii and azimuths. Examples of the mask surrounding the emission are shown in Fig. A.1, in which we show how the ^{12}CO emission in HD 121617 was masked in a few example channels from the image cube.

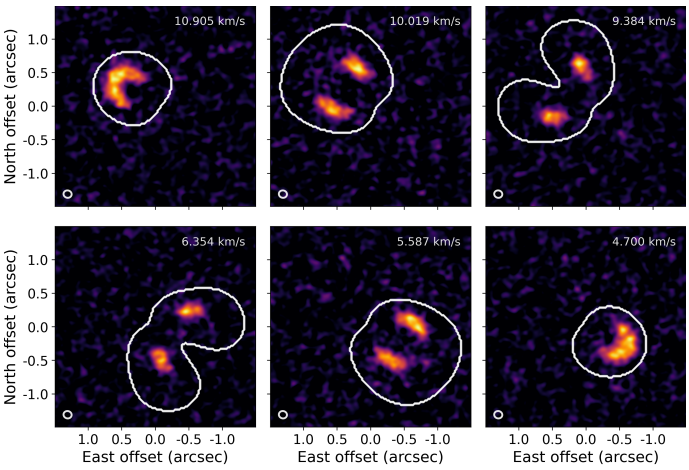

Fig. A.1: The Keplerian mask used during the imaging process shown here on channels from the HD 121617 ^{12}CO image cube. The mask is created using stellar parameters (see Table C.1) assumes the gas is moving in Keplerian rotation around the star. The masks were created using the `keplerian_mask` package (Teague 2020). The ellipse in the lower left corners is the synthesized beam of the observation.

Appendix B: Beam information

Appendix C: Disc parameters for ARKS

Appendix D: Spectra and upper limits for non-detected discs

Appendix E: Archival ^{12}CO integrated line fluxes

Appendix F: Discussion on individual discs

Appendix F.1: HD 9672 (49 Ceti)

HD 9672 is the only system for which the peaks of the ^{12}CO and ^{13}CO are not co-located (Fig. 2). The ^{12}CO is centrally peaked at ∼33 au, the ^{13}CO peaks much farther out in the system, at ∼73 au, while the dust continuum peaks at 135.2 ± 1.9 au (Marino et al. 2026b). Both ^{12}CO and (marginally) ^{13}CO are detected all the way to the central resolution element of the observations (the velocity-based inner radius of the ^{12}CO is ∼3 au) and out as far as ∼200 au. The difference in peak locations between ^{12}CO and ^{13}CO could be an effect of the ^{12}CO being optically thick, while the ^{13}CO is optically thin. Optically thick ^{12}CO would trace the temperature radial distribution (hotter closer to the star), while the optically thin ^{13}CO traces more closely the surface density of the gas. HD 9672's ^{12}CO/^{13}CO ratio displays (at least marginally) what we would expect from optically thick ^{12}CO co-located with optically thin ^{13}CO, with the ratio at its lowest at the peak location of the ^{13}CO and increasing away from the peak.

In its 1D spectral profiles (Fig. 2, left column), we see the ^{12}CO shows a very steep, V-shaped profile interior to its two spectral peaks, whereas ^{13}CO shows a shallower, U-shaped profile. This is further evidence towards ^{12}CO being optically thick with optically thinner ^{13}CO (Horne & Marsh 1986), making HD 9672 unique in the ARKS sample. 3D radiative transfer modelling and an analysis of the local line profiles is needed to determine the optical depth and more accurately determine the gas mass in this system, similar to what is presented in Brennan et al. (2026) and Jankovic et al. (2026) for HD 121617 and HD 131835.

Hughes et al. (2017) had previously measured the integrated flux of the ^{12}CO (3-2) in HD 9672 to be 6.0 ± 0.1 Jy km s^{-1} (though the 10% flux calibration uncertainty is not included in this error bar), measured from the flux enclosed by the 3σ contours on their integrated-intensity map. With the improved spectral and spatial resolution, we have measured a higher value of the integrated flux of ^{12}CO in the disc to be 8.9 ± 0.9 Jy km s^{-1}. The increased value is likely due to the 3 σ contour measurement by Hughes et al. (2017) missing some extended, low-level emission of the outer disc. They calculated an expected outer radius of the CO emission to be ∼220 au. With the improved spectral and spatial resolution offered by ARKS, we can reduce this outer

Table B.1: Overview of the beam information for the ARKS ^{12}CO and ^{13}CO line observations. θ_{maj} is the major axis and θ_{min} the minor axis of the synthesised beam. The beam size listed is the mean size of the beam.

	^{12}CO (13 m s^{-1} channels)				^{13}CO (443 m s^{-1} channels)			
Gas-Bearing Discs	θ_{maj} ["] × θ_{min}["]	Beam Size [au]	Beam PA [°]	RMS [mJy/beam]	θ_{maj} ["] × θ_{min}["]	Beam Size [au]	Beam PA [°]	RMS [mJy/beam]
HD 9672	0.16 × 0.13	8.3	-87.5	5.2	0.18 × 0.15	9.3	89.6	1.0
HD 32297	0.09 × 0.08	11.3	-56.5	3.8	0.09 × 0.08	11.1	-49.3	0.9
HD 121617	0.12 × 0.11	13.5	-76.5	4.7	0.13 × 0.12	14.8	-72.6	0.8
HD 131488	0.08 × 0.07	11.0	-69.8	2.9	0.08 × 0.07	10.9	-74.3	0.6
HD 131835	0.13 × 0.12	16.5	86.8	3.9	0.14 × 0.13	18.3	-89.8	0.9
Gas-Free Discs	^{12}CO (423 m s^{-1} channels)				^{13}CO (443 m s^{-1} channels)			
HD 10647	0.58 × 0.50	9.2	-65.8	0.9	0.61 × 0.52	9.7	66.1	1.0
HD 14055	0.37 × 0.24	10.4	2.0	0.6	0.39 × 0.26	11.0	4.3	0.8
HD 15115	0.20 × 0.18	9.2	59.0	0.4	0.22 × 0.20	10.0	58.1	0.5
HD 15257	1.07 × 0.82	47.3	-39.6	1.5	1.15 × 0.86	50.0	-39.8	1.6
HD 61005	0.33 × 0.22	9.9	86.4	1.3	0.40 × 0.26	12.0	86.6	1.5
HD 76582	0.80 × 0.67	35.9	61.8	1.0	0.83 × 0.70	37.5	62.1	1.1
HD 84870	0.81 × 0.57	62.2	1.1	0.9	0.85 × 0.60	65.3	1.8	0.9
HD 95086	0.49 × 0.30	38.1	17.2	1.2	0.51 × 0.41	39.8	17.5	1.6
HD 109573	0.14 × 0.12	9.5	83.6	1.3	0.16 × 0.15	11.3	88.9	1.4
HD 145560	0.16 × 0.13	17.2	74.4	0.6	0.17 × 0.15	19.0	72.3	0.7
HD 161868	0.80 × 0.54	20.0	-80.1	1.1	0.83 × 0.57	21.0	-78.0	1.2
HD 170773	0.45 × 0.39	15.6	-66.9	1.3	0.46 × 0.41	16.1	-67.7	1.5
TYC 93404371	0.73 × 0.98	31.6	-70.1	1.3	0.76 × 0.71	27.3	-73.1	1.7

Table C.1: Disc parameters of the ARKS disc sample employed in this work.

	i [°]	PA [°]	r [au]	Δr [au]	M_* [$M_\odot$]	d [pc]	L_* [$L_\odot$]	V_* [m s^{-1}]	Ref.
HD 9672	78.7 ± 0.2	107.9 ± 0.2	135.2 ± 1.9	158 ± 3	2.00	57.2	15	11906 ± 1	1
HD 32297	88.3 ± 0.0	47.5 ± 0.0	115.9 ± 0.3	37 ± 1	1.57	130	7.0	21558^{+4}_{-3}	1
HD 121617	44.1 ± 0.6	58.7 ± 0.7	76.3 ± 0.4	18 ± 1	1.90	118	14.9	7851^{+3}_{-2}	1
HD 131488	85.0 ± 0.1	97.2 ± 0.0	89.7 ± 0.1	13 ± 1	1.80	152	12	5860^{+7}_{-8}	1
HD 131835	74.2 ± 0.2	59.2 ± 0.2	77.1 ± 0.5	65 ± 2	1.70	130	9.5	3621^{+6}_{-5}	1
HD 10647	77.8 ± 0.1	57.3 ± 0.3	103.6 ± 0.4	65 ± 2	1.12	17.3	1.6	27600 ± 100	2
HD 14055	80.7 ± 0.2	162.2 ± 0.3	169.4 ± 2.9	162 ± 9	2.19	35.7	29	5100 ± 1700	2
HD 15115	86.7 ± 0.0	98.5 ± 0.0	80.7 ± 0.3	14 ± 1	1.43	48.8	3.7	6900 ± 300	2
HD 15257	59.4 ± 4.9	47.3 ± 5.5	184.2 ± 20.2	261 ± 41	1.75	49.0	14	−24800 ± 2800	3
HD 61005	85.9 ± 0.1	70.4 ± 0.1	72.4 ± 0.2	36 ± 1	0.95	36.5	0.62	22300 ± 100	2
HD 76582	72.6 ± 0.7	104.7 ± 0.7	203.6 ± 4.9	176 ± 9	1.61	48.9	9.9	−1700 ± 200	2
HD 84870	47.1 ± 2.6	−25.7 ± 4.1	199.3 ± 7.8	232 ± 15	1.66	88.8	7.9	500 ± 200	2
HD 95086	31.6 ± 3.5	100 ± 5.7	197.0 ± 4.6	173 ± 8	1.54	86.5	6.4	18000 ± 200	2
HD 109573	76.6 ± 0.1	26.5 ± 0.0	75.9 ± 0.1	7 ± 0	2.14	70.8	25	10900 ± 600	2
HD 145560	47.6 ± 0.6	39.4 ± 0.9	75.4 ± 0.5	29 ± 2	1.35	121	3.3	2800 ± 500	2
HD 161868	66.1 ± 1.5	57.6 ± 1.6	121.2 ± 3.7	134 ± 8	2.11	29.7	24	−12300 ± 500	2
HD 170773	32.9 ± 1.9	113.0 ± 2.9	191.9 ± 2.9	66 ± 4	1.4	36.9	3.6	−17700 ± 200	2
TYC 9340-437-1	18.0 ± 8.0	149.2 ± 20.2	95.7 ± 2.5	99 ± 5	0.75	36.7	0.19	7980 ± 20	4

Notes. The inclination, PA, disc radius (r) and disc width (Δr) (2nd, 3rd, 4th and 5th columns) are the best fit parameters derived from MCMC sampling carried out by Marino et al. (2026b). The listed values correspond to the median and the 16th and 84th percentiles to estimate the uncertainties. For sources with a double Gaussian (HD 107146, HD 92945 and HD 15115), r represents the average between the two Gaussian centres and Δr is the sum of the FWHM of the two Gaussians. Stellar masses in the 6th column were estimated as described in Appendix A in Marino et al. (2026b). The 7th column indicates the distance according to Gaia DR3 (Gaia Collaboration 2023). The stellar luminosity (8th column) were taken from Matrà et al. (2025). The 9th column indicates the stellar barycentric radial velocity. V_* for gas-bearing systems were measured by fitting a Gaussian to the discs spectro-spatailly stacked spectra, while V_* for gas-free systems were taken from the literature; the corresponding reference is listed in the 10th column.
Velocity references. 1. This work, 2. Gaia Collaboration (2023), 3. Gontcharov (2006), 4. Zúñiga-Fernández et al. (2021)

boundary: we find an outer radius of ∼200 au (Fig. 2). We confirm the existence of the asymmetry between the south-east and north-west limbs first reported in Hughes et al. (2017) in which the CO emission was twisted relative to the disc major axis. We observe that the ^{12}CO emission in the north west is brighter than the emission in the south east of the disc; in addition, on the NW side, the brightness peak is south of the disc major axis, which is in the same direction as the twist previously reported for ^{12}CO (Hughes et al. 2017) and now observed in the ARKS continuum observations (Lovell et al. 2026). This is clear for ^{12}CO from its integrated-intensity map, but not clearly seen for the fainter ^{13}CO

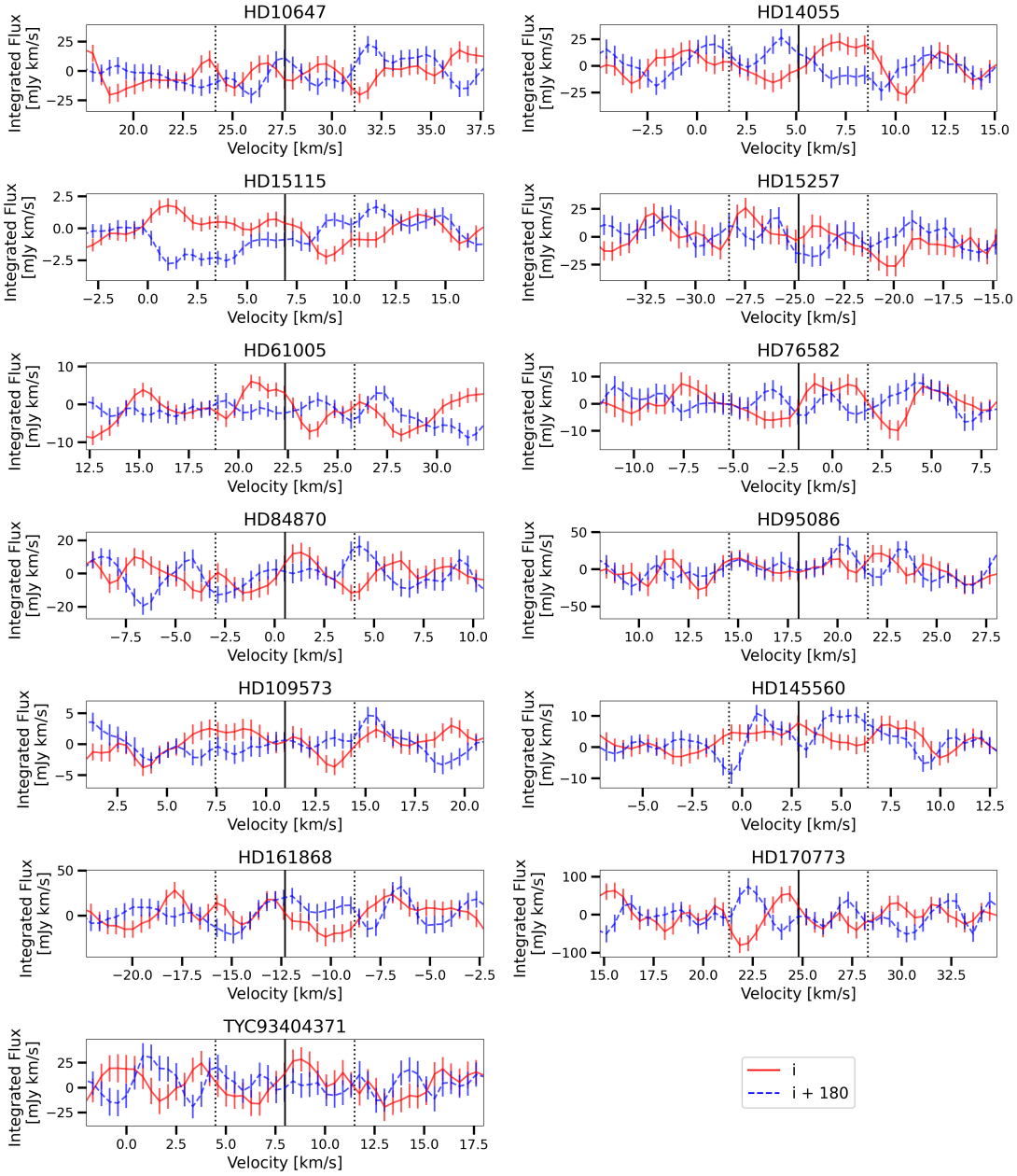

Fig. D.1: The spectro-spatially stacked spectra of the ARKS targets where no CO emission was detected. In each plot, we show both the spectrum shifted with the disc's inclination i and also with $i + 180°$, to eliminate the degeneracy between rotational direction and inclination. The black solid line indicates the stellar velocity, in the barycentric frame, which is where we would expect to see a peak if gas was detected in the system. The black dotted lines indicate the region of $V_* \pm 3.5$ km s^{-1} which was integrated over to calculate the line flux.

(Fig. 1), therefore it remains unclear for CO whether this reflects a surface density asymmetry or a temperature asymmetry.

Appendix F.2: HD 32297

HD 32297 is a close to edge-on ($i = 88.33°$), vertically thin disc when observed in the continuum (Zawadzki et al. 2026), though broader when observed through its ^{12}CO and ^{13}CO emission and in scattered light observations (Milli et al. 2026). From the on-sky (non-deprojected) radial profile, CO radially extends as far out as ~200 au, peaking around ~75 au and potentially all the way to the inner regions of the planetary system (Fig. 2), though the velocity-based upper limit on the inner radius of the ^{12}CO is ~68 au. This outer radius is consistent with what was observed with low resolution observations; Moór et al. (2019) also found an outer radius of ~200 au. The mm dust, however, peaks at $105.2^{+0.7}_{-0.5}$ au, in a much narrower belt ($\Delta R = 14 \pm 0.6$ au, Han et al. 2026).

We observe a asymmetry between the NE and SW sides of the disc in the gas, with the peak emission being brighter and more extended on the SW side of the disc, as seen in the moment maps (Fig. 1), and as was seen for CI in Fig. 1 of Cataldi et al. (2020). However, the radial profile shows that the NE side of the disc is brighter in the outer (> 100 au) regions of the disc

Table D.1: Upper limits on the integrated Line Flux of ^{12}CO.

Gas-free Discs	3 σ upper limit on Integrated line flux of ^{12}CO [mJy km s^{-1}]	Reference
HD 10647	84	1
HD 14055	83	1
HD 15115	20	1
HD 15257	85	1
HD 61005	59	1
HD 76582	49	1
HD 84870	44	1
HD 95086	100	1
HD 109573	20	1
HD 145560	67	1
HD 161868	230	1
HD 170773	130	1
TYC 93404371	160	1
HD 92945	69	2
HD 107146	74	3
HD 197481	70 [a]	4
HD 206893	40 [a]	5
HD 218396	–[b]	6

Notes. Archival upper limits on the ^{12}CO (J=3-2) line are included for the ARKS archival targets. [(a)] denotes ^{12}CO (J=2-1) is reported. [(b)] No upper limit is available for HD 218396, as discussed in Appendix B of Faramaz et al. (2021). **References:** 1. This work, 2. Marino et al. (2019), 3. Marino et al. (2018), 4. Daley et al. (2019), 5. Nederlander et al. (2021) 6. Faramaz et al. (2021)

(Fig. 2). This disc is observed to be asymmetric in other wavelengths; Lovell et al. (2026) determines the system to host an offset asymmetry while Milli et al. (2026) shows the disc is more extended in small grains in the NE (as is the case in the radial profiles in Fig. 2). All combined, this suggests that the disc is eccentric, with its orbital apocentre in the same direction as the asymmetries presented here.

HD 32297's ^{12}CO/^{13}CO ratio does not change with radius and is constant at ∼2. While this ratio is between the non-deprojected, on-sky radial profiles, it shows that both ^{12}CO and ^{13} CO are likely both optically thick or both optically thin, as discussed above.

Appendix F.3: HD 121617

The bulk of the ^{12}CO emission in HD 121617 is confined to a ring, peaking at ∼ 73 au and ∼48 au wide (FWHM from fitting a Gaussian to the radial profile) in ^{12}CO (Figs. 1, 2). However, interior to this ring the emission does not go down to zero, instead reaching a minimum at ∼34 au and rising again interior to that all the way to the central resolution element. The velocity-based upper limit on the inner radius of the ^{12}CO is ∼28 au. Similarly, outside the main ring, ^{12}CO emission is detected out to ∼160 au in a long, faint tail of emission. This is in contrast to the mm-sized dust grains, which peak at a slightly larger radius, $r = 75.3^{+0.4}_{-0.3}$ au, than the ^{12}CO intensity profile, but are much more narrowly distributed (FWHM = 14.1 ± 1.2 au for the mm grains vs ∼48 au for the ^{12}CO, Han et al. 2026).

The ^{12}CO/^{13}CO ratio is ∼2 at the peak location of the ^{12}CO and is largely consistent with being flat throughout the planetary system where both ^{12}CO and ^{13}CO are significantly detected. Between 60 au and 90 au, the ^{12}CO/^{13}CO ratio increases slightly to ∼3, which is likely caused by the ^{13}CO becoming less optically thick with radius. We observe two large peaks in the ^{12}CO/^{13}CO ratio for this system, located at ∼35 au and ∼105 au, in Fig. 3 but we note that these correspond to locations where the ^{13}CO becomes only marginally detected and should not be interpreted as a change in the optical depth of the isotopologues.

Brennan et al. (2026) carried out detailed radiative transfer modelling of this disc and found that the ^{12}CO and ^{13}CO emission are best explained by a narrow disc of gas, that resembles the thin dust disc, that is optically thick at all radii. They also analyse the intrinsic line profiles of the ^{12}CO and ^{13}CO and find them to be Gaussian, which was previously believed to indicate optically thin gas. However, they find their optically thick model can reproduce broad Gaussian line profiles. Their ^{13}CO RADMC-3D best-fit model reproduces the observations with $T_{\rm peak}$ = 38 K, and an optically thick ^{13}CO mass of $M_{^{13}\rm CO} = 2 \times 10^{-3}$ M$_\oplus$. This was then scaled by the ISM ^{12}CO/^{13}CO ratio of 77 to yield a total CO mass of $M_{\rm CO} = 1.48 \times 10^{-1}$ M$_\oplus$. We note here that the mass calculated in this work, presented in Table 1, assumed an optically thin ^{13}CO, with $\tau_{^{13}\rm CO} = 1$, whereas $\tau_{^{13}\rm CO} = 26$ in the best-fit model of Brennan et al. (2026), which explains the discrepancy in the reported mass values. Their $T_{\rm peak}$ is comparable with the $T_{\rm peak}$ measured for this system from the ^{12}CO peak-intensity/brightness temperature map.

The continuum observations for this disc show a strong asymmetry with a brighter arc of emission at the SW ansa of the main ring (Lovell et al. 2026; Marino et al. 2026a). However, this asymmetry is not seen in the CO emission (Fig. 1). By fitting a parametric radiative transfer model to the mm-sized dust grains, Marino et al. (2026a) constrained the arc morphology and found the arc to be radially narrow and only marginally resolved with a FWHM between ∼1 − 5 au. They examined the gas kinematics of the ring and found that the azimuthal velocity of the gas decreases radially more steeply than Keplerian, which could be explained by a strong pressure gradient. Marino et al. (2026a) concluded that the velocity deviations are consistent with a narrow ring of gas, and that this asymmetry could be caused by a vortex in the gas (Weber et al. 2026) or by planet-disc interactions, (Pearce et al, in prep.).

In addition, to investigate if the CO disc displays any shift in position due to the disc being eccentric (as found in scattered light emission, Perrot et al. 2023; Milli et al. 2026), Marino et al. (2026a) examined the differences between the radial profiles of the north east and south west sides of the disc and found there is a significant signal when examining these differences, indicating there could be an eccentricity in the CO emission. However, this finding is sensitive to the stellar location assumed and due to an uncertainty of $\lesssim$10 mas on the stellar location (Marino et al. 2026b), this eccentricity in the CO emission cannot be confirmed.

The asymmetry only being detected in the continuum observations and not in the gas emissions could be due to a) the high optical depth of CO emission, which could hide an overdensity; or b) the gas distribution is approximately axisymmetric. The latter is consistent with the study of Weber et al. (2026), who investigate the structure around HD 121617 via hydrodynamical simulations. Here, the narrow gas ring becomes unstable and generates a subtle azimuthal asymmetry in the form of a vortex. The size-dependent gas drag influences both the radial and azimuthal confinement of the dust particles. However, Weber et al. (2026) finds that the resultant dust structure is only consistent with the ALMA continuum and VLT/SPHERE scattered light image, if there is substantial unseen molecular hydrogen (i.e. if the total gas mass exceeds the measured CO mass

Table E.1: Archival ^{12}CO integrated line fluxes plotted in Figs. 5 and 6. ^{12}CO J=2-1 integrated line fluxes were multiplied by the average ^{12}CO J=3-2/J=2-1 ratio (1.67) before being plotted along side the ^{12}CO J=3-2 integrated line fluxes.

	Age [Myr]	Ref.	Fractional Luminosity	Ref.	^{12}CO Line	^{12}CO Integrated Flux [mJy km s^{-1}]	Ref.
HD 21997	42^{+6}_{-4}	1	$(5.8 \pm 0.1) \times 10^{-4}$	1	3-2	2513 ± 260	1
HD 36546	6 ± 4	2	$(4.7 \pm 0.1) \times 10^{-3}$	1	2-1	2670 ± 40	2
HD 38206	42^{+6}_{-4}	1	$(1.16 \pm 0.04) \times 10^{-4}$	1	2-1	< 18	3
HD 39060	23 ± 3	1	$(2.5 \pm 0.1) \times 10^{-3}$	1	3-2	5807 ± 606	4
HD 48370	36 ± 8	4	$(5.6 \pm 0.2) \times 10^{-4}$	2	2-1	< 338	1
HD 98363	15 ± 3	6	9.20×10^{-4}	3	2-1	< 36	7
HD 106906	15 ± 3	1	$(1.2 \pm 0.03) \times 10^{-3}$	1	2-1	< 43	8
HD 109085	1500^{+1000}_{-500}	7	$(1.7 \pm 0.4) \times 10^{-4}$	1	3-2	38 ± 9	9
H 109832	15	8	7.6×10^{-4}	4	2-1	< 33	7
HD 110058	15 ± 3	1	$(9^{22}_{-9}) \times 10^{-4}$	1	3-2	191 ± 17	1
HD 111520	15 ± 3	1	$(2.30 \pm 0.06) \times 10^{-3}$	1	2-1	< 43	8
HD 113766	15 ± 3	1	$(2.2^{+0.7}_{-0.3}) \times 10^{-2}$	1	2-1	< 45	8
HD 114082	15 ± 3	1	$(3.55^{+0.07}_{0.08}) \times 10^{-3}$	1	2-1	< 45	8
HD 115600	15 ± 3	1	$(1.95^{+0.05}_{-0.04}) \times 10^{-3}$	1	2-1	< 43	8
HD 117214	15 ± 3	1	$(2.66^{+0.07}_{-0.06}) \times 10^{-3}$	1	2-1	< 39	8
HD 121191	16 ± 2	1	$(3.2^{+0.6}_{-0.3}) \times 10^{-3}$	1	2-1	209 ± 19	10
HD 129590	16 ± 2	1	$(5.5^{+0.2}_{-0.1}) \times 10^{-3}$	1	2-1	< 54	8
HD 138813	10 ± 3	1	$(7.7 \pm 0.2) \times 10^{-4}$	1	2-1	1406 ± 78	8
HD 141569	5	9	8×10^{-3}	5	3-2	15800 ± 600	11
HD 142315	10 ± 3	1	$(6.6 \pm 0.1) \times 10^{-4}$	1	2-1	< 54	8
HD 146181	16 ± 2	1	$(1.9 \pm 0.2) \times 10^{-3}$	1	2-1	< 36	8
HD 146897	10 ± 3	1	$(8.0^{+0.4}_{-0.3}) \times 10^{-3}$	1	2-1	60 ± 15	8
HD 147137	10 ± 3	1	$(4.4^{+0.1}_{-0.2}) \times 10^{-4}$	1	2-1	< 43	8
HD 156623	16 ± 7	10	3.778×10^{-3}	6	2-1	1183 ± 37	8
HD 172555	23 ± 3	11	7.2×10^{-4}	7	2-1	170 ± 30	12
HD 181327	23 ± 3	1	$(2.71 \pm 0.05) \times 10^{-3}$	1	3-2	< 199	1
NO Lup	1-3	13	$(3.4 \pm 0.01) \times 10^{-3}$	8	3-2	290 ± 70	14
TWA7	10 ± 3	1	$(2.10 \pm 0.08) \times 10^{-3}$	1	3-2	91 ± 20	15
Fomalhaut	440 ± 40	14	$(1.41 \pm 0.02) \times 10^{-5}$	1	2-1	68 ± 16	16

Age References: 1. Matrà et al. (2025), 2. Currie et al. (2017), 3. Torres et al. (2008), 4. Gratton et al. (2024) 5. Booth et al. (2021a), 6. Melis et al. (2013), 7. Pearce et al. (2022) and references therein, 8. Pecaut & Mamajek (2016), 9. Flaherty et al. (2016), 10. Mellon et al. (2019), 11. Schneiderman et al. (2021), 12. Kennedy et al. (2018). 13. Lovell et al. (2021a), 14. Mamajek (2012). **Fractional Luminosity References:** 1. Matrà et al. (2025), 2. Moór et al. (2016), 3. Chen et al. (2014), 4. Ballering et al. (2013), 5. Sylvester et al. (1996), 6. McDonald et al. (2012), 7. Wyatt et al. (2007a), 8. Lovell et al. (2021b). **Flux References:** 1. Cataldi et al. (2023), 2. Rebollido et al. (2022), 3. Booth et al. (2021b), 4. Matrà et al. (2017a), 5. Booth et al. (2019), 6. Booth et al. (2021a) 7. Moór et al. (2017), 8. Lieman-Sifry et al. (2016), 9. Marino et al. (2016b), 10. Kral et al. (2020), 11. Flaherty et al. (2016), 12. Schneiderman et al. (2021), 13. Kennedy et al. (2018), 14. Lovell et al. (2021a), 15. Matrà et al. (2019b), 16. Matrà et al. (2017b)

by orders of magnitude). This assumption only makes sense in the primordial gas scenario. For the secondary gas scenario, the large dust and gas might be dynamically decoupled and hence evolve independently after being released through collisions.

Appendix F.4: HD 131488

HD 131488 is the system in which the CO peaks closest to the star, at ~15 au in the on-sky (non-deprojected) radial profile (Fig. 2). The CO extends outwards to 160 au and potentially extends inwards as far as the innermost resolution element (the highest velocity and on-sky along-midplane distance from the star at which a 3 σ detection is achieved anywhere in the system corresponds to $r_{\rm min} \sim 6$ au).

The ^{12}CO radial profile (Fig. 2) is similar to what might be expected in a primordial protoplanetary-like disc, and could point to a primordial origin if both ^{12}CO and ^{13}CO are optically thick (Sect. 4.2). In the radial profiles for HD 131488, we see that the CO extends to small radii ($r_{\rm min} < 6$ au), suggesting that gas might be accreting onto the star. However, Melis et al. (2013) presented the optical spectrum of HD 131488 and reported no evidence of accretion at a detectable level, as no noticeable emission lines tracing accretion nor any obvious filling of the Balmer absorption lines were present in their spectra.

For CO to be of second-generation origin, on the other hand, it needs to have had enough time to viscously spread inwards, from the thin dust disc, which peaks much farther out in the planetary system ($r_{\rm mm} = 90.84^{+0.18}_{-0.08}$ au, Han et al. 2026). To check

whether this viscous spreading could have propagated/evolved as far as the star, we calculate the viscous timescale, $t_\nu(r)$, at the location of the dust outer ring:

$$t_\nu(r) = \frac{r^2}{\upsilon_\nu} = \frac{\mu\sqrt{GM_* r}}{\alpha k_B T} \quad , \tag{F.1}$$

where $\upsilon_\nu = \alpha c_s H$ is the viscosity parametrized by the α parameter, α is the viscosity of the gas, c_s is the sound speed and $H = \frac{c_s}{\Omega}$ is the local disc scale height (Shakura & Sunyaev 1973; Kral et al. 2016). We calculate c_s by setting the molecular weight $\mu = 28$ and $T = 20$ K, measured from the ^{12}CO peak intensity/brightness temperature map at 90 au. We adopt the values of α that Kral et al. (2019) found can be used to explain the high CO mass in this disc due to its high CO input rate, $10^{-2} < \alpha < 1$. This yields viscous timescales for the ^{12}CO between 0.28 Myr and 28.23 Myr. This system is 16 Myr old (Matrà et al. 2025), so this simple calculation suggests that the gas may have had sufficient time to spread in as far as the star. A caveat here is that while this is the entirety of the gas, this applies to CO only as long as its photodissociation timescale is longer than this viscous timescale, which depends on its column density perpendicular to the midplane (leading to self-shielding), and the presence of CI shielding, whose derivations would require more detailed modelling than presented here (Marino et al. 2020, 2022).

Thus, if the viscosity of the gas were sufficiently high for the viscous timescale to be shorter than the system age, to not be accreting onto the star (Melis et al. 2013), the gas disc must be truncated and have an inner radius smaller than $r_{min} < 6$ au. A potential explanation for this truncation could be the presence of a planet in the inner regions of the system. Marino et al. (2020) reported that a planet orbiting interior to a debris disc could stop the inward flow of gas released by the disc's icy planetesimals. To calculate its mass, we must consider the viscous limit of the gaseous disc, which requires the gap be opened faster than the viscous gas can refill it (Lin & Papaloizou 1993; Duffell & MacFadyen 2013). We can also estimate the mass of a planet sculpting a gap in a gaseous disc by measuring the width of the gap and using the planet's Hill sphere (Bergez-Casalou & Kral 2024). We set Eq. 6 in Duffell & MacFadyen (2013) equal to Eq. 6 in Bergez-Casalou & Kral (2024) to calculate the required mass of a planet to open a gap in a viscous gas and to find where in the planetary system the planet is likely to be located. For this, we measure the temperature at the highest velocity and on-sky along-midplane distance from the star at which a 3 σ detection is achieved anywhere in the system, corresponding to $r_{\rm min} \sim 6$ au, by converting the 3 σ pixel's intensity to brightness temperature using Planck's law. We then extrapolate this temperature throughout the inner regions of the system by assuming a power law $T(r) \propto r^{-0.5}$. We assume that the gas is dominated by CO ($\mu = 28$), and that the viscosity of the gas is the minimum viscosity that would have allowed the gas to viscously spread throughout the system in the star's lifetime, $\alpha = 0.017$. We find that a $7M_\oplus$ planet located at 5.8 au is capable of opening a gap whose outer edge corresponds to the inner radius of the gas disc, 6 au. Thus, if such a planet exists in the system, we can infer its orbital radius is $\lesssim 5.8$ au and its mass $\gtrsim 7M_\oplus$, though we note that the viscous limit of the gaseous disc will scale linearly with the viscosity of the gaseous disc, so these planet parameters should be interpreted as a lower limit on the planet mass and an upper limit on the planets location. This disc also has two dust rings with a gap in-between them at ~69 au, which Han et al. (2026) estimates a planet with a mass of $1.3M_{\rm Jup}$ and orbital distance of 69.4 au could have sculpted. Thus, there are indications for multiple planets in this system.

As reported in Han et al. (2026), the dust disc in this system peaks at $90.84^{+0.18}_{-0.08}$ au. An entirely different possibility to explain the strong difference in peak location between CO and dust is that at least some of the gas is produced in situ in the inner region of the system, where planets may be forming. Melis et al. (2010) reported significant amounts of warm dust in the system, located at a radius of 0.6 au under the assumption that the dust grains temperature is given by their black body radiation. Departures from this assumption, however, may shift the radius further out, that is, closer to the observed CO peak location. Therefore, CO gas may be connected to the presence of warm dust and potentially giant impact(s) expected in the terrestrial region for a system of this age, and as observed more clearly for similarly aged A star HD 172555 (Schneiderman et al. 2021). However, this might not be sufficient to explain why gas extends as far out as > 160 au in this system, which likely requires an additional source of gas at such large distances.

Appendix F.5: HD 131835

HD 131835 is a moderately inclined disc, at $i = 74.2° \pm 0.2°$ (Marino et al. 2026b), which is now resolved over several resolution elements in the integrated-intensity and the peak-intensity maps (Fig. 1). The ^{12}CO peaks at ~63 au while the mm-sized dust peaks at 68.6 ± 0.4 au (Fig. 2, Han et al. 2026). We observe the CO out in the planetary system as far as ~220 au and calculate the velocity-based upper limit on the inner radius to be ~21 au. As in the other gas-bearing discs, the gas distribution is much broader than that of the mm-sized dust, which again could indicate a secondary origin for the CO which is now viscously spreading throughout the planetary system. This is consistent with spatially unresolved data analysed by Hales et al. (2019) of this disc, from which they argued that the partial co-location of the gas and dust supports a cometary origin for the gas.

The ^{12}CO radial profile (Fig. 2) shows a marginal dip at ~30 au. This dip is not seen clearly in the images of the ^{12}CO (Fig. 1), so higher resolution observations are needed to confirm its existence. In the ^{12}CO/^{13}CO ratio radial profile, we find the ratio is constant with radius until ~80 au, which as previously discussed in Sect. 4.2, could indicate both isotopologues being optically thin or both optically thick. However, exterior to ~80 au, we see a marginal increase in the ratio, which could indicate the ^{13}CO is becoming less optically thick at these large radii and is co-located with optically thick ^{12}CO, as discussed in Sect. 4.2, although within the 3σ uncertainties, the ^{12}CO/^{13}CO ratio remains consistent with being radially flat.

Moór et al. (2015) previously measured these using APEX and found the integrated line flux of ^{12}CO J=3-2 to be 2.74 ± 0.55 Jy km s^{-1}, which is consistent with our ARKS measurement at the 3 σ level (Table 1).

There is a large offset of ~35 au between the peak emission from mm-sized dust grains and the peak of scattered light from micron-sized dust grains in this system (Milli et al. 2026). Extensive modelling has been carried out to try to explain these differences, through two possible scenarios (Jankovic et al. 2026). In the first scenario, the disc contains two planetesimal belts which produce two dusty rings with very different size distributions, such that they appear very differently in mm emission and in scattered light. This scenario matches observations to a large degree, albeit the dust in the two planetesimal belts needs to have extremely different material strength, or alternatively the

belts need to have some combination of different dynamical excitation and different composition. It is not clear if these conditions can be fulfilled realistically.

In the second scenario, the peak of mm dust emission is tracing a planetesimal belt, and the outer ring is formed by smaller dust grains that have drifted outwards due to gas drag. Relatively simple dynamical models show that, while the location of the outer ring and the relative brightness of the rings in scattered light can be produced for reasonable assumptions, the outer ring would be much fainter in thermal emission than what is observed. This disagreement with observations could be resolved with a more detailed model that includes dust growth, or if there are planetesimals producing dust at large separations as well (but which do not need to be any different that the ones closer in, in this scenario). In any case, for this scenario to work, the gas mass cannot be as low as the optically thin CO mass found in this work, or else the gas drag would act too slowly on even the smallest grains.

A&A, 705, A197 (2026)
https://doi.org/10.1051/0004-6361/202556505
© The Authors 2026

Astronomy & Astrophysics

The ALMA survey to Resolve exoKuiper belt Substructures (ARKS)

III. The vertical structure of debris disks

B. Zawadzki[1,⋆], A. Fehr[2], A. M. Hughes[1], E. Mansell[1], J. Kittling[3], Y. Han[4], C. Hou[1], M. Pan[5], J. Milli[6], J. Olofsson[7], T. Pearce[8], A. A. Sefilian[9], A. Nurmohamed[1], J. Lee[1], Y. Mpofu[1], M. Bonduelle[6], M. Booth[10], A. Brennan[11], C. del Burgo[12,13], J. M. Carpenter[14], G. Cataldi[15,16], E. Chiang[17], S. Ertel[9,18], Th. Henning[19], M. R. Jankovic[20], G. M. Kennedy[21,8], Á. Kóspál[22,23,19], A. V. Krivov[24], J. B. Lovell[2], P. Luppe[11], M. A. MacGregor[25], S. Mac Manamon[11], S. Marino[26], J. P. Marshall[27], L. Matrà[11], A. Moór[22], S. Pérez[28,29,30], P. Weber[28,29,30], D. J. Wilner[2], and M. C. Wyatt[31]

(Affiliations can be found after the references)

Received 18 July 2025 / Accepted 12 September 2025

ABSTRACT

Context. Debris disks – collisionally sustained belts of dust and sometimes gas around main sequence stars – are remnants of planet formation processes and are found in systems ≳10 Myr old. Millimeter-wavelength observations are particularly important, as the grains probed by these observations are not strongly affected by radiation pressure and stellar winds, allowing them to probe the dynamics of large bodies producing dust. The ALMA survey to Resolve exoKuiper belt Substructures (ARKS) is analyzing high-resolution observations of 24 debris disks to enable the characterization of debris disk substructures across a large sample for the first time.

Aims. For the most highly inclined disks, it is possible to recover the vertical structure of the disk. We aim to model and analyze the most highly inclined systems in the ARKS sample in order to uniformly extract the vertical dust distributions for a sample of well-resolved debris disks.

Methods. We employed both parametric and nonparametric methods to constrain the vertical dust distributions for the most highly inclined ARKS targets.

Results. We find a broad range of aspect ratios, revealing a wide diversity in vertical structure, with a range of best-fit parametric values of $0.0026 \leq h_{\rm HWHM} \leq 0.193$ and a median best-fit value of $h_{\rm HWHM} = 0.021$. The results obtained by nonparametric modeling are generally consistent with the parametric modeling results. We find that five of the 13 disks are consistent with having total disk masses less than that of Neptune (17 $M_\oplus$), assuming stirring by internal processes (self-stirring and collisional and frictional damping). Furthermore, most systems show a significant preference for a Lorentzian vertical profile rather than a Gaussian.

Key words. circumstellar matter – submillimeter: general – submillimeter: planetary systems

1. Introduction

Debris disks offer a window into the final stages of planet formation, revealing details about the dynamical evolution of systems on timescales from tens of millions to billions of years (for reviews, see: Wyatt 2008; Matthews et al. 2014; Hughes et al. 2018). In particular, the vertical distribution of dust in debris disks contains information about the orbital distribution of planetesimals and collision rates within the disk (e.g., Thébault & Augereau 2007; Quillen et al. 2007; Moore et al. 2023). A measurement of the disk scale height at (sub)millimeter wavelengths is effectively a measurement of the inclination dispersion of the dust grains, which in turn enables constraints to be placed on the system dynamics (e.g., Quillen et al. 2007). At (sub)millimeter wavelengths, dust grains are largely unaffected by radiation pressure and allow direct probing of the mass distribution and level of dynamical excitation of large planetesimals in the system.

With high angular resolution (sub)millimeter observations from the Submillimeter Array (SMA) and the Atacama Large Millimeter/submillimeter Array (ALMA), dozens of debris disks have now been resolved, including some with marginally resolved or partially constrained vertical structures (e.g., Kennedy et al. 2018; Daley et al. 2019; Matrà et al. 2019; Vizgan et al. 2022; Hales et al. 2022; Marshall et al. 2023; Terrill et al. 2023; Matrà et al. 2025). Matrà et al. (2019) resolved the vertical structure in the disk around β Pictoris and found that a two-component vertical structure including both a dynamically cold and hot population was required to match the data – a structure that is reminiscent of the dual populations of planetesimals in the classical Kuiper belt caused by Neptune's migration early in the history of the Solar System (e.g., Brown 2001; Morbidelli et al. 2008; Petit et al. 2011). Daley et al. (2019) resolved the vertical structure of the edge-on debris disk around AU Mic using 1.3 mm data and used grain-size dependent velocity dispersions in the collisional cascade models of Pan & Schlichting (2012) to infer a total mass of stirring bodies in the debris belt no greater than 1.8 $M_\oplus$. Incorporating additional observations, Vizgan et al. (2022) examined the relationship between grain size and scale height by obtaining scale height values using both 1.3 mm and 450 μm data. Kennedy et al. (2018) modeled the HR 4796A (HD 109573) debris disk

⋆ Corresponding author: bzawadzki@wesleyan.edu

Open Access article, published by EDP Sciences, under the terms of the Creative Commons Attribution License (https://creativecommons.org/licenses/by/4.0), which permits unrestricted use, distribution, and reproduction in any medium, provided the original work is properly cited.
This article is published in open access under the Subscribe to Open model. Subscribe to A&A to support open access publication.

and determined that their modeling consistently returned a marginally resolved value for the scale height; however, this value was somewhat inconsistent with the indications from scattered light of a dynamically cold population of planetesimals (e.g., Kenyon et al. 1999). These observations revealed the promise of using vertical structure to interpret the dynamics of debris disk systems, although larger samples are needed to draw more robust conclusions.

While (sub)millimeter observations closely trace the masses and dynamical histories of debris disks, scattered light observations probe smaller grains that are sensitive to both radiation forces and collisions. At these wavelengths, debris disks are expected to have a minimum vertical aspect ratio full width at half maximum (FWHM) of $h_{\rm min} = 0.04 \pm 0.02$, which is driven by radiation pressure and collisions inflating inclinations and eccentricities of the small grains (Thébault 2009). The vertical structures of debris disks have already been characterized for several disks in scattered light, with most scale height measurements at or above the theoretically predicted minimum (e.g., Milli et al. 2014; Millar-Blanchaer et al. 2015, 2016; Engler et al. 2019; Boccaletti et al. 2019; Olofsson et al. 2020, 2022b).

However, a larger sample of scale height measurements at (sub)millimeter wavelengths is needed to complement this sample of scattered light scale heights and illuminate connections between grain size and system dynamics. For example, small grains may be stirred to higher inclinations by a giant planet in the disk, inflating the observed scale height (Quillen 2006; Pan & Schlichting 2012). Furthermore, comparing the vertical structures from millimeter and scattered light observations may enable constraints on the gas mass of debris disks as well as on the origins of the gas (Olofsson et al. 2022b). However, if grains are fully coupled to the gas or turbulent diffusion is significant, inclination damping could be reduced, preventing micron-sized grains from fully settling into the midplane and resulting in a more vertically extended grain distribution (Marino et al. 2022). More observational measurements of vertical disk structures at multiple wavelengths will reveal how these processes sculpt debris disks.

The ALMA survey to Resolve exoKuiper belt Substructures (ARKS) sample contains ALMA observations of 24 debris disks at a high enough resolution and sensitivity to carry out the detailed characterization of radial and vertical dust structures (Marino et al. 2026). In order to resolve the vertical distribution of dust, observations of highly inclined (i.e., close to edge-on) debris disks at high angular resolution are necessary. The most highly inclined debris disks in the ARKS sample provide the opportunity to begin building a larger sample of vertically well-resolved debris disks at millimeter wavelengths.

In this paper, we analyze these highly inclined ARKS debris disks in order to place new constraints on their vertical dust distributions. The observations and sample of debris disks are described in Sect. 2. Our modeling framework is detailed in Sect. 3, and our analyses are presented in Sect. 4. In Sect. 5 we relate our parametric modeling results to theoretical models of debris disk dynamics to infer the masses of stirring bodies and the dynamical history of the system, compare the parametric and nonparametric modeling results, and investigate the relationship between vertical structure at millimeter and scattered light wavelengths. Our main conclusions are summarized in Sect. 6. Some technical details are provided in the appendices.

2. Observations

ARKS (2022.1.00338.L, PI: S. Marino) aimed to resolve the FWHM of the vertical distribution of the most highly inclined ($i > 75°$) disks in the sample. The new Band 7 observations were configured to resolve the vertical FWHM of the disks with at least two resolution elements, assuming a vertical aspect ratio[1] of $h_\sigma = 0.05$. The observing strategy for ARKS targets with $i < 75°$was not optimized for vertical structure recovery, and observations of these targets often lack the resolution or S/N to firmly constrain vertical dust distributions (assuming the same vertical aspect ratio of $h_\sigma = 0.05$). However, parametric and/or nonparametric methods can recover vertical structure constraints for some disks at $i < 75°$. In addition to the methods described in this work, for example, azimuthal brightness variations in moderately inclined, optically thin dust rings can be exploited to estimate the disk scale height, provided that the belt is relatively vertically thick and radially narrow (Doi & Kataoka 2021; Villenave et al. 2025). In this paper, we include all disks with vertical structure constraints, though the focus is on the most highly inclined disks, which are amenable to detailed vertical characterization via parametric modeling.

The ARKS sample also includes six archival observations of well-resolved debris disks. The archival observations for HD 39060 (β Pic), HD 107146, HD 197481 (AU Mic), and HD 206893 were taken in Band 6. The vertical aspect ratio of a disk is known to vary with observing wavelength; this variation has been measured in AU Mic between 1.3 mm and 450 µm, with the scale height decreasing by a factor of ∼1.3 with a factor of about three decrease in wavelength (Vizgan et al. 2022). The difference between scale height measurements at Band 7 (0.89 mm) and Band 6 (1.3 mm) is likely more subtle given that the wavelength differs by less than a factor of two, but there are no Band 7 observations of these targets at sufficient resolution to confirm this. The full target selection and observing strategy is justified in Marino et al. (2026), as well as further details about the observations and data calibration. In this study, we use the corrected data produced and presented in Marino et al. (2026), which account for weights and phase center and flux offsets between execution blocks.

3. Modeling

3.1. Definitions of scale height

In general, a vertical scale height characterizes the thickness of the disk by quantifying the size of the region around the disk midplane from which the majority of disk emission originates. This can be defined in a number of ways, and can depend on the exact vertical distribution of disk material. Here, we parameterize the disk scale height, H, as

$$H(r) = hr \tag{1}$$

such that the vertical aspect ratio, h, is constant at all radii, r.

It is common to express a disk scale height as the standard deviation of a Gaussian distribution, H_σ. In this work, we consider multiple vertical distributions, including Lorentzian and multi-component vertical dust distributions which do not have a clearly defined standard deviation. Therefore, we report scale heights in terms of the half width at half maximum (HWHM) of

[1] Several common formulations of the aspect ratio, including h_σ, are defined in Sect. 3.1.

the vertical profile, $H_{\rm HWHM}$. We use the HWHM rather than the full width at half maximum (FWHM) to be more directly comparable with legacy H_σ values. The different scale height formats are related by

$$H_{\rm HWHM} = \frac{1}{2} H_{\rm FWHM} = \sqrt{2\ln 2}\, H_\sigma \qquad (2)$$
$$h_{\rm HWHM} = \frac{1}{2} h_{\rm FWHM} = \sqrt{2\ln 2}\, h_\sigma.$$

We use the above notation to express which scale height or aspect ratio definition is used. For a more direct comparison across different methodologies and archival studies, we preferentially use $H_{\rm HWHM}$ and $h_{\rm HWHM}$, converting to this format when possible. A complete list of aspect ratio values in their original and converted formats is available in Table C.1.

3.2. Parametric modeling

We use a parametric debris disk modeling code adapted from the publicly available code described in Flaherty et al. (2015)[2], which was developed from earlier disk modeling works (Dartois et al. 2003; Rosenfeld et al. 2012, 2013). The modeling framework, optimized for modeling the continuum (dust) emission of axisymmetric debris disks[3], is described in detail in Fehr (2023) and summarized below.

As debris disks are optically thin, their temperatures and densities are fully degenerate. Since we are modeling observations at a single wavelength, the geometric results are insensitive to the temperature structure and we assume a blackbody equilibrium temperature structure, allowing us to fit for the density structure. We computed the dust temperature by setting the flux received by the disk from its host star at some distance d from the star ($d = \sqrt{r^2 + z^2}$, where r and z are the radial and vertical distances in cylindrical coordinates, respectively) equal to the flux emitted by the dust grains at that distance. The bolometric flux emitted at the surface of a dust grain is

$$F_{\rm dust}(r) = \frac{L_*}{16\pi d^2}, \qquad (3)$$

where L_* is the bolometric luminosity of the host star. Assuming grains emit and absorb in a manner similar to black bodies, the dust temperature is then

$$T_{\rm dust}(r) = \left(\frac{L_*}{16\pi\sigma d^2}\right)^{\frac{1}{4}}, \qquad (4)$$

where σ is the Stefan-Boltzmann constant.

The density structure $\rho(r, z)$ of the disk is defined by two components: a radial profile form and a vertical profile form. Careful treatment of the radial structures is critical, as they can be degenerate with the vertical structure of the disk. Thus, the set of radial functional forms applied for the vertical parametric modeling presented here was informed by the ARKS radial structure analysis (Han et al. 2026). Most of our models use either a radial double power law or a radial double Gaussian; the functional forms and associated free parameters are shown in the top section of Table 1. For a more complete examination of the disk radial structures and functional forms, refer to Han et al. (2026).

For the disk vertical structure, we parameterize the disk scale height according to Eq. (1), such that the vertical aspect ratio h is constant throughout the disk in order to minimize additional free parameters. We discuss this assumption and its implications in Sect. 5.6. The vertical functional forms used in this study are shown in the bottom section of Table 1, and are motivated by the array of vertical functional forms used in other debris disk studies (e.g., Golimowski et al. 2006; Lagrange et al. 2012; Apai et al. 2015; Matrà et al. 2019).

3.2.1. Radiative transfer

Once the temperature and density structures of the disk have been defined, we compute the flux throughout the disk in order to obtain a model image of the disk with projected major axis x, projected minor axis y, and distance from disk center along the line of sight s. The intensity of the dust emission is

$$I_\nu(x, y) = \int_0^\infty S_\nu(x, y, s) \exp\left[-\tau_\nu(x, y, s)\right] K_\nu(x, y, s) ds, \qquad (5)$$

where $S_\nu(x, y, s)$ is the source function, $\tau_\nu(x, y, s)$ is the optical depth, and $K_\nu(x, y, s)$ is the absorption coefficient. We approximated the source function with the Planck function:

$$S_\nu(x, y, s) = \frac{2h_p\nu^3}{c^2} \frac{1}{\exp\left[\frac{h_p\nu}{k_B T(x,y,s)}\right] - 1}, \qquad (6)$$

where h_p is Planck's constant, c is the speed of light, and k_B is the Boltzmann constant.

The optical depth is

$$\tau_\nu(x, y, s) = \int_0^s K_\nu(x, y, s')\, ds'. \qquad (7)$$

We assumed

$$K_\nu(x, y, s) = \kappa_\nu \rho(x, y, r), \qquad (8)$$

where κ_ν is the dust mass opacity. We adopted κ_ν =1.9 cm^2 g^{-1} at 0.89 mm and κ_ν =1.3 cm^2 g^{-1} at 1.3 mm as in Marino et al. (2026), who assumed a power law grain size distribution with a slope of –3.5, and a composition of astrosilicates (70%), crystalline water ice (15%), and amorphous carbon (15%) by mass (Draine 2003; Li & Greenberg 1998).

After generating the model disk image and multiplying it by a Gaussian approximation of the primary beam[4], we used `galario` to obtain synthetic visibilities sampled at the same spatial frequencies as the data (Tazzari et al. 2018). The stellar flux is added to the image in the visibility domain at the disk center, which is set by free parameters that enable offsets in right ascension (dRA) and declination (dDec) from the phase center.

3.2.2. Model parameters

We fit the synthetic model visibilities to the observed visibilities using Markov Chain Monte Carlo (MCMC) methods. We used the affine-invariant MCMC implementation in `emcee` to

[2] https://github.com/kevin-flaherty/disk_model3

[3] While some ARKS debris disks are known to contain gas, we do not calculate hydrostatic equilibrium or the velocity field as we expect the dust mass to dominate over the gas mass.

[4] The archival Band 6 observations of HD 39060 are mosaicked. For this source, we apply a primary beam correction at each location in the mosaic field.

Table 1. Summary of the density functional forms used in the parametric modeling.

Radial Form	Surface Density Profile	Free Parameters
Double Power Law (DPL)	$\Sigma(r) = 10^{\Sigma_c}\left[\left(\frac{r}{R_c}\right)^{-\alpha_{in}\gamma} + \left(\frac{r}{R_c}\right)^{-\alpha_{out}\gamma}\right]^{-1/\gamma}$	$R_c, \alpha_{in}, \alpha_{out}, \gamma, \Sigma_c$
Double Gaussian (DG)	$\Sigma(r) = 10^{\Sigma_c}\left[C_1 \exp\left[\frac{-(r-R_1)^2}{2\sigma_1^2}\right] + (1-C_1)\exp\left[\frac{-(r-R_2)^2}{2\sigma_2^2}\right]\right]$	$R_1, R_2, \sigma_1, \sigma_2, C_1, \Sigma_c$
Error Function + Power Law (Erf)	$\Sigma(r) = 10^{\Sigma_c}\left[1 - \mathrm{erf}\left(\frac{R_c - r}{\sqrt{2}\sigma_{in}R_c}\right)\right]\left(\frac{r}{R_c}\right)^{-\alpha_{out}}$	$R_c, \sigma_{in}, \alpha_{out}, \Sigma_c$
Asymmetric Gaussian (AG)	$\Sigma(r) = \begin{cases} 10^{\Sigma_c}\exp\left[-\frac{(r-R_c)^2}{2\sigma_{in}^2}\right] & \text{if } r < R_c \\ 10^{\Sigma_c}\exp\left[-\frac{(r-R_c)^2}{2\sigma_{out}^2}\right] & \text{if } r \geq R_c \end{cases}$	$R_c, \sigma_{in}, \sigma_{out}, \Sigma_c$
Triple Power Law (TPL)	$\Sigma(r) = 10^{\Sigma_c}\left(\frac{R_{in}}{R_{out}}\right)^{-\alpha_{mid}}\left[\left(\frac{r}{R_{in}}\right)^{-\alpha_{in}\gamma_{in}} + \left(\frac{r}{R_{in}}\right)^{-\alpha_{mid}\gamma_{in}}\right]^{-1/\gamma_{in}} \times \left[\left(\frac{r}{R_{out}}\right)^{-\alpha_{mid}\gamma_{out}} + \left(\frac{r}{R_{out}}\right)^{-\alpha_{out}\gamma_{out}}\right]^{-1/\gamma_{out}}$	$R_{in}, R_{out}, \alpha_{in}, \alpha_{mid}, \alpha_{out}, \gamma_{in}, \gamma_{out}, \Sigma_c$
Gaussian (G)	$\Sigma(r) = 10^{\Sigma_c}\exp\left[-\frac{(r-R)^2}{2\sigma^2}\right]$	R, σ, Σ_c
Vertical Form	**Density Profile**	**Free Parameters**
Gaussian (vG)	$\rho(r,z) = \Sigma(r) \times \left[\exp\left[-\frac{1}{2}\left(\frac{z}{H_\sigma(r)}\right)^2\right] \Big/ \sqrt{2\pi}H_\sigma(r)\right]$	h_{HWHM}
Exponential (vE)	$\rho(r,z) = \Sigma(r) \times \left[\exp\left[-\frac{1}{2}\left(\frac{\lvert z\rvert}{H_\sigma(r)}\right)^\zeta\right] \Big/ \sqrt{2\pi}H_\sigma(r)\right]$	h_{HWHM}, ζ
Double Gaussian (vDG)	$\rho(r,z) = \Sigma(r) \times \left[\frac{C_{vert}\exp\left[-\frac{1}{2}(z/H_{\sigma1}(r))^2\right]}{\sqrt{2\pi}H_{\sigma1}(r)} + \frac{(1-C_{vert})\exp\left[-\frac{1}{2}(z/H_{\sigma2}(r))^2\right]}{\sqrt{2\pi}H_{\sigma2}(r)}\right]$	$h_{HWHM1}, h_{HWHM2}, C_{vert}$
Lorentzian (vL)	$\rho(r,z) = \Sigma(r) \times \frac{1}{\pi}\frac{H_{HWHM}(r)}{z^2 + H_{HWHM}(r)^2}$	h_{HWHM}

Notes. Top: Radial forms and free parameters. Bottom: Vertical forms and free parameters. For all radial DPL models, we fix $\gamma = 2$. We note that while the vertical aspect ratio free parameters are all listed as h_{HWHM}, some vertical forms are more conveniently expressed in terms of H_σ. The conversion to h_{HWHM} is described by Equations (2) and (1). In addition to the parameters shown in the table, all models fit for the disk inclination, PA, and stellar flux, as well as RA and declination offsets.

obtain best-fit model parameters and their posterior distributions (Foreman-Mackey et al. 2013). For each disk model, the free parameters included the disk inclination (i), position angle (PA), surface density normalization (Σ_c), stellar flux ($F_\star$) at the observing wavelength[5] (F_*), and offsets from the phase center (dRA and dDec). The additional free parameters for each model depend on the choice of radial and vertical density forms, presented in Table 1.

For each model, we initialized the MCMC with a 64 walker ensemble (more than double the number of free parameters for each model). To ensure that the parameter space was sufficiently sampled, we required at least 10^5 samples after convergence, which corresponds to approximately 1500 steps for each of the 64 walkers. Convergence was determined by visually inspecting the evolution of all walkers in both parameter space and log-likelihood space. We identified convergence once the log-likelihood stabilized and the walkers fluctuated around consistent parameter ranges, discarding earlier steps as burn-in. We further discarded walkers with log-likelihood values at least 5σ lower than the maximum log-likelihood value in order to prevent individual unconverged walkers from affecting the results.

The log-likelihood is proportional to $-0.5\chi^2$, where the model and data are compared using a χ^2 metric[6]:

$$\chi^2 = \sum_{j=1}^{N} w_j \left[\left(\mathrm{ReV}_{\mathrm{obs}\,j} - \mathrm{ReV}_{\mathrm{mod}\,j}\right)^2 + \left(\mathrm{ImV}_{\mathrm{obs}\,j} - \mathrm{ImV}_{\mathrm{mod}\,j}\right)^2\right], \tag{9}$$

where w_j are the visibility weights and $V_{\mathrm{obs}\,j}$ and $V_{\mathrm{mod}\,j}$ are the observed and model visibilities, respectively.

[5] AU Mic exhibited significant variations in the stellar flux across the three observations used here. Thus, we fit three separate stellar flux values as in Daley et al. (2019).

[6] `Using galario.double.chi2Image()`

3.2.3. Model comparison

We tested several model parameterizations for each source, typically beginning with two simple cases: a vertical Gaussian with a radial double power law, and a vertical Gaussian with a radial double Gaussian (Tables 1 and A.1). If radial parametric modeling results favored a different radial density distribution, we included additional models (see Han et al. 2026). After running the initial suite of models with a vertical Gaussian density distribution, we expanded the range of models to include additional vertical complexities.

We compared different model parameterizations using the Akaike and Bayesian Information Criteria (AIC and BIC, respectively), which quantify the trade-off between how well the different models fit the data and how many free parameters are needed (e.g., Akaike 1974; Schwarz 1978; Burnham et al. 2002; Liddle 2007). These criteria are defined as

$$\begin{aligned} \mathrm{AIC} &\equiv -2\ln\mathcal{L}_{\max} + 2k, \\ \mathrm{BIC} &\equiv -2\ln\mathcal{L}_{\max} + k\ln N, \end{aligned} \tag{10}$$

where $\mathcal{L}_{\max}$ is the maximum likelihood achievable by the model, k is the number of parameters of the model, and N is the number of data points (in this application, the number of visibilities).

The set of model parameterizations tested for each source are shown in Table A.1, including the AIC and BIC comparisons. These criteria were computed such that

$$\begin{aligned} \Delta\mathrm{AIC}_\mathrm{i} &= \mathrm{AIC}_\mathrm{i} - \mathrm{AIC}_\mathrm{min}, \\ \Delta\mathrm{BIC}_\mathrm{i} &= \mathrm{BIC}_\mathrm{i} - \mathrm{BIC}_\mathrm{min}, \end{aligned} \tag{11}$$

where $\mathrm{AIC}_\mathrm{min}$ and $\mathrm{BIC}_\mathrm{min}$ are the minimum values of the criteria across the full suite of models, indicating the best fit to the data. Thus, for both ΔAIC and ΔBIC, a value of 0 indicates a best-fit model. AIC comparisons can be converted to a relative likelihood, which is defined as $p_i = \exp\left[-\Delta\mathrm{AIC}_\mathrm{i}/2\right]$. Assuming a normal distribution with a mean of 0, we compute a symmetric interval which contains probability $1 - p_i$. We present AIC comparisons using the upper bound of this interval, which gives the relative likelihood in terms of a confidence level σ. BIC results are directly presented as ΔBIC. Generally, $\Delta\mathrm{BIC} > 10$ is regarded as strong evidence against a particular model (>99% confidence, see Kass & Raftery 1995; Raftery 1995).

We use the AIC and BIC to identify a fiducial model for each source. When the ΔAIC and ΔBIC are minimized for the same model, this model is selected as the fiducial model. When the ΔAIC and ΔBIC are minimized for different models, the model which is least strongly ruled out by the AIC and BIC (AIC confidence $< 3\sigma$ and $\Delta\mathrm{BIC} < 10$) is selected as the fiducial model.

3.3. Nonparametric modeling

Vertical information can also be extracted using nonparametric methods. We used both `frank`, which operates in the visibility domain, and `rave`, which operates in the image domain. Each is briefly summarized below. (For more detailed descriptions in the context of radial profile recovery, see Han et al. 2026.)

3.3.1. `frank`

`frank` is an open-source code which reconstructs the 1D (azimuthally averaged) radial intensity profile of a disk by fitting the visibilities with a Fourier-Bessel series (Jennings et al. 2020). While `frank` is primarily a tool for extracting radial profiles, we use an extension which enables constraints to be placed on the vertical aspect ratio of the disk (originally implemented in Terrill et al. 2023). The specific implementation of `frank` used for analyzing the ARKS sample (`arksia`, Jennings et al. 2024) is publicly available[7].

For all fits, we adopt the position angle, inclination, and RA and declination offsets presented in Marino et al. (2026). We assumed the disk to be vertically Gaussian, with the scale height H_σ proportional to the radius, thereby defining an aspect ratio of $h_\sigma = H_\sigma(r)/r$. Following the approach in Terrill et al. (2023), we repeated the radial profile fit over a range of scale height assumptions, computing the χ^2 value for each height and estimating its likelihood as $\exp(-\chi^2/2)$. The radial profile fits are presented in Han et al. (2026); here, we focus only on the vertical constraints obtained with `frank`.

Starting from a wide range in h_σ, we narrowed the height grid to more densely sample the region of h_σ in which the bulk of the probability mass is centered. The sample points were then interpolated quadratically to obtain a finer probability density distribution (PDF). For approximately half of the disks, the PDF exhibits a clear peak and approaches 0 or a value close to 0 on either side of the peak, and the best-fit height was estimated with the median and the uncertainties with the 16th and 84th percentiles. For the rest of the disks, the PDF does not approach 0 as h_σ approaches 0. In such cases, an upper limit was estimated with the 99.7th percentile if the PDF approaches 0 toward large values of h_σ. The fitted scale heights are listed in Table 3, and the PDFs are shown in Fig. B.2.

3.3.2. `rave`

`rave` is an open-source package for recovering the radial brightness profiles of edge-on disks by fitting models of concentric annuli in the image domain (Han et al. 2022). Like `frank`, `rave` also enables vertical height aspect ratio fitting. Assuming the disk to be vertically Gaussian, the radial profile was fit at a range of h_σ assumptions including 0, and nine additional points spaced uniformly in logarithmic space between 0.01 and 0.5. The χ^2 value for the model fit at each height assumption was calculated using the root mean square (rms) noise of the `CLEAN` image and assuming the number of independent elements to be equal to the number of beams in the region of the image containing disk flux (defined as a rectangle within $r_{\max}$ from the star along the major axis and $y_{\max}$ along the minor axis, as listed in the appendix of Han et al. 2026). The likelihood of each height was estimated to be proportional to $\exp(-\chi^2/2)$.

As with `frank`, the sample points were interpolated to obtain a finer PDF. For disks with PDFs that show a clear peak, the best-fit height was estimated with the median and the lower and upper uncertainties were estimated with the 16th and 84th percentiles. For the remainder of disks, the PDF does not approach 0 even when h_σ is 0. In such cases, if the PDF only drops to 0 at $h_\sigma \gtrapprox 0.3$, we take the 84th percentile to be an upper limit on h_σ; otherwise, the height was unconstrained. The scale heights fitted with `rave` are listed in Table 3, and the PDFs are shown in Fig. B.3.

4. Analysis

The fiducial parametric models are summarized briefly in Table 2. The fiducial images and residuals for each disk are

[7] https://github.com/jeffjennings/arksia

Table 2. Summary of the fiducial parametric models for each source along with the best-fit and median values of $h_{\rm HWHM}$ and inclination (errors showing the 16th and 84th percentiles).

Source	Radial Form	Vertical Form	$h_{\rm HWHM}$		i	
			Best-fit	50th Percentile	Best-fit	50th Percentile
HD 9672	DPL	vL	0.041	$0.046^{+0.008}_{-0.008}$	80.03°	$80.18^{\circ}{}^{+0.12}_{-0.14}$
HD 10647	DG	vDG	0.052 (91%) 0.226 (9%)	$0.053^{+0.006}_{-0.007}$ (88 ± 6%) $0.225^{+0.002}_{-0.002}$ (12 ± 6%)	78.74°	$8.83^{\circ}{}^{+0.21}_{-0.18}$
HD 14055	DPL	vG	0.059	$0.053^{+0.007}_{-0.008}$	80.0°	$80.0^{\circ}{}^{+0.2}_{-0.3}$
HD 15115	DG	vL	0.021	$0.022^{+0.002}_{-0.002}$	86.74°	$86.79^{\circ}{}^{+0.05}_{-0.04}$
HD 32297	DPL	vL	0.0098	$0.0092^{+0.0012}_{-0.0012}$	88.48°	$88.48^{\circ}{}^{+0.04}_{-0.03}$
HD 39060	DPL	vL	0.112	$0.112^{+0.002}_{-0.001}$	87.65°	$87.66^{\circ}{}^{+0.17}_{-0.13}$
HD 61005	DG	vL	0.0129	$0.0143^{+0.0020}_{-0.0021}$	86.23°	$86.24^{\circ}{}^{+0.03}_{-0.04}$
HD 76582	AG	vL	0.193	$0.192^{+0.009}_{-0.009}$	72.1°	$72.6^{\circ}{}^{+0.7}_{-0.6}$
HD 109573	DG	vG	0.0065	$0.0082^{+0.0033}_{-0.0038}$	76.57°	$76.62^{\circ}{}^{+0.09}_{-0.10}$
HD 131488	DG	vG	0.0048	$0.0059^{+0.0011}_{-0.0010}$	84.91°	$84.87^{\circ}{}^{+0.05}_{-0.05}$
HD 131835	DG	vL	0.017	$0.022^{+0.007}_{-0.006}$	74.5°	$74.6^{\circ}{}^{+0.2}_{-0.2}$
HD 161868	DPL	vL	0.192	$0.192^{+0.012}_{-0.016}$	66.7°	$66.7^{\circ}{}^{+0.9}_{-0.9}$
HD 197481	DPL	vL	0.0026	$0.0028^{+0.0009}_{-0.0002}$	88.16°	$88.13^{\circ}{}^{+0.08}_{-0.09}$

Notes. The full set of parametric modeling results, including all free parameters for the fiducial models and the AIC/BIC for each tested model, is presented in Table A.1.

shown in Figure 1 using the same imaging parameters as in Marino et al. (2026). For most sources the fiducial models closely match the observations, with no positive or negative features in the residuals at the 5σ level. Figure 2 shows the best-fit vertical profile for each disk at its reference radius (see Table 4), defined as the radial location of peak intensity in our models, which are axisymmetric. We find aspect ratios in the range between roughly $0.003 \leq h_{\rm HWHM} \leq 0.19$. We note that while we present h in terms of the HWHM of the vertical distribution, many previous studies (particularly those which assume a Gaussian vertical distribution) present h_σ, the standard deviation of the vertical profile. For comparison with other studies, we have converted the published h_σ values mentioned in this work to $h_{\rm HWHM}$ values.

For each source, the aspect ratio is meaningfully constrained, i.e., the posterior probability distribution of $h_{\rm HWHM}$ values has a nonzero peak (Figure 3). To determine whether the scale heights are fully or marginally resolved, we take the difference between the median and 16th percentile h values in order to approximate a 1σ confidence interval (this difference is equivalent to a 1σ confidence interval for a perfectly Gaussian posterior probability distribution, though not all of the posteriors are Gaussian). We use this interval to extrapolate to a 3σ confidence interval; for sources with a $h_{\rm HWHM} \leq 0$ at the 3σ lower bound, we consider $h_{\rm HWHM}$ to be marginally resolved, placing only an upper limit on $h_{\rm HWHM}$. We apply this extrapolation because $h_{\rm HWHM} \leq 0$ is not allowed by our model. Therefore, the 0.15th percentile (corresponding to $\sim 3\sigma$ for a Gaussian distribution) will always be positive and non-zero.

We additionally examine how well-resolved $h_{\rm HWHM}$ is with respect to the resolution of the observations. Importantly, the beams shown in Figure 1 do not reflect the smallest scales resolvable in our analyses. Because our parametric modeling occurs in the visibility domain, we retain spatial information up to the nominal resolution of the interferometer, $\theta_{\rm min} = \lambda_{\rm obs}/b_{\rm max}$, where $\lambda_{\rm obs}$ is the observing wavelength and $b_{\rm max}$ is the longest baseline in the array during the observations. As a result, $h_{\rm HWHM}$ is more easily resolved in Fourier space than in image space, and some values of $h_{\rm HWHM}$ may be resolvable even if the vertical extent of the disk is on roughly the same scale as the `CLEAN` beam (Figure 2). Furthermore, it is not necessary that $\theta_{\rm min} < h_{\rm HWHM}$ in order to resolve the aspect ratio, as $h_{\rm HWHM}$ does not represent the full vertical extent of the disk. Rather, $h_{\rm HWHM}$ only describes the distance from the disk mid-plane to the height at which the disk has half of its peak density. Depending on the vertical parametrization, the disk could thus host a substantial amount of material at several times $h_{\rm HWHM}$.

For example, a vertical Gaussian distribution contains about 95% of the material within $\pm 2\,h_\sigma$ from the midplane, equivalent to $\sim 3.4\,h_{\rm HWHM}$. In this case, a scale height may not be resolved by the observations if $\theta_{\rm min} > 3.4\,h_{\rm HWHM}$. A vertical Lorentzian distribution has thicker tails, with more disk material further from the midplane: ~95% within $\sim 25\,h_{\rm HWHM}$ centered on the midplane. In this case, a scale height may not be resolved by the observations if $\theta_{\rm min} > 25\,h_{\rm HWHM}$. Measurements of $h_{\rm HWHM}$ that are limited by the data resolution are diskussed in the source-specific sections, and values of $\theta_{\rm min}$ are provided in Table 4 for reference.

4.1. Marginally resolved scale heights

4.1.1. HD 109573 (HR 4796A)

Parametric models in Han et al. (2026) suggest that the radial density distribution of this source is well-fit by a double Gaussian, assuming vertical Gaussian profile with a fixed vertical aspect ratio of $h_{\rm HWHM} = 0.015$. Incorporating scale height as a free parameter, we examined double power law, double Gaussian, Gaussian, and asymmetric Gaussian radial profiles. We find

Table 3. Scale height aspect ratios obtained from parametric modeling, `frank`, and `rave`.

Target	Parametric	$h_{\rm HWHM}$ values `frank`	`rave`
HD 9672	$0.046^{+0.008}_{-0.008}$	$0.061^{+0.004}_{-0.004}$	$0.058^{+0.017}_{-0.024}$
HD 10647	$0.053^{+0.007}_{-0.007}$	<0.008	$0.040^{+0.016}_{-0.021}$
HD 14055	$0.054^{+0.008}_{-0.008}$	$0.037^{+0.010}_{-0.016}$	$0.047^{+0.038}_{-0.031}$
HD 15115	$0.022^{+0.002}_{-0.002}$	$0.019^{+0.001}_{-0.001}$	$0.022^{+0.002}_{-0.002}$
HD 15257	N/A	Unconst.	Unconst.
HD 32297	$0.009^{+0.002}_{-0.001}$	$0.010^{+0.001}_{-0.001}$	$0.015^{+0.003}_{-0.004}$
HD 39060	$0.112^{+0.002}_{-0.001}$	$0.073^{+0.002}_{-0.002}$	$0.086^{+0.005}_{-0.005}$
HD 61005	$0.015^{+0.002}_{-0.003}$	$0.019^{+0.001}_{-0.001}$	$0.020^{+0.005}_{-0.007}$
HD 76582	$0.192^{+0.010}_{-0.009}$	$0.065^{+0.012}_{-0.012}$	<0.097
HD 84870	N/A	Unconst.	Unconst.
HD 92945	N/A	$0.039^{+0.011}_{-0.013}$	<0.079
HD 95086	N/A	Unconst.	Unconst.
HD 107146	N/A	$0.134^{+0.021}_{-0.022}$	<0.167
HD 109573	<0.0116	<0.012	<0.022
HD 121617	N/A	$0.106^{+0.011}_{-0.011}$	$0.074^{+0.039}_{-0.044}$
HD 131488	<0.0070	<0.008	$0.016^{+0.005}_{-0.006}$
HD 131835	$0.022^{+0.007}_{-0.006}$	$0.039^{+0.006}_{-0.006}$	$0.057^{+0.020}_{-0.028}$
HD 145560	N/A	$0.070^{+0.015}_{-0.016}$	<0.103
HD 161868	$0.19^{+0.02}_{-0.02}$	<0.097	<0.135
HD 170773	N/A	<0.116	<0.143
HD 197481	$0.0028^{+0.0009}_{-0.0002}$	$0.023^{+0.002}_{-0.002}$	$0.026^{+0.005}_{-0.006}$
HD 206893	N/A	$0.113^{+0.034}_{-0.025}$	<0.212
HD 218396	N/A	Unconst.	Unconst.
TYC 9340	N/A	Unconst.	Unconst.

Notes. For all resolved scale heights, we show the median $h_{\rm HWHM}$, with uncertainties showing the 16th and 84th percentiles. The parametric scale heights are from the fiducial models shown in Table 2; sources marked with N/A do not have any vertical parametric models. For scale heights fitted with `frank` and `rave`, we show upper limits if the PDF only approaches zero at large h_σ, and we note the aspect ratio as unconstrained if the PDF does not approach zero at large h_σ.

that the double Gaussian continues to outperform the other radial density distributions even when incorporating vertical flexibility into the model. We then modeled HD 109573 with a radial double Gaussian density distribution and the four different vertical parameterizations presented in Table 1.

The AIC and BIC strongly favor the vertical Gaussian and vertical Lorentzian models over the other vertical forms, with the vertical Gaussian model preferred over the vertical Lorentzian only at low confidence (AIC σ = 0.09). However, the posterior probability distributions are broad, with a vertical aspect ratio of $h_{\rm HWHM} = 0.0082^{+0.0033}_{-0.0038}$ (vertical Gaussian) or $h_{\rm HWHM} = 0.0049^{+0.0016}_{-0.0014}$ (vertical Lorentzian). Both of these models exhibit a non-Gaussian posterior probability distribution for $h_{\rm HWHM}$, truncating near zero. As a result, we only marginally resolve the scale height for HD 109573. We take the upper limit to be the 84th percentile of the posteriors, $h_{\rm HWHM} < 0.0116$, using the fiducial vertical Gaussian model. Nonparametric fitting also constrains only upper limits, with `frank` finding $h_{\rm HWHM} < 0.012$ and `rave` finding $h_{\rm HWHM} < 0.022$.

The vertical structure of HD 109573 has previously been studied using Band 7 ALMA observations (~0.″17 resolution, Kennedy et al. 2018). Kennedy et al. (2018) modeled the disk with a radial Gaussian and a vertical Gaussian, finding $H_{\rm FWHM}$ = 7 ± 1 au at the radial location of the ring (78.6 au), corresponding to an aspect ratio of $h_{\rm HWHM} = 0.045^{+0.006}_{-0.006}$. Matrà et al. (2025) reanalyzed these observations, also modeling HD 109573 with radial and vertical Gaussians. At the radial ring location of 77.8 au, they obtain $H_{\rm HWHM}$ = 5.3 au, or $h_{\rm HWHM} = 0.068^{+0.002}_{-0.002}$. Han et al. (2025) used `fave`, an extension of `rave` optimized for less inclined disks, to fit the aspect ratio of HD 109573, finding $h_{\rm HWHM} = 0.057^{+0.016}_{-0.022}$. With the new Band 7 ARKS data (0.″08), we find a similar ring location (77.6 au), but a much smaller vertical extent ($H_{\rm HWHM}$ < 0.9 au). This discrepancy is likely due to the lower resolution of previous observations combined with the different best-fit functional form found here (double rather than single Gaussian); the degeneracy between radial and vertical structure makes it difficult to place strong constraints on the scale height, and this issue is more pronounced with lower-resolution data. Despite the improved resolution of the ARKS observations, we may still be limited by the data resolution of the data ($\theta_{\rm min}$ = 3.63 au). At a reference radius of 77.6 au (the location of peak brightness in the fiducial model), we obtain $H_{\rm HWHM}$ = 0.636 au. For a vertical Gaussian profile, 95% of the disk material would then lie within 2.16 au centered on the disk midplane, about 60% of the distance that could be resolved by the observations.

4.1.2. HD 131488

Parametric models in Han et al. (2026) suggest that the radial density distribution of this source is best fit by a double Gaussian, assuming a vertical Gaussian profile with a fixed vertical aspect ratio of $h_{\rm HWHM}$ = 0.005. We find that a double Gaussian radial density distribution is strongly preferred over a double power law or single Gaussian, assuming a vertical Gaussian profile with the vertical aspect ratio as a free parameter. We additionally modeled HD 131488 using a radial double Gaussian density distribution and both a vertical exponential and a vertical Lorentzian.

We find that the vertical Gaussian model performs best when considering both the AIC and BIC (AIC σ = 0.90 over the exponential, ΔBIC = 0), so we select this as the fiducial model for HD 131488. The radial double Gaussian with a vertical exponential is most strongly favored by the AIC, but disfavored by the BIC (ΔBIC = 11.63). The radial double Gaussian with a vertical Lorentzian form is not strongly ruled out by either the AIC or BIC tests (AIC σ = 1.26, ΔBIC = 1.14), but because the fiducial Gaussian model provides a better fit with the same number of parameters, we do not increase model complexity any further (i.e., we do not run a vertical double Gaussian model, which could have a similar vertical profile to the Lorentzian model at the cost of two additional free parameters). The aspect ratio is well-constrained, with $h_{\rm HWHM} = 0.0059^{+0.0011}_{-0.0010}$. The aspect ratio constraints from `frank` and `rave` are in agreement, finding $h_{\rm HWHM} < 0.008$ and $h_{\rm HWHM} = 0.016^{+0.005}_{-0.006}$, respectively. These values are consistent with the uncertain constraint reported in Worthen et al. (2024), $h_{\rm HWHM} = 0.09^{+0.05}_{-0.05}$, which was derived from Band 6 ALMA observations of HD 131488 (~0.″5 resolution).

We note that while our measurements of $h_{\rm HWHM}$ are constrained according to the posterior probability distributions, the interpretation of our measured values of $h_{\rm HWHM}$ may be limited by the resolution of the data. The observations of HD 131488

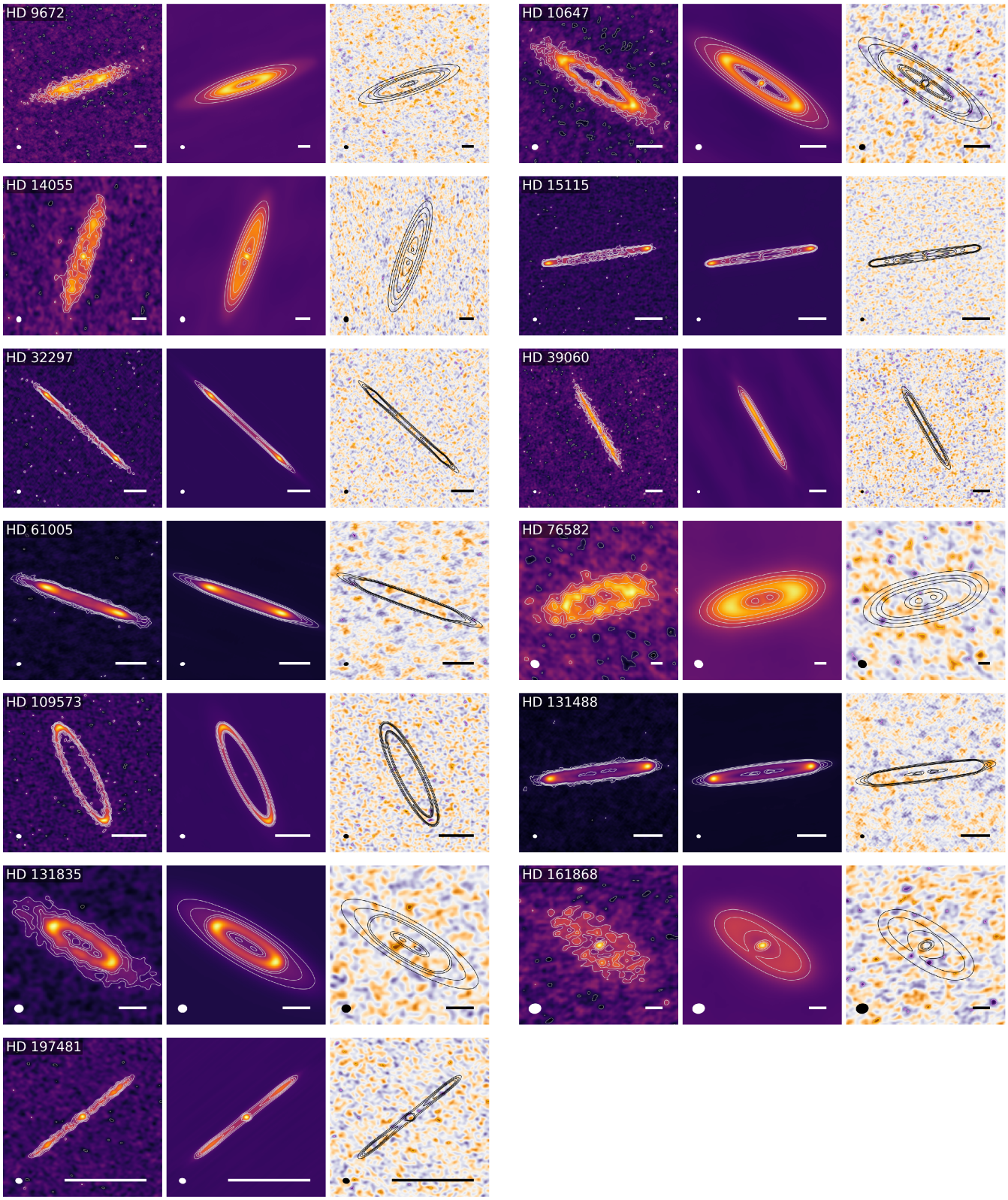

Fig. 1. Gallery of the data (left), models (center), and residuals (right, with model contours overplotted for reference) for the fiducial parametric vertical structure models for each source (models shown in Table 2). The effective beam is denoted by the shaded ellipse in the bottom-left corner of each panel, and the scale bars in the bottom right of each panel are 50 au in length. In the data and model panels, contours show three, five, seven, and nine times the rms (positive in light gray, negative in dark gray). In the residual panels, the purple and orange contours show +3 and −3 times the rms, respectively, though none of the sources show significant structure in the residuals. For each source, the data and model images are plotted on the same color scale, which spans the full dynamic range of each data image.

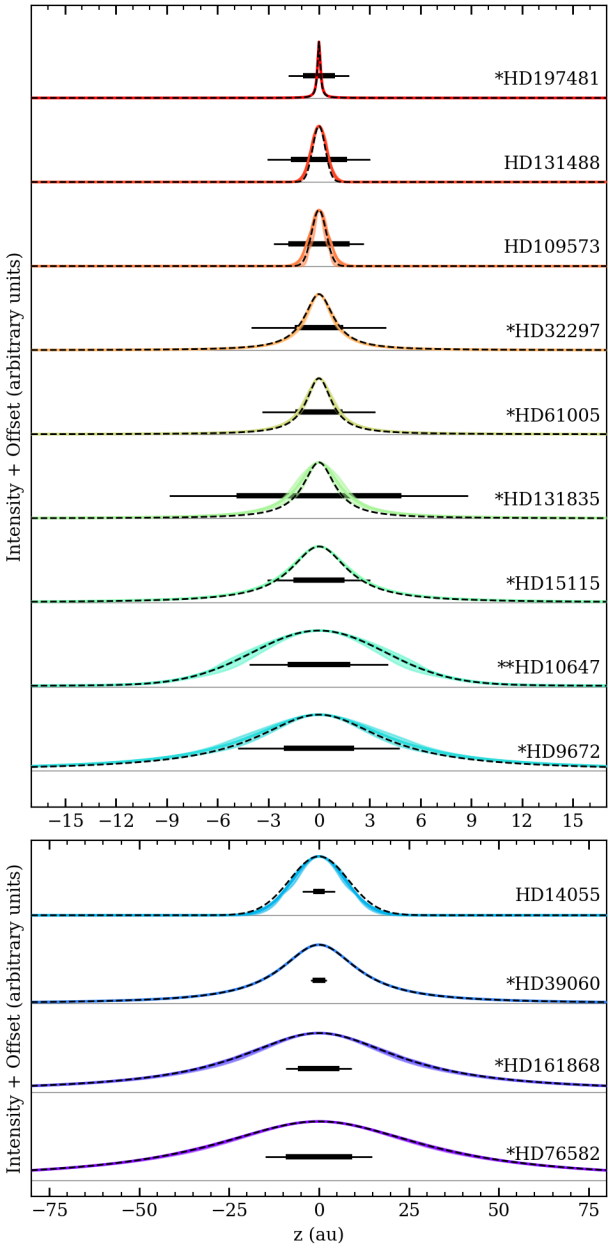

Fig. 2. Comparison of the fiducial vertical profiles for each disk at the reference radius $R_{\rm ref}$, defined as the location of peak intensity in the fiducial model (Table 4). Sources are ordered by $H_{\rm HWHM}(R_{\rm ref})$ and divided into two panels for visual clarity, with disks with $H_{\rm HWHM}(R_{\rm ref}) < 15$ au in the top panel and disks with $H_{\rm HWHM}(R_{\rm ref}) > 15$ au in the bottom panel. We denote extended or multi-component vertical profiles with asterisks (one asterisk for a Lorentzian profile, and two asterisks for a double Gaussian vertical profile). The remaining sources have Gaussian vertical profiles. Colored lines and the shaded regions denote the median profile $\pm1\sigma$, while the dashed black lines show the best-fit model. The thick horizontal black bars show the nominal resolution of the interferometer, $\lambda_{\rm obs}/b_{\rm max}$, where $\lambda_{\rm obs}$ is the observing wavelength and $b_{\rm max}$ is the longest baseline in the array. The thin horizontal black bars show the width of one beam along the vertical axis of the disk using the images shown in Figure 1.

have a nominal resolution of $\theta_{\rm min} = 3.32$ au. At a reference radius of 90.8 au, we obtain $H_{\rm HWHM} = 0.536$ au. For a vertical Gaussian profile, 95% of the disk material would then lie within 1.82 au centered on the disk midplane, nearly half the distance that could be resolved by the observations. We take the upper limit of $h_{\rm HWHM}$ to be the 84th percentile of the posteriors for the fiducial model, $h_{\rm HWHM} < 0.0070$, though follow-up observations at higher resolution are necessary to confirm this measurement.

4.2. Resolved Gaussian scale heights: HD 14055

The only source in our sample which is best fit with a vertical Gaussian distribution and has a fully resolved scale height is HD 14055. Parametric models in Han et al. (2026) suggest that the radial density distribution of this source is well-fit by a double power law, though a double Gaussian is not ruled out at high confidence. In the radial models, a vertical Gaussian profile was used with a fixed vertical aspect ratio of $h_{\rm HWHM} = 0.0475$. Incorporating scale height as a free parameter, we examined double power law and double Gaussian radial density distributions with a vertical Gaussian. The AIC favored the double Gaussian model, while the BIC favored the double power law model, so we modeled both radial double power law and radial double Gaussian density distributions with the four different vertical parameterizations presented in Table 1. Of these eight models, we select the radial double power law with a vertical Gaussian as the fiducial model, as it is favored at high confidence with the BIC and not strongly ruled out with the AIC ($\sigma = 0.56$ over a radial double Gaussian with a vertical Gaussian).

We measure $h_{\rm HWHM} = 0.053^{+0.007}_{-0.008}$ with the fiducial parametric model, using the 0.″23 ARKS observations in Band 7. The vertical aspect ratio is also resolved with `frank` and `rave`: `frank` finds $h_{\rm HWHM} = 0.037^{+0.010}_{-0.016}$, while `rave` finds $h_{\rm HWHM} = 0.047^{+0.038}_{-0.031}$. These values are in agreement with Terrill et al. (2023), Matrà et al. (2025), and Han et al. (2025), who used Band 6 observations (~2″ resolution) of HD 14055 to find limits of $h_{\rm HWHM} < 0.12$, $h_{\rm HWHM} = 0.04^{+0.02}_{-0.02}$, and $h_{\rm HWHM} = 0.131^{+0.073}_{-0.075}$, respectively.

4.3. Resolved complex structures

In this section we present sources that are consistent with having an extended or multi-component millimeter vertical emission profile (i.e., statistically preferred models use either a Lorentzian or a double Gaussian). We note that while we report a single $h_{\rm HWHM}$ for each vertical Lorentzian model, the broad tails of a Lorentzian can approximate a combination of broad and narrow components with different widths (see Sect. 5.1, where we also discuss the possible mechanisms that could generate these distributions).

4.3.1. HD 9672 (49 Ceti)

Parametric models in Han et al. (2026) suggest that the radial density distribution of this source is best fit by a double power law, assuming a vertical Gaussian profile with a fixed vertical aspect ratio of $h_{\rm HWHM} = 0.07$. We modeled HD 9672 using a radial double power law density distribution and the four different vertical parametrizations presented in Table 1, as well as with a radial double Gaussian and vertical Gaussian. We find that the vertical Lorentzian model is most favored by the BIC, and not strongly ruled out by the AIC ($\sigma = 0.27$). The vertical double Gaussian model is most strongly favored by the AIC, and disfavored by the BIC (ΔBIC = 25.81). We identify the vertical Lorentzian model as the fiducial model for HD 9672.

We obtained a vertical aspect ratio of $h_{\rm HWHM} = 0.046^{+0.008}_{-0.008}$ for the fiducial model. As the double Gaussian model is only disfavored by the BIC, which penalizes additional parameters more heavily than the AIC, we may tentatively resolve two

Table 4. Stellar, disk, and parametric model properties with derived solid mass and stirring estimates.

Source	$M_\star$ [$M_\odot$]	$\theta_{\rm min}$ [au]	$R_{\rm ref}$ [au]	$H_{\rm HWHM}(R_{\rm ref})$ [au]	$M_{\rm mm}$ [$M_\oplus$]	$M_{\rm disk}$ [$M_\oplus$]	$M_{\rm stir}$ [$M_\oplus$]	$R_{\rm stir}$ [km]	$T_{\rm stir}$ [Myr]
HD 9672	2.00	4.16	110.1	5.06	4.95×10^{-1}	86.6 ± 15.5	$3.11^{+1.85}_{-1.34} \times 10^{-4}$	606^{+102}_{-104}	1.23
HD 10647	1.12	3.67	88.2	4.67	4.07×10^{-2}	19.8 ± 2.6	$2.72^{+1.10}_{-0.97} \times 10^{-4}$	579^{+69}_{-79}	0.43
HD 14055	2.19	3.09	160.6	8.51	5.56×10^{-2}	25.3 ± 4.2	$3.18^{+1.53}_{-1.18} \times 10^{-4}$	609^{+85}_{-88}	40.0
HD 15115	1.43	3.05	97.9	2.15	6.17×10^{-3}	3.72 ± 0.26	$2.51^{+0.48}_{-0.46} \times 10^{-5}$	261^{+16}_{-17}	13.5
HD 32297	1.57	2.85	107.3	0.987	1.22×10^{0}	21.9 ± 3.0	$1.81^{+0.83}_{-0.61} \times 10^{-6}$	109^{+15}_{-14}	76.6
HD 39060	1.72	3.46	116.1	13.0	1.83×10^{-1}	104 ± 5	$3.32^{+0.12}_{-0.12} \times 10^{-3}$	1333^{+16}_{-16}	0.10
HD 61005	0.95	2.81	70.0	1.00	1.26×10^{-1}	10.2 ± 1.7	$6.02^{+2.94}_{-2.28} \times 10^{-6}$	163^{+23}_{-24}	6.38
HD 76582	1.61	18.51	188.5	36.2	2.25×10^{-1}	114 ± 12	$7.26^{+1.12}_{-0.96} \times 10^{-3}$	1730^{+85}_{-80}	1.20
HD 109573	2.14	3.63	77.6	0.636	4.68×10^{-2}	7.21 ± 3.1	$3.31^{+5.92}_{-2.80} \times 10^{-6}$	133^{+54}_{-62}	6.86
HD 131488	1.81	3.32	90.8	0.536	2.75×10^{-1}	9.01 ± 1.64	$7.41^{+4.80}_{-3.18} \times 10^{-7}$	81^{+15}_{-14}	70.5
HD 131835	1.70	9.75	69.2	1.52	4.08×10^{-1}	49.7 ± 15.3	$5.30^{+6.53}_{-3.12} \times 10^{-5}$	330^{+105}_{-90}	0.07
HD 161868	2.11	11.57	141.9	27.2	2.29×10^{-2}	87.1 ± 27.0	$1.68^{+0.33}_{-0.39} \times 10^{-2}$	2288^{+143}_{-190}	0.10
HD 197481	0.61	1.86	36.3	0.102	1.49×10^{-2}	0.830 ± 0.179	$6.01^{+7.62}_{-1.38} \times 10^{-8}$	35^{+11}_{-3}	117

Notes. Left: The stellar mass $M_\star$, nominal data resolution $\theta_{\rm min}$, reference radius $R_{\rm ref}$, scale height $H_{\rm HWHM}$, and millimeter dust mass $M_{\rm mm}$ for each source. $R_{\rm ref}$ is the location of peak brightness in the fiducial parametric model, and the location at which we report the fiducial scale height. $M_{\rm mm}$ is obtained from our fiducial parametric models. Right: Estimated total mass of disk solids $M_{\rm disk}$ assuming only internal processes (self-stirring, damping, etc.) are derived from the Pan & Schlichting (2012) collisional cascade model. Estimates on the lower limits of the largest stirring bodies in the disks ($M_{\rm stir}$ and $R_{\rm stir}$) are obtained from Eqs. (12) and (13). The stirring timescale $T_{\rm stir}$ is computed as described in Sect. 5.2.

distinct dynamical populations within the disk. The first has a measured aspect ratio of $h_{\rm HWHM} = 0.031^{+0.022}_{-0.013}$ containing 68^{+11}_{-15}% of the dust mass, and the other has an aspect ratio of $h_{\rm HWHM} = 0.105^{+0.021}_{-0.040}$ containing the rest of the mass. The nonparametric aspect ratios fall in between, with $h_{\rm HWHM} = 0.061^{+0.004}_{-0.004}$ from the `frank` fit and $h_{\rm HWHM} = 0.058^{+0.017}_{-0.024}$ from the `rave` fit.

The aspect ratio measured for the dynamically cooler population of the parametric vertical double Gaussian model is in agreement with the values reported in Delamer (2021) from an analysis of Band 8 (614 µm, ∼0.″25 resolution) and Band 7 (868 µm, ∼0.″13 resolution) continuum emission of HD 9672 ($h_{\rm HWHM} = 0.088^{+0.005}_{-0.005}$ and $h_{\rm HWHM} = 0.081^{+0.006}_{-0.008}$, respectively), assuming a Gaussian vertical profile.

With the same Band 8 observations, Terrill et al. (2023) found $h_{\rm HWHM} = 0.059^{+0.008}_{-0.008}$ and Han et al. (2025) found $h_{\rm HWHM} = 0.039^{+0.016}_{-0.021}$, with both studies using a nonparametric model with an assumed Gaussian vertical density distribution. Matrà et al. (2025) reanalyzed the Band 7 observations with radial and vertical Gaussians, finding an aspect ratio of $h_{\rm HWHM} = 0.089^{+0.011}_{-0.011}$. Finally, Delamer (2021) also analyzed Band 6 (1.33 mm, ∼0.″85 resolution) observations, finding a slightly larger aspect ratio of $h_{\rm HWHM} = 0.18^{+0.02}_{-0.02}$.

These differences could be partially driven by the range of observations represented, as the dust scale height may vary with observing wavelength. However, the variation among aspect ratios derived from Band 7 observations is likely driven by the fact that a Lorentzian or two Gaussians have broader tails, while a single Gaussian drops off more quickly away from the midplane. When fitting the disk with only one vertical Gaussian, the model may settle on a larger value of $h_{\rm HWHM}$ as it attempts to capture the more dynamically active population in the disk. HD 9672 also hosts a likely warp asymmetry, discussed in detail in Lovell et al. (2026). While we do not see significant features in the residual map (Fig. 1), we note that a subtle warp feature could bias our axisymmetric models to larger scale heights.

4.3.2. HD 10647

Parametric models in Han et al. (2026) suggest that the radial density distribution of HD 10647 is well-fit by a double Gaussian, assuming a vertical Gaussian profile with a fixed vertical aspect ratio of $h_{\rm HWHM} = 0.055$. We modeled the disk using radial double power law and double Gaussian density distributions with the four different vertical parametrizations presented in Table 1. The AIC strongly favors the model with both radial and vertical double Gaussian density distributions, while ΔBIC = 9.042. The BIC favors the radial double power law with a vertical Lorentzian, though the AIC strongly disfavors this model (AIC = 6.151σ). We thus identify the radial and vertical double Gaussian model as the fiducial model.

We resolve two distinct dynamical populations with the fiducial model of HD 10647, one with a measured scale height of $h_{\rm HWHM} = 0.053^{+0.006}_{-0.007}$ containing 88^{+6}_{-6}% of the dust mass, and the other with a scale height of $h_{\rm HWHM} = 0.225^{+0.002}_{-0.002}$ containing the rest of the mass. This is in line with the constraint from `rave`, $h_{\rm HWHM} = 0.040^{+0.016}_{-0.021}$. However, the upper limit derived from the `frank` fit is much smaller, $h_{\rm HWHM} < 0.008$. While we do not see significant features in the residual map of HD 10647 (Fig. 1), this source has a major axis asymmetry that could bias the results of our axisymmetric modeling (Lovell et al. 2026).

Several studies have already made measurements which are in agreement with our measurement of the dynamically cooler population of the fiducial model (which contains most of the disk mass): Lovell et al. (2021) found the scale height to be consistent with $h_{\rm HWHM} = 0.05^{+0.01}_{-0.01}$, while Han et al. (2025) found $h_{\rm HWHM} = 0.054^{+0.011}_{-0.012}$. Terrill et al. (2023) and Matrà et al. (2025) found marginal measurements of $h_{\rm HWHM} = 0.044^{+0.009}_{-0.008}$ and $h_{\rm HWHM} = 0.06^{+0.01}_{-0.01}$, respectively.

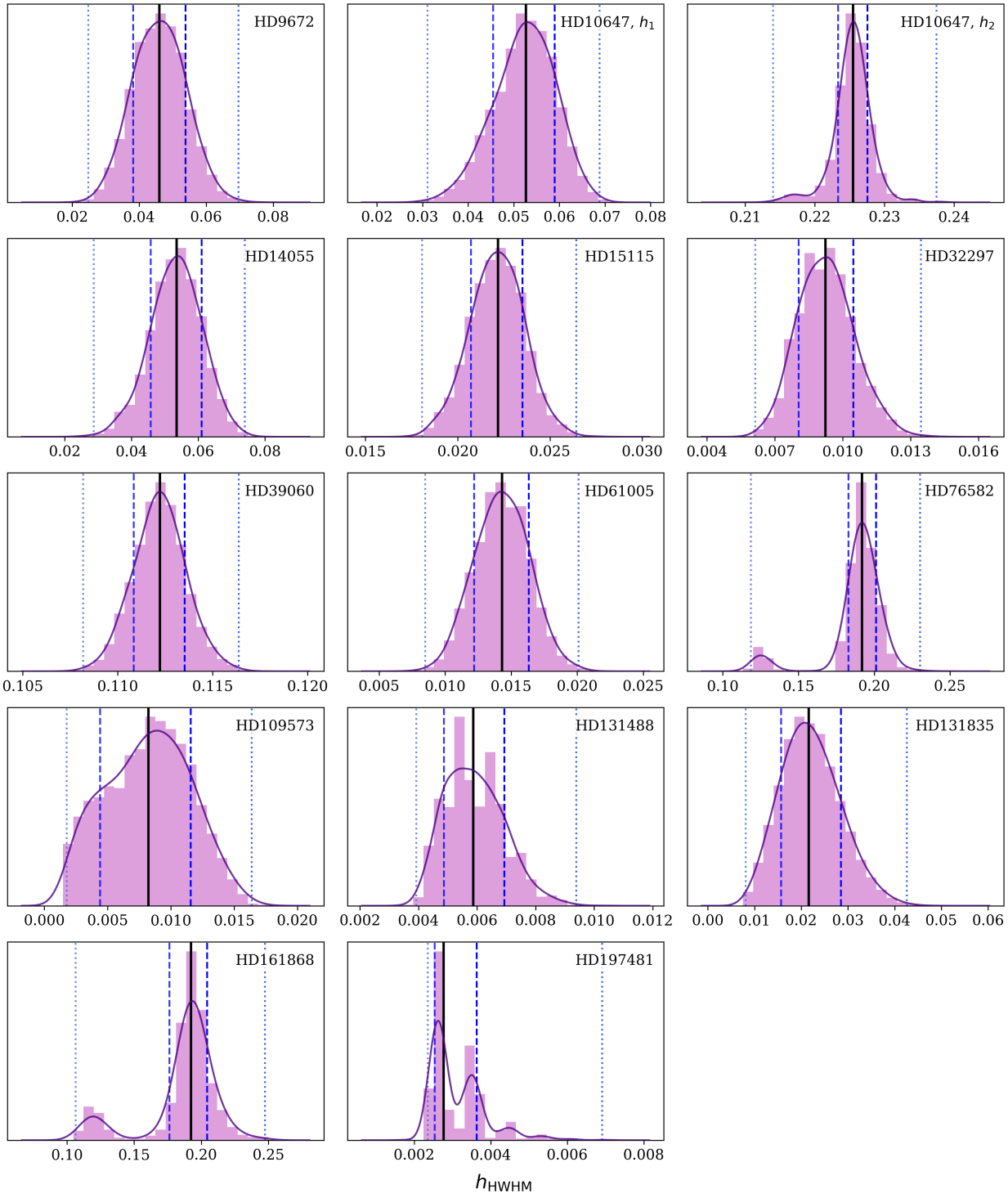

Fig. 3. Posterior distributions of the vertical aspect ratios for the fiducial parametric models. The histograms and KDEs are shown in light and dark purple, respectively. The median h_{HWHM} is shown by the vertical black line. The dark blue dashed line shows the 16th and 84th percentiles (equivalent to 1σ for Gaussian distributions), while the light blue dotted line shows the 0.15th and 99.85th percentiles (equivalent to 3σ for Gaussian distributions). Since the fiducial model for HD 10647 has two distinct vertical components, we show the posterior distributions for both h_{HWHM1} (top center panel) and h_{HWHM1} (top right panel).

4.3.3. HD 15115

The parametric modeling in Han et al. (2026) shows that HD 15115 is well-represented by a double Gaussian radial density distribution, assuming a vertical Gaussian profile with a fixed vertical aspect ratio of $h_{\mathrm{HWHM}} = 0.02$. We modeled HD 15115 using a radial double Gaussian density distribution and the four different vertical parametrizations presented in Table 1. We identify the vertical Lorentzian model as the fiducial model for HD 15115, as it is strongly favored by both the AIC and BIC. The scale height is well-constrained, with a vertical aspect ratio of $h_{\mathrm{HWHM}} = 0.0222^{+0.0013}_{-0.0015}$ for the vertical Lorentzian model. The `frank` and `rave` values are comparable, $h_{\mathrm{HWHM}} = 0.019^{+0.001}_{-0.001}$ and $h_{\mathrm{HWHM}} = 0.022^{+0.002}_{-0.002}$, respectively.

MacGregor et al. (2019) found that HD 15115 is not vertically resolved in 0.″6 (29 au) Band 6 observations. Using the same Band 6 observations, Matrà et al. (2025) marginally detected the scale height ($h_{\rm HWHM} = 0.06^{+0.01}_{-0.02}$) by modeling the disk with a radial and vertical Gaussian. This is in good agreement with results from Terrill et al. (2023) and Han et al. (2025), who used nonparametric methods with a vertical Gaussian assumption to measure $h_{\rm HWHM} = 0.056^{+0.008}_{-0.008}$ and $h_{\rm HWHM} = 0.079^{+0.035}_{-0.040}$, respectively. The differences between these values from previous observations and our measurement are likely due to the improved resolution of the ARKS data (0.″12), which is 5 times higher than the previous observations of HD 15115, combined with the different assumed radial and vertical distributions. In addition, there is evidence that HD 15115 is eccentric (Lovell et al. 2026), though this may be compensated for by the offset parameters dRA and dDec in our modeling (see Table A.1).

4.3.4. HD 32297

Parametric models in Han et al. (2026) suggest that the radial density distribution of HD 32297 is well-fit by a double power law, assuming a vertical Gaussian profile with a fixed vertical aspect ratio of $h_{\rm HWHM} = 0.012$. We modeled the disk using a radial double power law density distribution and the four different vertical parametrizations presented in Table 1. The vertical Lorentzian model is favored by both the AIC and BIC, so we select it as the fiducial model. The aspect ratio of the fiducial model is well-constrained ($h_{\rm HWHM} = 0.0092^{+0.0012}_{-0.0012}$) and in line with fits from `frank` ($h_{\rm HWHM} = 0.010^{+0.001}_{-0.001}$) and `rave` ($h_{\rm HWHM} = 0.015^{+0.003}_{-0.004}$).

The AIC score of the vertical double Gaussian model indicates that it also reproduces the data well (σ = 0.97); however, due to the additional parameters in the vertical double Gaussian model, the BIC score is significantly worse compared to the Lorentzian model (ΔBIC = 27.95). Nevertheless, we marginally resolve two independent dynamical populations within HD 32297: one with a scale height of $h_{\rm HWHM} = 0.0083^{+0.0018}_{-0.0034}$ containing 92^{+2}_{-3}% of the dust mass, and another with a scale height of $h_{\rm HWHM} = 0.146^{+0.027}_{-0.047}$ containing the remainder.

There exist several previous scale height measurements for HD 32297 at ~millimeter wavelengths. Terrill et al. (2023) and Han et al. (2025) use nonparametric methods (assuming a Gaussian vertical distribution) to find $h_{\rm HWHM} = 0.09^{+0.01}_{-0.01}$ and $h_{\rm HWHM} = 0.139^{+0.041}_{-0.052}$, respectively. Worthen et al. (2024) find $h_{\rm HWHM} = 0.018^{+0.002}_{-0.002}$ and Matrà et al. (2025) find $h_{\rm HWHM} = 0.09^{+0.01}_{-0.02}$, both modeling the disk with Gaussian radial and vertical density distributions. Our measured $h_{\rm HWHM}$ is smaller than all of the above, likely due to several factors. First, the ARKS data have a higher angular resolution (0.″06). Second, the vertical and radial distributions of disk material can be degenerate with disk inclination; uncertainties in the disk inclination make it more difficult to constrain the scale height and belt width, and all of the above studies find/use smaller inclinations than the value we obtain from our fiducial model ($i = 88.48^{\circ\,+0.04}_{-0.03}$, which does not appear to be affected by this degeneracy). We find that HD 32297 is best modeled with a vertical Lorentzian profile and a radial double power law profile; the common assumption of vertical and/or radial Gaussian profiles used for previous scale height measurements may be biasing the measurement of $h_{\rm HWHM}$, resulting in artificially high values. Lastly, there is evidence that HD 32297 is eccentric (Lovell et al. 2026), though this may be compensated for by the offset parameters dRA and dDec in our modeling (see Table A.1).

4.3.5. HD 39060 (Beta Pic)

Parametric models in Han et al. (2026) suggest that the radial density distribution of this source is well-represented by a double power law, assuming a vertical Gaussian profile with a fixed vertical aspect ratio of $h_{\rm HWHM} = 0.0445$. We modeled HD 39060 using a radial double power law density distribution and the four different vertical parametrizations presented in Table 1. The vertical Lorentzian (AIC σ = 1.55, ΔBIC = 0) and vertical double Gaussian (AIC σ = 0, ΔBIC = 22.85) models are both good fits to the data. For the fiducial vertical Lorentzian model, the aspect ratio is well-constrained with, $h_{\rm HWHM} = 0.1122^{+0.0013}_{-0.0013}$. The `frank` fit yields $h_{\rm HWHM} = 0.073^{+0.002}_{-0.002}$, while `rave` finds $h_{\rm HWHM} = 0.086^{+0.005}_{-0.005}$.

We identified two distinct dynamical populations within the disk with the vertical double Gaussian model; the first has a measured aspect ratio of $h_{\rm HWHM} = 0.046^{+0.005}_{-0.003}$ containing 58^{+4}_{-3}% of the dust mass, and the other has a scale height of $h_{\rm HWHM} = 0.212^{+0.002}_{-0.003}$ containing the rest of the mass. Matrà et al. (2019) also measured two distinct aspect ratios for this source, finding $h_{\rm HWHM} = 0.130^{+0.009}_{-0.007}$ containing 80^{+4}_{-5}% of the dust mass, and $h_{\rm HWHM} = 0.016^{+0.007}_{-0.007}$ containing the rest of the mass.

The differences are likely partially driven by the choice in radial density distribution. Here we use a double power law, finding a relatively shallow slope in the inner disk ($\alpha_{\rm in} = 1.78^{+0.14}_{-0.10}$) with a sharper decrease in density in the outer disk ($\alpha_{\rm out} = -5.2^{+0.6}_{-0.5}$). Matrà et al. (2019) use a radially Gaussian density distribution with $\sigma = 36.7^{+1.0}_{-1.3}$ au. Interestingly, Matrà et al. (2019) find that the broad component contains most of the disk mass, while we find that the narrow component contains slightly more mass. Matrà et al. (2019) also find marginal evidence of a radially varying aspect ratio in HD 39060, with $h(r) = h_0(r/r_0)^{\beta-1}$ and $\beta = 0.7^{+0.2}_{-0.2}$, which our model specification does not account for.

Asymmetries in the disk could also contribute to differences in the measured scale heights. Though the models presented both here and in Matrà et al. (2019) are axisymmetric, there is evidence of asymmetric structures in the millimeter emission of HD 39060 (Lovell et al. 2026). An asymmetric feature at the ~3σ level can be seen in the northeast of the residual map in Figure 1.

4.3.6. HD 61005

The parametric modeling in Han et al. (2026) shows that HD 61005 is well-represented by a double Gaussian radial density distribution, assuming a vertical Gaussian profile with a fixed vertical aspect ratio of $h_{\rm HWHM} = 0.02$. We modeled HD 61005 using a radial double Gaussian and the four different vertical parametrizations presented in Table 1. We find that the vertical Lorentzian model is favored by both the AIC and the BIC at high significance, corresponding to an aspect ratio of $h_{\rm HWHM} = 0.0143^{+0.0020}_{-0.0021}$. Compared to the vertical double Gaussian model, the AIC only favors the Lorentzian model at 1.31σ. We thus find marginal evidence of two resolved populations in the disk; the first has a measured scale height of $h_{\rm HWHM} = 0.014^{+0.005}_{-0.006}$ containing 90^{+6}_{-12}% of the dust mass, and the other has a scale height of $h = 0.117^{+0.043}_{-0.087}$ containing the rest of the mass. Aspect ratio fits from `frank` and `rave` find $h_{\rm HWHM} = 0.019^{+0.001}_{-0.001}$ and $h_{\rm HWHM} = 0.020^{+0.005}_{-0.007}$, respectively.

Assuming Gaussian radial and vertical density distributions, Matrà et al. (2025) find $h_{\rm HWHM} = 0.052^{+0.004}_{-0.005}$. Similarly, Terrill et al. (2023) and Han et al. (2025) find $h_{\rm HWHM} = 0.046^{+0.004}_{-0.005}$ and $h_{\rm HWHM} = 0.034^{+0.008}_{-0.011}$, respectively, using nonparametric methods and assuming a Gaussian vertical distribution. These values may be inflated due to the models fitting a more dynamically active disk to a simple vertical Gaussian, driving up the scale height measurement to account for the material further from the disk midplane.

It is also possible that asymmetries in the disk could bias our axisymmetric model toward a vertical structure indicative of multiple populations. While we do not identify structure in our model residuals (see Figure 1), Lovell et al. (2026) find evidence of asymmetry in HD 61005, which could affect the vertical structure measurements presented here.

4.3.7. HD 76582

Parametric models in Han et al. (2026) suggest that the radial density distribution of HD 76582 is well-fit by an asymmetric Gaussian (which is defined by some central radius and two different σ values inside and outside of the central radius), assuming a vertical Gaussian profile with a fixed vertical aspect ratio of $h_{\rm HWHM} = 0.015$. We examined the vertical structure of HD 76582 by first modeling the vertical structure of the disk with a Gaussian, and the radial structure with a variety of different radial forms. The best-fitting radial forms were a double power law, asymmetric Gaussian, and error function. We modeled HD 76582 using each of these radial density structures and the four different vertical parametrizations presented in Table 1. The model with a radial asymmetric Gaussian and vertical Lorentzian is favored by both the AIC and BIC, yielding $h_{\rm HWHM} = 0.192^{+0.009}_{-0.009}$; we thus selected this as the fiducial model for HD 76582. The `frank` aspect ratio fit ($h_{\rm HWHM} = 0.065^{+0.012}_{-0.012}$) and the `rave` upper limit ($h_{\rm HWHM} \leq 0.097$) are smaller.

The `rave` and `frank` results are in agreement with the upper limits identified by Matrà et al. (2025) ($h_{\rm HWHM} < 0.1$) and Han et al. (2025) ($h_{\rm HWHM} < 0.180$). All of these values were obtained by assuming Gaussian vertical density distributions. Furthermore, it is likely that the radial Gaussian density distribution assumed by Matrà et al. (2025) resulted in a biased scale height value. We found that an asymmetric Gaussian yields a good fit to the data, with substantially different widths on each side of the Gaussian peak ($\sigma_{\rm in} = 45 \pm 8$ au and $\sigma_{\rm out} = 114^{+23}_{-15}$ au). This corresponds to a FWHM of $\Delta R = 187^{+37}_{-27}$ au, while the Gaussian model of Matrà et al. (2025) has $\Delta R = 210 \pm 20$ au. Our asymmetric Gaussian model has its peak at $R = 181 \pm 11$ au, in contrast to $R = 219^{+9}_{-8}$ au in Matrà et al. (2025). As the Gaussian model of Matrà et al. (2025) is both marginally wider and significantly farther out compared to the best-fit asymmetric Gaussian model presented here, it is likely that the scale height measurement was underestimated to compensate for the extra radial width in the model.

4.3.8. HD 131835

Parametric models in Han et al. (2026) suggest that the radial density distribution of this source is well-fit by a double Gaussian, assuming vertical Gaussian profile with a fixed vertical aspect ratio of $h_{\rm HWHM} = 0.015$. We find that a radial double Gaussian continues to perform significantly better than a radial double power law or a radial triple Gaussian when the vertical aspect ratio is included as a free model parameter. We then modeled HD 131835 using a radial double Gaussian density distribution and the four different vertical parameterizations presented in Table 1.

The AIC and BIC strongly favor the vertical Gaussian and vertical Lorentzian models, with the Lorentzian model favored at low confidence over the Gaussian model (AIC $\sigma = 0.548$, ΔBIC = 1.077). Therefore, we select the Lorentzian model as the fiducial model for HD 131835. The posterior probability distributions are broad for both the fiducial and vertical Gaussian model, with an aspect ratio of $h_{\rm HWHM} = 0.022^{+0.007}_{-0.006}$ for the fiducial Lorentzian model and $h_{\rm HWHM} = 0.030^{+0.010}_{-0.010}$ for the vertical Gaussian model. `frank` and `rave` find $h_{\rm HWHM} = 0.039^{+0.006}_{-0.006}$ and $h_{\rm HWHM} = 0.057^{+0.020}_{-0.028}$, respectively.

4.3.9. HD 161868

Parametric models in Han et al. (2026) suggest that the radial density distribution of this source is well-fit by a double power law, assuming a vertical Gaussian profile with a fixed vertical aspect ratio of $h_{\rm HWHM} = 0.015$. We modeled HD 161868 with a radial double power law and the four different vertical parametrizations presented in Table 1. We find that the vertical Lorentzian model is favored by the BIC (AIC $\sigma = 1.255$), while the double Gaussian model is favored by the AIC (ΔBIC = 20.786). We select the vertical Lorentzian model as the fiducial model for HD 161868.

For the fiducial model, we measure a scale height of $h_{\rm HWHM} = 0.192^{+0.012}_{-0.016}$. The double Gaussian model is likely disfavored by the BIC more because of the additional parameters in the model rather than due to a poor fit to the data, as evidenced by the AIC. We thus find evidence that we resolve two distinct dynamical populations within the disk. The first has a measured aspect ratio of $h_{\rm HWHM} = 0.099^{+0.034}_{-0.045}$ containing 89^{+3}_{-2}% of the dust mass, and the other has an aspect ratio of $h_{\rm HWHM} = 0.380^{+0.037}_{-0.023}$ containing the rest of the mass. Fits with `frank` and `rave` yield only upper limits, finding $h_{\rm HWHM} < 0.097$ and $h_{\rm HWHM} < 0.135$, respectively.

Matrà et al. (2025) marginally resolve the scale height of HD 161868, finding $h_{\rm HWHM} = 0.15^{+0.05}_{-0.06}$ with a parametric fit assuming Gaussian radial and vertical density distributions. By nonparametrically fitting the visibilities and assuming a Gaussian vertical density distribution, Terrill et al. (2023) find a marginal measurement of $h_{\rm HWHM} = 0.18^{+0.04}_{-0.05}$ and Han et al. (2025) find $h_{\rm HWHM} = 0.16^{+0.04}_{-0.05}$. All three of these measurements are consistent with the aspect ratio of our fiducial model.

4.3.10. HD 197481 (AU Mic)

The parametric modeling in Han et al. (2026) shows that models of HD 197481 perform comparably well with a variety of radial density structures, assuming a vertical Gaussian profile with a fixed vertical aspect ratio of $h_{\rm HWHM} = 0.015$. We modeled HD 197481 using both radial double power law and double Gaussian density distributions with the four different vertical parametrizations presented in Table 1. There is no single model which stands out as a true best fit, but we identify the radial double power law and vertical Lorentzian model as the fiducial model due to its moderate AIC confidence ($\sigma = 2.491$) and strong BIC (ΔBIC = 0). For this model, we resolve an aspect ratio of $h_{\rm HWHM} = 0.0028^{+0.0009}_{-0.0002}$, the smallest in our sample.

The radial double Gaussian and vertical exponential model was favored by the AIC (ΔBIC = 23.328), yielding a scale height measurement of $h_{\rm HWHM} = 0.0338^{+0.0014}_{-0.0015}$ with a profile

that drops off sharply ($\gamma = 16^{+3}_{-3}$). `frank` and `rave` find similar aspect ratios: $h_{\rm HWHM} = 0.023^{+0.002}_{-0.002}$ and $h_{\rm HWHM} = 0.026^{+0.005}_{-0.006}$, respectively. Lastly, our model with a radial double power law and vertical double Gaussian density distribution also cannot be ruled out (AIC $\sigma = 1.196$, ΔBIC = 15.567), corresponding to two measured scale heights: one with $h_{\rm HWHM} = 0.0009^{+0.0005}_{-0.0003}$ containing 78^{+9}_{-14} % of the dust mass, and the other with $h_{\rm HWHM} = 0.058^{+0.022}_{-0.017}$ containing the rest of the mass.

Many of these measurements are comparable to other aspect ratio measurements of HD 197481; for example, Daley et al. (2019) model the 1.35 mm observations with a radial power law and vertical Gaussian, finding $h_{\rm HWHM} = 0.037^{+0.006}_{-0.005}$. Vizgan et al. (2022) repeated this analysis, with a resulting measurement of $h_{\rm HWHM} = 0.029^{+0.005}_{-0.006}$. They also analyze 450 µm observations of HD 197481, yielding a ratio of $h_{1.35{\rm mm}}/h_{450\ \mu{\rm m}} = 1.35$ ($h_{\rm HWHM} \approx 0.022$ at 450 µm). Recently, Matrà et al. (2025) reanalyzed the 1.35 mm data assuming a radially Gaussian belt with a vertical Gaussian density distribution, finding $h_{\rm HWHM} = 0.020^{+0.004}_{-0.004}$. Terrill et al. (2023) used a nonparametric approach to fit the radial structure of the 1.35 mm observations; assuming a vertical Gaussian profile, they find $h_{\rm HWHM} = 0.024^{+0.002}_{-0.002}$. Similarly, Han et al. (2025) find $h_{\rm HWHM} = 0.026^{+0.004}_{-0.004}$.

The variety of measured $h_{\rm HWHM}$ for HD 197481 suggest that the characterization of its vertical structure is highly dependent on the assumed density structure. Furthermore, while the fiducial measurement of $h_{\rm HWHM}$ – the smallest aspect ratio measured for this source – is resolved according to the criteria outlined in Sect. 4, it remains unclear whether the data resolution is sufficient to fully resolve such a small aspect ratio. The Band 6 observations of HD 197481 have a nominal resolution of $\theta_{\rm min} = 1.86$ au. At a reference radius of 36.3 au, an aspect ratio of $h_{\rm HWHM} = 0.0028$ yields a scale height of $H_{\rm HWHM} \approx 0.1$ au. A vertical Lorentzian profile with a HWHM of 0.1 au would contain 95% of the disk material within 2.5 au centered on the disk midplane. This is less than a factor of two larger than $\theta_{\rm min}$; while such small spatial scales could be supported by the longest baseline observations, they cannot be resolved with two resolution elements. Given the spread of measured $h_{\rm HWHM}$ values under different density distribution assumptions, higher resolution follow-up observations may be helpful in breaking this degeneracy.

5. Discussion

5.1. Non-Gaussian vertical distributions as the new norm

Previous debris disk studies commonly assume that the vertical density structure follows a Gaussian distribution (e.g., Kennedy et al. 2018; Daley et al. 2019; Terrill et al. 2023; Matrà et al. 2025). This common assumption arises because self-stirring processes can generate a Rayleigh inclination distribution (Ida & Makino 1992; Lissauer & Stewart 1993), which corresponds to a Gaussian vertical density distribution (Matrà et al. 2019). Furthermore, distinguishing between different vertical parameterizations may not have been possible in studies analyzing lower-resolution data, particularly since the radial dust distribution is also less certain in these conditions.

However, high resolution observations of debris disks have enabled a more detailed exploration of the precise dust distributions. We find that most sources analyzed here (10/13) are significantly better fit with a thick-tailed vertical density distribution (i.e., either a Lorentzian or a double Gaussian) compared to a single Gaussian distribution. For each of the three remaining disks, vertical Lorentzian models are not ruled out at high confidence (HD 14055 with a radial double power law and vertical Lorentzian, AIC $\sigma = 1.616$ and ΔBIC = 3.376; HD 109573 with a radial double Gaussian and vertical Lorentzian, AIC $\sigma = 0.090$ and ΔBIC = 0.149; and HD 131488 with a radial double Gaussian and vertical Lorentzian, AIC $\sigma = 1.255$ and ΔBIC = 1.141; see Table A.1).

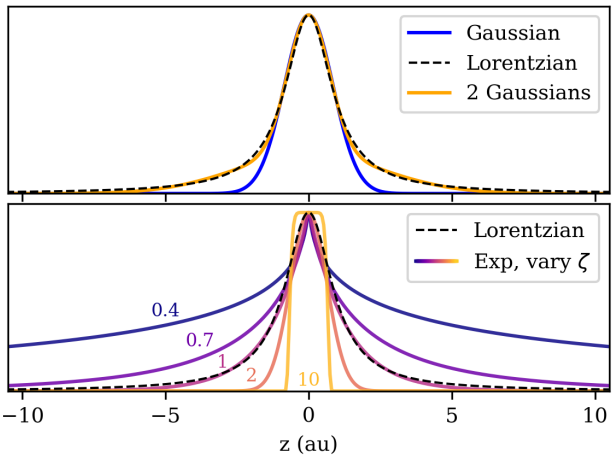

Fig. 4. Top: Arbitrary Gaussian, Lorentzian, and double Gaussian profiles that demonstrate how a Lorentzian can mimic a double Gaussian without the extra model parameters. The Gaussian (blue line) and Lorentzian (black line) profiles have a FWHM of 2 au, while the double Gaussian (orange dotted line) is composed of one Gaussian with a FWHM of 1.7 au and another with a FWHM of 6 au. Bottom: Various exponential forms with different ζ (colored lines, ζ values annotated on the panel). The wings of the Lorentzian (black line) are closely matched with an exponential with $\zeta = 1$. All profiles are normalized to the same maximum value.

Some studies have already used non-Gaussian vertical structures for debris disks, in particular for HD 39060 (β Pic). For example, scattered light observations of HD 39060 have been fit using two vertical Lorentzians (e.g., Golimowski et al. 2006; Lagrange et al. 2012) and two vertical Gaussians (e.g., Apai et al. 2015), though the authors emphasize that these parameterizations were not physically motivated, but rather chosen by qualitatively assessing the suitability of different profiles. Similarly, Matrà et al. (2019) find that modeling HD 39060 using two vertical Gaussians provides a significantly better fit to the 1.33 mm dust observations than a single Gaussian, and use this parameterization to find marginal evidence of a radially varying vertical aspect ratio.

Now equipped with a larger sample of highly resolved debris disk observations, we have begun teasing out trends in the vertical dust distributions of disks. In our detailed modeling of 13 disks, we find evidence that the millimeter-sized dust typically exhibits a more gradual decline from the midplane density compared to the commonly used, steeper Gaussian profile. Rather, the best models tend to have vertical dust distributions with the heavy-tailed behavior seen in a Lorentzian distribution, or in the combination of a narrow Gaussian with a broader Gaussian. While we do not resolve two distinct scale height values in many disks at high confidence (only HD 10647 is identified as having a fiducial model with a vertical double Gaussian), we note that a Lorentzian distribution can be qualitatively similar to 1) the sum of two Gaussians with different widths and 2) an exponential distribution with $\zeta < 2$, both of which are shown in Figure 4. Thus, some disks that are best fit by a Lorentzian may have multiple dynamical populations even if we are unable to measure multiple distinct scale heights at high confidence.

When comparing a model with fewer free parameters (e.g., one with a Gaussian vertical density distribution) to a more complex model like the vertical double Gaussian models presented here, the choice of model selection criteria may have a large impact on which model is identified as the best fit. Here, four of the 13 sources (HD 9672, HD 10647, HD 39060, and HD 161868) have a vertical double Gaussian model which is most strongly favored by the AIC, while no sources have a vertical double Gaussian model which is most strongly favored by the BIC. As the BIC penalizes model complexity more aggressively than the AIC, particularly for large datasets like ALMA observations (Eq. (10)), it may be useful to employ multiple selection criteria (e.g., both the AIC and BIC) to robustly evaluate model fit.

Multi-component fits have long been used for the classical Kuiper belt objects (KBOs), including double Gaussians, a Gaussian and a Lorentzian, and two von Mises–Fisher functions (Brown 2001; Kavelaars et al. 2009; Gulbis et al. 2010; Van Laerhoven et al. 2019; Malhotra & Roy 2023). Single Lorentzians have also been used to fit the classical KBOs (Adams et al. 2014). The inclinations and eccentricities of KBOs were likely inflated by Neptune's outward migration during the early history of the Solar System (e.g., Malhotra 1995; Hahn & Malhotra 2005; Levison et al. 2008; Nesvorný 2015). Therefore, one possible interpretation of the apparent preference for Lorentzian or multi-component distributions in debris disks is that Neptune-like migration histories are common in these systems.

However, such structures can also arise from secular (i.e., long-term) planet-disk interactions without invoking planetary migration. For instance, Farhat et al. (2023) find a two-component inclination distribution emerges for the case of HD 106906, accounting for the central binary star as well as the known external planetary companion, while assuming a massless disk. Sefilian et al. (2025) consider a scenario involving a massive, back-reacting (but not self-gravitating) debris disk with an internal planetary perturber, finding that non-Rayleigh inclinations and non-Gaussian vertical profiles emerge naturally regardless of the disk mass. The range of disk processes and conditions which could generate multiple vertical populations is still an active area of study. For example, most previous works on planet-debris disk interactions neglect at least one or more of: the disk's gravitational back-reaction and/or self-gravity, self-stirring processes, the possibility of multiple perturbers, and collisions within the disk. Gas-bearing debris disks should also be treated with care, as gas effects can also have a large impact on grain dynamics depending on the uncertain gas densities (though this may not have an observable effect on the vertical profile at millimeter wavelengths, Olofsson et al. 2022b). Regardless of the mechanisms driving the vertical grain distribution, non-Gaussianity appears to be nearly ubiquitous.

Furthermore, if the vertical distribution of solids changes with observing wavelength, then even a Gaussian vertical distribution of solids could produce a non-Gaussian emission profile (e.g., Terrill et al. 2023). This degeneracy could be broken by modeling well-resolved observations at multiple wavelengths. Currently, most debris disks which have been observed at multiple wavelengths lack the resolution for detailed vertical characterization at all wavelengths (Appendix C).

5.2. Constraints on the disk mass

The vertical thickness of debris disks can be influenced by a number of mechanisms, including early stirring in the protoplanetary disk phase (e.g., Walmswell et al. 2013; Booth & Clarke 2016), stirring by one or more planetary perturbers (e.g., Mustill & Wyatt 2009; Pearce & Wyatt 2014; Jílková & Portegies Zwart 2015; Dong et al. 2020; Chai et al. 2024, also see Sect. 5.5), or stellar flybys (e.g., Kenyon & Bromley 2002a; Lestrade et al. 2011; Moore et al. 2020; Batygin et al. 2020). Here, we primarily consider self-stirring of the disk, which is commonly invoked as a key mechanism driving disk scale heights (e.g., Ida 1990; Ida & Makino 1993; Kenyon & Bromley 2008; Kennedy & Wyatt 2010).

Under the assumption that the vertical thickness of disks is set by only self-stirring, measured scale height values can be used to place an upper limit on the mass of bodies stirring the disk. Following Daley et al. (2019), we defined the rms eccentricities and inclinations as $\bar{e} = \sqrt{\langle e^2 \rangle}$ and $\bar{i} = \sqrt{\langle i^2 \rangle}$, respectively, where $\langle e^2 \rangle$ and $\langle i^2 \rangle$ are the eccentricity and inclination dispersions of the grain population. We assume that grains are gravitationally excited isotropically in space such that $\bar{i} = \bar{e}/2$ (Inaba et al. 2001). At millimeter wavelengths, the inclination of a self-stirred disk is related to the observed aspect ratio by $\bar{i} \sim \sqrt{2} h_{\rm HWHM}$ (Quillen et al. 2007). The relative velocities of particles are then given by

$$\langle v_{\rm rel} \rangle \approx v_{\rm Kep}(r) \sqrt{\bar{i}^2 + 1.25\bar{e}^2} \approx 2\sqrt{3} v_{\rm Kep}(r) h_{\rm HWHM}, \tag{12}$$

where $v_{\rm Kep}(r)$ is the Keplerian velocity at radius r (Lissauer & Stewart 1993; Wetherill & Stewart 1993; Wyatt & Dent 2002).

In the absence of significant damping, $\langle v_{\rm rel} \rangle$ will be excited to roughly the escape velocity, $v_{\rm esc}$, of the largest bodies in the system (which dominate the disk dynamics and drive most of the stirring, e.g., Pan & Schlichting 2012; Schlichting 2014), at which point collisions begin to dominate, limiting the growth of $\langle v_{\rm rel} \rangle$. The escape velocity is given by

$$v_{\rm esc} = \sqrt{\frac{2\pi G D^2 \rho_d}{3}} \tag{13}$$

for a spherical object of diameter D and bulk density ρ_d. By equating $\langle v_{\rm rel} \rangle$ and $v_{\rm esc}$, we can obtain lower limits on the size and mass of the largest bodies in the disk. We assumed a bulk density of $\rho_d = 2.0$ g/cm^3, corresponding to the bulk densities of trans-Neptunian objects (Carry 2012). The minimum radii $R_{\rm stir}$ and masses $M_{\rm stir}$ of the largest bodies stirring each disk are presented in Table 4.

We also estimated the total mass of each disk using the collisional cascade model of Pan & Schlichting (2012). The model assumes a steady-state disk in which grains are stirred by close encounters with large bodies and damped by dynamical friction and collisions. Mass is conserved in all catastrophic collisions, and we assumed efficient collisional damping such that collisions with small bodies contribute significantly to the velocity damping (see Sect. 2 of Pan & Schlichting 2012). We adopted an eccentricity of 0.03 for all perturbing bodies. For each disk, we used Eq. (12) to estimate the typical random velocity of millimeter-sized grains within the disk, using the fiducial scale height values presented in Table 2. We used the stellar masses shown in Table 4, which were derived in Marino et al. (2026). Solving for the steady-state sizes and velocity distributions enabled the dust characteristics obtained from our parametric modeling (e.g., the millimeter dust mass and scale height) to be extrapolated to estimate the total amount of mass in the disk.

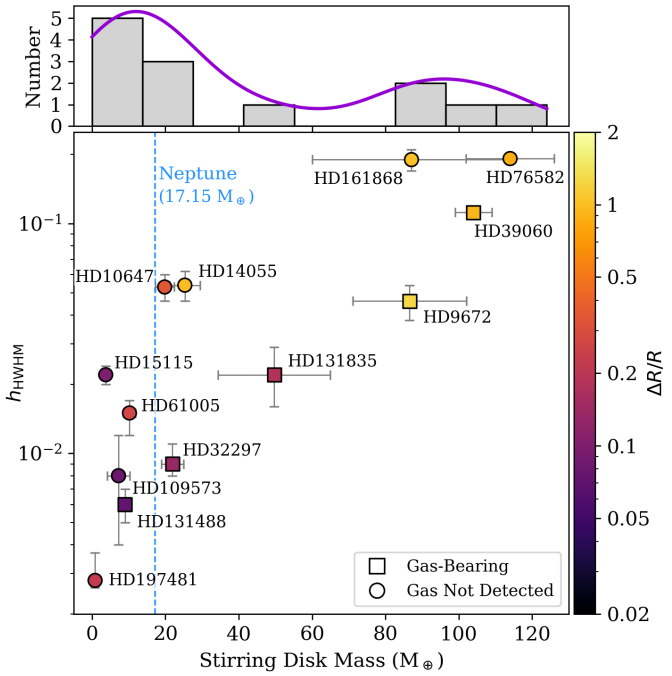

Fig. 5. Stirring disk masses obtained from the (Pan & Schlichting 2012) stirring model with the fiducial h_{HWHM} measurements for both the gas-bearing (square) and gas-poor (circles) debris disks. The color bar corresponds to the parametrically derived fractional widths ($\Delta R/R$) presented in Han et al. (2026). We took the average $\Delta R/R$ for disks with multiple reported rings (HD 15115 and HD 197481). The upper panel shows a histogram of disk masses in our sample overlaid with a KDE (purple line).

The derived masses, M_{disk}, for each disk are presented in Table 4 and plotted in Figure 5. The main panel shows the connection between h_{HWHM} and M_{disk} (we note that the positive correlation occurs due to the model specification, as h_{HWHM} is used to obtain the typical grain velocity, which directly affects the derived disk mass), while the top panel shows a histogram of the disk masses. Under half of the disks (5/13) contain less than the mass of Neptune, while the more massive disks reach up to several times the mass of Neptune. The color bar corresponds to the parametrically derived fractional widths ($\Delta R/R$) presented in Han et al. (2026). We find that belts which are vertically thicker and radially wider tend to be more massive. Furthermore, we see that the gas-bearing disks in the sample tend to be more massive than gas-poor disks with similar scale heights; however, gas is not considered in the collisional cascade model used to obtain our estimates on M_{disk}.

To verify whether the disk masses are large enough to stir the disks to their observed morphologies within the age of the system, we compute the stirring timescale T_{stir} using Eq. (28) in Krivov & Booth (2018). This calculation requires assumptions about the maximum planetesimal radius, belt location and fractional width, disk mass, stellar mass, bulk density, and fragmentation velocity v_{frag}. We use the values of R_{stir}, R_{ref}, M_{disk}, and $M_\star$ in Table 4, and the $\Delta R/R$ values from Han et al. (2026). As with our stirring mass estimates, we assume a bulk density of $\rho_d = 2.0$ g/cm^3. Because v_{frag} is not well-constrained, we adopt the nominal value of $v_{frag} = 30$ m/s used in Krivov & Booth (2018). Lastly, the equation includes the parameter γ, which ranges from $1 \leq \gamma \leq 2$ and bounds the upper and lower limits on T_{stir}; we choose an intermediate $\gamma = 1.5$. The stirring timescales are shown in Table 4. We find that all but three disks (HD 32297, HD 131488, and HD 197481) could have been self-stirred within the age of the system. The disks that cannot be explained solely by self-stirring require an alternative mechanism, such as the planet-disk stirring scenarios discussed in Sect. 5.5.

There exist other methods of estimating M_{disk}. For example, Krivov & Wyatt (2021, hereafter K21) compute a minimum disk mass M_{disk}^{min} contained within the collisional cascade by extrapolating the observed mm-sized dust, assuming a power law size distribution with $q = 3.7$ up to some maximum size at the top of the cascade (s_{max}, estimated using observables). The Pan & Schlichting (2012) model employed here, on the other hand, estimates the mass of the largest bodies driving the stirring within the disk, which may not necessarily contribute directly to the collisional cascade (as the collision timescale becomes larger than the age of the system at these sizes). In this case, we assume that the dust mass is negligible, such that $M_{disk} \approx M_{large}$.

These different modeling frameworks result in different mass estimates; for many of the disks, our estimates of M_{disk} are incompatible with the minimum masses reported in K21. However, much of this difference may stem from the choice of assumed millimeter dust mass, as the M_{disk}^{min} estimates from K21 use different millimeter dust masses than found here. To mitigate this effect, we rescaled the K21 estimates of M_{disk}^{min} to use the millimeter dust masses derived from our fiducial models (Table 4), finding that the estimates of M_{disk}^{min} are compatible with the estimates of M_{disk} found using the Pan & Schlichting (2012) model for four disks, and incompatible for the remaining three disks. These results are presented and discussed in more detail in Appendix D.

5.3. Comparison to other vertical measurements

The REASONS survey uniformly analyzed observations of 74 resolved debris disks (Matrà et al. 2025), many of which are also present in the ARKS sample. The modeling and analysis resulted in scale height measurements or constraints for many of the disks, including 11 out of the 13 disks in the sample presented here. In Figure 6, we compare the REASONS aspect ratios (circles) with the aspect ratios derived from the ARKS parametric modeling (stars).

We find that some sources with well-resolved aspect ratios from REASONS have significantly smaller (but still well resolved) values derived from the ARKS parametric modeling. The disks with the largest discrepancies tend to be some of the thinnest disks in the sample, according to the parametric constraints presented in this work (e.g., HD 197481, HD 109573, HD 32297). Some theoretical predictions suggest an increase in inclination dispersion (or scale height) with age (e.g., without considering damping and following $\sqrt{\langle i^2 \rangle} \propto t^{\frac{1}{4}}$ as in Ida & Makino 1993, assuming that stirrers form early in the disk lifetime). While this trend was not resolved with the REASONS sample, we find some evidence of an increase in $\langle i^2 \rangle$ with disk age in the ARKS scale height measurements.

The large differences between the REASONS and ARKS aspect ratios likely stems from differences in the model parametrizations, data resolution, and observing wavelength. Matrà et al. (2025) modeled each of the REASONS disks with a simple model that assumes the disk is both radially and vertically Gaussian. This had the advantage of enabling direct comparison between disks across a large sample of debris disks, including characterizing basic characteristics of the dust belts. However, the ARKS radial analysis reveals a diverse set of belt morphologies, very few of which are consistent with a Gaussian.

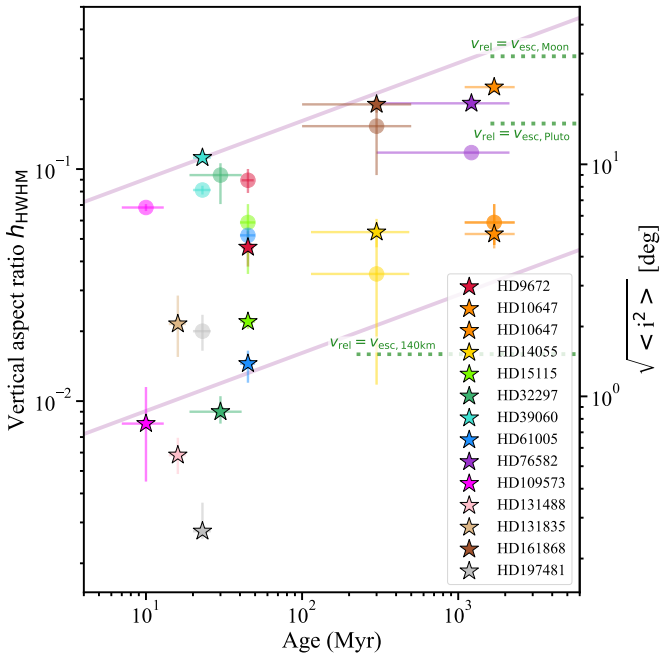

Fig. 6. Aspect ratio $h_{\rm HWHM}$ of the vertical profiles measured for the ARKS data (stars) compared to the values derived from the REASONS survey (circles, Matrà et al. 2025) with respect to host star age. ARKS values are the best-fit values presented in Table 2; we note that for HD 10647, two aspect ratios are plotted because the best-fit model is composed of a vertical double Gaussian with two measured aspect ratios. The corresponding rms inclination of dust grains assuming a Rayleigh distribution of inclinations is shown on the right y axis. Purple lines show the $\sqrt{\langle i^2 \rangle} \propto t^{\frac{1}{4}}$ increase with age expected for planetesimal belts stirred by large bodies (assuming that stirring bodies form early; Ida & Makino 1993), with mass × surface density $\Sigma M = 10^{-2}$ $M_\oplus^2$ au^2 (top) and $\Sigma M = 10^{-6}$ $M_\oplus^2$ au^2 (bottom). Green dotted lines represent the maximum rms inclinations expected from Moon-like, Pluto-like, and 140 km-sized stirring bodies (assuming the median stellar host mass and belt radius of the REASONS sample, Matrà et al. 2025).

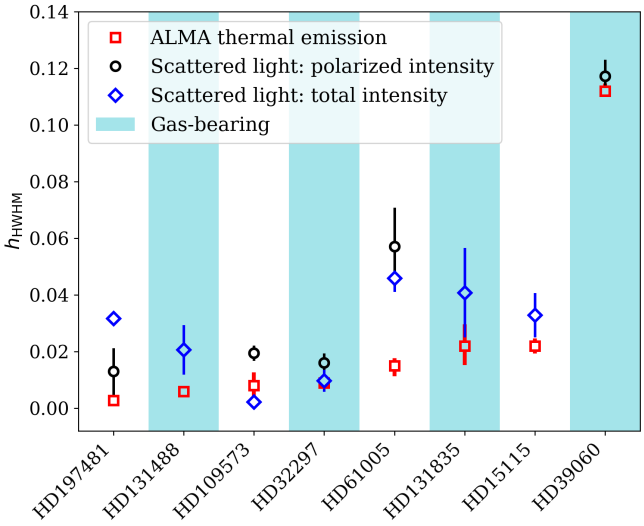

Fig. 7. Comparison of ALMA $h_{\rm HWHM}$ values (fiducial ARKS values, red squares) with $h_{\rm HWHM}$ constraints from scattered light observations (polarized intensity in black circles and total intensity in blue diamonds). Gas-bearing disks are indicated with a shaded blue background.

The work presented here further suggests that vertically, a Gaussian dust distribution may not be representative of many debris disks.

High resolution was not the focus of the REASONS survey, while the ARKS observing strategy focused specifically on resolving the belts well enough to conduct a more detailed analysis of each source (see Marino et al. 2026). On average, the resolution of the REASONS observations is several times poorer than the ARKS observations of a given target. In some cases, the angular resolution of the ARKS observations is nearly an order of magnitude higher (e.g., HD 32297 is resolved 0.″06 with ARKS and 0.″5 with REASONS). This resolution may have resulted in biased scale height measurements, even if they appear to be well-constrained using the simple Gaussian parametrization. Some of the aspect ratios recovered with the ARKS data still appear to be limited by the data resolution to some extent (Figure 2); follow-up observations of the thinnest disks at higher angular resolution may be useful to fully understand the dependence of measured scale height on resolution.

Lastly, variations in scale height with observing wavelength have already been observed (e.g., for AU Mic in ALMA Bands 6 and 9, Vizgan et al. 2022). The REASONS sample includes observations at $0.855 \leq \lambda$ [mm] ≤ 1.36, so differences in the observing wavelengths could contribute to differences in measured aspect ratios. However, this is likely only a minor contribution, as it is not clear that such a small difference in wavelength would result in a measurable difference in h. A list of ARKS targets with measured aspect ratios (both from this work and previous studies) is available in Table C.1, along with the corresponding data resolution and observing wavelength.

Many ARKS targets have also been detected in scattered light; a detailed comparison of the scattered light and thermal emission of these disks is presented in Milli et al. (2026). Here, we briefly discuss the vertical profiles and scale heights from the scattered light observations. The vertical profiles of the disks modeled in scattered light are parametrized with a Gaussian profile of standard deviation $r \tan \psi$ linearly increasing with the radius r, where ψ is the vertical opening angle of the disk. The HWHM of such a vertical profile is therefore $\sqrt{2 \ln 2} \times r \tan \psi$ and the corresponding aspect ratio is $h_{\rm HWHM} = \sqrt{2 \ln 2} \tan \psi$.

This quantity is plotted in Figure 7 together with the $h_{\rm HWHM}$ derived from the fiducial ARKS parametric models (Table 2). Systems are plotted with increasing millimeter scale height, and gas-bearing disks are highlighted with a light blue background. We find that most disks have a similar scale height or are thicker in scattered light compared to thermal imaging. HD 39060 has a substantially larger scale height in both thermal emission and scattered light compared to the rest of the targets.

Theoretical works predict the gas-bearing disks to have a smaller scale heights caused by dust vertical settling (Olofsson et al. 2022b). For second-generation gas present at a low level ($\lesssim 0.1 M_\oplus$, depending on the dust mass), this settling is expected to be most visible in scattered light while the larger grains seen in thermal images are less affected. On the other hand, we expect larger quantities of gas ($\gtrsim 0.1 M_\oplus$) to cause significant damping in both millimeter and scattered light observations. In Figure 7, no clear trend emerges from the comparison of the gas-bearing disks shown shaded in blue with the disks containing no detectable amount of CO.

These comparisons come with several caveats. First, not all disks are well resolved vertically in scattered light. For instance, this is the case for HD 32297, as mentioned in Olofsson et al. (2022a). Second, depending on the dataset used to model the

disk vertical distribution in scattered light (the spectral filter for HD 15115 or the choice between total or polarized light for most other disks, see details in Milli et al. 2026), the scale height may be different, mostly because the signal-to-noise of the scattered light observations is not the same.

5.4. Theoretical implications

One way to probe which dynamical effects are at work in these disks is to consider the ratio $\langle e_{\rm rms}\rangle/\langle i_{\rm rms}\rangle$. In self-stirred disks an energy equipartition between vertical and radial motion is expected, such that $\langle e_{\rm rms}\rangle/\langle i_{\rm rms}\rangle \sim 2$ (Ida & Makino 1992). If a disk is stirred by a (nearly) co-planar planet, eccentricities will be excited to a greater degree than the inclinations, and we may expect that $\langle e_{\rm rms}\rangle/\langle i_{\rm rms}\rangle > 1$ (Pearce et al. 2024). Alternatively, if a disk is pre-stirred (e.g., if the dynamical excitation is set during the protoplanetary phase), and if the eccentricity and the inclination distributions subsequently evolve due to fragmentation-dominated collisional evolution, we may expect that the ratio decreases to $\langle e_{\rm rms}\rangle/\langle i_{\rm rms}\rangle < 1$ with inefficient collisional damping (Jankovic et al. 2024). The vertical and radial constraints from this work and Han et al. (2026) enable observational constraints to be placed on this ratio.

We used the upper limit estimates of $\langle e_{\rm rms}\rangle$ presented in Han et al. (2026), which assume a self-stirred disk (Marino 2021; Rafikov 2023). For disks with no reported $\langle e_{\rm rms}\rangle$, we estimated the upper limit of $\langle e_{\rm rms}\rangle$ using the belt fractional width $\Delta R/R$ as in Marino (2021),

$$\langle e_{\rm rms}\rangle \leq 0.6\Delta R/R. \quad (14)$$

For these sources, we adopted the median fractional widths reported in Han et al. (2026). We estimated $\langle i_{\rm rms}\rangle$ as described in Sect. 5.2. We find that the majority of disks have an upper limit of $\langle e_{\rm rms}\rangle/\langle i_{\rm rms}\rangle > 2$, while four (HD 15115, HD 39060, HD 76582, and HD 161868) have $\langle e_{\rm rms}\rangle/\langle i_{\rm rms}\rangle \lesssim 2$ (Figure 8). While none of the disks have an upper limit of $\langle e_{\rm rms}\rangle/\langle i_{\rm rms}\rangle < 1$, the true ratio could be lower, so we cannot rule out that some disks in the sample may be dynamically dominated by catastrophic collisions.

We emphasize that the values of $\langle e_{\rm rms}\rangle$ and $\langle i_{\rm rms}\rangle$ shown in Figure 8 should be taken as estimates. Because $\langle e_{\rm rms}\rangle$ is derived from the radial distribution of material in the disk, there is a degeneracy between the semi-major axis distribution and the eccentricity distribution in the disk. Thus, the true values of $\langle e_{\rm rms}\rangle$ could be smaller. Similarly, while the errors on $\langle i_{\rm rms}\rangle$ shown in Figure 8 stem only from uncertainties in the measured scale height, there is additional uncertainty stemming from the approximations and assumptions used to compute $\langle i_{\rm rms}\rangle$. We calculate $\langle i_{\rm rms}\rangle$ using the approximation from Quillen et al. (2007), such that $\langle i_{\rm rms}\rangle \sim \sqrt{2}h_{\rm HWHM}$. Matrà et al. (2019), on the other hand, assume a Rayleigh distribution of inclinations in a self-stirred disk to derive $\langle i_{\rm rms}\rangle = \sqrt{2}h_\sigma$. We note that h_σ is approximately 85% of $h_{\rm HWHM}$. However, the non-Gaussianity of most vertical profiles means that neither of these equations are strictly true for this application.

Another way to compare different theoretical models to the observations is to consider how h varies with wavelength. If a disk is fragmentation-dominated with no significant collisional damping, h is expected not to vary with wavelength, in viscously stirred disks (Kenyon & Bromley 2002b, 2004, 2008; Kennedy & Wyatt 2010) as well as in pre-stirred disks (Jankovic et al. 2024). On the other hand, if h increases with wavelength, it could be a sign of efficient collisional damping in the system (Pan & Schlichting 2012).

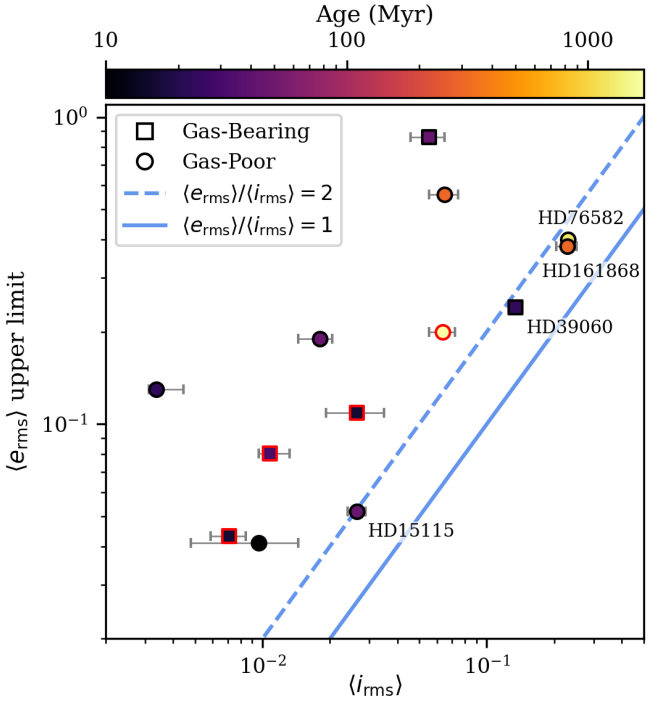

Fig. 8. Eccentricity and inclination dispersions estimated from the radial and vertical density distributions, respectively. Points with black outlines use the upper limits on $\langle e_{\rm rms}\rangle$ presented in Han et al. (2026), while points with red outlines have $\langle e_{\rm rms}\rangle$ estimated using Eq. (14). Disks may be dynamically dominated by catastrophic collisions when $\langle e_{\rm rms}\rangle/\langle i_{\rm rms}\rangle \lesssim 1$, rather than self-stirred or planet-stirred scenarios that result in a larger ratio of $\langle e_{\rm rms}\rangle/\langle i_{\rm rms}\rangle$. We note that the y-axis shows upper limits of $\langle e_{\rm rms}\rangle$, so we only find upper limits on $\langle e_{\rm rms}\rangle/\langle i_{\rm rms}\rangle$.

We compiled ALMA measurements of $h_{\rm HWHM}$, shown in Table C.1 and summarized in Figure C.1. A few systems show a consistent increase in measured $h_{\rm HWHM}$: HD 15115, HD 32297, HD 61005, and HD 131488. The remaining disks with multiwavelength constraints (HD 9672, HD 10647, HD 14055, HD 107146, HD 161868, and HD 197481[8]) appear more consistent with an aspect ratio that remains approximately constant with wavelength. The remaining disks do not have measurements in multiple ALMA bands.

The predictions come with the caveat that results are difficult to directly compare if the h measurements were obtained with different methods or with different data resolutions. Unfortunately, this makes it impossible to draw firm conclusions with the current data and analyses. Follow-up measurements at similar resolutions to the ARKS observations could help to confirm or rule out these tentative trends.

5.5. Constraints on planetary companions

In this work, we have assumed that disks have aspect ratios which are driven by internal processes. However, there is a rich literature exploring alternative scenarios in which planetary (or stellar) companions drive the required dynamical excitation. In these cases, the properties of the hypothetical planet(s) and the disk-to-planet mass ratio ($M_{\rm disk}/m_{\rm pl}$) set the disk particles'

[8] While not obvious here, there is evidence that HD 197481 is vertically thicker in Band 6 observations compared to Band 9 observations at a similar resolution (Vizgan et al. 2022).

eccentricities and inclinations. For example, low mass disks may have observable differences in their vertical structure depending on whether the planet's orbit is inclined with respect to the disk: a coplanar planet would excite the disk radially rather than vertically (Pearce & Wyatt 2014). On the other hand, initially misaligned, low-inclination planets can generate warps that propagate through the disk over time, causing the disk to settle into a vertically inflated configuration. This can occur regardless of whether the planet lies interior (Mouillet et al. 1997; Dawson et al. 2011; Pearce & Wyatt 2014; Smallwood 2023) or exterior to the disk (Nesvold et al. 2017; Farhat et al. 2023), assuming the dynamics are not significantly affected by the disk gravity (typically requiring $M_{\rm disk}/m_{\rm pl} \ll 1$; Sefilian et al. 2025). Assuming a given configuration, one can then use the measured vertical scale heights to infer the planet properties.

For relatively massive disks, the collective gravity of the disk may be significant enough to resist planetary perturbations, maintaining a low dispersion in both radial (Sefilian 2024) and vertical directions (Poblete et al. 2023; Sefilian et al. 2025). Alternatively, a massive disk could give rise to secular-inclination resonances and localized warps (Sefilian et al. 2025). This significantly complicates the interpretation of planetary parameters inferred from massless disk models, which typically result in artificially low planetary masses, particularly when the planet lies close to the disk (Sefilian et al. 2025). A full exploration of planet-driven dynamical excitation scenarios is outside the scope of this study. However, a future study will provide a detailed investigation on planetary inference in the ARKS sample, building on the vertical aspect ratio measurements presented in this work (Jankovic et al. in prep).

5.6. Limitations

We have presented the modeling and analysis of the vertical aspect ratios and dust distributions of the highly inclined ARKS targets. However, the analyses presented here have several limitations which could impact how the results are interpreted. First, we consider only axisymmetric disks with vertical distributions that peak at the disk midplane. The axisymmetric modeling could obscure more complex structures both radially and vertically. For example, the presence of a warp could bias the axisymmetric models to larger scale heights in order to account for the warped material sitting further from the midplane. An analysis of the asymmetric features in the ARKS sample is presented in Lovell et al. (2026).

Second, in this work we assume that aspect ratio is constant with radius. Using a constant aspect ratio is beneficial for enabling direct comparison with the majority of previous vertical structure measurements (see Table C.1), as well as for minimizing the number of free parameters in our models. However, recent work has called the validity of this assumption into question, as more disks with evidence of a variable h are identified. For example, Matrà et al. (2019) parametrized the aspect ratio of HD 39060 as $h \propto r^{\beta-1}$. In this parametrization, $\beta = 1$ corresponds to a constant aspect ratio (as in our Eq. (1)), $\beta > 1$ to a flared disk, and $\beta = 0$ to a constant H. The model fit yielded $\beta = 0.7 \pm 0.2$, which is consistent with a constant $h(r)$, but also provides marginal evidence (at $< 2\sigma$) of a slowly increasing scale height resulting in a radially varying $h(r)$. This, however, did not result in a significantly improved fit compared to models assuming a constant h. Similarly, Terrill et al. (2023) allowed for a varying aspect ratio with radius when fitting HD 9672 (49 Ceti), and found a loosely constrained value of $\beta = 0.79^{+0.29}_{-0.35}$.

More recently, Han et al. (2025) fit $H(r)$ nonparametrically, finding several disks that are not consistent with a constant aspect ratio. Some ARKS targets were included in this study: HD 14055 was found to be consistent with a constant aspect ratio, while HD 32297, HD 61005, and HD 197481 were found to have a steeper $H(r)$ (scale height increasing more sharply with radius). Interestingly, HD 15115 was found to have a decreasing $H(r)$, suggesting that the inner ring may be thicker than the outer ring.

From a theoretical perspective, Sefilian et al. (2025) find that in debris disks perturbed by inner planets, the aspect ratio can follow $h(r) \propto r^{-7/2}$, with the extent of this behavior depending on the disk-to-planet mass ratio, $M_{\rm disk}/M_{\rm planet}$. This effect arises from the disk's ability to mitigate planetary perturbations (see also Sefilian 2024). When $M_{\rm disk}/M_{\rm planet} \gtrsim 1$, this trend holds across the entire disk; for $M_{\rm disk}/M_{\rm planet} \lesssim 1$, it applies only in the disk's outer regions, while the inner parts maintain $h(r) \approx$ const. This suggests that planet-disk interactions can produce aspect ratios that vary and decrease with radius. The work presented here only considers the case of a radially constant h, but follow-up studies with nonconstant h would be beneficial to fully understand how common scale height variability is in debris disks.

Lastly, the specific radial and vertical density parametrizations can impact the measured scale heights. A poor choice of radial profile can result in biased vertical results, (and vice versa). This may explain some of the differences between $h_{\rm HWHM}$ measurements derived from REASONS and ARKS (Figure 6). Similar discrepancies can be seen in Figure C.1, which shows all of the measured $h_{\rm HWHM}$ listed in Table C.1. We have attempted to address this issue by leveraging the extensive radial structure analysis presented in Han et al. (2026) to ensure that we are using the most appropriate parametrizations for the radial dust distributions before extending the exploration to the vertical dust structures. However, it is possible that the radial and/or vertical density distributions adopted in this work do not fully capture the morphology of certain sources.

6. Conclusions

In this paper we have presented the detailed vertical structure analysis of the ARKS debris disks, including constraints from parametric modeling, `frank`, and `rave`. We successfully measured the scale heights for the 13 most highly inclined targets in the ARKS sample using all three methods, and we recovered scale height constraints for a handful of moderately inclined ARKS targets with `frank` and `rave` (Table 3). Our key results are summarized here:

- Many disks are quite thin ($h_{\rm HWHM} \lesssim 0.01$), while others host millimeter-sized dust grains much farther from the midplane ($h_{\rm HWHM} \gtrsim 0.1$);
- Lorentzian (or otherwise thick-tailed) vertical dust distributions are common, suggesting that systems may commonly host multiple dynamical populations within the disk. This could hint at Neptune-like migration histories in these systems or could be a remnant of long-term planet-disk interactions in general;
- We used our aspect ratio measurements to estimate the total mass of solids in the disk, and we placed limits on the mass of the bodies that could be gravitationally stirring the disks (Table 4, Figure 5). We find that fewer than half of the disks contain less mass than Neptune and that the most massive disks also have the broadest belts radially;
- We measure much smaller aspect ratios (thinner disks) than comparable measurements made with lower-resolution data

at the same observing wavelength. As a result, we may for the first time be observing the theoretically predicted increase in scale height with disk age. However, because the disks are so thin, follow-up observations at higher resolution could help us better understand this trend;
– Aspect ratios obtained from scattered light observations tend to be similar to or larger than the corresponding ALMA millimeter aspect ratios (Figure 7). We do not observe a clear trend when comparing the gas-bearing debris disks against those with no detected gas, though several of the disks are not well resolved vertically in scattered light.

These measurements provide new empirical constraints on the vertical structures of debris disks and the range of dynamical processes that are likely to sculpt them. Future high resolution and multiwavelength observations will help to further refine these measurements, strengthening our population level understanding of the debris disk morphologies and dynamics.

Data availability

The ARKS data used in this paper and others can be found in the ARKS dataverse. The data products produced by this work can be found at https://doi.org/10.7910/DVN/6NNKLY. For more information, visit arkslp.org.

Acknowledgements. This paper makes use of the following ALMA data: ADS/JAO.ALMA# 2022.1.00338.L, 2012.1.00142.S, 2012.1.00198.S, 2015.1.01260.S, 2016.1.00104.S, 2016.1.00195.S, 2016.1.00907.S, 2017.1.00167.S, 2017.1.00825.S, 2018.1.01222.S and 2019.1.00189.S. ALMA is a partnership of ESO (representing its member states), NSF (USA) and NINS (Japan), together with NRC (Canada), MOST and ASIAA (Taiwan), and KASI (Republic of Korea), in cooperation with the Republic of Chile. The Joint ALMA Observatory is operated by ESO, AUI/NRAO and NAOJ. The National Radio Astronomy Observatory is a facility of the National Science Foundation operated under cooperative agreement by Associated Universities, Inc. The project leading to this publication has received support from ORP, that is funded by the European Union's Horizon 2020 research and innovation programme under grant agreement No. 101004719 [ORP]. We are grateful for the help of the UK node of the European ARC in answering our questions and producing calibrated measurement sets. This research used the Canadian Advanced Network For Astronomy Research (CANFAR) operated in partnership by the Canadian Astronomy Data Centre and The Digital Research Alliance of Canada with support from the National Research Council of Canada the Canadian Space Agency, CANARIE and the Canadian Foundation for Innovation. Support for BZ was provided by The Brinson Foundation. This material is based upon work supported by the National Science Foundation Graduate Research Fellowship under Grant No. DGE 2140743. AMH, AJF, and EM acknowledges support from the National Science Foundation under Grant No. AST-2307920. EM acknowledges support from the NASA CT Space Grant. MP acknowledges support from NASA grant 80NSSC21K1334. JM acknowledges funding from the Agence Nationale de la Recherche through the DDISK project (grant No. ANR-21-CE31-0015) and from the PNP (French National Planetology Program) through the EPOPEE project. TDP is supported by a UKRI Stephen Hawking Fellowship and a Warwick Prize Fellowship, the latter made possible by a generous philanthropic donation. A.A.S. is supported by the Heising-Simons Foundation through a 51 Pegasi b Fellowship. MB acknowledges funding from the Agence Nationale de la Recherche through the DDISK project (grant No. ANR-21-CE31-0015). AB acknowledges research support by the Irish Research Council under grant GOIPG/2022/1895. CdB acknowledges support from the Spanish Ministerio de Ciencia, Innovación y Universidades (MICIU) and the European Regional Development Fund (ERDF) under reference PID2023-153342NB-I00/10.13039/501100011033, from the Beatriz Galindo Senior Fellowship BG22/00166 funded by the MICIU, and the support from the Universidad de La Laguna (ULL) and the Consejería de Economía, Conocimiento y Empleo of the Gobierno de Canarias. EC acknowledges support from NASA STScI grant HST-AR-16608.001-A and the Simons Foundation. S.E. is supported by the National Aeronautics and Space Administration through the Exoplanet Research Program (Grant No. 80NSSC23K0288, PI: Faramaz). MRJ acknowledges support from the European Union's Horizon Europe Programme under the Marie Sklodowska-Curie grant agreement no. 101064124 and funding provided by the Institute of Physics Belgrade, through the grant by the Ministry of Science, Technological Development, and Innovations of the Republic of Serbia. This work was also supported by the NKFIH NKKP grant ADVANCED 149943 and the NKFIH excellence grant TKP2021-NKTA-64. Project no.149943 has been implemented with the support provided by the Ministry of Culture and Innovation of Hungary from the National Research, Development and Innovation Fund, financed under the NKKP ADVANCED funding scheme. JBL acknowledges the Smithsonian Institute for funding via a Submillimeter Array (SMA) Fellowship, and the North American ALMA Science Center (NAASC) for funding via an ALMA Ambassadorship. SMM acknowledges funding by the European Union through the E-BEANS ERC project (grant number 100117693), and by the Irish research Council (IRC) under grant number IRCLA- 2022-3788. Views and opinions expressed are however those of the author(s) only and do not necessarily reflect those of the European Union or the European Research Council Executive Agency. Neither the European Union nor the granting authority can be held responsible for them. SM acknowledges funding by the Royal Society through a Royal Society University Research Fellowship (URF-R1-221669) and the European Union through the FEED ERC project (grant number 101162711). JPM acknowledges research support by the National Science and Technology Council of Taiwan under grant NSTC 112-2112-M-001-032-MY3. LM acknowledges funding by the European Union through the E-BEANS ERC project (grant number 100117693), and by the Irish research Council (IRC) under grant number IRCLA- 2022-3788. Views and opinions expressed are however those of the author(s) only and do not necessarily reflect those of the European Union or the European Research Council Executive Agency. Neither the European Union nor the granting authority can be held responsible for them. SP acknowledges support from FONDECYT Regular 1231663 and ANID – Millennium Science Initiative Program – Center Code NCN2024_001. PW acknowledges support from FONDECYT grant 3220399 and ANID – Millennium Science Initiative Program – Center Code NCN2024_001.

References

Adams, E. R., Gulbis, A. A. S., Elliot, J. L., et al. 2014, AJ, 148, 55
Akaike, H. 1974, IEEE Trans. Automatic Control, AC-19, 716
Apai, D., Schneider, G., Grady, C. A., et al. 2015, ApJ, 800, 136
Batygin, K., Adams, F. C., Batygin, Y. K., & Petigura, E. A. 2020, AJ, 159, 101
Boccaletti, A., Thébault, P., Pawellek, N., et al. 2019, A&A, 625, A21
Booth, R. A., & Clarke, C. J. 2016, MNRAS, 458, 2676
Brown, M. E. 2001, AJ, 121, 2804
Burnham, K. P., Anderson, D. R., & Burnham, K. P. 2002, Model Selection and Multimodel Inference: A Practical Information-Theoretic Approach
Carry, B. 2012, Planet. Space Sci., 73, 98
Chai, Y., Chen, C. H., Worthen, K., et al. 2024, ApJ, 976, 167
Daley, C., Hughes, A. M., Carter, E. S., et al. 2019, ApJ, 875, 87
Dartois, E., Dutrey, A., & Guilloteau, S. 2003, A&A, 399, 773
Dawson, R. I., Murray-Clay, R. A., & Fabrycky, D. C. 2011, ApJ, 743, L17
Delamer, M. 2021, Master's thesis, Wesleyan University, https://digitalcollections.wesleyan.edu/object/ir-3040
Doi, K., & Kataoka, A. 2021, ApJ, 912, 164
Dong, J., Dawson, R. I., Shannon, A., & Morrison, S. 2020, ApJ, 889, 47
Draine, B. T. 2003, ApJ, 598, 1017
Engler, N., Boccaletti, A., Schmid, H. M., et al. 2019, A&A, 622, A192
Farhat, M. A., Sefilian, A. A., & Touma, J. R. 2023, MNRAS, 521, 2067
Fehr, A. 2023, Bachelor's thesis, Wesleyan University, USA
Flaherty, K. M., Hughes, A. M., Rosenfeld, K. A., et al. 2015, ApJ, 813, 99
Foreman-Mackey, D., Hogg, D. W., Lang, D., & Goodman, J. 2013, PASP, 125, 306
Golimowski, D. A., Ardila, D. R., Krist, J. E., et al. 2006, AJ, 131, 3109
Gulbis, A. A. S., Elliot, J. L., Adams, E. R., et al. 2010, AJ, 140, 350
Hahn, J. M., & Malhotra, R. 2005, AJ, 130, 2392
Hales, A. S., Marino, S., Sheehan, P. D., et al. 2022, ApJ, 940, 161
Han, Y., Wyatt, M. C., & Matrà, L. 2022, MNRAS, 511, 4921
Han, Y., Wyatt, M. C., & Marino, S. 2025, MNRAS, 537, 3839
Han, Y., Mansell, E., Jennings, J., et al. 2026, A&A, 705, A196
Hughes, A. M., Duchêne, G., & Matthews, B. C. 2018, ARA&A, 56, 541
Ida, S. 1990, Icarus, 88, 129
Ida, S., & Makino, J. 1992, Icarus, 96, 107
Ida, S., & Makino, J. 1993, Icarus, 106, 210
Inaba, S., Tanaka, H., Nakazawa, K., Wetherill, G. W., & Kokubo, E. 2001, Icarus, 149, 235
Jankovic, M. R., Wyatt, M. C., & Löhne, T. 2024, A&A, 691, A302
Jennings, J., Booth, R. A., Tazzari, M., Rosotti, G. P., & Clarke, C. J. 2020, MNRAS, 495, 3209
Jennings, J., Marino, S., & Han, Y. 2024, https://doi.org/10.5281/zenodo.10993146
Jílková, L., & Portegies Zwart, S. 2015, MNRAS, 451, 804
Kass, R. E., & Raftery, A. E. 1995, J. Am. Statist. Assoc., 90, 773

Kavelaars, J. J., Jones, R. L., Gladman, B. J., et al. 2009, AJ, 137, 4917
Kennedy, G. M., & Wyatt, M. C. 2010, MNRAS, 405, 1253
Kennedy, G. M., Marino, S., Matrà, L., et al. 2018, MNRAS, 475, 4924
Kenyon, S. J., & Bromley, B. C. 2002a, AJ, 123, 1757
Kenyon, S. J., & Bromley, B. C. 2002b, ApJ, 577, L35
Kenyon, S. J., & Bromley, B. C. 2004, AJ, 127, 513
Kenyon, S. J., & Bromley, B. C. 2008, ApJS, 179, 451
Kenyon, S. J., Wood, K., Whitney, B. A., & Wolff, M. J. 1999, ApJ, 524, L119
Krivov, A. V., & Booth, M. 2018, MNRAS, 479, 3300
Krivov, A. V., & Wyatt, M. C. 2021, MNRAS, 500, 718
Lagrange, A. M., Boccaletti, A., Milli, J., et al. 2012, A&A, 542, A40
Lestrade, J. F., Morey, E., Lassus, A., & Phou, N. 2011, A&A, 532, A120
Levison, H. F., Morbidelli, A., Van Laerhoven, C., Gomes, R., & Tsiganis, K. 2008, Icarus, 196, 258
Li, A., & Greenberg, J. M. 1998, A&A, 331, 291
Liddle, A. R. 2007, MNRAS, 377, L74
Lissauer, J. J., & Stewart, G. R. 1993, in Protostars and Planets III, eds. E. H. Levy, & J. I. Lunine, 1061
Lovell, J. B., Hales, A. S., Kennedy, G. M., et al. 2026, A&A, 705, A200
Lovell, J. B., Marino, S., Wyatt, M. C., et al. 2021, MNRAS, 506, 1978
MacGregor, M. A., Weinberger, A. J., Nesvold, E. R., et al. 2019, ApJ, 877, L32
Malhotra, R. 1995, AJ, 110, 420
Malhotra, R., & Roy, S. 2023, RNAAS, 7, 143
Marino, S. 2021, MNRAS, 503, 5100
Marino, S., Cataldi, G., Jankovic, M. R., Matrà, L., & Wyatt, M. C. 2022, MNRAS, 515, 507
Marino, S., Matrà, L., Hughes, A. M., et al. 2026, A&A, 705, A195
Marshall, J. P., Milli, J., Choquet, E., et al. 2023, MNRAS, 521, 5940
Matrà, L., Wyatt, M. C., Wilner, D. J., et al. 2019, AJ, 157, 135
Matrà, L., Marino, S., Wilner, D. J., et al. 2025, A&A, 693, A151
Matthews, B. C., Krivov, A. V., Wyatt, M. C., Bryden, G., & Eiroa, C. 2014, in Protostars and Planets VI, eds. H. Beuther, R. S. Klessen, C. P. Dullemond, & T. Henning, 521
Millar-Blanchaer, M. A., Graham, J. R., Pueyo, L., et al. 2015, ApJ, 811, 18
Millar-Blanchaer, M. A., Wang, J. J., Kalas, P., et al. 2016, AJ, 152, 128
Milli, J., Lagrange, A. M., Mawet, D., et al. 2014, A&A, 566, A91
Milli, J., Olofsson, J., Bonduelle, M., et al. 2026, A&A, 705, A199
Moore, N. W. H., Li, G., & Adams, F. C. 2020, ApJ, 901, 92
Moore, N. W. H., Li, G., Hassenzahl, L., et al. 2023, ApJ, 943, 6
Morbidelli, A., Levison, H. F., & Gomes, R. 2008, in The Solar System Beyond Neptune, eds. M. A. Barucci, H. Boehnhardt, D. P. Cruikshank, A. Morbidelli, & R. Dotson, 275
Mouillet, D., Larwood, J. D., Papaloizou, J. C. B., & Lagrange, A. M. 1997, MNRAS, 292, 896
Mustill, A. J., & Wyatt, M. C. 2009, MNRAS, 399, 1403
Nesvold, E. R., Naoz, S., & Fitzgerald, M. P. 2017, ApJ, 837, L6
Nesvorný, D. 2015, AJ, 150, 73
Olofsson, J., Milli, J., Bayo, A., Henning, T., & Engler, N. 2020, A&A, 640, A12
Olofsson, J., Thébault, P., Kennedy, G. M., & Bayo, A. 2022a, A&A, 664, A122
Olofsson, J., Thébault, P., Kral, Q., et al. 2022b, MNRAS, 513, 713
Pan, M., & Schlichting, H. E. 2012, ApJ, 747, 113
Pearce, T. D., & Wyatt, M. C. 2014, MNRAS, 443, 2541
Pearce, T. D., Krivov, A. V., Sefilian, A. A., et al. 2024, MNRAS, 527, 3876
Petit, J. M., Kavelaars, J. J., Gladman, B. J., et al. 2011, AJ, 142, 131
Poblete, P. P., Löhne, T., Pearce, T. D., & Sefilian, A. A. 2023, MNRAS, 526, 2017
Quillen, A. C. 2006, MNRAS, 372, L14
Quillen, A. C., Morbidelli, A., & Moore, A. 2007, MNRAS, 380, 1642
Rafikov, R. R. 2023, MNRAS, 519, 5607
Raftery, A. E. 1995, Sociol. Methodol., 25, 111
Rosenfeld, K. A., Qi, C., Andrews, S. M., et al. 2012, ApJ, 757, 129
Rosenfeld, K. A., Andrews, S. M., Hughes, A. M., Wilner, D. J., & Qi, C. 2013, ApJ, 774, 16
Schlichting, H. E. 2014, ApJ, 795, L15
Schwarz, G. 1978, Ann. Statist., 6, 461
Sefilian, A. A. 2024, ApJ, 966, 140
Sefilian, A. A., Kratter, K. M., Wyatt, M. C., et al. 2025, MNRAS, 543, 3123
Smallwood, J. L. 2023, MNRAS, 523, 3526
Tazzari, M., Beaujean, F., & Testi, L. 2018, MNRAS, 476, 4527
Terrill, J., Marino, S., Booth, R. A., et al. 2023, MNRAS, 524, 1229
Thébault, P. 2009, A&A, 505, 1269
Thébault, P., & Augereau, J. C. 2007, A&A, 472, 169
Van Laerhoven, C., Gladman, B., Volk, K., et al. 2019, AJ, 158, 49
Villenave, M., Rosotti, G. P., Lambrechts, M., et al. 2025, A&A, 697, A64
Vizgan, D., Hughes, A. M., Carter, E. S., et al. 2022, ApJ, 935, 131
Walmswell, J., Clarke, C., & Cossins, P. 2013, MNRAS, 431, 1903
Wetherill, G. W., & Stewart, G. R. 1993, Icarus, 106, 190
Worthen, K., Chen, C. H., Brittain, S. D., et al. 2024, ApJ, 962, 166
Wyatt, M. C. 2008, ARA&A, 46, 339
Wyatt, M. C., & Dent, W. R. F. 2002, MNRAS, 334, 589

[1] Department of Astronomy, Van Vleck Observatory, Wesleyan University, 96 Foss Hill Dr., Middletown, CT 06459, USA
[2] Center for Astrophysics | Harvard & Smithsonian, 60 Garden St, Cambridge, MA 02138, USA
[3] Kavli Institute for Particle Astrophysics and Cosmology, 382 Via Pueblo Mall Stanford, CA 94305-4060, USA
[4] Division of Geological and Planetary Sciences, California Institute of Technology, 1200 E. California Blvd., Pasadena, CA 91125, USA
[5] Smithsonian Astrophysical Observatory, 60 Garden St, Cambridge, MA 02138, USA
[6] Univ. Grenoble Alpes, CNRS, IPAG, 38000 Grenoble, France
[7] European Southern Observatory, Karl-Schwarzschild-Strasse 2, 85748 Garching bei München, Germany
[8] Department of Physics, University of Warwick, Gibbet Hill Road, Coventry CV4 7AL, UK
[9] Department of Astronomy and Steward Observatory, The University of Arizona, 933 North Cherry Ave, Tucson, AZ 85721, USA
[10] UK Astronomy Technology Centre, Royal Observatory Edinburgh, Blackford Hill, Edinburgh EH9 3HJ, UK
[11] School of Physics, Trinity College Dublin, the University of Dublin, College Green, Dublin 2, Ireland
[12] Instituto de Astrofísica de Canarias, Vía Láctea S/N, La Laguna, 38200 Tenerife, Spain
[13] Departamento de Astrofísica, Universidad de La Laguna, La Laguna, 38200 Tenerife, Spain
[14] Joint ALMA Observatory, Avenida Alonso de Córdova 3107, Vitacura 7630355, Santiago, Chile
[15] National Astronomical Observatory of Japan, Osawa 2-21-1, Mitaka, Tokyo 181-8588, Japan
[16] Department of Astronomy, Graduate School of Science, The University of Tokyo, Tokyo 113-0033, Japan
[17] Department of Astronomy, University of California, Berkeley, Berkeley, CA 94720-3411, USA
[18] Large Binocular Telescope Observatory, The University of Arizona, 933 North Cherry Ave, Tucson, AZ 85721, USA
[19] Max-Planck-Insitut für Astronomie, Königstuhl 17, 69117 Heidelberg, Germany
[20] Institute of Physics Belgrade, University of Belgrade, Pregrevica 118, 11080 Belgrade, Serbia
[21] Malaghan Institute of Medical Research, Gate 7, Victoria University, Kelburn Parade, Wellington, New Zealand
[22] Konkoly Observatory, HUN-REN Research Centre for Astronomy and Earth Sciences, MTA Centre of Excellence, Konkoly-Thege Miklós út 15–17, 1121 Budapest, Hungary
[23] Institute of Physics and Astronomy, ELTE Eötvös Loránd University, Pázmány Péter sétány 1/A, 1117 Budapest, Hungary
[24] Astrophysikalisches Institut und Universitätssternwarte, Friedrich-Schiller-Universität Jena, Schillergäßchen 2-3, 07745 Jena, Germany
[25] Department of Physics and Astronomy, Johns Hopkins University, 3400 N Charles Street, Baltimore, MD 21218, USA
[26] Department of Physics and Astronomy, University of Exeter, Stocker Road, Exeter EX4 4QL, UK
[27] Academia Sinica Institute of Astronomy and Astrophysics, 11F of AS/NTU Astronomy-Mathematics Building, No.1, Sect. 4, Roosevelt Rd, Taipei 106319, Taiwan
[28] Departamento de Física, Universidad de Santiago de Chile, Av. Víctor Jara 3493, Santiago, Chile
[29] Millennium Nucleus on Young Exoplanets and their Moons (YEMS), Chile
[30] Center for Interdisciplinary Research in Astrophysics Space Exploration (CIRAS), Universidad de Santiago, Chile
[31] Institute of Astronomy, University of Cambridge, Madingley Road, Cambridge CB3 0HA, UK

Appendix A: Summary of parametric modeling

Table A.1: Summary of the parametric modeling (combinations of radial and vertical functional forms and the number of free parameters N_p) for each source.

Source	Radial Form	Vertical Form	N_p	AIC Conf.	ΔBIC	Fiducial Model Parameters	
						Best-Fit	50th Percentile
HD 9672	DPL	vG	10	7.52	60.62	$\alpha_{\rm in} = 2.11$	$\alpha_{\rm in} = 2.13^{+0.17}_{-0.17}$
	DG	vG	12	> 10	99.18	$\alpha_{\rm out} = -1.48$	$\alpha_{\rm out} = -1.45^{+0.09}_{-0.09}$
	DPL	vE	11	7.76	77.54	$R_{\rm c} = 107$ au	$R_{\rm c} = 107^{+4}_{-4}$ au
	DPL	**vL**	**10**	**0.27**	**0**	$h_{\rm HWHM} = 0.041$	$h_{\rm HWHM} = 0.046^{+0.008}_{-0.008}$
	DPL	vDG	12	0	25.81	$\Sigma_c = -4.170$	$\Sigma_c = -4.175^{+0.009}_{-0.009}$
						PA= 107.72°	PA= $107.74^{\circ+0.12}_{-0.09}$
						dRA= 0.″039	dRA= $0.''048^{+0.015}_{-0.016}$
						dDec= −0.″035	dDec= $-0.''037^{+0.006}_{-0.007}$
						$i = 80.03°$	$i = 80.18^{\circ+0.12}_{-0.14}$
						$F_\star = 5.2 \times 10^{-6}$ Jy	$F_\star = 1.0^{+1.0}_{-0.6} \times 10^{-5}$ Jy
HD 10647	DPL	vG	10	> 10	> 100	$R_1 = 87.9$ au	$R_1 = 87.6^{+0.9}_{-0.6}$ au
	DG	vG	12	> 10	> 100	$R_2 = 142.4$ au	$R_2 = 143^{+3}_{-3}$ au
	DPL	vE	11	> 10	> 100	$\sigma_1 = 10.4$ au	$\sigma_1 = 10.6^{+0.8}_{-0.8}$ au
	DG	vE	13	> 10	> 100	$\sigma_2 = 36.3$ au	$\sigma_2 = 35^{+2}_{-3}$ au
	DPL	vL	10	6.15	0	$C_1 = 0.650$	$C_1 = 0.654^{+0.011}_{-0.013}$
	DG	vL	12	7.74	47.94	$h_{\rm HWHM1} = 0.052$	$h_{\rm HWHM1} = 0.053^{+0.006}_{-0.007}$
	DPL	vDG	12	> 10	> 100	$h_{\rm HWHM2} = 0.226$	$h_{\rm HWHM2} = 0.225^{+0.002}_{-0.002}$
	DG	**vDG**	**14**	**0**	**9.04**	$C_{\rm vert} = 0.91$	$C_{\rm vert} = 0.88^{+0.06}_{-0.06}$
						$\Sigma_c = -4.406$	$\Sigma_c = -4.395^{+0.019}_{-0.019}$
						PA= 57.1°	PA= $56.8^{\circ+0.29}_{-0.19}$
						dRA= 0.″093	dRA= $0.''092^{+0.010}_{-0.010}$
						dDec= 0.″016	dDec= $0.''011^{+0.008}_{-0.009}$
						$i = 78.74°$	$i = 78.83^{\circ+0.21}_{-0.18}$
						$F_\star = 146 \times 10^{-6}$ Jy	$F_\star = 145^{+0.8}_{-1.0} \times 10^{-6}$ Jy
HD 14055	**DPL**	**vG**	**10**	**0.56**	**0**	$\alpha_{\rm in} = 1.31$	$\alpha_{\rm in} = 1.24^{+0.15}_{-0.12}$
	DG	vG	12	0.27	25.92	$\alpha_{\rm out} = -3.43$	$\alpha_{\rm out} = -3.2^{+0.7}_{-0.9}$
	DPL	vE	11	1.12	14.83	$R_{\rm c} = 177$ au	$R_{\rm c} = 180^{+9}_{-12}$ au
	DG	vE	13	0	38.72	$h_{\rm HWHM} = 0.059$	$h_{\rm HWHM} = 0.053^{+0.007}_{-0.008}$
	DPL	vL	10	1.62	3.38	$\Sigma_c = -5.051$	$\Sigma_c = -5.068^{+0.017}_{-0.018}$
	DG	vL	12	1.46	29.32	PA= 161.44°	PA= $161.59^{\circ+0.29}_{-0.16}$
	DPL	vDG	12	1.59	29.83	dRA= −0.″066	dRA= $-0.''062^{+0.009}_{-0.009}$
	DG	vDG	14	1.07	54.50	dDec= −0.″064	dDec= $-0.''067^{+0.013}_{-0.011}$
						$i = 80.0°$	$i = 80.0^{\circ+0.2}_{-0.3}$
						$F_\star = 1.00 \times 10^{-4}$ Jy	$F_\star = 1.01^{+0.1}_{-0.1} \times 10^{-4}$ Jy

Table A.1: continued.

Source	Radial Form	Vertical Form	N_p	AIC Conf.	ΔBIC	Fiducial Model Parameters	
						Best-Fit	50th Percentile
HD 15115	DPL	vG	10	> 10	> 100	R_1 = 97.83 au	$R_1 = 97.88^{+0.05}_{-0.07}$ au
	DG	vG	12	6.94	52.55	R_2 = 65.94 au	$R_2 = 66.0^{+0.60}_{-0.40}$ au
	DPL	vE	11	> 10	> 100	σ_1 = 4.68 au	$\sigma_1 = 4.59^{+0.18}_{-0.19}$ au
	DG	vE	13	6.05	54.77	σ_2 = 1.88 au	$\sigma_2 = 2.3^{+0.9}_{-0.8}$ au
	DPL	vL	10	> 10	> 100	C_1 = 0.78	$C_1 = 0.81^{+0.04}_{-0.07}$
	DG	vL	13	6.05	54.77	$h_{\rm HWHM}$ = 0.021	$h_{\rm HWHM} = 0.022^{+0.002}_{-0.002}$
	DPL	vL	10	> 10	> 100	Σ_c = −3.427	$\Sigma_c = -3.437^{+0.038}_{-0.028}$
	DG	**vL**	**12**	**0**	**0**	PA= 98.458°	PA= $98.463^{\circ}{}^{+0.013}_{-0.014}$
	DPL	vDG	12	> 10	> 100	dRA= 0.″038	dRA= $0.''036^{+0.002}_{-0.003}$
	DG	vDG	14	2.05	34.56	dDec= −0.″014	dDec= $-0.''014^{+0.001}_{-0.001}$
						i = 86.74°	$i = 86.79^{\circ}{}^{+0.05}_{-0.04}$
						$F_\star = 3.3 \times 10^{-5}$ Jy	$F_\star = 2.5^{+0.6}_{-0.6} \times 10^{-5}$ Jy
HD 32297	DPL	vG	10	3.02	11.96	$\alpha_{\rm in}$ = 71	$\alpha_{\rm in} = 66^{+22}_{-18}$
	DG	vG	12	5.27	57.36	$\alpha_{\rm out}$ = −6.4	$\alpha_{\rm out} = -6.3^{+0.13}_{-0.11}$
	DPL	vE	11	2.24	20.24	$R_{\rm c}$ = 105.2 au	$R_{\rm c} = 105.4^{+0.5}_{-0.4}$ au
	DG	vE	13	5.09	68.34	$h_{\rm HWHM}$ = 0.0098	$h_{\rm HWHM} = 0.0092^{+0.0012}_{-0.0012}$
	DPL	**vL**	**10**	**0**	**0**	Σ_c = −2.709	$\Sigma_c = -2.718^{+0.012}_{-0.016}$
	DG	vL	12	4.33	47.98	PA= 47.50°	PA= $47.50^{\circ}{}^{+0.02}_{-0.04}$
	DPL	vDG	12	0.97	27.95	dRA= 0.″0201	dRA= $0.''0202^{+0.0015}_{-0.0014}$
						dDec= 0.″0152	dDec= $0.''0151^{+0.0013}_{-0.0013}$
						i = 88.48°	$i = 88.48^{\circ}{}^{+0.04}_{-0.03}$
						$F_\star = 1.1 \times 10^{-5}$ Jy	$F_\star = 2.3^{+1.2}_{-1.2} \times 10^{-5}$ Jy
HD 39060 (Beta Pic)	DPL	vG	10	> 10	> 100	$\alpha_{\rm in}$ = 1.82	$\alpha_{\rm in} = 1.78^{+0.14}_{-0.10}$
	DPL	vE	11	> 10	91.82	$\alpha_{\rm out}$ = −5.4	$\alpha_{\rm out} = -5.2^{+0.6}_{-0.5}$
	DPL	**vL**	**10**	**1.55**	**0**	$R_{\rm c}$ = 125 au	$R_{\rm c} = 125^{+2}_{-3}$ au
	DPL	vDG	12	0	22.85	$h_{\rm HWHM}$ = 0.112	$h_{\rm HWHM} = 0.112^{+0.002}_{-0.001}$
						Σ_c = −4.020	$\Sigma_c = -4.031^{+0.014}_{-0.012}$
						PA= 29.76°	PA= $29.74^{\circ}{}^{+0.09}_{-0.09}$
						dRA= −0.″021	dRA= $-0.''017^{+0.010}_{-0.009}$
						dDec= −0.″007	dDec= $-0.''001^{+0.015}_{-0.015}$
						i = 87.65°	$i = 87.66^{\circ}{}^{+0.17}_{-0.13}$
						$F_\star = 7.5 \times 10^{-5}$ Jy	$F_\star = 7.5^{+1.3}_{-1.2} \times 10^{-5}$ Jy
HD 61005	DPL	vG	10	6.81	25.66	R_1 = 69.0 au	$R_1 = 69.4^{+0.5}_{-0.4}$ au
	DG	vG	12	2.64	9.61	R_2 = 97 au	$R_2 = 95^{+2}_{-2}$ au
	TG	vG	15	3.13	50.28	σ_1 = 7.8 au	$\sigma_1 = 7.5^{+0.5}_{-0.4}$ au
	DG	vE	13	3.03	24.52	σ_2 = 29.4 au	$\sigma_2 = 30.8^{+1.7}_{-1.5}$ au
	DG	**vL**	**12**	**0**	**0**	C_1 = 0.839	$C_1 = 0.837^{+0.011}_{-0.012}$
	DG	vDG	14	1.31	28.36	$h_{\rm HWHM}$ = 0.0129	$h_{\rm HWHM} = 0.0143^{+0.0020}_{-0.0021}$
						Σ_c = −3.351	$\Sigma_c = -3.349^{+0.016}_{-0.015}$
						PA= 70.286°	PA= $70.279^{\circ}{}^{+0.015}_{-0.020}$
						dRA= 0.″002	dRA= $-0.''001^{+0.006}_{-0.005}$
						dDec= −0.″017	dDec= $-0.''017^{+0.002}_{-0.003}$
						i = 86.23°	$i = 86.24^{\circ}{}^{+0.03}_{-0.04}$
						$F_\star = 2.3 \times 10^{-6}$ Jy	$F_\star = 2.0^{+8.0}_{-4.0} \times 10^{-6}$ Jy

Table A.1: continued.

Source	Radial Form	Vertical Form	N_p	AIC Conf.	ΔBIC	Fiducial Model Parameters	
						Best-Fit	50th Percentile
HD 76582	DPL	vG	10	7.99	68.74		
	DG	vG	12	8.08	93.10	$\sigma_{\rm in}$ = 47 au	$\sigma_{\rm in} = 45^{+8}_{-8}$ au
	Erf	vG	10	7.92	67.28	$\sigma_{\rm out}$ = 113 au	$\sigma_{\rm out} = 114^{+23}_{-15}$ au
	AG	vG	10	7.99	68.58	$R_{\rm c}$ = 182 au	$R_{\rm c} = 181^{+11}_{-11}$ au
	TPL	vG	15	> 10	> 100	$h_{\rm HWHM}$ = 0.193	$h_{\rm HWHM} = 0.192^{+0.009}_{-0.009}$
	Erf	vE	11	3.81	29.44	Σ_c = −4.690	$\Sigma_c = -4.692^{+0.019}_{-0.024}$
	AG	vE	11	3.50	27.01	PA= 103.2°	PA= $103.9^{\circ}{}^{+1.0}_{-0.7}$
	DPL	vL	10	2.09	6.61	dRA= −0.″029	dRA= $-0.''04^{+0.05}_{-0.05}$
	Erf	vL	10	1.63	4.52	dDec= 0.″036	dDec= $0.''04^{+0.03}_{-0.02}$
	AG	**vL**	**10**	**0**	**0**	i = 72.1°	$i = 72.6^{\circ}{}^{+0.7}_{-0.6}$
	DPL	vDG	12	2.98	35.04	$F_\star = 3.2 \times 10^{-5}$ Jy	$F_\star = 3.6^{+1.8}_{-1.6} \times 10^{-5}$ Jy
	Erf	vDG	12	2.94	34.75		
	AG	vDG	12	2.81	33.92		
HD 109573						R_1 = 77.63 au	$R_1 = 77.61^{+0.03}_{-0.10}$ au
						R_2 = 84.46 au	$R_2 = 83.0^{+1.9}_{-1.7}$ au
	DPL	vG	10	5.29	7.99	σ_1 = 3.2 au	$\sigma_1 = 3.0^{+0.2}_{-0.3}$ au
	DG	**vG**	**12**	**0**	**0**	σ_2 = 24 au	$\sigma_2 = 21^{+3}_{-4}$ au
	G	vG	9	> 10	42.41	C_1 = 0.977	$C_1 = 0.972^{+0.007}_{-0.010}$
	AG	vG	10	7.68	39.63	$h_{\rm HWHM}$ = 0.0065	$h_{\rm HWHM} = 0.0082^{+0.0033}_{-0.0038}$
	DG	vE	13	0.95	14.06	Σ_c = −2.810	$\Sigma_c = -2.784^{+0.023}_{-0.023}$
	DG	vL	12	0.09	0.15	PA= 26.52°	PA= $26.52^{\circ}{}^{+0.03}_{-0.04}$
	DG	vDG	14	1.54	28.03	dRA= 0.″0130	dRA= $0.''0137^{+0.0008}_{-0.0008}$
						dDec= −0.″0400	dDec= $-0.''0397^{+0.0012}_{-0.0011}$
						i = 76.57°	$i = 76.62^{\circ}{}^{+0.09}_{-0.10}$
						$F_\star = 2.3 \times 10^{-5}$ Jy	$F_\star = 3.6^{+1.6}_{-1.5} \times 10^{-5}$ Jy
HD 131488						R_1 = 90.77 au	$R_1 = 90.86^{+0.14}_{-0.10}$ au
						R_2 = 96.8 au	$R_2 = 95.9^{+0.70}_{-0.50}$ au
	DPL	vG	10	> 10	> 100	σ_1 = 1.03 au	$\sigma_1 = 1.17^{+0.18}_{-0.12}$ au
	DG	**vG**	**12**	**0.90**	**0**	σ_2 = 20.4 au	$\sigma_2 = 19.8^{+1.6}_{-1.3}$ au
	G	vG	9	> 10	> 100	C_1 = 0.968	$C_1 = 0.961^{+0.005}_{-0.006}$
	DPL	vE	11	> 10	> 100	$h_{\rm HWHM}$ = 0.0048	$h_{\rm HWHM} = 0.0059^{+0.0011}_{-0.0010}$
	DG	vE	13	0	11.63	Σ_c = −2.136	$\Sigma_c = -2.131^{+0.035}_{-0.063}$.
	DPL	vL	10	> 10	> 100	PA= 97.304°	PA= $97.298^{\circ}{}^{+0.013}_{-0.023}$
	DG	vL	12	1.26	1.14	dRA= 0.″0017	dRA= $0.''0011^{+0.0007}_{-0.0006}$
						dDec= −0.″007	dDec= $-0.''007^{+0.0002}_{-0.0003}$
						i = 84.91°	$i = 84.87^{\circ}{}^{+0.05}_{-0.05}$
						$F_\star = 4.3 \times 10^{-5}$ Jy	$F_\star = 3.8^{+0.9}_{-0.8} \times 10^{-5}$ Jy

Table A.1: continued.

Source	Radial Form	Vertical Form	N_p	AIC Conf.	ΔBIC	Fiducial Model Parameters	
						Best-Fit	50th Percentile
HD 131835	DPL	vG	10	> 10	> 100	R_1 = 69.0 au	$R_1 = 69.0^{+0.4}_{-0.3}$ au
	DG	vG	12	0.55	1.08	R_2 = 107.7 au	$R_2 = 109.1^{+2.2}_{-1.9}$ au
	TG	vG	15	1.67	43.94	σ_1 = 4.7 au	$\sigma_1 = 4.8^{+0.6}_{-0.6}$ au
	DG	vE	13	1.26	16.22	σ_2 = 42.7 au	$\sigma_2 = 42.0^{+1.4}_{-1.8}$ au
	DG	**vL**	**12**	**0**	**0**	C_1 = 0.877	$C_1 = 0.877^{+0.012}_{-0.012}$
	DG	vDG	14	1.46	30.01	$h_{\rm HWHM}$ = 0.017	$h_{\rm HWHM} = 0.022^{+0.007}_{-0.006}$
						Σ_c = −2.915	$\Sigma_c = -2.912^{+0.047}_{-0.043}$
						PA= 58.90°	PA= $58.96^{\circ+0.18}_{-0.18}$
						dRA= 0.″0007	dRA= $0.''0018^{+0.0018}_{-0.0018}$
						dDec= −0.″0063	dDec= $-0.''0056^{+0.0014}_{-0.0014}$
						i = 74.5°	$i = 74.6^{\circ+0.2}_{-0.2}$
						$F_\star = 4.3 \times 10^{-6}$ Jy	$F_\star = 1.0^{+1.2}_{-0.7} \times 10^{-5}$ Jy
HD 161868	DPL	vG	10	3.48	12.04	$\alpha_{\rm in}$ = 1.24	$\alpha_{\rm in} = 1.21^{+0.19}_{-0.15}$
	DG	vG	12	3.29	34.57	$\alpha_{\rm out}$ = −5.3	$\alpha_{\rm out} = -5.3^{+1.8}_{-2.5}$
	DPL	vE	11	1.94	14.71	$R_{\rm c}$ = 160 au	$R_{\rm c} = 160^{+11}_{-13}$ au
	DPL	**vL**	**10**	**1.26**	**0**	$h_{\rm HWHM}$ = 0.192	$h_{\rm HWHM} = 0.192^{+0.012}_{-0.016}$
	DPL	vDG	12	0	20.79	Σ_c = −4.896	$\Sigma_c = -4.902^{+0.025}_{-0.029}$
						PA= 57.8°	PA= $57.3^{\circ+1.0}_{-1.2}$
						dRA= −0.″004	dRA= $-0.''01^{+0.03}_{-0.02}$
						dDec= −0.″08	dDec= $-0.''08^{+0.02}_{-0.02}$
						i = 66.7°	$i = 66.7^{\circ+0.9}_{-0.9}$
						$F_\star = 1.7 \times 10^{-4}$ Jy	$F_\star = 1.6^{+0.2}_{-0.2} \times 10^{-4}$ Jy
HD 197481	DPL	vG	12	6.21	34.01	$\alpha_{\rm in}$ = 4.5	$\alpha_{\rm in} = 4.5^{+0.3}_{-0.2}$
	DG	vG	14	3.35	26.87	$\alpha_{\rm out}$ = −12.2	$\alpha_{\rm out} = -12.2^{+1.6}_{-1.9}$
	DPL	vE	13	3.13	14.65	$R_{\rm c}$ = 37.4 au	$R_{\rm c} = 37.2^{+0.6}_{-0.7}$ au
	DG	vE	15	0	23.33	$h_{\rm HWHM}$ = 0.0026	$h_{\rm HWHM} = 0.0028^{+0.0009}_{-0.0002}$
	DPL	**vL**	**12**	**2.49**	**0**	Σ_c = −3.756	$\Sigma_c = -3.711^{+0.045}_{-0.052}$
	DG	vL	14	2.95	24.17	PA= 128.73°	PA= $128.73^{\circ+0.02}_{-0.02}$
	DPL	vDG	14	1.20	15.57	dRA= −0.″019	dRA= $-0.''021^{+0.007}_{-0.007}$
	DG	vDG	16	1.09	36.58	dDec= −0.″012	dDec= $-0.''009^{+0.006}_{-0.005}$
						i = 88.16°	$i = 88.13^{\circ+0.08}_{-0.09}$
						$F_{\star1} = 3.5 \times 10^{-4}$ Jy	$F_{\star1} = 3.5^{+0.2}_{-0.2} \times 10^{-4}$ Jy
						$F_{\star2} = 1.5 \times 10^{-4}$ Jy	$F_{\star2} = 1.5^{+0.3}_{-0.2} \times 10^{-4}$ Jy
						$F_{\star3} = 2.0 \times 10^{-4}$ Jy	$F_{\star3} = 2.0^{+0.2}_{-0.2} \times 10^{-4}$ Jy

Notes. We use the AIC and BIC to identify a fiducial model for each source, shown in bold. We show the ΔAIC value in terms of a confidence level from the best-fit AIC model (the model with ΔAIC= 0), and we show the ΔBIC as a difference from the best-fit BIC model (the model with ΔBIC= 0). The rightmost columns show the best-fit and 50th percentile values for the fiducial models, with errors showing the 16th and 84th percentiles. The surface density normalization factor Σ_c is parametrized as an exponent; the units of 10^{Σ_c} are g cm^{-2}.

Appendix B: `frank` and `rave` vertical inference

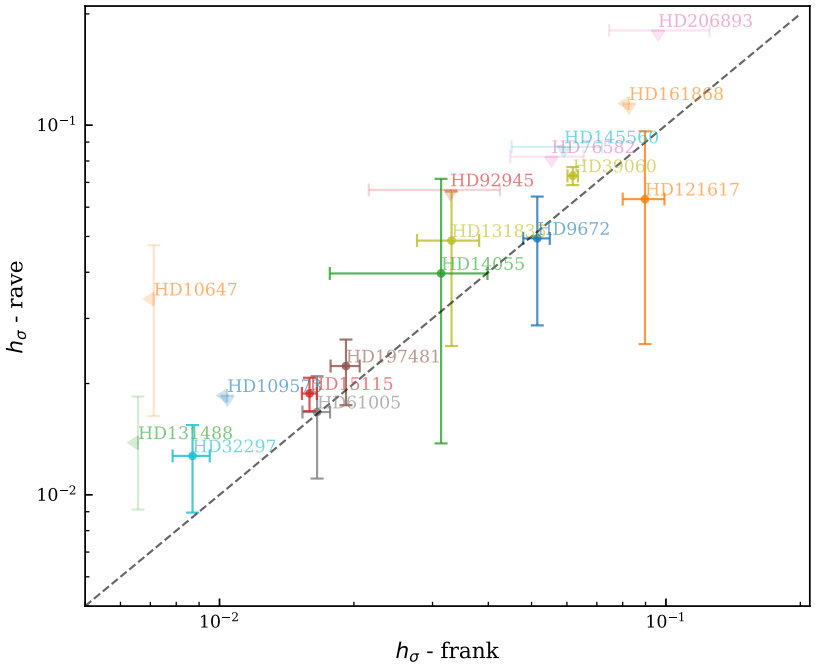

Fig. B.1: Comparison between the scale height aspect ratios h_σ fitted with `frank` and `rave`. Circular points indicate measurements with both methods, while triangles indicate constraints that are only upper limits (leftward and downward triangles for upper limits with `frank` and `rave`, respectively). The dashed line indicates where the fitted values from the two methods are equal.

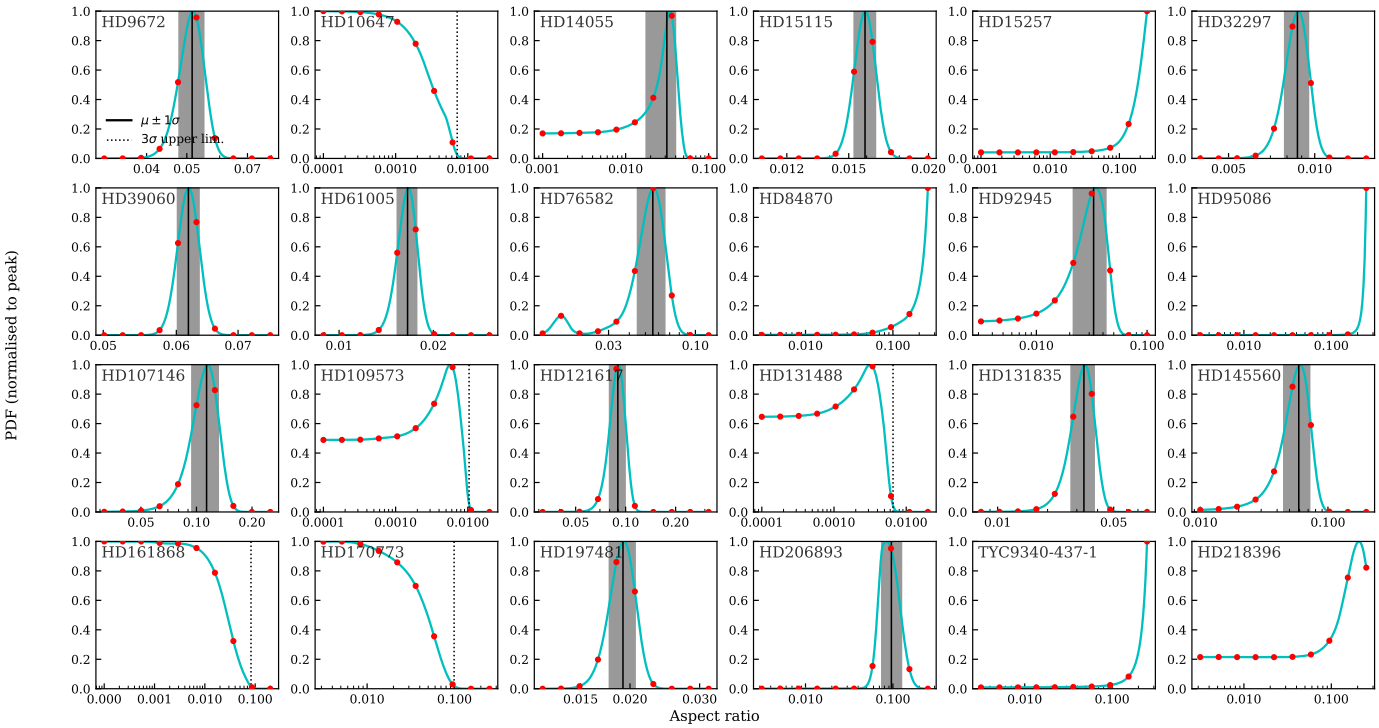

Fig. B.2: Probability density distributions of h_σ fitted with `frank`. The red dots indicate sample points where the `frank` model was fitted and the squared residuals computed, based on which the distribution was interpolated to obtain the cyan lines. The vertical solid black lines and shaded region indicate the median and 1σ uncertainty region for distributions with a clear peak, whereas black dotted lines indicate the 3σ upper limit for disks where only an upper limit can be placed.

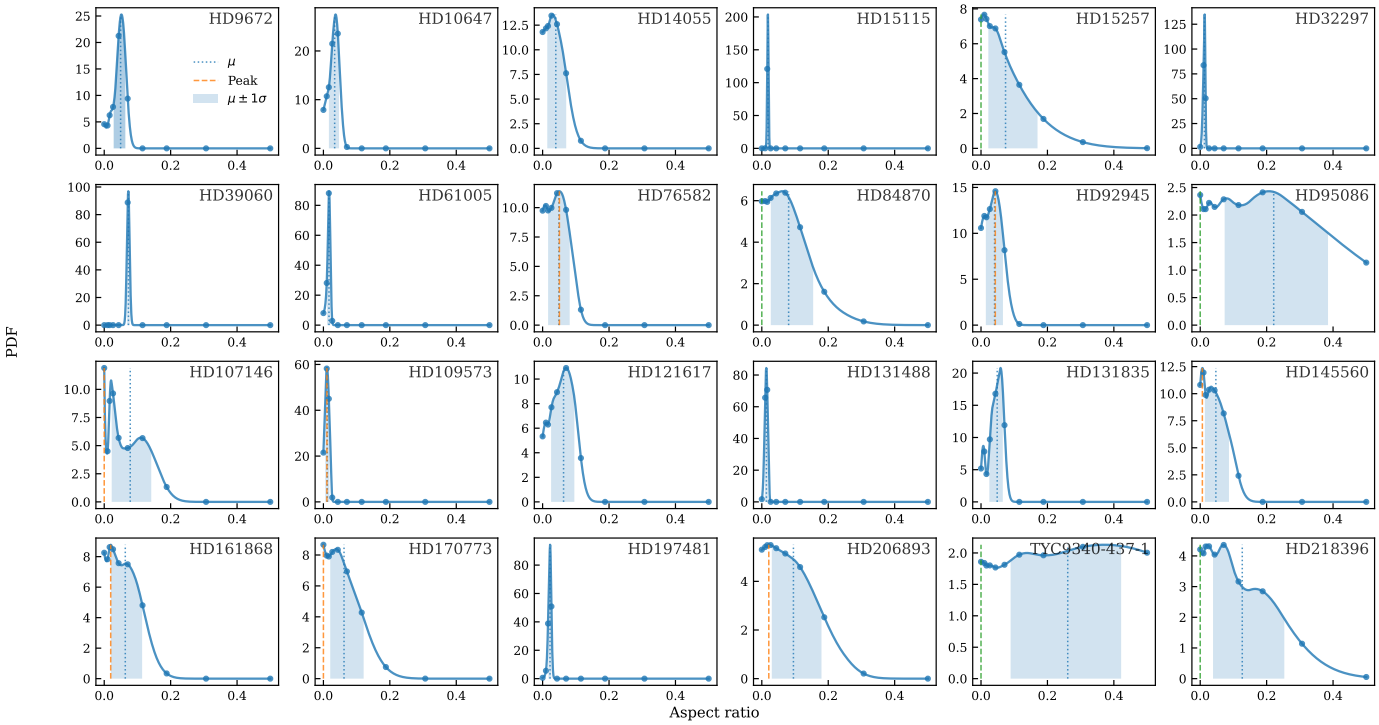

Fig. B.3: Probability density distributions of h_σ fitted with `rave`. The points in each panel indicate sample points where the `rave` model was fitted and the squared residuals computed, based on which the distribution was interpolated. The vertical blue dotted black lines and shaded region indicate the median and 1σ uncertainty region for distribution of each disk. An orange dashed line, when present in a panel, indicates the mode of the distribution, and is used as the height assumption when fitting the final model where only an upper bound can be placed. A green dashed line at h_σ=0, when present in a panel, indicates the height is unconstrained and a flat disk was assumed when fitting the final `rave` model. For all other disks, the median was used to estimate the scale height and fit the final `rave` model.

Appendix C: Summary of new and archival aspect ratio measurements

Table C.1: Compilation of h measurements for each source, along with the resolution and wavelength of the observations used.

Source	h_σ	h_{HWHM}	h_{FWHM}	Resolution (arcsec)	λ (mm)	Reference
HD 9672	0.039 ± 0.007	$\mathbf{0.046 \pm 0.008}$	0.092 ± 0.016	0.16	0.89	This work (parametric)
	$\mathbf{0.051^{+0.004}_{-0.003}}$	$0.060^{+0.005}_{-0.004}$	$0.120^{+0.009}_{-0.007}$	0.16	0.89	This work (`frank`)
	$\mathbf{0.051^{+0.033}_{-0.034}}$	$0.060^{+0.039}_{-0.040}$	$0.120^{+0.078}_{-0.080}$	0.16	0.89	This work (`rave`)
	$\mathbf{0.075 \pm 0.004}$	0.088 ± 0.005	0.177 ± 0.009	0.47	0.614	Delamer (2021)
	$\mathbf{0.050 \pm 0.007}$	0.059 ± 0.008	0.118 ± 0.016	0.47	0.614	Terrill et al. (2023)
	$\mathbf{0.033^{+0.014}_{-0.018}}$	$0.039^{+0.016}_{-0.021}$	$0.078^{+0.033}_{-0.042}$	0.47	0.614	Han et al. (2025)
	$\mathbf{0.069^{+0.005}_{-0.007}}$	$0.081^{+0.006}_{-0.008}$	$0.162^{+0.012}_{-0.016}$	0.5	0.868	Delamer (2021)
	$\mathbf{0.076 \pm 0.009}$	0.089 ± 0.011	0.179 ± 0.021	0.5	0.868	Matrà et al. (2025)
	$\mathbf{0.15 \pm 0.02}$	0.18 ± 0.02	0.35 ± 0.05	0.85	1.32	Delamer (2021)

Table C.1: continued.

Source	h_σ	$h_{\rm HWHM}$	$h_{\rm FWHM}$	Resolution (arcsec)	λ (mm)	Reference
HD 10647	$0.045^{+0.006}_{-0.005}$	$\mathbf{0.053^{+0.006}_{-0.007}}$	$0.106^{+0.014}_{-0.012}$	0.43	0.89	This work (parametric) [a]
	0.191 ± 0.002	$\mathbf{0.225 \pm 0.002}$	0.450 ± 0.004	0.43	0.89	This work (parametric) [b]
	$< \mathbf{0.007}$	< 0.008	< 0.016	0.43	0.89	This work (frank)
	$\mathbf{0.036^{+0.023}_{-0.024}}$	$0.042^{+0.027}_{-0.028}$	$0.085^{+0.054}_{-0.057}$	0.43	0.89	This work (rave)
	$\mathbf{0.048 \pm 0.004}$	$0.057^{+0.005}_{-0.005}$	$0.113^{+0.009}_{-0.009}$	0.5	0.86	Lovell et al. (2021)
	$\mathbf{0.037^{+0.007}_{-0.008}}$	$0.044^{+0.008}_{-0.009}$	$0.087^{+0.016}_{-0.019}$	0.5	0.86	Terrill et al. (2023)
	$\mathbf{0.05 \pm 0.01}$	0.06 ± 0.01	0.12 ± 0.02	1.0	1.26	Matrà et al. (2025)
	$\mathbf{0.046^{+0.009}_{-0.010}}$	$0.054^{+0.011}_{-0.012}$	$0.108^{+0.021}_{-0.024}$	0.5	0.86	Han et al. (2025)
HD 14055	$0.045^{+0.006}_{-0.007}$	$\mathbf{0.053^{+0.007}_{-0.008}}$	$0.106^{+0.014}_{-0.016}$	0.23	0.89	This work (parametric)
	$\mathbf{0.031^{+0.014}_{-0.008}}$	$0.037^{+0.016}_{-0.009}$	$0.073^{+0.033}_{-0.019}$	0.23	0.89	This work (frank)
	$\mathbf{0.040^{+0.026}_{-0.032}}$	$0.047^{+0.031}_{-0.038}$	$0.094^{+0.061}_{-0.075}$	0.23	0.89	This work (rave)
	$< \mathbf{0.10}$	< 0.12	< 0.024	1.85	1.27	Terrill et al. (2023)
	$\mathbf{0.03 \pm 0.02}$	0.04 ± 0.02	0.07 ± 0.05	1.85	1.27	Matrà et al. (2025)
	$\mathbf{0.111^{+0.062}_{-0.064}}$	$0.131^{+0.073}_{-0.075}$	$0.261^{+0.146}_{-0.151}$	1.85	1.27	Han et al. (2025)
HD 15115	$0.019^{+0.002}_{-0.002}$	$\mathbf{0.022 \pm 0.002}$	$0.044^{+0.004}_{-0.004}$	0.12	0.89	This work (parametric)
	$\mathbf{0.016 \pm 0.001}$	0.019 ± 0.001	0.038 ± 0.002	0.12	0.89	This work (frank)
	$\mathbf{0.018^{+0.007}_{-0.005}}$	$0.021^{+0.008}_{-0.006}$	$0.042^{+0.016}_{-0.012}$	0.12	0.89	This work (rave)
	$\mathbf{0.048 \pm 0.007}$	0.057 ± 0.008	$0.113^{+0.016}_{-0.016}$	0.6	1.3	Terrill et al. (2023)
	$\mathbf{0.05^{+0.01}_{-0.02}}$	$0.06^{+0.01}_{-0.02}$	$0.12^{+0.02}_{-0.05}$	0.6	1.3	Matrà et al. (2025)
	$\mathbf{0.067^{+0.030}_{-0.034}}$	$0.079^{+0.035}_{-0.040}$	$0.158^{+0.071}_{-0.080}$	0.6	1.3	Han et al. (2025)
HD 32297	$0.008^{+0.001}_{-0.002}$	$\mathbf{0.009^{+0.002}_{-0.001}}$	$0.018^{+0.002}_{-0.004}$	0.06	0.89	This work (parametric)
	$\mathbf{0.009 \pm 0.001}$	0.011 ± 0.001	0.021 ± 0.002	0.06	0.89	This work (frank)
	$\mathbf{0.012 \pm 0.007}$	0.014 ± 0.008	0.028 ± 0.016	0.06	0.89	This work (rave)
	$\mathbf{0.08 \pm 0.01}$	0.09 ± 0.01	0.19 ± 0.02	0.5	1.34	Terrill et al. (2023)
	$\mathbf{0.015 \pm 0.002}$	0.018 ± 0.002	0.035 ± 0.005	0.5	1.34	Worthen et al. (2024)
	$\mathbf{0.08^{+0.01}_{-0.02}}$	$0.09^{+0.01}_{-0.02}$	$0.19^{+0.02}_{-0.05}$	0.5	1.34	Matrà et al. (2025)
	$\mathbf{0.118^{+035}_{-0.044}}$	$0.139^{+0.041}_{-0.052}$	$0.278^{+0.082}_{-0.104}$	0.5	1.34	Han et al. (2025)
HD 39060	$0.095^{+0.001}_{-0.002}$	$\mathbf{0.112^{+0.002}_{-0.001}}$	$0.224^{+0.002}_{-0.004}$	0.22	1.33	This work (parametric)
	$\mathbf{0.062 \pm 0.002}$	0.073 ± 0.002	0.146 ± 0.005	0.22	1.33	This work (frank)
	$\mathbf{0.073 \pm 0.011}$	0.086 ± 0.013	0.172 ± 0.026	0.22	1.33	This work (rave)
	$\mathbf{0.014 \pm 0.006}$	0.016 ± 0.007	0.033 ± 0.014	0.3	1.33	Matrà et al. (2019) [c]
	$\mathbf{0.110^{+0.008}_{-0.006}}$	$0.130^{+0.009}_{-0.007}$	$0.259^{+0.019}_{-0.014}$	0.3	1.33	Matrà et al. (2019) [d]
HD 61005	$0.013^{+0.002}_{-0.003}$	$\mathbf{0.015^{+0.002}_{-0.003}}$	$0.030^{+0.004}_{-0.006}$	0.15	0.89	This work (parametric)
	$\mathbf{0.017 \pm 0.001}$	0.020 ± 0.001	0.040 ± 0.002	0.15	0.89	This work (frank)
	$\mathbf{0.016 \pm 0.010}$	0.019 ± 0.012	0.038 ± 0.024	0.15	0.89	This work (rave)
	$\mathbf{0.039^{+0.003}_{-0.004}}$	$0.046^{+0.004}_{-0.005}$	$0.092^{+0.007}_{-0.009}$	0.46	1.29	Terrill et al. (2023)
	$\mathbf{0.044^{+0.003}_{-0.004}}$	$0.052^{+0.004}_{-0.005}$	$0.104^{+0.007}_{-0.009}$	0.46	1.29	Matrà et al. (2025)
	$\mathbf{0.029^{+0.007}_{-0.009}}$	$0.034^{+0.008}_{-0.011}$	$0.068^{+0.016}_{-0.021}$	0.46	1.29	Han et al. (2025)
HD 76582	$0.163^{+0.008}_{-0.008}$	$\mathbf{0.192^{+0.010}_{-0.009}}$	$0.384^{+0.020}_{-0.018}$	0.56	0.89	This work (parametric)
	$\mathbf{0.055^{+0.011}_{-0.010}}$	$0.065^{+0.013}_{-0.012}$	$0.130^{+0.026}_{-0.024}$	0.56	0.89	This work (frank)
	$< \mathbf{0.116}$	< 0.137	< 0.273	0.56	0.89	This work (rave)

Table C.1: continued.

Source	h_σ	$h_{\rm HWHM}$	$h_{\rm FWHM}$	Resolution (arcsec)	λ (mm)	Reference
HD 92945	$\mathbf{0.033^{+0.011}_{-0.010}}$	$0.039^{+0.013}_{-0.012}$	$0.078^{+0.026}_{-0.024}$	0.40	0.86	This work (frank)
	$<\mathbf{0.096}$	<0.113	<0.226	0.40	0.86	This work (rave)
HD 107146	$\mathbf{0.113^{+0.019}_{-0.018}}$	$0.133^{+0.022}_{-0.021}$	$0.266^{+0.045}_{-0.042}$	0.59	0.86	This work (frank)
	$<\mathbf{0.184}$	<0.217	<0.433	0.59	1.00 [e]	This work (rave)
HD 109573	<0.0099	$<\mathbf{0.0116}$	<0.0232	0.08	0.89	This work (parametric)
	$<\mathbf{0.010}$	<0.012	<0.024	0.08	0.89	This work (frank)
	$<\mathbf{0.025}$	<0.029	<0.059	0.08	0.89	This work (rave)
	$\mathbf{0.038 \pm 0.005}$	0.045 ± 0.006	0.089 ± 0.012	0.17	0.88	Kennedy et al. (2018)
	$\mathbf{0.052 \pm 0.003}$	0.061 ± 0.004	0.122 ± 0.007	0.17	0.88	Terrill et al. (2023)
	$\mathbf{0.058 \pm 0.002}$	0.068 ± 0.002	0.137 ± 0.005	0.17	0.88	Matrà et al. (2025)
	$\mathbf{0.048^{+0.014}_{-0.019}}$	$0.057^{+0.016}_{-0.022}$	$0.113^{+0.033}_{-0.045}$	0.17	0.88	Han et al. (2025)
HD 121617	$\mathbf{0.090^{+0.010}_{-0.009}}$	$0.106^{+0.012}_{-0.011}$	$0.212^{+0.024}_{-0.021}$	0.12	0.89	This work (frank)
	$\mathbf{0.071^{+0.046}_{-0.049}}$	$0.084^{+0.054}_{-0.058}$	$0.167^{+0.108}_{-0.115}$	0.12	0.89	This work (rave)
HD 131488	$<\mathbf{0.0059}$	<0.0070	<0.014	0.04	0.89	This work (parametric)
	$<\mathbf{0.007}$	<0.008	<0.016	0.04	0.89	This work (frank)
	$\mathbf{0.014 \pm 0.008}$	0.016 ± 0.009	0.033 ± 0.019	0.04	0.89	This work (rave)
	$\mathbf{0.08 \pm 0.04}$	0.09 ± 0.05	0.19 ± 0.09	0.54	1.33	Worthen et al. (2024)
HD 131835	$0.019^{+0.006}_{-0.005}$	$\mathbf{0.022^{+0.007}_{-0.006}}$	$0.044^{+0.014}_{-0.012}$	0.13	0.89	This work (parametric)
	$\mathbf{0.033 \pm 0.005}$	0.039 ± 0.006	0.078 ± 0.012	0.13	0.89	This work (frank)
	$\mathbf{0.049^{+0.032}_{-0.031}}$	$0.058^{+0.038}_{-0.036}$	$0.115^{+0.075}_{-0.073}$	0.13	0.89	This work (rave)
HD 145560	$\mathbf{0.059^{+0.014}_{-0.013}}$	$0.069^{+0.016}_{-0.015}$	$0.139^{+0.033}_{-0.031}$	0.09	0.89	This work (frank)
	$<\mathbf{0.123}$	<0.145	<0.290	0.09	0.89	This work (rave)
HD 161868	$0.163^{+0.010}_{-0.014}$	$\mathbf{0.192^{+0.012}_{-0.016}}$	$0.384^{+0.024}_{-0.032}$	0.52	0.89	This work (parametric)
	$<\mathbf{0.083}$	<0.098	<0.195	0.52	0.89	This work (frank)
	$<\mathbf{0.187}$	<0.220	<0.440	0.52	0.89	This work (rave)
	$\mathbf{0.13^{+0.04}_{-0.05}}$	$0.15^{+0.05}_{-0.06}$	$0.31^{+0.09}_{-0.12}$	1.4	1.27	Matrà et al. (2025)
	$\mathbf{0.15^{+0.03}_{-0.04}}$	$0.18^{+0.04}_{-0.05}$	$0.35^{+0.07}_{-0.09}$	1.4	1.27	Terrill et al. (2023)
	$\mathbf{0.137^{+0.037}_{-0.042}}$	$0.161^{+0.044}_{-0.049}$	$0.323^{+0.087}_{-0.099}$	1.4	1.27	Han et al. (2025)
HD 170773	$<\mathbf{0.099}$	<0.117	<0.233	0.33	0.89	This work (frank)
	$<\mathbf{0.202}$	<0.238	<0.476	0.33	0.89	This work (rave)
HD 197481	$0.0024^{+0.0008}_{-0.0002}$	$\mathbf{0.0028^{+0.0009}_{-0.0002}}$	$0.0056^{+0.0018}_{-0.0004}$	0.35	1.35	This work (parametric)
	$\mathbf{0.019 \pm 0.001}$	0.022 ± 0.001	0.045 ± 0.002	0.35	1.35	This work (frank)
	$\mathbf{0.021 \pm 0.013}$	0.025 ± 0.015	0.049 ± 0.031	0.35	1.35	This work (rave)
	$\mathbf{0.031^{+0.005}_{-0.004}}$	$0.036^{+0.006}_{-0.005}$	$0.073^{+0.012}_{-0.009}$	0.35	1.35	Daley et al. (2019)
	$\mathbf{0.025^{+0.008}_{-0.002}}$	$0.029^{+0.009}_{-0.002}$	$0.059^{+0.019}_{-0.005}$	0.35	1.35	Vizgan et al. (2022)
	$\mathbf{0.017 \pm 0.003}$	0.020 ± 0.004	0.040 ± 0.007	0.35	1.35	Matrà et al. (2025)
	$\mathbf{0.020 \pm 0.002}$	0.024 ± 0.002	0.047 ± 0.005	0.35	1.35	Terrill et al. (2023)
	$\mathbf{0.022 \pm 0.003}$	0.026 ± 0.004	0.052 ± 0.007	0.35	1.35	Han et al. (2025)
	$\mathbf{0.019^{+0.006}_{-0.001}}$	$0.022^{+0.007}_{-0.001}$	$0.045^{+0.014}_{-0.002}$	0.23	0.45	Vizgan et al. (2022)
HD 206893	$\mathbf{0.096^{+0.021}_{-0.029}}$	$0.113^{+0.025}_{-0.034}$	$0.226^{+0.049}_{-0.068}$	0.45	1.35	This work (frank)
	$<\mathbf{0.271}$	<0.319	<0.638	0.45	1.35	This work (rave)

Notes. The originally reported value is shown in bold, while conversions from this value are provided such that h_σ, $h_{\rm HWHM}$, and $h_{\rm FWHM}$ are shown for each source. We note that for some entries, h_σ may not strictly be a standard deviation if a standard deviation is undefined for the method used (e.g., as in the parametric vertical Lorentzian fits shown in this work). For HD 10647, the contributions of the multicomponent fit contain [a] $88 \pm 6\%$ of the mass and [b] $12 \pm 6\%$ of the mass. For HD 39060, the contributions of the multicomponent fit from Matrà et al. (2019) contain [c] $20^{+5}_{-4}\%$ of the mass and [d] $80^{+4}_{-5}\%$ of the mass. [e] The rave analysis of HD 10746 used combined Band 6 and Band 7 observations.

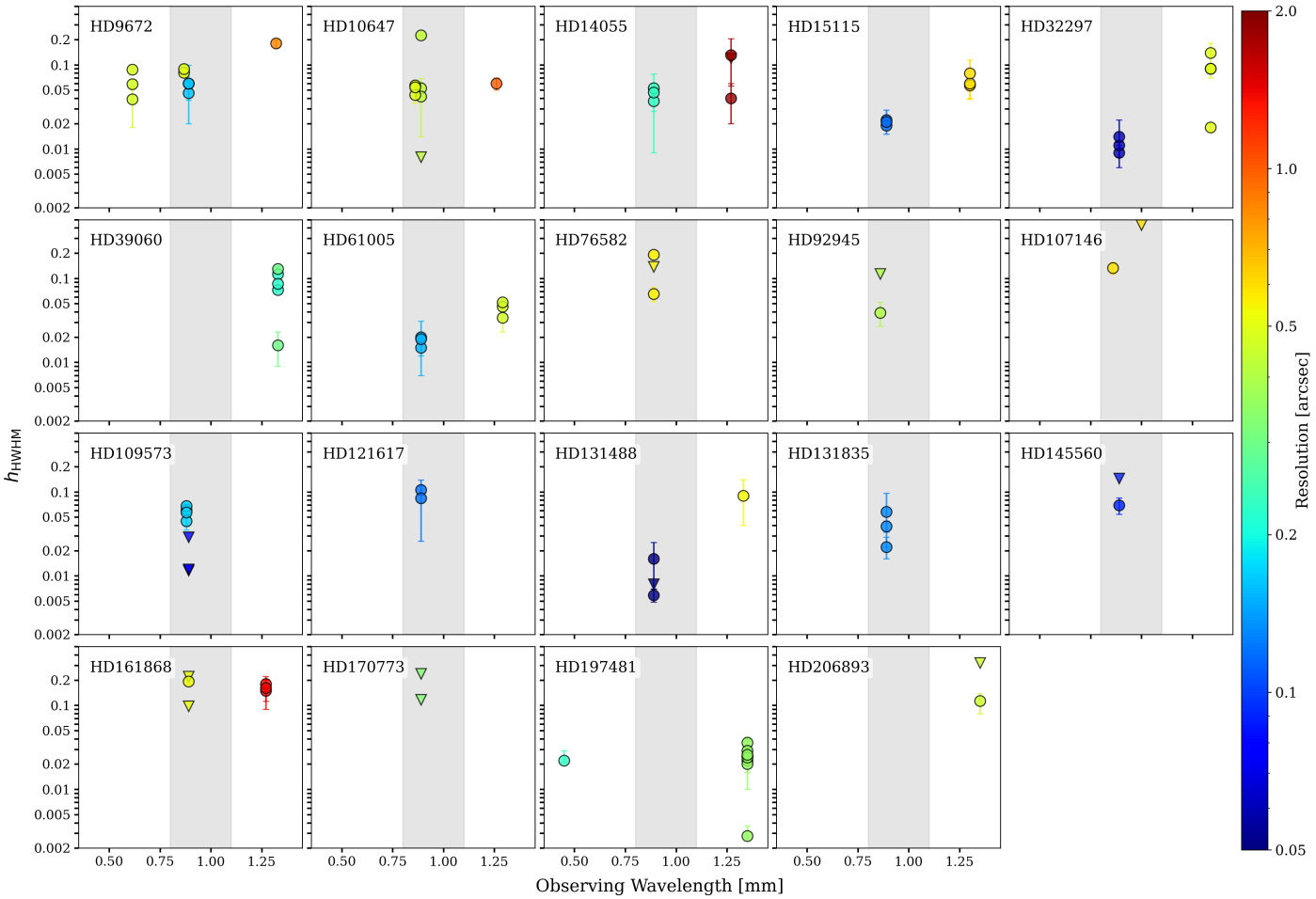

Fig. C.1: All values of h_{HWHM} measured in this work and previous studies (Table C.1) with respect to observing wavelength. The gray shaded region shows the wavelength range of ALMA Band 7. The color bar shows the angular resolution of the observations used for each measurement. Triangular points indicate measurements which are upper limits, while circular points show the upper and lower 1σ uncertainties associated with the measurement.

Appendix D: Comparison of disk mass estimates

Table D.1: Comparison of disk mass estimates from Pan & Schlichting (2012) (1) and K21 (2), as well as the assumed millimeter dust masses M_{mm} used in each of these models.

Target	M_{disk} $[M_\oplus]$ (1)	$M_{\mathrm{disk}}^{\mathrm{min}}$ $[M_\oplus]$ (2)	M_{mm} $[M_\oplus]$ (1)	M_{mm} $[M_\oplus]$ (2)	Rescaled $M_{\mathrm{disk}}^{\mathrm{min}}$ $[M_\oplus]$	Compatible?
HD 9672	86.6	14.3	4.95×10^{-1}	2.8×10^{-1}	25.3	yes
HD 15115	3.72	7.0	6.17×10^{-3}	8.5×10^{-2}	0.51	yes, rescaled
HD 39060	104	5.5	1.83×10^{-1}	7.9×10^{-2}	12.7	yes
HD 61005	10.2	14.2	1.26×10^{-1}	1.3×10^{-1}	13.8	no
HD 131488	9.01	85.8	2.75×10^{-1}	7.2×10^{-1}	32.8	no
HD 131835	49.7	39.1	4.08×10^{-1}	3.8×10^{-1}	42.0	yes
HD 197481	0.830	1.8	1.49×10^{-2}	1.4×10^{-2}	1.92	no

Notes. We rescale the originally reported $M_{\mathrm{disk}}^{\mathrm{min}}$ to use the M_{mm} obtained from our fiducial models. The rescaled $M_{\mathrm{disk}}^{\mathrm{min}}$ are compatible with the M_{disk} obtained from the Pan & Schlichting (2012) model for HD 9672, HD 15115, HD 39060, and HD 131835, and incompatible for HD 61005, HD 131488, and HD 197481. These discrepancies may stem from differences in model assumptions (see Sect. 5.2). For the Pan & Schlichting (2012) model, difficulties constraining the scale height aspect ratio (which sets model parameter $\langle v_{\mathrm{rel}} \rangle$) may also contribute, particularly for HD 131488 and HD 197481 which are both noted to have h measurements limited by the resolution of the observations.

A&A, 705, A196 (2026)
https://doi.org/10.1051/0004-6361/202556450
© The Authors 2026

Astronomy & Astrophysics

The ALMA survey to Resolve exoKuiper belt Substructures (ARKS)

II. The radial structure of debris discs

Yinuo Han[1,⋆], Elias Mansell[2], Jeff Jennings[3], Sebastian Marino[4], A. Meredith Hughes[2], Brianna Zawadzki[2], Anna Fehr[5], Jamar Kittling[2], Catherine Hou[2], Aliya Nurmohamed[2], Junu Lee[2], Allan Cheruiyot[2], Yamani Mpofu[2], Mark Booth[6], Richard Booth[7], Myriam Bonduelle[8], Aoife Brennan[9], Carlos del Burgo[10,11], John M. Carpenter[12], Gianni Cataldi[13,14], Eugene Chiang[15], Steve Ertel[16,17], Thomas Henning[18], Marija R. Jankovic[19], Ágnes Kóspál[20,21,18], Alexander V. Krivov[22], Joshua B. Lovell[5], Patricia Luppe[9], Meredith A. MacGregor[23], Sorcha Mac Manamon[9], Jonathan P. Marshall[24], Luca Matrà[9], Julien Milli[8], Attila Moór[20], Johan Olofsson[25], Tim Pearce[26], Sebastián Pérez[27,28,29], Antranik A. Sefilian[16], Philipp Weber[27,28,29], David J. Wilner[5], and Mark C. Wyatt[30]

(Affiliations can be found after the references)

Received 16 July 2025 / Accepted 28 October 2025

ABSTRACT

Context. Debris discs are populated by belts of planetesimals, whose structure carries dynamical imprints of planets and the formation and evolutionary history of the planetary system. The relatively faint emission of debris discs has previously made it challenging to obtain a large sample of high-resolution ALMA images to characterise their substructures.
Aims. The ALMA survey to Resolve exoKuiper belt Substructures (ARKS) was recently completed to cover the lack of high-resolution observations and to investigate the prevalence of substructures such as radial gaps and rings in a sample of 24 debris discs. This study characterises the radial structure of debris discs in the ARKS programme.
Methods. We modelled all discs with a range of non-parametric and parametric approaches, including those that deconvolve and deproject the image or fit the visibilities directly, in order to identify and quantify the disc substructures.
Results. Across the sample we find that of the 24 discs, 5 host multiple rings, 7 are single rings that display halos or additional low-amplitude rings, and 12 are single rings with at most tentative evidence of additional substructures. The fractional ring widths that we measured are significantly narrower than previously derived values, and they follow a distribution similar to the fractional widths of individual rings resolved in protoplanetary discs. However, there exists a population of rings in debris discs that are significantly wider than those in protoplanetary discs. We also find that discs with steep inner edges consistent with planet sculpting tend to be found at smaller (<100 au) radii, while more radially extended discs tend to have shallower edges more consistent with collisional evolution. An overwhelming majority of discs have radial profiles that are well-described by either a double power law or double-Gaussian parametrisation.
Conclusions. While our findings suggest that it may be possible for some debris discs to inherit their structures directly from protoplanetary discs, there exists a sizeable population of broad debris discs that cannot be explained in this way. Assuming that the distribution of millimetre dust reflects the distribution of planetesimals, mechanisms that cause rings in protoplanetary discs to migrate or debris discs to broaden soon after formation may be at play, possibly mediated by planetary migration or scattering.

Key words. methods: data analysis – planets and satellites: dynamical evolution and stability – planets and satellites: formation – planets and satellites: general – protoplanetary disks – planet-disk interactions

1. Introduction

Planetesimal belts analogous to the Solar System's Edgeworth-Kuiper belt provided some of the earliest hints of the presence of extrasolar planetary systems, which manifest as an infrared excess in the spectral energy distribution (SED) of main-sequence stars (Aumann et al. 1984; Harper et al. 1984). Subsequent decades of imaging campaigns have spatially resolved these belts from optical (e.g. GPIES, Crotts et al. 2024) to far-infrared (e.g. DEBRIS, Matthews et al. 2010; DUNES, Eiroa et al. 2013; Montesinos et al. 2016; Moór et al. 2015; Marshall et al. 2021) and (sub)millimetre (e.g. SONS, Holland et al. 2017; REASONS, Matrà et al. 2025) wavelengths, progressively achieving higher resolution that has revealed their morphology. In a handful of systems observed with sufficiently high resolution and sensitivity, substructures such as radial gaps (Marino et al. 2018, 2019, 2020; MacGregor et al. 2019; Nederlander et al. 2021), azimuthal asymmetries (Dent et al. 2014; MacGregor et al. 2017), and various vertical profiles (Kennedy et al. 2018; Matrà et al. 2019; Daley et al. 2019; Vizgan et al. 2022; Terrill et al. 2023) have been identified. These substructures could be caused by planets possibly residing in these discs, interacting with the planetesimals and the dust, and/or they could be an outcome of planetesimal formation processes, possibly linked with substructures commonly observed in protoplanetary discs (Bae et al. 2023).

The ALMA survey to Resolve exoKuiper belt Substructures (ARKS) is the most recent campaign in this effort to obtain a

⋆ Corresponding author: yinuo@caltech.edu

Open Access article, published by EDP Sciences, under the terms of the Creative Commons Attribution License (https://creativecommons.org/licenses/by/4.0), which permits unrestricted use, distribution, and reproduction in any medium, provided the original work is properly cited.
This article is published in open access under the Subscribe to Open model. Subscribe to A&A to support open access publication.

sample of high-resolution thermal emission images of debris discs and investigate the prevalence of substructures (Marino et al. 2026). This is the only ALMA large programme targeting debris discs, with targets selected from the sample of all ALMA- and SMA-resolved debris discs known as the REASONS sample (Matrà et al. 2025).

The term debris discs loosely refers to the collection of Kuiper belt, asteroid belt, and zodiacal dust analogues in a planetary system (Wyatt 2008; Hughes et al. 2018). In the context of this study, we use the term to refer specifically to analogues of the Kuiper belt at 10s to 100s of au, which extend over a large enough angular size for their detailed structure to be imaged. While substructures have been identified in debris discs at other observing wavelengths, ALMA observations are unique in imaging the distribution of millimetre-sized dust, which is thought to most closely trace the distribution of planetesimals, as smaller dust grains observed at shorter wavelengths are more significantly subject to radiative forces (Wyatt 2008; Krivov 2010; Hughes et al. 2018; Pawellek et al. 2019). This high-resolution ALMA survey is, therefore, well-suited for studying the detailed substructures of planetesimal belts, their dynamical interactions with planets in the system, and any structural similarities and differences with protoplanetary discs during the earlier phases of planet formation. This paper focuses on the radial structure of debris discs in the ARKS programme.

Perhaps the Solar System provides the most compelling examples of how the radial disc structure reflects the architecture and dynamical history of the planetary system. The Kuiper belt is known to host an extended scattered disc component that has been linked to the past migration of (Brown 2001; Morbidelli et al. 2004). Furthermore, a wide radial gap lies between the Kuiper belt and asteroid belt, within which the four giant planets of the Solar System reside. Even within the asteroid belt are a series of Kirkwood gaps, which are cleared by orbital resonances with Jupiter and Saturn (Wisdom 1983; Morbidelli & Henrard 1991).

Similar disc features have also been observed and modelled in extrasolar systems. The location and sharpness of the belt's edges could constrain the presence and migration history of planets, as an inner edge with a shallow slope is expected for debris discs evolving under steady-state collisions alone (Wyatt et al. 2007b; Löhne et al. 2008; Geiler & Krivov 2017; Imaz Blanco et al. 2023), whereas as a steeper slope is expected if a planet truncates the inner edge (Quillen 2006; Chiang et al. 2009; Mustill & Wyatt 2012; Rodigas et al. 2014; Marino 2021; Imaz Blanco et al. 2023; Pearce et al. 2024). Similarly, the outer edge of debris discs could record dynamical events such as the scattering of planetesimals possibly due to migrating planets (e.g. HR 8799, Geiler et al. 2019, and q^1 Eri, Lovell et al. 2021), whereas any azimuthal asymmetries could yield further constraints on planet migration (Wyatt 2003; Booth et al. 2023). For discs with sufficiently well-constrained radial profiles, it may be possible to retrieve the semi-major axis and eccentricity distributions of planetesimals within the belt (Rafikov 2023), which closely reflect the dynamical state of the system and any potential perturbing planets (Quillen 2006; Chiang et al. 2009; Faramaz et al. 2014; Pearce & Wyatt 2014; Kennedy 2020), as well as the disc's total mass (Sefilian 2024). Furthermore, radial gaps have been observed in debris discs (Marino et al. 2018, 2019, 2020) and used to infer the presence of <1 Jupiter mass planets at tens of au. These gaps could be carved by planets embedded within the disc (Faber & Quillen 2007; Shannon et al. 2016; Morrison & Kratter 2018; Friebe et al. 2022) or orbiting interior to its inner edge (Pearce & Wyatt 2015; Yelverton et al. 2019; Sefilian et al. 2021, 2023).

In addition to the link between disc structure and planetary architecture, we also consider the evolution of planetary systems from the few million-year-old protoplanetary discs to the more evolved debris disc phase (>10 Myr). The higher dust continuum luminosity of protoplanetary discs has enabled a number of ALMA programmes to map their detailed structure in dozens of systems (Bae et al. 2023). These observations have found that protoplanetary discs with multiple concentric rings appear to be common (Andrews et al. 2018; Huang et al. 2018; Long et al. 2018). Out of 479 young stellar objects surveyed in nearby star-forming regions, 355 discs have been detected and 62 have clearly identified ring-like structures, of which approximately half display multiple rings (Bae et al. 2023). However, debris discs known to unambiguously host multiple rings are comparatively few in number, and typical fractional widths (i.e. FWHM of a debris disc ring divided by its radius, or $\Delta R/R_c$) measured from available ALMA observations appear to be larger than in protoplanetary discs (Matrà et al. 2025). Prior to the ARKS programme, there were no debris disc surveys with comparable resolution and sample size to those targeting protoplanetary discs, so it was unclear whether the difference is real or due to limitations in the resolution and sensitivity of debris disc observations. Such a comparison of disc fractional widths is nonetheless important. If debris discs directly inherit the structure of protoplanetary rings, their radial distribution should be consistent if we are detecting systems of the same population and offset only in age (Najita et al. 2022; Orcajo et al. 2025). However, there could also exist mechanisms that broaden debris disc rings, such as debris self-scattering (Ida & Makino 1993) or the migration of planetesimal-forming dust traps in protoplanetary discs, which could form wider planetesimal belts than would be formed outside a non-migrating planet (Miller et al. 2021; Jiang & Ormel 2023).

The ARKS programme attempts to shed light on these questions. In this ARKS paper, we describe our modelling approach in Sect. 2, and show the deconvolved and deprojected radial profiles of the dust continuum emission in Sect. 3. The implications of these findings on our general understanding of debris disc structure are discussed in Sect. 4. Our findings are summarised in Sect. 5. Some further technical details are provided in Appendices A–H.

2. Extracting radial profiles

The primary quantity that we aim to determine in this section is the radial profile of the dust continuum emission for all discs in the ARKS programme. The reduced and corrected dataset and the `CLEAN` images of all discs are described and displayed in Marino et al. (2026), which include 18 discs with new observations and 6 with archival observations that meet the sensitivity and resolution requirements of the programme. The targets were selected to cover discs over a range of inclinations, and observations were designed to resolve gaps carved by Neptune-sized planets for face-on discs and to resolve the vertical height for edge-on discs (Marino et al. 2026).

Radial surface brightness profiles can be directly extracted from clean images by deprojecting and azimuthally averaging the emission (e.g. Marino et al. 2016). However, these beam-convolved profiles are limited by the beam size and do not perform well for highly inclined belts. Fortunately, there are

parametric and non-parametric methods that can circumvent these issues and robustly infer the deprojected and deconvolved radial profiles. This radial profile recovery can be performed either by modelling the visibilities measured by ALMA directly, or by going to image space and modelling reconstructed images. Both are non-trivial, as the source distribution is convolved with the beam (with the dirty beam taking a non-Gaussian form), and the radial distribution is partly degenerate with the vertical structure when the disc is not perfectly face-on. To obtain a radial brightness profile, non-parametric and parametric methods each have pros and cons. Non-parametric methods such as those in Jennings et al. (2020) and Han et al. (2022) avoid the risk of biasing a fitted profile towards specific shapes parametrised by certain functions, allowing them to more easily fit the observed visibilities accurately and identify features not obvious by eye from a `CLEAN` image. However, their lack of enforcement of a functional form (such as a Gaussian or power law radial profile) can give rise to erroneous features (such as oscillations in the fitted profile) in the absence of sufficient regularisation. To mitigate this, the balance between resolution and noise in the fitted profile can be tuned by varying hyperparameters specific to each method. Parametric methods provide a more direct quantification of specific features in the radial profile by allowing us to comparing different functional forms to theoretical models of debris disc evolution. Parametric models also typically allow for easier marginalisation over physical parameters like the system orientation and stellar flux.

In addition to deriving radial brightness profiles from `CLEAN` images, we applied both non-parametric and parametric approaches to recover deconvolved and deprojected radial profiles across the ARKS sample. We fit each source with:

(1) `frank` (Jennings et al. 2020; Terrill et al. 2023), a non-parametric method which operates in visibility space;

(2) `rave` (Han et al. 2022, 2025), a non-parametric method which operates in image space; and

(3) parametric models in visibility space, motivated by the shape of the non-parametric brightness profiles as well as theoretical predictions of debris disc structure.

Each of these methods enables radial profile recovery under the assumption of azimuthal symmetry, even if the disc is perfectly edge-on (due to the low optical depth of the discs in the sample). Together, they provide an informal type of verification to more reliably identify and quantify disc substructures. The assumption of azimuthal symmetry here is appropriate for the purpose of extracting the radial profile as any asymmetries of discs in the sample are generally subtle. Details on any asymmetries across the sample are analysed in an accompanying paper (Lovell et al. 2026). We describe the `CLEAN` profile extraction and the modelling approaches used in this study in the following sections. The resulting profiles are available for download from the Harvard Dataverse repository at `dataverse.harvard.edu/dataverse/arkslp` and the ARKS website at `arkslp.org`.

2.1. Extracting `CLEAN` profiles

We extracted deprojected radial profiles directly from the primary beam corrected `CLEAN` images by azimuthally averaging the emission (as in Marino et al. 2016). This was performed by drawing a set of ellipses with the same orientation as the discs and different semi-major axes (Marino et al. 2026). For sufficiently inclined belts, we additionally masked sectors of the disc near their minor axes where the deprojected beam is ≥30% the original beam major axis, as including these regions would artificially smooth the azimuthally averaged profile. The uncertainty was estimated as the square root of the average variance divided by the number of independent points being averaged. The latter was estimated from the length of the arcs being averaged divided by the beam major axis. We note that this method does not work for edge-on discs where the minor axis is not well resolved.

2.2. Non-parametric modelling: `frank`

The `frank` code recovers the deprojected and deconvolved radial profile of discs from ALMA visibilities under the assumption of axisymmetry by modelling the real component of the visibilities in 1D with a Fourier-Bessel series regularised by a fast Gaussian process (Jennings et al. 2020). Originally developed to model protoplanetary disc observations (Jennings et al. 2022a,b), the method has been adapted to model optically thin discs, such as debris discs, while also constraining the vertical aspect ratio (Terrill et al. 2023). Further adaptations of the method to fit the surface brightness in logarithmic space reduce oscillatory artefacts and prevent negative surface brightnesses from arising in the fitted profile[1] (Miley et al. 2024), which improves the quality of the fit over previous versions.

We adopted the updated `frank` method to fit all discs, which can be run specifically for the ARKS sample via the pipeline, `arksia`[2] (Jennings et al. 2024). The position angle, inclination and centering offset of the discs were assumed to be those fitted in Marino et al. (2026) for consistency. Before the radial profiles were fitted, stellar flux values (or, to be precise, emission of any unresolved central component) were subtracted from the real component of the visibilities as a constant offset in amplitude; these values were assumed to be those fitted in Marino et al. (2026) if they were well-constrained, or equal to the stellar flux fitted from the SED otherwise. We note that while the stellar flux value for HD 32297 was fitted in Marino et al. (2026), it is potentially overestimated. The fitted stellar flux for HD 32297 is consistent with 0 at 2σ, so we reverted to the SED flux value instead. For HD 109573, we found that the uncertainties of the radial profile better converged near the star when assuming no stellar emission detected, so we conservatively did not subtract any stellar flux before fitting the radial profile.

To fit the radial profile of each source, two hyperparameters were varied: α and $w_{\rm smooth}$. α sets the minimum signal-to-noise ratio (S/N) down to which `frank` attempts to fit the visibilities. $w_{\rm smooth}$ determines the amount of smoothing applied to the reconstructed power spectrum. We performed fits over a few sets of α and $w_{\rm smooth}$ values for each system, choosing the best values according to two criteria: the radial brightness profile should capture structural detail in the disc without introducing obvious oscillatory artefacts (a sign of over-fitting), and the reconstructed power spectrum should reasonably reproduce that from the observations without over-fitting to baselines that are undersampled and carry high uncertainty. Discriminating between oscillatory artefacts and real, narrow structures is not always trivial because the observed visibility distributions do not constrain structure in the radial brightness profile below some minimum spatial scale; across sources, we chose more conservative values of α and $w_{\rm smooth}$ such that the observed visibilities were accurately modelled by `frank` down to a S/N of ≈2. Two additional hyperparameters, the number of points in radius in a fit N and an outer radius $R_{\rm out}$ beyond which the brightness

[1] `https://github.com/discsim/frank`
[2] `https://github.com/jeffjennings/arksia`

is treated as 0, were chosen for each source to ensure the full radial extent of disc emission was modelled over a dense grid. Table G.1 summarises the most appropriate hyperparameters selected to model each disc.

We note a few caveats related to the `frank` fits. Firstly, `frank` does not account for the effect of the primary beam, which could bias the profiles of large discs (>5–10 arcsec) to lower surface brightnesses in their outer regions. However, comparison with other modelling methods used in this study shows that this effect is insignificant. Secondly, uncertainties on the `frank` radial profiles are estimated using the diagonal entries of the covariance matrix of the Gaussian process model evaluated using the best-fit power spectrum (Jennings et al. 2020), which is likely an underestimate of the true uncertainties. Finally, the updated `frank` code that significantly reduces artefacts by fitting the surface brightness in logarithmic space is only optimised for a scale height of 0 ($h = 0$). We find that for the range of scale heights measured in this sample (Zawadzki et al. 2026), the scale height assumption used when fitting the disc does not have a significant effect on the fitted radial profile. Considering that the reduction of oscillatory artefacts and avoidance of negative surface brightness values outweighs the potential inaccuracies of performing the fits under the assumption that the disc is thin, we proceeded with the updated version of `frank` assuming $h = 0$. The `frank` method can nonetheless be applied to constrain the vertical aspect ratio of discs, the details of which are described in Zawadzki et al. (2026).

2.3. Non-parametric modelling: `rave`

`rave` recovers the radial profile of a disc by fitting models of concentric annuli to its image, solving for the brightness required of each annulus to reproduce the image (Han et al. 2022). To mitigate the dependence of the fitted profile on the placement of annuli boundaries, the fit is repeated 100 times, each time with a different partitioning of annuli boundaries, which are chosen in a Monte Carlo fashion. The degree of scatter between the radial profiles fitted in each iteration was used to estimate the uncertainties on the radial profile (Han et al. 2022).

Designed to be compatible with observations over a range of wavelengths and imaging modes, `rave` works in image space and takes the `CLEAN` image as input when fitting to the ARKS sample. The values of the robust parameters used to generate the `CLEAN` images that are used by `rave` are listed in Table G.1. Similar to `frank`, stellar emission was subtracted from the `CLEAN` images before the radial profiles were fitted. The stellar flux values were assumed to be those fitted in Marino et al. (2026) if they were well-constrained, or the SED-fitted stellar flux otherwise.

Two versions of `rave`, optimised for edge-on (Han et al. 2022) and non-edge-on (Han et al. 2025) discs, respectively, are available. The former fits directly to the flux profile obtained by summing the image onto the major axis, which more effectively recovers the radial profile when the central cavity of the disc is not resolved, whereas the latter fits to the azimuthally averaged profile of the image, which is more suitable otherwise. Following the approach in Han et al. (2025), we applied the edge-on version to the only three highly inclined discs in the sample that do not have a resolved central cavity (HD 39060/β Pic, HD 197481/AU Mic and HD 32297). For the other discs, the non-edge-on optimisation was used. To confirm the validity of this choice, we fitted the edge-on discs with the non-edge-on version, and vice versa. Inspection of all discs fitted with both methods confirms that this choice of method produced lower uncertainties and oscillatory artefacts, and only the radials profiles fitted by the more appropriate method is used for the rest of the analysis in this paper.

`rave` requires disc images to be appropriately centred and rotated with a measured (or assumed) inclination for the appropriate model annuli to be simulated. We assumed the same position angle, centring offset and inclination as those fitted in Marino et al. (2026). Given a radial range over which disc emission is detected, the only hyperparameter of `rave` which determines the fitted radial profile was then the number of annuli used to fit the disc, N. We experimented with a range of N, choosing the maximum value of N that does not generate significant oscillatory artefacts in the fitted profile, beyond which the uncertainties on the radial profile increase, and which generally results in the average annuli being wider than half the beam size. The values of N used in the best-fit profiles are displayed in Table G.1.

We note a few caveats relating to the `rave` fits. Firstly, unlike `frank`, the `rave` fits account for the effect of the primary beam by fitting to the primary beam-corrected `CLEAN` images. Secondly, the `rave` fit depends on the `CLEAN` image. Empirically, the dependence of the fitted profile on the choice of the visibility weighting used to produce the `CLEAN` image is found to be low for reasonable robust parameter values. This is confirmed by experimenting with multiple `CLEAN` images with different robust parameters, since `rave` bins the image into discrete annuli that effectively smooths over resolution elements in the `CLEAN` image. Finally, unlike the `frank` radial profiles which were fitted assuming $h = 0$, the `rave` profiles presented here were fitted using the best-fit scale height aspect ratio derived with `rave`. Details of the scale height fitting procedure with `rave` are described in Zawadzki et al. (2026), in which Table 3 lists the best-fit aspect ratios. To briefly summarise, the likelihood of a given aspect ratio is assessed by fitting the radial profile assuming that scale height and computing the squared residuals, and the squared residuals across a range of aspect ratio values were assessed to find the best-fit aspect ratio.

2.4. Parametric models

2.4.1. Modelling code

We parametrically modelled radial structures in the continuum emission of our targets with the debris disc modelling code adapted by Fehr (2023). This approach complements our non-parametric models by allowing us to directly compare results to theoretical predictions and calculate the significance of substructures. We provide a brief overview of the radial aspects of the parametric modelling code in this section, which is described more fully by the companion paper Zawadzki et al. (2026).

The parametric modelling code creates a temperature profile and mass opacity for each disc, assuming that the dust emission is in blackbody equilibrium with the stellar emission. The code then employs the affine-invariant Markov chain Monte Carlo (MCMC) implementation in `emcee` (Foreman-Mackey et al. 2013) to fit vertical and radial surface density profiles, obtaining values for the physical parameters. These parameters are used to create a model image of the dust structure from the temperature and surface density profiles. The resulting parametric disc model is inclined and rotated based on free parameters and transformed into a two-dimensional sky-plane projection that, like `frank` and `rave` models, is axisymmetric. We use Galario (Tazzari et al. 2018) to convert the model image into synthetic visibilities

Table 1. Definitions of functional forms for radial parametric modelling.

Function	Surface density profile	Parameters
Double power law	$\Sigma(r) = \left[\left(\frac{r}{R_c}\right)^{-\alpha_{in}\gamma} + \left(\frac{r}{R_c}\right)^{-\alpha_{out}\gamma}\right]^{-1/\gamma}$	$R_c, \alpha_{in}, \alpha_{out}, \gamma = 2$
Triple power law	$\Sigma(r) = \left(\frac{R_{in}}{R_{out}}\right)^{-\alpha_{mid}} \left[\left(\frac{r}{R_{in}}\right)^{-\alpha_{in}\gamma_{in}} + \left(\frac{r}{R_{in}}\right)^{-\alpha_{mid}\gamma_{in}}\right]^{-1/\gamma_{in}} \times \left[\left(\frac{r}{R_{out}}\right)^{-\alpha_{mid}\gamma_{out}} + \left(\frac{r}{R_{out}}\right)^{-\alpha_{out}\gamma_{out}}\right]^{-1/\gamma_{out}}$	$R_{in}, R_{out}, \alpha_{in}, \alpha_{mid}, \alpha_{out}, \gamma_{in} = 2, \gamma_{out} = 2$
Power law + error function	$\Sigma(r) = \left[1 - \mathrm{erf}\left(\frac{R_c - r}{\sqrt{2}\sigma_{in}R_c}\right)\right]\left(\frac{r}{R_c}\right)^{-\alpha_{out}}$	$R_c, \sigma_{in}, \alpha_{out}$
Gaussian	$\Sigma(r) = \exp\left[-\frac{(r-R)^2}{2\sigma^2}\right]$	R, σ
Asymmetric Gaussian	$\Sigma(r) = \begin{cases} \exp\left[-\frac{(r-R_c)^2}{2\sigma_{in}^2}\right] & \text{if } r < R_c \\ \exp\left[-\frac{(r-R_c)^2}{2\sigma_{out}^2}\right] & \text{if } r \geq R_c \end{cases}$	$R_c, \sigma_{in}, \sigma_{out}$
Double Gaussian	$\Sigma(r) = C \times \exp\left[-\frac{(r-R_1)^2}{2\sigma_1^2}\right] + (1-C) \times \exp\left[-\frac{(r-R_2)^2}{2\sigma_2^2}\right]$	$R_1, R_2, \sigma_1, \sigma_2, C$
Triple Gaussian	$\Sigma(r) = C_1 \times \exp\left[-\frac{(r-R_1)^2}{2\sigma_1^2}\right] + C_2 \times \exp\left[-\frac{(r-R_2)^2}{2\sigma_2^2}\right] + (1-C_1-C_2) \times \exp\left[-\frac{(r-R_3)^2}{2\sigma_3^2}\right]$	$R_1, R_2, R_3, \sigma_1, \sigma_2, \sigma_3, C_1, C_2$
Gaussian + double power law	$\Sigma(r) = C_1 \times \exp\left[-\frac{(r-R)^2}{2\sigma^2}\right] + (1-C_1) \times \left[\left(\frac{r}{R_c}\right)^{-\alpha_{in}\gamma} + \left(\frac{r}{R_c}\right)^{-\alpha_{out}\gamma}\right]^{-1/\gamma}$	$R, \sigma, C_1, R_c, \alpha_{in}, \alpha_{out}, \gamma = 2$

Notes. All surface density profiles are multiplied by 10^{Σ_c}, the surface density normalisation. We fixed certain parameters at the values noted here to minimise degeneracies; exceptions for specific targets are stated explicitly.

sampled at the same antenna separations and orientations as the data. Then, we calculate a χ^2 metric by comparing the synthetic visibilities with observed visibilities at each MCMC step.

2.4.2. Radial profiles

We fit the radial surface density profile to a variety of functional forms – consisting of combinations of Gaussians, power laws, and error functions – implemented in the parametric modelling code. These functional forms are defined in Table 1 and visualised in Fig. 1.

We initially fit each disc with a double power law and with two independent Gaussians (hereafter referred to as a "double Gaussian"), as justified by theoretical models and further supported by the non-parametric results. Power laws allow us to measure the steepness of the inner and outer edges – which are important parameters in models of debris disc structure – while minimising the number of free parameters (e.g. Marino et al. 2019; MacGregor et al. 2019). Although Gaussians cannot always reproduce the inner and outer slopes of debris discs, these functions are simple and effective at measuring fractional widths, and are commonly used in the literature (e.g. Marino et al. 2016; White et al. 2017; Matrà et al. 2025).

The results of the non-parametric models motivated our choice of additional functional forms. Asymmetric Gaussians and power law + error functions were used to model discs without obvious substructures, while possible gaps were modelled through two approaches. We either modelled the rings with two or three Gaussians, or we modelled any gap by subtracting a Gaussian (G, with amplitude C) from the best-fitting functional form (Σ_0) as $\Sigma(r) = \Sigma_0(r) - C \times G(r)$. When we parametrised a gap, we assumed a Gaussian distribution because it modelled the

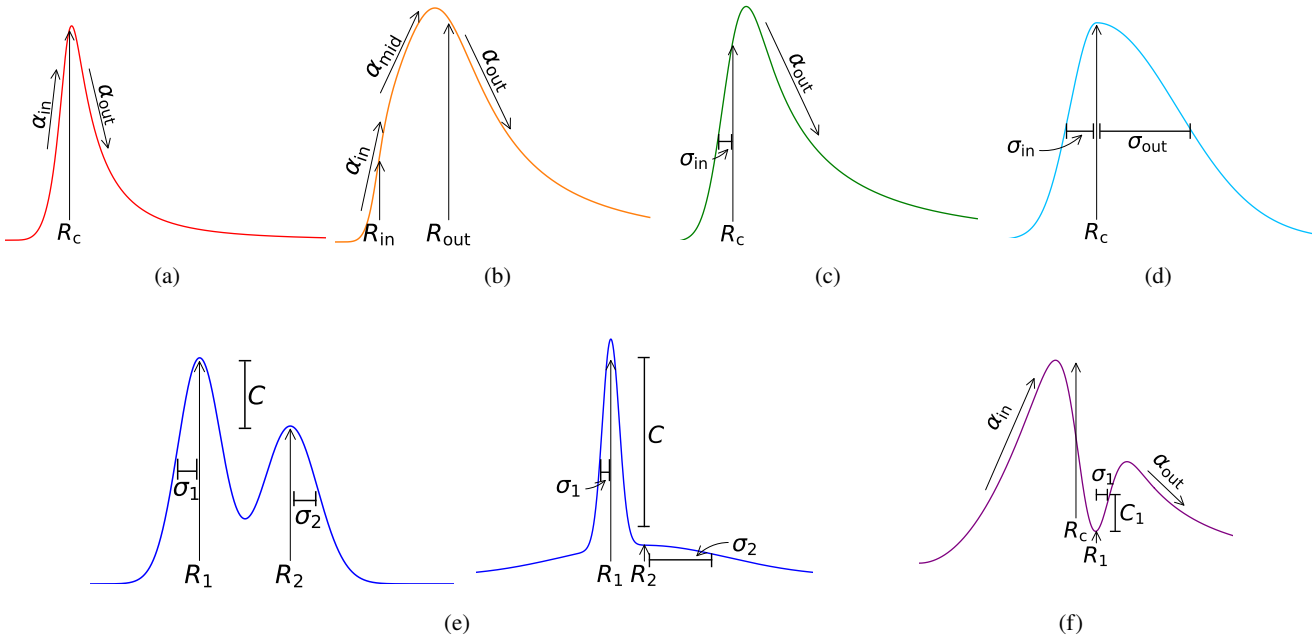

Fig. 1. Examples of the main radial functional forms from the parametric modelling code and their free parameters: double power law (a), triple power law (b), power law + error function (c), asymmetric Gaussian (d), double Gaussian (e), and double power law with Gaussian gap (f). The double Gaussian functional form is shown twice to demonstrate how it can model two rings or a ring with extended emission.

position, width, and depth of the gap with the fewest additional parameters.

For every target, we fitted the flux of the host star ($F_\star$), surface density normalisation of the disc (Σ_c), and the position of the disc in the sky, including position angle (PA), offset from the phase centre ($\Delta\alpha$ and $\Delta\delta$), and inclination (i), assuming that the star was located at the centre of the axisymmetric disc. Additional free parameters for the radial profile depend on the functional form and are outlined in Table 1. As an overview of the table, Gaussians were defined by radius (R), width (σ), and amplitude (C); power laws were defined by central radius (R_c) or transition radii (R_{in} and R_{out}), slope (α), and the sharpness of the transition (γ); and error functions were defined by central radius (R_c), width (σ), and slope (α).

2.4.3. Vertical profiles

We minimise degeneracies between radial and vertical structure by conducting separate steps of modelling, one in which we vary only radial parameters and another in which we vary both radial and vertical parameters. This paper is entirely focused on the former round of modelling; the latter is described by Zawadzki et al. (2026). We therefore assume that the vertical profile is Gaussian for all targets in this paper. We defaulted to fixing the vertical aspect ratio h_{HWHM} – defined as the half width at half max of the vertical profile and assumed to be constant throughout the disc – at 0.015, adjusting the value for certain discs based on results from Zawadzki et al. (2026). When h_{HWHM} = 0.015 did not fall between the 16th and 84th percentiles of the posterior distributions of the models that fit the vertical structure, we instead used approximate values obtained from preliminary vertical modelling. These exceptions were HD 9672 (h_{HWHM} = 0.07), HD 10647 (h_{HWHM} = 0.055), HD 14055 (h_{HWHM} = 0.0475), HD 15115 (h_{HWHM} = 0.02), HD 32297 (h_{HWHM} = 0.012), HD 39060 (h_{HWHM} = 0.0445), HD 61005 (h_{HWHM} = 0.02), and HD 131488 (h_{HWHM} = 0.005).

2.4.4. Parametric model comparison

We compared different parametrisations for each disc with the Akaike information criterion (AIC) and the Bayesian information criterion (BIC), which are statistical measures designed to compare the quality of fits for models with differing numbers of parameters and penalise unnecessary complexity. The AIC and the BIC are defined similarly, but the BIC takes the number of data points (in this case, the sum of the real and imaginary components in the visibility domain) into consideration and, therefore, penalises additional parameters more heavily than the AIC. BIC differences are considered to provide strong evidence of a better fit when greater than 10 (Kass & Raftery 1995), while AIC differences are converted to a Gaussian probability interval to obtain confidence levels.

Although AIC and BIC values were the primary basis for designating a functional form as the best fit for a given disc, we took into consideration radial profile visualisations (Fig. 2) and residuals (Fig. D.1) when the AIC and the BIC disagreed or when the differences between functional forms were not significant. This required considering parametric results on a case-by-case basis, and we describe the process of designating the best functional form for each disc in Sect. 3. While we designate only one functional form as the best for each disc, other functional forms often provided a good fit to the data as well. We report multiple results for several discs, and we sometimes use other functional forms to obtain radial parameters of interest. When a functional form with the radial parameter of interest was not available, we extracted it from the radial profile of the functional form designated as the best in Table E.1. We describe this methodology here.

For each disc, we find the inner and outer slope with a double power law or triple power law, sometimes with one or more Gaussian gaps added, and we find the outer transition radius with a triple power law where available or by measuring the radius at 5% of the peak in brightness from the radial profile of the best

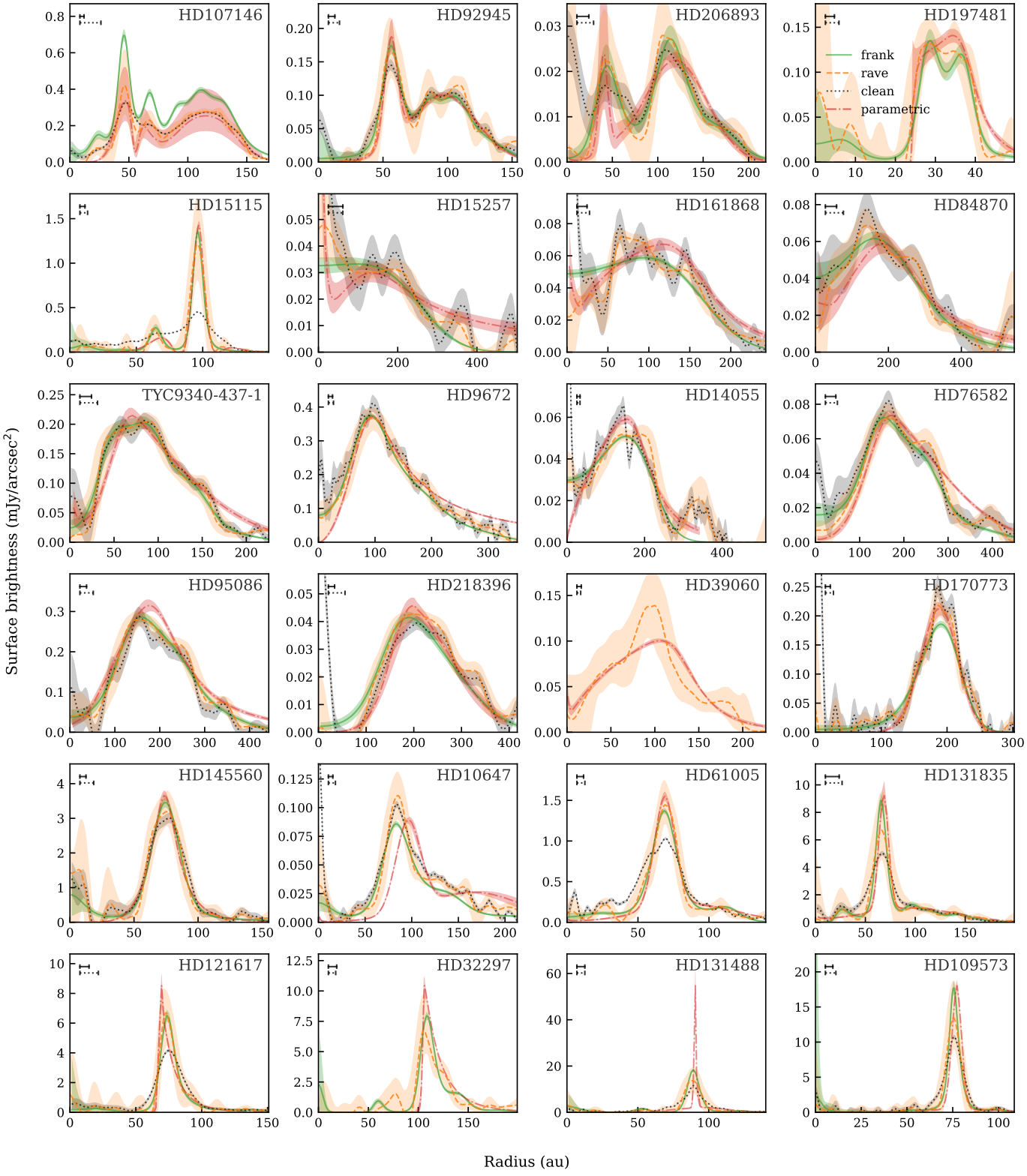

Fig. 2. Azimuthally averaged radial profiles derived from the `CLEAN` image (dotted black) and the deconvolved and deprojected surface brightness profiles fitted with `frank` (solid green), `rave` (dashed orange), and parametric models (dash-dotted red). The robust parameters used for `CLEAN` imaging are listed in Table G.1. The solid bars in the upper left corner of each panel indicate the FWHM resolved by `frank` if the radial profile were infinitesimally narrow (i.e. the `frank` PSF). The dotted bars indicate the synthesised beam size. In general, oscillations in the `CLEAN` profile that are likely due to noise (e.g. as seen in HD 15257 and HD 161868) are smoothed out in the `frank`, `rave`, and parametric models. The deconvolved peaks recovered by the `frank`, `rave`, and parametric models are often sharper than seen in the (beam-convolved) `CLEAN` images; the most extreme case is the best-fitting parametric model for HD 131488. We note that not all methods are applicable to every disc (e.g. azimuthal averaging was not applied to edge-on discs to extract the `CLEAN` profile, and `frank` was not applied to HD 39060 due to mosaicking being used in the observations). The offset between `rave` and `frank` for HD 107146 is due to the two methods fitting at different effective wavelengths.

functional form. This reliance on power laws limited our ability to measure slopes and outer radii for discs with more complicated structures; for example, we could only measure the inner slope of the innermost ring and the outer slope of the outermost ring for multi-ring discs. For each ring, we find the central radius with a double power law or with multiple Gaussians, and we find ΔR by multiplying σ by 2.355 for discs best fit by multiple Gaussians or by measuring the FWHM of the best functional form from its radial profile. In each case, the choice of a functional form to measure the slope or the central radius was based on the AIC and the BIC differences. The fitted radial profiles under the different parametrisations attempted for each disc are shown in Fig. E.1.

3. Results

3.1. Radial profiles

Figure 2 summarises our radial structure modelling results, displaying the surface brightness profiles determined using `CLEAN`, `frank`, `rave`, and the best parametric model for each disc. The gallery provides an overview of the kinds of radial structures suggested by the ARKS observations, based on which parametric models were developed and tested. We note that while the `frank`, `rave`, and parametric profiles are deconvolved, the `CLEAN` profiles are convolved with the beam. The model images and residuals of the fitted `frank`, `rave`, and parametric models are displayed in Figs. F.1, F.2, and D.1.

Fig. 3 displays a gallery of the non-parametric radial surface density profiles, which were converted from the surface brightness profiles in Fig. 2 assuming a blackbody equilibrium temperature profile, stellar luminosities listed in Marino et al. (2026) and the mass opacity described in Marino et al. (2026, $1.9\,\mathrm{cm^2\,g^{-1}}$ in Band 7, $1.3\,\mathrm{cm^2\,g^{-1}}$ in Band 6, and the mean value between the two for the combined Band 6 and 7 data for HD 39060, or β Pic). These profiles are based on `frank` fitting (except for β Pic, for which the `frank` model does not appropriately account for multiple pointings and the `rave` model was used instead), and are expected to represent the physical distribution of millimetre-sized dust in the disc under these temperature profile and opacity assumptions, and likely also the underlying planetesimal distributions from which the observed dust is produced (Hughes et al. 2018).

The horizontal bars in the lower left corner of each panel in Figs. 3 and 2 provide an indication of the resolution of the radial profiles. Specifically, the solid bar indicates the FWHM of the radial profile recovered by `frank` if an infinitesimally narrow ring (i.e. a radial profile described by a Dirac delta function) were to be observed by ALMA (under the same configuration as the data), with the same total flux as the disc, same noise level, and recovered by `frank` with the same hyperparameters (as done in Sierra et al. 2024). The longer dotted bar indicates the synthesised beam size when imaged with `CLEAN` under Briggs weighting and a robust parameter of 0.5.

The radial profiles obtained from each of the three deprojection and deconvolution approaches (`frank`, `rave` and parametric modelling) are generally in close agreement, confirming the robustness of the modelling for each system. The fitted non-parametric profiles typically smooth out noise in the `CLEAN` profile, and in many cases recover sharper peaks than the beam-convolved image, particularly for the radially narrower discs (e.g. HD 15115, HD 121617, HD 109573, HD 61005, HD 107146, HD 131835, and HD 131488). For several systems (e.g. HD 15257, HD 161868, and HD 84870), the `frank` and `rave` profiles differ in their balance between the smoothing of noise and the recovery of sharp features, which are partly controlled by the independent choice of hyperparameter values for each method. The `rave` uncertainties empirically reflect the range of values within which various possible radial profile shapes could take, and are not conditioned upon a particular radial profile shape. These uncertainties are generally larger than those derived by `frank`, as has also been discussed in previous work that compares the two methods (Han et al. 2025). The parametric models further explore the significance of each feature suggested by the non-parametric profiles, also yielding close agreement with the `frank` and `rave` profiles and sometimes finding even sharper features than non-parametric models (e.g. HD 131488, HD 121617 and HD 206893), particularly when the width of the parametric model is narrower than the resolution of the data.

Perhaps one of the strongest conclusions that could be drawn from the galleries of radial profiles is the diversity of radial structures exhibited by debris discs. None of the profiles appear to be fully described by a single Gaussian, which is a common assumption of previous works appropriate for lower-resolution observations. Figure 4 summarises the best-fit functional forms for the parametric models, demonstrating that double power laws and double Gaussians are the best-fit form for the vast majority of discs in the sample, and that only a minority (7/24) of discs require alternative parametrisation (with 4/24 best fitted by an asymmetric Gaussian and 3/24 requiring a gap to be explicitly parametrised).

We attempted to broadly classify the range of radial profiles within the sample. We first divided the sample into single-ring discs and multi-ring discs. Within the single-ring discs, we find that a sizeable subset shows evidence of additional low-amplitude features. Given the subtleness of such features, the `frank`, `rave`, and parametric fits do not always agree or cannot always clearly distinguish between whether these are additional faint rings or halos attached to the main ring. We therefore categorise these single-ring discs with low-amplitude features as a distinct category from those without such features in the radial profile.

To denote these features, we use an abbreviated notation which appends symbols that represent substructures onto the first-order single-ring (denoted R) vs. multi-ring (denoted M) classification of a given disc. As a general rule, superscripts denote the number of rings in a given disc (e.g. M^2 is a disc with 2 rings separated by a gap), but is omitted for discs with only one ring (e.g. R). Subscripts denote any additional structures, including any halos denoted as h either interior (e.g. ${}_hR$) or exterior (e.g. R_h) to a disc, or bumps or "shoulders" on the outer edge of a disc (e.g. R_s). Parentheses may be added to denote that a feature is tentative (e.g. $R_{(s)}$). To indicate the presence of gas in any disc for convenience of understanding its basic features, we use the g_+ tag to indicate gas-rich discs and g_- to indicate gas-poor discs. No gas tags are added to discs without gas detections. We note that this classification is purely phenomenological and is not designed to reflect their underlying physical origins and the fact that the boundaries between categories may be blurry and different features may lie on a continuum of shapes.

To clarify terminology used in the remainder of this section as we describe the characteristic inner and outer edges and central radius for each classification, we define discs with $\alpha > 15$ in parametric models with power-law edges as a steep slope based on the cut-off for planet sculpting (Pearce et al. 2024) and define $R > 100$ au as a disc with a large radius. Emission of a feature is considered low in amplitude if it is lower than 50% of the main

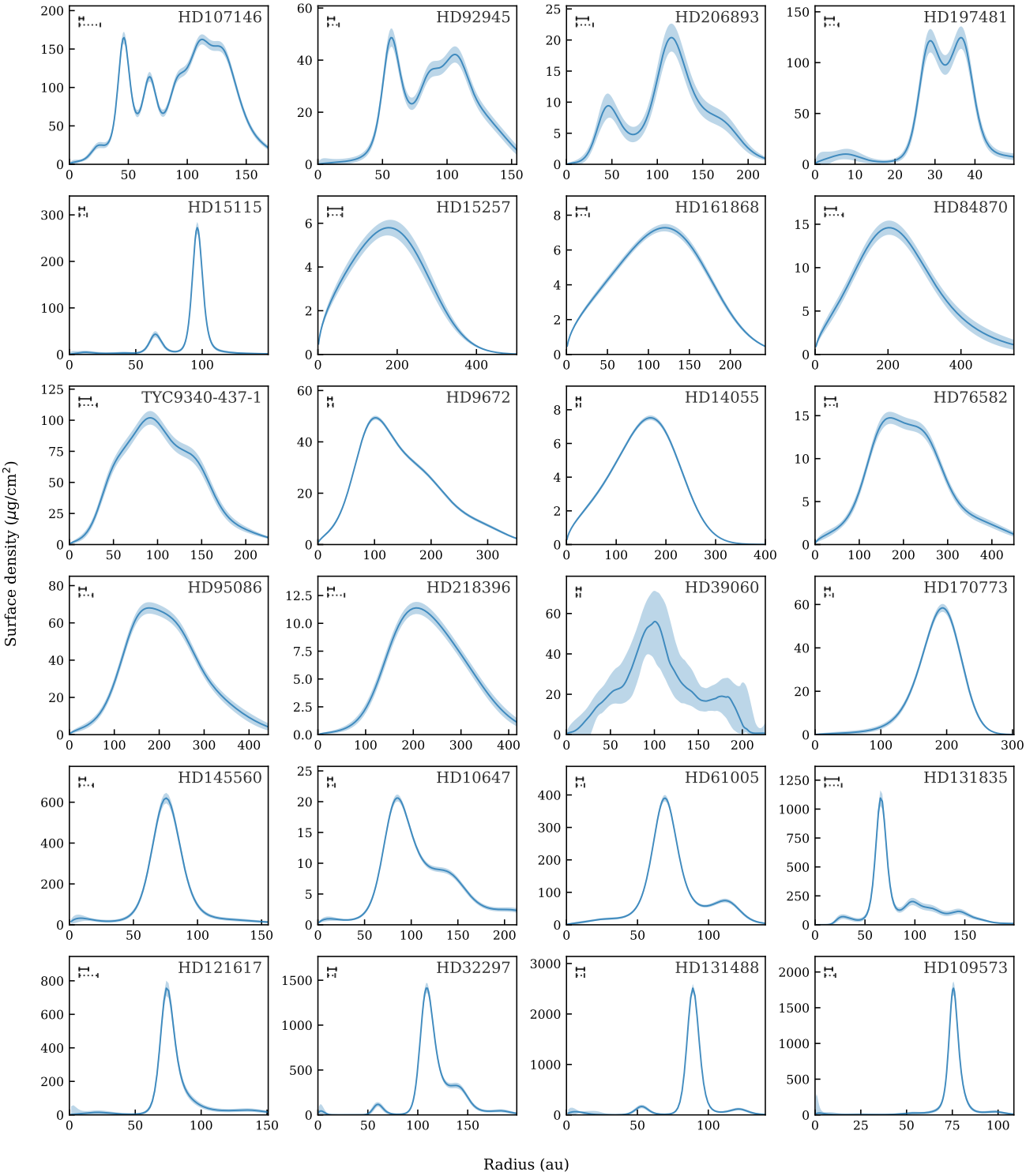

Fig. 3. Deconvolved and deprojected surface density profiles fitted with `frank`, except for β Pic (HD 39060) which was fitted with `rave`. These profiles are based on the surface brightness profiles presented in Fig. 2, but offers a cleaner and simpler alternative to that figure which includes a more comprehensive summary of the different approaches used to model the radial structure in this study. The bars in each panel are the same as those described in Fig. 2.

peak, and gas-rich is defined as an estimated gas mass above 10^{-4} $M_\oplus$, while gas-poor is defined by a gas detection lower than this threshold.

The remainder of this section describes the modelling for each individual system. We continue the discussion of the disc properties of the sample in Sect. 3.2.

3.1.1. Group [M^n]: multi-ring discs

This group includes discs with multiple rings separated by radial gaps. The non-parametric profiles suggest that eight discs in the ARKS sample have multiple rings based on their surface density profile, of which five have at least one significant gap when

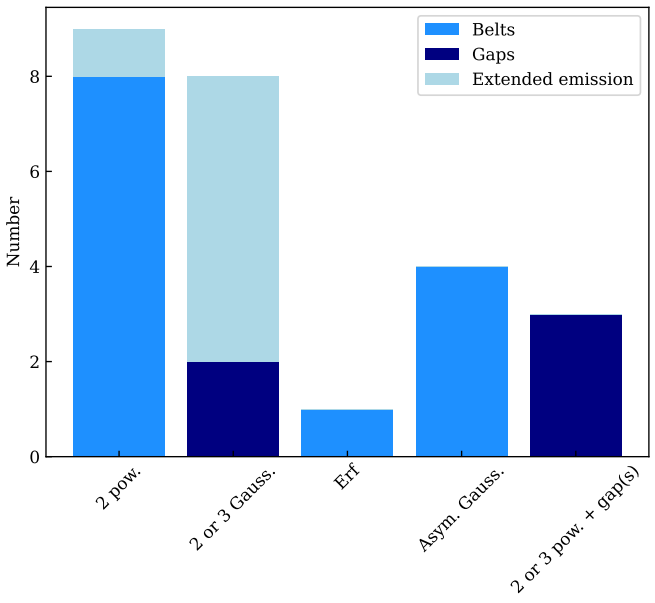

Fig. 4. Distribution of best functional forms for all targets, as determined by weighing the AIC confidence intervals, BIC differences, profile plots, and residuals (described in Sect. 2.4).

the parametric models are tested for statistical significance with the AIC and the BIC. These eight discs are listed in this section, with the remainder (parametrically not significant) discs discussed later in the single-ring discs with low-amplitude emission category (Sect. 3.1.3). The multi-ring discs are typically located at a small radius (mean R = 72 au), with steeper inner (mean $\alpha_{\rm in}$ = 16) and outer (mean $\alpha_{\rm out}$ = −11) edges than found among single-ring discs. The gap is often wide and deep in these discs. The inner ring is often narrower than the outer ring, with a mean $\Delta R/R$ = 0.21 for inner rings and a mean $\Delta R/R$ = 0.43 for outer rings. We measure the locations and widths of the peaks from Gaussian parametrisations, and we measure the locations and widths of the gaps from double power law and triple power law functional forms with Gaussian gaps added. The best-fit and median values for the double-Gaussian parametrisation of these discs are described in Table C.2.

(i) HD 107146 [M^3]

The outer regions of the disc were observed in scattered light by HST and modelled by Ertel et al. (2011). The disc was then imaged by ALMA and modelled parametrically as a wide belt with one gap in Marino et al. (2018); Marino (2021) and with two gaps in Imaz Blanco et al. (2023) following the discovery of a bump in the middle of a wide gap using `frank` and higher-resolution data. Here, we confirm the double gap structure. The intermediate belt is consistently recovered by both `frank` and `rave`, which manifests in the beam-convolved `CLEAN` profile as a low-amplitude bump and appears to be a real feature. The offset between the `frank` and `rave` profiles for this system in Fig. 2 is due to the fact that the `rave` profile was fitted to the `CLEAN` image created by combining band 6 and 7 observations (mean wavelength of 1.0 mm) which improves the S/N but lowers the brightness compared to using band 7 only (Marino et al. 2026), whereas the `frank` profile was fitted to the band 7 (mean wavelength of 0.86 mm) visibilities only.

We parametrically modelled HD 107146 with five functional forms – a double Gaussian, triple Gaussian, triple power law, triple power law with one gap, and triple power law with two gaps – to determine the significance of these previously observed gaps at the higher resolution of the ARKS observations. We find that the triple power law with two Gaussian gaps is significantly preferred over all other functional forms by both the AIC and the BIC, providing strong evidence that there are three rings in HD 107146. We therefore designate the triple power law with two Gaussian gaps as the best functional form for this disc (MCMC results described in Table C.3), although we rely on the triple Gaussian to describe the rings. This is the only disc in the ARKS sample with more than one significant gap

As parametrised by the triple Gaussian, the three rings are located at $46.2^{+0.3}_{-0.5}$ au, $66.3^{+0.6}_{-0.7}$ au, and $118.07^{+0.12}_{-0.11}$ au. The inner and centre rings are approximately the same width (ΔR = $13.2^{+0.9}_{-1.2}$ au and ΔR = $8.2^{+2.4}_{-1.9}$ au, respectively), while the outer ring is much wider (ΔR = $58.7^{+0.6}_{-0.4}$ au). The inner ring is the brightest. As parametrised by the triple power law with two Gaussian gaps, the two gaps are located at $56.1^{+0.5}_{-0.3}$ au and $78.1^{+0.6}_{-0.8}$ au. The inner gap (ΔR = $6.83^{+1.41}_{-0.94}$ au) is narrower than the outer gap (ΔR = $39.1^{+2.4}_{-1.9}$ au), while the outer gap (C = $0.693^{+0.025}_{-0.016}$) has a slightly greater amplitude than the inner gap (C = $0.57^{+0.7}_{-0.9}$). These results are consistent with the ARKS non-parametric models as well as modelling conducted by Imaz Blanco et al. (2023).

As high-resolution multiband data was available for this disc, we additionally fit the emissivity index with the parametric modelling code; results are described in Appendix A.

(ii) HD 92945 [M^2]

The disc has been modelled as a wide belt with a gap (Marino et al. 2018; Marino 2021), which is consistent with our non-parametric modelling. On top of that, the `CLEAN` profile suggests a possible dip in the relatively wide outer belt, which is deconvolved into a slightly deeper gap by `rave` and is also reflected in the `frank` profile, though to a lesser extent. Given the slightly lower S/N of the observations compared to HD 107146, as reflected in the larger uncertainties in the `CLEAN` profile, the possibility that there exist three rather than two rings in the system appears to be less certain than in HD 107146, so we label the disc as M^2 for now based on the present dataset.

We parametrically modelled HD 92945 with seven functional forms – a double Gaussian, double Gaussian with one gap, triple Gaussian, double power law, double power law with one gap, double power law with two gaps, and triple power law with one gap – to determine the significance of both possible gaps suggested by the non-parametric models. Both the AIC and the BIC indicate that the double power law is significantly worse than the other functional forms, providing strong evidence that there is at least one gap in the disc. The AIC and the BIC consistently prefer the double Gaussian parametrisation, indicating that the additional complexity of parametrising a second gap or a third ring is not justified by a reduction in χ^2. However, we emphasise that higher S/N data are necessary to confirm the presence or absence of a second gap around 100 au. We therefore designate the double Gaussian as the best functional form for this disc, although we rely on the triple power law with one gap to parametrise the gap itself.

As parametrised by the double Gaussian, the two rings are located at 57.0 ± 0.8 au and 102.7 ± 1.5 au, overlapping with two rings observed in infrared (Golimowski et al. 2011). The inner ring (ΔR = 13^{+3}_{-3} au) is wider than the outer ring (ΔR = 59^{+5}_{-4} au). As parametrised by the triple power law with one Gaussian gap, the gap is centred at R = 74.4 ± 2.0 au, with a width of ΔR = 21^{+7}_{-9} au and fractional depth of C = $0.52^{+0.05}_{-0.06}$. These results are consistent with previous modelling (Marino et al. 2019).

(iii) HD 206893 [M^2]

We find two belts at radial locations consistent with previous non-parametric modelling with `frank`, `rave`, and parametric modelling (Marino et al. 2020; Marino 2021; Nederlander et al. 2021). We parametrically modelled HD 206893 with six functional forms – a double power law, double power law with one gap, triple power law, triple power law with one gap, double Gaussian, and triple Gaussian – to explore various parametrisations of the gap. We find that the double Gaussian is strongly preferred over all other functional forms by the BIC, and marginally to moderately preferred by the AIC. We therefore designate the double Gaussian as the best functional form for this disc, although we rely on the double power law with a gap to describe the gap itself.

As parametrised by the double Gaussian, the rings are located at 42 ± 5 au and 127 ± 4 au. The inner ring ($\Delta R = 14^{+21}_{-9}$ au) is much narrower than the outer ring ($\Delta R = 85^{+9}_{-7}$ au), while the outer ring is brighter than the inner ring. As parametrised by the double power law with a Gaussian gap, the gap is centred at $R = 83^{+6}_{-7}$ au, with a width of $\Delta R = 24^{+26}_{-12}$ au and fractional depth $C = 0.50^{+0.30}_{-0.20}$.

(iv) HD 197481 (AU Mic) [M^2 (M^3)]

AU Mic has been extensively observed by ALMA (e.g. MacGregor et al. 2013; Daley et al. 2019; Vizgan et al. 2022). The main belt at 30 au is resolved into two separate peaks by `frank`, and to a lesser extent by `rave`, which is more similar to a plateau with relatively sharp edges on either side. Furthermore, our `frank` and `rave` modelling supports the presence of an inner component at <10 au, which has been suggested in previous parametric (MacGregor et al. 2013; Daley et al. 2019; Marino 2021) and non-parametric modelling (Han et al. 2022; Terrill et al. 2023). The oscillation of this inner emission in the `rave` profile is unlikely to be real, as reflected in the large uncertainty region, and more likely reflects the presence of inner emission that could be relatively sharp. Given the uncertainty of the inner emission, we label this disc as M^2 but include the M^3 label in brackets.

We parametrically modelled HD 197481 with five functional forms – a double power law, triple power law, double Gaussian, triple power law with one gap, and triple Gaussian – to explore the potential inner component suggested by previous observations and the potential gap at ~32 au suggested by the ARKS non-parametric models. We find that the addition of the inner component does not reduce the value of χ^2 enough to justify the increased number of parameters, as measured by both the AIC and the BIC. The significance of the gap at ~32 au is ambiguous, with the BIC significantly preferring the triple power law parametrisation and the AIC moderately preferring the triple power law parametrisation with a Gaussian gap. We therefore report results for both functional forms in Table C.3 and tentatively classify it as a disc with a gap, defaulting to the triple power law with a Gaussian gap where it is necessary to choose one functional form. We use the double Gaussian parametrisation to describe the rings.

As parametrised by the double Gaussian, HD 197481 has two rings located at $29.0^{+5.3}_{-0.7}$ au and $36.7^{+18.8}_{-0.6}$ au, with $\Delta R = 4.0^{+7.8}_{-1.4}$ au for the inner ring and $\Delta R = 11.1^{+5.7}_{-1.4}$ au for the outer ring. As parametrised by the triple power law with a Gaussian gap, there is a gap centred at 34^{+3}_{-2} au with $\Delta R = 19^{+3}_{-3}$. This gap was not detected by previous observations of HD 197481.

Because HD 197481 is a young, magnetically active red dwarf with variable stellar flux with archival observations from three dates (Cranmer et al. 2013; Daley et al. 2019), we fit the stellar flux for each observation separately. Our best-fit parametric model – a triple power law with one gap – found that the median stellar fluxes on these dates were 343^{+18}_{-19} μJy, 140^{+30}_{-20} μJy, and 205 ± 18 μJy, respectively (Table C.4). These fluxes are closest to the values obtained with the disc + Ring model run by Daley et al. (2019), although our median measurement for March, 2014 falls slightly below the uncertainty range calculated by Daley et al. (2019). The larger fluxes measured by previous studies may be attributable to bias from small flares (e.g. Cranmer et al. 2013).

(v) HD 15115 [M^2]

Both `frank` and `rave` profiles find two narrow rings separated by a deep radial gap, which is found to be clear of emission from parametric modelling. The ring radii found here (at 64 and 96 au) are slightly exterior to those fitted in prior parametric modelling of observations at lower resolution (with ring outer edges at 51 and 93 au, MacGregor et al. 2019) and are consistent with those found in previous non-parametric fitting (Terrill et al. 2023; Han et al. 2025).

We parametrically modelled HD 15115 with three functional forms – a double power law, double Gaussian, and double power law with one gap – and find that the double power law with one gap provided a significantly better fit according to both the AIC and the BIC. This disc consists of two narrow rings, which we characterise with the results of the double Gaussian functional form.

As parametrised by the double Gaussian, the two rings are located at $65.8^{+0.6}_{-0.3}$ au and $97.57^{+0.07}_{-0.05}$ au. The inner ring ($\Delta R = 6^{+2}_{-2}$ au) is slightly narrower than the outer ring ($\Delta R = 11.1^{+0.4}_{-0.5}$ au), while the outer ring is much brighter than the inner ring. As parametrised by a double power law with a Gaussian gap, the gap is located at 93.9 ± 0.3 au, with a width of $\Delta R = 25.7^{+0.9}_{-0.9}$ au and fractional depth of $C = 0.453^{+0.007}_{-0.008}$ (Table C.3). These results are consistent with `frank` and `rave` profiles, although the higher resolution of the ARKS observations indicate that the gap is somewhat wider and further out from the star than previously measured at lower resolution (MacGregor et al. 2019).

3.1.2. Group [R]: single-ring discs

This group includes single belts that have either no clear evidence of additional rings or extended halo-like emission. A subset of non-parametric profiles show a "shoulder", or abrupt steepening in slope, on the outer edge. We also find that a number of discs show tentative evidence of a sharp change in slope on the outer edge, giving the appearance of a bump or "shoulder". Although evidence for these features are tentative, similar features have been identified in protoplanetary discs, for which interactions with massive planets has been suggested to be a possible explanation (Bi & Lin 2024). We remain cautious, however, since these features were generally not found to be statistically significant when tested with parametric models. Parentheses are therefore added to denote that evidence of a feature is marginal (e.g. $R_{(s)}$).

Twelve debris discs in the ARKS sample are characterised by a single, relatively smooth belt and are well described by a double power law, asymmetric Gaussian, or power law + error function. The parametric results for these discs are described in Table C.1. The non-parametric models suggest the presence of possible substructures in several of these discs, including shoulders and plateaus. Although we parametrically fitted a triple power law functional form to 11 targets to describe these changes

in slope, the additional parameters were not justified by the improvement in fit according to either the AIC or the BIC. More sensitive observations may be necessary to detect these subtle features at high confidence.

The majority of these belts are broad, with a mean fractional width of 0.90, and have shallow inner (mean $\alpha_{\rm in} = 3.9$) and outer (mean $\alpha_{\rm out} = -4.1$) edges. The distributions for both slopes skew toward smaller values, with a median inner power law index of 1.9 and a median outer power law index of −3.25. We find that most of these belts without significant substructure are located at large radii, measuring a mean central radius of 160 au and a median central radius of 181 au.

(i) HD 15257 [R]

A central cavity is not resolved in the `frank` or `rave` profiles. The peak location in surface density at just under 200 au is slightly interior to the broad belt at 270^{+60}_{-40} fitted based on SMA observations in the REASONS survey (Matrà et al. 2025).

We parametrically modelled this disc with a double power law and power law + error function. The AIC and the BIC express no significant preference for either model over the other, indicating that both functional forms fit the data well. The power law + error function better recreates the peak, while the double power law adheres more closely to the outer edge (Fig. E.1). We therefore rely on both parametrisations to describe this low S/N disc, although we default to the power law + error function when it is necessary to choose just one functional form.

As parametrised by the power law + error function, HD 15257 is a broad belt ($\Delta R = 330^{+40}_{-70}$ au), with a large central radius ($R_{\rm c} = 110 \pm 30$ au). As parametrised by the double power law, the disc peaks in emission at a larger radius ($R_c = 250^{+50}_{-40}$ au), which agrees more closely with `frank` and REASONS (Matrà et al. 2025). The inner edge ($\alpha_{\rm in} = 0.8^{+0.4}_{-0.2}$) is much shallower than the outer edge ($\alpha_{\rm out} = -3.1^{+1.3}_{-2.9}$), which is characteristic of discs in this category.

(ii) HD 161868 (γ Oph) [$R_{(s)}$]

A broad disc peaking at ∼130 au, the disc radius measured here is significantly smaller than the ∼520 au radius based on *Spitzer* 70 μm observations (Su et al. 2008), but consistent with *Herschel* findings (Moór et al. 2015). The `rave` and `CLEAN` profiles suggest a possible subtle shoulder at 150 au.

We parametrically modelled this disc with an asymmetric Gaussian, power law + error function, and double power law to capture the single belt, having previously found that the shoulder suggested by the non-parametric models was not significant when fitted with a triple power law during an earlier iteration of the parametric modelling code. The AIC and the BIC express no significant preference for any of these models over the others, indicating that all three fit the data well. As the radial profiles are similar across the parametric models, we report results for all three, although we default to the double power law when it is necessary to choose just one functional form.

As parametrised by the double power law, HD 161868 is a broad belt ($\Delta R = 160^{+30}_{-10}$ au, wider than measured by REASONS), with a large central radius ($R_{\rm c} = 154^{+8}_{-10}$ au) that is consistent with results from *Herschel* (Moór et al. 2015). The asymmetric Gaussian ($R_{\rm c} = 120^{+11}_{-9}$ au) and power law + error function ($R_{\rm c} = 99^{+3}_{-4}$ au) measure a smaller central radius, although the asymmetric Gaussian adheres more closely to the peak found by the non-parametric models. The inner edge ($\alpha_{\rm in} = 0.99^{+0.14}_{-0.11}$) is shallower than the outer edge ($\alpha_{\rm out} = -3.7^{-0.7}_{-0.8}$), which is characteristic of other discs in this category.

(iii) HD 84870 [R]

A broad disc peaking at ∼200 au with the central cavity just resolved, the peak radius is slightly interior to the 260±50 au radius derived from REASONS (Matrà et al. 2025).

We parametrically modelled this disc with a double power law and a power law + error function to capture the single belt, having previously found that the shoulder suggested by `rave` was not significant when fitted with a triple power law during an earlier iteration of the parametric modelling code. The AIC and the BIC moderately prefer the double power law, indicating that this model provides a better fit to the data with the same number of parameters as the power law + error function. We therefore designate the double power law as the best functional form for this disc.

As parametrised by the double power law, HD 84870 is a broad belt ($\Delta R = 250^{+70}_{-30}$ au, in agreement with REASONS), with a large central radius ($R_{\rm c} = 220 \pm 30$ au) that is consistent with both the non-parametric results and REASONS. The inner ($\alpha_{\rm in} = 1.5 \pm 0.3$) and outer edges ($\alpha_{\rm out} = -2.0^{+0.5}_{-0.7}$) are smooth and fairly symmetric.

(iv) TYC 9340-437-1 [$R_{(s)}$]

The disc has previously been resolved and modelled as a large belt centred at 96 au with *Herschel* (Tanner et al. 2020) and at 130±20 au by ALMA in the REASONS survey (Matrà et al. 2025). Here, we find the radial profile to plateau between 50 and 100 au in surface brightness in both the `frank` and `rave` profiles, with the surface density peaking at 90 au and exhibiting a shoulder, or secondary bump, on the outer edge.

We parametrically modelled this disc with four functional forms: a double power law and an asymmetric Gaussian to capture the single belt, a triple power law to recreate the plateau suggested by `frank` and `rave`, and a double Gaussian to reflect any additional complexity. The AIC expresses moderate preference for the triple power law, but the BIC expresses significant preference for the asymmetric Gaussian and the double power law, indicating that all three models fit the data well. The triple power law recreates the plateau, while the asymmetric Gaussian adheres more closely to inner edge and the double power law adheres more closely to the peak. We therefore rely on all three functional forms to describe the disc, although we default to the asymmetric Gaussian when it is necessary to choose just one functional form.

As parametrised by the asymmetric Gaussian, TYC 9340 is broad ($\Delta R = 98 \pm 6$ au), with a central radius ($R_{\rm c} = 99^{+6}_{-7}$ au) that is somewhat smaller than measured by REASONS. The disc has an inner edge that is likely steeper than average for discs in this category ($\alpha_{\rm in} = 14^{+11}_{-8}$) and a characteristically shallow outer edge ($\alpha_{\rm out} = -3.3^{+0.5}_{-0.7}$), as measured by the triple power law parametrisation. The plateau has a slightly increasing slope ($\alpha_{\rm mid} = 0.41 \pm 0.14$) and is located between $R_{\rm in} = 36^{+5}_{-4}$ au and $R_{\rm out} = 128 \pm 12$ au.

(v) HD 9672 (49 Cet) [R, g_+]

Both the `frank` and `rave` profiles suggest a very smooth inner and outer edge, with the outer edge being significantly shallower in absolute terms than the inner edge, though they are similar in steepness when divided by the respective location of the edges (defined as emission at 50% of the peak). Our modelling is consistent with the ring radius in previous ALMA observations (Hughes et al. 2017; Nhung et al. 2017). A radial profile was not derived based on *Herschel* observations (Moór et al. 2015), but the position angle and inclination derived from the PACS 100 µm image are consistent with those derived from ARKS.

We parametrically modelled HD 9672 with a double power law and a double Gaussian. The AIC moderately prefers and the BIC significantly prefers the double power law, indicating that the additional parameters fit by the double Gaussian do not result in a significantly better fit to the data. We therefore designate the double power law as the best functional form for this disc.

As parametrised by the double power law, HD 9672 is broad ($\Delta R = 121 \pm 3$ au, narrower than measured by REASONS), with a central radius ($R_c = 96 \pm 4$ au) that is consistent with the peak measured by Hughes et al. (2017). The disc has a potentially shallow, but uncertain, inner edge ($\alpha_{in} > 1.79$) and a shallow outer edge ($\alpha_{out} = -1.11^{+0.08}_{-0.09}$) that are typical for discs in this category and consistent with the power law indices previously fitted by Hughes et al. (2017).

(iv) HD 14055 (γ Tri) [R]

The observations resolve a central cavity that is not completely clear of emission. The peak location is consistent with the belt radius of 180±10 au from REASONS (Matrà et al. 2025) and the radius of >170 au from DEBRIS (Booth et al. 2013). The `rave` profile suggests a possible plateau in surface brightness between 120 and 210 au, but this is marginal and not detected in `frank`. The `CLEAN` and `rave` profiles suggest the presence of an outer ring, but this is not detected in `frank` or favoured by parametric fits, so we label this disc as consisting of one rather than two rings for now.

We parametrically modelled this disc with a double power law and a double Gaussian. There is strong preference for the double power law over the double Gaussian as measured by the BIC but only marginal preference as measured with the AIC, indicating that the double power law fits the data well with fewer parameters. We note that the double Gaussian fits a single belt without additional features in this case, providing a profile that is very similar to the double power law. We therefore designate the double power law as the best functional form for this disc.

HD 14055 is broad ($\Delta R = 176^{+10}_{-9}$ au, in agreement with REASONS), with a central radius of $R_c = 181^{+9}_{-13}$ au that is consistent with measurements by REASONS and DEBRIS (Booth et al. 2013). The disc has shallow inner ($\alpha_{in} = 1.20^{+9}_{-0.11}$) and outer ($\alpha_{out} = -3.1^{+0.7}_{-1.0}$) slopes, which are characteristic of discs in this category. The parametric models were not able to constrain the significance of the plateau suggested by `rave`, while the failure of the double Gaussian to fit for a central cavity suggests that this non-parametric feature is not significant given the S/N of the observations.

(vii) HD 76582 [R_s]

Previous modelling based on far-infrared imaging by *Herschel*, submillimetre imaging by JCMT and the SED suggested two resolved components at 80 and 270 au, respectively, in addition to an unresolved inner component (Marshall et al. 2016). Our modelling based on the ALMA images supports the finding of resolved substructures, with the `frank` surface brightness profile suggesting a shoulder, which translates to almost a plateau in surface density between approximately 150 and 250 au. The `rave` surface brightness profile suggests a bump on the outer edge that is reminiscent of an additional ring peaking at approximately 250 au, in addition to the ring peaking at 150 au, although the uncertainties are sufficiently large such that a broad plateau rather than two rings is also possible.

We parametrically modelled this disc with a triple power law to capture the shoulder suggested by `frank` and with an asymmetric Gaussian, double power law, and power law + error function to capture the single belt. The BIC significantly prefers the asymmetric Gaussian, which the AIC moderately prefers over the double power law and significantly prefers over the power law + error function. Although the AIC only marginally prefers the asymmetric Gaussian over the triple power law, we cannot rule out this functional form and emphasise that higher-resolution observations are necessary to constrain the radial structure of this disc. We therefore report results for the triple power law here, although we default to the asymmetric Gaussian when it is necessary to choose just one functional form.

As parametrised by the asymmetric Gaussian, HD 76582 is broad ($\Delta R = 192^{+8}_{-7}$ au), with a large central radius ($R_c = 181^{+9}_{-8}$ au). The disc is symmetric, with characteristically shallow inner ($\alpha_{in} = 3.3^{+3.0}_{-0.7}$) and outer ($\alpha_{out} = -3.4 \pm 0.4$) edges, as measured by the triple power law. We note that the triple power law opted to fit a plateau rather than a shoulder, suggesting that the shoulder is not significant at the S/N of the ARKS observations. If present, the plateau is extremely shallow ($\alpha_{mid} = 0.1 \pm 0.2$), extending from $R_{in} = 137^{+19}_{-29}$ au to $R_{out} = 269^{+19}_{-16}$ au.

(viii) HD 95086 [$R_{(s)}$]

HD 95086 hosts a broad disc with a well-resolved central cavity. The belt radius is consistent with prior *Herschel* (Moór et al. 2015) and ALMA (Su et al. 2017) observations. Both the `rave` and `frank` profiles suggest a subtle shoulder on the outer edge; however, this profile could be biased by a background source which could be undersubtracted (Marino et al. 2026).

We parametrically modelled this disc with a double power law to fit the single belt, a triple power law to recreate the subtle shoulder, and a double Gaussian to capture additional complexity. The AIC marginally prefers the triple power law, while the BIC significantly prefers the double power law. We note that both the double Gaussian and the triple power law do not reproduce any substructures in this case but rather closely follow the profile of the double power law, indicating that a simpler structure is present at the S/N of the observations. We therefore designate the double power law as the best functional form for this disc.

As parametrised by the double power law, HD 95086 is broad ($\Delta R = 180^{+11}_{-11}$ au) with a large central radius ($R_c = 198^{+11}_{-7}$ au), in agreement with REASONS (Matrà et al. 2025), *Herschel* (Moór et al. 2015), and Su et al. (2017). The inner $\alpha_{in} = 1.93^{+0.20}_{-0.18}$ and outer $\alpha_{out} = -2.5^{+0.2}_{-0.3}$ edges are shallow, as characteristic of discs in this category. We note that we measure a much larger outer power law index than previous lower-resolution observations (Su et al. 2017).

(ix) HD 218396 (HR 8799) [R]

We find a broad disc with a large central cavity with the `frank` and `rave` profiles, which was previously modelled with a range of parametric profiles (Faramaz et al. 2021). Any potential bumps on the outer edge suggested by the `CLEAN` profile appear to be low in amplitude and do not exhibit a clear and sudden change in slope at the sensitivity of these observations.

We parametrically modelled this disc with a double power law, triple power law, asymmetric Gaussian, and double Gaussian. We find that the BIC strongly prefers the asymmetric Gaussian to the three other functional forms tested, while the AIC moderately prefers the asymmetric Gaussian and the double Gaussian to the other functional forms. We note that the double Gaussian recreates a shoulder on the outer edge, but this feature is not significant at the S/N of the observations. We therefore designate the asymmetric Gaussian as the best functional form for this disc, although we note that a more complex structure is possible.

As parametrised by the asymmetric Gaussian, HD 218396 is broad ($\Delta R = 150^{+10}_{-20}$ au), with a large central radius ($R_c = 208^{+11}_{-10}$ au). These values are smaller than those measured by

REASONS at lower resolution. The inner ($\alpha_{\rm in} = 9^{+4}_{-3}$) and outer ($\alpha_{\rm out} = -4.77^{+0.30}_{-0.17}$) edges are steeper than average for discs in this category, as measured by the triple power law.

(x) HD 39060 (β Pic) [$R_{(s)}, g_-$]

β Pic has been extensively observed by ALMA (e.g. Dent et al. 2014; Matrà et al. 2017; Hull et al. 2022), and its dust continuum radial profile has been modelled as a Gaussian peaking at 105 au (Matrà et al. 2019), consistent with the `rave` profile's peak (the `frank` profile is not displayed as the method is not optimised for mosaic observations at present), although the `rave` profile suggests a slightly more triangular shape than Gaussian, possibly with an additional bump on the outer edge.

We parametrically modelled this disc with a double power law and double Gaussian functional forms. While the AIC marginally prefers the double Gaussian, the BIC significantly prefers the double power law. We therefore report results for both functional forms, although we default to the double power law when it is necessary to choose just one functional form.

As parametrised by the double power law, β Pic is broad ($\Delta R = 122^{+5}_{-5}$ au, slightly wider than previously measured by REASONS), with a central radius ($R_{\rm c} = 130 \pm 5$ au) that is larger than the peak found by `rave` and Matrà et al. (2019). The double Gaussian captures the triangular shape indicated by `rave`, with a narrow Gaussian ($\sigma_1 = 16^{+14}_{-6}$ au) centred at $R_1 = 115^{+4}_{-6}$ au and a broad Gaussian ($\sigma_2 = 54^{+18}_{-3}$ au) centred at $R_2 = 106.4^{+1.9}_{-2.6}$ au. The inner edge ($\alpha_{\rm in} = 1.09^{+0.10}_{-0.07}$) is shallower than the unusually steep outer edge ($\alpha_{\rm out} = -4.8 \pm 0.8$), as measured by the double power law.

(xi) HD 170773 [R]

We find a smooth single belt with a shallower inner edge than outer edge. The peak location at 200 au is consistent with *Herschel* (Moór et al. 2015) and previous ALMA (Sepulveda et al. 2019) observations. We parametrically modelled this disc with an asymmetric Gaussian and a double power law. The AIC and the BIC prefer neither functional form significantly. We therefore report results for both, although we default to the asymmetric Gaussian when it is necessary to choose just one functional form.

As parametrised by the asymmetric Gaussian, HD 170773 is narrow ($\Delta R = 66^{+6}_{-5}$ au, in agreement with REASONS), with a large central radius ($R_{\rm c} = 194^{+7}_{-4}$ au). The double power law finds a similar central radius ($R_c = 200^{+13}_{-7}$ au). HD 170773 has an inner edge ($\alpha_{\rm in} = 5.6^{+1.0}_{-1.2}$) and outer edge ($\alpha_{\rm out} = -11^{+2}_{-5}$) that are steeper than average for discs in this category, as measured by the double power law. The asymmetric Gaussian is fairly symmetric, with an inner width of $\sigma_{\rm in} = 29^{+6}_{-3}$ au and an outer width of $\sigma_{\rm out} = 26^{+3}_{-4}$ au.

(xii) HD 145560 [R]

We find a smooth and symmetric single belt at a radius consistent with the value derived from previous observations (Matrà et al. 2025). Both the `frank` and `rave` profiles suggest possible low-amplitude inner emission. We parametrically modelled this disc with a double power law and a single Gaussian to capture a single belt and a double Gaussian to capture the possible low-amplitude emission. Both criteria agree that the single Gaussian does not provide a good fit to the data, despite having the fewest number of parameters. The AIC strongly prefers the double Gaussian over the double power law, while the BIC strongly prefers the double power law over the double Gaussian. We therefore report results for both functional forms and tentatively classify the disc as a single belt, although we emphasise that higher-resolution observations are necessary to determine whether the disc has a halo, as suggested by the AIC's preference for the double Gaussian functional form. We default to the double power law when necessary to choose just one functional form.

As parametrised by the double power law, HD 145560 is narrow ($\Delta R = 23.6^{+1.2}_{-1.0}$ au, consistent with measurements by REASONS at a lower resolution). The belt is centred at ~75 au according to both the double power law and double Gaussian parametrisations, which is consistent with the peak radius found by REASONS (Matrà et al. 2025). The inner ($\alpha_{\rm in} = 6^{+0.6}_{-0.5}$) and outer ($\alpha_{\rm out} = -7.1^{+0.4}_{-0.5}$) edges are steeper than average for discs in this category. If present, the halo is centred at 88^{+13}_{-12} au with a width of 180^{+30}_{-50} au, as measured by the double Gaussian parametrisation.

3.1.3. Group [R_x]: single-ring discs with additional low-amplitude emission (halo or possible ring)

This group includes single-ring discs with evidence of more extended low-amplitude emission, which could be in the form of a halo attached to the main ring or an additional low-amplitude ring separated from the main ring by a radial gap. The distinction between the two is often unclear given the low surface brightness of these features relative to the sensitivity of the observations, and the different modelling approaches may provide different suggestions on whether a halo or ring is more likely. Unlike the multi-ring discs which have shallow gaps, any additional rings appear to be separated by deeper gaps that appear to be largely clear of emission.

We define halos as a smooth, radially extended distribution of millimetre emission, typically reaching a larger radius than the main planetesimal ring. The parametric models indicate that halos are present in six of the seven discs in this category and find that the extended emission described by the non-parametric models is not significant in the remaining disc (HD 32297). These halos are best reproduced parametrically by the sum of two overlapping Gaussians: a narrow Gaussian reproduces the main ring, while a broad Gaussian describes the extended emission of the halo (see Fig. 1). The narrow component (mean $\Delta R/R = 0.18$) often has an extremely steep inner edge (mean $\alpha_{\rm in} = 56$) and shallower outer edge (mean $\alpha_{\rm out} = -8.6$), while the broad component (mean $\Delta R/R = 0.75$) has gradual slopes that extend to larger radii. Many of the discs described in this section have fractional widths that are much smaller than previously measured, likely because the low surface brightness of the broad halos skewed measurements at lower resolution. Although we report the FWHM of both the main belt and the halo throughout this section, as measured by the parametric models, we emphasise that the narrow/broad structure of these discs limits the efficacy of FWHM as a quantification of width.

We ran a single Gaussian for a selection of discs in this category with the lowest levels of extended emission to better understand the significance of this feature. Despite the single Gaussian parametrisation having the fewest number of parameters of any functional form in this paper, we find that the double Gaussian is strongly preferred over it in all cases that we tested. This indicates that the extended emission, while ambiguous in nature, is a significant feature in these discs and should be studied further.

We devote the rest of this section to discussing millimetre halos, although we reiterate that there could be unresolved low-amplitude rings in some of these systems. Theoretical models

have not typically predicted the narrow rings surrounded by extended millimetre emission that we find in this subset of the ARKS sample, although halos have been detected with optical and scattered-light observations in a large fraction of debris discs. Scattered-light halos are expected to consist primarily of small dust grains that are excited to high eccentricities by radiation pressure, which has only a negligible effect on the large dust grains observed in thermal emission. The detection of halos at longer wavelengths therefore suggests that a different dynamical process is responsible for these mm halos (Thebault et al. 2023).

Halos were first observed in millimetre emission by Marino et al. (2016) and MacGregor et al. (2018), which prompted Thebault et al. (2023) to re-analyse observations of halos in scattered light. They found that approximately 25% of scattered-light radial profiles with halos could not be explained by their models, which indicates that dynamical interactions may be responsible for the substructure, and predicted that higher-resolution ALMA observations would find more halos in thermal emission as well.

With the higher resolution of the ARKS sample, we now have evidence of narrow rings surrounded by millimetre halos in several targets, although more sensitive observations are necessary to confirm the nature of these features. All discs with low-level extended emission (7/7) described in this section are detected in scattered light as well, whereas a minority of single-ring discs (4/12) and multi-ring discs (2/5) are detected in scattered light (Milli et al. 2026). These detection rates may indicate that there are more small grains in systems with low-level extended emission. Approximately half (4/7) of discs with millimetre halos have scattered-light halos as well (HD 32297, HD 61005, HD 121617, and HD 131835, Thebault et al. 2023). Additionally, we find that this two-component radial structure is reminiscent of the vertical structure of the Kuiper Belt, in which two dynamical populations are present (Morbidelli et al. 2008). This may indicate that dynamical processes have shaped the discs, although further research is necessary to understand the mechanisms responsible for this substructure, which appears in approximately one-third of the ARKS sample.

(i) HD 10647 (q^1 Eri) [R_h]

The main features of our non-parametric profiles are broadly consistent with modelling based on prior observations (Lovell et al. 2021); however, we find that the outer edge slope abruptly becomes shallower at approximately 110 au, resulting a halo-like structure. This is notably different from the single-ring discs with potential shoulders, which show a steepening in slope from a plateau-like region to the outer edge. We note that the system hosts a giant planet at 2 au (Butler et al. 2006).

We parametrically modelled HD 10647 with a double power law, double Gaussian, and double power law with one gap. The AIC moderately prefers the double Gaussian, while the BIC moderately prefers the double power law. The double power law with a gap is not preferred by either criterion. Although we designate the double Gaussian as the best functional form and classify HD 10647 as a belt with a halo-like substructure, we emphasise that this previously unconstrained feature is ambiguous and that the eccentricity of the disc likely impacts our modelling efforts (Lovell et al. 2026). The main belt is centred at $89.2^{+0.7}_{-0.8}$ au with a width of $\Delta R = 28^{+2}_{-2}$ au, while the halo is centred at 164^{+6}_{-7} au with a width of $\Delta R = 108 \pm 7$ au. These results are consistent with observations by Lovell et al. (2021).

(ii) HD 61005 [$_hR_h$]

The disc appears to show emission both interior and exterior to the relatively narrow main belt, which is more similar to a "halo" than an additional ring according to our non-parametric models, although the `rave` profile and uncertainties suggest an additional faint outer and inner ring are also possible. Evidence of an outer halo (MacGregor et al. 2018; Han et al. 2025) or ring (Terrill et al. 2023) has also been suggested based on prior ALMA observations.

We parametrically modelled HD 61005 with a double power law, double Gaussian, and triple Gaussian. Both the AIC and the BIC find that the double power law is a significantly poorer fit. We find that the BIC significantly prefers the double Gaussian, while the AIC has no preference between the double Gaussian and triple Gaussian. The triple Gaussian recreates the same radial profile as the double Gaussian, which suggests that the faint outer and inner ring suggested by `rave` are not significant. We therefore designate the double Gaussian as the best functional form for this disc, which indicates the presence of a halo. Although MacGregor et al. (2018) previously observed the presence of a halo in HD 61005 with ALMA using shorter-baseline data, the higher resolution of the ARKS observations allows us to further constrain the locations and widths of the planetesimal belt and halo. Our parametric models find that the belt is narrower ($\Delta R = 17.4^{+1.2}_{-1.2}$ au) and centred at larger radius ($R = 69.4^{+0.5}_{-0.4}$ au) than MacGregor et al. (2018), while the halo is centred at 95^{+2}_{-3} au with a width of $\Delta R = 75 \pm 4$ au, extending across the planetesimal belt from ~20 to ~140 au. This suggests that the halo detected by ARKS observations is different than the halo measured by MacGregor et al. (2018), perhaps because of the difference in baselines.

(iii) HD 131835 [R^3, g_+ ($_hR_h, g_+$)]

Both the `frank` and `rave` fits suggest a narrow main ring with a low-amplitude inner ring and extended outer emission. The $83.7^{+0.9}_{-1.1}$ au radius fitted in REASONS (Matrà et al. 2025) is further out from the main belt than found from the non-parametric ARKS profiles, which peaks at 66 au, and is likely due to the presence of the extended outer emission.

It is not clear whether the outer emission is a separate ring or a halo attached to the main ring based on the non-parametric models. The `frank` profile suggests a shallow radial gap that separates the extended outer emission from the main ring; however, this gap is subtler in the `rave` profile and is contained within a region of large uncertainties. The outer emission at 100 au has been resolved to be the most prominent ring in scattered light using SPHERE (Feldt et al. 2017), whereas the main ring in ALMA at 65 au is significantly fainter in scattered light. The possible origin of this difference is discussed and modelled in detail in Jankovic et al. (2026). We tentatively label the disc as R^3, but note a likely alternative of $_hR_h$, given that parametric models (described below) favour describing the disc as a main belt with an extended halo.

We parametrically modelled HD 131835 with a double Gaussian, triple Gaussian, and double power law to explore three possible structures: an inner ring, an outer ring, and a halo, with the double power law acting as a benchmark for significance. The AIC and the BIC significantly prefer the other models to the double power law, indicating that the extended emission is significant. We find that the BIC significantly prefers and the AIC marginally prefers the double Gaussian over the triple Gaussian, indicating that the inner ring is not significant. Additionally, the double and triple Gaussian parametrisations both fit the inner emission at ~25 au as a part of the halo rather than a separate component, resulting in very similar radial profiles. This provides further evidence that the inner and outer components are not distinct from the main ring but rather part of a broad halo. We therefore designate the double Gaussian as the best functional

form for this disc. The main ring is centred at $R = 68.6 \pm 0.4$ au with a width of $\Delta R = 11.5^{+1.4}_{-1.4}$ au, while the halo is centred at $R = 105.8^{+2.0}_{-1.7}$ au with a width of $\Delta R = 102^{+3}_{-4}$ au. The main ring is much narrower than measured by REASONS ($\Delta R = 87 \pm 4$ au, Matrà et al. 2025), likely due to the previously unresolved broad component.

(iv) HD 121617 [R_h, g_+]

Our non-parametric profiles fitted with both `frank` and `rave` suggest a single narrow belt. Low-level emission possibly extends out to at least twice the belt radius on the outer edge. The belt radius is consistent with modelling based on previous observations (Moór et al. 2017).

We parametrically modelled HD 121617 with a double Gaussian, single Gaussian, power law + error function, double power law, and asymmetric Gaussian. Although we find that the asymmetric Gaussian and single Gaussian provide significantly poorer fits to the data according to both the AIC and the BIC, the statistical criteria differ on the significance of the other three functional forms: the AIC strongly prefers the double Gaussian (which models a halo), but the BIC strongly prefers the power law + error function. The double power law is not ruled out either. We report results for all three functional forms, although we designate the double Gaussian as the best parametric model for the disc based on a visual evaluation of the radial profiles (Fig. E.1). This indicates that the low-level emission found by the non-parametric profiles and by the double Gaussian functional form is of ambiguous significance at the S/N of the data.

As parametrised by the double power law, this disc has steep inner ($\alpha_{\rm in} > 20$) and outer ($\alpha_{\rm out} = -6.9^{+0.2}_{-0.4}$) edges, similar to those found in scattered light by Perrot et al. (2023). We find comparable central radii with the double power law ($R_{\rm c} = 68.5^{+0.7}_{-0.5}$ au), power law + error function ($R_{\rm c} = 67.8^{+0.6}_{-0.4}$ au), and double Gaussian ($R = 75.3^{+0.4}_{-0.3}$ au). As parametrised by the double Gaussian, the main ring is centred at $R = 75.3^{+0.4}_{-0.3}$ au with a width of $\Delta R = 14.1^{+1.2}_{-1.2}$ au, while the halo is centred at $R = 103^{+8}_{-5}$ au with a width of $\Delta R = 100^{+20}_{-20}$ au. The main ring is much narrower than measured by REASONS (Matrà et al. 2025), likely due to the previously unresolved broad component.

(v) HD 32297 [R_h^2, g_+ (R_h, g_+)]

The `frank` and `rave` profiles show a narrow ring with a faint outer halo, consistent with suggestions based on prior ALMA observations (MacGregor et al. 2018). The non-parametric models also suggest the presence of inner emission, likely as a separate faint ring component interior to the main belt, although it is not significantly detected in parametric models.

We parametrically modelled this disc with a double power law as a default model, a double Gaussian to explore the presence of a halo, and a sum of a Gaussian and a double power law to explore the presence of an inner component suggested by non-parametric modelling. We find strong evidence that the double Gaussian does not fit the data well, according to both the AIC and the BIC. Although the AIC marginally prefers a Gaussian with a double power law, the BIC significantly prefers the simpler structure provided by a double power law. We therefore designate the double power law as the best parametric model, but we note that higher-resolution observations may be necessary to further constrain the radial substructures present in this disc, including the outer halo and inner emission suggested by the non-parametric models. As parametrised by the double power law, HD 32297 is centred at $R_{\rm c} = 105.2^{+0.7}_{-0.5}$ au with a width of $\Delta R = 14.1^{+0.6}_{-0.6}$ au, significantly narrower than measured by REASONS (Matrà et al. 2025). The discrepancy in width is more characteristic of discs with halos, and the low-amplitude emission found by the non-parametric models – although not significantly detected by the parametric models – may have skewed measurements at lower resolution toward a broader width. The inner ($\alpha_{\rm in} > 27$) and outer edges ($\alpha_{\rm out} = -6.3 \pm 0.12$) are among the steepest found in the ARKS sample.

(vi) HD 131488 [R^2, g_+ ($_hR_h, g_+$)]

Previous continuum maps observed at lower resolution were modelled by a ring at 84±3 au (Moór et al. 2017), consistent with the radius of the very narrow ring resolved here. Both `rave` and `frank` resolve a small bump at approximately 50 au, interior to the inner edge of the main belt. A slight outer bump in the `frank` profile is not reproduced in the `rave` fit.

We parametrically modelled HD 131488 with a double power law to recreate a simple belt, a double Gaussian to recreate a halo, and a triple Gaussian to recreate a halo as well as the inner bump resolved by `rave` and `frank`. Both the AIC and the BIC strongly prefer the double Gaussian parametrisation to the double power law and to the triple Gaussian, indicating that the halo is significant. We therefore designate the double Gaussian as the best functional form for this disc. The profile produced by the double Gaussian (Fig. E.1) suggests that the inner bump resolved by the non-parametric models and the outer bump found by `frank` is part of a broad halo. The main ring is centred at $R_c = 90.84^{+0.18}_{-0.08}$ au with a width of $\Delta R = 2.3^{+0.7}_{-0.4}$ au, while the halo is centred at $R = 96.1^{+0.6}_{-0.7}$ au with a width of $\Delta R = 45 \pm 4$ au. Although the location of the main ring is consistent with previous modelling in both thermal emission and scattered light (Moór et al. 2017; Pawellek et al. 2024; Matrà et al. 2025), the ring is much narrower with the ARKS modelling, likely due to the previously unresolved broad component. However, we note that the width of the main ring measured by ARKS is smaller than the angular resolution of the data (with a beam size of 6 au, Marino et al. 2026). We therefore consider the width to be marginally resolved, as it appears to be smaller than the resolution of the data.

(vii) HD 109573 (HR 4796) [R_h]

We find a narrow belt consistent with previous modelling based on lower-resolution observations (Kennedy et al. 2018), with possible very low-level emission on the outer edge. We parametrically modelled HD 109573 with a double Gaussian, single Gaussian, and double power law. Both the AIC and the BIC strongly prefer the double Gaussian parametrisation over the double power law and the single Gaussian, indicating the presence of a halo. The main ring is centred at $R = 77.61^{+0.04}_{-0.16}$ au with a width of $\Delta R = 6.8^{+0.4}_{-0.4}$ au, while the halo is centred at $R = 84^{+2.1}_{-1.8}$ au with a width of $\Delta R = 52 \pm 9$ au. The main ring is much narrower than measured by REASONS (Matrà et al. 2025), likely due to the previously unresolved broad component.

3.2. Quantifying disc features

The results of Sect. 3.1 show that there is a great diversity of radial profiles observed across the sample. One way to systematically characterise the radial properties of the sample is to quantify features of interest, including the width of each ring and its inner and outer edges, in a way that is analogous to what has been performed for protoplanetary discs (Huang et al. 2018). We performed these measurements with both the non-parametric profiles, as represented by the `frank` surface density profiles, and the best fitting parametric model selected with the AIC and BIC. We describe the approach used for the non-parametric models here; for the use of parameters from the parametric models; see Sect. 2.4.

Table 2. Gap location and widths, and inferred single planet masses.

Target	Gap	$r_{\rm gap}$ (au)	$\Delta r_{\rm gap}$ (au)	$M_{\rm pl}$ ($M_{\rm J}$)	Consistent with direct imaging
HD 15115	1	$79.3^{+4.0}_{-4.3}$	$22.2^{+0.7}_{-0.6}$	$0.37^{+0.09}_{-0.07}$	Y
HD 32297	1	$79.9^{+6.4}_{-8.5}$	$35.4^{+1.3}_{-1.2}$	$2.0^{+0.9}_{-0.6}$	Y
HD 92945	1	$72.6^{+4.7}_{-4.1}$	$19.6^{+2.3}_{-1.7}$	$0.20^{+0.10}_{-0.07}$	Y
HD 107146	1	$57.3^{+2.8}_{-1.8}$	$12.3^{+0.6}_{-0.6}$	$0.11^{+0.03}_{-0.02}$	Y
	2	$79.2^{+3.1}_{-2.6}$	$18.9^{+2.7}_{-1.4}$	$0.15^{+0.07}_{-0.05}$	Y
HD 131488	1	$69.4^{+3.6}_{-6.2}$	$26.1^{+1.0}_{-0.8}$	$1.3^{+0.4}_{-0.3}$	Y
HD 131835	1	$42.2^{+6.8}_{-9.1}$	$25.2^{+3.3}_{-3.9}$	$6.3^{+8.6}_{-3.5}$	Y
	2	$84.8^{+4.9}_{-4.2}$	$18.9^{+2.3}_{-1.8}$	$0.20^{+0.10}_{-0.07}$	N
HD 197481	1	$17.0^{+3.6}_{-6.0}$	$14.1^{+2.1}_{-1.4}$	$7.1^{+16.7}_{-4.5}$	N
	2	$32.5^{+1.8}_{-1.8}$	$4.1^{+1.3}_{-1.2}$	$0.010^{+0.015}_{-0.007}$	Y
HD 206893	1	$73.5^{+10.8}_{-12.0}$	$40.4^{+4.6}_{-4.3}$	$3.7^{+3.6}_{-1.8}$	Y

Notes. Gap location and widths are measured from the `frank` surface density profiles. The planet masses correspond to a single planet required to clear the measured widths (see Eq. (1)). These values are not tested for consistency with the gap depth. The rightmost column lists whether such a planet is consistent with current constraints from the available direct imaging observations based on the detection probability maps in Milli et al. (2026), i.e. 'Y' means not expected to be detected by available observations at 50%.

For discs with a single ring, we measured the peak radius and the radii where the inner and outer edges reach 25, 50, and 75% of the peak, respectively. For discs with multiple rings, it may not be appropriate to assume that the base of the belt is at a surface density of 0, given that neighbouring belts could superimpose. For each ring within a multi-belt disc, we measured its peak radius and treated the inner and outer edges separately when measuring the radius of 25, 50, and 75% surface density for either edge. For either edge of the ring, if the edge immediately borders a radial gap, the baseline surface density value was assumed to be the local minimum value of the gap; otherwise, the edge of the ring is assumed to be the edge of the entire disc and the baseline surface density value was assumed to be 0. The radii of 25, 50 and 75% surface density were measured as percentages of the difference between the peak surface density of the gap and the baseline.

We used the 50% radii at the inner and outer edges to calculate the FWHM of the disc, and the difference between the 25 and 75% radii of either edge to define the width of the edge (the inverse of it being the slope of the edge). The ring location was defined using the centroid radius of the disc if the disc only has a single ring, or the peak radius of the ring if the ring is in a multi-belt system. The inner and outer edge locations were defined using the 50% radii of the edge. These measurements also enable the characterisation of the radial gaps found between neighbouring rings. We used the local minimum within the gap to define its location, and the 50% radius of the outer/inner edge of the inner/outer neighbouring rings of each gap to define the width of the gap. The measurements of these disc features are summarised in Tables I.1 and 2, which will be studied at the population level in the following section. Fig. I.1 provides a visualisation of the slope and width measurements on the radial profile.

3.3. The prevalence of substructures and distribution of fractional widths

The radial profiles described in Sect. 3.1 demonstrate that substructures are prevalent in the sample. We find that 5/24 discs show strong evidence of multi-ring structures and 7/24 are single rings with evidence of additional low-amplitude rings or extended halos. The two categories together account for 50% of the sample, meaning that the radial structure of half the sample cannot be simply described by a single ring. Even for the single-ring discs, potential features such as shoulders and inner and outer edge asymmetries suggest that the incidence rate of substructures could be even higher.

These findings provide an updated understanding of debris disc structures, both in terms of the basic properties such as the fractional width of rings in debris discs and the prevalence of substructures. The REASONS sample contains the most complete set of debris discs resolved by ALMA (though biased towards bright discs), which have been modelled by assuming that they follow Gaussian radial profiles, which is appropriate given its more limited sensitivity and resolution (Matrà et al. 2025).

Fig. 5 shows the distribution of the fractional width of debris discs based on the REASONS and ARKS samples. Discs in the REASONS sample with relative uncertainties on the fractional width that are larger than 50% (i.e. HD 15257 and TYC 9340-437-1) have been excluded. HD 36546 was also excluded as the disc was centrally peaked and a Gaussian fit did not adequately measure its fractional width (Matrà et al. 2025). The subset of REASONS values for discs that are also covered by ARKS is distributed similarly to the full REASONS sample. The updated distribution based on the ARKS dataset, however, is shifted significantly towards the narrower end while also retaining the wide end, almost exhibiting a bimodal distribution overall. The different between the REASONS and ARKS fractional widths is largely because previously unresolved (sub)structure such as multiple rings could result in REASONS measuring wider rings, and the presence of low surface brightness, extended emission could cause the same effect when observing at lower resolution. We discuss the implications of these findings in more detail in Sect. 4.

4. Discussion

In this section we discuss several implications of our findings in the context of both debris disc formation from protoplanetary discs and the dynamical interaction between planets and the debris disc in mature planetary systems. Section 4.1 compares the rings seen in debris discs with those in protoplanetary

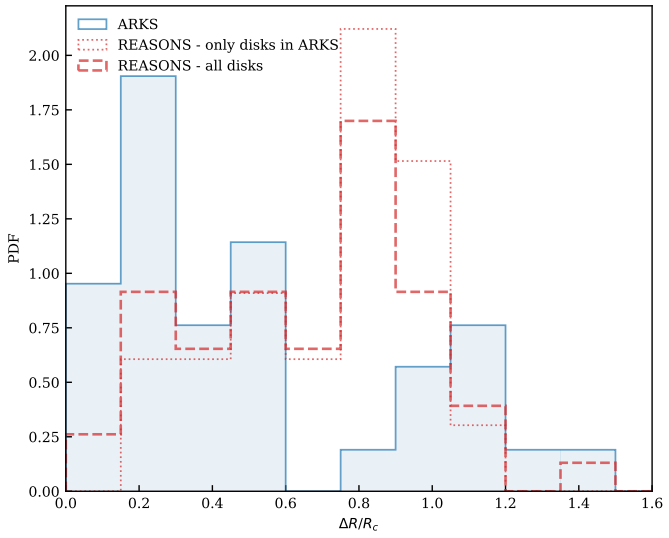

Fig. 5. Comparison between the distribution of fractional widths found from the REASONS (Matrà et al. 2025) and ARKS datasets. The vertical axis shows the probability density function (PDF). Discs found to have multiple rings in ARKS are separated into their constituent rings. Two distributions are shown for REASONS, which correspond to the distribution of all REASONS discs, and the REASONS values for discs that overlap with those in ARKS respectively. REASONS discs with fractional uncertainties greater than 0.5 have been excluded from the REASONS distributions.

discs. Section 4.2 explores any potential correlations between structural features among debris discs. Sections 4.3 and 4.4 place constraints on potential perturbing planets based on any radial gaps and the slope of the inner edge of debris discs in the sample. Section 4.5 constrains the eccentricity dispersion of planetesimals based on the outer edge slope. We note that we expect follow-up studies to perform more detailed dynamical modelling to interpret the disc structures more wholistically than is considered here.

4.1. Comparison with protoplanetary discs

Prior to the analysis based on the ARKS sample, the distribution of the fractional widths of rings in debris disc appeared to peak at approximately 0.8 to 1.0, with a median of 0.71 and 70% of the discs with fractional widths of above 0.5 (Fig. 5, Matrà et al. 2025). This is significantly larger than the fractional widths of rings in protoplanetary discs, which exhibit a median fractional width of 0.29, with 24% of rings characterised by a fractional width larger than 0.5 based on the sample of resolved protoplanetary discs compiled by Bae et al. (2023). It has been unclear whether this trend is due to the low resolution of these debris disc observations or reflects an evolutionary process occurring between the protoplanetary and debris stages.

The higher-resolution observations in the ARKS dataset have significantly shifted this distribution towards smaller fractional widths (Fig. 5). A comparison of the fractional widths between the protoplanetary and debris ring populations is shown in Fig. 6. Based on our non-parametric (`frank`) modelling, we find a median fractional width of 0.40 for debris disc rings, with 37% being wide (13/35 rings across the 24 discs with $\Delta R/R_c > 0.5$). The parametric modelling offers a slightly more conservative classification of whether a disc hosts multiple belts via rigorous model comparison with statistical criteria such as the

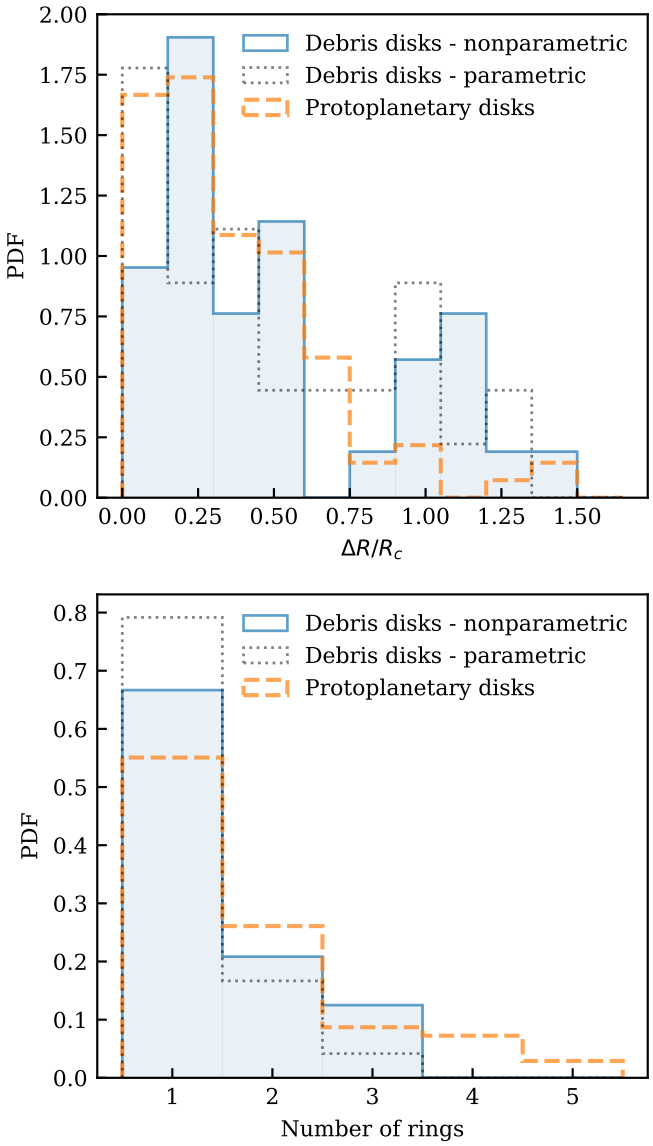

Fig. 6. Comparison between rings in debris discs from ARKS and the sample of resolved protoplanetary discs compiled by Bae et al. (2023). Discs with multiple rings are separated into their constituent rings. The top panel shows the distribution of fractional widths, where both the distributions derived from `frank` and parametric modelling are shown for debris discs. The bottom panel shows the distribution of the number of rings in a disc, where the ring counts in debris discs are based on the `frank` profiles, as labelled in Fig. I.1.

AIC and BIC, finding a median fractional width of 0.33, with 40% of the rings (12/30 rings) being wide. The distribution of fractional widths derived from the non-parametric and parametric approaches are in broad agreement, as shown in Fig. 6. These results suggest that, compared to the REASONS distribution, which is abundant in fractionally wide discs, the updated distribution based on ARKS is significantly shifted towards fractionally narrower discs, and is more similar to the distribution of protoplanetary discs than previously thought, particularly within the range of fractional widths between 0 and 0.8.

The large overlap between debris disc and protoplanetary disc fractional width suggests that in some cases, the debris rings may inherit the general distribution seen in the protoplanetary phase. The prevalent concentric rings in protoplanetary

discs (Andrews et al. 2018) have been interpreted as either gaps carved by newly formed planets (Dong et al. 2015), or local pressure bumps formed through instabilities (e.g. Flock et al. 2015) but could nonetheless be conducive to planetesimal formation (Stammler et al. 2019; Miller et al. 2021) by trapping dust and undergoing streaming instabilities (Youdin & Goodman 2005). These rings could therefore be the predecessors of the planetesimals producing mm dust that we observe in debris discs, resulting in debris discs that inherit protoplanetary disc structures (Marino et al. 2018, 2019).

However, given the presence of a population of debris disc rings which are significantly fractionally wider than their protoplanetary counterparts, this is unlikely to explain all discs. Planets likely play a significant role in setting the location and width of the planetesimal belts that form from protoplanetary rings (Wyatt et al. 2015). Simulations have suggested that dust traps could produce planetesimals while moving, which could occur due to planet migration, leaving a trail of planetesimals in their path that span a wide range of radii and form a planetesimal belt with a large fractional width (Miller et al. 2021). Even in the absence of planet migration in protoplanetary discs, other simulations have found that planets could eventually scatter the ring and leave a fractionally wider planetesimal belt, whereas inward migration of the newly formed planet away from the ring could sustain the ring for longer and potentially leave a fractionally narrower planetesimal belt (Jiang & Ormel 2023). The exact effect of planet migration therefore appears to be nuanced as suggested by both the differing setups in these theoretical studies and the large range of debris ring widths observed in reality, and one that would require further theoretical work to more clearly explain.

We discuss a few caveats related to the comparison above. Firstly, the debris disc and protoplanetary disc samples are not studied with uniform resolution. However, typical resolutions in protoplanetary disc surveys (e.g. 5 au for high-resolution observations such as DSHARP, Andrews et al. 2018) can be comparable to ARKS resolutions (which lie between 4 au and 36 au). The fractional widths derived for debris discs in this study are deconvolved, whereas the protoplanetary disc values are generally not (Huang et al. 2018; Bae et al. 2023). Jennings et al. (2022a) found that the ring widths recovered by `frank` in the DSHARP sample are on average 26% narrower than by `CLEAN`. This could mean that the protoplanetary disc fractional widths used here are biased to be slightly larger than they are. However, this should not fundamentally shift the conclusions of the comparison discussed here, since the fractional ring width distribution of protoplanetary discs is relatively wide, and reducing their values by approximately one quarter would still result in a distribution comparable to that of the fractionally narrow population of debris discs.

Secondly, while there exists the possibility that the discs in our sample could still consist of more unresolved rings, our `frank` resolution tests (benchmarking the fractional width recovered when observing an infinitesimally thin ring, as described in Sect. 3.1) suggest that if the broad discs were to consist of 2–3 very narrow rings instead, our observations should have resolved these radial substructures (although if they were to consist of a large number of rings, e.g. $\gtrsim$10 rings, these very narrow rings would not have been individually resolved). The presence of the fractionally broad population of debris disc rings is thus likely to be real.

Thirdly, the protoplanetary disc sample of Bae et al. (2023) contains a higher fraction of lower-mass stars (with a median stellar mass of 0.9 $M_\odot$) than the ARKS sample (with a median stellar mass of 1.6 $M_\odot$), which could bias the protoplanetary discs in this comparison to be at smaller radii. However, we find that when comparing only the A stars (for which the ARKS sample is most abundant in) to control for the effect of stellar mass (including only protoplanetary disc host stars with masses equivalent to those of main-sequence A stars), the findings based on the comparison of fractional width distribution still hold, although in a less robust way given the more limited sample size.

Relatedly, this comparison loosely assumes that the protoplanetary and debris discs observed are from the same population and offset only in time, i.e. the protoplanetary discs in the Bae et al. (2023) sample will evolve into debris discs analogous to those in the ARKS sample. In practice, the evolutionary pathway could be diverse. For example, a number of possible formation and evolutionary pathways of debris discs could exist (Michel et al. 2021; Najita et al. 2022), and the observed debris discs could represent only the population of systems emerging from bright and extended protoplanetary discs. A broader range of evolutionary pathways could, therefore, also exist, but may not be captured by the sample studied here.

Finally, it is important to note that this comparison relies on defining the width of a belt based on its FWHM. Low-amplitude extended emission, which we have found to be common in the sample as discussed in Sect. 3.1, is not accounted for by the FWHM metric. If we are to more wholistically connect protoplanetary rings to debris rings, the formation of the broad faint distributions in debris discs will also need to be accounted for.

4.2. Ring width correlations

In addition to the comparison between debris discs and protoplanetary discs, the relatively large span in age of the ARKS sample allows us to investigate the evolution of debris discs subsequent to their formation from protoplanetary discs. Fig. 7a displays the fractional widths of all discs in the ARKS sample measured from the `frank` profiles as a function of the centroid radius. A positive correlation is seen among the single-ring systems (at 3.3σ, which is important to isolate from the multi-ring systems given that some of the low-amplitude rings from non-parametric modelling are of lower significance than the main belts), and at lower significance when all rings in multi-ring systems suggested by non-parametric (`frank`) fits are also considered (at 1.9σ), where the significance was estimated using the ratio between the least-squares slope and its standard error when fitting a linear model in logarithmic space. This suggests that wider discs are not only wider in absolute terms, but they are also fractionally wider, i.e. with the larger radius adjusted for.

Age appears to be a basis for this correlation. Figs. 7b and c display the radius and fractional widths as a function of age, and both tentatively increase with age (at 2.4σ and 2.0σ respectively, where the significance is effectively unchanged even if the only M star, AU Mic, is removed in panel b). The increase in age of the fractional width in panel c also holds when the rings from multi-ring systems are also included (at 2.6σ). In Fig. 7b, the black dashed line indicates the evolution of the radius of peak optical depth expected in self-stirred discs (Kennedy & Wyatt 2010). A positive correlation between fractional width and age has previously been observed among relatively well-resolved ALMA images (Han et al. 2025), though not among the full REASONS sample (Matrà et al. 2025). Analysing the REASONS fractional width measurements based on only its subsample that constitute the ARKS sample (excluding the 2 discs with relative uncertainties above 50%), there is no correlation between the fractional width and age for the ARKS single rings (at 0.1σ) and only a weak correlation for all rings (modelled as single Gaussians,

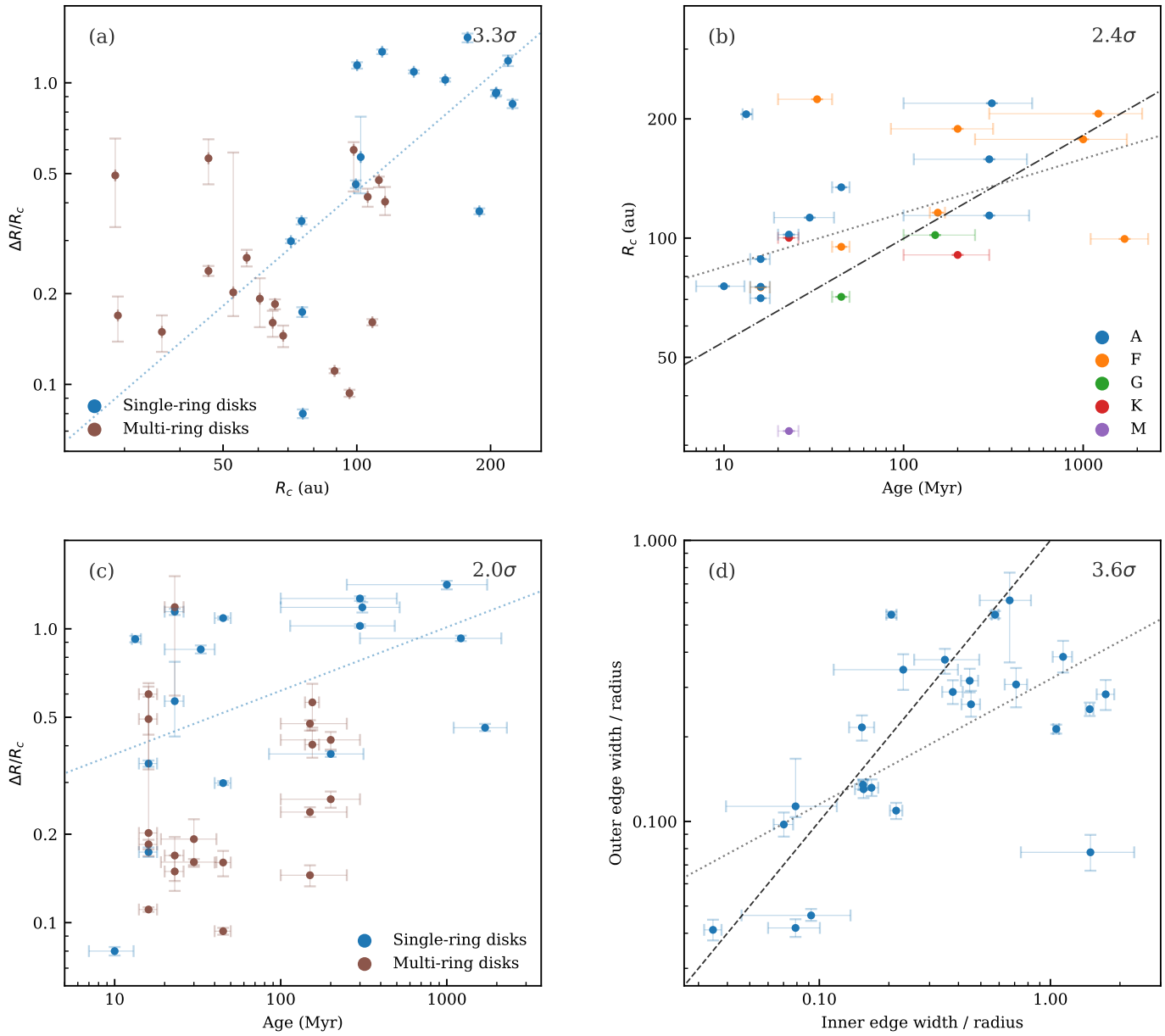

Fig. 7. Radial properties across the ARKS sample. Linear models were fitted in linear or log space (as appropriate for the way the data in each panel are plotted) and displayed as dotted lines. The significance is evaluated as the ratio of the slope to its uncertainties, as displayed in the upper right corner of each panel. In panels a and c, the linear model shown is that fitted to single-ring discs only, whereas in panels b and d, the line is fitted to all points. In panel b, the dash-dotted line has a slope of 6/23, as predicted for self-stirred discs (Kennedy & Wyatt 2010). In panel d, the dashed line indicates where the fractional inner and outer edge widths are equal. The width of an edge is defined as the number of au for the radial profile to rise (fall) from 25 (75%) to 75% (25%) of the peak, and the radius of an edge is defined as where the radial profiles crosses 50% of the peak.

at 1.5σ). The lower significance among the REASONS sample could either reflect the fact that the REASONS modelling included a sizeable fraction of marginally resolved discs, or that the tentative correlation found in ARKS is affected by a biased sample.

Also seen across this sample (but not plotted) is a weak negative correlation between fractional width and dust mass, which could be explained by the decreasing dust mass with age due to collisional depletion (Dominik & Decin 2003; Wyatt et al. 2007a; Löhne et al. 2008; Holland et al. 2017). The anti-correlation may also be consistent with theoretical expectations based on planet-induced secular stirring of self-gravitating discs (Sefilian 2024). Tentative positive correlations are also seen between the fractional inner and outer widths and the fractional width of the belt (and therefore with age), resulting in an apparent coordinated evolution of the radial profile. However, as noted in earlier discussion, the majority of radial profiles appear to be asymmetric. Although the fractional inner and outer edge widths appear to be correlated with each other across the sample, we find that the fractional inner edge width appears to be more typically broader than the fractional outer edge width, as shown in Fig. 7d. We note that these fractional edge widths correspond to their absolute width divided by the edge location, rather than the centroid location of the whole belt, thereby accounting for the

difference in location of the inner and outer edges. This finding could arise from a higher dynamical excitation close to the inner than outer edges which would make inner edges appear smoother than the outer edges (Marino 2021).

The overall picture in this sample therefore appears to be that the disc radially broadens while its centroid moves further out over timescales of the order of ~100 Myr. Collisional evolution could cause the peak emission to propagate to larger radii over time as the inner regions of the disc are collisionally depleted over faster timescales (Kenyon & Bromley 2008; Kennedy & Wyatt 2010; Imaz Blanco et al. 2023). Similarly, collisional evolution could also cause the smaller discs to collisionally deplete below the detection threshold faster, resulting in the average radius of a population of narrow belt debris discs to increase with age (Wyatt et al. 2007b). However, it is not clear that this could also explain any potential increase in fractional widths observed. It is possible that the fractional width increase could relate to the scattering between planetesimals or by planets. The fractionally shallower inner edge relative to outer edge could reflect a larger eccentricity dispersion closer to the inner system, or that the effect of collisional evolution, which tends to make the surface density converge to a power law index of 2 (Marino et al. 2017; Imaz Blanco et al. 2023). However, it is important to note that the more extended halos, which could correspond to higher-eccentricity components on the outer edge, may not be fully captured by the edge width measurements, which are not affected by low-level emission under 25% of the peak surface density of the belt.

Of the 5 gas-rich debris discs (HD 121617, HD 131835, HD 131488, HD 32297, and HD 9672), 4 are classified as narrow discs. Conversely, among the 5 fractionally narrowest single-ring discs (R and R_x), 4 are gas-rich. These gas-bearing discs are young (<50 Myr). On top of the potential fractional width and age correlation, this tentative correlation between narrowness and the presence of gas could potentially also relate to the concentration of dust due to gas drag (Olofsson et al. 2022). Gas has also been detected in β Pic's relatively broad disc, although the gas mass is relatively low. The gas-rich debris discs are discussed in more detail in an accompanying paper (Mac Manamon et al. 2026).

4.3. Planet constraints from gaps

The radial profiles derived in this study enable detailed dynamical modelling in each individual system to infer their planetary architecture. We expect dedicated work in future studies to model potential interactions between the disc and unseen planets in more detail; however, it is possible to make some simple predictions based on several basic assumptions.

In part motivated by the recent example of a potential planet in a debris disc gap (Lagrange et al. 2025; Crotts et al. 2025), if we were to assume that all gaps identified in the sample are created by a single planet which formed in situ on a circular orbit, and that the mechanism of gap clearing is scattering driven by the chaotic evolution due to the overlap of first-order mean-motion resonances, then it is possible to use the width of each gap to estimate the mass of the corresponding planet clearing the gap. The total width of the chaotic zone (i.e. summed over the chaotic regions both interior and exterior to the planet's orbit) is described by

$$\Delta a \approx 3 a_{\rm pl} \left(\frac{M_{\rm pl}}{M_*} \right)^{2/7}, \quad (1)$$

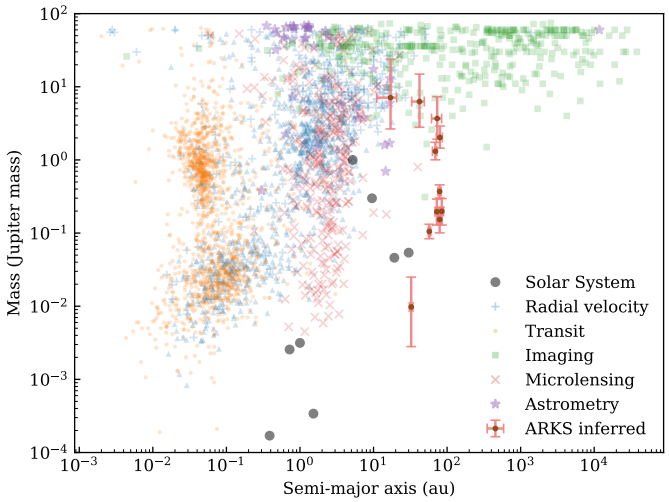

Fig. 8. Planet population inferred from the ARKS sample (red points) assuming all gaps suggested by non-parametric (`frank`) profiles are cleared by a single planet due to overlap of first-order mean motion resonances, overplotted on the sample of confirmed exoplanets observed with common detection methods as of March 2025 (retrieved from exoplanet.eu).

where $a_{\rm pl}$ is the semi-major axis of the planet, $M_{\rm pl}$ is the mass of the planet and M_* is the mass of the star (Wisdom 1980; Morrison & Malhotra 2015). Assuming this relation, we mapped the disc widths listed in Table 2 to the planet masses required to produce the gaps under these assumptions, which are overplotted on the population of known exoplanets[3] in Fig. 8. The orbit of these hypothetical planets lie between 20 and 80 au and their masses range widely from a few Earth masses to a few Jupiter masses. They are typically near the edge of or below current direct imaging limits.

It is important to emphasise a few caveats on the nuances that this basic analysis ignores. Firstly, these mass estimates are not tested for compatibility of the depth of the gap and are based solely on its width. It is possible that some of the masses estimated from the gap width are high enough to clear a deeper gap than that observed over the age of the system, thus making it unlikely for such a planet to exist in the gap. For these shallower gaps, a chain of lower-mass planets may be more likely than a single higher-mass planet (Shannon et al. 2016); however, planetesimal-driven migration of planets could also complicate such a picture (Morrison & Kratter 2018; Friebe et al. 2022).

Secondly, it is also important to recognise that the multi-ring structures that we find in the ARKS sample could also be inherited from the protoplanetary disc phase in which the dynamical evolution is shaped by gas, rather than purely by planet clearing as has been assumed here (see discussion in Marino et al. 2019). Mean motion resonances beyond the chaotic zone (Tabeshian & Wiegert 2016), secular interactions (Pearce & Wyatt 2015; Zheng et al. 2017; Yelverton & Kennedy 2018; Sefilian et al. 2021, 2023) and low-mass planets migrating through the disc (Morrison & Kratter 2018; Friebe et al. 2022) could also play a major role in clearing material both close to the planet and at more distant locations, thereby further complicating the picture. It is, therefore, important for future work to systematically model the radial profile, rather than only the gap location and its width

[3] Retrieved from `exoplanet.eu`.

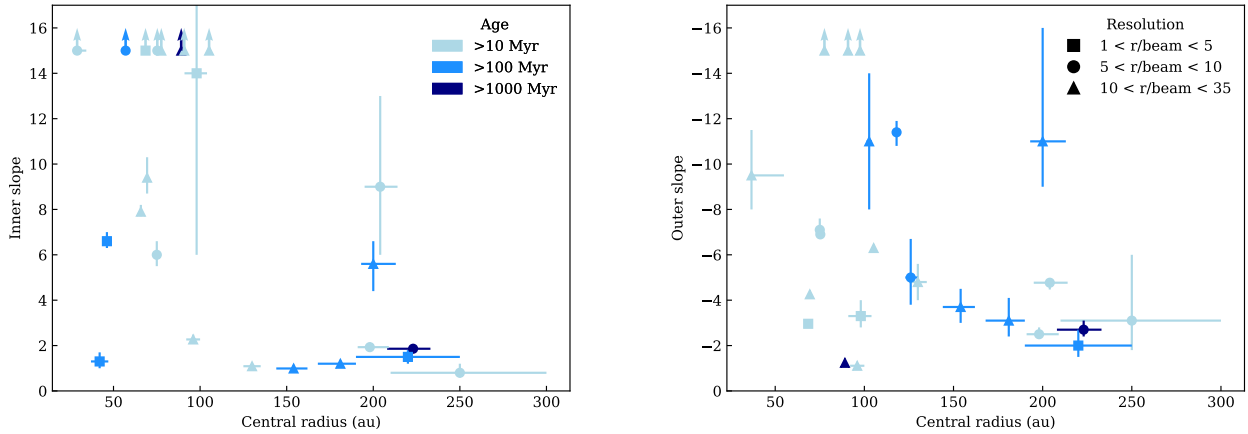

Fig. 9. Sharpness of inner and outer slopes as a function of distance from the host star. The slopes are measured with a double power law or triple power law ($\alpha_{\rm in}$ and $\alpha_{\rm out}$), while the central radii are measured with a double power law ($R_{\rm c}$) or multiple Gaussians (R). For discs with multiple rings, only the innermost ring is plotted on the left and only the outermost ring is plotted on the right; for discs with halos, only the main planetesimal belts are plotted. This is due to the limitations of power-law parametrisations. The colours indicate the age of the system (Table A.2 in Matrà et al. 2025), while the marker shapes indicate the resolution of the ARKS observations (Table 2 in Marino et al. 2026). Discs with median power-law indices greater than 15 – the cut-off for pure planet sculpting of the inner edge – are indicated by arrows for both plots. We note that the x-error bars on the steepest discs are too small to be seen.

as performed in this study, to reach a more comprehensive conclusion on potential planetary configurations consistent with the disc structures observed.

Finally, available direct imaging observations already provide constraints on the range of possible planets within these systems. Based on the detection probability maps computed in Milli et al. (2026), one hypothetical planet in Table 2 (in the inner gap of HD 197481, or AU Mic) should have been detected by SPHERE with 95% probability, although considering the uncertainties on the planet mass and orbit, the detection probability could be at 50% or lower. Another possible planet (in the inner gap of HD 131835) should have been detected by SPHERE with a probability between 50 and 95%, and the detection probability could be lower than 50% considering uncertainties on the constraints on such a planet. The detection probabilities of all other such gap-inferred planets in Fig. 8 are lower than 50%.

4.4. Trends in the steepness of the inner edge

The sharpness of the inner edges of debris discs can indicate sculpting by planets (e.g. Quillen 2006; Chiang et al. 2009; Pearce et al. 2024). We compare the slopes of the ARKS targets based on the results of power law parametrisations, with gaps added as necessary. Although double power laws and triple power laws did not provide the best fit to the data for several discs, we find that the models can still place constraints on the slopes. Because the implementation of the double power law described in Table 1 is smooth across radii, we additionally tested whether introducing a sharp cut-off on the inner and outer edges would affect the power law indices. We found that this did not impact the values obtained for the indices. We therefore take $\alpha_{\rm in}$ and $\alpha_{\rm out}$ values from double power law fits in most cases, except for HD 92945, HD 107146, HD 197481, TYC 9340-437-1, and HD 218396, where a triple power law provided a better fit to the data according to the AIC and the BIC.

We find a bimodal distribution of inner slopes: discs that are closer to their host stars ($R_{\rm c} < 100$ au) have sharper inner edges ($\alpha_{\rm in} > 15$), while discs that are further out have shallower inner edges (Fig. 9). We propose four explanations for these results, although we emphasise that self-stirring and secular interactions may also play an important role in shaping inner edges.

First, planets may be more likely to have orbits closer to their host stars, so the sharp inner edges observed in discs at smaller radii might simply reflect the underlying distribution of planet semi-major axes. Direct imaging has shown that planets at large distances from their host stars are rare (Vigan et al. 2021; Currie et al. 2023), so discs at large radii may not experience planet truncation to the same extent as discs at small radii, or the timescale for sculpting inner edges at large radii may simply be too large: For example, a Jupiter-mass planet located just interior to a disc will truncate an inner edge at 50 au in 3.9 Myr and an inner edge at 200 au in 31 Myr (from Eq. (3) in Pearce et al. 2024).

Second, secular resonances can allow planets to sculpt the inner edges of discs at large radii (Zheng et al. 2017; Sefilian et al. 2021, 2023; Pearce et al. 2024), but these discs may experience excitation that flattens the inner edge or may not have visibly sharp inner edges due to delays related to the distance from the host star.

Third, collisional evolution may be responsible for the shallow inner edges we observe in debris discs at large radii. Models by Marino et al. (2017) and Imaz Blanco et al. (2023) have shown that the inner regions of debris discs lose material faster, resulting in a power law index of $\alpha_{\rm in} \approx 2$. As seen in Fig. 9, most discs centred at large radii in the ARKS sample have inner slopes consistent with those expected from collisional evolution.

Fourth, these discs with large radii and shallow slopes are the only systems in the ARKS sample with directly imaged planets. It is possible that the presence of a massive planet shaped the radial structure of these discs, creating shallow slopes.

The higher resolution of the ARKS observations finds much steeper inner edges than previous studies of debris discs. Although Pearce et al. (2024) found that many debris discs observed at lower resolutions have inner edges that are too flat to be explained by planet sculpting alone, we calculate that seven discs in the ARKS sample have inner edges that are steep enough to constrain planet masses. The maximum flatness of $\sigma_i \leq 0.05$ derived by Pearce et al. (2024) for pure planet sculpting corresponds to a power-law index of $\alpha_{\rm in} \geq 15$, due to the inverse

Table 3. Planet sculpting constraints for the seven discs with the steepest inner edges in the ARKS sample.

Disc	α_{in}		M_{pl}	a_{pl}
	`frank`	Parametric	(M_J)	(au)
HD 10647	5.4	>18	<2.5	<48
HD 32297	22	>27	<1.0	< 74
HD 107146	14	>13.91	<5.0	<32
HD 109573	28	34^{+5}_{-3}	$0.68^{+0.30}_{-0.18}$	<50
HD 121617	14	>20	<3.1	< 49
HD 131488	22	28^{+5}_{-4}	$1.2^{+0.6}_{-0.5}$	<63
HD 197481	14	>14	<3.2	<19

Notes. Non-parametric slopes are derived from the inner edge definitions in Table I.1.

relationship between the parameters:

$$\sigma_i = \sqrt{\frac{2}{\pi}}\frac{1}{\alpha_{in}}. \quad (2)$$

We additionally calculate a power-law slope from the steepest part of the inner edge described by `frank` profiles for each target to compare the results of the parametric and non-parametric models. While parametric models suggest steeper slopes than those derived from `frank`, the seven discs described in Table 3 generally meet the criterion of $\alpha_{in} \geq 15$ with both methods.

We note that the seven discs that are likely candidates for planet sculpting include five of the seven discs with extended, low-amplitude emission and two of the five discs with multiple statistically significant rings described in Sect. 3.1. This result suggests that the presence of gaps or extended emission in debris discs may indicate the influence of planets, assuming that sharp inner edges are caused by planet sculpting. Additionally, we find that the seven candidates for planet sculpting have some of the smallest widths in the ARKS sample. Because these discs are centred at small radii, this suggests that there may be a correlation between planet sculpting and disc width. Perhaps truncation by planets cleared the inner regions of discs centred at small radii, removing enough dust to decrease the widths of these objects. However, we emphasise that this explanation is extremely tentative and that the correlation observed here requires theoretical exploration beyond the scope of this paper.

We estimate upper limits on the masses and semi-major axes of the predicted planets sculpting these seven discs with Eq. (17) in Pearce et al. (2024) and with the publicly available planet-truncation model from Pearce et al. (2022)[4], respectively. These constraints rely on the assumption that a planet is located just interior to the inner edge of the disc and has cleared debris out to the inner edge. We report these calculations in Table 3, and we compare our results with constraints from other studies in Appendix B. We find that planets around these discs need to be <5 M_J and at <74 au to sculpt the inner edge.

4.5. The outer edge and eccentricity

The steepness of the outer edges of debris discs can provide insights into the levels of stirring, which can reveal the dynamical history of planetary system (Marino 2021). We find a variety of outer power-law indices among the discs in the ARKS sample, ranging from −1 to −22, which we use to estimate the mean particle eccentricities (e_{rms}) near the outer edges. The limitations of the power law parametrisations mean that eccentricity can be calculated only for the outermost ring of multi-ring discs and only for the main planetesimal belt of discs with halos. We use the approximation derived by Marino (2021) for a model of a stirred disc that assumes a Rayleigh distribution of particle eccentricities and inclinations (see also Rafikov 2023),

$$e_{rms} = 0.77\frac{l_{out}}{R_{out}}, \quad (3)$$

where R_{out} is either the parameter fit by the triple power law or the radius of the disc at 0.5% of the peak surface density and where $l_{out} = R_{out}/\alpha_{out}$. Because this relation breaks down as e_{rms} approaches $\Delta R/R$, we only report e_{rms} for discs with $\Delta R/R < e_{rms}$ in Table 4. A higher e_{rms} corresponds to a shallower outer edge, with particles distributed across a wider range of radii.

Our calculated particle eccentricities for HD 107146, HD 206893, HD 218396, and HD 197481 are systematically smaller than those calculated by Marino (2021) by a factor ∼2. These differences are likely due to the different parametric model chosen here (edges modelled as a power law instead of hyperbolic tangents or error functions) and how the values of R_{out} and α_{out} are approximated to an equivalent l_{out}.

We find that discs with multiple statistically significant rings or extended emission are often narrower and have steeper outer edges that correspond to low particle eccentricities, as shown in Fig. 9. This may indicate that the possible halos observed in the ARKS sample are not due to scattering, which can produce eccentricities greater than 1 (Gladman et al. 2001). However, we note that the observed eccentricities for these discs with extended emission or multiple significant rings are extremely close to the maximum constraint placed by their FWHM (represented by the dashed line in Fig. 10) and that we do not have outer slopes for the extended emission itself. We additionally find that discs with $\Delta R/R > 0.65$ shown in Fig. 10 are the same as the discs with $\alpha_{in} \leq 4$ shown in Fig. 9, with the exception of TYC 9340-437-1 and HD 218396. This suggests two distinct populations of discs: narrow belts with significant radial substructures – either gaps or halos – located at small radii with

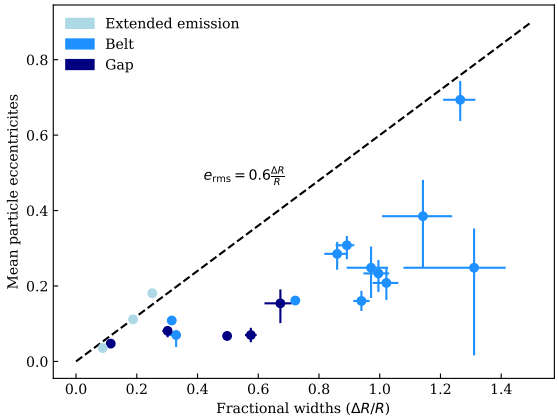

Fig. 10. Eccentricities and fractional widths of the discs with $e_{rms} < \Delta R/R$. The maximum eccentricity (Marino 2021) is represented by the black dashed line, and the error bars correspond to 1σ. For discs with gaps, we only plot $\Delta R/R$ for the outer ring as this is the only outer edge modelled by power-law parametrisations. For discs with low-amplitude emission, the eccentricities are derived from the outer slope of the planetesimal belt, not the faint emission.

[4] https://github.com/TimDPearce/SculptingPlanet/tree/main

Table 4. Outer slopes, mean particle eccentricities, and fractional widths for the ARKS sample.

Disc	$\alpha_{\rm out}$	$e_{\rm rms}$		$\Delta R/R$
		Median	Upper limit	
HD 9672	$-1.11^{+0.08}_{-0.09}$	$0.69^{+0.05}_{-0.06}$	0.86	$1.27^{+0.06}_{-0.06}$
HD 10647	$-1.24^{+0.04}_{-0.08}$			$0.34^{+0.02}_{-0.02}$
HD 14055	$-3.1^{+0.7}_{-1.0}$	$0.24^{+0.06}_{-0.08}$	0.56	$0.99^{+0.08}_{-0.09}$
HD 15115	$-16.3^{+0.6}_{-0.8}$	$0.047^{+0.002}_{-0.002}$	0.052	$0.114^{+0.004}_{-0.005}$ $0.086^{+0.036}_{-0.029}$
HD 15257	$-3.1^{+1.3}_{-2.9}$	$0.25^{+0.10}_{-0.23}$	1.2	$1.3^{+0.3}_{-0.4}$
HD 32297	$-6.30^{+0.12}_{-0.12}$			$0.134^{+0.006}_{-0.006}$
HD 39060	$-4.8^{+0.8}_{-0.8}$	$0.16^{+0.03}_{-0.03}$	0.24	$0.94^{+0.05}_{-0.06}$
HD 61005	$-4.26^{+0.08}_{-0.09}$	$0.181^{+0.003}_{-0.004}$	0.19	$0.269^{+0.017}_{-0.015}$
HD 76582	$-2.7^{+0.3}_{-0.4}$	$0.29^{+0.03}_{-0.04}$	0.40	$0.86^{+0.05}_{-0.07}$
HD 84870	$-2.0^{+0.5}_{-0.7}$	$0.39^{+0.10}_{-0.13}$	1.1	$1.1^{+0.4}_{-0.2}$
HD 92945	-11^{+3}_{-3}	$0.07^{+0.02}_{-0.02}$	0.14	$0.23^{+0.05}_{-0.05}$ $0.58^{+0.05}_{-0.04}$
HD 95086	$-2.5^{+0.2}_{-0.3}$	$0.31^{+0.02}_{-0.04}$	0.41	$0.89^{+0.07}_{-0.06}$
HD 107146	$-11.4^{+0.6}_{-0.5}$	$0.068^{+0.003}_{-0.003}$	3.0	$0.29^{+0.02}_{-0.03}$ $0.497^{+0.005}_{-0.003}$ $0.12^{+0.04}_{-0.03}$
HD 109573	$-21.7^{+1.2}_{-1.5}$	$0.035^{+0.002}_{-0.002}$	0.041	$0.081^{+0.002}_{-0.003}$
HD 121617	$-6.9^{+0.2}_{-0.4}$	$0.112^{+0.003}_{-0.006}$	0.12	$0.117^{+0.017}_{-0.018}$
HD 131488	$-16.6^{+0.8}_{-0.7}$			$0.072^{+0.003}_{-0.003}$
HD 131835	$-2.96^{+0.05}_{-0.05}$			$0.182^{+0.016}_{-0.015}$
HD 145560	$-7.1^{+0.4}_{-0.5}$	$0.108^{+0.006}_{-0.008}$	0.13	$0.315^{+0.017}_{-0.015}$
HD 161868	$-3.7^{+0.7}_{-0.8}$	$0.21^{+0.04}_{-0.04}$	0.38	$1.02^{+0.19}_{-0.10}$
HD 170773	-11^{+2}_{-5}	$0.07^{+0.01}_{-0.03}$	0.12	$0.33^{+0.04}_{-0.03}$
HD 197481	$-9.5^{+1.5}_{-2.0}$	$0.08^{+0.01}_{-0.02}$	0.13	$0.14^{+0.27}_{-0.05}$ $0.30^{+0.21}_{-0.04}$
HD 206893	$-5.0^{+1.2}_{-1.7}$	$0.15^{+0.04}_{-0.05}$	0.30	$0.3^{+0.5}_{-0.2}$ $0.67^{+0.08}_{-0.06}$
TYC 9340-437-1	$-3.3^{+0.5}_{-0.7}$	$0.23^{+0.04}_{-0.05}$	0.35	$1.00^{+0.09}_{-0.09}$
HD 218396	$-4.77^{+0.30}_{-0.17}$	$0.161^{+0.010}_{-0.006}$	0.20	$0.72^{+0.08}_{-0.10}$

Notes. Multiple fractional widths ($\Delta R/R$) are reported for discs with multiple rings, but the mean particle eccentricity ($e_{\rm rms}$) and the outer power-law index ($\alpha_{\rm out}$) are reported only for the outermost ring. Median eccentricities are calculated from the 50th percentile of $\alpha_{\rm out}$ with 1 σ uncertainties, and upper limits on eccentricities are calculated from the 99.7th percentile of $\alpha_{\rm out}$. Eccentricities are not reported for discs with $e_{\rm rms} > \Delta R/R$ as the relation between outer slope and eccentricity no longer holds in this case.

steep inner edges and low mean particle eccentricities, and wide belts without significant substructures located at large radii with shallow inner edges and high mean particle eccentricities. The correlation between wide belts and smooth outer edges may suggest an evolutionary explanation. If debris discs widen over time, then their outer edges will become smoother. However, further research is necessary to confirm the existence of this bimodal population, determine the origins of these substructures, and understand the underlying dynamical processes.

5. Conclusions

We summarise the main findings of this study in the following points.

– We modelled the 24 debris discs in the ARKS sample and obtained deprojected and deconvolved radial profiles with the visibility-space non-parametric method, `frank`, the image-space non-parametric method, `rave`, and a range of parametric models. The results from the different modelling

approaches generally yielded close agreement, confirming the robustness of the modelling of the main radial features.
- Among the sample of 24 discs, we found that 8 discs exhibit multiple rings from non-parametric models, 5 of which were found to be statistically significant when tested with parametric modelling. Additionally, 7 discs show low-amplitude extended emission on the inner or outer edge, which could correspond to either a halo or additional low-amplitude rings (which are often difficult to distinguish between). Substructures that deviate from a single symmetric ring are therefore abundant in this sample.
- The majority of discs appear to be well-fitted by either a double power law or a double-Gaussian radial profile, the latter of which can account for either two rings separated by a gap or a single ring with a radial profile that deviates from a Gaussian. Both the radius and the fractional width of the debris discs show a tentative positive correlation with age.
- The distribution of fractional widths of individual rings in the sample is significantly more skewed towards the narrower end than was previously understood to be the case in debris discs. The distribution that we find appears to be similar to known protoplanetary discs for fractional widths below 0.8, but we also find a small population of broad belts that have no counterpart among the existing population of protoplanetary discs. These widths are based on the FWHM of rings and do not account for the low-amplitude extended emission found in 7 of the 24 debris discs in the ARKS sample.
- Assuming that the gaps found in the debris discs are carved by planets via scattering (driven by the chaotic overlap of mean-motion resonances near the planet), we inferred a population of planets at tens of au with masses that mostly lie between a few Neptune masses and a few Jupiter masses. We used the inner edge to provide additional constraints based on planet sculpting models and the outer edge to constrain the eccentricities within the disc. Future work may wish to model the dynamical scenario in each disc more holistically by taking into account the full radial profile and age of each system.

Acknowledgements. This study made use of `NumPy` (Walt et al. 2011), `SciPy` (Virtanen et al. 2019), `Matplotlib` (Hunter 2007), `Astropy` (Astropy Collaboration 2013, 2018, 2022), `CASA` (McMullin et al. 2007), `frank` (Jennings et al. 2020), `rave` (Han et al. 2022, 2025), `MPoL` (Czekala et al. 2023; Zawadzki et al. 2023), `arksia` (Jennings et al. 2024), NASA's Astrophysics Data System Bibliographic Services and Karl Stapelfeldt's Catalog of Circumstellar discs. This paper makes use of the following ALMA data: ADS/JAO.ALMA# 2022.1.00338.L, 2012.1.00142.S, 2012.1.00198.S, 2015.1.01260.S, 2016.1.00104.S, 2016.1.00195.S, 2016.1.00907.S, 2017.1.00167.S, 2017.1.00825.S, 2018.1.01222.S and 2019.1.00189.S. ALMA is a partnership of ESO (representing its member states), NSF (USA) and NINS (Japan), together with NRC (Canada), MOST and ASIAA (Taiwan), and KASI (Republic of Korea), in cooperation with the Republic of Chile. The Joint ALMA Observatory is operated by ESO, AUI/NRAO and NAOJ. The National Radio Astronomy Observatory is a facility of the National Science Foundation operated under cooperative agreement by Associated Universities, Inc. The project leading to this publication has received support from ORP, that is funded by the European Union's Horizon 2020 research and innovation programme under grant agreement No 101004719 [ORP]. We are grateful for the help of the UK node of the European ARC in answering our questions and producing calibrated measurement sets. This research used the Canadian Advanced Network For Astronomy Research (CANFAR) operated in partnership by the Canadian Astronomy Data Centre and The Digital Research Alliance of Canada with support from the National Research Council of Canada the Canadian Space Agency, CANARIE and the Canadian Foundation for Innovation. This research made use of the Wesleyan University high-performance computing cluster. Y.H. is supported by a Caltech Barr Fellowship and this work was made possible by support from a Gates Cambridge Scholarship enabled by the Bill & Melinda Gates Foundation (OPP1144). E.M. acknowledges support from the NASA CT Space Grant. S.M. acknowledges funding by the Royal Society through a Royal Society University Research Fellowship (URF-R1-221669) and the European Union through the FEED ERC project (grant number 101162711). A.M.H., A.J.F. and E.M. gratefully acknowledge support from the National Science Foundation through Grant No. AST-2307920. Support for B.Z. was provided by The Brinson Foundation. This material is based upon work supported by the National Science Foundation Graduate Research Fellowship under Grant No. DGE 2140743. M.B. acknowledges funding from the Agence Nationale de la Recherche through the Ddisc project (grant No. ANR-21-CE31-0015). A.B. acknowledges research support by the Irish Research Council under grant GOIPG/2022/1895. C.d.B. acknowledges support from the Agencia Estatal de Investigación del Ministerio de Ciencia, Innovación y Universidades (MCIU/AEI) under grant WEAVE: EXPLORING THE COSMIC ORIGINAL SYMPHONY, FROM STARS TO GALAXY CLUSTERS and the European Regional Development Fund (ERDF) with reference PID2023-153342NB-I00/10.13039/501100011033, as well as from a Beatriz Galindo Senior Fellowship (BG22/00166) from the MICIU. The University of La Laguna (ULL) and the Department of Economy, Knowledge, and Employment of the Government of the Canary Islands are also gratefully acknowledged for the support provided to CdB (2024/347). E.C. acknowledges support from NASA STScI grant HST-AR-16608.001-A and the Simons Foundation. S.E. is supported by the National Aeronautics and Space Administration through the Exoplanet Research Program (Grant No. 80NSSC23K0288, PI: Faramaz). This material is based upon work supported by the National Science Foundation Graduate Research Fellowship under Grant No. DGE 2140743. M.R.J. acknowledges support from the European Union's Horizon Europe Programme under the Marie Sklodowska-Curie grant agreement no. 101064124 and funding provided by the Institute of Physics Belgrade, through the grant by the Ministry of Science, Technological Development, and Innovations of the Republic of Serbia. This work was also supported by the NKFIH NKKP grant ADVANCED 149943 and the NKFIH excellence grant TKP2021-NKTA-64. Project no.149943 has been implemented with the support provided by the Ministry of Culture and Innovation of Hungary from the National Research, Development and Innovation Fund, financed under the NKKP ADVANCED funding scheme. J.B.L. acknowledges the Smithsonian Institute for funding via a Submillimeter Array (SMA) Fellowship, and the North American ALMA Science Center (NAASC) for funding via an ALMA Ambassadorship. S.M.M. and L.M. acknowledge funding by the European Union through the E-BEANS ERC project (grant number 100117693), and by the Irish research Council (IRC) under grant number IRCLA- 2022-3788. Views and opinions expressed are however those of the author(s) only and do not necessarily reflect those of the European Union or the European Research Council Executive Agency. Neither the European Union nor the granting authority can be held responsible for them. J.P.M. acknowledges research support by the National Science and Technology Council of Taiwan under grant NSTC 112-2112-M-001-032-MY3. J.M. acknowledges funding from the Agence Nationale de la Recherche through the DDISK project (grant No. ANR-21-CE31-0015) and from the PNP (French National Planetology Program) through the EPOPEE project. T.D.P. is supported by a UKRI Stephen Hawking Fellowship and a Warwick Prize Fellowship, the latter made possible by a generous philanthropic donation. S.P. acknowledges support from FONDECYT Regular 1231663 and ANID – Millennium Science Initiative Program – Center Code NCN2024_001. A.A.S. is supported by the Heising-Simons Foundation through a 51 Pegasi b Fellowship. P.W. acknowledges support from FONDECYT grant 3220399 and ANID – Millennium Science Initiative Program – Center Code NCN2024_001.

References

Andrews, S. M., Huang, J., Pérez, L. M., et al. 2018, ApJ, 869, L41
Astropy Collaboration (Robitaille, T. P., et al.) 2013, A&A, 558, A33
Astropy Collaboration (Price-Whelan, A. M., et al.) 2018, AJ, 156, 123
Astropy Collaboration (Price-Whelan, A. M., et al.) 2022, ApJ, 935, 167
Aumann, H. H., Gillett, F. C., Beichman, C. A., et al. 1984, ApJ, 278, L23
Bae, J., Isella, A., Zhu, Z., et al. 2023, ASP Conf. Ser., 534, 423
Bhowmik, T., Boccaletti, A., Thébault, P., et al. 2019, A&A, 630, A85
Bi, J., & Lin, M.-K. 2024, ApJ, 971, 76
Booth, M., Kennedy, G., Sibthorpe, B., et al. 2013, MNRAS, 428, 1263
Booth, M., Pearce, T. D., Krivov, A. V., et al. 2023, MNRAS, 521, 6180
Brown, M. E. 2001, AJ, 121, 2804
Butler, R. P., Wright, J. T., Marcy, G. W., et al. 2006, ApJ, 646, 505
Chiang, E., Kite, E., Kalas, P., Graham, J. R., & Clampin, M. 2009, ApJ, 693, 734
Cranmer, S. R., Wilner, D. J., & MacGregor, M. A. 2013, ApJ, 772, 149
Crotts, K. A., Matthews, B. C., Duchêne, G., et al. 2024, ApJ, 961, 245
Crotts, K. A., Carter, A. L., Lawson, K., et al. 2025, ApJ, 987, L41
Currie, T., Biller, B., Lagrange, A., et al. 2023, ASP Conf. Ser., 534, 799
Czekala, I., Jennings, J., Zawadzki, B., et al. 2023, https://doi.org/10.5281/zenodo.3594081

Daley, C., Hughes, A. M., Carter, E. S., et al. 2019, ApJ, 875, 87
Dent, W. R. F., Wyatt, M. C., Roberge, A., et al. 2014, Science, 343, 1490
Dominik, C., & Decin, G. 2003, ApJ, 598, 626
Dong, R., Zhu, Z., & Whitney, B. 2015, ApJ, 809, 93
Draine, B. T. 2006, ApJ, 636, 1114
Eiroa, C., Marshall, J. P., Mora, A., et al. 2013, A&A, 555, A11
Ertel, S., Wolf, S., Metchev, S., et al. 2011, A&A, 533, A132
Faber, P., & Quillen, A. C. 2007, MNRAS, 382, 1823
Faramaz, V., Beust, H., Thébault, P., et al. 2014, A&A, 563, A72
Faramaz, V., Marino, S., Booth, M., et al. 2021, AJ, 161, 271
Fehr, A. 2023, Bachelor's thesis, Wesleyan University, USA
Feldt, M., Olofsson, J., Boccaletti, A., et al. 2017, A&A, 601, A7
Flock, M., Ruge, J. P., Dzyurkevich, N., et al. 2015, A&A, 574, A68
Foreman-Mackey, D., Hogg, D. W., Lang, D., & Goodman, J. 2013, PASP, 125, 306
Friebe, M. F., Pearce, T. D., & Löhne, T. 2022, MNRAS, 512, 4441
Geiler, F., & Krivov, A. V. 2017, MNRAS, 468, 959
Geiler, F., Krivov, A. V., Booth, M., & Löhne, T. 2019, MNRAS, 483, 332
Gilbert, K. M., Quirk, A. C. N., Guhathakurta, P., et al. 2022, ApJ, 924, 116
Gladman, B., Kavelaars, J. J., Petit, J.-M., et al. 2001, AJ, 122, 1051
Golimowski, D. A., Krist, J. E., Stapelfeldt, K. R., et al. 2011, AJ, 142, 30
Han, Y., Wyatt, M. C., & Matrà, L. 2022, MNRAS, 511, 4921
Han, Y., Wyatt, M. C., & Marino, S. 2025, MNRAS, 537, 3839
Harper, D. A., Loewenstein, R. F., & Davidson, J. A. 1984, ApJ, 285, 808
Holland, W. S., Matthews, B. C., Kennedy, G. M., et al. 2017, MNRAS, 470, 3606
Huang, J., Andrews, S. M., Dullemond, C. P., et al. 2018, ApJ, 869, L42
Hughes, A. M., Lieman-Sifry, J., Flaherty, K. M., et al. 2017, ApJ, 839, 86
Hughes, A. M., Duchêne, G., & Matthews, B. C. 2018, ARAA, 56, 541
Hull, C. L. H., Yang, H., Cortés, P. C., et al. 2022, ApJ, 930, 49
Hunter, J. D. 2007, Comput. Sci. Eng., 9, 90
Ida, S., & Makino, J. 1993, Icarus, 106, 210
Imaz Blanco, A., Marino, S., Matrà, L., et al. 2023, MNRAS, 522, 6150
Jankovic, M. R., Pawellek, N., Zander, J., et al. 2026, A&A, 705, A204
Jennings, J., Booth, R. A., Tazzari, M., Rosotti, G. P., & Clarke, C. J. 2020, MNRAS, 495, 3209
Jennings, J., Booth, R. A., Tazzari, M., Clarke, C. J., & Rosotti, G. P. 2022a, MNRAS, 509, 2780
Jennings, J., Tazzari, M., Clarke, C. J., Booth, R. A., & Rosotti, G. P. 2022b, MNRAS, 514, 6053
Jennings, J., Marino, S., & Han, Y. 2024, https://doi.org/10.5281/zenodo.10993146
Jiang, H., & Ormel, C. W. 2023, MNRAS, 518, 3877
Kass, R. E., & Raftery, A. E. 1995, J. Am. Stat. Assoc., 90, 773
Kennedy, G. M. 2020, R. Soc. Open Sci., 7, 200063
Kennedy, G. M., & Wyatt, M. C. 2010, MNRAS, 405, 1253
Kennedy, G. M., Marino, S., Matrà, L., et al. 2018, MNRAS, 475, 4924
Kenyon, S. J., & Bromley, B. C. 2008, ApJS, 179, 451
Krivov, A. V. 2010, Res. Astron. Astrophys., 10, 383
Lagrange, A.-M., Wilkinson, C., Mâlin, M., et al. 2025, Nature, 642, 905
Löhne, T. 2020, A&A, 641, A75
Löhne, T., Krivov, A. V., & Rodmann, J. 2008, ApJ, 673, 1123
Long, F., Pinilla, P., Herczeg, G. J., et al. 2018, ApJ, 869, 17
Lovell, J. B., Marino, S., Wyatt, M. C., et al. 2021, MNRAS, 506, 1978
Lovell, J. B., Hales, A. S., Kennedy, G. M., et al. 2026, A&A, 705, A200
Mac Manamon, S., Matrà, L., Marino, S., et al. 2026, A&A, 705, A198
MacGregor, M. A., Wilner, D. J., Rosenfeld, K. A., et al. 2013, ApJ, 762, L21
MacGregor, M. A., Wilner, D. J., Chandler, C., et al. 2016, ApJ, 823, 79
MacGregor, M. A., Matrà, L., Kalas, P., et al. 2017, ApJ, 842, 8
MacGregor, M. A., Weinberger, A. J., Hughes, A. M., et al. 2018, ApJ, 869, 75
MacGregor, M. A., Weinberger, A. J., Nesvold, E. R., et al. 2019, ApJ, 877, L32
Marino, S. 2021, MNRAS, 503, 5100
Marino, S., Matrà, L., Stark, C., et al. 2016, MNRAS, 460, 2933
Marino, S., Wyatt, M. C., Panić, O., et al. 2017, MNRAS, 465, 2595
Marino, S., Carpenter, J., Wyatt, M. C., et al. 2018, MNRAS, 479, 5423
Marino, S., Yelverton, B., Booth, M., et al. 2019, MNRAS, 484, 1257
Marino, S., Zurlo, A., Faramaz, V., et al. 2020, MNRAS, 498, 1319
Marino, S., Matrà, L., Hughes, A. M., et al. 2026, A&A, 705, A195
Marshall, J. P., Booth, M., Holland, W., et al. 2016, MNRAS, 459, 2893
Marshall, J. P., Wang, L., Kennedy, G. M., Zeegers, S. T., & Scicluna, P. 2021, MNRAS, 501, 6168
Matrà, L., Dent, W. R. F., Wyatt, M. C., et al. 2017, MNRAS, 464, 1415
Matrà, L., Wyatt, M. C., Wilner, D. J., et al. 2019, AJ, 157, 135
Matrà, L., Marino, S., Wilner, D. J., et al. 2025, A&A, 693, A151
Matthews, B. C., Sibthorpe, B., Kennedy, G., et al. 2010, A&A, 518, L135
McMullin, J. P., Waters, B., Schiebel, D., Young, W., & Golap, K. 2007, ASP Conf. Ser., 376, 127
Michel, A., van der Marel, N., & Matthews, B. C. 2021, ApJ, 921, 72
Miley, J. M., Carpenter, J., Booth, R., et al. 2024, A&A, 682, A55
Miller, E., Marino, S., Stammler, S. M., et al. 2021, MNRAS, 508, 5638
Milli, J., Vigan, A., Mouillet, D., et al. 2017, A&A, 599, A108
Milli, J., Olofsson, J., Bonduelle, M., et al. 2026, A&A, 705, A199
Montesinos, B., Eiroa, C., Krivov, A. V., et al. 2016, A&A, 593, A51
Moór, A., Kóspál, Á., Ábrahám, P., et al. 2015, MNRAS, 447, 577
Moór, A., Curé, M., Kóspál, Á., et al. 2017, ApJ, 849, 123
Morbidelli, A., & Henrard, J. 1991, Celest. Mech. Dyn. Astron., 51, 169
Morbidelli, A., Emel'yanenko, V. V., & Levison, H. F. 2004, MNRAS, 355, 935
Morbidelli, A., Levison, H. F., & Gomes, R. 2008, in The Solar System Beyond Neptune, eds. M. A. Barucci, H. Boehnhardt, D. P. Cruikshank, A. Morbidelli, & R. Dotson (Tucson: University of Arizona Press), 275
Morrison, S., & Malhotra, R. 2015, ApJ, 799, 41
Morrison, S. J., & Kratter, K. M. 2018, MNRAS, 481, 5180
Mustill, A. J., & Wyatt, M. C. 2012, MNRAS, 419, 3074
Najita, J. R., Kenyon, S. J., & Bromley, B. C. 2022, ApJ, 925, 45
Nederlander, A., Hughes, A. M., Fehr, A. J., et al. 2021, ApJ, 917, 5
Nhung, P. T., Hoai, D. T., Tuan-Anh, P., et al. 2017, MNRAS, 469, 4726
Olofsson, J., Thébault, P., Kral, Q., et al. 2022, MNRAS, 513, 713
Orcajo, S., Cieza, L. A., Guilera, O., et al. 2025, ApJ, 984, L57
Pan, M., & Schlichting, H. E. 2012, ApJ, 747, 113
Pawellek, N., Moór, A., Pascucci, I., & Krivov, A. V. 2019, MNRAS, 487, 5874
Pawellek, N., Moór, A., Kirchschlager, F., et al. 2024, MNRAS, 527, 3559
Pearce, T. D., & Wyatt, M. C. 2014, MNRAS, 443, 2541
Pearce, T. D., & Wyatt, M. C. 2015, MNRAS, 453, 3329
Pearce, T. D., Launhardt, R., Ostermann, R., et al. 2022, A&A, 659, A135
Pearce, T. D., Krivov, A. V., Sefilian, A. A., et al. 2024, MNRAS, 527, 3876
Perrot, C., Olofsson, J., Kral, Q., et al. 2023, A&A, 673, A39
Plavchan, P., Barclay, T., Gagné, J., et al. 2020, Nature, 582, 497
Quillen, A. C. 2006, MNRAS, 372, L14
Rafikov, R. R. 2023, MNRAS, 519, 5607
Ricci, L., Maddison, S. T., Wilner, D., et al. 2015, ApJ, 813, 138
Rodigas, T. J., Malhotra, R., & Hinz, P. M. 2014, ApJ, 780, 65
Sefilian, A. A. 2024, ApJ, 966, 140
Sefilian, A. A., Rafikov, R. R., & Wyatt, M. C. 2021, ApJ, 910, 13
Sefilian, A. A., Rafikov, R. R., & Wyatt, M. C. 2023, ApJ, 954, 100
Sepulveda, A. G., Matrà, L., Kennedy, G. M., et al. 2019, ApJ, 881, 84
Shannon, A., Bonsor, A., Kral, Q., & Matthews, E. 2016, MNRAS, 462, L116
Sierra, A., Pérez, L. M., Sotomayor, B., et al. 2024, ApJ, 974, 306
Stammler, S. M., Drążkowska, J., Birnstiel, T., et al. 2019, ApJ, 884, L5
Su, K. Y. L., Rieke, G. H., Stapelfeldt, K. R., et al. 2008, ApJ, 679, L125
Su, K. Y. L., MacGregor, M. A., Booth, M., et al. 2017, AJ, 154, 225
Tabeshian, M., & Wiegert, P. A. 2016, ApJ, 818, 159
Tanner, A., Plavchan, P., Bryden, G., et al. 2020, PASP, 132, 084401
Tazzari, M., Beaujean, F., & Testi, L. 2018, MNRAS, 476, 4527
Terrill, J., Marino, S., Booth, R. A., et al. 2023, MNRAS, 524, 1229
Thebault, P., Olofsson, J., & Kral, Q. 2023, A&A, 674, A51
Vigan, A., Fontanive, C., Meyer, M., et al. 2021, A&A, 651, A72
Virtanen, P., Gommers, R., Oliphant, T. E., et al. 2019, SciPy 1.0–Fundamental Algorithms for Scientific Computing in Python
Vizgan, D., Hughes, A. M., Carter, E. S., et al. 2022, ApJ, 935, 131
Walt, S. v. d., Colbert, S. C., & Varoquaux, G. 2011, Comput. Sci. Eng., 13, 22
White, J. A., Boley, A. C., Dent, W. R. F., Ford, E. B., & Corder, S. 2017, MNRAS, 466, 4201
Wisdom, J. 1980, AJ, 85, 1122
Wisdom, J. 1983, Icarus, 56, 51
Wyatt, M. C. 2003, ApJ, 598, 1321
Wyatt, M. C. 2008, ARA&A, 46, 339
Wyatt, M. C., Smith, R., Greaves, J. S., et al. 2007a, ApJ, 658, 569
Wyatt, M. C., Smith, R., Su, K. Y. L., et al. 2007b, ApJ, 663, 365
Wyatt, M. C., Panić, O., Kennedy, G. M., & Matrà, L. 2015, Ap&SS, 357, 103
Yelverton, B., & Kennedy, G. M. 2018, MNRAS, 479, 2673
Yelverton, B., Kennedy, G. M., Su, K. Y. L., & Wyatt, M. C. 2019, MNRAS, 488, 3588
Youdin, A. N., & Goodman, J. 2005, ApJ, 620, 459
Zawadzki, B., Czekala, I., Loomis, R. A., et al. 2023, PASP, 135, 064503
Zawadzki, B., Fehr, A., Hughes, A. M., et al. 2026, A&A, 705, A197
Zheng, X., Lin, D. N. C., Kouwenhoven, M. B. N., Mao, S., & Zhang, X. 2017, ApJ, 849, 98

[1] Division of Geological and Planetary Sciences, California Institute of Technology, 1200 E. California Blvd., Pasadena, CA 91125, USA
[2] Department of Astronomy, Van Vleck Observatory, Wesleyan University, 96 Foss Hill Dr., Middletown, CT, 06459, USA
[3] Center for Computational Astrophysics, Flatiron Institute, 162 Fifth Ave., New York, NY 10010, USA

[4] Department of Physics and Astronomy, University of Exeter, Stocker Road, Exeter EX4 4QL, UK
[5] Center for Astrophysics | Harvard & Smithsonian, 60 Garden St, Cambridge, MA 02138, USA
[6] UK Astronomy Technology Centre, Royal Observatory Edinburgh, Blackford Hill, Edinburgh EH9 3HJ, UK
[7] School of Physics and Astronomy, University of Leeds, Leeds LS2 9JT, UK
[8] Univ. Grenoble Alpes, CNRS, IPAG, F-38000 Grenoble, France
[9] School of Physics, Trinity College Dublin, the University of Dublin, College Green, Dublin 2, Ireland
[10] Instituto de Astrofísica de Canarias, Vía Láctea S/N, La Laguna, 38200, Tenerife, Spain
[11] Departamento de Astrofísica, Universidad de La Laguna, La Laguna, E-38200, Tenerife, Spain
[12] Joint ALMA Observatory, Avenida Alonso de Córdova 3107, Vitacura 7630355, Santiago, Chile
[13] National Astronomical Observatory of Japan, Osawa 2-21-1, Mitaka, Tokyo 181-8588, Japan
[14] Department of Astronomy, Graduate School of Science, The University of Tokyo, Tokyo 113-0033, Japan
[15] Department of Astronomy, University of California, Berkeley, Berkeley, CA 94720-3411, USA
[16] Department of Astronomy and Steward Observatory, The University of Arizona, 933 North Cherry Ave, Tucson, AZ, 85721, USA
[17] Large Binocular Telescope Observatory, The University of Arizona, 933 North Cherry Ave, Tucson, AZ, 85721, USA
[18] Max-Planck-Insitut für Astronomie, Königstuhl 17, 69117 Heidelberg, Germany
[19] Institute of Physics Belgrade, University of Belgrade, Pregrevica 118, 11080 Belgrade, Serbia
[20] Konkoly Observatory, HUN-REN Research Centre for Astronomy and Earth Sciences, MTA Centre of Excellence, Konkoly-Thege Miklós út 15-17, 1121 Budapest, Hungary
[21] Institute of Physics and Astronomy, ELTE Eötvös Loránd University, Pázmány Péter sétány 1/A, 1117 Budapest, Hungary
[22] Astrophysikalisches Institut und Universitätssternwarte, Friedrich-Schiller-Universität Jena, Schillergäßchen 2-3, 07745 Jena, Germany
[23] Department of Physics and Astronomy, Johns Hopkins University, 3400 N Charles Street, Baltimore, MD 21218, USA
[24] Academia Sinica Institute of Astronomy and Astrophysics, 11F of AS/NTU Astronomy-Mathematics Building, No.1, Sect. 4, Roosevelt Rd, Taipei 106319, Taiwan
[25] European Southern Observatory, Karl-Schwarzschild-Strasse 2, 85748 Garching bei München, Germany
[26] Department of Physics, University of Warwick, Gibbet Hill Road, Coventry CV4 7AL, UK
[27] Departamento de Física, Universidad de Santiago de Chile, Av. Víctor Jara 3493, Santiago, Chile
[28] Millennium Nucleus on Young Exoplanets and their Moons (YEMS), Chile
[29] Center for Interdisciplinary Research in Astrophysics Space Exploration (CIRAS), Universidad de Santiago, Chile
[30] Institute of Astronomy, University of Cambridge, Madingley Road, Cambridge CB3 0HA, UK

Appendix A: Emissivity index of HD 107146

HD 107146 was observed in Band 6 in April 2017 and in Band 7 in October through December 2016 and in May 2021 (Marino et al. 2018; Imaz Blanco et al. 2023). Because these data are comparable in resolution and sensitivity, we can include both in our parametric models to improve our interpretation of the structure of the disc. The availability of multi-frequency data for HD 107146 additionally provides an opportunity to measure the emissivity index, β. Because the spectral index and emissivity index depend on the density of the material and the distribution of dust grain sizes (Löhne 2020), we can relate these indices to the tensile strength of the dust and better constrain the masses of the bodies producing dust in debris discs (Pan & Schlichting 2012).

While the emissivity index is incorporated into the parametric modelling code, it is a fixed variable used to calculate the dust mass opacity κ (Zawadzki et al. 2026). We modified the parametric modelling code to accept β as an additional free parameter for HD 107146. Although spectral index has been measured with ALMA for several discs (e.g. Ricci et al. 2015; MacGregor et al. 2016; Vizgan et al. 2022), the emissivity index has not often been fit directly. Fitting β allows us to then calculate the grain-size distribution parameter q (Draine 2006), defined as

$$q = \frac{\beta}{\beta_s} + 3, \tag{A.1}$$

where β_s is the dust opacity spectral index of small particles, assumed to be 1.8 (MacGregor et al. 2016). We obtain a best-fit and median value of $\beta = 0.3 \pm 0.2$ for the emissivity index, which corresponds to a grain-size distribution slope of $q = 3.17 \pm 0.11$.

We compare this result to previous studies of spectral indices and emissivity indices in other debris discs here. MacGregor et al. (2016) measured the spectral indices of 15 debris discs and calculated the grain-size distribution slope for each. They found a weighted mean of $\langle q \rangle = 3.36 \pm 0.02$, with slopes in the sample ranging from 2.84–3.64. Our measured grain-size distribution slope for HD 107146 is somewhat smaller than this weighted mean but within the range observed by MacGregor et al. (2016). We note that HD 107146 has a grain-size distribution slope that is among the smallest measured in debris discs: HD 141569 has a slope of 2.84 ± 0.05 (MacGregor et al. 2016) and HD 197481 has a slope of $q = 3.03 \pm 0.02$ (Vizgan et al. 2022).

Our measurement of the grain-size distribution slope for HD 107146 places this disc within the gravity regime of $3 < q < 3.21$ described by (Pan & Schlichting 2012), in which small bodies have greater velocities than large bodies and catastrophic collisions significantly damp the velocities of all bodies in the disc. The relatively small β value we measure for HD 107146 could also result if material strength does not dominate colliding bodies or from inhomogeneities in densities and fragmentation energies (MacGregor et al. 2016). However, additional research is necessary to understand the implications for the collisional cascade in HD 107146.

Appendix B: Planet constraints from the inner edge

We compare the planet masses and semi-major axes calculated from the properties of the inner edges in Sect. 4.4 to previous detections or constraints. All masses are below the detection limits at both the 99.7% and 50% confidence levels calculated by the companion paper Milli et al. (2026), unless these limits are unavailable due to observation sensitivities.

HD 10647 has an inner radius of 79 au and an inner power law index of > 18, corresponding to an upper limit of 2.5 M_J on a planet sculpting its inner edge and an upper limit of 48 au on the semi-major axis of its orbit. The 1 M_{Jup} planet previously observed in this system (Butler et al. 2006) has an orbit of ~ 2 au that is too small to affect the inner edge of the disc. (Pearce et al. 2024).

HD 32297 has an inner radius of 102 au and an inner power law index of > 27, corresponding to an upper limit of 1 M_J on a planet sculpting its inner edge and an upper limit of 74 au on the semi-major axis of its orbit. Although no planets have been previously observed in this system, the planet mass derived here is consistent with both the detection limit of 1 M_J based on previous scattered light observations of the discs (Bhowmik et al. 2019) and the minimum planet mass of $0.04^{+0.03}_{-0.10}$ M_J for secular stirring (Pearce et al. 2022). The latter estimate assumes a massless disc; adopting a maximum disc mass of $100M_\oplus$ increases the minimum required planet mass to 0.63 M_J (Sefilian 2024).

HD 107146 has an inner radius of 44 au and an inner power law index of > 13.91, corresponding to an upper limit of 5 M_J on a planet sculpting its inner edge and an upper limit of 32 au on the semi-major axis of its orbit. No planets have been previously observed in this system.

HD 109573 has an inner radius of 69 au and a median inner power law index of 34^{+5}_{-3}, corresponding to an upper limit of $0.68^{+0.30}_{-0.18}$ M_J on a planet sculpting its inner edge and an upper limit of 50 au on the semi-major axis of its orbit. Although no planets have been previously observed in this system, the planet mass derived here further constrains the maximum planet mass of $0.4^{+8.4}_{-0.4}$ M_J calculated by Milli et al. (2017) based on truncation of the inner slope observed in scattered light.

HD 121617 has an inner radius of 65 au and an inner power law index of > 20, corresponding to an upper limit of 3.1 M_J on a planet sculpting its inner edge and an upper limit of 49 au on the semi-major axis of its orbit. Although no planet has been previously observed in this system, the planet mass derived here is consistent with the minimum planet mass of 0.3 ± 0.2 M_J necessary for secular stirring (Pearce et al. 2022). The latter estimate assumes a massless disc; adopting a maximum disc mass of $100M_\oplus$ increases the minimum required planet mass to 1 M_J (Sefilian 2024).

HD 131488 has an inner radius of 79 au and a median inner power law index of 28^{+5}_{-4}, corresponding to an upper limit of $1.2^{+0.6}_{-0.5}$ M_J on a planet sculpting its inner edge and an upper limit of 63 au on the semi-major axis of its orbit. No planet has been previously observed in this system.

HD 197481 has an inner radius of 25 au and an inner power law index of > 14, corresponding to an upper limit of 3.2 M_J on a planet sculpting its inner edge and an upper limit of 19 au on the semi-major axis of its orbit. Although two Neptune-sized planets have been detected in this system (Plavchan et al. 2020; Gilbert et al. 2022), these objects have orbits that are too small to affect the inner edge of the disc according to the model of Pearce et al. (2024).

Appendix C: Best-fit parameters from parametric modelling

This appendix lists the fitted model parameters from parametric modelling. Details of the fitting methods are described in Sect. 2.4.

Table C.1: MCMC results for discs with a clear single peak.

Double power law

Disc	R_c (au)		α_{in}		α_{out}		Σ_c		PA (°)		$\Delta\alpha$ (mas)		$\Delta\delta$ (mas)		i (°)		F_* (μJy)	
HD 9672	95	96^{+4}_{-4}	2.4	$2.27^{+0.21}_{-0.19}$	−1.1	$-1.11^{+0.08}_{-0.09}$	−4.188	$-4.191^{+0.009}_{-0.009}$	108.02	$107.95^{+0.12}_{-0.15}$	46	51^{+16}_{-15}	−38	-39^{+7}_{-6}	79.1	$79.13^{+0.12}_{-0.11}$	16	14^{+10}_{-9}
HD 10647	74.5	$73.7^{+0.8}_{-0.7}$	120	140^{+100}_{-90}	−1.22	$-1.24^{+0.04}_{-0.08}$	−4.584	$-4.578^{+0.015}_{-0.010}$	57.48	$57.04^{+0.46}_{-0.07}$	118	123^{+10}_{-10}	−23	-22^{+8}_{-8}	79.69	$79.37^{+0.37}_{-0.13}$	142	138^{+10}_{-9}
HD 14055	189	181^{+9}_{-13}	1.19	$1.20^{+0.14}_{-0.11}$	−3.7	$-3.1^{+0.7}_{-1.0}$	−5.074	$-5.075^{+0.014}_{-0.014}$	161.93	$161.60^{+0.27}_{-0.14}$	−56	-62^{+9}_{-10}	−67	-66^{+12}_{-12}	80.2	$80.0^{+0.2}_{-0.3}$	100	101^{+9}_{-10}
HD 15257	240	250^{+50}_{-40}	0.9	$0.8^{+0.4}_{-0.2}$	−2.3	$-3.1^{+1.3}_{-2.9}$	−5.11	$-5.12^{+0.05}_{-0.06}$	51	49^{+3}_{-4}	100	100^{+80}_{-70}	130	100^{+90}_{-90}	65	63^{+3}_{-3}	100	100^{+30}_{-30}
HD 32297	105.1	$105.2^{+0.7}_{-0.5}$	110	100^{+60}_{-50}	−6.33	$-6.30^{+0.12}_{-0.12}$	−2.719	$-2.722^{+0.013}_{-0.014}$	47.45	$47.47^{+0.05}_{-0.03}$	20.2	$20.5^{+1.6}_{-1.4}$	15.3	$15.3^{+1.3}_{-1.3}$	88.46	$88.39^{+0.07}_{-0.05}$	23	23^{+13}_{-11}
HD 39060	134	130^{+5}_{-5}	1.07	$1.09^{+0.10}_{-0.07}$	−5.4	$-4.8^{+0.8}_{-0.8}$	−4.202	$-4.201^{+0.012}_{-0.011}$	29.66	$29.73^{+0.07}_{-0.06}$	29	26^{+13}_{-12}	3	-4^{+19}_{-18}	86.06	$86.06^{+0.04}_{-0.07}$	73	66^{+12}_{-13}
HD 84870	220	220^{+30}_{-30}	1.5	$1.5^{+0.3}_{-0.3}$	−1.9	$-2.0^{+0.5}_{-0.7}$	−4.70	$-4.70^{+0.03}_{-0.04}$	134	137^{+4}_{-3}	390	360^{+70}_{-80}	−360	-280^{+100}_{-100}	55	53^{+3}_{-2}	0	8^{+10}_{-6}
HD 95086	199	198^{+11}_{-7}	1.84	$1.93^{+0.20}_{-0.18}$	−2.6	$-2.5^{+0.2}_{-0.3}$	−3.966	$-3.972^{+0.015}_{-0.017}$	99	97^{+3}_{-2}	−120	-110^{+40}_{-40}	90	90^{+30}_{-30}	30	31^{+3}_{-2}	22	20^{+16}_{-13}
HD 121617	68.5	$68.5^{+0.7}_{-0.5}$	70	60^{+30}_{-20}	−6.9	$-6.9^{+0.2}_{-0.4}$	−2.993	$-2.995^{+0.019}_{-0.021}$	58.7	$58.4^{+0.7}_{-0.6}$	−1	0^{+2}_{-3}	−4	-3^{+2}_{-3}	44.5	$44.6^{+0.4}_{-0.7}$	22	27^{+10}_{-10}
HD 145560	74.5	$75.0^{+1.2}_{-1.2}$	6.1	$6^{+0.6}_{-0.5}$	−6.8	$-7.1^{+0.4}_{-0.5}$	−3.058	$-3.056^{+0.015}_{-0.016}$	40	$39.2^{+0.8}_{-0.8}$	16	17^{+3}_{-3}	−19	-18^{+4}_{-3}	47.5	$47.5^{+0.5}_{-0.5}$	24	26^{+9}_{-8}
HD 161868	154	154^{+8}_{-10}	0.97	$0.99^{+0.14}_{-0.11}$	−3.9	$-3.7^{+0.7}_{-0.8}$	−4.97	$-4.98^{+0.02}_{-0.03}$	55.1	$56.1^{+1.9}_{-1.5}$	10	0^{+30}_{-20}	−90	-100^{+30}_{-20}	65.1	$65.7^{+1.2}_{-1.1}$	151	152^{+20}_{-20}
HD 170773	197	200^{+13}_{-7}	6.3	$5.6^{+1.0}_{-1.2}$	−10	-11^{+2}_{-5}	−3.99	$-4.00^{+0.02}_{-0.03}$	113.4	$113.4^{+1.8}_{-9.8}$	−130	-130^{+30}_{-40}	20	20^{+30}_{-30}	32.9	$31.7^{+1.9}_{-1.6}$	90	80^{+20}_{-20}
TYC 9340	99	98^{+6}_{-7}	1.73	$1.77^{+0.17}_{-0.14}$	−1.9	$-1.8^{+0.3}_{-0.3}$	−3.834	$-3.840^{+0.020}_{-0.020}$	152	147^{+8}_{-16}	−10	-20^{+50}_{-60}	−30	-50^{+40}_{-50}	29	32^{+3}_{-4}	1	7^{+11}_{-5}

Asymmetric Gaussian

disc	R_c (au)		σ_{in} (au)		σ_{out} (au)		Σ_c		PA (°)		$\Delta\alpha$ (mas)		$\Delta\delta$ (mas)		i (°)		F_* (μJy)	
HD 76582	184	181^{+9}_{-8}	55	53^{+6}_{-6}	143	145^{+10}_{-10}	−4.825	$-4.822^{+0.013}_{-0.014}$	104.8	$104.7^{+0.3}_{-0.5}$	0	-20^{+50}_{-50}	−40	-50^{+30}_{-20}	73.8	$73.7^{+0.4}_{-0.7}$	53	57^{+18}_{-17}
HD 161868	115	120^{+11}_{-9}	50	54^{+9}_{-8}	74	72^{+10}_{-11}	−5.12	$-5.12^{+0.02}_{-0.03}$	55.1	$57.0^{+2.3}_{-1.9}$	0	10^{+30}_{-30}	−100	-110^{+30}_{-20}	65.4	$66.4^{+1.2}_{-1.4}$	150	140^{+20}_{-30}
HD 170773	191	194^{+7}_{-4}	27	29^{+6}_{-3}	27	26^{+3}_{-4}	−4.185	$-4.191^{+0.018}_{-0.018}$	115.1	$113.3^{+1.7}_{-2.9}$	−120	-130^{+40}_{-30}	10	20^{+30}_{-20}	32.1	$32.2^{+1.6}_{-1.6}$	90	80^{+20}_{-20}
TYC 9340	78	81^{+4}_{-5}	25	26^{+2}_{-3}	91	88^{+9}_{-9}	−4.012	$-4.017^{+0.020}_{-0.020}$	151	137^{+16}_{-13}	−50	-60^{+60}_{-50}	20	40^{+60}_{-60}	28	30^{+4}_{-5}	1	9^{+12}_{-7}
HD 218396	205	208^{+11}_{-10}	45	48^{+5}_{-6}	89	96^{+14}_{-9}	−4.91	$-4.93^{+.03}_{-0.02}$	95	92^{+3}_{-13}	−30	-60^{+50}_{-50}	−90	-100^{+60}_{-70}	12	12^{+16}_{-6}	58	55^{+10}_{-10}

Power law + error function

disc	R_c (au)		σ_{in} (au)		α_{out}		Σ_c		PA (°)		$\Delta\alpha$ (mas)		$\Delta\delta$ (mas)		i (°)		F_* (μJy)	
HD 15257	130	110^{+30}_{-30}	0.46	$0.51^{+0.35}_{-0.12}$	0.9	$0.6^{+0.5}_{-0.4}$	−5.33	$-5.40^{+0.10}_{-0.12}$	47	47^{+3}_{-3}	130	80^{+70}_{-70}	80	80^{+80}_{-90}	61.4	$62.4^{+1.9}_{-2.1}$	50	50^{+40}_{-30}
HD 121617	67.5	$67.8^{+0.6}_{-0.4}$	0.007	$0.018^{+0.014}_{-0.011}$	6.7	$6.9^{+0.4}_{-0.3}$	−3.268	$-3.264^{+0.017}_{-0.016}$	58.6	$58.4^{+0.7}_{-0.6}$	0	0^{+2}_{-3}	−4	-3^{+2}_{-3}	44.4	$44.6^{+0.4}_{-0.6}$	22	27^{+10}_{-10}
HD 161868	100	99^{+3}_{-4}	0.299	$0.297^{+0.015}_{-0.014}$	1.89	$1.90^{+0.16}_{-0.17}$	−5.13	$-5.12^{+0.02}_{-0.03}$	58.9	$58.5^{+1.1}_{-1.2}$	60	70^{+30}_{-30}	−160	-150^{+20}_{-30}	67.7	$66.8^{+1.1}_{-1.1}$	20	27^{+29}_{-19}

Notes. The left column under each parameter is the best fit—defined as having the lowest χ^2 value—while the right column is the median. Uncertainties are calculated from the 16th and 84th percentiles of the posterior distribution. We report multiple parametrisations for discs where the significance between these models, as measured by the AIC and the BIC, was minimal or ambiguous. The surface density normalisation Σ_c is parametrised as an exponent, with 10^{Σ_c} in units of g cm^{-2}.

Table C.2: MCMC results for discs with gaps or extended emission fit by a double Gaussian.

Best Fits

Disc	R_1 (au)	R_2 (au)	σ_1 (au)	σ_2 (au)	C	Σ_c	PA (°)	$\Delta\alpha$ (mas)	$\Delta\delta$ (mas)	i (°)	F_* (μJy)
HD 10647	89.2	168	12	48	0.659	−4.433	56.93	121	−17	79.08	128
HD 15115	65.8	97.54	1.6	4.75	0.26	−3.40	98.466	37	−14	86.7	23
HD 61005	69.7	94	7.3	32.3	0.836	−3.358	70.29	2	−16	86.2	1
HD 92945	57.1	102.7	5.6	24.1	0.52	−4.09	100.9	−70	−87	66.3	39
HD 109573	77.65	85	2.98	24	0.979	−2.77	26.52	13.8	−39.9	76.54	52
HD 121617	75.2	100	6	42	0.948	−3.17	58.0	0	−2	43.9	5
HD 131488	90.8	95.1	0.69	17.3	0.97	−1.96	97.305	1.1	−7.3	84.84	40
HD 131835	68.7	104.2	4.9	44.7	0.866	−2.9	58.94	1.4	−5.9	74.47	4
HD 206893	42	125	6	36	0.43	−4.53	64	−50	20	44	17

Medians

Disc	R_1 (au)	R_2 (au)	σ_1 (au)	σ_2 (au)	C	Σ_c	PA (°)	$\Delta\alpha$ (mas)	$\Delta\delta$ (mas)	i (°)	F_* (μJy)
HD 10647	$89.1^{+0.7}_{-0.8}$	164^{+6}_{-8}	$11.9^{+1.0}_{-0.9}$	46^{+3}_{-3}	$0.664^{+0.009}_{-0.010}$	$-4.438^{+0.012}_{-0.012}$	$56.93^{+0.06}_{-0.05}$	121^{+10}_{-10}	-23^{+9}_{-7}	$79.00^{+0.12}_{-0.18}$	130^{+10}_{-10}
HD 15115	$65.8^{+0.6}_{-0.3}$	$97.57^{+0.07}_{-0.05}$	$2.4^{+1.0}_{-0.8}$	$4.73^{+0.18}_{-0.20}$	$0.19^{+0.06}_{-0.04}$	$-3.44^{+0.04}_{-0.02}$	$98.460^{+0.011}_{-0.013}$	36^{+2}_{-3}	$-14^{+0.9}_{-0.9}$	$86.71^{+0.03}_{-0.02}$	28^{+5}_{-6}
HD 61005	$69.4^{+0.5}_{-0.4}$	95^{+2}_{-3}	$7.4^{+0.5}_{-0.5}$	$31.7^{+1.6}_{-1.5}$	$0.837^{+0.012}_{-0.012}$	$-3.359^{+0.016}_{-0.015}$	$70.29^{+0.02}_{-0.03}$	0^{+5}_{-5}	-17^{+2}_{-2}	$86.17^{+0.05}_{-0.07}$	5^{+7}_{-4}
HD 92945	$57.0^{+0.8}_{-0.8}$	$102.7^{+1.5}_{-1.5}$	$5.5^{+1.2}_{-1.1}$	$25.1^{+2.0}_{-1.9}$	$0.52^{+0.04}_{-0.03}$	$-4.10^{+0.04}_{-0.03}$	$100.5^{+0.5}_{-0.5}$	-80^{+30}_{-30}	-78^{+17}_{-16}	$66.0^{+0.5}_{-0.6}$	36^{+15}_{-15}
HD 109573	$77.61^{+0.04}_{-0.16}$	$84^{+2.1}_{-1.8}$	$2.89^{+0.18}_{-0.19}$	22^{+4}_{-4}	$0.977^{+0.006}_{-0.009}$	$-2.77^{+0.02}_{-0.02}$	$26.51^{+0.05}_{-0.07}$	$13.9^{+0.8}_{-0.8}$	$-39.6^{+1.2}_{-1.2}$	$76.65^{+0.09}_{-0.09}$	38^{+17}_{-17}
HD 121617	$75.3^{+0.4}_{-0.3}$	103^{+8}_{-5}	$6^{+0.5}_{-0.5}$	42^{+8}_{-7}	$0.952^{+0.008}_{-0.010}$	$-3.17^{+0.03}_{-0.02}$	$58.3^{+0.6}_{-0.6}$	-1^{+2}_{-2}	-2^{+3}_{-2}	$44.1^{+0.6}_{-0.5}$	12^{+11}_{-8}
HD 131488	$90.84^{+0.18}_{-0.08}$	$96.1^{+0.6}_{-0.7}$	$0.96^{+0.28}_{-0.19}$	$19.3^{+1.9}_{-1.3}$	$0.966^{+0.006}_{-0.006}$	$-2.08^{+0.08}_{-0.10}$	$97.301^{+0.012}_{-0.029}$	$1.2^{+0.6}_{-0.6}$	$-7.1^{+0.3}_{-0.3}$	$84.87^{+0.06}_{-0.03}$	38^{+8}_{-8}
HD 131835	$68.5^{+0.4}_{-0.4}$	$105.8^{+2.0}_{-1.7}$	$4.9^{+0.6}_{-0.6}$	$43.5^{+1.3}_{-1.5}$	$0.869^{+0.011}_{-0.010}$	$-2.939^{+0.04}_{-0.04}$	$58.95^{+0.18}_{-0.18}$	$1.6^{+1.8}_{-1.8}$	$-5.6^{+1.3}_{-1.4}$	$74.41^{+0.20}_{-0.20}$	10^{+11}_{-7}
HD 206893	42^{+5}_{-5}	126^{+4}_{-3}	6^{+9}_{-4}	36^{+4}_{-3}	$0.38^{+0.22}_{-0.17}$	$-4.57^{+0.20}_{-0.12}$	62^{+3}_{-3}	-10^{+60}_{-60}	30^{+50}_{-50}	46^{+3}_{-2}	14^{+6}_{-6}

Notes. The top half of the table describes the best fits, while the bottom half describes the median values and their uncertainties, as calculated from the 16th and 84th percentiles of the posterior distribution. The surface density normalisation Σ_c is parametrised as an exponent, with 10^{Σ_c} in units of g cm^{-2}. Although HD 15115, HD 107146, and HD 197481 are included in this table, these discs are better fit by variations of the triple power law or double power law functional forms. These results can be found in Table C.3.

Table C.3: MCMC results from the best parametric models for HD 15115, HD 107146, and HD 197481.

	HD 15115		HD 107146		HD 197481			
	2 pow. + 1 gap		3 pow. + 2 gaps		3 pow. + 1 gap		3 pow.	
Parameter	Best fit	Median	Best fit	Median	Best fit	Median	Best fit	Median
R_c (au)	98.11	$98.09^{+0.16}_{-0.19}$						
R_{in} (au)			44.4	$43.8^{+0.8}_{-0.9}$	25.4	$25.1^{+0.8}_{-1.0}$	26.7	$26.9^{+0.5}_{-0.7}$
R_{out} (au)			137.8	$137.5^{+1.0}_{-1.0}$	38.7	$38.1^{+1.2}_{-1.4}$	38.3	$39.0^{+1.1}_{-1.3}$
α_{in}	7.9	$7.9^{+0.3}_{-0.2}$	6.7	$6.6^{+0.4}_{-0.3}$	25	28^{+14}_{-11}	28	25^{+4}_{-5}
α_{mid}			0	$0.02^{+0.04}_{-0.05}$	0.9	$0.8^{+0.3}_{-0.4}$	0.8	$0.5^{+0.4}_{-0.3}$
α_{out}	−16.2	$-16.3^{+0.6}_{-0.8}$	−11.3	$-11.4^{+0.6}_{-0.5}$	−9.3	$-9.5^{+1.5}_{-2.0}$	−11.1	$-11.4^{+1.4}_{-2.1}$
R_1 (au)	94	$93.9^{+0.3}_{-0.3}$	55.9	$56.1^{0.5}_{-0.3}$	36	34^{+3}_{-2}		
σ_1 (au)	11	$10.9^{+0.4}_{-0.4}$	2.7	$2.9^{+0.6}_{-0.4}$	7.5	$8^{+1.2}_{-1.1}$		
C_1	0.448	$0.452^{+0.007}_{-0.008}$	0.64	$0.57^{+0.7}_{-0.9}$	0.8	$0.6^{+0.3}_{-0.3}$		
R_2 (au)			77.9	$78.1^{+0.6}_{-0.8}$				
σ_2 (au)			16.2	$16.6^{+1.0}_{-0.8}$				
C_2			0.692	$0.693^{+0.025}_{-0.016}$				
Σ_c	−3.04	$-3.02^{+0.02}_{-0.02}$	−4.17	$-4.18^{+0.04}_{-0.04}$	−3.82	$-3.89^{+0.11}_{-0.10}$	−4.05	$-3.99^{+0.06}_{-0.08}$
PA (°)	98.478	$98.464^{+0.019}_{-0.033}$	163.2	$163.29^{+0.19}_{-0.16}$	128.72	$128.73^{+0.03}_{-0.02}$	128.72	$128.74^{+0.05}_{-0.03}$
$\Delta\alpha$ (mas)	36	36^{+3}_{-2}	12	11^{+7}_{-6}	−19	-20^{+6}_{-7}	−17	-22^{+7}_{-7}
$\Delta\delta$ (mas)	−14.0	$-14.0^{+0.09}_{-0.09}$	−20	-29^{+5}_{-5}	−9	-9^{+5}_{-6}	−10	-8^{+5}_{-6}
i (°)	86.753	$86.735^{+0.017}_{-0.041}$	14.5	$14.4^{+1.1}_{-0.3}$	88.4	$88.42^{+0.03}_{-0.06}$	88.41	$88.40^{+0.04}_{-0.08}$
F_* (μJy)	21	25^{+6}_{-6}	23.1	$23.6^{+1.7}_{-1.3}$	See Table C.4			

Notes. The surface density normalisation Σ_c is parametrised as an exponent, with 10^{Σ_c} in units of g cm^{-2}. For HD 197481, the significance of the gap centred at 36 au is ambiguous, so we report results for two parametrisations here.

Table C.4: Stellar fluxes for HD 197481.

Date	ARKS Fitting		Disc + Ring		Fiducial	
	Best Fit	Median	Best Fit	Median	Best Fit	Median
March 26, 2014	327	343^{+18}_{-19}	370	390^{+20}_{20}	400	390^{+20}_{-20}
August 18, 2014	130	140^{+30}_{-20}	140	150^{+20}_{-30}	170	160^{+20}_{-30}
June 24, 2015	196	205^{+18}_{-18}	210	220^{+20}_{-20}	240	240^{+20}_{-20}

Notes. ARKS fitting results are from the best parametric model for HD 197481, a triple power law with one gap. Disc + ring and fiducial model results are from Daley et al. (2019). All fluxes are in units of μJy.

Appendix D: Model and residual maps from parametric modelling

This appendix displays the model images and residual maps from parametric modelling. Details of the fitting methods are described in Sect. 2.4.

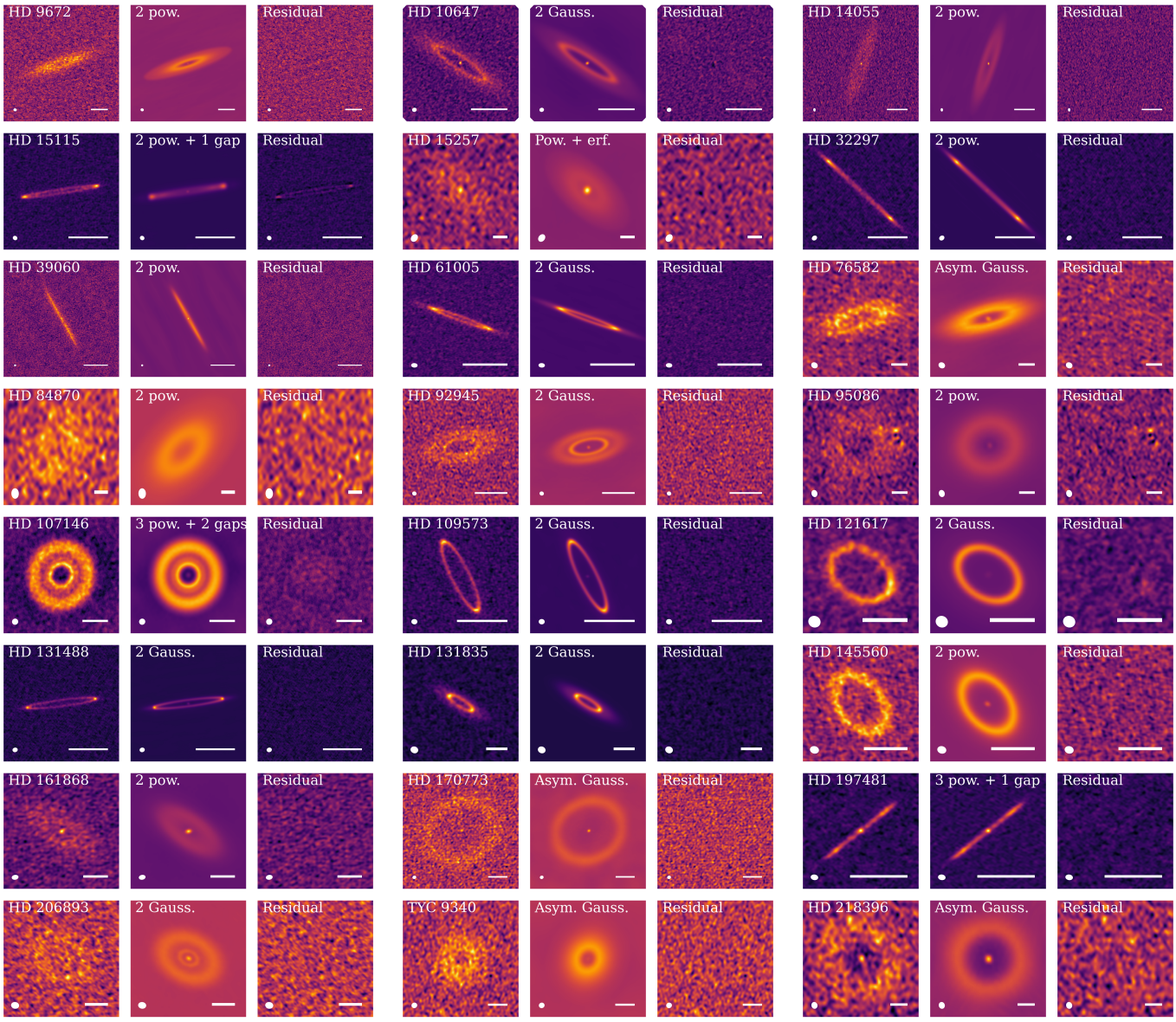

Fig. D.1: Data (left), model (middle), and residual (right) images for the best-fit parametric model for each disc. We compare the images in the visibility domain, and we apply a Briggs weighting with a robust parameter of 0.5 by default. Scale bars are 100 au for all discs, except HD 197481, which has a scale bar of 50 au.

Appendix E: AIC and BIC parametric model comparison

This Appendix lists the results of model comparison among the parametric models fitted to each system in Table E.1 and displays the fitted parametric radial profiles in Fig. E.1. Details of the fitting methods are described in Sect. 2.4.

Table E.1: AIC and BIC comparison of parametric models.

Disc	Functional Forms	AIC Confidence (σ)	ΔBIC
HD 9672	**Double power law**	—	—
	Double Gaussian	2.9	> 10
HD 10647	**Double Gaussian**	—	8.2
	Double power law	3.6	—
	Double power law + 1 gap	2.7	> 10
HD 14055	**Double power law**	—	—
	Double Gaussian	0.77	> 10
HD 15115	**Double power law + 1 gap**	—	—
	Double Gaussian	4.9	> 10
	Double power law	> 5	> 10
HD 15257	**Power law + error function**	—	—
	Double power law	0.97	0.16
HD 32297	**Double power law**	1.4	—
	Double Gaussian	4.7	> 10
	Gaussian + double power law	—	> 10
HD 39060	**Double power law**	1.8	—
	Double Gaussian	—	> 10
HD 61005	**Double Gaussian**	—	—
	Double power law	> 5	> 10
	Triple Gaussian	0.17	> 10
HD 76582	**Asymmetric Gaussian**	—	—
	Double power law	2.8	> 10
	Power law + error function	4.1	> 10
	Triple power law	1.1	> 10
HD 84870	**Double power law**	—	—
	Power law + error function	1.7	4.7
HD 92945	**Double Gaussian**	—	—
	Double Gaussian + 1 gap	1.9	> 10
	Triple Gaussian	1.8	> 10
	Double power law	> 5	> 10
	Double power law + 1 gap	4.2	> 10
	Double power law + 2 gaps	2.3	> 10
	Triple power law + 1 gap	2.4	> 10
HD 95086	**Double power law**	1.9	—
	Double Gaussian	2.2	> 10
	Triple power law	—	> 10
HD 107146	**Triple power law + 2 gaps**	—	—
	Triple power law + 1 gap	> 5	> 10
	Triple power law	> 5	> 10
	Double Gaussian	> 5	> 10
	Triple Gaussian	> 5	> 10
HD 109573	**Double Gaussian**	—	—
	Single Gaussian	> 5	> 10
	Asymmetric Gaussian	> 5	> 10
	Double power law	5.0	4.7
HD 121617	**Double Gaussian**	—	7.3
	Single Gaussian	> 5	> 10
	Power law + error function	3.9	—
	Double power law	4.0	0.15
	Asymmetric Gaussian	> 5	> 10
HD 131488	**Double Gaussian**	—	—
	Triple Gaussian	> 5	> 10
	Double power law	> 5	> 10
HD 131835	**Double Gaussian**	—	—
	Triple Gaussian	1.4	> 10
	Double power law	> 5	> 10
HD 145560	**Double power law**	3.9	—
	Double Gaussian	—	7.1
	Single Gaussian	> 5	> 10

Table E.1: Continued.

Disc	Functional Forms	AIC Confidence (σ)	ΔBIC
HD 161868	**Double power law**	—	—
	Power law + error function	0.72	1.5
	Asymmetric Gaussian	1.1	2.5
HD 170773	**Asymmetric Gaussian**	—	—
	Double power law	0.33	0.61
HD 197481	**Triple power law + 1 gap**	—	> 10
	Triple power law	3.4	—
	Double power law	6.6	> 10
	Double Gaussian	4.2	6.2
	Triple Gaussian	2.8	> 10
HD 206893	**Double Gaussian**	—	> 10
	Triple Gaussian	1.3	> 10
	Double power law	2.5	—
	Double power law + 1 gap	1.1	> 10
	Triple power law	3.3	> 10
	Triple power law + 1 gap	1.3	> 10
TYC 9340-437-1	**Asymmetric Gaussian**	2.2	—
	Double power law	2.3	0.85
	Triple power law	—	> 10
	Double Gaussian	3.3	> 10
HD 218396	**Asymmetric Gaussian**	0.18	—
	Double Gaussian	—	> 10
	Double power law	3.0	> 10
	Triple power law	1.2	> 10

Notes. We calculated AIC and BIC differences for each disc relative to the functional form with the lowest criterion value, indicated by a dash (—). The best-fit functional form is determined on a case-by-case basis for each disc, as described throughout the results section, and is indicated by bold text. We convert AIC differences to a confidence interval, while BIC differences > 10 are considered to be a strong indicator of significance.

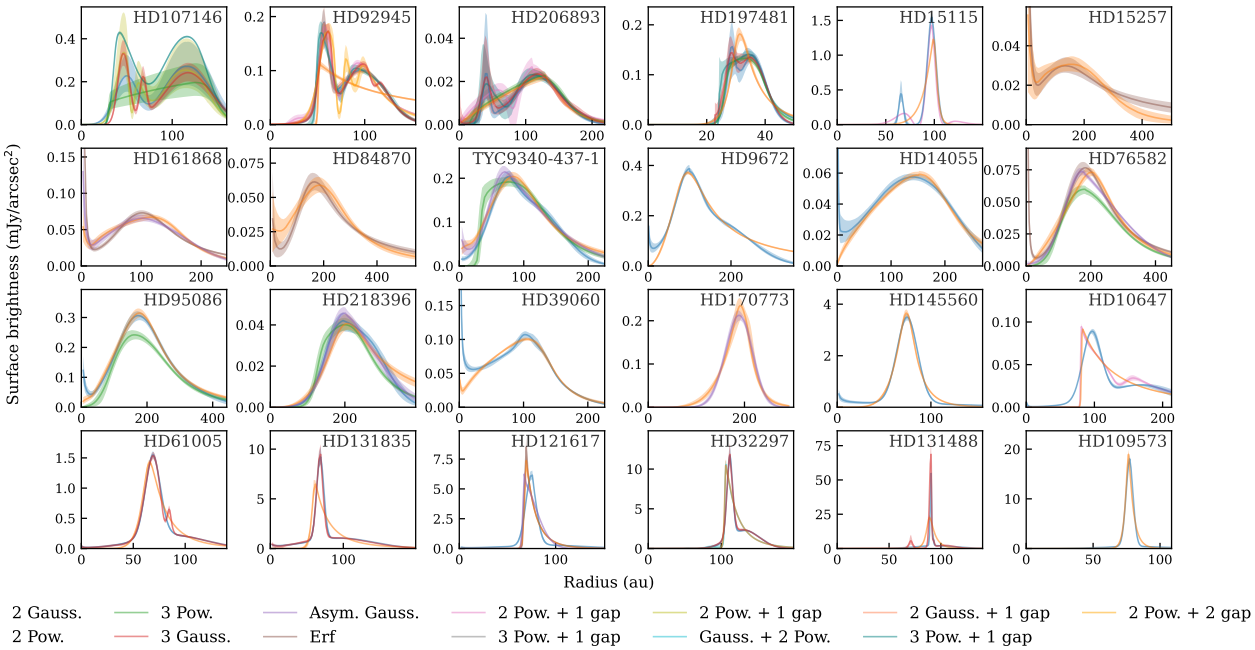

Fig. E.1: Deprojected radial profiles fitted under various parametric models attempted for each disc.

Appendix F: Model and residuals maps from `frank` and `rave` models

This appendix displays the model images and residual maps for the radial profile methods used in this study. These methods are described in Sect. 2.

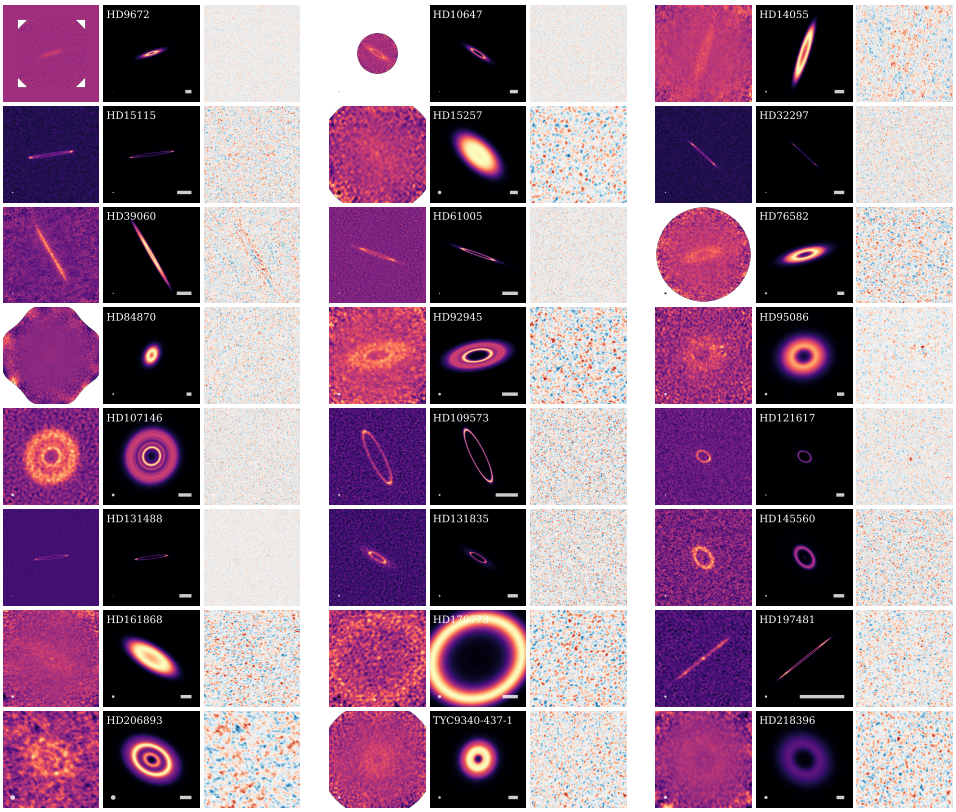

Fig. F.1: `CLEAN` image, `frank` model (convolved), and `frank` imaged residuals. The scale bars indicate 50 au and the ellipses at the bottom left of each panel indicate the beam size.

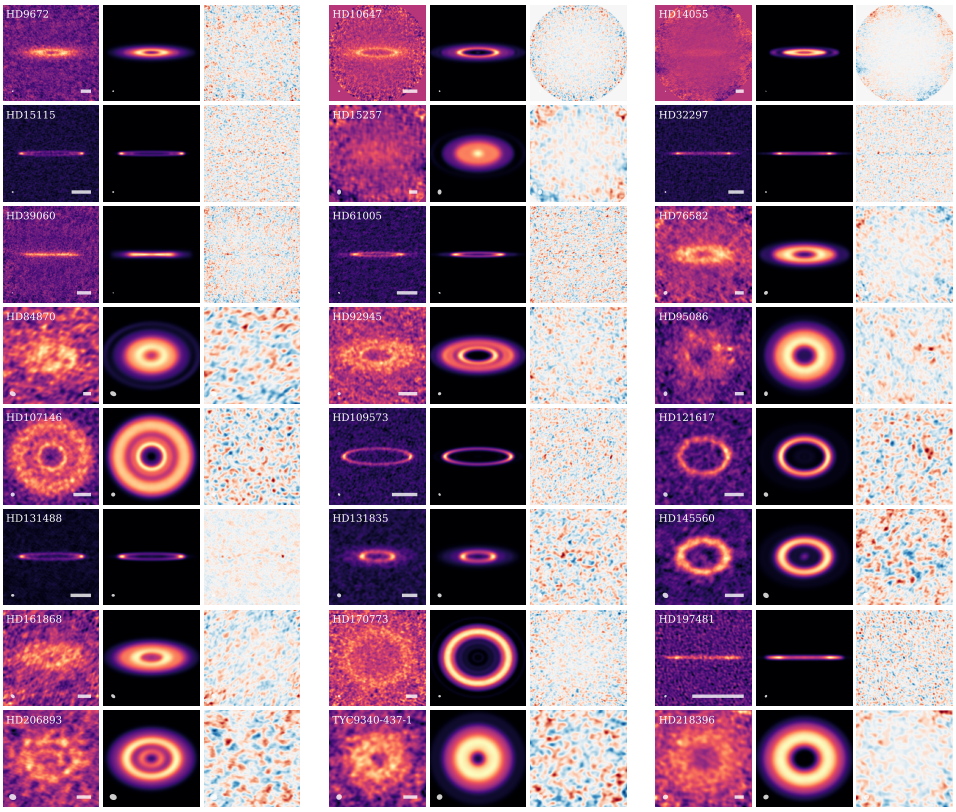

Fig. F.2: `CLEAN` image, `rave` model (convolved), and `rave` residuals with the major axis aligned horizontally. The scale bars indicate 50 au.

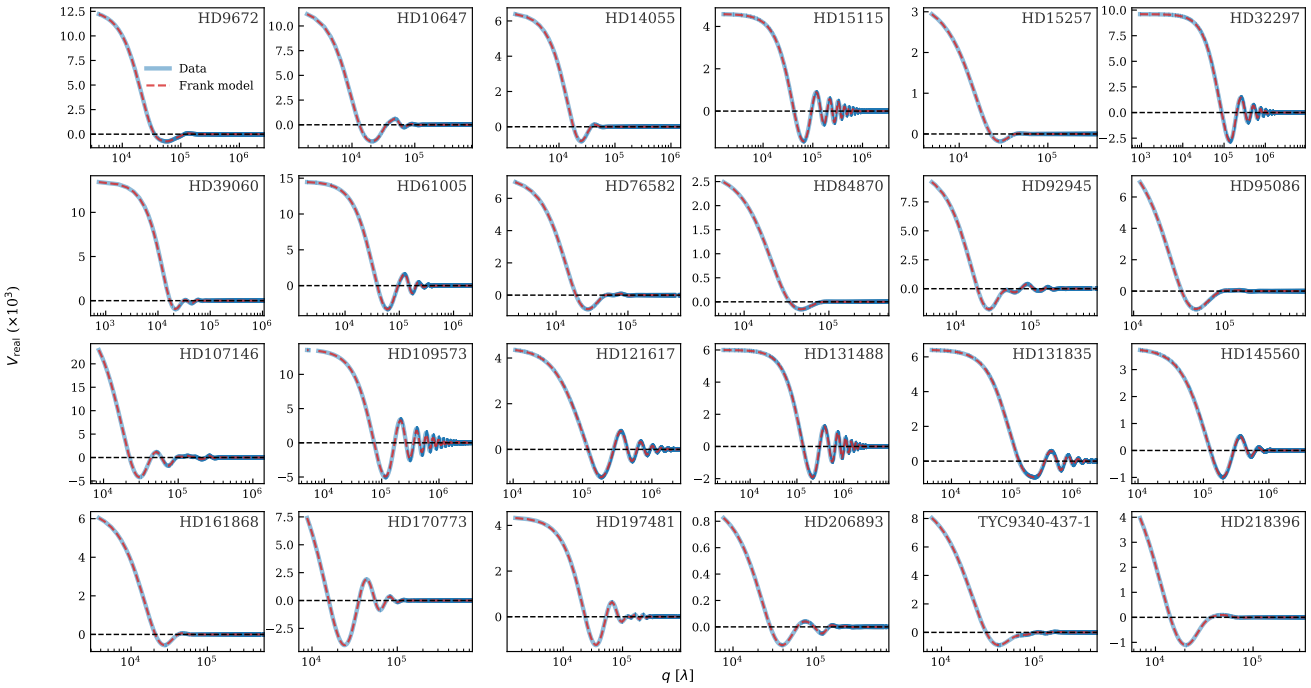

Fig. F.3: `frank` visibility amplitudes of the observations (solid blue line) and `frank` models (dotted orange line).

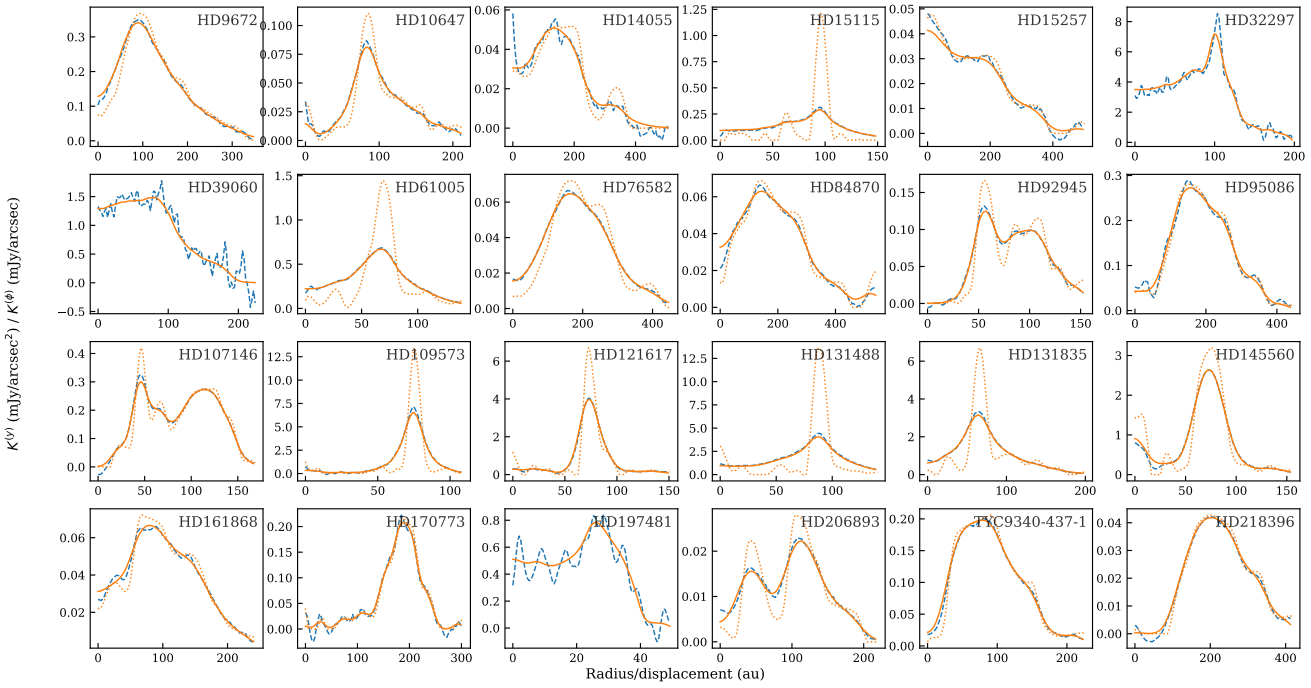

Fig. F.4: 1D quantities that `rave` fits to. This includes the vertically summed flux ($K^{(y)}$) of the `CLEAN` image (blue dashed line) and `rave` model (solid orange line) for the edge-on discs (HD 39060, HD 197481, and HD 32297), and the azimuthally averaged profiles ($K^{(\phi)}$) of the `CLEAN` image (blue dashed line) and (convolved) `rave` model image (solid orange line), with the (deconvolved) `rave` profile overplotted (dotted orange line), for all other discs.

Appendix G: `frank` and `rave` hyperparameters

This Appendix lists the hyperparameters used in the non-parametric fitting in Table G.1. Details of the fitting methods are described in Sects. 2.2 and 2.3.

Table G.1: `frank` and `rave` hyperparameters used to fit the deconvolved and deprojected radial profiles.

	`frank`				`rave`			`CLEAN`	
Target	α	$w_{\rm smooth}$	N	$r_{\rm out}$ [″]	N	$r_{\rm max}$ [″]	$y_{\rm max}$ [″]	`rave` robust	Display profile robust
HD 9672	1.05	0.001	300	10	10	6.1	1.5	1.0	0.5
HD 10647	1.05	0.001	200	20	15	12.3	5.5	0.5	0.5
HD 14055	1.05	0.1	300	12	10	14.3	2.9	2.0	2.0
HD 15115	1.01	0.1	300	5	20	3.1	0.5	0.5	0.5
HD 15257	1.05	0.1	300	12	7	10.2	5.1	2.0	0.5
HD 32297	1.05	0.001	300	3	17	1.5	0.2	0.5	0.5
HD 39060	1.3	0.1	300	12	7	11.5	2.3	2.0	1.0
HD 61005	1.05	0.1	200	6	15	3.8	0.8	0.5	0.0
HD 76582	1.01	0.0001	300	15	10	9.2	3.7	2.0	0.5
HD 84870	1.01	0.1	300	12	10	6.1	3.7	2.0	0.5
HD 92945	1.01	0.1	200	10	15	7.2	3.6	1.0	1.0
HD 95086	1.01	0.1	200	8	10	5.1	4.1	2.0	0.5
HD 107146	1.03	0.01	300	10	20	6.1	6.1	-0.5	-0.5
HD 109573	1.01	0.1	300	2	20	1.5	0.4	0.5	0.0
HD 121617	1.01	0.1	200	3	18	1.3	0.8	0.5	0.5
HD 131488	1.1	0.1	200	2	15	0.9	0.2	1.0	0.0
HD 131835	1.03	0.0001	200	3	15	1.5	0.5	0.5	0.0
HD 145560	1.01	0.1	200	3	15	1.3	0.8	2.0	0.5
HD 161868	1.05	0.1	300	12	10	8.2	4.1	2.0	0.5
HD 170773	1.02	0.1	300	9	20	8.2	6.5	2.0	0.5
HD 197481	1.01	0.1	300	10	9	5.1	0.5	0.0	0.0
HD 206893	1.01	0.001	300	8	10	5.4	4.3	2.0	1.0
TYC 9340-437-1	1.01	0.0001	300	12	10	6.1	6.1	2.0	0.5
HD 218396	1.01	0.1	100	15	10	10.2	10.2	2.0	0.5

Appendix H: Mean-motion resonances

Undetected planets could exist in mean-motion resonances and shape the structure of the debris discs that we observe. Three discs in the ARKS sample exhibit more than one radial gap as suggested by the `frank` profiles (see Table 2). We find that the radial location of the two gaps in HD 131835 and HD 197481 (AU Mic) could coincide with a 2:1 resonance, whereas the two gaps in HD 107146 could coincide with the 3:2 resonance. While these commensurabilities between orbital periods at key locations in the discs could exist, it must be remembered that by chance, a fraction of radial features based on an arbitrary sample of radial profiles are expected to fall close to a resonance. A discussion on the probability and implications of these resonances is beyond the scope of this work, and we simply list these potential resonances as topics of investigation to encourage future work on this subject.

Appendix I: Disc features measured from non-parametric profiles

This appendix lists the radial features measured from the `frank` surface density profiles in Table I.1, with a visualisation of these measurements shown in Fig. I.1. Details of these measurements are described in Sect. 3.2.

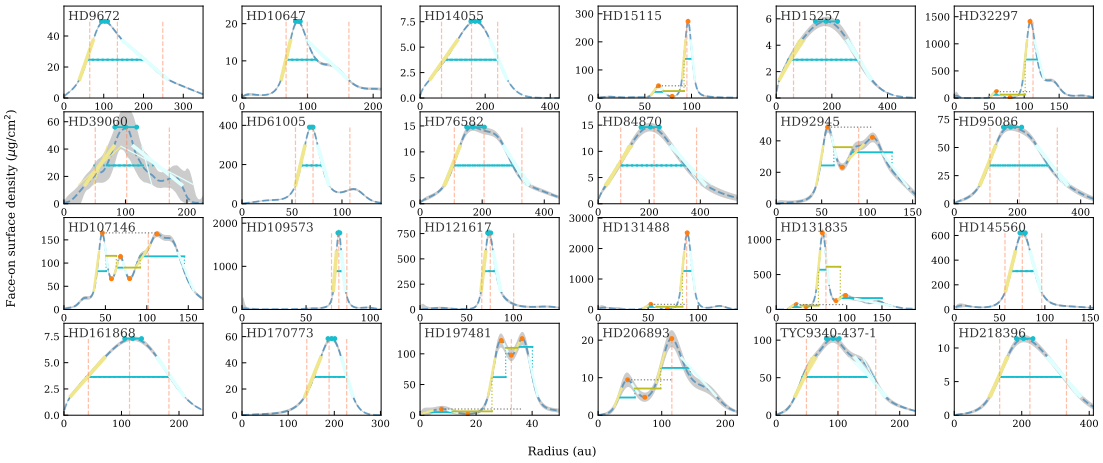

Fig. I.1: `frank` surface density profiles labelled with measured disc features. Orange dots at peaks and troughs indicate the individual rings and gaps in multi-ring systems. The line segments labelled on each profile indicate the edges, fractional widths, and the uncertainties in the peak radius detected from the radial profiles (see Sect. 3.2 for details).

Table I.1: Ring and edge locations and widths in units of au measured from the `frank` surface density profiles.

Target	Ring	$r_{\rm peak}$	$r_{\rm centroid}$	Δr	$r_{\rm inner}$	$\Delta r_{\rm inner}$	$r_{\rm outer}$	$\Delta r_{\rm outer}$
HD 9672	1	$102.3^{+7.4}_{-8.1}$	134.4	$146.2^{+1.7}_{-1.8}$	$58.2^{+0.7}_{-0.8}$	$33.5^{+1.2}_{-1.1}$	$204.4^{+2.7}_{-2.8}$	$111.2^{+3.4}_{-3.3}$
HD 10647	1	$86.0^{+2.9}_{-4.4}$	99.5	$45.8^{+1.4}_{-1.2}$	$67.7^{+0.5}_{-0.5}$	$13.9^{+0.7}_{-0.7}$	$113.6^{+2.2}_{-1.9}$	$61.8^{+1.5}_{-1.5}$
HD 14055	1	$169.3^{+12.1}_{-13.1}$	158.1	$161.8^{+2.2}_{-2.2}$	$77.7^{+2.6}_{-2.6}$	$82.4^{+2.4}_{-2.4}$	$239.5^{+1.8}_{-1.8}$	$51.1^{+1.9}_{-1.9}$
HD 15115	1	$64.7^{+2.5}_{-2.3}$		$10.4^{+1.0}_{-1.1}$	$59.5^{+1.0}_{-0.9}$	$2.2^{+1.3}_{-1.1}$	$69.8^{+1.0}_{-1.1}$	$4.2^{+1.4}_{-1.2}$
	2	$96.3^{+1.1}_{-1.0}$		$9.0^{+0.2}_{-0.2}$	$92.0^{+0.2}_{-0.2}$	$0.5^{+0.3}_{-0.3}$	$101.0^{+0.3}_{-0.3}$	$4.2^{+0.3}_{-0.3}$
HD 15257	1	$179.4^{+41.1}_{-38.4}$	177.5	$250.9^{+7.7}_{-9.1}$	$45.1^{+7.8}_{-6.4}$	$78.1^{+7.0}_{-6.7}$	$296.0^{+9.0}_{-10.4}$	$83.8^{+10.5}_{-10.1}$
HD 32297	1	$60.5^{+3.4}_{-4.3}$		$11.6^{+2.0}_{-2.3}$	$54.5^{+2.2}_{-1.8}$	$4.3^{+2.2}_{-2.1}$	$66.1^{+2.1}_{-2.3}$	$5.1^{+2.6}_{-2.5}$
	2	$108.4^{+2.7}_{-1.4}$		$17.4^{+0.4}_{-0.4}$	$101.5^{+0.3}_{-0.3}$	$0.7^{+0.4}_{-0.4}$	$118.9^{+0.5}_{-0.5}$	$13.5^{+6.4}_{-1.1}$
HD 39060	1	$100.5^{+18.7}_{-20.3}$	102.4	$62.3^{+16.3}_{-13.8}$	$66.1^{+12.0}_{-16.7}$	$44.1^{+12.8}_{-19.9}$	$128.4^{+15.9}_{-15.7}$	$78.5^{+17.2}_{-26.6}$
HD 61005	1	$69.5^{+1.6}_{-2.1}$	71.1	$21.2^{+0.3}_{-0.3}$	$58.9^{+0.3}_{-0.3}$	$9.1^{+0.4}_{-0.4}$	$80.1^{+0.3}_{-0.3}$	$10.8^{+0.5}_{-0.5}$
HD 76582	1	$170.1^{+37.1}_{-20.0}$	206.1	$191.3^{+4.1}_{-4.0}$	$107.4^{+3.4}_{-3.5}$	$48.7^{+4.6}_{-4.4}$	$298.7^{+4.7}_{-4.7}$	$78.0^{+9.1}_{-7.5}$
HD 84870	1	$204.6^{+35.0}_{-36.6}$	219.0	$259.1^{+10.8}_{-10.3}$	$81.8^{+8.7}_{-8.9}$	$92.9^{+8.7}_{-9.1}$	$340.9^{+12.6}_{-11.9}$	$131.3^{+18.4}_{-15.8}$
HD 92945	1	$56.5^{+3.3}_{-2.3}$		$14.9^{+0.9}_{-1.0}$	$48.5^{+0.8}_{-0.7}$	$1.8^{+1.0}_{-0.9}$	$63.4^{+1.1}_{-1.2}$	$5.1^{+1.5}_{-1.2}$
	2	$105.8^{+5.7}_{-6.4}$		$44.3^{+2.8}_{-3.2}$	$83.0^{+3.4}_{-2.2}$	$13.1^{+4.0}_{-6.5}$	$127.3^{+3.5}_{-3.1}$	$27.5^{+2.8}_{-2.8}$
HD 95086	1	$178.3^{+35.1}_{-22.8}$	205.5	$189.6^{+4.8}_{-4.7}$	$108.4^{+3.5}_{-3.5}$	$48.5^{+4.2}_{-4.0}$	$298.0^{+6.1}_{-5.9}$	$94.4^{+9.7}_{-8.6}$
HD 107146	1	$46.4^{+1.4}_{-1.7}$		$11.0^{+0.4}_{-0.4}$	$39.9^{+0.4}_{-0.4}$	$1.0^{+0.6}_{-0.5}$	$50.9^{+0.5}_{-0.5}$	$3.7^{+0.6}_{-0.5}$
	2	$68.3^{+2.0}_{-2.4}$		$9.9^{+0.8}_{-0.8}$	$63.2^{+0.8}_{-0.8}$	$1.7^{+1.0}_{-0.8}$	$73.1^{+0.8}_{-0.8}$	$3.7^{+1.1}_{-0.9}$
	3	$112.1^{+6.9}_{-3.8}$		$53.3^{+1.5}_{-2.8}$	$92.0^{+4.6}_{-1.9}$	$2.6^{+1.3}_{-1.3}$	$145.3^{+1.0}_{-1.1}$	$18.9^{+1.4}_{-1.3}$
HD 109573	1	$75.7^{+0.7}_{-0.8}$	75.6	$6.0^{+0.2}_{-0.2}$	$72.7^{+0.2}_{-0.2}$	$2.5^{+0.2}_{-0.2}$	$78.8^{+0.2}_{-0.2}$	$3.2^{+0.3}_{-0.3}$
HD 121617	1	$73.6^{+2.3}_{-1.0}$	75.4	$13.1^{+0.5}_{-0.5}$	$68.2^{+0.4}_{-0.4}$	$4.8^{+0.5}_{-0.5}$	$81.3^{+0.6}_{-0.6}$	$7.9^{+0.8}_{-0.8}$
HD 131488	1	$52.7^{+3.5}_{-2.8}$		$10.6^{+20.3}_{-1.8}$	$47.7^{+1.7}_{-39.1}$	$4.4^{+2.1}_{-2.2}$	$58.3^{+1.5}_{-1.8}$	$4.3^{+2.1}_{-1.8}$
	2	$89.1^{+0.8}_{-0.7}$		$9.9^{+0.2}_{-0.2}$	$84.4^{+0.2}_{-0.2}$	$0.4^{+0.2}_{-0.2}$	$94.3^{+0.2}_{-0.2}$	$4.4^{+0.2}_{-0.2}$
HD 131835	1	$28.6^{+7.4}_{-6.2}$		$14.1^{+4.6}_{-4.6}$	$20.7^{+3.0}_{-1.8}$	$4.8^{+3.5}_{-2.4}$	$34.8^{+7.4}_{-6.2}$	$5.4^{+4.1}_{-2.7}$
	2	$65.4^{+2.4}_{-1.0}$		$12.1^{+0.4}_{-0.5}$	$60.0^{+0.4}_{-0.4}$	$1.1^{+0.5}_{-0.6}$	$72.0^{+0.5}_{-0.5}$	$5.0^{+0.6}_{-0.5}$
	3	$98.4^{+6.5}_{-6.5}$		$59.0^{+3.6}_{-16.1}$	$90.9^{+4.1}_{-3.0}$	$4.3^{+4.6}_{-2.2}$	$149.9^{+4.1}_{-28.0}$	$52.0^{+7.0}_{-7.9}$
HD 145560	1	$75.6^{+2.8}_{-3.2}$	75.1	$26.1^{+0.6}_{-0.7}$	$62.7^{+0.6}_{-0.6}$	$10.5^{+0.7}_{-0.8}$	$88.8^{+0.7}_{-0.7}$	$11.7^{+0.8}_{-0.8}$
HD 161868	1	$119.6^{+15.3}_{-13.8}$	114.0	$144.6^{+2.5}_{-2.6}$	$39.4^{+2.9}_{-2.7}$	$58.3^{+2.2}_{-2.2}$	$184.1^{+2.3}_{-2.4}$	$46.2^{+2.6}_{-2.5}$
HD 170773	1	$194.3^{+6.9}_{-7.9}$	188.7	$70.8^{+1.6}_{-1.6}$	$156.0^{+1.6}_{-1.6}$	$33.5^{+2.1}_{-2.0}$	$226.8^{+1.5}_{-1.6}$	$24.8^{+1.6}_{-1.7}$
HD 197481	1	$7.7^{+4.1}_{-6.8}$		$9.1^{+2.5}_{-4.5}$	$2.5^{+5.2}_{-2.5}$	$3.7^{+2.0}_{-1.8}$	$11.6^{+2.5}_{-3.9}$	$2.9^{+3.1}_{-1.5}$
	2	$29.0^{+1.4}_{-1.4}$		$4.9^{+0.8}_{-0.9}$	$25.7^{+0.3}_{-0.3}$	$0.7^{+0.4}_{-0.4}$	$30.6^{+1.2}_{-1.4}$	$1.2^{+1.2}_{-0.6}$
	3	$36.4^{+1.4}_{-1.5}$		$5.4^{+0.7}_{-0.8}$	$34.7^{+1.2}_{-1.1}$	$1.3^{+1.3}_{-0.7}$	$40.1^{+0.4}_{-0.4}$	$3.1^{+0.5}_{-0.4}$
HD 206893	1	$46.4^{+8.5}_{-8.4}$		$26.1^{+4.1}_{-4.7}$	$31.8^{+3.3}_{-2.4}$	$5.9^{+4.5}_{-2.9}$	$57.8^{+5.8}_{-6.1}$	$9.0^{+9.1}_{-4.5}$
	2	$115.8^{+8.8}_{-8.5}$		$46.7^{+5.6}_{-4.6}$	$98.2^{+3.2}_{-2.9}$	$6.5^{+3.8}_{-3.2}$	$145.0^{+8.3}_{-6.0}$	$54.5^{+5.1}_{-5.9}$
TYC 9340-437-1	1	$91.9^{+10.1}_{-10.5}$	100.1	$114.5^{+2.7}_{-2.9}$	$42.8^{+2.4}_{-2.2}$	$30.4^{+3.5}_{-3.3}$	$157.3^{+3.1}_{-3.4}$	$48.3^{+7.0}_{-8.2}$
HD 218396	1	$205.4^{+28.0}_{-21.0}$	224.1	$190.8^{+6.0}_{-6.0}$	$133.1^{+4.5}_{-4.4}$	$50.3^{+5.2}_{-5.1}$	$323.9^{+7.6}_{-7.6}$	$93.5^{+9.4}_{-8.8}$

A&A, 705, A195 (2026)
https://doi.org/10.1051/0004-6361/202556489
© The Authors 2026

Astronomy & Astrophysics

The ALMA survey to Resolve exoKuiper belt Substructures (ARKS)

I. Motivation, sample, data reduction, and results overview

S. Marino[1,⋆], L. Matrà[2], A. M. Hughes[3], J. Ehrhardt[4], G. M. Kennedy[5,6], C. del Burgo[7,8], A. Brennan[2], Y. Han[9], M. R. Jankovic[10], J. B. Lovell[11], S. Mac Manamon[2], J. Milli[12], P. Weber[13,14,15], B. Zawadzki[3], R. Bendahan-West[1], A. Fehr[11], E. Mansell[3], J. Olofsson[4], T. D. Pearce[6], A. Bayo[4], B. C. Matthews[16,17], T. Löhne[18], M. C. Wyatt[19], P. Ábrahám[20,21,22], M. Bonduelle[12], M. Booth[23], G. Cataldi[24,25], J. M. Carpenter[26], E. Chiang[27], S. Ertel[28,29], A. S. Hales[30,26,14], Th. Henning[31], Á. Kóspál[20,22,31], A. V. Krivov[18], P. Luppe[2], M. A. MacGregor[32], J. P. Marshall[33], A. Moór[20], S. Pérez[13,14,15], A. A. Sefilian[28], A. G. Sepulveda[34], and D. J. Wilner[11]

(Affiliations can be found after the references)

Received 8 July 2025 / Accepted 1 November 2025

ABSTRACT

Context. The outer regions of planetary systems host dusty debris discs analogous to the Kuiper belt (exoKuiper belts), which provide crucial constraints on planet formation and evolution processes. ALMA dust observations have revealed a great diversity in terms of radii, widths, and scale heights. At the same time, ALMA has also shown that some belts contain CO gas, whose origin and implications are still highly uncertain. Most of this progress, however, has been limited by low angular resolution observations that hinder our ability to test existing models and theories.

Aims. High-resolution observations of these belts are crucial for understanding the detailed distribution of solids and for constraining the gas distribution and kinematics.

Methods. We conducted the first ALMA large programme dedicated to debris discs: the ALMA survey to Resolve exoKuiper belt Substructures (ARKS). We selected the 24 most promising belts to best address our main objectives: analysing the detailed radial and vertical structure, and characterising the gas content. The data were reduced and corrected to account for several systematic effects, and then imaged. Using parametric and non-parametric models, we constrained the radial and vertical distribution of dust, as well as the presence of asymmetries. For a subset of six belts with CO gas, we constrained the gas distribution and kinematics. To interpret these observations, we used a wide range of dynamical models.

Results. The first results of ARKS are presented as a series of ten papers. We discovered that up to 33% of our sample exhibits substructures in the form of multiple dusty rings that may have been inherited from their protoplanetary discs. For highly inclined belts, we found that non-Gaussian vertical distributions are common and could be indicative of multiple dynamical populations. Half of the derived scale heights are small enough to be consistent with self-stirring in low-mass belts ($M_{\rm belt} \leq M_{\rm Neptune}$). We also found that 10 of the 24 belts present asymmetries in the form of density enhancements, eccentricities, or warps. We find that the CO gas is radially broader than the dust, but this could be an effect of optical depth. At least one system shows non-Keplerian kinematics due to strong pressure gradients, which may have triggered a vortex that trapped dust in an arc. Finally, we find evidence that the micron-sized grains may be affected by gas drag in gas-rich systems, pushing the small grains to wider orbits than the large grains.

Conclusions. ARKS has revealed a great diversity of radial and vertical structures in exoKuiper belts that may arise when they are formed in protoplanetary discs or subsequently via interactions with planets and/or gas. We encourage the community to explore the reduced data and data products that we have made public through a dedicated website.

Key words. methods: observational – techniques: interferometric – surveys – planet-disk interactions – circumstellar matter – planetary systems

1. Introduction

Young and mature planetary systems contain tenuous dust belts called debris discs, frequently revealed by their infrared excess (Aumann et al. 1984). Due to the dust's short lifetime against radiation and collisional processes, it has long been known that the dust is likely a product of collisions between kilometre-sized or even larger planetesimals (Harper et al. 1984; Weissman 1984; Backman & Paresce 1993). Debris discs are therefore the extrasolar analogues of the Solar System's asteroid and Kuiper belts. With ages ranging from tens to thousands of millions of years, debris discs provide a unique window into the final assembly of planetary systems (Wyatt 2008; Hughes et al. 2018). Moreover, they allow us to connect the structure seen in protoplanetary discs with the currently known mature exoplanet population.

At these ages, the gas densities are generally so low that the dynamics are no longer governed by gas, but rather by gravitational interactions (e.g. with planets) and radiation forces. Therefore, debris discs probe a different epoch in the planet

⋆ Corresponding author: s.marino-estay@exeter.ac.uk

Open Access article, published by EDP Sciences, under the terms of the Creative Commons Attribution License (https://creativecommons.org/licenses/by/4.0), which permits unrestricted use, distribution, and reproduction in any medium, provided the original work is properly cited.
This article is published in open access under the Subscribe to Open model. Subscribe to A&A to support open access publication.

formation process: giant planets have already formed, but may still be migrating and scattering material (like Neptune's migration into the Kuiper belt, Fernandez & Ip 1984; Ida et al. 2000), and terrestrial planets may be in the final stages of formation (e.g. undergoing dust-producing giant impacts like the Earth's Moon-forming impact, Jackson et al. 2014; Genda et al. 2015).

Despite the apparent distinction between protoplanetary discs and debris discs, defining which objects are or are not debris discs is not always easy as the evolution from protoplanetary to debris disc is a chaotic process that progresses at different rates throughout the system. Therefore, they share multiple properties (Wyatt et al. 2015). They can both have gas (Kóspál et al. 2013; Lieman-Sifry et al. 2016; Ansdell et al. 2016), and their ages overlap (Lovell et al. 2021c; Michel et al. 2021; Matrà et al. 2025). For example, protoplanetary discs can be found at ages as old as 30 Myr (Silverberg et al. 2020; Long et al. 2025), and debris discs can be found at ages as young as ~6 Myr in the TW Hydrae association (Miret-Roig et al. 2025) and in even younger associations, for example class III sources (Lovell et al. 2021c). A working distinction lies in the amount of dust in their discs as measured by the dust fractional luminosity (Hughes et al. 2018). Debris discs typically exhibit fractional luminosities below 1%[1], which makes them generally optically thin at all wavelengths. In contrast, protoplanetary discs have fractional luminosities generally above 1%, making them optically thick at short wavelengths. In practice, the transition between protoplanetary and debris discs is physical and gradual rather than categorical as systems evolve from being gas-rich and optically thick to dust populations increasingly dominated by second-generation grains produced by planetesimal collisions.

Beyond quantifying the amount of dust in debris discs, resolving its distribution has been fundamental to understanding these systems, starting with the first image of the archetype debris disc β Pictoris (in scattered light, Smith & Terrile 1984). Detailed models provided strong support for the dust-producing planetesimals scenario (e.g. Lecavelier Des Etangs et al. 1996). These models also suggested the potential importance of imaging debris discs at (sub)millimetre wavelengths to trace the parent planetesimals. The first submillimetre images of debris discs with single-dish telescopes resolved belt-like morphologies at Solar System scales in some very nearby systems (Fomalhaut and ϵ Eridani, Holland et al. 1998; Greaves et al. 1998). Early millimetre interferometry provided sufficient resolution to firmly establish the connection between scattered light and the millimetre belt structures, as predicted by size-dependent dust dynamics (e.g. β Pictoris, Wilner et al. 2011).

In the last 10 years, ALMA has revolutionised the study of cold debris discs analogous to the Kuiper belt (exoKuiper belts). Thanks to its unprecedented sensitivity and angular resolution at millimetre wavelengths, ALMA is uniquely suited to reveal the spatial distribution of millimetre-sized grains (Terrill et al. 2023). These large dust grains are mostly unaffected by radiation forces, and thus are ideal tracers of their parent planetesimals and the gravitational interactions in these systems (Krivov 2010). ALMA observations have revealed a wide range of structures, such as narrow belts (Marino et al. 2016; Kennedy et al. 2018), wide and smooth belts (Hughes et al. 2017; Faramaz et al. 2021), eccentric belts (MacGregor et al. 2017, 2022; Faramaz et al. 2019), belts with gaps (Marino et al. 2018, 2019, 2020b; MacGregor et al. 2019; Nederlander et al. 2021), belts with possible clumps (Dent et al. 2014; Lovell et al. 2021b; Booth et al. 2023), and a wide diversity of vertical distributions (Daley et al. 2019; Matrà et al. 2019b; Hales et al. 2022; Han et al. 2022; Terrill et al. 2023; Marshall et al. 2023).

Similarly, ALMA high-resolution observations of dust in protoplanetary discs, the predecessors of debris discs, have demonstrated the ubiquity of substructures in the form of rings, gaps, spirals, crescent-shaped features, and warps (see review by Bae et al. 2023). Constraining whether this ubiquity of substructures is passed along to the second-generation dust in exoKuiper belts is fundamental to understanding the evolution of circumstellar discs and planet formation processes.

In addition, ALMA's unprecedented sensitivity to gas has revealed that several exoKuiper belts contain CO and CI gas that is roughly co-located with the dust (e.g. Kóspál et al. 2013; Dent et al. 2014; Lieman-Sifry et al. 2016; Moór et al. 2017; Higuchi et al. 2017; Cataldi et al. 2018). Most systems with detected gas are young (<50 Myr) A-type stars, but a few exceptional detections have extended this sample to later types (Marino et al. 2016; Kral et al. 2020; Matrà et al. 2019a) and older systems (Matrà et al. 2017b; Marino et al. 2017). The origin of this gas is still unclear. For systems with low CO gas masses, the short photodissociation lifetime of CO implies that CO is continuously replenished via the destruction of volatile-rich solids (i.e. of secondary origin, Marino et al. 2016; Kral et al. 2016; Matrà et al. 2017b). Systems with high levels of CO gas are all young enough (10–50 Myr) that the gas could plausibly be part of a protoplanetary disc that has not yet dispersed, with CO molecules shielded by H_2 (i.e. of primordial origin, Kóspál et al. 2013; Nakatani et al. 2021). The high CO gas levels could also be achieved in the secondary scenario since CO is subject to self- and CI-shielding (Kral et al. 2019; Marino et al. 2020a); shielding also explains the non-detection of molecules other than CO in debris discs (Klusmeyer et al. 2021; Smirnov-Pinchukov et al. 2022). However, CI shielding is only efficient if vertical mixing is weak, which is currently unconstrained (Marino et al. 2022), and the CI inferred abundance from observations seems insufficient to shield the CO significantly (Cataldi et al. 2023; Brennan et al. 2024).

These recent advancements have triggered fundamental questions in our understanding of exoKuiper belts, but most of what we know about dust and gas substructures is based on a handful of the brightest belts. Most belts observed by ALMA have been resolved only enough to determine their widths (Matrà et al. 2025). Therefore, it is unclear how common the radial and vertical structures of dust and gas are that have been well resolved in these few systems. Due to the faintness of debris discs, determining the prevalence of these structures over a broader sample requires a significant time investment that only an ALMA large programme can achieve.

Here we present the first ALMA large programme dedicated to debris discs, The ALMA survey to Resolve exoKuiper belt Substructures (ARKS), to study their detailed dust and gas distribution. This paper is structured as follows. Section 2 describes the motivation and goals of this programme. Section 3 presents the observing strategy and Sect. 4 the sample selection. Section 5 describes the observations, data reduction, and imaging procedure. Section 6 describes the data products that we have made available to the community. Section 7 presents an overview of the results of ARKS presented in nine additional companion papers. Finally, Sect. 8 summarises the main conclusions of this programme.

[1] There is a class of debris discs known as extreme debris discs that exhibit fractional luminosities above this threshold and that can vary in time (e.g. Moór et al. 2021).

2. ARKS motivation and goals

ARKS was motivated by three core components of exoKuiper belts: the radial distribution of dust, the vertical distribution of dust, and the overall distribution and kinematics of CO gas. Below, we describe the most important findings in these areas that motivated ARKS and our programme design.

The radial and vertical structure of exoKuiper belts had been studied through several ALMA studies on individual systems and a few studies of small samples, until the ALMA survey REsolved ALMA and SMA Observations of Nearby Stars (REASONS, Matrà et al. 2025). REASONS compiled and expanded the sample of resolved belts with ALMA and SMA to 74 and performed uniform parametric modelling to constrain their central radius (R), full width at half maximum (ΔR), inclination (i), position angle (PA), and belt flux ($F_{\rm belt}$). This analysis resulted in a series of important findings for the radial and vertical structure of exoKuiper belts.

First, REASONS found that most millimetre bright belts are broad discs rather than narrow rings, with fractional widths ($\Delta R/R$) much greater than both the Kuiper belt and rings in protoplanetary discs. This result comes as a surprise, as narrow rings in protoplanetary discs are ubiquitous (Huang et al. 2018; Long et al. 2019; Cieza et al. 2021) and are thought to be the birthplace of planetesimals at tens of au (Stammler et al. 2019). If planetesimals in exoKuiper belts truly formed in these rings, their larger width could be explained by: (a) the migration of rings in protoplanetary discs, leaving behind planetesimals and thus producing wide exoKuiper belts (Miller et al. 2021); (b) dynamical perturbations by planets, massive planetesimals or flybys widen these belts (e.g. Booth et al. 2009; Lestrade et al. 2011); or (c) many broad exoKuiper belts may have unresolved substructures in the form of narrow rings and gaps, as shown for a handful of systems with high-resolution observations (Marino et al. 2018, 2019, 2020b; Nederlander et al. 2021).

Second, REASONS was also able to constrain the vertical thickness or scale height (H, vertical standard deviation) for a small subsample of highly inclined belts. The belt vertical aspect ratio ($h = H/R$) is a direct result of the dispersion of orbital inclinations ($i_{\rm rms}$), and thus, constraints on h are translated into constraints on the dynamical excitation of belts. REASONS found $i_{\rm rms}$~1−20°, implying a diversity of stirring levels (see also Terrill et al. 2023). However, these values could be biased by the low resolution of most observations and model assumptions (e.g. Gaussian radial and vertical distributions). Moreover, they could hide more complex vertical distributions, such as the one found in β Pic that deviates significantly from Gaussian and suggests at least two dynamical populations (Matrà et al. 2019b).

ALMA observations of gas have also suffered from similar limitations, with generally low spatial and spectral (velocity) resolution. Spatial resolution is key to assessing how correlated the dust and gas spatial distributions are. In the secondary origin scenario, for instance, CO gas is expected to be co-located with dust unless it is shielded and can viscously spread (Kral et al. 2016, 2019; Marino et al. 2020a). There are mixed results when comparing the gas and dust distribution. In some systems, the gas distribution appears to be more extended inwards or outwards (Kóspál et al. 2013; Moór et al. 2013). In others, the gas distribution appears to be less extended than that of the dust (Hughes et al. 2017; Higuchi et al. 2019; Hales et al. 2022), and in some cases, they are consistent with each other (Marino et al. 2016; Matrà et al. 2017a, 2019b). These results are, however, limited by low spatial resolution, hindering a detailed and model-free comparison between the gas and dust (despite the high surface brightness of CO line emission, Moór et al. 2017). The low spectral resolution has also hindered kinematic studies of the gas, which can constrain its kinetic temperature, Keplerian deviations due to planets (Perez et al. 2015), strong pressure gradients (Teague et al. 2018), and outflows (Lovell et al. 2021a). It is yet to be seen whether such kinematic features are common among gas-rich exoKuiper belts.

ARKS aims to expand our understanding of debris discs' radial and vertical dust structures, as well as gas distribution and kinematics by performing an ALMA high-resolution survey of 24 belts (new observations of 18 targets and archival data of 6; see Sect. 4 for details). In particular, ARKS has the following goals:

- Dust radial structure: determine what types of dust substructures such as rings/gaps are present in wide belts, down to the level of $\Delta R/R \sim 0.2$ that corresponds to the median of the ring width distribution for bright protoplanetary discs (Matrà et al. 2025). If wide belts have narrow rings similar to protoplanetary discs (Bae et al. 2023), this would suggest that planetesimal belts inherit some of the dust structures. Conversely, smooth and featureless belts may, for instance, favour a ring migration or scattered-disc scenarios (Miller et al. 2021; Geiler et al. 2019). Gaps could also indicate the presence of planets embedded in these discs, clearing their orbits from debris (Marino et al. 2018; Friebe et al. 2022), or closer-in opening gaps through secular interactions (Pearce & Wyatt 2015; Yelverton & Kennedy 2018; Sefilian et al. 2021, 2023). Finally, the sharpness of inner and outer edges can inform us about the collisional evolution and dynamics of these belts (Marino 2021; Rafikov 2023; Imaz Blanco et al. 2023; Pearce et al. 2024).
- Dust vertical structure: determine the scale heights and vertical dust distributions of highly inclined belts, thus constraining their dynamical excitation level. The excitation level can be used to place constraints on the mass and number of bodies stirring the belts (Ida & Makino 1993; Quillen et al. 2007; Daley et al. 2019; Matrà et al. 2019b). In addition, we can also search for multiple dynamical populations as found in β Pic (Matrà et al. 2019b). This can provide insights into the birth conditions of planetesimals and their interactions with planets, including scenarios involving Neptune-like migration through the belt (Malhotra 1995; Matrà et al. 2019b; Sefilian et al. 2025).
- Gas distribution and kinematics: determine the spatial extent and kinematics of the previously known CO gas in six belts in our sample. By assessing the gas spatial extent relative to dust, we can test whether viscous spreading has taken place (if gas is secondary, Kral et al. 2016; Marino et al. 2020a) and whether gas plays a role in shaping the dust distribution (Takeuchi & Artymowicz 2001; Krivov et al. 2009). The velocity information can also constrain the dynamics of the gas, kinetic temperature, the stellar mass, and the presence of planets.
- Dust and gas asymmetries: determine if asymmetries are common among the brightest exoKuiper belts at millimetre wavelengths. Asymmetries come in different forms, for example, belt eccentricities (Kalas et al. 2005; MacGregor et al. 2017, 2022; Faramaz et al. 2019), density enhancements (Dent et al. 2014; Lovell et al. 2021b; Booth et al. 2023), and warps (Matrà et al. 2019b; Hales et al. 2022). These asymmetries encode information about the dynamical history of these systems, and they are typically interpreted as evidence of interactions with massive companions (e.g. Wyatt et al. 1999; Pearce & Wyatt 2014; Sefilian et al. 2025).

3. Observing strategy

We defined the following observing strategy to study the radial and vertical distribution of dust and the distribution and kinematics of CO gas.

To study the radial structure of wide belts and determine if they are made of multiple radial components, we first focus on belts with a fractional width larger than 0.3 and that are only moderately inclined, here defined as having an inclination (i) lower than 75°, to ease the extraction of radial information[2]. The spatial resolution was set with two considerations. First, the beam should be at least as small as the gap width that a Neptune-mass planet would carve in a massless disc if placed on an orbit at the belt central radius R (~20% of R for a stellar mass of $\approx 1 M_\odot$, Morrison & Malhotra 2015) to search for Neptune analogues. Second, the beam should be small enough to resolve ΔR into at least five resolution elements to study the sharpness of the inner and outer edges. Finally, we requested a sensitivity such that, after deprojecting and azimuthally averaging the emission, we can measure its radial profile with an average signal-to-noise ratio (S/N_r) of ~10 per resolution element. This strategy meant that each disc was observed with a tailored resolution (θ) and sensitivity (or rms per beam) set by the following[3]:

$$\mathrm{rms} = 0.37 \frac{F_{\mathrm{belt}}}{S/N_r} \frac{\theta^{3/2}}{\Delta R \sqrt{R}}, \quad (1)$$

$$\theta = 0.2 \min(\Delta R, R). \quad (2)$$

To study the vertical structure, we focus on highly inclined belts (here defined as $i > 75°$) since those are easier to resolve vertically. We aim to resolve the FWHM of the vertical distribution with two resolution elements at the belt central radius R, assuming a vertical aspect ratio ($h = H/r$ or vertical standard deviation) of 0.05, and with a S/N of 20 on h (S/N_h). This would allow us to measure an inclination dispersion ($i_{\mathrm{rms}} = \sqrt{2}h$) as low as 1°. The required sensitivity to achieve this was found by simulating observations and forward-modelling them, arriving at the empirical relation:

$$\mathrm{rms} = 0.63 \frac{F_{\mathrm{belt}}}{S/N_h} \frac{\sqrt{h}\theta^{3/2}}{\sqrt{R}(R + \Delta R/2)}, \quad (3)$$

$$\theta = 1.18 hR, \quad (4)$$

where we assume $h = 0.05$ for our sample, a value found for belts that have been marginally resolved vertically (Terrill et al. 2023; Matrà et al. 2025).

It should be noted that the constraints on i were in place only when choosing the best targets for observation and constraining the radial and vertical distribution of dust. Nevertheless, we still extract the dust radial distribution of highly inclined belts (Han et al. 2026) and the dust vertical distribution for some belts with inclinations below 75° (Zawadzki et al. 2026).

[2] Radial information can also be extracted from edge-on belts by performing a deconvolution in the image or visibility space (Han et al. 2022; Terrill et al. 2023).

[3] This equation was derived by assuming a face-on disc, defining the belt average surface brightness within ΔR as $I_\nu = kF_{\mathrm{belt}}/(2\pi R \Delta R)$, the beam area as $\Omega_{\mathrm{b}} = \pi\theta^2/(4\ln(2))$, the signal to noise $S/N_r = I_\nu \Omega / \mathrm{rms}_{\mathrm{av}}$, and the rms after azimuthally averaging $\mathrm{rms}_{\mathrm{av}} = \mathrm{rms}\sqrt{\theta/(2\pi R)}$. The factor k was found numerically to be 0.8, assuming a Gaussian distribution. The factor $2\pi R/\theta$ in the rms after azimuthally averaging represents the number of independent points being averaged at radius R. We note that for more inclined discs, this number will be lower, but this will be roughly counterbalanced by the higher surface brightness.

We chose to use band 7 for ARKS observations to optimise the required observation time. Band 7 offers the best S/N for a fixed integration time given the typical spectral index/slope of exoKuiper belts (~2.5, Matrà et al. 2025). However, some systems had already good enough archival band 6 observations, in which case we analysed those (see Sect. 4).

Finally, to study the gas, we targeted the ^{12}CO and ^{13}CO J=3–2 lines in parallel to the continuum, and thus, with the same spatial resolution and integration times. For systems with previously known abundant CO gas, we used the highest spectral resolution available of 26 m/s for ^{12}CO to extract as much kinematic information as possible. For ^{13}CO (and ^{12}CO for targets without abundant gas), we set a lower spectral resolution of 0.9 km/s to maximise the bandwidth and hence the continuum sensitivity.

4. Sample selection

Given the above observing strategy, we selected the most suitable targets from the REASONS sample as those that require the shortest integration times. REASONS comprises nearly all debris discs observed by ALMA with publicly available observations from different programmes, which inherently resulted in a biased sample of the brightest discs, observed in a heterogeneous way. Nevertheless, all these observations were modelled uniformly by fitting a belt model with surface and vertical density distributions described as a Gaussian.

We started our sample selection by removing those belts in REASONS whose outer edge is larger than 9″, beyond which the sensitivity drops below 50% due to the 12 m antennas' primary beam in band 7. Smaller belts can be efficiently observed with a single pointing instead of mosaicking. In addition, we removed HD 38858 and HD 36546. The first was only marginally detected with ALMA, and a background source likely contaminated its derived parameters. The second was not well fit by a Gaussian belt model, and thus its derived radius and width are heavily biased by the unsuitable model choice.

To estimate the required sensitivity and thus the integration time of the remaining sample, we used the radius, width, and inclination information from REASONS and the measured and predicted fluxes at 0.88 mm using the existing millimetre fluxes measured between 0.86–1.36 mm and assuming a spectral index of 2.5. Finally, we focus only on belts with constrained inclinations whose widths have been marginally resolved with an error smaller than 50%. These considerations left us with 53/74 belts from which we selected our targets.

To obtain a sufficiently large sample, we set the minimum requested rms to 10 μJy. This resulted in a complete sample of 24 belts: 14 moderately inclined belts (0–75°) and ten highly inclined belts (>75°), six of which have previously detected CO gas. Six of the 24 systems had archival observations that already met our observation requirements for our goals (Sect. 3)[4], and thus we did not request new observations. The properties of this sample are summarised in Table 1.

Figure 1 shows the distribution of fractional widths (top panel) vs. the expected belt fluxes at 0.88 mm for moderately inclined (middle panel) and highly inclined belts (bottom panel). Blue markers show systems in ARKS, while grey markers represent systems in REASONS that were excluded from ARKS.

[4] One of the systems with sufficient archival observations (HD 206893) had a flux below our threshold (Fig. 1 top panel), but its observations met our resolution and S/N_r criterium.

Table 1. Main system parameters of the ARKS sample.

Name	Dist [pc]	Spt	$L_\star$ [$L_\odot$]	$M_\star$ [$M_\odot$]	Age [Myr]	$L_{\rm cold}/L_\star$ [$\times 10^{-4}$]	$a_{\rm p}$ [au]	Expected from REASONS $F_{\rm belt}$ [mJy]	i [°]	PA [°]	R [au]	$\Delta R/R$
Moderately inclined belts ($i < 75°$)												
HD 15257	49.0	F1V	14	1.75	1000^{+800}_{-800}	0.61		7.5	40	60	270	0.81
HD 76582	48.9	A7V	9.9	1.61	1200^{+900}_{-900}	2.0		8.0	72	104	219	0.96
HD 84870	88.8	A9V	7.9	1.66	300^{+200}_{-200}	4.3		4.8	50	10	260	1.00
HD 92945	21.5	K0V	0.37	0.85	200^{+100}_{-100}	6.6	PMa: 2–30	10.1	67	100	96	0.83
HD 95086	86.5	A9V	6.4	1.54	$13.3^{+1}_{-0.6}$	16	52(1)	8.1	29	93	206	0.87
HD 107146	27.5	G0V	1.00	1.04	150^{+100}_{-50}	9.8	PMa: 2.5–20	39.3	22	149	107	1.03
HD 121617[g]	118	A1V	14	1.90	16^{+2}_{-2}	51		4.8	37	60	78	0.77
HD 131835[g]	130	A8V	8.9	1.70	16^{+2}_{-2}	23		5.5	74	60	84	1.04
HD 145560	121	F5V	3.3	1.35	16^{+2}_{-2}	20		4.1	47	28	76	0.66
HD 161868	29.7	A1V	24	2.11	300^{+200}_{-200}	0.65	PMa: 3–25	6.3	68	57	124	0.89
HD 170773	36.9	F4V	3.6	1.40	200^{+100}_{-100}	4.9		15.8	33	114	194	0.35
HD 206893	40.8	F5V	2.8	1.33	160^{+20}_{-20}	2.7	3.5,9.7(2)	2.9	24	60	108	0.93
TYC 9340-437-1	36.7	K7V	0.19	0.75	23^{+3}_{-3}	10		11.0	40	130	130	0.77
HD 218396 (HR 8799)	40.9	A9V	5.5	1.50	33^{+7}_{-10}	2.5	15,27,41,72(3)	11.2	39	51	290	0.86
Highly inclined belts ($i > 75°$)												
HD 9672 (49 Ceti)[g]	57.2	A2V	15	2.00	45^{+5}_{-5}	7.2		15.2	79	107	136	1.08
HD 10647 (q^1 Eri)	17.3	F8V	1.6	1.12	1700^{+600}_{-600}	2.6	2.0(4)	12.8	77	57	100	0.70
HD 14055	35.7	A1V	29	2.19	300^{+200}_{-200}	0.89		8.5	81	163	180	0.89
HD 15115	48.8	F3V	3.7	1.43	45^{+5}_{-5}	4.7		5.8	88	98	93	0.23
HD 32297[g]	130	A8V	7.0	1.57	30^{+10}_{-10}	61		9.9	87	48	122	0.51
HD 39060 (β Pic)[g]	19.6	A4V	8.7	1.72	23^{+3}_{-3}	25	2.7,10(5)	56.2	87	30	105	0.88
HD 61005	36.5	G6V	0.62	0.95	45^{+5}_{-5}	25		16.4	86	70	73	0.52
HD 109573 (HR 4796)	70.8	B9.5V	25	2.14	10^{+3}_{-3}	42	PMa: 4–38	15.4	76	27	78	0.19
HD 131488[g]	152	A3V	12	1.80	16^{+2}_{-2}	26		8.1	84	96	92	0.50
HD 197481 (AU Mic)	9.71	M1V	0.098	0.61	23^{+3}_{-3}	3.9	0.070,0.12(6)	17.4	88	129	35	0.36

Notes. Column 2 indicates the distance according to *Gaia* DR3 (Gaia Collaboration 2023). The approximate spectral types are shown in Column 3, estimated using the stellar effective temperatures of REASONS and the main sequence from Pecaut & Mamajek (2013). The stellar luminosity and fractional luminosity of the cold dust component (Columns 4 and 7) were taken from spectral energy distribution fits using the same methodology as in REASONS (Matrà et al. 2025), but with updated disc fluxes based on ARKS (see Appendix D). The stellar age (Column 6) was taken from REASONS (Matrà et al. 2025). The stellar masses in Column 5 were inferred as described in Appendix C. Column 8 shows the semi-major axes of known planets in these systems. Systems with unknown planets but with a significant ($>3\sigma$) proper motion anomaly are labelled as PMa (Kervella et al. 2022), with the values originating from Milli et al. (2026). The last five columns show the expected belt flux at 0.88 mm, the belt inclination, position angle, central radius and fractional width from REASONS. Systems with archival data only and not observed by ARKS are highlighted in grey, and systems with CO gas are flagged '[g]'. (1): Chauvin et al. (2018); (2): Hinkley et al. (2023); (3): Zurlo et al. (2022); (4): Marmier et al. (2013); (5): Brandt et al. (2021); (6): Mallorquín et al. (2024).

Our sample is biased towards the brightest belts ($\gtrsim$3 mJy). However, as shown in Fig. 2, the selected sample (blue) is not significantly biased relative to REASONS in terms of stellar luminosities and ages. That said, both samples favour early-type stars with $L_\star > 1\ L_\odot$ and display a bimodal age distribution, with a notable gap between 50 and 100 Myr. The luminosity bias arises because early-type stars are more likely to host bright exoKuiper belts, which are easier to detect and resolve with ALMA. The gap in the age distribution, on the other hand, reflects the absence of moving groups within the 50–100 Myr range in the REASONS sample, resulting in an apparent bimodality (Matrà et al. 2025). Of the nearby moving groups, only the recently discovered Volans-Carina falls within this age interval (as it is ~90 Myr old, Gagné et al. 2018). Overall, the ARKS sample does not show significant biases relative to REASONS in terms of fractional widths, stellar luminosities, or ages.

In terms of companions, 8 out of the 24 systems have confirmed companions with a wide range of mass ratios and separations (see Appendix G for details). Four of these eight systems (HD 10647, HD 76582, HD 109573 and HD 197481) have stellar companions at wide separations and at least 6 times

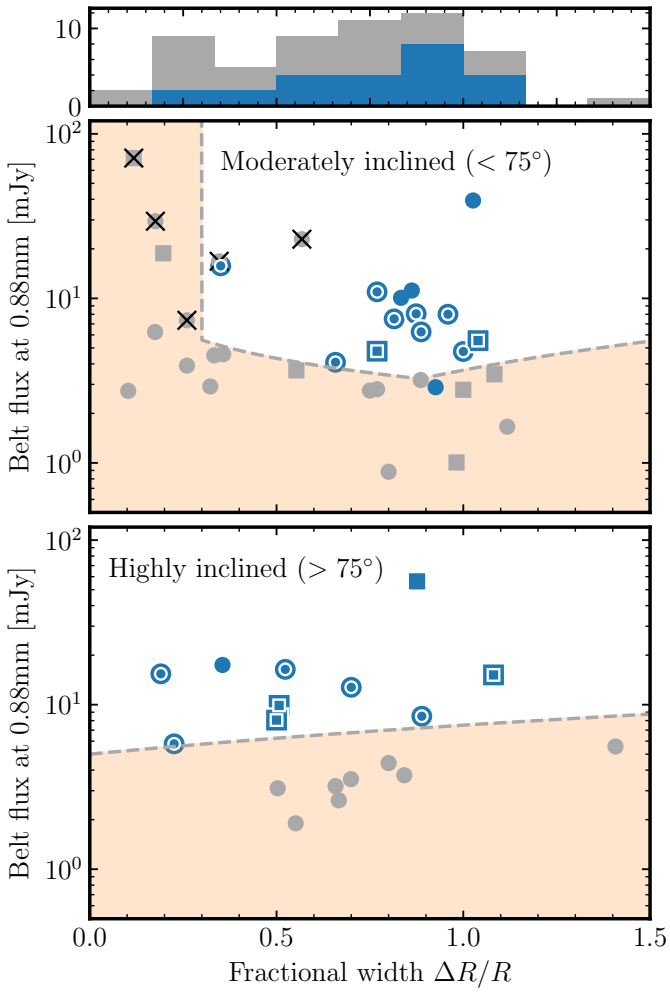

Fig. 1. Distribution of fractional widths vs belt fluxes at 0.88 mm. Top: histogram of all REASONS belts with resolved widths (grey) and those analysed in ARKS (blue, including six with archival observations). Middle: distribution of fractional widths vs expected belt fluxes for moderately inclined belts. Bottom: distribution of fractional widths vs expected belt fluxes for highly inclined belts. The blue markers represent ARKS targets (double markers: newly observed; single markers: archival data). The square symbols represent systems with CO gas, and the black crosses represent systems too large to be observed without mosaicking. The dashed line represents the 10 μJy sensitivity limit chosen for ARKS (Eqs. (1) and (3)), below which belts were excluded unless already observed (orange shaded region). The grey markers represent belts in REASONS that were excluded for being too large, too wide, or too faint for high-resolution observations.

further than their belts. One of these eight systems has a brown dwarf companion (HD 206893) interior to the belt. Six of the eight systems (HD 10647, HD 39060, HD 95086, HD 197481, HD 206893 and HD 218396) contain companions in the planetary mass regime interior to their belts, at separations that are not greater than 50% of the belts' inner edge. Milli et al. (2026) presents a summary of the known substellar mass companions in the sample, and their location relative to the belts. In addition, Milli et al. (2026) presents mass upper limits based on SPHERE direct imaging observations, that constrain the possible mass of companions at the disc inner edge (and gaps if present), and semi-major axes and mass constraints for companions causing the PMa in four systems where these have not been confirmed yet via direct imaging.

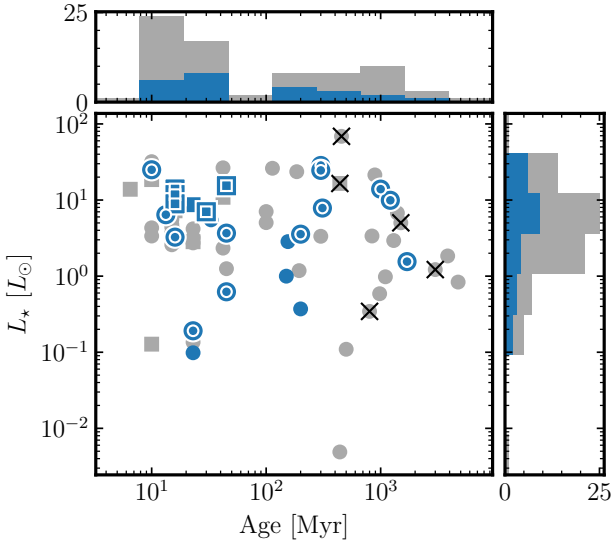

Fig. 2. Distribution of stellar luminosities and ages for all systems in REASONS (grey) and in ARKS (blue). The symbols follow the same convention as in Fig. 1. The top and right panels show histograms of the stellar age and luminosities, respectively.

5. Observations, data reduction, and imaging

In this section we summarise the observations of ARKS and those archival observations that we included.

5.1. Observations

ARKS observations (2022.1.00338.L, PI: S. Marino, co-PIs: A. M. Hughes & L. Matrà) were carried out during cycles 9 and 10 from October 2022 to July 2024. Table A.1 summarises the observations of the 18 ARKS and 6 archival targets. For two of the ARKS targets (HD 9672 and HD 10647), we included archival band 7 observations to improve their S/N. The last column of Table A.1 indicates the project code of the archival observations that were included.

ARKS observations used a wide range of antenna configurations, from the 7m Atacama Compact Array (ACA, with baselines as short as 8m) for the largest belts, to configuration C-8 of the 12m array (with baselines as long as 8.5 km) for the smallest belts. These provided a wide range of resolutions tailored to each system, from 0.″85 down to 0.″04.

ARKS observations used two different spectral setups depending on the CO content of each system, which had been established by previous observations. For gas-poor systems (i.e. no detected CO gas), two of the four spectral windows were dedicated to studying the dust continuum emission only, with a bandwidth of 1.875 GHz and 120 channels each and centred at 343.2 and 333.2 GHz. The other two were set to cover the ^{12}CO and ^{13}CO J=3–2 lines to search for gas with a bandwidth of 1.875 GHz, centred at 345.2 and 331.3 GHz, with 3840 channels and a channel spacing of 488 kHz, providing a spectral resolution of 0.84 and 0.85 km/s, respectively. The total continuum bandwidth for these systems was 7.5 GHz.

For systems regarded to be gas-rich (HD 9672, HD 32297, HD 121617, HD 131488, HD 131835), the spectral window covering the ^{12}CO J=3–2 emission at 345.789 GHz was set with the highest spectral resolution of 31 kHz or 26 m/s (15 kHz or 13 m/s channel spacing). This spectral window had a total bandwidth of 59 MHz or 51 km/s, with 3840 channels and was centred at the line central frequency, taking into account the radial velocity of

each system. The total continuum bandwidth for these systems was 5.7 GHz.

In addition to the new ARKS observations, we include ALMA archival observations for 2 of the 18 systems observed by ARKS. These systems had previous observations at a similar resolution in band 7, although at a lower sensitivity. However, these observations still enhance our S/N due to the increased integration time. These systems are HD 9672 (49 Ceti, Cataldi et al. 2023; Delamer 2023) and HD 10647 (q^1 Eri, Lovell et al. 2021b). For the 6 additional archival targets, we preferentially use their band 7 data with two exceptions. For HD 206893, its band 6 data has a higher S/N at the desired resolution, and thus we use this only (Marino et al. 2020b; Nederlander et al. 2021). For HD 107146, we use both bands 6 and 7 since they are complementary: the former has high S/N, low-resolution observations, while the latter includes higher-resolution data at a moderate S/N (Marino et al. 2018; Marino 2021; Imaz Blanco et al. 2023). The spectral setup of these observations varied, with most of them including ^{12}CO observations while maximising the continuum sensitivity. Finally, 5 of the 6 archival targets were observed with a single pointing, the exception being HD 39060 (β Pic), which included a 2-point mosaic for its 12m antenna short baseline observations.

5.2. Data reduction

The data were calibrated by the UK ARC Node using the ALMA pipeline and corresponding CASA version (6.4.1.12 for those observed during cycle 9 and 6.5.4.9 for cycle 10, CASA Team 2022). For archival data, the calibrated measurement set (MS) files were delivered by the ESO ARC. No additional steps were done for the calibration of the data, except for some flagging of some archival data (see below).

We reduced the calibrated MS files using CASA version 6.4.1.12 as follows. We first transformed the MS files to the barycentric reference frame using the task MSTRANSFORM and kept only the target observations. We then time averaged the data using the task SPLIT. The time binning (Δt) was calculated for each source and antenna configuration such that the effect of time averaging smearing is kept below 5% at a radius equal to twice the size of the belts' outer edges (following Eq. (6.80) in Thompson et al. 2017). We also constrained the maximum value of Δt to 60 s, which was the case for most of our sources. For HD 61005 and β Pic long baseline observations, Δt was set to 45 and 30 s, respectively, to keep the effect of time averaging smearing below 5%.

Each target observation was centred at the predicted stellar position using the available stellar astrometry in cycle 9. For the targets observed as part of ARKS, this was done using *Gaia* DR2 (Gaia Collaboration 2018), except for HD 14055 and HD 161868 for which we used the Hipparcos astrometric solution (van Leeuwen 2007). These two stars have the largest apparent magnitudes, which makes their *Gaia* DR2 astrometric solution less accurate than Hipparcos. We find that the DR2 positions match well with the DR3 positions, with differences smaller than 5 mas. The Hipparcos predicted positions of HD 14055 and HD 161868, and the phase centres used in the archival observations, differed by larger values up to 81 mas. The final phase centre coordinates (after the data correction described in Sect. 5.3) and the offsets relative to *Gaia* DR3 are summarised in Table D.1.

To study the dust continuum emission, we flagged channels within 15 km/s of the ^{12}CO and ^{13}CO J=3–2 lines[5] for systems with known gas, and within 50 km/s for systems with no known CO gas. Subsequently, we spectrally averaged the data by $\Delta\nu$, which was calculated for each source and antenna configuration such that the effect of bandwidth smearing is kept below 5% at a radius equal to twice the size of the belts' outer edges (following Eq. (6.75) in Thompson et al. 2017). The spectral averaging is also constrained to be at most the bandwidth of any spectral window (~2 or 0.06 GHz), which sets $\Delta\nu$ for most of our sources. The exceptions to this were the long baseline observations of HD 9672, HD 15115, HD 32297, HD 61005, HD 109573 and HD 131488 with a frequency averaging of 1 GHz and HD 39060 long baseline observations with a 0.5 GHz averaging.

To study the CO gas, we split the time-averaged MS files into two new files containing the spectral windows dedicated to ^{12}CO and ^{13}CO J=3–2 lines (or ^{12}CO J=2–1 for HD 39060's archival data). We used the task UVCONTSUB to fit and subtract the continuum emission, excluding the same channels that were flagged to study the continuum as described above.

An additional step was taken to reduce the data of HD 107146, HD 10647 and HD 197481 (AU Mic) that involved flagging. For HD 107146's band 7 12m short baseline observations, we flagged visibilities at baselines shorter than 20 kλ to reduce some low-frequency ripples in the image that were not caused by the uv coverage but rather systematic noise in the data. This solves most of the problem, but we note that some large-scale artefacts remain in the data, especially in images constructed with more weight towards the band 7 short baselines (Imaz Blanco et al. 2023). For HD 10647 long baseline observations in cycle 3 taken on 12 Jul 2016 at 11:34 (UTC), we flagged the baselines corresponding to the antenna pair DA46 and DA54 since they produced strong ripples in the continuum image (Lovell et al. 2021b). For HD 197481 (AU Mic), we flagged scan 27 in the long baseline observations taken on 24 Jun 2015 (UTC) to remove a stellar flare from our data (Daley et al. 2019; MacGregor et al. 2020). We also searched for stellar variability on all the data, but found no significant variability for any target other than HD 197481 (see Appendix F). Finally, we note that HD 218396 has background CO J=3–2 emission at −12.5 km/s in the barycentric reference frame (Faramaz et al. 2019), which was flagged as part of our standard reduction.

ExoKuiper belts are not typically bright enough for successful self-calibration. Nevertheless, as an experiment, we tested whether self-calibration could improve our data's S/N. We tried self-calibrating our brightest targets using the package AUTO_SELFCAL[6] but found no improvements in the image rms. Therefore, we continue using the non-self-calibrated data.

5.3. Data correction

Before imaging and analysing the continuum and gas data, we applied a final data correction step, which aims to correct any astrometric offsets, flux offsets, and rescale the visibility weights of each execution block to truly represent the noise or dispersion in the continuum and CO data. For sources with background galaxies, this step also includes subtracting their emission from the continuum data. To determine these corrections, we use the continuum data as a reference.

We start this process by extracting the continuum visibilities of each execution block[7] and forward-fitting them simultaneously using a simple belt model (see below), leaving as free

[5] Or the J=2-1 lines for archival sources with band 6 observations.

[6] Available at https://github.com/jjtobin/auto_selfcal/

[7] Each system can be observed with multiple antenna configurations (scheduling blocks), and multiple executions per configuration (execution blocks).

parameters astrometric (phase centre) offsets, flux scale offsets, and weights scale offsets for each execution block (in addition to system parameters), and exploring the parameter space with an MCMC (as in Marino 2021). This fitting and correction step is effectively a low-order self-calibration using a simple model as a reference.

The belt model was computed using `disc2radmc` (a Python wrapper to use RADMC3D[8], Marino et al. 2022). For most systems, we assumed a belt with a Gaussian surface density distribution (with central radius and FWHM as free parameters) and a Gaussian vertical distribution with a free and radius-independent aspect ratio for sufficiently inclined systems (a similar strategy to REASONS). The exceptions to this were HD 15115, HD 92945 and HD 107146, for which we fit a double Gaussian radial distribution with additional free parameters for the central radius, FWHM, and relative scale of the second Gaussian; HD 206893, for which we fit a Gaussian gap with additional free parameters for its centre, width, and depth; and HD 121617, for which we included a sinusoidal azimuthal variation (with additional parameters for the phase and amplitude of the variation). Without these additional components, the best fits to these systems showed strong residuals and, thus, could strongly bias our correction process. For systems where central emission was detected using uncorrected clean images, we kept the stellar flux as a free parameter. We also considered the belt's inclination and position angle as free parameters. Finally, we left the dust mass as a free parameter to fit the belt flux, assuming a dust opacity of 1.9 $\mathrm{cm^2\ g^{-1}}$ at 0.89 mm or 1.3 $\mathrm{cm^2\ g^{-1}}$ at 1.3 mm[9]. Since we fit two bands for HD 107146, we included an extra parameter to fit the belt flux in band 6 (1.3 mm) instead of fitting the spectral index or grain size distribution.

In addition, we account for background submillimetre galaxies (SMGs) present near the belts of HD 76582, HD 84870, HD 92945, HD 95086, HD 107146, HD 206893, TYC 9340-437-1, and HD 218396, by including 2D elliptical Gaussians in the model images. We left as free parameters their flux, position relative to the stars, (taking into account the SMG's relative motion to these stars due to the stellar proper motions, Gaia Collaboration 2023), major and minor axes, and position angle. Fitting these background sources had the advantage of providing an additional lever to determine any systematic astrometry or flux offsets between observations. Appendix E explains why these are likely SMGs and presents the best-fit values for these sources.

The model images were multiplied by the antenna primary beam (computed using CASA) and then Fourier transformed with Galario to produce model visibilities to fit the ALMA data (Tazzari et al. 2018). To account for any systematic phase centre offsets between observations, we left as free parameters a right ascension and declination offset for each execution block. This is applied to the model by Galario in Fourier space.

For each model evaluation, Galario computes a χ^2 for each execution j that is defined as

$$\chi^2_j(x) = \sum_k^{N_j} \|V_{\mathrm{d},k,j} f_{\mathrm{flux},j} - V_{\mathrm{m},k,j}(\boldsymbol{x}) P_{k,j}\|^2 \frac{W_{k,j}}{f^2_{\mathrm{flux},j} f^2_{\sigma,j}}, \quad (5)$$

where $V_{\mathrm{d},k,j}$ and $V_{\mathrm{m},k,j}(x)$ are the measured and model complex visibilities k of the execution j, $f_{\mathrm{flux},j}$ is the flux correction factor, $\boldsymbol{x}$ represents the system's free parameters (including background sources), $P_{k,j}$ represents the phase centre offset with free parameters $\Delta\mathrm{RA}_j$ and $\Delta\mathrm{Dec}_j$[10], $W_{k,j}$ is the associated weight (1/uncertainty^2), $f_{\sigma,j}$ is a factor to rescale the weights (see below), and N_j is the number of visibilities for a particular execution. Each system was typically observed with two antenna configurations and multiple executions per configuration. Because each execution was observed and calibrated independently, they may have different systematic astrometric offsets.

Similarly, each execution can have different absolute flux calibration errors of the order of ∼10% (Francis et al. 2020). To account for this, we fit a flux correction factor $f_{\mathrm{flux},j}$ to each execution $j > 0$ while fixing $f_{\mathrm{flux},0} = 1$ to anchor these factors. We arbitrarily assigned $j = 0$ to one of the executions taken with the longest baseline configuration of each target[11]. For HD 107146, we had to set $f_{\mathrm{flux}} = 1$ for one band 7 execution and one band 6 execution.

Finally, the factors $f_{\sigma,j}$ in Eq. (5) account for the fact that the weights in the calibrated MS files do not necessarily match the true dispersion and uncertainty in the data. While the task STATWT in CASA can empirically determine the weights, here we choose to conserve the relative weights between different measured visibilities and only adjust their absolute level (e.g. Marino et al. 2018; Matrà et al. 2019b). We tested whether this offset varies with spectral window and found it did not, and thus, we chose to use a single factor per execution. Fitting for $f_{\sigma,j}$ is equivalent to forcing the reduced χ^2_j to be one, which is an adequate choice for ALMA observations of exoKuiper belts where the S/N per visibility is $\ll 1$ (i.e. each value is dominated by noise, Marino 2021). This means that the choice of the model has little influence on the best-fit value of $f_{\sigma,j}$.

We use the Python package EMCEE (Foreman-Mackey et al. 2013) to fit all these parameters using the Affine Invariant MCMC Ensemble sampler (Goodman & Weare 2010) and recover the posterior distribution defined as

$$\log P = -\frac{1}{2}\sum_j [\chi^2_j(x) + 2N_j \log(f_{\sigma,j})] + \mathrm{prior}, \quad (6)$$

where the prior is uniform for all parameters except for the flux offsets ($f_{\mathrm{flux,j}}$), for which we assume a Gaussian prior with a standard deviation of 10%[12]. Typically, each system requires between 50 and 100 free parameters, depending on the number of executions, and the MCMC was run with 200–400 walkers and for 2000–10 000 iterations, depending on how fast the chains converged. After removing the burn-in phase that typically lasted half the iteration length, we extracted the median and 16th and 84th percentiles for each parameter.

We used the medians of the fitted parameters to correct the continuum and CO data[13]. The medians of $\Delta\mathrm{RA}_j$ and $\Delta\mathrm{Dec}_j$

[8] https://www.ita.uni-heidelberg.de/~dullemond/software/radmc-3d/

[9] Computed using Mie Theory for a power law grain size distribution ranging from 1 µm to 1 cm, with a slope of −3.5, and composed of astrosilicates (70%), crystalline water ice (15%) and amorphous carbon (15%) by mass (Draine 2003; Li & Greenberg 1998).

[10] In Eq. (5), $P_{k,j} = \exp[-2\pi i(u_{k,j}\Delta\mathrm{RA}_j + v_{k,j}\Delta\mathrm{Dec})]$, where $u_{k,j}$ and $v_{k,j}$ are the $u - v$ coordinates of each visibility.

[11] Although we make sure we do not use as a reference execution an observation with a significantly higher noise than the average.

[12] The second term inside the brackets in Eq. (6) arises from the normalisation of a Gaussian distribution where the standard deviation has been scaled by $f_{\sigma,j}$, which are free parameters. Thus, they must be included explicitly in the definition of $\log P$.

[13] The medians approximate very well the values with the highest likelihood with differences within one σ in most cases, and combined they produce a high-likelihood fit.

were used to align each execution with our reference execution ($j = 0$). In this way, if there was a true offset in the disc relative to the predicted stellar location, this would be conserved, but only with the accuracy that the single $j = 0$ execution provides. We also copy the coordinates of this reference execution to all other executions using the CASA task FIXPLANET. Typically, these offsets were found to be smaller than the beam size and consistent with the expected systematic astrometric uncertainty (see Sect. 5.4). Two systems, HD 14055 and HD 39060, showed offsets with a standard deviation between executions larger than 30% of the beam size (i.e. 3 times the expected absolute astrometric accuracy of 5–10% of the beam, ALMA Technical Handbook). For HD 14055, we attribute the large dispersion to the low elevation (~30°) of its observations due to its declination, which may have increased the phase noise, and to a low S/N per execution. For HD 39060 (β Pic), this is due to one of three executions that has a much higher noise. The coordinates of the final phase centre and the date of the reference execution of each system are presented in Table D.1.

The medians of $f_{\mathrm{flux},j}$ were used to correct for the relative flux offsets. These were found to be typically centred at 1 and have a dispersion of 8% between executions. Finally, the weights of each execution were corrected by using the medians of $f_{\sigma,j}$. We find $f_{\sigma,j} = 1.86-1.88$ for the 12m array and $f_{\sigma,j} = 1.65-1.70$ for the 7m array ARKS observations. These factors mean that the visibility uncertainties are typically underestimated by 70–90%, which would impact any analysis performed using the uncorrected visibility weights. For archival observations, there is a wider range of values from 0.99 to 33.3, likely due to differences in the calibration of weights in earlier ALMA cycles.

For systems with SMGs, we also produce corrected continuum MS files with those sources subtracted using their model visibilities. For most sources, the SMG subtraction performed well, leaving no significant residuals. The two exceptions were HD 95086 and HD 107146. The results of this step, including the best-fit parameters of these sources, are presented in Appendix E. We note that the CO data did not require subtracting the SMGs, as the continuum subtraction step subtracted their emission.

HD 39060 (β Pic) observations used a mosaic strategy (Matrà et al. 2019b) for the compact 12m observations: two pointings set along the disc major axis and offset by 5″ from the star. We found that our offset parameters for the pointing centred on the SW side (single execution) were significantly different from the nominal phase centre by 0.5″(~2 beams). This could be due to our axisymmetric disc assumption as β Pic's disc presents slight asymmetries (Dent et al. 2014; Matrà et al. 2019b). Therefore, for the mosaic observations, we fixed $\Delta\mathrm{RA}_j$ and $\Delta\mathrm{Dec}_j$ to zero.

The inferred central radius, FWHM, disc aspect ratio, and stellar flux for the ARKS sample can be found in Table B.1. Overall, we find good agreement between the derived central radius and FWHM of the dust radial distribution and the estimated values from REASONS in Table 1. However, for some systems, we find significant differences in the FWHM that we attribute to the radial profiles being far from Gaussian distributions (see detailed radial profiles in the companion paper by Han et al. 2026). This is the case for HD 131835, HD 109573, HD 121617, HD 131488 and HD 32297, which display narrow peaks surrounded by extended low-level emission. This translates into ARKS observations being best fit by narrower Gaussians than the lower-resolution REASONS data that are more (less) sensitive to the wide (narrow) component.

For those systems in which we fit a stellar flux, we find values consistent (within 3σ) with the fluxes expected from their SEDs. These predicted fluxes are extrapolations of their fitted photometry assuming a Rayleigh-Jeans behaviour (presented in brackets in the eighth column of Table B.1). Three stars, however, present significant differences: HD 9672, HD 10647, and HD 197481. Though we do not detect the star in HD 9672 (49 Ceti), we constrain its flux to be <19 μJy, which is significantly lower than the 28 μJy expected from its photosphere (as has been found before for other A-type stars, White et al. 2018). For HD 10647 (q[1] Eri), we find a stellar flux of 131 ± 9 μJy (±16 μJy when considering the absolute flux uncertainty) that is higher than the predicted photospheric emission of 96 μJy, but still within 3σ. A higher flux could arise from an unresolved inner belt (Lovell et al. 2021b). For HD 197481 (AU Mic), we find a significantly higher flux of 245 ± 14 μJy (±29 μJy when considering the absolute flux uncertainty) than the expected photospheric emission of 50 μJy. HD 197481 is known to have variable non-photospheric emission at mm wavelengths, which may explain this higher flux (Daley et al. 2019; see also our Appendix F).

5.4. Continuum imaging

Image reconstruction was performed using the CLEAN algorithm implemented in the task TCLEAN in CASA (CASA Team 2022). We used Briggs weighting using robust parameters[14] tailored to each source to find the right balance between resolution and S/N for the different data analyses. For example, the analysis of the radial distribution of dust benefits from higher resolution as one can azimuthally average the emission (Han et al. 2026). Conversely, the analysis of asymmetries benefits more from a higher S/N than higher resolution (Lovell et al. 2026). Typically, we used robust values of 0.5, 1.0 and 2.0, except for a few sources where the S/N was sufficient to reduce the robust value to 0 (e.g. for HD 121617 or HD 32297). We also applied a uvtaper for other sources to boost the S/N per beam and better recover the emission in the reconstructed images (e.g. HD 95086). We used the standard gridder by default, except for sources where we combined 12m and 7m array observations (10/24). For those, we used the mosaic gridder option to account for the different primary beams (this also includes HD39060/β Pic observations that included a mosaic). Finally, we also used the multiscale option, setting the scales to roughly 0, 1, 3 and 9 times the size of the robust=0.5 beam to recover better larger-scale structures.

While cleaning, we manually masked the dirty image, only including regions with positive emission and updated these masks between cleaning cycles to include lower surface brightness regions as imaging artefacts disappeared. We stopped cleaning once the residuals outside the mask appeared like Gaussian noise to visual inspection without large-scale artefacts.

For the particular case of HD 107146, we combine its band 6 and 7 data into a single multi-band image using the 'mtmfs' deconvolver with two terms and a reference frequency of 300 GHz (1.0 mm). Combining both bands was advantageous as it incorporated the high-resolution information from the band 7 observations and the high signal-to-noise short baseline observations from the band 6 observations. The resulting image was

[14] This parameter can take values from −2 to 2, with higher values resulting in a lower resolution but higher S/N. A value of 0.5 is the standard used for observation planning and the quality assessment of the data.

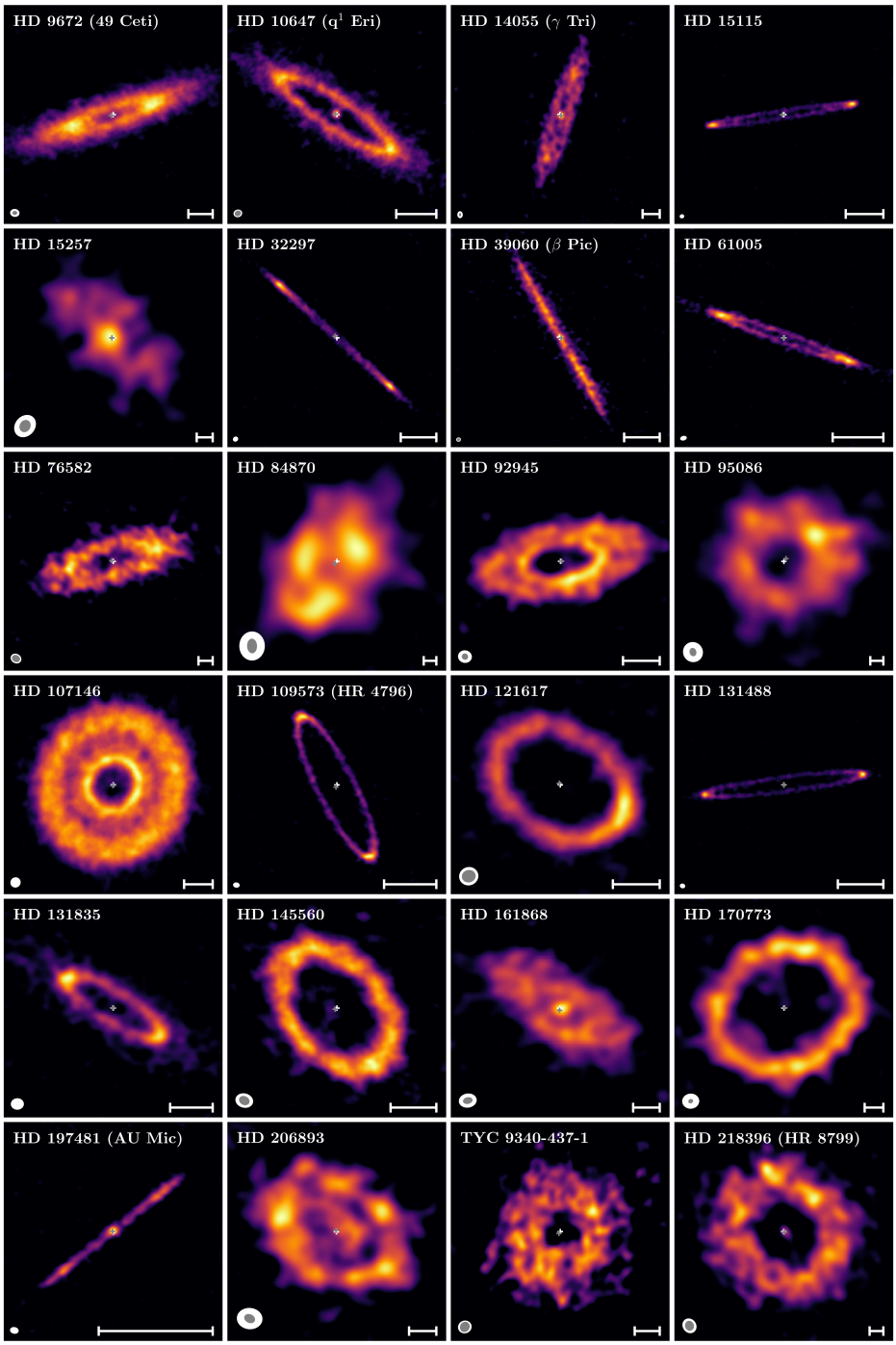

Fig. 3. ARKS continuum clean images of the 24 systems in the sample after correction and subtraction of any SMG. The beam size is shown as a white ellipse in the bottom left corner. For sources imaged with a robust parameter greater than 0.5, an additional grey ellipse represents the beam size using a robust value of 0.5. The white ticks at the edges are spaced by 1″, while the scale bar at the bottom right corner represents a projected distance of 50 au. The white cross represents the expected stellar position according to *Gaia* DR3, while the grey cross represents the best-fit centre of the system assuming a circular belt. For better clarity, each panel uses its own colour scale from 3×rms to the image peak.

significantly better in S/N than the band 7-only image while keeping the beam size almost unchanged. We note, however, that the multi-band images suffer slightly from large-scale artefacts due to systematic noise in the band 7 data (see Sect. 5.2). For this reason, when searching for asymmetries in this system, we use the band 6 data only (Lovell et al. 2026).

Figure 3 presents the continuum images of the SMG-subtracted and corrected data using different robust values to highlight the overall disc emission. The corresponding beam is shown as a white ellipse. The white cross in the image centre shows the expected stellar location according to *Gaia* DR3 for the ARKS targets (Gaia Collaboration 2023), while the grey cross shows the best-fit centre from our Gaussian fit. These differences are small but significant[15] for HD 15115, HD 32297, HD 39060 (β Pic), HD 76582, HD 95086, HD 109573

[15] $>3\sigma$ when looking at the 2D posterior distribution of ΔRA vs. ΔDec for the multiple long baseline observations of each system.

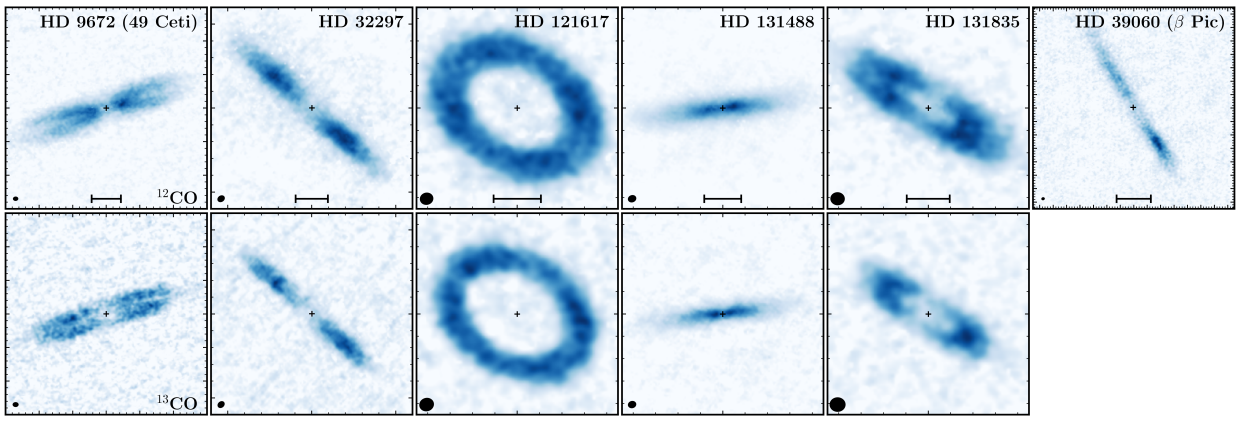

Fig. 4. ARKS CO moment 0 images of the six systems with gas in the sample after subtracting the continuum (^{12}CO at the top and ^{13}CO at the bottom row). We selected an appropriate robust parameter for each system to enhance the S/N per beam if necessary. The beam size is shown as a black ellipse in the bottom left corner. The black cross represents the expected stellar position according to *Gaia* DR3. The bar at the bottom of the top panels represents 50 au. The large and small ticks are spaced by 1 and 0.″2, respectively. The imaging process is described in Mac Manamon et al. (2026). We note that HD 39060 does not have a ^{13}CO image as it was not included in the archival observations that we use for ARKS.

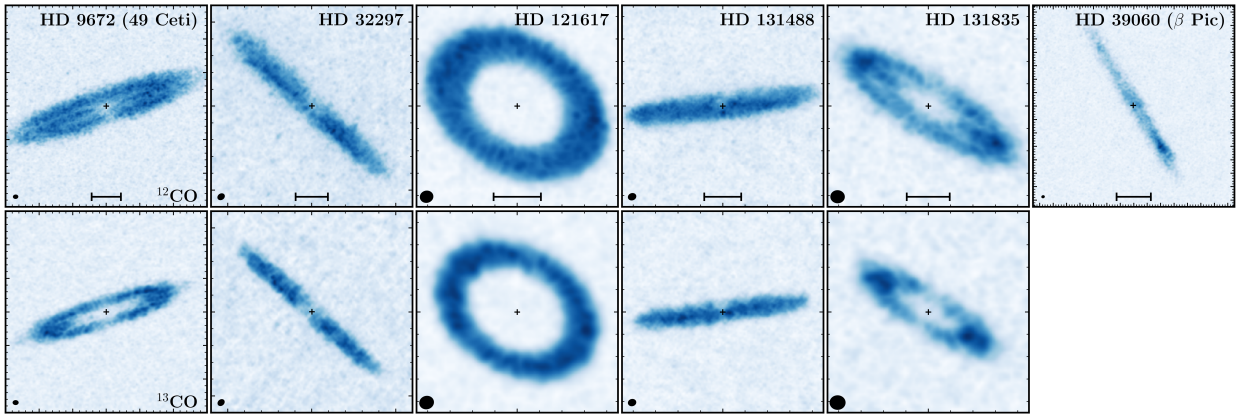

Fig. 5. Same as Fig. 4, but showing the moment 8 (peak intensity) images of the six systems with gas (Mac Manamon et al. 2026).

(HR 4796), HD 161868, and HD 197481 (AU Mic). These offsets may be due to systematic errors (e.g. errors from baseline uncertainties or phase referencing errors) or disc asymmetries (e.g. disc eccentricities or crescents) that bias the Gaussian fit away from the star. Systematic pointing errors are not expected to be larger than 30% of the beam (3 times the expected absolute astrometric accuracy of 5–10% of the beam), which would suggest that the offsets in HD 15115, HD 32297, HD 95086 and HD 109573 are due to asymmetric emission. These offsets and the presence of asymmetries are discussed in detail in the companion paper by Lovell et al. (2026).

5.5. Line imaging

Line imaging was performed using the CLEAN algorithm and the continuum-subtracted data. We used Keplerian masks tailored to each source, producing line cubes that we used to generate moment maps. The details of this process and gas analysis are described in the companion paper by Mac Manamon et al. (2026). Detailed analysis of the gas distribution, line profile and kinematics of the only source significantly away from edge-on, HD 121617, can be found in Brennan et al. (2026) and Marino et al. (2026). Figures 4 and 5 show the moment 0 and 8 images (integrated intensity and peak intensity, respectively) of the ^{12}CO and ^{13}CO J=3–2 emission for the 6 systems with gas detections in ARKS. We note that the HD 39060 band 6 data did not include the ^{13}CO J=2–1 line. Our observations did not reveal any new, previously unknown, CO-bearing system, likely because the higher resolution achieved in ARKS spread any signal over more resolution elements than prior observations, leading to a disc-integrated detection capability not significantly deeper than prior observations, despite the longer integration times.

6. Data release

We have made the corrected data and other data products publicly available on our dedicated website arkslp.org and ARKS dataverse. The data products include:

- The continuum and CO gas measurement sets (MS files), time averaged, frequency averaged for the continuum, and corrected for astrometric offsets, flux offsets, weights rescaling, and with and without the subtraction of SMGs (see Sect. 5.3).
- Corrected continuum visibility tables in a text format.
- Clean continuum and CO gas images with various resolutions (robust parameter), uv-tapering, and before and after subtracting SMGs.
- Reduction and correction scripts to run in CASA to regenerate the data, and best-fit values that we used to correct the data as json files.

– A master table with the most relevant information presented in Tables 1, A.1 and B.1.

7. Initial results overview

In this section we provide an overview of the results from the first ARKS paper series.

7.1. ARKS II: The radial structure of debris discs, Han et al. (2026)

In this paper, we analyse the radial distribution of dust using parametric and non-parametric models. We find many structures, such as multiple rings and gaps, halos, and sharp or smooth edges. Overall, we find that 5/24 belts have multiple rings, 7/24 belts have low-amplitude emission (either a halo or additional faint rings), and the remaining 12/24 are consistent with being single belts (some of which have substructures such as shoulders or plateaus). We find a bimodal distribution in the fractional width of rings across the whole sample, with our new observations revealing that the population of narrow rings is more prevalent than the lower-resolution REASONS data suggested. This is not only because several belts are resolved into multiple components, but also because some broad belts have been resolved into a very narrow peak surrounded by extended and faint components that biased lower-resolution observations. The distribution of fractional widths is similar to that of rings in protoplanetary discs, but the wide population is still more prevalent than in protoplanetary discs as found in REASONS (Matrà et al. 2025).

7.2. ARKS III: The vertical structure of debris discs, Zawadzki et al. (2026)

In this paper, we analyse the vertical distribution of dust using parametric models. We resolve the vertical structure of 13 belts, finding a wide distribution of vertical aspect ratios (H/r), with values ranging between 0.003–0.2, with a median of 0.02. Moreover, we find that for most belts, their vertical distribution approximates better to a Lorentzian than a Gaussian distribution, hinting at the presence of multiple dynamical populations. The inferred dynamical excitation of these belts could be explained by self-stirring, with half of them requiring belt masses below 20 $M_{\oplus}$.

7.3. ARKS IV: CO gas imaging and overview, Mac Manamon et al. (2026)

In this paper, we present and analyse the ^{12}CO and ^{13}CO J=3–2 CO gas observations of HD 9672, HD 32297, HD 121617, HD 131488, and HD 131835. We describe how the image cubes were generated and how their integrated and peak intensity maps were calculated. We analyse the spatial distribution of CO and compare it with that of the millimetre dust, finding that the CO gas intensity is broader than the dust emission and its peak is shifted inwards in comparison to the dust, though the offset between the dust and the gas peaks varies with system. If the gas is secondary, this could be evidence of viscous spreading. However, these differences could at least be partially explained by the high optical depth of CO emission.

We present radially resolved ^{12}CO/^{13}CO isotopologue ratios for the five systems with new ARKS observations (i.e. excluding HD 39060/β Pic) and find that the ^{12}CO and ^{13}CO in all but one system, HD 9672 (49 Ceti), must both be either optically thin or optically thick. Using spectrospatial stacking, we measured the integrated line flux of ^{12}CO and ^{13}CO in each gas-rich system and conducted a deep search for ^{12}CO in every disc that did not previously have a CO detection. No new CO detections were made, although this allowed us to constrain upper limits on the ^{12}CO integrated line flux in all systems without detected CO.

7.4. ARKS V: Comparison between scattered light and thermal emission, Milli et al. (2026)

In addition to ARKS observations, we have collected scattered light data of all systems in our sample, tracing the distribution of small micron-sized grains. Of the 24 belts, 15 have been detected in scattered light. The reported detections were made with at least one of these three facilities: the Very Large Telescope (VLT) SPHERE instrument, the Gemini Planet Imager (GPI), or the Hubble Space Telescope (HST), noting that the entire ARKS sample has been observed by the VLT/SPHERE instrument. In this paper, we focus on those 15 detections and present the data reduction, forward-modelling, and comparison of the spatial distribution of small and large grains. For gas-poor systems, we find only subtle differences in peak surface density locations. However, for gas-rich systems, we find that the distribution of small grains is significantly shifted outwards by $\gtrsim$10%, suggesting that the interplay of radiation pressure and gas drag has a significant effect on the dynamics of µm-grains (Takeuchi & Artymowicz 2001; Krivov et al. 2009). We also detect for the first time the scattered light emission of the belt surrounding the K-type star TYC 9340-437-1 with HST/NICMOS. Lastly, we summarise the mass and orbital properties of the known planets in the 24 systems, their location relative to the disc edges and gaps, and present additional constraints from *Gaia* astrometry, *Gaia*-Hipparcos proper motion anomalies, and direct imaging.

7.5. ARKS VI: Asymmetries and offsets, Lovell et al. (2026)

In this paper, we investigate whether the (sub)millimetre dust emission of the sample contains asymmetries, and if the discs contain stellocentric offsets (eccentricities). We use a series of empirical diagnostics to search for different types of asymmetric features in the data. We find that 10/24 systems present significant asymmetries in the form of disc eccentricities, arcs, and global emission asymmetries (i.e. along either their major or minor axes, or azimuthally). Tentative asymmetries (at the 3−5σ level) are found in four other discs. We characterise these asymmetries and briefly discuss plausible dynamical scenarios that could explain these features. We find that the presence of an asymmetry/offset in the ARKS sample appears to be correlated with the fractional luminosity of cold dust. We also find a tentative enhancement in the fraction of systems hosting a continuum asymmetry, and those that are CO-rich. Overall, this study, the first (sub)millimetre population analysis of debris disc asymmetries, highlights that asymmetries and offsets in debris discs are likely common.

7.6. ARKS VII: Optically thick gas in the HD 121617 disc with broad CO Gaussian local line profiles, Brennan et al. (2026)

In this paper, we analyse the intrinsic line profile of ^{12}CO in the HD 121617 disc. The observed line profile is very broad, displaying a FWHM of 1.1 km/s, which could be interpreted as the gas having a very high kinetic temperature of ~380 K at 73 au. However, the integrated intensity images (moment 0's) of both ^{12} and ^{13}CO display an azimuthal modulation that is typical of optically

thick discs (also seen in the other 2 non-edge-on gas-rich discs in ARKS). Using radiative transfer models, we show how a massive ($\gtrsim$0.1 $M_\oplus$), cold (~38 K), and narrow (FWHM of 17 au) ring of CO gas can reproduce the line width, moment 0 and peak intensity images. These results confirm the previous findings of a low excitation temperature for CO gas (e.g. Cataldi et al. 2023) and that the ^{12}CO emission must be optically thick. Additionally, these results would imply that CO is thermally decoupled from the dust, displaying a significantly lower temperature.

7.7. ARKS VIII: A dust arc and non-Keplerian gas kinematics in HD 121617, Marino et al. (2026)

In this paper, we investigate the asymmetric dust distribution and CO kinematics in the HD 121617 disc. We find that the dust arc has a morphology similar to that attributed to vortices in protoplanetary discs, and that it is absent or much less pronounced in the distribution of small grains and gas (although the CO gas emission is optically thick and thus could hide an arc in the gas distribution). The CO gas kinematics show strong deviations from Keplerian rotation due to strong pressure gradients at the inner and outer edges of the ring. We retrieve the rotation curve and use it to derive profiles for the pressure gradient and gas surface density. We can reconcile this surface density with that of the CO gas depending on the assumed stellar mass and gas sound speed (determined by the gas temperatures and mean molecular weight). If the gas densities are high enough, requiring a primordial origin, the dust radial confinement and azimuthal arc may result from dust grains responding to gas drag (Weber et al. 2026). Alternatively, the asymmetry may be due to planet-disc interactions via mean motion resonances (Pearce et al., in prep.).

7.8. Paper IX: Gas-driven origin for continuum arc in the debris disc HD 121617, Weber et al. (2026)

A key finding presented in Lovell et al. (2026) and Marino et al. (2026) is that the mm-emission from the dust ring around HD 121617 shows a significant asymmetry with an arc of increased emission. This suggests that dust accumulates at a preferred azimuth within the ring, which itself is embedded in a gas ring with steep pressure gradients on either side. We explore two explanations for this feature: in Weber et al. (2026), we investigate whether a shallow gas vortex, similar to those seen in protoplanetary discs, could generate such an azimuthal dust over-density. Through hydrodynamical simulations with varying gas masses, we find that this scenario only works if the total gas mass in HD 121617 is around ~25 $M_\oplus$, roughly 10^2 times the estimated minimum CO mass. Hence, this scenario implies a hydrogen-dominated composition and a primordial origin for the CO. By contrast, an alternative explanation involving an outward-migrating planet can also account for the observed asymmetry, as it would trap dust grains in mean-motion resonances; this alternative will be explored in a forthcoming study (Pearce et al., in prep.).

7.9. Paper X: Interpreting the peculiar dust rings around HD 131835, Jankovic et al. (2026)

HD 131835 contains at least two distinct rings, with the outermost being brightest in scattered light, indicating that micron-sized grains reside mostly in that outer ring, while the innermost is much brighter at millimetre wavelengths, indicating that millimetre-sized grains instead reside mostly in the inner ring (Milli et al. 2026). In this paper, we explore two possible explanations for this grain size segregation. We (i) use collisional models to test under which conditions two planetesimal belts can produce two dust rings with such different properties, and (ii) use dynamical models of dust migration under the influence of gas drag to investigate if the gas present in this disc could explain this behaviour instead. We find that gas drag can form an outer ring out of small dust (as in Takeuchi & Artymowicz 2001), but the simple dynamical model cannot reproduce the brightness of HD 131835's outermost ring. Nevertheless, the gas-driven explanation is promising, and we discuss how a more comprehensive model may change this result. The collisional scenario might reproduce observations, although it requires an extreme difference in the dynamical excitation and/or material strength between the two rings, which remains to be explained.

8. Conclusions

The ARKS ALMA large programme was motivated by a series of questions that have arisen over the last decade while studying exoKuiper belts. Below, we summarise these questions, how ARKS has contributed to answering them, and what new questions have arisen.

What type of radial substructures are present in exoKuiper belts? ARKS has shown that there is a great diversity of radial structures. Up to one-third of the belts in ARKS show substructures in the form of multiple rings or local maxima with gaps of varied depths in between, one-third display narrow rings surrounded by low-amplitude additional rings or halos, and the rest are consistent with wide and smooth single belts (Han et al. 2026). The high fraction of multi-ring belts and narrow single rings (~60%) suggests that a high fraction of exoKuiper belts may inherit their solid distribution from that in protoplanetary discs that predominantly show substructures in the form of multiple or single narrow rings. Alternatively, these structures may appear at a later stage (e.g. gaps cleared by planets). The other ~40% of wide and smooth belts may have formed or evolved in very different ways, for example in migrating protoplanetary rings or scattered by planets. Finally, ARKS has also shown a diversity in the steepness of belt edges. Belt inner edges within 100 au tend to be steep and consistent with planet sculpting, whereas inner edges at larger distances tend to be shallower and consistent with being shaped by collisional evolution. We do not find clear correlations between these structures and the system properties (e.g. age, spectral type, presence of planets), which leaves the origin of these structures unconstrained.

How dynamically excited are exoKuiper belts? ARKS has shown that belts have a wide range of dynamical excitation as inferred from their vertical thickness (Zawadzki et al. 2026). These levels overlap those measured for the Kuiper belt, from a few degrees to tens of degrees. Moreover, ARKS has shown that the dust vertical distributions are better reproduced by non-Gaussian distributions such as a Lorentzian, which suggests the presence of multiple dynamical populations. Similar to the radial structures, we do not find clear correlations between the derived vertical structures and the system properties. However, we do find that the radial and vertical widths of belts are correlated, which may indicate that the processes that excite the orbits of solids are also responsible for making these belts wider. Despite these important insights, it is still an open question whether the dynamical excitation is set by planets not embedded in the belts or by dwarf planets within the belts.

Are asymmetries common in exoKuiper belts? ARKS has shown that asymmetries in the dust distribution are common; 10 of the 24 belts show a significant asymmetry in the form of arcs, belt eccentricities, and warps (Lovell et al. 2026). Whether these asymmetries are caused by planet–disc interactions, stellar flybys, or gas drag is an open question. Asymmetries in the gas distribution are yet to be examined in detail, but at least one system shows tentative evidence of an eccentricity in its gas distribution (HD 121617, Marino et al. 2026), while other edge-on ones show azimuthal asymmetries (HD 39060/β Pic, HD32297, HD131488, Mac Manamon et al. 2026).

What is the origin of the gas? ARKS has shown that the CO gas emission spans a larger range of radii than the dust, with a peak intensity slightly closer to the star than the dust (Mac Manamon et al. 2026). This may be partly explained by the CO emission being optically thick, as demonstrated for one system by Brennan et al. (2026). However, in a few systems, CO emission is detected close to the star, which strongly suggests that the gas and dust distributions are different. This wider span is a feature seen in primordial and secondary gas models. In the former, the dust distribution can be shaped by gas drag, producing a narrower distribution of large grains trapped in pressure maxima if gas densities are high enough (Weber et al. 2026). In the secondary scenario, CO gas is expected to have a wider distribution if it is shielded, allowing it to viscously spread before being photodissociated (Kral et al. 2019; Marino et al. 2020a).

Does gas affect the dust dynamics? ARKS has found that in gas-bearing systems, the spatial distribution of micron-sized grains is significantly shifted outwards compared to millimetre-sized grains (Milli et al. 2026). This is a feature expected in optically thin gas-rich discs, due to the combined effect of radiation pressure and gas drag (Jankovic et al. 2026). Moreover, for one of these gas-bearing belts, we found an overdensity in the distribution of millimetre-sized dust that resembles the expected morphology of dust trapped in a vortex (Lovell et al. 2026; Marino et al. 2026; Weber et al. 2026). These findings suggest that gas may play an important role in shaping the distribution of small and large dust in gas-bearing exoKuiper belts. These results have also triggered the question of whether the wider span of gas relative to dust is a consequence of gas viscous spreading or dust trapping.

Does the gas display non-Keplerian kinematics? For at least one system, HD 121617, we find strong deviations from Keplerian rotation due to strong pressure gradients that are consistent with the CO gas intensity distribution (Marino et al. 2026). These kinematic features, combined with the intensity distribution and radiative transfer models, could allow us to break degeneracies and determine the mean molecular weight of the gas.

Perhaps the most important question that is yet to be answered is whether any or most of the observed structures are linked to the presence of planets in these systems. Some of these systems host planets, but most reside far from the edges of these belts. The James Webb Space Telescope and soon the Extremely Large Telescope may reveal or rule out the presence of planets actively shaping these discs.

Data availability

The ARKS data used in this paper and others can be found in the ARKS dataverse. The continuum data products produced by this work can be found within the ARKS I's dataset (doi.org/10.7910/DVN/VNGHPQ). The data reduction scripts can be found at github.com/SebaMarino/ARKS-data-reduction (doi.org/10.5281/zenodo.17432148). For more information, visit arkslp.org.

Acknowledgements. We thank the referee for their constructive review of this manuscript that helped improve the quality and clarity of this work. This paper makes use of the following ALMA data: ADS/JAO.ALMA# 2022.1.00338.L, 2012.1.00142.S, 2012.1.00198.S, 2015.1.01260.S, 2016.1.00104.S, 2016.1.00195.S, 2016.1.00907.S, 2017.1.00167.S, 2017.1.00825.S, 2018.1.01222.S and 2019.1.00189.S. ALMA is a partnership of ESO (representing its member states), NSF (USA) and NINS (Japan), together with NRC (Canada), MOST and ASIAA (Taiwan), and KASI (Republic of Korea), in cooperation with the Republic of Chile. The Joint ALMA Observatory is operated by ESO, AUI/NRAO and NAOJ. The National Radio Astronomy Observatory is a facility of the National Science Foundation operated under cooperative agreement by Associated Universities, Inc. The project leading to this publication has received support from ORP, that is funded by the European Union's Horizon 2020 research and innovation programme under grant agreement No 101004719 [ORP]. We are grateful for the help of the UK node of the European ARC in answering our questions and producing calibrated measurement sets. This research used the Canadian Advanced Network For Astronomy Research (CANFAR) operated in partnership by the Canadian Astronomy Data Centre and The Digital Research Alliance of Canada with support from the National Research Council of Canada the Canadian Space Agency, CANARIE and the Canadian Foundation for Innovation. S.M. acknowledges funding by the Royal Society through a Royal Society University Research Fellowship (URF-R1-221669) and the European Union through the FEED ERC project (grant number 101162711). L.M. acknowledges funding by the European Union through the E-BEANS ERC project (grant number 100117693), and by the Irish research Council (IRC) under grant number IRCLA- 2022-3788. Views and opinions expressed are however those of the author(s) only and do not necessarily reflect those of the European Union or the European Research Council Executive Agency. Neither the European Union nor the granting authority can be held responsible for them. A.M.H. acknowledges support from the National Science Foundation under Grant No. AST-2307920. C.d.B. acknowledges support from the Spanish Ministerio de Ciencia, Innovación y Universidades (MICIU) and the European Regional Development Fund (ERDF) under reference PID2023-153342NB-I00/10.13039/501100011033, from the Beatriz Galindo Senior Fellowship BG22/00166 funded by the MICIU, and the support from the Universidad de La Laguna (ULL) and the Consejería de Economía, Conocimiento y Empleo of the Gobierno de Canarias. A.B. acknowledges research support by the Irish Research Council under grant GOIPG/2022/1895. M.R.J. acknowledges support from the European Union's Horizon Europe Programme under the Marie Sklodowska-Curie grant agreement no. 101064124 and funding provided by the Institute of Physics Belgrade, through the grant by the Ministry of Science, Technological Development, and Innovations of the Republic of Serbia. J.B.L. acknowledges the Smithsonian Institute for funding via a Submillimeter Array (SMA) Fellowship, and the North American ALMA Science Center (NAASC) for funding via an ALMA Ambassadorship. SMM acknowledges funding by the European Union through the E-BEANS ERC project (grant number 100117693), and by the Irish research Council (IRC) under grant number IRCLA- 2022-3788. Views and opinions expressed are however those of the author(s) only and do not necessarily reflect those of the European Union or the European Research Council Executive Agency. Neither the European Union nor the granting authority can be held responsible for them. J.M. acknowledges funding from the Agence Nationale de la Recherche through the DDISK project (grant No. ANR-21-CE31-0015) and from the PNP (French National Planetology Program) through the EPOPEE project. P.W. acknowledges support from FONDECYT grant 3220399 and ANID – Millennium Science Initiative Program – Center Code NCN2024_001. Support for B.Z. was provided by The Brinson Foundation. R.B.W. was supported by a Royal Society Grant (RF-ERE-221025). This material is based upon work supported by the National Science Foundation Graduate Research Fellowship under Grant No. DGE 2140743. E.M. acknowledges support from the NASA CT Space Grant. T.D.P. is supported by a UKRI Stephen Hawking Fellowship and a Warwick Prize Fellowship, the latter made possible by a generous philanthropic donation. This work was also supported by the NKFIH research grant K-147380. M.B. acknowledges funding from the Agence Nationale de la Recherche through the DDISK project (grant No. ANR-21-CE31-0015). E.C. acknowledges support from NASA STScI grant HST-AR-16608.001-A and the Simons Foundation. S.E. is supported by the National Aeronautics and Space Administration through the Exoplanet Research Program (Grant No. 80NSSC23K0288, PI: Faramaz). This work was also supported by the NKFIH NKKP grant ADVANCED 149943 and the NKFIH excellence grant TKP2021-NKTA-64. Project no.149943 has been implemented with the support provided by the Ministry of Culture and Innovation of Hungary from the National Research, Development and Innovation Fund, financed under

the NKKP ADVANCED funding scheme. J.P.M. acknowledges research support by the National Science and Technology Council of Taiwan under grant NSTC 112-2112-M-001-032-MY3. S.P. acknowledges support from FONDECYT Regular 1231663 and ANID – Millennium Science Initiative Program – Center Code NCN2024_001. A.A.S. is supported by the Heising-Simons Foundation through a 51 Pegasi b Fellowship.

References

Ansdell, M., Williams, J. P., van der Marel, N., et al. 2016, ApJ, 828, 46
Astropy Collaboration (Price-Whelan, A. M., et al.) 2022, ApJ, 935, 167
Aumann, H. H., Beichman, C. A., Gillett, F. C., et al. 1984, ApJ, 278, L23
Backman, D. E., & Paresce, F. 1993, in Protostars and Planets III, eds. E. H. Levy, & J. I. Lunine (Tucson: University of Arizona Press), 1253
Bae, J., Isella, A., Zhu, Z., et al. 2023, ASP Conf. Ser., 534, 423
Baig, S., Smart, R. L., Jones, H. R. A., et al. 2024, MNRAS, 533, 3784
Baraffe, I., Homeier, D., Allard, F., & Chabrier, G. 2015, A&A, 577, A42
Baron, F., Artigau, É., Rameau, J., et al. 2018, AJ, 156, 137
Belokurov, V., Penoyre, Z., Oh, S., et al. 2020, MNRAS, 496, 1922
Bertini, L., Roccatagliata, V., & Kim, M. 2023, A&A, 671, L2
Biller, B. A., Liu, M. C., Wahhaj, Z., et al. 2013, ApJ, 777, 160
Blanton, M. R., Bershady, M. A., Abolfathi, B., et al. 2017, AJ, 154, 28
Booth, M., Wyatt, M. C., Morbidelli, A., Moro-Martín, A., & Levison, H. F. 2009, MNRAS, 399, 385
Booth, M., Matrà, L., Su, K. Y. L., et al. 2019, MNRAS, 482, 3443
Booth, M., Pearce, T. D., Krivov, A. V., et al. 2023, MNRAS, 521, 6180
Brandt, T. D. 2021, ApJS, 254, 42
Brandt, G. M., Brandt, T. D., Dupuy, T. J., Li, Y., & Michalik, D. 2021, AJ, 161, 179
Brennan, A., Matrà, L., Marino, S., et al. 2024, MNRAS, 531, 4482
Brennan, A., Matrà, L., Mac Manamon, S., et al. 2026, A&A, 705, A201
Bressan, A., Marigo, P., Girardi, L., et al. 2012, MNRAS, 427, 127
Butler, R. P., Wright, J. T., Marcy, G. W., et al. 2006, ApJ, 646, 505
CASA Team (Bean, B., et al.) 2022, PASP, 134, 114501
Cataldi, G., Brandeker, A., Wu, Y., et al. 2018, ApJ, 861, 72
Cataldi, G., Aikawa, Y., Iwasaki, K., et al. 2023, ApJ, 951, 111
Chauvin, G., Vigan, A., Bonnefoy, M., et al. 2015, A&A, 573, A127
Chauvin, G., Gratton, R., Bonnefoy, M., et al. 2018, A&A, 617, A76
Chen, Y., Girardi, L., Bressan, A., et al. 2014, MNRAS, 444, 2525
Chen, Y., Bressan, A., Girardi, L., et al. 2015, MNRAS, 452, 1068
Cieza, L. A., González-Ruilova, C., Hales, A. S., et al. 2021, MNRAS, 501, 2934
Cifuentes, C., Caballero, J. A., González-Payo, J., et al. 2025, A&A, 693, A228
Daley, C., Hughes, A. M., Carter, E. S., et al. 2019, ApJ, 875, 87
Dallant, J., Langlois, M., Flasseur, O., & Thiébaut, É. 2023, A&A, 679, A38
De Rosa, R. J., Patience, J., Wilson, P. A., et al. 2014, MNRAS, 437, 1216
del Burgo, C., & Allende Prieto, C. 2016, MNRAS, 463, 1400
del Burgo, C., & Allende Prieto, C. 2018, MNRAS, 479, 1953
Delamer, M. 2023, Master's thesis, Wesleyan University, USA
Dent, W. R. F., Wyatt, M. C., Roberge, A., et al. 2014, Science, 343, 1490
Donati, J. F., Cristofari, P. I., Finociety, B., et al. 2023, MNRAS, 525, 455
Draine, B. T. 2003, ApJ, 598, 1017
Ducourant, C., Teixeira, R., Galli, P. A. B., et al. 2014, A&A, 563, A121
Elliott, P., Bayo, A., Melo, C. H. F., et al. 2014, A&A, 568, A26
Elliott, P., Huélamo, N., Bouy, H., et al. 2015, A&A, 580, A88
Elliott, P., Bayo, A., Melo, C. H. F., et al. 2016, A&A, 590, A13
Faramaz, V., Krist, J., Stapelfeldt, K. R., et al. 2019, AJ, 158, 162
Faramaz, V., Marino, S., Booth, M., et al. 2021, AJ, 161, 271
Fernandez, J. A., & Ip, W.-H. 1984, Icarus, 58, 109
Fernandez, M. A., Covey, K. R., De Lee, N., et al. 2017, PASP, 129, 084201
Foreman-Mackey, D., Hogg, D. W., Lang, D., & Goodman, J. 2013, PASP, 125, 306
Francis, L., Johnstone, D., Herczeg, G., Hunter, T. R., & Harsono, D. 2020, AJ, 160, 270
Friebe, M. F., Pearce, T. D., & Löhne, T. 2022, MNRAS, 512, 4441
Gagné, J., Faherty, J. K., & Mamajek, E. E. 2018, ApJ, 865, 136
Gaia Collaboration 2022, VizieR On-line Data Catalog: I/357
Gaia Collaboration (Brown, A. G. A., et al.) 2018, A&A, 616, A1
Gaia Collaboration (Vallenari, A., et al.) 2023, A&A, 674, A1
Geiler, F., Krivov, A., Booth, M., & Löhne, T. 2019, MNRAS, 483, 332
Genda, H., Kobayashi, H., & Kokubo, E. 2015, ApJ, 810, 136
Ginsburg, A., Sipőcz, B. M., Brasseur, C. E., et al. 2019, AJ, 157, 98
González-Payo, J., Caballero, J. A., Gorgas, J., et al. 2024, A&A, 689, A302
Goodman, J., & Weare, J. 2010, Comm Appl. Math. Comput. Sci., 5, 65
Grandjean, A., Lagrange, A. M., Beust, H., et al. 2019, A&A, 627, L9
Gratton, R., Squicciarini, V., Nascimbeni, V., et al. 2023, A&A, 678, A93
Gratton, R., Bonavita, M., Mesa, D., et al. 2024, A&A, 685, A119
Greaves, J. S., Holland, W. S., Moriarty-Schieven, G., et al. 1998, ApJ, 506, L133
Hales, A. S., Marino, S., Sheehan, P. D., et al. 2022, ApJ, 940, 161
Han, Y., Mansell, E., Jennings, J., et al. 2026, A&A, 705, A196
Han, Y., Wyatt, M. C., & Matrà, L. 2022, MNRAS, 511, 4921
Harper, D. A., Loewenstein, R. F., & Davidson, J. A. 1984, ApJ, 285, 808
Higuchi, A. E., Sato, A., Tsukagoshi, T., et al. 2017, ApJ, 839, L14
Higuchi, A. E., Saigo, K., Kobayashi, H., et al. 2019, ApJ, 883, 180
Hinkley, S., Lacour, S., Marleau, G. D., et al. 2023, A&A, 671, L5
Holland, W. S., Greaves, J. S., Zuckerman, B., et al. 1998, Nature, 392, 788
Huang, J., Andrews, S. M., Dullemond, C. P., et al. 2018, ApJ, 869, L42
Hughes, A. M., Lieman-Sifry, J., Flaherty, K. M., et al. 2017, ApJ, 839, 86
Hughes, A. M., Duchêne, G., & Matthews, B. C. 2018, ARA&A, 56, 541
Ida, S., & Makino, J. 1993, Icarus, 106, 210
Ida, S., Bryden, G., Lin, D. N. C., & Tanaka, H. 2000, ApJ, 534, 428
Imaz Blanco, A., Marino, S., Matrà, L., et al. 2023, MNRAS, 522, 6150
Jackson, A. P., Wyatt, M. C., Bonsor, A., & Veras, D. 2014, MNRAS, 440, 3757
Jankovic, M. R., Pawellek, N., Zander, J., et al. 2026, A&A, 705, A204
Janson, M., Brandt, T. D., Moro-Martín, A., et al. 2013a, ApJ, 773, 73
Janson, M., Lafrenière, D., Jayawardhana, R., et al. 2013b, ApJ, 773, 170
Jiménez-Esteban, F. M., Solano, E., & Rodrigo, C. 2019, AJ, 157, 78
Jura, M., Zuckerman, B., Becklin, E. E., & Smith, R. C. 1993, ApJ, 418, L37
Kalas, P., Graham, J. R., & Clampin, M. 2005, Nature, 435, 1067
Kastner, J. H., Zuckerman, B., & Bessell, M. 2008, A&A, 491, 829
Kennedy, G. M., Marino, S., Matrà, L., et al. 2018, MNRAS, 475, 4924
Kervella, P., Arenou, F., Mignard, F., & Thévenin, F. 2019, A&A, 623, A72
Kervella, P., Arenou, F., & Thévenin, F. 2022, A&A, 657, A7
Klusmeyer, J., Hughes, A. M., Matrà, L., et al. 2021, ApJ, 921, 56
Kóspál, Á., Moór, A., Juhász, A., et al. 2013, ApJ, 776, 77
Kral, Q., Wyatt, M., Carswell, R. F., et al. 2016, MNRAS, 461, 845
Kral, Q., Marino, S., Wyatt, M. C., Kama, M., & Matrà, L. 2019, MNRAS, 489, 3670
Kral, Q., Matrà, L., Kennedy, G. M., Marino, S., & Wyatt, M. C. 2020, MNRAS, 497, 2811
Krivov, A. V. 2010, Res. Astron. Astrophys., 10, 383
Krivov, A. V., Herrmann, F., Brandeker, A., & Thébault, P. 2009, A&A, 507, 1503
Lagrange, A. M., Gratadour, D., Chauvin, G., et al. 2009, A&A, 493, L21
Lagrange, A. M., Meunier, N., Rubini, P., et al. 2019, Nat. Astron., 3, 1135
Lagrange, A. M., Rubini, P., Nowak, M., et al. 2020, A&A, 642, A18
Latham, D. W., Stefanik, R. P., Torres, G., et al. 2002, AJ, 124, 1144
Lecavelier Des Etangs, A., Vidal-Madjar, A., & Ferlet, R. 1996, A&A, 307, 542
Leclerc, A., Babusiaux, C., Arenou, F., et al. 2023, A&A, 672, A82
Lestrade, J. F., Morey, E., Lassus, A., & Phou, N. 2011, A&A, 532, A120
Li, A., & Greenberg, J. M. 1998, A&A, 331, 291
Lieman-Sifry, J., Hughes, A. M., Carpenter, J. M., et al. 2016, ApJ, 828, 25
Long, F., Herczeg, G. J., Harsono, D., et al. 2019, ApJ, 882, 49
Long, F., Pascucci, I., Houge, A., et al. 2025, ApJ, 978, L30
Loomis, R. A., Öberg, K. I., Andrews, S. M., et al. 2018, AJ, 155, 182
Lovell, J. B., Kennedy, G. M., Marino, S., et al. 2021a, MNRAS, 502, L66
Lovell, J. B., Marino, S., Wyatt, M. C., et al. 2021b, MNRAS, 506, 1978
Lovell, J. B., Wyatt, M. C., Ansdell, M., et al. 2021c, MNRAS, 500, 4878
Lovell, J. B., Hales, A. S., Kennedy, G. M., et al. 2026, A&A, 705, A200
Mac Manamon, S., Matrà, L., Marino, S., et al. 2026, A&A, 705, A198
MacGregor, M. A., Matrà, L., Kalas, P., et al. 2017, ApJ, 842, 8
MacGregor, M. A., Weinberger, A. J., Nesvold, E. R., et al. 2019, ApJ, 877, L32
MacGregor, A. M., Osten, R. A., & Hughes, A. M. 2020, ApJ, 891, 80
MacGregor, M. A., Hurt, S. A., Stark, C. C., et al. 2022, ApJ, 933, L1
Malhotra, R. 1995, AJ, 110, 420
Mâlin, M., Boccaletti, A., Perrot, C., et al. 2024, A&A, 690, A316
Mallorquín, M., Béjar, V. J. S., Lodieu, N., et al. 2024, A&A, 689, A132
Marcussen, M. L., & Albrecht, S. H. 2023, AJ, 165, 266
Marino, S. 2021, MNRAS, 503, 5100
Marino, S., Matrà, L., Stark, C., et al. 2016, MNRAS, 460, 2933
Marino, S., Wyatt, M. C., Panić, O., et al. 2017, MNRAS, 465, 2595
Marino, S., Carpenter, J., Wyatt, M. C., et al. 2018, MNRAS, 479, 5423
Marino, S., Yelverton, B., Booth, M., et al. 2019, MNRAS, 484, 1257
Marino, S., Flock, M., Henning, T., et al. 2020a, MNRAS, 492, 4409
Marino, S., Zurlo, A., Faramaz, V., et al. 2020b, MNRAS, 498, 1319
Marino, S., Cataldi, G., Jankovic, M. R., Matrà, L., & Wyatt, M. C. 2022, MNRAS, 515, 507
Marino, S., Gupta, V., Weber, P., et al. 2026, A&A, 705, A202
Marmier, M., Ségransan, D., Udry, S., et al. 2013, A&A, 551, A90
Marois, C., Macintosh, B., Barman, T., et al. 2008, Science, 322, 1348
Marois, C., Zuckerman, B., Konopacky, Q. M., Macintosh, B., & Barman, T. 2010, Nature, 468, 1080
Marshall, J. P., Milli, J., Choquet, E., et al. 2023, MNRAS, 521, 5940
Martioli, E., Hébrard, G., Correia, A. C. M., Laskar, J., & Lecavelier des Etangs, A. 2021, A&A, 649, A177

Mason, B. D., Wycoff, G. L., Hartkopf, W. I., Douglass, G. G., & Worley, C. E. 2001, AJ, 122, 3466
Matrà, L., Dent, W. R. F., Wyatt, M. C., et al. 2017a, MNRAS, 464, 1415
Matrà, L., MacGregor, M. A., Kalas, P., et al. 2017b, ApJ, 842, 9
Matrà, L., Öberg, K. I., Wilner, D. J., Olofsson, J., & Bayo, A. 2019a, AJ, 157, 117
Matrà, L., Wyatt, M. C., Wilner, D. J., et al. 2019b, AJ, 157, 135
Matrà, L., Marino, S., Wilner, D. J., et al. 2025, A&A, 693, A151
Michel, A., van der Marel, N., & Matthews, B. C. 2021, ApJ, 921, 72
Miller, E., Marino, S., Stammler, S. M., et al. 2021, MNRAS, 508, 5638
Milli, J., Hibon, P., Christiaens, V., et al. 2017, A&A, 597, L2
Milli, J., Olofsson, J., Bonduelle, M., et al. 2026, A&A, 705, A199
Miret-Roig, N., Alves, J., Ratzenböck, S., et al. 2025, A&A, 694, A60
Moór, A., Juhász, A., Kóspál, Á., et al. 2013, ApJ, 777, L25
Moór, A., Curé, M., Kóspál, Á., et al. 2017, ApJ, 849, 123
Moór, A., Ábrahám, P., Szabó, G., et al. 2021, ApJ, 910, 27
Morrison, S., & Malhotra, R. 2015, ApJ, 799, 41
Nakatani, R., Kobayashi, H., Kuiper, R., Nomura, H., & Aikawa, Y. 2021, ApJ, 915, 90
Nederlander, A., Hughes, A. M., Fehr, A. J., et al. 2021, ApJ, 917, 5
Nielsen, E. L., De Rosa, R. J., Macintosh, B., et al. 2019, AJ, 158, 13
Pearce, T. D., & Wyatt, M. C. 2014, MNRAS, 443, 2541
Pearce, T. D., & Wyatt, M. C. 2015, MNRAS, 453, 3329
Pearce, T. D., Krivov, A. V., Sefilian, A. A., et al. 2024, MNRAS, 527, 3876
Pecaut, M. J., & Mamajek, E. E. 2013, ApJS, 208, 9
Perez, S., Dunhill, A., Casassus, S., et al. 2015, ApJ, 811, L5
Plavchan, P., Barclay, T., Gagné, J., et al. 2020, Nature, 582, 497
Quillen, A. C., Morbidelli, A., & Moore, A. 2007, MNRAS, 380, 1642
Rafikov, R. R. 2023, MNRAS, 519, 5607
Rameau, J., Chauvin, G., Lagrange, A. M., et al. 2013, ApJ, 772, L15
Riello, M., De Angeli, F., Evans, D. W., et al. 2021, A&A, 649, A3
Rodriguez, D. R., & Zuckerman, B. 2012, ApJ, 745, 147
Sefilian, A. A., Rafikov, R. R., & Wyatt, M. C. 2021, ApJ, 910, 13
Sefilian, A. A., Rafikov, R. R., & Wyatt, M. C. 2023, ApJ, 954, 100
Sefilian, A. A., Kratter, K. M., Wyatt, M. C., et al. 2025, MNRAS, 543, 3123
Shaya, E. J., & Olling, R. P. 2011, ApJS, 192, 2
Silverberg, S. M., Wisniewski, J. P., Kuchner, M. J., et al. 2020, ApJ, 890, 106
Skrutskie, M. F., Cutri, R. M., Stiening, R., et al. 2006, AJ, 131, 1163
Smirnov-Pinchukov, G. V., Moór, A., Semenov, D. A., et al. 2022, MNRAS, 510, 1148
Smith, B. A., & Terrile, R. J. 1984, Science, 226, 1421
Stammler, S. M., Drążkowska, J., Birnstiel, T., et al. 2019, ApJ, 884, L5
STSci 2020, Digitized Sky Survey, NASA IPAC DataSet, IRSA441
Takeuchi, T., & Artymowicz, P. 2001, ApJ, 557, 990
Tang, J., Bressan, A., Rosenfield, P., et al. 2014, MNRAS, 445, 4287
Tazzari, M., Beaujean, F., & Testi, L. 2018, MNRAS, 476, 4527
Teague, R., Bae, J., Bergin, E. A., Birnstiel, T., & Foreman-Mackey, D. 2018, ApJ, 860, L12
Terrill, J., Marino, S., Booth, R. A., et al. 2023, MNRAS, 524, 1229
Thompson, A. R., Moran, J. M., & Swenson, George W., J. 2017, Interferometry and Synthesis in Radio Astronomy, 3rd edn. (Berlin: Springer)
Tokovinin, A. 2018, ApJS, 235, 6
van Leeuwen, F. 2007, A&A, 474, 653
Vigan, A., Patience, J., Marois, C., et al. 2012, A&A, 544, A9
Waisberg, I., Klein, Y., & Katz, B. 2023, MNRAS, 521, 5232
Weber, P., Pérez, S., Baruteau, C., et al. 2026, A&A, 705, A203
Weissman, P. R. 1984, Science, 224, 987
White, J. A., Aufdenberg, J., Boley, A. C., et al. 2018, ApJ, 859, 102
Whiting, M. L., Hill, J. B., Bromley, B. C., & Kenyon, S. J. 2023, AJ, 165, 193
Wilner, D. J., Andrews, S. M., & Hughes, A. M. 2011, ApJ, 727, L42
Winterhalder, T. O., Lacour, S., Mérand, A., et al. 2024, A&A, 688, A44
Wyatt, M. C. 2008, ARA&A, 46, 339
Wyatt, M. C., Dermott, S. F., Telesco, C. M., et al. 1999, ApJ, 527, 918
Wyatt, M. C., Panić, O., Kennedy, G. M., & Matrà, L. 2015, Ap&SS, 357, 103
Yelverton, B., & Kennedy, G. M. 2018, MNRAS, 479, 2673
Zakhozhay, O. V., Launhardt, R., Müller, A., et al. 2022, A&A, 667, A63
Zapata, L. A., Ho, P. T. P., & Rodríguez, L. F. 2018, MNRAS, 476, 5382
Zawadzki, B., Fehr, A., Hughes, A. M., et al. 2026, A&A, 705, A197
Zúñiga-Fernández, S., Bayo, A., Elliott, P., et al. 2021, A&A, 645, A30
Zurlo, A., Goździewski, K., Lazzoni, C., et al. 2022, A&A, 666, A133

[1] Department of Physics and Astronomy, University of Exeter, Stocker Road, Exeter EX4 4QL, UK
[2] School of Physics, Trinity College Dublin, the University of Dublin, College Green, Dublin 2, Ireland
[3] Department of Astronomy, Van Vleck Observatory, Wesleyan University, 96 Foss Hill Dr., Middletown, CT, 06459, USA
[4] European Southern Observatory, Karl-Schwarzschild-Strasse 2, 85748 Garching bei München, Germany
[5] Malaghan Institute of Medical Research, Gate 7, Victoria University, Kelburn Parade, Wellington, New Zealand
[6] Department of Physics, University of Warwick, Gibbet Hill Road, Coventry CV4 7AL, UK
[7] Instituto de Astrofísica de Canarias, Vía Láctea S/N, La Laguna, 38200 Tenerife, Spain
[8] Departamento de Astrofísica, Universidad de La Laguna, La Laguna, 38200 Tenerife, Spain
[9] Division of Geological and Planetary Sciences, California Institute of Technology, 1200 E. California Blvd., Pasadena, CA 91125, USA
[10] Institute of Physics Belgrade, University of Belgrade, Pregrevica 118, 11080 Belgrade, Serbia
[11] Center for Astrophysics | Harvard & Smithsonian, 60 Garden St, Cambridge, MA 02138, USA
[12] Univ. Grenoble Alpes, CNRS, IPAG, 38000 Grenoble, France
[13] Departamento de Física, Universidad de Santiago de Chile, Av. Víctor Jara 3493, Santiago, Chile
[14] Millennium Nucleus on Young Exoplanets and their Moons (YEMS), Chile
[15] Center for Interdisciplinary Research in Astrophysics Space Exploration (CIRAS), Universidad de Santiago, Chile
[16] Herzberg Astronomy & Astrophysics, National Research Council of Canada, 5071 West Saanich Road, Victoria, BC, V9E 2E9, Canada
[17] Department of Physics & Astronomy, University of Victoria, 3800 Finnerty Rd, Victoria, BC V8P 5C2, Canada
[18] Astrophysikalisches Institut und Universitätssternwarte, Friedrich-Schiller-Universität Jena, Schillergäßchen 2-3, 07745 Jena, Germany
[19] Institute of Astronomy, University of Cambridge, Madingley Road, Cambridge CB3 0HA, UK
[20] Konkoly Observatory, HUN-REN Research Centre for Astronomy and Earth Sciences, MTA Centre of Excellence, Konkoly-Thege Miklós út 15-17, 1121 Budapest, Hungary
[21] Institute for Astronomy (IfA), University of Vienna, Türkenschanzstrasse 17, 1180 Vienna, Austria
[22] Institute of Physics and Astronomy, ELTE Eötvös Loránd University, Pázmány Péter sétány 1/A, 1117 Budapest, Hungary
[23] UK Astronomy Technology Centre, Royal Observatory Edinburgh, Blackford Hill, Edinburgh EH9 3HJ, UK
[24] National Astronomical Observatory of Japan, Osawa 2-21-1, Mitaka, Tokyo 181-8588, Japan
[25] Department of Astronomy, Graduate School of Science, The University of Tokyo, Tokyo 113-0033, Japan
[26] Joint ALMA Observatory, Avenida Alonso de Córdova 3107, Vitacura 7630355 Santiago, Chile
[27] Department of Astronomy, University of California, Berkeley, Berkeley, CA 94720-3411, USA
[28] Department of Astronomy and Steward Observatory, The University of Arizona, 933 North Cherry Ave, Tucson, AZ, 85721, USA
[29] Large Binocular Telescope Observatory, The University of Arizona, 933 North Cherry Ave, Tucson, AZ, 85721, USA
[30] National Radio Astronomy Observatory, 520 Edgemont Road, Charlottesville, VA 22903-2475, USA
[31] Max-Planck-Insitut für Astronomie, Königstuhl 17, 69117 Heidelberg, Germany
[32] Department of Physics and Astronomy, Johns Hopkins University, 3400 N Charles Street, Baltimore, MD 21218, USA
[33] Academia Sinica Institute of Astronomy and Astrophysics, 11F of AS/NTU Astronomy-Mathematics Building, No.1, Sect. 4, Roosevelt Rd, Taipei 106319, Taiwan
[34] The University of Texas School of Law. 727 E. Dean Keeton Street, Austin, Texas 78705, USA

Appendix A: Observation details

Table A.1 presents a summary of all the new and archival observations used for ARKS.

Appendix B: Data correction parameters

Table B.1 presents the best-fit disc parameters for the model used to correct the data as described in Sect. 5.3.

Appendix C: Fundamental stellar parameters

In order to determine the fundamental stellar parameters for the ARKS sample of stars, we applied the Bayesian inference code of del Burgo & Allende Prieto (2016, 2018) on a grid of PARSEC 1.2S stellar evolution models (Bressan et al. 2012; Chen et al. 2014, 2015; Tang et al. 2014). This choice is based on the reasonably good statistical match of the measured dynamical masses with the corresponding predictions for detached eclipsing binaries. In particular, for binary stars on the main-sequence, with a small discrepancy of 4% on average (del Burgo & Allende Prieto 2018).

The grid of PARSEC v1.2S models arranged for this analysis comprises ages ranging from 2 to 13,800 million years and steps of 5%, and [M/H] from -2.18 to 0.51 with steps of 0.02 dex, adopting the photometric passband calibration of Riello et al. (2021), with the zero points of the VEGAMAG system. We used this grid to infer the stellar fundamental parameters of all stars through the aforementioned Bayesian code, fed by the following three input parameters: the absolute G magnitude M_G, the colour $G_{\rm BP} - G_{\rm RP}$, and the stellar age compiled from the literature. We did not constrain the stellar evolution stage. Given the relatively small distances, we assumed null extinction when deriving the colour $G_{\rm BP} - G_{\rm RP}$ and M_G from the Gaia DR3 photometry and astrometry (Gaia Collaboration 2023). M_G was determined from the apparent G magnitude by subtracting the distance modulus, which was calculated from the Gaia DR3 trigonometric parallaxes. The resulting stellar parameters are shown in Table C.1.

Appendix D: ALMA measured fluxes

We derive integrated fluxes for each system as follows. We use the corresponding clean image produced with a robust parameter of 2.0, primary beam corrected, and with SMGs subtracted. We then create a series of concentric elliptical masks with increasing semi-major axes. These masks match the ellipticity of the discs given their inclination (as constrained by the MCMC fits) and also take into account the beam size and a scale height as large as 10% of the disc radius. We integrate the intensity within these masks to derive an integrated flux as a function of aperture size and the flux uncertainty taking into account the beam size and image rms, which increase towards the edge of the images due to the primary beam response. This curve is then used to determine the final aperture size, set as the radius at which the minimum flux (defined as flux minus 3 times the uncertainty) stops increasing. Finally, we add in quadrature a 10% flux calibration error to the flux uncertainty. The wavelength, measured fluxes and aperture sizes are summarised in Table D.1.

We find that all the measured fluxes of the 24 systems in ARKS are within 3σ of those expected from or measured by REASONS (taking into account REASONS and ARKS uncertainties). The only fluxes that have more than a 30% difference are those of HD 15257 and HD 84870, which ARKS measures to be ~50% fainter but still within 2σ. The measured fluxes are also within 15% of the flux of our best-fit simple models for all systems, except for HD 131488. For this system, the model flux is 5.5 mJy instead of the 7.4 mJy measured from the image. The lower model flux could be due to it missing the emission interior and exterior of the main ring, as it was modelled as a Gaussian (Han et al. 2026). Similarly, the smaller differences for the other systems can be explained by the model assumptions of the surface density profile being a Gaussian.

Appendix E: Background sources

The compact, bright sources detected in the field of view of eight of our targets were identified as background submillimetre galaxies. We are confident that these sources are not related to the discs for the following reasons. First, those in HD 84870, HD 92945, and HD 206893 images have projected distances that would put these objects at hundreds of au. Second, the spectral indices derived by previous studies in the three systems with multi-band data are larger than 3 and thus consistent with SMGs (this is the case of HD 95086, HD 107146, and HD 218396, Booth et al. 2019; Marino 2021; Faramaz et al. 2021). Third, those with archival and ARKS data spanning years show negligible proper motion (this is the case for HD 76582, HD 95086, HD 107146, and HD 218396, Matrà et al. 2025; Zapata et al. 2018; Imaz Blanco et al. 2023; Faramaz et al. 2021). Finally, the source detected near TYC 9340-437-1 has recently been detected with JWST/NIRCam at 4μm at a location that indicates it is not co-moving with the system (Zhang et al. in prep).

Table E.1 presents the best-fit parameters of the SMGs identified in 8 of our targets. Figure E.1 shows the clean continuum images without the SMGs subtracted and using Briggs weighting with a robust value of 2.0. The location and best-fit morphology of the SMGs are highlighted with grey ellipses; HD107146's observations span multiple years, and thus, the SMG's location changed relative to the star. We note that for two systems, the subtractions were not optimal and left significant residuals: HD 95086 and HD 107146.

For HD 107146, the fit converged to a total SMG flux of 0.36 mJy at 0.87 mm, which is significantly lower than the 0.79 mJy estimated at a similar wavelength in a previous study (Marino 2021). The lower retrieved flux is likely due to the choice of disc model. Marino (2021) fit a more flexible disc model to the data that included an inner edge that was parametrised such that it could be smooth or sharp independently of the outer edge and gap. Here, instead, we used a simpler double Gaussian to fit the disc, which effectively imposes a smooth disc inner edge. Therefore, it is likely that our disc model overpredicted the disc surface brightness just interior to the disc where the SMG is found in some epochs. This could explain why the fit converged to a lower SMG flux. This lower SMG flux is likely the reason why the radial profile presented in Han et al. (2026) shows emission at ~20 au that is not present in previous analyses (Marino 2021; Imaz Blanco et al. 2023).

For HD 95086, we fit two components to the two brightest features in the data that are found ~3″ to the west. Our model converged to SMG fluxes of 3.8 and 0.4 mJy, which are consistent with the fluxes derived by Zapata et al. (2018) using lower-resolution observations. However, the SMG subtracted image in Fig. 3 still displays excess emission towards the west and near the brightest SMG, which is likely additional background emission. Recent JWST/MIRI observations support the idea of more extended and complex background emission (Mâlin et al. 2024). While the 23 μm image shows two background sources

Table A.1: All new and archival observations used for ARKS.

Name	ΔR [au ($''$)]	$\Delta z \sin(i)$ [au ($''$)]	Beam [au ($''$)]	rms [μJy/beam]	Band	Antenna conf.	N_{exe}	ToS [h]	Date range	Archival data
HD 9672[g]	147(2.6)	16(0.27)	9(0.16)	12	7	5-6,2	6,1	3.1, 0.8	10/2018-06/2024	1
HD 10647	70(4.0)	11(0.66)	8(0.43)	10	7	4,1,7m	6,3,6	4.1, 2.0, 4.4	07/2016-05/2024	2,3
HD 14055	160(4.5)	21(0.59)	8(0.23)	10	7	4,1,7m	11,0,21	8.5,0,17.3	10/2022-07/2024	
HD 15115	21(0.4)	11(0.22)	6(0.12)	6	7	6,3	12,3	9.5,1.8	10/2022-06/2024	
HD 15257	220(4.5)	20(0.42)	36(0.74)	24	7	2,7m	4,11	2.7,8.8	10/2022	
HD 32297[g]	62(0.5)	14(0.11)	7(0.06)	17	7	7,4	4,2	2.6,1.0	06/2023-12/2023	
HD 39060[g]	92(4.7)	12(0.63)	4(0.22)	13	6	5,2,7m	3,1,2	1.9,0.5,0.9	10/2013-08/2015	4
HD 61005	38(1.0)	9(0.23)	6(0.15)	21	7	6,3	3,1	1.7,0.3	10/2022-05/2023	
HD 76582	210(4.3)	25(0.50)	27(0.56)	18	7	2,7m	2,9	1.7,7.0	10/2022-12/2022	
HD 84870	260(2.9)	23(0.26)	49(0.56)	14	7	3,7m	7,14	5.8,10.5	10/2022-12/2022	
HD 92945	80(3.7)	10(0.48)	9(0.40)	17	7	3,7m	3,5	2.4, 4.1	10/2016-03/2017	5
HD 95086	180(2.1)	12(0.14)	30(0.34)	19	7	3	3	2.4	01/2023	
HD 107146	110(4.0)	5(0.17)	16(0.59)	13	7	5,3,2,7m	1,1,2,4	0.7,0.8,1.6,2.3	10/2016-05/2021	6,7
HD 107146	110(4.0)	5(0.17)	18(0.65)	6	6	3	5	4.0	04/2017	8
HD 109573	15(0.2)	9(0.13)	6(0.08)	20	7	7,4	2,1	1.0,0.2	01/2023-06/2023	
HD 121617[g]	60(0.5)	6(0.05)	14(0.12)	11	7	6,3	7,2	5.8,1.4	10/2022-05/2023	
HD 131488[g]	46(0.3)	11(0.07)	6(0.04)	9	7	8,5	6,3	4.8,1.9	04/2023-06/2023	
HD 131835[g]	87(0.7)	9(0.07)	17(0.13)	11	7	6,3	9,2	6.6,1.6	12/2022-05/2023	
HD 145560	50(0.4)	7(0.05)	11(0.09)	9	7	6,3	7,3	5.5,2.0	10/2022-05/2023	
HD 161868	110(3.7)	14(0.46)	15(0.52)	19	7	2,7m	3,11	2.0,7.9	10/2022	
HD 170773	68(1.8)	12(0.34)	12(0.33)	22	7	3,7m	2,3	1.0,2.5	10/2022-01/2023	
HD 197481	12(1.3)	4(0.42)	3(0.35)	16	6	5,2	2,1	0.9,0.5	03/2014-06/2015	9
HD 206893	100(2.5)	5(0.13)	18(0.45)	6	6	5,2	4,2	3.2,1.3	06/2018-09/2018	10
TYC 9340-437-1	100(2.7)	10(0.27)	20(0.55)	24	7	3,7m	2,4	1.7,3.0	10/2022	
HD 218396	250(6.1)	21(0.53)	35(0.85)	11	7	1,7m	6,30	4.6,21.7	10/2016-06/2018	11

Notes. Column 2 shows the estimated radial FWHM from REASONS. Column 3 shows the expected projected vertical FWHM, where we assume $h = 0.05$. Column 4 shows the clean beam size obtained after imaging all the data using a robust value of 0.5 (see Sect. 5.4) and averaging the beam major and minor axes. Column 5 shows the corresponding image rms for the robust=0.5 images. The last six columns show the band, the approximate antenna configurations, the number of executions per configuration, the time on source per configuration, the range of observing dates, and the references to archival data that we use, respectively. Systems with archival data only and not observed by ARKS are highlighted in grey, and systems with CO gas are flagged '[g]'.
Archival data used: (1): 2018.1.01222.S (Cataldi et al. 2023; Delamer 2023); (2,3): 2015.1.01260.S, 2017.1.00167.S (Lovell et al. 2021b); (4): 2012.1.00142.S (Matrà et al. 2019b); (5): 2016.1.00104.S (Marino et al. 2019); (6,7): 2016.1.00104.S, 2019.1.00189.S (Marino et al. 2018; Imaz Blanco et al. 2023); (8): 2016.1.00195.S (Marino et al. 2018); (9): 2012.1.00198.S (Daley et al. 2019); (10): 2017.1.00825.S (Nederlander et al. 2021; Marino et al. 2020b); (11): 2016.1.00907.S (Faramaz et al. 2021).

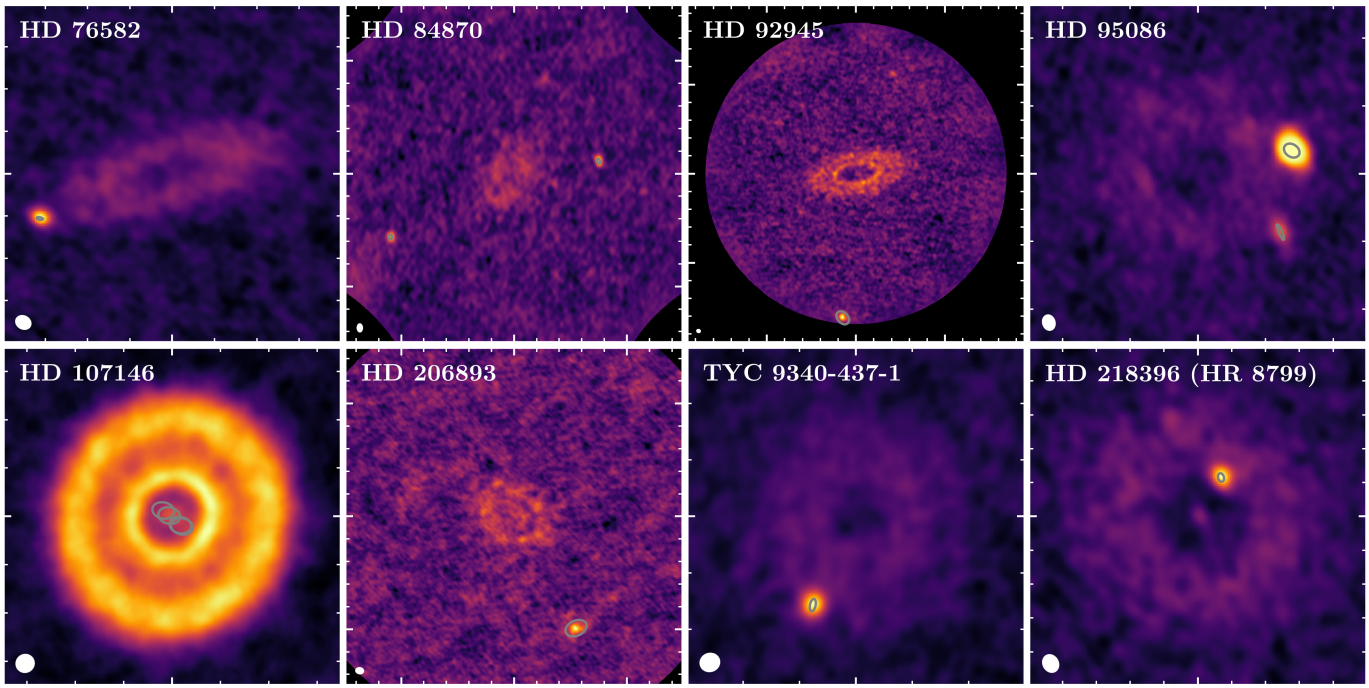

Fig. E.1: ARKS continuum clean images of the eight systems in the sample with background sources before their subtraction. The data were imaged with a robust value of 2 and the white ellipse in the bottom left corner represents the corresponding beam. The grey ellipses represent the best-fit location and size (FWHM) of the SMGs at the different epochs of observations. For HD 95086 the image has a non-linear scale to increase the dynamic range and to visualise both SMGs. The white minor and major ticks in all panels are spaced by 2″ and 10″, respectively.

Table B.1: Continuum best-fit parameters

Name	R [au]	ΔR [au]	h	i [°]	PA [°]	$M_{\rm dust}$ [$M_\oplus$]	$F_\star$ [μJy]	ΔRA [mas]	ΔDec [mas]
HD 9672[g]	135.2 ± 1.9	158 ± 3	0.066 ± 0.004	78.7 ± 0.2	107.9 ± 0.2	0.21	< 19 (28)	68 ± 76	−33 ± 30
HD 10647	103.6 ± 0.4	65 ± 2	0.062 ± 0.003	77.8 ± 0.1	57.3 ± 0.1	0.03	131 ± 9 (96)	90 ± 56	28 ± 51
HD 14055	169.4 ± 2.9	162 ± 9	0.048 ± 0.007	80.7 ± 0.2	162.2 ± 0.3	0.05	87 ± 11 (111)	−57 ± 59	−84 ± 155
HD 15115	80.7 ± 0.3	14 ± 1	0.017 ± 0.001	86.7 ± 0.0	98.5 ± 0.0	0.07	24 ± 4 (22)	44 ± 12	−8 ± 5
HD 15257	184.2 ± 20.2	261 ± 41		59.4 ± 4.9	47.3 ± 5.5	0.06	79 ± 35[m] (73)	86 ± 134	14 ± 180
HD 32297[g]	115.9 ± 0.3	37 ± 1	0.011 ± 0.001	88.3 ± 0.0	47.5 ± 0.0	0.87	24 ± 13[m] (3)	19 ± 4	18 ± 4
HD 39060[g]	104.3 ± 1.4	97 ± 3	0.059 ± 0.003	86.4 ± 0.2	29.9 ± 0.1	0.12	86 ± 14 (70)	−54 ± 14	−2 ± 20
HD 61005	72.4 ± 0.2	36 ± 1	0.020 ± 0.002	85.9 ± 0.1	70.4 ± 0.1	0.15	(12)	8 ± 22	−4 ± 8
HD 76582	203.6 ± 4.9	176 ± 9		72.6 ± 0.7	104.7 ± 0.7	0.12	(37)	100 ± 46	54 ± 33
HD 84870	199.3 ± 7.8	232 ± 15		47.1 ± 2.6	−25.7 ± 4.1	0.13	(9)	81 ± 57	−103 ± 63
HD 92945	78.2 ± 1.0	73 ± 6	0.032 ± 0.013[m]	65.4 ± 0.6	100.0 ± 0.6	0.06	45 ± 13 (25)	−84 ± 55	12 ± 35
HD 95086	197.0 ± 4.6	173 ± 8		31.6 ± 3.5	100.0 ± 5.7	0.49	(9)	−91 ± 45	127 ± 34
HD 107146	84.2 ± 0.2	89 ± 1		19.3 ± 0.6	153.2 ± 1.7	0.22	(29)	36 ± 35	−48 ± 35
HD 109573	75.9 ± 0.1	7 ± 0	< 0.02	76.6 ± 0.1	26.5 ± 0.0	0.23	(20)	11 ± 2	−32 ± 2
HD 121617[g]	76.3 ± 0.4	18 ± 1		44.1 ± 0.6	58.7 ± 0.7	0.21	(6)	8 ± 8	14 ± 7
HD 131488[g]	89.7 ± 0.1	13 ± 1	0.011 ± 0.001	85.0 ± 0.1	97.2 ± 0.0	0.58	(3)	0 ± 2	1 ± 1
HD 131835[g]	77.1 ± 0.5	65 ± 2	0.049 ± 0.005	74.2 ± 0.2	59.2 ± 0.2	0.45	(5)	6 ± 6	3 ± 6
HD 145560	75.4 ± 0.5	29 ± 2	< 0.11	47.6 ± 0.6	39.4 ± 0.9	0.28	(4)	15 ± 12	−9 ± 11
HD 161868	121.2 ± 3.7	134 ± 8		66.1 ± 1.5	57.6 ± 1.6	0.03	161 ± 18 (146)	49 ± 40	−131 ± 42
HD 170773	191.9 ± 2.6	66 ± 4		32.9 ± 1.9	113.0 ± 2.9	0.16	84 ± 21 (39)	−77 ± 40	26 ± 35
HD 197481	33.6 ± 0.2	13 ± 1	0.015 ± 0.003	88.3 ± 0.1	128.6 ± 0.1	0.012	245 ± 14 (50)	32 ± 15	6 ± 13
HD 206893	105.1 ± 6.0	116 ± 10		45.2 ± 2.5	60.3 ± 3.6	0.04	(12)	40 ± 132	53 ± 106
TYC 9340-437-1	95.7 ± 2.5	99 ± 5		18.0 ± 8.0	149.2 ± 20.2	0.17	(10)	81 ± 65	−98 ± 64
HD 218396	240.4 ± 4.6	182 ± 9		28.8 ± 3.3	49.7 ± 5.7	0.11	59 ± 10 (35)	−41 ± 65	−57 ± 69

Notes. Best-fit parameters derived from the MCMC sampling, using the median and the 16th and 84th percentiles to estimate the uncertainties. For sources fitted with a double Gaussian (HD 107146, HD 92945, and HD 15115), R represents the average between the two Gaussian centres and ΔR is the sum of the FWHMs of the two Gaussians. Column 8 shows the stellar flux at the shortest available ALMA wavelength as derived from the MCMC if it was included as a free parameter and the photospheric flux expected from extrapolating the stellar SED in brackets. For marginalised distributions of h and $F_\star$ peaking at zero, we present upper limits estimated with the 99.7 percentile. If their marginalised distributions peaked above zero but still extended to zero, we flagged those marginal values '[m]'. The last two columns show the best-fit right ascension and declination offsets for the long baseline execution used as a reference. Systems with CO gas are flagged '[g]'.

Table C.1: Fundamental stellar parameters of the 24 host stars of the ARKS sample.

Name	$T_{\rm eff}$ [K]	$M_\star$ [$M_\odot$]	$R_\star$ [$R_\odot$]	$L_\star$ [$L_\odot$]	log(g) [cgs]	[Fe/H] [dex]
HD 9672	8924±32	1.9955±0.0004	1.643±0.007	15.43±0.11	4.307±0.003	0.182±0.013
HD 10647	6154±15	1.116±0.019	1.085±0.005	1.521±0.006	4.415±0.010	0.02±0.05
HD 14055	9120±64	2.19±0.09	2.06±0.04	26.3±0.9	4.153±0.026	0.21±0.19
HD 15115	6764±15	1.426±0.005	1.380±0.005	3.592±0.016	4.312±0.004	0.19±0.03
HD 15257	7256±35	1.75±0.13	2.37±0.04	13.99±0.28	3.93±0.05	0.1±0.3
HD 32297	7874±22	1.57±0.06	1.451±0.013	7.29±0.10	4.311±0.024	-0.15±0.24
HD 39060	7951±32	1.724±0.005	1.534±0.008	8.47±0.06	4.303±0.005	0.157±0.018
HD 61005	5577±17	0.95±0.007	0.834±0.006	0.6060±0.0011	4.573±0.008	0.01±0.03
HD 76582	7796±21	1.61±0.15	1.715±0.02	9.79±0.17	4.17±0.05	-0.1±0.4
HD 84870	7741±20	1.66±0.04	1.566±0.011	7.93±0.06	4.268±0.016	0.11±0.13
HD 92945	5175±9	0.850±0.007	0.747±0.004	0.3609±0.0013	4.62±0.008	-0.00±0.06
HD 95086	7674±22	$1.541^{+0.020}_{-0.002}$	$1.455^{+0.007}_{-0.005}$	$6.614^{+0.019}_{-0.014}$	$4.3^{+0.008}_{-0.003}$	$-0.19^{+0.07}_{-0.02}$
HD 107146	5885^{+22}_{-15}	$1.04^{+0.03}_{-0.01}$	$0.935^{+0.012}_{-0.006}$	$0.944^{+0.011}_{-0.006}$	$4.515^{+0.024}_{-0.009}$	$-0.01^{+0.15}_{-0.05}$
HD 109573	9641±61	2.14±0.09	1.694±0.011	22.3±0.5	4.311±0.022	0.09±0.23
HD 121617	9029±34	1.901±0.009	1.526±0.011	13.94±0.13	4.350±0.005	0.024±0.020
HD 131488	8713±30	1.804±0.016	1.493±0.015	11.56±0.17	4.346±0.008	-0.00±0.03
HD 131835	8284±28	1.698±0.013	1.464±0.010	9.09±0.10	4.337±0.007	-0.02±0.03
HD 145560	6467±19	1.35±0.08	1.422±0.016	3.18±0.04	4.26±0.03	0.09±0.15
HD 161868	8658±56	2.11±0.07	2.075±0.027	21.8±0.4	4.129±0.021	0.29±0.17
HD 170773	6667±28	1.40±0.05	1.396±0.021	3.47±0.05	4.293±0.028	0.17±0.25
HD 197481	3615±14	0.614±0.026	0.805±0.005	0.0998±0.0005	4.414±0.023	-0.15±0.08
HD 206893	6571±27	1.329±0.011	1.281±0.011	2.757±0.007	4.346±0.004	0.14±0.05
TYC9340-437-1	4091±12	0.753±0.009	0.855±0.006	0.1844±0.001	4.451±0.010	0.25±0.06
HD 218396	7366^{+31}_{-33}	$1.495^{+0.011}_{-0.034}$	$1.414^{+0.010}_{-0.012}$	$5.299^{+0.020}_{-0.040}$	$4.312^{+0.010}_{-0.018}$	$-0.05^{+0.05}_{-0.16}$

Notes. Effective temperature $T_{\rm eff}$, mass $M_\star$, radius $R_\star$, luminosity $L_\star$, surface gravity log(g), and iron-to-hydrogen abundance [Fe/H], all output parameters from the Bayesian inference code of del Burgo & Allende Prieto (2016, 2018).

Table D.1: Phase centres and integrated fluxes of the 24 systems analysed in ARKS derived from the primary beam corrected images.

Name	Date [d/m/y]	RA [h:m:s]	Dec [d:m:s]	ΔRA_G [mas]	ΔDec_G [mas]	Wavelength [mm]	Flux [mJy]	Aperture size [au (″)]
HD 9672	17/06/2024	01:34:37.9394	-15:40:34.967	1	0	0.89	13.9 ± 1.4	411 (7.2)
HD 10647	08/05/2024	01:42:29.7722	-53:44:29.508	1	0	0.89	14.8 ± 1.5	197 (11.3)
HD 14055	26/07/2024	02:17:18.9573	+33:50:48.612	17	10	0.89	8.1 ± 0.9	333 (9.3)
HD 15115	09/05/2023	02:26:16.3839	+06:17:32.012	-1	1	0.89	4.8 ± 0.5	144 (2.9)
HD 15257	19/10/2022	02:28:09.9531	+29:40:07.632	-3	-3	0.89	3.8 ± 0.5	352 (7.2)
HD 32297	23/09/2023	05:02:27.4455	+07:27:39.119	-1	2	0.89	10.8 ± 1.1	308 (2.4)
HD 39060	08/08/2015	05:47:17.0931	-51:03:58.137	67	46	1.33	18.6 ± 1.9	194 (9.9)
HD 61005	11/05/2023	07:35:47.3591	-32:12:12.298	0	1	0.89	14.8 ± 1.5	135 (3.7)
HD 76582	16/10/2022	08:57:35.2957	+15:34:53.094	0	0	0.89	8.1 ± 0.9	489 (10.0)
HD 84870	24/12/2022	09:49:02.7913	+34:05:06.134	0	0	0.89	2.6 ± 0.3	413 (4.7)
HD 92945	17/12/2016	10:43:27.9966	-29:03:52.304	-8	5	0.86	11.1 ± 1.1	156 (7.3)
HD 95086	09/01/2023	10:57:02.8496	-68:40:02.161	0	0	0.89	9.3 ± 1.0	467 (5.4)
HD 107146	03/05/2021	12:19:06.2413	+16:32:50.707	-1	-1	1.00	22.1 ± 2.2	182 (6.6)
HD 109573	04/06/2023	12:36:00.9175	-39:52:10.778	0	-1	0.89	13.8 ± 1.4	116 (1.6)
HD 121617	11/05/2023	13:57:41.0610	-47:00:34.792	0	0	0.89	4.2 ± 0.4	157 (1.3)
HD 131488	27/06/2023	14:55:07.9902	-41:07:13.925	0	0	0.89	7.4 ± 0.8	364 (2.4)
HD 131835	30/04/2023	14:56:54.4230	-35:41:44.244	0	0	0.89	6.6 ± 0.7	298 (2.3)
HD 145560	19/05/2023	16:13:34.2891	-45:49:04.446	0	0	0.89	4.6 ± 0.5	270 (2.2)
HD 161868	01/10/2022	17:47:53.5203	+02:42:24.505	27	4	0.89	7.5 ± 0.8	283 (9.5)
HD 170773	23/01/2023	18:33:01.0908	-39:53:33.111	0	0	0.89	14.2 ± 1.5	252 (6.8)
HD 197481	18/08/2014	20:45:09.8511	-31:20:32.517	5	-19	1.35	4.7 ± 0.5	52 (5.3)
HD 206893	30/08/2018	21:45:22.0239	-12:47:00.064	15	-6	1.35	1.0 ± 0.1	200 (4.9)
TYC 9340-437-1	02/10/2022	22:42:49.3897	-71:42:22.415	0	0	0.89	9.5 ± 1.0	227 (6.2)
HD 218396	29/05/2018	23:07:28.8587	+21:08:02.399	15	-2	0.88	7.1 ± 0.8	412 (10.1)

Notes. Columns 2–6 display the date and the phase centre coordinates of the reference execution block in the ICRS frame used to align the observations during the correction step, and the offset relative to the predicted stellar position according to Gaia DR3 (the RA offset has been multiplied by cos(Dec), Gaia Collaboration 2023). Columns 7–9 show the wavelength, integrated flux, and aperture size. For systems with submillimetre galaxies, we used the subtracted images. The flux errors include a nominal 10% absolute flux calibration error added in quadrature to the statistical error that arises from the image rms. The aperture size corresponds to the semi-major axis of an elliptical mask used to measure the flux.

Table E.1: Submillimetre galaxies best-fit parameters.

Name	ID	RA [h:m:s]	Dec [d:m:s]	λ [mm]	SMG Flux [mJy]	σ_{maj} [″]	σ_{min} [″]	PA [°]
HD 76582	1	08:57:35.73	+15:34:50.97	0.89	0.74 ± 0.04	0.131 ± 0.018	0.052 ± 0.008	80 ± 16
HD 84870	1	09:49:02.19	+34:05:07.24	0.89	0.34 ± 0.03	0.189 ± 0.042	0.108 ± 0.017	19 ± 18
HD 84870	2	09:49:03.67	+34:05:00.51	0.89	0.75 ± 0.08	0.187 ± 0.045	0.113 ± 0.023	4 ± 48
HD 92945	1	10:43:28.11	-29:04:08.49	0.86	6.60 ± 0.60	0.708 ± 0.140	0.499 ± 0.171	41 ± 34
HD 95086	1	10:57:02.34	-68:40:01.48	0.89	3.84 ± 0.06	0.210 ± 0.004	0.157 ± 0.003	57 ± 3
HD 95086	2	10:57:02.40	-68:40:03.89	0.89	0.43 ± 0.04	0.209 ± 0.034	0.043 ± 0.027	23 ± 6
HD 107146	1	12:19:06.27	+16:32:50.95	0.87	0.36 ± 0.04	0.388 ± 0.047	0.285 ± 0.032	78 ± 15
HD 206893	1	21:45:21.65	-12:47:09.97	1.35	0.34 ± 0.04	0.832 ± 0.112	0.567 ± 0.093	115 ± 13
TYC 9340-437-1	1	22:42:49.71	-71:42:25.56	0.89	0.87 ± 0.04	0.191 ± 0.022	0.085 ± 0.023	−12 ± 9
HD 218396	1	23:07:28.76	+21:08:04.70	0.88	0.30 ± 0.02	0.216 ± 0.036	0.148 ± 0.035	17 ± 27

Notes. Best-fit parameters were derived from our MCMC using the median and the 16th and 84th percentiles to estimate the uncertainties. Columns 7–9 show the standard deviation of the major axis, the standard deviation of the minor axis, and the position angle of the deconvolved elliptical Gaussian.

that match the SMG positions (labelled "g" and "g2" in Mâlin et al. 2024), at 11 µm g is shifted towards the NE and it appears more extended than in the ALMA images. We thus conclude that there may be a third extended source in the ALMA images (labelled g at 11 µm) or additional extended emission associated with the brightest SMG.

Appendix F: Stellar variability

We performed a search for stellar variability on all data, using spectrally averaged MS files with no time averaging[16]. In most cases the star is not detected by ALMA, so this search is primarily for large positive variations in flux that make the star temporarily visible, i.e. flares. Each MS was further averaged down to one channel per spectral window to reduce the data

[16] The code is publicly available at https://github.com/drgmk/alma_var.

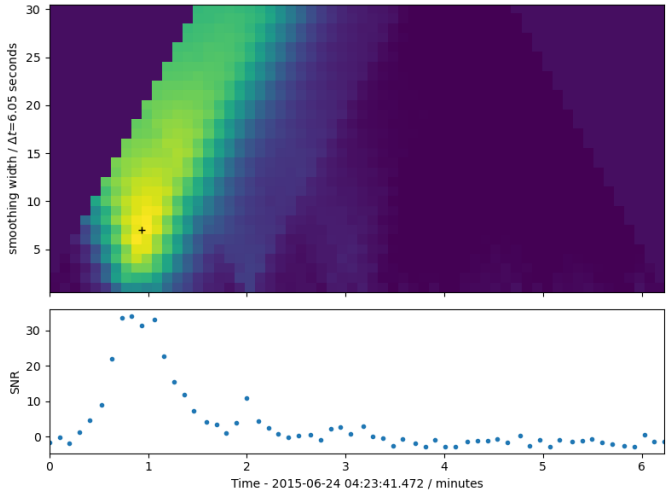

Fig. F.1: Example of the stellar variability search output for scan 27 from the 2015 AU Mic data. The lower panel shows the S/N vs. time for a single scan (27), with one large flare visible. The colour scale in the upper panel shows the mean-filtered data from the lower panel using a window of the width given on the y-axis to increase the S/N for flares with a duration greater than 6 seconds. The flare is mostly strongly detected for a window of 7×6 s, as indicated by the plus sign (+) in the upper panel.

volume, and a model based on a clean image from the full MS was subtracted to produce the MS to be searched, which in the absence of variability is simply Gaussian noise (which is verified with a Shaprio-Wilk test). Each model-subtracted MS was then split into individual files for every scan (duration ~5 minutes), for which there is typically one measurement every 6 seconds (i.e. 50 time steps per scan). These scans were searched in visibility space for variability using a matched filter for a point source (e.g. Loomis et al. 2018), assuming equal flux in each spectral window, at the locations of any Gaia DR3 sources within the primary beam (which includes our target star in each case). The matched filter for each u, v point is therefore a complex number with unit length that is rotated according to the search location in sky coordinates. The filter spans only a single time point (i.e. we are not trying to match the time-dependent decay of a flare), so the output is an S/N for each time step. These S/N's were then time averaged with a mean filter for windows up to half the scan length, to improve the S/N for variability on timescales longer than an individual time step. S/N values greater than 4 for any window length were flagged for visual inspection. An example of the output for a single scan is shown in Fig. F.1. This method recovered the flare seen for HD 197481 (Daley et al. 2019), and this scan was removed from the data. We did not detect significant variability for any other targets. It is possible that this method could miss small flares if the average stellar flux were biased upwards by flares, as the S/N's would be biased downwards (e.g. the post-flare S/N values in Fig. F.1 are below zero). We do not see any evidence that marginally significant flares were missed in this way, but an improved method could iteratively exclude scans with S/N's significantly different from zero in creating the model that is subtracted from the original MS. The upper limits set on the flux of any flares in each case varies, depending on the point source sensitivity of the observations and the stellar flux. For example, for HD 145560 the stellar flux is expected to be about 4 mJy, but the rms is 9 mJy, so in that case any flares would need to be 7 times the stellar flux to have been detected. Flares stronger than this could also have been missed if their timescale were significantly shorter than 6 seconds.

Appendix G: Multiplicity

To understand the architecture of the 24 systems studied in ARKS, we performed a literature search for any information on stellar or substellar companions. These can usually be detected through radial velocities with spectroscopy (e.g. Latham et al. 2002; Fernandez et al. 2017),[17] through astrometry including astrometric accelerations or proper motion anomalies (PMa, Kervella et al. 2019; Brandt 2021), astrometric excess noise (e.g. as measured by Gaia's RUWE parameter, Belokurov et al. 2020), or resolving a companion using adaptive optics, speckle imaging or interferometry (Jiménez-Esteban et al. 2019; Dallant et al. 2023).

Our literature search focused on studies with electronic catalogues available, which we queried using `astroquery` within ASTROPY (Ginsburg et al. 2019; Astropy Collaboration 2022) and complemented with a simple visual inspection of the fields in Gaia Data Release 3 (Gaia Collaboration 2023), in the images of the Two Micron All Sky Survey (2MASS) in the J, H, and K bandpasses (Skrutskie et al. 2006), in the Sloan Digital Sky Survey (SDSS) images in the r and g bandpass (Blanton et al. 2017), and in the Digitized Sky Survey (DSS) image (STSci 2020). Table G.1 presents the queried catalogues containing ARKS targets.

In addition to the catalogues listed in Table G.1, we searched the following catalogues but did not recover any entry in common with the ARKS sample:

- Gaia DR3: Gaia Data Release 3: Non-single stars (2022). Vizier: "I/357" Gaia Collaboration (2022);
- Gaia EDR3 nearby accelerating stars: A Catalogue of Nearby Accelerating Star Candidates in Gaia DR3 (2023). Vizier: "J/AJ/165/193" Whiting et al. (2023);
- The Gaia ultracool dwarf sample - V: the ultracool dwarf companion catalogue. No VizieR entry at the time of writing. Tables extracted from the body of the paper Baig et al. (2024);
- Combining HIPPARCOS and Gaia data for the study of binaries: The BINARYS tool. No VizieR entry at the time of writing. Tables extracted from the body of the paper Leclerc et al. (2023);
- Spectroscopic Follow-up of Gaia Exoplanet Candidates: Impostor Binary Stars Invade the Gaia DR3 Astrometric Exoplanet Candidates. No Vizier entry at the time of writing. Tables in the paper Marcussen & Albrecht (2023);
- Binarity and beyond in A stars - I. Survey description and first results of VLTI/GRAVITY observations of VAST targets with high Gaia-Hipparcos accelerations. No VizieR entry at the time of writing. Tables extracted from the body of the paper Waisberg et al. (2023);
- Multiples among B-stars in Sco-Cen. Vizier: "J/A+A/678/A93", Gratton et al. (2023);
- Combining Gaia and GRAVITY: Characterising five new directly detected substellar companions. No VizieR entry at the time of writing. Tables extracted from the body of the paper Winterhalder et al. (2024).

[17] Spectroscopic binaries are abbreviated as SB1s when only one component is detected, SB2 when two are detected, and so on.

Table G.1: Queried catalogues containing ARKS targets.

Reference	Vizier Catalog ID
[R01] Gratton et al. (2024)	Not in VizieR (as of 2024)
[R02] Kervella et al. (2022)	J/A+A/657/A7
[R04] González-Payo et al. (2024)	J/A+A/689/A302
[R05] Gaia Collaboration (2023)	I/355/gaiadr3
[R07] Elliott et al. (2016)	J/A+A/590/A13
[R08] Biller et al. (2013)	J/ApJ/777/160
[R09] Baron et al. (2018)	J/AJ/156/137
[R12] Elliott et al. (2014)	J/A+A/568/A26
[R13] Zúñiga-Fernández et al. (2021)	J/A+A/645/A30
[R17] Brandt (2021)	J/ApJS/254/42
[R27] Elliott et al. (2015)	J/A+A/580/A88
[R37] Tokovinin (2018)	J/ApJS/235/6
[R38] Mason et al. (2001)	B/wds
Cifuentes et al. (2025)	Not in VizieR (as of 2024)
[R03] Butler et al. (2006)	J/ApJ/646/505
[R06] Vigan et al. (2012)	J/A+A/544/A9
[R10] De Rosa et al. (2014)	J/MNRAS/437/1216
[R11] Lagrange et al. (2020)	Not in VizieR (as of 2024)
[R14] Chauvin et al. (2015)	Not in VizieR (as of 2024)
[R15] Rodriguez & Zuckerman (2012)	J/ApJ/745/147
[R16] Rameau et al. (2013)	Not in VizieR (as of 2024)
[R18] Jura et al. (1993)	Not in VizieR (as of 2024)
[R19] Kastner et al. (2008)	Not in VizieR (as of 2024)
[R20] Zakhozhay et al. (2022)	J/A+A/667/A63
[R21] Janson et al. (2013b)	Not in VizieR (as of 2024)
[R22] Janson et al. (2013a)	Not in VizieR (as of 2024)
[R23] Plavchan et al. (2020)	Not in VizieR (as of 2024)
[R24] Martioli et al. (2021)	Not in VizieR (as of 2024)
[R25] Grandjean et al. (2019)	Not in VizieR (as of 2024)
[R26] Zurlo et al. (2022)	Not in VizieR (as of 2024)
[R29] Bertini et al. (2023)	J/A+A/671/L2
[R30] Lagrange et al. (2009)	Not in VizieR (as of 2024)
[R31] Lagrange et al. (2019)	Not in VizieR (as of 2024)
[R33] Nielsen et al. (2019)	J/AJ/158/13
[R34] Ducourant et al. (2014)	Not in VizieR (as of 2024)
[R36] Shaya & Olling (2011)	J/ApJS/192/2
[R39] Hinkley et al. (2023)	Not in VizieR (as of 2024)
[R40] Milli et al. (2017)	Not in VizieR (as of 2024)
[R41] Marois et al. (2008)	Not in VizieR (as of 2024)
[R42] Marois et al. (2010)	Not in VizieR (as of 2024)
[R28] Marmier et al. (2013)	
[R32] Chauvin et al. (2018)	
[R35] Mallorquín et al. (2024)	

Notes. The first part of the table lists the main catalogues queried and the second part those queried at a second instance since they were referenced by the main catalogues. The third part lists the references that were used in the multiplicity study, due to their occurrence in Table 1.

Appendix G.1. Multiplicity results

A total of eight systems were identified to have confirmed companions, exhibiting a wide range of mass ratios and separations (see Table G.3 for details). Four of these eight systems (HD 10647, HD 76582, HD 109573 and HD 197481) have stellar companions at wide separations from $\sim 500 - 4 \times 10^4$ au. One of these eight systems has a brown dwarf companion (HD 206893) interior to the belt detected via RV, PMa and direct imaging. Six of the eight systems (HD 10647, HD 39060, HD 95086, HD 197481, HD 206893 and HD 218396) contain companions in the planetary mass regime interior to their belts, at separations that are no more than 50% the inner edge of the belts.

Table G.2: Multiplicity status per system and range of separations.

Name	Status per range of separation [1] Close $\lesssim$ 1 au	Intermediate ~ few au - tens au	Wide $\gtrsim$ 100 au
HD 9672	?	N	?
	RV ^{R01}	AO+RUWE ^{R01}	
HD 10647	Y?	Y	Y
	PMa ^{R02}	PMa+CPM^{R02}, RV^{R03}	PMa+CPM ^{R02}, CPM^{R04}
HD 14055	Y?	N	N
	RUWE ^{R05}	AO ^{R06}	CPM ^{R07}
HD 15115	?	N	N
	RV ^{R01}	AO^{R06}, RUWE^{R01}, CPM^{R08}	CPM ^{R09}
HD 15257	N?	N	N
	PMa+RUWE ^{R02}	AO^{RTW3}	CPM ^{R10}
HD 32297	N?	N	?
	PMa+RUWE ^{R02}	AO^{RTW1,RTW2}	?
HD 39060	N	Y	N
	RV^{R11}	AO+RV^{R11}	CPM^{R09}
HD 61005	N	N	N
	RV ^{R12R13}	AO+CPM ^{R14}	CPM ^{R07R09}
HD 76582	N?	N	Y
	PMa ^{R02}	AO^{RTW3}	CPM ^{R02R36}
HD 84870	N?	N	N
	PMa+RUWE ^{R02}	AO^{R15}	AO ^{R15}
HD 92945	Y?	N	?
	PMa ^{R02}	AO^{RTW1,RTW2}	
HD 95086	?	Y	N
	?	AO ^{R16}	AO ^{R16}
HD 107146	Y?	N	?
	PMa ^{R02R17}	AO^{RTW1,RTW2}	
HD 109573	A: ?, B: N	N	Y
	B: RV^{R13}	AO^{RTW1}	CPM^{R18R07R19}
HD 121617	?	?	?
HD 131488	?	N	?
		AO^{RTW1,RTW2}	
HD 131835	?	N	?
		AO^{RTW2}	
HD 145560	?	N	N
	RV^{R20}	AO^{R21}	AO^{R21}
HD 161868	Y?	N	N
	RUWE+PMa ^{R02}	AO^{RTW3}	AO ^{R22}
HD 170773	?	N	?
		AO^{RTW1,RTW2}	
HD 197481	Y	N	Y
	T^{R23R24}	AO^{RTW1,RTW2}	AO^{R12}
HD 206893	N	Y	N
	RV^{R25}	AO^{R25}	AO^{R25}
HD 218396	Y?	Y	Y? N
	RUWE^{R02}	AO^{R26}	Y?: CPM^{R02}, CPM^{R07R09}
TYC 9340-437-1	N	N	N
	RV^{R13}	AO^{RTW1,RTW2}	AO^{R27}, CPM^{R07}

Notes. References^{RX} for the quoted techniques as in Table G.1. Flags: ? = no data available and/or no conclusion on the (non)presence of a companion. Y = existing surveys report detected (gravitationally bound) stellar and/or substellar companions. Y? = RUWE and/or PMa and/or χ^2 and/or searches for CPM candidates indicate possible companions. N = existing surveys probing this separation range report non-detections $\rightarrow$ with (high) probability there are no companions. N? = values exist of PMa and/or RUWE that do not show signs of multiplicity Techniques: RV = Radial Velocity; AO = Adaptive Optics; PMa = Proper Motion Anomaly (mostly between HIPPARCOS and Gaia); RUWE = Renormalized Unit Weight Error (from Gaia); CPM = Common Proper Motion; T = Transit. Flags with the reference '^{RTW}' correspond to contrast limits obtained homogeneously with the data available in the SPHERE data centre, stellar properties from Table 1, and the predictions in mass from the Baraffe et al. (2015) model using broad-band H filter (and if not available *H_D*2 and *H_D*3 filter) observations: we separated the outcomes into three regimes: RTW1: Objects for which we can discard stellar companions down to 3au; RTW2: Objects for which we can discard companions with masses > 13 Mjup as close as 5au; RTW3: Objects for which we can discard stellar companions down to ~10au.

Table G.3: Architecture of multiple system and properties of the companion.

Properties of confirmed multiple systems [1]							
Name	M_P [$M_\odot$]	Config.	Sep [au]	M_c [M_{Jup}]	ΔM_c [M_{Jup}]	M_c [$M_\odot$]	$(R-\Delta R/2)$–$(R+\Delta R/2)$ [2] [au]
HD 10647	1.12	Ab^{R03}	2.0^{R28}	0.93^{R03}	0.18		71–136
		B ^{R02}	3.7×10^4 ^{R02,R29}			[0.2,0.4]^{R29}	
HD 39060	1.72	b^{R30}	10.3^{R17}	10–11^{R11}			56–153
		c^{R31}	2.7^{R17}	7.8^{R11}	0.4		
HD 76582[3]	1.61	B ^{R02}	4.8×10^4 ^{R02}	?			116–292
HD 95086	1.54	b^{R16}	52^{R32}	2.6^{R33}	0.4		110–284
HD 109573	2.14	B^{R18}	490-560^{R18,R02}			0.37 ^{R34}	72–79
		C^{R18}	$1.2–1.4\times10^4$ ^{R07,R19,R02}			0.1 ^{R34}	
HD 197481[4]	0.61	Ab^{R23}	0.07^{R35}	0.028^{R35}	0.009		27–40
		Ac^{R23}	0.12^{R35}	0.04^{R35}	0.02		
		AB = AT Mic^{R36}	$4.0–4.5\times10^4$ ^{R37,R38,R36}			0.37 ^{R37}, 0.36^{R36}	
		BC^{R37}	20–24^{R02}			0.20 ^{R37}	
HD 206893	1.33	Ab^{R25}	3.5^{R39}	12.7^{R39}	1.2		47–163
		B^{R40}	9.7^{R39}	28.0^{R39}	2.2		
HD 218396	1.50	b ^{R41}	72^{R26}	6^{R26}			149–331
		c ^{R41}	41^{R26}	8^{R26}			
		d ^{R41}	27^{R26}	9^{R26}			
		e ^{R42}	16^{R26}	8 ^{R26}			

Notes. References^{RX} for the quoted values are provided as in Table G.1. Column 8 shows the disc extent.
[1] M_P: Primary Mass: same as in Table C.1: estimated as described in Appendix C; Config.: Architecture of the system: lower case letters indicate planetary companions, capital letters indicate stellar or brown dwarf companions; Sep: semi-major axis for those companions with orbital constraints (Sep< 100 au) or separation for those on wider orbits (homogenised to angular units with parallaxes from Gaia DR3); M_c: Companion Mass: for substellar companions the units are given in Jupiter masses, while for stellar companions the mass is given in solar masses. If provided in the referenced literature, the uncertainties are given in ΔM_c [2]Approximated disc extent. Values of R and ΔR are taken from Table B.1 [3] HD 76582 and HD 76543 reported by Kervella et al. (2022) and Shaya & Olling (2011) as a common proper motion pair. In addition to the finding from Gaia Collaboration (2023), the two stars are at the same distance and have radial velocities that are consistent within the errors. No mass is reported for the companion; instead, a placeholder ('?') is used. This is because Kervella et al. (2022) does not provide a mass estimate, and the masses for both components reported in other studies, such as Shaya & Olling (2011) and De Rosa et al. (2014), are inconsistent with the primary star adopted here and with each other. [4] Hierarchical stellar triple system: The primary star HD 197481 (AU Mic) hosts two confirmed planets; and there are hints for two additional planets (Donati et al. 2023). It has a very wide companion HD 196982 (AT Mic), which is itself a binary system. Elliott et al. (2016) suggest a limit for wide binaries in the beta Pic moving group that agrees with HD 197481 (AU Mic) and HD 196982 (AT Mic) being bound in the past. However, the systems are considered comoving but not bound in Tokovinin (2018).

A&A, 691, A302 (2024)
https://doi.org/10.1051/0004-6361/202451080
© The Authors 2024

Astronomy & Astrophysics

Collisional damping in debris discs: Only significant if collision velocities are low

Marija R. Jankovic[1,⋆], Mark C. Wyatt[2], and Torsten Löhne[3]

[1] Institute of Physics Belgrade, University of Belgrade, Pregrevica 118, 11080 Belgrade, Serbia
[2] Institute of Astronomy, University of Cambridge, Madingley Road, Cambridge CB3 0HA, UK
[3] Astrophysikalisches Institut und Universitätssternwarte, Friedrich-Schiller-Universität Jena, Schillergäßchen 2–3, 07745 Jena, Germany

Received 12 June 2024 / Accepted 4 October 2024

ABSTRACT

Context. Dusty debris discs around main sequence stars are observed to vary widely in terms of their vertical thickness. Their vertical structure may be affected by damping in inelastic collisions. Although kinetic models have often been used to study the collisional evolution of debris discs, these models have not yet been used to study the evolution of their vertical structure.
Aims. We extend an existing implementation of a kinetic model of collisional evolution to include the evolution of orbital inclinations and we use this model to study the effects of collisional damping in pre-stirred discs.
Methods. We evolved the number of particles of different masses, eccentricities, and inclinations using the kinetic model and used Monte Carlo simulations to calculate collision rates between particles in the disc. We considered all relevant collisional outcomes including fragmentation, cratering, and growth.
Results. Collisional damping is inefficient if particles can be destroyed by projectiles that are of much lower mass. If that is the case, catastrophic disruptions shape the distributions of eccentricities and inclinations, and their average values evolve slowly and at the same rate for all particle sizes.
Conclusions. The critical projectile-to-target mass ratio (Y_c) and the collisional timescale jointly determine the level of collisional damping in debris discs. If Y_c is much smaller than unity, a debris disc retains the inclination distribution that it is born with for much longer than the collisional timescale of the largest bodies in the disc. Such a disc should exhibit a vertical thickness that is independent of wavelength even in the absence of other physical processes. Collisional damping is efficient if Y_c is of order unity or larger. For millimetre-sized dust grains and common material strength assumptions, this requires collision velocities of lower than ∼40 m s^{-1}. We discuss the implications of our findings for exo-Kuiper belts, discs around white dwarfs, and planetary rings.

Key words. methods: numerical – minor planets, asteroids: general

1. Introduction

Dusty discs have been detected around numerous main sequence stars. These are believed to be merely the observable component of discs populated with larger bodies, planetesimals, and perhaps even dwarf planets. Such systems are commonly called debris discs (Wyatt 2008; Hughes et al. 2018). In debris discs, planetesimals and dust are respectively at the top and bottom of a collisional cascade, a system in which collisions and fragmentation of larger objects resupply the abundance of smaller objects. Thus, through characterisation of the small dust in these discs, it is possible to probe the structure of the large planetesimals. The vertical structure of these discs in particular can be useful to constrain their dynamical state, as the vertical profile of a disc reveals the inclination distribution of the orbits of its particles, and this distribution is directly related to the velocities at which particles collide. That is, the vertical structure and the dynamical state of a debris disc are closely related to its collisional evolution and the transfer of mass down the collisional cascade.

Observationally, the vertical structure of debris discs is most easily probed for discs that are seen near edge-on, for which a disc scale-height or aspect ratio can be measured. Measurements so far show a great diversity among discs. At millimetre (mm) wavelengths, aspect ratios range from 0.02 for AU Mic (Terrill et al. 2023) and 0.08 for HR 4796 (Kennedy et al. 2018), up to 0.13 for HD 16743 (Marshall et al. 2023) and 0.13–0.28 for HD 110058 (Hales et al. 2022). At wavelengths in the near-infrared (NIR), for which the highest resolutions have been achieved, it has been shown that discs are diverse in terms of not only their aspect ratios, but also the shape of their vertical density profile (Olofsson et al. 2022). Vertical profile shapes at mm wavelengths can also be nontrivial, as found for the disc around β Pic (Matrà et al. 2019). In some systems, the aspect ratio may also vary with distance from the star, which can be inferred with sophisticated nonparametric methods (Han et al. 2022).

Discs observed at multiple wavelengths can provide a substantial amount of information, as they probe the scale-height of particles of different sizes in a single dynamical system. So far, there appears to be diversity in these results as well. For example, for HR 4796 (HD109573), the aspect ratio inferred from ALMA observations of 0.08 (at the wavelength of 880 µm; Kennedy et al. 2018) is comparable to the SPHERE value of 0.06 (at the wavelength of ∼0.7 µm; Olofsson et al. 2022). On the other hand, in AU Mic the aspect ratio appears to be increasing as a function of wavelength (Olofsson et al. 2022; Daley et al. 2019; Vizgan et al. 2022). All in all, the amount of available observational data on the vertical structure of debris discs is steadily growing, and theoretical models are needed to understand them.

⋆ Corresponding author; marija.jankovic@ipb.ac.rs

Open Access article, published by EDP Sciences, under the terms of the Creative Commons Attribution License (https://creativecommons.org/licenses/by/4.0), which permits unrestricted use, distribution, and reproduction in any medium, provided the original work is properly cited.
This article is published in open access under the Subscribe to Open model. Subscribe to A&A to support open access publication.

It has long been argued that the velocity evolution of a debris disc (and thus the evolution of its scale-height) is governed by the largest bodies in the disc (the largest planetesimals or perhaps even dwarf planets), which increase the inclinations and eccentricities of all the bodies through gravitational interactions, a process known as viscous stirring (Kenyon & Bromley 2002b, 2004, 2008, 2010; Kennedy & Wyatt 2010; Krivov & Booth 2018). In the absence of damping mechanisms (or if these are inefficient), an initially thin disc will be viscously stirred by the largest bodies in the disc, so that its scale-height (and the particles' inclinations, eccentricities, and the velocity dispersion) may depend on the age of the system, as well as on the properties of the bodies doing the stirring. Thus, assuming the absence of damping mechanisms, the properties of the largest bodies in the disc can be constrained through measurement of the scale-height (Nakano 1988; Artymowicz 1997; Quillen et al. 2007; Matrà et al. 2019).

One damping mechanism is certain to exist: collisions among particles are inelastic and this has the effect of damping particle inclinations and eccentricities over time. The efficiency with which collisional damping impedes viscous stirring depends on the size distribution of the bodies in the belt (Lissauer & Stewart 1993). Using an analytic model, Pan & Schlichting (2012) proposed that there could be an equilibrium between viscous stirring and collisional damping in a collisional cascade, such that, among small dust grains, particle velocity increases with particle size. On the other hand, time-dependent simulations of debris-disc evolution that account for both viscous stirring and collisional damping, as well as continued accretion of the largest bodies (Kenyon & Bromley 2002b, 2004, 2008, 2010), typically show collisional damping to only be important early on, while viscous stirring dominates at later stages due to efficient (dwarf) planet formation, making the velocity independent of particle size for the small dust. However, the results vary based on the exact mixture of planetesimals and pebbles that the disc initially consists of Najita et al. (2022), meaning that in these simulations there can be a phase in the disc evolution during which particle velocity increases as a function of particle size. Therefore, there is no clear consensus on the degree to which collisional damping may affect the debris-disc scale-heights that are being observed.

As physical collisions are one of the most fundamental processes in debris discs, it is important to understand their role in the evolution of particle eccentricities and inclinations (and thus in the evolution of the disc scale-heights). One numerical method in particular is well suited for this – the kinetic approach (Krivov et al. 2005), whereby the collisional and dynamical evolution of particles are considered in a fully coupled manner in the parameter space of particle size and selected orbital elements. This method allows arbitrary distributions of orbital elements to be considered on a discretised grid. In comparison, in the mixed statistical approach (e.g. Kenyon & Bromley 2002a,b, 2004), the evolution of mass and the evolution of velocity are considered concurrently but separately[1], and it is assumed that the functional form of the distributions of eccentricities and inclinations is fixed. However, the kinetic approach has so far not been used to study the evolution of particle inclinations or debris disc scale-heights.

In this paper, we aim to study the effects of physical collisions on particle eccentricities and inclinations in debris discs in detail. To do so, we extend a previous implementation of the kinetic approach (van Lieshout et al. 2014) to include particle inclinations in the parameter space, using Monte Carlo simulations (Wyatt et al. 2010) to calculate particle collision rates. There are two major aims of this paper: to present this extended numerical model and to study the importance of collisional damping in collisional cascades. We start by discussing the underlying physics of collisional damping in Sect. 2, and present the methods of our numerical approach in Sect. 3. In Sects. 4 and 5 we present and discuss our results. Finally, in Sect. 6, we summarise our findings.

2. Theoretical expectations

In this section we discuss some of the well-known results from the literature about collisional damping and we discuss collisional damping in collisional cascades whose evolution is governed by destructive collisions. We are only concerned with physical collisions and not with close encounters and gravitational scattering. A simple model of such a physical collision is a collision of two indestructible spheres, with the normal and the transversal components of the relative velocity at the point of impact changing in the collision proportionally to coefficients of restitution (e.g. Trulsen 1971; Brahic 1977; Brahic & Henon 1977; Hornung et al. 1985). We further simplify this model by assuming physical collisions are completely inelastic.The total kinetic energy of colliders pre-collision is a sum of the energy associated with centre-of-mass motion and with their relative velocity. In a completely inelastic collision the latter term is entirely dissipated and post-collision both bodies are moving at their centre-of-mass velocity. This assumption may not be fully realistic for all types of collisional outcomes in real discs, but this does not affect the main takeaways of this work (see the discussion in Sect. 5.4). Thus, we leave exploration of more detailed prescriptions for future work.

Even a completely inelastic collision does not always lead to a lower velocity for both bodies. For example, if a population of larger bodies has higher velocity dispersion than a population of smaller bodies, it will collisionally stir the smaller bodies. But, each collision loses energy and the overall effect is collisional damping, meaning, reduction in the velocity dispersion. In a circumstellar disc in which the velocity dispersion arises from particles having different eccentricities and inclinations, this means a decrease in the typical particle orbital eccentricity and inclination with time (Brahic 1977; Hornung et al. 1985).

We wish to estimate the rate at which the velocity dispersion and the typical eccentricity and inclination decrease with time. To do so, we first consider the rate at which particles collide in a circumstellar disc, which can be easily estimated with a particle-in-a-box model (e.g. Wyatt et al. 2007; Rigley & Wyatt 2020). In such a model we can consider a power-law size distribution of particles, $n(s)\mathrm{d}s \propto s^{-q}\mathrm{d}s$, with a bulk material density ρ_b, a total mass M, and with minimum and maximum radius of s_min and s_max, respectively. This material is assumed to be spread out over a circumstellar belt centred at stellocentric radius a with a width Δa and average inclination $\langle i \rangle$. The volume of the disc can then be estimated as $V \sim 4\pi a^2 \Delta a \langle i \rangle$. The average impact velocity depends, in general, on the average eccentricity and the average inclination of particle orbits (e.g. Lissauer & Stewart 1993). Assuming the ratio between the average eccentricity and the average inclination to be a constant of order unity, the average impact velocity can be estimated as $v_\mathrm{rel} \sim v_\mathrm{kep}(a)\langle i \rangle$. The rate at which a target particle of size s_t collides with other particles

[1] For the most part, some redistribution of the kinetic energy of the colliders to their fragments can be included in this method directly within the collisional outcome prescription (Kenyon & Luu 1999).

in the size range of $s_{\rm min}$ to $s_{\rm max}$ is then given by

$$R_{\rm coll}(s_{\rm t}) = C \int_{s_{\rm min}}^{s_{\rm max}} s_{\rm p}^{-q}(s_{\rm p} + s_{\rm t})^2 {\rm d}s_{\rm p}, \tag{1}$$

where subscript p stands for the projectile particle colliding with the target and

$$C = \frac{3(4-q)}{16\pi}(GM_*)^{0.5}\rho_{\rm b}^{-1}a^{-3.5}\left(\frac{\Delta a}{a}\right)^{-1} M s_{\rm max}^{q-4}. \tag{2}$$

Next, we account for the fact that different collisions contribute differently to collisional damping, because the degree of velocity damping depends on the mass ratio of the colliders. For a rigorous, more general derivation based on kinetic theory we refer the reader to Hornung et al. (1985). Here we merely sketch out how this dependence on the mass ratio arises by deriving an order-of-magnitude estimate, assuming all particles to have an identical Gaussian velocity distribution. In a thin circumstellar disc, the velocity dispersion ($\langle \delta v^2 \rangle$) around the Keplerian velocity ($v_{\rm K}(a)$) arises from the eccentricity and inclination dispersions ($\langle e^2 \rangle$ and $\langle i^2 \rangle$). In this simplified model we also assume that the ratio of the eccentricity and the inclination dispersion is a constant. In a collision of a target of mass $m_{\rm t}$ with a projectile of mass $m_{\rm p}$, $\langle e^2 \rangle$ and $\langle i^2 \rangle$ change by a factor of the order of the fraction of the average kinetic energy associated with the random velocities that is lost on average in a single collision ($\langle \Delta \delta v_{\rm t}^2 \rangle / \langle \delta v_{\rm t}^2 \rangle$). We can calculate this fraction by considering a single collision in which particles collide with velocities $\mathbf{v}_{\rm t}$ and $\mathbf{v}_{\rm p}$ (in the inertial frame of reference), in which the energy loss for the target is given by

$$\begin{aligned} &\frac{1}{2}m_{\rm t}v_{\rm t}^2 - \frac{1}{2}m_{\rm t}v_{\rm CM}^2 \\ &\quad = \frac{1}{2}\frac{m_{\rm t}}{(m_{\rm t}+m_{\rm p})^2}\left(m_{\rm p}^2(v_{\rm t}^2 - v_{\rm p}^2) + 2m_{\rm t}m_{\rm p}\mathbf{v}_{\rm t}(\mathbf{v}_{\rm t} - \mathbf{v}_{\rm p})\right). \end{aligned} \tag{3}$$

Averaging the above expression over the velocity distributions of the colliders, using our assumptions of Gaussian velocity distributions independent of particle size and disregarding a numerical factor of order unity, the fraction we are looking for is given by

$$\frac{\langle \Delta \delta v_{\rm t}^2 \rangle}{\langle \delta v_{\rm t}^2 \rangle} \sim \frac{m_{\rm t}m_{\rm p}}{(m_{\rm t}+m_{\rm p})^2}. \tag{4}$$

It follows that the eccentricity, the inclination and the velocity dispersion decrease over time approximately at a rate given by

$$R_{\rm damp}(s_{\rm t}) = C \int_{s_{\rm min}}^{s_{\rm max}} s_{\rm p}^{-q}(s_{\rm p} + s_{\rm t})^2 \frac{m_{\rm t}m_{\rm p}}{(m_{\rm t}+m_{\rm p})^2} {\rm d}s_{\rm p}. \tag{5}$$

From this it can be shown that collisions with equal-size bodies dominate collisional damping. It is useful to consider the number of particles in a logarithmic size bin, that is, to change the variable of integration to $\ln s_{\rm p}$. For $q < 4$, one obtains an integrand that is a non-monotonous function peaking approximately at $s_{\rm p} \sim s_{\rm t}$. This is to be intuitively expected. A much smaller projectile cannot change significantly the velocity of a massive target, while, on the other hand, for $q < 4$ smaller particles dominate the cross-section area and collisions with more massive 'projectiles' occur at a much lower rate.

If it is further assumed that particle velocities are *only* damped in collisions with particles in the same logarithmic unit size bin (Pan & Schlichting 2012),

$$\begin{aligned} R_{\rm damp}(s_{\rm t}) &= C \int_{s_{\rm min}}^{s_{\rm max}} s_{\rm p}^{1-q}(s_{\rm p} + s_{\rm t})^2 \frac{s_{\rm t}^3 s_{\rm p}^3}{(s_{\rm t}^3 + s_{\rm p}^3)^2} {\rm d}\ln s_{\rm p} \\ &\sim C s_{\rm t}^{3-q}. \end{aligned} \tag{6}$$

For the standard value of $q = 3.5$ (Dohnanyi 1969), $R_{\rm damp}(s_{\rm t}) \propto s_{\rm t}^{-1/2}$. This simple size-dependence is valid as long as $s_{\rm t}$ is not too close to either $s_{\rm min}$ or $s_{\rm max}$. One clear consequence of this size-dependence is that the velocity distributions of particles of different sizes do not remain identical, and the damping rate itself will change over time. Nevertheless, Eq. (5) provides a simple estimate for how quickly the eccentricities and the inclinations should change initially in a disc in which particles of all sizes are pre-stirred to the same velocity dispersion.

The above damping rate is applicable if the particle remains intact after each collision. But, for the debris discs to be observable, there must be destructive collisions producing dust. The change in particle mass in collisions is thus critical. As with damping, only a fraction of all collisions are important. For the body to be fragmented, the impact energy has to be greater than some size- and velocity-dependent critical specific energy $Q_{\rm D}^*$ (e.g. Benz & Asphaug 1999; Stewart & Leinhardt 2009). Equivalently, for some typical impact velocity in the disc, a target can only be destroyed by a projectile larger than some critical size $s_{\rm c}$. For projectiles that are much less massive than the target the impact energy is roughly the kinetic energy of the projectile and

$$\frac{s_{\rm c}}{s_{\rm t}} = \left(\frac{2Q_{\rm D}^*}{v_{\rm rel}^2}\right)^{\frac{1}{3}}. \tag{7}$$

The rate of destructive collisions is then given by

$$R_{\rm frag}(s_{\rm t}) = C \int_{s_{\rm c}}^{s_{\rm max}} s_{\rm p}^{-q}(s_{\rm p} + s_{\rm t})^2 {\rm d}s_{\rm p}. \tag{8}$$

For $q > 1$, the fragmentation rate is dominated by collisions with bodies of critical size $s_{\rm c}$. Analogous to Eq. (6), not too close to either the top or the bottom of the cascade, the fragmentation rate is approximately given by

$$R_{\rm frag}(s_{\rm t}) \sim C s_{\rm c}^{1-q}(s_{\rm c} + s_{\rm t})^2. \tag{9}$$

It follows directly that, at the very least, the damping rate from Eq. (5) should be modified so that the upper limit of the integral equals $s_{\rm c}$, if $s_{\rm c} < s_{\rm t}$. The rate $R_{\rm damp}$ is then dominated by bouncing or cratering collisions with bodies just below the critical projectile size. More importantly, the fragmentation rate is then higher than the damping rate. If $s_{\rm c} \lesssim s_{\rm t}$, particles are destroyed faster than their velocities are damped[2]. Their velocities are then inherited from their parent bodies and change very little before mass proceeds down the collisional cascade. Collisional damping would occur jointly with the transfer of mass down the collisional cascade, although if $s_{\rm c} \ll s_{\rm t}$ fragments will simply inherit the velocity distribution of the more massive of two colliders. Additionally, the more the impact energy exceeds the critical energy, the smaller the fragments and the further down the cascade the target's velocity is copied, hence equalising

[2] In the limiting case of $s_{\rm t} = s_{\rm max}$ for which the fragmentation rate diminishes for $s_{\rm c} = s_{\rm t}$, $R_{\rm frag} > R_{\rm damp}$ for $s_{\rm c}$ below $\approx 0.6 s_{\rm t}$.

the velocities across the cascade. All in all, we expect that collisional damping is inefficient if the critical projectile-target size ratio is much smaller than unity. Velocities may still evolve in this case, but their evolution would depend on how the destruction and production rates shape the distributions of eccentricities and inclinations.

Now, in some discs it may happen that $s_c \gtrsim s_t$. In that case $R_{frag} \lesssim R_{damp}$, and the average eccentricity and inclination of particles would indeed fall off at the rate R_{damp} (provided these collisions are fully dissipating as assumed here). The key question is then if collisions still produce a collisional cascade and observable dust. For example, Eq. (7) is in fact no longer applicable, since it is derived under the assumption that $s_c \ll s_t$. For large values of $2Q_D^*/v_{rel}^2$, the impact energy is insufficient to disrupt the target mass for any projectile mass. On the other hand, in this simplified model we only consider collisions at the average/typical collision velocity v_{rel}, whereas particles in real discs have a distribution of velocities. Moreover, cratering/erosion can still produce dust in this case. In fact, studies have found that even when fragmenting collisions are present, cratering collisions can dominate the mass flux through the cascade (Thébault et al. 2003; Thébault & Augereau 2007; Kobayashi & Tanaka 2010). All in all, to investigate this further we need a more comprehensive model, which we present in the next section.

Lastly, collisional damping also affects particles' semi-major axes. As particles lose energy in inelastic collisions, their semi-major axes are expected to shrink over time. More precisely, most of the mass can be expected to shift inwards, while some of the particles will end up on wider orbits, to conserve total angular momentum. This evolution of semi-major axes happens on much longer timescales than the damping of eccentricity and inclination, as found in N-body simulations (Brahic 1977). N-body simulations of Lithwick & Chiang (2007) also support this large difference in timescales, and they also find analytically that the radial diffusion timescale of the ring will be longer than the damping timescale by a factor of $(\Delta a/(ae))^2$, where e is the average eccentricity. For wide enough rings, therefore, it is justified to neglect the evolution of semi-major axis while focusing on the short-term evolution of eccentricities and inclinations. In numerical simulations presented in our work, $\Delta a/(ae) \gg 1$ in all physical models where damping is efficient. To further support neglecting semi-major axis evolution, note that Pan & Schlichting (2012) argued that the ratio of the timescale of inclination damping to the timescale of semi-major axis damping is equal to the fraction of the orbital energy lost in a single collision, which is roughly the average inclination of particle orbits. That is typically observed to be less than ~ 0.1 in debris discs (e.g. Terrill et al. 2023; Kennedy et al. 2018; Olofsson et al. 2022; Daley et al. 2019). Based on these arguments, we neglect the evolution of semi-major axis in this work. However, we also note that in the N-body simulations of Brahic (1977) and Lithwick & Chiang (2007) all bodies are of equal size. Damping rates are size-dependent and in a collisional cascade of bodies spanning many orders of magnitude in size it may indeed occur that semi-major axes of the smallest bodies evolve faster than the evolution of the eccentricities and inclinations of the largest bodies. We further discuss this possibility in Sect. 5.

3. Methods

To model collisional evolution of particles in a circumstellar disc, we employ a modified version of the kinetic model implemented by van Lieshout et al. (2014) (based on the approach developed by Krivov et al. 2005, 2006; Löhne 2008). The spatial and size distributions of particles (n) in a phase space of particle masses (m) and orbital elements ($\boldsymbol{k}$) are evolved using the continuity equation

$$\frac{\mathrm{d}n}{\mathrm{d}t} = \left(\frac{\mathrm{d}n}{\mathrm{d}t}\right)_{\mathrm{gain}} - \left(\frac{\mathrm{d}n}{\mathrm{d}t}\right)_{\mathrm{loss}}, \tag{10}$$

where the gain (source) and the loss (sink) terms describe changes in the distribution function due to collisions. In this study we focus on the evolution of large particles in the outer regions of gas-free debris discs, and so we do not consider P-R drag, gas drag, nor sublimation of dust. To solve the continuity equation, the phase space $(m, \mathbf{k})$ is discretised into a grid of bins, and the distribution function is discretised as a number of particles in each bin. The continuity equation becomes a series of ODEs.

The key assumption of the kinetic approach is that the collisional timescales, as well as the timescales of the drag processes, are much longer than orbital timescales. We further assume that the disc is axisymmetric. Under these assumptions, the evolution of the dust can be followed in a reduced phase space consisting of 4 variables: particle mass (m), eccentricity (e), semi-major axis (a) (or, alternatively, periastron distance) and inclination (i). The remaining orbital elements, which determine the orientations of the orbits, can be averaged over in the treatment of particle collisions.

The inclusion of inclination in the kinetic model phase space is the key difference between the model used in this work and the model used by van Lieshout et al. (2014). The latter assumed that the particle inclination distribution was fixed. This allowed to use a simplified, analytic approach to calculate collisional probabilities and other relevant quantities (Krivov et al. 2006). To consider collisions between particles with arbitrary inclinations, we perform Monte Carlo simulations which sample the distributions of particle velocities and collision locations (Wyatt et al. 2010). In this work, we also account for a greater variety of collisional outcomes, including erosion and growth, bringing the model up-to-date with state-of-the-art debris disc kinetic models in this respect (e.g. Löhne et al. 2017). We also make minor corrections to the code with regards to the calculation of collision terms.

Our treatment of particle collisions is detailed in Sect. 3.1. While the model is implemented to work with a four-dimensional phase space, due to computational costs we limit ourselves to using only a single semi-major axis bin. In other words, semi-major axis does not evolve in the results presented here (but we still take into account the reduction in the radial width of a belt if particle eccentricities are damped). This should not affect the main findings of our study, which concern chiefly the evolution of particles' eccentricities and inclinations, because the evolution of semi-major axis due to collisional damping happens on much longer timescales (Brahic 1977, see discussion in Sect. 2). The exact phase-space grid we use is defined in Sect. 3.2. Several tests of our model are considered in Appendices A and B.

3.1. Collisions

First, we discuss the collision terms in the kinetic model and introduce the quantities characterising the collisions. Then, we discuss the calculation of the collisional probabilities and impact velocities using the Monte Carlo method, and finally the collisional outcomes considered in this model. Figure C.1 shows

the overview of how the kinetic model and the Monte Carlo simulations are coupled.

3.1.1. Collision terms in the kinetic model

Without the transport terms, in the discretised form of the continuity equation, the number of particles in each bin evolves according to

$$\frac{\mathrm{d}n_i}{\mathrm{d}t} = \sum_p \sum_t G(p,t,i) - \sum_p L(p,i), \tag{11}$$

where indices i, p and t numerate bins in the phase space, and G and L denote the gain and the loss rates, respectively. Essentially, the first term on the right-hand side loops over various combinations of targets (t) and projectiles (p) whose collisions produce fragments in the bin with index i, and the second term loops over various projectiles (p) which can destroy or crater particles in the bin with index i. A factor 1/2 is applied for $p = t$ collisions in the first term and for $p = i$ collisions in the second term. The gain (G) and the loss (L) rates are averaged over all of the orbital elements not included in our phase space. This averaging is performed using a Monte Carlo simulation, which samples the distributions of the redundant orbital elements, producing a large number of particle pairs colliding at different locations and velocities. The gain and loss rates are given by

$$\begin{aligned} L(p,t) = n_p n_t \sigma(m_p, m_t) \sum_j \Delta(\boldsymbol{k}_p, \boldsymbol{k}_t; j) \\ \times v_{\mathrm{imp}}(m_p, \boldsymbol{k}_p, m_t, \boldsymbol{k}_t; j) \\ \times c(m_p, \boldsymbol{k}_p, m_t, \boldsymbol{k}_t; j), \end{aligned} \tag{12}$$

$$\begin{aligned} G(p,t,i) = n_p n_t \sigma(m_p, m_t) \sum_j \Delta(\boldsymbol{k}_p, \boldsymbol{k}_t; j) \\ \times v_{\mathrm{imp}}(m_p, \boldsymbol{k}_p, m_t, \boldsymbol{k}_t; j) \\ \times c(m_p, \boldsymbol{k}_p, m_t, \boldsymbol{k}_t; j) \\ \times f(m_p, \boldsymbol{k}_p, m_t, \boldsymbol{k}_t, m_i, \boldsymbol{k}_i; j), \end{aligned} \tag{13}$$

where the sum over j counts over particle pairs produced in a Monte Carlo simulation. Here, σ is the collisional cross section, Δ is the geometric probability of the collision (similar in its meaning to the Δ-integral of Krivov et al. 2006), v_{imp} is the impact velocity, c is the probability that the collision results in loss of mass and f is the probability that a collision of a particular target and projectile will result in the formation of a fragment with phase-space variables m_i and $\boldsymbol{k}_i$ (see Sect. 3.1.3). The probability Δ and the impact velocity are obtained from the Monte Carlo simulation, as described in the following section. The impact velocity only depends on particle masses for small dust particles affected by radiation pressure; in the results presented in this paper that is neglected.

3.1.2. Collisional probabilities and impact velocities

To calculate geometric collision probabilities and particle velocities, and ultimately the gain and the loss rates due to collisions, we use a Monte Carlo approach based on the work of Wyatt et al. (2010). The goal is to characterise collisions between two populations of particles with given semi-major axes (or pericentre distances), eccentricities and inclinations. With these orbital elements fixed, particles still collide at a range of distances from the central star (i.e. at different radii) and at different heights from the disc midplane, as the orbit orientations and the positions of particles along their orbits vary. The relative (or impact) velocity varies as well, and with it the collisional outcome. These variations are captured in a Monte Carlo simulation as follows.

We start with a pre-defined grid of orbital elements (the grid to be used in the kinetic model). Each grid bin is defined by its edges and its centre for the eccentricity (e), semi-major axis (a) (or pericentre distance, q) and inclination (i). For a total of N grid bins ($N = N_e N_a N_i$), there are $N(N+1)/2$ unique grid bin combinations. In this work limit the grid of semi-major axes to $N_a = 1$, but the methods are general with respect to use of more bins. For each grid bin combination we run a Monte Carlo simulation as follows.

First, we generate two populations of particles for the two sets of orbital elements defining the grid bins. Typically we use 10^4 particles for the 'first' and 10^5 particles for the 'second' population[3]. The semi-major axes in a population are sampled uniformly from the a-bin, while the inclinations and eccentricities are sampled from a very narrow range around the centres of the e- and i-bins[4]. The rest of the Keplerian orbital elements and the particle locations along the orbit are uniformly distributed in their respective ranges. These populations are used to calculate the fraction of particles in the region of the space where particle orbits overlap, determined radially by particles' pericentres and apocentres and vertically by the smaller of the two inclinations. Then, two new populations of particles are generated in a similar manner, except that they are constrained to the overlapping region. This ensures that the number of particles in the overlapping region remains consistently large to accurately capture collision probabilities and velocities, while the fraction calculated above is accounted for at a later stage. For some parameters, the overlapping region is very narrow and few particles are produced in the overlapping region, which can severely reduce the accuracy of the method; if fewer than 1% of particles fall into the overlapping region, we repeat the calculation with 10^6 particles. However, the number of particles produced in the second step (in the overlapping region) remains the same (as set on input).

Second, for each particle in the first population we find its nearest neighbour from the other population. As long as the number of particles is large, the choice of the first population here should be unimportant. These pairs of particles represent collisions between the two populations. The finding of the nearest neighbour for each particle is optimised by dividing the space into a grid, and only searching for the nearest neighbour among the particles in the same or the neighbouring grid cell. The size of the grid cell is set to 1% of the radius of the outer boundary of the overlapping region. If there are no neighbours found for some of the particles, the grid cell size is increased and the process repeated for these particles.

[3] This balances the need to increase the accuracy with the need to reduce the computer memory requirements; the latter depends on the number of particles in the 'first' population, as explained later.

[4] This choice reduces artificial diffusion of fragments through the grid. If inclinations and eccentricities are sampled uniformly from their respective bins, very small changes in these orbital elements (including due to small numerical errors) cause particles near bin edges (or the fragments they produce) to 'jump' into a neighbouring bin. With limited grid resolution this manifests as numerical diffusion and artificially speeds up the evolution. This artificial diffusion would also occur along the semi-major axis grid, but in this work we only consider a single a-bin, as discussed above. Furthermore, the way inclination and eccentricity bins are sampled does not strongly affect the collisional probabilities and velocities.

Third, we calculate the collision probability for each pair of particles. The orbit-overlapping region is divided into $N_r = 100$ radial (r) and $N_\phi = 20$ vertical (i.e., polar angle, ϕ) bins. The fraction of particles in each bin is calculated for each of the populations, and further multiplied by the initial fraction of particles in the entire overlapping region (calculated in the first step). We denote these fractions as $\sigma_1(r)$ and $\sigma_2(r)$. The probability of a collision in each of the bins is then

$$\Delta(r,\phi) = \frac{\sigma_1(r,\phi)\sigma_2(r,\phi)}{\mathrm{d}V(r,\phi)}, \tag{14}$$

where $dV(r,\phi)$ is the volume of the bin. This quantity is analogous to the Δ-integral calculated analytically in two dimensions by Krivov et al. (2006). Then, if there are $N_1(r,\phi)$ particles from the 'first' population in the given bin, each pair of nearest neighbours identified above is assigned a collision probability

$$\Delta(j) = \frac{\Delta(r,\phi)}{N_1(r,\phi)}, \tag{15}$$

where j counts over all of the particles from the 'first' population in this bin (whereas its nearest neighbour from the 'second' population need not be from the same $r-\phi$ bin, and can also be the nearest neighbour to more than one particle from the first population).

Furthermore, note that the collision probability assigned in this manner to all $N_1(r,\phi)$ particle pairs is the same, but their relative velocities are not. In each r-ϕ bin there is a distribution of velocities at which particles collide. This is analogous to how in two dimensions, for a fixed relative orientation of the orbits (or at a fixed radius), particles may collide at up to two different relative velocities (Krivov et al. 2006). The particle pairs are a sample of that velocity distribution.

Finally, for each orbit combination, for each particle in the 'first' population we store the components of its position and velocity, the position and velocity of its nearest neighbour from the 'second' population, and the probability of their encounter $\Delta(j)$. These data are pre-calculated and stored for use in the kinetic model.

In this work we only consider large particles for which radiation pressure is negligible. If smaller dust particles were considered in the model, the actual velocity of particles in each collision would also depend on their mass, due to radiation pressure. However, in such cases, the Monte Carlo code still needs only to be run once, assuming no radiation pressure for all particles, and the velocities can be scaled using particle β parameters when required in the kinetic model (the velocities are simply multiplied by $\sqrt{1-\beta}$). This effect is negligible for large particles and in this work we set $\beta = 0$ for all particles, for simplicity. Additionally, in this work the grid of eccentricities for which the Monte Carlo code is run only extends up to the chosen maximum initial eccentricity. That does not need to be the case. If smaller particles were included, which also end up on high-eccentricity orbits because of radiation pressure, the collision rates and velocities would simply be pre-calculated for a grid of eccentricities up to unity. In principle, one could in a similar manner also account for collisions with particles that end up on unbound orbits, but that is not presently implemented.

Furthermore, if very large bodies are considered, the impact velocity calculated from particle velocities from the Monte Carlo simulation should also be corrected for gravitational focusing. The modification to the cross-section is given by $1 + v_{\rm esc}^2/v_{\rm imp}^2$, where $v_{\rm esc}^2 = 2G(m_{\rm p}+m_{\rm t})/(s_{\rm p}+s_{\rm t})$. For $M_* = M_\odot$, $r = 50$ au, $s_{\rm t} = s_{\rm p} = 1$ km, $v_{\rm imp}^2 \sim 2\langle i^2\rangle v_{\rm K}^2$, $\sqrt{\langle i^2\rangle} = 10^{-3}$, this correction is only a few percent. Assuming the correction to the particle velocities is similarly small for these parameters, in this work we can safely neglect the role of gravitational focusing.

Table 1. Models we consider for the specific critical disruption energy, $Q_{\rm D}^*$.

Model	$Q_{\rm D}^*$
1	$10^7\,\frac{\rm erg}{\rm g}$
2	$5\times10^6\,\frac{\rm erg}{\rm g}\left(\left(\frac{s}{1\,\rm m}\right)^{-0.37}+\left(\frac{s}{1\,\rm km}\right)^{1.38}\right)$
3	$5\times10^6\,\frac{\rm erg}{\rm g}\left(\left(\frac{s}{1\,\rm m}\right)^{-0.37}+\left(\frac{s}{1\,\rm km}\right)^{1.38}\right)\left(\frac{v_{\rm imp}}{3\,\rm km/s}\right)^{0.5}$

3.1.3. Collisional outcomes

Collisions among particles result in catastrophic fragmentation, erosion and/or growth. To determine the outcome of a particular collision, we follow an algorithm employed in other state-of-the-art kinetic models of debris discs (see Löhne 2008; Löhne et al. 2017) with some minor variations.

The collisional outcome depends on the parameters of the collision (the impact velocity $v_{\rm imp}$ and the impact energy $E_{\rm imp} = m_{\rm t}m_{\rm p}/(m_{\rm t}+m_{\rm p})v_{\rm imp}^2/2$) and on the properties of the material out of which particles are assumed to be made. The key property of the material here is the critical specific energy for dispersal, Q^*, for which we consider 3 different models shown in Table 1 (with the most realistic model based on the results of Benz & Asphaug 1999). Following Stewart & Leinhardt (2009), we further define a joint critical specific energy for dispersal of both colliders, $Q_{\rm tp}^* = Q^*(s_{\rm tp})$, where $s_{\rm tp} = (s_{\rm t}^3 + s_{\rm p}^3)^{1/3}$.

If the specific impact energy is greater than the joint critical specific energy ($E_{\rm imp} > (m_{\rm t}+m_{\rm p})Q_{\rm tp}^*$), both colliders are catastrophically disrupted, and their total mass is distributed into a distribution of smaller fragments. The mass of the largest fragment is given by (Paolicchi et al. 1996)

$$m_{\rm lf} = \frac{1}{2}(m_{\rm t}+m_{\rm p})\left(\frac{E_{\rm imp}}{(m_{\rm t}+m_{\rm p})Q_{\rm tp}^*}\right)^{-1.24}. \tag{16}$$

If the above condition is not fulfilled, colliders lose some mass to erosion. We consider first the case where the target remains largely intact, yet the projectile may still be completely disrupted. We consider this to happen if half of the impact energy is sufficient to disrupt the projectile ($E_{\rm imp}/2 > m_{\rm p}Q^*(s_{\rm p})$). In this case, the target and the projectile are assumed to be eroded as a single body, with the eroded mass given by

$$m_{\rm frag} = \frac{1}{2}(m_{\rm t}+m_{\rm p})\left(\frac{E_{\rm imp}}{(m_{\rm t}+m_{\rm p})Q_{\rm tp}^*}\right), \tag{17}$$

and the mass of the largest fragment given by $m_{\rm lf} = 0.2m_{\rm frag}$. The single remnant of such a collision has mass $m_{\rm rem} = m_{\rm t}+m_{\rm p}-m_{\rm frag}$. In some cases, this may lead to net growth of the target ($m_{\rm rem} > m_{\rm t}$; Stewart & Leinhardt 2009).

The same outcome happens if the impact velocity is less than the critical sticking velocity (for which we adopt $v_{\rm stick} = 1\,\rm m\,s^{-1}$). However, note that in such a case the impact energy is so small that very little erosion is expected and the resulting remnant should be larger than either of the colliders.

Finally, if neither of the above conditions is fulfilled, both the target and the projectile are eroded and post-collision their remnants separate. In this case, it is assumed that half of the impact energy is spent on eroding the target and the other half on eroding the projectile. The eroded mass for each is calculated analogous to Eq. (17), but, using the values of the individual mass of each collider and their individual critical energy for dispersal, and only half of the impact energy. The total eroded mass is distributed into smaller fragments as above.

In this way, every collision results in loss of mass and the mass of the colliders is distributed over the phase-space grid as remnants and as fragments. First, the mass is distributed across the mass bins (we adopt the same power-law mass distribution of fragments as van Lieshout et al. 2014, $n(m) \propto m^{-11/6}$, corresponding to the power-law exponent of −3.5 for the distribution of sizes, extending up to $m_{\rm lf}$ and with the normalisation constant such that the total mass of fragments equals the eroded mass). Then, orbital elements of these remnants and fragments are determined and distributed over the grid. If a remnant is found to fall into the same bin as its parent body, a fraction of the cratered/accreted mass is moved to a lower/higher mass bin in order to more accurately model the transport of mass in a coarse grid.

A fragment orbit is determined by the location of the collision and the velocities and masses of the colliders (the particle pairs from the Monte Carlo simulation), and also by the effect of radiation pressure on the fragment. The location of the collision is estimated as being the centre-of-mass of the colliders, based on their positions from the Monte Carlo simulation[5]. The location of the collision represents the initial position of the fragments, **R**. The initial velocity, **V**, of each of the fragments is calculated from conservation of momentum, assuming maximal collisional damping (following Krivov et al. 2006; van Lieshout et al. 2014),

$$(m_1 + m_2)\mathbf{V} = m_1\mathbf{V}_1 + m_2\mathbf{V}_2, \tag{18}$$

where m_1 and m_2 are the masses of the colliders. Velocities of the colliders, $\mathbf{V}_1$ and $\mathbf{V}_2$, are the velocities of Monte Carlo particles scaled by their respective β parameters to account for the effect of radiation pressure, if radiation pressure is considered.

From the fragment's initial position and velocity the fragment's specific angular momentum **h** is calculated, and finally the orbital elements (Murray & Dermott 2000),

$$a = \left(\frac{2}{R} - \frac{V^2}{GM_*(1-\beta)}\right)^{-1}, \tag{19}$$

$$e = \sqrt{1 - \frac{h^2}{GM_*(1-\beta)a}}, \tag{20}$$

$$i = \arccos\left(\frac{h_z}{h}\right). \tag{21}$$

Here the scaling factor $(1-\beta)$ is added to account for the radiation pressure acting on the fragment; in this work we only consider large bodies for which radiation pressure is negligible and we simply set $\beta = 0$ for all particles.

The orbits of the remnants post-collision are calculated in the same way as for the orbits of the fragments. In other words, every collision results in maximal collisional damping of particle velocities.

[5] This choice minimises deviation from the conservation of momentum, which arises due to the finite difference in positions of the nearest neighbours in the Monte Carlo simulation.

3.2. The phase-space grid

We use the following grid for the discretisation of the phase space. For the mass we use 26 bins between the (mass corresponding to) particle radius of $s = 1$ mm and $s = 100$ m. The bins are log-spaced such that $m_{i+1}/m_i \approx 4$ ($s_{i+1}/s_i \approx 1.6$). The bulk density of particles is taken to be 3 g cm^{-3}.

For the eccentricity and the inclination we use 10 linearly spaced bins for each, between zero and $e_{\rm max}$ or $i_{\rm max} = e_{\rm max}/2$; these maximum values differ between models. Lastly, for the semi-major axis we use a single bin between 36 and 44 au. The numerical model described in this section can be run for multiple semi-major axis bins, in principle. In practice, collisional damping leads to artificially enhanced diffusion of particles through the semi-major axis grid, for the simple fragment distribution method implemented in this model. Since the evolution of semi-major axes is expected to be slow compared to evolution of particle eccentricities and inclinations (see Sect. 2), we limit our particles to a single semi-major axis bin.

4. Results

In all our models, we follow the evolution of a disc around a $M_* = 1\,{\rm M}_\odot$ star. All simulations start with a power-law mass distribution ($n(m){\rm d}m \propto m^{-11/6}{\rm d}m$) of bodies 1 mm to 100 m in size (spanning our entire mass grid), placed into a single semi-major axis bin extending from $a_{\rm min} = 36$ au to $a_{\rm min} = 44$ au, with a total mass of the disc $M_{\rm d} = 1\,M_\oplus$. As discussed in previous sections, the evolution of the semi-major axes of particles due to collisional damping is neglected in this work. These model parameters have been chosen so that even the largest bodies damping timescales (calculated using Eq. (5)) are shorter than 1 Gyr, which is for how long we run all our simulations.

The eccentricities and inclinations of the particles are initially uniformly distributed between zero and $e_{\rm max}$ and $i_{\rm max} = e_{\rm max}/2$, respectively. We consider two sets of values for these parameters: a high-excitation disc with $e_{\rm max} = 0.2$ and a low-excitation disc with $e_{\rm max} = 0.01$. Together with the rest of the model parameters, these two sets of values ensure that we probe both systems in which the damping rate is faster and slower than the fragmentation rate, or in other words, both systems in which the critical projectile-to-target mass ratio is larger and smaller than unity. For both low-excitation and high-excitation discs we further consider three different, increasingly realistic models for the specific critical disruption energy, $Q^*_{\rm D}$, shown in Table 1. First, for simplicity, we consider a constant value (model 1), then we consider a more realistic size-dependent function (model 2), and, lastly, the full size and velocity-dependent function (model 3). In Fig. 1 we illustrate how the approximate initial critical projectile-to-target mass ratio ($Y_{\rm c} = 2Q^*_{\rm D}/v^2_{\rm imp}$) varies with particle size in these 6 different disc models. This approximate critical ratio aids the discussion of our results throughout this section, although it is not directly used in our kinetic model (for the description of how collisional outcomes are implemented in the model, see Section 3.1.3).

We present our results in the following order. First, in Sect. 4.1, as a test of our model, we consider a disc in which particles can only bounce off each other, inelastically, but without any cratering or fragmentation. Then, in Sects. 4.2 and 4.3 we consider a collisional cascade with fragmentation and cratering, with different excitation levels and with different, increasingly realistic, material strength prescriptions, as outlined above.

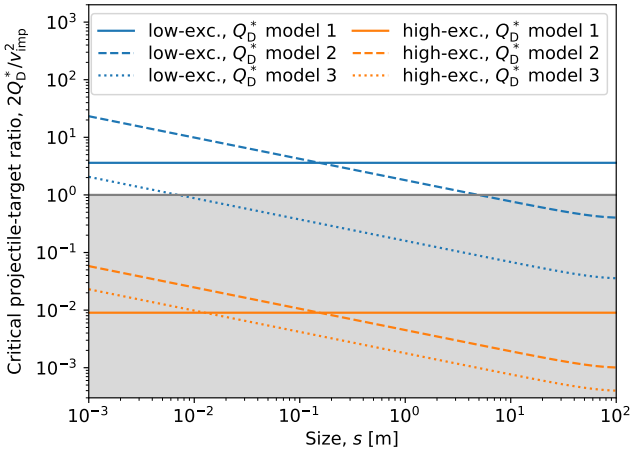

Fig. 1. Approximate initial critical projectile-to-target mass ratio (Y_c) for the models considered in Sects. 4.2 and 4.3. Blue and orange lines are for low-excitation ($e_{max} = 0.01$) and high-excitation discs ($e_{max} = 0.2$), respectively, and the different line styles are for different Q_D^* models shown in Table 1; see plot legend. Here for the average impact velocity we adopt $v_{imp} = v_K e_{max}/2$, evaluated at the centre of the belt, at 40 au. The nearly power-law size-dependence is due to only considering sizes up to 100 m, which are all in the strength regime of material strength. Where the mass ratio shown is higher than unity, the exact value of it is unphysical, as the assumptions behind the simple formula break down, as discussed in Sect. 2. Nevertheless, this figure shows for which parameters we expect the disc evolution to be dominated by fragmentation, as opposed to bouncing or cratering.

4.1. Inelastic bouncing of indestructible particles

To test our numerical model, we first consider a disc of indestructible particles. Each collision leads to complete damping of the relative velocity between particles, but the particles remain whole and separate, there is no mass evolution. As expected, this leads to damping of the average eccentricity and inclination, as shown in Fig. 2. Particles are only damped down to the lowest-value grid bins of the kinetic model, and so the damping is limited artificially (this is an unfortunate consequence of discretisation which is present in other work as well, e.g. Brahic 1977; Lithwick & Chiang 2007). As the average eccentricities and inclinations approach these artificial lowest values, the damping slows down. To some degree this is also due to discretisation (see Fig. B.3), but for the smaller bodies there is also a physical reason for this – collisional stirring by the larger bodies whose eccentricities and inclinations are damped more slowly. Overall, the model results in damping by a factor of 10 within 1 Gyr.

We can compare these results to a damping timescale from a simple particle-in-a-box model, that is, to the inverse of rate R_{damp} given by Eq. (5). In Fig. 2, the particle-in-a-box damping timescales for different particle sizes are shown as filled circles. Particle eccentricities fall off by a factor of ∼2 in a single particle-in-a-box damping timescale, and it takes about 10 times longer than the damping timescale to completely damp eccentricity and inclination for any given particle size; this is in line with results from N-body simulations (Brahic 1977; Lithwick & Chiang 2007). We do not make a direct, quantitative comparison with these studies because of differing assumptions (complete damping is assumed in our model, while the N-body simulations assume nonzero elasticity).

Far above our artificial size distribution cut-off at the size of 1 mm, the particle-in-a-box damping timescale depends on the particle size as $\propto s^{1/2}$ (see Sect. 2). The results of our kinetic model agree well with this in both the low-excitation and the high-excitation disc. However, there is a factor of ∼2 difference in the damping timescale in the high-excitation and the low-excitation numerical model (the left and the right-hand-side panel of Fig. 2). This is contrary to the simple particle-in-a-box estimate of the damping rate, which does not depend on the level of excitation in the disc. We ascribe this to over-simplification in the particle-in-a-box model. In obtaining Eq. (2), both the volume of interaction and the relative velocity are assumed to be proportional to the average inclination, which then cancels out. In the kinetic model (and in reality), both quantities depend in a more complex way on both eccentricity and inclination. For example, in the particle-in-a-box model we set the disc width to be the width of our semi-major axis bin, whereas particle pericentres and apocentres are outside of that range, and depend on particle eccentricities.

4.2. Collisional cascade with fixed material strength

Here and in the following section, we consider collisional cascades where the mass of particles in each size bin evolves due to fragmentation, cratering, and, if velocities are sufficiently damped, growth. In this section, we assume a constant specific critical disruption energy Q_D^* for all particles (model 1 in Table 1). We consider the full realistic Q_D^* prescription (models 2 and 3 in Table 1) in the following section.

The overall mass evolution of our collisional cascades agrees well with previous analytic and numerical work (e.g. Dominik & Decin 2003; Krivov et al. 2006; Thébault & Augereau 2007; Wyatt et al. 2007, see Appendix B for a more detailed comparison). The time-evolving size distributions for the low-excitation and the high-excitation models are shown in Fig. 3. On the collisional timescale of largest bodies a steady-state is established, and after that the size distribution shape varies very little. The total mass in the system decreases steadily with time, as the mass in the largest bodies is ground down to the lowest sizes, below which it is considered to be lost. In reality mass is lost when particles are fragmented below the radiation pressure blowout size. In our models the lower-size cutoff is set instead to 1 mm. This should not affect the evolution of the disc model overall, although it does introduce an artificial over-abundance of 1 mm grains, as there are no smaller projectiles to collide with for them. This is analogous to the over-abundance of grains just above the blowout size limit that is present when modelling the full size distribution (e.g. Campo Bagatin et al. 1994; Krivov et al. 2006; van Lieshout et al. 2014).

The evolution of the average eccentricities and inclinations for particles of various sizes are shown in Fig. 4 for the low-excitation and the high-excitation disc model, in the left-hand-side and right-hand-side panels, respectively. The results are entirely consistent with the basic theory laid out in Sect. 2. For the low-excitation disc, the approximate critical projectile-to-target mass ratio evaluates to $Y_c \sim 4$ for the approximate average impact velocity (see Fig. 1). Indeed, in the low-excitation disc, eccentricities and inclinations are efficiently damped, on practically the same timescales as in our inelastic-bouncing models (compare with left-hand-side panel of Fig. 2). Looking at the distributions of eccentricity and inclination (see left-hand-side column in Fig. 5), we also find that mass is redistributed into lower-e and lower-i bins faster than it is lost to destructive-collisional evolution of the disc.

Conversely, in the high-excitation disc the eccentricities and the inclinations are not damped by the end of the simulation, and

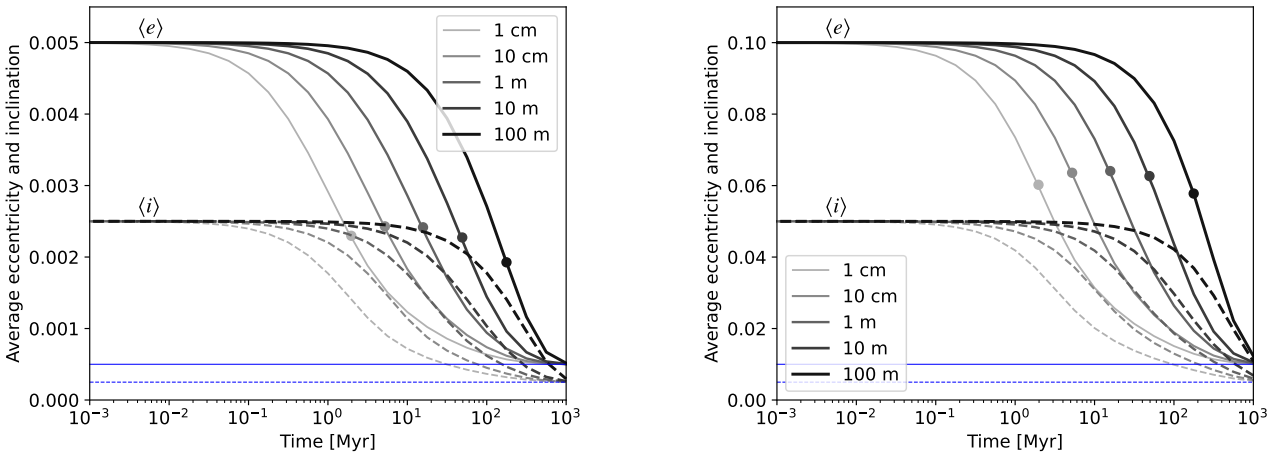

Fig. 2. Evolution of average eccentricity (solid lines) and inclination (in radians; dashed lines) in a disc of indestructible particles, inelastically bouncing off each other in collisions. The left- and right-hand-side panels show a low-excitation disc and high-excitation disc, respectively. Horizontal blue lines show the lowest grid bin values, i.e. the lowest values to which eccentricity and inclination can be damped in the model. Circles on solid curves indicate damping timescales predicted by a simple particle-in-a-box model. See Sect. 4.1.

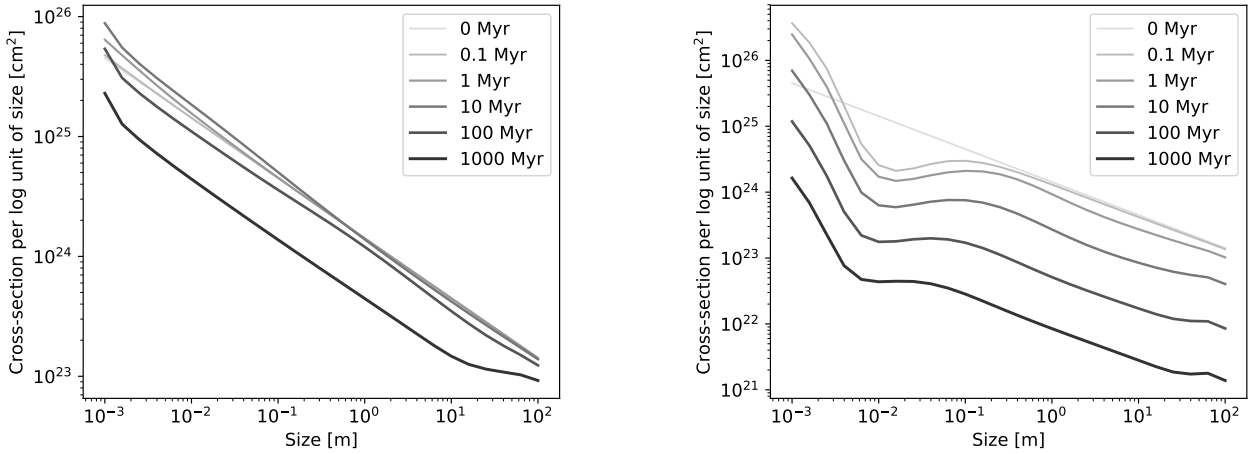

Fig. 3. Cross-section area per base-10 logarithmic unit of size at different times (see plot legend) in a model of a collisional cascade with constant $Q_{\rm D}^*$ (model 1 in Table 1). The left- and right-hand-side panels show a low-excitation disc and high-excitation disc, respectively. See Sect. 4.2.

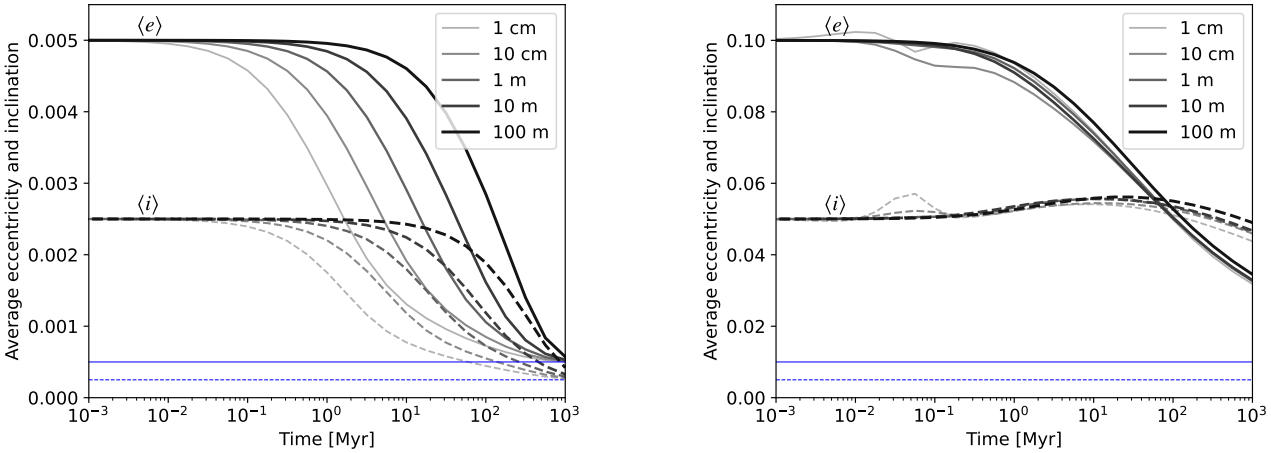

Fig. 4. Evolution of average eccentricity (solid lines) and inclination (in radians; dashed lines) in a model of a collisional cascade with constant $Q_{\rm D}^*$ (model 1 in Table 1). The left- and right-hand-side panels show the low-excitation disc and high-excitation disc, respectively. Horizontal blue lines show the lowest grid bin values, i.e. the lowest values to which eccentricity and inclination can be damped in the model. See Sect. 4.2.

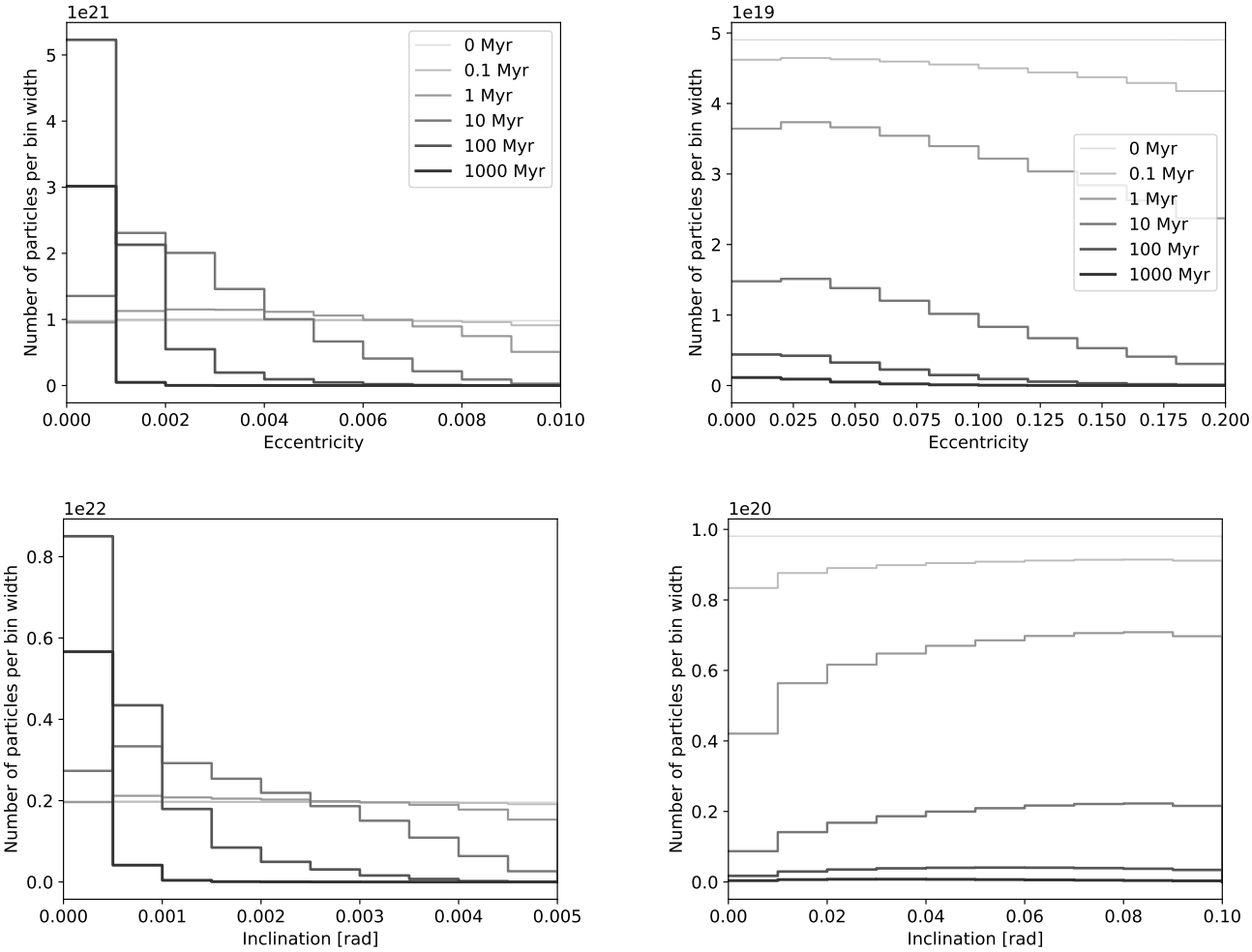

Fig. 5. Evolution of eccentricity (top panels) and inclination (bottom panels) distributions for 1 m bodies in the models shown in Figs. 3 and 4. The left- and right-hand-side panels show low-excitation disc and high-excitation disc, respectively. See Sect. 4.2.

the inclinations in particular change very little over the course of 1 Gyr. The initial approximate critical projectile-to-target mass ratio is $Y_c \sim 10^{-2}$ for this disc (see Fig. 1). In this case, distributions of eccentricity and inclination are shaped by destructive collisions. The right-hand-side top and bottom panel of Fig. 5 show how the number of 1 m bodies monotonously decreases with time in all eccentricity and inclination bins. The decrease is faster for higher eccentricities and for lower inclinations, consistent with the damping of the average eccentricity and the slight increase in the average inclination seen in Fig. 4; the reasons for this are discussed in detail in the rest of this section. The results are also remarkably independent of particle size.

The different evolution of eccentricities and inclinations can be explained by how the destruction rate depends on a particle's eccentricity and inclination. We illustrate this using the Monte Carlo code described in Sect. 3.1.2. We calculate the geometric part of the collision rate of a target on orbits of varying eccentricity and inclination with a population of projectiles with uniform distributions as in the initial conditions of our kinetic models. Figure 6 shows how the geometric collision probability (top panel) mainly depends on the target inclination, peaking for targets on low-inclination orbits, moving through the densest region of the disc near midplane, and the impact velocity (middle panel) mainly depends on target eccentricity. The geometric collision probability also decreases with increasing eccentricity of the target, because the particles on high-eccentricity orbits spend considerable time outside of the high-density centre of the belt (for these particular parameters, for which the width of the belt in terms of semi-major axes, $a_{max} - a_{min}$, is comparable to the radial width of high-eccentricity orbits being considered). Nevertheless, the geometric part of the collision rate (bottom panel) peaks for high eccentricities and for low inclinations of the target. The destruction rate, as opposed to the collision rate shown here, has further dependence on the velocity, as only collisions above the critical impact velocity will result in fragmentation. This further amplifies the loss rate for particles on high-eccentricity orbits. Overall, thus, Fig. 6 shows why in our high-excitation disc the average eccentricity decreases with time, and why the average inclination initially increases. At later times, the average inclination is also decreasing with time, perhaps because some of these trends in how the destruction rates depend on inclination change after the eccentricities are damped to some degree. In general, as the eccentricity and inclination distributions of both targets and projectiles change over time so do the collision and destruction rates of objects on different orbits. Because of this, our results may be sensitive to our initial conditions and different initial distributions should be explored in future work.

Destructive collisions do not only destroy particles, they also produce them (i.e., they produce fragments and remnants). We find that the production of particles typically has the opposite

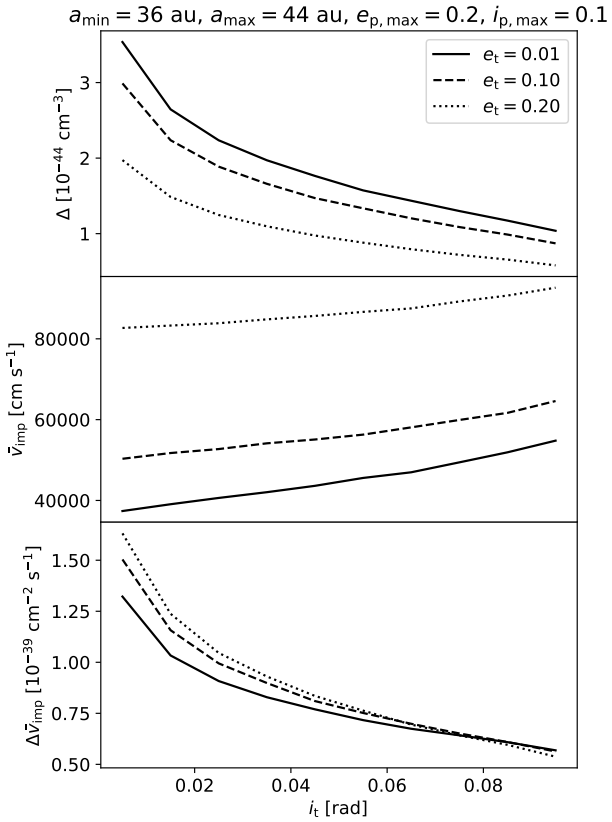

Fig. 6. Geometric collision probability (top), average impact velocity (middle), and the geometric part of the collision rate (bottom) in the high-excitation simulation discussed in Sect. 4.2, as a function of the eccentricity e_t and the inclination i_t of target particles colliding with projectiles with uniform distributions of eccentricity and inclination from 0 to $e_{p,max} = 0.2$ and $i_{p,max} = 0.1$, respectively, calculated using the Monte Carlo code described in Sect. 3.1.2. Both targets and projectiles have uniform distributions of semi-major axis with $a_{min} = 36$ au and $a_{max} = 44$ au, as in our disc models. In these simulations, we use 10^5 particles in each Monte Carlo population. The collision rate is maximised for high eccentricities and low inclinations of the target. See Sect. 4.2.

effect from destruction: if destruction damps eccentricities of bodies of a particular size, production will typically increase them. This is likely a consequence of the fragments inheriting the velocity distribution of their larger parent bodies: the parent bodies are also being preferentially destroyed at higher eccentricities, producing fragments at higher eccentricities. Nevertheless, through inspection of loss and gain rates in our kinetic model we find that the destruction dominates the change rates of the average eccentricity and inclination, although the effects are of the same order of magnitude. This is to be expected in a collisional cascade, where the disc is losing mass and for each size bin the loss rate is at least somewhat higher than the gain rate. An additional possible reason for this imbalance in the evolution of the average eccentricities may be that bodies are indeed inheriting the eccentricity distribution of the destroyed larger bodies, but not exactly. Due to collisional damping the newly created particles should have at least somewhat lower eccentricities than the destroyed ones. However, given the small projectile-target mass ratio in our high-excitation disc, most fragments will simply have inherited a velocity distribution very close to that of the massive target.

Another key feature of how the high-excitation disc evolves is that the ratio of the average eccentricity to the average inclination drops from the initial factor of 2 to a bit below unity. This is contrary to findings of, for example, Brahic (1977), where the system that initially has a different eccentricity-to-inclination ratio evolves towards the value of ∼2. This is a simple consequence of our assumption of complete collisional damping. With zero elasticity in physical collisions (and also from not having any gravitational interactions as in, for example, Ida & Makino 1992), there is nothing pushing the system towards energy equipartition.

We can further confirm our interpretation of these results by looking into what types of collisional outcomes govern the evolution of the average eccentricity and inclination. In our kinetic model phase space the average eccentricity as a function of particle size is calculated as

$$\langle e\rangle(j_m) = \frac{\sum_{j_e,j_i} n(j_m, j_e, j_i) e(j_e)}{\sum_{j_e,j_i} n(j_m, j_e, j_i)}, \tag{22}$$

where the denominator equals $n(j_m)$, the number of particles in mass bin j_m, and j_e and j_i are eccentricity and inclination bin indices. Its change rate is given by

$$\frac{\mathrm{d}\langle e\rangle(j_m)}{\mathrm{d}t} = \frac{1}{n(j_m)} \sum_{j_e,j_i} \frac{\mathrm{d}n(j_m, j_e, j_i)}{\mathrm{d}t} \left(e(j_e) - \langle e\rangle(j_m)\right). \tag{23}$$

Analogous equations can be written down for the average inclination. Here we can separate the change rate of the number of particles, $\mathrm{d}n(j_m, j_e, j_i)/\mathrm{d}t$, into contributions from different collisional outcomes. However, it is technically difficult to separate this into the exact collisional outcomes itemised in Sect. 3.1.3. After the pre-calculation phase in our code, during time evolution, this information is not kept, to reduce computational costs. Instead, we can separate the change rate into:

(1) the rate at which particles of size j_m are produced in collisions in which neither of the colliders is from the same size bin (this is production through fragmentation or cratering),
(2) the rate at which mass is removed from size bin j_m and moved to a different size bin (this is destruction of particles), and
(3) the rate at which mass is removed from and re-added to size bin j_m in collisions where at least one of the colliders is from the same size bin (i.e. mass is being moved across the eccentricity and inclination grid, but not the mass grid).

We show the results of this analysis in Fig. 7. As expected, in the high-excitation disc, the change rate is determined by the balance between pure destruction and production of particles by fragmentation and cratering.

In the low-excitation model the change rate of both eccentricity and inclination is governed by the third 'category' of collisions. These collisions are associated with some of the mass remaining in the same mass bin. This is in line with our theoretical expectations that collisions in low-excitation discs mostly result in cratering/bouncing, with efficient collisional damping. However, the rates included in category 3 on Fig. 7 also include collisions in which a projectile from the size bin j_m is completely destroyed in a collision with a larger body, but then a fragment of the same size is created in that collision (i.e. a part of the larger body). We cannot differentiate between those two collisional outcomes at runtime in our simulations.

4.3. Collisional cascade with size- and velocity-dependent material strength

In this section, we continue our exploration of collisional damping in collisional cascades, now with more realistic material

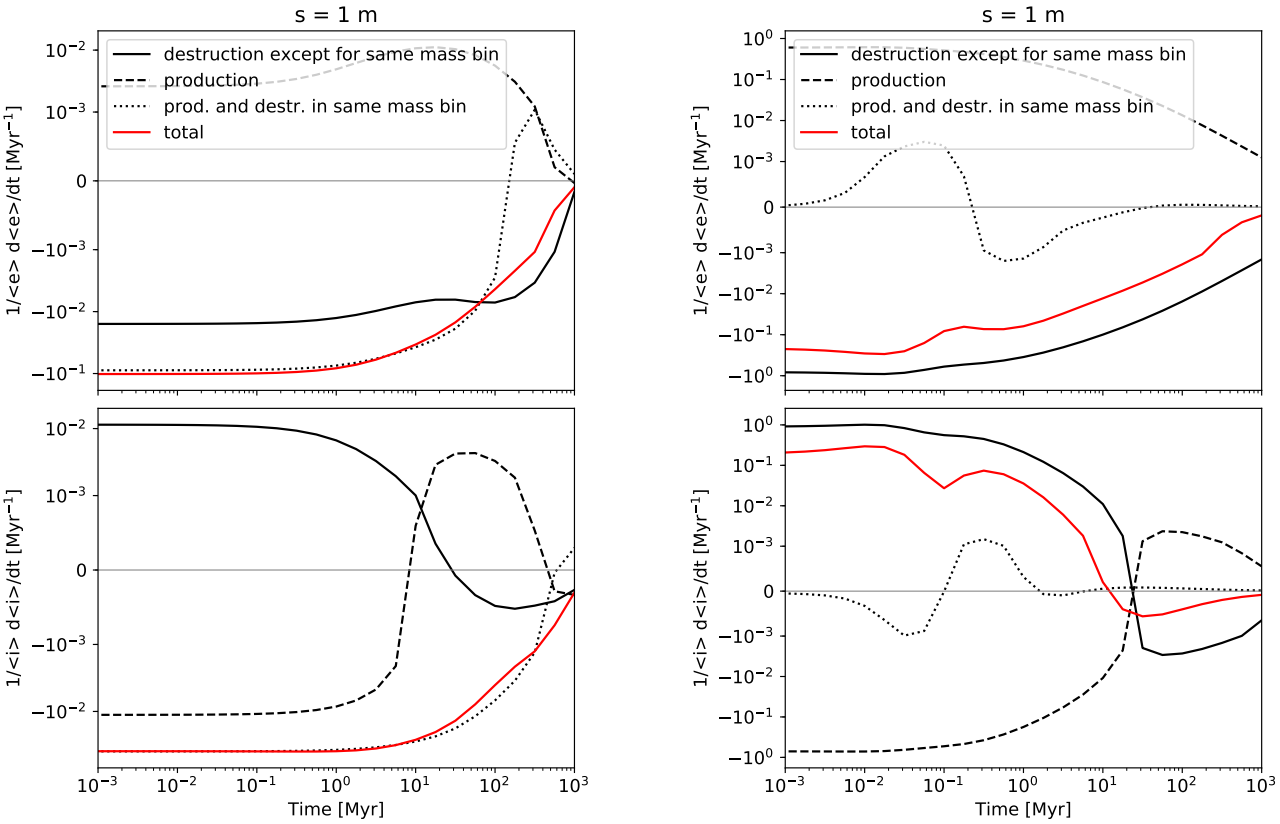

Fig. 7. Rate of change of average eccentricity (top panels) and inclination (bottom panels) for 1 m bodies in the models shown in Figs. 3 and 4. The left- and right-hand-side panels show low-excitation disc and high-excitation disc, respectively. The total rate of change is shown in red colour, while the black lines show how different types of collisions contribute to the total rate (see plot legend and the explanation of the classification of collisions in Sect. 4.2).

properties. To produce the results shown in Figs. 8 and 9, we use models 2 and 3 for $Q_{\rm D}^*$ from Table 1, respectively. Model 2 for $Q_{\rm D}^*$ accounts for the size-dependence of material strength, and model 3 additionally includes the velocity dependence.

We find that the eccentricities and the inclinations in the high-excitation disc evolve similarly regardless of the exact values of $Q_{\rm D}^*$ (see the similarity in the right-hand-side panel of Fig. 4 with the right-hand-side panels of Figs. 8 and 9). In all 3 models of the high-excitation disc the particle projectile-to-target mass ratio is much smaller than unity for all particles (see the orange lines in Fig. 1) and in all 3 models collisional damping is much less efficient than predicted by the indestructible-particles model (compare with the right-hand-side panel of Fig. 2).

For our low-excitation disc parameters, with these realistic prescriptions for material strength we probe an interesting regime where the expected critical projectile-to-target mass ratio is above unity for smaller particles, and below unity for larger ones (see the dashed and the dotted blue lines in Fig. 1). In such systems we expect the efficiency of damping to depend on particle size (in addition to how the collisional/damping timescale depends on particle size even if damping is efficient). Indeed, in our low-excitation disc, with our model 2 for $Q_{\rm D}^*$ (the dashed blue line in Fig. 1), we find that the velocities of the smallest bodies are damped on practically the same timescale as in our test indestructible-particles model, while for the largest bodies the average eccentricity and the inclination are not fully damped by 1 Gyr (compare the left panel of Fig. 2 with the left panel of Fig. 8). The differences are quite small, however, because the critical projectile-to-target mass ratio is still near unity even for the largest bodies.

In our low-excitation disc with our model 3 for $Q_{\rm D}^*$ the critical projectile-to-target mass ratio is (initially) less than one for all but the smallest particles (see the dotted blue line in Fig. 1), and in this case we find that the damping efficiency depends on particle size more strongly, albeit still weakly overall. The results for this model are shown in the left panel of Fig. 9. Interestingly, for all sizes, but especially for the largest particles, the evolution of the average eccentricities and inclinations evidently resembles more the evolution in the high-excitation disc than in the previously discussed low-excitation models (compare the left and the right panel of Fig. 9). In other words, there is a gradual transition in our results as a function of the projectile-to-target mass ratio across different models. In this particular model, large bodies evolve the same as in our high-excitation disc, because they are easily disrupted in collisions. Small bodies' inclinations are initially damped, but that damping slows down at one point, likely because the larger bodies are easily disrupted (on their own longer collisional timescale), producing smaller bodies with larger inclinations (because the larger bodies' inclinations are not damped).

Overall, comparing the different models presented here, we find that collisional damping becomes gradually less efficient (the damping timescale gradually increases) as the initial typical critical projectile-to-target mass ratio decreases below unity, when more bodies can be catastrophically disrupted. However, if the projectile-to-target ratio is much smaller than unity, the evolution of the average eccentricity and inclination appear to

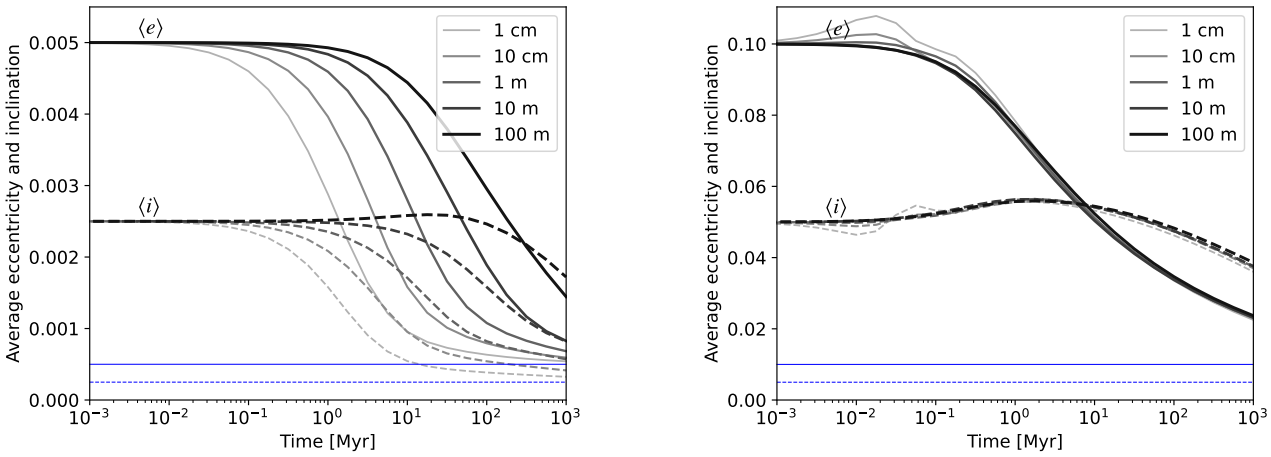

Fig. 8. Same as Fig. 4, but for size-dependent material strength ($Q^*_{\rm D}$ model 2 in Table 1). See Sect. 4.3.

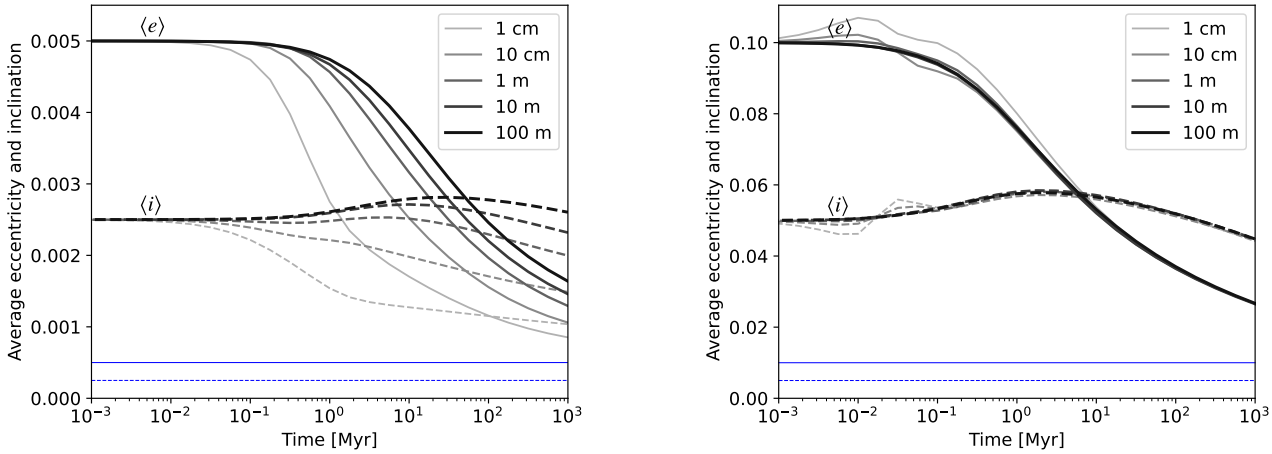

Fig. 9. Same as Fig. 4, but for size- and velocity-dependent material strength ($Q^*_{\rm D}$ model 3 in Table 1). See Sect. 4.3.

not depend on its value (see the similarity in our results for the high-excitation disc when using different $Q^*_{\rm D}$ models). In this regime any damping occurs because of how the eccentricity and inclination distributions are shaped by destructive collisions, as discussed in the previous section.

5. Discussion

In this section we discuss how our results apply to pre-stirred debris discs, implications for stirred discs, implications for small dust grains affected by radiation pressure, and lastly we discuss some of the limitations of our numerical approach.

5.1. Pre-stirred debris discs

The results presented in this work can be directly applied to pre-stirred discs, as we assume that discs start out with some distributions of eccentricities and inclinations and we do not account for any subsequent stirring that may occur through gravitational interactions between bodies in the disc. Here we discuss what our results imply for potential observations of pre-stirred discs. While our results are not directly applicable to evolution or observations of ∼µm-sized dust grains (since such grains are not included in the model), those are discussed separately further below.

We find that if the critical projectile-to-target mass ratio for dust particles is well below unity the disc evolution is fragmentation-dominated rather than damping-dominated, the average particle inclination evolves very slowly, and it is approximately the same for all particle sizes at any given time. As observations at a given wavelength probe mostly particles of size of the order of that wavelength, these discs would be observed to have a scale-height that does not vary with observing wavelength. Therefore, a vertically thick disc with wavelength-independent scale-height does not necessarily imply a viscously stirred disc to maintain that height.

Additionally, for such discs our model predicts that the ratio of the average eccentricity and the average inclination decreases over time to less than unity, in contrast with the value of $\langle e\rangle/\langle i\rangle \sim 2$ expected from energy equipartition in a disc of gravitationally interacting particles (Ida & Makino 1992). This ratio could be observationally constrained, in principle, by measuring radial and vertical widths of narrow debris rings. If found to be unexpectedly small, it could be a sign of catastrophic collisions shaping the distributions of eccentricities and inclinations. However, it should also be recognised that such narrow rings could be different to the model discs in this work, in which we assume a non-negligible dispersion of particle semi-major axes.

If the critical projectile-to-target mass ratio approaches unity, collisional damping becomes more efficient. Because smaller particles are stronger in collisions (in the strength regime)

and because their collision rate is higher, smaller particles are damped faster than larger ones. These discs may be observed to have a scale-height that increases with observing wavelength.

For the critical projectile-to-target mass ratio above unity, and for collisional timescales shorter than system age, particle inclinations are strongly damped. In observations this would appear as a very thin disc with an unresolved scale-height. The eccentricities would also be damped, but the disc would still be radially wide if its semi-major axis distribution is wide. Overall, if debris discs are in general pre-stirred, we may expect to observe two types of discs: vertically thick discs where the collision velocity is higher than the critical velocity derived above, and discs with very small vertical heights, perhaps unresolved in observations (with caveats discussed further below).

The critical projectile-to-target mass ratio is size-dependent and velocity-dependent. This has two important consequences. Firstly, in this work we only considered particles held together by material strength which become weaker with increasing size. However, above a few 100s of metres particles are held together by gravity, and they become stronger with increasing size. Therefore, at the top of the collisional cascade damping may be more efficient than for the intermediate particle sizes. This may have implications for the collisional evolution of the disc, its dust production and its observability, as discussed further below.

Secondly, due to the velocity dependence of the critical projectile-to-target mass ratio, the *true* damping rate (unlike the classical damping rate, $R_{\rm frag}$) may be a non-monotonous function of semi-major axis. In a wide disc it may have a minimum at some distance from the star, and so the dust scale-height may have a minimum at some distance from the star, increasing both radially inwards and outwards. This is because at shorter distances collision velocities are higher, the critical projectile-to-target mass ratio is lower and damping becomes less efficient. Conversely, if damping is efficient, the damping timescale increases radially outwards because the collision velocities and collision rate are lower radially outwards. This is illustrated with an example in Fig. 10.

We have focused on the importance of the critical projectile-to-target mass ratio as the parameter controlling the level of collisional damping. Equivalently, given a model for $Q^*_{\rm D}(s, v_{\rm imp})$ (e.g. the commonly used expression named model 3 in Table 1), damping will be inefficient if collision velocities are above a critical impact velocity that is a solution to $1 = 2Q^*_{\rm D}(s, v_{\rm imp})/v^2_{\rm imp}$. For mm-sized dust grains, using the model 3 from Table 1, we find a critical velocity of $v_{\rm crit} \sim 40\,{\rm m\,s^{-1}}$. We use this value in the discussion further below, but note that it is derived using a $Q^*_{\rm D}$ model designed for much higher ($\sim {\rm km\,s^{-1}}$) impact velocities. Therefore, this specific threshold could change if a collisional model more suitable for low-velocity disruptive impacts were adapted.

Using this critical velocity and the simple collisional model discussed in Sect. 2, we can consider if collisional damping is efficient or inefficient (relative to the classical damping rate given by Eq. (5)) in different types of debris discs. The typical collision velocity in a disc can be estimated as $v_{\rm rel} \sim v_{\rm kep} i \sim v_{\rm kep} h$, where i is the typical inclination and h the aspect ratio of the disc (and the latter can be measured for some discs). Thus, for a given mass of the central object M_* and disc radius a, there is a critical value of the aspect ratio, $h_{\rm crit} = v_{\rm crit}/v_{\rm kep}$. For an exo-Kuiper belt ($M_* = 2\,{\rm M}_\odot$, $a = 100\,{\rm au}$), $h_{\rm crit} = 0.01$; for a disc around a white dwarf ($M_* = 0.6\,{\rm M}_\odot$, $a = 1\,{\rm R}_\odot$), $h_{\rm crit} = 10^{-4}$; for a planetary ring ($M_* = 1\,{\rm M}_{\rm Saturn}$, $a = 10^5\,{\rm km}$), $h_{\rm crit} = 0.002$. If $h < h_{\rm crit}$, collision velocities are small in the system and collisional damping is efficient. This does not necessarily mean that such a disc would be observed to be very thin and unresolved, because that would still require the damping timescale to be shorter than the system age. In our example exo-Kuiper belt (assuming disc mass of $M = 1\,{\rm M}_\oplus$, $\Delta a/a = 0.2$, $\rho_{\rm b} = 3\,{\rm g\,cm^{-3}}$, $s_{\rm max} = 1\,{\rm km}$), the damping timescale of mm-sized dust grains is about 30 Myr, so damping may be ongoing in young exo-Kuiper belts.

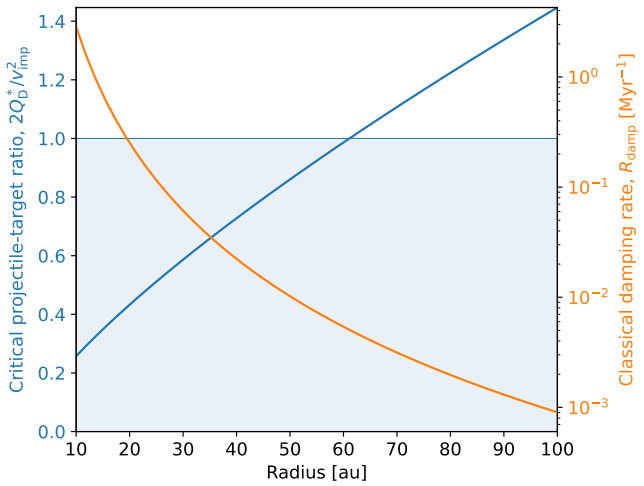

Fig. 10. Example calculation of critical projectile-to-target mass ratio (in blue) and the classical damping rate given by Eq. (5) for 1 mm grains as functions of radius in a wide disc around a solar-mass star, with particle $Q^*_{\rm D}$ given by model 3 in Table 1, an average eccentricity of $\langle e \rangle = 0.01$, particles ranging from 1 µm to 100 m in size with a power-law size distribution exponent $q = 3.5$, and a disc mass of $0.1\,{\rm M}_\oplus$. This example illustrates how, in a wide disc, collisional damping may be a non-monotonous function of radius: inefficient at short radii due to low projectile-to-target ratio and slow at large radii due to low collisional rate, with a 'sweet spot' in the middle where damping is both efficient and fast enough to be observed assuming, for example, a system age of 100 Myr. See Sect. 5.1.

If $h > h_{\rm crit}$, collision velocities are high and damping is inefficient. However, this does not mean that the typical inclination or the disc thickness has not decreased within the system age. Even in high-excitation discs we found eccentricities and inclinations can decrease due to preferential destruction of particles on certain orbits. This decrease occurs on a timescale much longer than the classical damping timescale of the largest bodies in the disc. For exo-Kuiper belts this *true* damping timescale is too long, but for other debris systems that timescale may still be much shorter than the system age. In our example discs around a white dwarf and a planetary ring, assuming a disc mass of $M = 1\,{\rm M}_{\rm Moon} = 0.01\,{\rm M}_\oplus$ (and other disc parameters as above), the classical damping rate of 1 km bodies evaluates to 10^{-3} and 10^{-4} yr, respectively. These are tiny fractions of Gyr-long lifetimes of these debris discs and so, even if it takes much longer to reduce the average particle inclination, we may expect that the disc thickness has decreased significantly within the system lifetime, despite the high collision velocities.

Furthermore, to be observable, debris discs also need to remain bright enough, that is, the fragmentation timescale of the largest bodies in the disc must not bee too short, or else the disc loses mass too quickly (e.g. Wyatt et al. 2007). On the other hand, if a disc initially consists only of large bodies, their fragmentation timescale also needs to be short enough for the bodies to have produced the observable small dust; in this case there is a lower limit on the initial excitation of the disc. Furthermore, to observe any damping, the damping timescale (the real

one, not the idealised one from Eq. (5)) must be shorter than the system age. However, if the damping timescale is too short and particle velocities are severely damped, collisions of large bodies would not produce the small dust that can be observed. Growth, instead of fragmentation, may then govern the evolution of the disc, reducing the disc luminosity (Kenyon & Bromley 2002a), followed potentially by a revival if this leads to formation of (dwarf) planets that can stir the disc (Kenyon & Bromley 2004). Even before damping occurs in such a disc there may be very little dust – since efficient damping requires a critical projectile-to-target mass ratio of unity or higher, such a disc would rely on cratering to create smaller particles. These timescales depend on several poorly constrained factors, such as the size of the largest bodies present in the disc, see Eq. (2).

Several previous studies considered the evolution of mass and velocity in pre-stirred discs. Kenyon & Bromley (2002a) and Kenyon & Bromley (2004) found that very-high-excitation discs lose mass and become non-observable before inclinations are damped. This is consistent with the fragmentation rate being much higher than the damping rate if the critical projectile-to-target mass ratio is much less than unity. In less extreme cases, they found that making bodies weaker led to particles damping more rapidly. This appears to be a consequence of assuming that damping acts at the rate equivalent to the one given by Eq. (5) in catastrophic collisions. However, if mass and velocity evolution are fully coupled and both catastrophic and cratering collisions are assumed to be fully dissipating, as in our simulations, the opposite occurs (making bodies weaker results in slower damping). It is less clear why in their results the eccentricity is found to decrease with increasing particle size for the smallest particles. This may be due to the collisional/damping timescale for the smallest particles being increased due to the lower-size cut-off (we observe this effect to some degree in our simulations), or perhaps due to other effects included in their simulations and not in ours, such as dynamical friction.

Furthermore, Krivov et al. (2005) studied pre-stirred discs using the same sort of kinetic approach as in our work, except that they did not include orbital inclinations in their phase space. Their disc models are similar to our high-excitation, fragmentation-dominated discs in which the eccentricity distribution is shaped by how the collisional probability depends on the eccentricity. They found that particles on orbits with both the smallest and largest eccentricities are preferentially depleted, in contrast to our models where only particles with the largest eccentricities are preferentially removed. This is because the collision probability in their models, calculated analytically, increases for low eccentricities. However, in a belt that is wider than the typical eccentricity, we do not expect and do not observe that dependence (see Fig. 6).

5.2. Viscously stirred discs

Our numerical simulations model pre-stirred discs, but many studies have argued that the large bodies present in debris discs gravitationally stir all particles in the disc, and that this viscous self-stirring can explain the levels of excitation in the observed debris discs (e.g. Kenyon & Bromley 2002b, 2004, 2008, 2010; Kennedy & Wyatt 2010; Krivov & Booth 2018). Damping mechanisms can still act in viscously stirred discs, although it is often found in numerical simulations that they are not significant if very large bodies are formed through accretion (Kenyon & Bromley 2002b, 2004, 2008, 2010). For such discs our results imply that collisional damping becomes less and less important over time as the velocities in the disc become more excited by viscous stirring.

Pan & Schlichting (2012) argued, using an analytical model, that the velocity dispersion (or, equivalently, the inclination dispersion) of particles of different sizes is determined by an equilibrium between viscous stirring and collisional damping. For bodies participating in the collisional cascade (all except for, maybe, the largest bodies) and for $q < 4$ (q being the size distribution exponent), they considered two types of damping: collisional damping through collisions with equal-sized bodies and collisional damping through catastrophic collisions. Based on our results, the former would occur only if the projectile-to-target size ratio is of the order unity or larger. Notably, in that regime collisional cascades might be driven purely by cratering/erosion, which might require a different form of mass conservation to be considered, compared to the one used in their study.

If the projectile-to-target size ratio is less than one (or it becomes less than one due to stirring), the second type of damping applies. However, it should be noted that velocities are not really damped in this case. Rather, it should be understood as the case in which particles are destroyed at the same rate at which they are stirred. That is analogous to our study of the balance between damping and destruction rates. However, it is unlikely that stirring can be balanced in this way. Indeed, it could occur that particles of a certain size are being destroyed faster than their velocities can be increased by stirring, but at the same time these particles would be continually produced in collisions of larger bodies. Newly created fragments would have a velocity dispersion inherited from their parent bodies, which is not accounted for by the analytical model. If the critical projectile-to-target mass ratio is much less than one, fragments in the collisional cascade inherit the velocities of the large bodies. Since these large bodies can be stirred to higher velocities (their damping and fragmentation rates are lower), the small particles would also be effectively stirred to higher velocities than implied by the equilibrium calculated using this analytical model. Ultimately, the velocities of all particles may be equal to the velocities of particles at the top of the collisional cascade in this case.

Either way, it should also be noted that the equilibrium might not be reached in the observed debris discs. For example, the fragmentation rate might be lower than the viscous rate, but fast enough to deplete the disc before it is stirred to the equilibrium value. The viscous stirring rate may also increase over time as the largest bodies grow (Kenyon & Bromley 2002b, 2004, 2008, 2010).

5.3. Small dust grains

The smallest sub-micron-sized dust grains produced in collisions in debris discs are expelled from the disc by radiation pressure, on orbital timescales, and the smallest micron-sized grains that remain bound are put on high-eccentricity orbits (e.g. Krivov et al. 2006). As a result, their fragmentation timescale is fairly independent of the level of excitation in the disc (Thébault & Wu 2008). Due to these high eccentricities, the critical projectile-to-target size ratio is likely to be less than unity for these particles (although material strength is found to increase with decreasing particle size for small bodies, and these micron-sized grains are inferred to be be quite strong; Benz & Asphaug 1999). Therefore, based on our results in this paper, we hypothesise that collisional damping is inefficient for these particles. Instead, these particles likely inherit their inclinations from their parent bodies. Their observed scale-height may decrease with time if the

inclinations of their parent bodies are damped. That would occur on the fragmentation timescale of the parent bodies.

It has been proposed that if physical collisions of these particles are not maximally damping (i.e., if there is some elasticity), some of the kinetic energy associated with their high eccentricities is redistributed into vertical direction, so that collisions increase their inclinations instead of damping them (Thébault 2009). A consequence of this would be, for example, that the average inclination decreases as a function of size for these particles, which could be measured with scattered light observations. Implications of our findings are not straight-forward in this case. On the one hand, numerical models of Thébault (2009) only included bouncing collisions and we expect these particles to fragment and become smaller in collisions, instead of bouncing off and increasing their inclination dispersion. Any increase in the scale-height should be reflected in the distribution of their fragments, which are likely to be unbound and leave the system quickly. On the other hand, it has been argued by Thébault (2009) that these dust grains may act as projectiles in collisions in which grains of the same size are ultimately produced as fragments, with similar inclinations as would result from bouncing collisions. This deserves further study with a numerical method that incorporates both the velocity and mass evolution of these particles – such as the method employed in our work.

5.4. Limitations

Throughout the paper we stressed the advantages of the kinetic approach (Krivov et al. 2005, 2006; van Lieshout et al. 2014) used in this work. It allows to model concurrently and in a fully coupled manner both the mass and the velocity evolution of a circumstellar disc. The results presented show the importance of this in our understanding of the collisional evolution of debris discs. However, there are several important limitations.

The kinetic approach considers the evolution of particles in a phase space of particle size and select orbital elements. For an axisymmetric disc it is sufficient to consider semi-major axis, eccentricity and inclination. The numerical approach necessitates discretisation of this phase space. As a consequence, changes in particle eccentricities and inclinations that are smaller than the bin widths are neglected. Additionally, if a particle moves to a different bin, it is instantly assumed to be moved to the centre of that bin. To check how this influences our results, we run some of our models at different grid resolutions, that is, with different number of eccentricity and inclination bins. These tests are shown and discussed in Appendix B. In short, we find that for those models where damping is efficient (critical projectile-to-target ratio of order unity or larger) the damping rate in our models is to some degree influenced by grid resolution: with smaller bin widths, damping is slightly faster. In spite of that, our main conclusions still hold, and the lack of significant damping when the critical projectile-to-target ratio is much smaller than one does not appear to depend on grid resolution.

Furthermore, in this work we neglected the evolution of semi-major axis. This has been justified by the findings of Brahic (1977) and Lithwick & Chiang (2007) that semi-major axes evolve on much longer timescales than eccentricities and inclinations, and this study focuses on the evolution of the latter. However, for real debris discs, it is still possible that the semi-major axis distribution may evolve within system ages. This is especially true for smaller bodies whose collisional timescales are short. General expectations for that case have been outlined by Brahic (1977), who show how long-term spreading of the disc eventually leads to some particles falling onto the star, as well as to a decrease of collisional rates. In the case of high-excitation discs in which collisional damping is inefficient, the findings of Krivov et al. (2005) apply: particles at shorter semi-major axis are preferentially depleted due to shorter collisional timescales.

There are several other assumptions in our work that may need to be questioned in future work. We assume that particles have initially uniform distributions of eccentricities and inclinations, whereas assuming something akin to a Rayleigh distribution may be more appropriate (e.g. Brahic 1977; Ida & Makino 1992; Lissauer & Stewart 1993). Ideally, after some time these distributions are independent of the initial conditions in the model, but this might also not be the case in the models where they evolve slowly, such as our high-excitation disc models. Furthermore, we neglect any elasticity in collisions, assuming maximal efficiency of collisional damping in each single collision. The impact energy is assumed to be fully dissipated and the velocity of all particles post-collision is assumed to equal the pre-collision centre-of-mass velocity of the colliders; orbits of both remnants and fragments in both catastrophic and cratering collisions are determined by this. This assumption maximises the rate at which the average eccentricity and inclination decrease with time. In reality, the level of dissipation likely depends on the collisional outcome and collision geometry (e.g. catastrophic collisions dissipate more energy than cratering ones, and more energy is dissipated in head-on versus grazing impacts; Fujiwara 1986; Leinhardt & Stewart 2012). We expect that our results in the high-velocity regime would not change with different dissipation assumptions, because in that regime the low projectile-to-target mass ratio makes damping insignificant in any case. At low collision velocities damping could be less significant in real discs than it is in the results of our simulations, although it would always be present to some degree as collisions are always inelastic. All in all, most of these limitations can be addressed in future work, and the general kinetic approach used in this work is a very important tool for studying the collisional mass and velocity evolution of debris discs.

6. Conclusions

We present a kinetic model of the collisional evolution of debris discs that includes the evolution of orbital inclinations in addition to the evolution of particle masses and orbital eccentricities. We applied this model to pre-stirred discs with different levels of excitation and with particles of different material strengths. We explored how inelastic collisions change particle eccentricities and inclinations over time. Our main results can be summarised as follows:

1. Our model reproduces the basic theoretical expectations regarding the collisional damping of indestructible particles in discs. In discs in which particle mass can be changed by cratering and catastrophic disruption, the critical projectile-to-target mass ratio determines how efficient collisional damping is.
2. If the critical projectile-to-target mass ratio is of order unity or larger (low-excitation discs and/or particles with high material strength), collisions mostly leave colliders intact and particle eccentricities and inclinations are damped over time at a similar rate to the case where particles are indestructible.
3. As the critical projectile-to-target mass ratio falls below unity, the damping timescale becomes longer. This is because collisional damping is most efficient in collisions of bodies of similar mass, and in this case those collisions result in catastrophic disruption. Collisions with projectiles smaller

than the critical size leave targets largely intact, but they do not result in significant damping, and overall the destruction rate is higher than the damping rate.
4. If the critical projectile-to-target mass ratio is much smaller than one (high-excitation discs and/or discs in which particles are made of weak materials), eccentricities and inclinations evolve slowly, and their evolution is driven by the destruction probability being slightly different for particles on different orbits. In this regime, the damping rate does not depend on the exact value of the projectile-to-target ratio in the range explored. Furthermore, the average eccentricity and inclination are independent of size at all times, meaning that the scale-height of such a disc would appear the same at different wavelengths. We also find that the average eccentricity decreases faster than the average inclination.
5. For mm-sized dust grains, we expect the critical projectile-to-target mass ratio to fall below unity at impact velocities higher than $\sim 40\,\mathrm{m\,s^{-1}}$. For impact velocities much higher than this critical velocity, we expect collisional damping to be inefficient in changing the velocity distribution with which mm-sized grains are produced, or in counteracting viscous stirring from large bodies in the disc.
6. Both the collisional timescales and the critical projectile-to-target mass ratio are important factors in determining whether collisional damping can significantly affect eccentricities and inclinations and vertical scale-heights in a debris disc.

Acknowledgements. We thank the referee for their helpful and constructive comments. We thank Jessica Rigley, Rik van Lieshout, Sebastian Marino and Nicole Pawellek for helpful discussions. MRJ acknowledges support from the European Union's Horizon Europe Programme under the Marie Sklodowska-Curie grant agreement no. 101064124, funding provided by the Institute of Physics Belgrade, through the grant by the Ministry of Science, Technological Development, and Innovations of the Republic of Serbia, and support by the UK Science and Technology Research Council (STFC) via the consolidated grant ST/S000623/1.

References

Artymowicz, P. 1997, Annu. Rev. Earth Planet. Sci., 25, 175
Benz, W., & Asphaug, E. 1999, Icarus, 142, 5
Bottke, W. F., Nolan, M. C., Greenberg, R., & Kolvoord, R. A. 1994, Icarus, 107, 255
Brahic, A. 1977, A&A, 54, 895
Brahic, A., & Henon, M. 1977, A&A, 59, 1
Campo Bagatin, A., Cellino, A., Davis, D. R., Farinella, P., & Paolicchi, P. 1994, Planet. Space Sci., 42, 1079
Daley, C., Hughes, A. M., Carter, E. S., et al. 2019, ApJ, 875, 87
Dohnanyi, J. S. 1969, J. Geophys. Res., 74, 2531
Dominik, C., & Decin, G. 2003, ApJ, 598, 626
Fujiwara, A. 1986, Mem. Soc. Astron. Italiana, 57, 47
Hales, A. S., Marino, S., Sheehan, P. D., et al. 2022, ApJ, 940, 161
Han, Y., Wyatt, M. C., & Matrà, L. 2022, MNRAS, 511, 4921
Hornung, P., Pellat, R., & Barge, P. 1985, Icarus, 64, 295
Hughes, A. M., Duchêne, G., & Matthews, B. C. 2018, ARA&A, 56, 541
Ida, S., & Makino, J. 1992, Icarus, 96, 107
Kennedy, G. M., & Wyatt, M. C. 2010, MNRAS, 405, 1253
Kennedy, G. M., Marino, S., Matrà, L., et al. 2018, MNRAS, 475, 4924
Kenyon, S. J., & Bromley, B. C. 2002a, AJ, 123, 1757
Kenyon, S. J., & Bromley, B. C. 2002b, ApJ, 577, L35
Kenyon, S. J., & Bromley, B. C. 2004, AJ, 127, 513
Kenyon, S. J., & Bromley, B. C. 2008, ApJS, 179, 451
Kenyon, S. J., & Bromley, B. C. 2010, ApJS, 188, 242
Kenyon, S. J., & Luu, J. X. 1999, AJ, 118, 1101
Kobayashi, H., & Tanaka, H. 2010, Icarus, 206, 735
Krivov, A. V., & Booth, M. 2018, MNRAS, 479, 3300
Krivov, A. V., Sremčević, M., & Spahn, F. 2005, Icarus, 174, 105
Krivov, A. V., Löhne, T., & Sremčević, M. 2006, A&A, 455, 509
Leinhardt, Z. M., & Stewart, S. T. 2012, ApJ, 745, 79
Lissauer, J. J., & Stewart, G. R. 1993, in Protostars and Planets III, eds. E. H. Levy, & J. I. Lunine, 1061
Lithwick, Y., & Chiang, E. 2007, ApJ, 656, 524
Löhne, T., Krivov, A. V., Kirchschlager, F., Sende, J. A., & Wolf, S. 2017, A&A, 605, A7
Löhne. 2008, PhD thesis, Friedrich-Schiller-Universität Jena, Germany
Marshall, J. P., Milli, J., Choquet, E., et al. 2023, MNRAS, 521, 5940
Matrà, L., Wyatt, M. C., Wilner, D. J., et al. 2019, AJ, 157, 135
Murray, C. D., & Dermott, S. F. 2000, Solar System Dynamics (Cambridge University Press)
Najita, J. R., Kenyon, S. J., & Bromley, B. C. 2022, ApJ, 925, 45
Nakano, T. 1988, MNRAS, 230, 551
Olofsson, J., Thébault, P., Kral, Q., et al. 2022, MNRAS, 513, 713
Pan, M., & Schlichting, H. E. 2012, ApJ, 747, 113
Paolicchi, P., Verlicchi, A., & Cellino, A. 1996, Icarus, 121, 126
Quillen, A. C., Morbidelli, A., & Moore, A. 2007, MNRAS, 380, 1642
Rigley, J. K., & Wyatt, M. C. 2020, MNRAS, 497, 1143
Stewart, S. T., & Leinhardt, Z. M. 2009, ApJ, 691, L133
Terrill, J., Marino, S., Booth, R. A., et al. 2023, MNRAS, 524, 1229
Thébault, P. 2009, A&A, 505, 1269
Thébault, P., & Augereau, J. C. 2007, A&A, 472, 169
Thébault, P., & Wu, Y. 2008, A&A, 481, 713
Thébault, P., Augereau, J. C., & Beust, H. 2003, A&A, 408, 775
Trulsen, J. 1971, Ap&SS, 12, 329
van Lieshout, R., Dominik, C., Kama, M., & Min, M. 2014, A&A, 571, A51
Vizgan, D., Hughes, A. M., Carter, E. S., et al. 2022, ApJ, 935, 131
Wyatt, M. C. 2008, ARA&A, 46, 339
Wyatt, M. C., Smith, R., Greaves, J. S., et al. 2007, ApJ, 658, 569
Wyatt, M. C., Booth, M., Payne, M. J., & Churcher, L. J. 2010, MNRAS, 402, 657

Appendix A: Tests of the Monte Carlo code

We first test the Monte Carlo calculation of collision probabilities and impact velocities in two dimensions, by reproducing Fig. A.3 of Krivov et al. (2006), see Fig. A.1. The top panel shows the Δ-integral defined by Krivov et al. (2006), and the bottom panel shows the average impact velocity $\bar{v}_{\rm imp}$ between two test populations of particles on planar, eccentric orbits, calculated as (see Eq. (31), (32) in Wyatt et al. (2010) and Sect. 3.1.2)

$$\Delta = \sum_{r,\phi} \sigma_1(r,\phi)\sigma_2(r,\phi)/dV(r,\phi), \tag{A.1}$$

$$\bar{v}_{\rm imp} = \sum_{r,\phi} \sigma_1(r,\phi)\sigma_2(r,\phi)\langle v_{\rm imp}(r,\phi)\rangle/dV(r,\phi)/\Delta. \tag{A.2}$$

To obtain their figure A.3, Krivov et al. (2006) used 3D Monte Carlo simulations in which they assumed uniform distributions of particle latitudes. To obtain our Fig. A.1, we used 2D Monte Carlo simulations which implicitly assume the same, uniform distributions of particle latitudes. Our results do not account for the vertical components of particle velocities, but these are negligible for these test parameters, and the agreement between their results and ours is very good.

Next, we test the Monte Carlo code in three dimensions by reproducing (with reasonably good accuracy) a distribution of relative velocities between two populations of particles on inclined orbits given in figure 1 of Bottke et al. 1994, see Fig. A.2. This figure has already been reproduced by Wyatt et al. (2010), who first published the Monte Carlo code used here. Here the figure is recalculated directly from the output that feeds as input to the kinetic model, thereby testing the connection between the codes, and we also use it to illustrate the effect of varying the number of particles in the simulation. Throughout this paper we use $N = 10^4$ particles in each population in each Monte Carlo simulation, and Fig. A.2 shows that such sparse sampling is sufficiently accurate to reasonably approximate the velocity distribution and collision probability of colliding particles.

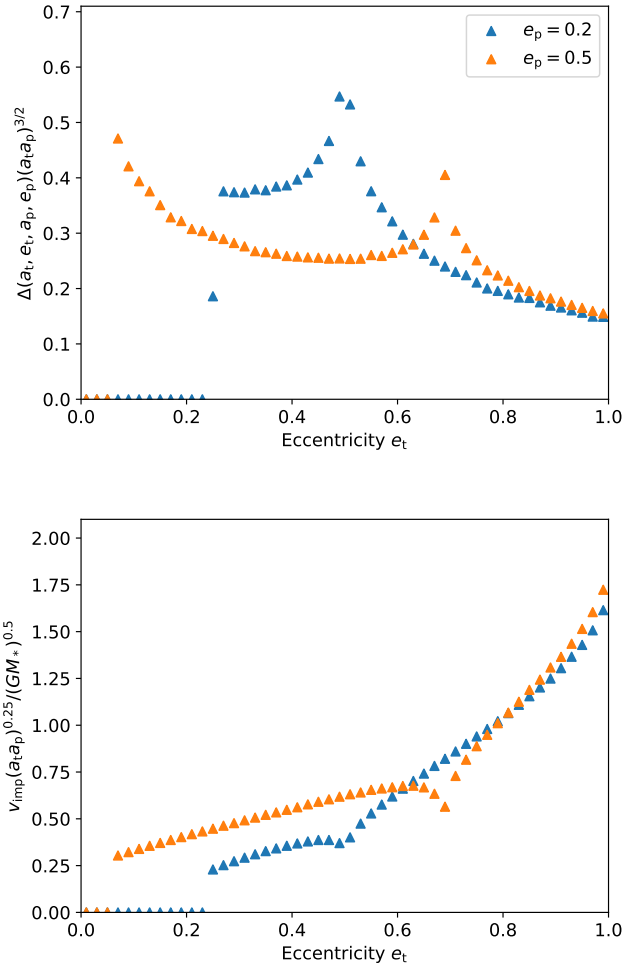

Fig. A.1. Test of the Monte Carlo code in 2D: geometric probability Δ (top panel) and the average impact velocity $\bar{v}_{\rm imp}$ (bottom panel), calculated for test populations with semi-major axes $a_t = 1.6, a_p = 1.0$ and assumed semi-opening angle $\epsilon = 8.5°$, using the Monte Carlo code in two dimensions, for comparison with figure A.3 of Krivov et al. (2006).

Appendix B: Tests of the kinetic model

Under the assumptions that a disc is vertically thin and that the vertical distribution of particles is fixed and uniform in particle latitude, collision rates can be calculated in '2D' using analytic formulae with approximate corrections for the vertical component (Krivov et al. 2006). To model the evolution of the disc, it is then sufficient to consider the phase space consisting only of semi-major axis (or pericentre distance) and eccentricity. In Figs. B.1 and B.2 we compare results of such '2D' models, obtained using the Monte Carlo approach presented in this paper and using the analytic approach as implemented by van Lieshout et al. (2014) with minor corrections. The parameters of the models are the same ones used throughout the paper for our high-excitation disc, and for the realistic specific critical disruption energy given by the model 3 in Table 1. We find that the results agree well.

Also shown in Figs. B.1 and B.2 are results of our full '3D' model of a high-excitation disc. In comparison with '2D' models, this model may be expected to feature somewhat faster evolution, because the '3D' model assumes a uniform distribution of inclinations, meaning the distribution of particle latitudes is strongly peaked around the disc midplane, leading to higher collision probabilities (Wyatt et al. 2010). Nevertheless, the distribution of inclinations in this particular '3D' model remains fairly flat throughout the duration of the simulation, and the results agree well with '2D' models.

We further compare all of these results with two analytic results on the evolution of collisional cascades. Firstly, in Fig. B.1, the thin blue line shows the power-law size distribution expected in a steady-state disc in which the specific critical disruption energy depends on the particle size as a power law, $Q^*_{\rm D}(s) \propto s^{\gamma}$, and in which the particle velocities are independent of particle size (see e.g. Pan & Schlichting 2012, we insert $\gamma = -0.37$, corresponding to the strength regime). The assumption of the particle velocities being independent of particle size is appropriate because the eccentricities and the inclinations do not evolve significantly in these high-excitation disc models. We find that over time all three models evolve to this power-law size distribution, with the exception of the smallest particle sizes. The relative uptick in the number of smallest-size particles is a well known feature of collisional cascades with a lower-size cutoff Campo Bagatin et al. (e.g. 1994); Krivov et al. (e.g. 2006); Thébault & Augereau (e.g. 2007). In real debris discs such a feature is expected at $\sim$ µm sizes, where the size distribution is expected to be cut off by radiation pressure. In our models the size cutoff and this feature are artificial numerical necessities.

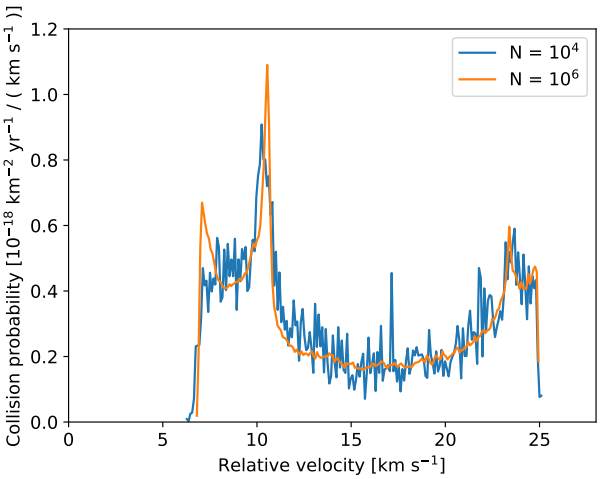

Fig. A.2. Test of the Monte Carlo code in 3D: distribution of intrinsic probability as a function of impact velocity between two test populations of particles with orbital elements $a_t = 3.42$ au, $e_t = 0.578$, $i_t = 0.435$ rad, and $a_p = 1.59$ au, $e_p = 0.056$, $i_p = 0.466$ rad, obtained using the Monte Carlo code, using 10^4 and using 10^6 particles in each population for the blue and the orange line, respectively, for comparison with figure 1 of Bottke et al. (1994), see also figure 4 of Wyatt et al. (2010).

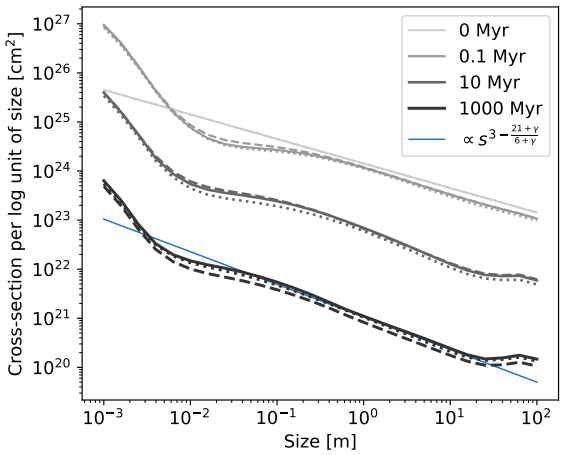

Fig. B.1. Cross-section area per base-10 logarithmic unit of size for '2D' models, for our high-excitation disc parameters, obtained using Monte Carlo collision rates (solid lines) and using analytically calculated collision rates (dashed lines), and also for a corresponding '3D' model (dotted lines). Results from the three models are shown as function of time (various shades of grey, see plot legend). Also shown is an analytically derived, arbitrarily scaled power-law describing a disc at steady-state, with bodies' critical specific disruption energy in the strength regime ($\gamma = -0.37$; thin blue line).

Secondly, it is well known that the total mass of a debris disc should decrease as a function of time approximately as $M(t) = M_0/(1 + ct)$ (Dominik & Decin 2003; Wyatt et al. 2007; Löhne 2008). Here the constant c has the meaning of the inverse of the initial collisional timescale of the largest bodies in the disc. In Fig. B.2, we compare the mass evolution of discs from the three '2D' and the '3D' models with this functional form, shown with the thin red dotted curve. For this we use a value of c obtained by fitting the thick green dotted curve (the '3D' model). Therefore, the overall shape of $M(t)$ from our models is in reasonably good agreement with the functional form derived analytically.

Finally, we test how our results depend on the grid resolution. In Fig. B.3 we show results for the evolution of average inclinations for 3 of our models presented in this paper with varying number of bins in the eccentricity (n_e) and the inclination (n_i) grids. We pick these 3 models so that we test convergence in 3 different evolution scenarios we encounter: efficient damping (top panel in Fig. B.3, shown in the main text in left panel in Fig. 4), inefficient damping (bottom panel in Fig. B.3, and right panel in Fig. 9) and a regime in between (middle panel in Fig. B.3, and left panel in Fig. 9).

We find that some of our results (in the top and the middle panel of Fig. B.3) do vary somewhat with the grid resolution. This is because of the limitation of the kinetic approach where we only consider particles to move to a different bin if the level of damping in a single collision is sufficiently large. Therefore, higher resolution (smaller bins) results in faster damping in our models, and the damping timescales are overestimated in our models. Nevertheless, there appears to exist a trend of convergence with increasing number of eccentricity and inclination bins, and the difference between $n_e = n_i = 10$ results (the resolution used throughout the paper) and $n_e = n_i = 20$ results is not too large with respect to all of the other uncertainties present in these numerical models. Importantly, the qualitative picture we established in the main text does not change with grid resolution: efficiency of collisional damping decreases with increasing collision velocities and decreasing material strength (i.e. there is a clear change in damping efficiency going from the top to the bottom panel of Fig. B.3, at any of the tested grid resolutions).

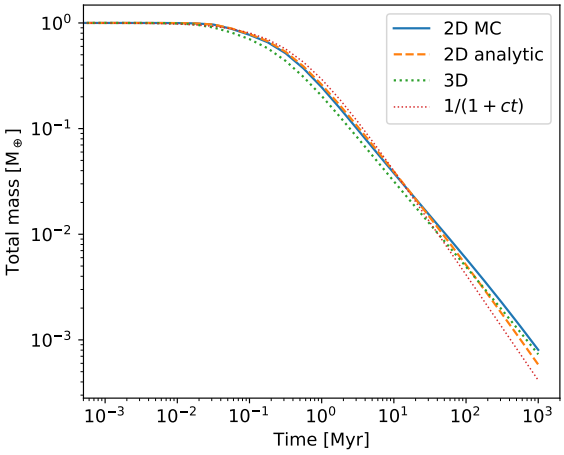

Fig. B.2. Total mass in the disc as function of time for the '2D' and the '3D' models, for our high-excitation disc parameters, and also the basic expectation for the evolution of disc mass from an analytic model (Wyatt et al. 2007), see plot legend.

Appendix C: Flowchart of numerical model

Figure C.1 illustrates the details of the numerical calculations in our model, including how the Monte Carlo simulations of Wyatt et al. (2010) and the kinetic model of van Lieshout et al. (2014) are coupled.

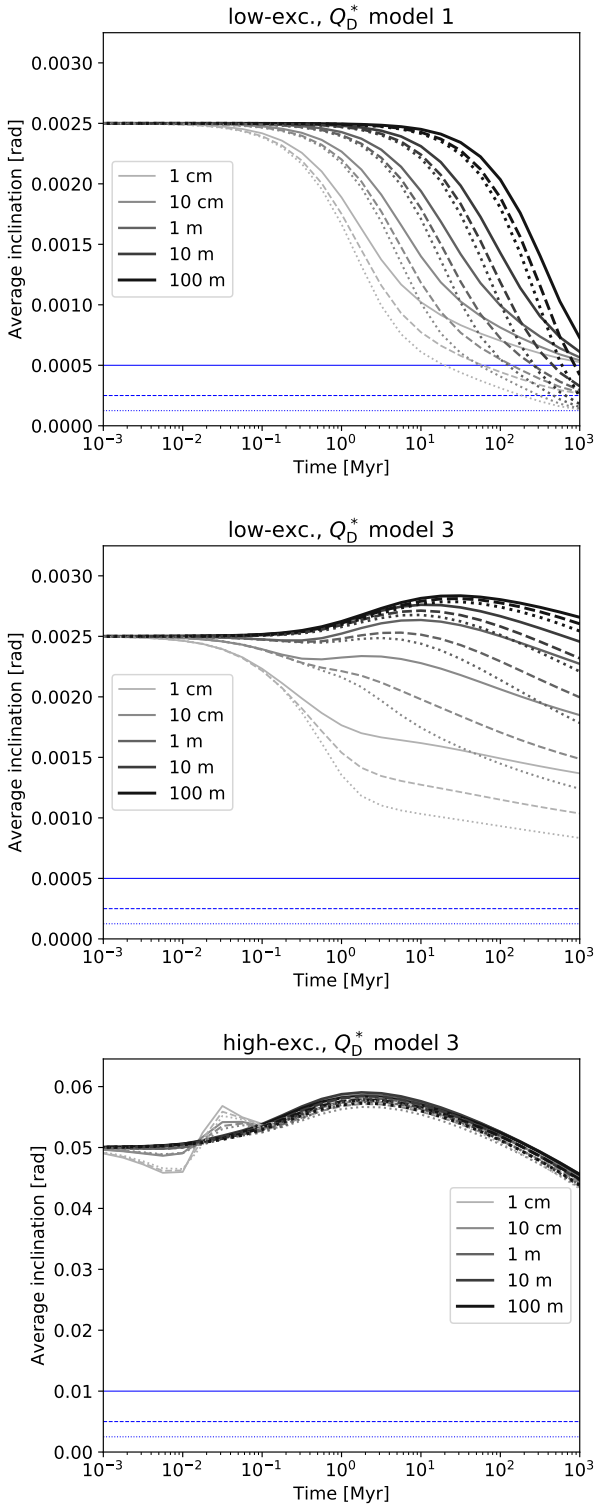

Fig. B.3. Resolution tests show average inclination as function of time, for different particle sizes (see plot legend), for three of our models (top panel: low-excitation disc using Q_D^* model 1; middle panel: low-excitation disc using Q_D^* model 3; bottom panel: high-excitation disc using Q_D^* model 3) for three different grid resolutions (solid lines: $n_e = n_i = 5$; dashed lines: $n_e = n_i = 10$; dotted lines: $n_e = n_i = 20$). Horizontal blue lines show the lowest grid bin values, i.e. the lowest values to which the average inclination can be damped in each model.

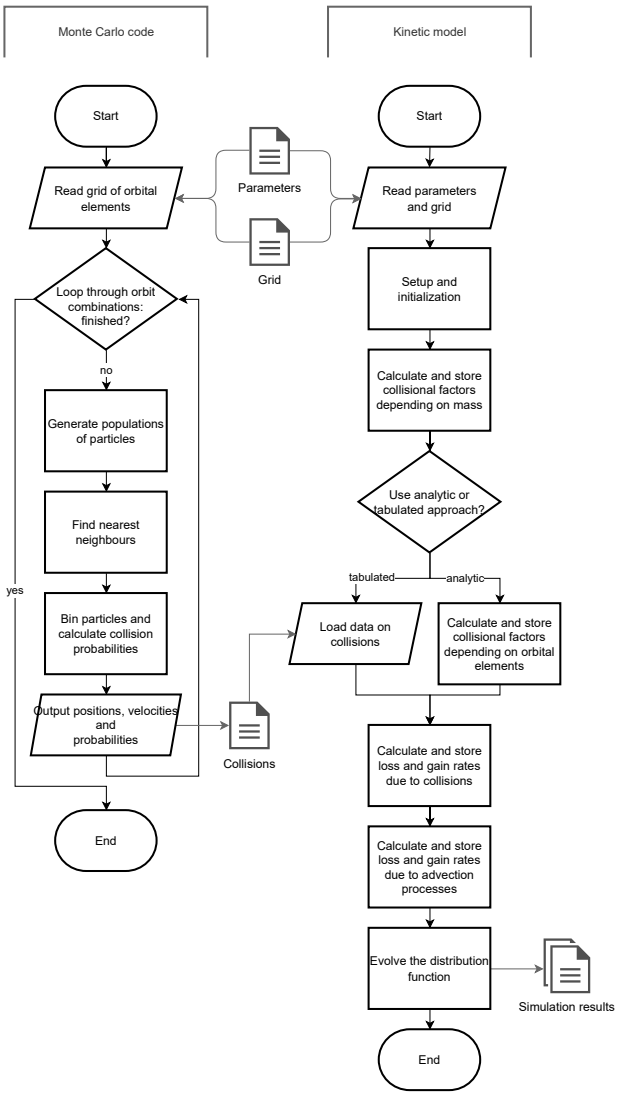

Fig. C.1. Flowchart illustrating the numerical model used in this work: Monte Carlo simulations (Wyatt et al. 2010, left column) are used to pre-calculate samples of collisional pairs and collision probabilities, and these are fed as input to the kinetic model of collisional evolution (van Lieshout et al. 2014, right column).

Monthly Notices of the ROYAL ASTRONOMICAL SOCIETY

MNRAS **515,** 507–524 (2022)
Advance Access publication 2022 June 25

https://doi.org/10.1093/mnras/stac1756

Vertical evolution of exocometary gas – I. How vertical diffusion shortens the CO lifetime

S. Marino [1,2]★ G. Cataldi [3,4] M. R. Jankovic [2] L. Matrà[5] and M. C. Wyatt [2]

[1]*Jesus College, University of Cambridge, Jesus Lane, Cambridge CB5 8BL, UK*
[2]*Institute of Astronomy, University of Cambridge, Madingley Road, Cambridge CB3 0HA, UK*
[3]*Department of Astronomy, Graduate School of Science, The University of Tokyo, Tokyo 113-0033, Japan*
[4]*National Astronomical Observatory of Japan, Osawa 2-21-1, Mitaka, Tokyo 181-8588, Japan*
[5]*School of Physics, Trinity College Dublin, the University of Dublin, College Green, Dublin 2, Ireland*

Accepted 2022 June 22. Received 2022 June 17; in original form 2022 February 25

ABSTRACT

Bright debris discs can contain large amounts of CO gas. This gas was thought to be a protoplanetary remnant until it was recently shown that it could be released in collisions of volatile-rich solids. As CO is released, interstellar UV radiation photodissociates CO producing CI, which can shield CO allowing a large CO mass to accumulate. However, this picture was challenged because CI is inefficient at shielding if CO and CI are vertically mixed. Here, we study for the first time the vertical evolution of gas to determine how vertical mixing affects the efficiency of shielding by CI. We present a 1D model that accounts for gas release, photodissociation, ionization, viscous evolution, and vertical mixing due to turbulent diffusion. We find that if the gas surface density is high and the vertical diffusion weak ($\alpha_{\rm v}/\alpha < [H/r]^2$) CO photodissociates high above the mid-plane, forming an optically thick CI layer that shields the CO underneath. Conversely, if diffusion is strong ($\alpha_{\rm v}/\alpha > [H/r]^2$) CI and CO become well mixed, shortening the CO lifetime. Moreover, diffusion could also limit the amount of dust settling. High-resolution ALMA observations could resolve the vertical distribution of CO and CI, and thus constrain vertical mixing and the efficiency of CI shielding. We also find that the CO and CI scale heights may not be good probes of the mean molecular weight, and thus composition, of the gas. Finally, we show that if mixing is strong the CO lifetime might not be long enough for CO to spread interior to the planetesimal belt where gas is produced.

Key words: methods: numerical – planetary systems – circumstellar matter – radiative transfer – astrochemistry.

1 INTRODUCTION

Over the last decade, it has become increasingly clear that circumstellar gas is present beyond the short ($\lesssim$10 Myr) protoplanetary disc phase in exoplanetary systems. This gas was first found decades ago (Slettebak 1975; Zuckerman, Forveille & Kastner 1995), but its ubiquity in systems with bright debris discs was only recently revealed (e.g. Moór et al. 2017; Iglesias et al. 2018; Rebollido et al. 2020). These dusty discs were known to be the result of collisions of large (at least km-sized) planetesimals (Wyatt 2008; Hughes, Duchêne & Matthews 2018; Marino 2022), but for a long time were considered gas free. Today, gas has been discovered in tens of systems mainly through CO emission lines around AFGM-type stars tracing cold gas (e.g. Dent et al. 2014; Marino et al. 2016; Matrà et al. 2019; Kral et al. 2020b), and UV and optical absorption lines tracing hot gas mainly around BA-type stars (Montgomery & Welsh 2012; Iglesias et al. 2018; Rebollido et al. 2018). The presence of gas for hundreds or thousands of Myr could have strong implications for the atmospheres of exoplanets as these could accrete this gas delivering volatiles to their atmospheres (Kral, Davoult & Charnay 2020a). Moreover, gas could also shape the dust spatial distribution (Takeuchi & Artymowicz 2001; Thébault & Augereau 2005; Krivov et al. 2009; Lyra & Kuchner 2013; Pearce, Krivov & Booth 2020; Olofsson et al. 2022), and thus understanding its evolution is important to correctly interpret the dynamics of these systems. In addition, in a few systems gas absorption lines have been shown to be variable and Doppler shifted, indicating that the hot gas originates from sublimating exocomets on highly eccentric orbits (e.g. Kennedy 2018). In this paper, we focus on the study of cold gas found at tens of au.

Where this cold gas originates from and how it evolves are one of the key current questions in debris disc studies. Two main scenarios have been proposed to explain it. First, the gas could be a leftover from the protoplanetary disc phase and dominated by hydrogen. In this scenario, some debris discs could be hybrid containing primordial gas that has not dispersed yet and secondary dust created by collisions (Kóspál et al. 2013). The hybrid scenario is motivated by the fact that a considerable fraction of debris discs around young A-type stars are gas-rich, containing vast amounts of CO gas that are comparable to protoplanetary discs around Herbig AeBe stars (Moór et al. 2017). Recent simulations have shown that primordial gas could survive for longer than expected in optically thin discs around A-type stars due to a weaker photoevaporation compared to later-type stars (Nakatani et al. 2021). This could potentially explain why gas-rich discs are found around A-type stars

★ E-mail: sebastian.marino.estay@gmail.com

© 2022 The Author(s)
Published by Oxford University Press on behalf of Royal Astronomical Society

Downloaded from https://academic.oup.com/mnras/article/515/1/507/6617989 by University of Cambridge user on 12 August 2022

preferentially. This model, however, has not yet been tested against the measured CO gas masses and constraints on its composition. As a way to determine the gas origin, recent surveys have searched for multiple molecules (apart from CO) that are normally detected in protoplanetary discs (Klusmeyer et al. 2021; Smirnov-Pinchukov et al. 2022). Those studies, however, have only led to non-detections implying abundances relative to CO orders of magnitude lower than those in protoplanetary discs. These results do not rule-out that the gas is primordial since, as shown by Smirnov-Pinchukov et al. (2022), the optically thin nature of debris discs means most molecules will be short lived and scarce.

On the other hand, the gas could be of secondary origin, i.e. released from volatile-rich solids as they fragment and grind down in the collisional cascade (Zuckerman & Song 2012; Dent et al. 2014). In this scenario, hydrogen-poor gas is continuously released and could viscously evolve spreading beyond the planetesimal belt (Kral et al. 2016), or could be blown out via stellar winds or radiation pressure if densities are low or the star has a high luminosity (Kral et al. 2021; Youngblood et al. 2021). This exocometary origin scenario has successfully explained the low levels of CO gas found in a few systems (e.g. Dent et al. 2014; Marino et al. 2016; Matrà et al. 2017). Once the CO gas is released, it should only survive for ∼130 yr due to interstellar UV photodissociating radiation (Visser, van Dishoeck & Black 2009; Heays, Bosman & van Dishoeck 2017), and thus the observed amount has been used to infer the rate at which CO gas was released. Since the gas release requires collisions between solids to free trapped gas or expose ices from their interiors, the gas release rate is a fraction of the rate at which mass is lost in the cascade. This fraction is approximately the mass fraction of volatiles in the planetesimals feeding the cascade, and was found to be consistent with Solar System comets (Marino et al. 2016; Matrà et al. 2017). If these planetesimals are similar in composition to Solar System comets, we would expect other molecules to be released as well. However, their short lifetime and low abundance in comets relative to CO makes their detection very challenging (Matrà et al. 2018).

The main problem with the secondary origin scenario has been to explain the several A-type stars with vast amounts of CO gas (e.g. Moór et al. 2017), which suggest CO lifetimes are much longer or gas release much higher than expected. Kral et al. (2019) found a solution by proposing that it is the carbon atoms, from previously photodissociated CO, that act as a shield. Carbon in neutral form (CI) has an ionization cross-section that covers all the CO photodissociation bands, and thus could become an effective shield prolonging the CO lifetime (Rollins & Rawlings 2012). In fact, CI has been found in some of these gas-rich/shielded discs adding supporting evidence to this scenario (Higuchi et al. 2019; Kral et al. 2019; Moór et al. 2019). This model is also successful at explaining the amounts of gas in the population of A-type and FGK-type stars with debris discs (Marino et al. 2020).

This solution and success of the secondary origin scenario to explain even the CO-rich systems has been recently challenged. Cataldi et al. (2020) pointed out that carbon is only an effective shield if it is vertically distributed in a geometrically thin, but optically thick surface layer completely far above and below the CO-rich mid-plane. Instead, if carbon and CO are vertically mixed, carbon shielding is weak and the observed vertical column densities may not be enough to explain the amount of CO gas in these discs. This finding emphasizes the importance of the vertical processes, in addition to the radial ones, in the evolution of the gas. Previous theoretical studies on exocometary gas have only looked at the radial evolution (e.g. Kral et al. 2016; Marino et al. 2020). This is why in this paper we focus for the first time in trying to understand the vertical evolution of the gas and how vertical diffusion affects carbon shielding. In Section 2, we present and describe a new model that takes into account photodissociation, vertical diffusion, ionisation, and viscous evolution of gas continuously released in a planetesimal belt. Section 3 presents the main findings and evolution of the gas for different model parameters. We discuss these results in Section 4 in terms of its implications for the known gas-rich debris discs, its uncertainties, how observations could shed light on the vertical mixing of carbon and CO, and some of the limitations of our model. Finally, in Section 5 we summarize the main conclusions of this paper.

2 MODEL DESCRIPTION

In this work, we focus on the vertical evolution of the exocometary gas taking into account the release of CO gas, its photodissociation, ionization of CI, viscous evolution, and vertical mixing through turbulent diffusion. This evolution is simulated with EXOGAS, a PYTHON package that we have developed and made available at https://github.com/SebaMarino/exogas. EXOGAS consists of two main modules, one to model the radial evolution of gas based on the simulations developed in Marino et al. (2020), and a new one that focuses on the vertical evolution that is presented below.

The vertical model consists of a one-dimensional distribution of gas as a function of height z in the middle of a planetesimal belt of radius r, where gas is being released. We assume that the released gas is pure CO and thus the C/O ratio of the gas is equal to one throughout our simulations. Note that the C/O ratio could be different in reality if other gas species that are abundant in comets were released as well (e.g. CO_2, H_2O). The presence of these additional species is, however, very uncertain due to the lack of observational constraints and the uncertain mechanism through which gas is released in the cold outer regions. Therefore, the gas in our model is composed of CO, its photodissociation products CI and OI, and ionized species CII and electrons. Note that since the C/O ratio is equal to one and we do not expect oxygen to be ionized (Kral et al. 2016), the number density of oxygen is simply equal to the carbon (CI + CII) number density and the number density of electrons is equal to the number density of CII. Therefore, of these five species only CO, CI, and CII need to be explicitly modelled and the total gas density (ρ) is equal to $\rho_{\rm CO} + \frac{28}{12}(\rho_{\rm CI} + \rho_{\rm CII})$.

The evolution of these three species is summarized in equations (1), (2), and (3). The CO gas evolution is ruled by the release of new CO gas ($\dot{\rho}^{+}$), the photodissociation of CO ($\dot{\rho}_{\rm ph}$), viscous evolution in the radial direction ($\dot{\rho}_{\rm vis,CO}$), and vertical diffusion ($\dot{\rho}_{{\rm CO},D}$). The CI gas evolution is ruled by the CO photodissociation, viscous evolution, diffusion, and ionization/recombination ($\dot{\rho}_{\rm ion}$). Finally, the evolution of CII is ruled by viscous evolution, diffusion, and ionization/recombination.

$$\frac{\partial \rho_{\rm CO}}{\partial t} = \dot{\rho}^{+} - \dot{\rho}_{\rm ph} - \dot{\rho}_{\rm vis,CO} + \dot{\rho}_{{\rm CO},D}, \quad (1)$$

$$\frac{\partial \rho_{\rm CI}}{\partial t} = \frac{12}{28}\dot{\rho}_{\rm ph} - \dot{\rho}_{\rm vis,CI} - \dot{\rho}_{\rm ion} + \dot{\rho}_{{\rm CI},D}, \quad (2)$$

$$\frac{\partial \rho_{\rm CII}}{\partial t} = \dot{\rho}_{\rm ion} - \dot{\rho}_{\rm vis,CII} + \dot{\rho}_{{\rm CII},D}. \quad (3)$$

These equations are solved numerically using finite differences and each individual processes (CO gas release, photodissociation, ionization, viscous evolution, and diffusion) is described below. Table A1 summarizes the definition and units of the most important parameters and variables.

Downloaded from https://academic.oup.com/mnras/article/515/1/507/6617989 by University of Cambridge user on 12 August 2022

2.1 Gas release

We assume the gas is released with a Gaussian vertical distribution with a scale height equal to H, i.e. with the same vertical distribution as in hydrostatic equilibrium. This assumption together with our viscous evolution treatment (Section 2.4) keeps the total gas density in hydrostatic equilibrium throughout the simulation and allows us to avoid having to model net vertical motions of the gas by solving the Navier–Stokes equations of classical fluid dynamics. Thus, CO gas is released in our 1D grid at a rate of

$$\dot{\rho}_+(z) = \dot{\Sigma}_+ \frac{e^{-\frac{z^2}{2H^2}}}{\sqrt{2\pi}H}, \tag{4}$$

$$H = c_s / \Omega_K, \tag{5}$$

where $\dot{\Sigma}_+$ is the gas release rate per unit surface at the centre of the belt, H is the gas scale height, Ω_K is the Keplerian frequency, and c_s is the isothermal sound speed. The sound speed and temperature (T) are set by

$$c_s = \sqrt{\frac{k_B T}{\mu m_p}}, \tag{6}$$

$$T = 278.3 \text{ K} \left(\frac{L_\star}{L_\odot}\right)^{1/4} \left(\frac{r}{1 \text{ au}}\right)^{-1/2}, \tag{7}$$

where for simplicity we have assumed a constant temperature as a function of height and time, and equal to the mid-plane equilibrium temperature for a blackbody. This temperature is simply set by the stellar luminosity, $L_\star$, and belt radius, r. The mean molecular weight in equation (6), μ, is assumed to be equal to 14, i.e. equivalent to a gas dominated by carbon and oxygen in equal proportions. A different temperature or μ (e.g. 28 if the gas is CO dominated) would change the scale height and the gas disc could become thicker or thinner. Nevertheless, the evolution of the gas surface density and its overall vertical distribution (relative to H) is not very sensitive to the value of H itself. This is because the CO photodissociation depends mainly on the optical depths and column densities rather than the volumetric densities, and the vertical diffusion time-scale is independent of T and μ. This is discussed and demonstrated in Section 4.8.

In this paper, we consider a scenario where collisions between solids are responsible for the release of gas and thus the gas input rate is proportional to the mass-loss rate of solids (e.g. as discussed in Zuckerman & Song 2012; Matrà et al. 2015; Marino et al. 2016). Since the collisional rates are proportional to the disc mass or its density (Wyatt et al. 2007), $\dot{\Sigma}_+$ is thus proportional to the squared density of solids. We assume that the radial distribution of solids follows a Gaussian distribution with a full width at half-maximum (FWHM), Δr, and the total gas release rate is $\dot{M}_+$. Therefore, $\dot{\Sigma}_+$ can be defined as

$$\dot{\Sigma}_+ = \frac{\dot{M}_+ \sqrt{2\ln(2)}}{\pi^{3/2} r \Delta r}. \tag{8}$$

2.2 CO photodissociation

We want to estimate the photodissociation rate of CO molecules at each height in the disc. In order to do this, we first define the unshielded CO photodissociation rate per molecule due to the interstellar radiation field (ISRF) as

$$R_{ph,0} = \int \sigma_{ph}(\lambda)\phi_\lambda \, d\lambda, \tag{9}$$

where $\sigma_{ph}(\lambda)$ is the photodissociation cross-section of CO (Heays et al. 2017),[1] and ϕ_λ is the ISRF (Draine 1978; van Dishoeck & Black 1982).[2] This rate is equal to the inverse of the photodissociation time-scale of 130 yr.

If the CO or CI column densities are high enough, CO molecules will become partly or fully shielded from the UV photodissociating radiation. In general, this type of disc is relatively flat with vertical aspect ratios (H/r) $\ll 1$, and thus radiation entering the disc horizontally through the disc mid-plane will encounter much higher column densities than radiation entering vertically. Therefore, shielding will be a function of the direction considered and the height above the mid-plane. In order to simplify the calculations of the CO photodissociation rate, we assume a plane-parallel model, i.e. all disc quantities are constant within a plane at height z. This means that at a given height z, the column density (or optical depth) away from that point will only vary as a function of the polar angle, θ, measured with respect to the vertical direction. This is an approximation, since in reality the density will also vary (at least) radially. Nevertheless, we expect this to be a minor effect, especially at the belt central radius. Therefore, the CO photodissociation rate per molecule is defined as

$$R_{ph}(z) = \frac{1}{4\pi} \int \int \sigma_{ph}(\lambda)\phi_\lambda e^{-\tau(\lambda,\theta,z)} \, d\lambda \, d\Omega, \tag{10}$$

where the optical depth (τ) is defined from a point at height z outwards in a direction θ and at a wavelength λ. Note that τ is the sum of the optical depth of all species (e.g. H_2, H, dust, CO, CI) that can absorb the ISRF at the UV wavelengths that cause CO photodissociation. These are only CO and CI in our model, and thus τ is defined as

$$\tau(\lambda, \theta, z) = \tau_{CO}(\lambda, \theta, z) + \tau_{CI}(\lambda, \theta, z). \tag{11}$$

Using the plane–parallel approximation, the optical depths are simply

$$\tau_i(\lambda, \theta, z) = N_i^{\pm}(z)\sigma_i(\lambda)/|\cos(\theta)|, \tag{12}$$

where $N_i^{\pm}(z)$ is the vertical column density above (+) z for $\theta < \pi/2$ or below (−) z for $\theta > \pi/2$

$$N_i^+(z) = \int_z^\infty n_i(z') \, dz', \tag{13}$$

$$N_i^-(z) = \int_{-\infty}^z n_i(z') \, dz'. \tag{14}$$

Since the CI cross-section is roughly constant across the UV wavelength range where CO photodissociation happens due to the ISRF (90−110 nm), we can write

$$R_{ph}(z) = \frac{1}{2} \int_0^\pi \sin(\theta) e^{-\tau_{CI}(\theta,z)} \int_{90 \text{ nm}}^{110 \text{ nm}} \sigma_{ph}(\lambda)\phi_\lambda e^{-\tau_{CO}(\lambda,\theta,z)} \, d\theta \, d\lambda, \tag{15}$$

where the solid angle integral was converted to an integral over the polar angle only as nothing depends on the azimuthal angle (plane–parallel approximation). To simplify this further, we define the CO self-shielding factor K as

$$K(N_{CO}^{\pm}(z)/|\cos(\theta)|) = \frac{\int \sigma_{ph}\phi_\lambda e^{-\tau_{CO}(\lambda,\theta,z)} \, d\lambda}{\int \sigma_{ph}\phi_\lambda \, d\lambda}, \tag{16}$$

[1]The cross-section of CO was downloaded from https://home.strw.leidenuniv.nl/~ewine/photo/cross_sections.html. They correspond to an excitation temperature of 100 K and a Doppler broadening of 1 km s^{-1}.
[2]Downloaded from https://home.strw.leidenuniv.nl/~ewine/photo/radiation_fields.html

Downloaded from https://academic.oup.com/mnras/article/515/1/507/6617989 by University of Cambridge user on 12 August 2022

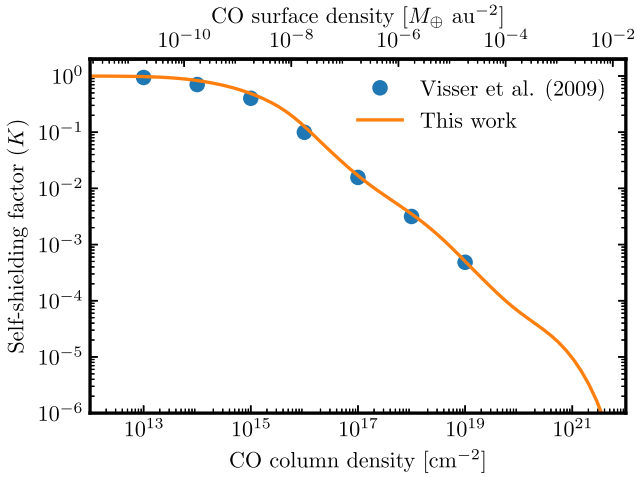

Figure 1. Self-shielding factor K as a function of CO column density (orange). The blue points correspond to values in table 6 of Visser et al. (2009) for an excitation temperature of 50 K, Doppler broadening of 0.3 km s^{-1} and ^{12}CO/^{13}CO abundance ratio of 69.

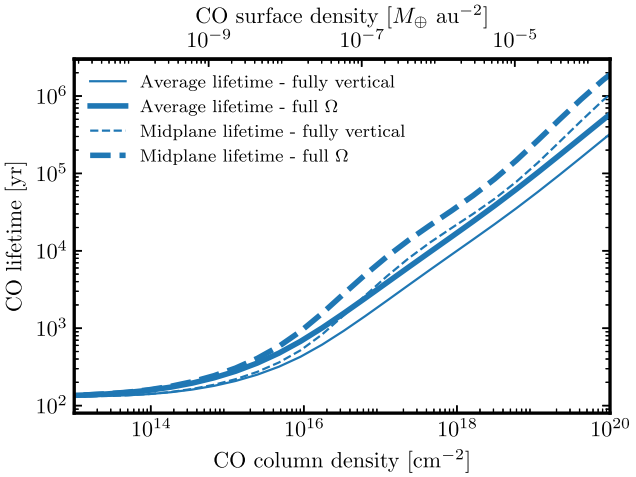

Figure 2. CO lifetime as a function of the CO vertical column density in the absence of CI. The solid lines show the average lifetime, while the dashed lines show the lifetime in the mid-plane. The thin and thick lines correspond to considering ISRF photons enter the disc only vertically or from all directions, respectively.

which corresponds to the self-shielding function from Visser et al. (2009). The CO self-shielding factor can be understood as the photodissociation rate (relative to the unshielded rate) for a CO molecule if it was surrounded by a spherical cloud with a given column density from its centre. Fig. 1 compares K with the values from Visser et al. (2009) as a function of the CO column density, showing a good agreement between the two. The self-shielding factor is slightly higher (less shielding) at intermediate column densities. This difference is likely due to the absence of CO isotopologues ^{13}C^{16}O and ^{12}C^{18}O in our calculations, and the use of an updated CO cross-sections table from Heays et al. (2017).

Finally, we can write the photodissociation rate per molecule and the CO mass photodissociation rate per unit volume as

$$R_{\rm ph}(z) = \frac{R_{\rm ph,0}}{2} \int_0^\pi \sin(\theta) K \left(\frac{N^{\pm}_{\rm CO}}{|\cos(\theta)|} \right) e^{-N^{\pm}_{\rm CI}\sigma_{\rm CI}/|\cos(\theta)|} \, {\rm d}\theta \tag{17}$$

$$\dot{\rho}_{\rm ph}(z) = \rho_{\rm CO}(z) R_{\rm ph}(z). \tag{18}$$

Fig. 2 shows the CO lifetime as a function of the CO vertical column density in the absence of CI. The solid lines correspond to the average lifetime defined as $\tau_{\rm CO,mean} = \int \rho_{\rm CO}(z)\,{\rm d}z / \int \dot{\rho}_{\rm ph}(z)\,{\rm d}z$, when considering the ISRF photons to enter the disc only vertically (thin line) or to be distributed in all directions (thick line). We find that the CO lifetime can be underestimated by a factor $\sim$1.8 for column densities above 10^{16} cm^{-2} when the ISRF is assumed to enter the disc only vertically (where the optical depth is lowest) as done in Kral et al. (2019), Marino et al. (2020), and Cataldi et al. (2020). The dashed lines show the CO lifetime at the mid-plane. These show that the mid-plane lifetime is longer by a factor of 1.5$-$3 for column densities above 10^{16} cm^{-2}. Thus, considering the mid-plane lifetime as representative (as done in Kral et al. 2019; Marino et al. 2020) would overestimate the true CO lifetime in the disc. Nevertheless, both effects balance out and the average lifetime considering all directions of radiation is very close to the mid-plane lifetime when assuming all UV radiation enters the disc vertically.

Fig. 3 shows the CO average lifetime as a function of the CI column density in the absence of CO shielding. The solid lines correspond to a case where the CI gas is on a thin layer above and below all the CO gas (as assumed in Kral et al. 2019; Marino et al. 2020), whereas the dashed lines show a case where CI and CO are well mixed (as assumed in Cataldi et al. 2020). We find that the assumption on how

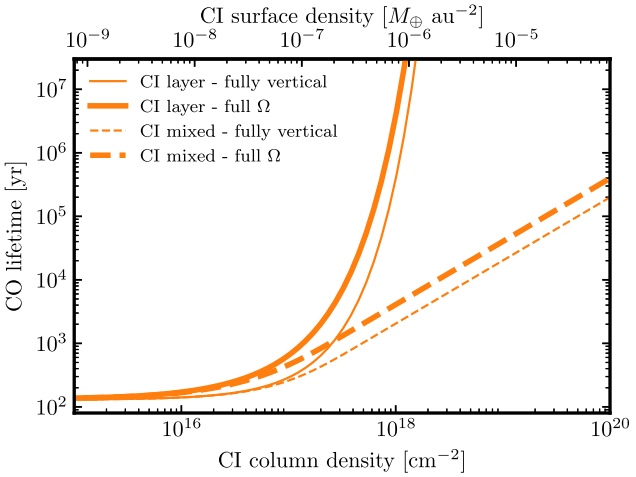

Figure 3. CO lifetime as a function of the CI vertical column density in the absence of CO shielding. The solid lines show the average lifetime when CI is in two surface layers above and below the CO gas. The dashed lines show a case where CO and CI are well mixed. The thin and thick lines correspond to considering ISRF photons enter the disc only vertically or from all directions, respectively.

CI is distributed has profound implications for the lifetime of CO gas, as pointed out by Cataldi et al. (2020). If CO and CI are well mixed, the average lifetime of CO increases only linearly with the CI column density as the photodissociation layer moves higher up in the disc.[3] In fact, we find that self-shielding is more effective than CI-shielding for the same column density by a factor $\sim$1.5. This strong dependency of the CO lifetime on the CI vertical distribution means that it is crucial to study the vertical structure of the gas both theoretically and observationally to advance in our understanding of the gas evolution.

[3]This can be demonstrated using equation (9) in Cataldi et al. (2020) that shows that the photodissociation rate is proportional to $1 - \exp(-\tau)$ and $\tau_{\rm CO}/\tau$. For $\tau_{\rm CO} \ll \tau_{\rm CI}$ and $\tau_{\rm CI} \gg 1$, the CO photodissociation rate becomes inversely proportional to $\tau_{\rm CI}$.

Downloaded from https://academic.oup.com/mnras/article/515/1/507/6617989 by University of Cambridge user on 12 August 2022

The model presented above does not include the photodissociating UV photons from the star. These can dominate the UV radiation field at 100 au for early A-type stars. Nevertheless, Marino et al. (2020) showed that for the typical CO-rich debris discs where gas is detected, this component is negligible at tens of au due to the high column densities in the radial direction. Therefore, we omit it from our calculations.

2.3 C ionization and recombination

The ionization rate per CI atom is calculated as

$$R_{\rm ion}(z) = \frac{R_{\rm ion,0}}{2} \int_0^{\pi} \sin(\theta) e^{-N_{\rm CI}^{\pm}\sigma_{\rm CI}/|\cos(\theta)|}\, {\rm d}\theta, \tag{19}$$

where $R_{\rm ion,\,0}$ is ionization rate per CI atom in the optically thin regime

$$R_{\rm ion,0} = \int \phi_\lambda \sigma_{\rm CI}\ {\rm d}\lambda, \tag{20}$$

and corresponds to an ionization time-scale of 100 yr. Recombination is calculated as

$$R_{\rm rc}(z) = \alpha_{\rm rc}(T) n_{\rm e^-}(z), \tag{21}$$

where $\alpha_{\rm rc}(T)$ is the recombination rate of CII that is dependent on the temperature and is taken from Badnell (2006). The number density of electrons $n_{\rm e^-}(z)$ is set equal to the number density of CII. In other words, we assume that electrons only originate from CI ionization and that CII and electrons are co-located. Finally, the net ionization rate is given by

$$\dot{\rho}_{\rm ion}(z) = \rho_{\rm CI}(z) R_{\rm ion}(z) - \rho_{\rm CII}(z) R_{\rm rc}(z). \tag{22}$$

2.4 Viscous evolution

As the gas viscously evolves, angular momentum is transported outwards while gas mass is mostly moved inwards. This process effectively removes gas from the centre of the belt forming an accretion disc interior to the belt and a decretion disc exterior to it. This process has been studied in detail using 1D simulations that model the radial evolution of gas (e.g. Kral et al. 2016; Moór et al. 2019; Marino et al. 2020). Here, we use a similar approach to Kral et al. (2019) and Cataldi et al. (2020), and we approximate the viscous removal of gas at the belt central radius with

$$\dot{\rho}_{\rm vis,i}(z) = \frac{\rho_i(z)}{t_{\rm vis}}, \tag{23}$$

where $t_{\rm vis}$ is a viscous time-scale. An expression for $t_{\rm vis}$ can be found by considering that in steady state, the gas accretion rate ($3\pi\nu\Sigma$, Armitage 2011) must be equal to the gas input rate $\dot{M}_+$, and that $\dot{\Sigma}_+$ must be equal to $\Sigma/t_{\rm vis}$. Combining these two equalities, we find

$$t_{\rm vis} = \frac{\sqrt{\pi} r \Delta r}{3\sqrt{2\ln(2)}\nu} \approx \frac{r\Delta r}{2\nu}. \tag{24}$$

With this definition, the steady-state surface density ($\dot{M}_+/(3\pi\nu)$) is independent of Δr, and matches the surface density obtained solving the radial viscous evolution and the analytic solution presented in equation (B13) in Metzger + 2012 (valid when $\Delta r \to 0$). Note that when approximating the viscous evolution through equation (23) (only truly valid at steady-state), the densities tend to grow faster and steady state is reached earlier than if we were to solve the viscous evolution radially. Finally, the kinematic viscosity is parametrized with the standard α viscosity as $\nu = \alpha c_{\rm s} H$ (Shakura & Sunyaev 1973).

2.5 Gas vertical diffusion

The last effect to consider is the vertical diffusion, which will mix the different species. The diffusion term in equations (1), (2), and (3) can be written as (Ilgner & Nelson 2006; Armitage 2011)

$$\dot{\rho}_{i,D} = \tfrac{\partial}{\partial z}\left[\rho D \tfrac{\partial}{\partial z}\left(\tfrac{\rho_i}{\rho}\right)\right], \tag{25}$$

where D is the mass diffusivity, which we assume arises from turbulent mixing. Hence, we set D equal to the vertical kinematic viscosity, $\nu_{\rm v}$, which is parametrized as $\alpha_{\rm v} c_{\rm s} H$. We will assume $\alpha_{\rm v} = \alpha$ unless otherwise stated, i.e. the vertical diffusivity is as strong as the radial kinematic viscosity. This means that the viscosity is isotropic, but it is possible that the vertical and radial viscosity and diffusion could differ (see discussion in Section 4.2). Therefore, we also explore scenarios where $\alpha_{\rm v}$ is independent of α. Finally, we can define the vertical diffusion time-scale as $t_{\rm diff} = H^2/D = 1/(\alpha_{\rm v}\Omega_{\rm K})$, which translates to

$$t_{\rm diff} = 1.3 \times 10^4\ {\rm yr} \left(\frac{\alpha_{\rm v}}{10^{-2}}\right)^{-1} \left(\frac{r}{100\ {\rm au}}\right)^{3/2} \left(\frac{M_\star}{1.5\ {\rm M}_\odot}\right)^{-1/2}. \tag{26}$$

3 RESULTS

With the model presented above, we now proceed to simulate its evolution. We consider a system around a 1.5 $M_\odot$ star with a luminosity of 10 $L_\odot$. The system has a planetesimal belt centred at 100 au, with an FWHM of 50 au. We assume an alpha viscosity of 10^{-2}, which translates to a viscous time-scale of 1.5 Myr as defined in equation (24). Note that although the viscosity parameter is kept constant, below we present the evolution for different values of $\alpha_{\rm v}$ and different gas input rates to cover the different scenarios. Our vertical grid consists of only one hemisphere since the disc is symmetric with respect to the mid-plane, and is divided into 50 bins from the midplane to 5 scale heights. The polar angle θ is sampled with 20 bins from 0 to π. We evolve the system for 10 Myr.

3.1 Without diffusion

Fig. 4 shows a case in which CO gas is input at a rate of 10^{-3} $M_\oplus$ Myr^{-1} and diffusion is switched off. The top panels show the vertical distribution of CO, CI, and CII at five different epochs. The three species have a vertical distribution that approximates a Gaussian. The bottom left-hand panel shows the column density as a function of height. The horizontal dotted lines show the critical column density to shield the CO (below z) via self-shielding (blue) and CI-shielding (orange) by a factor $\geq e$. From this we can see that CO is only marginally shielded by CI as the column density of CI at the mid-plane is close to the critical column density. The bottom right-hand panel shows the evolution of the surface density of the three species. This shows how the surface density of CO stays roughly constant at a value where the photodissociation rate is balanced by the CO input rate. While CO photodissociates, carbon is produced and quickly ionized in a 100 yr time-scale. Ionized carbon dominates the first Myr of evolution, while CI dominates afterwards as recombination becomes more effective within 1.5 scale heights. After 3 Myr, the CI gas is close to steady state at surface density of 2×10^{-8} $M_\oplus$ au^{-2}. At this level CO is marginally shielded and its surface density increases by 50 per cent. This case represents the systems with low CO masses, where CO is released by planetesimals and destroyed in time-scales of $\sim$100 yr like in β Pic, HD 181327, and Fomalhaut (Dent et al. 2014; Marino et al. 2016; Matrà et al. 2017).

Downloaded from https://academic.oup.com/mnras/article/515/1/507/6617989 by University of Cambridge user on 12 August 2022

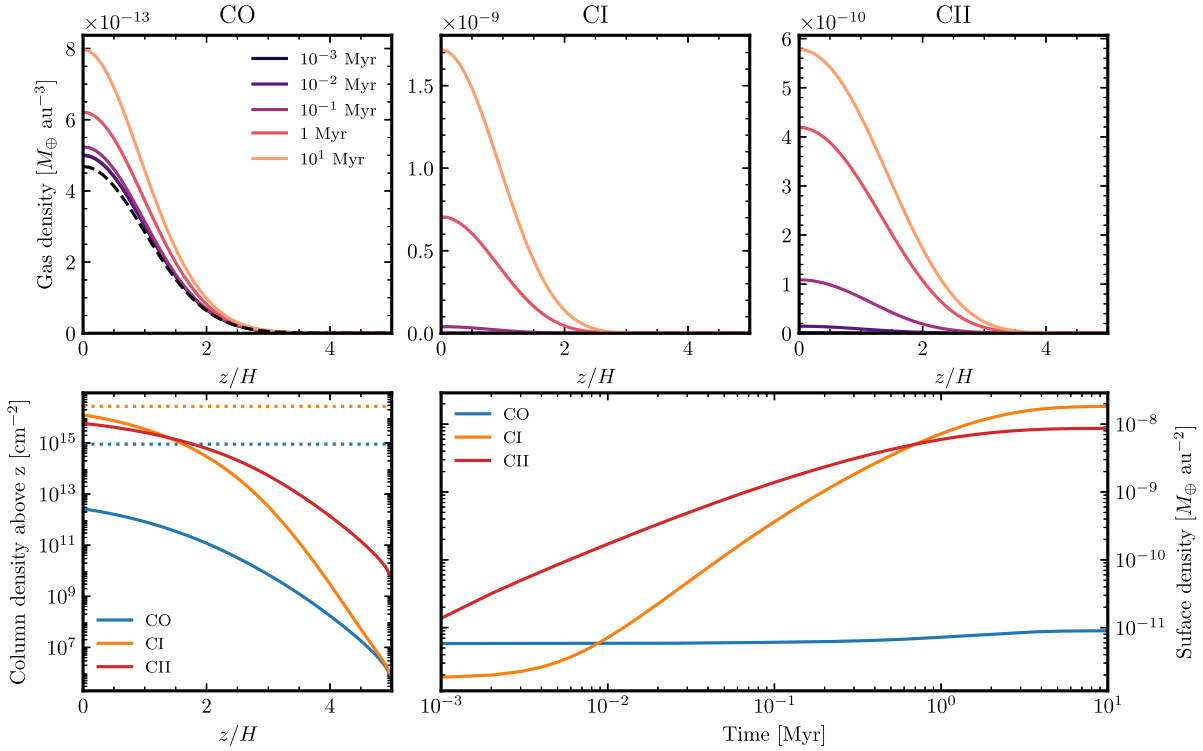

Figure 4. Evolution of CO, CI, and CII for $\dot{M}_+ = 10^{-3}$ M$_\oplus$ Myr^{-1}, $\alpha = 10^{-2}$, and no vertical diffusion. The top panels show the vertical density profile at different epochs as a function of z/H. The black dashed line in the top left-hand panel shows the expected CO density if there was no shielding. The bottom left-hand panel shows the vertical column density above z as a function of z/H (the total column density is twice the value reached at $z = 0$) for CO (blue), CI (orange), and CII (red). The horizontal dotted lines show the critical column density of CO (blue) and CI (orange) to shield the CO underneath it by a factor of $\geq e$. The bottom right-hand panel shows the evolution of the surface density of CO, CI, and CII.

Fig. 5 shows a case with a hundred times higher CO release rate ($\dot{M}_+ = 0.1\,M_\oplus$ Myr^{-1}). In this case CO becomes shielded after 1 Myr by CI and it reaches a photodissociation timescale of 6 Myr by the end of the simulation. This time-scale is longer than the viscous timescale and thus CO is mainly lost via viscous evolution. As CI becomes optically thick to UV radiation, it forms a layer at $1.5H$ where CI production peaks, i.e. $\dot{\rho}_{\rm ph}(z) - \dot{\rho}_{\rm ion}(z)$ reaches its maximum. CII is mostly produced above this layer at $2H$ where carbon is still produced via photodissociation of new CO, and ionization and recombination rates are comparable. This evolution confirms that it is possible that CI is in a layer above the mid-plane that is dominated by CO, as assumed in Kral et al. (2019) and Marino et al. (2020). This shielded case would correspond to the gas-rich discs, where CO masses and surface densities are found to be comparable to protoplanetary disc levels. Note that the height at which these layers are (relative to the scale height) will depend on the rate at which CO gas is released. The higher the release rate is, the higher these layers will be (see Section 3.3).

3.2 With diffusion

Now we focus on the effect of vertical diffusion. Vertical diffusion happens on a time-scale of 10^4 yr for $\alpha = 10^{-2}$ (equation 26). It is worth noting that since H is typically an order of magnitude smaller than r, vertical diffusion can be two orders of magnitude faster than viscous evolution. Vertical diffusion is, nevertheless, longer than CO photodissociation and ionisation time-scales in the unshielded case. We thus do not see differences between a case with diffusion and without when the CO release rate is low, as in the case shown in Fig. 4. On the other hand, if the gas release rate is high both ionisation and photodissociation rates become longer than the diffusion time-scale, and thus CO and CI can easily mix.

Fig. 6 shows this latter scenario where CO gas is released at a high rate of 0.1 M$_\oplus$ Myr^{-1}. Diffusion mixes CO and CI, moving CO to upper layers where it becomes exposed and CI is transported towards the mid-plane reducing its effectiveness at shielding CO. Both CO and CI show a vertical distribution close to Gaussian with a standard deviation similar to H. Given the less effective shielding by CI, the photodissociation time-scale drops to 0.09 Myr (almost a factor of 100 shorter than the case without diffusion). The CO surface density, however, drops by a smaller factor close to 10. This difference is because in the scenario without diffusion, CO was being lost via viscous evolution (i.e. in a viscous time-scale of $\sim$1 Myr), while with diffusion it is being lost via photodissociation. The CII distribution remains unaffected since carbon ionization and recombination occur on a shorter time-scales than diffusion.

It is also possible to consider a case where the vertical and radial values of α differ as mentioned in Section 2.5. In Fig. 7, we show a case where vertical diffusion (parametrized now by $\alpha_{\rm v}$) is weaker and equal to 10^{-4}. Since H is a factor of $\sim$10 smaller than the radius and width, the now hundred times weaker vertical diffusion leads to a vertical diffusion time-scale similar to the viscous time-scales and close to 1 Myr. At this critical value, mixing is significant causing the CI density to peak at the mid-plane but slow enough for CI to have a wide vertical distribution. Compared to the case with $\alpha_{\rm v} = \alpha = 10^{-2}$, CO is better shielded and reaches a surface density similar to the case with no vertical diffusion. Therefore, we conclude that for $\alpha_{\rm v} < \alpha(H/r)^2$ vertical diffusion plays a minor role.

Downloaded from https://academic.oup.com/mnras/article/515/1/507/6617989 by University of Cambridge user on 12 August 2022

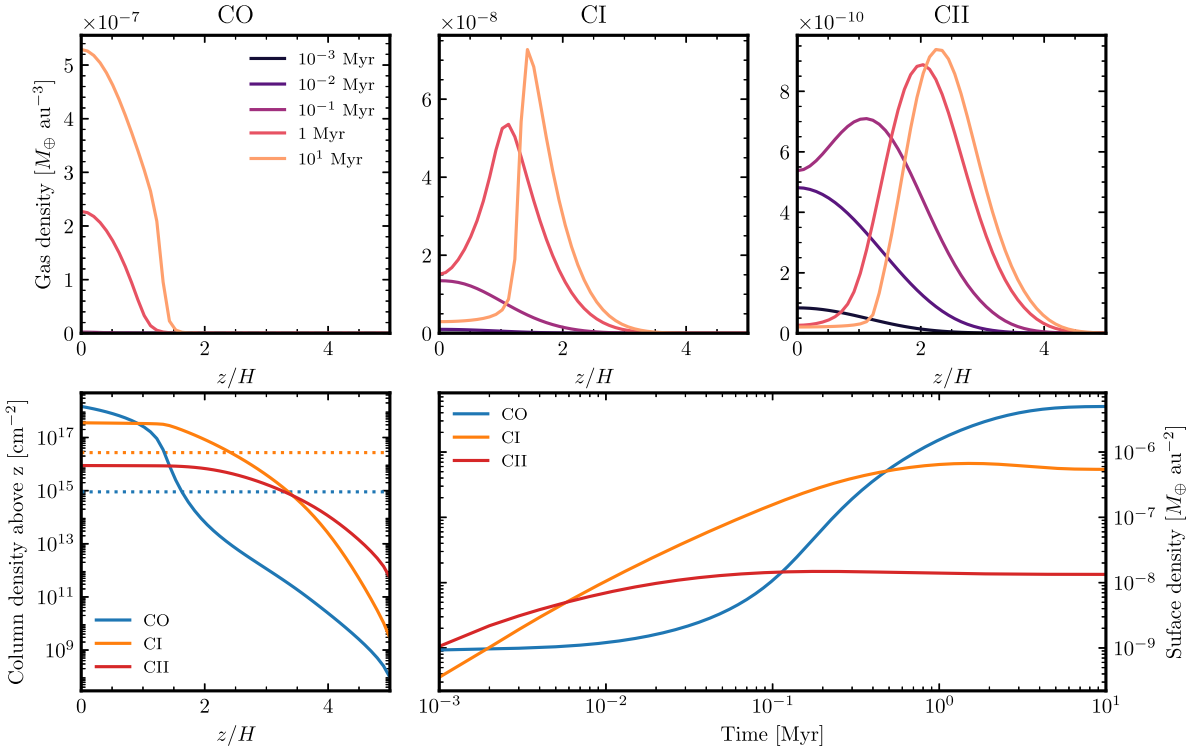

Figure 5. Same as Fig. 4, but for $\dot{M}_+ = 0.1$ M$_\oplus$ Myr^{-1}, $\alpha = 10^{-2}$, and no vertical diffusion.

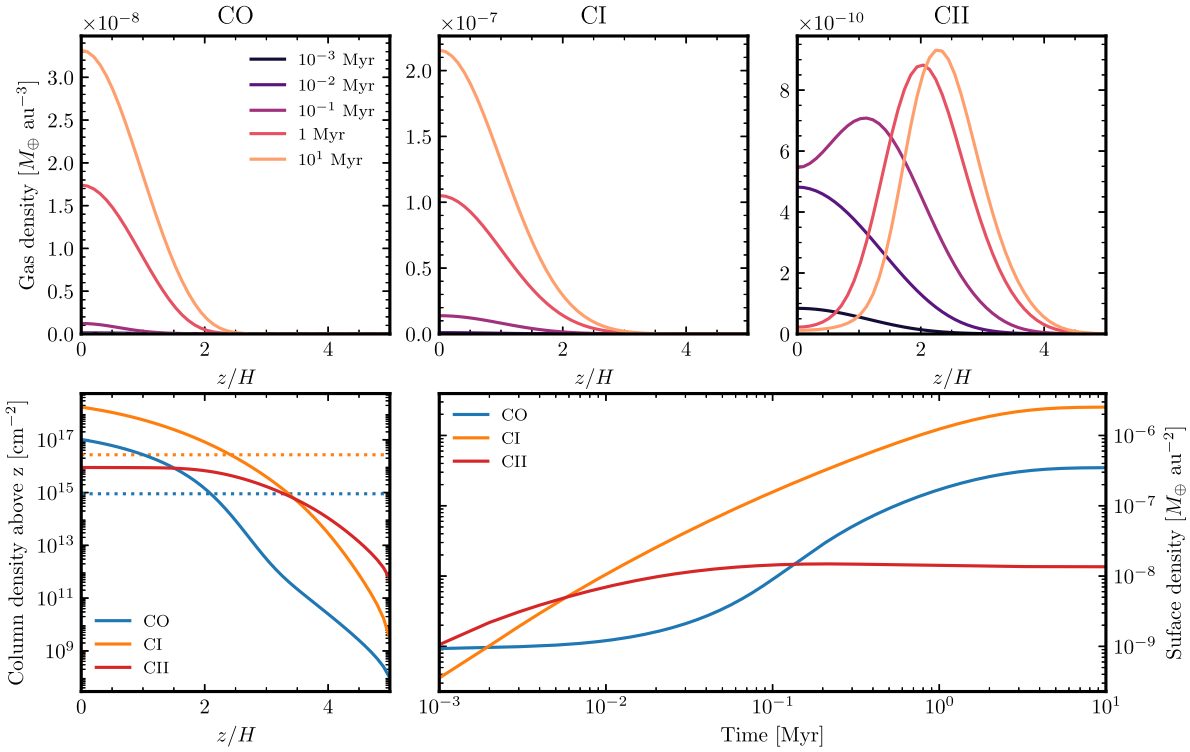

Figure 6. Same as Fig. 4, but for $\dot{M}_+ = 0.1$ M$_\oplus$ Myr^{-1}, $\alpha = 10^{-2}$, and with vertical diffusion.

Conversely, if $\alpha_v > \alpha(H/r)^2$ and the diffusion time-scale is shorter than the age of the system, vertical diffusion mixes CO and CI. For systems younger than the diffusion time-scale ($\sim 10^2/\alpha_v$ yr at 100 au, equation 26), or systems in which gas has been released for a shorter time-scale, vertical mixing will not be able to effectively mix CO and CI.

Downloaded from https://academic.oup.com/mnras/article/515/1/507/6617989 by University of Cambridge user on 12 August 2022

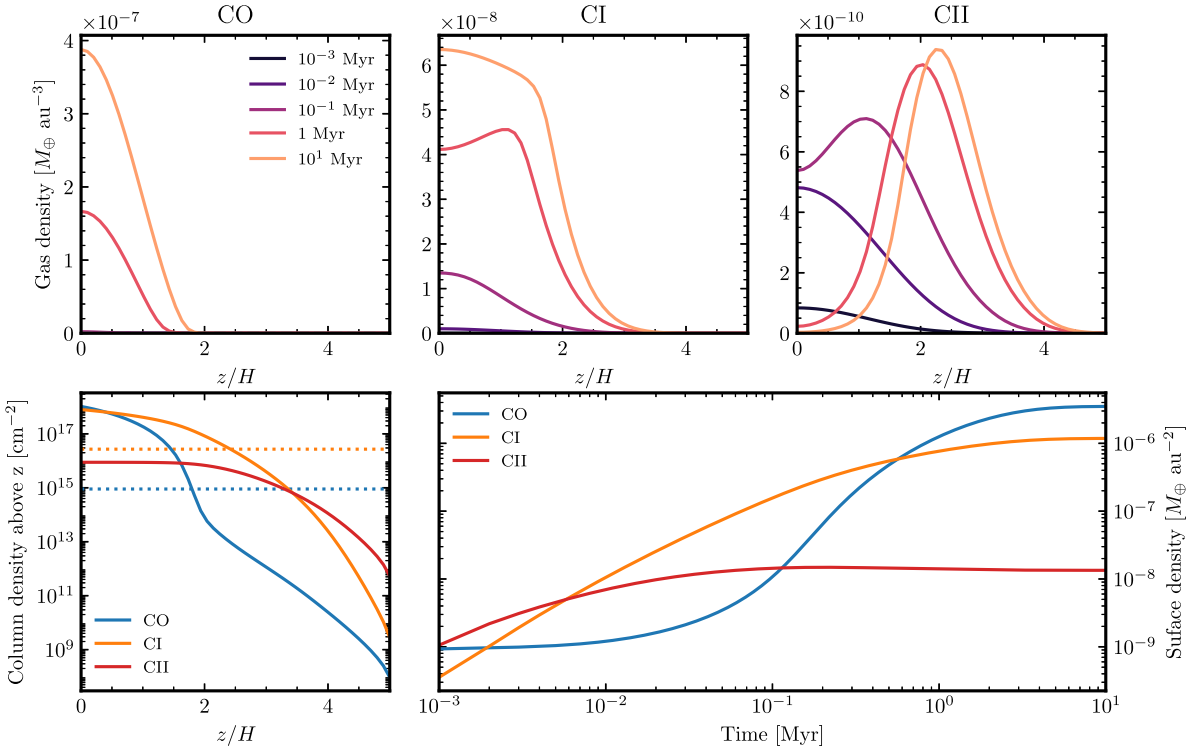

Figure 7. Same as Fig. 4, but for $\dot{M}_+ = 0.1$ M$_\oplus$ Myr^{-1}, $\alpha = 10^{-2}$ and with a vertical diffusion strength of $\alpha_v = 10^{-4}$.

3.3 The vertical distribution of CO and CI

In order to understand how the vertical distribution of CO and CI depend on the gas input rate and α_v we run EXOGAS for a sample of different values fixing $\alpha = 10^{-2}$ and evolving the system until it reaches steady state. The main effect of changing the gas input rate is to change the steady state surface density of gas (Σ_{SS}), which is simply the product of the gas input rate ($\dot{\Sigma}_+$ as defined in equation 8) and the viscous time-scale. Therefore, below we will focus on how the CO and CI distribution change as a function of this steady-state surface density. Fig. 8 shows where the CO (blue) and CI (orange) densities peak (solid lines) as a function of the steady state surface density. The shaded area represents the region where the density is at least 60 per cent of the peak density (equivalent to a $\pm H$ range for a Gaussian distribution), and the dashed lines the height at which CO and CI become optically thick to photodissociating radiation in the vertical direction (i.e. the $\tau = 1$ layer for each species).

The top panel shows cases with low vertical diffusion ($\alpha_v = \alpha/1000 = 10^{-5}$). For low gas densities, CO and CI have the same vertical distribution as shown in Fig. 4. As the surface density increases, we find an intermediate stage where CI gas becomes optically thick and can shield CO, which becomes highly peaked at the disc mid-plane. At higher surface densities, the CI density peaks in a surface layer at a height just below its $\tau = 1$ layer, which increases with the surface density. This layer traces the location where the CO photodissociation rate is the highest. As CO is well shielded under this layer, the CO vertical extent becomes wider, closer to a Gaussian and with a standard deviation equal to H.

The middle panel shows cases with an intermediate vertical diffusion ($\alpha_v = \alpha/100 = 10^{-4}$). The behaviour is similar to the one with low vertical diffusion, e.g. the CO vertical distribution and $\tau = 1$ layer are almost identical. However, the CI distribution now peaks at the mid-plane, still extending to heights similar to the case with low vertical diffusion. This intermediate case demonstrates how even if the CI density peaks at the mid-plane, the CI equivalent scale height can be much larger than the true gas scale height.

The bottom panel shows a case with a high vertical diffusion ($\alpha_v = \alpha/10 = 10^{-3}$). In this case, both CO and CI have an almost identical vertical distribution, except in the intermediate stage when CI starts to become optically thick. In this range of surface densities, CO is moderately shielded near the mid-plane and thus its density strongly peaks at $z = 0$. Note that the diffusion time-scale is not short enough compared to the photodissociation time-scale to smear out this peak. Only for $\alpha_v \sim 1$, the vertical diffusion time-scale would become ~100 yr, i.e. comparable to the CO photodissociation time-scale, and thus short enough to widen the vertical distribution of CO in this range of surface densities. Note that a stronger vertical diffusion (e.g. $\alpha_v = \alpha = 10^{-2}$) leads to very similar results where CO and CI are well mixed. The main difference is that at the intermediate stage the vertical spread of CO is slightly wider.

Finally, although the example shown in Fig. 8 shows a case with $\alpha = 10^{-2}$, we find similar results for higher and lower α's if we keep α_v/α constant. An example of this is shown in the Appendix B, where we show that with $\alpha = 10^{-1}$ the same vertical structures are obtained. In other words, for a fixed H/r whether CI will form a surface layer or will be bound to the mid-plane will ultimately depend on the ratio α_v/α, the viscosity (or gas removal time-scale) and the gas production rate. As mentioned in Section 3.2, in systems younger than the vertical diffusion time-scale (equation 26), i.e. not yet in steady state, the CI could form a surface layer regardless of the ratio α_v/α if the gas surface density is high enough for CI to become optically thick in the vertical direction.

Downloaded from https://academic.oup.com/mnras/article/515/1/507/6617989 by University of Cambridge user on 12 August 2022

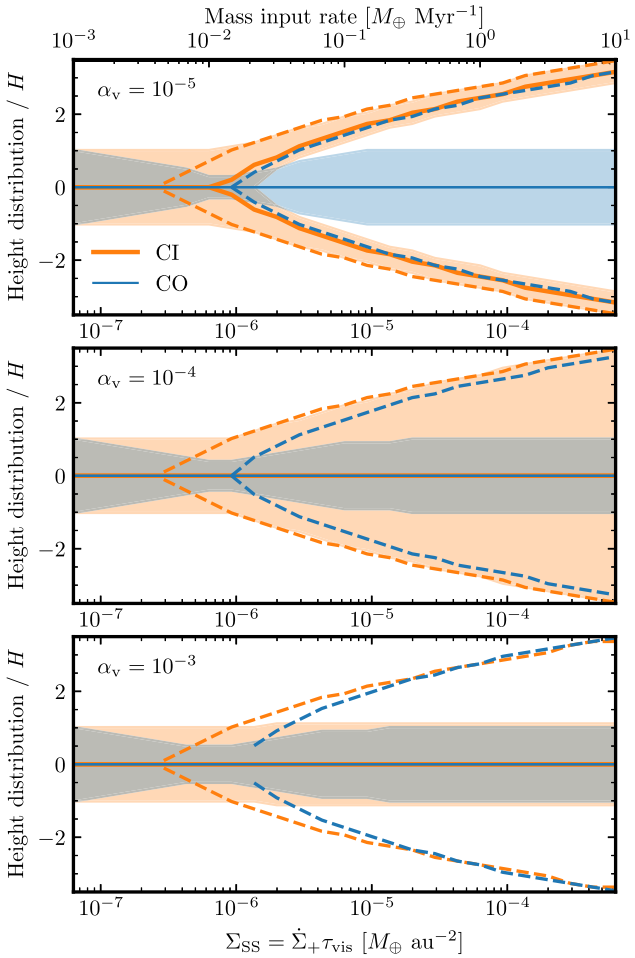

Figure 8. Vertical distribution in steady state of CO (blue) and CI (orange) normalized by the scale height (H) as a function of the steady state surface density of gas, in a case with $\alpha = 10^{-2}$. The solid line shows where the density distribution peaks, while the shaded region represents the region where the density is at least 60 per cent of the peak density (1σ drop). The dashed lines represent the height at which CI and CO become optically thick to photodissociating radiation in the vertical direction. The top, middle, and bottom panels show scenarios where α_v is 10^{-5}, 10^{-4}, and 10^{-3}, respectively. The upper x-axis in the top panel shows the mass input rates as reference. Note that the orange solid line in the middle and bottom panels lies behind the solid blue line.

3.4 The surface density of CO and CI

With a better understanding of how the vertical distribution of CI depends on α_v, we now focus on how the surface density of CO and CI will depend on α_v. Fig. 9 shows the surface density of CO (blue) and CI (orange) as a function of the steady state surface density of gas, for different values of α_v, assuming $\alpha = 10^{-2}$. As expected, the lower α_v is, the better CI is at shielding CO as it is mostly in a surface layer that absorbs most UV photons. The upper and lower black diagonal lines show the expected surface density of CO if it is lost through viscous evolution or if it is unshielded and lost through photodissociation, respectively. For a low α_v (solid line), as Σ_{SS} increases the CI production rate stalls as most UV photons are absorbed by CI rather than CO. This is why the surface density of CI is almost constant for $\Sigma_{SS} \geq 10^{-6}\,M_\oplus$ au^{-2}. This also causes the CO lifetime to increase exponentially up to a viscous time-scale, and the surface density quickly converges to the upper black line.

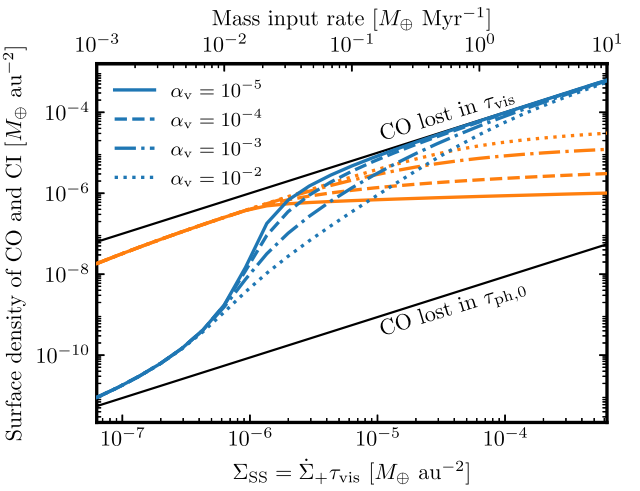

Figure 9. Surface density of CO (blue) and CI (orange) as a function of the steady state surface density of gas, in a case with $\alpha = 10^{-2}$. The solid, dashed, dot–dashed and dotted lines represent cases with $\alpha_v = 10^{-5}$, 10^{-4}, 10^{-3}, and 10^{-2}, respectively. The upper and lower black solid lines represent the maximum and minimum surface density of CO, i.e. when it is lost in a viscous timescale or unshielded and lost in a 130 yr photodissociation time-scale. The upper x-axis shows the mass input rates as reference.

On the other hand, as described before, with a high value of α_v (dotted line) CI is well mixed with CO and thus it is not as effective at shielding it from photodissociating radiation. Thus, for the same Σ_{SS} or gas input rate, the CO surface density is much lower than in the case with a weak vertical diffusion. This is effectively the result obtained by Cataldi et al. (2020).

The difference between the blue curves is the largest near $\Sigma_{SS} = 2 \times 10^{-6}\,M_\oplus$ au^{-2}, where the surface density of CO for $\alpha_v = 10^{-5}$ is ∼30 times larger than for $\alpha_v = 10^{-2}$. How big this difference is also depends on α. The lower the viscosity, the larger this difference becomes as shielding can extend the CO lifetime to an even longer viscous time-scale.

4 DISCUSSION

In this section, we discuss the implications of our findings, what is known about vertical diffusion in circumstellar discs, and the level of ionization of the gas obtained from our simulations. We also discuss the effect vertical diffusion can have on the vertical settling of dust and on the radial evolution of CO, how high-resolution observations could constrain the strength of vertical diffusion, but might be unable to constrain the gas scale height, and finally, we discuss some of the limitations of our model.

4.1 Implications for shielded/hybrid discs

As pointed out by Cataldi et al. (2020) and demonstrated in detail here, if CO and CI are well mixed shielding is much less effective than if CI is in a surface layer. To achieve the same level of shielding, much higher quantities of CI gas are needed. However, CI observations of gas-rich discs seem to suggest lower CI quantities than those needed if CO and CI are well mixed. Two scenarios might solve this tension. On one hand, Cataldi et al. (2020) suggested that if CI was captured by dust grains and then used to re-form CO that is then released, this could maintain a high CO production rate in the system. In this recycling scenario, CO would be predominately self-shielded. This scenario, however, still needs to be tested via physical simulations or

Downloaded from https://academic.oup.com/mnras/article/515/1/507/6617989 by University of Cambridge user on 12 August 2022

experiments. On the other hand, the gas could be primordial or hybrid in origin, containing still large amounts of hydrogen that shield the CO (Kóspál et al. 2013). Note that although the CI mass has been constrained, its value is still largely dependent on assumptions such as its temperature and vertical structure that can change its optical depth when viewed close to edge-on. Therefore, it is possible that the real mass of CI in the gas-rich discs is much larger than the current observational estimates.

If diffusion is weak, nevertheless, we expect the CI density to peak above and below the CO-dominated mid-plane, as implicitly assumed in the simple shielded secondary scenario presented by Kral et al. (2019). A weak diffusion could thus explain the population of gas-rich discs and account for the current CI mass estimates. Unfortunately, there are no clear predictions for how strong vertical diffusion will be (see Section 4.2). This will ultimately depend on the relative strength of the turbulence in the vertical and radial direction. Therefore, high-resolution ALMA observations are crucial since they reveal the true nature of gas-rich debris discs and provide constraints on the hydrodynamics (see Section 4.6).

4.2 Vertical diffusion

Since the strength of the vertical diffusion in debris discs is not well known, we may look for some guidance from the study of protoplanetary discs, keeping in mind that the gas densities and especially the dust optical depths are significantly higher than in debris discs. One way to constrain the vertical diffusion in protoplanetary discs is by considering the disc chemistry. For example, in order to explain the high CH_3CN abundance observed towards MWC 480, the disc model by Öberg et al. (2015) requires efficient vertical transport ($\alpha_v \sim 10^{-3}$–10^{-2}) of CH_3CN ice from the mid-plane to UV-exposed regions in the disc atmosphere where the ice can be photodesorbed. Similarly efficient vertical mixing is also believed to contribute to the observed C depletion in protoplanetary discs by transporting CO from the disc atmosphere to the mid-plane where it can freeze out and be sequestered into pebbles (e.g. Kama et al. 2016; Van Clepper et al. 2022). Dust settling has also been used to constrain vertical diffusion. For example, Pinte et al. (2016) report that their dust settling model best fits the small dust scale height of the HL Tau protoplanetary disc if weak vertical diffusion is assumed (α_v a few times 10^{-4}).

Recent observations aimed at detecting non-thermal gas motion form CO line emission suggest that relatively weak turbulence (corresponding to $\alpha \lesssim 10^{-3}$) may be common in protoplanetary discs (Flaherty et al. 2018, 2020). In general, it is often assumed that α_v is approximately equal to the turbulent α parameter. This can be justified from numerical simulations of protoplanetary discs subject to the magnetorotational instability (MRI), showing that α_v is usually within an order of magnitude of α (e.g. Okuzumi & Hirose 2011; Zhu, Stone & Bai 2015; Xu, Bai & Murray-Clay 2017). To the best of our knowledge, the only study looking at the MRI in debris discs was presented by Kral & Latter (2016). They showed that the MRI could be at work in the debris disc around β Pictoris, although a weak magnetic field would be sufficient to stabilize the disc. However, their results might not be directly applicable to the CO-rich discs we consider here due to the significantly higher gas densities and lower ionization compared to the disc around β Pic (see Section 4.3).

As a further complication, the turbulence strength could vary vertically as the ionization level increases with z (Flock et al. 2015; Delage et al. 2021). Also, if turbulent motion is driven by a mechanism different from the MRI, α could be very different from α_v. Numerical simulations by Stoll, Kley & Picogna (2017) show that

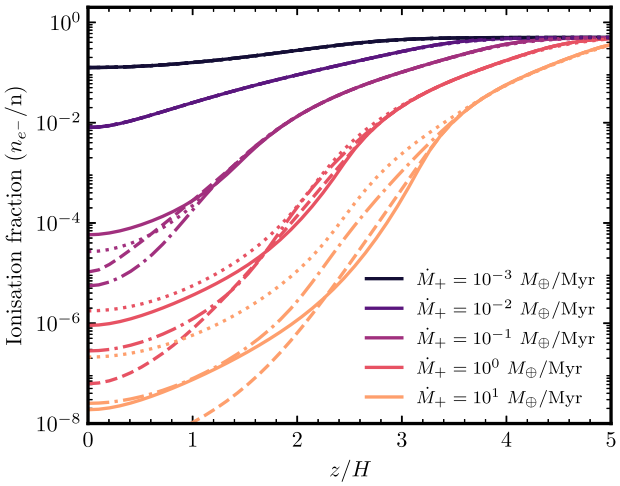

Figure 10. Ionization fraction as a function of height for a disc with $\alpha = 10^{-2}$. The different colours correspond to different gas input rates. The solid, dashed, dot–dashed, and dotted lines represent cases with $\alpha_v = 10^{-5}$, 10^{-4}, 10^{-3}, and 10^{-2}, respectively. The ionization fraction is calculated as the number density ratio between CII (equivalent to the electron number density) and CO+CI+CII+O.

turbulence induced by the vertical shear instability could be highly anisotropic (α_v more than two orders of magnitude larger than α).

In summary, the strength of vertical diffusion in debris discs is essentially unknown. Thus, in this study we explored a range of plausible values for α_v to understand the gas evolution in different regimes. Future observations of highly inclined gas-rich debris discs could provide the first constraints on α_v and the hydrodynamics (see Section 4.6).

4.3 Ionization fraction

As discussed above, one possible driver of vertical (and radial) diffusion in debris discs is turbulence due to the MRI. Well-ionized debris discs such as β Pic may be unstable to the MRI, provided that the magnetic field is not too strong (Kral & Latter 2016). If, however, the ionization fraction is too low, the gas decouples from the magnetic field and the disc is stable to the MRI (in protoplanetary discs, such regions are known as 'dead zones'; Gammie 1996).

Consideration of the disc vertical structure is important for the calculation of the ionisation fraction in debris discs. Kral et al. (2019) found that the ionization fraction near the disc mid-plane can be several orders of magnitude lower than that at the disc surface, due to the self-shielding of the atomic carbon. This effect is also present in the models presented in this paper (see Fig. 10), where both the atomic carbon and CO in the upper disc layers shield the disc mid-plane from the ISRF. We find that the ionisation fraction at the disc mid-plane can vary greatly with the disc mass (which is, at fixed α, proportional to the gas mass input rate shown in Fig. 10). In a more massive disc, the disc mid-plane is better shielded and this results in both lower rate of carbon production and lower ionization rate of the produced carbon. Vertical diffusion also influences the mid-plane ionization fraction, to a lesser degree. We find that the relationship between the degree of vertical diffusion (i.e. α_v) and the mid-plane ionization fraction is non-monotonous. This is due to the relative importance of two competing effects. As the vertical diffusion coefficient first increases from 10^{-5} to 10^{-4} (solid to dashed line), diffusion is strong enough for CI from upper layers to diffuse downwards decreasing the shielding of CO, which in turn increases

Downloaded from https://academic.oup.com/mnras/article/515/1/507/6617989 by University of Cambridge user on 12 August 2022

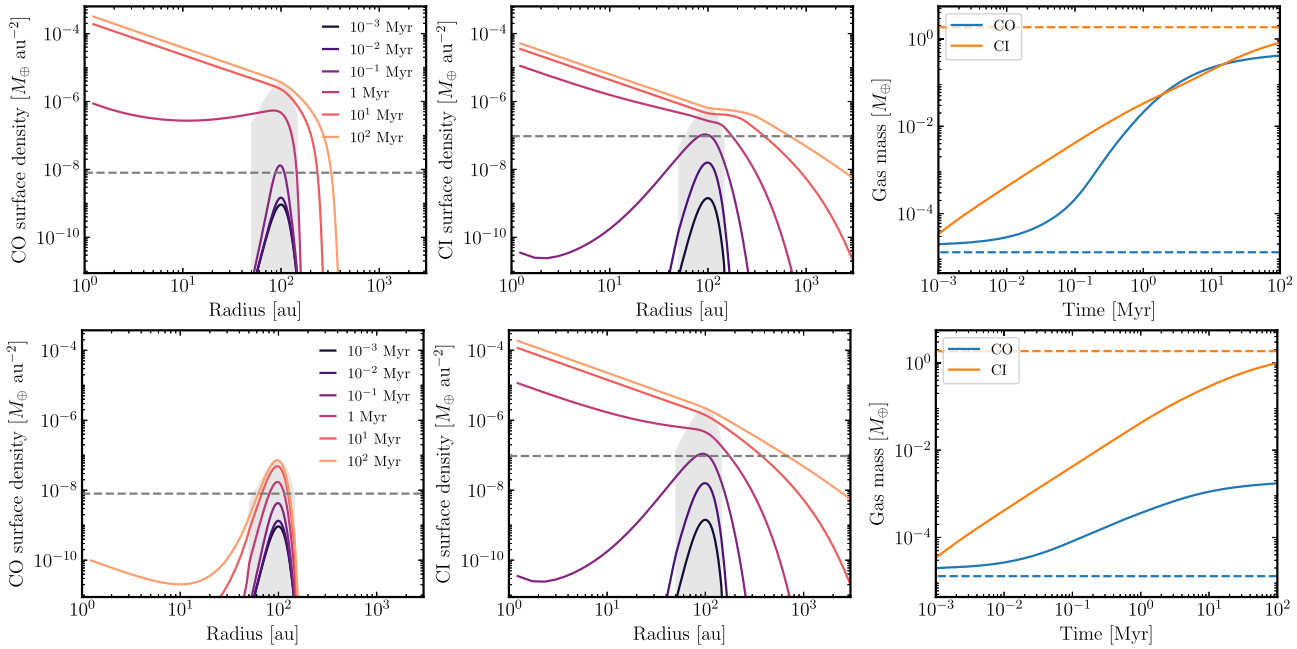

Figure 11. Radial evolution of the surface density of CO (left), CI (middle), and their masses (right), in a system where CO gas is released at a rate of 0.1 $M_\oplus$ Myr^{-1} from a belt centred at 100 and 50 au wide (FWHM) (grey-shaded region), with $\alpha = 10^{-2}$. The top panel represents a case where CI is in the surface of the disc, while in the bottom panel CO and CI are perfectly mixed. The horizontal grey dashed lines represent the surface density at which CO becomes shielded by a factor e. The horizontal blue and orange lines in the right panels show the expected steady-state mass if CO was unshielded.

the CO photodissociation rate and thus the surface density of CI. The higher CI surface density translates to a higher optical depth that lowers the ionization rate of carbon and thus the ionization fraction. However, as α_v increases further (dashed to dotted line), the diffusion time-scale is short enough for ionized carbon to diffuse downwards, increasing the ionization fraction at the mid-plane despite the much lower ionization rate.

This variation of the ionization fraction with height above the disc mid-plane is reminiscent of the ionization state of protoplanetary discs. In vast regions of protoplanetary discs cosmic rays and stellar X-rays ionize only the disc upper layers, but do not reach the disc mid-plane, leading to MRI-dead zones (Gammie 1996; Igea & Glassgold 1999). If the mid-plane regions of debris discs are similarly MRI-dead, any vertical mixing or radial diffusion driven by the MRI would be considerably weaker than in a well-ionized disc. However, the low mid-plane ionization fractions (as low as $\sim 10^{-8}$), we find here may still be well above the critical value required to make the disc unstable to the MRI. In protoplanetary discs, that critical value can be of the order of only 10^{-12} (e.g. Gammie 1996). The stability of weakly ionized debris discs against the MRI remains to be explored, taking into account the chemical composition that differs largely from protoplanetary discs and to a lesser degree from well ionized debris discs considered by Kral & Latter (2016).

4.4 Dust scale height

Whilst in this paper we have focused only on the gas evolution, the dynamics and evolution of dust can be strongly affected by the presence of gas (Takeuchi & Artymowicz 2001; Thébault & Augereau 2005; Krivov et al. 2009; Lyra & Kuchner 2013; Pearce et al. 2020). In particular, Olofsson et al. (2022) recently showed how gas can cause dust grains to settle towards the mid-plane if their inclinations are damped by the gas in a time-scale (the stopping time) shorter than their collisional lifetime. This effect is strongest for the smallest grains in contrast to what happens in protoplanetary discs where it is the largest grains that readily settle towards the mid-plane. In debris discs, the gas densities are low enough such that all grains larger than the blow-out size have Stokes numbers larger than unity (see fig. 11 in Marino et al. 2020); therefore, all bound grains are decoupled from the gas. However, only the smallest grains have stopping times shorter than their collisional lifetime. Therefore, if gas densities are high enough we expect small grains to be more concentrated towards the mid-plane than large grains and planetesimals.

One important effect that was neglected by Olofsson et al. (2022) is the stirring by turbulent diffusion that could reduce the amount of inclination damping (Youdin & Lithwick 2007). In the presence of turbulent diffusion (as considered in this paper), the scale height of dust is expected to be (equation 24 in Youdin & Lithwick 2007)[4]

$$H_\mathrm{d} = H\sqrt{\frac{\alpha_\mathrm{v}}{\mathrm{St}}}\sqrt{\frac{1+\mathrm{St}}{1+2\mathrm{St}}}, \tag{27}$$

where St is the Stokes number or the dimensionless stopping time. The Stokes number is defined as $\frac{\pi}{2}\frac{a\rho_\mathrm{s}}{\Sigma}$, where a, ρ_s, and Σ are the grain size, the internal density of grains and the gas surface density, respectively. Since we expect $\mathrm{St} \gg 1$, we have $H_\mathrm{d} \approx H\sqrt{\frac{\alpha_\mathrm{v}}{2\mathrm{St}}}$. We can evaluate this for a gas-rich debris disc with a surface density of 10^{-5} $M_\oplus$ au^{-2} (i.e. $M_\mathrm{gas} \sim 1$ $M_\oplus$) to obtain

$$\frac{H_\mathrm{d}}{H} = 0.1\left(\frac{a}{1\ \mu\mathrm{m}}\right)^{-1/2}\left(\frac{\alpha_\mathrm{v}}{10^{-2}}\right)^{1/2}\left(\frac{\Sigma}{10^{-5}\ M_\oplus\ \mathrm{au}^{-2}}\right)^{1/2}\left(\frac{\rho_\mathrm{s}}{1\ \mathrm{g\ cm}^{-3}}\right)^{-1/2} \tag{28}$$

This means that although gas drag will damp the inclinations of μm-sized grains, these will not completely settle towards the mid-plane if the gas surface densities are high ($\gtrsim 10^{-5}$ $M_\oplus$ au^{-2}) and turbulent diffusion is strong ($\alpha_\mathrm{v} \gtrsim 10^{-2}$). Note that these equations are only

[4]Note that we have taken the dimensionless eddy time as 1, which is consistent with MRI simulations (Fromang & Papaloizou 2006; Zhu et al. 2015).

Downloaded from https://academic.oup.com/mnras/article/515/1/507/6617989 by University of Cambridge user on 12 August 2022

valid for those dust grains with a collisional lifetime much longer than the stopping time. Therefore, observational estimates of the scale height of gas and small dust grains could help to constrain the strength of vertical diffusion and gas models.

4.5 Radial evolution

Throughout this paper we have shown the importance of the vertical evolution on the effectiveness of shielding of CO by atomic carbon. Whether carbon is well mixed or in a layer has profound implications for how the gas will evolve. Here, we investigate how the radial evolution could be affected by the vertical diffusion of gas. To this end, we focus on two extreme scenarios: one where CI is in a layer completely far above and below the CO-rich mid-plane, and another where CO and CI are well mixed. For both scenarios, we consider a system where CO gas is released at a rate of 0.1 $M_\oplus$ Myr^{-1} in a belt centred at 100 and 50 au wide (FWHM), around a 1.5 $M_\odot$ star (10 $L_\odot$), and with $\alpha = 10^{-2}$.

We solve the radial evolution of CO and CI in these two scenarios using the radial module of the PYTHON package EXOGAS that is based on the model developed in Marino et al. (2020). Because the photodissociation of CO strongly depends on the disc vertical structure, which this module does not solve, we need to precompute the CO photodissociation time-scales. We do this using the vertical evolution module for a grid of 50 x 50 different surface densities of CO and CI that are logarithmically spaced. Here is where the two scenarios differ. In order to compute these time-scales, we need to define the vertical distribution of CO and CI. First, we assume all CI is distributed in two surface layers on top of and below the CO gas. Secondly, we assume CI and CO are well mixed. In Fig. 3, we showed how the CO lifetime could be very different in these two scenarios. EXOGAS then uses these precomputed grids and interpolates its values to estimate the CO photodissociation time-scale. These grids provide realistic photodissociation time-scales similar to the ones obtained through photon counting (Cataldi et al. 2020), but that also account for UV radiation entering the disc at different angles that lengthens the CO lifetime by a factor of ∼2 (see Section 2.2).

Fig. 11 shows the surface density profiles of CO (left), CI (middle), and the mass evolution of CO and CI as a function of time. The top panels show the case where CI is in a surface layer, and thus the shielding is most effective. Once CI reaches a high enough surface density (10^{-7} $M_\oplus$ au^{-2}), CO starts to become shielded. With a longer lifetime, CO viscously evolves spreading inwards and outwards beyond the planetesimal belt where CO is released (grey-shaded region). The resulting surface densities at the belt centre after 10 Myr of evolution are very similar to those obtained when simulating the vertical evolution without vertical diffusion (Section 3.1). Similar to the simulation results in Marino et al. (2020), we find a plateau in the CI surface density from 100 to 200 au after 100 Myr of evolution. This feature can be understood by examining the top left and middle panels. In the first 1 Myr of evolution, CI accumulates forming an accretion disc that is massive enough to shield CO within 150 au, allowing it to accumulate, viscously accrete, and dominate the gas surface densities. Beyond the belt centre, the released CO gas slowly flows outwards, but at a time-scale much longer than the CO lifetime (which decreases exponentially with radius), resulting in an exponential drop in the surface density of CO. In this drop between 100 and 300 au the gas composition changes from being CO dominated to being carbon and oxygen dominated. It is the balance between the decrease in the overall gas surface density and the increase in the abundance of CI that creates the plateau. Therefore, the plateau starts at the belt centre (where gas starts to flows outwards) and stops, where CI and OI dominate the bulk of the gas density.

If CI and CO are well mixed (bottom panel), the average CO lifetime at the belt centre is only 0.02 Myr, which is too short compared to the viscous time-scale (6 Myr). This is why CO does not viscously spread significantly after 100 Myr. This scenario is the most problematic for explaining gas-rich discs since their estimated CI levels would not be enough to shield CO (Cataldi et al. 2020). We note one caveat in this calculation that results in an underestimation in the level of shielding compared to the case with a strong diffusion ($\alpha_\nu = \alpha$) and a high gas input rate (0.1 $M_\oplus$ Myr^{-1}) presented in Section 3. We assume that CI and CO are perfectly mixed, however, when simulating the vertical evolution with $\alpha_\nu = \alpha$, CO is still more concentrated towards the mid-plane than CI. This is because the photodissociation time-scale in the top layers is still shorter than the diffusion time-scale, therefore CO becomes depleted there relative to the mid-plane. This behaviour is also shown in Fig. 8 for values of $\Sigma_{ss} = 10^{-6}$ $M_\oplus$ au^{-2}. The carbon-dominated upper layer can significantly contribute to shielding CO. In order to completely mix CO and CI, the diffusion time-scale should be shorter than the unshielded photodissociation time-scale. At ∼100 au, that would only be obtained with $\alpha \gtrsim 10^{-1}$. Therefore, perfect mixing might never happen in debris discs unless they are strongly turbulent in the vertical direction.

We conclude that the vertical structure of the gas has a large impact on the radial evolution. The two extreme scenarios explored here lead to significantly different results, particularly for the CO distribution. Constraining the vertical structure of the gas is thus crucial to advance our understanding of the gas evolution in debris discs.

4.6 Observability

In this section, we produce radiative transfer predictions and discuss how the vertical distribution of CO and CI would translate into real observations. To this end, we use RADMC-3D[5] that allows to produce synthetic images of dust and gas emission based on several parameters and input files such as the dust distribution, opacity, gas distribution, velocity field, molecular information, and stellar spectrum. We produce these files and run RADMC-3D calculations using the PYTHON package DISC2RADMC[6] (based on Marino et al. 2018), which allows to define these input files and run multiple RADMC-3D calculations in a simple and concise manner.

We focus on and compare the two main scenarios presented in Section 3. In these two scenarios, CO gas has been released at a rate of 0.1 $M_\oplus$ Myr^{-1} for 10 Myr and $\alpha = 10^{-2}$ (i.e. it is in steady state). They differ in that in one gas evolves without vertical diffusion, while in the other there is strong vertical diffusion ($\alpha_\nu = \alpha = 10^{-2}$). Since our vertical simulations presented above were one dimensional, we need to extrapolate their density distribution of CO and CI in order to define their density as a function of r and z. For simplicity, we assume the vertical distribution (relative to $H(r)$) is independent of radius and the surface density distribution of both species follows a Gaussian distribution centred at 110 au and with a standard deviation of 34 au (FWHM of 80 au). We further assume a scale height of 5 au at 100 au, which scales linearly with radius, and a turbulence corresponding to $\alpha = 10^{-2}$ that broadens slightly the line emission. Note that although the true gas temperature could be different (hotter or colder) and the mean molecular weight higher (if CO dominated), the vertical

[5] http://www.ita.uni-heidelberg.de/dullemond/software/radmc-3d
[6] https://github.com/SebaMarino/disc2radmc

Downloaded from https://academic.oup.com/mnras/article/515/1/507/6617989 by University of Cambridge user on 12 August 2022

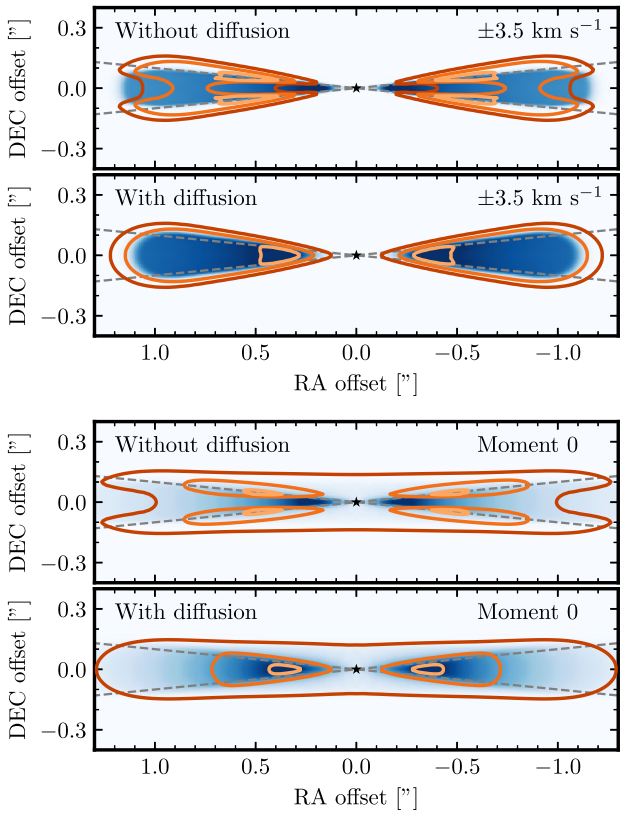

Figure 12. Radiative transfer prediction of CO and CI emission for an edge-on disc. The top two panels show the emission at line-of-sight velocities of ±3.5 km s^{-1}, while the bottom two show the moment 0 (velocity integrated emission). CO J = 2−1 emission is shown in blue colours, while CI $^3P_1-^3P_0$ emission is shown in orange contours at 10, 50, and 90 per cent of the peak value. The first/third and second/fourth panels show a case without and with vertical diffusion (respectively), assuming $\alpha = 10^{-2}$ and $\dot{M}^+ = 10^{-1}$ M$_\oplus$ Myr^{-1} after 10 Myr (in steady state). The grey dashed line represent 2 scale heights from the mid-plane.

distribution relative to H will remain roughly the same as shown in Section 4.8. This means that while the vertical extent of CO and CI is uncertain and could vary as $\sqrt{T/\mu}$, their predicted morphologies presented below are robust. A higher (lower) temperature would only stretch (compress) their vertical distributions. Finally, we assume a 1.7 M$_\odot$ central star, at a distance of 133 pc, and that is viewed edge-on. The radial distribution, stellar mass, and distance approximate the values for HD 32297, a gas-rich edge-on disc (Greaves et al. 2016; MacGregor et al. 2018; Cataldi et al. 2020).

Under these assumptions and density distributions, we compute synthetic images of CO J = 2−1 (λ = 1300 μm) and CI $^3P_1-^3P_0$ emission (λ = 609 μm), both readily accessible through ALMA observations. When calculating the emission from these species, RADMC-3D assumes Local Thermodynamic Equilibrium (LTE), i.e. the population levels of each gas species are set by the local temperature. It is well-known that non-LTE can be important when gas densities are low (Matrà et al. 2015), but the densities considered here should be high enough for the different energy levels to be collisionally excited and in thermal equilibrium.

Fig. 12 shows the expected emission at line-of-sight velocities of ±3.5 km s^{-1} (close to the Keplerian velocity at the belt centre of 3.7 km s^{-1}) and the moment 0 (i.e. the velocity-integrated emission) for a case without and with diffusion (scenarios presented in Figs 5 and 6, respectively). The CO intensity is displayed with a blue colour map, while CI is shown with orange contours. In both the channel maps and moment 0's, we find a similar morphology. Without diffusion, the CO emission peaks at the mid-plane and is located within 2 scale heights from the mid-plane (grey-dashed lines), while CI emission is almost absent within one scale height and peaks near the upper and lower edges of the CO emission. Note that the height at which this happens, relative to the scale height, can vary depending on the gas input rate and viscosity (Section 3.3). Since CO is very optically thick, its emission peaks towards the inner regions where the gas is hotter. Conversely, with diffusion the CI and CO emissions peak in the mid-plane displaying a very similar intensity distribution. The only difference is that CI emission extends vertically slightly further compared to CO since the latter has a slightly narrower vertical distribution due to photodissociation. Finally, the observed vertical morphology is not sensitive to the radial distribution of CO and CI. A different radial distribution would change how the emission is distributed radially, but the vertical morphology would still be the same. This is especially true for individual channel maps where each pixel traces approximately a single radius.

These radiative transfer simulations show that it is possible to distinguish these two scenarios by looking at the vertical distribution of CO and CI. Both emission lines have been already detected and resolved radially in multiple shielded discs. So far, only Hughes et al. (2017) and Higuchi et al. (2019) have tried to constrain the vertical extent of CO and CI. Doing a similar analysis for both lines, Higuchi et al. (2019) found their heights to be consistent with each other, although with large uncertainties that prevent assessing the strength of vertical diffusion. Future observations at high-resolution should reveal if CI is located in a surface layer and thus indicate the strength of vertical diffusion. Note that with images that do not resolve the vertical distribution of CO and CI, it is impossible to distinguish between these two scenarios due to the unknown gas temperatures and gas scale height.

Whilst in the radiative transfer predictions presented above we focus in an edge-on case, vertical information can also be obtained for discs with moderate inclinations. It has been shown that the characteristic height of emission lines can be obtained from line-of-sight velocity maps, as well as from individual channels (e.g. Teague et al. 2018; Pinte et al. 2018; Casassus & Pérez 2019; Izquierdo et al. 2021). Therefore, ALMA observations at a resolution comparable or better than the disc scale height offer a unique chance to determine how strong vertical diffusion is, and thus how important shielding by CI is.

4.7 Is the observed gas scale height a good indicator of gas origin?

It has been suggested that a powerful way to determine the origin of gas in debris discs is to measure its scale height (e.g. Hughes et al. 2017; Kral et al. 2019; Smirnov-Pinchukov et al. 2022). By knowing the scale height and the temperature of a disc, one could estimate the mean molecular weight. This would allow to determine if the gas is dominated by molecular Hydrogen or by heavier species such as C, O, or CO (e.g. Hughes et al. 2017). In addition to the difficulty of estimating the gas kinetic temperature, a key problem lies in measuring the gas scale height. To measure it, one would need to use a gas tracer such as CO or CI, but as shown here the vertical distribution of these species can differ significantly from the gas true vertical distribution. For example, in the results presented in Section 3.3 we found that the distribution of CO can be skewed towards the mid-plane due to its higher shielding at the mid-plane if vertical mixing is weak, mimicking a small-scale height. A similar phenomenon could

Downloaded from https://academic.oup.com/mnras/article/515/1/507/6617989 by University of Cambridge user on 12 August 2022

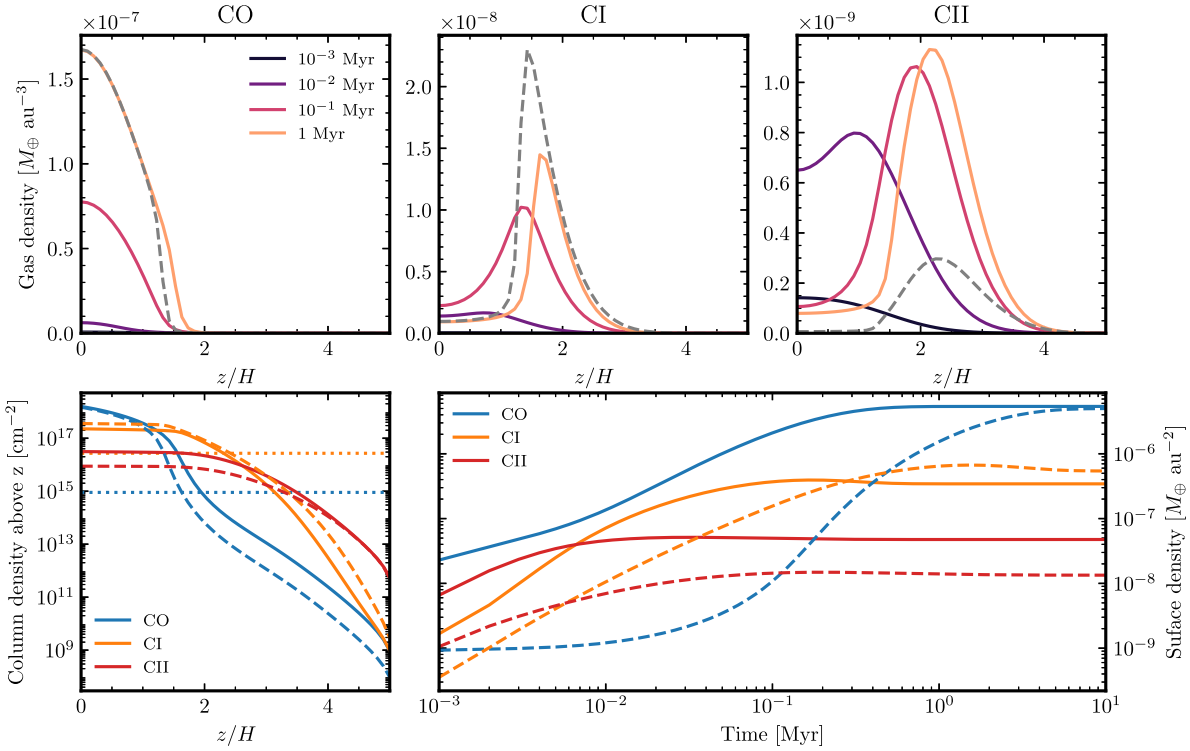

Figure 13. Same as Fig. 4, but for $T = 500$ K instead of 50 K, $\dot{M}_+ = 1$ M$_\oplus$ Myr^{-1}, $\alpha = 10^{-2}$, and no vertical diffusion. The grey dashed lines in the top panels show the steady-state gas density when $T = 50$ K and scaled by a factor of $1/\sqrt{10}$ for comparison. Similarly, the dashed coloured lines in the bottom left-hand and right-hand panels show the steady-state column density profiles and the surface density evolution for $T = 50$ K.

occur in a primordial gas scenario as well if vertical diffusion is weak since the CO lifetime will also be longer near the mid-plane. This means that the small CO scale height measured in 49 Ceti by Hughes et al. (2017) might be very different from the true gas scale height (even if primordial). Hence, one should be careful interpreting a small CO scale height as evidence of a high mean molecular weight (and thus gas of secondary origin). On the other hand, the vertical distribution of CI can be much wider mimicking a larger scale height. Moreover, a high optical depth would rise the emitting surface of optically thick species making the apparent vertical distribution wider than in reality. Therefore, we recommend that scale height values derived directly from observations should be used with caution, and ideally interpreted using gas models and radiative transfer simulations. Otherwise, estimates could suffer from great systematic errors.

4.8 How does temperature affects the evolution?

Throughout the paper, we have assumed a gas temperature equal to the blackbody equilibrium temperature at 100 au of 50 K, which translates to a scale height of 5 au. However, the gas temperature could be significantly different from the blackbody and dust temperature in reality, depending on the gas heating and cooling rates (e.g. Kral et al. 2016). Therefore, in this section, we examine the evolution of the gas with a temperature 10 times higher (500 K) in order to understand its effects. The increased temperature changes the sound speed, which in turn changes other important quantities. First, the gas scale height is increased by a factor of $\sqrt{10}$ from approximately 5 to 15 au. Secondly, the viscosity is 10 times higher (as we keep α fixed), which translates to a viscous time-scale 10 times shorter.

We now compare the gas evolution in the case of no vertical diffusion and a high gas input rate, as presented in Section 3.1 and in Fig. 5. In order to focus on the effect of the temperature alone, we increase the mass input rate by a factor of 10 to keep the total gas surface density in steady-state constant. Fig. 13 shows the evolution of CO, CI, and CII for $T = 500$ K. The dashed lines show our standard model with $T = 50$ K for comparison. The grey dashed lines in the top panels have been scaled by a factor of $1/\sqrt{10}$ to account for the difference in scale height and ease the comparison. We find that the gas evolution is very similar to the case with a lower temperature. The main differences are that the CI surface density is ∼30 per cent smaller, the CII surface density is a factor of 5 greater, the CO, CI and CII volumetric densities are lower (due to the increased scale height), and that the steady state is reached earlier due to the 10 times shorter viscous time-scale. The increase in the surface density of CII (and decrease of CI) can be explained by the lower volumetric densities and higher temperature that decrease the recombination rate of CII. Conversely, reducing the temperature (or increasing μ) would have the opposite effect: CII recombination rates would be higher, increasing (reducing) the surface density of CI (CII). These findings confirm that the evolution of CO and CI is more sensitive to the column (or surface) densities rather than the volumetric densities.

If we considered vertical diffusion, the increase in the temperature would leave the vertical diffusion time-scale unchanged ($1/(\alpha_\mathrm{v}\Omega_\mathrm{K})$). However, the vertical diffusion time-scale relative to the viscous time-scale would become longer, and thus the CO and CI would become less mixed. We note that this conclusion is only valid if α and α_v are kept fixed. The high uncertainty in the relative values of α_v and α, and their dependence on the temperature makes it impossible to know how different the evolution of a colder versus a

Downloaded from https://academic.oup.com/mnras/article/515/1/507/6617989 by University of Cambridge user on 12 August 2022

hotter disc will be. Nevertheless, our main conclusion that CO and CI will become well mixed if $\alpha_v > \alpha(H/r)^2$ still holds.

4.9 Limitations

The model presented here provides a useful tool to estimate and quantify the importance of vertical diffusion on the evolution of CO in exocometary discs. This model, nevertheless, has some limitations which we discuss here.

First, our model assumes that CO gas is released with a vertical profile that matches the hydrostatic equilibrium. In reality, the release of gas will depend on the vertical distribution of solids that dominate the gas release. If CO gas was released with a high vertical dispersion, the upper layers would be enriched in CO compared to our model. Therefore, shielding by carbon would be less effective. Conversely, if CO was released with a small vertical dispersion, it would be better shielded by CI. Moreover, we assumed a constant temperature. The temperature could vary as a function of height (reaching hundreds or thousands of K at the disc surface, Kral et al. 2019) or time as the gas densities and composition change (Kral et al. 2016). Both effects could have an impact on the level of mixing and thus on the gas evolution if they changed the ratio of the vertical diffusion and viscous time-scales as discussed in Section 4.8. Exploring these scenarios would require solving the Navier–Stokes equations together with radiative transfer equations. Such demanding computations go beyond the scope of this paper. Additionally, the uncertainty would remain over how α and α_v vary as a function of the temperature, density, and ionization fraction (Section 4.3).

Second, our model is one dimensional and thus we cannot track the radial evolution of the gas. To approximate the viscous evolution, we remove gas on a viscous time-scale at all heights. This might not necessarily be the case if the viscosity is height dependent. Nevertheless, this approximation provides a simple way to remove gas on a certain time-scale. Moreover, our model is only strictly valid at the center of the belt, where CO gas is being released and there is negligible inflow of gas from another region. To model the gas interior or exterior to the belt, we would need to know the composition with which it arrives at that radius. Future modelling could solve self-consistently the radial and vertical evolution, allowing to study in more detail this evolution.

5 CONCLUSIONS

In this paper, we have studied for the first time the vertical evolution of gas in debris discs, focusing on how the vertical distribution of carbon strongly affects the photodissociating radiation that CO receives. To this end, we developed a new 1D model and python package (EXOGAS) that contains a module to simulate the vertical evolution of gas (in addition to a module to simulate the radial evolution as in Marino et al. 2020). Our model takes into account the release of CO gas from solids in a planetesimal belt, the photodissociation of CO, the ionization/recombination of carbon, the radial viscous evolution, and the vertical mixing due to turbulent diffusion. Below we summarize our main findings.

First, we determined the efficiency of shielding by CI in two extreme hypothetical scenarios and confirmed previous findings. If carbon is primarily located in the surface layer below and above the CO gas, the lifetime of CO increases exponentially with the column density of CI (as argued by Kral et al. 2019). However, if CI and CO are vertically well mixed, shielding by CI is inefficient (Cataldi et al. 2020) and the CO lifetime increases only linearly with the CI column density. This demonstrates the importance of knowing the true vertical distribution of gas in debris discs to understand its evolution.

In order to understand what the true vertical distribution should be, we developed a 1D model to simulate the gas evolution. We showed for the first time how ISRF photodissociating radiation creates a surface layer dominated by atomic carbon and oxygen if gas densities are high and vertical diffusion is negligible. This surface layer acts as an efficient shield, where CI atoms absorb most of the interstellar UV photons and become ionized. This process creates three layers where carbon is in different forms: a top layer dominated by CII where the recombination rate is slow compared to ionization, a surface or middle layer dominated by CI where recombination is efficient and where most UV radiation is absorbed, and a bottom layer that extends to the mid-plane and is dominated by CO. This layered structure allows the build-up of a CO-rich mid-plane. However, if diffusion is strong CI and CO become well mixed, exposing CO to a stronger UV radiation. In this case, shielding by CI is inefficient and thus higher gas release rates would be required to achieve the same CO gas surface densities than with a weak vertical diffusion.

Since the strength of the turbulent diffusion (α_v) is uncertain in debris discs, we explored a wide range of values to characterize the different behaviours. We found that in steady state the vertical structure of the gas is mainly set by the vertical diffusion time-scale (H^2/D) relative to the viscous time-scale (i.e. the gas removal/replenishment time-scale, r^2/ν). In other words, if $\alpha_v/\alpha > (H/r)^2$ diffusion happens faster than the gas replenishment and thus CO and CI are well mixed. Conversely, if $\alpha_v/\alpha < (H/r)^2$ diffusion plays a minor role and a surface layer forms that is dominated by CI and oxygen, which shields the CO underneath. If the vertical diffusion time-scale is longer than the age of the system, the CI gas could still form a surface layer if it is optically thick. Note that if gas densities are low enough such that the gas is optically thin to UV radiation in the vertical direction, CI and CO have very similar distributions independently of the diffusion strength.

Based on our results, we discussed what these findings imply for the known gas-rich debris discs. If diffusion is weak, the simple secondary scenario could still explain the population of gas-rich debris discs and account for the estimated CI masses. However, if observations of gas-rich debris discs indicate that CI and CO are well mixed, the standard secondary origin scenario might need reevaluation. Unfortunately, the strength of vertical diffusion in debris discs is unknown. If turbulence is driven by the MRI, α_v might be similar to α which would result in a well-mixed CO and CI gas. However, this picture could be even more complicated since we find that the ionization varies greatly with height, which could make any MRI-driven diffusion height dependent.

We also discussed how turbulent diffusion could affect the vertical distribution of small grains. Those grains are susceptible to gas drag that damps their inclinations and thus should settle towards the mid-plane (Olofsson et al. 2022). However, turbulent diffusion can counterbalance this effect and limit the amount of settling. Measurements of the gas and small dust heights could provide constraints to the strength of vertical diffusion.

Whilst our simulations focused on the gas evolution at the belt centre, we showed how the efficiency of shielding has an effect on the viscous radial evolution of CO. Using radial evolution simulations, we showed that if CO and CI are well mixed (and thus shielding by CI is weak) the CO lifetime might not be long enough for it to spread interior to the planetesimal belt. Therefore, the vertical evolution of the gas can have a profound effect on the radial distribution of CO.

Although vertical diffusion is largely unconstrained, using our simulations and radiative transfer predictions we showed that high-

Downloaded from https://academic.oup.com/mnras/article/515/1/507/6617989 by University of Cambridge user on 12 August 2022

resolution ALMA observations could reveal if CO and CI are well mixed or segregated into different layers. Such observations would constrain α_v/α and ultimately determine how efficient shielding by CI is. This could confirm the exocometary origin of the gas, or favour a primordial origin where shielding is mostly done by hydrogen.

Finally, we discussed how attempts to infer the gas scale height directly from observations could suffer from large systematic errors. This is because the vertical distribution of CO and CI can be significantly different from the total gas distribution in gas-rich discs. CO gas can be concentrated towards the midplane, while CI can have an effective scale height much larger than the true value. We thus recommend the use of multiple species and the comparison with models as the one presented in this paper.

ACKNOWLEDGEMENTS

S. Marino is supported by a Junior Research Fellowship from Jesus College, University of Cambridge. G. Cataldi is supported by the NAOJ ALMA Scientific Research grant code 2019-13B. M. Jankovic is supported by the UK Science and Technology Research Council (STFC) via the consolidated grant ST/S000623/1.

DATA AVAILABILITY

The data underlying this article will be shared on reasonable request to the corresponding author. EXOGAS can be downloaded from https://github.com/SebaMarino/exogas, where readers can also find examples of how to use it. DISC2RADMC can be downloaded from https://github.com/SebaMarino/disc2radmc, where examples are also available.

REFERENCES

Armitage P. J., 2011, ARA&A, 49, 195
Badnell N. R., 2006, ApJS, 167, 334
Casassus S., Pérez S., 2019, ApJ, 883, L41
Cataldi G. et al., 2020, ApJ, 892, 99
Delage T. N., Okuzumi S., Flock M., Pinilla P., Dzyurkevich N., 2021, A&A, 658, A97
Dent W. R. F. et al., 2014, Science, 343, 1490
Draine B. T., 1978, ApJS, 36, 595
Flaherty K. M., Hughes A. M., Teague R., Simon J. B., Andrews S. M., Wilner D. J., 2018, ApJ, 856, 117
Flaherty K. et al., 2020, ApJ, 895, 109
Flock M., Ruge J. P., Dzyurkevich N., Henning T., Klahr H., Wolf S., 2015, A&A, 574, A68
Fromang S., Papaloizou J., 2006, A&A, 452, 751
Gammie C. F., 1996, ApJ, 457, 355
Greaves J. S. et al., 2016, MNRAS, 461, 3910
Heays A. N., Bosman A. D., van Dishoeck E. F., 2017, A&A, 602, A105
Higuchi A. E. et al., 2019, ApJ, 883, 180
Hughes A. M. et al., 2017, ApJ, 839, 86
Hughes A. M., Duchêne G., Matthews B. C., 2018, ARA&A, 56, 541
Igea J., Glassgold A. E., 1999, ApJ, 518, 848
Iglesias D. et al., 2018, MNRAS, 480, 488
Ilgner M., Nelson R. P., 2006, A&A, 445, 223
Izquierdo A. F., Testi L., Facchini S., Rosotti G. P., van Dishoeck E. F., 2021, A&A, 650, A179
Kama M. et al., 2016, A&A, 592, A83
Kennedy G. M., 2018, MNRAS, 479, 1997
Klusmeyer J. et al., 2021, ApJ, 921, 56
Kóspál Á. et al., 2013, ApJ, 776, 77
Kral Q., Latter H., 2016, MNRAS, 461, 1614
Kral Q., Wyatt M., Carswell R. F., Pringle J. E., Matrà L., Juhász A., 2016, MNRAS, 461, 845
Kral Q., Marino S., Wyatt M. C., Kama M., Matrà L., 2019, MNRAS, 489, 3670
Kral Q., Davoult J., Charnay B., 2020a, Nature Astron., 4, 769
Kral Q., Matrà L., Kennedy G. M., Marino S., Wyatt M. C., 2020b, MNRAS, 497, 2811
Kral Q. et al., 2021, A&A, 653, L11
Krivov A. V., Herrmann F., Brandeker A., Thébault P., 2009, A&A, 507, 1503
Lyra W., Kuchner M., 2013, Nature, 499, 184
MacGregor M. A. et al., 2018, ApJ, 869, 75
Marino S., 2022, preprint (arXiv:2202.03053)
Marino S. et al., 2016, MNRAS, 460, 2933
Marino S. et al., 2018, MNRAS, 479, 5423
Marino S., Flock M., Henning T., Kral Q., Matrà L., Wyatt M. C., 2020, MNRAS, 492, 4409
Matrà L., Panić O., Wyatt M. C., Dent W. R. F., 2015, MNRAS, 447, 3936
Matrà L. et al., 2017, ApJ, 842, 9
Matrà L., Wilner D. J., Öberg K. I., Andrews S. M., Loomis R. A., Wyatt M. C., Dent W. R. F., 2018, ApJ, 853, 147
Matrà L., Öberg K. I., Wilner D. J., Olofsson J., Bayo A., 2019, AJ, 157, 117
Montgomery S. L., Welsh B. Y., 2012, PASP, 124, 1042
Moór A. et al., 2017, ApJ, 849, 123
Moór A. et al., 2019, ApJ, 884, 108
Nakatani R., Kobayashi H., Kuiper R., Nomura H., Aikawa Y., 2021, ApJ, 915, 90
Öberg K. I., Guzmán V. V., Furuya K., Qi C., Aikawa Y., Andrews S. M., Loomis R., Wilner D. J., 2015, Nature, 520, 198
Okuzumi S., Hirose S., 2011, ApJ, 742, 65
Olofsson J. et al., 2022, MNRAS, 513, 713
Pearce T. D., Krivov A. V., Booth M., 2020, MNRAS, 498, 2798
Pinte C., Dent W. R. F., Ménard F., Hales A., Hill T., Cortes P., de Gregorio-Monsalvo I., 2016, ApJ, 816, 25
Pinte C. et al., 2018, A&A, 609, A47
Rebollido I. et al., 2018, A&A, 614, A3
Rebollido I. et al., 2020, A&A, 639, A11
Rollins R. P., Rawlings J. M. C., 2012, MNRAS, 427, 2328
Shakura N. I., Sunyaev R. A., 1973, A&A, 24, 337
Slettebak A., 1975, ApJ, 197, 137
Smirnov-Pinchukov G. V., Moór A., Semenov D. A., Ábrahám P., Henning T., Kóspál Á., Hughes A. M., Di Folco E., 2022, MNRAS, 510, 1148
Stoll M. H. R., Kley W., Picogna G., 2017, A&A, 599, L6
Takeuchi T., Artymowicz P., 2001, ApJ, 557, 990
Teague R., Bae J., Bergin E. A., Birnstiel T., Foreman-Mackey D., 2018, ApJ, 860, L12
Thébault P., Augereau J. C., 2005, A&A, 437, 141
Van Clepper E., Bergner J. B., Bosman A. D., Bergin E., Ciesla F. J., 2022, ApJ, 927, 206
van Dishoeck E. F., Black J. H., 1982, ApJ, 258, 533
Visser R., van Dishoeck E. F., Black J. H., 2009, A&A, 503, 323
Wyatt M. C., 2008, ARA&A, 46, 339
Wyatt M. C., Smith R., Greaves J. S., Beichman C. A., Bryden G., Lisse C. M., 2007, ApJ, 658, 569
Xu Z., Bai X.-N., Murray-Clay R. A., 2017, ApJ, 847, 52
Youdin A. N., Lithwick Y., 2007, Icarus, 192, 588
Youngblood A., Roberge A., MacGregor M. A., Brandeker A., Weinberger A. J., Pérez S., Grady C., Welsh B., 2021, AJ, 162, 235
Zhu Z., Stone J. M., Bai X.-N., 2015, ApJ, 801, 81
Zuckerman B., Song I., 2012, ApJ, 758, 77
Zuckerman B., Forveille T., Kastner J. H., 1995, Nature, 373, 494

APPENDIX A: PARAMETERS

In Table A1, we summarize the most important parameters that we use.

Downloaded from https://academic.oup.com/mnras/article/515/1/507/6617989 by University of Cambridge user on 12 August 2022

Table A1. Model parameters, their default units, and description.

Parameter	Unit	Description
r	au	Planetesimal belt radius
Δr	au	FWHM of planetesimal belt
z	au	Height above the disc mid-plane
H	au	Vertical disc scale-height as defined in equation (5)
Σ	$M_\oplus$ au^{-2}	Total surface density of gas
$\rho(z)$	$M_\oplus$ au^{-3}	Total density of gas at height z
$\rho_i(z)$	$M_\oplus$ au^{-3}	Density of species i (CO, CI or CII gas) at height z
Ω_K	rad yr^{-1}	Keplerian frequency
c_s	m s^{-1}	Isothermal sound speed as defined in equation (6)
μ	–	Mean molecular weight
m_p	kg	Proton mass
$L_\star$	$L_\odot$	Stellar luminosity
T	K	Gas temperature as defined in equation (7)
λ	nm	Wavelength
θ	rad	Polar angle measured from the vertical direction
$\sigma_{ph}(\lambda)$	cm^2	CO photodissociation cross-section from Heays et al. (2017)
σ_{CI}	cm^2	CI ionisation cross-section from Heays et al. (2017)
$\sigma_i(\lambda)$	cm^2	cross-section of species i
ϕ_λ	s^{-1} cm^{-2} nm^{-1}	Interstellar radiation field from Draine (1978) with extension from van Dishoeck & Black (1982)
$\tau_i(\lambda, \theta, z)$	–	Optical depth of species i in the direction θ at height z and wavelength λ as defined in equation (12)
$R_{ph,0}$	yr^{-1}	Unshielded CO photodissociation rate per molecule as defined in equation (9)
$R_{ph}(z)$	yr^{-1}	CO photodissociation rate per molecule at height z as defined in equation (10)
$K(N_{CO})$	–	Shielding factor due to CO self-shielding as defined in equation (16)
$\dot{\rho}_{ph}(z)$	$M_\oplus$ au^{-3} yr^{-1}	CO photodissociation rate per unit volume at height z as defined in equation (18)
$R_{ion,0}$	yr^{-1}	Ionization rate per CI atom in the optically thin regime as defined in equation (20)
$R_{ion}(z)$	yr^{-1}	Ionization rate per CI atom as defined in equation (19)
$R_{rc}(z)$	yr^{-1}	Recombination rate per CII atom as defined in equation (21)
$\alpha_{rc}(T)$	au^3 yr^{-1}	Recombination rate coefficient
$n_{e^-}(z)$	au^{-3}	Electron number density
$\dot{\rho}_{ion}(z)$	$M_\oplus$ au^{-3} yr^{-1}	Net ionization rate per unit volume at height z as defined in equation (22)
$\dot{\rho}^+$	$M_\oplus$ au^{-3} yr^{-1}	CO gas release rate per unit volume as defined in equation (4)
$\dot{\Sigma}^+$	$M_\oplus$ au^{-2} yr^{-1}	CO gas release rate per unit surface as defined in equation (8)
$\dot{M}^+$	$M_\oplus$ yr^{-1}	CO gas release rate
$\dot{\rho}_{vis,i}(z)$	$M_\oplus$ au^{-3} yr^{-1}	Mass-loss due to viscous evolution as defined in equation (23)
t_{vis}	yr	Viscous time-scale as defined in equation (24)
t_{diff}	yr	Vertical diffusion timescale as defined in equation (26)
ν	au^2 yr^{-1}	Kinematic viscosity defined as $\alpha c_s H$
α	–	Dimensionless viscosity parameter
D	au^2 yr^{-1}	Diffusion coefficient defined as $\alpha_v c_s H$
α_v	–	Dimensionless vertical diffusion parameter
$\dot{\rho}_{i,D}$	$M_\oplus$ au^{-3} yr^{-1}	Diffusion term as defined in equation (25)

APPENDIX B: VERTICAL STRUCTURE WITH $\alpha = 10^{-1}$

In Fig. B1, we show the vertical distribution of CO and CI as a function of the steady-state surface density of gas, and for three different values of α_v: 10^{-4}, 10^{-3}, and 10^{-2}. These correspond to the same ratios of α_v/α than those shown in Section 3.3. This demonstrates how the vertical distribution of CO and C will mostly depend on α_v/α rather than their absolute values.

Downloaded from https://academic.oup.com/mnras/article/515/1/507/6617989 by University of Cambridge user on 12 August 2022

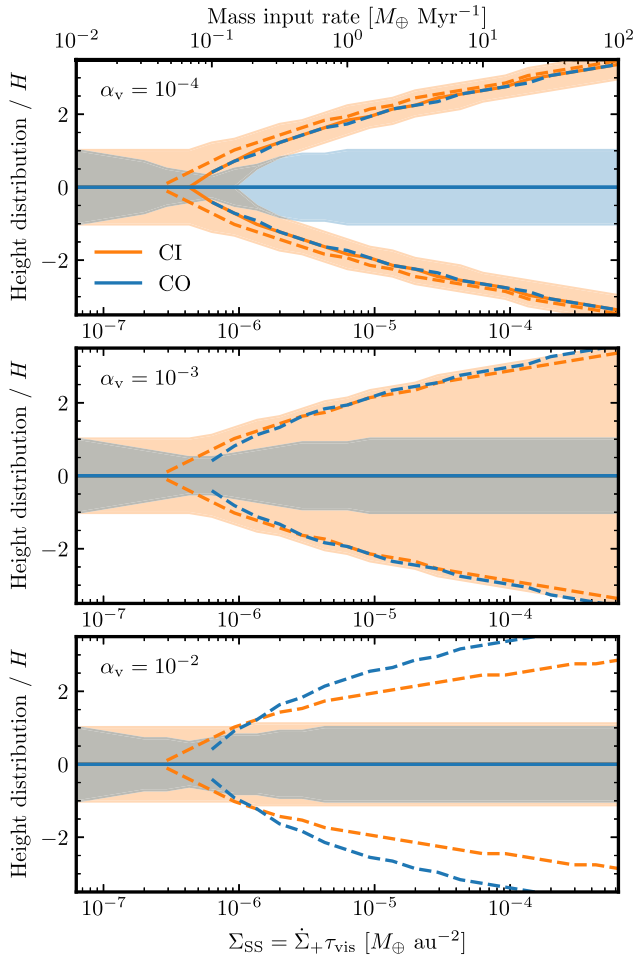

Figure B1. Vertical distribution in steady state of CO (blue) and CI (orange) normalized by the scale height (H) as a function of the steady state surface density of gas, in a case with $\alpha = 10^{-1}$. The solid line shows where the density distribution peaks, while the shaded region represents the region where the density is at least 60 per cent of the peak density (1σ drop). The dashed lines represent the height at which CI and CO become optically thick to photodissociating radiation in the vertical direction. The top, middle, and bottom panels show scenarios where α_v is 10^{-4}, 10^{-3}, and 10^{-2}, respectively. The upper x-axis intop panel shows the mass input rates as reference.

This paper has been typeset from a TEX/LATEX file prepared by the author.

Downloaded from https://academic.oup.com/mnras/article/515/1/507/6617989 by University of Cambridge user on 12 August 2022

MNRAS **000**, 1–19 (2020) Preprint 17 November 2021 Compiled using MNRAS LATEX style file v3.0

MRI-active inner regions of protoplanetary discs. II. Dependence on dust, disc and stellar parameters

Marija R. Jankovic[1]★, Subhanjoy Mohanty[2], James E. Owen[2] and Jonathan C. Tan[3,4]
[1]*Institute of Astronomy, University of Cambridge, Madingley Road, Cambridge CB3 0HA, UK*
[2]*Astrophysics Group, Imperial College London, Blackett Laboratory, Prince Consort Road, London SW7 2AZ, UK*
[3]*Dept. of Astronomy, University of Virginia, Charlottesville, Virginia 22904, USA*
[4]*Dept. of Space, Earth & Environment, Chalmers University of Technology, Gothenburg SE-412 96, Sweden*

Accepted XXX. Received YYY; in original form ZZZ

ABSTRACT

Close-in super-Earths are the most abundant exoplanets known. It has been hypothesized that they form in the inner regions of protoplanetary discs, out of the dust that may accumulate at the boundary between the inner region susceptible to the magneto-rotational instability (MRI) and an MRI-dead zone further out. In Paper I we presented a model for the viscous inner disc which includes heating due to both irradiation and MRI-driven accretion; thermal and non-thermal ionization; dust opacities; and dust effects on ionization. Here we examine how the inner disc structure varies with stellar, disc and dust parameters. For high accretion rates and small dust grains, we find that: (1) the main sources of ionization are thermal ionization and thermionic and ion emission; (2) the disc features a hot, high-viscosity inner region, and a local gas pressure maximum at the outer edge of this region (in line with previous studies); and (3) an increase in the dust-to-gas ratio pushes the pressure maximum outwards. Consequently, dust can accumulate in such inner discs without suppressing the MRI, with the amount of accumulation depending on the viscosity in the MRI-dead regions. Conversely, for low accretion rates and large dust grains, there appears to be an additional steady-state solution in which: (1) stellar X-rays become the main source of ionization; (2) MRI-viscosity is high throughout the disc; and (3) the pressure maximum ceases to exist. Hence, if planets form in the inner disc, larger accretion rates (and thus younger disks) are favoured.

Key words: planets and satellites: formation – protoplanetary discs

1 INTRODUCTION

Exoplanet discoveries have shown that close-in super-Earths, planets with radii of 1–4 $R_\oplus$ and orbital periods shorter than $\sim$100 days, are extremely common (Fressin et al. 2013; Dressing & Charbonneau 2013, 2015; Mulders et al. 2018; Hsu et al. 2019). To form the solid cores of these planets requires more mass in solids than is expected to exist at short orbital periods in the initial phases of planet formation in protoplanetary discs (Raymond et al. 2008; Chiang & Laughlin 2013; Schlichting 2014; Raymond & Cossou 2014). Because of this, it has been proposed that these super-Earths form further away from the star, in regions where the temperature in the protoplanetary disc is low enough for water ice to condense, which increases the total amount of solids. In this hypothesis, ice-rich planets migrate inwards, to their present orbits, through gravitational interactions with the disc (Terquem & Papaloizou 2007; Ogihara & Ida 2009; McNeil & Nelson 2010; Cossou et al. 2014; Izidoro et al. 2017, 2019; Bitsch et al. 2019). However, when compared against atmospheric evolution models, the observed radius distribution of close-in super-Earths is found to be consistent with their cores being rocky, with very little ice present (Owen & Wu 2017; Van Eylen et al. 2018; Wu 2019; Rogers & Owen 2021).

This possibly implies that close-in super-Earths form in the inner, hot regions of protoplanetary discs, near their present orbits. As noted above, it is not expected that these inner regions contain, initially, enough mass in solids to form the super-Earths. However, the inner disc can be enriched by pebbles from the outer disc (Hansen & Murray 2013; Boley & Ford 2013; Chatterjee & Tan 2014; Hu et al. 2018; Jankovic et al. 2019), as pebbles are prone to inwards radial drift due to gas drag (Weidenschilling 1977). It has been hypothesized (Chatterjee & Tan 2014) that the radial drift of pebbles could be stopped at a local gas pressure maximum in the inner disc. Over time the pressure maximum could accumulate enough material to form a super-Earth-sized planet.

A gas pressure maximum is expected to form in an inner disc that accretes viscously via turbulence induced by the magneto-rotational instability (MRI; Balbus & Hawley 1991; Kretke et al. 2009; Dzyurkevich et al. 2010; Chatterjee & Tan 2014). The sus-

★ E-mail: mj577@cam.ac.uk

© 2020 The Authors

ceptibility of the disc to the MRI depends on the coupling between the gas and the magnetic field, and thus on the ionization fraction in the disc. In the hot innermost disc, the MRI is expected to drive high viscosity (i.e., efficient accretion) as a result of thermal ionization. At larger distances, where gas is colder and the ionization fraction drops, the viscosity is expected to be low (such a region is called a dead zone; Gammie 1996). In steady-state, a local gas pressure maximum forms at the transition between the high-viscosity and the low-viscosity regions (the dead zone inner edge) (e.g. Terquem 2008).

The pressure maximum will only trap pebbles which are prone to radial drift relative to the gas. Smaller dust grains that are well coupled to the gas may be advected and diffused through the pressure maximum by the gas accreting onto the star. In the inner disc, the size of dust grains is limited by fragmentation due to relative turbulent velocities (Birnstiel et al. 2010, 2012; Drazkowska et al. 2016). Pebbles that radially drift from the outer to the inner disc become smaller due to fragmentation, and the effect of radial drift weakens. Jankovic et al. (2019) showed that, in an inner disc in which the gas accretion and the grain turbulent velocities are driven by the MRI, the grains can become small enough to escape the pressure trap through advection and radial mixing by the turbulent gas. Additionally, it was found that this leads to an enhanced dust-to-gas ratio of small dust grains throughout the inner disc, interior to the pressure maximum.

Jankovic et al. (2019) did not explicitly take into account the effects of dust on the MRI, whereas it can be expected that the accumulation of dust could quench the MRI in the innermost disc since dust grains adsorb free charges from the gas phase (Sano et al. 2000; Ilgner & Nelson 2006; Wardle 2007; Salmeron & Wardle 2008; Bai & Goodman 2009; Mohanty et al. 2013). As a consequence of quenching the MRI, the strength of the turbulence would fall allowing some grain growth. However, this would concurrently push the MRI-active region and the pressure maximum inwards, possibly eliminating it from the inner disc. Evidently, the outcome is a function of the size and the abundance of the dust grains.

In a previous paper (Jankovic et al. 2021, Paper I) we presented a model of a steady-state viscously accreting disc which includes both the MRI-driven viscosity and the effects of dust on the MRI. This accounts for the adsorption of free charges onto dust grains, and also for the electron (thermionic) and ion emission from dust grains into the gas phase. The thermionic and ion emission become important at temperatures above $\sim$1000 K (so at the temperatures present in the inner disc) and act to increase the ionization fraction of the gas (Desch & Turner 2015). We found that for 1 μm grains, comprising 1% of the disc mass, these dust effects balance out and result in a pressure maximum at roughly the same location as predicted from thermal ionization. Additionally, this model also self-consistently considers the disc opacity due to dust grains, thus accounting for the effects of dust on the disc thermal structure.

In the above work, we focused on a fiducial disc model. Building on this, in this paper we investigate how the inner disc structure changes with dust-to-gas ratio, dust grain size, and other disc and stellar parameters, in order to narrow down the region of parameter space where the formation of planetary cores in the inner disc is more likely. In section 2 we discuss the theoretical expectations about the location of the pressure maximum based on the results of Paper I. We briefly overview our disc model in section 3 and present our results in section 4. In section 5 we focus on the existence and location of the gas pressure maximum as a function of the above parameters, exploring the entire parameter space in detail. In section 6 we discuss the implications of our results for the formation of the super-Earths and the limitations of our work, and in section 7 we summarize our conclusions.

2 THEORETICAL EXPECTATIONS

A local gas pressure maximum is expected to form in an accretion disc at steady-state if the material in the inner regions accretes faster than the material in the outer regions. In the context of viscous accretion discs, for the pressure maximum to form, the disc viscosity should decrease with distance from the star. If the viscosity is driven by the MRI, the requirement is for the coupling between the magnetic field and the gas (i.e., the ionization fraction) to decrease radially outwards.

Such a configuration has been predicted to arise in protoplanetary discs as the innermost regions can be hot enough to thermally ionize potassium, whereas outer regions are not (Gammie 1996). Desch & Turner (2015) have shown that, in fact, at the temperatures present in the inner disc, the dominant sources of ionization are thermionic and ion emission from small dust grains, and not thermal ionization. Nevertheless, the resulting ionization fraction sharply increases above a certain critical temperature, the same as in the case of thermal ionization. Moreover, for the materials out of which we expect the small grains to be made of in the inner disc, this critical temperature is likely close to the temperature required for thermal ionization of potassium (about 1000 K; see the discussion in Desch & Turner 2015). This suggests that the pressure maximum should arise at roughly the same distance from the star as in the case of thermal ionization. In Paper I we showed that, for fiducial stellar, disc and dust parameters, this is indeed the case.

Therefore, we expect that a local gas pressure maximum indeed forms at the distance from the star at which the disc temperature reaches about $\sim$ 1000 K. In the inner disc, the MRI is active around the disc midplane (if the vertical temperature distribution is calculated self-consistently, see Paper I, and also Terquem 2008), and so it is the disc midplane temperature that sets the location of the pressure maximum. Furthermore, as we show in Paper I, the midplane temperature is set by the heat released by the accretion and the disc cooling, while the heating by stellar irradiation has a small effect on the location of the pressure maximum, due to the inner disc being vertically optically thick. We also find that the inner disc is unstable to vertical convection.

Given the above findings, it is useful to consider how the disc midplane temperature (and thus the location of the pressure maximum) scales with different disc, stellar and dust parameters using the simple Shakura & Sunyaev (1973) viscous thin disc model, modified to account for vertical convection. In this model, the viscosity ν is parametrized by the dimensionless α parameter and given by $\nu = \alpha c_s^2/\Omega$, where c_s is the sound speed and Ω the angular Keplerian velocity. It is assumed that the disc is at steady-state, i.e., has a radially-constant gas accretion rate $\dot{M}$, and that the only source of heating is the accretion, that the disc is strongly optically thick (such that the majority of the discs mass is below the photosphere) and is convective up to the cooling radiation photosphere. Under these assumptions, Garaud & Lin (2007) showed that the disc's midplane temperature (T) is approximately related to the effective temperature ($T_{\rm eff}$, determined by viscous dissipation) via $T \propto \tau_0^{2/7} T_{\rm eff}^{(7+2\beta)/7}$ where β encapsulates the temperature dependence of the opacity via $\kappa = \kappa_0 (T/T_0)^\beta$, with T_0 a reference temperature and $\tau_0 \equiv \kappa_0 \Sigma/2$ (with Σ the disc surface density) the optical depth to radiation at

the reference temperature[1]. For constant β the disc structure is then described by a set of power-law relations. For the disc midplane temperature, away from the disc inner edge, we have

$$T \propto \kappa_0^{2/9} \alpha^{-2/9} \dot{M}^{\frac{15+2\beta}{36}} M_*^{\frac{11+2\beta}{36}} r^{-\frac{11+2\beta}{12}}, \quad (1)$$

where M_* the stellar mass, $\dot{M}$ the disc accretion rate and r the cylindrical radius. Then, if the pressure maximum arises at a fixed temperature, its radial location scales with other parameters as:

$$r_{P_{\max}} \propto \kappa_0^{\frac{8}{3(11+2\beta)}} \alpha^{-\frac{8}{3(11+2\beta)}} \dot{M}^{\frac{15+2\beta}{3(11+2\beta)}} M_*^{1/3}. \quad (2)$$

Inspection of our Rosseland mean opacities in Figure 1 indicates values of $\beta \sim 0.5$ for temperatures around 1000 K, thus for this choice of β we find:

$$r_{P_{\max}} \propto \kappa_0^{2/9} \alpha^{-2/9} \dot{M}^{4/9} M_*^{1/3}. \quad (3)$$

Therefore, for this choice of β, we obtain an expression that is exactly the same as the one found by Chatterjee & Tan (2014), who assumed that the disc was cooled radiatively. This agreement arises because for values of β of order unity or smaller, the radiative $T(\tau)$ relation in discs $T \propto \tau^{1/4} T_{\rm eff}$ is a reasonable approximation for the mid-plane temperature in a very optically thick convective disc (e.g. Cannizzo & Wheeler 1984). Putting in the correct constants and fiducial disc parameters for a Solar mass star into eq. (3), one arrives at a value of a few tenths of an AU, which falls within the range of the observed orbital radii of the close-in super-Earths (see Chatterjee & Tan 2014).

Equation (3) tells us how the radius of the pressure maximum depends on the various disc and stellar parameters. If the pressure maximum arises at a fixed temperature, a disc that is hotter will feature a pressure maximum at a larger distance from the star, and a disc that is too cold will not feature a pressure maximum at all. The disc midplane is hotter if the heating rate is higher, or if radiative cooling is less efficient. The heating rate due to viscous dissipation is directly proportional to the accretion rate and the stellar mass. On the other hand, the cooling rate is reduced by increasing the optical depth of the disc. At a fixed value of viscosity parameter α, higher accretion rate and stellar mass yield a disc with a higher surface density and thus a disc that is more optically thick and less efficient at cooling. Higher opacity also makes the disc more optically thick. Therefore, higher accretion rate, stellar mass and opacity all lead to a larger radius of the pressure maximum.

Conversely, higher value of the viscosity parameter α makes the disc surface density lower and thus it makes the disc less optically thick. The radius of the pressure maximum is thus inversely related to α. Note that the value of α discussed here is the value at the location of the pressure maximum, i.e., at the location where the MRI is (largely) suppressed. It thus refers to the small viscosity driven either by propagation of turbulence from the adjacent MRI-active inner region or by other, hydrodynamical processes. In this work, it is a free parameter, and we refer to it as the minimum or dead-zone viscosity parameter.

Furthermore, we can expand on eq. (3) by considering how the mass opacity (κ) depends on the properties of dust. First, we assume that the dust grain size distribution follows a power-law distribution $n(a) \propto a^{-3.5} da$ with a minimum grain size $a_{\min}$ and a maximum grain size $a_{\max}$. Second, we neglect gas opacities and scattering (or assume a constant albedo). Under these assumptions, the opacity can be approximated as the ratio of the surface area of all dust grains larger than the wavelength of peak local radiation (smaller grains, if there are any, contribute much less to the absorption cross section) and the total dust mass. For the above grain size distribution, this surface area is dominated by the grains of the size of the peak wavelength, while the mass is dominated by the largest grains. Then, if we also assume that the maximum dust grain size ($a_{\max}$) is much larger than the peak wavelength, at a fixed temperature, the opacity κ has a simple dependence on $a_{\max}$ and the dust-to-gas ratio $f_{\rm dg}$, $\kappa_0 \propto f_{\rm dg} a_{\max}^{-1/2}$. Finally, for the radial location of the pressure maximum we obtain

$$r_{P_{\max}} \propto f_{\rm dg}^{2/9} a_{\max}^{-1/9} \alpha^{-2/9} \dot{M}^{4/9} M_*^{1/3}. \quad (4)$$

Evidently, this scaling does not take into account how the critical ionization temperature (at which thermionic and ion emission become efficient) depends on the dust properties. Even if the disc is thermally ionized, the above derivation neglects the dependence of the critical temperature on the density and the complexity of the criteria for the onset of the MRI. However, for the case of thermal ionization, we can compare eq. (4) with fits to the numerical results of Mohanty et al. (2018), who self-consistently coupled the simple Shakura-Sunyaev disc model with thermal ionization of potassium and a detailed prescription for MRI-driven viscosity (the same one used in this work). The fits were obtained for the viscosity parameter, accretion rate and stellar mass, which combined together yield

$$r_{P_{\max}} \propto \alpha^{-1/4} \dot{M}^{1/2} M_*^{1/3}. \quad (5)$$

While the exponents here deviate somewhat from eq. (4), the deviations are small (see also Kretke et al. 2009). Therefore, for the case of thermal ionisation, the scaling of $r_{P_{\max}}$ with α, $\dot{M}$ and M_* given in eq. (4) remains approximately correct. In this work, we use our new model to determine whether these deviations from the simple scaling become larger when thermionic and ion emission are accounted for, and also explore the dependence on the dust parameters.

Finally, note that the entire discussion so far has been made under an assumption that the disc's ionization fraction rises sharply above a fixed critical temperature. However, non-thermal sources of ionization are also present in protoplanetary discs (most importantly stellar X-rays; Glassgold et al. 1997; Ercolano & Glassgold 2013). Non-thermal sources of ionization increase the ionization fraction at all orbital radii, not only in the high-temperature inner region. In Paper I we explored how this affects the MRI-driven viscosity in the inner disc, for a set of fiducial model parameters. The effect of any of the ionisation sources on the MRI-driven viscosity depends on the magnetic field strength. Under the assumptions made in Paper I about the field strength (that it is vertically constant and evolves to maximize the MRI-driven α), the stellar X-rays only contribute to the MRI-driven accretion in the outer regions, outwards from the pressure maximum, and also at the location of the pressure maximum, since α has to be a continuous function. If this is indeed the case, the role of the X-rays is simply to increase the α in eq. (4), which pushes the pressure maximum inwards. Since the contribution of the X-rays to accretion in the inner regions is neglected, the above assumptions maximize the effect of the X-rays on the location of the pressure maximum. Nevertheless, in Paper I we showed that, for fiducial disc and stellar parameters, this effect is completely negligible. Firstly, for those fiducial parameters, the surface densities in the inner disc are much higher than the column that the X-rays can penetrate. Second, in the X-ray ionized regions,

[1] The optical depth to cooling radiation can be calculated through the evaluation of $\tau = \int_0^\infty \kappa(T(z))\rho(z)\mathrm{d}z$.

dust grains act as an efficient recombination pathway for the ions, which significantly suppresses the MRI (Sano et al. 2000; Ilgner & Nelson 2006; Wardle 2007; Salmeron & Wardle 2008; Bai & Goodman 2009; Mohanty et al. 2013). The adsorption of gas-phase ions onto the dust grain surfaces depends primarily on the total dust grain surface area. Therefore, we can expect that the stellar X-rays become more important in a less massive disc (e.g., for disc accretion rates that are lower than our fiducial one), and also for lower dust-to-gas ratios and larger dust grains. As we explore the disc parameter space in this paper, we identify the limits in which the ionization due to stellar X-rays becomes important for the location (and the existence) of the pressure maximum.

3 METHODS

Our disc model is presented in Paper I. Here, we only summarize the main points. It is assumed that the viscously-accreting disc is in steady-state, i.e., that the gas accretion rate $\dot{M}$ is radially constant. The disc structure is calculated self-consistently with disc opacities, ionization state and the viscosity due to the MRI. The disc is assumed to be in vertical hydrostatic and thermal equilibrium, heated by viscous dissipation and stellar irradiation, and cooled radiatively and/or via convection.

We account for heating by stellar irradiation using the grazing angle prescription (Calvet et al. 1992; Chiang & Goldreich 1997; D'Alessio et al. 1999). For the first radial point we assume the flat-disc approximation. The disc structure and the grazing angle at every other radial point are determined self-consistently. To calculate the grazing angle, we perform a smoothing over a number of grid points (see Paper I for details). As such, the first few grid points in our calculation are sensitive to how we perform this smoothing, and we indicate the affected region in our figures throughout this paper.

We consider disc opacities due to silicate dust grains, and we calculate the opacities for a MRN grain size distribution (Mathis et al. 1977), with a minimum grain size $a_{\rm min} = 0.1\,\mu$m and a maximum grain size $a_{\rm max}$, using optical constants from Draine (2003, see Paper I for details), and assuming bulk density of dust grains $\rho_{\rm s} = 3.3\,{\rm g\,cm^{-3}}$. In the calculation of the Rosseland-mean opacity we include the scattering coefficient, but assume that the scattering is isotropic. Figure 1 shows the opacities, calculated per unit mass of gas, for different maximum grain sizes $a_{\rm max}$, assuming a dust-to-gas ratio $f_{\rm dg} = 0.01$ and stellar effective temperature $T_* = 4400\,{\rm K}$. We only consider the structure of the disc beyond the silicate sublimation line, when dust opacities typically dominate over those of the gas, and so neglect the opacities due to gas molecular and atomic lines (but see section 6.3). Additionally, the water ice and carbonaceous grains have sublimation temperatures that are much lower than the temperatures expected in the hot MRI-active regions (e.g. Pollack et al. 1994). These grains may condense in the colder layers such as the photosphere to the disc radiation. Still, for simplicity, we neglect the contribution from other dust species.

The disc ionization state is calculated using a simple chemical network (Desch & Turner 2015) that includes thermal (collisional) ionization of potassium; ionization of molecular hydrogen by stellar X-rays, cosmic rays and radionuclides (producing metal (magnesium) ions by charge transfer); gas-phase recombinations; adsorption onto dust grains and thermionic and ion emission from dust grains. Both charged and neutral species can be adsorbed (or condensed) in collisions with dust grains. Neutral potassium atoms, potassium ions and electrons can also be emitted back into the gas phase. The rates at which the latter processes occur increase with

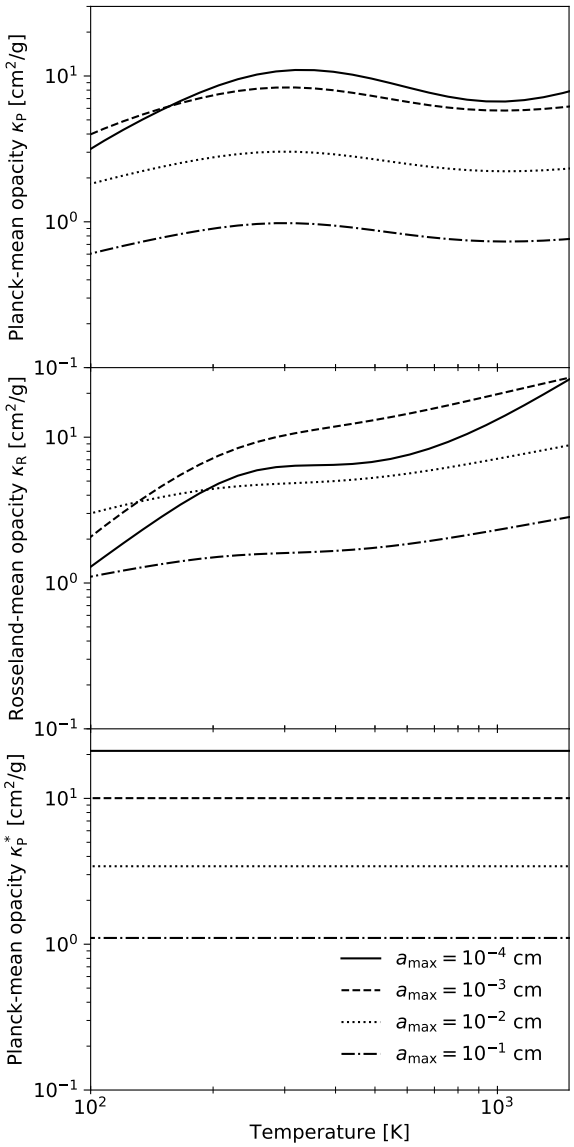

Figure 1. Planck-mean opacity $\kappa_{\rm P}$ (top), Rosseland-mean opacity $\kappa_{\rm R}$ (middle), and Planck-mean opacity at the stellar effective temperature $\kappa_{\rm P}^*$ (i.e., the absorption coefficient for the stellar irradiation; bottom), per unit mass of gas, as functions of disc temperature, for different maximum grain sizes $a_{\rm max}$ as indicated in plot legend, assuming a dust-to-gas ratio $f_{\rm dg} = 0.01$ and stellar effective temperature $T_* = 4400\,{\rm K}$. Absorption is dominated by small grains, and so the Planck-mean opacities decrease with increasing maximum grain size. The Rosseland-mean opacity is a non-monotonic function of grain size for $a_{\rm max} \lesssim 10^{-2}$ cm.

increasing temperature, as determined by 3 different activation energies and the charge state of the dust grains. Firstly, evaporation of potassium atoms from dust grains is determined by our adopted binding energy of potassium ($E_{\rm a} = 3.26\,{\rm eV}$), whose value is chosen to match the condensation temperature of a common potassium-bearing mineral (see Desch & Turner 2015). Furthermore, a fraction of the potassium atoms evaporating from dust grains may be ionised in the process. This is referred to as ion emission, and it is a function of the ionization potential (IP $= 4.34\,{\rm eV}$) of potassium, as well as the work function of the material of which the dust is composed (for the discussion of the adopted value, $W = 5\,{\rm eV}$, see Desch &

Turner 2015). Thermionic emission, i.e., emission of electrons from heated dust grains, is also determined by the work function. Additionally, the charge state of the grains effectively changes the work function. For example, ion emission results in negatively charged grains, which reduces the effective work function and increases the thermionic emission rate.

Only a single dust grain species of size $a_{\rm gr} = 0.1\,\mu$m is considered in the chemical network, but an effective dust-to-gas ratio $f_{\rm eff}$ is chosen to mimic the full size distribution stated above (see Paper I for details). This approach is based on an assumption that multiple grain species behave independently in the chemical network, and that it is a combination of the grain abundance and the grain size that controls the chemistry of the disc (see also Bai & Goodman 2009). Specifically, we choose $f_{\rm eff}$ here such that the ionisation threshold temperature (above which thermionic and ion emission become efficient) approximately mimics that expected for the full range of grain sizes (see Paper I).

Among the non-thermal sources of ionization, stellar X-rays appear to be the most important one for the models investigated here where the focus is on the inner regions of the disc. The ionization rate of molecular hydrogen by stellar X-rays is calculated using Bai & Goodman (2009) fits to the Igea & Glassgold (1999) Monte Carlo simulations (using the fits for $kT_X = 3\,$keV), so at any point in the disc it is a function of the cylindrical radius and the vertical mass column from the disc surface to that point. We ignore the X-rays coming through the bottom side of the disc and note that in a low-surface-density disc this may increase the ionization fraction by a factor of 2 at most. For the stellar X-ray luminosity we adopt $L_{\rm X} = 10^{-3.5} L_{\rm bol}$ (e.g. Wright et al. 2011; Güdel et al. 2007; Preibisch et al. 2005, but note that there is significant scatter in the observed luminosities and for a single star this luminosity may also be variable due to stellar flares).

Finally, the viscosity due to the MRI, parametrized using the Shakura & Sunyaev (1973) α parameter, is calculated using a prescription based on the results of magnetohydrodynamic simulations (see Paper I). This accounts for the suppression of the MRI by Ohmic and ambipolar diffusion. In the MRI-dead zones (where the MRI is suppressed), we assume the gas can still accrete due to a small constant viscosity parameter $\alpha_{\rm DZ}$, induced either by the adjacent MRI-active zone or by purely hydrodynamical instabilities. The viscous α is calculated both as a function of radius and height, and we define a vertically-averaged viscosity parameter

$$\bar{\alpha} \equiv \frac{\int_0^{z_{\rm surf}} \alpha P dz}{\int_0^{z_{\rm surf}} P dz}, \tag{6}$$

where $z_{\rm surf}$ is the height of the disc surface, defined as the height above the mid-plane where the gas pressure falls below a small constant value ($P(z_{\rm surf}) = 10^{-10}\,$dyn cm^{-2}). The weighting of the viscosity parameter α by pressure is motivated by the relationship between the α and the accretion rate: in steady-state, the accretion rate is proportional to the numerator in the above expression.

4 RESULTS

Here, we explore the effects of varying the important physical parameters on the inner disc structure. Initially, we vary the parameters one-by-one: dust-to-gas ratio $f_{\rm dg}$ and maximum dust grain size $a_{\rm max}$ in section 4.1, and the gas accretion rate $\dot{M}$, stellar mass M_*, and the dead-zone viscosity $\alpha_{\rm DZ}$ in section 4.2. We then extend the exploration of the parameter space by concurrently considering a larger dust grain size and a lower gas accretion rate, in section 4.3, discovering an X-ray dominated solution. As our fiducial model, taken from Paper I, we consider a disc with a gas accretion rate $\dot{M} = 10^{-8}\,{\rm M}_\odot\,{\rm yr}^{-1}$, stellar mass $M_* = 1\,{\rm M}_\odot$, stellar radius $R_* = 3\,{\rm R}_\odot$, effective stellar temperature $T_* = 4400\,{\rm K}$[2], viscosity parameter in the MRI-dead zone $\alpha_{\rm DZ} = 10^{-4}$, dust-to-gas ratio $f_{\rm dg} = 10^{-2}$, and maximum dust grain size $a_{\rm max} = 10^{-4}\,$cm. In Paper I, this model was used to discuss the impact of various physical and chemical processes on the inner disc structure.

4.1 Dust-to-gas ratio and dust size

As noted in section 2, dust has two effects on the disc structure in our model: it determines opacities in the disc, and it affects the disc ionization state. To better understand the results of varying dust properties, we first consider only the dust opacities. That is, in section 4.1.1, we consider a model with a vastly simplified chemical network, in which the only source of ionization is thermal ionization of potassium and free charges recombine only in the gas phase. Then, in section 4.1.2 we present the results of our full model which also accounts for the adsorption of charges onto dust grains, thermionic and ion emission from dust grains, and ionization of molecular hydrogen by stellar X-rays, cosmic rays and radionuclides.

4.1.1 Thermally-ionized model

In this section we consider a model which includes dust opacities, but does not include dust effects on the disc chemistry, nor ionization of molecular hydrogen. Thus, the ionization fraction is set exclusively by thermal ionization. The results of varying the dust-to-gas ratio, $f_{\rm dg}$, in the range $10^{-4} - 1$ are shown in the left column of Fig. 2.

In this simplified, thermally-ionized disc model, the MRI is only active at small radii. Therefore, the viscosity is highest in the innermost region where the midplane ionization fraction and the midplane temperature (shown in the second and third row, respectively) are highest, and it decreases with distance from the star. At some radius the ionization fraction drops below that needed to sustain the MRI, and the viscosity parameter $\bar{\alpha}$ falls to the minimum, dead-zone value $\alpha_{\rm DZ}$. That radius is the location of the local gas pressure maximum, shown in the bottom panel.

We find that a higher dust-to-gas ratio results in a larger MRI-active zone (the region where $\bar{\alpha} > \alpha_{\rm DZ}$). This is the behaviour expected from eq. (4). Because the inner disc is optically-thick, the disc midplane temperature is set by the accretion heat released near midplane and the optical depth of the disc to its own radiation (with a caveat that the vertical temperature gradient is additionally limited by convection; see Paper I). The disc's opacity is directly proportional to the dust-to-gas ratio, i.e., a disc with more dust is more optically-thick. As discussed in section 2, increasing optical depth makes the cooling less efficient, and the midplane hotter and more ionized, leading to a higher MRI-induced viscosity at a given radius. At lower dust-to-gas ratios gas opacities (which are neglected here) should become more important than at higher dust-to-gas ratios, but the main results shown here would likely be unaffected if the gas opacities were included (see Section 6.3).

[2] These specific stellar parameters correspond to a Solar-mass star at an age of 0.5 Myr in the stellar evolution models of Baraffe et al. (2015). Over the first 5 Myr the luminosity of a Solar-mass star decreases by a factor of 5 in these models, and so the adopted parameters are roughly valid throughout the disc lifetime.

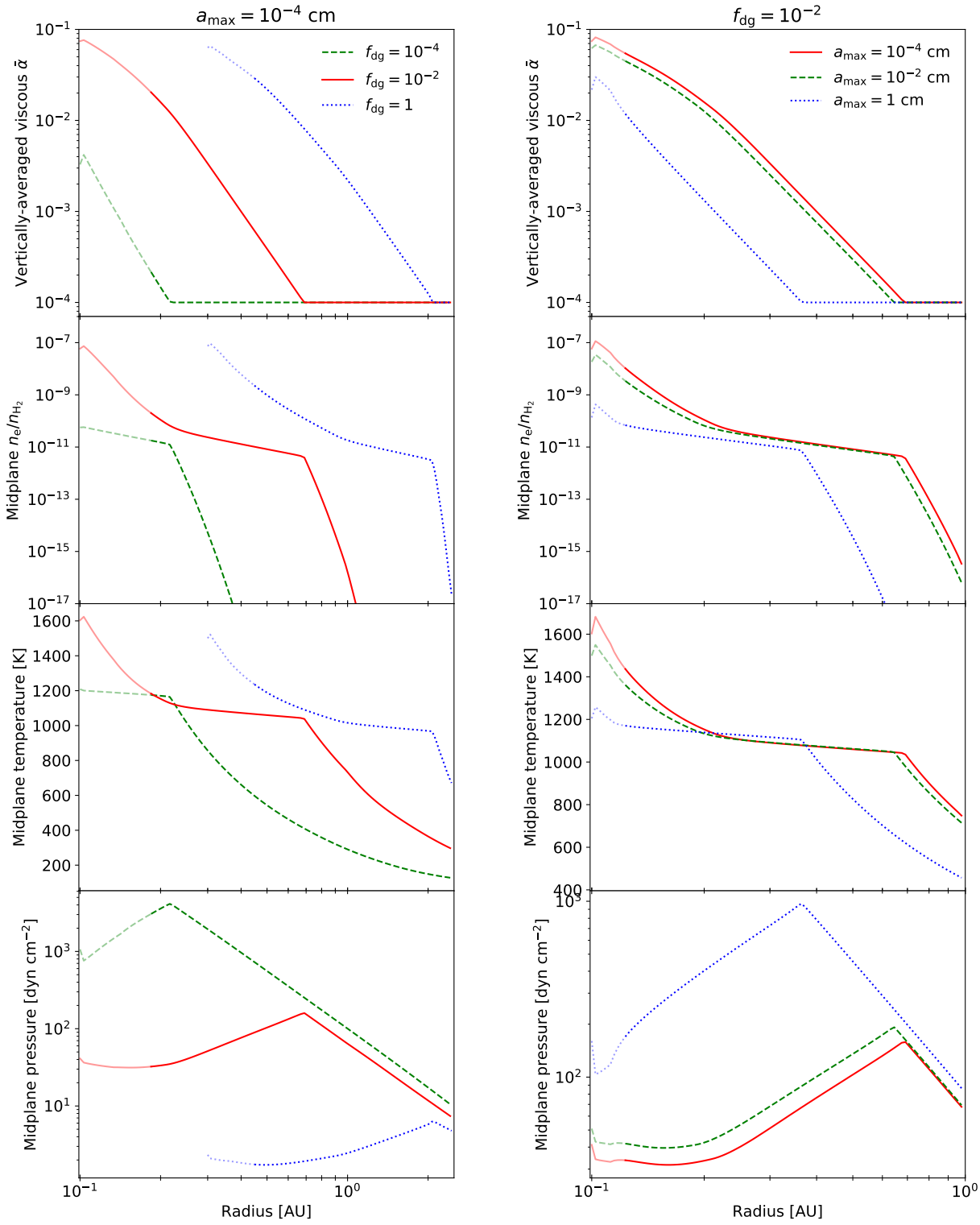

Figure 2. Results for a thermally-ionized disc (where the only source of ionization is thermal ionization of potassium, and dust effects on the disc chemistry are not included). The left column shows models with a constant maximum grain size $a_{\rm max} = 10^{-4}$ cm and varying dust-to-gas ratio $f_{\rm dg}$ as indicated in plot legend. The right column shows models with a constant dust-to-gas ratio $f_{\rm dg} = 10^{-2}$ and varying maximum grain size $a_{\rm max}$ as indicated in plot legend. The rows show radial profiles of (from top to bottom) vertically-averaged viscosity parameter $\bar{\alpha}$, midplane free electron fraction $n_{\rm e}/n_{\rm H_2}$, midplane temperature and midplane pressure. The inner edge of the $f_{\rm dg} = 1$ model is set to ~ 0.3 AU, since radially inwards temperature increases above the sublimation temperature of silicates. The light lines indicate the regions affected by the inner boundary condition (see Section 3). The radius of the pressure maximum is larger for a larger dust-to-gas ratio and a smaller maximum grain size. Note that the axis ranges are different in the left and the right column. See Section 4.1.1.

Furthermore, the right column of Fig. 2 shows models with a constant dust-to-gas ratio of $f_{\rm dg} = 10^{-2}$, but varying the maximum dust grain size $a_{\rm max}$ in the range $10^{-4} - 1$ cm. For the three values of $a_{\rm max}$ considered here, the MRI-active region becomes smaller if dust grains are larger. This is because, for these values of $a_{\rm max}$, larger dust grains have lower opacities (see Fig. 1), making the inner disc less optically thick. Just as in a disc with a lower dust-to-gas ratio, this makes the disc midplane cooler and less ionized.

Therefore, in these simplified, thermally-ionized models, if dust growth were to happen, this would result in the MRI-active zone edge being pushed inwards. We emphasize that it is the changes to the dust opacities alone that lead to these significant changes in the extent of the MRI-active zone. The effects of including dust grains in our chemical network are explored next.

4.1.2 *Full model*

In this section, we consider our full model that additionally includes (direct) effects of dust on the ionization fraction (adsorption of free charges onto dust grains, thermionic and ion emission), and also ionization of molecular hydrogen. Three sources of ionization are considered for the latter (stellar X-rays, cosmic rays and radionuclides), the X-rays being the most important (see Paper I). The results of varying the dust-to-gas ratio and maximum dust grain size in this full model are shown in the left and the right column of Fig. 3, respectively.

As in the simplified, thermally-ionized models discussed above, in the innermost regions the viscosity parameter decreases with distance from the star. Here, however, the viscosity parameter reaches a minimum value close to the dead-zone viscosity, and then increases again radially outwards, due to ionization by stellar X-rays (this is true in all models, even if not always evident in the plots). As discussed in Section 2 (Paper I; Desch & Turner 2015), in the full model the main source of ionization are thermionic and ion emission from dust grains in the inner disc. While this is a fundamentally different mechanism from gas-phase thermal ionization, the ionization states of the disc are quantitatively similar in the two cases due to their similar activation energies. As a result, the viscosity parameter in these innermost regions is similar to the models with no dust in the chemical network. In Paper I, we discussed this case for the fiducial maximum grain size $a_{\rm max} = 10^{-4}$ cm. The results presented in this work show that this conclusion holds at a wide range of dust-to-gas ratios and grain sizes (e.g., compare Fig. 3 with Fig. 2).

The case of high dust-to-gas ratio of $f_{\rm dg} = 1$ deviates somewhat from the above scenario. In this model, the midplane free electron fraction decreases substantially already at the distance of ~ 0.9 AU (see the left panel, second row in Fig. 3). However, the viscous $\bar{\alpha}$ remains high out to ~ 2 AU in this model (the top left panel in Fig. 3). In this high-$\bar{\alpha}$ region, the MRI is indeed active at the disc midplane (as shown in the top panel of Fig. 4), despite the large decrease in the midplane electron number density. What drives the MRI in this case?

The bottom panel of Fig. 4 shows that between ~ 0.4 AU and ~ 2 AU the main ionized species are the potassium ions and the dust grains. As expected, the number density of electrons decreases with increasing dust-to-gas ratio (keeping other parameters fixed). However, the opposite is true for the number density of potassium ions evaporating from dust grains, above ~ 900 K (see Desch & Turner 2015), which increases with increasing dust density. In the resulting disc ionization state, due to charge conservation, the total charge of potassium ions equals the total charge on dust grains. Clearly, since the dust grains have a much higher inertia than potassium ions, it is the potassium ions that couple the gas to the magnetic field. Overall, these results show that emission of potassium from dust grains is sufficient to sustain the MRI out to large radii, at high dust-to-gas ratios. Although, we note that at dust-to-gas ratios approaching unity the dynamical back reaction of the dust on the gas would need to be included, an effect which is poorly studied in the context of MRI turbulence and by extension not included in our parameterisation of the how the viscosity depends on the ionization structure. Clearly, MHD simulations of this disc state are warranted to study its behaviour. Particularly as our previous work in Jankovic et al. (2019) has indicated dust-to-gas ratios approaching unity in the inner MRI active regions is a possible outcome of disc evolution.

Furthermore, as noted above, in our full model the viscosity parameter $\bar{\alpha}$ reaches a minimum value, outwards from which it increases with radius. The minimum in the viscosity parameter corresponds to the location of the gas pressure maximum, shown in the bottom panels of Fig. 3. Outwards of the pressure maximum, the temperature at the disc midplane is too low for efficient ionization, and so the MRI is only active in an X-ray-ionized layer high *above* disc midplane (seen near ~ 2 AU in the top panel of Fig. 4). Inwards of the pressure maximum, this X-ray-ionized layer does not appear; as discussed in Paper I, this is due to our assumption that the magnetic field strength is vertically constant, and the fact that the magnetic field strengths required for the MRI differ greatly in the high-density midplane and the low-density upper layers. In the outer, X-ray-ionized regions, the viscosity parameter increases with decreasing dust-to-gas ratio and increasing dust grain size. This is because the main source of ionization are the stellar X-rays, and dust only acts as a recombination pathway. For lower dust-to-gas ratios and, equivalently, higher maximum grain size, the total grain surface area (onto which free charges adsorb) decreases, leading to higher ionization fraction and higher MRI-driven viscosity (Sano et al. 2000; Ilgner & Nelson 2006). As expected from eq. (4), this increase in the value of $\bar{\alpha}$ at the location of the pressure maximum pushes the pressure maximum inwards. This effect is somewhat exaggerated since the effect of the X-rays on $\bar{\alpha}$ is neglected inwards of the pressure maximum (due to the model limitations noted above). Nevertheless, for the majority of the parameter space explored so far the contribution to the accretion rate from the X-ray-ionized layer is low in all cases and the viscosity parameter $\bar{\alpha} \sim \alpha_{\rm DZ}$ in the outer regions. In other words, in these outer regions the gas primarily accretes through the dead zone, and the stellar X-rays do not affect strongly the location of the pressure maximum (for the given gas accretion rate).

Overall, the extent of the high-viscosity inner region and the location of the pressure maximum is dictated by the dependence of disc's vertical optical thickness on the dust-to-gas ratio and dust grain size through the effects discussed in the previous section. In our full model the location of the pressure maximum is approximately the same for $a_{\rm max} = 10^{-4}$ cm and $a_{\rm max} = 10^{-2}$ cm (see the top right panel in Fig. 3). This is because a larger grain size results in a lower effective dust-to-gas ratio in our chemical network. This slightly decreases the critical temperature at which the thermionic and ion emission make the gas sufficiently ionized to start the MRI at disc midplane. Concurrently, the dust opacity for the case of $a_{\rm max} = 10^{-2}$ cm is only slightly smaller than for $a_{\rm max} = 10^{-4}$ cm in the relevant temperature range (see Fig. 1). The location of the pressure maximum as a function of dust grain size is considered in more detail in section 5.

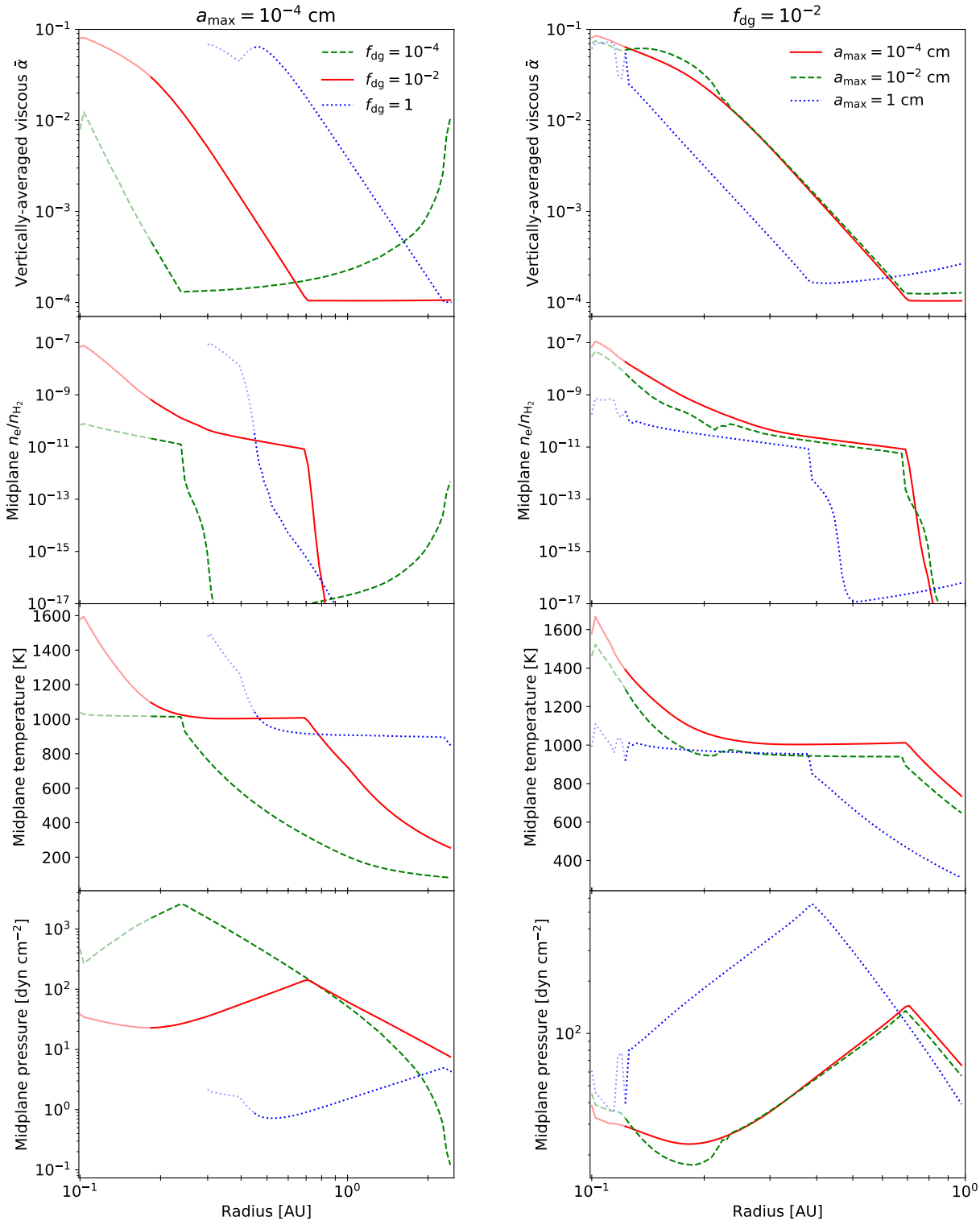

Figure 3. Results for our full model which includes dust effects on disc chemistry and ionization of molecular hydrogen. The left column shows models with a constant maximum grain size $a_{\rm max} = 10^{-4}$ cm and varying dust-to-gas ratio $f_{\rm dg}$ as indicated in plot legend. The right column shows models with a constant dust-to-gas ratio $f_{\rm dg} = 10^{-2}$ and varying maximum grain size $a_{\rm max}$ as indicated in plot legend. The rows show radial profiles of (from top to bottom) vertically-averaged viscosity parameter $\bar{\alpha}$, midplane free electron fraction $n_{\rm e}/n_{\rm H_2}$, midplane temperature and midplane pressure. The light lines indicate the regions affected by the inner boundary condition (see Section 3). The radius of the pressure maximum is larger for a larger dust-to-gas ratio; it is approximately the same for the maximum grain size of 10^{-4} cm and 10^{-2} cm, but much smaller for the maximum grain size of 1 cm. Note that the axis ranges are different in the left and the right column. See Section 4.1.2.

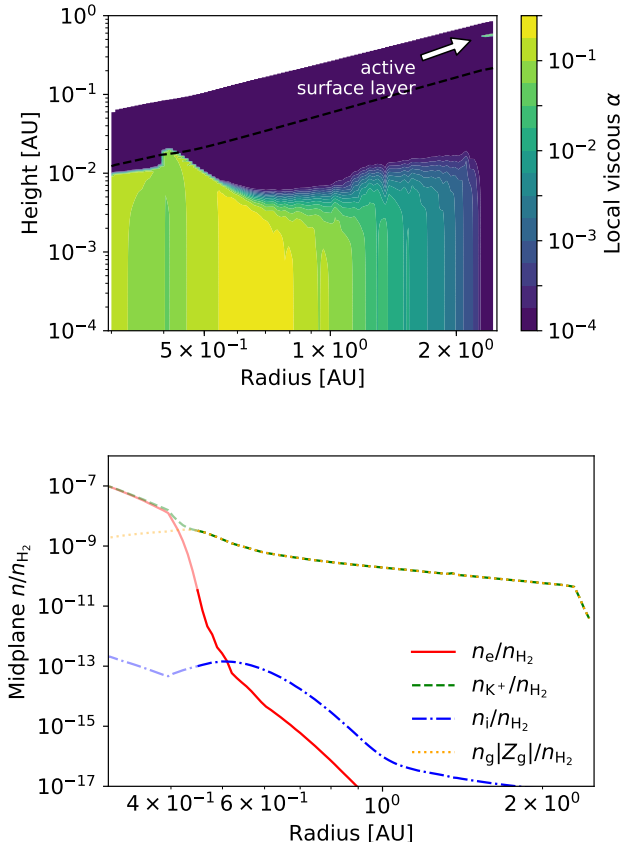

Figure 4. Local viscosity parameter α as a function of location in the disc (top) and the fractional number densities of various ionized species at the disc midplane as a function of radius (bottom), in a model with a dust-to-gas ratio of $f_{\rm dg} = 1$ (with other parameters equal to the fiducial values). The species shown in the bottom panel are free electrons ($n_{\rm e}$), potassium ions ($n_{\rm K^+}$), magnesium ions ($n_{\rm i}$) and dust grains ($n_{\rm g}$, carrying a mean charge $Z_{\rm g}$). See Section 4.1.2.

4.2 Gas accretion rate, stellar mass, dead-zone viscosity

In this section we keep the dust-to-gas ratio and the maximum dust grain size constant and equal to our fiducial values, and investigate how the structure of the inner disc changes with varying gas accretion rate, stellar mass and dead-zone viscosity. Fig. 5 shows the results of our fiducial model compared to three other models in which we vary these three parameters. The different panels show, from top to bottom, the vertically-averaged viscosity parameter ($\bar{\alpha}$), midplane free electron fraction ($n_{\rm e}/n_{\rm H_2}$), midplane temperature and midplane pressure, as functions of radius.

In each panel the dashed line shows a model with a gas accretion rate $\dot{M} = 10^{-9}\,{\rm M}_\odot\,{\rm yr}^{-1}$, lower than in our fiducial model with $\dot{M} = 10^{-8}\,{\rm M}_\odot\,{\rm yr}^{-1}$, shown by the solid line. The lower gas accretion rate results in a smaller high-viscosity inner region, and a gas pressure maximum at a shorter radius. This is in line with the theoretical expectations discussed in Section 2. In the optically-thick inner disc, the midplane temperature (and consequently the ionization fraction and the viscosity) is set by the rate of viscous dissipation, and the latter is directly proportional to the gas accretion rate. Additionally, fixing other parameters, gas accretion rate also sets the gas surface density, and thus the disc optical depth and

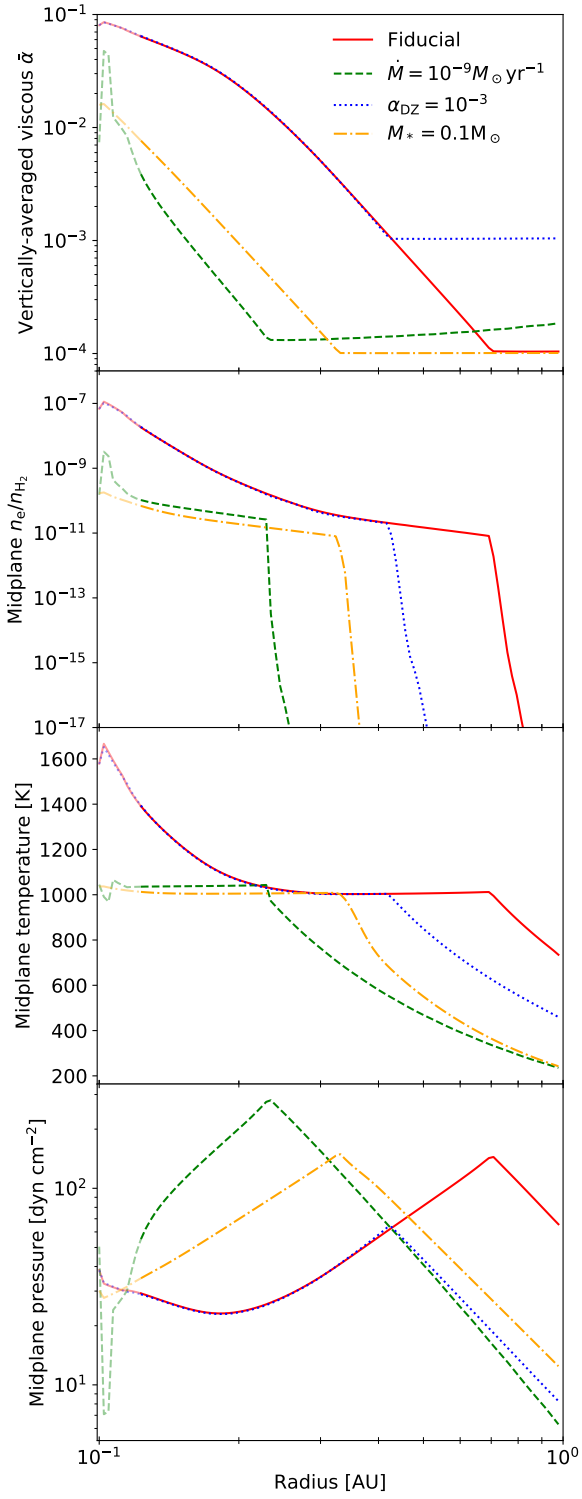

Figure 5. Results for our full model which includes dust effects on disc chemistry and ionization of molecular hydrogen. The different panels show radial profiles of (from top to bottom) vertically-averaged viscosity parameter $\bar{\alpha}$, midplane free electron fraction $n_{\rm e}/n_{\rm H_2}$, midplane temperature and midplane pressure. Fiducial model (solid lines) has a gas accretion rate $\dot{M} = 10^{-8}\,{\rm M}_\odot\,{\rm yr}^{-1}$, stellar mass $M_* = 1\,{\rm M}_\odot$ and dead-zone viscosity $\alpha_{\rm DZ} = 10^{-4}$. Models with a lower gas accretion rate (dashed line), a smaller stellar mass (dash-dotted line) or a larger dead-zone viscosity (dotted line) all yield the gas pressure maximum at a smaller radius. The light lines indicate the regions affected by the inner boundary condition (see Section 3). See Section 4.2.

how efficiently the disc cools. Therefore, the lower gas accretion rate yields a colder, less ionized disc. The radius of the gas pressure maximum scales with the gas accretion rate approximately as $r_{P\max} \propto \dot{M}^{1/2}$. This is close to the prediction given by eq. (4) and, in fact, the same as the scaling given by eq. (5), previously found by Mohanty et al. (2018), who neglected heating by stellar irradiation, dust effects and ionization of molecular hydrogen. While we find that stellar irradiation and ionization of molecular hydrogen are indeed unimportant for the model parameters chosen here, the dust effects are not. However, as discussed in Section 2, while the chemistry setting the ionization state of the disc is qualitatively different in their simple models (thermal ionization of potassium) and in the models presented here (thermionic and ion emission), in both cases the ionization fraction increases sharply above roughly the same temperature (~ 1000 K), yielding the same approximate scaling.

X-ray ionization of molecular hydrogen becomes more important at the lower gas accretion rate. X-rays activate the MRI in a layer high above the disc midplane outwards of the pressure maximum, increasing the viscosity parameter $\bar{\alpha}$ compared to the dead-zone value $\alpha_{\rm DZ}$. For an accretion rate of 10^{-9} $\mathrm{M_\odot\ yr^{-1}}$ the vertically averaged viscosity has increased by a factor of 2 outside the dead-zone over the model with an accretion rate of 10^{-8} $\mathrm{M_\odot\ yr^{-1}}$. This is because in these outer regions a lower gas accretion rate results in lower gas surface densities. Since the accretion rate carried by the X-ray ionized layer is roughly constant (e.g. set by the penetration depth of the X-rays) at lower accretion rates it has a larger relative contribution to the total accretion rate. This contribution remains small for the small maximum grain size assumed here; in the next section we discuss how this finding changes if grains are larger.

We find that the structure of the inner disc surrounding a $M_* = 0.1\,\mathrm{M_\odot}$ star[3] (shown by the dash-dotted lines in Fig. 5) is merely shifted radially inwards compared to our fiducial model with $M_* = 1\,\mathrm{M_\odot}$. Similar to the gas accretion rate, the stellar mass determines the disc heating rate due to accretion, as well as the disc optical depth through the dependence of the disc surface density on the stellar mass. The resulting approximate scaling $r_{P_{\max}} \propto M_*^{-1/3}$ is identical to the one given by eq. (4), stressing again that (for the chosen $\dot{M}$, dust parameters etc.) stellar irradiation and ionization by stellar X-rays are unimportant in setting the location of the pressure maximum. Note that in Fig. 5 we vary the disc parameters one-by-one from our fiducial values, whereas observations show that stellar mass and gas accretion rate are correlated (e.g. Mohanty et al. 2005; Manara et al. 2012; Alcalá et al. 2014, 2017; Manara et al. 2017). We investigate the combined effect of a lower stellar mass and a lower gas accretion rate in our detailed parameter study in Section 5.

Finally, the dotted line in Fig. 5 shows a model with a dead-zone viscosity $\alpha_{\rm DZ} = 10^{-3}$ (higher than our fiducial $\alpha_{\rm DZ} = 10^{-4}$). As in the simple models of Mohanty et al. (2018), the exact value of $\alpha_{\rm DZ}$ is unimportant in the innermost, well-ionized region. In the outer regions the accretion stress is dominated by that in the dead zone, and so $\alpha_{\rm DZ}$ sets the disc structure there. This includes the disc midplane temperature, and so $\alpha_{\rm DZ}$ sets the location where, going radially inwards, the midplane temperature reaches the critical value above which the disc midplane becomes well ionized. Once again, the approximate scaling that we find, $r_{P_{\max}} \propto \alpha_{\rm DZ}^{-0.22}$ is close to the one expected from simple arguments laid out in Section 2.

[3] Here we adopt a stellar radius of $R_* = 1\,\mathrm{R_\odot}$ and an effective temperature of $T_* = 2925$ K.

4.3 Large dust grains and low accretion rates

Within the parameter space explored above, the steady-state solution for the inner disc structure remains qualitatively the same, with a local gas pressure maximum at the transition between the high-viscosity inner region and the low-viscosity outer region. Non-thermal sources of ionization (dominated by stellar X-rays) can suppress this picture by increasing the viscosity in the outer region and removing the pressure maximum. Within the parameter space explored above, the importance of non-thermal ionization increases for larger grains and lower gas accretion rates, but overall remains very small.

However, for large enough grains and low enough gas accretion rate, the above picture changes entirely. We find that for a maximum grain size $a_{\max} = 1$ cm and a gas accretion rate of $\dot{M} = 10^{-9}\,\mathrm{M_\odot\,yr^{-1}}$ (with other model parameters equal to the fiducial values) our model produces a steady-state solution in which the viscosity parameter is of the order of $\bar{\alpha} \sim 7 \times 10^{-2}$ throughout the inner disc, and consequently there is no local gas pressure maximum (see Fig. 6). Stellar X-rays are the main source of ionization in this low-surface-density solution and they drive the MRI down to the disc midplane (Fig. 7 shows that the metal ions vastly outnumber the potassium ions at the midplane). The disc is hot enough to ionise potassium inwards of 0.1 AU and there is a drop in the midplane ionisation fraction at this radius (see Fig. 7). However, there is no pressure maximum associated with this drop in ionisation, as the ionisation fraction remains high enough to yield a high viscosity. Moreover, the midplane ionisation fraction increases again radially outwards from this location, suggesting that the viscosity remains high in the outer disc, beyond our computational domain. Overall, these results may be interpreted as the MRI-dead zone being completely wiped out from the disc by high ionisation rate (due to low gas surface densities) and low recombination rate (due to the total surface area of the dust grains being reduced for larger maximum dust grain size).

This steady-state solution does not appear to be a unique steady-state solution for these model parameters. Multiple solutions can arise, for example, because the various thermal and non-thermal sources of ionization produce an ionisation fraction that is a complex function of temperature, density and column density (an example was discussed in Paper I). The disc ionization state is further convolved with complex MRI criteria, our assumptions about the magnetic field strength, and possibly with artefacts of the numerical procedures used (e.g. the vertical smoothing of the viscosity parameter). The uniqueness of the solution is affected both in terms of the equilibrium steady-state solution at a fixed orbital radius and a fixed value of the magnetic field strength, and in terms of the number of local maxima of the MRI-driven viscosity parameter $\bar{\alpha}$ as a function of the magnetic field strength. The steady-state solution shown in Fig. 6 is favoured by our assumption that the disc structure and the magnetic field strength adapt to maximize $\bar{\alpha}$ at any given orbital radius. Further investigation of this issue (e.g. determining whether a steady-state solution featuring a pressure maximum can be constructed for these model parameters) is hampered by computational cost of root-solving and optimization of functions with non-unique solutions. Regardless of the existence of other solutions, the abrupt change in the steady-state structure as model parameters are varied implies that time-dependent simulations are required to examine what configuration the disc would evolve into once the X-ray-driven solution becomes viable.

Nevertheless, we can analyse under which conditions the X-ray-ionized steady-state solution can arise. This solution does not

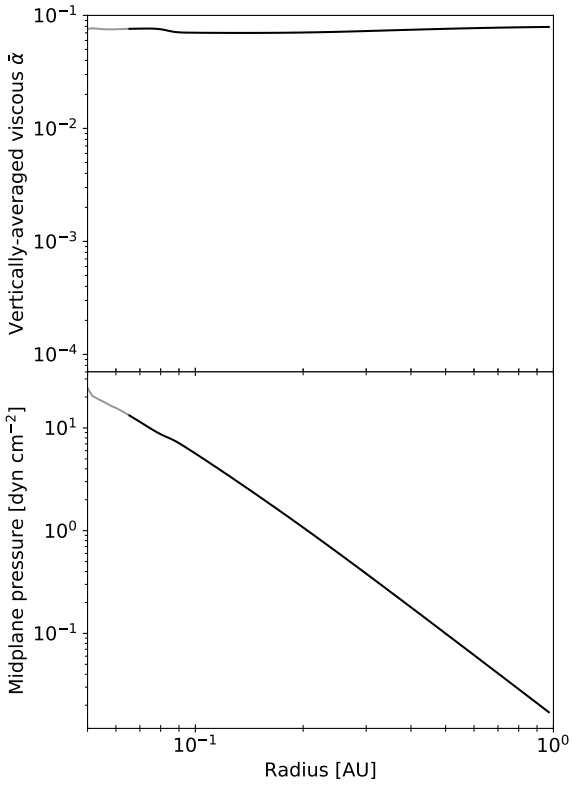

Figure 6. Vertically-averaged viscosity parameter $\bar{\alpha}$ (top) and midplane pressure (bottom) for a disc model with a gas accretion rate $\dot{M} = 10^{-9}\,\mathrm{M}_\odot\,\mathrm{yr}^{-1}$, stellar mass $M_* = 1\,\mathrm{M}_\odot$, dead-zone viscosity $\alpha_{\mathrm{DZ}} = 10^{-4}$, dust-to-gas ratio $f_{\mathrm{dg}} = 10^{-2}$ and maximum grain size $a_{\mathrm{max}} = 1\,\mathrm{cm}$. There is no local gas pressure maximum in the inner disc for these model parameters. The light lines indicate the regions affected by the inner boundary condition (see Section 3). See Section 4.3.

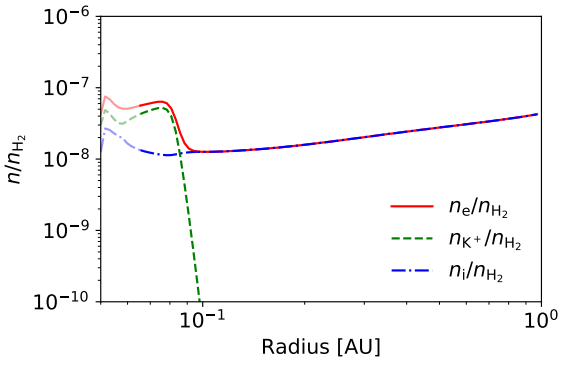

Figure 7. The fractional number densities of various ionized species at the disc midplane as a function of radius for the disc model shown in Fig. 6. The light lines indicate the regions affected by the inner boundary condition (see Section 3). See Section 4.3.

appear in a disc with small dust grains, because the higher surface area of the grains enhances the adsorption of charges onto dust grains and lowers the ionisation fraction, as discussed in previous sections. This solution also does not seem to exist at higher gas accretion rates. This can be understood as there being a maximum accretion rate that can be driven by the X-rays and the MRI, essentially due to the X-rays only ionising a limited column in the disc.

We can estimate this maximum accretion rate as a function of model parameters and the orbital radius using a simplified model, akin to the approach of Perez-Becker & Chiang (2011). Perez-Becker & Chiang (2011) focused on the role of both X-ray and UV ionisation and a much more detailed chemical network in their work, but the physics setting the maximum accretion rate is similar. First, note that the gas accretion rate is given in steady-state by $\dot{M} = 3\pi\alpha\Sigma c_s^2/(\Omega f_r)$, where Σ is the total gas surface density, c_s is the sound speed, Ω the Keplerian velocity at a given orbital radius and $f_r = 1 - \sqrt{R_*/r}$ a factor accounting for the inner disc edge boundary condition. Second, note that this solution must feature low surface densities, so that the X-rays can ionise the disc midplane. At these low surface densities the disc is only marginally optically thick, and the disc midplane temperature is set by stellar irradiation. In fact, neglecting stellar irradiation largely suppresses the X-ray-ionized steady-state solution, since the temperature (and thus the sound speed) produced by viscous dissipation in a marginally optically thick disc is much lower than the one produced by stellar irradiation, which lowers the accretion rate given by the above expression. Therefore, in this regime, we estimate the disc temperature as $T = (\phi/2)^{1/4}(R_*/r)^{1/2}T_*$ (Chiang & Goldreich 1997), assuming for simplicity that the incident angle of stellar irradiation ϕ is given by the flat-disc approximation (valid for the inner regions). As this yields a fixed radial temperature profile, at a given radius the accretion rate is maximised by maximising the product $\alpha\Sigma$.

In this regime, the MRI is primarily suppressed by ambipolar diffusion. The maximum viscosity parameter α that can be driven by the MRI increases with an increasing ambipolar Elsasser number Am, according to a simple function given by Bai & Stone (2011). Assuming that the only important charged species are electrons and atomic ions and that we are in the ambipolar-diffusion-dominated regime, $\mathrm{Am} \approx n_{\mathrm{i}}\langle\sigma v\rangle_{\mathrm{i}}/\Omega$, where n_{i} is the number density of ions and $\langle\sigma v\rangle_{\mathrm{i}}$ is the rate coefficient for momentum transfer in collisions between ions and neutrals. Therefore, the ambipolar Elsasser number is directly proportional to the number density of ions. On the other hand, in a disc ionised by stellar X-rays, the number density of ions at disc midplane decreases with increasing gas surface density, due to attenuation of the stellar X-rays. As a result, the product of the viscosity parameter and the surface density, $\alpha(\mathrm{Am}(\Sigma))\Sigma$, is maximized at some value of Σ, and so is the gas accretion rate.

Furthermore, we can estimate Am and n_{i} at disc midplane, by assuming the only source of ionization are X-rays and atomic ions recombine on dust grains, and using the reaction rates given in Paper I (but here we ignore the charge state of the dust grains). In our chemistry calculations we use an effective dust-to-gas ratio to mimic the grain size distribution; for the purpose of this calculation we use the effective dust-to-gas ratio that corresponds to dust grains of different sizes being weighted by their surface area (different than in the rest of our calculations), which is a more appropriate choice when dust grains only act as a recombination pathway (see section 2.4.2 in Paper I). We calculate the product $\alpha(\mathrm{Am}(\Sigma))\Sigma$ for a range of values of Σ and pick the maximum value. For our fiducial stellar (Solar-mass) parameters and a maximum grain size $a_{\mathrm{max}} = 1\,\mathrm{cm}$, at the radius of 0.1 AU we find that the maximum

accretion rate that can be obtained via an X-ray-dominated solution is $\dot{M}_{\rm max} \approx 3 \times 10^{-9}\,{\rm M}_\odot\,{\rm yr}^{-1}$. This simple estimate thus appears to be in agreement with the results of our full numerical model.

Notably, $\dot{M}_{\rm max}$ increases with orbital radius, due to the dependence of the accretion rate on the Keplerian angular velocity, and in spite of the decrease in the X-ray ionisation rate at larger radii (see also Perez-Becker & Chiang 2011). Therefore, at large enough radii the X-ray-dominated steady-state solution should arise even for our fiducial accretion rate (and higher values). For the same parameters as above, within 1 AU from the star, $\dot{M}_{\rm max}$ remains below our fiducial value of $\dot{M} = 10^{-8}\,{\rm M}_\odot\,{\rm yr}^{-1}$, and so the simple estimate also confirms our results from the previous sections. However, more generally, such a configuration where the disc would adopt an X-ray-dominated solution only outwards from some radius is unphysical, as it would require a sharp and large drop in the gas surface density at the transition between the different steady-state solutions. In the following section we discuss further the importance of this X-ray-dominated solution for the existence of the pressure maximum, and in Section 6 we discuss how it could fit into the general picture of disc evolution.

5 PRESSURE MAXIMUM

The above results show that, for a wide range of disc, stellar and dust parameters, an MRI accreting protoplanetary disc features a high-viscosity inner region, a low-viscosity outer region, and a gas pressure maximum at the transition between the two regions. This gas pressure maximum has been hypothesized to have a key role in the formation of the super-Earths inside the water ice line (Chatterjee & Tan 2014, 2015; Hu et al. 2016, 2018). In this section, we wish to examine in more detail the existence and location of the pressure maximum.

As discussed in Section 2, the existence of the pressure maximum in the inner disc requires two conditions. First, the ionization fraction should increase (sharply) above some critical temperature. Second, the disc should be hot enough so that the ionization fraction in the innermost region increases above a value required to sustain the MRI. The first of these conditions is not fulfilled if the disc evolves into a steady-state structure primarily ionized by stellar X-rays, discussed in Section 4.3. As noted in Section 4.3, time-dependent simulations are required to establish whether the stellar X-rays could indeed overtake the disc structure and at what point in the disc evolution this could happen. Still, it is important to consider this possibility when discussing the existence of the pressure maximum in the inner disc. Due to computational cost, it is not possible to calculate a large grid of models which include the possibility of multiple equilibrium solutions, as well as heating by stellar irradiation (which is, as discussed above, key for the existence of X-ray-dominated solutions). Therefore, we proceed as follows.

In this section, we neglect the heating by stellar irradiation and the ionization of the disc by the stellar X-rays, and use our model to find the radial location of the pressure maximum for various combinations of disc and stellar parameters. Then, for each combination of parameters, we estimate the maximum gas accretion rate that can be attained in an irradiated X-ray-ionized disc, at that radial location, using the simplified model outlined in Section 4.3. If this maximum gas accretion rate of an X-ray-ionized solution is larger than the given, input accretion rate, we note that the pressure maximum *might* not exist for those parameters. This condition for the existence of the pressure maximum is likely too strict. The maximum accretion rate of an X-ray-dominated solution increases with increasing orbital radius, and so the above condition does not guarantee that this solution would exist all the way to the inner disc edge for the given parameters. Nevertheless, this condition can also be understood as an estimate of whether a surface X-ray-ionized layer may become more important than the accretion through an MRI-dead midplane, i.e., whether the X-rays could perturb the steady-state solution featuring a pressure maximum. Ultimately, time-dependent simulation and a more complex chemical network will be needed to investigate how a real disc would behave, and we discuss this further in Section 6.3.

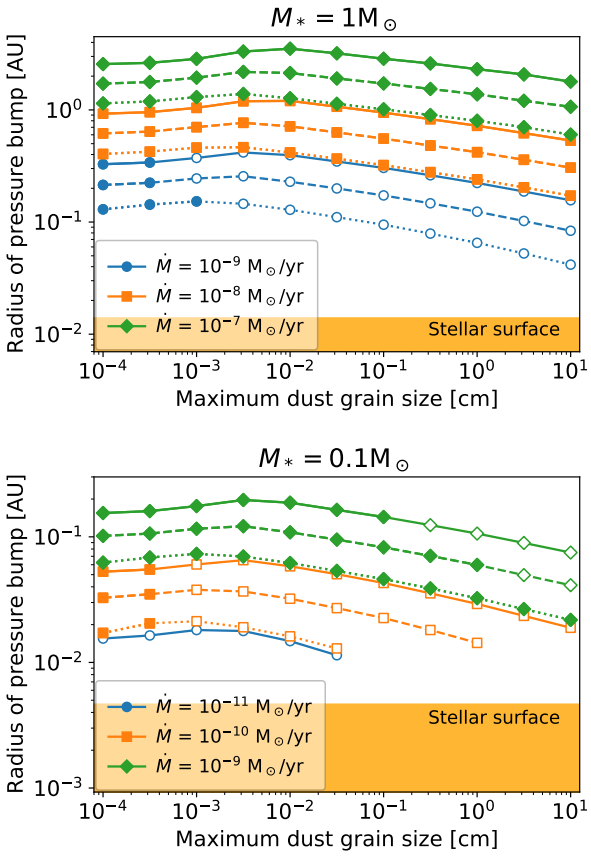

Figure 8. Radius of gas pressure bump as a function of maximum dust grain size. Top panel shows the results for a stellar mass $M_* = 1\,{\rm M}_\odot$, bottom panel for $M_* = 0.1\,{\rm M}_\odot$. In all models the dust-to-gas ratio is 10^{-2}. Solid, dashed and dotted lines show results for the dead-zone viscosity parameter $\alpha_{\rm DZ} = 10^{-5}$, 10^{-4} and 10^{-3}, respectively. Blue, green and red lines indicate different gas accretion rates $\dot{M}$ as indicated in plot legends for each panel. To obtain these results, we neglect stellar irradiation in our disc model, and use a simple calculation to estimate if including the irradiation would produce a steady-state solution ionized primarily by stellar X-rays and featuring no pressure maximum (shown as empty symbols). This is indeed found to be the case for lower accretion rates and larger dust grains. For $M_* = 0.1\,{\rm M}_\odot$, there may be no pressure maximum for the lower end of the observed accretion rates ($\dot{M} = 10^{-11}\,{\rm M}_\odot\,{\rm yr}^{-1}$) for any maximum grain size. See Section 5.

Fig. 8 shows the radial location of the pressure maximum (or pressure bump) as a function of the maximum dust grain size (see Section 3 for details of the dust grain distribution and how it is mimicked in our chemical network), for a stellar mass of $1\,{\rm M}_\odot$ (the top panel) and $0.1\,{\rm M}_\odot$ (the bottom panel). Those models in which the X-rays *may* erase the pressure maximum are indicated by empty

symbols. In all models shown here, we adopt our fiducial dust-to-gas ratio of 10^{-2}. The solid, dashed and dotted lines correspond to different values of the dead-zone viscosity parameter ($\alpha_{\rm DZ} = 10^{-5}$, 10^{-4} and 10^{-3}, respectively). For the different stellar masses we explore different ranges of the gas accretion rate $\dot{M}$, as indicated in plot legends next to each panel. The chosen ranges are motivated by observational studies, which find that for a Solar-mass star typically $\dot{M} \sim 10^{-8}\,{\rm M}_\odot\,{\rm yr}^{-1}$ and for the stellar mass of $0.1\,{\rm M}_\odot$, typically $\dot{M} \sim 10^{-10}\,{\rm M}_\odot\,{\rm yr}^{-1}$ (e.g. Mohanty et al. 2005; Manara et al. 2012; Alcalá et al. 2014, 2017; Manara et al. 2017). There is a significant spread both in the reported mean values in these studies (± 1 dex for the stellar mass of $0.1\,{\rm M}_\odot$, and somewhat less for a Solar-mass star) and within the observed samples in each study (up to 2 dex). However, the correlation with the stellar mass appears robust, and so we adopt the above typical values as mean values and vary the gas accretion by ± 1 dex for each stellar mass.

For the Solar-mass star we find that, for the upper end of the observed range of gas accretion rates ($\dot{M} \gtrsim 10^{-8}\,{\rm M}_\odot\,{\rm yr}^{-1}$) and a wide range of $\alpha_{\rm DZ}$, the existence of the pressure maximum is robust for a wide range of grain sizes. For the lower gas accretion rate ($\dot{M} = 10^{-9}\,{\rm M}_\odot\,{\rm yr}^{-1}$) and grain sizes larger than a few microns, the simple estimate described above suggests that accretion through an X-ray-ionized surface layer may perturb the disc structure. Therefore, we caution that a pressure maximum may not always occur for these parameters. For $M_* = 0.1\,{\rm M}_\odot$ the portion of the parameter space within which the pressure maximum is always present is even smaller, since the observed mean gas accretion rate is two orders of magnitude lower. Note that the range of grain sizes for which the pressure maximum is unperturbed for $\dot{M} = 10^{-9}\,{\rm M}_\odot\,{\rm yr}^{-1}$ around the lower-mass star is larger than for the Solar mass star, due to the lower-mass star having a lower (X-ray) luminosity.

The radius of the pressure maximum as a function of the maximum dust grain size ($a_{\rm max}$) shows a similar trend across the various values of the stellar mass, accretion rate and dead-zone viscosity: it weakly increases with increasing $a_{\rm max}$ for small grains, peaks at about $a_{\rm max} \sim 10^{-2}$ cm, and then steadily decreases for larger dust grains. The factors causing this have already been briefly discussed in section 4.1. First, recall that an increase in the disc opacity means that accretion heat can escape less easily, making the disc midplane hotter and pushing the pressure maximum outwards. In addition, for small dust grains, larger dust grain size leads to a moderate increase in the opacity (here, the relevant opacity is the opacity of the disc to its own radiation in the optically-thick regions, i.e., the Rosseland-mean opacity, see Fig. 1). At the same time, the increase in dust grain size reduces the critical temperature at which ionization fraction rises due to thermionic and ion emission (as the increase in dust grain size is equivalent to a reduction in the effective dust-to-gas ratio in our chemical network; see also Desch & Turner 2015), pushing the pressure maximum outwards. When these factors are compounded, for small grains, the radius of the pressure maximum increases with $a_{\rm max}$. However, if the grains grow beyond $a_{\rm max} \sim 10^{-2}$ cm, dust opacities are severely decreased with increasing grain size and the net effect is a decrease in the radius of the pressure maximum. Additionally, note that the exact value of $a_{\rm max}$ at which the radius of the pressure bump peaks varies somewhat with $\dot{M}$ and $\alpha_{\rm DZ}$; this can be expected, since both determine the gas surface density and thus the optical depth at disc midplane and the relative importance of the above two effects. It is also important to note that including heating due to stellar irradiation seems to somewhat modify the trend for small dust grains, as can be seen by comparing Fig 8 to the models discussed in the previous section. Specifically, Fig. 3 shows that for our fiducial disc and stellar parameters, micron-size grains result in a pressure maximum at a larger radius. The resulting differences in the radial location of the pressure maximum are, however, small, and certainly for larger grains the pressure maximum moves inwards.

6 DISCUSSION

In this work we have investigated how the structure of the inner disc, accreting primarily through the MRI, changes with various disc, stellar and dust parameters. Of particular interest are the existence and the location of a local gas pressure maximum and a highly-turbulent region inwards of it, which could accumulate dust grains drifting in radially from the outer disc, possibly leading to the formation of planetary cores (Chatterjee & Tan 2014; Hu et al. 2018; Jankovic et al. 2019). The models presented in this work are steady-state models, each with a distribution of dust grains that is fixed throughout the disc. However, as discussed in Sections 6.1 and 6.2, these models provide us with important insights into how the inner disc could evolve as the dust grains grow, if and how the dust will accumulate, how this accumulation could feedback on the gas structure, and the disc parameters that are favourable for the formation of planetary cores. In Section 6.3 we discuss the various limitations of these models.

Before we proceed, we re-iterate that dust is incredibly important for the inner disc structure. Thermionic and ion emission from dust grains and the adsorption of charges from the gas onto the dust grains control the ionization fraction, and thus the extent of the inner region where the MRI can drive efficient accretion. These processes yield an ionization fraction that increases sharply above a critical temperature, similar to thermal ionization. This critical temperature appears to be a slowly varying function of dust properties, however, and so it is the effect of the dust on the disc opacity that largely determines the location of the pressure maximum. Increasing the dust opacity results in a more optically-thick, hotter inner disc, with a radius of the pressure maximum at a larger distance from the star.

6.1 Dust growth

As discussed in Section 5, dust growth to $a_{\rm max} \sim 10^{-2}$ cm increases the extent of the high-viscosity inner region and the radius at which the pressure maximum is located, as an increase in dust grain size leads to a moderate increase in the disc opacity and a decrease in the threshold temperature at which thermionic and ion emission become efficient. Growth beyond that size has the opposite effect, as it leads to a significant decrease in the disc opacity, making the disc midplane colder, and thus less ionized. Therefore, in the inner disc, if dust grows larger than $\sim 100\,\mu$m sizes, the dead-zone inner edge moves inwards.

Note that this is the opposite of what happens in the outer regions of protoplanetary discs. The outer regions are ionized primarily by the stellar X-rays and cosmic rays. These sources of ionization become more important further away from the star, as the disc column density decreases and high-temperature effects become unimportant. These regions are expected to be optically thin to their own radiation, and the primary source of heat is stellar irradiation. Therefore, the dust acts primarily to lower the ionization fraction by adsorbing free charges from the gas. Because of this, in the outer regions the dead zone is expected to shrink as the dust grains grow (Sano et al. 2000; Ilgner & Nelson 2006).

We can calculate the location of the pressure maximum under an assumption that the maximum dust grain size has reached a

growth limit. In the inner disc, dust growth is limited by collisional fragmentation of dust grains due to relative turbulent velocities (Birnstiel et al. 2010, 2012; Drazkowska et al. 2016). Here, the relative grain velocities are induced by the MRI-driven turbulence, as well as the lower levels of turbulence assumed to persist in the MRI-dead zone. Since this growth limit depends on the velocities of dust grains due to turbulent velocities of the gas, it is given in terms of the particles "Stokes number" (St), the ratio between the particle gas drag stopping time and the eddy turnover time (where the eddy turnover time is taken to be $1/\Omega$ Zhu et al. 2015). In a turbulent disc, typical collisional relative velocity between dust grains is given by $V_{\rm dd}^2 \approx 3V_{\rm g}^2{\rm St}$ (for ${\rm St} < 1$, Ormel & Cuzzi 2007), where $V_{\rm g}$ is the typical turbulent gas velocity (given by $V_{\rm g}^2 = \alpha c_{\rm s}^2$). There is a critical velocity $u_{\rm frag}$ above which a collision between dust grains results in their fragmentation, rather than sticking/growth. For silicate grains of similar size, $u_{\rm frag} \sim 1\,{\rm m\,s^{-1}}$ (Blum & Münch 1993; Beitz et al. 2011; Schräpler et al. 2012; Bukhari Syed et al. 2017, although note that grains might become more sticky at the high temperatures present in the inner disc (Demirci et al. 2019)). Since the Stokes number St is directly related to the grain size, and the collision velocity to St, fragmentation imposes an upper limit on dust growth. At the fragmentation limit (Birnstiel et al. 2009, 2012),

$$ {\rm St}_{\rm frag} = \frac{u_{\rm frag}^2}{3\alpha c_{\rm s}^2}. \tag{7} $$

The exact relationship between the Stokes number and the particle size depends on the relevant drag law (Weidenschilling 1977). Typically, the dust grains in protoplanetary discs are smaller than the mean free path of gas molecules, and therefore couple to the gas according to the Epstein drag law. However, due to the high densities in the inner disc, dust grains may enter the Stokes regime. Importantly, the above approximate expression for the turbulent relative velocity between dust grains ($V_{\rm dd}$) has been derived under an assumption that St does not depend on the relative velocity between the dust grain and the gas, $V_{\rm dg}$. This assumption is true for grains in the Epstein drag regime. In the Stokes regime, it is true only if the Reynolds number Re of the particle is less than unity. We always check that this condition is fulfilled for our particles in the Stokes regime, and that we may employ the above expression for $V_{\rm dd}$. The Reynolds number of a particle itself depends on the velocity $V_{\rm dg}$, for which we adopt another approximate expression, $V_{\rm dg}^2 = V_{\rm g}^2{\rm St}/(1+{\rm St})$ (Cuzzi & Hogan 2003, note that this expression was derived analytically for ${\rm St} \ll 1$, but also shown to be applicable for a wide range of St through a comparison with numerical simulations).

To calculate the location of the pressure maximum in a disc in which grain growth is limited by fragmentation, we proceed as follows. At the location of the pressure maximum for various combinations of stellar mass, accretion rate, dead-zone viscosity parameter and maximum dust grain size (i.e., for every point in Fig. 8), we calculate the fragmentation limit for the particle Stokes number, ${\rm St}_{\rm frag}$ (assuming $\alpha = \bar{\alpha}$), and the corresponding grain size, $a_{\rm frag}$ (for an appropriate drag law). For each combination of the disc and stellar parameters (stellar mass, accretion rate and dead-zone viscosity parameter), this yields a set of points describing a function $a_{\rm frag}(a_{\rm max})$. We connect these points using linear interpolation, and find the maximum grain size such that $a_{\rm frag}(a_{\rm max}) = a_{\rm max}$. Then, again using the results shown in Fig. 8 and linear interpolation, we find the radius of the pressure maximum at that value of $a_{\rm max}$. Similarly, we find the corresponding midplane temperature and density.

This calculation utilizes models in which the maximum dust grain size is assumed to be constant everywhere in the disc, and so the obtained solutions also formally correspond to models in which the maximum dust grain size is radially constant (and equal to the fragmentation limit $a_{\rm frag}$ at the pressure maximum). In a real disc, the fragmentation limit to which particles can grow would be a function of the turbulence levels and other parameters which vary as functions of radius. While this calculation does not take this radial variation of dust size into account, the fragmentation limit at the pressure maximum and the location of the pressure maximum would remain the same as in the solutions found here. In particular, note that radially inwards from the pressure maximum, $a_{\rm frag}$ should decrease compared to the value at the pressure maximum, as the turbulence parameter α increases. Furthermore, for large maximum grain sizes $a_{\rm max}$ (which is the regime pertaining to the solutions found here), a decrease in $a_{\rm max}$ yields an increase in α at a fixed radius. Thus, if we accounted for the decrease in $a_{\rm max} = a_{\rm frag}$ inwards of the pressure maximum, this would only make the radial gradient of α steeper inwards of the pressure maximum, but it would not change the location of its minimum, and therefore not the location of the pressure maximum obtained here.

The results for the radius of the pressure maximum and the grain size are shown in Fig. 9, as functions of the gas accretion rate, for different values of stellar mass and the dead-zone viscosity parameter. The maximum grain size at the pressure maximum is limited by turbulent fragmentation (middle panel) and thus sensitive to the dead-zone viscosity parameter $\alpha_{\rm DZ}$ (results for $\alpha_{\rm DZ} = 10^{-5}$, 10^{-4} and 10^{-3} are shown by the solid, dashed and dotted lines, respectively). This is because, in these models, at the location of the pressure maximum, the vertically-averaged viscosity (and turbulence) parameter $\bar{\alpha} = \alpha_{\rm DZ}$.

Remarkably, despite the sensitivity of the grain size to $\alpha_{\rm DZ}$, the radius of the pressure maximum depends very weakly on this parameter. This is a result of three different inter-dependencies. At a fixed maximum grain size (and other parameters), a lower $\alpha_{\rm DZ}$ yields a larger radius of the pressure bump, and also a larger fragmentation-limited grain size. Concurrently, a larger maximum grain size yields a smaller radius of the pressure bump (for maximum dust grain size larger than about 10^{-2} cm, see Fig. 8). Evidently, compounding these inter-dependencies results in a weakly-varying radius of the pressure bump.

We can also compare these results against simple theoretical expectations, by coupling eq. (4) with the expressions for the fragmentation-limited dust grain size (obtained from eq. (7) and the appropriate drag laws). In the Epstein drag regime (pertaining to the solution for $\alpha_{\rm DZ} = 10^{-3}$ in Fig. 9), we obtain for the radius of the pressure bump

$$ r_{P_{\rm max}} \propto f_{\rm dg}^{4/15}\dot{M}^{2/5}M_*^{1/3} \propto f_{\rm dg}^{0.27}\dot{M}^{0.4}M_*^{0.33}, \tag{8} $$

and in the Stokes regime (pertaining to the solutions for $\alpha_{\rm DZ} \leqslant 10^{-4}$),

$$ r_{P_{\rm max}} \propto f_{\rm dg}^{8/39}\alpha^{-2/13}\dot{M}^{16/39}M_*^{1/3} \propto f_{\rm dg}^{0.2}\alpha^{-0.15}\dot{M}^{0.41}M_*^{0.33}. \tag{9} $$

These simple predictions agree with our finding that the dependency of the radius of the pressure bump on $\alpha_{\rm DZ}$ is very weak, and in fact expected to be non-existent in the Epstein drag regime. The dependencies on the other parameters also seem to match fairly well. Small deviations are to be expected since in the numerical models the pressure bump does not occur precisely at a constant fixed temperature.

Furthermore, for the Solar-mass star, the pressure maximum is

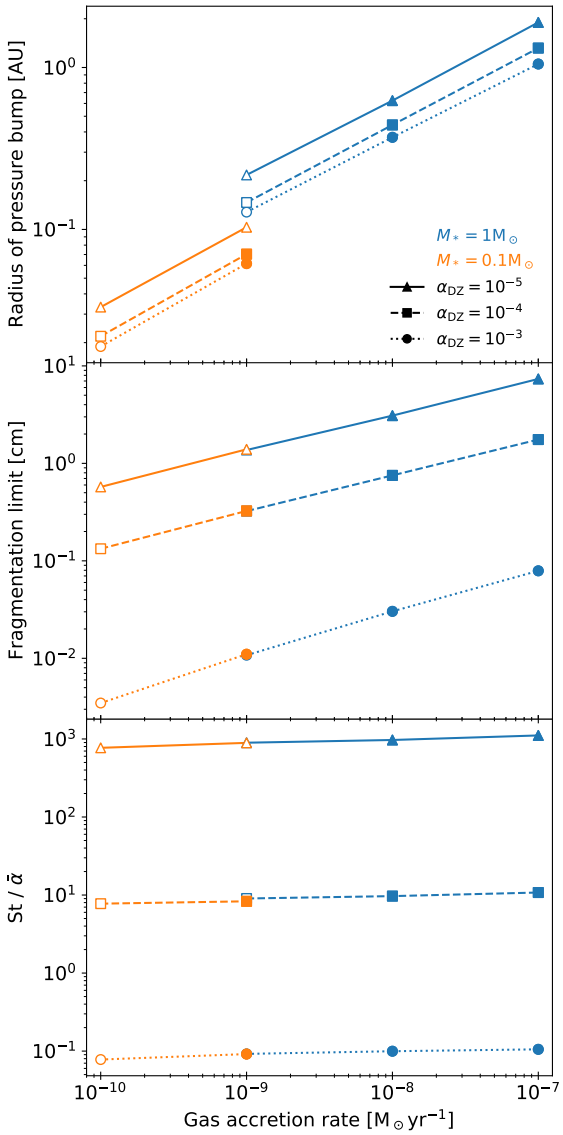

Figure 9. Radius of the pressure bump (top), maximum dust grain size (middle) and ratio of the Stokes number to the viscosity parameter ($\mathrm{St}/\bar{\alpha}$) at the pressure bump (bottom) as functions of the gas accretion rate, for a maximum dust grain size that corresponds to the grain growth limit due to turbulent fragmentation. Solid, dashed and dotted lines correspond to different values of the dead-zone viscosity parameter α_{DZ} as shown in the plot legend. The dust grain size and $\mathrm{St}/\bar{\alpha}$ are highly sensitive to the dead-zone viscosity parameter α_{DZ}. Conversely, varying α_{DZ} affects the location of the pressure bump only weakly. Blue lines show the results for a stellar mass $M_* = 1\,\mathrm{M}_\odot$, orange lines for $M_* = 0.1\,\mathrm{M}_\odot$. Empty symbols denote solutions where an alternative steady-state solution may exist that is ionized primarily by stellar X-rays and featuring no pressure maximum, same as in Fig. 8. There is no solution for $M_* = 0.1\,\mathrm{M}_\odot$ and $\dot{M} = 10^{-11}\,\mathrm{M}_\odot\,\mathrm{yr}^{-1}$. See Sections 6.1 and 6.2.

located at radii between ~ 0.3 AU and ~ 2 AU in the upper end of the range of the observationally-motivated gas accretion rates considered here. However, for the accretion rate of $\dot{M} = 10^{-9}\,\mathrm{M}_\odot\,\mathrm{yr}^{-1}$ the pressure maximum may be perturbed and possibly removed from the inner disc altogether. As discussed in Section 5, for lower gas accretion rates and larger dust grain sizes, we find that the disc could assume a high-viscosity X-ray-dominated steady-state solution which features no pressure maximum (in Fig. 9, this is indicated by empty symbols).

For a lower-mass star, $M_* = 0.1\,\mathrm{M}_\odot$, at a fixed gas accretion rate, dust grains grow to similar sizes as for the Solar-mass star. Overall, the radius of the pressure maximum is expected to be smaller, due to the lower viscous dissipation rate and the lower observed gas accretion rates (see the discussions in sections 4.2 and 5). Analogously to the case of the Solar-mass star, there might not be a pressure maximum at lower accretion rates.

6.2 Dust accumulation

For dust grains to become trapped within the pressure maximum, the outwards radial drift velocity of dust grains just inwards of the pressure maximum should be higher than the velocity with which the accreting gas advects the grains inwards. The ratio of the radial drift and the gas advection velocities is roughly equal to the ratio of the particle Stokes number and the viscous α (Jacquet et al. 2012). Therefore, for the particle radial drift to overcome advection with the gas inwards of the pressure maximum, it is required that $\mathrm{St}/\alpha > 1$. To check whether this condition is fulfilled, in the bottom panel of Fig. 9 we show the ratio between the Stokes number at the fragmentation limit $\mathrm{St}_{\mathrm{frag}}$ and the vertically averaged viscosity and turbulence parameter $\bar{\alpha}$ at the location of the pressure maximum.

The ratio $\mathrm{St}_{\mathrm{frag}}/\bar{\alpha}$ is most sensitive to the value of the dead-zone viscosity parameter α_{DZ}. The Stokes number at the fragmentation limit $\mathrm{St}_{\mathrm{frag}}$ is given by eq. (7). At a fixed critical fragmentation velocity u_{frag}, it is a function only of the viscosity parameter $\bar{\alpha}$ and the speed of sound c_{s} (i.e., the temperature) at the pressure maximum. Since these solutions are extracted from models which neglect ionization by stellar X-rays, $\bar{\alpha} = \alpha_{\mathrm{DZ}}$, the value of the dead-zone viscosity parameter. Hence, $\mathrm{St}_{\mathrm{frag}}/\bar{\alpha} \propto 1/\alpha_{\mathrm{DZ}}^2$. This ratio also varies slightly with gas accretion rate, which we can attribute to the fact that the pressure maximum does not occur precisely at a fixed critical temperature. Instead, the ionization fraction, driven primarily by thermionic and ion emission, also depends on the dust properties and the disc density.

Overall, whether the dust grains become trapped in the pressure maximum depends on an assumed value of α_{DZ}. We may consider how the disc might evolve forward, depending on this value. First, if the dead-zone viscosity parameter is low, $\alpha_{\mathrm{DZ}} = 10^{-5}$, $\mathrm{St}_{\mathrm{frag}}/\bar{\alpha} \gg 1$. In this case, dust grains could readily accumulate at the pressure maximum. This accumulation might lead to an unstable configuration, as an increase in the dust-to-gas ratio leads to an increase in $\bar{\alpha}$ at a given radius (see Fig. 3). As the dust-to-gas ratio would increase at the pressure maximum, and decrease either side, this could lead to an emergence of an additional minimum in $\bar{\alpha}$ outwards from the original minimum, and thus to a formation of an additional pressure trap. Time-dependent simulations are needed to examine further evolution of the disc. In general, if the pressure maximum efficiently traps the radially-drifting dust, one observable consequence would be that the gas accreting onto the star would be depleted in elements of which the dust is composed: such a mechanism has been proposed to be at work in the inner disc of TW Hya, where the levels of depletion of refractory and volatile elements suggest a dust trap inside of the water ice line (McClure et al. 2020), and also in transition discs surrounding Herbig Ae/Be stars (Kama et al. 2015).

Second, consider a case in which $\mathrm{St}_{\mathrm{frag}}/\bar{\alpha} \sim 1$, which would occur if the dead-zone viscosity parameter is slightly above the middle of the plausible range, $\alpha_{\mathrm{DZ}} = 10^{-4}$. In this case, considered by Jankovic et al. (2019), the gas pressure maximum does not trap

large amounts of dust. This is because $\bar{\alpha}$ increases inwards of the pressure maximum, and $\mathrm{St}_{\mathrm{frag}}$ decreases. This limits the radial width of the pressure trap. Dust advection with the accreting gas is not sufficient to remove the dust grains from the trap; however, the grains are also mixed radially by the turbulence. The dust-to-gas ratio at the pressure maximum is then limited by the corresponding radial diffusion term. Nevertheless, dust would still accumulate in the entire region interior to the pressure maximum, as in the highly-turbulent innermost region dust grains become small enough to couple to the gas, reducing the radial drift relative to the outer disc. However, in this case, the amount of dust that can be accumulated in the inner disc is limited by the flux of dust drifting inwards from the outer disc. Moreover, the small size of the dust grains is detrimental to planet formation.

In this work, we also find that a higher dust-to-gas ratio yields a larger extent of the high-viscosity inner region (see Section 4.1.2). This is highly beneficial for planet formation in the inner disc, as it implies that the accumulation of dust is not only sustainable, but also leads to a radial expansion of the high-viscosity, high-turbulence region inside of which the dust accumulates. In particular, this expansion is beneficial for the growth of the small fragmentation-limited dust grains into larger, more rigid solid bodies, i.e., into planetesimals. Specifically, planetesimals may form out of dust grains through a combination of the streaming instabilities (SI) and the gravitational instability (Youdin & Goodman 2005; Johansen & Youdin 2007; Bai & Stone 2010; Johansen et al. 2012; Simon et al. 2016, 2017; Schäfer et al. 2017). Under certain conditions, the SI leads to localized concentrations of dust grains susceptible to gravitational collapse. Jankovic et al. (2019) pointed out that this process is unlikely in the inner disc if the pressure (and the density) maximum is located at very short orbital distances, as too close to the star the tidal effect of the star prevents the gravitational collapse. Therefore, the shift of the pressure maximum to larger orbital distances due to the accumulation of dust could potentially help to overcome this barrier and form planetesimals.

Finally, if the dead-zone viscosity parameter is high, $\alpha_{\mathrm{DZ}} = 10^{-3}$, $\mathrm{St}_{\mathrm{frag}}/\bar{\alpha} \ll 1$. In this case, dust grains are so small and well-coupled to the gas that they are advected through the pressure maximum inwards. Dust may still accumulate interior to the pressure maximum, as a consequence of fragmentation in the innermost regions, as noted above. However, it is unlikely that this could lead to the formation of larger solid bodies. While the exact value of the dead-zone viscosity is unimportant for the location of the pressure maximum (see Fig. 9 and Section 6.1), in this case the grains would likely be too small, too well-coupled to the gas to start the streaming instabilities (Carrera et al. 2015; Yang et al. 2017).

6.3 Limitations

In this work, we have assumed that the MRI-accreting inner disc is in an equilibrium, steady state. However, there are several processes whose further study requires to consider the time dependence of the disc structure.

First, even if variations in the dust properties are neglected, the steady-state MRI-accreting inner disc is unstable to surface density perturbations (Mohanty et al. 2018). At a fixed radius, the MRI-driven accretion rate decreases with an increasing surface density (as calculated using the steady-state models). Therefore, a perturbation in the disc surface density might lead out of the steady-state, creating a pile up of mass in a certain region. This so-called viscous instability (Lightman & Eardley 1974; Pringle 1981) could have important consequences for the inner disc structure and planet formation, as it is likely to produce rings and gaps on the viscous timescale.

Second, the results presented in this work show that the accumulation of dust in the inner disc is possibly a highly dynamical process. The dust grain size and the dust-to-gas ratio strongly affect the MRI-driven viscosity at a given radius, and, concurrently, the extent of the innermost region within which the dust may accumulate. The evolution of the disc is particularly unclear if the dust is trapped in the pressure maximum, e.g., whether further evolution of gas and dust might lead to a modified equilibrium state, or creation of multiple pressure maxima.

Third, while we considered the effects of dust on the disc thermal and chemical structure, we did not account for the dynamical effects. If dust grains drift radially due to gas drag, there is also a back-reaction on the gas (Nakagawa et al. 1986). This becomes increasingly important at high dust-to-gas ratios. In particular, drag back-reaction acts to flatten the radial gas pressure profile, and so it would affect accumulation of dust in the pressure maximum (Taki et al. 2016). Further study of the early stages of planet formation in the inner disc should account for the self-consistent, time-dependent evolution of the gas and the dust.

Fourth, it was shown that for some disc parameters dust growth could lead to steady-state solutions in which the disc is primarily ionized by stellar X-rays and no pressure maximum would exist. This deserves further study through time-dependent simulations, and also using a more detailed chemical network than considered here. In the regime in which the high-temperature effects are unimportant, at low dust-to-gas ratios (equivalent to larger grain sizes) simplified chemical networks (such as the one used here) overestimate the disc ionization fraction, and the MRI-driven accretion efficiency, compared to the more complex networks (Ilgner & Nelson 2006). The stellar X-ray luminosity may also need to be more carefully considered, as the stellar parameters used here are adopted from very early times in the stellar evolution models, while low gas accretion rates (for which the X-ray-dominated solutions appear) are observed at later stages of protoplanetary disc evolution. Lastly, propagation of the X-rays may need to be treated more accurately at short periods, and the penetration of X-rays from the "bottom" side of the disc should be taken into account when X-rays can reach the disc midplane.

Furthermore, we showed that the inner disc structure is sensitive to the disc opacities. Yet the radiative properties of the disc are determined only by silicate dust grains in this work. Other important species (e.g. carbonaceous grains; Pollack et al. 1994) could condense in some of the colder regions of the disc (e.g. near the disc photosphere - below the upper layers heated by stellar irradiation and above the hot, optically-thick disc midplane), and their contribution to the opacities could alter the details of the location of the pressure maximum. Opacities due to atomic and molecular lines have also been neglected. In the optically-thick regions (such as the disc midplane in our models), this is a good assumption since the Rosseland-mean opacity of the gas is always negligible compared to that of the dust where the pressure maximum is located. However, in the optically-thin regions (in the disc upper layers), Planck-mean opacity of the gas at high temperatures is comparable to that of micron-sized dust, and the absorption coefficient κ_{P}^{*} greatly exceeds that of cm-sized dust (e.g. Malygin et al. 2014). Since the gas accretes primarily through the dense, optically-thick regions around the disc midplane, we can expect that including the gas opacities would not change our results, as the higher absorption of stellar light would only increase the temperature in the uppermost disc layers. Nevertheless, note that the gas opacities are

strongly non-monotonic, and the upper disc layers might not be in thermal equilibrium (Malygin et al. 2014), which is assumed to be the case here.

Another limitation of this work in modelling of the disc upper layers is that the possibility of shadowing neglected. As in other 1+1D models (e.g. Chiang & Goldreich 1997; D'Alessio et al. 1998), when heating by stellar irradiation is considered, there is an underlying assumption that the disc is flaring, so that stellar rays can reach the disc surface at all radii. However, Terquem (2008) showed that the inner boundary of the MRI-dead zone may be puffed up sufficiently to throw a shadow over the outer regions of the disc. In our models, we can look for this possibility by inspecting the irradiated surface of the disc arising from the integration of the disc structure in the vertical direction (as opposed to the adopted irradiated surface, constructed by ray-tracing in two dimensions under the assumption that the disc is flaring, see Paper I; D'Alessio et al. 1999). Indeed, we find that, in the vicinity of the pressure maximum there is an inconsistency between the two surfaces, with the former surface implying that the region immediately outwards from the pressure maximum should be in a shadow. Nonetheless, we do not expect that correcting for the shadowing would change any of the conclusions of this work due to the same reason as above: temperature at the disc midplane is primarily determined by viscous dissipation, and not by stellar irradiation.

Furthermore, in this work we have assumed that the disc accretes viscously, via the MRI, and that the resulting viscosity is well described by criteria extracted from local magnetohydrodynamic simulations. Accretion in protoplanetary discs may also be driven by non-viscous processes, e.g. by large scale laminar flows if Hall effect is the dominant non-ideal MHD effect (Lesur et al. 2014), or, in the presence of a magnetic field threading the disc, by magnetic winds (Suzuki & Inutsuka 2009; Suzuki et al. 2010; Bai & Stone 2013; Fromang et al. 2013; Lesur et al. 2013). It is likely that both the Hall effect and magnetic winds play a significant role in the overall evolution of protoplanetary discs, driving gas accretion at a much larger range of radii than the MRI (e.g. Bai 2017). Magnetic winds in particular could be shaping the inner disc structure along with the MRI (Suzuki et al. 2016). Nevertheless, the structure of the innermost regions of discs is still likely to be strongly affected by the MRI, and especially so the disc midplane where planets are expected to form. Therefore, while we do not consider non-viscous drivers of accretion in this work, the models presented here should still offer important insights for future work on the inner disc structure.

Finally, in this work we have also assumed that where the disc is not sufficiently ionized to drive the MRI, the viscosity parameter obtains a minimum, floor value ($\alpha_{\rm DZ}$). The value of this parameter determines whether dust will accumulate at the inner edge of the dead zone (i.e., at the pressure maximum; see Section 6.2). An assumption of a fixed, non-zero $\alpha_{\rm DZ}$ in the MRI-dead zone is reasonable if such a viscosity can be driven by non-magnetic instabilities. The range of values explored in this paper covers the values observed in simulations of various hydrodynamic instabilities (e.g. Lesur & Papaloizou 2010; Nelson et al. 2013; Stoll & Kley 2014). However, outwards from the pressure maximum accretion may also be driven by propagation of waves from the adjacent MRI-active zone, and/or those outer regions may be heated by radial transport of heat from the MRI-active zone (e.g. Latter & Balbus 2012; Faure et al. 2014). This would be contrary to our assumptions that the outer regions are heated by an uncorrelated source of viscosity and that the disc structure at different radii is uncorrelated except for the heating by stellar irradiation. In this case, the physics setting the location of the pressure maximum is more complex and the pressure maximum would likely occur at shorter orbital distances than predicted here. Ultimately though, at larger radii non-viscous drivers of accretion discussed above are likely to take over the evolution of the disc. If these are relevant at the outer edge of the MRI-active zone, the pressure maximum may still exist, provided that the gas still accretes faster in the inner region than in the outer. In this case, the disc midplane could be non-turbulent, allowing grain growth beyond the sizes predicted in Section 6.1 and promoting accumulation of grains at the pressure maximum. Lastly, the inner edge of the MRI-dead zone is possibly unstable to formation of vortices (Lyra & Mac Low 2012; Faure et al. 2014), which would invalidate our assumption of an azimuthally symmetric disc, but also possibly further promote accumulation of dust and planet formation.

7 SUMMARY

We have explored how the structure of the MRI-accreting inner regions of protoplanetary discs changes as a function of the dust-to-gas ratio, dust grain size, and other disc and stellar parameters. We have especially focused on the location of the gas pressure maximum arising at the boundary between the highly-viscous innermost region and the low-viscosity outer region. The existence and the location of the pressure maximum, and the disc structure in its vicinity, are key to the formation of the super-Earths inside the water ice line.

At fixed dust parameters, the radius of the pressure maximum is directly related to the stellar mass M_* and the gas accretion rate $\dot{M}$. This is because the stellar mass and the accretion rate determine the total viscous dissipation at a given radius, and thus the temperature and the ionization fraction at disc midplane. The radius of the pressure maximum is inversely related to the assumed viscosity parameter in the MRI-dead zone $\alpha_{\rm DZ}$. The location of the pressure maximum corresponds to a minimum in the viscosity parameter. Even though in our model there is an MRI-active layer at all radii, in the outer regions this is a (X-ray ionized) layer high above the disc midplane (in the vicinity of the pressure maximum), and the disc primarily accretes through the dense MRI-dead regions around the midplane. Therefore, the minimum viscosity parameter is close in value to the dead-zone $\alpha_{\rm DZ}$.

However, this picture of the highly-viscous innermost region and the low-viscosity outer region may change qualitatively for some disc and stellar parameters. Specifically, for low gas accretion rates ($\leqslant 10^{-9}\,{\rm M}_\odot\,{\rm yr}^{-1}$), we find that a steady-state solution could exist in which there is no gas pressure maximum. In these solutions the disc features low gas surface densities and high viscosity driven by X-ray ionization. Such solutions are more likely to exist for larger grain sizes (and, equivalently, at lower dust-to-gas ratios).

At fixed stellar and disc parameters, as long as the pressure maximum does exist, its location moves radially outwards as the dust grains grow to $a_{\rm max} \sim 10^{-2}$ cm. Grain growth to still larger sizes results in the pressure maximum moving inwards, towards the star. This behaviour is primarily driven by the effects of dust opacities on the disc thermal structure.

We calculate the location of the pressure maximum for the case of dust growth being limited by turbulent fragmentation. For a Solar-mass star and gas accretion rates in the range $10^{-9}-10^{-7}\,{\rm M}_\odot\,{\rm yr}^{-1}$, this always places the pressure maximum outwards of 0.1 AU. In this fragmentation-limited regime, the radius of the pressure maximum depends very weakly on the dead-zone viscosity parameter, and it is most sensitive to the gas accretion rate. The pressure maximum may possibly not exist for a Solar-mass star and a gas accretion rate of $\leqslant 10^{-9}\,{\rm M}_\odot\,{\rm yr}^{-1}$, nor for a stellar mass of $0.1\,{\rm M}_\odot$ for gas accretion

rates $\leqslant 10^{-10}\,M_\odot\,yr^{-1}$, if the disc evolves into the high-viscosity X-ray ionized structure as soon as such structure can match the required disc accretion rate. This suggests that planet formation in the inner disc is more likely early in the disc lifetime.

The fragmentation-limited dust grain size and its Stokes number are most sensitive to the value of the viscosity (and turbulence) parameter at the pressure maximum. As noted above, this roughly equals the assumed value of the viscosity parameter in the MRI-dead zone (α_{DZ}). Therefore, whether the dust grains can become trapped in the pressure maximum is determined by this uncertain parameter. Dust trapping is likely for the lower end of plausible values ($\alpha_{DZ} = 10^{-5}$) and will not happen for the higher end ($\alpha_{DZ} = 10^{-3}$).

Importantly, the pressure maximum does not move inwards for higher dust-to-gas ratios. That is, dust accumulation near the pressure maximum (and/or inwards of it) should result in an expansion of the dust-enriched region and/or dynamical evolution of the disc structure. However, time-dependent simulations are needed to further study the potential outcomes, and the viability of planetesimal formation in the inner disc.

ACKNOWLEDGEMENTS

We thank the reviewer for their thoughtful comments. We thank Richard Booth, Thomas Haworth, Zhaohuan Zhu, Steven Desch, Neal Turner, Colin McNally and Henrik Latter for helpful discussions. MRJ acknowledges support from the President's PhD scholarship of the Imperial College London and the UK Science and Technology research Council (STFC) via the consolidated grant ST/S000623/1. JEO is supported by a Royal Society University Research Fellowship. This project has received funding from the European Research Council (ERC) under the European Union's Horizon 2020 research and innovation programme (Grant agreement No. 853022, ERC-STG-2019 grant, PEVAP). JCT acknowledges support from NASA ATP grant Inside-Out Planet Formation (80NSSC19K0010).

DATA AVAILABILITY

The data underlying this article will be shared on reasonable request to the corresponding author.

REFERENCES

Alcalá J. M., et al., 2014, A&A, 561, A2
Alcalá J. M., et al., 2017, A&A, 600, A20
Bai X.-N., 2017, ApJ, 845, 75
Bai X.-N., Goodman J., 2009, ApJ, 701, 737
Bai X.-N., Stone J. M., 2010, ApJ, 722, 1437
Bai X.-N., Stone J. M., 2011, ApJ, 736, 144
Bai X.-N., Stone J. M., 2013, ApJ, 767, 30
Balbus S. A., Hawley J. F., 1991, ApJ, 376, 214
Baraffe I., Homeier D., Allard F., Chabrier G., 2015, A&A, 577, A42
Beitz E., Güttler C., Blum J., Meisner T., Teiser J., Wurm G., 2011, ApJ, 736, 34
Birnstiel T., Dullemond C. P., Brauer F., 2009, A&A, 503, L5
Birnstiel T., Dullemond C. P., Brauer F., 2010, A&A, 513, A79
Birnstiel T., Klahr H., Ercolano B., 2012, A&A, 539, A148
Bitsch B., Raymond S. N., Izidoro A., 2019, A&A, 624, A109
Blum J., Münch M., 1993, Icarus, 106, 151
Boley A. C., Ford E. B., 2013, arXiv e-prints, p. arXiv:1306.0566
Bukhari Syed M., Blum J., Wahlberg Jansson K., Johansen A., 2017, ApJ, 834, 145
Calvet N., Magris G. C., Patino A., D'Alessio P., 1992, Rev. Mex. Astron. Astrofis., 24, 27
Cannizzo J. K., Wheeler J. C., 1984, ApJS, 55, 367
Carrera D., Johansen A., Davies M. B., 2015, A&A, 579, A43
Chatterjee S., Tan J. C., 2014, ApJ, 780, 53
Chatterjee S., Tan J. C., 2015, ApJ, 798, L32
Chiang E. I., Goldreich P., 1997, ApJ, 490, 368
Chiang E., Laughlin G., 2013, MNRAS, 431, 3444
Cossou C., Raymond S. N., Hersant F., Pierens A., 2014, A&A, 569, A56
Cuzzi J. N., Hogan R. C., 2003, Icarus, 164, 127
D'Alessio P., Cantö J., Calvet N., Lizano S., 1998, ApJ, 500, 411
D'Alessio P., Calvet N., Hartmann L., Lizano S., Cantó J., 1999, ApJ, 527, 893
Demirci T., Krause C., Teiser J., Wurm G., 2019, A&A, 629, A66
Desch S. J., Turner N. J., 2015, ApJ, 811, 156
Draine B. T., 2003, ApJ, 598, 1017
Drazkowska J., Alibert Y., Moore B., 2016, A&A, 594, A105
Dressing C. D., Charbonneau D., 2013, ApJ, 767, 95
Dressing C. D., Charbonneau D., 2015, ApJ, 807, 45
Dzyurkevich N., Flock M., Turner N. J., Klahr H., Henning T., 2010, Astronomy and Astrophysics, 515, A70
Ercolano B., Glassgold A. E., 2013, MNRAS, 436, 3446
Faure J., Fromang S., Latter H., 2014, A&A, 564, A22
Fressin F., et al., 2013, ApJ, 766, 81
Fromang S., Latter H., Lesur G., Ogilvie G. I., 2013, A&A, 552, A71
Gammie C. F., 1996, ApJ, 457, 355
Garaud P., Lin D. N. C., 2007, ApJ, 654, 606
Glassgold A. E., Najita J., Igea J., 1997, ApJ, 480, 344
Güdel M., et al., 2007, A&A, 468, 353
Hansen B. M. S., Murray N., 2013, ApJ, 775, 53
Hsu D. C., Ford E. B., Ragozzine D., Ashby K., 2019, AJ, 158, 109
Hu X., Zhu Z., Tan J. C., Chatterjee S., 2016, ApJ, 816, 19
Hu X., Tan J. C., Zhu Z., Chatterjee S., Birnstiel T., Youdin A. N., Mohanty S., 2018, ApJ, 857, 20
Igea J., Glassgold A. E., 1999, ApJ, 518, 848
Ilgner M., Nelson R. P., 2006, A&A, 445, 205
Izidoro A., Ogihara M., Raymond S. N., Morbidelli A., Pierens A., Bitsch B., Cossou C., Hersant F., 2017, MNRAS, 470, 1750
Izidoro A., Bitsch B., Raymond S. N., Johansen A., Morbidelli A., Lambrechts M., Jacobson S. A., 2019, arXiv e-prints, p. arXiv:1902.08772
Jacquet E., Gounelle M., Fromang S., 2012, Icarus, 220, 162
Jankovic M. R., Owen J. E., Mohanty S., 2019, MNRAS, 484, 2296
Jankovic M. R., Owen J. E., Mohanty S., Tan J. C., 2021, Monthly Notices of the Royal Astronomical Society, 504, 280
Johansen A., Youdin A., 2007, ApJ, 662, 627
Johansen A., Youdin A. N., Lithwick Y., 2012, A&A, 537, A125
Kama M., Folsom C. P., Pinilla P., 2015, A&A, 582, L10
Kretke K. A., Lin D. N. C., Garaud P., Turner N. J., 2009, ApJ, 690, 407
Latter H. N., Balbus S., 2012, MNRAS, 424, 1977
Lesur G., Papaloizou J. C. B., 2010, A&A, 513, A60
Lesur G., Ferreira J., Ogilvie G. I., 2013, A&A, 550, A61
Lesur G., Kunz M. W., Fromang S., 2014, A&A, 566, A56
Lightman A. P., Eardley D. M., 1974, ApJ, 187, L1
Lyra W., Mac Low M.-M., 2012, ApJ, 756, 62
Malygin M. G., Kuiper R., Klahr H., Dullemond C. P., Henning T., 2014, A&A, 568, A91
Manara C. F., Robberto M., Da Rio N., Lodato G., Hillenbrand L. A., Stassun K. G., Soderblom D. R., 2012, ApJ, 755, 154
Manara C. F., et al., 2017, A&A, 604, A127
Mathis J. S., Rumpl W., Nordsieck K. H., 1977, ApJ, 217, 425
McClure M. K., Dominik C., Kama M., 2020, A&A, 642, L15
McNeil D. S., Nelson R. P., 2010, MNRAS, 401, 1691
Mohanty S., Jayawardhana R., Basri G., 2005, ApJ, 626, 498
Mohanty S., Ercolano B., Turner N. J., 2013, ApJ, 764, 65
Mohanty S., Jankovic M. R., Tan J. C., Owen J. E., 2018, ApJ, 861, 144
Mulders G. D., Pascucci I., Apai D., Ciesla F. J., 2018, AJ, 156, 24

Nakagawa Y., Sekiya M., Hayashi C., 1986, Icarus, 67, 375
Nelson R. P., Gressel O., Umurhan O. M., 2013, MNRAS, 435, 2610
Ogihara M., Ida S., 2009, ApJ, 699, 824
Ormel C. W., Cuzzi J. N., 2007, A&A, 466, 413
Owen J. E., Wu Y., 2017, ApJ, 847, 29
Perez-Becker D., Chiang E., 2011, ApJ, 735, 8
Pollack J. B., Hollenbach D., Beckwith S., Simonelli D. P., Roush T., Fong W., 1994, ApJ, 421, 615
Preibisch T., et al., 2005, ApJS, 160, 401
Pringle J. E., 1981, ARA&A, 19, 137
Raymond S. N., Cossou C., 2014, MNRAS, 440, L11
Raymond S. N., Barnes R., Mandell A. M., 2008, MNRAS, 384, 663
Rogers J. G., Owen J. E., 2021, MNRAS, 503, 1526
Salmeron R., Wardle M., 2008, MNRAS, 388, 1223
Sano T., Miyama S. M., Umebayashi T., Nakano T., 2000, ApJ, 543, 486
Schäfer U., Yang C.-C., Johansen A., 2017, A&A, 597, A69
Schlichting H. E., 2014, ApJ, 795, L15
Schräpler R., Blum J., Seizinger A., Kley W., 2012, ApJ, 758, 35
Shakura N. I., Sunyaev R. A., 1973, A&A, 500, 33
Simon J. B., Armitage P. J., Li R., Youdin A. N., 2016, ApJ, 822, 55
Simon J. B., Armitage P. J., Youdin A. N., Li R., 2017, ApJ, 847, L12
Stoll M. H. R., Kley W., 2014, A&A, 572, A77
Suzuki T. K., Inutsuka S.-i., 2009, ApJ, 691, L49
Suzuki T. K., Muto T., Inutsuka S.-i., 2010, ApJ, 718, 1289
Suzuki T. K., Ogihara M., Morbidelli A., Crida A., Guillot T., 2016, A&A, 596, A74
Taki T., Fujimoto M., Ida S., 2016, A&A, 591, A86
Terquem C. E. J. M. L. J., 2008, ApJ, 689, 532
Terquem C., Papaloizou J. C. B., 2007, ApJ, 654, 1110
Van Eylen V., Agentoft C., Lundkvist M. S., Kjeldsen H., Owen J. E., Fulton B. J., Petigura E., Snellen I., 2018, MNRAS, 479, 4786
Wardle M., 2007, Ap&SS, 311, 35
Weidenschilling S. J., 1977, MNRAS, 180, 57
Wright N. J., Drake J. J., Mamajek E. E., Henry G. W., 2011, ApJ, 743, 48
Wu Y., 2019, ApJ, 874, 91
Yang C.-C., Johansen A., Carrera D., 2017, A&A, 606, A80
Youdin A. N., Goodman J., 2005, ApJ, 620, 459
Zhu Z., Stone J. M., Bai X.-N., 2015, ApJ, 801, 81

This paper has been typeset from a TEX/LATEX file prepared by the author.

Monthly Notices of the ROYAL ASTRONOMICAL SOCIETY

MNRAS **528,** 1249–1263 (2024) https://doi.org/10.1093/mnras/stae095
Advance Access publication 2024 January 10

On the likely magnesium–iron silicate dusty tails of catastrophically evaporating rocky planets

Beatriz Campos Estrada [1,2,3,4]★ James E. Owen [4] Marija R. Jankovic [5] Anna Wilson[4] and Christiane Helling[2,3]

[1]*Centre for ExoLife Sciences, Niels Bohr Institute, Øster Voldgade 5, DK-1350 Copenhagen, Denmark*
[2]*Space Research Institute, Austrian Academy of Sciences, Schmiedlstrasse 6, A-8042 Graz, Austria*
[3]*TU Graz, Fakultät für Mathematik, Physik und Geodäsie, Petersgasse 16, A-8010 Graz, Austria*
[4]*Astrophysics Group, Imperial College London, Blackett Laboratory, Prince Consort Road, London SW7 2AZ, UK*
[5]*Institute of Physics Belgrade, University of Belgrade, Pregrevica 118, 11080 Belgrade, Serbia*

Accepted 2024 January 3. Received 2023 December 22; in original form 2023 July 5

ABSTRACT

Catastrophically evaporating rocky planets provide a unique opportunity to study the composition of small planets. The surface composition of these planets can be constrained via modelling their comet-like tails of dust. In this work, we present a new self-consistent model of the dusty tails: we physically model the trajectory of the dust grains after they have left the gaseous outflow, including an on-the-fly calculation of the dust cloud's optical depth. We model two catastrophically evaporating planets: KIC 1255 b and K2-22 b. For both planets, we find the dust is likely composed of magnesium–iron silicates (olivine and pyroxene), consistent with an Earth-like composition. We constrain the initial dust grain sizes to be ~ 1.25–$1.75\ \mu$m and the average (dusty) planetary mass-loss rate to be $\sim 3\ M_{\oplus}\mathrm{Gyr}^{-1}$. Our model shows that the origin of the leading tail of dust of K2-22 b is likely a combination of the geometry of the outflow and a low radiation pressure force to stellar gravitational force ratio. We find the optical depth of the dust cloud to be a factor of a few in the vicinity of the planet. Our composition constraint supports the recently suggested idea that the dusty outflows of these planets go through a greenhouse effect–nuclear winter cycle, which gives origin to the observed transit depth time variability. Magnesium–iron silicates have the necessary visible-to-infrared opacity ratio to give origin to this cycle in the high mass-loss state.

Key words: planets and satellites: composition – planets and satellites: surfaces.

1 INTRODUCTION

The nature and composition of small planets' ($R_p \lesssim 1.5\ \mathrm{R}_{\oplus}$) interiors remain uncertain. Measurements of planetary densities (e.g. Dressing et al. 2015; Van Eylen et al. 2021) and modelling constraints (e.g. Rogers 2015; Dorn et al. 2019; Gupta & Schlichting 2019; Rogers & Owen 2021; Rogers et al. 2023a; Rogers, Schlichting & Owen 2023b) show most have an 'Earth-like' composition of 2/3 silicate rock and 1/3 iron. However, density measurements alone do not provide enough information to determine a planet's bulk composition because planets with similar densities can vary greatly in terms of their bulk composition (e.g. Seager et al. 2007; Valencia, Sasselov & O'Connell 2007; Rogers & Seager 2010; Unterborn, Dismukes & Panero 2016; Dorn et al. 2017a; Dorn, Hinkel & Venturini 2017b; Neil & Rogers 2020; Neil, Liston & Rogers 2022). One way around this degeneracy would be to constrain the elemental abundance ratios of the bodies. For example, this analysis can be performed for the material accreted by polluted white dwarfs (e.g. Gänsicke et al. 2012; Farihi et al. 2016; Harrison, Bonsor & Madhusudhan 2018; Bonsor et al. 2020). However, it is uncertain what planetary reservoirs polluted white dwarfs probe (e.g Jura & Young 2014; Buchan et al. 2022; Brouwers, Bonsor & Malamud 2023), and they are unlikely to represent close-in planets.

Alternatively, ultra-short-period (USP) planets (planets with an orbital period of less than one day) provide a unique opportunity to study the composition of small planets. USP planets are tidally locked and highly irradiated by their host stars, often achieving sub-stellar (day-side) surface temperatures $\gtrsim 2000$ K. Their primordial atmosphere is expected to be lost quickly (e.g. Valencia et al. 2010; Owen & Wu 2013), leaving a 'bare' core exposed to stellar radiation. Under these conditions, the surface of the planet becomes molten on its day-side, and a rock-vapour atmosphere forms from magma outgassing (e.g. Schaefer & Fegley 2009; Miguel et al. 2011; Ito et al. 2015; Kite et al. 2016; Mahapatra, Helling & Miguel 2017; Zilinskas et al. 2022). Measuring the composition of this rock-vapour atmosphere could directly probe the planetary interior composition since the planet's atmosphere is likely in vapour pressure equilibrium with the magma. Zieba et al. (2022) recently argued the small ($1.5\ R_{\oplus}$) rocky USP planet K2-141 b probably has a thin rock-vapour atmosphere. Further, JWST observations will likely unveil more about the nature of these planets (Zilinskas et al. 2022). However, current observations have yielded no evidence for thick atmospheres (Kreidberg et al. 2019; Crossfield et al. 2022). Furthermore, detailed

★ E-mail: beatriz.estrada@nbi.ku.dk

© The Author(s) 2024.
Published by Oxford University Press on behalf of Royal Astronomical Society. This is an Open Access article distributed under the terms of the Creative Commons Attribution License (https://creativecommons.org/licenses/by/4.0/), which permits unrestricted reuse, distribution, and reproduction in any medium, provided the original work is properly cited.

Downloaded from https://academic.oup.com/mnras/article/528/2/1249/7515287 by guest on 01 February 2024

modelling of these planets' interior–atmosphere interaction and evolution is required to interpret the observations and understand their planetary interiors.

In 2012, Rappaport et al. (2012) reported the discovery of KIC 12557548 b (often shortened to KIC 1255 b and more recently Kepler-1520 b), a transiting object with an orbital period of approximately 15.7 h which displays an asymmetric light curve. The KIC 1255 b light curve presents a sharp transit ingress and a slow egress. Additionally, the light curve shows a positive bump in stellar flux before the transit occurs and high transit depth time variability. Rappaport et al. (2012) suggested this light curve could be explained by the existence of a low-mass (similar to Mercury) evaporating USP planet with a comet-like tail of dust. The comet-like tail scenario can be explained as follows: dust from the planet's molten surface condenses in a thermally driven wind (Rappaport et al. 2012; Perez-Becker & Chiang 2013; Booth, Owen & Schulik 2023) and is transported by a gaseous outflow out to the point where the gas density is low enough that dust dynamically decouples from the gas. At this point, the trajectory of the dust is dictated by the stellar radiation pressure and the stellar gravity, which shapes the dust into a cometary tail, trailing the planet (e.g Brogi et al. 2012; Rappaport et al. 2012; Budaj 2013; Sanchis-Ojeda et al. 2015; Lieshout & Rappaport 2018). As the gas density decreases away from the planet, the sublimation temperature decreases (e.g. Booth, Owen & Schulik 2023). This results in the gradual sublimation of the dust as it moves along the tail, ultimately resulting in a tail where the optical depth drops with distance from the planet (Rappaport et al. 2012; van Lieshout et al. 2016). The optical depth pattern of the dust cloud can explain the sharp ingress and slow egress observed. Furthermore, the forward scattering of stellar photons by the dust grains towards the line-of-sight of the observer can give rise to the pre-transit brightening (e.g. van Lieshout et al. 2016). This dusty-tail scenario has been validated by studies of the colour dependence of the transit depth (e.g. Bochinski et al. 2015). In addition to this, van Werkhoven et al. (2014) obtained an upper limit on the KIC 1255 b's radius of 4600 km, supporting the idea that we are observing the dust cloud and not the planet.

Since the discovery of KIC 1255 b, two more examples of evaporating rocky planets have been observed: KOI-2700 b (Rappaport et al. 2014) and K2-22 b (Sanchis-Ojeda et al. 2015). KOI-2700 b presents a very similar light curve to KIC 1255 b. K2-22b presents a symmetric light curve, with increased observed flux both before and after the transit, where the post-transit brightening is explained with a leading tail of dust (Sanchis-Ojeda et al. 2015).

To explain the high transit depth time variability, Rappaport et al. (2012) state an erratic variation in the dust production rate is needed, and a detailed understanding of the origin of this variability remains uncertain. Perez-Becker & Chiang (2013) speculated and Booth, Owen & Schulik (2023) found the planetary outflow can be unsteady. For fast dust growth rates and moderate optical depths, there is a cycle between periods of dust production and no dust production, which could give rise to the observed transit depth variability. The variability was investigated further by Bromley & Chiang (2023), following the speculation of heterogeneous condensation by Booth, Owen & Schulik (2023). Bromley & Chiang (2023) demonstrated a chaotic evolution could arise when iron-poor silicates condensed at low-mass loss rates (low optical depths), while iron-rich silicate dust condensed at high mass-loss rates (high optical depths).

Using models of the planetary outflow, Perez-Becker & Chiang (2013), Kang et al. (2021) and Booth, Owen & Schulik (2023) constrained the mass of KIC 1255 b and the planetary mass-loss rate. In addition to this, the models agree with a scenario where the outflows are marginally optically thick in the planet's vicinity.Morphological models of KIC 1255 b's dusty-tail reproduce the characteristics of the observed light curve and place constraints on the size of the dust grains by comparing synthetic light curves to the observed ones (e.g. Brogi et al. 2012; Budaj 2013; van Werkhoven et al. 2014). These models do not attempt to model the formation and launch of the dusty outflow but to study the properties of the dust under the assumption it is launched from the planets. The models indicate the dust grains are around micron-sized.

K2-22 b's dust tail properties have also been studied using similar morphological models. Sanchis-Ojeda et al. (2015) determined K2-22 b has a leading dust tail, giving origin to the observed post-transit brightening in flux. This implies the ratio of radiation pressure forces to stellar gravity (β) to be less than 2 per cent. The value of β can be this small for low-luminosity host stars and small particle sizes ($\lesssim 0.1\mu$m) or large particle sizes ($\gtrsim 1.0\mu$m). More recently, observations and models of K2-22 b by Schlawin et al. (2021) show the average particle size must be larger than about 0.5 - 1.0μm, leading to mass-loss rates of about 1.6 - 1.8 $M_\oplus$ Gyr^{-1}.

The dust in the planetary outflow is a direct sample of the magma pool on the planet's surface. Therefore, studying the dusty tails can be used to directly place constraints on the planetary composition. The composition of the dust was investigated in detail by van Lieshout, Min & Dominik (2014); van Lieshout et al. (2016). This work was done by assuming the planet launched an outflow with dust particles of a certain size and composition and studying how long they survived before they completely sublimated. van Lieshout, Min & Dominik (2014) used the dust's survival time-scale to compute the distance it could travel from the planet, and compared this to the length of the tail inferred from the light curve. They found the models where the dust was composed of corundum (Al_2O_3[s]) or iron-rich silicates to be consistent with the observations of KIC 1255 b and KOI-2700 b. Pure iron, graphite or silicon carbide grains were ruled out. van Lieshout et al. (2016) directly simulated the dynamics and size evolution of dust particles in KIC 1255 b's tail to study the dust composition, the dust grain sizes and the planetary mass-loss rate of the planet. They found the dusty tail to be most likely composed of Al_2O_3[s] micron-sized grains, with a planetary mass-loss rate ranging from 0.6 to 15.6 $M_\oplus$Gyr^{-1}. Enstatite ($MgSiO_3$[s]) and forsterite (Mg_2SiO_4[s]) had previously been suggested as potential compositions of the dust grains by Rappaport et al. (2012), Brogi et al. (2012) and Perez-Becker & Chiang (2013). However, van Lieshout et al. (2016) found iron-free magnesium-silicates were too cold to sublimate efficiently due to their low optical, but high IR opacities, and hence survived too long in the dust cloud to be consistent with the observed transit duration.

All previous dusty-tail models are limited because they assume the dusty-tail to be optically thin throughout. In addition to this, many of the previous models use a simplified formulation for the complex refractive index in the calculation of dust optical properties. Considering the dust cloud to be optically thin throughout is an assumption that requires detailed investigation. The trajectory of a dust grain is highly dictated by the radiation pressure force, which is obviously highly sensitive to the optical depth to stellar light once it reaches moderate values. Thus, even moderate optical depths can cause significant changes in the morphology of the dusty tail. In addition to this, the temperature of a dust grain, and hence the sublimation rate of the dust, is highly sensitive to moderate or higher optical depths. Therefore, the more optically thick the environment, the cooler the dust grains will be, causing them to survive longer in the dusty tail.

Downloaded from https://academic.oup.com/mnras/article/528/2/1249/7515287 by guest on 01 February 2024

In this work, we construct a new model of the dusty tails. We couple the dust particle dynamics to the self-consistently determined optical depth. Introducing the optical depth evolution allows for robust compositional constraints to be derived from the observations. Our methods are presented in Section 2. In Section 3 we apply our model to KIC 1255 b and in Section 4 to K2 22 b. In Section 5, we discuss our results in the context of the observations. Finally, in Section 6, we summarize our findings.

2 MODEL AND METHODS

We aim to develop a model with all the necessary physics to compare directly to the observations, but that is still computationally feasible. To achieve this, we adopt a hybrid method, where similar to van Lieshout et al. (2016), the dust grains are modelled as Lagrangian 'super-particles', but the optical depth is computed by ray tracing on a grid of dust densities. Our super-particle is a collection of dust grains that share the same but evolving properties. The number of actual dust grains (N_d) inside a super-particle depends on the planetary mass-loss rate, the grain's initial size and composition, and how often/many super-particles we introduce into the simulation. Thus, we introduce the super-particle mass $m_{sp} = m_d N_d$, where m_d is the mass of an individual dust grain.

2.1 Dust motion

The stellar radiation pressure force and the stellar gravity dominate the trajectory of the dust grains. For full consistency, we include planetary gravity and the Poynting–Robertson drag (Robertson 1937) acting on the dust grains, but we ignore collisions between the individual dust grains. Following the results from Booth, Owen & Schulik (2023), we assume the planet to have a mass of $0.03 M_\oplus$ although we note the choice does not affect our results. Using the Fortney, Marley & Barnes (2007) mass–radius relationship, we estimate the planetary radius to be $0.33\,R_\oplus$, assuming mass fractions of 2/3 silicate rock and 1/3 iron. The equation of motion for the dust grain is solved in the co-rotating frame of reference, centred at the centre of mass of the star–planet system. The planetary and stellar orbits are assumed to be circular. The equation of motion of a dust grain is given by

$$\begin{aligned}\ddot{\mathbf{r}} = &-\frac{GM_\star}{|\,\mathbf{r}-\mathbf{r}_\star\,|^3}(\mathbf{r}-\mathbf{r}_\star) - \frac{GM_{\rm planet}}{|\,\mathbf{r}-\mathbf{r}_{\rm planet}\,|^3}(\mathbf{r}-\mathbf{r}_{\rm planet})\\ &-\boldsymbol{\omega}\times(\boldsymbol{\omega}\times\mathbf{r}) - 2(\boldsymbol{\omega}\times\dot{\mathbf{r}})\\ &+\beta\frac{GM_\star}{|\,\mathbf{r}-\mathbf{r}_\star\,|^2}\left[\left(1-\frac{\dot{\mathbf{r}}_{\rm radial}}{c}\right)\frac{(\mathbf{r}-\mathbf{r}_\star)}{|\,\mathbf{r}-\mathbf{r}_\star\,|} - \left(\frac{\dot{\mathbf{r}}+(\boldsymbol{\omega}\times\mathbf{r})}{c}\right)\right]\end{aligned} \tag{1}$$

where $\mathbf{r}$ is the position vector of the dust grain, $\mathbf{r}_{\star,\rm planet}$ are the position vectors of the star and planet, respectively; $M_{\star,\rm planet}$ are the mass of the star and planet respectively; $\boldsymbol{\omega}$ is the rotation vector of the frame-of-reference, β is the ratio between the norms of the direct radiation pressure force and the star's gravitational force, G is the gravitational constant and c is the speed of light. The final term on the RHS of equation (1) represents the radiation forces acting on the dust grains (Robertson 1937; Burns, Lamy & Soter 1979).

We assume our dust grains are spherical, and as such, β is given by

$$\beta = \frac{1}{4\pi cG}\frac{L_\star}{M_\star}e^{-\tau_\star}\kappa(T_\star, s) \tag{2}$$

where $L_\star$ is stellar luminosity, $\tau_\star$ is the optical depth of the dust cloud to stellar irradiation at the grain's position, and κ is the radiation-pressure Planck-mean opacity at the stellar temperature $T_\star$, for a particle of radius s.

2.2 Dust sublimation

We take a similar approach to van Lieshout et al. (2016) for determining the sublimation rate of a spherical dust grain in a gas-free environment. In thermodynamical equilibrium, when the partial pressure of a molecule equals its equilibrium vapour pressure, the condensation rate must equal the sublimation rate; thus, the sublimation rate can be expressed in terms of the condensation rate using the principle of detailed balance (c.f. Booth, Owen & Schulik 2023). In our models, the dust grains have large numbers of atoms ($\sim 10^9$ atoms for a $0.1\,\mu$m particle); thus, we assume their sublimation rate is solely dependent on the dust's internal properties (e.g. its temperature, Gail & Sedlmayr 2013). Consequently, the sublimation rate for a dust grain in thermodynamical equilibrium with the gas surrounding it is equal to its sublimation rate in a gas-free environment (Langmuir 1913). Therefore, the change of the radius of a dust grain (s) can be written as (Kimura et al. 2002; Gail & Sedlmayr 2013; van Lieshout, Min & Dominik 2014),

$$\frac{\mathrm{D}s}{\mathrm{D}t} = -\frac{\alpha\, p_{\rm v}(T_{\rm d})}{\rho_{\rm d}}\left(\frac{\mu m_{\rm u}}{2\pi k_{\rm B} T_{\rm d}}\right)^{1/2} \tag{3}$$

where α is the evaporation coefficient which parametrizes the kinetic inhibition of the sublimation.[1], $p_{\rm v}$ is the equilibrium vapour pressure, μ is the molecular weight of the sublimating molecules in atomic mass units[2], $m_{\rm u}$ is the atomic mass unit, $k_{\rm B}$ is Boltzmann's constant, and $T_{\rm d}$ is the dust grain's temperature. The equilibrium vapour pressure is given by the Clausius-Claperyon relation (Kimura et al. 2002),

$$p_{\rm v}(T) = \exp(-\mathcal{A}/T + \mathcal{B})\ [\rm cgs] \tag{4}$$

where $\mathcal{A}$ and $\mathcal{B}$ are material-specific parameters. Quantities α, $\mathcal{A}$ and $\mathcal{B}$ are assumed to be temperature independent.

The balance between the received and emitted energy by a dust grain is used to determine the dust's temperature, which we approximate as:

$$\kappa_{\rm abs}(T_\star, s)\,\frac{L_\star}{4\pi r_{\rm d}^2}\,e^{-\tau_\star} = 4\,\kappa_{\rm abs}(T_{\rm d}, s)\,\sigma_{\rm SB}\,T_{\rm d}^4 \tag{5}$$

where $\kappa_{\rm abs}(T_\star, s)$ is the Planck-mean absorption opacity at the stellar temperature $T_\star$, $\kappa_{\rm abs}(T_{\rm d}, s)$ is the absorption opacity at the dust temperature $T_{\rm d}$, $r_{\rm d}$ is the dust grain-star distance and $\sigma_{\rm SB}$ is Stefan–Boltzmann's constant. This equation assumes that while we are including the attenuation of stellar light due to the dust cloud's optical depth, we are assuming the dust cloud is optically thin to its own cooling radiation. This assumption is justified, as for our best-fitting models, the dusty outflow is optically thin to its re-emitted thermal emission. As discussed in our results, the dust's temperature (and hence sublimation rate) depends critically on the opacity ratio $\kappa_{\rm abs}(T_\star, s)/\kappa_{\rm abs}(T_{\rm d}, s)$, which at higher ratios gives higher

[1] α has been experimentally measured to be approximately the same as the growth/sticking coefficient (Gail & Sedlmayr 2013).
[2] Following van Lieshout, Min & Dominik (2014) and for simplicity, we assume μ to be the molecular weight of the dust sublimating. In reality, μ is the average molecular weight of the molecules recondensing from the gas phase in the sublimation–condensation equilibrium.

Downloaded from https://academic.oup.com/mnras/article/528/2/1249/7515287 by guest on 01 February 2024

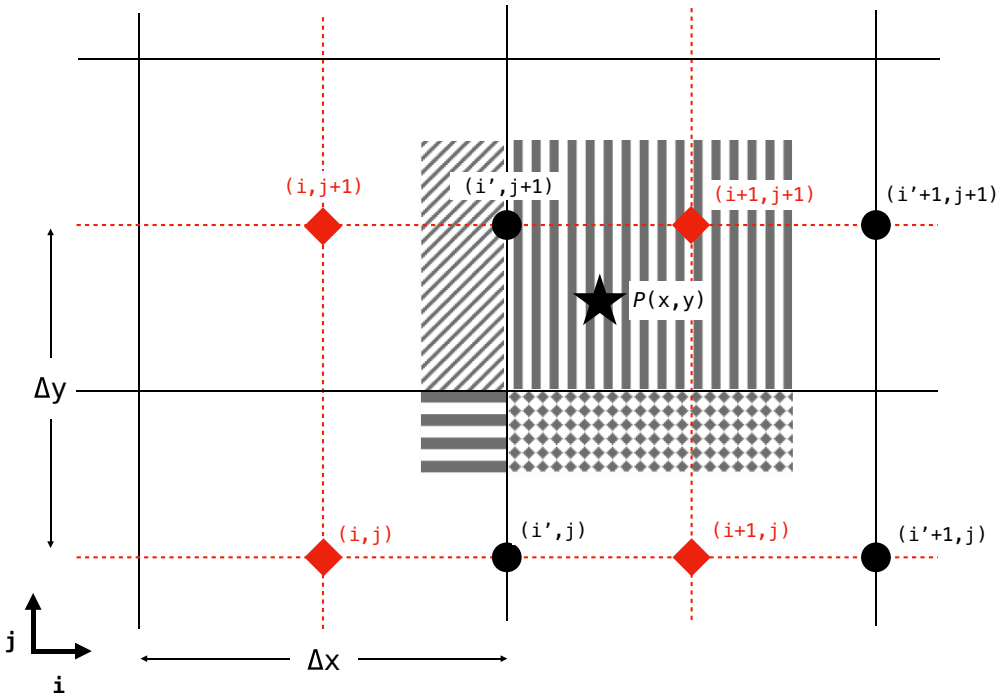

Figure 1. A 2D representation of our staggered mesh, similar to the 3D one used to estimate the dust cloud's optical depth. Scalar variables are measured at the centres of the grid cells, represented by the red diamonds. Vector quantities/direction-dependent variables are measured at the grid-cell interfaces, represented by the black circles. We apply the clouds-in-cells method (Section 2.3) where the extinction contribution of a dust grain in position $P(x, y)$ (black star) is shared between the grid cells surrounding it (shaded area) with the value determined between the volume assigned to the grain and the volume of the cell.

temperatures and hence faster sublimation. It is this opacity ratio that ultimately allows us to constrain the dust's composition and size through its impact on the temperature and, subsequently, the sublimation rate.

2.3 Optical depth evolution

To calculate the optical depth of the dust cloud, we implement the clouds-in-cells (CIC) method (Birdsall & Fuss 1969). Consider a staggered-mesh grid, where scalar variables (e.g. extinction) are defined at the grid-cell centres (red diamonds in Fig. 1) and direction-dependent variables (e.g. optical depth) at the centres of the grid-cell interfaces (black circles in Fig. 1). The extinction to be attributed to the grid-cell centres is obtained by sharing a dust super-particle's extinction over the grid points surrounding it. A 2D representation of our 3D method is shown in Fig. 1. Considering a dust grain at a position $P(x, y)$, we can regard the grain as a small cloud and spread it over an area of $\Delta x \Delta y$, the shaded area surrounding the black star. The extinction in the horizontal-lines-shaded area is assigned to point (i, j); that in the diamond-shaded area to point $(i + 1, j)$; that in the vertical-lines-shaded area to point $(i + 1, j + 1)$ and that in the diagonal-lines-shaded area to point $(i, j + 1)$.

We adapt and apply the method described above to a uniform three-dimensional spherical polar grid centred at the star, i.e. the volume of each grid cell is approximately the same. Here, r is the radial distance from the star's centre, θ is the polar angle, and ϕ is the azimuthal angle. The contribution to the extinction of a super-particle at a position (r_d, θ_d, ϕ_d) is given by

$$\chi_{\rm sp}(r_{\rm d}, \theta_{\rm d}, \phi_d) = \frac{m_{\rm sp}\, \kappa_{\rm ext}(T_\star, s)}{\Delta V}, \tag{6}$$

where $\kappa_{\rm ext}$ is the extinction opacity of the dust grains in a super-particle, and ΔV is the 'volume'[3] of the superparticle, taken to be the volume element of the cell in which it resides. For better numerical accuracy, volumes are calculated with the spherical volume element in the following form (cf. Stone & Norman 1992):

$$\Delta V = \Delta(R^3/3)\, \Delta(-\cos\theta)\, \Delta\phi. \tag{7}$$

The extinction of the grid cell centred at $(r(i), \theta(j), \phi(k))$ can now be written as

$$\chi(i, j, k) = \sum_{\rm sp} V^f_{ijk}\, \chi_{\rm sp}(r_{\rm d}, \theta_{\rm d}, \phi_{\rm d}) \tag{8}$$

where V^f_{ijk} is the fraction of the superparticle's volume that resides in cell (i, j, k) (see Fig. 1). The sum is performed over all super-particles that have any volume that overlaps with that cell. Once the extinction grid is computed via equation (8), we obtain the optical depth by numerically integrating the extinction over the radial distance from the star to the grid-cell interface centres in the radial direction **i**, using:

$$\tau(i, j, k) = \sum_{i'=0}^{i-1} \chi(i', j, k)\, \Delta r, \ \text{for}\ i \geq 1 \tag{9}$$

where $\tau(i, j, k)$ is the optical depth at the grid-cell interface centred at $(r(i), \theta(j), \phi(k))$ and Δr is grid-cell size in the radial direction **i**. The grid boundaries are set as

[3]It is important not to confuse this 'volume' with any physical volume. This 'volume' is used to smooth the extinction over our grid in the CIC method and thus scales with the grid's resolution. Our choice for its size is confirmed by our resolution tests.

Downloaded from https://academic.oup.com/mnras/article/528/2/1249/7515287 by guest on 01 February 2024

$$r(i=0) = R_{\rm min},\ r(i=N_{\rm R}) = R_{\rm max};$$
$$\theta(j=0) = \theta_{\rm min} + \frac{\Delta\theta}{2},\ \theta(j=N_\theta - 1) = \theta_{\rm max} - \frac{\Delta\theta}{2};$$
$$\phi(j=0) = \phi_{\rm min} + \frac{\Delta\phi}{2},\ \phi(j=N_\phi - 1) = \phi_{\rm max} - \frac{\Delta\phi}{2};$$

where $N_{\rm R,\,\theta,\,\phi}$ are the number of grid cells in the radial **i**, polar **j**, and azimuthal **k** directions, respectively, $(R,\,\theta,\,\phi)_{\rm min}$ are the lower boundaries in each direction and similarly $(R,\,\theta,\,\phi)_{\rm max}$ are the upper boundaries. We note that $r(i') = r(i) + \frac{\Delta r}{2}$. In this case, at $i = 0$, $\tau = 0$ for all j and k. After testing, we set $N_{\rm R} = 75$, $N_\theta = 25$, and $N_\phi = 250$, and the grid limits to be

$$R_{\rm min} = 0.95\,a,\ R_{\rm max} = 1.10\,a;$$
$$\theta_{\rm min} = 1.55\ {\rm rad},\ \theta_{\rm max} = 1.60\ {\rm rad};$$

$$\phi_{\rm min} = -0.40\ {\rm rad},\ \phi_{\rm max} = 0.10\ {\rm rad};$$

where a is the semimajor axis of the planet's orbit. These values allow for approximately cubic grid cells with constant grid-cell sizes in each direction, where $\Delta r = 0.002\,a$ and $\Delta\theta = \Delta\phi = 0.002$ rad. The grid limits were chosen according to where the optical depth is dynamically important. A lower limit of 0.001 for the optical depth is placed. Outside the chosen grid limits, the optical depth of the dust cloud is set to 0.001. To obtain the optical depth at the position of a super-particle, we perform a tri-cubic spline interpolation (Press et al. 2002) over the optical depth grid.

2.4 Dust opacities

Dust opacities are calculated for the materials listed in Table 1 as follows. First, using the MIESCAT module of RADMC3DPY[4], which applies Mie theory, we calculate the dust absorption ($\kappa^{\lambda}_{\rm abs}$) and scattering opacities ($\kappa^{\lambda}_{\rm sca}$), as well as the scattering g-factor ($g^{\lambda}_{\rm sca}$), as functions of wavelength ($\lambda = 10^{-5}$–10 cm) and grain size ($s = 0.1$–$10\,\mu$m)[5] Where the optical constants are not available for the entire wavelength range indicated above, they are extrapolated by keeping them constant at shorter wavelengths and with a log–log function at longer wavelengths, as would be expected from simple diffraction theory (e.g. Bohren & Huffman 1983). The extrapolation of optical constants to shorter wavelengths may somewhat affect the opacities at the stellar temperatures, especially for corundum (Al_2O_3[s]), for which the optical constants are only available down to 0.5 μm, but they do not change our conclusions. At the lower end of relevant temperatures, the calculated values are unaffected by the extrapolation since the available data covers the relevant range of wavelengths.

For each grain size s, the opacities are averaged over a Gaussian size distribution centred at s, and of width $\Delta\ln(s) = 0.02$ to avoid 'ringing'. We adopt the dust bulk densities shown in Table 1.

To obtain the Planck-mean opacities as functions of temperature and grain size, we integrate $\kappa^{\lambda}_{\rm abs}$, $\kappa^{\lambda}_{\rm sca}$ and $g^{\lambda}_{\rm sca}$ over frequency. In our problem, we have four relevant opacities:

(i) The absorption opacity to stellar light, $\kappa_{\rm abs}(T_\star,\,s)$, used in equation (5);

(ii) The absorption opacity at the grain's temperature, $\kappa_{\rm abs}(T_d,\,s)$, used in equation (5);

(iii) The extinction opacity to the star light, $\kappa_{\rm ext}(T_\star,\,s) = \kappa_{\rm abs}(T_\star,\,s) + \kappa_{\rm sca}(T_\star,\,s)$, used in equation (6);

(iv) The radiation pressure opacity, $\kappa(T_\star,\,s) = \kappa_{\rm abs}(T_\star,\,s) + \kappa_{\rm sca,\,eff}(T_\star,\,s)$, used in equation (2), where $\kappa_{\rm sca,\,eff}(T_\star,\,s)$ is given by $(1 - g_{\rm sca}(T_\star,\,s))\,\kappa_{\rm sca}(T_\star,\,s)$.

2.5 Numerical methods

To determine the trajectory of a super-particle, we solve its equations of motion (equation (1)) and sublimation (equation (3)) simultaneously. To solve equations (1) and 3, we use the Dormand–Prince (DP) method (Dormand & Prince 1980) with an absolute and relative tolerance of 10^{-8}. We apply Brent's method (Brent 1973) to solve equation (5) numerically for the temperature of a dust grain with an absolute tolerance of 10^{-4} and a relative tolerance of 10^{-8}. Each super-particle has an optimal time-step for the DP solver. In order to make the model as efficient as possible, we use the optimal time-step for each individual super-particle and synchronize the time-step between particles when obtaining the optical depth of the dust cloud and calculating the transit depth (see Section 2.6). This approach only updates the optical depth at every synchronized time-step; however, we confirmed this does not affect our results by varying the synchronized time-step.

The model's free parameters are the distribution of the grain's initial positions and velocities, the initial dust grain sizes, the planetary mass-loss rate and the dust composition. To ensure the dust grains are not gravitationally bound to the planet, we start them off at a distance of 1.1 Hill radii from the planet's centre. We assume the dust grains have left the planetary atmosphere at the thermal velocity of the gas particles (Booth, Owen & Schulik 2023) in the radial direction. The super-particles are either randomly distributed to leave from the entire planetary surface (spherical outflow) or just the planet's day-side, both at the level of the Hill radius (see Section 4).

The simulations are initialized by obtaining the optical depth grid of the initial dust cloud. The planetary mass-loss rate is set to be constant throughout our simulations. We launch 250 super-particles every 100th of a planetary orbit, enough to guarantee convergence in the light curve (see Fig. 2). We trace the optical depth every 200$^{\rm th}$ of an orbit. We consider a dust grain completely sublimated when it is smaller than 0.1 μm, at which point it does not significantly contribute to the extinction or scattering of the dust cloud. We run the simulations until the transit profile is converged, i.e. it has reached a steady state and does not significantly change from one transit to the next; this typically requires five orbits (or until it becomes apparent there is no steady state for a given material; see Section 3.2).

2.6 Transit profile calculation

The final stage is to compute a synthetic light curve from our simulations. We adopt a two-stage method, including extinction and forward scattering. For the extinction calculation, we implement the CIC method once again (see Section 2.3). We grid the star into cells with area $A_{\rm cell}$ and spread each super-particle over an area $A_{\rm cell}$. If a super-particle overlaps with a given grid cell, the optical depth contribution from the super-particle in that cell is given by

$$\tau_{\rm sp} = \frac{f\,\kappa_{\rm ext}(T_\star,\,s)\,m_{\rm sp}}{A_{\rm cell}}, \tag{10}$$

where f is the fraction of the super-particle's area which overlaps with the grid cell. To obtain the total optical depth τ in a grid cell,

[4] https://www.ita.uni-heidelberg.de/~dullemond/software/radmc-3d/manual_rmcpy/

[5] For some materials, in some wavelength ranges, optical constants are different for different crystal axes. In such cases, we follow van Lieshout et al. (2016) and combine the optical constants for different axes using the Bruggeman (1935) mixing rule.

Downloaded from https://academic.oup.com/mnras/article/528/2/1249/7515287 by guest on 01 February 2024

Table 1. Dust species used in this study and the corresponding densities, sublimation parameters, and references for optical data and sublimation parameters.

Dust species	Density [g cm^{-3}]	Optical data ref.	Sublimation parameters $\mathcal{A}$ [10^4 K]	$\mathcal{B}$	α	ref.	Notes
Al_2O_3[s] (Corundum)[1]	4.00	K95	7.74	39.3	0.1	S04, L08	
$MgSiO_3$[s] (Enstatite)[1,2]	3.20	J94, D95, J98	6.89	37.8	0.1	M88	(a)
$Mg_{[0.5,0.7,0.95]}Fe_{[0.5,0.3,0.05]}SiO_3$[s] (Pyroxene)[1]	3.20, 3.01, 2.74	J94, D95	6.89	37.8	0.1	M88	(a), (b)
Mg_2SiO_4[s] (Forsterite)[1]	3.27	F01	6.53	34.1	0.1	N94	
$Mg_{1.72}Fe_{0.21}SiO_4$[s] (San Carlos Olivine)[2]	3.30	F01, Z11	6.53	34.1	0.1	N94	(a), (c), (d)
$Mg_{1.56}Fe_{0.40}Si_{0.91}O_4$[s] (Sri Lanka Olivine)[2]	3.30	Z11	6.53	34.1	0.1	N94	(a), (c),(d)
$Mg_{[1.0,0.8]}Fe_{[1.0,1.2]}SiO_4$[s] (Olivine)[1]	3.71, 3.80	J94, D95	6.53	34.1	0.1	N94	(a), (d)
Fe_2SiO_4[s] (Fayalite)[2]	4.39	F01	6.04	37.7	0.1	N94	(a)

Notes. [1]Amorphous. [2]Crystalline. (a) Following van Lieshout, Min & Dominik (2014), $\alpha = 0.1$ is adopted for materials with no evaporation coefficient measurement. (b) Following Kimura et al. (2002), the sublimation parameters of enstatite are adopted for all other types of pyroxene. (c) The density chosen for this olivine is the average density of low-Fe olivine. (d) Following Kimura et al. (2002), the sublimation parameters of forsterite are adopted for all other types of olivine.

References. K95, Koike et al. (1995); S04, Schaefer & Fegley (2004); L08, Lihrmann (2008); J94, Jaeger et al. (1994); D95, Dorschner et al. (1995); J98, Jaeger et al. (1998); M88, Mysen & Kushiro (1988); F01, Fabian et al. (2001); N94, Nagahara, Kushiro & Mysen (1994); Z11, Zeidler et al. (2011).

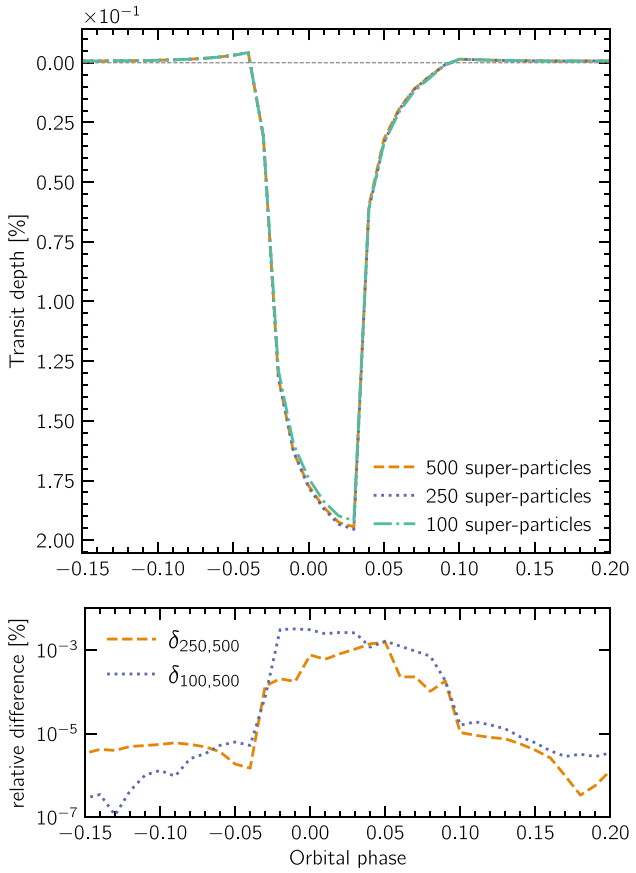

Figure 2. Top: Simulated transit of KIC 1255 b for different numbers of super-particles launched every 100$^{\text{th}}$ of an orbit. The dust is assumed to be composed of olivine ($Mg_{0.8}Fe_{1.2}SiO_4$[s]). The dust cloud is assumed to be optically thin throughout ($\tau = 0.1$) and the outflow is assumed to be radially outwards from the entire planetary surface (spherical outflow). Bottom: The relative percentage difference between the transits simulated on the top plot. The difference is smaller than the observed error ($\approx$ 200 ppm; Rappaport et al. 2012), therefore, we launch 250 superparticles every 100$^{\text{th}}$ of an orbit.

we sum all the individual τ_{sp}'s corresponding to that cell. The flux from that cell is then attenuated by a factor of $e^{-\tau}$. Finally, the total stellar flux is obtained by adding all the individual fluxes from each grid cell.

Forward scattering of light by dust grains can increase the observed stellar flux. The increase in flux is proportional to the scattering opacity of the dust grain, $\kappa_{\text{sca}}(T_\star, s)$ (Section 2.4), and the scattering phase function at the scattering angle. We use the Henyey–Greenstein analytical scattering phase function for dust grain mixtures (Henyey & Greenstein 1941), which is solely dependent on g_{sca} and the scattering angle, and use the single scattering approximation (van Lieshout et al. 2016). We ignored limb-darkening effects for both the extinction and forward scattering computations. The extinction and forward scattering components are combined into synthetic transit profiles.

3 KIC 1255 B: DUST COMPOSITION, GRAIN SIZES AND MASS-LOSS RATE CONSTRAINTS

One of our key goals is to determine the dust composition and size. The size of the dust grains has been constrained through measurements of the transit depth dependence on wavelength, i.e. colour dependence. Croll et al. (2014) and Schlawin et al. (2016) observed the transit depths of KIC 1255 b not to be colour dependent and set a lower limit of the dust grain size of ~0.2-0.5 μm. Previous modelling efforts (e.g. Brogi et al. 2012; Budaj 2013) predict the dust grain sizes to be 0.1 - 1.0 μm based on the shape of the forward-scattering bump. However, these models did not consider the sublimation rate of the dust grains and simply assumed an exponential decay of the size distribution. Furthermore, van Lieshout et al. (2016) curiously found corundum (Al_2O_3 [s]) to be the best fit with the observations for KIC 1255 b, using a model that didn't include the dust tail's optical depth self-consistently on the dust dynamics.

Therefore, using our new, self-consistent approach, we constrain the tail's dust composition, grain sizes and planetary mass-loss rate. We run a grid of models and compare the synthetic light curves with observations. The dust's optical properties, which are highly dependent on the dust grain sizes and compositions, control the morphology of the white light curve, specifically the pre-transit brightening and the long egress. On the other hand, the planetary mass-loss rate mainly influences the transit depth (see Section 3.3).

Downloaded from https://academic.oup.com/mnras/article/528/2/1249/7515287 by guest on 01 February 2024

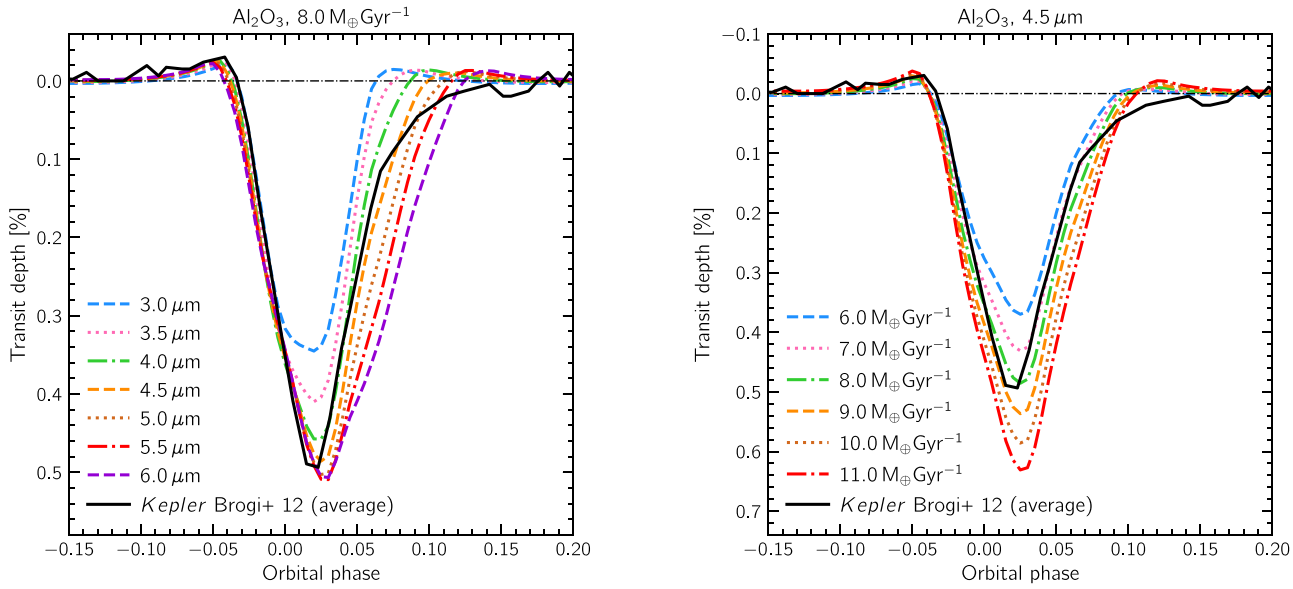

Figure 3. Synthetic light curves of KIC 1255 b for dust composed of corundum (Al_2O_3[s]). The observed *Kepler* light curve averaged over six quarters by Brogi et al. (2012) is shown as the black solid curve. Left: Synthetic light curves for models at a constant planetary mass-loss rate of 8.0 $M_\oplus Gyr^{-1}$ and different initial dust grain sizes. Right: Synthetic light curves for models at a constant initial dust grain size of 4.5 μm and different planetary mass-loss rates.

We define the best-fit models to be the ones where the pre-transit brightening and the long egress shapes are best represented with a transit depth comparable to that of the average observed light curves. Therefore, the reported mass-loss rate is an attempt to estimate the *average* dusty mass-loss rates (see Section 3.3).

Since the planet itself is not detected, we do not know exactly when, in its orbit, the planet is at mid-transit in the observations. Thus, one needs to align the models with the observations by defining when an orbital phase of 0 occurs. We do this by aligning our synthetic light curves with the observations by the pre-transit brightening (if necessary). Additionally, we also align our out-of-eclipse flux to that of the observations.

In our simulations, we compute the transit depth every 5 min. To obtain the synthetic light curves to compare to the observations, we smooth the data over the *Kepler* long cadence (30 min).

We first apply our model to KIC 1255 b. KIC 1255 b orbits a K-type star with $T_\star \approx 4550\,K$, $R_\star \approx 0.66\,R_\odot$, and $M_\star \approx 0.67\,M_\odot$ (Thompson et al. 2018). We run the model for the dust compositions listed in Table 1. We study the parameter space of initial dust grain sizes ranging from 0.5 to 8.0 μm, and (dusty) planetary mass-loss rates from 1.0 to 15.0 $M_\oplus Gyr^{-1}$. The models we discuss throughout Section 3 assume the outflow is spherical. We also explored models with a day-side outflow geometry, but we found the spherical outflow to consistently be a better fit for KIC 1255 b (Appendix A). This is because the day-side outflow models produce a more symmetric transit, which is less consistent with KIC 1255 b's light curve. We discuss the issue of outflow geometry further in Section 4.

3.1 Corundum

We find corundum dust grains with initial sizes below 2.0 μm sublimate too fast to produce the observed light curve of KIC 1255 b. This is expected as small corundum grains achieve very high temperatures (fig. 4 in Booth, Owen & Schulik 2023), due to their low IR opacity. We find corundum could give origin to the observed light curve of KIC 1255 b with initial dust grain sizes of ∼3.5–5.5 μm and an average mass-loss rate of 8.0 $M_\oplus Gyr^{-1}$ (Fig. 3). This result arises because as the particles get larger, the ratio between their optical and IR opacity falls resulting in lower temperatures and longer lifetimes; however, larger particles have a lower opacity and we must increase the mass-loss rate to match the observed transit depth.

The initial dust grain sizes we estimate for dust composed of corundum are above the lower limit estimated from colour dependence measurements. The average dust mass-loss rate we estimate is within the findings of van Lieshout et al. (2016) but considerably higher than the theoretical models of Perez-Becker & Chiang (2013) and Booth, Owen & Schulik (2023). The estimate of the dust mass-loss rate in other studies (e.g. Kawahara et al. 2013) is generally obtained solely from the transit depth, ignoring any forward scattering effects. Forward scattering reduces the transit depth and therefore, higher mass-loss rates are needed to fit the observations (Appendix B).

As discussed by van Lieshout et al. (2016), aluminium has a low cosmic abundance and is likely a minor component of rocky planets (e.g. Schaefer & Fegley 2009; Jura & Young 2014). In addition to this, corundum is measured to have a relatively low abundance in the bulk silicate earth (BSE) composition (see table 1.7 in O'Neill & Palme 1998). Therefore, the existence of a corundum dust tail combined with such high mass-loss rates would be surprising. While corundum can fit the data, we consider it an unlikely candidate for the composition of the dust in the tail.

3.2 Olivine and pyroxene

We have studied compounds we know are pre-dominant in the Earth's mantle (e.g. O'Neill & Palme 1998): olivine, $(Mg, Fe)_2SiO_4$[s], and pyroxene, $(Mg, Fe)SiO_3$[s].

First, we consider the end-members of these two types of minerals. The iron end-member of olivine (fayalite), Fe_2SiO_4 [s], is too volatile in the entire parameter space studied, i.e. it sublimates too fast to explain an observable dusty tail. On the other hand, the magnesium end-members of olivine (forsterite), Mg_2SiO_4[s], and pyroxene (enstatite), $MgSiO_3$[s], have low optical to IR opacity ratio and do not achieve high enough temperatures to sublimate. The dust survives for multiple orbits, accumulating over time, and the transit profile never

Downloaded from https://academic.oup.com/mnras/article/528/2/1249/7515287 by guest on 01 February 2024

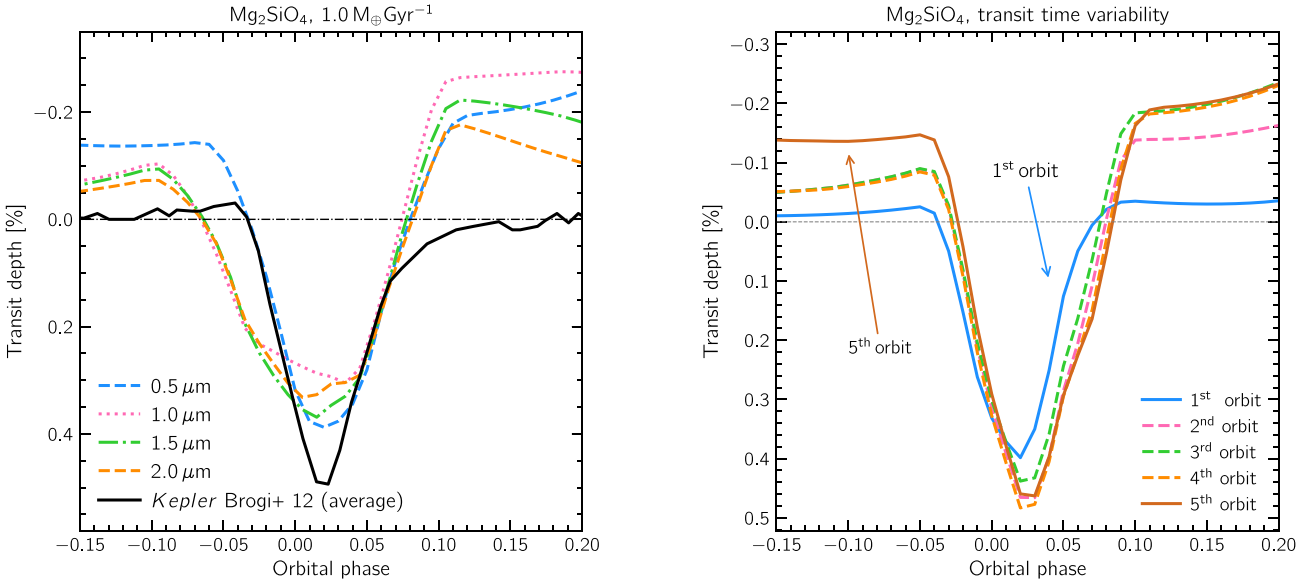

Figure 4. Synthetic light curves of KIC 1255 b for dust composed of forsterite (Mg_2SiO_4[s]). Left: Synthetic light curves for models at a constant planetary mass-loss rate of 1.0 $M_\oplus Gyr^{-1}$ and different initial dust grain sizes after five orbits. The observed *Kepler* light curve averaged over six quarters by Brogi et al. (2012) is shown as the black solid curve. Right: Synthetic light curves over five orbits at an initial dust grain size of 0.5 μm and a planetary mass-loss rate of 1.0 $M_\oplus Gyr^{-1}$. Note how the light curve does not converge, particularly for the pre-transit brightening region.

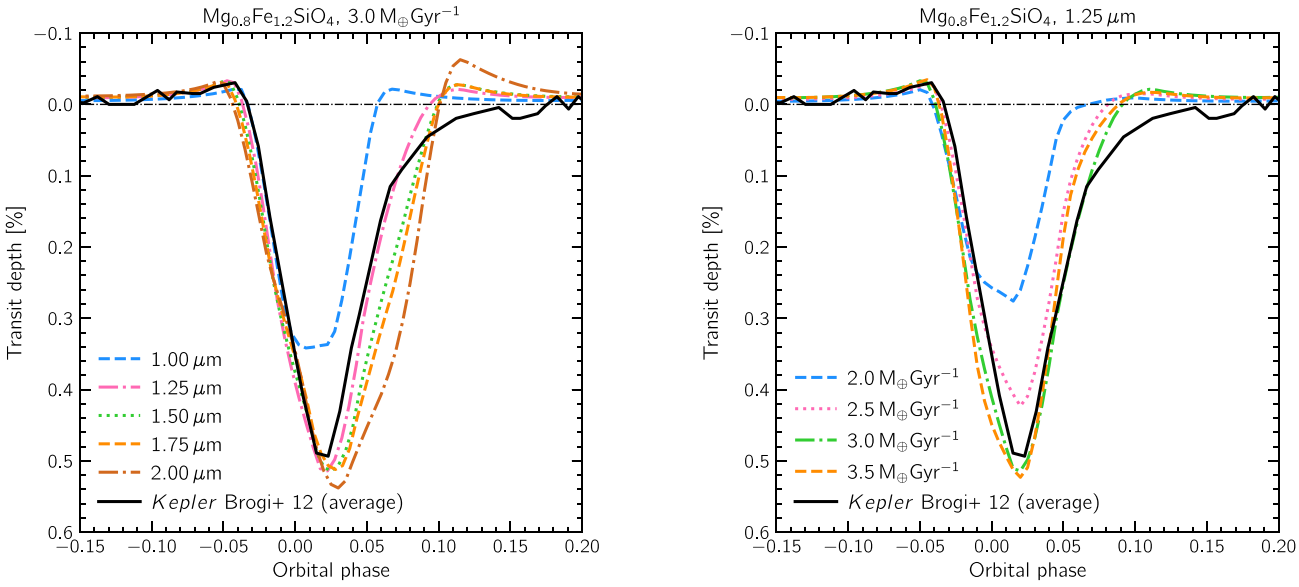

Figure 5. Synthetic light curves of KIC 1255 b for dust composed of iron-rich olivine ($Mg_{0.8}Fe_{1.2}SiO_4$[s]). The observed *Kepler* light curve averaged over six quarters by Brogi et al. (2012) is shown as the black solid curve. Left: Synthetic light curves for models at a constant planetary mass-loss rate of 3.0 $M_\oplus Gyr^{-1}$ and different initial dust grain sizes. Right: Synthetic light curves for models at a constant initial dust grain size of 1.25 μm and different planetary mass-loss rates.

converges (see the right panel of Fig. 4). Additionally, the synthetic light curves produced show no agreement with the observations at any time-point (see the left panel of Fig. 4). The pre-transit brightening occurs earlier than expected for most of the parameter space. Furthermore, there is a significant post-transit brightening, which does not match the observations. Therefore, we rule out dust grains predominately composed of fayalite, forsterite, or enstatite.

We test other types of pyroxene (see Table 1). For $Mg_{0.95}Fe_{0.05}SiO_3$[s], the scenario is similar to that of forsterite and enstatite, i.e. the dust is too cold due to its low optical to IR opacity ratio. $Mg_{0.7}Fe_{0.3}SiO_3$[s] and $Mg_{0.5}Fe_{0.5}SiO_3$[s] behave similarly to fayalite—these compounds are too volatile and do not survive long enough to create the dusty-tail observed. Given the contrasting behaviours of the different types of pyroxene tested here, we believe low–iron pyroxene with an iron content between 0.05 and 0.3 should be explored in future work.

The dust compositions tested which best fit with the observations of KIC 1255 b are magnesium–iron olivines, i.e. compounds of the form $(Mg, Fe)_2SiO_4$[s] with an iron content of at least 10 per cent. Fig. 5 shows that for $Mg_{0.8}Fe_{1.2}SiO_4$[s], the pre-transit brightening

Downloaded from https://academic.oup.com/mnras/article/528/2/1249/7515287 by guest on 01 February 2024

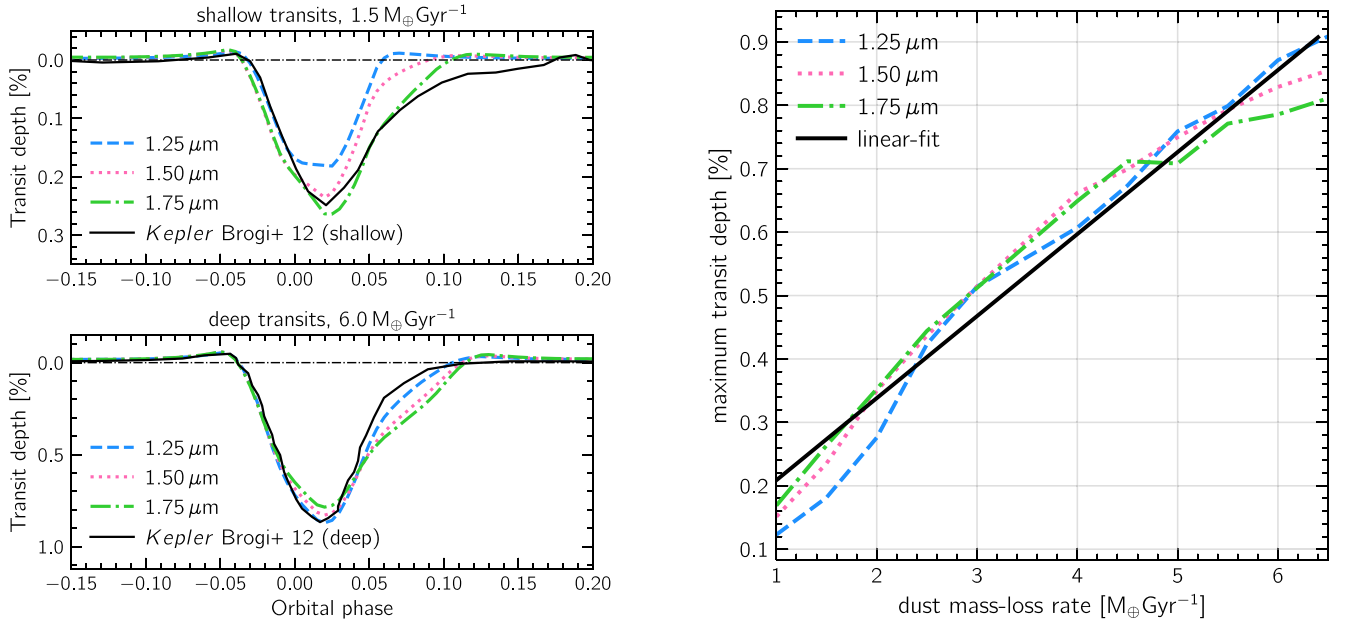

Figure 6. Left: Synthetic light curves for models at a constant planetary mass-loss rate of 1.5 $M_{\oplus}$Gyr^{-1} (top) and 6.0 $M_{\oplus}$Gyr^{-1} (bottom) at different initial dust grain sizes. The observed *Kepler* light curve averaged over six quarters by Brogi et al. (2012) is shown as the black solid curve. Shallow transits correspond to observed light curves with transit depths between 0.2 and 0.5 per cent, deep transits correspond to observed light curves with transit depths larger than 0.8 per cent (see Brogi et al. 2012). Right: The maximum transit depth for the synthetic light curves of $Mg_{0.8}Fe_{1.2}SiO_4$ versus the dust mass-loss rate, at different initial dust grain sizes. The black solid curve represents a linear fit to the data.

and the long-egress match the observation for dust grain sizes between 1.25 and 1.75 μm and an average planetary mass-loss rate of 3.0 $M_{\oplus}$Gyr^{-1}. Similar results are obtained for Sri Lanka olivine, San Carlos olivine and $MgFeSiO_4$[s].

These results are in agreement with the BSE abundances (e.g Kargel & Lewis 1993) and white dwarf measurements for evaporating exoplanets (e.g Bonsor et al. 2020). Curry et al. (2023) show that the observed dust is coming from a localized region where the planet has been evaporated down to. This supports the idea that the dust originates from the mantle of the planet, where magnesium–iron silicates like olivine and pyroxene are expected to be abundant. In addition to this, Bromley & Chiang (2023) argued iron-rich silicates are required to be able to produce an observable mass loss rate for catastrophically evaporating exoplanets.

3.3 Estimating the average mass-loss rate

Since the transits are variable, and the precision on an individual transit is poor, we must compare our model to phase-folded, average light curves. Therefore, we must evaluate whether the mass-loss rate reported by our model, when compared to averaged light curves, is representative of the average mass-loss rate. We did this by computing the relationship between the mass-loss rates and the transit depth in our models. As shown in the right panel in Fig. 6, we find the transit depth has an approximately linear relation with the dust mass-loss rate. A linear relationship implies that average light curves can be used to estimate average mass-loss rates. Additionally, we compared our synthetic light curves for $Mg_{0.8}Fe_{1.2}SiO_4$ to two sets of observed light curves of KIC 1255 b as divided by Brogi et al. (2012): a set where the transit depths are shallow (0.2 per cent,- 0.5 per cent) and a set where the transit depths are deep (> 0.8 per cent). We find the best-fit for the shallow and deep transits require smaller and larger mass-loss rates, respectively, but the same range of dust grain sizes as for the average mass-loss rate case (left panel, Fig. 6). Therefore, our reported best-fit mass-loss rates to the average light curves are a reasonable approximation to the average mass-loss rate.

3.4 Synthetic JWST spectra: corundum versus magnesium–iron silicates

While we have argued corundum is an unlikely composition, we suggest that this can be directly confirmed with additional observations. Corundum and magnesium–iron silicates have distinct absorption features in the near-infrared and mid-infrared regions. In particular, silicates show a very broad absorption feature at about 10 μm. Observing the dusty tails in these wavelengths can help us understand what the dust is composed of and validate our models. We produce synthetic JWST absorption spectra of KIC 1255 b for the $Mg_{0.8}Fe_{1.2}SiO_4$[s] best-fit model with an initial dust grain size of 1.25 μm and an average mass-loss rate of 3.0 $M_{\oplus}$Gyr^{-1} (pink dot-dashed curve in Fig. 5 left), and the corundum best-fit model with an initial dust grain size of 4.5 μm and an average mass-loss rate of 8.0 $M_{\oplus}$Gyr^{-1} (green dot-dashed curve in Fig. 3 left). We use the wavelength range and resolution of the MIRI-MRS mode and the NIRSpec-PRISM mode. The spectra are shown in Fig. 7. The synthetic spectra show that we would be able to distinguish if the dust is composed of corundum or magnesium–iron silicates with JWST observations if a bright target is identified.[6] This inference is in line with the results of Bodman et al. (2018) and Okuya et al. (2020), who also found JWST observations could help constrain the dust composition.

[6]It is likely KIC 1255 b is too faint to perform this experiment with a small number of transits; however, K2-22 b may be bright enough.

Downloaded from https://academic.oup.com/mnras/article/528/2/1249/7515287 by guest on 01 February 2024

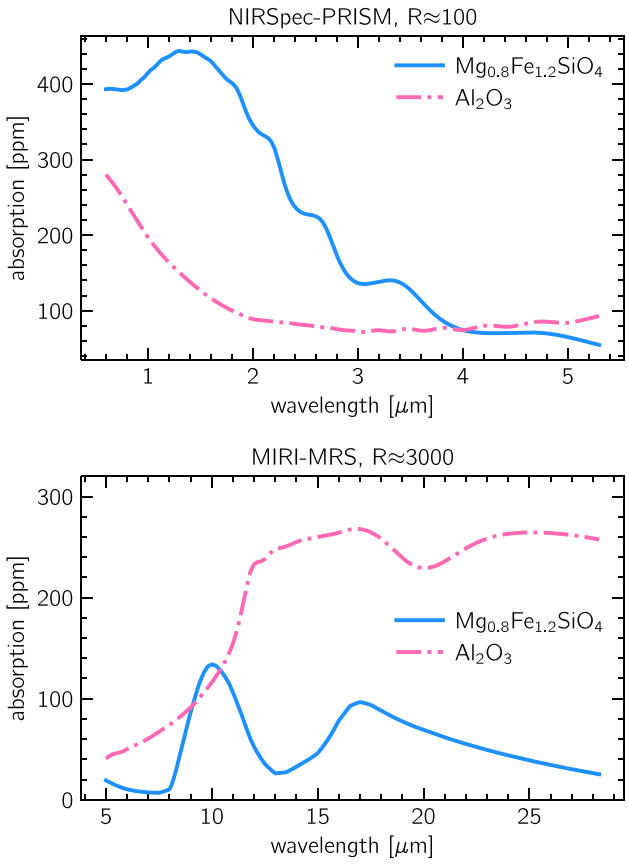

Figure 7. Top: NIRSpec-PRISM synthetic absorption spectra of KIC 1255 b for the best-fitting model of corundum (4.5 μm and 8.0 $M_{\oplus}\mathrm{Gyr}^{-1}$ – green dot-dashed curve in Fig. 3 left) and iron-rich olivine (1.25 μm and 3.0 $M_{\oplus}\mathrm{Gyr}^{-1}$ – pink dot-dashed curve in Fig. 5 left). The resolution used was 100. Bottom: Same as the top panel but for the MIRI-MRS mode. The resolution used was 3000. Note the distinct absorption feature of the olivine at about 10 μm.

4 THE LEADING DUST TAIL OF K2-22B AND THE OUTFLOW GEOMETRY

In addition to modelling KIC 1255 b, we also model K2-22 b. As mentioned earlier, K2-22 b shows a light curve with increases in the observed flux both before and after the transit (Sanchis-Ojeda et al. 2015). This agrees with a scenario where there is a tail of dust also leading the planet. K2-22 b orbits an M-type star with $T_{\star} \approx 3830\,K$, $R_{\star} \approx 0.58\,R_{\odot}$ and $M_{\star} \approx 0.60\,\mathrm{M}_{\odot}$, with an orbital period of approximately 9.2h (Sanchis-Ojeda et al. 2015).

Sanchis-Ojeda et al. (2015) state a 'substantial' ($\beta \gtrsim 0.05$) radiation pressure force necessarily blows the dust into orbits trailing the planet. However, they find if β is sufficiently small ($\lesssim 0.02$) some dust can fall into faster orbits than that of the planet, creating a tail of dust leading the planet.

The best-fit models we find for the K2-22 b average light curve (Sanchis-Ojeda et al. 2015), assuming the dust is composed of $Mg_{0.8}Fe_{1.2}SiO_4$[s], are for initial dust grain sizes $\sim$1.0 - 1.5μm and a mass-loss rate $\sim$2.5–3.0 $M_{\oplus}\mathrm{Gyr}^{-1}$. These results compare favourably to Schlawin et al. (2021), who observationally constrained the dust grain sizes of K2-22 b to be larger than 0.5–1.0 μm. Based on this measurement, they constrained the average mass-loss rate of K2-22 b to be $\sim 1.6\,M_{\oplus}\mathrm{Gyr}^{-1}$.

Here, we investigate if the origin of the leading tail is a consequence of the launch geometry of the dusty outflow. We test two outflow geometries: a spherical outflow, where the super-particles leave from the Hill sphere radially outwards over the full 4π, and a day-side outflow, where the super-particles leave the Hill sphere only from the day-side of the planet, radially outwards. As discussed in our methods, we always launch our super-particles from just outside the planet's Hill sphere. Physically, the outflow is always launched from the day-side surface of the planet; however, multidimensional simulations of photoevaporating planets with H/He-rich atmospheres (e.g. Stone & Proga 2009; Owen & Adams 2014; Tripathi et al. 2015) indicate the outflow can wrap around to the nightside, yielding a quasi-spherical outflow through the Hill sphere. Thus, we speculate a high-mass planet could have an outflow similar to those seen in these photoevaporation simulations, while a low-mass planet might have an outflow geometry that is day-side dominated at the Hill sphere (Fig. 8, right).

We find the spherical outflow is a better fit for the pre-transit brightening of K2-22 b. However, we find the day-side outflow to be a better fit for the egress and post-transit brightening (Fig. 8, left). We find a post-transit brightening and a symmetric light curve (i.e. a leading tail of dust) can exist for both geometries in certain ranges of the parameter space, even though they don't fit the light curve perfectly. Thus, even in the spherical outflow scenario, this implies that changing the stellar parameters and the planet's orbital period is enough to give rise to a leading tail of dust. This result is a consequence of the strength of the radiation pressure force. The radiation pressure is weaker for K2-22 compared to KIC 1255 because K2-22 is cooler than KIC 1255 by about 700K. Therefore, dust grains can occupy orbits closer to the star. While we cannot produce a model light curve that matches all the features of K2-22b, we speculate that K2-22 b's outflow geometry probably lies somewhere between a spherical and a day-side outflow. Coupling this launching geometry with a lower radiation pressure force to stellar gravitational force ratio than KIC 1255 b, would likely yield K2-22 b's light curve.

We find a day-side outflow at the level of the Hill sphere is not a good fit with the observations of KIC 1255 b (Appendix A). Thus, the fact that KIC 1255 b is consistent with a spherical outflow and K2-22b with an outflow geometry that sits between our spherical and day-side models might imply KIC 1255 b is more massive than K2-22b. In this scenario KIC 1255 b is massive enough for a significant fraction of the escaping dust grains to wrap around the planet as they escape, as seen in hydrodynamic simulations (e.g. Stone & Proga 2009; Owen & Adams 2014; Tripathi et al. 2015), while for K2-22 b they are effectively unbound when they leave the planet's surface.

5 OPTICAL DEPTH AND TRANSIT DEPTH TIME VARIABILITY

As speculated by Rappaport et al. (2012), Perez-Becker & Chiang (2013) and van Lieshout et al. (2016), we find the dust cloud to be optically thick in the vicinity of the planet (see Fig. 9). This affects the transit light curve of the planet and its tail in our models significantly, as shown in Fig. 10. The transit depth for the models where the optical depth is traced is consistently larger than the transit depth in the models in which we assume a fixed low value for the optical depth. This is because the dust is cooler in the optically thicker environment, and the grains do not sublimate as fast. Although the optical depth also affects the radiation pressure force (i.e. β parameter, see equation (2)), its effect on the sublimation is stronger as the sublimation rate is exponentially dependent on the dust temperature (although radiation

Downloaded from https://academic.oup.com/mnras/article/528/2/1249/7515287 by guest on 01 February 2024

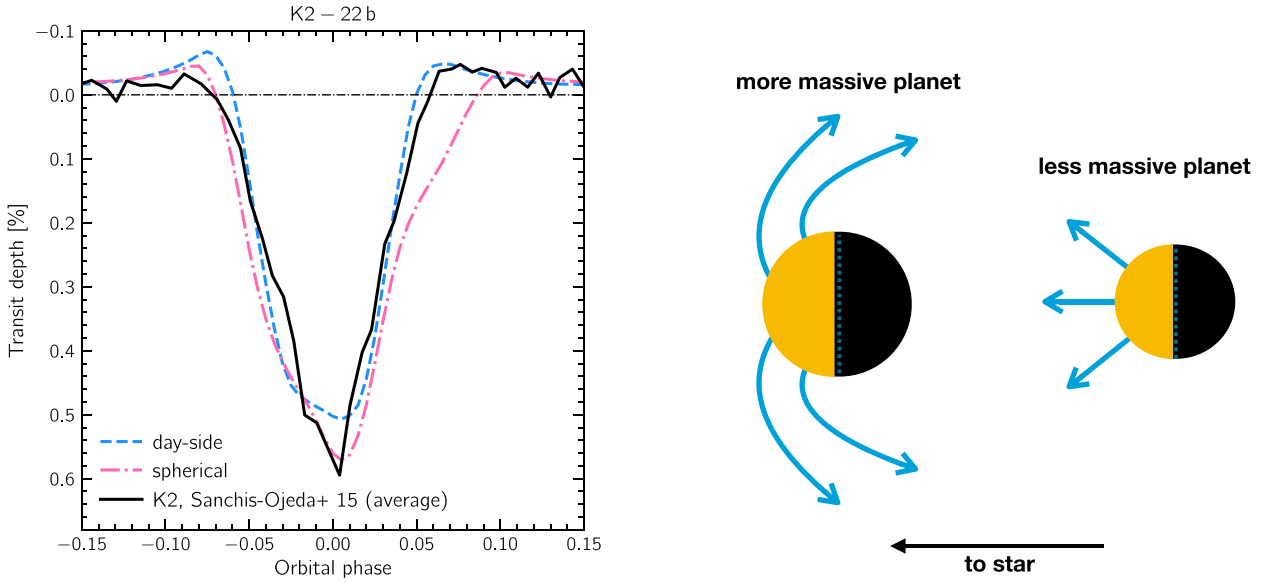

Figure 8. Left: Synthetic light curves of K2-22 b for dust composed of iron-rich olivine ($Mg_{0.8}Fe_{1.2}SiO_4$[s]). The blue dashed curve is for a day-side outflow with an initial dust grain size of 1.5 μm and a mass-loss rate of 3.0 $M_\oplus Gyr^{-1}$. The pink dot-dashed curve is for a spherical outflow with an initial dust grain size of 1.0 μm and a mass-loss rate of 2.5 $M_\oplus Gyr^{-1}$. The observed *K2* light curve is the black solid curve (Sanchis-Ojeda et al. 2015). Right: Cartoon of the dust outflow trajectory. The yellow represents the planet's day-side. The dust forms on the planet's day-side. If the planet is massive enough, the dust will follow a trajectory similar to that shown on the planet on the left – this is what the spherical outflow in our model depicts. If the planet is not massive enough, the dust will follow a trajectory similar to that shown on the planet on the right – this is what the day-side outflow in our model assumes.

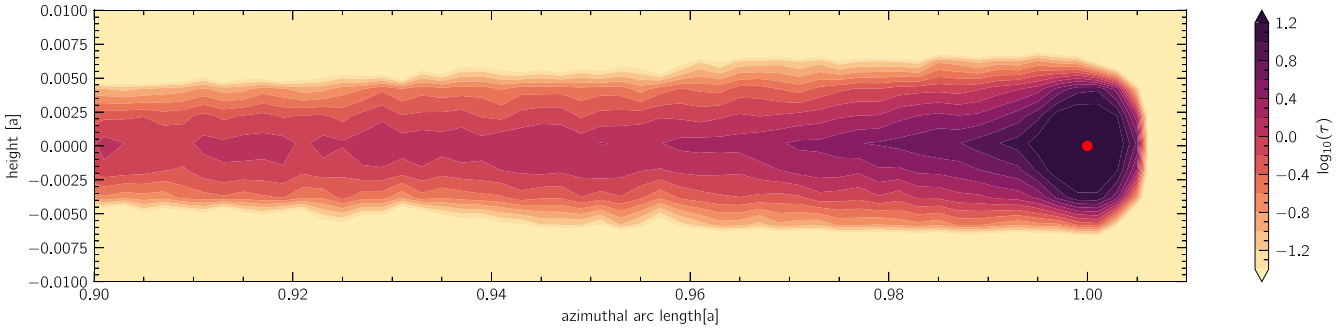

Figure 9. Optical depth density map at the radial edge of the optical depth grid ($R = 1.10\,a$) for the best-fitting $Mg_{0.8}Fe_{1.2}SiO_4$[s] model (1.25 μm, 3.0 $M_\oplus Gyr^{-1}$, dot-dashed pink curve in the left panel of Fig. 5). The red circle indicates the position of the planet. Note how the optical depth is moderate in the vicinity of the planet, implying attenuation of stellar light is important for controlling the dust's dynamics.

pressure is also exponentially sensitive to optical depth, our models only reach moderate optical depths).

Although we have included the optical depth evolution of the dusty tail, we do not find a transit depth time variability in our simulations. One of the limitations of our model is the fact that the planetary mass-loss rate is a free parameter and, therefore, independent of the optical depth of the dust cloud. In reality, the planetary mass-loss rate of the planet is dependent on the optical depth of the dust cloud. The rock vapour pressure is exponentially dependent on the surface temperature of the planet. So, a fractional change in the dust cloud's optical depth could cause large differences in the planetary mass-loss rate (e.g. Perez-Becker & Chiang 2013). Furthermore, we have disregarded the dynamical impact of the stellar wind on the dust grains as for micron-sized particles, the stellar wind pressure is generally negligible compared to the radiation pressure (e.g. Strubbe & Chiang 2006). However, the stellar wind may become relevant for extremely large stellar wind rates. These rates can happen during, for example, coronal mass ejections, which can be a source of the observed variability (cf. Kawahara et al. 2013; Croll, Rappaport & Levine 2015; Schlawin et al. 2018).

The observations of KIC 1255 b show that its transit depth variability presents no pattern (e.g Lieshout & Rappaport 2018). Both Perez-Becker & Chiang (2013) and Booth, Owen & Schulik (2023) have argued the variability might be driven by a cycle involving stellar insolation and mass loss. In addition to this, Booth, Owen & Schulik (2023) found that non-steady outflows can arise for fast dust growth rates and moderate optical depths. However, a chaotic behaviour, like the one the observations show, was not reproduced. Recently, Bromley & Chiang (2023) found a chaotic behaviour for the transit depth when they consider the planetary surface temperature to increase with increasing optical depth when the atmosphere is optically thin, and when it decreases with increasing optical depth when the atmosphere is optically thick. Such behaviour is only possible if, when the atmosphere is optically thin, the dust has

Downloaded from https://academic.oup.com/mnras/article/528/2/1249/7515287 by guest on 01 February 2024

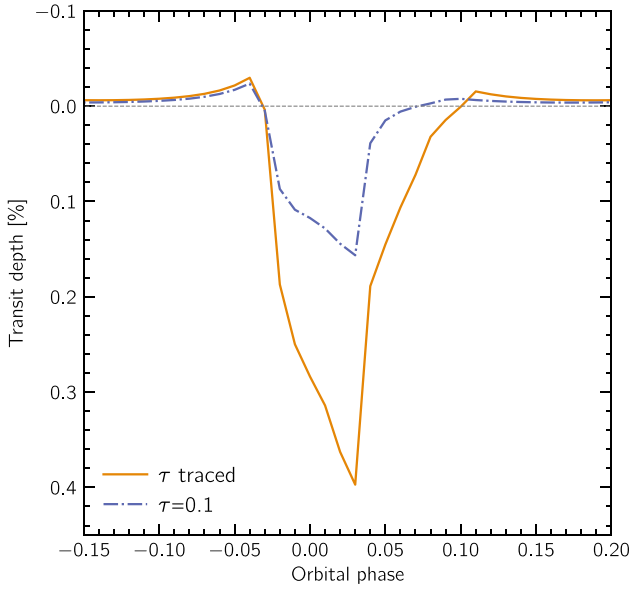

Figure 10. Comparison of two synthetic light curves for a model where the optical depth of the dust cloud is kept thin at 0.1 (dash-dotted curve) and a model where the optical depth is traced (solid curve).

lower opacities in the visible wavelengths than in the infrared. This is because, in order to condense, the dust grains need to radiate away their energy more efficiently than they absorb visible light. In addition to this, for the planetary surface temperature to increase with increasing optical depth in an optically thin atmosphere, the dust needs to induce a greenhouse effect, which will raise the planetary surface temperature via infrared back-warming. Iron-poor silicate-rich dust presents the ideal visible-to-infrared opacity ratio to give rise to the conditions described above. When enough dust grains have condensed, and the atmosphere has therefore become optically thick to starlight, more iron can condense onto the grains. The dust will begin to absorb more efficiently in the visible than in the infrared, and the planetary surface temperature will decrease, inducing what Bromley & Chiang (2023) denominate a nuclear winter. Bromley & Chiang (2023) state this cycle between the greenhouse effect and the nuclear winter is the most likely cause of the transit depth time variability.

Booth, Owen & Schulik (2023) discuss heterogeneous condensation might give rise to the transit depth time variability. They argue stable iron-free or iron-poor silicates will condensate first in the wind (e.g. Mg_2SiO_4[s]) at low temperatures. This will allow iron to condense into these grains, causing the dust temperature to rise. However, iron evaporates more promptly than magnesium from silicates (e.g. Costa, Jacobson & Fegley 2017) which will increase the dust temperature, causing the iron content to decrease. This means the dust grains might reach a composition that is controlled by the feedback between the iron content and the temperature of the dust.

We find the dust is likely composed of magnesium–iron silicates (iron-poor or iron-rich) (Section 3). This is in agreement with both the greenhouse effect-nuclear winter cycle (Bromley & Chiang 2023) and heterogeneous condensation (Booth, Owen & Schulik 2023). A complete model which couples the dust formation to the outflow dynamics and tail morphology is needed to accurately study which processes are giving rise to the transit depth time variability. In addition to this, compositionally heterogeneous dust grains should be considered.

6 SUMMARY

Catastrophically evaporating rocky planets provide a unique opportunity to study the composition of rocky worlds. We have developed a self-consistent model of the dusty tails of catastrophically evaporating rocky planets. For the first time, we have introduced the optical depth evolution of the dust cloud in a model of this kind. We apply the model to two catastrophically evaporating exoplanets: KIC 1255 B and K2-22 b.

For both planets, we find the dust is likely composed of magnesium–iron silicates. The synthetic light curves of KIC 1255 b match the observed light curve for average (dusty) planetary mass-loss rates of $\sim 3\ M_{\oplus}\mathrm{Gyr}^{-1}$ and initial dust grain sizes between ~ 1.25 and $\sim 1.75\ \mu$m. Although corundum also produces models that fit the *Kepler* observations, this is for very large initial dust grain sizes ($\sim 4\ \mu$m) and large planetary mass-loss rates ($\sim 8\ M_{\oplus}\mathrm{Gyr}^{-1}$). The existence of a corundum dust tail combined with such high mass-loss rates would be surprising as aluminimum is likely a minor component of rocky planets (e.g. Schaefer & Fegley 2009). JWST observations in the wavelength range of 1–28 μm could explicitly rule out corundum as the composition of the dust.

We show K2-22 b probably has a different outflow geometry than KIC 1255 b. Thus, K2-22b is likely less massive than KIC 1255 b and presents a leading tail of dust. We find the leading tail of dust is likely a consequence of the outflow geometry and low radiation pressure force to stellar gravity force ratios (β).

We find the dust cloud is marginally optically thick to stellar light in the vicinity of the planet, as first speculated by Rappaport et al. (2012). This has a significant impact on the light curve, and therefore, future models of dusty tails should account for the optical depth of the tail, as was done in this work. Furthermore, Bromley & Chiang (2023) recently showed the observed transit depth time variability could have an origin in a greenhouse effect–nuclear winter cycle. Magnesium–iron silicates have the ideal visible-to-infrared opacity ratio to give rise to this cycle in the high mass-loss regime. In order to fully validate this hypothesis, we need to combine the model here developed with a model of the outflow dynamics and dust formation (e.g. Booth, Owen & Schulik 2023).

ACKNOWLEDGEMENTS

We thank the anonymous reviewer for their comments, which improved the manuscript. We are grateful to Richard Booth, Subhanjoy Mohanty, Alfred Curry, Francisco Ardévol Martínez, David A. Lewis, and Courtney J. Rundhaug for interesting discussions. We thank Eugene Chiang and Joshua Bromley for helpful comments on an earlier version of the manuscript. BCE is part of the CHAMELEON MC ITN EJD which received funding from the European Union's Horizon 2020 - Research and Innovation Framework Programme under the Marie Sklodowska-Curie grant agreement no. 860470. BCE was supported by a Royal Society 2020 Enhancement Award. JEO is supported by a Royal Society University Research Fellowship. MRJ acknowledges support from the European Union's Horizon Europe Programme under the Marie Sklodowska-Curie grant agreement no. 101064124, and funding provided by the Institute of Physics Belgrade, through the grant by the Ministry of Science, Technological Development, and Innovations of the Republic of Serbia. This project has received funding from the European Research Council (ERC) under the European Union's Horizon 2020 - Research and Innovation Framework Programme (grant agreement no. 853022, PEVAP). Storage and computing resources at the University of Copenhagen HPC centre, funded in

Downloaded from https://academic.oup.com/mnras/article/528/2/1249/7515287 by guest on 01 February 2024

part by Villum Fonden (VKR023406), were used to carry out part of the data analysis. For the purpose of open access, the authors have applied a Creative Commons Attribution (CC-BY) licence to any Author Accepted Manuscript version arising.

DATA AVAILABILITY

The synthetic light curves data presented in the paper are available at the Electronic Research Data Archive (ERDA) of the University of Copenhagen at https://erda.ku.dk/archives/0bc047ed0bc096717e073d2d462f3913/published-archive.html.

REFERENCES

Birdsall C. K., Fuss D., 1969, J. Comput. Phys., 3, 494
Bochinski J. J., Haswell C. A., Marsh T. R., Dhillon V. S., Littlefair S. P., 2015, ApJ, 800, L21
Bodman E. H. L., Wright J. T., Desch S. J., Lisse C. M., 2018, AJ, 156, 173
Bohren C. F., Huffman D. R., 1983, Absorption and scattering of light by small particles, Research supported by the University of Arizona and Institute of Occupational and Environmental Health. Wiley-Interscience, New York, p. 541
Bonsor A., Carter P. J., Hollands M., Gänsicke B. T., Leinhardt Z., Harrison J. H. D., 2020, MNRAS, 492, 2683
Booth R. A., Owen J. E., Schulik M., 2023, MNRAS, 518, 1761
Brent R. P., 1973, SIAM J. Numer. Anal., 10, 327
Brogi M., Keller C. U., de Juan Ovelar M., Kenworthy M. A., de Kok R. J., Min M., Snellen I. A. G., 2012, A&A, 545, L5
Bromley J., Chiang E., 2023, MNRAS, 521, 5746
Brouwers M. G., Bonsor A., Malamud U., 2023, MNRAS, 519, 2646
Bruggeman D. A. G., 1935, Ann. Phys., 416, 636
Buchan A. M., Bonsor A., Shorttle O., Wade J., Harrison J., Noack L., Koester D., 2022, MNRAS, 510, 3512
Budaj J., 2013, A&A, 557, A72
Burns J. A., Lamy P. L., Soter S., 1979, Icarus, 40, 1
Costa G. C. C., Jacobson N. S., Fegley Bruce J., 2017, Icarus, 289, 42
Croll B. et al., 2014, ApJ, 786, 100
Croll B., Rappaport S., Levine A. M., 2015, MNRAS, 449, 1408
Crossfield I. J. M. et al., 2022, ApJ, 937, L17
Curry A., Booth R., Owen J. E., Mohanty S., 2023, preprint (arXiv:2303.15200)
Dormand J., Prince P., 1980, J. Comput. Appl. Math., 6, 19
Dorn C., Venturini J., Khan A., Heng K., Alibert Y., Helled R., Rivoldini A., Benz W., 2017a, A&A, 597, A37
Dorn C., Hinkel N. R., Venturini J., 2017b, A&A, 597, A38
Dorn C., Harrison J. H. D., Bonsor A., Hands T. O., 2019, MNRAS, 484, 712
Dorschner J., Begemann B., Henning T., Jaeger C., Mutschke H., 1995, A&A, 300, 503
Dressing C. D. et al., 2015, ApJ, 800, 135
Fabian D., Henning T., Jäger C., Mutschke H., Dorschner J., Wehrhan O., 2001, A&A, 378, 228
Farihi J., Koester D., Zuckerman B., Vican L., Gänsicke B. T., Smith N., Walth G., Breedt E., 2016, MNRAS, 463, 3186
Fortney J. J., Marley M. S., Barnes J. W., 2007, ApJ, 659, 1661
Gail H.-P., Sedlmayr E., 2013, Physics and Chemistry of Circumstellar Dust Shells. Cambridge University Press (Cambridge Astrophysics), Cambridge, p. 332
Gänsicke B. T., Koester D., Farihi J., Girven J., Parsons S. G., Breedt E., 2012, MNRAS, 424, 333
Gupta A., Schlichting H. E., 2019, MNRAS, 487, 24
Harrison J. H. D., Bonsor A., Madhusudhan N., 2018, MNRAS, 479, 3814
Henyey L. G., Greenstein J. L., 1941, ApJ, 93, 70
Ito Y., Ikoma M., Kawahara H., Nagahara H., Kawashima Y., Nakamoto T., 2015, ApJ, 801, 144
Jaeger C., Mutschke H., Begemann B., Dorschner J., Henning T., 1994, A&A, 292, 641
Jaeger C., Molster F. J., Dorschner J., Henning T., Mutschke H., Waters L. B. F. M., 1998, A&A, 339, 904
Jura M., Young E. D., 2014, Annu. Rev. Earth Planet. Sci., 42, 45
Kang W., Ding F., Wordsworth R., Seager S., 2021, ApJ, 906, 67
Kargel J. S., Lewis J. S., 1993, Icarus, 105, 1
Kawahara H., Hirano T., Kurosaki K., Ito Y., Ikoma M., 2013, ApJ, 776, L6
Kimura H., Mann I., Biesecker D. A., Jessberger E. K., 2002, Icarus, 159, 529
Kite E. S., Fegley Bruce J., Schaefer L., Gaidos E., 2016, ApJ, 828, 80
Koike C., Kaito C., Yamamoto T., Shibai H., Kimura S., Suto H., 1995, Icarus, 114, 203
Kreidberg L. et al., 2019, Nature, 573, 87
Langmuir I., 1913, Phys. Rev., 2, 329
Lieshout R. v., Rappaport S. A., 2018, Disintegrating Rocky Exoplanets. Springer International Publishing, Cham, p. 1527
Lihrmann J.-M., 2008, J. Euro. Ceram. Soc., 28, 633
Mahapatra G., Helling C., Miguel Y., 2017, MNRAS, 472, 447
Miguel Y., Kaltenegger L., Fegley B., Schaefer L., 2011, ApJ, 742, L19
Mysen B. O., Kushiro I., 1988, Am. Mineral., 73, 1
Nagahara H., Kushiro I., Mysen B. O., 1994, Geochim. Cosmochim. Acta, 58, 1951
Neil A. R., Rogers L. A., 2020, ApJ, 891, 12
Neil A. R., Liston J., Rogers L. A., 2022, ApJ, 933, 63
O'Neill H. S. C., Palme H., 1998, Composition of the Silicate Earth: Implications for Accretion and Core Formation. Cambridge University Press, Cambridge, p. 3
Okuya A., Okuzumi S., Ohno K., Hirano T., 2020, ApJ, 901, 171
Owen J. E., Adams F. C., 2014, MNRAS, 444, 3761
Owen J. E., Wu Y., 2013, ApJ, 775, 105
Perez-Becker D., Chiang E., 2013, MNRAS, 433, 2294
Press W. H., Teukolsky S. A., Vetterling W. T., Flannery B. P., 2002, Numerical Recipes in C++ : The Art of Scientific Computing. Cambridge University Press, Cambridge
Rappaport S. et al., 2012, ApJ, 752, 1
Rappaport S., Barclay T., DeVore J., Rowe J., Sanchis-Ojeda R., Still M., 2014, ApJ, 784, 40
Robertson H. P., 1937, MNRAS, 97, 423
Rogers L. A., 2015, ApJ, 801, 41
Rogers J. G., Owen J. E., 2021, MNRAS, 503, 1526
Rogers L. A., Seager S., 2010, ApJ, 712, 974
Rogers J. G., Janó Muñoz C., Owen J. E., Makinen T. L., 2023a, MNRAS, 519, 6028
Rogers J. G., Schlichting H. E., Owen J. E., 2023b, ApJ, 947, L19
Sanchis-Ojeda R. et al., 2015, ApJ, 812, 112
Schaefer L., Fegley B., 2004, Icarus, 169, 216
Schaefer L., Fegley B., 2009, ApJ, 703, L113
Schlawin E., Herter T., Zhao M., Teske J. K., Chen H., 2016, ApJ, 826, 156
Schlawin E., Hirano T., Kawahara H., Teske J., Green E. M., Rackham B. V., Fraine J., Bushra R., 2018, AJ, 156, 281
Schlawin E., Su K. Y. L., Herter T., Ridden-Harper A., Apai D., 2021, AJ, 162, 57
Seager S., Kuchner M., Hier-Majumder C. A., Militzer B., 2007, ApJ, 669, 1279
Stone J. M., Norman M. L., 1992, ApJS, 80, 753
Stone J. M., Proga D., 2009, ApJ, 694, 205
Strubbe L. E., Chiang E. I., 2006, ApJ, 648, 652
Thompson S. E. et al., 2018, ApJS, 235, 38
Tripathi A., Kratter K. M., Murray-Clay R. A., Krumholz M. R., 2015, ApJ, 808, 173
Unterborn C. T., Dismukes E. E., Panero W. R., 2016, ApJ, 819, 32
Valencia D., Sasselov D. D., O'Connell R. J., 2007, ApJ, 665, 1413
Valencia D., Ikoma M., Guillot T., Nettelmann N., 2010, A&A, 516, A20
Van Eylen V. et al., 2021, MNRAS, 507, 2154
Zeidler S., Posch T., Mutschke H., Richter H., Wehrhan O., 2011, A&A, 526, A68
Zieba S. et al., 2022, A&A, 664, A79
Zilinskas M., van Buchem C. P. A., Miguel Y., Louca A., Lupu R., Zieba S., van Westrenen W., 2022, A&A, 661, A126

Downloaded from https://academic.oup.com/mnras/article/528/2/1249/7515287 by guest on 01 February 2024

van Lieshout R., Min M., Dominik C., 2014, A&A, 572, A76
van Lieshout R. et al., 2016, A&A, 596, A32
van Werkhoven T. I. M., Brogi M., Snellen I. A. G., Keller C. U., 2014, A&A, 561, A3

APPENDIX A: KIC 1255 B, DAY-SIDE OUTFLOW

The simulations for KIC 1255 b that assume a day-side outflow fail to reproduce the observed long-egress. This happens consistently in the parameter space explored. Fig. A1 shows the synthetic spectra for different dust mass-loss rates and initial dust grain sizes when assuming a day-side outflow for KIC 1255 *b*.

APPENDIX B: THE EXTINCTION AND FORWARD SCATTERING COMPETITION

While the extinction increases the transit depth, forward scattering fills up the light curve. When including forward scattering in the modelling of dusty-tails, we require larger mass-loss rates to fit the observations (see also fig. 3, van Lieshout et al. 2016). Fig. B1 shows the contribution from scattering and extinction for the best-fitting models of corundum and iron-rich olivine.

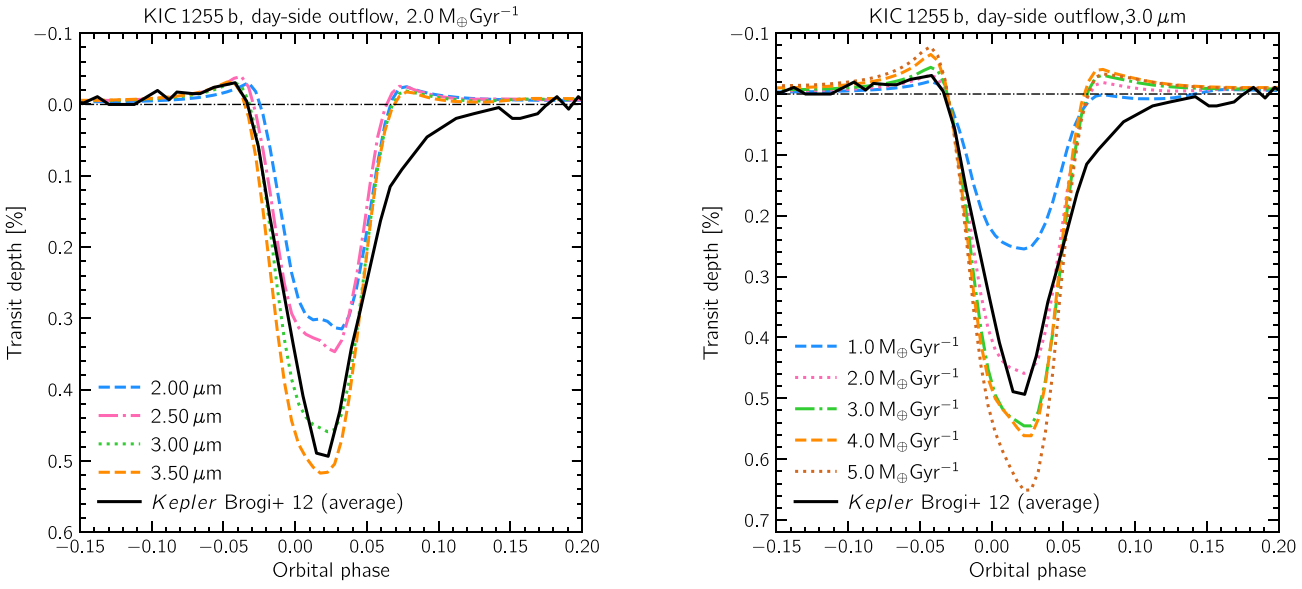

Figure A1. Synthetic light curves of KIC 1255 b for dust composed of iron-rich olivine ($Mg_{0.8}Fe_{1.2}SiO_4$[s]) and a day-side dusty outflow. Left: Synthetic light curves for models at a constant planetary mass-loss rate of 2.0 $M_\oplus Gyr^{-1}$ and different initial dust grain sizes. The observed *Kepler* light curve averaged over six quarters by Brogi et al. (2012) is shown as the black solid curve. **Right**: Synthetic light curves over five orbits at an initial dust grain size of 0.5 μm and a planetary mass-loss rate of 1.0 $M_\oplus Gyr^{-1}$.

Downloaded from https://academic.oup.com/mnras/article/528/2/1249/7515287 by guest on 01 February 2024

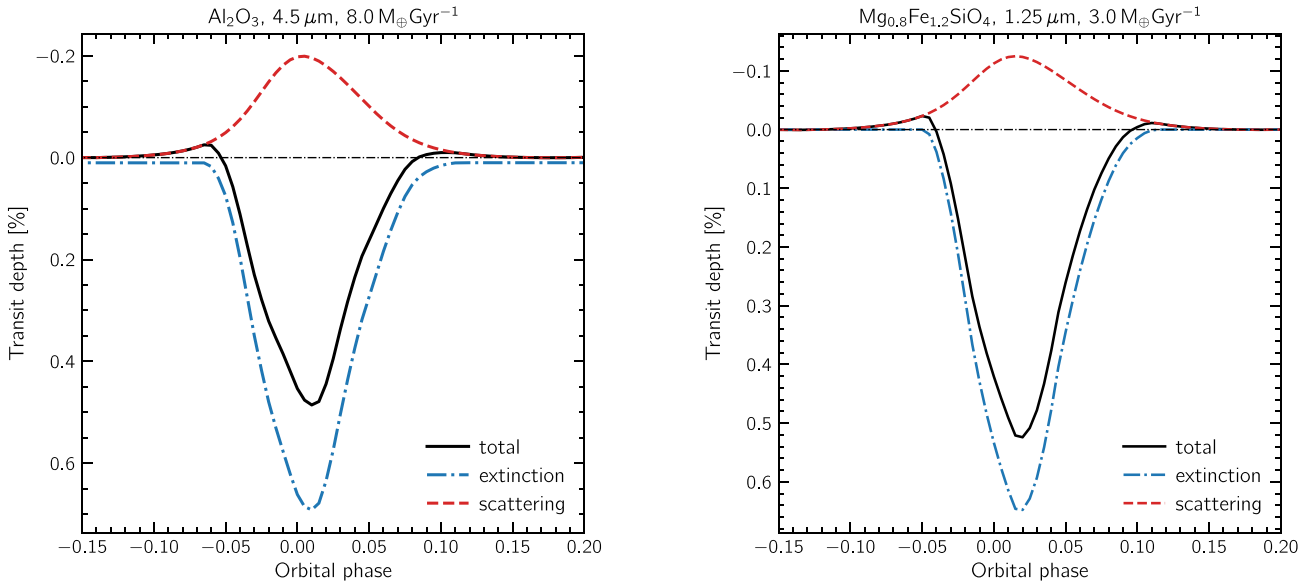

Figure B1. Synthetic light curves (black solid curves) of the best-fitting corundum (left) and iron-rich olivine (right) models, and the scattering (dashed red curves) and extinction (dot-dashed blue curves) components. The components are smoothed to *Kepler*'s long cadence. Note how the scattering component reduces the transit depth by a significant factor in both cases.

This paper has been typeset from a TEX/LATEX file prepared by the author.

Downloaded from https://academic.oup.com/mnras/article/528/2/1249/7515287 by guest on 01 February 2024

© The Author(s) 2024.
Published by Oxford University Press on behalf of Royal Astronomical Society. This is an Open Access article distributed under the terms of the Creative Commons Attribution License (https://creativecommons.org/licenses/by/4.0/), which permits unrestricted reuse, distribution, and reproduction in any medium, provided the original work is properly cited.

Monthly Notices of the ROYAL ASTRONOMICAL SOCIETY

MNRAS **527,** 3876–3899 (2024) https://doi.org/10.1093/mnras/stad3462
Advance Access publication 2023 November 08

The effect of sculpting planets on the steepness of debris-disc inner edges

Tim D. Pearce [1,2★] Alexander V. Krivov,[2] Antranik A. Sefilian [2,3] Marija R. Jankovic [4] Torsten Löhne [2] Tobias Morgner,[2] Mark C. Wyatt [5] Mark Booth[2,6] and Sebastian Marino [7]

[1]*Department of Physics, University of Warwick, Gibbet Hill Road, Coventry CV4 7AL, UK*
[2]*Astrophysikalisches Institut und Universitätssternwarte, Friedrich-Schiller-Universität Jena, Schillergäßchen 2-3, D-07745 Jena, Germany*
[3]*Center for Advanced Mathematical Sciences, American University of Beirut, PO Box 11-0236, Riad El-Solh, Beirut 11097 2020, Lebanon*
[4]*Institute of Physics Belgrade, University of Belgrade, Pregrevica 118, 11080 Belgrade, Serbia*
[5]*Institute of Astronomy, University of Cambridge, Madingley Road, Cambridge CB3 0HA, UK*
[6]*UK Astronomy Technology Centre, Royal Observatory Edinburgh, Blackford Hill, Edinburgh EH9 3HJ, UK*
[7]*Department of Physics and Astronomy, University of Exeter, Stocker Road, Exeter, EX4 4QL, UK*

Accepted 2023 November 7. Received 2023 October 31; in original form 2023 September 13

ABSTRACT

Debris discs are our best means to probe the outer regions of planetary systems. Many studies assume that planets lie at the inner edges of debris discs, akin to Neptune and the Kuiper Belt, and use the disc morphologies to constrain those otherwise-undetectable planets. However, this produces a degeneracy in planet mass and semimajor axis. We investigate the effect of a sculpting planet on the radial surface-density profile at the disc inner edge, and show that this degeneracy can be broken by considering the steepness of the edge profile. Like previous studies, we show that a planet on a circular orbit ejects unstable debris and excites surviving material through mean-motion resonances. For a non-migrating, circular-orbit planet, in the case where collisions are negligible, the steepness of the disc inner edge depends on the planet-to-star mass ratio and the initial-disc excitation level. We provide a simple analytic model to infer planet properties from the steepness of ALMA-resolved disc edges. We also perform a collisional analysis, showing that a purely planet-sculpted disc would be distinguishable from a purely collisional disc and that, whilst collisions flatten planet-sculpted edges, they are unlikely to fully erase a planet's signature. Finally, we apply our results to ALMA-resolved debris discs and show that, whilst many inner edges are *too steep* to be explained by collisions alone, they are *too flat* to arise through completed sculpting by non-migrating, circular-orbit planets. We discuss implications of this for the architectures, histories, and dynamics in the outer regions of planetary systems.

Key words: planets and satellites: dynamical evolution and stability – planet–disc interactions – circumstellar matter.

1 INTRODUCTION

Debris discs, like the Solar System's Asteroid and Kuiper Belts, are circumstellar populations of sub-planet-mass objects (Wyatt 2008). These objects undergo destructive collisions that release observable dust, and such dust is detected around 20 per cent of main-sequence stars (Hughes, Duchêne & Matthews 2018; Wyatt 2020). Extrasolar debris discs can be resolved in scattered light and thermal emission (e.g. Esposito et al. 2020; Lovell et al. 2021; Booth et al. 2023), and are invaluable probes of processes in the outer regions of planetary systems; modern planet-detection techniques are insensitive to mid-sized planets orbiting at 10s or 100s of au from stars, but such planets can be inferred from their influence on observed debris (e.g. Mouillet et al. 1997; Wyatt et al. 1999; Quillen 2006; Pearce & Wyatt 2014; Sefilian, Rafikov & Wyatt 2021; Stuber, Löhne & Wolf 2023). The launch of the *JWST* has prompted renewed interest in such hypothetical planets, because if they exist, then many should be detectable by this facility for the first time (Pearce et al. 2022).

Many theoretical studies have used the shapes and locations of debris discs to infer the properties of unseen planets. If such planets orbit just interior to debris discs, and are responsible for sculpting debris-disc inner edges, then the shapes and locations of these edges can be used to infer the planets' minimum-possible mass, maximum semimajor axis, and minimum eccentricity (e.g. Pearce & Wyatt 2014; Faramaz et al. 2019; Pearce et al. 2022). However, this approach suffers from several key unknowns. First, whilst Neptune dominates the Kuiper Belt's inner edge (Malhotra 1993), it is unclear whether planets actually *do* reside just interior to extrasolar debris discs. It could be that the disc shapes and locations are instead set by other, non-planetary processes, such as debris–debris collisions or system formation. Second, even if exoplanets do sculpt debris-disc edges, it is unclear whether they do so on fixed orbits (as often assumed in planet–disc interaction studies), or whether they migrate over time. Third, even if planetary sculpting occurs, it is unclear whether this process has finished in observed discs (as often assumed), or whether disc edges are still evolving under planet–debris interactions. These distinctions have significant implications for the morphology of debris discs, and the masses and locations of any responsible planets today. Such questions are difficult to answer using only debris-disc shapes and inner-edge locations.

★ E-mail: tim.pearce@warwick.ac.uk

© The Author(s) 2023.
Published by Oxford University Press on behalf of Royal Astronomical Society. This is an Open Access article distributed under the terms of the Creative Commons Attribution License (https://creativecommons.org/licenses/by/4.0/), which permits unrestricted reuse, distribution, and reproduction in any medium, provided the original work is properly cited.

Downloaded from https://academic.oup.com/mnras/article/doi/10.1093/mnras/stad3462/7382221 by guest on 23 November 2023

However, we can gain more insight by also considering the *radial surface-density profile* of debris-disc edges. If an edge were sculpted by a non-migrating planet, then this profile would have a characteristic steepness that depends on planet mass (Quillen 2006; Chiang et al. 2009; Mustill & Wyatt 2012; Rodigas, Malhotra & Hinz 2014). Conversely, if the edge were set by non-planetary processes like collisions, then its steepness would be different (Wyatt et al. 2007; Löhne, Krivov & Rodmann 2008; Geiler & Krivov 2017; Imaz Blanco et al. 2023). Similarly, the profiles of edges sculpted by migrating planets would be distinct from those due to non-migrating planets (Friebe, Pearce & Löhne 2022), and edges set by combinations of both planetary and non-planetary effects would also have different profiles (Thebault, Kral & Ertel 2012; Nesvold & Kuchner 2015). The profiles of debris-disc edges are therefore powerful tools for probing the architectures, histories, and processes in the outer regions of planetary systems.

Recently, several studies used the Atacama Large Millimeter/submillimeter Array (ALMA) to resolve the radial profiles of debris-disc edges (e.g. Faramaz et al. 2021; Lovell et al. 2021; Marino 2021). These observations trace millimetre-sized grains that are unaffected by radiation forces (Hughes et al. 2018), so offer our best means to probe the distribution of larger, unseen planetesimals in the discs. Such studies show that some debris discs have flatter inner edges that are consistent with pure collisional evolution, whilst others have steeper profiles potentially indicative of planetary sculpting (Imaz Blanco et al. 2023). Our aim in this paper is to thoroughly investigate the dynamical effects of sculpting planets on the steepness of debris-disc inner edges, and establish whether any of the observed ALMA steepnesses are consistent with planetary sculpting. We will show that, whilst many inner edges are *too steep* to be explained through collisions alone, they are *too flat* to be purely the result of completed sculpting by non-migrating, circular-orbit planets. This potentially implies that different processes, or combinations of processes, are actually operating in these discs.

Several previous studies also explored the effect of sculpting planets on the steepness of debris-disc inner edges (e.g. Quillen 2006; Quillen & Faber 2006; Chiang et al. 2009; Mustill & Wyatt 2012; Rodigas et al. 2014; Nesvold & Kuchner 2015; Regály et al. 2018). Our study differs from these in several ways. First, since we do not know debris-disc masses or the sizes of the largest planetesimals (Krivov & Wyatt 2021), both of which are critical for quantifying collisional evolution, we choose to decouple the dynamical and collisional modelling in this paper. Instead, we initially model the interaction between a planet and a collisionless disc, to isolate the effect of a planet on the edge steepness. We then apply a collisional model, to demonstrate how collisions would change the steepness from the planet-only regime. Second, we explore a very broad parameter space in both the dynamical and collisional simulations, to provide general predictive models that are valid across a wide range of scenarios. Third, we parametrize our results in a form that directly relates to those fitted to ALMA data, to facilitate the application of our results to upcoming observations. Finally, we apply our predictive model to recent ALMA observations of debris discs.

The layout of this paper is as follows. Section 2 describes our n-body simulations of a circular-orbit planet and a collisionless debris disc. Section 3 provides a predictive model relating the steepness of a disc's edge to the parameters of a circular-orbit planet, and specifically Section 3.2.1 gives a step-by-step method demonstrating how to infer an unseen sculpting planet from a debris disc's inner edge. Section 4 addresses how collisions would affect planet-sculpted edges. In Section 5, we apply our results to observed debris discs, and in Section 6, we discuss our results (including what the observed-disc profiles may be telling us about planetary systems). We conclude in Section 7.

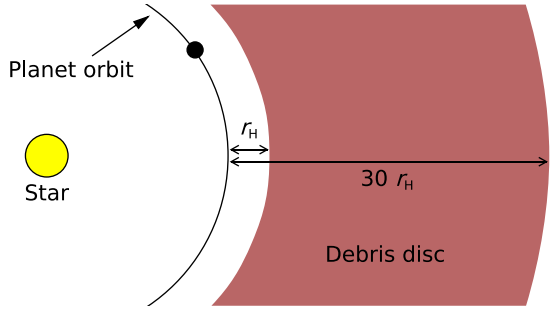

Figure 1. Initial setup of our n-body simulations with a circular-orbit planet. A single planet (black circle) is initialized just interior to a massless debris disc, which spans 1–30 Hill radii exterior to the planet orbit.

2 n-BODY SIMULATIONS

We use a large suite of n-body simulations to explore the dynamical interaction between a circular-orbit planet and a collisionless debris disc. The effects of debris–debris collisions will be assessed later (Section 4). We describe the circular-planet simulation setup in Section 2.1, discuss two example simulations in Section 2.2, and present the surface-density profiles of all simulated discs in Section 2.3. We measure the debris-excitation level at the simulated inner edges in Section 2.4, and show this to arise through mean-motion resonance (MMR) interactions with the circular-orbit planet. In addition, we also extend the n-body analyses to eccentric planets in Appendix B.

2.1 Setup of n-body simulations

The initial setup of our n-body simulations with circular-orbit planets is shown on Fig. 1. Each simulation comprises one star, one planet, and a disc of 20 000 massless debris particles. We run over 300 simulations, each with a different combination of star mass, planet mass, planet semimajor axis, and initial-disc excitation level.

Each debris particle is initialized with a semimajor axis between 1 and 30 Hill radii (r_H) exterior to the planet;

$$r_H \equiv a_p \left(\frac{m_p}{3m_*} \right)^{1/3}, \quad (1)$$

where a_p is the planet semimajor axis, and m_p and m_* are the planet and star masses, respectively. The inner edge of 1 Hill radius ensures that Trojans are omitted, which would otherwise bias the axisymmetric surface-density profiles that we fit later (we discuss Trojans in Section 6.1.9). The outer edge of 30 Hill radii ensures that the outer edge does not affect the inner-edge profile; a circular-orbit planet is expected to scatter all non-resonant material originating within approximately 3 Hill radii of its orbit (Gladman 1993; Ida et al. 2000; Kirsh et al. 2009; Malhotra et al. 2021; Friebe et al. 2022), so setting the outer edge at $30r_H$ ensures that this is well beyond the inner region. Debris semimajor axes are drawn such that the initial surface-density distribution goes as approximately $r^{-1.5}$ (where r is stellocentric distance), akin to the Minimum-Mass Solar Nebula (MMSN, Weidenschilling 1977; Hayashi 1981). Each debris particle has an initial eccentricity uniformly drawn between 0 and a maximum value $e_{max,0}$, and an initial inclination (relative to the planet's orbital plane) uniformly drawn between 0 and

Downloaded from https://academic.oup.com/mnras/article/doi/10.1093/mnras/stad3462/7382221 by guest on 23 November 2023

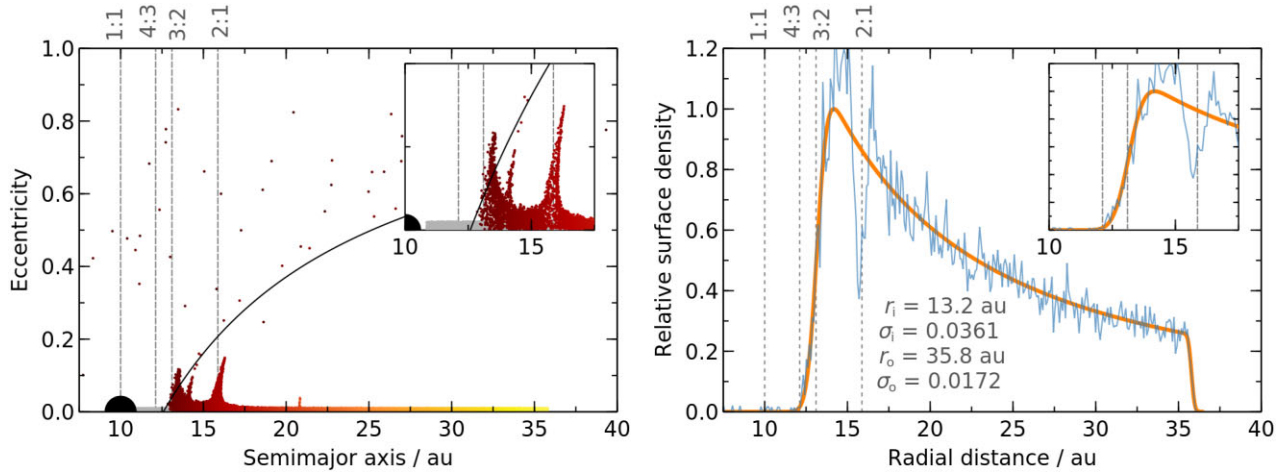

Figure 2. Simulation of a circular-orbit planet interacting with an exterior debris disc, for an initially weakly excited disc. The simulation is of a solar-mass star, a 2 M_{Jup} planet on a circular orbit at 10 au ($m_p/m_* = 2 \times 10^{-3}$), and 20 000 massless debris particles initially spanning 1–30 Hill radii exterior to the planet, with an initial surface-density profile of approximately $r^{-1.5}$. Initial debris eccentricities were each uniformly drawn between 0 and 0.01, and the plot shows the final state after 8.7×10^5 yr (10 diffusion time-scales). The planet clears nearby debris through scattering, and excites the eccentricities of surviving material through MMRs. Left panel: semimajor axes and eccentricities of the planet (large circle) and debris (small points, coloured by initial semimajor axis). Grey points show debris at the start of the simulation. Solid black lines are the minimum eccentricities required for debris to come within 3 Hill radii of the planet, and dashed grey lines are nominal MMR locations. Right panel: radial surface-density profile of the disc, $\Sigma(r)$. The thin blue line shows the simulation data, and the thick orange line is the fit (equation 6). Insets show the inner-edge region in more detail. The fitted model parameters are shown on the right panel; α was fixed to 1.5 in the fit.

$e_{max,0}/2$ radians . Each particle's initial longitude of ascending node, argument of pericentre, and mean anomaly are uniformly drawn between 0° and 360°.

To ensure that scattering is essentially complete by the end of the simulations, we set each simulation end time depending on the diffusion time-scale t_{diff}. The value t_{diff} characterizes the scattering time-scale, and is roughly the time taken for a planet to significantly scatter or eject 70 per cent of material originating within 3 Hill radii of its orbit (Costa, Pearce & Krivov, submitted). The diffusion time for a planet acting on a body with semimajor axis a is

$$t_{diff} \approx 0.01 T_p \left(\frac{a_p}{a}\right)^{1/2} \left(\frac{m_p}{m_*}\right)^{-2}, \quad (2)$$

where T_p is the planet's orbital period (Tremaine 1993). Equivalently,

$$t_{diff} \approx 1.1 \times 10^4 \text{ yr } \left(\frac{a_p}{\text{au}}\right)^2 \left(\frac{a}{\text{au}}\right)^{-1/2} \left(\frac{m_*}{M_\odot}\right)^{3/2} \left(\frac{m_p}{M_{Jup}}\right)^{-2}. \quad (3)$$

We run each simulation for at least $10 t_{diff}$ calculated at $a = a_p$, to ensure that scattering is essentially complete by the end. Simulations are run in REBOUND (Rein & Liu 2012) using WHFAST (a symplectic Wisdom–Holman integrator, Wisdom & Holman 1991; Rein & Tamayo 2015), with a time-step of 1 per cent of the planet's orbital period.[1] Simulations are conducted and analysed in the centre-of-mass frame.

We run simulations with star masses of 1–2 $M_\odot$, planet-to-star mass ratios of 3×10^{-5} to 10^{-1}, planet semimajor axes of 1–100 au, and maximum initial debris eccentricities of $e_{max,0} = 0.001$–0.3. In addition, we also re-weight debris particles in post-simulation analyses, so we can test different initial surface-density profiles; we consider initial surface-density profiles between r^0 and $r^{-1.5}$. We assume the planet and debris to be point-like particles; this lets us apply simple scaling laws to our results, but also means that the potential removal of debris via accretion rather than ejection is ignored in our simulations (see Morrison & Malhotra 2015).

[1] REBOUND does not define several orbital parameters in the case of a perfectly circular orbit. To ensure correct behaviour, for our 'circular-planet' simulations we actually implement a planet eccentricity of 10^{-4}.

2.2 Example simulation results

Figs 2 and 3 show two example simulations after 10 diffusion time-scales. Both have a solar-mass star and a 2 M_{Jup} planet ($m_p/m_* = 2 \times 10^{-3}$), which is on a circular orbit at 10 au. The simulation on Fig. 2 starts with an initially unexcited debris disc ($e_{max,0} = 0.01$), and that on Fig. 3 has the same setup but an initially excited disc ($e_{max,0} = 0.1$). The main qualitative features of these simulations are typical of all our runs.

The left panels of Figs 2 and 3 show the semimajor axes and eccentricities of the simulated bodies, which demonstrate the two main effects of a circular-orbit planet on debris. The planet:

(i) scatters and ejects most debris coming within ∼3 Hill radii of its orbit; this clears the region above the solid black lines on the left panels;

(ii) excites the eccentricities of surviving debris via MMRs, particularly near the inner edge of the sculpted disc.

The role of MMRs in exciting debris eccentricity is clearest in the initially unexcited-disc simulation (Fig. 2, left panel). Here, populations of debris in the 2:1 and 3:2 MMRs are clearly visible. For the initially excited disc (Fig. 3), these MMR populations are similar to those in the initially unexcited simulation, only now they are less distinct due to the higher intrinsic eccentricity of the disc. The evolution of debris inclination is much less significant than eccentricity; there is some very small inclination excitation at specific resonances in these simulations, but the disc still remains thin across its entire width.

Downloaded from https://academic.oup.com/mnras/article/doi/10.1093/mnras/stad3462/7382221 by guest on 23 November 2023

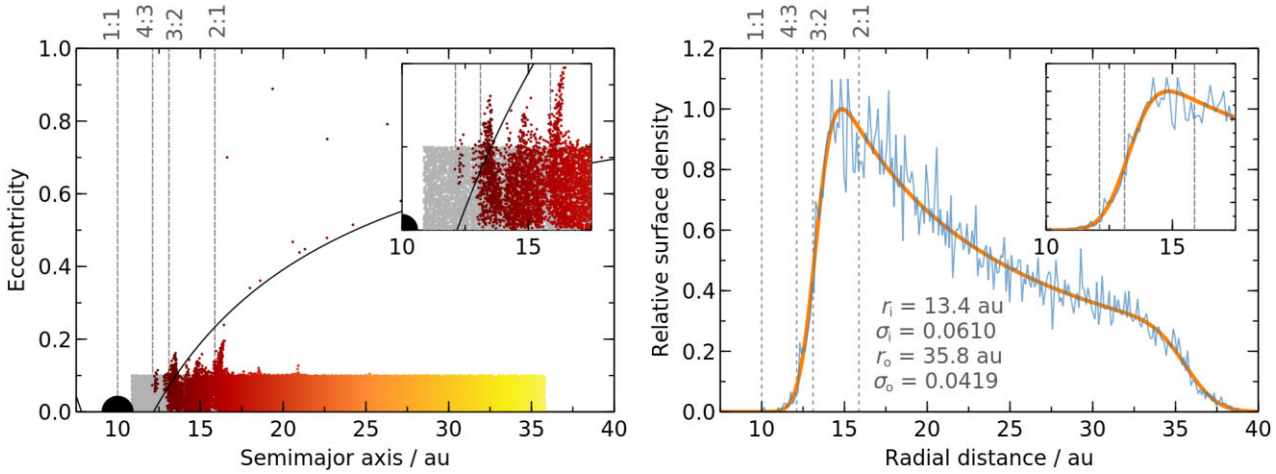

Figure 3. Simulation with the same setup as that on Fig. 2, except that the debris disc is initially more excited (maximum initial eccentricities of 0.1, rather than the value of 0.01 on Fig. 2). The planet still excites debris through MMRs (left panel), but these populations are less significant against the background excitation level of the disc. The resulting inner edge is flatter than in the low-initial-excitation case.

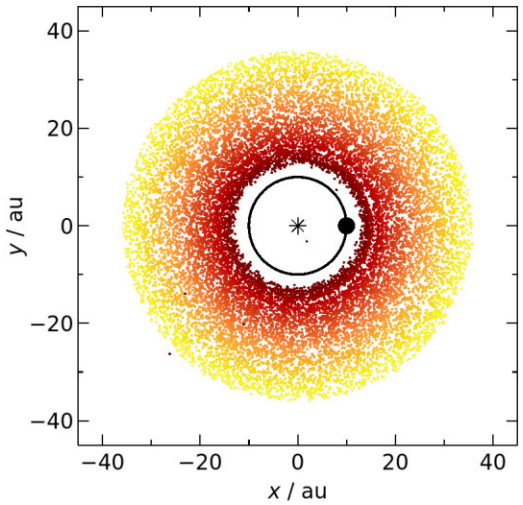

Figure 4. Positions of bodies from the simulation with a low-eccentricity disc (Fig. 2). The asterisk, filled black circle, and solid line denote the star, planet, and planet orbit, respectively, and small points are debris (coloured by initial semimajor axis). The disc is almost axisymmetric, with a slight asymmetry between the left and right sides due to MMRs. This causes a small difference in the inner-edge steepness between the two sides; the right side (aligned with the planet position) has $\sigma_i = 0.0286$, whilst the value for the opposite side is 0.0354.

The right panels of Figs 2 and 3 show the azimuthally averaged surface-density profiles of the simulated debris discs (thin blue lines). The planet imposes a profile on the disc inner edge, whilst the central and outer regions retain their initial profiles. Individual, strong MMRs can also impose additional structure, such as the 2:1 MMR at 15.9 au on Fig. 2; in this example that MMR does not affect the inner-edge fit, but it can do in other simulations. The thick orange lines are parametric fits to the surface-density profiles, as detailed in Section 2.3.

Fig. 4 shows the final positions of bodies in the initially unexcited-disc simulation (that on Fig. 2). The disc is almost axisymmetric, with a slight asymmetry between the directions aligned and anti-aligned with the planet due to MMR structure (an effect noted by Tabeshian & Wiegert 2016, 2017). This leads to a small difference in the steepness of the inner-edge profile between the two sides of the disc, which we discuss further in Section 6.2.1. For the initially excited-disc simulation from Fig. 3, the asymmetry is less pronounced.

2.3 Surface-density profile fitting

We aim to quantify how the properties of a sculpting planet affect the steepness and location of the debris disc's inner edge. To proceed, we use a parametric model to fit the radial surface-density profiles of debris in the n-body simulations, and examine how the model parameters change as functions of system properties. Section 2.3.1 describes the model, Section 2.3.2 the dependence of the fitted models on system parameters, and Section 2.3.3 the time-scale for a disc edge takes to reach its final state.

2.3.1 Surface-density profile model

To quantify the disc surface-density profile, we follow the approach of Rafikov (2023). They show that, for a low-eccentricity disc with a sharp semimajor-axis cut-off at the outer edge, the radial surface-density profile around that edge can be characterized as:[2]

$$\Sigma(r) \propto 1 - \mathrm{erf}\left(\frac{r - r_\mathrm{o}}{\sqrt{2}\sigma_\mathrm{o} r_\mathrm{o}}\right). \quad (4)$$

Here, r_o characterizes the radial location of the outer edge, σ_o is the 'flatness' of the surface-density profile at that edge, and erf is the Gauss error function:

$$\mathrm{erf}(z) \equiv \frac{2}{\sqrt{\pi}} \int_0^z \exp(-t^2)\mathrm{d}t. \quad (5)$$

Equation (4) is an 'S-shape' profile centred on r_o, which is steeper for smaller σ_o and flatter for larger σ_o. The value of σ_o is strongly linked to debris eccentricity; if debris has a sharp cut-off in semi-major axis, and its root-mean-square (rms) eccentricity is e_rms, then $\sigma_\mathrm{o} = e_\mathrm{rms}/\sqrt{2}$ (Rafikov 2023). This means that, for discs with sharp cut-offs in semimajor axis, lower rms eccentricities mean steeper

[2]Rafikov (2023) derived equation (4) analytically. Marino (2021) fitted edges numerically using hyperbolic tangents instead, but the two profiles have similar forms.

Downloaded from https://academic.oup.com/mnras/article/doi/10.1093/mnras/stad3462/7382221 by guest on 23 November 2023

edges (and smaller σ_o). If the eccentricities are uniformly spread from 0 to e_{max}, then $e_{rms} = e_{max}/\sqrt{3}$ and hence $\sigma_o = e_{max}/\sqrt{6}$. We will later show that a planet-sculpted disc does not have a sharp cut-off in semimajor axis at the inner edge, so the corresponding relationship between the edge profile and debris eccentricity is slightly modified, but the two remain strongly linked.

To parametrize the surface density across a whole disc, we use profiles similar to equation (4) at the two edges, combined with an $r^{-\alpha}$ profile describing the surface density between the edges. By multiplying these three local profiles together, we arrive at the following model for the overall surface-density profile:

$$\Sigma(r) = \frac{\Sigma_0}{2}\left[1-\mathrm{erf}\left(\frac{r_i - r}{\sqrt{2}\sigma_i r_i}\right)\right]\left[1-\mathrm{erf}\left(\frac{r - r_o}{\sqrt{2}\sigma_o r_o}\right)\right]\left(\frac{r}{r_i}\right)^{-\alpha}, \tag{6}$$

where subscripts i and o denote terms characterizing the inner and outer edges, respectively, and Σ_0 is the the surface density at $r \approx r_i$.

We numerically fit a radial profile of this form to each of our simulated discs, treating Σ_0, r_i, r_o, σ_i, and σ_o as free parameters. We typically fix α to the initial surface-density index of the disc (i.e. $\alpha = 1.5$ for an initially MMSN profile). The fitting procedure is described in Appendix A, and the orange lines on the right panels of Figs 2 and 3 show the resulting fitted profiles for those simulations.

2.3.2 *Dependence of the final inner-edge profile on system parameters*

Having fitted surface-density profiles to each of our *n*-body discs, we now assess how the profile of a planet-sculpted inner edge depends on system parameters. The inner-edge profiles are fully characterized by r_i and σ_i, and in this section we show how those fitted parameters vary with simulation setup.

Fig. 5 shows how the location of the inner edge of a planet-sculpted disc, r_i, scales with the planet-to-star mass ratio, planet semimajor axis, and the initial disc-excitation level. The location r_i is just exterior to the 'chaotic zone' around the planet's circular orbit, which can be defined as either ∼3 Hill radii or via the Wisdom overlap criterion (Wisdom 1980). The value r_i is larger for discs with higher initial-excitation levels, and kinks occur when r_i is close to the nominal location of a strong MMR; this is especially true for discs with low initial eccentricities. Note that r_i/a_p is independent of the planet's semimajor axis, and so depends only on the planet-to-star mass ratio and the disc's initial-excitation level.

Fig. 6 shows how the flatness of the inner-edge profile, σ_i, scales with the planet-to-star mass ratio and the initial disc-excitation level. It is independent of all other parameters. The inner edges are generally steeper if sculpted by lower-mass planets, and flatter for higher-mass planets. The inner edges are also flattest for discs with the highest initial-excitation levels, although there is less of a dependence for discs with low initial-excitation levels. The relationships between σ_i and m_p/m_* are also not smooth, but show complicated spikes. These spikes are not numerical effects, because they are replicated across simulations with the same mass ratios but different planet semimajor axes and star masses; the spikes actually occur when the inner edge is near the nominal location of a strong MMR.

The values of r_i and σ_i on Figs 5 and 6 were fitted for discs with initial surface-density profiles of $r^{-\alpha}$, where $\alpha = 1.5$, but they are actually independent of α for realistic setups. This is because the planet-induced edges are typically much steeper than the overall disc profiles. To check this, we re-scaled the simulated discs to

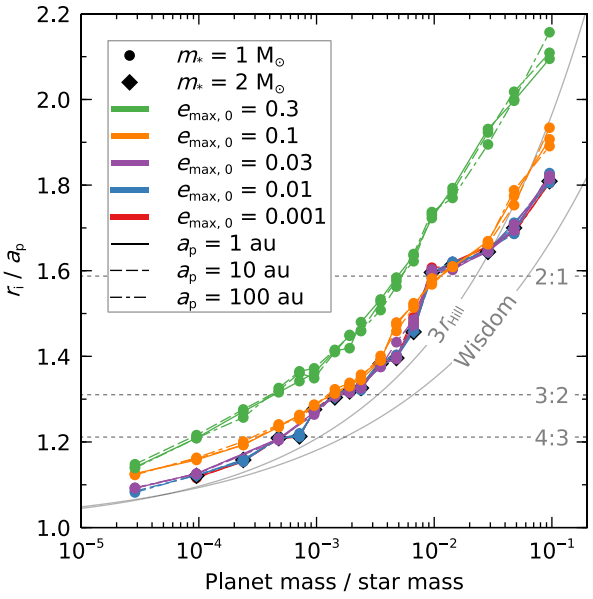

Figure 5. Location of the sculpted disc's inner edge r_i (in terms of planet semimajor axis a_p), from fits to surface-density profiles at the end of our *n*-body simulations. Coloured points and lines show simulations with different initial setups, as denoted in the key. Grey solid lines denote different definitions of the outer edge of the chaotic zone; after the planet has ejected unstable debris, the disc's inner edge is typically just outside this chaotic zone. Dashed horizontal lines denote where r_i coincides with the nominal location of a strong MMR; these resonances can significantly affect the edge location.

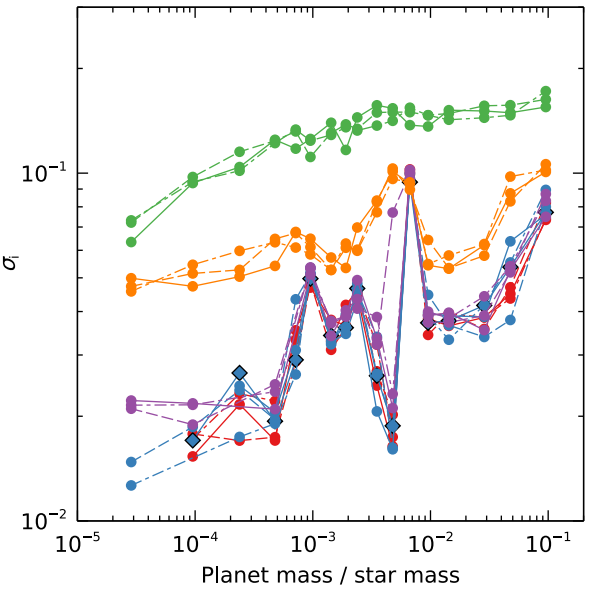

Figure 6. Flatness of the sculpted disc's inner edge, σ_i, from fits to surface-density profiles at the end of our *n*-body simulations. A smaller value of σ_i corresponds to a sharper edge. Lines and symbols have the same meanings as on Fig. 5. The edge steepness only depends on the planet-to-star mass ratio and the disc's initial-excitation level, and spikes in the plotted relationships occur when the inner edge is near the nominal location of a strong MMR.

Downloaded from https://academic.oup.com/mnras/article/doi/10.1093/mnras/stad3462/7382221 by guest on 23 November 2023

have initially flat surface-density profiles (i.e. $\alpha = 0$) and re-fitted the edges. This resulted in values of r_i and σ_i that are within a few per cent of the $\alpha = 1.5$ values, and hence the profiles of planet-sculpted edges do not strongly depend on the broader disc profiles. We further checked this analytically, and show that planet-sculpted inner edges should be much steeper than the overall disc provided that the initial-disc profile is flatter than r^{-4} (and also r^4); this calculation is presented in Appendix C. Most measured debris-disc profiles are shallower than this, so the steepness of a planet-sculpted edge should typically not depend on the overall disc profile.

2.3.3 *Edge-sculpting time-scale*

The time-scale for a circular-orbit planet to sculpt the disc inner edge is expected to scale with the diffusion time-scale (equations 2 and 3), which quantifies how quickly a planet scatters and ejects debris. We find that this is reflected in our simulations; after some number of diffusion times, the inner edges settle into their final configurations. However, the number of diffusion time-scales required appears to have some dependence on the planet-to-star mass ratio, with different regimes for ratios above and below 10^{-2}.

For planet-to-star mass ratios below 10^{-2}, we find that the inner edge settles into its final shape within 1 diffusion time-scale; therefore, for the majority of realistic planets, equations (2) and (3) are reasonable estimates of the sculpting time-scale. However, for mass ratios above 10^{-2}, more diffusion time-scales are needed; such planets appear to take closer to 10 diffusion times to sculpt the disc. For this reason, we ran all simulations that had $m_p/m_* \geq 10^{-2}$ until a time of $100t_{diff}$, whilst all simulations with $m_p/m_* < 10^{-2}$ were run for $10t_{diff}$. Regardless, despite the difference in the number of diffusion times required, large planets still sculpt discs much faster than small planets, because the diffusion time-scale strongly decreases with increasing planet mass.

There may be two reasons for this behaviour change around $m_p/m_* = 10^{-2}$. First, it may mark the transition between a star–planet interaction, where $m_p/m_* \ll 1$, to a binary interaction, where the two bodies have comparable mass. In the latter case, dynamical definitions like the Hill radius break down, so the interaction dynamics may fundamentally change.

The second reason relates to the ratio of t_{diff} to the planet's orbital period. For $m_p/m_* = 10^{-2}$, the diffusion time is approximately 100 planet periods, and for $m_p/m_* = 10^{-1}$, the diffusion time is just 1 planet period. For such mass ratios the approximations used to define the diffusion time-scale start to break down. For example, a planet with $m_p/m_* = 10^{-1}$ must take more than one period (and hence more than one t_{diff}) to clear unstable material, because it can only eject material that passes close to it; any material that is nearly co-orbital with the planet but located on the opposite side of the star must therefore take several orbital periods (and hence several diffusion times) to pass close to the planet and get ejected. Conversely, for a small mass ratio, the diffusion time is much longer than the planet period, so such effects are less important.

2.4 Debris eccentricity at the disc inner edge

To understand the profiles of the simulated inner edges, we must understand the dynamical processes occurring there. Like Marino (2021) and Rafikov (2023), we expect the edge steepness to be related to debris eccentricity, so understanding the planet-induced eccentricity is vital for understanding how planets shape disc inner edges. In this section, we quantify the eccentricity excitation at the simulated inner edges (Section 2.4.1), and show that this excitation is caused by MMR interactions (Section 2.4.2). Later, in Section 3, we will use these results to produce a predictive model relating planet properties to inner-edge profiles.

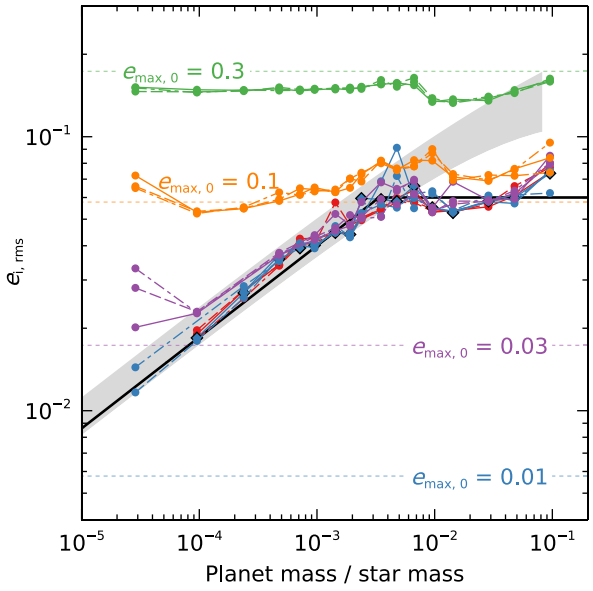

Figure 7. Rms eccentricities of surviving debris at the disc inner edges, at the end of our n-body simulations. Lines and symbols are defined on Fig. 5. Dotted horizontal lines are the values expected if the discs maintain their initial-excitation levels; these should be compared to simulation lines of the matching colour. The shaded region is a theoretical prediction for the rms eccentricity acquired by bodies in the planet's 3:2 or 2:1 MMRs; its width is the spread of these values. The planet excites surviving debris through MMRs; the black line is a rough fit to the eccentricity it imparts on debris at the inner edge (equation 7). If this planet-induced eccentricity is smaller than the initial-disc excitation level, then the planet does not significantly increase the excitation level above that of the pre-interaction disc.

2.4.1 *Measuring debris eccentricity at the simulated inner edges*

We first directly measure the eccentricities of inner-edge debris at the final snapshot of each of our n-body simulations. To do this, we fit the erf-power-law surface-density model (equation 6) to each simulated disc, then use this to define the inner-edge region; the inner edge has a characteristic width of several times $r_i\sigma_i$, so we define the 'inner-edge region' as that centred on r_i with an arbitrary full width $3r_i\sigma_i$. We then calculate the rms eccentricity of all debris bodies that are instantaneously located in this radial range, which we define as the rms eccentricity of the debris-disc inner edge, $e_{i,\,rms}$. As an example, for this definition the simulation on Fig. 2 has an inner-edge region spanning from 12.5 to 13.9 au, with $e_{i,\,rms} = 0.0433$.

Fig. 7 shows the rms eccentricities at the inner edges of each of our simulated discs, calculated using the above method. These rms eccentricities depend only on the planet-to-star mass ratio and the initial-disc excitation level. For discs with low initial-excitation levels, the eccentricity imparted by the planet increases with the planet-to-star mass ratio, up to mass ratios of $\sim 3.3 \times 10^{-3}$; above this, the inner-edge eccentricity is roughly independent of mass ratio. Conversely, if the disc's initial eccentricity exceeds the level that would be imparted on the edge by the planet, then the resulting edge

Downloaded from https://academic.oup.com/mnras/article/doi/10.1093/mnras/stad3462/7382221 by guest on 23 November 2023

eccentricity is essentially independent of the planet, and remains close to the initial level throughout the simulation.

2.4.2 *Mean-motion resonances as the edge-excitation mechanism for circular-orbit planets*

We now identify the mechanism that excites inner-edge debris. Despite the significant eccentricities of this material (Fig. 2, left panel), this excitation is not caused by planet-debris scattering, because the semimajor axes of this debris remains essentially unchanged. Excitation is also not due to secular interactions, because the low-eccentricity planet cannot sufficiently excite debris through secular interactions. This leaves MMRs as the only possible excitation mechanism, in agreement with previous studies (Quillen 2006; Quillen & Faber 2006). The idea that MMRs are responsible is also supported by the presence of debris populations with similar excited eccentricities near nominal MMR locations (e.g. the 2:1 MMR on Fig. 2). Note that a single MMR does not usually dominate all surviving debris at the disc edge; rather, several nearby MMRs excite debris across a range of semimajor axes.

Given the resonant nature of debris at the inner edge, we can dynamically explain the dependence of $e_{\rm i,\,rms}$ on planet-to-star mass ratio. The specific MMRs at the edge depend on the mass ratio, because as the mass ratio increases, the nominal MMR locations remain unchanged but the width of the chaotic zone around the planet increases. However, for low-mass ratios, the excitation level appears similar to that expected from the 2:1 or 3:2 MMRs, even if these are not the specific resonances at the edge. To show this, the grey region on Fig. 7 is a theoretical prediction for the rms debris eccentricity expected for a population of bodies in the 2:1 or 3:2 MMRs, found by integrating the equations of motion for those MMRs (Pearce et al., in preparation). This is similar to the $(m_{\rm p}/m_*)^{1/3}$ scaling from Petrovich, Malhotra & Tremaine (2013, their equations 19 and 34), and agrees with our simulation results for lower planet-to-star mass ratios. Specifically, if a circular-orbit, non-migrating planet sculpts a debris-disc inner edge, then the rms eccentricity at that edge increases with planet mass, provided $m_{\rm p}/m_* \lesssim 3.3 \times 10^{-3}$.

For planet-to-star mass ratios above $\sim 3.3 \times 10^{-3}$, the inner-edge excitation is below that expected of 2:1 and 3:2 MMRs; this is because those MMRs would now lie inside the chaotic zone, and higher-order MMRs at semimajor axes outside the nominal 2:1 location are weaker and less effective at exciting debris (Fig. 2). Hence for planet-to-star mass ratios above $\sim 3.3 \times 10^{-3}$, the debris eccentricity at the disc edge does not further increase with mass ratio.

Given this behaviour, we can roughly quantify the eccentricity that a planet on a circular orbit induces on initially unexcited debris at the disc inner edge:

$$e_{\rm i,rms,p} \approx \begin{cases} 0.4\left(m_{\rm p}/m_*\right)^{1/3}, & \text{if } m_{\rm p}/m_* \leq 3.3 \times 10^{-3}; \\ 0.06, & \text{else.} \end{cases} \tag{7}$$

This is the black line on Fig. 7, which is a good match to the simulations where the planet-induced excitation dominates over the intrinsic disc excitation (e.g. the purple lines for mass ratios above 10^{-4}). Conversely, since the initial-disc excitation would dominate over the planet-induced excitation if the former were high enough, we can generally predict the eccentricity of surviving debris at the inner edge of a planet-sculpted debris disc as

$$e_{\rm i,rms} = \max\left(e_{\rm i,rms,p}, e_{\rm i,rms,0}\right), \tag{8}$$

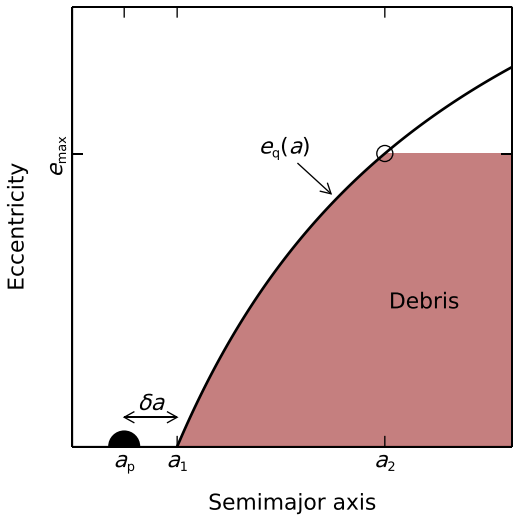

Figure 8. Schematic of our simple model for predicting the disc's inner-edge profile (Section 3). The black circle is the planet, and the red region surviving debris. Debris has eccentricities between 0 and $e_{\rm max}$. The planet eventually ejects all debris originating within its chaotic zone, which is any debris above the solid line (equations 9 and 10). The value a_1 is the smallest semimajor axis of any surviving particle (a circular orbit just exterior to the chaotic zone), and a_2 is the largest semimajor axis of any unstable particle (an orbit with the highest eccentricity $e_{\rm max}$, whose pericentre is at the outer edge of the chaotic zone).

where $e_{\rm i,\,rms,\,0}$ is the 'intrinsic' rms eccentricity at the disc edge (i.e. the pre-interaction eccentricity), and the planet-induced eccentricity $e_{\rm i,\,rms,\,p}$ is given by equation (7).

3 ANALYTIC MODEL RELATING THE INNER-EDGE PROFILE TO THE SCULPTING PLANET

In Section 2, we showed that, if a circular-orbit planet sculpts a collisionless debris disc, then the steepness and relative location of the disc's inner edge depend only on the planet-to-star mass ratio and the disc's initial-excitation level. We also quantified how the planet excites debris eccentricities at the inner edge. Using these results, we now produce a simple analytical model to infer the properties of sculpting planets from inner-edge profiles. Section 3.1 details our analytical model, and Section 3.2 demonstrates how to use it to infer the properties of an unseen sculpting planet from an observed inner-edge profile.

3.1 Model setup and predictions

We assume a simplified model of the inner-edge region, as shown on Fig. 8. We consider a planet on a circular orbit, and a debris disc that initially extends from the planet's semimajor axis out to some larger distance. The debris particles have initial eccentricities uniformly distributed between 0 and some $e_{\rm max}$; for this model, the origin of these eccentricities is unimportant. To predict the location and steepness of such a planet-sculpted disc edge, we consider which particles would be scattered by the planet, and which would survive.

In our model, any particle whose orbit comes within the planet's chaotic zone would be scattered and eventually ejected. This means that, at late times, no particles should occupy the parameter space above the solid line on Fig. 8; this line is the eccentricity $e_{\rm q}(a)$ that

Downloaded from https://academic.oup.com/mnras/article/doi/10.1093/mnras/stad3462/7382221 by guest on 23 November 2023

results in a particle's pericentre coinciding with the outer edge of the chaotic zone, defined by

$$e_{\rm q}(a) \equiv 1 - \frac{a_{\rm p} + \delta a}{a}. \tag{9}$$

Here, a is the semimajor axis, and δa is the half-width of the chaotic zone, taken as 3 Hill radii for a circular-planet orbit:

$$\delta a \equiv 3 r_{\rm H} = 3 a_{\rm p} \left(\frac{m_{\rm p}}{3 m_*} \right)^{1/3}. \tag{10}$$

Since the planet eccentricity is zero, any non-scattered debris would retain its initial semimajor axis and eccentricity. Hence, any debris with initial eccentricity above equation (9) line would eventually get ejected, whilst any with eccentricity below the line would remain unperturbed. So in our model, at late times debris only occupies the shaded region of Fig. 8.

In the following sections, we use this model to infer the location and steepness of the planet-sculpted inner edge. Before doing so, we must first define two final parameters: the semimajor axes a_1 and a_2, as shown on Fig. 8. The span a_1 to a_2 roughly defines the inner-edge region in semimajor-axis space. The values of a_1 and a_2 correspond to the semimajor axes of orbits at the edge of the chaotic zone; a_1 corresponds to a circular orbit, and a_2 to an orbit with eccentricity equal to the maximum debris eccentricity $e_{\rm max}$. Expressions for a_1 and a_2 are given in Appendix D1.

3.1.1 *Predicted radial location of the disc inner edge,* $r_{\rm i}$

We now use the simple model on Fig. 8 to predict $r_{\rm i}$, the characteristic location of a planet-sculpted inner edge. A full derivation of the $r_{\rm i}$ prediction is presented in Appendix D2; our basic method is to first calculate the time-averaged radial location of all debris at a single semimajor axis a, and then average these for all debris with $a_1 \leq a \leq a_2$. This yields our prediction:

$$r_{\rm i} \approx a_{\rm p} \left[1 + 3^{2/3} \left(\frac{m_{\rm p}}{m_*} \right)^{1/3} \right] \left(1 + \frac{2}{\sqrt{3}} e_{\rm i,rms} \right), \tag{11}$$

where we used $e_{\rm i,rms} = e_{\rm max}/\sqrt{3}$ for a uniform e distribution to convert $e_{\rm max}$ into $e_{\rm i,\,rms}$. Equation (11) predicts that the edge location depends on planet semimajor axis, planet mass, and debris eccentricity. The origin of this eccentricity is unimportant, provided that the eccentricity-semimajor axis distribution resembles that on Fig. 8. We can therefore evaluate the eccentricity term in equation (11) using equations (7) and (8). If the debris eccentricity is set by the intrinsic (i.e. pre-interaction) eccentricity of the disc, which would occur if the intrinsic eccentricity is higher than that induced by the planet, then $e_{\rm i,\,rms}$ in equation (11) can simply be replaced by the intrinsic disc eccentricity $e_{\rm i,\,rms,\,0}$. Alternatively, for a disc with sufficiently low pre-interaction eccentricity, we can substitute $e_{\rm i,\,rms} = e_{\rm i,\,rms,\,p}$ from equation (7) to predict the location of the planet-sculpted inner edge:

$$r_{\rm i} \approx \begin{cases} a_{\rm p} \left[1 + 2.5 \left(\frac{m_{\rm p}}{m_*} \right)^{1/3} \right], & \text{if } m_{\rm p}/m_* \leq 3.3 \times 10^{-3}; \\ a_{\rm p} \left[1.1 + 2.2 \left(\frac{m_{\rm p}}{m_*} \right)^{1/3} \right], & \text{else,} \end{cases} \tag{12}$$

where we omit higher-order terms in $(m_{\rm p}/m_*)^{1/3}$.

Having made a prediction for $r_{\rm i}$, we now compare this prediction to the results of our n-body simulations. For each simulation, we predict $r_{\rm i}$ by evaluating equation (11); to do this, we take $a_{\rm p}$ and $m_{\rm p}$ from the simulation setup, and also use the value of $e_{\rm i,\,rms}$ measured directly from the simulation. The results are shown on Fig. 9. We see that the prediction generally works well; the predicted value of $r_{\rm i} - a_{\rm p}$ for simulations with $e_{\rm max,\,0} < 0.3$ is typically within 10 per cent of that from simulations. However, the prediction is less accurate for discs with very high intrinsic eccentricities ($e_{\rm max,\,0} = 0.3$) that are interacting with low-mass planets ($m_{\rm p}/m_* \lesssim 10^{-4}$); for such high eccentricities there is considerable overlap of debris orbits, so our simple $r_{\rm i}$ approximation using only the average debris position probably no longer holds. There is also a noticeable divergence for planet-to-star mass ratios above 10^{-2}, which could be due to a fundamental shift in the dynamics; this is discussed in Section 2.3.3. None the less, equation (11) holds across the large majority of our explored parameter space, so offers a reasonable means to predict the location of a planet-sculpted inner edge.

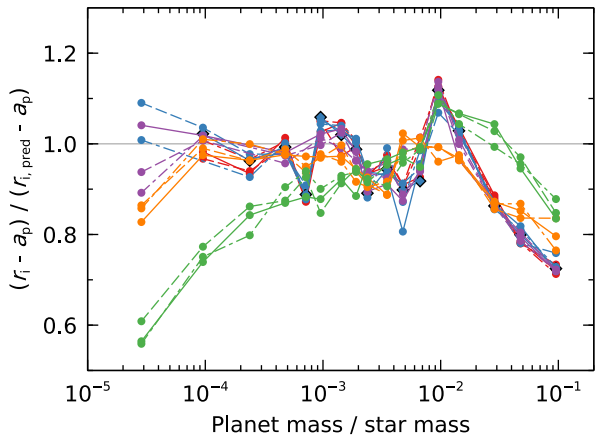

Figure 9. Comparison of our predicted inner-edge location to the results of n-body simulations. The vertical axis is the difference between the planet orbit and the inner-edge location $r_{\rm i}$ fitted from the simulations, divided by the equivalent value predicted by equation (11). The horizontal grey line denotes unity; all other symbols and lines are defined on Fig. 5. Our predicted edge locations are generally similar to those from the simulations, with the predictions typically within 10 per cent of the simulated values for planets below 1 per cent of the stellar mass and initial debris-excitation levels of $e_{\rm max,\,0} < 0.3$. Predictions are worse for larger mass ratios, and also for simulations with both high initial-debris eccentricities and low-mass planets.

3.1.2 *Predicted steepness of the disc inner edge,* σ_i

In this section, we use our simple model to predict the shape of the planet-sculpted inner edge, as quantified by $\sigma_{\rm i}$. Near the inner edge, our fitted profile (equation 6) is essentially an erf function; this has characteristic width $x r_{\rm i} \sigma_{\rm i}$, where x is a scalar of order unity. We hypothesize that this width should be roughly equivalent to the distance between the pericentre of the innermost stable particle and the apocentre of the outermost unstable particle, that is, $x r_{\rm i} \sigma_{\rm i} \approx a_2(1 + e_{\rm max}) - a_1$ from Fig. 8. Substituting expressions for $r_{\rm i}$, a_1 and a_2 yields $\sigma_{\rm i} \propto e_{\rm max}$ to first order in $e_{\rm max}$, that is, the steepness of a planet-sculpted inner edge depends entirely on the eccentricity of debris around that edge. Marino (2021) and Rafikov (2023) reached a similar conclusion for edges with sharp cut-offs in semimajor axis, but we show that this proportionality is also expected from the smooth distribution arising from scattering.

Since we expect $\sigma_{\rm i} \propto e_{\rm max}$, we use our n-body simulations to directly relate $\sigma_{\rm i}$ to debris eccentricity. Fig. 10 shows the rms eccentricities measured at the inner edges of our simulated discs, divided by the $\sigma_{\rm i}$ values fitted to those simulations. This ratio is

Downloaded from https://academic.oup.com/mnras/article/doi/10.1093/mnras/stad3462/7382221 by guest on 23 November 2023

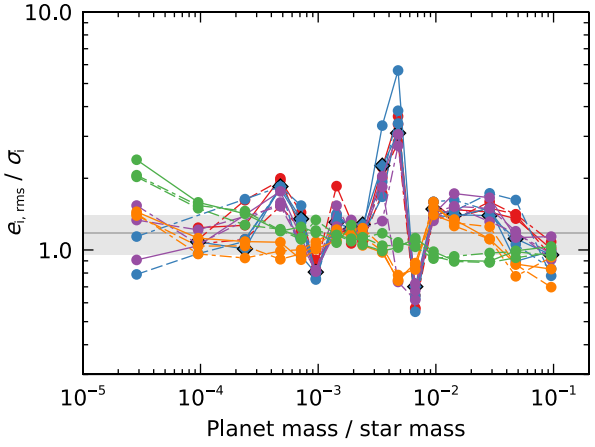

Figure 10. Relating the steepness of sculpted-disc inner edges to the debris eccentricities at those edges, from our n-body simulations. Smaller σ_i values correspond to steeper edges. Our simple model predicts σ_i and $e_{i,\,rms}$ to be proportional, in agreement with the simulations. The horizontal grey line and shaded region show the value and uncertainty of the pre-factor 1.2 ± 0.2 in equation (13), which is empirically measured from the simulations. All other lines and symbols are defined on Fig. 5. The breakdown in the fit at planet-to-star mass ratios between 10^{-3} and 10^{-2} for low-eccentricity simulations is due to the 2:1 MMR imposing additional structure on the edge (discussed in Section 2.3.2).

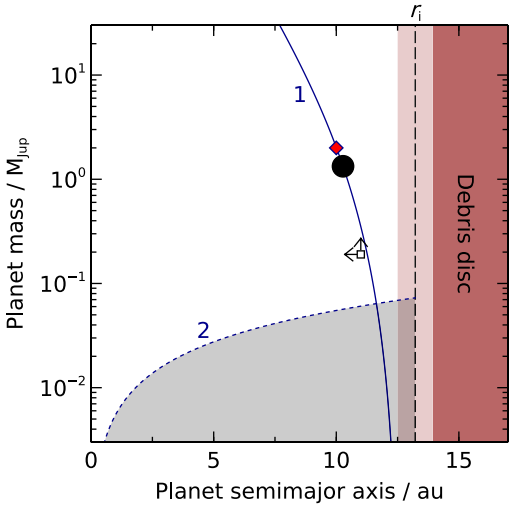

Figure 11. Example application of our results: using a debris disc's inner-edge profile to infer the properties of an unseen sculpting planet. The plot shows the disc from the n-body simulation on Fig. 2, for which we attempt to constrain the planet using the step-by-step method from Section 3.2.1. The disc has a fitted inner-edge radius $r_i = 13.2$ au and flatness $\sigma_i = 0.0361$. The dashed vertical line is r_i, and the light brown region around it is the approximate full width of the inner edge ($3r_i\sigma_i$). The large black circle shows the planet properties we infer, and the red diamond is the actual planet in the n-body simulation. The white square is the planet's minimum-possible mass and maximum semimajor axis found using the alternative method of Pearce et al. (2022), which accounts for the edge location but not its steepness. Line 1 shows the planet properties required to set the edge at r_i (equation 14), and Line 2 is the minimum planet mass required to have sculpted the disc edge within the age of the star (equation 15); for this example the age is arbitrarily taken as 100 Myr.

roughly constant for all simulations, verifying our prediction that σ_i depends only on e_{max} (and hence $e_{i,\,rms}$). Taking the median of this ratio from our simulations, we find that the flatness of the inner edge of a planet-sculpted disc depends on the eccentricity of debris at that edge as

$$e_{i,rms} \approx (1.2 \pm 0.2)\,\sigma_i. \tag{13}$$

Here, the uncertainty on the empirical pre-factor is defined from the inter-quartile range on $e_{i,\,rms}/\sigma_i$ from our simulations.

3.2 Inferring the properties of a sculpting planet from the location and shape of a debris-disc inner edge

Section 3.1 related the disc inner edge to the properties of a sculpting planet. Since it has historically been easier to resolve a cold debris disc than to detect a distant planet, it is common to use observed debris discs to infer the properties of unseen planets (e.g. Pearce et al. 2022). In this section, we provide a method to constrain a sculpting planet on a circular orbit from the shape and location of a debris-disc inner edge.

To demonstrate the method, we apply it to the simulation on Fig. 2 as a example. We assume that the simulated disc has been observed, but that the sculpting planet is undetectable. We will constrain the properties of the unseen planet from the disc alone, then compare these to the known parameters of the simulated planet to gauge the effectiveness of the method. The various steps in the calculation are shown on Fig. 11, and described below. For this example, we assume that the planet has finished sculpting the disc by the time the observations are made.

3.2.1 Step-by-step method

The first step is to fit the disc surface-density profile with some function that quantifies the location and steepness of the inner edge. In this paper, we use an erf-power-law function (equation 6), which yields inner-edge location r_i and flatness σ_i; other parametrizations could alternatively be used, and in Appendix E we provide equations to convert the outputs of common parametric models into r_i and σ_i values. For our example simulation, the fitted inner-edge profile has $r_i = 13.2$ au and $\sigma_i = 0.0361$.

The second step, now that we have the edge profile, is to infer the sculpting-planet mass as a function of its semimajor axis. This step makes the implicit assumption that the planet has a circular orbit and has not migrated, but it otherwise applies regardless of whether the planet or some other process is responsible for debris eccentricities. Equation (11) relates planet mass and semimajor axis to the location and rms eccentricity of the disc inner edge; using this equation, and noting the relation between $e_{i,\,rms}$ and σ_i (equation 13), we can infer the sculpting-planet mass using

$$m_p \approx 116\,M_{Jup}\left(\frac{m_*}{M_\odot}\right)\left[\frac{r_i}{a_p}\,(1+1.35\sigma_i)^{-1}-1\right]^3. \tag{14}$$

This is Line 1 on Fig. 11 (noting that $m_* = 1\,M_\odot$ in our example).

The next step is to put a lower bound on the planet mass, assuming that the planet has finished sculpting the observed-disc edge. This means that the sculpting time-scale must be shorter than the star age t_*. In Section 2.3.3, we showed that the sculpting time-scale is approximately the diffusion time if $m_p/m_* \lesssim 10^{-2}$, and $\sim$10 diffusion times otherwise; we can therefore re-arrange equation (3) and evaluate it at $a = r_i$ to show that

$$m_p \gtrsim 0.105\sqrt{k}\,M_{Jup}\left(\frac{t_*}{Myr}\right)^{-1/2}\left(\frac{a_p}{au}\right)\left(\frac{m_*}{M_\odot}\right)^{3/4}\left(\frac{r_i}{au}\right)^{-1/4}, \tag{15}$$

Downloaded from https://academic.oup.com/mnras/article/doi/10.1093/mnras/stad3462/7382221 by guest on 23 November 2023

where

$$k \approx \begin{cases} 1, & \text{if } m_{\rm p}/m_* \lesssim 10^{-2}; \\ 10, & \text{else.} \end{cases} \quad (16)$$

For our example, we ascribe an arbitrary stellar age of 100 Myr, which results in Line 2 on Fig. 11.

The final step is to use the edge shape to break the degeneracy between planet mass and semimajor axis. Unlike previous steps, this step requires the implicit assumption that the planet is solely responsible for exciting debris. It is also only valid if $\sigma_{\rm i} \lesssim 0.05$ (i.e. $e_{\rm i,\,rms} \lesssim 0.06$); this is the flattest profile that a non-migrating, circular-orbit planet could impart on an initially low-eccentricity disc (Fig. 7), so if $\sigma_{\rm i} \gtrsim 0.05$ then some other process must have excited debris and this step cannot be applied. If $\sigma_{\rm i} \lesssim 0.05$, then re-arranging equation (7) yields the planet mass as

$$m_{\rm p} \approx 2.64 \times 10^4\ {\rm M_{Jup}} \left(\frac{m_*}{\rm M_\odot}\right) \sigma_{\rm i}^3; \quad (17)$$

we can then substitute this mass into equation (14) to yield the planet's semimajor axis as

$$a_{\rm p} \approx r_{\rm i}\,(1 + 1.35\sigma_{\rm i})^{-1} \left[1 + 0.205 \left(\frac{m_{\rm p}}{\rm M_{Jup}}\right)^{1/3} \left(\frac{\rm m_*}{\rm M_\odot}\right)^{-1/3}\right]^{-1}. \quad (18)$$

For our example, this yields a planet mass of 1.24 $\rm M_{Jup}$ and semimajor axis 10.3 au; these are in good agreement with the actual values of 2 $\rm M_{Jup}$ and 10 au from the simulation, as shown on Fig. 11. Note that caution must be applied if $\sigma_{\rm i} \sim 0.05$ (i.e. $e_{\rm i,\,rms} \sim 0.06$), because such an edge profile could be imparted by any planet with $m_{\rm p}/m_* \gtrsim 3.3 \times 10^{-3}$ (Fig. 7); in this case, the mass estimate from equation (17) should be interpreted as a lower bound rather than a single value.

3.2.2 *Accuracy of planet parameters inferred from disc edges*

The above example showed that planet parameters can be well inferred from inner-edge profiles in at least some setups. We now repeat the above process for a large fraction of our simulations, to test how well the method applies in general. We omit simulations where the initial disc-excitation level is larger than the expected excitation generated by the planet, because for those simulations, equation (17) cannot be used to infer planet mass. The results are shown on Fig. 12. The top panel shows that the inferred debris-excitation level $e_{\rm i,\,rms}$, calculated from the edge profile using equation (13), agrees with the actual simulation values in almost all cases; the largest discrepancy is for planet-to-star mass ratios around 5×10^{-3}, which is where additional structure from the strong 2:1 MMR coincides with the disc edge. The bottom panel shows that the planet masses inferred using equation (17) agree with the actual planet masses for low-mass ratios, but that the two diverge if the actual planet has $m_{\rm p}/m_* \gtrsim 3.3 \times 10^{-3}$. For the highest mass ratios, equation (17) can underpredict the planet mass by over one order of magnitude. The reason for this is that, for planets with mass ratios above 3.3×10^{-3}, the level of eccentricity excitation imparted on the disc edge is independent of planet mass (Fig. 7); this can cause equation (17) to significantly underpredict the planet mass if debris at the disc edge has an excitation level of $e_{\rm i,\,rms} \approx 0.06$. Note that this degeneracy only affects the use of equation (17); regardless of the mass ratio, and whether or not the planet was responsible for exciting debris, a sculpting planet should still lie close to the mass–semimajor axis relation from equation (14) (Line 1 on Fig. 11).

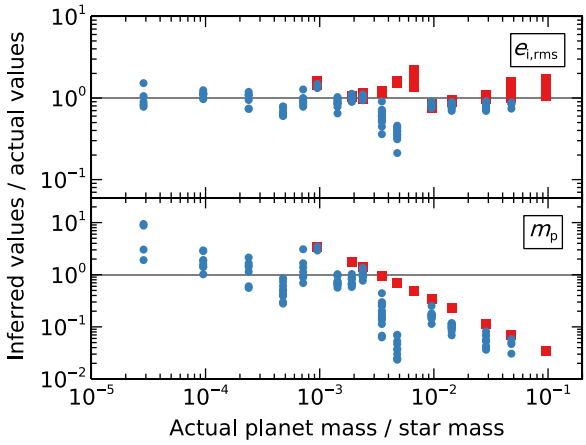

Figure 12. Planet properties inferred from simulated-disc inner edges using the process in Section 3.2, compared to the actual planets. Top panel: $e_{\rm i,\,rms}$ values inferred from our fitted inner-edge profiles (equation 13), which agree well with the actual values. Bottom panel: planet masses inferred from the edge steepnesses (equation 17), which agree well with the actual values for planet-to-star mass ratios below 3.3×10^{-3} (equivalent to 3.5 $\rm M_{Jup}$ around a Sun-like star). For higher ratios, equation (17) can significantly underpredict the planet mass, because the edge excitation level becomes constant with planet mass (Fig. 7). Note that this degeneracy only affects planet masses that were directly inferred from the edge steepness (black circle on Fig. 11); regardless of this, all planets would still lie along the mass–semimajor axis relation (Line 1 on Fig. 11). Blue circles and red squares are simulations where the inferred debris excitation $e_{\rm i,\,rms}$ at the disc inner edge is below and above 0.06, respectively (where $e_{\rm i,\,rms} \approx 0.06$ corresponds to an edge profile with $\sigma_{\rm i} \approx 0.05$).

4 COLLISIONS

Sections 2 and 3 assessed how a circular-orbit planet would sculpt the inner edge of a debris disc, if the interaction were purely n-body dynamics. For that scenario we showed that the edge steepness could be directly related to the planet mass. However, in a real disc, there are also collisions between debris bodies, which would alter the edge profile. In this section, we consider the collisional evolution, and answer two basic questions: could a collision-dominated disc edge be differentiated from a planet-dominated edge, and how would collisions change the profile of a planet-sculpted edge?

4.1 Could a purely collisional disc be differentiated from a purely planet-sculpted disc?

Destructive collisions cause debris discs to lose mass over time; material grinds down to dust, which is eventually removed by radiation forces (Wyatt et al. 1999; Wyatt 2008; Krivov 2010). The rate at which this process occurs depends on several main factors: the number density of debris bodies, their size distribution, and their relative velocities.

For an initially broad debris disc, these factors result in well-defined collisional evolution. At early times, the surface density is expected to decrease with distance, for example, going as $r^{-1.5}$ in the MMSN. Relative velocities are also higher in the inner regions, and this combination makes the initial collisional depletion faster closer to the star. However, this means that the surface density closer to the star drops faster than that further out, reducing the inner collision rate. The result is that the initially negative surface-density slope gradually transforms into a positive one; a 'collision front' moves outwards across the disc, where the region interior to the front tends

Downloaded from https://academic.oup.com/mnras/article/doi/10.1093/mnras/stad3462/7382221 by guest on 23 November 2023

towards a positive surface-density slope, whilst the exterior region still has its original profile. In the collisionally processed region, this profile is well characterized as a power law r^{p_i}, with index $p_i = 7/3 = 2.3$ in Wyatt et al. (2007) and Kennedy & Wyatt (2010), or $p_i = 2$ in more-recent models (Löhne et al. 2008; Imaz Blanco et al. 2023).

Conversely, if a planet sculpts a collisionless disc, then the inner-edge steepness is set by the planet mass. To answer whether such a planet-dominated disc can be differentiated from a collision-dominated disc, we must compare the inner-edge slopes. Using equation (E5) to relate an erf-fitted slope to a power-law slope, we see that a planet-dominated disc will have a steeper inner edge than a collision-dominated disc if $\sigma_i < 0.40$ (assuming $p_i = 2$ for the collisional disc; if $p_i = 7/3$ were used instead, then $\sigma_i < 0.35$ for the sculpted edge to be steeper). Fig. 6 shows that these conditions are satisfied by the end of all of our circular-planet simulations, meaning that the inner edge of a purely planet-sculpted disc is steeper than that of a purely collisional disc if sculpting has completed. In some cases, it would be much steeper; our steepest n-body discs have $\sigma_i \sim 10^{-2}$, which would correspond to $p_i > 10$ in r^{p_i} notation. So we should be able to differentiate purely planet-sculpted discs from purely collision-dominated discs, with the former having much steeper inner edges.

4.2 How would collisions affect a planet-sculpted edge?

The previous section compared a collisionless, planet-sculpted disc to a collisional disc without a planet. However, in reality a planet-sculpted disc would also undergo collisions. In this section, we consider collisions in more detail, to assess how they would affect a planet-sculpted disc.

A fully self-consistent model, where a disc undergoes n-body interactions whilst simultaneously collisionally evolving, is difficult to properly implement. In particular, there are several parameters that are critical for quantifying the collisional evolution, but that are fundamentally unknown for real debris discs; these include the debris-disc mass, and the sizes of the largest planetesimals (Krivov & Wyatt 2021). For this reason, we chose to decouple the dynamical and collisional modelling in this paper. Instead, we will take the disc morphologies arising from our n-body simulations, and then input these into a collisional model to estimate how collisions would modify a planet-sculpted disc edge. This approach is not fully self-consistent, but would be valid if the planet-sculpting time-scale were much shorter than the collisional time-scale; we will later show that this condition holds for many plausible scenarios.

4.2.1 *Collisional model*

To model collisions, we use a MATHEMATICA implementation of the Löhne et al. (2008) collisional model. The model takes an axisymmetric surface-density profile, and splits it into radial bins. Each bin is then treated separately, and the dust mass in each bin is determined after some time. We then use the masses in each radial bin to calculate the dust surface-density profile. In this section, we briefly describe the model and the parameters we use; we refer the reader to Löhne et al. (2008) for a much more detailed description.

We assume the eccentricity e and inclination I of the debris population are related by $I \approx e/2$, and treat e as a free parameter. Following Löhne et al. (2012), Schüppler et al. (2016), and Krivov et al. (2018), we assume a critical fragmentation energy of

$$Q_D^* = \left(\frac{v_{col}}{v_0}\right)^{1/2} \left[A_s \left(\frac{s}{1\,\mathrm{m}}\right)^{3b_s} + A_g \left(\frac{s}{1\,\mathrm{km}}\right)^{3b_g}\right], \tag{19}$$

with $v_0 = 3\,\mathrm{km\,s^{-1}}$, $A_s = A_g = 5 \times 10^6\,\mathrm{erg\,g^{-1}}$, $b_s = -0.12$, and $b_g = 0.46$. The planetesimal-collision speed v_{col} is given by

$$v_{col} = \sqrt{\frac{\mathcal{G}m_*}{r}}\, f(e, I), \tag{20}$$

where $\mathcal{G}$ is the gravitational constant and

$$f(e, I) = \sqrt{\frac{5}{4}e^2 + I^2}. \tag{21}$$

The value of Q_D^* is dominated by the material strength for smaller bodies, and gravity for larger bodies. The transition between these can be defined either as the size at which the strength and gravity terms in equation (19) are equal, or as the size at which Q_D^* is minimized. Following Löhne et al. (2008), here we use the former definition. For our parameters, the strength-gravity transition then occurs at the 'breaking' radius $s_b = 232\,\mathrm{m}$.

We assume that debris in each bin follows a three-slope size distribution as in Löhne et al. (2008), with slope $q_p = 1.87$ for primordial bodies, $q_g = 1.68$ in the gravity-dominated quasi-steady state and $q_s = 1.89$ in the strength-dominated quasi-steady state. We choose minimum and maximum dust-grain radii of $s_{min} = 2\,\mu\mathrm{m}$ and $s_{dust} = 1\,\mathrm{mm}$, and treat the largest-planetesimal radius s_{max} as a free parameter. We use a bulk density of solids $\rho = 3.5\,\mathrm{g\,cm^{-3}}$.

According to the model, there are two key time-scales that determine the collisional evolution. The shorter, τ_b, is the time when the weakest bodies begin to collide. At this time, the collisional decay of the dust density sets in (if $q_p \leq q_s$) or at least speeds up (if $q_p > q_s$); see equation (43) and fig. 9 in Löhne et al. (2008). The value of τ_b is given by equation (31) in Löhne et al. (2008):

$$\tau_b = \frac{16\pi\rho}{3M_0}\left(\frac{s_b}{s_{max}}\right)^{3q_p-5} \frac{s_{max} r^{7/2}}{\sqrt{\mathcal{G}m_*}} \frac{\delta r}{r} \times \frac{q_p - 5/3}{2 - q_p}\left[1 - \left(\frac{s_{min}}{s_{max}}\right)^{6-3q_p}\right] \frac{I}{f(e, I) G(q_p, s_b, r)}, \tag{22}$$

where M_0 is the total initial mass of solids in the bin, δr is the radial width of the bin,

$$G(q, s, r) = \left[X_c(s, r)^{5-3q} - \left(\frac{s_{max}}{s}\right)^{5-3q}\right] + 2\frac{q - 5/3}{q - 4/3}\left[X_c(s, r)^{4-3q} - \left(\frac{s_{max}}{s}\right)^{4-3q}\right] + \frac{q - 5/3}{q - 1}\left[X_c(s, r)^{3-3q} - \left(\frac{s_{max}}{s}\right)^{3-3q}\right], \tag{23}$$

and

$$X_c(s, r) = \left[\frac{2Q_D^*(s, r) r}{f^2(e, I)\mathcal{G}m_*}\right]^{1/3}. \tag{24}$$

We arbitrarily use $\delta r/r = 0.1$ in our code, but this later cancels out so its value does not affect any results.

Downloaded from https://academic.oup.com/mnras/article/doi/10.1093/mnras/stad3462/7382221 by guest on 23 November 2023

The longer time-scale is $\tau_{\rm max}$: the collisional lifetime of the largest planetesimals. This is equation (42) in Löhne et al. (2008):[3]

$$\tau_{\rm max} = \frac{16\pi\rho}{3M_0}\frac{s_{\rm max}r^{7/2}}{\sqrt{\mathcal{G}m_*}}\frac{\delta r}{r} \times \frac{q_{\rm g}-5/3}{2-q_{\rm p}}\left[1-\left(\frac{s_{\rm min}}{s_{\rm max}}\right)^{6-3q_{\rm p}}\right]\frac{I}{f(e,I)G(q_{\rm g},s_{\rm max},r)}. \quad (25)$$

We will later show that $\tau_{\rm max}$ is the most important factor for determining the collisional behaviour. We provide an open-access PYTHON code to calculate $\tau_{\rm max}$ given the assumptions in this paper,[4] and in Section 4.2.3, we write $\tau_{\rm max}$ in an alternative form to make its dependencies more explicit.

Given the above setup, the model yields the dust mass $m_{\rm dust}$ in each radial bin after some time t. This is equation (43) in Löhne et al. (2008):

$$m_{\rm dust}(t) = \frac{M_0}{1+t/\tau_{\rm max}}\mathcal{T}^{(q_{\rm g}-q_{\rm p})/[q_{\rm p}-5/3+(q_{\rm p}-1)b_{\rm g}]}\frac{2-q_{\rm p}}{2-q_{\rm s}} \times \left(\frac{s_{\rm b}}{s_{\rm max}}\right)^{6-3q_{\rm p}}\left[\left(\frac{s_{\rm dust}}{s_{\rm b}}\right)^{6-3q_{\rm s}}-\left(\frac{s_{\rm min}}{s_{\rm b}}\right)^{6-3q_{\rm s}}\right]^{-1}, \quad (26)$$

for $\tau_{\rm b} < t < \tau_{\rm max}$, where $\mathcal{T} = t/\tau_{\rm b}$ if $t < \tau_{\rm max}$ or $\tau_{\rm max}/\tau_{\rm b}$, otherwise.[5] For $t < \tau_{\rm b}$, $q_{\rm g}$ and $b_{\rm g}$ should be replaced by $q_{\rm s}$ and $b_{\rm s}$, respectively.

For each collisional simulation, we initialize the disc with a surface-density profile similar to the outcomes of our n-body simulations. This is a power law with a truncated inner edge:

$$\Sigma(r) = x_{\rm m}\left(\frac{r}{\rm au}\right)^{-\alpha}\frac{\rm M_\oplus}{\rm au^2} \times \frac{1}{2}\left[1-{\rm erf}\left(\frac{r_{\rm i}-r}{\sqrt{2}\sigma_{\rm i}r_{\rm i}}\right)\right], \quad (27)$$

where a disc with $x_{\rm m} = 1$ and $\alpha = 3/2$ would have the MMSN profile beyond the inner edge. This initial profile sets M_0 in the above equations. The initial values of $x_{\rm m}$ and α are free parameters that we vary between models. After setting up the disc, we use equation (26) to determine the dust mass in each radial bin after some time. Using these bin masses, we compute the dust surface-density profile. Finally, we fit this profile with an erf-power-law function similar to equation (27), to measure $r_{\rm i}$, $\sigma_{\rm i}$ and α at that time.

4.2.2 *Collision results*

The previous section described the collisional model. In this section, we apply the model to assess the impact of collisions on planet-sculpted disc edges.

We first apply it to the n-body disc from Fig. 2 as an example. We initialize the disc with $x_{\rm m} = 1$ and $\alpha = 3/2$, with an inner edge defined by $r_{\rm i} = 13.2$ au and $\sigma_{\rm i} = 0.0361$, and set the largest-planetesimal radius to $s_{\rm max} = 50$ km. We also set the debris eccentricity to 0.043, the rms eccentricity at the disc inner edge in the n-body simulation. This results in $\tau_{\rm max} = 1.1$ Gyr and $\tau_{\rm b} = 0.14$ Myr at 13.2 au (equations 22 and 25). We then use the collisional model to calculate the edge profile at various times up to 10 Gyr, the lifetime of the solar-type star. The first snapshot is made shortly after $\tau_{\rm b}$, to ensure there is sufficient dust in the system. Fig. 13 shows the results; the inner edge is largely unchanged for the first 100 Myr, but from 1 Gyr collisions begin to make the edge flatter. We quantify this flattening using the erf-power-law function; at 0.2, 10, 100, 10^3, and 10^4 Myr, the respective fitted values are $r_{\rm i} = 13.1$, 13.0, 13.0, 13.0, and 13.2 au, and $\sigma_{\rm i} = 0.034$, 0.042, 0.043, 0.064, and 0.11. Note that the erf function is an increasingly poor fit to the edge shape as $\tau_{\rm max}$ is approached, due to the complex edge profile.

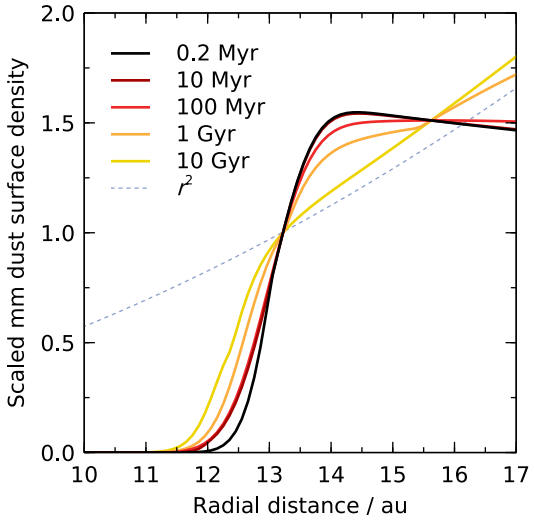

Figure 13. Collisional evolution of the planet-sculpted disc from Fig. 2, according to the Löhne et al. (2008) model (Section 4.2). We initialize the disc with $r_{\rm i} = 13.2$ au and $\sigma_{\rm i} = 0.0361$, and assume $m_* = 1\,{\rm M}_\odot$, $x_{\rm m} = 1$, and $s_{\rm max} = 50$ km. This yields $\tau_{\rm max} = 1.1$ Gyr and $\tau_{\rm b} = 0.14$ Myr at 13.2 au. Solid lines show the edge at various times; collisions flatten the edge, tending towards an r^2 profile (dashed line). Note that our simulated collisions only deplete material; the lines are scaled to the same value at 13.2 au for gradient comparison, giving the impression that the surface density increases with time at some radii, but in reality it decreases at each successive snapshot and unscaled lines would not cross (the lines are scaled because the surface density drops considerably with time, and a logarithmic plot would skew the gradient comparison). The edge undergoes little evolution until the time becomes comparable to $\tau_{\rm max}$; after that, the edge starts to flatten.

Fig. 13 demonstrates the importance of $\tau_{\rm max}$ in setting the collisional evolution. Before $\tau_{\rm max}$, collisions have little effect on the inner-edge profile. However, once $\tau_{\rm max}$ is reached, collisions start to have a significant effect, making the edge flatter. This collisional profile is expected to eventually tend towards r^2, the profile for a broad collisional disc, as shown by the dashed line on Fig. 13. However, in this example the profile is never reached within the stellar lifetime; in fact, the inner edge assumes two slopes, with an erf-like profile interior to $r_{\rm i}$ and a flatter, positive profile beyond this. This means that, in this example, the effect of planet sculpting would still be visible on the disc's inner-edge even at very late times.[6]

Fig. 13 was for one example setup. Fig. 14 shows how the inner-edge steepness collisionally evolves in a number of different setups, demonstrating that this evolution is both qualitatively and quantitatively similar across a broad parameter space. Starting with the setup from Fig. 13 as a reference, we vary the input parameters and re-run the collisional simulation multiple times. We see that all of the setups have the same general collisional evolution. First, between

[3]Equation (42) in Löhne et al. (2008) has an erroneous index of -1 around the square bracket, which we omit here; this does not affect our results because $s_{\rm min} \ll s_{\rm max}$.

[4]http://www.tdpearce.uk/public-code

[5]Equation (43) in Löhne et al. (2008) has erroneous indices of $2-q$ instead of $6-3q$, for $q_{\rm p}$ and $q_{\rm s}$.

[6]Since dust mass, and hence brightness, decreases with time, a real observation of a collisionally evolved disc might require a high signal-to-noise ratio to detect the deviation from an r^2 profile at $r_{\rm i}$.

Downloaded from https://academic.oup.com/mnras/article/doi/10.1093/mnras/stad3462/7382221 by guest on 23 November 2023

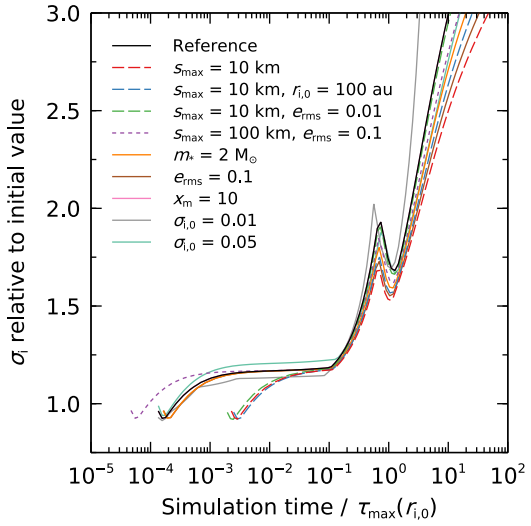

Figure 14. General collisional evolution of the inner edge of a planet-sculpted debris disc. The plot shows the evolution of the inner-edge profile over time, where time is expressed relative to $\tau_{\max}(r_{\mathrm{i},0})$, the collisional lifetime of the largest planetesimals at the initial inner edge. The simulations start at time τ_{b}. The black line is the reference simulation from Fig. 13, and other lines show simulations that differ from the reference setup by the parameters listed in the key. At early times collisions make the edge slightly flatter (i.e. increase σ_{i}), before making it significantly flatter as the time approaches $\tau_{\max}(r_{\mathrm{i},0})$. The local peak around $\tau_{\max}$ should be ignored; it arises because the erf-power-law function used to fit the profile struggles with the complex edge shape at this time.

τ_{b} and $\tau_{\max}$ the inner edge becomes slightly flatter, with σ_{i} increasing by a factor of $\sim$1.2. This remains constant, until the time approaches $\tau_{\max}$; around this time the edge becomes much flatter, and tends towards the r^2 collisional profile. The plot shows the importance of $\tau_{\max}$ in setting the collisional evolution of the sculpted-disc edge.

4.2.3 *Implications of collisions for planet-sculpted debris discs*

The previous sections showed that collisions have a very small effect on the inner-edge profile, until the time $\tau_{\max}$. After this, a planet-sculpted edge would become significantly flatter. Consideration of $\tau_{\max}$, the stellar lifetime and the planet-sculpting time-scale t_{diff} are therefore vital for assessing the effect of collisions on the edge profile.

We can use the above time-scales to identify three possibilities for the evolution of the debris-disc inner edge, depending on t_{diff} and $\tau_{\max}$:

(i) $t_{\mathrm{diff}} \ll \tau_{\max}$: the planet sculpts the disc, producing a sharp inner edge like our n-body simulations. This edge then gradually gets flatter due to collisions, but does not change significantly until the time approaches $\tau_{\max}$. Then, if left long enough, it may eventually assume an r^2 profile.

(ii) $t_{\mathrm{diff}} \sim \tau_{\max}$: unknown outcome. In this regime planetary sculpting and collisions are equally important at all times, and our simulations are insufficient to model this.

(iii) $t_{\mathrm{diff}} \gg \tau_{\max}$: the disc collisionally evolves almost as if no planet were present. The disc tends toward an r^2 profile.

So if t_{diff} and $\tau_{\max}$ are known, then the relative importance of collisions to planetary sculpting can be ascertained, and the evolution of the disc edge predicted. However, whilst t_{diff} is straightforward, equations (23)–(25) show that $\tau_{\max}$ is a complicated function depending on many parameters, several of which are interdependent and unknown.

We can gain deeper insight by rewriting $\tau_{\max}$, to make its dependencies more explicit. Equations (23)–(25) give $\tau_{\max}$, G, and X_{c} in their general forms; we can simplify these by substituting our assumed form for the initial $\Sigma(r)$, as well as Q_{D}^*, f, I/e, etc. We also assume $s_{\max} \gg s_{\min}$. For the region beyond the inner edge, this yields

$$\tau_{\max} = \frac{649\ \mathrm{yr}}{x_{\mathrm{m}}} \frac{q_{\mathrm{g}} - 5/3}{2 - q_{\mathrm{p}}} \left(\frac{r}{\mathrm{au}}\right)^{3/2+\alpha} \left(\frac{s_{\max}}{\mathrm{km}}\right) \left(\frac{m_*}{\mathrm{M}_\odot}\right)^{-1/2} \times \left(\frac{\rho}{\mathrm{g\ cm^{-3}}}\right) G^{-1}(q_{\mathrm{g}}, s_{\max}, r), \tag{28}$$

where

$$G(q_{\mathrm{g}}, s_{\max}, r) = \left[X_{\mathrm{c}}(s_{\max}, r)^{5-3q_{\mathrm{g}}} - 1\right] + 2\frac{q_{\mathrm{g}} - 5/3}{q_{\mathrm{g}} - 4/3}\left[X_{\mathrm{c}}(s_{\max}, r)^{4-3q_{\mathrm{g}}} - 1\right] + \frac{q_{\mathrm{g}} - 5/3}{q_{\mathrm{g}} - 1}\left[X_{\mathrm{c}}(s_{\max}, r)^{3-3q_{\mathrm{g}}} - 1\right] \tag{29}$$

and

$$X_{\mathrm{c}}(s_{\max}, r) = 0.0138\, e^{-1/2} \left(\frac{s_{\max}}{\mathrm{km}}\right)^{b_{\mathrm{g}}} \left(\frac{r}{\mathrm{au}}\right)^{1/4} \left(\frac{m_*}{\mathrm{M}_\odot}\right)^{-1/4}. \tag{30}$$

Expressing the equations in this form demonstrates that $\tau_{\max}$ is inversely proportional to the unknown x_{m}, which is related to the initial mass of the debris disc in MMSN units. We use this to better visualize $\tau_{\max}$.

Fig. 15 shows $\tau_{\max}$ multiplied by x_{m}, for a Solar-type star and a disc with an initial surface-density profile of $r^{3/2}$. The figure shows that, for reasonable debris parameters, $\tau_{\max}$ is typically extremely long, unless $s_{\max}$ is very small or x_{m} very large. However, $s_{\max}$ is unlikely to be smaller than a few kilometres, otherwise it would violate planetesimal-formation models and the statistics of discs of various ages (Krivov & Wyatt 2021, and references therein). A 100 au disc with debris eccentricity 0.01 would therefore have $x_{\mathrm{m}}\tau_{\max} \sim 10^{10}$ yr. Furthermore, $x_{\mathrm{m}} > 10$ is unlikely because such debris discs would have masses exceeding those of solids in the preceding, protoplanetary stage (Krivov & Wyatt 2021). As a result, for many observed debris discs $\tau_{\max}$ may be longer than the $\sim 10^7$ to 10^9 yr system age. In fact, $\tau_{\max}$ can even be infinite, which means that collisions never disrupt the largest bodies; this occurs in the large regions of parameter space where $X_{\mathrm{c}}(s_{\max}) \geq 1$ (for which $G \leq 0$). Re-arranging equation (24), $\tau_{\max}$ becomes infinite if

$$Q_{\mathrm{D}}^*(s_{\max}) \geq \frac{f^2 G m_*}{2r}, \tag{31}$$

which yields the solid lines on Fig. 15.

Conversely, calculating t_{diff} (equation 2) shows that a Jupiter-mass planet located within 100 au of a Solar-mass star would finish sculpting a disc within <10 Myr. So if such planets were sculpting debris discs, then they would likely do so long before collisions had any effect on the inner edges. This would make the inner-edge profiles long lived, and since even $10\tau_{\max}$ is insufficient to fully erase the planet's signature in the example on Fig. 13, it is likely that a disc sculpted by a massive planet would maintain a distinctive shape even if collisions were fully accounted for. For such cases, the planet can be constrained using the process in Section 3.2. For smaller, Neptune-mass planets the sculpting time-scale is 100 times longer, in which case both collisions and planets could simultaneously sculpt the discs. Such systems may not have reached their final configurations by the time they are observed, meaning that the disc edges would be

Downloaded from https://academic.oup.com/mnras/article/doi/10.1093/mnras/stad3462/7382221 by guest on 23 November 2023

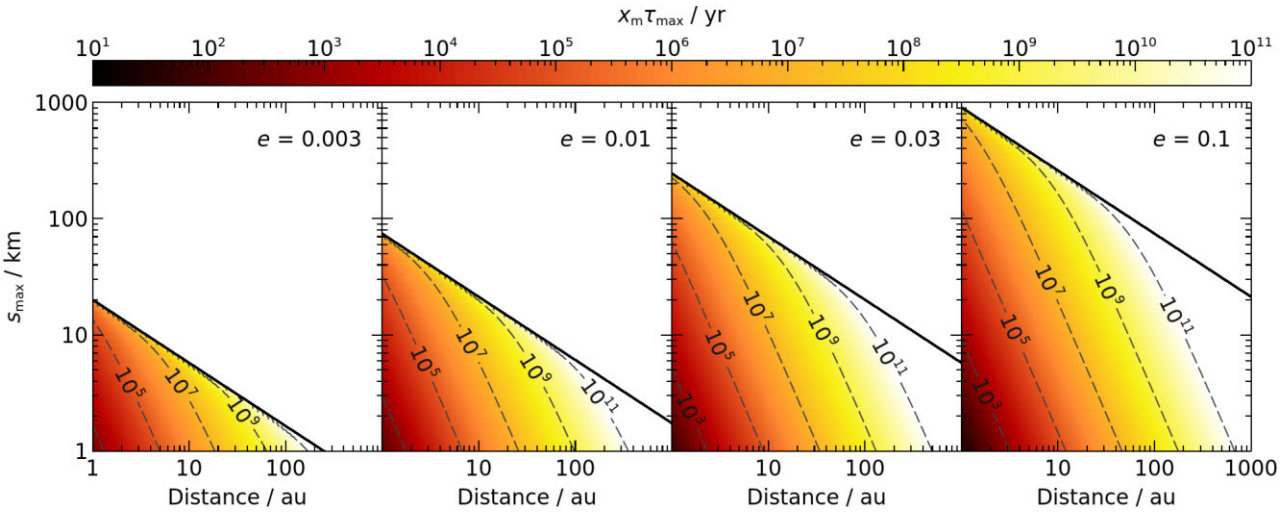

Figure 15. Plots of τ_{max} (collisional lifetime of the largest debris) multiplied by x_m (initial surface density relative to the MMSN), for a Solar-type star and a disc with an initial surface-density profile of $r^{3/2}$. The plots show that τ_{max} strongly depends on distance, s_{max} and debris eccentricity, and can sometimes be very long. It is unlikely that $x_m > 10$, so τ_{max} can be much longer than the $\sim 10^7$ to 10^9 yr ages of debris-disc systems. If the largest bodies lie above the solid line (equation 31), then they would never be destroyed and τ_{max} becomes infinite. Note that x_m and s_{max} cannot be arbitrarily varied for an observed debris disc; only certain combinations are allowed, since they set the observed-dust mass at the system age (equation 26). Increasing or decreasing the star mass respectively raises or lowers the contours slightly, but does not have a large effect.

somewhere between the very steep values expected for such planets, and the r^2 profile expected from collisions. This is discussed further in Section 6.1.

5 APPLICATION TO OBSERVED DEBRIS DISCS

Finally, we now compare the inner-edge slopes we predict from planetary sculpting to the inner edges of observed debris discs. We consider seven ALMA-resolved, extrasolar debris discs, each of which has a literature measurement of its inner-edge steepness. The systems are listed in Table 1, and were analysed by Lovell et al. (2021), Faramaz et al. (2021), and Imaz Blanco et al. (2023).

The literature works used various parametrizations to quantify disc profiles, which we must first convert to erf-power-law functions for comparison with our simulations. The literature works generally fitted the inner edges using a radial power law, with some turnover occurring further out; this turnover could be the disc outer edge, or a gap within the disc. For our analyses, the nature of the turnover is unimportant, but its location is needed to define the 'inner' region of the disc. Following Lovell et al. (2021), we quantify the surface densities around the inner edges of the literature discs using a double power law:

$$\Sigma(r) \propto \left[\left(\frac{r}{r_t} \right)^{-\eta p_i} + \left(\frac{r}{r_t} \right)^{-\eta p_o} \right]^{-1/\eta}, \quad (32)$$

where p_i is the slope of the inner edge, r_t is the radial location of the turnover, p_o is the slope exterior to the turnover, and η sets how sharp the turnover is. The assumed values for each disc are listed in Table 1; for fits where η was undefined or unconstrained, we assumed a value of 2 as in Lovell et al. (2021).

We next convert these power-law fits into erf-power-law profiles for comparison with our simulations. This is not strictly valid as we should really fit our erf-power-law profile to the underlying data, but it should be sufficient for this simple analysis. We consider the profile

$$\Sigma(r) \propto \left[1 - \mathrm{erf} \left(\frac{r_i - r}{\sqrt{2}\sigma_i r_i} \right) \right] \left(\frac{r}{r_i} \right)^{p_o}, \quad (33)$$

which is equivalent our equation (6) near the inner edge. We set p_o to the literature values describing the region just beyond the edge, noting that p_o is typically negative. We then use equation (C1) to convert the inner-edge power-law index p_i to an equivalent flatness σ_i, which approximates how the inner edge would appear if fitted with an erf function instead. Finally, we deduce r_i, which characterizes the location of the inner edge in the erf model, such that equations (32) and (33) peak at the same radial location. A comparison of the erf-power-law and double-power-law profiles for an example system is shown on Fig. E1, and the inferred values of σ_i and r_i are listed for all systems in Table 1. In some cases r_i could not be fitted because the region beyond the turnover was so steep that equation (33) does not turn over; however, this does not affect the edge flatness σ_i, which is the parameter of interest in this section.

Fig. 16 shows the inferred σ_i values for the observed discs, which exhibit a range of inner-edge slopes. At least two have relatively flat slopes consistent with pure collisional evolution, which would yield power-law indices of $p_i \approx 2$ as described in Section 4 (equivalent to $\sigma_i \approx 0.4$, shown as the dashed line on Fig. 16). Several have much steeper inner edges, which Imaz Blanco et al. (2023) argued are indicative of planetary sculpting. However, whilst those edges are indeed steeper than expected from collisions alone, they are still *flatter* than our simulations predict for *in-situ* sculpting of low-eccentricity discs by planets on circular orbits. The shaded region on Fig. 16 shows the maximum σ_i expected if a $m_p/m_* \leq 10^{-3}$ planet sculpts a disc with $e_{max,0} \leq 0.1$; all of the observed inner edges are flatter than this.[7] In Section 6.1, we discuss the potential implications of these flatter edges, which could teach us about architectures,

[7]Whilst a planet with mass $m_p/m_* \approx 0.07$ could drive σ_i to required values of 0.11 (Fig. 6), we disfavour this possibility because it seems unlikely that planets with such specific masses exist in two of our seven systems.

Downloaded from https://academic.oup.com/mnras/article/doi/10.1093/mnras/stad3462/7382221 by guest on 23 November 2023

Table 1. Constraints on the inner edges of several axisymmetric, extrasolar debris discs. The parameters r_t, p_i, p_o, and η are from literature fits to the surface-density profiles in the inner-edge regions (equation 32), and r_i and σ_i are the equivalent parameters in our erf-power-law model for comparison with our simulations (equation 33). Note that p_i and p_o are often 0.5 larger than the values provided in disc-imaging papers, because we consider the surface-density slope, whilst those papers often give the intensity slope (e.g. Imaz Blanco et al. 2023).

System	Name	Star mass ($M_\odot$)	Age (Myr)	r_t (au)	p_i	p_o	η	r_i (au)	σ_i	References
HD 9672	49 Ceti	1.98 ± 0.01	45 ± 5	131^{+13}_{-12}	$1.3^{+0.4}_{-0.3}$	$-3.0^{+0.4}_{-0.5}$	2	–	$0.6^{+0.1}_{-0.2}$	1, 3
HD 10 647	q^1 Eri	$1.13^{+0.03}_{-0.04}$	1700 ± 600	76 ± 1	>5.6	-2.1 ± 0.2	2	70	<0.14	1, 4
HD 92 945	V419 Hya	0.87 ± 0.01	250 ± 100	54 ± 2	8 ± 2	$-0.8^{+0.4}_{-0.6}$	2	52	0.11 ± 0.03	1, 3
HD 107 146	–	$1.03^{+0.02}_{-0.04}$	150^{+100}_{-50}	44 ± 2	$7.2^{+0.9}_{-0.7}$	$-0.2^{+0.1}_{-0.2}$	$2.8^{+1.2}_{-0.7}$	41	0.11 ± 0.01	1, 3
HD 197 481	AU Mic	0.59 ± 0.03	24 ± 3	36.4 ± 0.7	1.4 ± 0.4	-9 ± 1	2	–	0.6 ± 0.3	1, 3
HD 206 893	–	$1.32^{+0.07}_{-0.05}$	160 ± 20	35^{+7}_{-10}	>1.1	-2.2 ± 0.2	2	–	<0.76	2, 3
HD 218 396	HR 8799	1.59 ± 0.02	42^{+6}_{-4}	180^{+10}_{-20}	$3.0^{+0.9}_{-0.5}$	$-0.6^{+0.5}_{-0.3}$	2	160	$0.27^{+0.04}_{-0.08}$	1, 5

Notes. References: Star masses and ages from (1) Pearce et al. (2022) and (2) Hinkley et al. (2023). ALMA surface-density fits from (3) Imaz Blanco et al. (2023),
(4) Lovell et al. (2021), and (5) Model 2 in Faramaz et al. (2021).

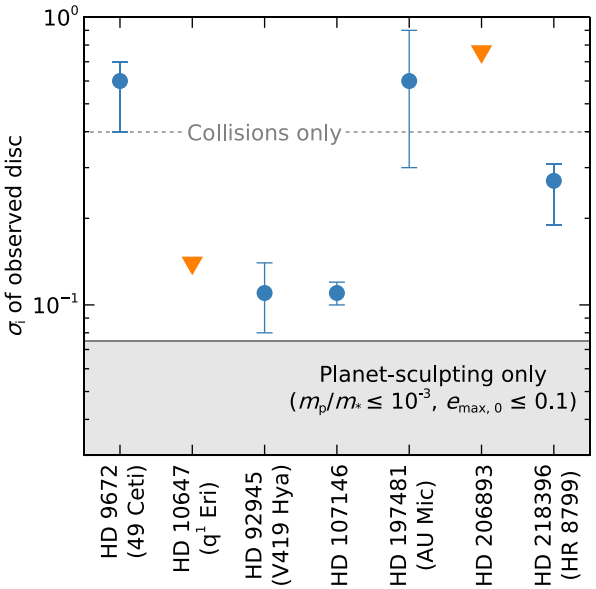

Figure 16. Flatness of the inner edges of observed discs (Table 1). Blue circles and orange triangles are σ_i values and upper limits, respectively. Several discs (49 Ceti, AU Mic, and HD 206893) have flat inner-edge slopes consistent with pure collisional evolution, as shown by the dashed horizontal line. Other discs (q^1 Eri, HD 92945, and HD 107146) have much steeper profiles, but these are still flatter than expected from *in-situ* sculpting of low-eccentricity discs by circular-orbit planets.

dynamical processes, and histories in the outer regions of planetary systems.

6 DISCUSSION

In Section 6.1, we discuss the possible implications of observed discs having flatter-than-expected edge profiles, and in Section 6.2, we compare the analyses in this paper to previous studies.

6.1 Why are observed inner edges flatter than expected from sculpting planets?

In Section 5 we showed that, whilst the edges of several ALMA-resolved discs are steeper than expected from collisions alone, they are flatter than expected from planetary sculpting of an initially low-eccentricity disc. Here, we discuss several possible reasons for this, and what these could teach us about planetary systems.

6.1.1 *Debris discs have high intrinsic-excitation levels*

One possibility is that planetesimals in debris discs have higher intrinsic excitation levels than is often assumed. For example, if debris at a disc inner edge had $e_{i,\,rms} \approx 0.13$, then that edge would have $\sigma_i \approx 0.11$, which is similar to the steepest discs in Table 1. This value of $e_{i,\,rms}$ is higher than the maximum of 0.06 that could be imparted by a non-migrating, circular-orbit planet (Fig. 7), raising the possibility that these eccentricities arise through non-planetary processes. Examples of possible excitation mechanisms include self-stirring by the debris disc's self-gravity, or processes that occurred during system formation. Marino (2021) used the *outer* edges of several observed discs to infer the debris-excitation levels, and found these to be consistent with $e_{i,\,rms} \gtrsim 0.1$; that sample included HD 92945 and HD 107146, which have the steepest edges in Table 1. It is therefore plausible that *in-situ* planets sculpted the inner edges of some observed discs, but that this debris has separately been excited by some non-planetary processes.

One means to test this would be to measure scale heights at the *inner* edges of debris discs. We find that MMRs of a coplanar planet excite debris eccentricity but not inclination (Section 2.2), so if *in situ*, coplanar planets sculpt debris-disc inner edges, then these edges would be more excited radially than vertically.

6.1.2 *Planets are present at the inner edges, but sculpting has not yet finished*

Planets take time to eject debris and fully sculpt a debris-disc inner edge. The required time is characterized by 1–10 diffusion timescales (Section 2.3.3). Until this time, the disc's inner edge could have almost any profile, which would depend on its initial configuration. It is therefore possible that planets reside just interior to debris discs, but the planets have not yet finished sculpting the edges into steep profiles. This is particularly plausible for young systems, or those with low-mass planets.

The observed discs in Table 1 with the flattest inner-edge profiles are also the youngest, with ages less than 100 Myr. These are 49 Ceti, AU Mic, and HR 8799. Equation (15) shows that, if planets with masses below 0.1–1 M_{Jup} lie at the inner edges of those discs,

Downloaded from https://academic.oup.com/mnras/article/doi/10.1093/mnras/stad3462/7382221 by guest on 23 November 2023

then these systems would be younger than one diffusion time and hence planetary sculpting would not yet have finished. It is therefore plausible that inner-edge profiles are flatter than expected not because sculpting planets are absent, but because sculpting has not yet finished. If true, then care must be taken when inferring planet properties from debris discs, because the hypothesized planet–disc interactions may not have reached their final state. This may be a prevalent problem because the discs most favourable for observation are generally the youngest, for which the dust mass (and hence brightness) is highest.

6.1.3 Discs are sculpted by migrating planets

In this paper, we modelled planets on non-evolving orbits, but a migrating planet would impose a very different morphology on the disc inner edge. Specifically, a migrating planet causes MMR sweeping, where the nominal locations of MMRs move across the debris disc and trap large numbers of bodies in resonance. During this process, resonant debris is excited to increasingly high eccentricities (e.g. Wyatt 2003; Reche et al. 2008; Friebe et al. 2022), which would result in a flatter edge profile.

An example of this occurred in the Solar System. Neptune is located at the inner edge of the Kuiper Belt, but the orbits of Kuiper-Belt objects (KBOs) show that the planet migrated outwards in the past (Malhotra 1993). As a result, KBOs at the Kuiper Belt's inner edge have relatively high eccentricities, which make the Belt's inner edge flatter than would be expected from perturbations by a non-migrating Neptune. In an upcoming paper (Morgner et al., in preparation), we take the observed KBOs and, using a method similar to Vitense, Krivov & Löhne (2010), de-bias these observations to estimate the true KBO population distribution. We then fit the surface density of this de-biased population with equation (33), to get the steepness of the Kuiper-Belt inner edge. This yields $\sigma_{\rm i} = 0.076$, which is much flatter than would be expected for a non-migrating Neptune; Neptune has $m_{\rm p}/m_* = 5 \times 10^{-5}$, so the inner edge should have $\sigma_{\rm i} < 0.02$ if Neptune's orbit never changed (Fig. 6). The reason for this difference is that Neptune excited KBOs through MMR sweeping as it migrated, resulting in eccentricities at the Kuiper Belt's inner edge of $e_{\rm i,\,rms} \sim 0.2$, compared to just 0.01 expected from excitation by a non-migrating Neptune (equation 7).

It is possible that some extrasolar discs were also sculpted by migrating planets, which made their edge profiles flatter than our *in-situ* model predicts. Dust clumps that may be indicative of planetary migration are inferred in debris discs (Lovell et al. 2021; Booth et al. 2023), and Pearce et al. (2022) argue that migration may be required to relate the location of debris-disc edges to system-formation theory. These results, combined with debris-disc edges being flatter than expected for sculpting by non-migrating planets, could imply that planetary migration is common in the outer regions of debris-disc systems. Such migration could be caused by planetesimal scattering (e.g. Friebe et al. 2022), planet–gas interactions in the protoplanetary disc phase, or planet–planet scattering.

It may be possible to test exoplanet-migration scenarios in the near future. *JWST* will search for planets in the outer regions of debris-disc systems, and should detect many of the inferred planets if they exist (Pearce et al. 2022). If a planet were found just interior to a debris disc, and that disc had a flatter edge profile than would be expected from *in-situ* planetary sculpting, then it could be evidence that the planet migrated outwards in the past, exciting debris as it did so.

6.1.4 Collisions have flattened the planet-sculpted edges

Debris-disc edges could initially have been sculpted by planets, and these edges could since have undergone significant collisional evolution. The steepest edges of the Table 1 discs have $\sigma_{\rm i} \approx 0.11$, which is at least 1.3 times flatter than expected from sculpting by non-migrating planets (Fig. 6). However, Fig. 14 shows that collisions can quickly increase $\sigma_{\rm i}$ by a factor of 1.2, long before the largest bodies start colliding at $\tau_{\rm max}$. This could explain the steepest inner edges in Table 1; in these cases, the system ages could be longer than $\tau_{\rm b}$ but shorter than $\tau_{\rm max}$. After $\tau_{\rm max}$, collisions would flatten the edge further, increasing $\sigma_{\rm i}$ by a factor of 3–6 within $10\tau_{\rm max}$; this could potentially reproduce some of the flatter edges in Table 1, if those systems are already older than $\tau_{\rm max}$. Since some observed edges are too steep to be explained by collisions alone, yet too flat to be explained by non-migrating planets alone, this could suggest that both processes play a significant role in some systems.

6.1.5 Planets are present at debris-disc inner edges, but the edges are set by planet formation rather than scattering

A circular-orbit planet would eject debris that initially lies within 3 Hill radii of its orbit (Fig. 5). Therefore, if a newly formed system had a planetesimal disc extending down to less than 3 Hill radii exterior to a planet's orbit, then that planet would eventually impart a sharp inner edge on the disc. This is the scenario we modelled in our simulations. However, a real planet would also have accreted material from around its orbit as it formed. If the forming planet's feeding zone were wider than 3 Hill radii, then much of the debris within the scattering radius would already have been accreted by the time the planet formed. Also, other processes in the protoplanetary disc phase could further affect planetesimal profiles, such as the forming and trapping of material in planet-induced pressure bumps near a planet. Therefore, it is possible that a debris disc's edge profile is set by processes occurring during planet formation, rather than by pure planetary scattering; in this case, its edge profile could differ from those that we model (e.g. Eriksson, Johansen & Liu 2020).

6.1.6 Debris-disc edges are set by planetesimal formation alone

Planets are often invoked to explain the shapes and locations of debris-disc inner edges, motivated in part by Neptune dominating the inner edge of the Kuiper Belt. However, an alternative possibility is that planetesimals naturally form in distinct radial zones; in this case debris-disc edges may be completely unrelated to planets, but instead mark locations were planetesimal formation transitioned from being inefficient to efficient. Such formation zones are predicted by some streaming-instability models (Carrera et al. 2017), as well as models involving snowlines (Ida & Guillot 2016; Drążkowska & Alibert 2017; Schoonenberg & Ormel 2017; Schoonenberg, Ormel & Krijt 2018; Izidoro et al. 2022; Morbidelli et al. 2022). This possibility can soon be tested because, if sculpting planets exist, then many should be detectable by *JWST* (Pearce et al. 2022); the absence of such detections would potentially imply that other processes set disc-edge locations.

6.1.7 Debris discs do not have sharp cut-offs in semimajor axis

Debris-disc inner edges could be broad in semimajor-axes space, meaning that the number density of debris gradually increases with semimajor axis. The radial profile of such a disc would mimic that of a higher-eccentricity disc with a sharper semimajor-axis distribution.

Downloaded from https://academic.oup.com/mnras/article/doi/10.1093/mnras/stad3462/7382221 by guest on 23 November 2023

Shallow semimajor-axis distributions could be a natural outcome of system formation (Section 6.1.6), arise through MMR sweeping during planet migration (Friebe et al. 2022), or result from debris diffusion during self-stirring (Ida & Makino 1993). Since the average eccentricities and inclinations would be related in a relaxed debris disc, the disc vertical thickness would test this; Marino (2021) argued that the outer region of the AU Mic disc is more extended radially than vertically, which could imply low eccentricities and hence a slowly changing semimajor-axis profile.

6.1.8 Debris discs are sculpted by planets with low but non-zero eccentricities

Eccentric planets can excite debris to higher eccentricities than circular-orbit planets, due to additional secular perturbations (eccentric planets are considered in Appendix B). This would result in flatter disc inner edges. Combining equations (13) and (B3), we can show that a Neptune-mass planet orbiting a solar-type star with eccentricity 0.10 could induce an inner-edge steepness of $\sigma_{\rm i} \approx 0.11$, like the sharpest observed edges. Such a planet would make the inner edge elliptical with global eccentricity 0.052 (equation B5), which is high enough to detect with modern observations (e.g. Lovell et al. 2021). Therefore, it should be possible to rule out an eccentric planet as being responsible for a flat disc edge if the disc's global eccentricity were robustly measured as negligible.

However, an intriguing possibility arises if the star position is poorly constrained. In this scenario, a disc with a low global eccentricity could masquerade as axisymmetric, owing to a poorly constrained stellar offset. Were this the case, then an eccentric planet could flatten the disc inner edge, whilst no global disc eccentricity would be detected. One way to rule out this scenario would be to measure the azimuthal variation in the disc profile, because a planet sculpting a truly eccentric disc would make the inner edge flatter at pericentre than apocentre (Appendix B2). Depending on the disc width and the intrinsic debris excitation, the eccentric planet may also flatten the outer edge, which could be observable (compare Fig. 2 and Fig. B1).

6.1.9 Unresolved Trojans are present interior to the inner edges

Unresolved Trojans could be present at the disc inner edges. In our simulations, we purposefully truncated the initial-disc edge at one Hill radius exterior to the planet, to omit any Trojans and ensure that our fitted $\sigma_{\rm i}$ values describe the 'true' inner-edge slopes. However, if sculpting planets are present at the inner edges of real discs, but there are also unresolved Trojans co-orbiting with the planets, then the Trojans would flatten the azimuthally averaged inner-edge profiles. The degree of flattening would depend on the surface density of Trojans relative to the disc.

6.1.10 Dust transport is important

Dust-transport processes could be operating in addition to planetary sculpting, which would make the disc edges more radially extended and their profiles flatter. Poynting–Robertson (PR) drag can be significant for small grains, causing discs to be radially extended in scattered light; whilst the larger, ALMA-imaged grains we consider should be unaffected by PR drag, they could be affected in a similar way by stellar winds. Winds would be particularly important for discs around late-type stars, and would drag material inwards from the planetesimal belt (e.g. Plavchan, Jura & Lipscy 2005; Reidemeister et al. 2011; Schüppler et al. 2015). This would flatten the inner-edge profile. Similarly, CO gas is detected in many debris discs around early-type stars, which could also cause radial drift through gas drag (e.g. Krivov et al. 2009; Marino et al. 2020; Pearce, Krivov & Booth 2020). Again, this would flatten the inner edges.

6.1.11 More complex disc–planet interactions occur in some debris discs

The inner edges of some specific systems in Table 1 could be excited by more complex planet–disc interactions. There are gaps in the discs of both HD 92945 and HD 107146, which are the discs with the steepest inner edges. Friebe et al. (2022) showed that the simplest and most self-consistent way to explain the morphology of HD 107146 is if a planet has migrated across the gap; such migration would cause sweeping by MMRs, which would excite debris at the disc inner edge (their fig. 9, lower-right panel). In that model, the planet would now lie just exterior to the inner edge of the gap, and may have swept up a Trojan population which could resemble the additional gap features in Imaz Blanco et al. (2023). It is therefore possible that planets lying further out in more-complex discs could excite debris at the inner edge, leading to flatter edge profiles.

Alternatively, planets could excite inner-edge debris through secular resonances rather than MMRs, which could lead to higher debris eccentricities and thus flatter edges. A secular resonance occurs where the apsidal precession rate of debris (due to the planet and disc self-gravity) matches that of the planet (due to the disc or other planets), and such resonances can drive up debris eccentricities and even open remote gaps in broad discs (Pearce & Wyatt 2015; Yelverton & Kennedy 2018; Sefilian et al. 2021, 2023). If a secular resonance were located near the disc inner edge, then it could dominate over scattering and MMRs, and hence produce a different edge location and profile to those in our simulations (e.g. Smallwood 2023). Given the very large uncertainties on both debris-disc masses and orbital architectures in the outer regions of systems, we cannot state for certain whether this secular-resonance excitation occurs, but we can estimate the disc masses that could lead to this scenario.

In a coplanar system with a single planet and an external, self-gravitating disc, a secular resonance occurs at semimajor axis $a_{\rm res}$. The location of $a_{\rm res}$ depends on the total disc mass $M_{\rm d}$ relative to that of the planet, as well as the planetary semimajor axis. A general expression describing this relationship is derived in Sefilian et al. (2021, their equation 19) which, assuming a power-law disc with surface density $\propto a^{-1.5}$ spanning semimajor axes $a_{\rm in}$ to $a_{\rm out}$, with $a_{\rm p} \approx a_{\rm in}$, reads as

$$\frac{M_{\rm d}}{m_{\rm p}} \approx \frac{1.5}{|\psi_1(a_{\rm res})|}\left(\frac{a_{\rm out}}{a_{\rm in}}\right)^{1/2}\left(\frac{a_{\rm res}}{a_{\rm in}}\right)^{-2.5}, \tag{34}$$

where $\psi_1(a)$ is a factor of order unity (see also Sefilian et al. 2023). A secular resonance will hence lie near the disc inner edge if $M_{\rm d}/m_{\rm p} \gtrsim 0.89(a_{\rm out}/a_{\rm in})^{1/2}$; here we arbitrarily define 'near' as $a_{\rm res} < 1.2a_{\rm in}$, where $\psi_1(1.2a_{\rm in}) \approx -1.07$ (computed using equation 18 in Sefilian & Rafikov 2019, assuming $H = 0.05$ for the disc scale height).[8] This implies that, for disc-to-planet mass ratios of roughly unity or higher, secular resonances could play a role in shaping the disc inner edge. Since debris discs could have masses up to 1000 $M_\oplus$ (Krivov & Wyatt 2021), this effect could be significant even for Jupiter-mass planets. We will further investigate the effect of secular

[8]For comparison, defining the inner-edge region as $<1.5a_{\rm in}$ instead yields $M_{\rm d}/m_{\rm p} \gtrsim 0.75(a_{\rm out}/a_{\rm in})^{1/2}$, with $\psi_1(1.5a_{\rm in}) \approx -0.73$.

Downloaded from https://academic.oup.com/mnras/article/doi/10.1093/mnras/stad3462/7382221 by guest on 23 November 2023

resonances on debris-disc edges in a future work (Sefilian et al., in preparation).

6.2 Comparison to literature studies

Several literature studies also assessed the effect of a sculpting planet on debris-disc inner edges. These used various different approaches, and yielded various different results. In this section, we compare our paper to literature works, specifically focusing on the *n*-body results (Section 6.2.1), collisional modelling (Section 6.2.2), and the planet-inferring technique of Pearce et al. (2022), which uses the locations of debris-disc inner edges but not their steepnesses (Section 6.2.3).

6.2.1 Gravitational effects

The fact that MMRs of planets on circular orbits excite debris at disc inner edges, and that more-massive planets cause higher excitation and hence flatter edge profiles, was also identified in previous works. Mustill & Wyatt (2012) used encounter maps to demonstrate this effect on planetesimals (their fig. 4), and showed that a similar effect arises in the prescription of Wisdom (1980). Chiang et al. (2009) and Rodigas et al. (2014) consider small dust released from a population of planet-sculpted planetesimals, and show that this decrease in edge steepness with increasing planet mass is also expected in scattered-light observations (their figs 3 and 1b, respectively).

Quillen (2006) and Quillen & Faber (2006) used MMR theory to predict that a low-eccentricity planet should impose an eccentricity dispersion at the disc inner edge that is proportional to $(m_p/m_*)^{3/7}$, which is slightly steeper than our empirical $(m_p/m_*)^{1/3}$ for a circular-orbit planet (equation 7). However, we note that the zero-planet-eccentricity simulations of Quillen & Faber (2006) appear more consistent with our flatter index of 1/3 (filled pentagons on their fig. 2), and this index is also predicted theoretically by Petrovich et al. (2013, their equations 19 and 34). We therefore argue that $(m_p/m_*)^{1/3}$ is a better estimate of debris eccentricities at the inner edge of a disc sculpted by a circular, non-migrating planet, provided that $m_p/m_* \lesssim 3.3 \times 10^{-3}$. Above this mass ratio, we observe a turnover where increasing the planet mass no longer excites debris to higher eccentricities; this is due to the inner edge of the planet's chaotic zone extending beyond the location of strong MMRs, and was not observed by the above authors because their simulations did not extend to such high-mass ratios.

Tabeshian & Wiegert (2016, 2017) modelled the interaction between a planet and a planetesimal disc, and showed that the MMRs of a circular-orbit planet can impose asymmetric structure on an external disc (fig. 5 in Tabeshian & Wiegert 2016). In particular, they show that MMRs can carve crescent-shaped gaps in the disc, and that the inner-edge profile can vary with azimuth. We find the same result; in the simulation on Fig. 4, a crescent-shaped gap can be seen aligned with the planet, and the inner-edge steepness differs slightly on the left and right sides of the disc. However, we do not investigate this asymmetry in more detail, because the difference is small enough that it is unlikely to significantly affect any inferred-planet parameters. Also, Tabeshian & Wiegert (2016) show that the degree of asymmetry scales with the planet-to-star mass ratio, and this asymmetry is already small for the comparatively high-mass ratio on Fig. 4; for smaller mass ratios, the asymmetry would be even less pronounced.

6.2.2 Collisional effects

We find that collisions make the disc edge flatter, and move its characteristic radius outwards (Figs 13 and 14). This is in qualitative agreement with fig. 3 of Nesvold & Kuchner (2015), which shows that the same effects manifest in the SMACK collision prescription; that prescription simultaneously models the collisional and *n*-body dynamical evolution of debris (Nesvold et al. 2013). Nesvold & Kuchner (2015) also find that it takes 10–100 collisional time-scales for this process to occur (their fig. 4). However, our collisional models, and our definitions of collisional time-scales, are fundamentally different.

We employ the analytical model of Löhne et al. (2008), where the most relevant collisional time-scale is $\tau_{\rm max}$, the collisional lifetime of the largest bodies. This predominantly depends on disc location, debris eccentricity, the disc's initial mass, and the size of the largest bodies. The latter two are unknown, but for physically plausible values, a disc with inner edge at 50 au would have $\tau_{\rm max}$ of at least $\sim 10^7$ yr, and potentially much longer (Fig. 15). This means that $\tau_{\rm max}$ should be at least comparable to the ages of debris-disc stars (Table 1), and may be much longer; based on this, we argue that collisions should *not* significantly reduce the steepness of planet-sculpted edges in many observed discs.

This conclusion differs from Nesvold & Kuchner (2015), who suggest that collisions typically *would* have a significant effect on the observed edges of planet-sculpted discs. They model the collisional cascade in detail and self-consistently with the dynamical evolution, unlike our simulations. However, the difference between our conclusions is unlikely to be due to our separation of dynamics and collisions, but rather differences between our collisional assumptions and those of Nesvold & Kuchner (2015).

There are two main reasons for this difference. First, the maximum grain radius in Nesvold & Kuchner (2015) is $s_{\rm max} = 10$ cm (their table 1); these pebbles are depleted much faster than the $\gtrsim 1$ km planetesimals in our model, so their collisional erosion occurs on much shorter time-scales. Second, the amount of dust in the Nesvold & Kuchner (2015) models is higher because they assume a greater minimum grain size; extrapolating from their $s_{\rm min} = 1$ mm to the typical $s_{\rm min} = 1$–$10\ \mu$m expected from radiation pressure blowout corresponds to vertical optical depths that are higher than ours by factors of 10–30, assuming a size distribution index of 3.5.

Accounting for the respective differences in $s_{\rm min}$ and $s_{\rm max}$ each increase the ratio between the collision time-scales of smallest dust (their equation 3) and that of the biggest objects (which govern the long-term evolution). Nesvold & Kuchner (2015) define smallest-grain collisional time-scales of 10^3–10^6 yr for a sample of observed discs (their section 4); instead of the factors of 10–100 in their fig. 4, planetesimals would evolve collisionally on time-scales that are longer by several orders of magnitude, in line with our results. So this difference in time-scales appears to be the cause of our different conclusions regarding the relative effects of planets and collisions on the disc inner edge.

None the less, the Nesvold & Kuchner (2015) model captures additional physics that is omitted in our simpler prescription. In particular, our model would not capture the expected collisional enhancement in resonant populations (Stark & Kuchner 2009); this means we probably underestimate collision rates at the MMR-dominated inner edges, and therefore overestimate collisional time-scales. This effect could be significant in some cases, because the inner-edge eccentricities in our low-eccentricity planet simulations are determined by MMRs. Detailed, self-consistent modelling is therefore required in future, to properly assess the balance between

Downloaded from https://academic.oup.com/mnras/article/doi/10.1093/mnras/stad3462/7382221 by guest on 23 November 2023

collisions and planet-debris interactions at the inner edges of debris discs.

6.2.3 *Comparison to Pearce et al. (2022) planet predictions*

Pearce et al. (2022) give a general model to infer the minimum mass, maximum semimajor axis, and minimum eccentricity of a perturbing planet based on the shape and location of a debris disc's inner edge. Those predictions are based on Pearce & Wyatt (2014), and do not consider the steepness of the disc edge; as a result they have a degeneracy in planet mass and semimajor axis, because they cannot distinguish a low-mass planet near the disc from a high-mass planet away from the disc. However, in this paper we make predictions that also include information about the edge steepness; this can break the degeneracy, because edge steepness can be directly related to planet mass (at least in the collisionless regime).

Section 3 describes our simple analytic model to predict planet properties from an observed-disc edge. These predictions are comparable to those of Pearce et al. (2022), with three important differences. First, we have an extra dependence on the edge profile, and hence the debris eccentricity $e_{\rm i,\,rms}$; our predicted inner-edge location (equation 11) is increased by a factor of $(1 + 2e_{\rm i,rms}/\sqrt{3})$ relative to that in Pearce et al. (2022).

Second, Pearce & Wyatt (2014) use a stricter definition of the sculpting time-scale; they assume sculpting takes 10 diffusion times, which is the time it takes an eccentric planet to eject 95 per cent of unstable material. However, we find that an edge sculpted by a circular-orbit planet with mass $m_{\rm p}/m_* < 10^{-2}$ takes just one diffusion time-scale to assume roughly its final configuration (equation 15). This is because it takes a planet exponentially longer to clear increasingly large fractions of unstable debris; a circular-orbit planet removes ~ 70 per cent of unstable debris within 1 diffusion time, but takes 10 diffusion times to remove ~ 90 per cent (Costa, Pearce & Krivov, submitted). Hence our minimum-allowed planet mass can be a factor of $\sqrt{10} \approx 3$ times smaller than Pearce et al. (2022).

Finally, we take the width of the chaotic zone around the planet's orbit to be 3 Hill radii, whilst Pearce et al. (2022) used 5. The reason for this is that Pearce & Wyatt (2014) studied eccentric planets, for which the innermost stable semimajor axis is 5 eccentric Hill radii exterior to planet apocentre (their fig. 9), whilst for circular-orbit planets a value of 3 provides a better fit (Gladman 1993; Ida et al. 2000; Kirsh et al. 2009; Malhotra et al. 2021; Friebe et al. 2022). It is unclear at what planet eccentricities the transition from 3 to 5 Hill radii occurs, though Fig. B1 shows that a planet eccentricity of 0.2 is already high enough for 5 Hill radii to provide a better estimate. This is consistent with Regály et al. (2018), who find the transition occurs at planet eccentricities somewhere between 0 and 0.2 (their fig. 5c).

The result of these three differences is that any planets predicted using our model will differ slightly from the Pearce et al. (2022) model. However, the mass predictions should typically be within an order of magnitude or so of each other. For the example on Fig. 11, the lower bound on planet mass predicted by the Pearce et al. (2022) model is 10 times smaller than the mass predicted from our model; the two predictions still lie in a similar region of parameters space, along Line 1 on that figure.

6.3 Application to narrow discs

We only considered broad discs in our simulations, to isolate the inner edge from the outer edge. This ensured that our inner-edge profiles were dominated by planet–disc interactions, rather than the initial profile of the disc. However, this means that our quantitative results may not hold for very narrow discs, where the outer- and inner-edge profiles could overlap.

In Section 2.4, we argued that the characteristic inner-edge width is several times $r_{\rm i}\sigma_{\rm i}$. Hence our results should hold if the disc is sufficiently wide for the edges to be well separated, that is,

$$r_{\rm o} - r_{\rm i} \gtrsim r_{\rm i}\sigma_{\rm i} + r_{\rm o}\sigma_{\rm o}. \tag{35}$$

Equation (13) shows that $\sigma_{\rm i}$ is proportional to the eccentricity of inner-edge debris, and a similar relation holds for the outer edge. Therefore, if the eccentricity distribution were constant across the disc, then equation (35) implies that our results should hold provided the disc fractional width is larger than the rms debris eccentricity; this is in agreement with Marino (2021). Our full criterion (equation 35) is slightly more complicated, because the debris-eccentricity level would vary across a planet-sculpted disc.

6.4 Range of explored mass ratios

We explored planet-to-star-mass ratios ranging from 3×10^{-5} to 10^{-1}. We did not consider lower-mass planets, because in many cases the dynamical time-scales would then become comparable to the stellar lifetimes. For example, an Earth-mass planet at 10 au from a Solar-type star ($m_{\rm p}/m_* = 3 \times 10^{-6}$) would have a diffusion time-scale of 40 Gyr, which would exceed the stellar lifetime of $\sim$10 Gyr. Hence our results would not hold for very low-mass ratios, because the interaction we study would not have time to occur.

Our upper limit of $m_{\rm p}/m_* = 10^{-1}$ represents the upper end of what could realistically be called a 'planet'. For example, this could be a $10\,{\rm M_{Jup}}$ super-Jupiter orbiting a $0.1\,{\rm M_\odot}$ M6 dwarf. In many cases, such high-mass companions would be detectable via imaging, radial velocity or astrometry, particularly in younger systems (e.g. Carter et al. 2023).

Were a companion detected, then our results could be used to infer its evolutionary history. For example, if a debris disc in the system had an edge steepness consistent with sculpting by the observed companion, but the companion were detected far interior to the disc, then this could be evidence that the detected companion sculpted the disc historically but has since migrated inward. This scenario has been suggested as a way to explain non-detections of planets at the inner edges of debris discs (Pearce et al. 2022).

7 CONCLUSIONS

We perform a dynamical investigation into the effect of planets on the profiles of debris-disc inner edges. We consider both planet–disc interactions and debris collisions, and explore the interaction across a broad parameter space. We quantify our simulated surface-density profiles using an erf function, as in Rafikov (2023), for direct comparison with ALMA-resolved inner edges. Our main conclusions are as follows:

(i) For a non-migrating, circular-orbit planet, in the case where collisions are negligible, the steepness of the disc inner edge is set by the planet-to-star mass ratio and the initial-disc excitation level. Lower-mass planets lead to steeper inner edges, with the edge width proportional to $(m_{\rm p}/m_*)^{1/3}$ (equations 7, 8, and 13).

(ii) There is a maximum eccentricity that a planet on a circular, non-migrating orbit can generally impart on the population of planetesimals at a debris-disc inner edge, which is an rms eccentricity of 0.06 (equation 7).

Downloaded from https://academic.oup.com/mnras/article/doi/10.1093/mnras/stad3462/7382221 by guest on 23 November 2023

(iii) Considering the steepness of a debris disc's inner edge when inferring the properties of unseen sculpting planets can break the degeneracy between planet mass and semimajor axis. We provide a step-by-step method for inferring such planets from disc inner edges in Section 3.2.1.

(iv) Eccentric planets make inner-edge profiles flatter, and introduce azimuthal asymmetries (Appendix B).

(v) The inner edge of a purely planet-sculpted debris disc is much steeper than that of a purely collisional debris disc.

(vi) Collisions flatten the profile of a planet-sculpted inner edge. The effect of collisions is small before the largest bodies start to collide; after this time, collisions start to significantly flatten the inner edge.

(vii) In most cases, collisions would never fully erase the signature of a sculpting planet on a debris-disc inner edge.

(viii) Whilst the inner edges of many ALMA-resolved debris discs are *too steep* to be caused by collisions alone, they are also *too flat* to arise through pure sculpting by non-migrating, circular-orbit planets, unless sculpting is still ongoing. Possible implications of this for the outer regions of planetary systems are discussed in Section 6.1.

ACKNOWLEDGEMENTS

We thank the anonymous referee, whose comments improved the paper. We are grateful for exploratory work by Zuzanna Jonczyk as a summer intern at the Institute of Astronomy, University of Cambridge; her work helped identify some of the challenges in connecting inner-edge profiles to sculpting planets. We also thank Brenda Matthews for useful discussions. TDP, AVK, TL, and MB were supported by Deutsche Forschungsgemeinschaft (DFG) grants Kr 2164/13-2, Kr 2164/14-2, Kr 2164/15-2, and Lo 1715/2-2. TDP is also supported by a Warwick Prize Fellowship, made possible by a generous philanthropic donation. MB also received funding from the European Union's Horizon 2020 research and innovation programme under grant agreement no. 951815 (AtLAST). AAS acknowledges support by the Alexander von Humboldt Foundation through a Humboldt Research Fellowship for postdoctoral researchers. MRJ acknowledges support from the European Union's Horizon Europe programme under the Marie Sklodowska-Curie grant agreement no. 101064124, and funding provided by the Institute of Physics Belgrade, through the grant by the Ministry of Science, Technological Development, and Innovations of the Republic of Serbia. SM is supported by a Royal Society University Research Fellowship (URF-R1-221669).

DATA AVAILABILITY

The data underlying this article will be shared upon reasonable request to the corresponding author.

REFERENCES

Booth M. et al., 2023, MNRAS, 521, 6180
Carrera D., Gorti U., Johansen A., Davies M. B., 2017, ApJ, 839, 16
Carter A. L. et al., 2023, ApJ, 951, L20
Chiang E., Kite E., Kalas P., Graham J. R., Clampin M., 2009, ApJ, 693, 734
Drążkowska J., Alibert Y., 2017, A&A, 608, A92
Eriksson L. E. J., Johansen A., Liu B., 2020, A&A, 635, A110
Esposito T. M. et al., 2020, AJ, 160, 24
Faramaz V. et al., 2014, A&A, 563, A72
Faramaz V. et al., 2019, AJ, 158, 162
Faramaz V. et al., 2021, AJ, 161, 271
Friebe M. F., Pearce T. D., Löhne T., 2022, MNRAS, 512, 4441
Geiler F., Krivov A. V., 2017, MNRAS, 468, 959
Gladman B., 1993, Icarus, 106, 247
Hayashi C., 1981, Prog. Theor. Phys. Suppl., 70, 35
Hinkley S. et al., 2023, A&A, 671, L5
Hughes A. M., Duchêne G., Matthews B. C., 2018, ARA&A, 56, 541
Ida S., Guillot T., 2016, A&A, 596, L3
Ida S., Makino J., 1993, Icarus, 106, 210
Ida S., Bryden G., Lin D. N. C., Tanaka H., 2000, ApJ, 534, 428
Imaz Blanco A. et al., 2023, MNRAS, 522, 6150
Izidoro A., Dasgupta R., Raymond S. N., Deienno R., Bitsch B., Isella A., 2022, Nat. Astron., 6, 357
Kennedy G. M., Wyatt M. C., 2010, MNRAS, 405, 1253
Kirsh D. R., Duncan M., Brasser R., Levison H. F., 2009, Icarus, 199, 197
Krivov A. V., 2010, Rev. Astron. Astrophys., 10, 383
Krivov A. V., Wyatt M. C., 2021, MNRAS, 500, 718
Krivov A. V., Herrmann F., Brandeker A., Thébault P., 2009, A&A, 507, 1503
Krivov A. V., Ide A., Löhne T., Johansen A., Blum J., 2018, MNRAS, 474, 2564
Löhne T., Krivov A. V., Rodmann J., 2008, ApJ, 673, 1123
Löhne T. et al., 2012, A&A, 537, A110
Lovell J. B. et al., 2021, MNRAS, 506, 1978
Malhotra R., 1993, Nature, 365, 819
Malhotra R., Castro-Cisneros J. D., Fitzgerald J., Rosengren A. J., Ross S., Todorovic N., Wu D., 2021, in AAS/Division of Dynamical Astronomy Meeting. p. 305.04
Marino S., 2021, MNRAS, 503, 5100
Marino S., Flock M., Henning T., Kral Q., Matrà L., Wyatt M. C., 2020, MNRAS, 492, 4409
Morbidelli A., Baillié K., Batygin K., Charnoz S., Guillot T., Rubie D. C., Kleine T., 2022, Nat. Astron., 6, 72
Morrison S., Malhotra R., 2015, ApJ, 799, 41
Mouillet D., Larwood J. D., Papaloizou J. C. B., Lagrange A. M., 1997, MNRAS, 292, 896
Murray C. D., Dermott S. F., 1999, Solar System Dynamics. Cambridge University Press, Cambridge, UK
Mustill A. J., Wyatt M. C., 2012, MNRAS, 419, 3074
Nesvold E. R., Kuchner M. J., 2015, ApJ, 798, 83
Nesvold E. R., Kuchner M. J., Rein H., Pan M., 2013, ApJ, 777, 144
Pearce T. D., Wyatt M. C., 2014, MNRAS, 443, 2541
Pearce T. D., Wyatt M. C., 2015, MNRAS, 453, 3329
Pearce T. D., Krivov A. V., Booth M., 2020, MNRAS, 498, 2798
Pearce T. D., Beust H., Faramaz V., Booth M., Krivov A. V., Löhne T., Poblete P. P., 2021, MNRAS, 503, 4767
Pearce T. D. et al., 2022, A&A, 659, A135
Petrovich C., Malhotra R., Tremaine S., 2013, ApJ, 770, 24
Plavchan P., Jura M., Lipscy S. J., 2005, ApJ, 631, 1161
Quillen A. C., 2006, MNRAS, 372, L14
Quillen A. C., Faber P., 2006, MNRAS, 373, 1245
Rafikov R. R., 2023, MNRAS, 519, 5607
Reche R., Beust H., Augereau J. C., Absil O., 2008, A&A, 480, 551
Regály Z., Dencs Z., Moór A., Kovács T., 2018, MNRAS, 473, 3547
Reidemeister M., Krivov A. V., Stark C. C., Augereau J. C., Löhne T., Müller S., 2011, A&A, 527, A57
Rein H., Liu S. F., 2012, A&A, 537, A128
Rein H., Tamayo D., 2015, MNRAS, 452, 376
Rodigas T. J., Malhotra R., Hinz P. M., 2014, ApJ, 780, 65
Schoonenberg D., Ormel C. W., 2017, A&A, 602, A21
Schoonenberg D., Ormel C. W., Krijt S., 2018, A&A, 620, A134
Schüppler C. et al., 2015, A&A, 581, A97
Schüppler C., Krivov A. V., Löhne T., Booth M., Kirchschlager F., Wolf S., 2016, MNRAS, 461, 2146
Sefilian A. A., Rafikov R. R., 2019, MNRAS, 489, 4176
Sefilian A. A., Rafikov R. R., Wyatt M. C., 2021, ApJ, 910, 13
Sefilian A. A., Rafikov R. R., Wyatt M. C., 2023, ApJ, 954, 100
Smallwood J. L., 2023, MNRAS, 523, 3526
Stark C. C., Kuchner M. J., 2009, ApJ, 707, 543
Stuber T. A., Löhne T., Wolf S., 2023, A&A, 669, A3
Tabeshian M., Wiegert P. A., 2016, ApJ, 818, 159

Downloaded from https://academic.oup.com/mnras/article/doi/10.1093/mnras/stad3462/7382221 by guest on 23 November 2023

Tabeshian M., Wiegert P. A., 2017, ApJ, 847, 24
Thebault P., Kral Q., Ertel S., 2012, A&A, 547, A92
Tremaine S., 1993, in Phillips J. A., Thorsett S. E., Kulkarni S. R.eds, ASP Conf. Ser., Vol. 36, Planets Around Pulsars. California Institute of Technology, Pasadena, CA, p. 335
Vitense C., Krivov A. V., Löhne T., 2010, A&A, 520, A32
Weidenschilling S. J., 1977, Ap&SS, 51, 153
Wisdom J., 1980, AJ, 85, 1122
Wisdom J., Holman M., 1991, j, 102, 1528
Wyatt M. C., 2003, ApJ, 598, 1321
Wyatt M. C., 2008, ARA&A, 46, 339
Wyatt M., 2020, in Prialnik D. , et al., eds, The Trans-Neptunian Solar System, p. 351
Wyatt M. C., Dermott S. F., Telesco C. M., Fisher R. S., Grogan K., Holmes E. K., Piña R. K., 1999, ApJ, 527, 918
Wyatt M. C., Smith R., Su K. Y. L., Rieke G. H., Greaves J. S., Beichman C. A., Bryden G., 2007, ApJ, 663, 365
Yelverton B., Kennedy G. M., 2018, MNRAS, 479, 2673

APPENDIX A: SURFACE-DENSITY PROFILE FITTING

We fit surface-density profiles to our simulations through several rounds of χ^2 minimization, using the following process. First, we perform an initial χ^2 minimization, which typically provides a good fit to the broad disc as a whole. However, this generally produces poor fits at the edges, because the edges make up a small fraction of the overall profile; the inner edge on Fig. 2 spans just 25 radial bins, compared to the 400 bins across the entire disc, so even a poor edge fit would not significantly impact the overall χ^2. To properly fit the inner edge, we then repeat the fitting using the parameters of the first fit as our initial guess, except for σ_i for which we use a value between 10^{-8} and 10^2. We repeat this several times for different initial guesses of σ_i, and the fit with the lowest χ^2 is taken as the new reference fit. Finally, this whole process is repeated for the outer edge, using the new reference fit as our initial guess and testing different guesses for σ_o. The fit with the lowest χ^2 after this process is the fit we use. This technique avoids local minima, and ensures that the edge profiles are properly fitted. It is also considerably faster than performing a full MCMC fit to each of our simulations. The fitting is performed using the PYTHON module SCIPY.OPTIMIZE.

APPENDIX B: ECCENTRIC PLANETS

We showed that a planet on a circular orbit excites debris eccentricities through MMRs, and that these eccentricities set the steepness of the disc inner edge. However, an eccentric planet would also drive up eccentricities through secular interactions. Whilst we focus on circular-orbit planets in this paper, in this section we briefly consider how planet eccentricity would affect the inner-edge profiles. We will show that a low- to moderate-eccentricity planet can excite debris more than a circular-orbit planet, resulting in a flatter inner edge, and that the planet eccentricities required to do this can be low enough that they do not necessarily impose a clear asymmetry on the disc.

B1 *N*-body simulation with an eccentric planet

To demonstrate the effect of an eccentric planet, we re-run the simulation from Fig. 2, but with the planet eccentricity increased to 0.2. We also initialize the disc inner edge to be slightly further outwards than before; we still place it one Hill radius exterior to the planet's apocentre, but since the planet is now eccentric, we switch to the definition of the eccentric Hill radius at apocentre from Pearce & Wyatt (2014):

$$r_{\mathrm{Hill,Q}} \approx a_\mathrm{p}(1+e_\mathrm{p})\left[\frac{m_\mathrm{p}}{(3-e_\mathrm{p})m_*}\right]^{1/3}, \tag{B1}$$

where e_p is the planet eccentricity. We do this because the Hill radius of an eccentric planet varies around the planet orbit; the above equation is the Hill radius at the planet's apocentre, and the equivalent at planet pericentre is found by changing e_p to $-e_\mathrm{p}$ in this equation.

We run the eccentric-planet simulation for 16.5 Myr, which is much longer than the 0.868 Myr for the circular case. We do this because an eccentric planet would drive spiral density waves in a massless disc through secular interactions, in addition to sculpting the inner edge through scattering. Pearce & Wyatt (2014) show that such a disc would settle into its final state after at least 10 secular times have elapsed at its outer edge (by which time the spirals are tightly wound and indistinct), *and* at least 10 diffusion times have elapsed at the inner edge (by which time scattering would be largely complete). We compute the secular time-scale using equation (17) in Pearce & Wyatt (2014), and run our simulation to 10 times that value.

Fig. B1 shows the simulation with an eccentric planet, for comparison with the equivalent circular-planet simulation of Fig. 2. As well as ejecting debris, the eccentric planet drives the disc into a broad, eccentric structure aligned with the planet orbit, as described in Pearce & Wyatt (2014) and Faramaz et al. (2014). Debris eccentricities are much higher than in the circular-planet case (Fig. B1, middle panel, compared to Fig. 2, left panel), with implications for the inner-edge profile as discussed below. Another difference is that the inner edge is truncated at a semimajor axis corresponding to 5 eccentric Hill radii outside the planet's apocentre, rather than 3 Hill radii as in the circular case; this behaviour is discussed in Pearce & Wyatt (2014). The eccentric-planet simulation also has resonant debris surviving on planet-crossing orbits (e.g the 3:2 MMR), and such populations can be stable even for highly eccentric planets (Pearce et al. 2021).

We now assess the profile of the eccentric-disc inner edge. In our circular-planet simulations, we simply azimuthally averaged the entire disc to produce radial surface-density profiles, but this approach is insufficient for asymmetric discs. Instead, we follow Tabeshian & Wiegert (2016, 2017) and divide the disc into several sectors. We define one sector as everything 45° either side of the planet's pericentre direction, and another as everything 45° either side of the planet's apocentre. These sectors are coloured orange and green, respectively, on the left panel of Fig. B1. For each of these sectors we azimuthally average the particles within them, to produce one radial surface-density profile for the region around pericentre and another for the region around apocentre. These profiles are shown on the right panel of Fig. B1. We fit each profile with equation (6) as before, again fixing the power-law index α to 1.5. The result is that the inner edge has a different steepness on the apocentre and pericentre sides of the disc; we fit $\sigma_\mathrm{i} = 0.137$ on the pericentre side, compared to 0.106 on the apocentre side. Both are much flatter than the circular-planet case, which had $\sigma_\mathrm{i} = 0.0361$. In the next section, we quantify the general impact of planet eccentricity on the inner-edge profile.

B2 Effect of planet eccentricity on the inner-edge profile

The inner-edge steepness is set by the eccentricity of surviving debris. A circular-orbit planet excites debris eccentricities through MMRs, whilst an eccentric planet also excites eccentricities through secular interactions. If the secular excitation were greater than the MMR

Downloaded from https://academic.oup.com/mnras/article/doi/10.1093/mnras/stad3462/7382221 by guest on 23 November 2023

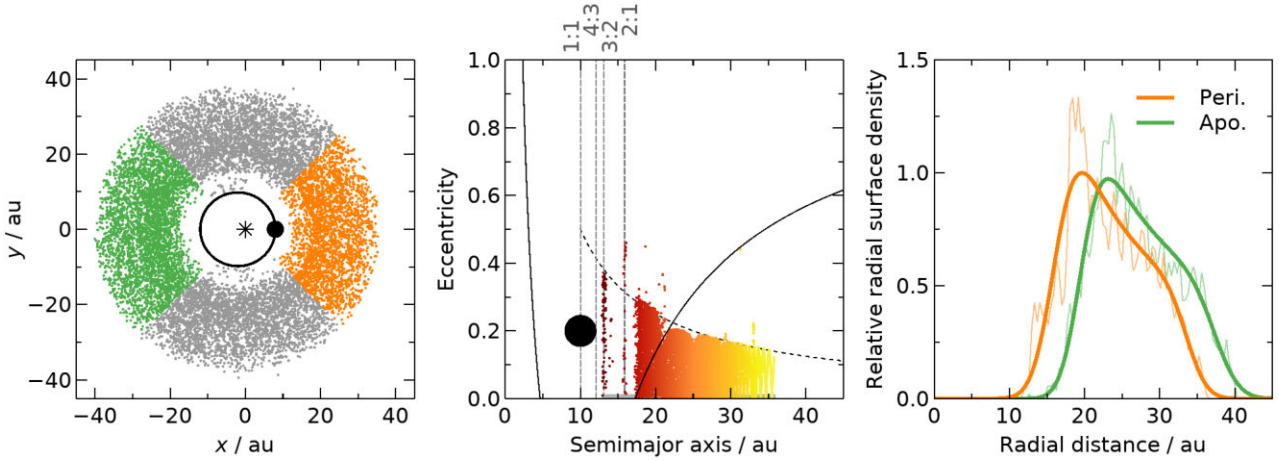

Figure B1. Simulation with an eccentric planet. The simulation has the same setup as that on Fig. 2, except here the planet has eccentricity 0.2, and the initial disc lies further out (see Appendix B1). The eccentric planet excites debris through secular interactions, resulting in higher eccentricities and flatter edges than the circular-planet case. Left panel: positions at the end of the simulation. Orange and green points are debris within 45° of the planet's pericentre and apocentre directions, respectively. Middle panel: the dotted black line is $2e_{\rm forced}(a)$, the maximum debris eccentricity expected from secular interactions (equation B2). The solid lines define the chaotic region, which is 5 (rather than 3) times the eccentric Hill radius either side of the eccentric planet's orbit. Right panel: separate surface-density profiles for material within 45° of the planet's pericentre and apocentre. The thick and thin lines are the simulation data and fitted models respectively, relative to the peak of the pericentre model. The fit to the pericentre side has $r_{\rm i} = 16.6$ au, $\sigma_{\rm i} = 0.137$, $r_{\rm o} = 33.9$ au, and $\sigma_{\rm o} = 0.0625$, whilst that to the apocentre side has $r_{\rm i} = 20.0$ au, $\sigma_{\rm i} = 0.106$, $r_{\rm o} = 37.7$ au, and $\sigma_{\rm o} = 0.0666$; the peak fitted surface density on the apocentre side is 0.973 times that on the pericentre side. All remaining lines and symbols are defined on previous figures.

excitation, then the eccentric planet would produce a flatter edge than a circular-orbit planet. In this section, we calculate how eccentric a planet can be before the inner-edge profile deviates from the circular-planet case, and the effect of an eccentric planet on the inner edge.

Secular interactions with an eccentric planet cause debris eccentricities to oscillate, whilst their semimajor axes remain constant. Specifically, debris initialized on a circular orbit with semimajor axis a would oscillate in eccentricity between zero and twice the forcing eccentricity $e_{\rm forced}$, where

$$2e_{\rm forced}(a) \approx \frac{5}{2}\frac{a_{\rm p}}{a}e_{\rm p} \tag{B2}$$

(Murray & Dermott 1999). This is shown on the middle panel of Fig. B1, where the dotted line is $2e_{\rm forced}$. We can use this to derive the maximum eccentricity of secular debris at the disc inner edge; the innermost stable semimajor axis is about 5 eccentric Hill radii beyond planet apocentre, that is, $a_{\rm in} \approx a_{\rm p}(1+e_{\rm p}) + 5r_{\rm Hill,\,Q}$ (Pearce & Wyatt 2014), so we can use equation (B1) to get the innermost stable semimajor axis, then substitute this into equation (B2). The result is that, to first order in planet eccentricity, the maximum debris eccentricity from secular effects at the disc inner edge is

$$e_{\rm max,sec} \approx 2e_{\rm forced}(a_{\rm in}) \approx \frac{5}{2}e_{\rm p}\left[1 + 3.47\left(\frac{m_{\rm p}}{m_*}\right)^{1/3}\right]^{-1}. \tag{B3}$$

For the scenario on Fig. B1 ($e_{\rm p} = 0.2$, $m_{\rm p}/m_* = 1.9 \times 10^{-3}$), equation (B3) yields $e_{\rm max,\,sec} \approx 0.35$, in good agreement with the simulation.

We can use equation (B3) to determine how eccentric a planet must be for the inner-edge profile to differ significantly from the circular-planet case. Equation (7) gives the rms eccentricity at the inner edge arising from MMRs from a circular-orbit planet; if an eccentric planet excited debris to higher values through secular interactions, then the edge profile would be flatter than in the circular-planet case. Comparing equations (7) and (B3), the disc inner edge would be flatter than the circular-planet case if the planet has eccentricity

$$e_{\rm p} > 0.277\left(\frac{m_{\rm p}}{m_*}\right)^{1/3} + 0.961\left(\frac{m_{\rm p}}{m_*}\right)^{2/3}. \tag{B4}$$

For the examples on Fig. 2 and Fig. B1 with a 2 $M_{\rm Jup}$ planet orbiting a solar-type star, $m_{\rm p}/m_* = 1.9 \times 10^{-3}$ and so equation (B4) predicts a critical planet eccentricity of 0.05 (equal to the eccentricity of Jupiter). So for this example, if the planet eccentricity were below 0.05 then the inner-edge profile would be similar to the circular-planet case (Fig. 2), whilst higher planet eccentricities would result in a flatter inner edge (Fig. B1).

The actual inner-edge steepnesses on the pericentre and apocentre sides are comparable to that predicted by equation (13); for the example on Fig. B1, inserting $e_{\rm i,rms} \approx e_{\rm max,sec}/\sqrt{3} = 0.17$ into equation (13) predicts $\sigma_{\rm i} \approx 0.144$, comparable to the simulation values of 0.137 and 0.106 on the pericentre and apocentre sides, respectively.[9]

Generally, the inner edge of an eccentric disc would be steeper on the apocentre side than the pericentre side, due to how the innermost debris evolves. Pearce & Wyatt (2014) showed that the inner edge is set by debris with the innermost stable semimajor axis $a_{\rm in}$, which oscillates in eccentricity between 0 and $2e_{\rm forced}$. This debris also evolves in orientation, being maximally aligned with the planet orbit when its eccentricity is high, and minimally aligned when low. The result is that the disc inner edge assumes an eccentric shape; combining equations (5) and (6) in Pearce & Wyatt (2014) shows that an ellipse fitted to the disc inner edge will have eccentricity

$$e_{\rm i} = \frac{e_{\rm forced}(a_{\rm in})}{1 - e_{\rm forced}(a_{\rm in})}, \tag{B5}$$

[9]Strictly the rms eccentricity of a secular population scales with $e_{\rm max,\,sec}$ by a factor $\sqrt{2}$ rather than $\sqrt{3}$, since the eccentricity distribution is not uniform, but for this simple estimate we neglect this difference.

Downloaded from https://academic.oup.com/mnras/article/doi/10.1093/mnras/stad3462/7382221 by guest on 23 November 2023

which is $e_{\rm forced}(a_{\rm in})$ to first order.[10] This means that at apocentre the inner edge is a superposition of low-eccentricity orbits at the innermost stable semimajor axis, so its profile is relatively sharp; conversely, at pericentre the inner edge is a diffuse superposition of higher-eccentricity orbits and is flatter. There may also be additional surface-density features that would manifest in particularly narrow and/or eccentric discs (Pearce & Wyatt 2014).

APPENDIX C: CRITERION FOR PLANET-SCULPTED EDGES TO BE STEEPER THAN THE OVERALL DISC

In Appendix E1, we show that the steepness of the erf function is equivalent to that of a power law r^p if

$$\sigma_{\rm i} = \sqrt{\frac{2}{\pi}}\frac{1}{p}, \tag{C1}$$

and so the inner edge is much steeper than the overall disc profile if $\sigma_{\rm i} \ll \sqrt{2/\pi}/\alpha$. Since all of our simulated inner edges have $\sigma_{\rm i} < 0.2$ (Fig. 6), the planet-sculpted edges should be much steeper than the overall disc provided that the initial-disc profile is flatter than r^{-4} (and also r^4).

APPENDIX D: DERIVING INNER-EDGE PARAMETERS FROM OUR SIMPLE SCATTERING MODEL

Here, we use our simple scattering model to predict inner-edge parameters, yielding the results in Sections 3.1.1 and 3.1.2. These parameters are derived with reference to Fig. 8.

D1 Semimajor axes a_1 and a_2, and the fraction of surviving debris with semimajor axis a

We define

$$a_1 \equiv a_{\rm p} + \delta a, \tag{D1}$$

to be the semimajor axis where $e_{\rm q}(a_1) = 0$, that is, the semimajor axis of a circular orbit at the outer edge of the chaotic zone (recalling that $e_{\rm q}(a)$ is given by equation 9). Then, we define

$$a_2 \equiv \frac{a_{\rm p} + \delta a}{1 - e_{\rm max}} = \frac{a_1}{1 - e_{\rm max}}, \tag{D2}$$

as the semimajor axis where $e_{\rm q} = e_{\rm max}$, that is, the semimajor axis of an orbit with pericentre at the outer edge of the chaotic zone and eccentricity equal to the maximum eccentricity $e_{\rm max}$.

Next, we assume that the fraction of surviving particles with semimajor axis a transitions from 0 per cent for $a \leq a_1$ to 100 per cent for $a \geq a_2$. Since we assume that all debris with initial eccentricity above $e_{\rm q}(a)$ is ejected, for particles with initial eccentricities uniformly distributed between 0 and $e_{\rm max}$ the probability density function of surviving particles goes as

$$S(a) \propto \frac{e_{\rm q}(a)}{e_{\rm max}}, \tag{D3}$$

for $a_1 \leq a \leq a_2$. Similarly, $S(a) = 0$ for $a \leq a_1$ and is constant for $a \geq a_2$.

[10]The equivalent equation for the eccentricity of the outer edge is $e_{\rm out} = e_{\rm forced}(a_{\rm out})/[1 + e_{\rm forced}(a_{\rm out})]$, where $a_{\rm out}$ is the outermost semimajor axis; similarly, this reduces to $e_{\rm out} \approx e_{\rm forced}(a_{\rm out})$ to first order.

D2 Inner-edge location $r_{\rm i}$

For an orbit with semimajor axis a and eccentricity e, the time-averaged value of some parameter x over a single orbit is

$$\langle x \rangle = \frac{1}{2\pi a^2\sqrt{1-e^2}} \int_0^{2\pi} r^2(f)x(f){\rm d}f, \tag{D4}$$

where r and f are the radial distance and true anomaly, respectively (e.g. Murray & Dermott 1999). Hence, the time-averaged radial distance of a single body is

$$\langle r_{a,e} \rangle = a\left(1 + \frac{e^2}{2}\right). \tag{D5}$$

For a collection of bodies with the same semimajor axis but with eccentricities uniformly drawn between 0 and $e_{\rm q}$, we can integrate equation (D5) to get the average radial position of the bodies in this group; this is $\langle r_a \rangle = \int_0^{e_{\rm q}} \langle r_{a,e} \rangle(e){\rm d}e/e_{\rm q}$, which yields

$$\langle r_a \rangle = a\left[1 + \frac{e_{\rm q}^2(a)}{6}\right]. \tag{D6}$$

Next, we integrate equation (D6) to find the average position of all particles with semimajor axes between a_1 and a_2, which we hypothesize to be similar to the characteristic inner-edge radius $r_{\rm i}$. This is $r_{\rm i} \approx \int_{a_1}^{a_2} \langle r_a \rangle(a) S(a){\rm d}a$. Finally, we replace $e_{\rm max}$ in the above equations with $\sqrt{3}e_{\rm i,rms}$ for a uniform eccentricity distribution, and expand to first order in eccentricity. This yields our prediction for the characteristic radius of the sculpted disc's inner edge:

$$r_{\rm i} \approx a_{\rm p}\left(1 + \frac{\delta a}{a_{\rm p}}\right)\left(1 + \frac{2}{\sqrt{3}}e_{\rm i,rms}\right). \tag{D7}$$

APPENDIX E: RELATING THE VARIOUS LITERATURE MODELS USED TO QUANTIFY EDGE PROFILES

Various parametric models are used in the literature to quantify the steepness of debris-disc inner edges. Here, we provide conversions of commonly used steepness parameters to the $\sigma_{\rm i}$ we use. We also show a radial profile quantified by a power-law function, and also the equivalent erf-power-law function with parameters derived using the following equations, to show the two are similar (Fig. E1).

E1 Relating erf to a radial power law

Consider an inner edge fitted with the erf function

$$\Sigma_{\rm E}(r) = \Sigma_0\left[1 - {\rm erf}\left(\frac{r_{\rm i} - r}{\sqrt{2}\sigma_{\rm i} r_{\rm i}}\right)\right], \tag{E1}$$

where Σ_0 is the surface density at the characteristic edge radius $r_{\rm i}$ (e.g. Rafikov 2023). The profile could alternatively be quantified by a power law:

$$\Sigma_{\rm P}(r) = \Sigma_0\left(\frac{r}{r_{\rm i}}\right)^{p_{\rm i}}. \tag{E2}$$

Equations (E1) and (E2) can be differentiated to yield the slopes at $r_{\rm i}$:

$$\left.\frac{\rm d}{{\rm d}r}\Sigma_{\rm E}(r)\right|_{r=r_{\rm i}} = \sqrt{\frac{2}{\pi}}\frac{\Sigma_0}{r_{\rm i}\sigma_{\rm i}}, \tag{E3}$$

and

$$\left.\frac{\rm d}{{\rm d}r}\Sigma_{\rm P}(r)\right|_{r=r_{\rm i}} = \frac{\Sigma_0 p_{\rm i}}{r_{\rm i}}. \tag{E4}$$

Downloaded from https://academic.oup.com/mnras/article/doi/10.1093/mnras/stad3462/7382221 by guest on 23 November 2023

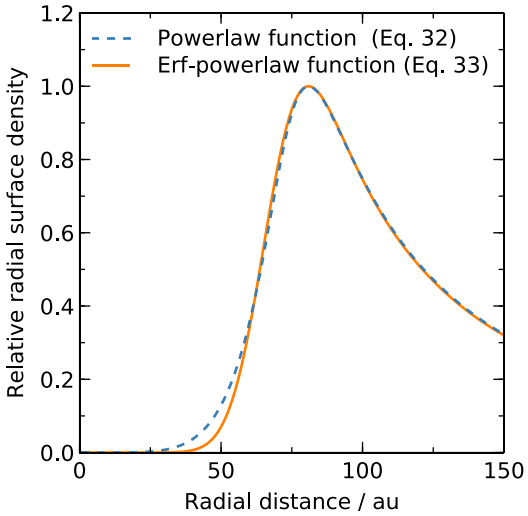

Figure E1. The double-power-law model for the observed q^1 Eri disc from Lovell et al. (2021), compared to our erf-power-law model inferred using the method in Section 5.

Hence, the erf function (equation E1) has the same steepness as the power-law function (equation E2) at r_i if

$$\sigma_\mathrm{i} = \sqrt{\frac{2}{\pi}}\frac{1}{p_\mathrm{i}}. \tag{E5}$$

E2 Relating erf to tan*h*

Consider an inner edge fitted with a hyperbolic-tangent function

$$\Sigma_\mathrm{T}(r) = \Sigma_0\left[1 + \tanh\left(\frac{r - r_\mathrm{i}}{l_\mathrm{i}}\right)\right], \tag{E6}$$

where l_i characterizes the edge flatness (e.g. Marino 2021). Differentiating this yields the slope at $r = r_\mathrm{i}$:

$$\frac{\mathrm{d}}{\mathrm{d}r}\Sigma_\mathrm{T}(r)\bigg|_{r=r_\mathrm{i}} = \frac{\Sigma_0}{l_\mathrm{i}}. \tag{E7}$$

Equating this to equation (E3) shows that the erf function has the same slope as the hyperbolic-tangent function at $r = r_\mathrm{i}$ if

$$\sigma_\mathrm{i} = \sqrt{\frac{2}{\pi}}\frac{l_\mathrm{i}}{r_\mathrm{i}}. \tag{E8}$$

E3 Relating tan*h* to a radial power law

Equating equations (E4) and (E7) show that a radial power law has the same slope as the hyperbolic-tangent function at $r = r_\mathrm{i}$ if

$$p_\mathrm{i} = \frac{r_\mathrm{i}}{l_\mathrm{i}}. \tag{E9}$$

This paper has been typeset from a TEX/LATEX file prepared by the author.

Downloaded from https://academic.oup.com/mnras/article/doi/10.1093/mnras/stad3462/7382221 by guest on 23 November 2023

© The Author(s) 2023.
Published by Oxford University Press on behalf of Royal Astronomical Society. This is an Open Access article distributed under the terms of the Creative Commons Attribution License (https://creativecommons.org/licenses/by/4.0/), which permits unrestricted reuse, distribution, and reproduction in any medium, provided the original work is properly cited.

American Journal of Physics

PAPERS | AUGUST 01 2022

Perihelion precession in power-law potentials: Hénon's theorem

V. Dmitrašinović; Marija R. Janković

Check for updates

Am. J. Phys. 90, 580–586 (2022)
https://doi.org/10.1119/5.0080691

View Online
Export Citation

Articles You May Be Interested In

Einstein's perihelion formula and its generalization

Am. J. Phys. (April 2015)

Expanding the range of validity of the simplest computation of the perihelion precession in Schwarzschild spacetime

Am. J. Phys. (January 2024)

Nonrelativistic contribution to Mercury's perihelion precession

Am. J. Phys. (June 1979)

18 February 2026 10:25:56

AAPT PHYSICS EDUCATION®

Perihelion precession in power-law potentials: Hénon's theorem

V. Dmitrašinović[a)]
Institute of Physics, Belgrade University, Pregrevica 118, Zemun, P.O. Box 57, 11080 Beograd, Serbia

Marija R. Janković
Institute of Astronomy, University of Cambridge, Madingley Road, Cambridge CB3 0HA, United Kingdom

(Received 2 December 2021; accepted 11 May 2022)

In 1977, Michel Hénon proved a remarkable theorem for planar N-body orbits in power-law potentials that relates the rate of change of the perihelion angle (the precession rate), the rate of change of the period evaluated at constant energy, the angular momentum of an orbit, and the power law of the potential. We provide a simple proof of this theorem for two bodies in periodic orbits that interact via a radial power-law force, which is, of course, equivalent to a one-body problem with a power-law central potential. We discuss this theorem's underlying assumptions and implications, including its relation to Bertrand's and Bohlin's theorems, and we illustrate it with several numerically calculated examples. © *2022 Published under an exclusive license by American Association of Physics Teachers.*
https://doi.org/10.1119/5.0080691

I. INTRODUCTION

The classical mechanics of two bodies interacting via a radial force law has been studied in great detail over the past 300 years.[1,2] Bertrand's theorem[2] states that central potentials result in closed, elliptical orbits for all two-body bound systems only for potentials proportional to $1/r$ (Newtonian gravity) or r^2 (harmonic oscillator). Therefore, for these two potentials, precession of the perihelion occurs only when there is an external perturbation. A range of particular results about the rate of change of this precession angle is known,[3] so much so that one might be forgiven for believing that everything that can be known about orbits has been known for at least one century.

Yet, there is one comparatively recent (1977) non-trivial result in this field: Hénon's theorem[4] relates the rate of change of the perihelion/aphelion angle to the rate of change of the period at fixed energy for an N-body system moving in a plane. Hénon's theorem holds for any power-law potential, not only for the two precession-free potentials discussed above.

Power-law potentials form an important subset in classical mechanics: It is well known that power-law or homogeneous[5] potentials lead to simple scaling laws.[1,6] It is perhaps less well known that these scaling laws lead to certain duality relations between periodic orbits in power-law potentials of the form $V(r) \sim r^{\alpha}$ and $V(r) \sim r^{\bar{\alpha}}$ when the powers α and $\bar{\alpha}$ are related by $(\alpha+2)(\bar{\alpha}+2) = 4$. This duality was discovered by Bohlin[7,8] and Kasner[9] in the early 20th century and discussed at length in this journal[10–12] and elsewhere.[13–16] In some presentations, this duality appears as a mere mathematical curiosity, but it is a direct consequence of the homogeneity of the potential, i.e., of the underlying scaling symmetry.

Normally, the properties of physical systems implied by symmetry are studied in some detail in textbooks, but the scaling symmetry appears to be an exception, perhaps because of the prevailing attitude that its consequences must be trivial. However, as the example of Hénon's theorem shows, the consequences of classical or "engineering" scaling in point particle dynamics are far from fully understood, and still farther from being well known, even among experts in classical dynamics, let alone the wider physics community.

The purpose of this article is to present Hénon's theorem, provide an undergraduate-level proof for the two-body case, and connect it with other results based on scaling arguments. In particular, we shall show that Hénon's theorem is consistent with the aforementioned (power-law) conformal duality in Newtonian two-body dynamics. Indeed, Bertrand's theorem receives a new meaning in view of Hénon's theorem. We also show how to use Hénon's theorem and the duality law to find all power-law potentials integrable by means of elliptic integrals.

This paper consists of six sections. After the Introduction, in Sec. II, we briefly review the preliminaries. Then in Sec. III, we state Hénon's theorem for two body motion and discuss some of its basic consequences. In Sec. IV, we show the proof of this version of Hénon's theorem. In Sec. V, we present several examples of integrable motions in power-law potentials. In Sec. VI, we put these results into their wider historical perspective, summarize, and draw conclusions.

II. PRELIMINARIES

The original Hénon's theorem addresses planar periodic N-body orbits, where $N = 1, 2, 3, \ldots$, with non-zero angular momentum in power-law binary potentials including, but not limited to, Newtonian gravity. Here, we only address the case of two bodies ($N = 2$) interacting via a radial force, and, of course, the equivalent case of one body in a fixed central potential. First, in Sec. II A, we remind the reader of some basic facts of two-body motion in central potentials. Then in Sec. II B, we specialize to power-law potentials, of which the Newtonian gravity is a special case. Power-law potentials allow similar solutions when parameters are scaled, and in this discussion, we will hold fixed masses, coupling constant, and energy. The scale-invariant period and angular momentum that facilitate this stipulation are shown in Sec. II C.

A. Periodic two-body orbits in central potentials

It is well known[1,3] that the problem of two bodies ($N = 2$) interacting via a central potential $V(r)$ is integrable (in Liouville's sense), because it can be reduced to the problem of a single body moving in an effective potential $V_{\text{eff.}}(r) = L^2/(2mr^2) + V(r)$ with only one degree of freedom, r.

18 February 2026 10:25:56

 © 2022 Published under an exclusive license by AAPT

Angular momentum conservation implies planar motion of the particles.[1,2] After removing the center-of-mass motion, the $N=2$-body problem turns into a planar one-body problem that can be parametrized with two variables: The radius r (from the center of attraction) and an angle θ. The equations of motion in these two variables can be separated. In bounded motion, the radius moves between some minimum (perihelion) and maximum (aphelion), whereas the angle generally increases or decreases monotonically.

In an inertial frame of reference, the trajectories of periodic orbits form closed curves such as ellipses or Rosetta-like curves as shown in Fig. 1. Because the trajectories are periodic, the period T_r of radial oscillation and the time T_θ for the angle θ to increase by 2π are commensurate. Equivalently, when viewed in a co-rotating frame of reference, the trajectory is a closed curve with a period that is commensurate with the inverse of the angular frequency of the frame's rotation. When we refer to the "period" of such a system, we will always mean T_r rather than the time required for the orbit to return to precisely the same conditions.

In quasi-periodic orbits, on the other hand, these two periods are incommensurate—such orbits have perihelia that slowly precess in such a way that the curves never close and fill up the plane after sufficiently long time, see Fig. 1(b). Equivalently, when viewed in a co-rotating frame of reference, the trajectory is a closed curve with a period that is incommensurate with the inverse angular velocity of the rotation.

As far as Hénon's theorem is concerned, there is no intrinsic difference between periodic and quasi-periodic orbits, as both may have precessing perihelia, and in both cases, we will refer to the radial period, T_r, simply as the period. The shift of the angle of the perihelion, ϕ, during one radial period will be called the precession angle $\Phi = \Delta\phi = \phi(T_r) - \phi(0)$. In two-body problems, both $\Phi(E,L,\alpha)$ and $T_r(E,L,\alpha)$ can be expressed as definite integrals over the radius r that depend parametrically on the energy E and the angular momentum L, see Eqs. (1) and (3). When the motion proceeds in a power-law central potential, there are additional constraints on these dependences.

B. Two-body trajectories in power-law potentials

When the potential is a power law, $V(r) = V_\alpha(r) = \mathrm{sgn}(\alpha) g_\alpha r^\alpha$, where $\mathrm{sgn}(x) = x/|x|$ and $g_\alpha > 0$, the solutions are generally (for a range of angular momenta and energies) bounded and quasi-periodic for powers $-2 < \alpha < +\infty$. For powers $-2 > \alpha > -\infty$, the motion is generally unbounded, and thus, non-periodic, though there may exist individual periodic orbits (at specific values of energy and angular momentum) which are unstable. For future convenience, we set $g_\alpha = \bar{g} a^{-\alpha}$, where a is the length scale and $\bar{g}$ is the (universal) coupling strength with dimension of energy; $\bar{g}$ and a are set to fixed constant values, whereas the energy E and the angular momentum L are non-vanishing and apparently independent variables that are also constants of the motion. However, due to the power-law nature of the potential, there are non-trivial relations among these nominally independent constants. Section II C will explain the interdependence of the mass m, the coupling $\bar{g}$, the length scale a, and the dynamical constants of the motion E and L.

The period T_r of the radial motion and the perihelion shift angle Φ can be expressed as integrals over one period[1,2] with upper and lower integration limits depending on the angular momentum L: Eq. (14.6) in Ref. 1 for the period T of a periodic orbit reads

$$T_r(L,E,\alpha) = 2\int_{r_{\min}}^{r_{\max}} \frac{dr}{\sqrt{\frac{2}{m}\left(\mathrm{E} - \frac{L^2}{2mr^2} - \mathrm{sgn}(\alpha) g_\alpha r^\alpha\right)}}, \tag{1}$$

where $r_{\min}$ and $r_{\max}$ are the two extremal solutions to the equation

$$E - \frac{L^2}{2mr^2} - \mathrm{sgn}(\alpha) g_\alpha r^\alpha = 0, \tag{2}$$

and Eq. (14.10) in Ref. 1 for the perihelion precession angle Φ of an orbit during one period

$$\Phi(L,E,\alpha) = 2\int_{r_{\min}}^{r_{\max}} \frac{L\,dr}{mr^2\sqrt{\frac{2}{m}\left(\mathrm{E} - \frac{L^2}{2mr^2} - \mathrm{sgn}(\alpha) g_\alpha r^\alpha\right)}}. \tag{3}$$

In the following, these two integrals will be of paramount interest, but there are other dimensional integrals that can be related to these two by way of partial integration with respect to the energy E and angular-momentum L.

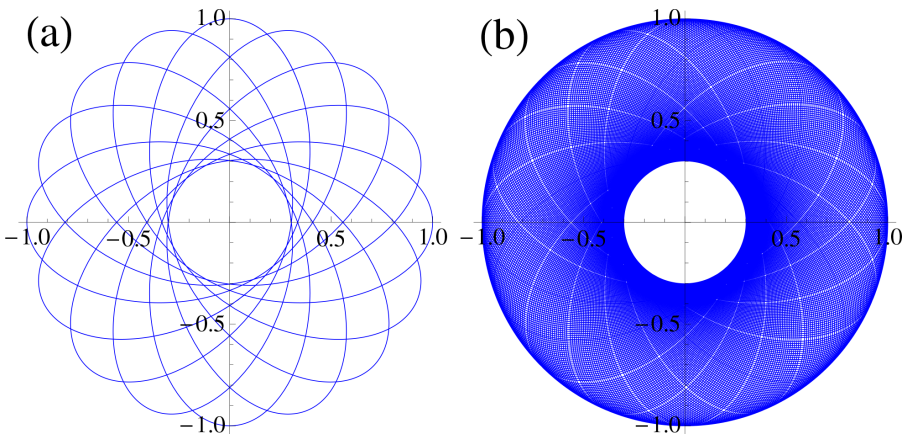

Fig. 1. Precessing one-body orbits in the central logarithmic potential: (a) closed, absolutely periodic orbit, with commensurate T_r and T_θ, (b) infinite, quasi-periodic orbit, with incommensurate T_r and T_θ, after a finite time. The initial conditions are: (a) $x_0 = \dot{y}_0 = 0, y_0 = 1, \dot{x}_0 = 0.488\,00$; (b) $x_0 = \dot{y}_0 = 0, y_0 = 1, \dot{x}_0 = 0.490$. The coupling g and mass m were set to unity.

18 February 2026 10:25:56

(1) The auxiliary integral (the so-called radial action):

$$I_r(E,L,\alpha) = \frac{1}{\pi}\int_{r_{\min}}^{r_{\max}} dr\sqrt{2m\left(\mathrm{E} - \frac{L^2}{2mr^2} - \mathrm{sgn}(\alpha)g_\alpha r^\alpha\right)} \sim \int_{r_{\min}}^{r_{\max}} \mathbf{p}\cdot d\mathbf{r}. \tag{4}$$

(2) The precession angle:

$$\Phi(E,L,\alpha) = 2\pi f(E,L,\alpha), \tag{5}$$

where

$$f(E,L) = -\left(\frac{\partial I_r(E,L)}{\partial L}\right)_E. \tag{6}$$

(3) The (radial) period:

$$T_r = T_r(E,L) = \frac{2\pi}{\omega_r}, \tag{7}$$

which is inversely proportional to the (radial) frequency

$$\omega_r(E,L) = \left(\frac{\partial I_r(E,L)}{\partial E}\right)_L^{-1}. \tag{8}$$

C. Scaling of orbits in power-law potentials

The Newtonian equation of motion for a nonrelativistic particle in a homogeneous potential $V_\alpha(r)$ is

$$m\ddot{\mathbf{r}} = -\nabla_{\mathbf{r}} V_\alpha(\mathbf{r}) = -\alpha\,\mathrm{sgn}(\alpha) g_\alpha r^{\alpha-1}\hat{\mathbf{r}}.$$

Scaling the spatial coordinates in this equation according to $\mathbf{r}\to\lambda\mathbf{r}$ demands a temporal rescaling as $t\to\lambda^{(1-\alpha/2)}t$ in order to preserve the form of the equation of motion. In this scaling, we see

$$\begin{aligned} &\mathbf{r}\to\lambda\mathbf{r},\\ &t\to\lambda^{(1-\alpha/2)}t,\\ &\mathbf{p}\to\mathbf{p}\lambda^{\alpha/2},\\ &E\to\lambda^\alpha E,\\ &L\to\lambda^{1+\alpha/2}L,\\ &I_r\to\lambda^{1+\alpha/2}I_r. \end{aligned} \tag{9}$$

Alternatively, we may introduce a new scaling parameter s under which energy E scales linearly

$$\begin{aligned} &\mathbf{r}\to s^{1/\alpha}\mathbf{r},\\ &t\to s^{1/\alpha-1/2}t,\\ &\mathbf{p}\to s^{1/2}\mathbf{p},\\ &E\to sE,\\ &L\to s^{1/2+1/\alpha}L,\\ &I_r\to s^{1/2+1/\alpha}I_r. \end{aligned} \tag{10}$$

Using these relationships, one can build scale-invariant combinations of independent dynamical variables such as $T|E|^{1/2-1/\alpha}$, $TR^{-(1-\alpha/2)}$, and $|E||L|^{(-2\alpha/(2+\alpha))}$. These scaling invariants depend on dimensional variables in a unique way, however. For example,

(1) The energy dependence $T\sim|E|^{1/\alpha-1/2}$ of the period T is determined by the spatial scaling rules. It has a unique prefactor (see, e.g., Problem 2 in Sec. 11 of Ref. 1)

$$T\sim\sqrt{\frac{m}{E}}\left(\frac{E}{g_\alpha}\right)^{1/\alpha}\sim|E|^{1/\alpha-1/2}\sqrt{m}(g_\alpha)^{-1/\alpha}, \tag{11}$$

so the mass m and coupling constant g_α dependences of T also follow from scaling laws. Since the dimensional coupling $g_\alpha=\bar{g}a^{-\alpha}$ can be replaced by $\bar{g}$, which has the dimension of energy, and a length unit a, we have uniquely determined the dependences not just on the energy E but also on the coupling g_α, and/or the length scale a, and on the mass m. In other words, and as advertised earlier, homogeneity of the potential implies scaling rules that imply the change of mass and of the coupling constant, as well as the spatiotemporal scaling.

(2) The dimensionless phase Φ has no dimensional prefactor: It can only depend on dimensionless scale-invariant quantities, such as $2ma^2E/L^2$, $2ma^2\lambda/L^2$, or $r_{\min/\max}/a$, i.e.,

$$\Phi = \Phi_\alpha\left(\frac{2ma^2E}{L^2}, \frac{2ma^2\lambda}{L^2}, \frac{r_{\max}}{a}, \frac{r_{\min}}{a}\right). \tag{12}$$

Thus, even though the energy E and the angular momentum L are independent variables, under scaling transformations they change such that the constraint $|E||L|^{(-2\alpha/(2+\alpha))}=\text{const.}$ remains fulfilled. This relation can be rewritten as $L|E|^{(-1/2-1/\alpha)}=L_{\text{s.i.}}=\text{const.}$, which serves as a definition of the scale-invariant angular momentum $L_{\text{s.i.}}$. Different values of the scale-invariant angular momentum $L_{\text{s.i.}}$ reflect its independence of energy E. Therefore, we must take into account this and all other constraints stemming from scaling symmetry.

III. HÉNON'S THEOREM

A. Statement

For the two-body problem in a homogeneous potential $V(r)\sim g_\alpha r^\alpha$, Hénon's theorem reads

$$\left(\frac{\partial T}{\partial\Phi}\right)_E = \left(\frac{1}{\alpha}+\frac{1}{2}\right)\frac{L}{E}. \tag{13}$$

This equation will be proven in Sec. IV. Note that:

(1) This result implies $L\sim(\partial T/\partial\Phi)_E$, whereas one might have naively expected $L\sim\Phi\sim(\partial\Phi/\partial T)$. The explanation for this counter-intuitive inverse proportionality is that it is not a derivative with respect to time t, but with respect to the period T;

(2) Both sides of Eq. (13) are homogeneous of degree $1-\alpha/2$, i.e., they transform as $\lambda^{(1-\alpha/2)}$ under scaling Eq. (9). This means that one could have written entirely in terms of scale-invariant variables $T_{\text{s.i.}}=T|E|^{(1/2-1/\alpha)}$ and $L_{\text{s.i.}}=L|E|^{(-1/2-1/\alpha)}$, i.e., as $(\partial T_{\text{s.i.}}/\partial\Phi)=(1/\alpha+1/2)L_{\text{s.i.}}$.

18 February 2026 10:25:56

B. Some consequences

There are four special values of α worthy of discussion:

(1) In the case of the so-called "strong" force ($\alpha = -2$), the pre-factor on the right-hand side of Eq. (13) vanishes, thus leading to the statement $(\partial T/\partial\Phi)_E = 0$. The only periodic solution is a circular orbit with $E = 0$ and a fixed value of angular momentum L. Its dual $\bar{\alpha} = \pm\infty$ case corresponds to a hard sphere (or solid-wall) potential.[12]

(2) In the self-dual case $\alpha = 0$, $\bar{\alpha} = 0$, the right-hand side of this formula goes to infinity, thus implying $(\partial T/\partial\Phi)_E \to \infty$. Note, however, that $\alpha = 0$ corresponds to free motion, as the potential is a constant. Consequently, there can be no periodic orbits, and the corresponding notions such as the period T and perihelion shift Φ are both undefined.[17] Therefore, this singularity is illusory.

(3) For Newtonian gravity or the Coulomb force, the perihelion of the elliptic orbit does not precess $\Phi(T, L, E) = 0$, which would seem to imply $(\partial\Phi/\partial T)_E = 0$, which in Eq. (13) implies $E/L = 0$ for arbitrary finite values of L at finite fixed values of E. This apparent paradox is resolved by examining Hénon's theorem for the case $\alpha = -1$

$$\left(\frac{\partial T}{\partial\Phi}\right)_E = -\frac{L}{2E}, \tag{14}$$

and noticing that the period $T(L, E)$ is also independent of the angular momentum at fixed value of energy E, i.e., that both $(\partial\Phi/\partial L)_E = 0$ and $(\partial T/\partial L)_E = 0$ hold.[18] Therefore, Eq. (14) is an identity of the $0 = 0$ type, whereas Eq. (13) has the form of $0/0 = E/L < \infty$. Thus, there is no paradox. Indeed, this means that the $E(L)$ function for the Keplerian two-body orbits is (infinitely) multivalued, and that one cannot deduce $\Phi(T, L, E) = const.(= 0)$ from Hénon's theorem alone.

(4) The harmonic oscillator potential $\bar{\alpha} = 2$, is the dual of Newtonian potential; there is no perihelion precession in the harmonic oscillator and the angular momentum is arbitrary at fixed values of energy for arbitrary number of particles N. For this reason, we have $(\partial\Phi/\partial T)_E = 0/0$ here, just as in the $N = 2$ Newtonian potential.

Note, moreover, that Eq. (13) for exponents α and $\bar{\alpha}$ can be connected by means of the duality relation $(\alpha + 2)(\bar{\alpha} + 2) = 4$. This implies an identity relating the rates of change of the periods dT_α and $dT_{\bar{\alpha}}$, to the rates of change of the perihelion shifts $d\Phi_\alpha$ and $d\Phi_{\bar{\alpha}}$. This is the differential form of the conformal duality relations.[10,11,13]

IV. PROOF

In the special case, we are considering of two-body systems in power-law potentials, and the proof can be reduced to a series of (purely) algebraic operations, i.e., Eq. (13) becomes an identity, albeit a non-trivial one to prove.[19]

The radial action $I_r(L, E)$, Eq. (4), can be expressed explicitly in terms of the previously defined ω_r, Eq. (8), and $f(L)$, Eq. (6), by means of the following identity (this is Eq. (B3) in Ref. 20, modulo the energy E factor)

$$I_r = \frac{2\alpha}{2+\alpha}\frac{E}{\omega_r} - Lf(L). \tag{15}$$

Proof of identity Eq. (13):

We start from Eq. (10) for the scaling of the radial action

$$I_r(sE, s^{1/2+1/\alpha}L) = s^{1/2+1/\alpha} I_r(E, L).$$

Differentiating this with respect to s and then setting $s = 1$

$$\frac{\partial}{\partial s} I_r(sE, s^{1/2+1/\alpha}L)\bigg|_{s=1} = \frac{\partial}{\partial s} s^{1/2+1/\alpha}\bigg|_{s=1} I_r(E, L),$$

we find[21]

$$E\left(\frac{\partial I_r(E,L)}{\partial E}\right)_L + L\left(\frac{1}{2}+\frac{1}{\alpha}\right)\left(\frac{\partial I_r(E,L)}{\partial L}\right)_E = \left(\frac{1}{2}+\frac{1}{\alpha}\right) I_r(E, L).$$

Next, we use Eq. (7) for the radial period T_r, and Eq. (8) for the radial frequency, ω_r^{-1} to rewrite

$$\frac{2\alpha}{2+\alpha}\frac{E}{\omega_r} = I_r - L\frac{\partial I_r}{\partial L}.$$

Next use the definition Eq. (6) to find Eq. (15). *q.e.d.* Now we are set for the Proof of identity Eq. (13).

Start from the identity Eq. (15), without setting $E = 1$, to express $f(L) = -\partial I_r(E, L)/\partial L$ as follows:

$$-f(L) = \frac{\partial I_r(E,L)}{\partial L} = \frac{\partial}{\partial L}\left(\frac{2\alpha}{2+\alpha}\frac{E}{\omega_r} - Lf(L)\right),$$

i.e.,

$$\frac{\partial}{\partial L}\left(\frac{2\alpha}{2+\alpha}\frac{E}{\omega_r} - Lf(L)\right) = \left(\frac{2\alpha}{2+\alpha}\right)\frac{\partial}{\partial L}\frac{E}{\omega_r} - f(L) - L\frac{\partial f(L)}{\partial L},$$

implying

$$L\frac{\partial f(L)}{\partial L} = \left(\frac{2\alpha}{2+\alpha}\right) E\left(\frac{\partial}{\partial L}\frac{1}{\omega_r}\right)_E.$$

Next use the definition Eq. (8) of the period T in terms of ω_r and Eq. (6) in $\partial f(L)/\partial L$ to find

$$\frac{L}{2\pi}\frac{\partial\Phi(L)}{\partial L} = \left(\frac{2\alpha}{2+\alpha}\right)\frac{E}{2\pi}\frac{\partial T}{\partial L},$$

which is Hénon's theorem (13) for the two-body problem, provided $\partial\Phi/\partial L \neq 0$. *q.e.d.*

The above proofs amount to repeated applications of (several) identities among partial derivatives of functions of two real independent variables E, L. This may give one the false impression that Hénon's theorem for two-body motion is a mere identity. That is not so, because in deriving Eq. (15) we

Table I. Nine integer-valued exponents α in power-law potentials, and their duals $\bar{\alpha}$, integrable in terms of elliptic integrals. Here, $(\alpha + 2)(\bar{\alpha} + 2) = 4$ holds.

α	6	4	2	1	−1	−2	−3	−4	−6
$\bar{\alpha}$	−3/2	−4/3	−1	−2/3	2	$\pm\infty$	−6	−4	−3

18 February 2026 10:25:56

Table II. Five fractional-valued powers α and their duals $\bar{\alpha}$ in power-law potentials integrable in terms of elliptic integrals. Here, $(\alpha+2)(\bar{\alpha}+2)=4$ holds.

α	$-3/2$	$-4/3$	$-2/3$	$-1/2$	$2/3$
$\bar{\alpha}$	6	4	1	2/3	$-1/2$

have repeatedly used the scaling symmetry, by way of Eqs. (9) and (10), which do not hold for inhomogeneous potentials.

V. EXAMPLES

Let us now show a few examples that illustrate why this is a non-trivial result. According to Whittaker[22] and Broucke,[23] there are exactly 14 values of the power α that can be expressed in terms of elliptic functions and/or elliptic integrals.[24] The nine integer values are shown in Table I, and the five fractional values are shown in Table II. Note that some of the same values appear also in the second row, the so-called dual powers $\bar{\alpha}$, in these tables. Manifestly, only $9+2=11$ of these exponents are independent, whereas the remaining three can be obtained by way of conformal transformations.

The Coulomb and harmonic oscillator, which are solved in terms of trigonometric functions, are but two of these 14. They have been treated in Refs. 10, 11, and 25 and shall not be repeated here. As discussed in Sec. III B, these two examples are indeed trivial, albeit only for $N=2$ bodies. Another special case, the so-called "strong potential," $\alpha=-2$, has been treated by Wu and Sprung,[12] again, so it will not be repeated here.

Whereas the remaining eight cases are expressible in terms of elliptic functions and/or integrals, their derivatives generally lead to very complicated expressions that have to be evaluated numerically, which we do here for three values of α, which equals six when their duals are taken into account. These examples ought to serve as a benchmark for the interested reader to compare with their own calculations.

A. Numerical check of Hénon's theorem for elliptic integrals $\alpha=-3/2, -1/2, 1/2$

Henon's equation (13) can be checked by numerical calculations: First, calculate $T(L)$ by numerically integrating Eq. (1) with integration boundaries shown in Eq. (2) and then invert it to find $L(T)$ (at fixed energy E). This will be used to compare $-(1/2+1/\alpha)L/E$ and $dT/d\Phi$, where $\Phi(L)$ is integrated from Eq. (3), again using integration boundaries shown in Eq. (2).

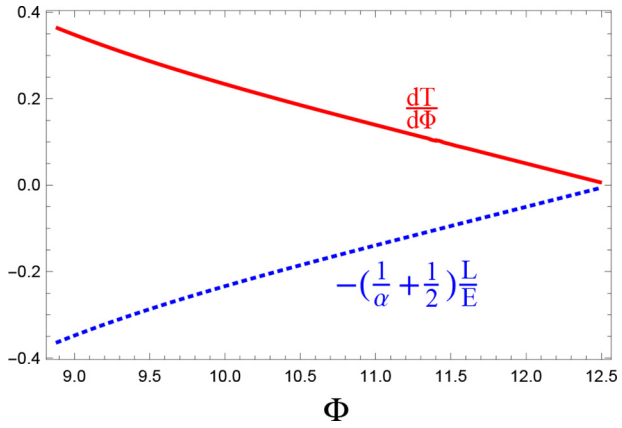

Fig. 3. Comparison of $-(1/2+1/\alpha)(L/E)$ (the negative left-hand side of Hénon's equation (13)—blue dotted line) with the derivative $dT/d\Phi$ (red solid line) in the power-law potential with $\alpha=-3/2$, at fixed energy $E=-1/2$.

Case $\alpha=-3/2$

We show the angular momentum $L(T)$ and the perihelion precession angle $\Phi(T)$ as functions of period T for relative periodic two-body orbits in the homogeneous potential with $\alpha=-3/2$ at fixed energy $E=-1/2$ in Fig. 2.

Note that in Fig. 2, the perihelion precession angle Φ is effectively negative at $\alpha=-3/2$: We have $\Phi(L=0)/(2\pi)=2$ and, as the angles are only defined modulo 2π, we may set it equal to zero: $\Phi(L=0)/(2\pi)=0$. In Fig. 3, we compare the negative of the quantity $(1/2+1/\alpha)(L/E)$ as directly calculated and the same quantity calculated by way of Hénon's identity, Eq. (13)—note the symmetry of curves above and below the horizontal axis, which confirms Hénon's theorem.

Cases $\alpha=-1/2$ and $\alpha=1/2$

Similarly, we show in Fig. 4 the perihelion precession angle $\Phi(T)$ as a function of period T for relative periodic two-body orbits for $\alpha=-1/2$ and $\alpha=1/2$. We see that Φ has the same sign and the same sign of its slope for both $\alpha=-1/2$ and $\alpha=1/2$. Assuming continuity in α, it follows that Φ is also non-zero with the same sign of slope at $\alpha=0$ in agreement with the argument based on Bertrand's theorem presented in Sec. III B.

VI. SUMMARY, DISCUSSION, AND CONCLUSIONS

Hénon's theorem is a consequence of scaling symmetry in a simple power-law mechanical system, just like the conformal duality, but it has not reached a wider audience as yet;

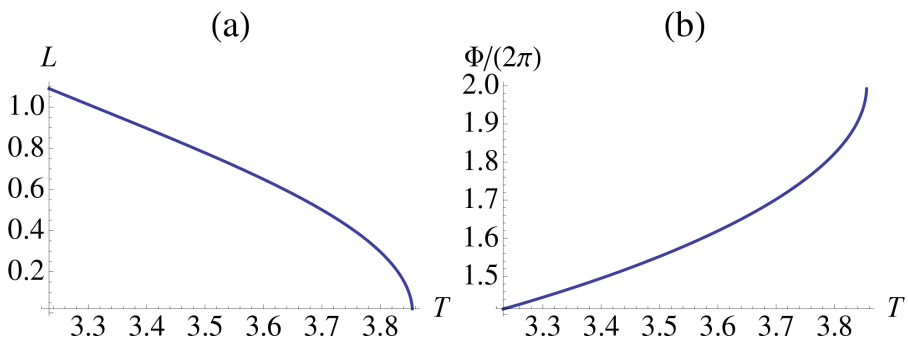

Fig. 2. (a) Angular momentum $L(T)$ and (b) the perihelion precession angle $\Phi(T)/(2\pi)$ as functions of period T for (quasi)periodic two-body orbits in the homogeneous potential with $\alpha=-3/2$, at fixed energy $E=-1/2$.

18 February 2026 10:25:56

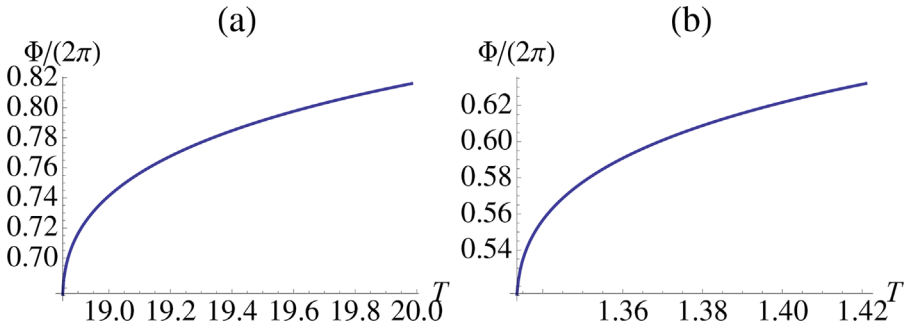

Fig. 4. (a) The perihelion precession angle $\Phi(T)$ as a function of period T for periodic two-body orbits in the power-law potential with $\alpha = -1/2$, at fixed energy $E = -1/2$ and (b) with $\alpha = 1/2$, at fixed energy $E = 1/2$.

herewith we hope to provoke curiosity among teachers and students of physics alike.

Hénon explained[4] his path towards this theorem: His formulation and subsequent derivation of the general formula followed an initial observation of a special case in his study of the "isochron" model of spherical star clusters[26] and in his studies of planar three-body problem.[27] Yet, Hénon's original proof of his theorem was based on Routh's formalism[28] of integrating out ignorable degrees of freedom (cyclic variables), which is not standard fare in undergraduate, or even graduate-level textbooks (for an exception, see Ref. 29).

Hénon was not the only person interested in this topic due to Einstein's calculation of Mercury's perihelion shift in General Relativity. Indeed, there was at least one close encounter[30] (but still a miss) before Hénon's formulation, and another one[20] thereafter. There are other consequences of homogeneity of power-law potentials, such as the conformal duality relations,[10–13,16] which was used in Tables I and II. Hénon's theorem fits nicely into this line of thought, though Hénon did not mention duality explicitly in his paper. Indeed, neither have the many authors of subsequent papers about conformal duality.[10–13,16] All of this leaves us with the question: Why was Hénon's theorem discovered so late, in the historical development of the subject, and why has it been missed and/or overlooked so often?

ACKNOWLEDGMENTS

The authors thank Igor Salom for careful reading of the manuscript and valuable suggestions. The results of the present paper were largely worked out during the academic years 2014–2015 and 2015–2016, during which time M.R.J. was a recipient of the "Professor Dr. Djordje Živanović" scholarship, awarded jointly by the Faculty of Physics and the Institute of Physics, Belgrade University and was also supported by a City of Belgrade studentship (Gradska stipendija grada Beograda, for 2013), as well as the "Dositeja" stipend from the Fund for Young Talents of the Serbian Ministry for Youth and Sport for the academic year 2015–2016 (Fond za mlade talente-stipendija "Dositeja"). V.D. was supported by the Serbian Ministry of Science and Technological Development, Grant No. 451-03-68/2020-14/200024.

[a]Electronic mail: dmitrasin@ipb.ac.rs, ORCID: 0000-0003-0192-921X.

[1]L. D. Landau and E. M. Lifshitz, *Mechanics*, 3rd ed. (Butterworth-Heinemann, Oxford, 1976), Sec. 10.
[2]H. Goldstein, *Classical Mechanics*, 2nd ed. (Addison-Wesley, Reading, MA, 1980).
[3]G. L. Kotkin and V. G. Serbo, *Collection of Problems in Classical Mechanics* (Pergamon, Oxford, 1971); see, e.g., problems 2.17, 2.19, 2.20, and 2.21 in Sec. II.
[4]M. Hénon, "A relation in families of periodic solutions," Celest. Mech. **15**, 99–105 (1977).
[5]"Power-law" and "homogeneous" are synonyms in the context of one- and two-body problems, as there is only one distance variable involved. That is not the case anymore as the number of bodies increases.
[6]Indeed, these scaling laws are so simple that they are often overlooked in textbooks on theoretical physics, one significant exception being Landau–Lifshitz (Ref. 1); whereas, at the other extreme, they are called "engineering" rules (Ref. 31) and/or are widely ignored. In stark contrast, the scaling properties of continua, both classical and quantum, such as those of phase transitions in statistical mechanics, or of quantum fields, are highly non-trivial—having been the subject of intense research for decades with many significant new results and no end in sight.
[7]M. K. Bohlin, "Note sur le probléme des deux corps et sur une intégration nouvelle dans le probléme des trois corps," Bull. Astron. **28**, 113–119 (1911).
[8]A forerunner of the duality relation (credited above to Bohlin) is published in Newton's Principia, as "the same otherwise, proof of proposition XI"; see footnote 18 in Ref. 11, as well as Refs. 14 and 15.
[9]E. Kasner, *Differential-Geometric Aspects of Dynamics* (American Mathematical Society, Providence, 1913).
[10]Laurence Mittag and Michael J. Stephen, "Conformal transformations and the application of complex variables in mechanics and quantum mechanics," Am. J. Phys. **60**, 207–211 (1992).
[11]Aaron K. Grant and Jonathan L. Rosner, "Classical orbits in power-law potentials," Am. J. Phys. **62**, 310–315 (1994).
[12]Hua Wu and D. W. L. Sprung, "Comment on 'Classical orbits in power-law potentials,'" Am. J. Phys. **63**, 564–567 (1995).
[13]V. I. Arnol'd, *Huyghens & Barrow, Newton & Hooke* (Birkäuser Verlag, Basel, 1990).
[14]T. Needham, "Newton and the transmutation of force," Amer. Math. Mon. **100**, 119–137 (1993).
[15]Tristan. Needham, *Visual Complex Analysis* (Clarendon, Oxford U. P., Oxford, 1997), Sec. X.3, p. 244.
[16]P. A. Horvathy, "The laws of planetary motion, derived from those of a harmonic oscillator (following Arnold)," arXiv:1404.2265 (2014).
[17]The logarithmic potential is also often associated with scale invariance, i.e., with the $\alpha \to 0$ limit of the power-law potential. However, in this potential, an additive constant appears under scaling transformations. Of course, the equations of motion are invariant under such additive constants, but the energy E is not. Thus, the above proof of Hénon's theorem must be modified for the logarithmic potential. One can pass from the logarithmic potential to the limit $\alpha = 0$ of the power-law if one subtracts a constant which tends to ∞, however.
[18]Of course, the deeper reason for these perhaps somewhat confusing facts is the existence of the conserved Laplace–Runge–Lenz vector, which exists in the two-body case only and implies a period that depends only on the energy E and not on the angular momentum: $T = T(E)$.
[19]The fact that in spite of great attention paid to the two-body problem over the years (centuries), Hénon's theorem was not discovered in that context is testimony to its non-triviality.

18 February 2026 10:25:56

[20]A. G. Magner, A. A. Vlasenko, and K. Arita, "Semiclassical trace formula for the two-dimensional radial power-law potentials," Phys. Rev. E **87**, 062916 (2013).
[21]This is just a variant of Euler's identity for homogeneous functions.
[22]E. T. Whittaker, *Analytical Dynamics of Particles* (Cambridge U. P., Cambridge, 1959).
[23]R. Broucke, "Notes on the central force r^n," Astrophys. Space Sci. **72**, 33–53 (1980).
[24]The $\alpha = 4$ case was explicitly solved in terms of elliptic functions in the Appendix of Ref. 20.
[25]O. L. de Lange and J. Pierrus, *Solved Problems in Classical Mechanics* (Oxford U. P., Oxford, 2010).
[26]M. Hénon, Ann. Astrophys. **22**, 491 (1959).
[27]M. Hénon, "A family of periodic solutions of the planar three-body problem, and their stability," Celest. Mech. **13**, 267–285 (1976).
[28]Edward John Routh, *Dynamics of a System of Rigid Bodies*, 6th ed. (MacMillan and Co., London, 1905).
[29]L. A. Pars, *Analytical Dynamics* (Heinemann, London, 1965), Chap. XXIX.
[30]See Problem 2.19 in Ref. 3 (the original authors of this problem were not cited). Only references to textbooks can be found in Ref. 3, though many of the problems contained therein had been research ones at some point in time.
[31]S. R. Coleman, "Dilatations," in *Aspects of Symmetry* (Cambridge U. P., Cambridge, 1985), pp. 67–98.

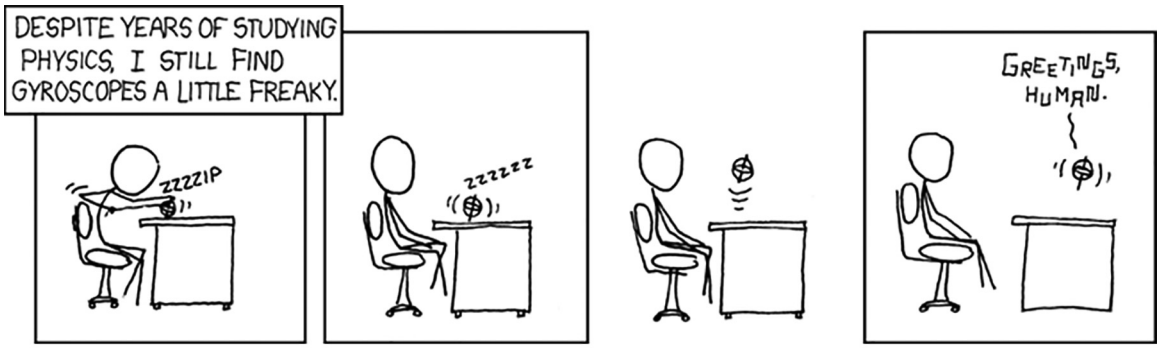

We didn't actually land on the moon — it just looked like we did because of precession. Also, gyroscopes caused 9/11. (Source: https://xkcd.com/332/)

18 February 2026 10:25:56